



Power and Energy Series 69



# The Lightning Flash

2nd Edition

Edited by Vernon Cooray

# **The Lightning Flash**

## Other volumes in this series:

- Volume 1 **Power circuit breaker theory and design** C.H. Flurscheim (Editor)  
Volume 4 **Industrial microwave heating** A.C. Metaxas and R.J. Meredith  
Volume 7 **Insulators for high voltages** J.S.T. Looms  
Volume 8 **Variable frequency AC motor drive systems** D. Finney  
Volume 10 **SF<sub>6</sub> switchgear** H.M. Ryan and G.R. Jones  
Volume 11 **Conduction and induction heating** E.J. Davies  
Volume 13 **Statistical techniques for high voltage engineering** W. Hauschild and W. Mosch  
Volume 14 **Uninterruptible power supplies** J. Platts and J.D. St Aubyn (Editors)  
Volume 15 **Digital protection for power systems** A.T. Johns and S.K. Salman  
Volume 16 **Electricity economics and planning** T.W. Berrie  
Volume 18 **Vacuum switchgear** A. Greenwood  
Volume 19 **Electrical safety: a guide to causes and prevention of hazards** J. Maxwell Adams  
Volume 21 **Electricity distribution network design, 2nd edition** E. Lakervi and E.J. Holmes  
Volume 22 **Artificial intelligence techniques in power systems** K. Warwick, A.O. Ekwue and R. Aggarwal (Editors)  
Volume 24 **Power system commissioning and maintenance practice** K. Harker  
Volume 25 **Engineers' handbook of industrial microwave heating** R.J. Meredith  
Volume 26 **Small electric motors** H. Moczala *et al.*  
Volume 27 **AC-DC power system analysis** J. Arrillaga and B.C. Smith  
Volume 29 **High voltage direct current transmission, 2nd edition** J. Arrillaga  
Volume 30 **Flexible AC transmission systems (FACTS)** Y-H. Song (Editor)  
Volume 31 **Embedded generation** N. Jenkins *et al.*  
Volume 33 **Overvoltage protection of low-voltage systems, revised edition** P. Hasse  
Volume 36 **Voltage quality in electrical power systems** J. Schlabbach *et al.*  
Volume 37 **Electrical steels for rotating machines** P. Beckley  
Volume 38 **The electric car: development and future of battery, hybrid and fuel-cell cars** M. Westbrook  
Volume 39 **Power systems electromagnetic transients simulation** J. Arrillaga and N. Watson  
Volume 40 **Advances in high voltage engineering** M. Haddad and D. Warne  
Volume 41 **Electrical operation of electrostatic precipitators** K. Parker  
Volume 43 **Thermal power plant simulation and control** D. Flynn  
Volume 44 **Economic evaluation of projects in the electricity supply industry** H. Khatib  
Volume 46 **Distribution switchgear** S. Stewart  
Volume 48 **Wood pole overhead lines** B. Wareing  
Volume 49 **Electric fuses, 3rd edition** A. Wright and G. Newbery  
Volume 50 **Wind power integration: connection and system operational aspects** B. Fox *et al.*  
Volume 51 **Short circuit currents** J. Schlabbach  
Volume 52 **Nuclear power** J. Wood  
Volume 53 **Condition assessment of high voltage insulation in power system equipment** R.E. James and Q. Su  
Volume 55 **Local energy: distributed generation of heat and power** J. Wood  
Volume 56 **Condition monitoring of rotating electrical machines** P. Tavner, L. Ran, J. Penman and H. Sedding  
Volume 57 **The control techniques drives and controls handbook, 2nd edition** W. Drury (Editor)  
Volume 58 **Lightning protection** V. Cooray (Editor)  
Volume 59 **Ultracapacitor applications** J.M. Miller  
Volume 62 **Lightning electromagnetics** V. Cooray  
Volume 63 **Energy storage for power systems, 2nd edition** A. Ter-Gazarian  
Volume 65 **Protection of electricity distribution networks, 3rd edition** J. Gers  
Volume 66 **High voltage engineering testing, 3rd edition** H. Ryan (Editor)  
Volume 67 **Multicore simulation of power system transients** F. Uriate  
Volume 68 **Distribution system analysis and automation** J. Gers  
Volume 905 **Power system protection, 4 volumes**

# The Lightning Flash

2nd Edition

Edited by Vernon Cooray

The Institution of Engineering and Technology

Published by The Institution of Engineering and Technology, London, United Kingdom

The Institution of Engineering and Technology is registered as a Charity in England & Wales (no. 211014) and Scotland (no. SC038698).

© The Institution of Engineering and Technology 2003

© The Institution of Engineering and Technology 2014

First published 2003

Second edition 2014

This publication is copyright under the Berne Convention and the Universal Copyright Convention. All rights reserved. Apart from any fair dealing for the purposes of research or private study, or criticism or review, as permitted under the Copyright, Designs and Patents Act 1988, this publication may be reproduced, stored or transmitted, in any form or by any means, only with the prior permission in writing of the publishers, or in the case of reprographic reproduction in accordance with the terms of licences issued by the Copyright Licensing Agency. Enquiries concerning reproduction outside those terms should be sent to the publisher at the undermentioned address:

The Institution of Engineering and Technology  
Michael Faraday House  
Six Hills Way, Stevenage  
Herts, SG1 2AY, United Kingdom

[www.theiet.org](http://www.theiet.org)

While the author and publisher believe that the information and guidance given in this work are correct, all parties must rely upon their own skill and judgement when making use of them. Neither the author nor publisher assumes any liability to anyone for any loss or damage caused by any error or omission in the work, whether such an error or omission is the result of negligence or any other cause. Any and all such liability is disclaimed.

The moral rights of the author to be identified as author of this work have been asserted by him in accordance with the Copyright, Designs and Patents Act 1988.

#### **British Library Cataloguing in Publication Data**

A catalogue record for this product is available from the British Library

**ISBN 978-1-84919-691-8 (hardback)**

**ISBN 978-1-84919-692-5 (PDF)**

Typeset in India by MPS Limited

Printed in the UK by CPI Group (UK) Ltd, Croydon

---

# Contents

---

<b>Preface to the first edition</b>	<b>xviii</b>
<b>Preface to the second edition</b>	<b>xix</b>
<b>Contributors</b>	<b>xx</b>
<b>Biographies of contributors</b>	<b>xxi</b>
<b>1 Charge structure and geographical variation of thunderclouds</b>	<b>1</b>
<i>Earle Williams</i>	
1.1 The formation of clouds	1
1.2 Local conditions necessary for thunderclouds	1
1.3 The gross charge structure of thunderclouds	2
1.4 Sprite-producing thunderclouds: mesoscale convective systems	4
1.5 Geographical variability of thunderclouds	6
1.5.1 Environmental controls	6
1.5.2 Tropical thunderstorms	8
1.5.3 Midlatitude thunderstorms	10
1.5.4 Winter thunderstorms	11
References	11
<b>2 Thunderstorm electrification mechanisms</b>	<b>15</b>
<i>Rohan Jayaratne</i>	
2.1 Introduction	15
2.2 The suggested mechanisms	16
2.2.1 The inductive mechanism	16
2.2.2 The convective mechanism	19
2.2.3 The selective ion capture theory	20
2.2.4 Drop breakup theory	20
2.2.5 Melting of ice	21
2.2.6 The Workman–Reynolds effect	21
2.2.7 The thermoelectric effect	22
2.2.8 Surface potential theories	22
2.2.9 The quasi-liquid layer theory	25
2.2.10 Charging due to the fragmentation of ice	28
2.3 Riming experiments	29
2.4 Droplet size effect	31
2.5 Effect of chemical impurities	34
References	35
<b>3 Mechanism of electrical discharges</b>	<b>41</b>
<i>Vernon Cooray</i>	
3.1 Introduction	41

3.2	Basic definitions	41
3.2.1	Mean free path and cross section	41
3.2.2	Drift velocity and mobility	42
3.2.3	Thermal equilibrium and local thermal equilibrium	43
3.3	Ionisation processes	45
3.3.1	Ionisation due to electron impact	45
3.3.2	Photoionisation	48
3.3.3	Thermal ionisation	48
3.3.4	Ionisation caused by meta-stable excited atoms	50
3.3.5	Ionisation due to positive ions	51
3.4	De-ionisation processes	51
3.4.1	Electron–ion recombination	51
3.5	Other processes that can influence the process of ionisation	52
3.5.1	Electron attachment and detachment	52
3.5.2	Excitation of molecular vibrations	54
3.5.3	Diffusion	55
3.6	Cathode processes	56
3.6.1	Photoelectric emission	58
3.6.2	Thermionic emission	58
3.6.3	Schottky effect	58
3.6.4	Field emission	59
3.6.5	Incidence of positive ions	59
3.7	Electrical breakdown	60
3.7.1	Electron avalanche	61
3.7.2	The space charge electric field due to an avalanche	63
3.7.3	Formation of a streamer	64
3.7.4	Characteristics of the streamers	69
3.7.5	Streamer to spark transition and thermalisation	74
3.7.6	Electrical breakdown criterion in the presence of streamer discharges	76
3.8	Electrical breakdown in very small gaps: Townsend's breakdown mechanism	78
3.8.1	Townsend's experiment	78
3.8.2	Townsend's theory of electrical breakdown	79
3.9	Paschen's law	85
3.9.1	Physical interpretation of the shape of the Paschen curve	86
3.9.2	Validity of Paschen's law	87
3.10	Voltage and current (V–I) characteristics and the post breakdown stage (low pressures)	87
3.10.1	The glow discharge	88
3.10.2	Abnormal glow	90
3.10.3	The glow to arc transition	91
3.11	Resistance of spark channels	93
3.12	Corona discharges	94
3.12.1	Negative corona modes	95
3.12.2	Positive corona modes	97
3.12.3	Electrical breakdown and corona	99

3.13	Dependence of electrical breakdown conditions on atmospheric conditions	99
3.14	Statistical nature of electrical breakdown	101
3.14.1	Electrical breakdown under the application of impulse voltages	102
3.14.2	Statistical nature of the electrical breakdown	103
3.15	The long spark	103
3.15.1	Streamer to leader transition and the initiation of the leader	103
3.15.2	General characteristics of impulse breakdown in rod-plane gaps	104
3.15.3	Some features of mathematical modelling of positive leader discharges	111
3.16	Humidity effects	114
3.16.1	Critical electric field necessary for streamer propagation	114
3.16.2	Influence on the corona development at the initiation of long sparks	114
3.16.3	Influence on leader propagation	115
	References	115
<b>4</b>	<b>Mechanism of the lightning flash</b>	<b>119</b>
	<i>Vernon Cooray</i>	
4.1	Introduction	119
4.2	Ground flash	119
4.3	Cloud flash	121
4.4	Frequency of lightning discharges	123
4.4.1	Cloud to ground flash ratio	124
4.4.2	Ground flash density	124
4.4.3	Total lightning activity	125
4.5	Inception of lightning discharges in clouds	125
4.5.1	The particle interaction or classical mechanism	125
4.5.2	The runaway electron hypothesis	131
4.6	Physical processes and the electromagnetic fields of ground flashes	132
4.6.1	Preliminary breakdown process	132
4.6.2	Stepped leader	137
4.6.3	Return stroke	152
4.6.4	Continuing current	177
4.6.5	M-Components	178
4.6.6	K changes	182
4.6.7	Subsequent strokes	183
4.6.8	Dart leaders	184
4.7	Electromagnetic fields generated by cloud flashes	193
4.7.1	General features	193
4.7.2	Radiation field pulse characteristics	194
4.8	Difference between the ground flashes and cloud flashes	199
4.9	Energy dissipation in return strokes and lightning flashes and cloud potential	200
4.9.1	Potential of the cloud	202



4.10	Measuring lightning-generated electric and magnetic fields	204
4.10.1	Electric field mill or generating voltmeter	204
4.10.2	Plate or whip antenna	205
4.10.3	Crossed loop antennas to measure the magnetic field	209
4.11	Detection of lightning flashes	210
4.11.1	Lightning flash counters	211
4.11.2	Magnetic direction finding	212
4.11.3	Time of arrival technique: VLF range	212
4.11.4	Time of arrival technique: VHF range	213
4.11.5	VHF radio interferometry	214
	References	215
<b>5</b>	<b>Features of lightning flashes obtained from high-speed video recordings</b>	<b>231</b>
	<i>Marcelo M. F. Saba, Tom A. Warner and Carina Schumann</i>	
5.1	Introduction	231
5.2	Negative and positive cloud-to-ground flashes	233
5.2.1	Leaders	233
5.2.2	Return stroke	237
5.2.3	Number of return strokes per flash	238
5.2.4	Flash duration	239
5.2.5	Multigrounded lightning flashes	240
5.2.6	Interstroke time intervals	244
5.2.7	Continuing current	244
5.3	Bipolar cloud-to-ground flashes	251
5.4	Upward lightning flashes	253
5.4.1	Upward leader initiation characteristics	254
5.4.2	Upward leader characteristics	255
5.4.3	Corona brush and leader branching	258
5.4.4	Recoil leaders in upward lightning flashes	259
5.4.5	M-components, dart leaders and return strokes in upward lightning flashes	260
	References	262
<b>6</b>	<b>Rocket-and-wire triggered lightning experiments</b>	<b>267</b>
	<i>Vladimir A. Rakov</i>	
6.1	Introduction	267
6.2	Triggering techniques	269
6.2.1	Classical triggering	269
6.2.2	Altitude triggering	272
6.2.3	Triggering facility at Camp Blanding, Florida	274
6.3	Overall current waveforms	276
6.3.1	Classical triggering	276
6.3.2	Altitude triggering	278
6.4	Parameters of return-stroke current waveforms	279
6.5	Return-stroke current peak versus grounding conditions	289
6.6	Characterization of the close lightning electromagnetic environment	295

6.7	Studies of interaction of lightning with various objects and systems	296
6.7.1	Overhead power distribution lines	297
6.7.2	Underground cables	308
6.7.3	Power transmission lines	309
6.7.4	Residential building	309
6.7.5	Airport runway lighting system	311
6.7.6	Miscellaneous experiments	313
6.8	Concluding remarks	314
	Acknowledgment	314
	References	314
<b>7</b>	<b>Tower initiated lightning discharges</b>	<b>325</b>
	<i>Gerhard Diendorfer</i>	
7.1	Introduction	325
7.2	Concept of effective height of tall objects	326
7.3	Initiation of upward lightning	330
7.4	Seasonal occurrence of upward lightning	331
7.5	General characterization of upward negative lightning	332
7.6	Characteristics of impulsive current components in negative upward lightning	336
7.6.1	Parameters of ICC pulses	336
7.6.2	Parameters of return strokes following the ICC	337
7.7	Characteristics of upward positive lightning	339
7.8	Characteristics of upward bipolar lightning	341
7.9	Detection of upward lightning	343
7.10	Summary	343
	References	344
<b>8</b>	<b>Computation of electromagnetic fields from lightning discharge</b>	<b>351</b>
	<i>Rajeev Thottappillil</i>	
8.1	Electrostatics and magnetostatics	351
8.1.1	Electrostatic field from a dipole	351
8.1.2	Magnetostatic field from a line current	352
8.1.3	Electrostatic and magnetostatic fields from a semi-infinite vertical thin-wire antenna above a conducting plane	354
8.2	Time varying fields from lightning	357
8.2.1	Introduction	357
8.3	Treatment of retardation effects	359
8.4	Fields in terms of current (the Lorentz condition approach)	361
8.4.1	Magnetic field	364
8.4.2	Image channel	364
8.4.3	Fields at ground level	364
8.5	Fields in terms of current and charge (the continuity equation approach)	365
8.5.1	Image channel	368
8.5.2	Fields at ground level	368
8.6	Non-uniqueness of electrostatic, induction, and radiation field components	369
8.7	The continuity equation	371

8.8	Fields in terms of apparent charge distribution	374
8.8.1	Theory	374
8.8.2	Return stroke electric and magnetic fields	377
8.8.3	Magnetic field	381
8.8.4	Image channel	382
8.8.5	Leader electric fields	383
8.9	Calculation of fields from lightning return stroke	385
8.9.1	Numerical calculation of fields at different elevations and distances from the lightning return stroke	387
8.9.2	Electric fields	387
8.9.3	Magnetic fields	392
8.10	Transmission line model of the return stroke	398
8.10.1	Pulse propagation on a vertical wire antenna above a conducting plane: exact formulation	399
8.10.2	Pulse propagation along a vertical lightning channel above conducting ground at certain speed $v$ : exact expressions using electromagnetic fields of accelerating charges	401
	References	401

**9 Return stroke models with special attention to engineering applications** **405**

*Vernon Cooray*

9.1	Introduction	405
9.2	Modelling of return strokes	405
9.3	Electro-thermodynamic models	407
9.4	Transmission line or LCR models	410
9.5	Electromagnetic models	419
9.6	Engineering models	420
9.6.1	Current propagation models (CP models)	420
9.6.2	Current generation models (CG models)	425
9.6.3	CG models in practice	431
9.6.4	Inadequacy of the CG models used in practice to represent first return strokes	440
9.6.5	A CG model to represent first return strokes	441
9.7	Current dissipation models (CD models)	452
9.7.1	General description	452
9.7.2	Mathematical background	455
9.7.3	Current dissipation concept in practice – introducing current reflection from ground level into return stroke models	456
9.8	Generalisation of any model to current generation type	459
9.9	Generalisation of any model to a current dissipation type model	460
9.10	Current propagation models as a special case of current dissipation models	461
9.11	Advantage of utilising current dissipation concept in constructing models in comparison to current propagation concept	462
9.12	Introducing ground conductivity in CG type return stroke models	463
9.12.1	Model predictions	464

9.13 Linear charge density deposited by the first return stroke along the leader channel	468
9.14 Future of return stroke models	470
References	470
<b>10 Return stroke speed models</b>	<b>477</b>
<i>Vernon Cooray</i>	
10.1 Introduction	477
10.2 Subsequent return stroke speed profile as predicted by current generation type engineering return stroke models	477
10.3 Return stroke speed as predicted by models taking into consideration the processes taking place at the return stroke front	480
10.3.1 Lundholm and Wagner	480
10.3.2 Rai	481
10.3.3 Cooray – first model	482
10.3.4 Cooray – second model	490
References	497
<b>11 On the various approximations to calculate lightning return stroke-generated electric and magnetic fields over finitely conducting ground</b>	<b>499</b>
<i>Vernon Cooray</i>	
11.1 Introduction	499
11.2 Exact expressions for the electromagnetic fields of a dipole located over finitely conducting ground and their extension to return stroke fields	500
11.2.1 Exact expressions for the vector potential of a dipole over finitely conducting ground	500
11.2.2 The exact expressions for the electromagnetic fields of a dipole over finitely conducting ground	501
11.2.3 Electromagnetic fields of return strokes	503
11.3 Return stroke models utilised in testing the approximate expressions	504
11.4 Summary of exact propagation effects in the vicinity of the channel	505
11.5 Simplified procedures to calculate electric and magnetic fields over finitely conducting ground	508
11.5.1 Norton's and Bannister's approximations	508
11.5.2 Simplified expressions to calculate vertical electric field and horizontal magnetic field over finitely conducting ground	512
11.5.3 Propagation effects on radiation fields of the first return strokes of negative and positive lightning flashes	517
11.5.4 The reason why propagation effects vary with the shape of the radiation field	521
11.5.5 The effect of propagation on electromagnetic fields generated by cloud flashes	523

11.5.6	Simplified expressions to calculate the horizontal electric field	526
11.5.7	Barbosa and Paulino expression to calculate the horizontal electric field	529
11.5.8	Approximate time domain expressions to calculate underground electric fields	532
11.6	Propagation over vertically stratified ground or multi-section path	540
11.6.1	Expressions for the attenuation function for a dipole at ground level	540
11.6.2	Simplified expression for the electromagnetic fields from lightning over vertically stratified ground	542
11.6.3	Some interesting effects of vertically stratified ground on radiation fields	542
11.7	Propagation effects over horizontally stratified ground	547
11.7.1	Wait's simplified expressions for the attenuation function for a dipole at ground level	547
11.7.2	Simplified expression for the electromagnetic fields from lightning over vertically stratified ground	548
11.7.3	Some interesting effects of horizontally stratified ground on radiation fields	548
11.8	Future studies	555
	References	556
<b>12</b>	<b>Interaction of electromagnetic fields generated by lightning with overhead electrical networks</b>	<b>559</b>
	<i>Carlo Alberto Nucci and Farhad Rachidi</i>	
12.1	Introduction	559
12.2	Field-to-transmission line coupling models	560
12.2.1	Use of the transmission line theory	560
12.2.2	Case of single-wire line above a perfectly conducting ground	561
12.2.3	Agrawal et al. model	561
12.2.4	Taylor, Satterwhite, and Harrison model	563
12.2.5	Rachidi model	563
12.2.6	Contribution of the different components of the electromagnetic field in the coupling mechanism	564
12.2.7	Other models	565
12.2.8	Inclusion of losses	567
12.2.9	Discussion on the relative importance of different transmission line parameters when calculating lightning-induced voltages	569
12.2.10	Case of multiconductor lines	571
12.2.11	Time-domain representation of coupling equations	573
12.2.12	Experimental validation of the field-to-transmission line coupling models	575

12.3	Lightning-induced voltages on overhead power lines	578
12.3.1	Return stroke current model, computation of the incident electromagnetic field, and coupling model	578
12.3.2	Mechanism of voltage induction by a nearby lightning return stroke on an overhead line	579
12.3.3	Preliminary remarks on the influence of the ground resistivity on the induced voltages	581
12.3.4	Sensitivity analysis and discussion	584
12.3.5	Influence of additional factors (downward leader, corona, channel inclination and tortuosity)	595
12.3.6	Application to realistic cases: use of the LIOV–EMTP	598
	References	601
<b>13</b>	<b>Principles of protection of structures against lightning</b>	<b>611</b>
	<i>Carlo Mazzetti</i>	
13.1	Parameters of lightning current	611
13.2	Classification of structures	612
13.3	Damage due to lightning	613
13.3.1	Effects of lightning	613
13.3.2	Causes and types of damage	613
13.3.3	Types of loss	614
13.4	Risk	615
13.4.1	Number of flashes	615
13.4.2	Probability of damage	616
13.4.3	Amount of loss	617
13.4.4	Risk components	617
13.4.5	Tolerable value of risk	618
13.5	Basic criteria of protection	619
13.5.1	Protection of structures against physical damages and life hazard	619
13.5.2	Protection of electrical and electronic systems within the structure against lightning electromagnetic impulse (LEMP)	621
13.5.3	Protection of services entering the structure	623
13.6	Protection by means of SPD	623
13.7	Main features of lightning protection system (LPS)	624
13.7.1	External lightning protection system	624
13.7.2	Positioning of the air termination system	624
13.7.3	Down conductor systems	627
13.7.4	Protection measures against touch and step voltages	628
13.7.5	Earth termination system	628
13.7.6	Materials and dimensions	634
13.8	Internal lightning protection system	634
13.8.1	General	634
13.8.2	Lightning equipotential bonding	635
13.8.3	Electrical insulation of the external LPS	636
13.9	Shielding	636

13.10	Maintenance and inspection of LPS	636
13.11	Annex A: parameters of lightning current	637
13.11.1	Lightning flashes to earth	637
13.11.2	Lightning current parameters	638
13.11.3	Maximum lightning current parameters used for dimensioning lightning protection systems	639
13.11.4	Minimum lightning current parameters used for interception efficiency of air terminals	643
13.12	Annex B: models for the evaluation of lightning exposure of structures and interception probability of air terminals	643
13.12.1	Electrogeometric model	643
13.12.2	Improved electrogeometric model	645
13.12.3	Generalised leader inception model	646
13.12.4	Leader progression model	646
	References	646
<b>14</b>	<b>Attachment of lightning flashes to grounded structures</b>	<b>649</b>
	<i>Vernon Cooray</i>	
14.1	Introduction	649
14.2	Striking distance	650
14.3	Leader inception models	652
14.3.1	Critical radius and critical streamer length concepts	652
14.3.2	Rizk's generalized leader inception equation	653
14.3.3	Lalande's stabilization field equation	654
14.3.4	Leader inception model of Becerra and Cooray (SLIM)	654
14.4	Leader progression or lightning attachment models	655
14.4.1	Recent developments	657
14.5	The potential of the stepped leader channel and the striking distance	657
14.6	Charge distribution on the stepped leader channel as a function of cloud potential	660
14.7	Striking distance of subsequent return strokes	661
14.8	The effect of the height of the structure	662
14.8.1	Variation of striking distance with height	663
14.8.2	Variation of attractive radii with distance	664
14.9	Comparison of different lightning attachment models	666
14.9.1	Comparison of attractive radii calculated using EGM and SLIM with CVM	666
14.9.2	Comparison of the predictions of SLIM with the predictions of other lightning attachment models	670
14.10	Experimental test of lightning attachment models	670
14.11	Lightning strikes to the side of the structure	675
	References	675
<b>15</b>	<b>Lightning and EMC</b>	<b>679</b>
	<i>Michel Ianoz</i>	
15.1	Introduction	679
15.2	Short overview of EMC history	679

15.3	Lightning as a disturbance source	680
15.4	Types of coupling between lightning and circuits or installations	682
15.4.1	Coupling modes	682
15.4.2	Effects due to conductive coupling	683
15.4.3	Calculation of the average number of lightning strokes per year on an overhead line	683
15.4.4	Effects due to electromagnetic field coupling	684
15.5	Typical EMC problems due to lightning	687
15.5.1	Lightning effects in power networks	687
15.5.2	Lightning effects on power network substation equipment	689
15.5.3	Lightning effects on telecommunication networks	690
15.5.4	Lightning effects on low-voltage power networks	690
15.5.5	Lightning effects on aircraft	691
15.6	Specific EMC lightning protection parameters	693
15.6.1	General	693
15.6.2	Peak current	694
15.6.3	Peak current derivative	694
15.6.4	Peak rate of change of voltage	695
15.6.5	Total charge	695
15.6.6	The action integral: $\int i^2 \times dt$	695
15.6.7	Time to half value of the current	695
15.6.8	Conclusions on LEMP and fast transients protection comparison	696
15.7	Specific EMC lightning protection concepts	696
15.7.1	General EMC protection concepts	696
15.7.2	Suppressors	697
15.7.3	Shielded cages	698
	References	698
<b>16</b>	<b>Electrical aspects of lightning strikes to humans</b>	<b>701</b>
	<i>Chris Andrews</i>	
16.1	Introduction	701
16.2	Strike mechanisms – descriptive outline	701
16.2.1	Direct strike	702
16.2.2	Contact potential and side flash	702
16.2.3	Earth potential rise	703
16.2.4	Aborted upward streamer	703
16.2.5	Other classifications	704
16.3	Current behaviour in biological material	705
16.4	Models for lightning shock current estimates	706
16.4.1	Body model	706
16.4.2	Factors for modelling	708
16.5	Current estimates	708
16.5.1	Direct strike including side flash and contact potential	708
16.5.2	EPR mediated shock	713
16.5.3	Aborted upward streamer	714
16.5.4	Telephone mediated strike	716



16.6	Experimental support	720
16.7	Conclusion	721
	Acknowledgement	721
	References	721
<b>17</b>	<b>Upper atmospheric electrical discharges</b>	<b>725</b>
	<i>Ningyu Liu</i>	
17.1	Introduction	725
17.2	General phenomenology	727
	17.2.1 Jets and gigantic jets	727
	17.2.2 Sprites	737
	17.2.3 Elves	751
17.3	Elementary discharge processes	753
	17.3.1 Similarity laws	754
	17.3.2 Electron density growth at subbreakdown condition at high altitudes	755
17.4	Modeling sprites and sprite streamers	757
	17.4.1 Introduction	757
	17.4.2 Large-scale modeling of sprites/sprite halos	759
	17.4.3 Modeling of sprite streamers	763
	Acknowledgments	771
	References	771
<b>18</b>	<b>Energetic radiation from thunderstorms and lightning</b>	<b>787</b>
	<i>Joseph R. Dwyer and Hamid K. Rassoul</i>	
18.1	Introduction	787
18.2	Observations	788
	18.2.1 X-rays from lightning	788
	18.2.2 Gamma-ray flashes from thunderstorms	793
18.3	Discharges in air	795
18.4	Propagating electrons	796
18.5	Avalanche multiplication	798
18.6	Feedback mechanisms	801
18.7	Streamers	803
18.8	Development of hot channels	805
18.9	High-energy versus low-energy discharges	806
18.10	Modeling	807
18.11	Dark lightning	809
18.12	Future work	811
	Acknowledgments	811
	References	811
<b>19</b>	<b>Global lightning nitrogen oxides production</b>	<b>819</b>
	<i>William Koshak</i>	
19.1	The importance of lightning nitrogen oxides	819
19.2	Estimating global annual LNO <sub>x</sub> production	821
	19.2.1 Flash extrapolation method	821
	19.2.2 Thunderstorm extrapolation method	825
	19.2.3 Global model fit method	825

19.3	Observations and inferences of LNO <sub>x</sub>	825
19.3.1	Early examinations of thunderstorm rainwater	826
19.3.2	Clarifying observations	826
19.3.3	Some field campaigns	827
19.4	The Lightning Nitrogen Oxides Model (LNOM)	831
19.4.1	Motivations	832
19.4.2	Functionality	834
19.4.3	Data products	836
19.4.4	Data archive	837
19.4.5	Future evolution	841
19.5	Benefits of satellite observations	842
19.5.1	Two early studies employing photometers	842
19.5.2	Space-based lightning mappers	842
19.5.3	Top-down constraints on LNO <sub>x</sub>	844
19.5.4	Discriminating flash type from space	846
	References	850
<b>20</b>	<b>Lightning and global temperature change</b>	<b>861</b>
	<i>Colin Price</i>	
20.1	Introduction	861
20.2	Global distribution of thunderstorms	861
20.3	Microphysics and dynamics of thunderstorms	864
20.4	Temperature and lightning	865
20.4.1	Diurnal variations	865
20.4.2	Semi-annual variations	867
20.4.3	Annual variations	869
20.4.4	ENSO variations	869
20.4.5	Inter-annual variations	871
20.4.6	Future predictions	872
20.5	Conclusions and discussion	875
	References	875
	<b>Index</b>	<b>879</b>

---

## **Preface to the first edition**

---

Lightning research is an interdisciplinary subject where the needs of various branches of engineering and physics converge.

For power engineers, the mechanism of the lightning flash and the characteristics of electromagnetic fields generated by lightning are vital for the design of protection measures in power lines. For the electromagnetic specialists, lightning is a long radio antenna that generates a broadband electromagnetic signal, which can be utilised to characterise the effects of the propagation path on electromagnetic fields. For the telecommunication engineer, an understanding of the interaction of these fields with overhead and underground wires is of importance in protecting electrical instruments connected to overhead power lines and underground cables from induced overvoltages. For the high voltage engineer, lightning is a current and voltage generator that disrupts various components located on high voltage power lines. For the physicists, lightning is a laboratory in which one can test the fundamentals of discharge physics. Thus the researchers and students who seek information about lightning come from different backgrounds and disciplines and require tailor-made information. I hope this book will help diffuse knowledge across such boundaries.

The topics of the chapters in this book are based on a graduate course given to the engineering students at Uppsala University. I also hope that this book may serve as a text in graduate courses on lightning, given to power engineering students.

---

## **Preface to the second edition**

---

It gives me great pleasure to introduce the second edition of the lightning flash. The second edition is significantly expanded by the addition of nine new chapters on various subjects related to lightning including triggered lightning, high-speed video observations, nitrogen oxide production, energetic radiation emissions, upper atmospheric electrical discharges, lightning attachment and influence of lightning on climate. All but four chapters of the previous edition have been modified to include the latest research work on the subject. I hope that the lightning research community will find this edition of the book to be both educational and instrumental in tackling new challenges in lightning research.

Vernon Cooray  
29 November 2013

---

## Contributors

---

Dr. Chris Andrews	Family Practitioner (GP), Queensland, Australia Senior Lecturer, School of Medicine, University of Queensland, Australia
Professor Vernon Cooray	Uppsala University, Uppsala, Sweden
Dr. Gerhard Diendorfer	Austrian Electrotechnical Association (OVE), Vienna, Austria
Professor Joseph R. Dwyer	Florida Institute of Technology, Melbourne, Florida, USA
Dr. Rohan Jayaratne	International Laboratory for Air Quality and Health, Queensland University of Technology, Brisbane, Australia
Professor Michel Ianoz	Swiss Federal Institute of Technology, Lausanne, Switzerland
Dr. William Koshak	NASA George C. Marshall Space Flight Center (MSFC), Huntsville, Alabama, USA
Professor Carlo Mazzetti	University of Roma 'La Sapienza', Rome, Italy
Dr. Ningyu Liu	Florida Institute of Technology, Melbourne, Florida, USA
Professor Carlo Alberto Nucci	University of Bologna, Bologna, Italy
Professor Colin Price	Tel Aviv University, Israel
Professor Farhad Rachidi	Swiss Federal Institute of Technology, Lausanne, Switzerland
Professor Vladimir A. Rakov	University of Florida, Gainesville, USA
Professor Hamid K. Rassoul	Florida Institute of Technology, Melbourne, Florida, USA
Professor Marcelo M. F. Saba	National Institute for Space Research, INPE, Brazil
Ms. Carina Schumann	National Institute for Space Research, INPE, Brazil
Professor Rajeev Thottappillil	KTH Royal Institute of Technology, Stockholm, Sweden
Mr. Tom A Warner	ZT-Research, Rapid City, South Dakota, US
Dr. Earle Williams	Lincoln Laboratory, MIT, Massachusetts, USA

---

## Biographies of contributors

---



**Chris Andrews** graduated with honours in Electrical Engineering in 1973, and then Master of Engineering Science, and Diploma in Computer Science, in 1976. After this, he studied Medicine, and graduated MBBS with honours in 1982. He now practices medicine in daily life as a Family Practitioner.

Chris received the PhD degree in the area of Lightning and Electrical Injuries, with a special interest in Telephone-Related Injuries. He is internationally regarded in the area of Lightning and Electrical Injuries. Chris is a regular Medico-Legal Expert having examined some hundreds of cases on five continents.

He has contributed one major joint-edited text, and personal or joint authorship of 11 book chapters and updates, and 46 papers, letters, and conference presentations to the literature. He is an invited member of MT4 of IEC TC64 which examines the effects of electric current on the human body. He has been awarded the Kitagawa Medal for his contributions to the area of keraunomedicine.



**Vernon Cooray** received the PhD degree in Electricity with special attention to Electrical Transients and Electrical Discharges from Uppsala University, Sweden, in 1982. In the year 2000, he was promoted to the rank of Full Professor in Electricity with special attention to Transients and Electrical Discharges at the division for electricity of Uppsala University. From 2000 to 2002 he was the Head of the Division for Electricity in the Department of Engineering Sciences.

Vernon Cooray has authored and co-authored more than 400 scientific papers and 22 book chapters on Physics of Lightning and Electrical Discharges, Lightning Interaction and Electromagnetic Compatibility. He is the editor of three books, *The Lightning Flash*, published by IEE (London) in 2003, *Lightning Protection* published by IET (London) in 2009 and *Lightning Electromagnetics* published by IET (London) in 2012. His latest book, *An Introduction to Lightning*, will be published by Springer in 2014. Vernon Cooray was a guest editor of two issues of *Atmospheric Research* and two issues of the *Journal of Electrostatics*. He was the recipient of the prestigious *Berger Award* from the scientific committee of the International Conference on Lightning Protection (ICLP) in 2012.



**Gerhard Diendorfer** was born in Austria in 1957. He received the Diploma and PhD degrees in electrical engineering from the Vienna University of Technology, Vienna, Austria, in 1982 and 1987, respectively.

During 1982–1990, he was a Research Assistant at the Vienna University of Technology, where he was engaged in the field of Electromagnetic Coupling of Lightning-Radiated Electromagnetic Fields to Power Lines. During 1988–1989, he was at the Lightning Research Laboratory at University of Florida, Gainesville, working on Return Stroke Modelling. Since then he

has focused primarily on the performance of lightning location systems and measurements of lightning on an instrumented tower. He is currently the Head of the Austrian Lightning Detection and Information System. He is a member of IEEE, AGU, and the Austrian National Committee on Lightning Protection. He is a member of several CIGRE working groups and received the CIGRE Technical Committee Award in 2008.



**Joseph R. Dwyer** received his PhD from the University of Chicago in 1994 and worked as a Research Scientist at Columbia University and the University of Maryland before joining the faculty at the Florida Institute of Technology in 2000. His research interests are primarily in the field of High-Energy Atmospheric Physics, which includes terrestrial Gamma-ray flashes (TGFs) and the X-ray/Gamma-ray emissions from thunderstorms and lightning. He is currently Department Head and Professor of Physics and Space Sciences at Florida Tech.



**Michel Ianoz** (SM'86–F'96–LM'11) received the BS degree from the Politechnic Institute of Bucarest, Romania in 1958 and the PhD degree from the Moscow State University, Moscow, Russia, in 1968.

He taught Electromagnetic Compatibility (EMC) as a Professor at the Swiss Federal Institute of Technology of Lausanne, Lausanne, Switzerland, until 2001, where he is now an Honorary (Emeritus) Professor. He is a Consultant Professor at the North China Electric Power University and Doctor Honoris Causa of the Technical University of Saint-Petersburg, Petersburg, Russia. He is the co-author of two books and about 165 scientific papers (more than 60 in referenced journals). His research interests include Calculation of Electromagnetic Fields, Transient Phenomena, Lightning, and EMP Effects on Power and Telecommunication Networks.

He was a Chairman of the Subcommittee 77B (HF phenomena) of the IEC (1997–2006), an Associate Editor of the *IEEE Transactions on Electromagnetic Compatibility* (1997–2002) and the Distinguished Lecturer of the EMC-S in 2003–2004.



**Rohan Jayaratne** obtained his PhD in Atmospheric Physics from the University of Manchester (UMIST) in 1981. He has published widely in the areas of Thunderstorm Electricity, Lightning and Air Quality. He has worked on four different continents. Having obtained an Honours Degree (First Class) in Physics from the University of Colombo, Sri Lanka, in 1976, he worked there as a Lecturer in Physics until 1984. After a further short stint in Thunderstorm Electrification Research at UMIST, he took up an academic position at the Department of Physics at the University of Botswana in 1986. While there, he was appointed Associate Professor in Physics in 1995. Having moved to Australia in 2000, he is presently a Research Scientist at the International Laboratory for Air Quality and Health at the Queensland University of Technology in Brisbane. Dr Jayaratne served as an elected member of the International Commission of Atmospheric Electricity from 1992 to 2000.



**William Koshak** is an Atmospheric Physicist at the NASA George C. Marshall Space Flight Center (MSFC) in Huntsville, Alabama. He has over 60 published articles, papers, and technical reports in his specialty discipline of lightning research. In the past approximately 24 years with NASA, his research has included a broad range of topics including Remote Sensing of Lightning, Mathematical Inversion Theory and Applications, Lightning Nitrogen Oxides Production, Lightning Radiative Transfer in Optically Thick Thundercloud Scattering Media, the Retrieval of Charges Deposited by Lightning, Space-Based Lightning Flash-Typing, the Impact of Lightning on Air Quality, Aircraft Electric Field Mill Calibration, Lightning/Climate Relations, Lightning Location Retrieval, and Space Sensor Calibration/Validation. Dr Koshak is a recognized leader in the development of algorithms for retrieving the physical characteristics of lightning and thunderstorms.



**Ningyu Liu** is an Associate Professor in the Department of Physics and Space Sciences at Florida Institute of Technology. He received the BS and MS degrees from Zhejiang University in China, and the PhD degree from The Pennsylvania State University in the United States. His research interests include Atmospheric Electricity, Plasma Discharges, Applied Electromagnetics, Numerical Analysis, and High-Performance Computing. He is a member of American Geophysical Union, IEEE and US Commissions G and H of International Union of Radio Science.





**Carlo Mazzetti di Pietralata**, born in Rome on 5 May 1943, is Full Professor of ‘High Voltage Technique’ at University of Roma ‘La Sapienza’ since 1986. From the academic year 2004–2005 he has also the charge of teaching the course on ‘Electrical Systems for Energy’. From 1986 to 1989 he was Director of Electrical Engineering Department of the same University. Since 1981 he takes part in the activities of CT 81 (Lightning Protection) of CLC and IEC as Convener of two Working Groups. From 1996 to 2008 he was President of the International Conference on Lightning Protection (ICLP). He is responsible

for two Agreements of Cooperation between the University of Roma ‘La Sapienza’ and the Warsaw University of Technology and the University of Piura (Perù).

Since several years he acts as Referee of important international journals. He was Associate-Guest Editor of Special Issue on ‘Dielectric Liquids’ of IEEE – Dielectric and Electrical Insulation Society published in the *IEEE – DEIS Transactions on* in 1988 and of Special Issue on ‘Lightning’ of IEEE – Electromagnetic Compatibility Society published in the *IEEE – EMC Transactions on* in 1988.

Prof. Mazzetti has been responsible of several research projects of University of Roma ‘La Sapienza’ and supported by important electrical industries and utilities. He is the author and co-author of several scientific publications on the following subjects: High Voltage Impulse Generators, Partial Discharge Tests on Fluids and Electrical HV Components (Cables, Bushings), Assessment of Risk due to Lightning, Modelling and Computation of Overvoltages Induced by Lightning on Power and Telecommunication Lines.



**Carlo Alberto Nucci** is Full Professor and Head of the Power Systems Laboratory of the Department of Electrical, Electronic and Information Engineering ‘Guglielmo Marconi’ of the University of Bologna. He is the author or co-author of over 300 scientific papers published on peer-reviewed journals or on proceedings of international conferences, of five book chapters edited by IEE (two), Kluwer, Rumanian Academy of Science and WIT press and of a couple of IEEE Standards and some CIGRE technical brochures. He is a Fellow of the IEEE and of the IET, and a CIGRE Honorary Member and has

received some best paper/technical international awards, including the CIGRE Technical Committee Award. From January 2006 to September 2012 he has served as Chairman of CIGRE Study Committee C4 ‘System Technical Performance’. Since January 2010 he is serving as Editor-in-Chief of the *Electric Power Systems Research* journal of Elsevier. Prof. Nucci is Doctor *Honoris Causa* of the University Politehnica of Bucharest and member of the Bologna Science Academy. Since January 2013 he serves as President of the Italian Group of University Professors of Electrical Power Systems. He also serves as Coordinator of the Working Group ‘Smart City’ of the University of Bologna.



**Colin Price** is a Full Professor in the Department of Geophysical, Atmospheric and Planetary Science at Tel Aviv University, Israel. Prof. Price grew up in South Africa, but received his BSc and MSc from Tel Aviv University in Geophysics and Atmospheric Sciences. He received his PhD from Columbia University in New York while carrying out research at NASA's Goddard Institute for Space Studies. After completing his postdoc at Lawrence Livermore National Laboratory in California, he joined the faculty of Tel Aviv University in 1995. His field of research is related to Thunderstorms, Severe Weather, and Climate Change.

Prof. Price sits on the Executive Committee of the International Commission on Atmospheric Electricity, and the International Association of Meteorology and Atmospheric Science. He has published more than 100 peer-reviewed scientific papers.



**Farhad Rachidi** (IEEE Fellow) received the MS degree in Electrical Engineering and the PhD degree from the Swiss Federal Institute of Technology, Lausanne, in 1986 and 1991 respectively. He is a Titular Professor and the Head of the EMC Laboratory at the Swiss Federal Institute of Technology, Lausanne, Switzerland.

He was the recipient of the 2005 IEEE Technical Achievement Award, the 2005 Technical Committee Award of the CIGRE and the 2006 Blondel Medal from the French Association of Electrical Engineering, Electronics, Information Technology and Communication (SEE).

He is currently the President of the International Conference on Lightning Protection (ICLP), the Editor-in-Chief of the *IEEE Transactions on Electromagnetic Compatibility*, the President of the Swiss National Committee of the International Union of Radio Science. He is the author or co-author of over 100 scientific papers published in peer-reviewed journals and over 300 papers presented at international conferences.



**Vladimir A. Rakov** received the Masters and PhD degrees in Electrical Engineering from the Tomsk Polytechnical University, Russia, in 1977 and 1983, respectively, where he was also teaching and for a number of years directed the Lightning Research Laboratory. He is currently a Professor at the Department of Electrical and Computer Engineering, University of Florida, Gainesville, and Co-Director of the International Center for Lightning Research and Testing. He is the author or co-author of 2 books, 19 book chapters, 32 patents, and over 600 other publications on various aspects of lightning, with over 220

papers being published in reviewed journals. Dr. Rakov is Co-Chairman of URSI WG E.4 'Lightning Discharges and Related Phenomena' and Convener of CIGRE WG C4.407 'Lightning Parameters for Engineering Applications'. He is a Fellow of

four major professional societies, the IEEE, the American Meteorological Society, the American Geophysical Union, and the Institution of Engineering and Technology.



**Hamid K. Rassoul**, a veteran Space Physicist, joined the Florida Institute of Technology in 1988 following a two-year research fellowship at the University of Texas and the NASA Marshall Space Flight Center in Huntsville, Alabama. His current research interests include X-ray and Gamma-ray Emissions Produced by Thunderstorms and Lightning, Initiation and Propagation of Lightning and Spark Discharges, Terrestrial Gamma-ray Flashes (TGFs), Solar Modulation of Galactic and Anomalous Cosmic Rays, Instrument Development and Space Science Education. In addition to teaching and research, Rassoul serves as Dean of Florida Tech's College of Science.



**Marcelo M. F. Saba** received a BA degree in Physics from the University of São Paulo, Brazil, in 1985, and MS and PhD degrees in Space Science from the National Institute for Space Research, INPE, in 1993 and 1997, respectively. He is a Professor at INPE, where he conducts research on the Physics of Lightning, Thundercloud Electricity, Lightning Imaging and Detection, and other topics in Atmospheric Electricity. He is the author of over 50 scientific papers in refereed journals and over 150 papers in conference proceedings. He is now studying upward flashes characteristics in Brazil and in the United States seeking to understand how upward lightning is triggered by nearby flash activity.



**Carina Schumann** received a degree in Physics from Federal University of Itajuba, Brazil, in 2010 and a Master degree in Geophysical Space Science from the National Institute for Space Research, INPE, in 2012. Her Master dissertation was about positive cloud-to-ground flashes. Since then, she is a PhD candidate in the Atmospheric Electricity Group at INPE, studying upward flashes characteristics and how upward lightning is triggered by nearby flash activity. She has been participating in international lightning data acquisition campaigns in US and Brazil during the last 4 years. During these 4 years she published 5 articles in scientific journals and more than 20 papers in international conferences.



**Rajeev Thottappillil** received PhD in Electrical Engineering from University of Florida, Gainesville, USA, in 1992. His Bachelor's degree in Electrical Engineering was from University of Calicut, India. After some years of postdoctoral research, he moved to the High Voltage Research Institute at Uppsala University, Sweden in 1995 where he became Full Professor in 2000 in the subject area Electricity with Special Emphasis on Transients and Discharges. In 2008, he moved to KTH Royal Institute of Technology where he holds the Chair in Electric Power Engineering and Design.

Prof. Thottappillil has published more than 200 scientific articles related to Lightning and Electromagnetic Compatibility. He was the Chairman of the European Science Foundation COST Action P18 'Physics of Lightning Flash and its Effects during 2005–2009'. He was a Member of the CIGRE committee WG C4.407 on Lightning Parameters for Engineering Applications.



**Tom A. Warner** received a BS degree in Atmospheric Sciences from the University of California, Davis, in 1988. He served as a United States Air Force pilot from 1989 to 1997 and then piloted the T-28 Storm Penetrating Aircraft from 2000 to 2003. He received a MS degree in Atmospheric Sciences from the South Dakota School of Mines and Technology in 2003. Since 2004, he has studied upward lightning from tall structures and is currently working collaboratively with INPE Brazil on the Upward Lightning Triggering Study (UPLIGHTS), which seeks to understand how upward lightning is triggered by nearby

flash activity. He specializes in optical observation techniques, which include high-speed camera operations. He is an author of 13 scientific papers in refereed journals.



**Earle Williams** is a Physical Meteorologist, currently dividing his time between the MIT campus and the Aviation Weather group at MIT Lincoln Laboratory. He has been engaged in research on Thunderstorm Electrification and Atmospheric Electricity for nearly 40 years. These interests have taken him to all of the predominant tropical thunderstorm regions (Africa (Niger), South America (Brazil) and the Maritime Continent (Northern Australia)) for radar field experiments. Williams is presently focused on the Earth's Schumann resonances, a naturally occurring electromagnetic phenomenon trapped

between the conductive Earth and the ionosphere, and on the use of that phenomenon for the continuous monitoring of the global lightning activity.



---

## *Chapter 1*

# **Charge structure and geographical variation of thunderclouds**

*Earle Williams*

---

### **1.1 The formation of clouds**

Clouds in the Earth's atmosphere are composed of water droplets and ice crystals. Clouds are commonly white in appearance because these liquid and solid particles are large relative to the wavelengths of visible light, and so no selective scattering occurs to colour the cloud. Owing to the abundance of cloud condensation nuclei, clouds appear whenever the air becomes locally supersaturated in water vapour. This supersaturation condition is most often achieved by a lifting process in which air parcels subsaturated with respect to water vapour cool by adiabatic expansion. The lifting process is usually caused by the heating of air near the Earth's surface, which is itself warmed by sunlight. The warmed air parcels become buoyant relative to their surroundings and rise. A second mechanism for lifting depends on the forced ascent of air by horizontal pressure gradient forces. Regardless of the lifting mechanism, the altitude at which the supersaturation condition is achieved in the rising air parcel and cloud begins to form is the lifted condensation level (LCL).

In many circumstances where clouds are frequent occurrences, the LCL is within 1000 m of the Earth's surface, and substantially lower than the altitude of the 0°C isotherm, typically 4000–5000 m above ground. As a consequence, the great majority of clouds form at temperatures above freezing and consist entirely of liquid droplets. The weight of the evidence shows that such clouds are not strongly electrified and rarely, if ever, produce lightning.

### **1.2 Local conditions necessary for thunderclouds**

Clouds in which lightning occurs – thunderclouds by definition – are the largest and most convectively vigorous in the atmosphere. Numerous observations in many geographical locations disclose that a cumulonimbus cloud must extend at least 2–3 km into the subfreezing portion of the atmosphere before the first lightning is observed. This observation is consistent with the most favoured mechanism for electrical charge separation leading to lightning: the collisions between graupel particles and ice crystals or other smaller graupel particles. The presence of such particles requires a mixed-phase condition – the simultaneous presence of water substance in all three phases: vapour, liquid and solid. Graupel particles form when supercooled liquid droplets are accreted by large ice crystals and subsequently freeze. Continual accretion can lead to graupel growth to sizes of millimetres and,

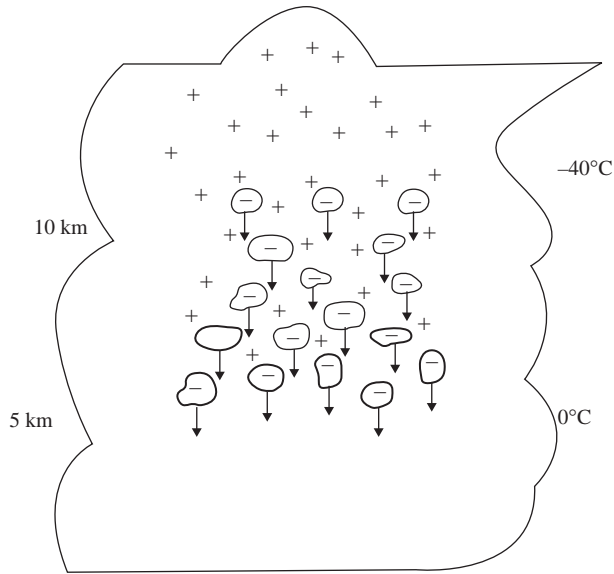


*Figure 1.1 Illustration of charge separation by particle collisions and differential motions under gravity. Negative charge is selectively transferred to larger graupel particles to create the positive thunderstorm dipole*

in extreme cases of high supercooled water concentrations, to centimetre-sized particles known as hail. Ice crystals grow at the expense of the supercooled water by the Bergeron process in a mixed-phase environment because the equilibrium vapour pressure with respect to ice is less than that with respect to liquid water. The selective transfer of negative electricity to the graupel particles in collisions with the smaller ice particles then provides for gravitational separation of oppositely charged particles until an electric field sufficient for dielectric breakdown is present and lightning develops. A more detailed discussion of the mechanisms for charge transfer during particle collisions may be found in Chapter 2. Charge separation by differential motions under gravity to form a positive dipole is illustrated in Figure 1.1.

A surprisingly wide variety of meteorological conditions are favourable for lightning – ordinary summer thunderstorms, severe (hail and tornadoes) thunderstorms, the hurricane eyewall and rainbands, winter snowstorms, oceanic convection and mesoscale convective systems. The common ingredient in all these situations is an active mixed-phase region. Deep convection without sufficient updraft and vigorous mixed-phase process does not result in lightning. The best examples are the tropical oceanic hot towers which may attain heights of 15 km or more and not produce lightning.

### **1.3 The gross charge structure of thunderclouds**

The electrostatic structure of thunderclouds was exposed over the course of the twentieth century by remote sensing methods. Two distinct methods were pioneered independently by two British scientists who for more than two decades held opposite views on the polarity of the thunderstorm dipole moment [1]. The two scientists were G.C. Simpson and C.T.R. Wilson. Simpson [2] measured the charge

on rain beneath thunderclouds. He later designed an instrument to measure the vertical component of the electric field from a balloon released at the ground which ascended through the depth of the cloud. Wilson [3, 4] measured the changes in electrostatic field accompanying lightning flashes and, with estimates of the distance to the lightning based on observations of the thunder delay, interpreted these measurements to extract the magnitude and the polarity of the charge moment for both intracloud and cloud-to-ground lightning flashes. Within the latter part of the twentieth century, Simpson's method has been extended to vector electric field measurements and the use of Poisson's equation to extract estimates of space charge density [5, 6]. Wilson's method has also been extended to multistation measurements of lightning field change [7, 8] which enable determinations of the magnitudes and heights of the charge transferred by lightning in different phases of the lightning flash.

The long-standing disagreement between Wilson and Simpson [1] was resolved by a series of electric field soundings by Simpson and Scrase [9] and Simpson and Robinson [10] in which a tripolar electrostatic structure for thunderclouds was identified – positive charge uppermost, main negative charge at midlevel and a region of smaller positive charge at lower levels as shown in Figure 1.2. For measurements at some distance from the cloud (a necessary condition with Wilson's method as his instruments would not have worked properly if wet by rain) the tripole structure is dominated by the upper positive dipole. For measurements directly beneath the cloud, where Simpson made numerous measurements of the electric charge carried by raindrops, the lower (inverted) dipole would be most apparent. The tripole picture brought consistency to the measurements of these two scientists [1].

More recent measurements with the refined methods previously described lend further support to the basic tripolar structure in isolated thunderclouds. The main negative charge is found in the cold part of the cloud where the temperature is in the range of  $-10^{\circ}\text{C}$  to  $-20^{\circ}\text{C}$ , with a tendency for slightly higher altitudes (and lower temperatures) in deeper, more vigorous storms. The main negative charge is frequently vertically confined, often less than 1 km in vertical extent. The upper positive charge is more diffuse and can extend to the top of the cloud.

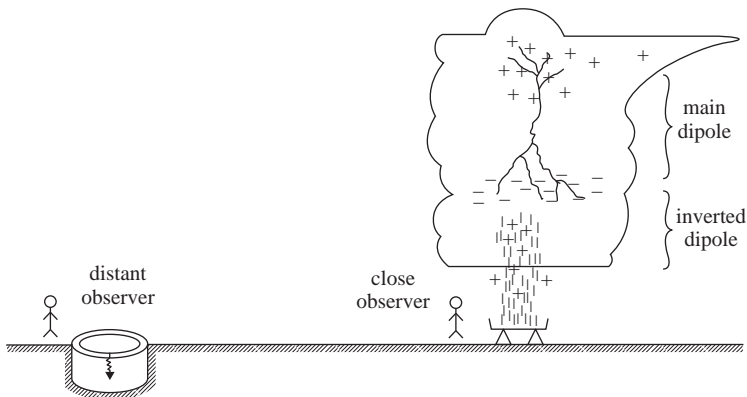
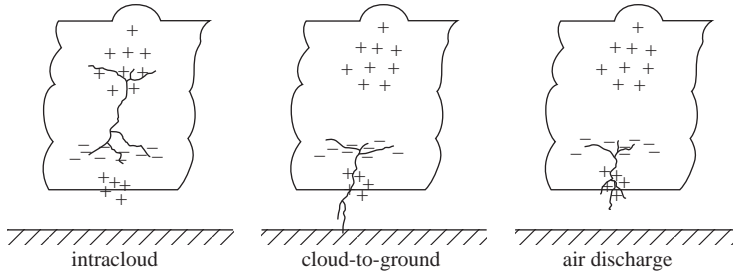


Figure 1.2 The tripole structure of the thundercloud (first identified by Simpson and Scrase [9]) and the predominant behaviour for observers at different distances from the storm. The inverted dipole dominates for the close observer and the main dipole for the distant observer





*Figure 1.3 Predominant lightning types within the tripole structure of a thunderstorm: the intracloud flash, the negative ground flash and the air discharge*

The upper positive and main negative charge regions are often separated by a quasi-neutral zone in the central mixed-phase region, consistent with the picture for charge separation by particle collisions illustrated in Figure 1.1. The lower positive charge is typically smaller in magnitude than the main negative charge (consistent with the common presence of upward-pointing electric fields beneath thunderclouds), and can extend below the  $0^{\circ}\text{C}$  isotherm.

The tripole structure is also broadly consistent with the dominant lightning types now recognised in isolated thunderclouds [11], as illustrated in Figure 1.3. The most common lightning type is the intracloud flash, a discharge between the upper positive charge and the main negative charge. The most common ground flash transfers negative charge from the main negative charge region to ground, but the initial discharge between the main negative charge and the lower positive charge may be an essential aspect of the overall process. A discharge between the main negative charge and the lower positive charge which does not succeed in contacting ground is called an air discharge. Had Wilson been able to make his field-change measurements closer to the cloud, he probably would have recognised this third common lightning type in early work. A less frequent type of air discharge is the lightning that propagates upward into clear air above the cloud top. A fifth lightning type is the positive ground discharge which occurs about one tenth as frequently as does the negative ground discharge. It has not yet been established whether positive ground flashes draw on the upper positive charge or the lower positive charge, or still another positive charge reservoir. The answer may well depend on the meteorological context [12–14].

As previously discussed, the main charge regions in thunderclouds are often confined in the vertical in comparison with their horizontal extents. The main evidence for this behaviour has come from balloon soundings of electric field, but the various observations of lightning paths within the cloud corroborate this behaviour [8, 15–17]. The evidence for vertical confinement of charge contradicts earlier ideas of Malan and Schonland [18] about an extended vertical column of electric charge which originated on the basis of a misinterpretation of the electric field changes during the lightning discharge [8].

#### **1.4 Sprite-producing thunderclouds: mesoscale convective systems**

Although vertical confinement of charge regions characteristic of ordinary thunderclouds is depicted in Figures 1.1–1.3, this behaviour is most pronounced

in the stratiform region of mesoscale convective systems (MCSs) – clouds whose width-to-height ratio may be 10 or 20 to 1 instead of 1 to 1. MCSs are the result of the aggregation of isolated thunderstorms forming earlier in the diurnal cycle, and hence are most prevalent very late in the afternoon and evening. The laterally extensive layers of space charge in an MCS allow for larger and more energetic lightning than is possible in ordinary thunderclouds. Charge transfers of hundreds of coulombs are possible [19–22], in contrast with the few tens of coulombs in ordinary thundercloud lightning. Lightning with horizontal extents exceeding 100 km has been documented in these very broad thunderstorms [23].

The charge structure of the MCS stratiform region is often more complicated than that depicted for ordinary thunderclouds in Figure 1.1 [5], although the dominant charge layers are still found in the mixed-phase region of the storms [24]. A pronounced layer of positive space charge is often found (by balloon soundings of the electric field) near the melting level at the lower boundary of the mixed-phase zone. A negative layer is often found above this positive layer [24]. The latter positive layer appears to be an important reservoir for the very energetic positive ground flashes with laterally extensive spider lightning and long continuing currents which predominate in MCS stratiform clouds [14, 25].

The discovery of sprites in the mesosphere in recent years [25–29] has intensified interest in the electrification and charge structure of the MCS stratiform region. Sprites are a luminous discharge phenomenon at 70–90 km altitude clearly caused by the large energetic positive ground flashes typical of this meteorological stage of convection [21, 30]. A video camera image of an energetic sprite is shown in Figure 1.4. Sprites do not appear to be produced by lightning in ordinary thunderclouds, but rather require clouds with more substantial lateral extents as shown in Figure 1.5. The energetic positive discharges make sprites simultaneously excite

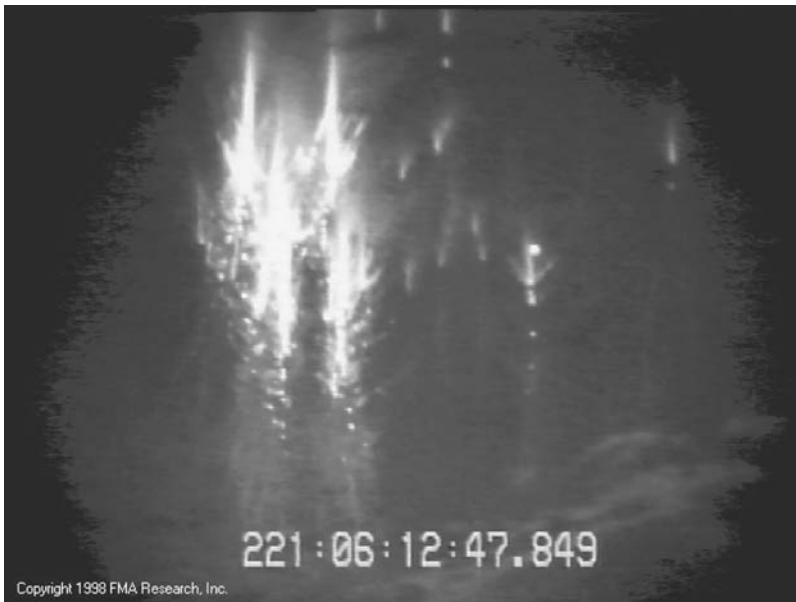


*Figure 1.4 A video camera image of a sprite in the mesosphere over a large mesoscale convective system*

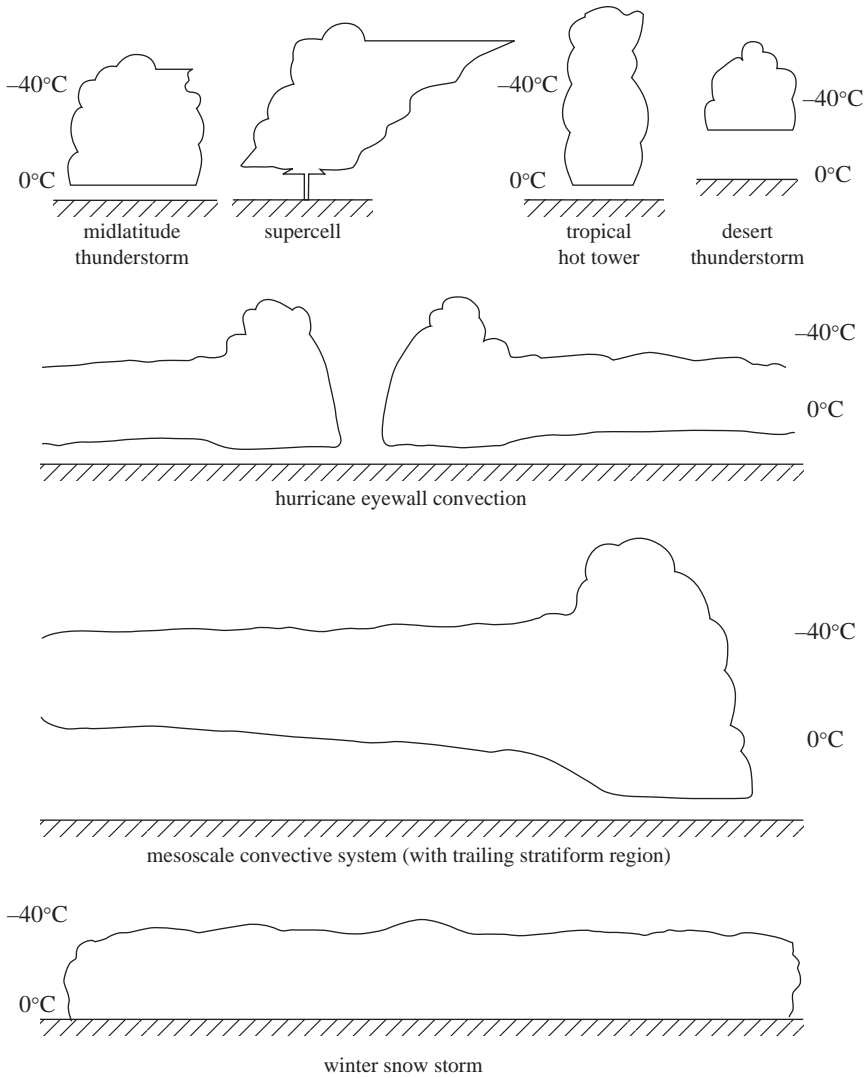


*Figure 1.5 Shapes and sizes of thunderstorms in different meteorological environments and different geographical locations. A viable mixed-phase region appears to be a common feature*

the extremely low-frequency resonances of the Earth–ionosphere cavity and thereby enable the worldwide detection of sprite locations with single station ELF measurements [21, 29–31].

## 1.5 Geographical variability of thunderclouds

### 1.5.1 Environmental controls

The shape, size, intensity and prevalence of thunderstorms all exhibit geographical variations which are best understood by first considering environmental controls on thunderstorm characteristics. Thunderstorms are still notoriously difficult to

predict, but this kind of information is invaluable towards that end. Important controls are the following:

*Availability of water vapour:* The energy made available for thunderstorms is ultimately the latent heat released when water vapour reverts to its liquid and solid phases through the processes of condensation, vapour deposition, and freezing (riming). The most important single factor in influencing the seasonal and geographical variability of thunderstorms is the physical law governing the temperature dependence of the water vapour concentration at saturation – the Clausius–Clapeyron relation. This relationship is exponential – a rough rule-of-thumb is a doubling of water vapour concentration for each  $10^{\circ}\text{C}$  increase in temperature. For a  $50^{\circ}\text{C}$  temperature difference between the Earth's equator and pole, this amounts roughly to a  $2^5 = 32$  fold contrast in water vapour concentration.

*Atmospheric instability:* Vertical air motions in thunderstorms are caused primarily by cloud buoyancy forces which themselves are set up by differences in temperature, water vapour concentration and condensate between ascending and descending air parcels and their environment. One often used measure of integrated cloud buoyancy, obtained from thermodynamic soundings in the environment of a developing storm, is CAPE (Convective Available Potential Energy) [32, 33]. In general, an atmosphere with larger CAPE is likely to produce a stronger updraft and a more vigorous and electrically active storm. The updrafts in turn will influence the vertical development of precipitation in the mixed-phase region of the cloud where the impact on charge separation appears to be greatest. Large CAPE can result from either strong surface heating and hot boundary-layer air, and/or by the presence of cold air aloft. The nature of the surface is influential here; land surfaces heat more rapidly when exposed to sunlight than water surfaces because of the rigidity, opacity and smaller heat capacity of the land surface.

*The vertical extent of cloud buoyancy:* Air parcels experiencing upward buoyancy forces over a greater vertical extent [34] are expected to achieve larger vertical velocities, and thereby contribute to more vigorous thunderstorms. The height at which the buoyancy force vanishes is the level of neutral buoyancy (LNB). Owing to the vertical temperature structure of the atmosphere, the LNB is in general found just beneath the local tropopause, where the temperature begins to increase into the stratosphere. The tropopause height varies considerably with geographical latitude – 17 km in the tropics to 12–13 km in midlatitude summer to about 6–7 km in midlatitude winter conditions.

*Altitude of the mixed-phase region:* As noted earlier and illustrated in Figure 1.5, mixed-phase microphysics appears to be essential for vigorous charge separation and lightning. The mixed-phase region is bounded by the  $0^{\circ}\text{C}$  and  $-40^{\circ}\text{C}$  isotherms, which translates to a vertical extent in the atmosphere of 5–6 km. In summer this region is 4–5 km above the Earth's surface. In winter, this region begins near the Earth's surface and extends upward. This effect alone will obviously contribute greatly to both the seasonal and geographical variability of thunderstorms.

*Boundary-layer aerosol concentration:* The Earth's atmosphere is polluted with submicroscopic particles whose concentration varies widely. Because the sources for many of these particles are land-based, the continental aerosol concentrations are systematically greater than those over the ocean. A subset of the aerosol particles is the cloud condensation nuclei which strongly influence the spectra of cloud [35, 36]

droplets (both number concentrations and sizes) in developing moist convection. In this way the aerosol particles can influence the precipitation formed by the cloud. Recent speculation and observation suggest that the aerosol may also affect both lightning activity [37, 38] and cloud-to-ground lightning polarity [39]. This issue is presently an active area of research.

*Land versus ocean effects:* It is now well established that lightning is far more prevalent over land than over ocean, as shown in Figure 1.6. The explanation for the order-of-magnitude contrast is not well established. The traditional explanation is based on the stronger heating over land, larger CAPE, larger updraft and greater invigoration of mixed-phase microphysics. However, a large land/ocean lightning contrast is evident even at midnight [40], when the land surface is not strongly heated by the Sun. It has also been pointed out that even when CAPE is large over warm ocean water, the lightning activity there is still very modest [41]. The most recent work on this issue [42] emphasises an important role in cloud basic height (low over ocean, high over land) in influencing the conversion of CAPE to updraft kinetic energy.

One alternative explanation [36, 43] for the large lightning contrast is based on differences in continental and oceanic aerosol concentration. Over land where the air is more polluted, the available condensed liquid will be shared among a larger number of droplets, leading to smaller droplet sizes. The coalescence process to form rain is suppressed in the presence of small droplets and this may enable more liquid water to access the mixed-phase region where it is able to participate in the ice processes that promote charge separation. The results of field experiments cast doubt on the aerosol mechanism as the primary cause of the land–ocean lightning contrast [38] but recent modeling work supports a role for variable CCN concentration in modifying cloud electrification [37].

Yet another explanation for the land–ocean lightning contrast rests on the convective theory for electrification [44] and the differences in point discharge current expected for the smooth ocean surface and the rough and irregular land surface.

*Baroclinity of the atmosphere:* An atmosphere whose temperature is laterally uniform is referred to in meteorology as ‘barotropic’. Thunderstorms in a purely barotropic atmosphere grow vertically and frequently collapse on themselves to terminate their life cycle. The tropical atmosphere is the most barotropic region on the Earth. More common at midlatitude is the baroclinic atmosphere characterised by strong horizontal temperature gradients. Large-scale latitudinal temperature gradients are the direct result of differential heating of the Earth by the Sun – the tropics are hot and the poles are cool, with gradient regions in between. In baroclinic zones where hot and cold air masses of synoptic scale ( $\sim 1000$  km) interact, extraordinarily large CAPE can develop and storms can be strongly tilted from the vertical. Severe weather of all kinds (hail, wind and tornadoes) is strongly encouraged by baroclinic conditions. Recent studies have shown the severe storm to be the most electrically active in the atmosphere [45], and usually produces more than ten times more intracloud lightning than ground flashes.

### 1.5.2 *Tropical thunderstorms*

As a population of storms, the deep tropical clouds dominate the global thunderstorm category, in no small part because of the temperature dependence of the

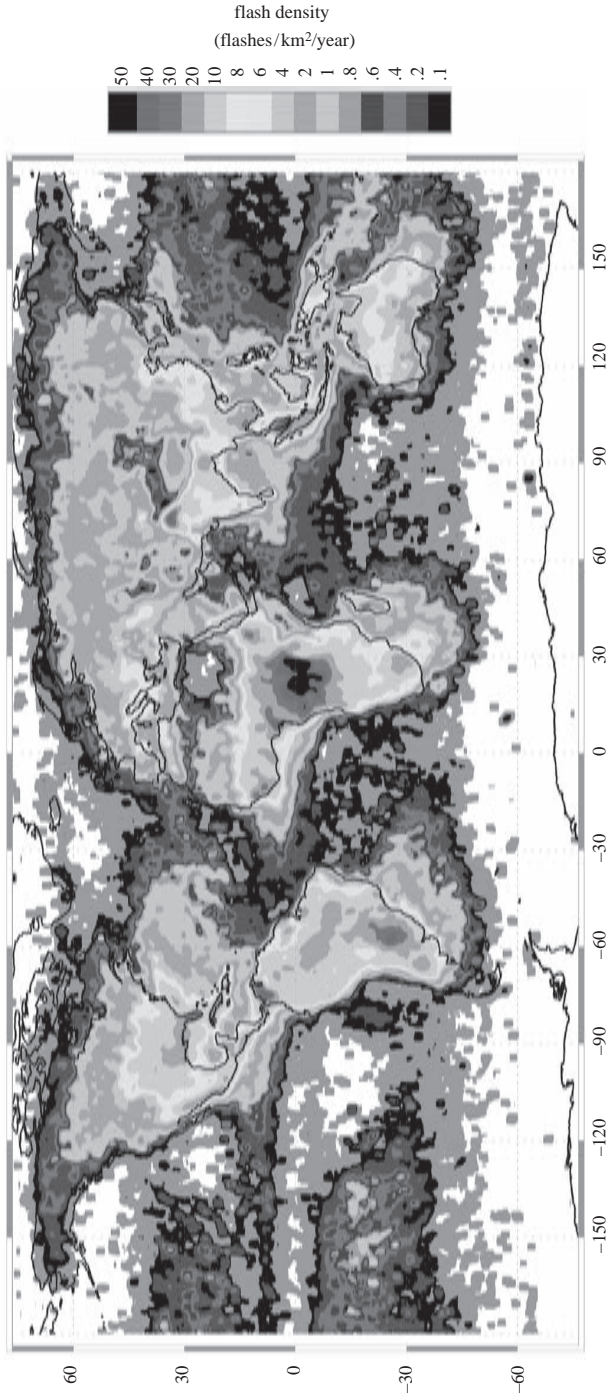


*Figure 1.6 Global lightning distribution depicted by the Optical Transient Detector in space showing a predominance of lightning activity over land areas (Dr's H. Christian and D. Boccippio, NASA/Marshall Space Flight Center)*

Clausius–Clapeyron relation. According to the satellite observations of Orville and Henderson [40], two of every three lightning flashes are found within the tropical belt. Tropical lightning is also dominant because, in many regions, thunderstorms develop nearly every day. Such is not the case at higher latitudes.

The flash rates of tropical thunderstorms vary widely. For storms close to and within the intertropical convergence zone (ITCZ) – the main region of synoptic scale upwelling and widespread persistent rainfall – the flash rates are quite modest, a few per minute or less. The active overturn of the troposphere on a large scale prevents the development of large CAPE (and attendant vigorous updrafts) and values here are often 1000 J/kg or less. For storms sufficiently displaced in latitude from the ITCZ to find themselves in large-scale subsidence of the ITCZ but still close enough for adequate moisture supply, the CAPE values may be 1000–3000 J/kg and the flash rates are substantially greater, 20–60 flashes per minute.

Owing to the high tropical tropopause (16–17 km), the cloud buoyancy is often distributed over a great range in height [33, 34]. In the barotropic environment typical of the tropics, the storms grow vertically to great depth but the modest cloud buoyancy often limits the vigour of mixed-phase development (almost always in the range 4.5–10 km altitude) and the associated flash rate. The skinny nature of tropical thunderstorms [46] may well be largely responsible for the high ratio of intracloud to ground lightning which they exhibit [47]. An elevated and narrow main negative charge region (Figure 1.5) may not promote flashes to ground with the same vigour as a broader midlatitude storm.

The often modest CAPE, the high melting level (4.5–5 km) and, in particular, the lack of baroclinity all contribute to the rarity of severe thunderstorms (hail, wind and tornadoes) in the tropical environment [48, 49]. The hurricane and typhoon are producers of severe wind, but their vertical winds are often quite modest in comparison with ordinary thunderstorms. Lightning is often more prevalent in the outer convective rain bands of a hurricane than in the eyewall region (Figure 1.5).

### 1.5.3 *Midlatitude thunderstorms*

At the higher latitudes of the extratropics, the tropopause height is lower –  $\sim 12$  km in summer – and so thunderstorms are generally less tall than in the tropics. For the same total CAPE, one finds greater cloud buoyancy at midlatitude than in the tropics and larger vertical velocity on average within the mixed-phase region. The squatter clouds at midlatitude (Figure 1.5) with somewhat lower mixed-phase regions probably contribute to the tendency for smaller ratios of intracloud to cloud-to-ground lightning at midlatitude.

The clash of warm and cold synoptic scale air masses is a prevalent phenomenon at midlatitude, and the associated strong baroclinity exerts a strong influence on thunderstorms there. In North America, warm moist air flows northward at low levels from the Gulf of Mexico and cold air aloft streams eastward off the Rocky Mountains to set up extraordinary atmospheric instability, with CAPE values occasionally in the 3000–5000 J/kg range. The combination of strong baroclinity and strong instability set up conditions for giant storms with rotating updrafts called supercells (Figure 1.5). These storms exhibit the largest updrafts, most strongly developed mixed-phase regions and the largest lightning flash rates anywhere in the world [49]. For reasons still not well understood but believed to be linked with mixed-phase microphysics [49], the most exceptional of these storms also produce

clusters of positive ground flashes in addition to their prodigious intracloud lightning displays [22, 50].

Dry desert regions would appear to be unfavourable for thunderstorm development, but occasionally small storms do develop there. On account of the reduced water vapour in the lower atmosphere, the LCL (and cloud base) for such storms is quite high, and the mixed-phase region dominates the depth of these clouds, as illustrated in Figure 1.5.

#### 1.5.4 Winter thunderstorms

Snowstorms are also the product of a baroclinic atmosphere but in the winter rather than in the summer season. Now the 0°C isotherm is often very close to the Earth's surface and so storm observers are immersed in the mixed-phase region. The winter tropopause is often quite low and the lifting process is often widespread, so winter storms have aspect ratios quite distinct from those of tropical towers (Figure 1.5). On account of Clausius–Clapeyron, the available water vapour in winter is substantially less and this dilutes the mixed-phase activity relative to the usual situation in summer. Nevertheless, the available observations demonstrate that locally intensified convection and riming conditions to form small graupel particles are present when snowstorm lightning occurs. Less vigorous snowstorms which produce predominantly vapour-grown crystals that aggregate into snowflakes (without appreciable riming) are only weakly electrified and rarely (if ever) become thunderstorms.

Lightning discharges are difficult to observe in winter storms because the visibility is so poor. Cloud base is often close to the Earth's surface. As a further consequence, the ratio of intracloud to ground flashes is poorly known. Based on measurements with lightning detection networks, it is well established that ground flashes of positive polarity are relatively more prevalent in the winter than in the summer. The reasons for this behaviour are not well established, and only little is known about the gross charge structure in winter storms [12, 51]. These uncertainties and the direct accessibility of the mixed-phase region to ground observers indicate that winter storms are deserving of greater study.

## References

- [1] WILLIAMS, E.R.: 'C.T.R. Wilson versus G.C. Simpson: Fifty years of controversy in atmospheric electricity', *Atmos. Res.*, 2009, **91**, pp. 259–271
- [2] SIMPSON, G.C.: 'On the electricity of rain and its origins in thunderstorms', *Philos. Trans. A*, 1909, **209**, pp. 379–413
- [3] WILSON, C.T.R.: 'On some determinations of the sign and magnitude of electric discharges in lightning flashes', *Proc. R. Soc. London*, 1916, **92**, p. 555
- [4] WILSON, C.T.R.: 'Investigations on lightning discharges and the electric field of thunderstorms', *Philos. Trans. A*, 1920, **221**, pp. 73–115
- [5] MARSHALL, T.C., and RUST, W.D.: 'Two types of vertical electrical structures in stratiform precipitation regions of mesoscale convective systems', *Bull. Am. Meteorol. Soc.*, 1993, **74**, pp. 2159–2170
- [6] STOLZENBURG, M., MARSHALL, T.C., RUST, W.D., and SMULL, B.F.: 'Horizontal distribution of electrical and meteorological conditions across the stratiform region of a mesoscale convective system', *Mon. Weather Rev.*, 1994, **122**, pp. 1777–1797



- [7] JACOBSON, E.A., and KRIDER, E.P.: 'Electrostatic field changes produced by Florida lightning', *J. Atmos. Sci.*, 1976, **33**, p. 103
- [8] KREHBIEL, P.R., BROOK, M., and McCRORY, R.A.: 'An analysis of the charge structure of lightning discharges to ground', *J. Geophys. Res.*, 1979, **84**, pp. 2432–2456
- [9] SIMPSON, G.C., and SCRASE, F.J.: 'The distribution of electricity in thunderclouds', *Proc. R. Soc. London, Ser. A*, 1937, **161**, pp. 309–352
- [10] SIMPSON, G.C., and ROBINSON, G.D.: 'The distribution of electricity in thunderclouds II', *Proc. R. Soc. London, Ser. A*, 1941, **177**, pp. 281–329
- [11] WILLIAMS, E.R., ORVILLE, R.E., and WEBER, M.E.: 'The relationship between lightning type and convective state of thunderclouds', *J. Geophys. Res.*, 1989, **94**, pp. 13213–13220
- [12] BROOK, M., NAKANO, M., KREHBIEL, P., and TAKEUTI, T.: 'The electrical structure of the Hokuriku winter thunderstorms', *J. Geophys. Res.*, 1982, **87**, pp. 1207–1215
- [13] WILLIAMS, E.R.: 'The tripole structure of thunderstorms', *J. Geophys. Res.*, 1989, **94**, pp. 13151–13167
- [14] WILLIAMS, E.R.: 'The positive charge reservoir for sprite-producing lightning', *J. Atmos. Sol. Terr. Phys.*, 1998, **60**, pp. 689–692
- [15] TEER, T.L., and FEW, A.A.: 'Horizontal lightning', *J. Geophys. Res.*, 1974, **79**, pp. 3436–3441
- [16] MACGORMAN, D.R., FEW, A.A., and TEER, T.L.: 'Layered lightning activity', *J. Geophys. Res.*, 1981, **86**, pp. 9900–9910
- [17] KREHBIEL, P.R., *et al.*: 'GPS-based mapping system reveals lightning inside storms', *EOS Trans. Am. Geophys. Union*, 2000, **81**, p. 21
- [18] MALAN, D.J., and SCHONLAND, B.F.J.: 'The electrical processes in the intervals between the strokes of a lightning discharge', *Proc. R. Soc. London, Ser. A*, 1951, **206**, pp. 145–163
- [19] BURKE, C.P., and JONES, D.L.: 'On the polarity and continuous current in unusually large lightning flashes deduced from ELF events', *J. Atmos. Terr. Phys.*, 1996, **58**, pp. 531–540
- [20] CUMMER, S.A., and INAN, U.S.: 'Measurement of charge transfer in sprite-producing lightning using ELF radio atmospheric', *Geophys. Res. Lett.*, 1997, **24**, p. 1731
- [21] HUANG, E., *et al.*: 'Criteria for sprites and elves based on Schumann resonance measurements', *J. Geophys. Res.*, 1999, **104**, pp. 16943–16964
- [22] STOLZENBURG, M.: 'Observations of high ground flash densities of positive lightning in summer thunderstorms', *Mon. Weather Rev.*, 1994, **122**, pp. 1740–1750
- [23] LIGDA, M.G.H.: 'The radar observation of lightning', *J. Atmos. Terr. Phys.*, 1956, **9**, pp. 329–346
- [24] SHEPHERD, T.R., RUST, W.D., and MARSHALL, T.C.: 'Electric fields and charges near 0°C in stratiform clouds', *Mon. Wea. Rev.*, **124**, 920–938, 1996.
- [25] LYONS, W.A., NELSON, T.E., WILLIAMS, E.R., CUMMER, S.A., and STANLEY, M.A.: 'Characteristics of sprite-producing positive cloud-to-ground lightning during 19th July 2000 STEPS Mesoscale Convective Systems,' *Mon. Weather Rev.*, 2003

- [26] FRANZ, R.C., NEMZEK R.J., and WINKLER, J.R.: 'Television image of a large upward electrical discharge above a thunderstorm system', *Science*, 1990, **249**, pp. 48–51
- [27] SENTMAN, D.D., and WESCOTT, E.M.: 'Observations of upper atmosphere optical flashes recorded from an aircraft', *Geophys. Res. Lett.*, 1993, **20**, p. 2857
- [28] LYONS, W.A.: 'Low light video observations of frequent luminous structures in the stratosphere above thunderstorms', *Mon. Weather Rev.*, 1994, **122**, pp. 1940–1946
- [29] WILLIAMS, E.R., 'Sprites, elves and glow discharge tubes', *Physics Today*, 2001, November, pp. 41–47
- [30] BOCCIPPIO, D.J., *et al.*: 'Sprites, ELF transients and positive ground strokes', *Science*, 1995, **269**, pp. 1088–1091
- [31] HOBARA, Y., HAYAKAWA, M., WILLIAMS, E., BOLDI, R., and DOWNES, E.: 'Location and electrical properties of sprite-producing lightning from a single ELF site', in FULLEKRUG, M., MAREEV, E.A., and RYCROFT, M.J. (Eds): *Sprites, Elves and Intense Lightning Discharges*. NATO Science Series, II. Mathematics, Physics and Chemistry 225, Springer, 398 pp., 2006
- [32] RIEMANN-CAMPE, K., FRAEDRICH, K., and LUNKEIT, F.: 'Global climatology of Convective Available Potential Energy (CAPE) and Convective Inhibition (CIN) in ERA-40 reanalysis', *Atmos. Res.*, 2009, **93**, pp. 534–545
- [33] WILLIAMS, E.R., and RENNO, N.O.: 'An analysis of the conditional instability of the tropical atmosphere', *Mon. Weather Rev.*, 1993, **121**, pp. 21–36
- [34] WILLIAMS, E.R.: 'Meteorological aspects of thunderstorms', in VOLLAND, H. (Ed.): *CRC Handbook on Atmospheric Electrodynamics* (CRC Press, Boca Raton, FL, 1995), vol. I, pp. 27–60
- [35] HOGAN, A.: 'Meteorological variation of maritime aerosols', in RODDY, A.F. and O'CONNOR, P.C. (Eds): *Atmospheric Aerosols and Nuclei*, Galway Univ. Press, Galway, Ireland, 1977, pp. 503–507
- [36] WILLIAMS, E.R.: Franklin Lecture, 2012. <http://fallmeeting.agu.org/2012/events/franklin-lecture-ae31a-lightning-and-climate-video-on-demand/>
- [37] MANSELL, E. and ZIEGLER, C.: 'Aerosol effects on simulated storm electrification and precipitation in a two-moment bulk microphysics model'. *J. Atmos. Sci.*, 2013, **70**, pp. 2032–2050
- [38] WILLIAMS, E.R., *et al.*: 'Contrasting convective regimes over the Amazon: Implications for cloud electrification', *J. Geophys. Res.*, 2002, LBA Special Issue 107 (D20), 8082, doi 1029/2001JD000380
- [39] LYONS, W.A., NELSON, T.E., WILLIAMS, E.R., CRAMER, J.A., and TURNER, T.R.: 'Enhanced positive cloud-to-ground lightning in thunderstorms ingesting smoke from fires', *Science*, 1998, **282**, pp. 77–80
- [40] ORVILLE, R.E., and HENDERSON, R.W.: 'Global distribution of midnight lightning: September 1977 to August 1978', *Mon. Weather Rev.*, 1986, **114**, pp. 2640–2653
- [41] LUCAS, C., ZIPSER, E.J., and LEMONE, M.A.: 'Convective available potential energy in the environment of oceanic and continental clouds: Correction and comments', *J. Atmos. Sci.*, 1994, **51**, pp. 3829–3830

- [42] WILLIAMS, E., and STANFILL, S.: 'The physical origin of the land-ocean contrast in lightning activity', *C. R. Phys.*, 2002, **3**, pp. 1277–1292
- [43] ROSENFELD, D.: Personal Communication, 1998
- [44] VONNEGUT, B.: 'Some facts and speculations regarding the origin and role of thunderstorm electricity', *Meteorol. Monogr.* **5**, 1963, pp. 224–241
- [45] WILLIAMS, E., *et al.*: 'The behavior of total lightning in severe Florida thunderstorms', *J. Atmos. Res.*, 1999, **51**, pp. 245–265
- [46] WILLIAMS, E.R., *et al.*: 'A radar and electrical study of tropical hot towers', *J. Atmos. Sci.*, 1992, **49**, pp. 1386–1395
- [47] RUTLEDGE, S.A., WILLIAMS, E.R., and KEENAN, T.D.: 'The down under Doppler and electricity experiment (DUNDEE): Overview and preliminary results', *Bull. Am. Meteorol. Soc.*, 1992, **73**, pp. 3–16
- [48] BARNES, G.: 'Severe local storms in the tropics', in DOSWELL, C.A. III (Ed.): *Monograph on Severe Convective Storms*, American Meteorological Society, 2001, pp. 359–432
- [49] WILLIAMS, E.R.: 'The electrification of severe storms', in DOSWELL, C.A. III (Ed.): *Monograph on Severe Convective Storms*, American Meteorological Society, 2001, pp. 527–561
- [50] MACGORMAN, D.R., and BURGESS, D.W.: 'Positive cloud-to-ground lightning in tornadic storms and hailstorms', *Mon. Weather Rev.*, 1994, **122**, pp. 1671–1697
- [51] TAKAHASHI, T., TAJIRI, T., and SONOI, Y.: 'Charges on graupel and snow crystals and the electrical structure of winter thunderstorms', *J. Atmos. Sci.*, 1999, **56**, pp. 1561–1578

---

## Chapter 2

# Thunderstorm electrification mechanisms

*Rohan Jayaratne*

---

### 2.1 Introduction

The origin of thunderstorm electrification has long been an unsolved problem in atmospheric physics. Despite a number of simulated laboratory experiments, together with the vast amount of field data collected over the past few decades, our knowledge of how these convective cloud masses get charged still remains sparse at the microphysical level.

Sir John Mason in the Bakerian Lecture [48] identified thunderstorm electrification as one of the three leading unsolved problems in cloud physics. He had this to say about the problem:

This is, for me, the most intriguing and challenging problem in cloud physics, with a strong incentive to understand one of the most spectacular of natural phenomena, but made all the more interesting by the fact that the search for a continuing solution has led us into a number of rather difficult areas of classical physics, and to a deeper study of the fundamental properties of water and ice.

A satisfactory theory must be able to explain all of the observed electrical characteristics of a typical thunderstorm. Such a list of requirements, first drawn up by Mason [47] and later extended by Moore and Vonnegut [50], is as follows:

- (i) For lightning to occur, the cloud depth must be greater than 3–4 km. Very tall thunderclouds produce far more frequent lightning than those of ordinary height.
- (ii) Although lightning may occur in warm clouds, strong electrification is not observed unless the cloud extends above the freezing level.
- (iii) Highly electrified regions of thunderstorms almost always coincide with the coexistence of ice and supercooled water.
- (iv) Strong electrification occurs when the cloud exhibits strong convective activity with rapid vertical development.
- (v) The charge generation and separation processes are closely associated with the development of precipitation, probably in the form of soft hail. Lightning generally originates in the vicinity of high-precipitation regions.
- (vi) The first lightning stroke very often occurs within 12–20 min of the appearance of precipitation particles of radar-detectable size. The initial rate of electrification has a time constant of about 2 min.
- (vii) The average duration of precipitation and electrical activity from a single thunderstorm cell is about 30 min.

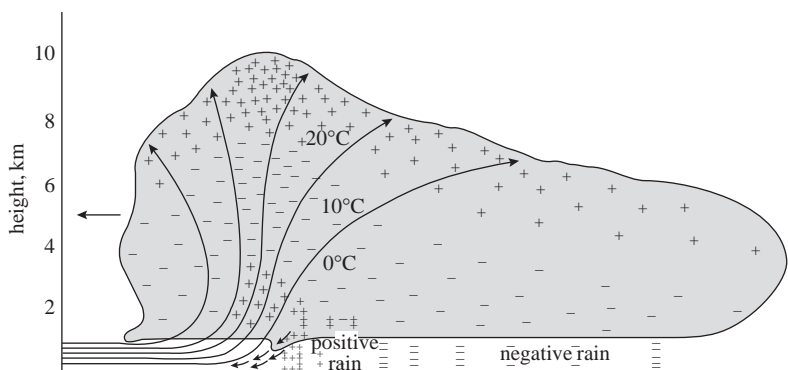


Figure 2.1 *The classical tripolar charge structure of a thunderstorm (from [63])*

- (viii) The location of the charge centres appear to be determined by temperature and not height above the ground. The main negative charge centre is generally located between the  $-5^{\circ}\text{C}$  and  $-25^{\circ}\text{C}$  isotherms with the main positive some kilometres higher up. There is a small pocket of positive charge below the main negative centre, close to the freezing level, that appears to be associated with the precipitation shaft (Figure 2.1).
- (ix) In the mature stage of a storm, electric fields as high as  $400\text{ kV}\cdot\text{m}^{-1}$  may occur, giving rise to a flash rate of several per minute requiring an average charging current of the order of 1 A. The required charging rate is about  $1\text{ C}\cdot\text{km}^{-3}\cdot\text{min}^{-1}$ .
- (x) The average electric moment destroyed in a lightning flash is about 100 C km; the corresponding charge being 20–30 C.
- (xi) The dipole destroyed by the flash may depart from the vertical in some cases by as much as  $90^{\circ}$ .

These requirements suggest strongly a fundamental role for an ice-based precipitation mechanism of thunderstorm electrification. There have been reports of lightning from clouds everywhere warmer than  $0^{\circ}\text{C}$  [20, 51, 54] but these observations have been rare and the electrification very weak. The overwhelming observational evidence seems to favour a mechanism closely related to the presence of ice within clouds. The key points of this evidence have been aptly summarised by Williams [72] and are essentially in line with the list of requirements above.

Over the past several decades, a number of mechanisms have been proposed to explain these observed features. Most of these have had to be discarded owing to various difficulties. In this chapter, we shall look at each of these mechanisms in turn and discuss their merits and demerits in terms of the results from laboratory experiments and field observations.

## 2.2 The suggested mechanisms

### 2.2.1 *The inductive mechanism*

The inductive mechanism was one of the first theories of thunderstorm electrification and has proved to be very popular even up to the present day. It was first proposed by Elster and Geitel [18] in 1913 and has been modified by several workers since then. Figure 2.2 shows a schematic representation of their model. A water drop falling

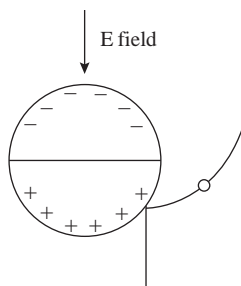


*Figure 2.2 Schematic representation of the inductive charging mechanism. Charge polarisation occurs on the larger particle in the external electric field. During a rebounding collision, a smaller particle removes some of the positive charge from the lower half of the larger particle and is swept up in the air currents. The larger particle falls with a net negative charge. Both particles move in directions that reinforce the external electric field*

through the vertical electric field region of a thundercloud has oppositely polarised charges at its top and underside. In a downward directed electric field, that is with the positive charge above the negative in the cloud, the underside of the drop will carry a positive charge. Smaller droplets rebounding off the lower half of the drop will remove some of this positive charge which will get swept up to the top of the cloud to augment the upper positive charge centre, leaving the falling drop with a net negative charge which will be transported to the base of the cloud to enhance the lower negative charge. This provides a positive feedback mechanism that will enhance the existing electric field. The theory was later extended to ice particles by Muller-Hillebrand [52] and Latham and Mason [38]. Here, the heavier hailstones will fall with respect to the lighter ice crystals which are usually swept to the top of the cloud. The above workers calculated the magnitude of the charge separated when two spherical particles interacted in a given electric field in terms of their radii, time of contact and point of impact. Several workers have since shown that it is possible to account for the observed electric fields in thunderstorms within the required time intervals in terms of the inductive mechanism [14, 53, 57, 61, 77]. These models have been based on the three possible combinations of cloud particle interactions: water–water, water–ice and ice–ice. However, each of these cases has strong limitations, as we shall discuss now.

In the water–water case, a droplet colliding with a larger drop is more likely to coalesce than rebound. This is even more likely in an external electric field. Jennings [34] showed that the probability of coalescence tends to one in the presence of electric fields greater than about  $25 \text{ kV}\cdot\text{m}^{-1}$ . A similar problem limits the efficiency of the water–ice case. A supercooled water droplet colliding with a falling hailstone is far more likely to freeze on impact than to rebound. Aufdermaur and Johnson [1] showed that not more than 1 in 100 droplets bounce off and these are the droplets that make grazing collisions off regions of the hailstone where there are very few polarised charges to give a significant charge separation. Further, as the hailstone acquires a net charge, the electrical equator will move down. Droplets making grazing collisions may now remove the opposite charge from the regions above the electrical equator – a process that will oppose the positive feedback to the electric field. There is also the strong possibility of a rebounding droplet

subsequently coalescing with another hail pellet, placing a further limit on the amount of charge that may be transferred to the top of the cloud.

Many workers have attempted to test the ice–ice-based inductive mechanism experimentally. Latham and Mason [38] showed that two ice particles brought into contact with each other for various time intervals in an electric field separated charges in accordance with the theory. However, the bouncing collisions did not yield satisfactory results. No appreciable charge transfers were found when ice crystals were made to bounce off a cylindrical ice target at speeds up to  $30 \text{ m}\cdot\text{s}^{-1}$  in electric fields up to  $70 \text{ kV}\cdot\text{m}^{-1}$ . Aufdermaur and Johnson [1] impacted frozen water drops on an ice covered target and found charges of  $50 \text{ fC}$  per collision, but this value was not affected by the electric field raising some questions as to the source of the charging process. Gaskell [21] showed that the charge separated was significantly less than that predicted under the conditions used and attributed it to the short contact times between the two particles. For a reasonable amount of charge to be transferred, the time of contact must be of the same order as the relaxation time for the redistribution of charge. Gross [24] showed that, for pure ice, the relaxation time was significantly longer than the estimated contact times in ice–ice collisions. Illingworth and Caranti [27] found that, in general, the conductivity of pure ice was too low for a complete charge transfer during the contact times available. Brooks and Saunders [7] showed that when the impacting ice particles were replaced by conducting metal spheres, the mean charge separated was appreciably larger. They attributed this to the shorter relaxation times in metals over ice. Also, most of these experiments have been conducted using radial fields around the larger particle. Experimental conditions make it difficult to produce a vertical electric field across a particle while smaller particles fall vertically to impact on it. The radial configuration creates unrealistically large electric fields near the electrical equator of the larger particle – where smaller particles are most likely to make contact. Figure 2.3 illustrates this problem schematically.

The main difficulty in accepting the inductive mechanism has been with respect to field observations of particle charges and electric fields. The theory predicts a maximum charge that a particle of a particular size may acquire in a given electric field. However, measured charges on precipitation particles are often

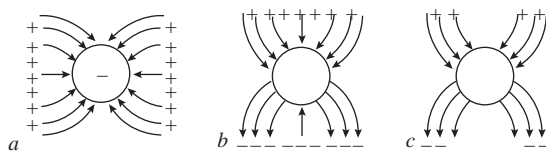


*Figure 2.3 Problems encountered due to various electrode configurations in laboratory studies of the inductive charging mechanism. The smaller particle falls or is sucked by the air moving vertically downwards through a tube and is more likely to make a glancing collision at the equator of the target. (a) The electric field is applied between the target and the walls of the tube; this leads to an unrealistically high field at the equator of the target. (b) Horizontal plate electrodes best represent natural thunderstorm fields but make it impossible to allow the particle to interact with the target. (c) Leaving gaps in the plates allows the particle to fall through but again leads to a distortion of the field, enhancing the fields at the equator*

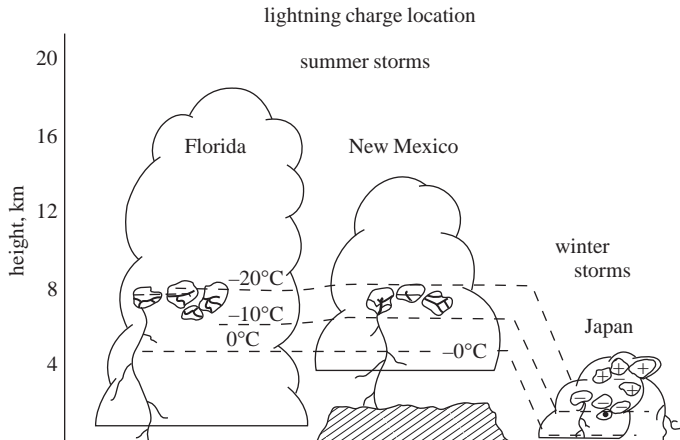


Figure 2.4 Schematic representations of the vertical locations of charge sources giving rise to lightning in storms at three different locations – Florida, New Mexico and in wintertime in Japan. Note that the charge centres are correlated with temperature and not altitude (from [35])

much too large to be explicable in terms of the inductive mechanism [23, 45]. The inductive mechanism requires the recovery of the electric field between lightning flashes to be exponential. However, Winn and Byerley [74] using instrumented balloons in New Mexico thunderstorms found that the recovery was linear and thus not proportional to the existing electric field. The theory also fails to explain the temperature dependence of the location of the main negative charge centre. Krehbeil *et al.* [35] showed that the temperature at the negative charge centre is restricted to a narrow range within thunderstorms forming over various climatic conditions and geographical locations (Figure 2.4).

The inductive mechanism is attractive because it is simple but in view of the above difficulties it is hard to imagine how it may operate as a viable charge generation mechanism in thunderstorms.

### 2.2.2 The convective mechanism

First proposed by Grenet [25] and later extended by Vonnegut [70], the convective mechanism has for many years been the foremost non-precipitation-based theory of thunderstorm electrification. The theory is based on the vertical transport of atmospheric ions by the strong updraughts inside thunderstorms and by the compensating downdraughts outside. The basic features of the theory are schematically illustrated in the idealised sketch shown in Figure 2.5 after Vonnegut [71]. It supposes that positive ions released by point discharge at the ground are carried into the cloud and towards the cloud top by the updraughts. There, these charges attract small negative ions to the cloud's upper surface from the clear upper atmosphere. The negative ions rapidly become immobilised by attachment to cloud particles which are caught up in the downdraughts and transported to the lower part of the cloud. This causes more positive ions to be produced by point discharge at the ground, thus leading to a positive feedback mechanism.

Wormell [76] points out that the concentration of ions present around a thundercloud is insufficient to account for the observed rate of regeneration of charge within the cloud. Standler and Winn [64] showed that the total point discharge



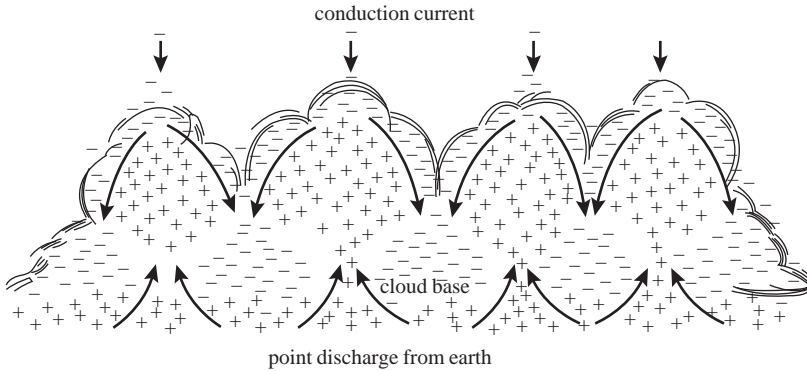


*Figure 2.5 Schematic diagram illustrating the convective charging mechanism (from [71])*

current by itself is too small to account for the observed lightning currents and that the resulting positive space charge does not form a deep vertical column from the ground up to the cloud but rather a layer of thickness 100–200 m near the ground. Chalmers [13] has questioned the validity of the theory on the grounds that the updraughts should carry not just the positive charges but also the negative charged particles that have been transported in the downdraughts. There has also been some concern regarding the time frame of the process. Point discharge currents do not occur until the electric field at the ground has built up to about  $800 \text{ V}\cdot\text{m}^{-1}$ . By this time, the electric fields within the cloud are high enough to give rise to lightning. Further, the resulting positive ions take a considerable time to reach the cloud. Thus, the theory fails to explain the initial electrification of the cloud.

### *2.2.3 The selective ion capture theory*

Wilson [73] suggested that a raindrop polarised in a vertical electric field may acquire a net charge by a selective ion capture process. For example, a raindrop falling through a downward directed electric field would be polarised in such a way that it would attract negative ions while repelling positive ions from its lower half. The drop would, thus, gain a net negative charge and carry this down to enhance the ambient electric field. However, there is a limit to which the drop can be charged in this manner. Once it has acquired a large enough negative charge, it will begin to repel negative ions away from its vicinity. Moreover, if the mobility of the ions in the ambient electric field is too high, they will not be captured by the falling drop. This imposes a constraint on the maximum electric field at which the mechanism can be viable. For a raindrop falling at a terminal velocity of  $8 \text{ m}\cdot\text{s}^{-1}$  past small ions of mobility  $1.5 \text{ cm}^2\cdot\text{s}^{-1}\cdot\text{V}^{-1}$ , this maximum electric field is about  $50 \text{ kV}\cdot\text{m}^{-1}$ . There is a further difficulty in that, as Wormell [76] has pointed out, the concentration of ions in the atmosphere may not be sufficiently high. Thus, although this mechanism is thought to be partly responsible for bringing down some of the ions that may have otherwise been swept up to the top of the cloud, it falls far short of accounting for the large electric fields and charge centres present in thunderstorms.

### *2.2.4 Drop breakup theory*

An uncharged water drop suspended in a downward directed electric field will be polarised in such a way that its lower hemisphere will carry a positive charge while

the upper hemisphere will be negative. If the drop were to break up along its equator, the two resulting droplets would carry roughly equal and opposite charges. It can be shown that a drop of diameter 6 mm, breaking up in an electric field of  $500 \text{ V}\cdot\text{cm}^{-1}$ , would produce two fragments with about 0.3 nC each or a charge density of about  $0.3 \text{ nC}\cdot\text{g}^{-1}$  of ruptured water. This is equivalent to a cloud charge density of about  $1 \text{ C}\cdot\text{km}^{-3}$  if the liquid water content is  $5 \text{ g}\cdot\text{m}^{-3}$  [55]. Matthews and Mason [49] show that the charge separated increases with electric field and that the larger fragment generally carries the positive charge. They conclude that the process may explain the formation of the lower positive charge centre in thunderstorms. A major problem with this theory is that large drops do not break up very easily unless they are involved in a collision with another drop. Moreover, the drops are not always likely to break up at the equator, thus reducing the expected amount of charge that may be separated.

### 2.2.5 *Melting of ice*

Dinger and Gunn [16] showed that when ice melts it acquires a net positive charge. This was later confirmed by Drake [17]. Iribarne and Mason [28] showed that the charge is separated by tiny air bubbles in the ice bursting at the surface during the melting process. The minute droplets produced by the bursting bubbles remove a negative charge leaving the ice positive. The mechanism was attributed to an electric double layer at the water–air interface which gives rise to the excess of negative ions at the surface. Electric charges up to about  $2 \text{ nC}\cdot\text{g}^{-1}$  of melted water were found depending on the bubble content of the ice. Mason [48], assuming a charge concentration of  $0.7 \text{ nC}\cdot\text{g}^{-1}$  of melted water from millimetre-sized graupel in an ice concentration of  $2 \text{ g}\cdot\text{m}^{-3}$ , estimated a spatial charge concentration of approximately  $1 \text{ C}\cdot\text{km}^{-3}$  and suggested that this may explain the lower positive charge centre in a thundercloud. Indeed, the lower positive charge centre appears to be closely associated with the melting layer in many instances [62] but there are cases where it has been observed well above this level [39, 42, 45, 65]. Moreover, the polarity of the charge separation in the melting process is the wrong way around to account for the positive charge accumulations near the freezing level that appears to be widespread in stratiform regions with radar bright bands at or below this level.

### 2.2.6 *The Workman–Reynolds effect*

Workman and Reynolds [75] observed that an electric double layer was set up across the ice–liquid interface during the freezing of dilute aqueous solutions. The sign and magnitude of the potential was found to be sensitive to the nature and concentration of the solute. Distilled water showed negligible effects. The potential appeared during the progress of the freezing front and disappeared soon after the freezing ended. The effect was attributed to the selective incorporation of ions from the liquid into the ice during freezing; the ice attained a negative potential with respect to most solutes, ammonium salts being a notable exception. During the freezing of  $5 \times 10^{-5} \text{ N}$  solution of ammonium hydroxide the ice acquired a potential of +240 V with respect to the liquid and a  $10^{-4} \text{ N}$  solution of sodium chloride gave a corresponding potential of about –30 V. The sensitivity to solute concentration was apparent when a sodium chloride solution of  $5 \times 10^{-4} \text{ N}$  hardly showed any effect.

It is well known that hail pellets are warmer than their environment owing to the latent heat released by the accretion of supercooled water droplets. As a hail

pellet falls towards the base of the cloud, if the cloud water content is high enough, the latent heat acquired may be sufficient to raise its temperature to 0°C. The pellet will begin to melt and carry a sizable water skin at its surface. It is then said to be in a state of wet growth. Workman and Reynolds suggested that, when this water skin became thick enough, the pellet would shed some of the water as it fell through the cloud. Considering the nature and concentration of chemical impurities present in cloud water, the potential difference at the ice–water interface would ensure that the water flung off was positively charged, leaving the pellet with a net negative charge. Subsequent gravitational separation would result in the observed dipolar charge distribution within the thundercloud.

The difficulty with this mechanism is that it can occur only at temperatures close to 0°C. The cloud water content present in a typical thunderstorm at colder temperatures is insufficient to raise the temperature of graupel pellets to ensure wet growth. Reynolds *et al.* [56] showed that the mechanism was inadequate to account for negative charge centres at temperatures colder than about –16°C.

### 2.2.7 *The thermoelectric effect*

The mobility of the H<sup>+</sup> ions in ice is much greater than that of the OH<sup>–</sup> ions and they both increase with temperature. In a block of ice with a temperature gradient down its length, the warmer end would acquire a net negative charge due to the faster diffusion of H<sup>+</sup> ions away from that end. If two pieces of ice at different temperature were brought into momentary contact they would separate with the warmer carrying a net negative charge. Latham and Mason [36] calculated that a potential difference of about 2Δ*T* mV would be set up across the ends of a piece of ice having a steady temperature difference of Δ*T*°C. Several simulated laboratory experiments have been conducted with small ice particles in the form of vapour-grown ice crystals or frozen droplets made to bounce off an artificially warmed ice target [6, 32, 37, 43, 56].

In all these experiments, the warmer ice particle acquired the negative charge. However, a major drawback to the thermoelectric effect theory is that the concentration of ions in ice is grossly inadequate to explain the observed charge separation during interactions between ice particles. The magnitudes of charge transfer observed in the simulated experiments cannot be explained in terms of the Latham and Mason calculations based on the known concentrations of ions in ice.

### 2.2.8 *Surface potential theories*

Takahashi [67] used a vibrating capacitor method to determine the surface electrical potential of an ice surface under various conditions. When the ice was warmed to form a thin liquid film on its surface, it acquired a negative potential of –100 mV with respect to a dry surface. He explained the observation as follows: H<sup>+</sup> and OH<sup>–</sup> ions are more concentrated in water than in ice because of their different activation energies. At the same time, H<sup>+</sup> ions have a greater mobility than OH<sup>–</sup> in ice and so will diffuse more readily from the water into the ice. He calculated a potential of –150 mV for the water with respect to ice, in fair agreement with experiment. Takahashi suggested that this mechanism may explain how hailstones in wet growth become positively charged in the lower regions of thunderstorms.

Takahashi [66] also used this technique to measure the surface potential of an ice surface rubbed with another piece of ice or with a planer. He noted a negative potential which increased to about –200 mV on the surface being rubbed.

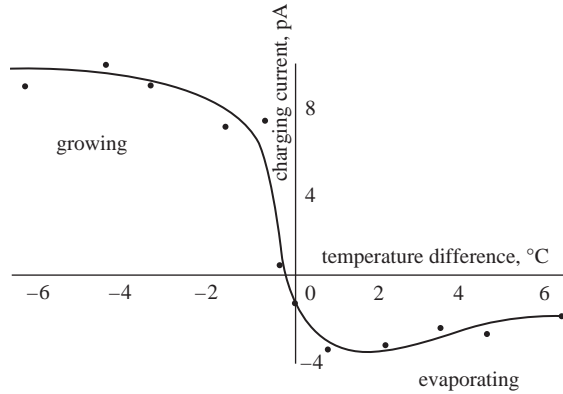


Figure 2.6 The charging current  $I$  to an ice target as a function of temperature difference  $\Delta T$  between the target and a cloud of ice crystals. Ambient temperature =  $-10^{\circ}\text{C}$ ; impact speed =  $15\text{ m}\cdot\text{s}^{-1}$ . The warmer target was sublimating and charged negatively. The colder target was growing and charged positively (from [6])

He suggested that pairs of negatively charged dislocations and positively charged D-defects were produced at the point of rubbing. D-defects diffused faster than the dislocations into the ice due to their greater mobility, leaving the surface with a net negative charge.

Using an ionisation method, Takahashi [68] observed that, in ionised air, a sublimating ice surface acquires a negative charge and a growing one becomes positively charged with a potential difference of about 200 mV between the two cases. Caranti and Illingworth [10] repeated this experiment and failed to detect any difference in surface potential between a sublimating and growing ice surface. However, they reported a very large effect during riming where the rimed surface acquired a potential of a few hundred millivolt with respect to an unrimed ice surface. The potential increased as the temperature decreased reaching a saturation value of about  $-400\text{ mV}$  at  $-15^{\circ}\text{C}$ .

Buser and Aufdermaur [9] bounced frozen droplets off an ice target and concluded that the target charged negatively if it was sublimating and positively if it was growing from the vapour. This observation has subsequently been confirmed by several others [6, 12, 22, 32, 43]. Figure 2.6 shows a result obtained by Baker *et al.* [6] where a cloud of vapour-grown ice crystals was drawn past a stationary ice target in a wind tunnel. When the target was artificially warmed with respect to the air, it charged negatively and when it was cooled it charged positively. Caranti *et al.* [12] impacted frozen ice spheres of diameter  $100\text{ }\mu\text{m}$  at a speed of  $8\text{ m}\cdot\text{s}^{-1}$  on an ice target at various air temperatures. They noted that the target charged increasingly positive as it was cooled below the environmental temperature (Figure 2.7). An ice target warmed above its ambient temperature will be in a state of sublimation. Even in a supersaturated environment it is necessary to warm it by just  $1^{\circ}\text{C}$  at  $-10^{\circ}\text{C}$  and  $2^{\circ}\text{C}$  at  $-20^{\circ}\text{C}$  to make it sublimate. Thus, it follows that the negative charging of a warmed ice target exposed to rebounding collisions with ice crystals may be a consequence of its surface state and not temperature. Jayaratne [29] performed a series of experiments and showed that the sign of charging was not controlled by the temperature difference between the two ice particles, nor the direction of the temperature gradient in the ice on the target. Baker *et al.* [6]

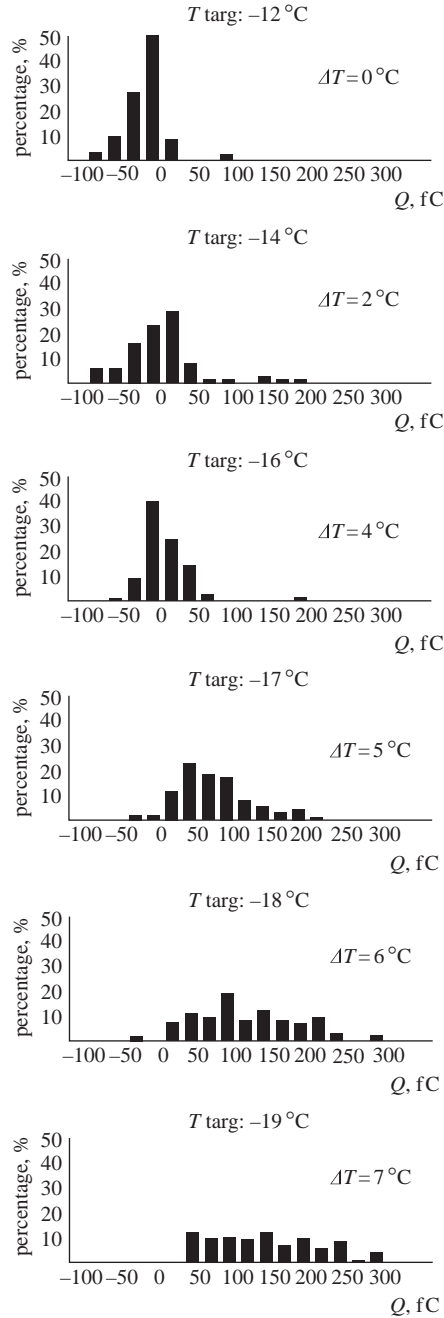


Figure 2.7 *Histograms showing the percentage of charging events of each sign and magnitude when an ice sphere of diameter  $100 \mu\text{m}$  impacted at a speed of  $8 \text{ m}\cdot\text{s}^{-1}$  on an ice target that was cooled with respect to the ambient temperature of  $-12^\circ\text{C}$ . The target charged mostly negatively at first but became increasingly positive as it was cooled towards  $-19^\circ\text{C}$  (from [ 12])*

suggested that the sign was controlled by the relative growth rates of the two particles with the faster growing particle acquiring the positive charge.

### 2.2.9 *The quasi-liquid layer theory*

Theoretical and experimental studies have shown that ice in equilibrium with the vapour has a disordered quasi-liquid layer at the ice–vapour interface. The thickness of this layer increases with temperature and also with growth rate from the vapour [15]. Baker and Dash [4] proposed an explanation for the relative growth rate dependence of charge transfer between colliding ice particles based on this phenomenon. Fletcher [19] showed that it was energetically favourable for water molecules in the liquid close to the water–vapour interface to orient themselves with the  $H^+$  ions pointing towards the vapour side. Such a preferred dipolar orientation would result in a drift of free negative ions towards the liquid–vapour interface in order to equalise the potential difference. Thus, ice would carry a net negative charge in the quasi-liquid layer. Baker and Dash [5] modified their hypothesis somewhat by suggesting that segregation effects at the solid–liquid interface may be more important than the dipolar orientation effect at the liquid–vapour interface. In general, if the molecular orientations near the solid–liquid interface were such as to provide a net negative charge at this interface, this negative charge would diffuse into the more polarisable liquid. Although the origin was different, each of the hypotheses could plausibly explain the presence of a net negative charge in the quasi-liquid layer on ice.

During the impact and separation of two ice particles it seems reasonable to assume that some mass would be exchanged between the quasi-liquid layers of the two particles. In general, mass would flow from the thicker layer (or the layer with the higher chemical potential) to the thinner (the layer with the lower chemical potential). Since the thickness of the quasi-liquid layer increases with temperature, the particle at the higher temperature would lose mass and negative charge to the colder particle and acquire a net positive charge. Further, the thickness of the layer increases with growth rate, so that the particle that was growing faster from the vapour would lose mass and negative charge to the slower growing particle and acquire a net positive charge. In the absence of any riming, ice particles growing from the vapour are slightly warmer than the environment due to the release of latent heat from the sublimating vapour. Similarly, sublimating ice particles are slightly colder than the environment owing to the latent heat carried away by the vapour. Thus, the Baker–Dash hypothesis was to explain the observed sign of charge transfer in each of the possible combinations where the two interacting ice particles were growing/sublimating, fast-growing/slow-growing and fast-sublimating/slow-sublimating. However, it should be noted that when one of the ice particles was cooled with respect to the ambient temperature and the other particle, it acquired a positive charge during the interaction. Similarly, an artificially warmed target acquired a negative charge. This suggests that the surface state of the particles was having a dominant effect on the thickness of the quasi-liquid layer over the temperature. Although it has not been experimentally established as yet, recent studies by Jayaratne [29] and Mason and Dash [46] indeed suggest that the sign of the charge transfer is overwhelmingly controlled by the relative growth rates between the two particles rather than temperature differences.

Supercooled water has a higher vapour pressure than ice at the same temperature. Thus the two cannot remain in equilibrium and in clouds both graupel and ice crystals will grow at the expense of the droplets. When a supercooled droplet comes into contact with and accretes on to a graupel pellet, the temperature of the droplet will initially shoot up to  $0^{\circ}\text{C}$  and then remain there until it has completely frozen, whence it will cool to the temperature of the graupel. During the time when it is at  $0^{\circ}\text{C}$ , a freezing droplet forms an intense vapour source bathing the surrounding dry graupel surface which will grow rapidly by vapour diffusion. Although ice crystals grow from the vapour supplied by the supercooled droplets in the cloud, areas around freezing droplets on the graupel surface will grow not only from the supercooled cloud droplets but also from the vapour supplied by the freezing droplets at  $0^{\circ}\text{C}$  (Figure 2.8). Baker *et al.* [6] showed that this latter term is expected to be dominant over a distance of several droplet diameters around a freezing droplet. Ice crystals bouncing off these rapidly growing areas are likely to charge the graupel positively in accordance with the Baker *et al.* hypothesis. If the cloud water content is high enough, riming may produce sufficient latent heat to warm the graupel surface sufficiently to cause sublimation. However, since droplets freeze at  $0^{\circ}\text{C}$ , whatever the surface temperature of graupel, the areas around freezing droplets would still be growing. Thus, on a graupel surface during riming, the expected picture would be many annular growing regions on an overall sublimating surface. It is interesting to note that Caranti *et al.* [12] found charging events of both signs at any given temperature (Figure 2.7). The probability of an ice crystal encountering a rapidly growing annular region around a freezing droplet is greater at higher cloud water contents because there will be more such sites. It will also be greater at higher temperatures because droplet freezing times decrease rapidly with decreasing temperature. Thus, the higher the temperature the better the chance of an impacting crystal finding an annular area around a still freezing droplet and charging the graupel positively. The Baker *et al.* hypothesis is therefore able to explain the dependence of charge sign on temperature and cloud water

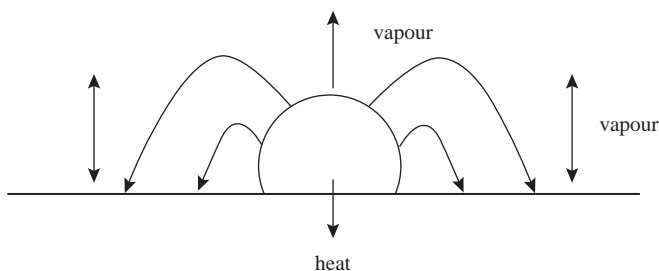


*Figure 2.8 Schematic diagram showing a droplet freezing on a graupel surface. Much of the latent heat released by riming droplets is conducted into the graupel substrate. At high cloud water contents (high riming rates) the heat absorbed may be high enough to raise the surface temperature of the graupel sufficiently above ambient to cause it to sublimate. However, the temperature of a droplet remains at  $0^{\circ}\text{C}$  while freezing and so forms an intense source of vapour to the annular area immediately surrounding a freezing droplet. Thus, a sublimating graupel surface may be scattered with many such growing spots*

content observed by Jayaratne *et al.* [32]. There are some minor discrepancies in different studies. For example, Takahashi [69] and Saunders *et al.* [60] found positive charging of graupel at low temperatures at low cloud water contents. Saunders and Peck [58] have attempted to explain these observations in terms of the Baker *et al.* hypothesis by considering the increased growth rate of the graupel surface owing to the reduced latent heat available from fewer droplets present at lower cloud water contents. Figure 2.9 compares the results of Jayaratne *et al.*

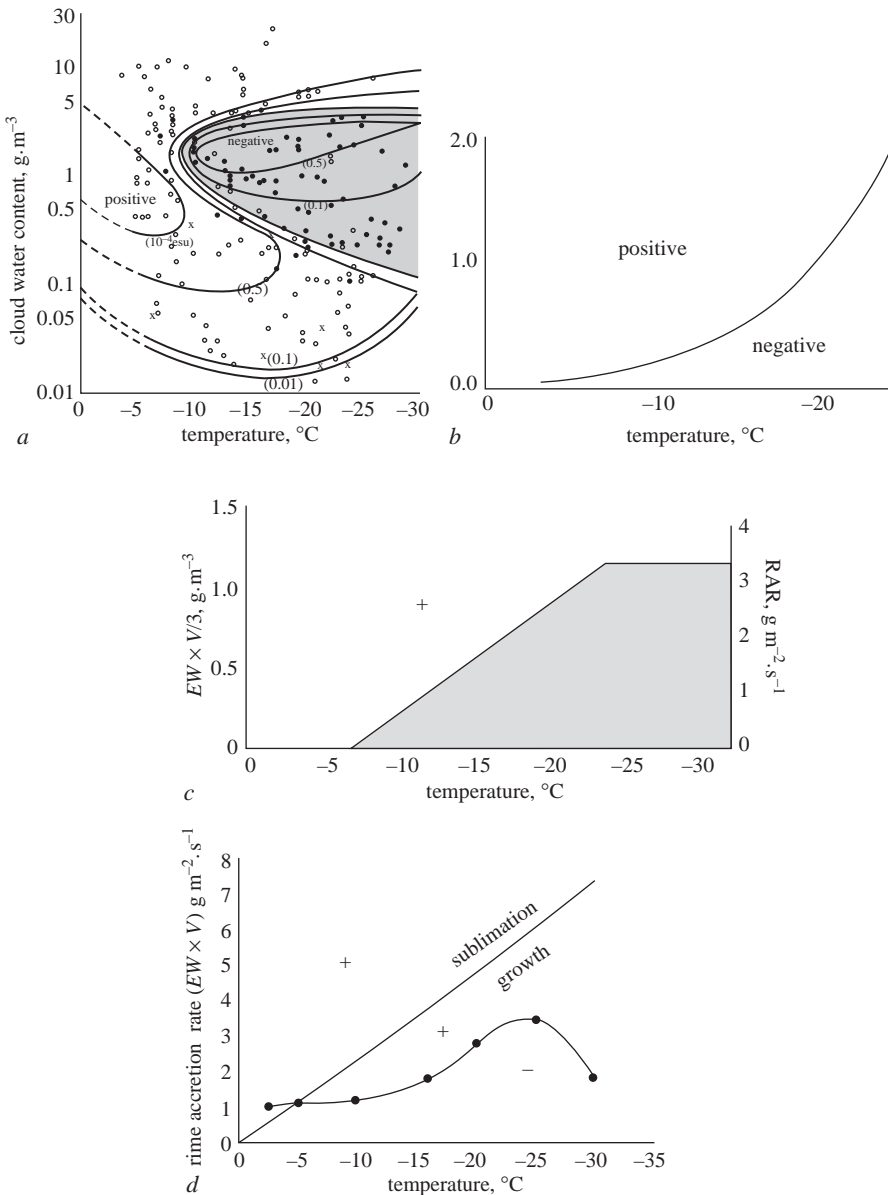


Figure 2.9 Charge sign reversal lines according to (a) Takahashi [69]; (b) Jayaratne *et al.* [32]; (c) Brooks *et al.* [8]; (d) Saunders and Peck [58]



[32], Takahashi [69], Brooks *et al.* [8] and Saunders and Peck [58], and shows that in all studies using clouds of ice crystals and supercooled droplets interacting with a graupel pellet, we see an overall pattern where the graupel is more likely to charge positively when the temperature or the cloud water content is high and negatively when these parameters are low in accordance with the Baker *et al.* hypothesis.

### 2.2.10 *Charging due to the fragmentation of ice*

Caranti *et al.* [12] studied individual collisions between 100  $\mu\text{m}$  diameter ice spheres and an ice target growing by vapour diffusion and showed that most charging events were accompanied by tiny frost fragments that were breaking off the target surface. The sign of charge acquired by the target was increasingly positive as its temperature was progressively decreased below ambient (Figure 2.7). The growing frost tips would be warmer than the substrate due to the latent heat generated at such points. This would give rise to an inwardly directed temperature gradient along frost fibres on the target surface. Caranti *et al.* suggested that breaking these protuberances across the temperature gradient would separate charge with the colder side, which would be the target in this case, acquiring the positive charge. They showed that reversing the temperature gradient reversed the charging sign as expected. Here, warming the target internally led to sublimation of the frost tips which cooled with respect to the substrate due to the latent heat released on sublimation. The sign of the charge transfer observed was explicable in terms of the thermoelectric theory but, as had been shown before, the observed magnitude of the charge separated was too high to be explained in terms of the theory. Caranti *et al.* proposed a modified hypothesis based on the breaking of hydrogen bonds in ice during the fracture process. It was assumed that the protons tunnelling back and forth across a double potential well in the temperature gradient had a slightly higher probability of remaining on the colder side as the fracture progressed, resulting in the observed sign of charge separation. Using a simplified calculation, they showed that the process could account for the magnitude of the charge observed.

Caranti *et al.* showed that the fragments breaking off were in fact carrying an equal and opposite charge to that acquired by the target. There seemed no doubt that their 100  $\mu\text{m}$  ice spheres impacting at a speed of  $8\text{ m}\cdot\text{s}^{-1}$  were capable of breaking frost fragments off the target. However, charge is transferred in experiments where the impacting particles are ice crystals no larger than 10  $\mu\text{m}$ . These have much lower energy than the 100  $\mu\text{m}$  ice spheres used by Caranti *et al.* and are quite unlikely to break any fragments. Griggs and Choulaton [26] showed experimentally that frost and rime protuberances on ice can be surprisingly strong. Glass beads of diameter 485  $\mu\text{m}$  required a minimum speed of about  $20\text{ m}\cdot\text{s}^{-1}$  to fracture even the most fragile of the rime deposits studied. Frost deposits grown on a target fractured more easily but still required beads of diameter 485  $\mu\text{m}$  at speeds of  $4\text{--}6\text{ m}\cdot\text{s}^{-1}$ . Jayaratne *et al.* [33] detected no ice fragments when they impacted frost or rime-covered targets with small ice crystals of size  $10\text{--}20\text{ }\mu\text{m}$  and light lycopodium spores. However, when these particles were replaced with 250  $\mu\text{m}$  grains of sand, many fragments were observed. They concluded that, although it may occur, fragmentation was not a necessary requirement for charge transfer during ice–ice collisions.

### 2.3 Riming experiments

The Baker *et al.* hypothesis successfully explains the sign of the charge transfer between two interacting ice particles in terms of their relative growth rates in the absence of riming. Experiments where the target was allowed to rime at the same time require further explanation.

The first simulated riming experiment was conducted by Reynolds *et al.* [56]. They whirled an ice-covered metal sphere through a cloud of supercooled droplets and ice crystals in a chest freezer which could be cooled down to  $-25^{\circ}\text{C}$ . The sphere acquired an electric charge that was negative when the cloud water content was high and positive when it was low. In the latter case, the sign could be reversed to negative by heating the sphere with a lamp.

Takahashi [69] whirled a 3 mm diameter rod through a cloud of supercooled droplets and vapour-grown ice crystals at a speed of  $9\text{ m}\cdot\text{s}^{-1}$  and showed that the sign and magnitude of the charge acquired by the rod was controlled by the temperature and the cloud water content (Figure 2.10). At temperatures higher than about  $-10^{\circ}\text{C}$  the rod charged positively at all cloud water contents. At lower temperatures, the sign was positive at high and low cloud water contents but negative in an intermediate range as shown in the figure. In a similar study, Jayaratne *et al.* [32] showed that a simulated graupel pellet subject to ice crystal interactions charged positively at higher temperatures and higher cloud water contents and negatively at

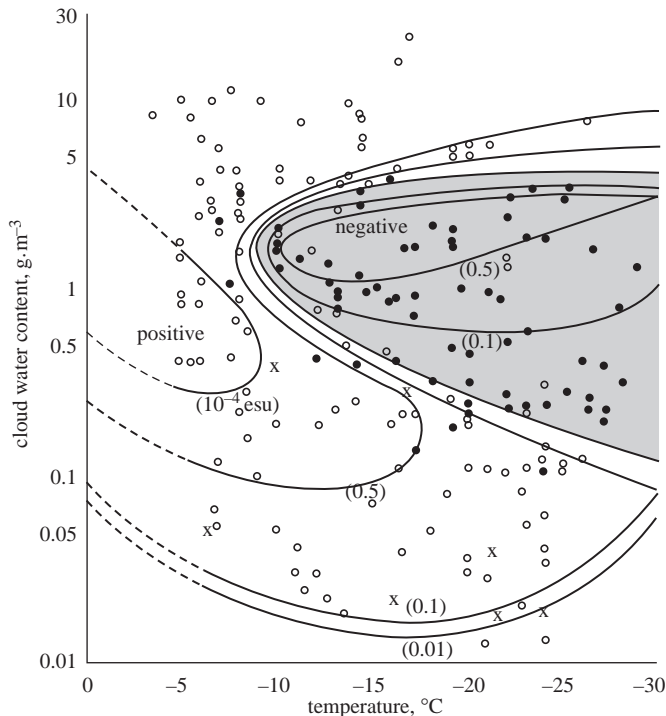


Figure 2.10 The charge acquired per crystal rebounding event by a simulated graupel particle moving through a mixed cloud at  $9\text{ m}\cdot\text{s}^{-1}$  shown on a cloud water content versus temperature diagram (from [69])

lower temperatures and lower cloud water contents (Figure 2.11). At a cloud water content of  $1 \text{ g}\cdot\text{m}^{-3}$ , the charge sign reversal temperature was about  $-20^\circ\text{C}$ . Baker *et al.* [6] extended this study down to  $-35^\circ\text{C}$  and found a charge sign reversal temperature of  $-18^\circ\text{C}$  (Figure 2.12). It is clear from Figure 2.11 that the reversal temperature was higher at lower cloud water contents. At  $0.2 \text{ g}\cdot\text{m}^{-3}$  the reversal temperature was close to  $-10^\circ\text{C}$ . These observations were used to explain the existence of the classical tripolar charge structure in thunderclouds [63]. At temperatures higher than the reversal temperature, graupel would acquire a net positive charge and the rebounding crystals would carry the negative charge in the updraughts. In the

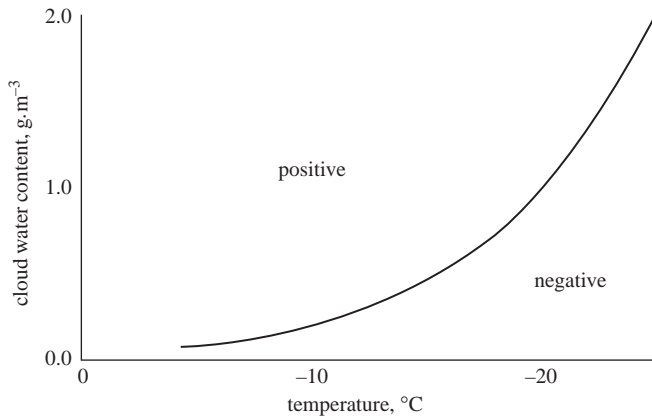


Figure 2.11 *The charge acquired per crystal rebounding event by a simulated graupel particle moving through a mixed cloud at  $3 \text{ m}\cdot\text{s}^{-1}$  shown on a cloud water content versus temperature diagram (from [32])*

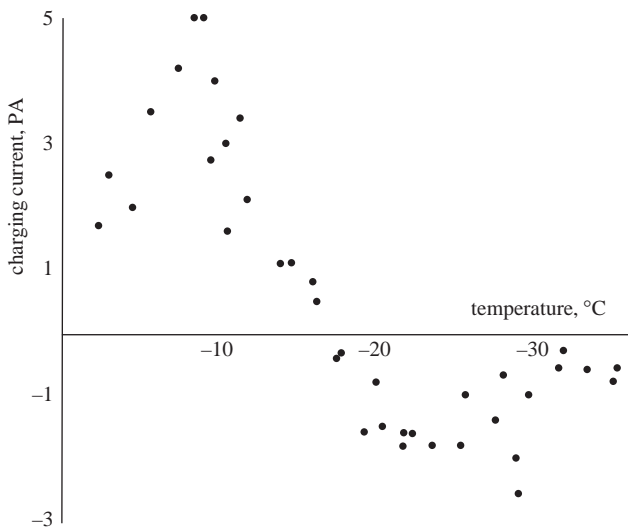


Figure 2.12 *The charging current to the graupel as a function of temperature according to Jayaratne *et al.* [32] extended by Baker *et al.* [6]. Cloud water content =  $0.3 \text{ g}\cdot\text{m}^{-3}$ , mean crystal size =  $40 \mu\text{m}$ , crystal concentration =  $50 \text{ ml}^{-1}$ , impact speed =  $3 \text{ m}\cdot\text{s}^{-1}$*

upper parts of the cloud at lower temperatures, the crystals would carry a positive charge to the top of the cloud forming the upper positive charge centre and the falling graupel would carry a negative charge, augmented by the ice crystals from below to form the main negative charge centre at the reversal temperature.

## 2.4 Droplet size effect

Jayaratne and Saunders [31] showed that, in addition to the temperature and cloud water content, the droplet size spectrum played an important role in determining the sign of the charge separated during ice crystal–graupel collisions. The Jayaratne *et al.* [32] experiments were carried out with a cloud of droplets of mean diameter 10  $\mu\text{m}$  extending up to about 30  $\mu\text{m}$ . Jayaratne and Saunders [31] repeated this study with a droplet size spectrum shifted to smaller sizes with a maximum droplet diameter of less than 4  $\mu\text{m}$ . They showed that at  $-10^\circ\text{C}$  the graupel now charged negatively. Jayaratne [30] noted that, with such a spectrum, the corresponding charge–temperature dependence was startlingly different to that observed with the normal droplet size spectrum with four charge sign reversal temperatures instead of the single reversal temperature observed by Jayaratne *et al.* [32] and Takahashi [69] using larger droplets (Figure 2.13). Saunders *et al.* [59] noted a similar trend, with smaller droplets giving negative charged graupel at  $-10^\circ\text{C}$  and at  $-20^\circ\text{C}$  at a comparable cloud water content of about  $1\text{ g}\cdot\text{m}^{-3}$ . These observations do not allow us to conclude that larger/smaller droplets favour positive/negative charging of graupel. Although it may be true at  $-10^\circ\text{C}$  and at  $-20^\circ\text{C}$ , the opposite occurs at  $-15^\circ\text{C}$  and at  $-30^\circ\text{C}$ . The picture became more complicated when Avila *et al.* [2, 3] reported negative charging of graupel at all temperatures when the droplet size spectrum was shifted to sizes significantly larger than that used by Jayaratne *et al.* [32] (Figure 2.14). This behaviour is puzzling but not unexpected when we consider what a change in the droplet size can do to the relative growth rate between a riming graupel and the vapour-grown ice crystals in the cloud.

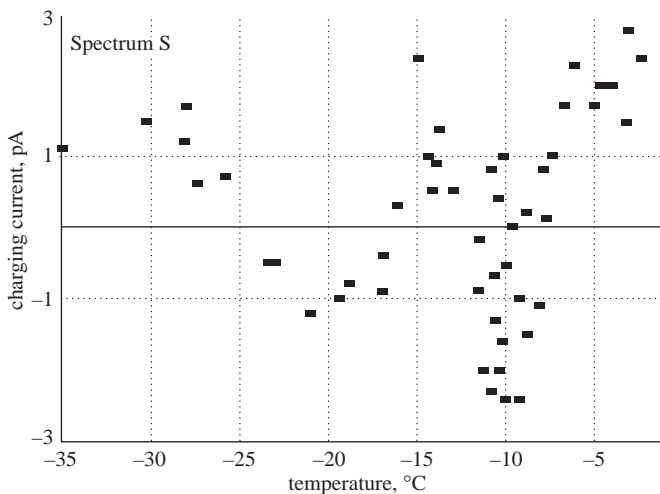


Figure 2.13 The temperature dependence of the graupel charging current with a smaller droplet size spectrum (from [3])

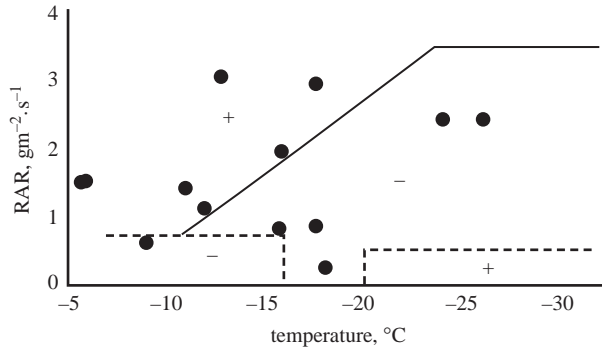


Figure 2.14 *The charge sign zones as a function of rime accretion rate (RAR) and temperature from Saunders et al. [60] and Brooks et al. [8] together with the negative charging events (solid circles) found by Avila et al. [2] using large spray droplets*

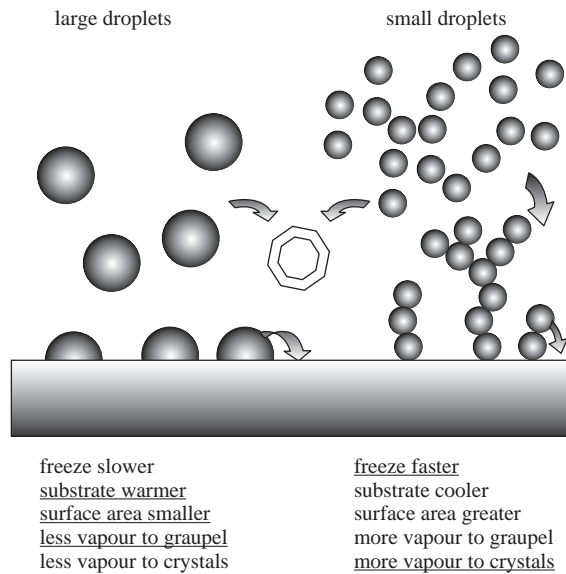
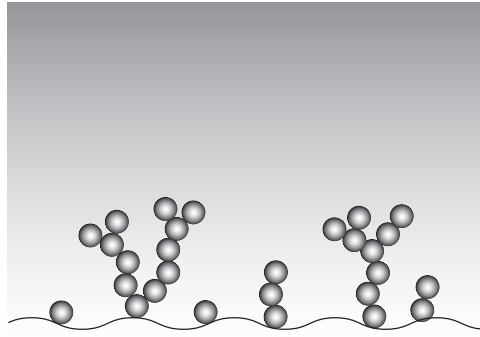


Figure 2.15 *Summary of the possible effects of droplet size on the relative growth rates of the two interacting ice particles. Cases favouring negative charging of graupel are underlined. See text for explanation*

The droplet size affects the relative growth rates of the two particles in several ways and these are summarised in Figure 2.15. We shall consider these in turn. Some of these have been discussed in Avila *et al.* [2]:

- (i) Large droplets take longer to freeze than smaller droplets and so allow the crystals a longer time to find a fast-growing area on the graupel surface. Thus, according to the Baker *et al.* [6] relative growth rates hypothesis, this effect predicts positive/negative charging of the graupel with larger/smaller droplets.
- (ii) During accretion, larger droplets tend to spread more than smaller droplets and freeze as hemispheres; smaller droplets freeze as spheres very often showing a buildup into a chain-like structure as shown in Figure 2.16 [40].



*Figure 2.16 Schematic diagram showing the structure of rime formed by small droplets. Note the chain-like growth which restricts flow of latent heat into the graupel substrate*

The contact area between the droplet and the graupel will increase with droplet size. This allows a greater fraction of the latent heat to conduct into the rime substrate for larger droplets than for smaller droplets. Thus, at the same ambient temperature and rime accretion rate, larger droplets will make a graupel particle warmer and, hence, allow it to grow slower than when the droplet size was smaller. This predicts negative/positive graupel charging with larger/smaller droplets.

- (iii) A number of small droplets (of the same mass as one large droplet) will present a larger fast-growing area on the graupel surface than the larger droplet. Thus, at the same temperature and rime accretion rate, impacting crystals have a greater chance of finding a faster growing area when the droplets are smaller than when they are larger. The prediction due to this effect is again negative/positive graupel with larger/smaller droplets.
- (iv) A large droplet has a smaller surface area than several smaller droplets of the identical total mass. Thus, at the same temperature and rime accretion rate, the large droplet is likely to provide less vapour to the graupel surface than all the smaller droplets together. This effect predicts negative/positive graupel charging with larger/smaller droplet sizes.
- (v) Finally, let us consider what effect the cloud droplet size could have on the growth rate of the crystals. Marshall and Langleben [44] showed that ice crystal growth was enhanced when there were more droplets in the cloud. At the same cloud water content, smaller droplets present a greater surface area and, thus, a greater vapour flux to the crystals than larger droplets. Crystals would grow faster in a cloud of smaller droplets than larger droplets. This would still be true if we keep the rime accretion rate the same in the presence of both droplet size clouds because smaller droplets have a lower collision efficiency than larger droplets and would need to be present in even larger numbers to maintain the same rime accretion rate. So, whether it was at the same cloud water content or the same rime accretion rate, crystals would grow faster when the droplet size was smaller. Faster growing crystals are likely to charge the graupel more negatively according to the relative growth rate hypothesis, so our prediction in this case is positive/negative graupel charging with larger/smaller droplets.

So, we see that the droplet size spectrum plays a complex role in determining the relative growth rate of the two particles. A change in any one or more of the above conditions may flip the sign of charging. Predicting the exact sign of charging under a given set of conditions becomes extremely difficult. The matter may be further complicated if it is the shape of the droplet size spectrum rather than just the mean droplet size that may be relevant in determining the sign of charging. For example, a normal size distribution and a bimodal distribution can have the same mean droplet size but the resulting charging sign could well be very different. This presents a major hurdle to numerical modellers of thunderstorm electrification. Representing the droplet size spectrum in a model requires multidimensional parameters that are very difficult to manipulate.

## 2.5 Effect of chemical impurities

Many laboratory workers have shown that the presence of chemical impurities has a profound effect on the sign of the charge transfer during ice–ice collisions. In general, the presence of trace quantities of NaCl in the rime made the graupel charge negatively, but most ammonium salts made it charge positively [32, 41, 56, 69]. Jayaratne *et al.* [32] investigated the effect of temperature and showed that the magnitude of the charging generally increased sharply as the temperature was decreased (Figure 2.17). At present, there is no plausible explanation for these observations except a similarity with the Workman–Reynolds effect (see section 2.2.6) where NaCl and ammonium salts indeed produced potentials of opposite

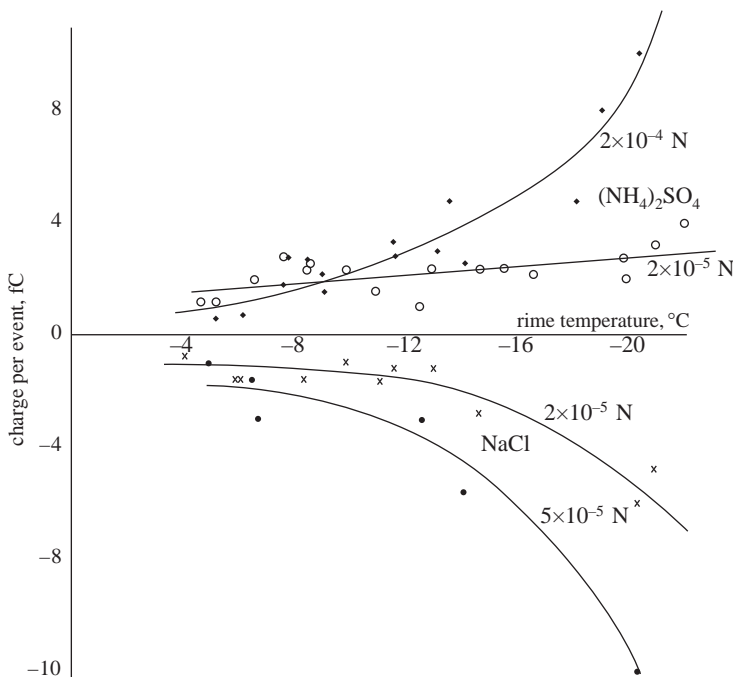


Figure 2.17 *The charge per crystal collision as a function of temperature when the droplets in the cloud contained dilute ammonium sulphate and sodium chloride solution (from [32])*

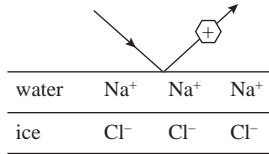


Figure 2.18 Schematic diagram showing the separation of ions near an ice surface contaminated with sodium chloride

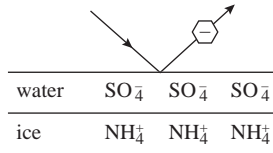


Figure 2.19 Schematic diagram showing the separation of ions near an ice surface contaminated with ammonium sulphate

signs. However, the Workman–Reynolds potentials decayed as soon as the freezing ended. The probability of an ice crystal impacting on a still-freezing droplet on the graupel surface is negligibly small and, so, it becomes difficult to relate the sign of the charge separation to the Workman–Reynolds potentials. Caranti and Illingworth [11] attempted to measure a possible remnant potential on a rimed surface. They found no such potential once the supercooled droplets had completely frozen. Considering the resolution of their measurements in time, they concluded that if there was such a potential, it would have disappeared within a fraction of a second – too short an interval of time to have an appreciable effect on the charge transfer due to ice crystal impacts. However, we do know that ions have different mobilities in ice and water. For example, Cl<sup>-</sup> ions diffuse into ice more easily than Na<sup>+</sup> ions. Thus, an ice surface contaminated with NaCl will have an excess positive ion concentration near its surface on the quasi-liquid layer (Figure 2.18). Impacting ice crystals may remove some of this positively charged mass off the quasi-liquid layer, leaving the graupel negative. Also, NH<sub>4</sub><sup>+</sup> ions are readily incorporated into the ice. Following the same argument as for NaCl we could expect a graupel particle containing ammonium salts to acquire a net positive charge during ice crystal interactions (Figure 2.19).

The role played by chemical impurities in determining the sign and magnitude of the charge separated during rebounding collisions between ice particles remains a major mystery and so far it has not been possible to explain it in terms of any of the existing hypotheses. Furthermore, it is reasonable to imagine that thunderstorms in various geographical locations must contain cloud condensation nuclei of varying chemical content such as the excess salt nuclei found in coastal and maritime clouds. However, thunderstorms all over the world show a remarkably similar charge structure. These questions pose a major difficulty for explaining the electrification of thunderstorms in terms of the noninductive ice–ice charging mechanism.

## References

- [1] AUFDERMAUR, A.N., and JOHNSON, D.A.: ‘Charge separation due to riming in an electric field’, *Q. J. R. Meteorol. Soc.*, 1972, **98**, pp. 369–382



- [2] AVILA, E.E., CARANTI, G.M., and CASTELLANO, N.E.: 'Laboratory studies of the influence of cloud droplet size on charge transfer during crystal-graupel collisions', *J. Geophys. Res.*, 1998, **103**, pp. 8985–8996
- [3] AVILA, E.E., CASTELLANO, N.E., and SAUNDERS, C.P.R.: 'Effects of cloud droplet spectra on the average surface temperature of ice accreted on fixed cylindrical collectors', *Q. J. R. Meteorol. Soc.*, 1999, **125**, pp. 1059–1074
- [4] BAKER, M.B., and DASH, J.G.: 'Charge transfer in thunderstorms and the surface melting of ice', *J. Cryst. Growth*, 1989, **97**, pp. 770–776
- [5] BAKER, M.B., and DASH, J.G.: 'Mechanism of charge transfer between colliding ice particles in thunderstorms', *J. Geophys. Res.*, 1994, **99**, pp. 10621–10626
- [6] BAKER, B., BAKER, M.B., JAYARATNE, E.R., LATHAM, J., and SAUNDERS, C.P.R.: 'The influence of diffusional growth rate on the charge transfer accompanying rebounding collisions between ice crystals and hailstones', *Q. J. R. Meteorol. Soc.*, 1987, **113**, pp. 1193–1215
- [7] BROOKS, I.M., and SAUNDERS, C.P.R.: 'An experimental investigation of the inductive mechanism of thunderstorm electrification'. *Proceedings of the Ninth International Conference on Atmospheric Electricity*, St Petersburg, Russia, 1992, pp. 92–95
- [8] BROOKS, I.M., SAUNDERS, C.P.R., MITZEVA, R.P., and PECK, S.L.: 'The effect on thunderstorm charging of the rate of rime accretion by graupel', *Atmos. Res.*, 1997, **43**, pp. 277–295
- [9] BUSER, O., and AUFDERMAUR, A.N.: 'Electrification by collisions of ice particles on ice or metal targets', in DOLEZALEK, H., and REITER, R. (Eds.): *Electrical Processes in Atmospheres* (Steinkopff, Darmstadt, 1977), pp. 294–301
- [10] CARANTI, J.M., and ILLINGWORTH, A.J.: 'Surface potentials of ice and thunderstorm charge separation', *Nature*, 1980, **284**, pp. 44–46
- [11] CARANTI, J.M., and ILLINGWORTH, A.J.: 'Transient Workman–Reynolds freezing potentials', *J. Geophys. Res.*, 1983, **88**, pp. 8483–8489
- [12] CARANTI, G.M., AVILA, E.E., and RÉ, M.A.: 'Charge transfer during individual collisions in ice growing from vapour deposition', *J. Geophys. Res.*, 1991, **96**, pp. 15365–15375
- [13] CHALMERS, J.A.: *Atmospheric Electricity* (Pergamon Press, 1963, 2nd edn.)
- [14] CHIU, C.S.: 'Numerical study of cloud electrification in an axisymmetric, time-dependent cloud model', *J. Geophys. Res.*, 1978, **83**, pp. 5025–5049
- [15] DASH, J.G.: 'Surface melting', *Contemp. Phys.*, 1989, **30**, pp. 89–100
- [16] DINGER, J.E., and GUNN, R.: 'Electrical effects associated with a change of state of water', *Terr. Magn. and Atmos. Elect.*, 1946, **51**, pp. 477–494
- [17] DRAKE, J.C.: 'Electrification accompanying the melting of ice particles', *Q. J. R. Meteorol. Soc.*, 1968, **94**, pp. 176–191
- [18] ELSTER, J., and GEITEL, H.: 'Zur Influenztheorie Der Niederschlagsselektrizität', *Phys. Z.*, 1913, **14**, p. 1287
- [19] FLETCHER, N.H.: 'Surface structure of water and ice II: A revised model', *Philos. Mag.*, 1968, **18**, pp. 1287–1300
- [20] FOSTER, H.: 'An unusual observation of lightning', *Bull. Am. Meteorol. Soc.*, 1950, **31**, pp. 140–141

- [21] GASKELL, W.: 'A laboratory study of the inductive theory of thunderstorm electrification', *Q. J. R. Meteorol. Soc.*, 1981, **107**, pp. 955–966
- [22] GASKELL, W., and ILLINGWORTH, A.J.: 'Charge transfer accompanying individual collisions between ice particles and its role in thunderstorm electrification', *Q. J. R. Meteorol. Soc.*, 1980, **106**, pp. 841–854
- [23] GASKELL, W., ILLINGWORTH, A.J., LATHAM, J., and MOORE, C.B.: 'Airborne studies of electric fields and the charge and size of precipitation elements in thunderstorms', *Q. J. R. Meteorol. Soc.*, 1978, **104**, pp. 447–460
- [24] GROSS, G.W.: 'Role of relaxation and contact times in charge separation during collision of precipitation particles with ice targets', *J. Geophys. Res.*, 1982, **87**, pp. 7170–7178
- [25] GRENET, G.: 'Essai d'explication de la charge électrique des nuages d'orages', *Ann. Geophys.*, 1947, **3**, pp. 306, 307
- [26] GRIGGS, D.J., and CHOULARTON, T.W.: 'A laboratory study of secondary ice particle production by the fragmentation of rime and vapour-grown ice crystals', *Q. J. R. Meteorol. Soc.*, 1986, **112**, pp. 149–163
- [27] ILLINGWORTH, A.J., and CARANTI, J.M.: 'Ice conductivity restraints on the inductive theory of thunderstorm electrification', *J. Geophys. Res.*, 1985, **90**, pp. 6033–6039
- [28] IRIBARNE, J.V., and MASON, B.J.: 'Electrification accompanying the bursting of bubbles in water and dilute aqueous solutions', *Trans. Faraday Soc.*, 1967, **63**, pp. 2234–2245
- [29] JAYARATNE, E.R.: 'Temperature gradients in ice as a charge generation process in thunderstorms', *Atmos. Res.*, 1993, **29**, pp. 247–260
- [30] JAYARATNE, E.R.: 'Possible laboratory evidence for multipole electric charge structures in thunderstorms', *J. Geophys. Res.*, 1998, **103**, pp. 1871–1878
- [31] JAYARATNE, E.R., and SAUNDERS, C.P.R.: 'Thunderstorm electrification: The effect of cloud droplets', *J. Geophys. Res.*, 1985, **90**, pp. 13063–13066
- [32] JAYARATNE, E.R., SAUNDERS, C.P.R., and HALLETT, J.: 'Laboratory studies of the charging of soft-hail during ice crystal interactions', *Q. J. R. Meteorol. Soc.*, 1983, **109**, pp. 609–630
- [33] JAYARATNE, E.R., PECK, S.L., and SAUNDERS, C.P.R.: 'Comment on "a laboratory study of static charging by fracture in ice growing by riming" by AVILA, E.E., and CARANTI, G.M.', *J. Geophys. Res.*, 1996, **101**, pp. 9533–9535
- [34] JENNINGS, S.G.: 'Charge separation due to water drop and cloud droplet interactions in an electric field', *Q. J. R. Meteorol. Soc.*, 1975, **101**, pp. 227–233
- [35] KREHBIEL, P.R., BROOK, M., and McCRRORY, R.A.: 'An analysis of the charge structure of lightning discharges to ground', *J. Geophys. Res.*, 1979, **84**, pp. 2432–2456
- [36] LATHAM, J., and MASON, B.J.: 'Electric charge transfer associated with temperature gradients in ice', *Proc. R. Soc., Ser. A*, 1961, **260**, pp. 523–536
- [37] LATHAM, J., and MASON, B.J.: 'Generation of electric charge associated with the formation of soft hail in thunderclouds', *Proc. R. Soc., Ser. A*, 1961, **260**, pp. 537–549
- [38] LATHAM, J., and MASON, B.J.: 'Electrical charging of hail pellets in a polarizing electric field', *Proc. R. Soc., Ser. A*, 1962, **266**, pp. 387–401

- [39] MACCREADY, P.B., Jr., and PROUDFIT, A.: 'Observations of hydrometeor charge evolution in thunderstorms', *Q. J. R. Meteorol. Soc.*, 1965, **91**, pp. 44–53
- [40] MACKLIN, W.C.: 'The density and structure of ice formed by accretion', *Q. J. R. Meteorol. Soc.*, 1962, **88**, pp. 30–50
- [41] MAGONO, C., and TAKAHASHI, T.: 'On the electrical phenomena during riming and glazing in natural supercooled clouds', *J. Meteorol. Soc. Japan*, 1963, **41**, pp. 71–81
- [42] MARSH, S.J., and MARSHALL, T.C.: 'Charged precipitation measurements before the first lightning flash in a thunderstorm', *J. Geophys. Res.*, 1993, **98**, pp. 16605–16611
- [43] MARSHALL, B.J.P., LATHAM, J., and SAUNDERS, C.P.R.: 'A laboratory study of charge transfer accompanying the collision of ice crystals with a simulated hailstone', *Q. J. R. Meteorol. Soc.*, 1978, **104**, pp. 163–178
- [44] MARSHALL, J.S., and LANGLEBEN, M.P.: 'A theory of snow crystal habit and growth', *J. Meteorol.*, 1954, **11**, pp. 104–120
- [45] MARSHALL, T.C., and WINN, W.P.: 'Measurements of charged precipitation in a New Mexico thunderstorm: Lower positive charge centers', *J. Geophys. Res.*, 1982, **87**, pp. 7141–7157
- [46] MASON, B., and DASH, J.: 'An experimental study of charge and mass transfer during ice contact interactions'. *Proceedings of the 11th International Conference on Atmospheric Electricity*, Guntersville, AL, USA, 1999, pp. 264–267
- [47] MASON, B.J.: 'A critical examination of theories of charge generation in thunderstorms', *Tellus*, 1953, **5**, pp. 446–460
- [48] MASON, B.J.: 'The physics of the thunderstorm', *Proc. R. Soc., Ser. A*, 1972, **327**, pp. 433–466
- [49] MATHEWS, J.B., and MASON, B.J.: 'Electrification accompanying melting of snow and ice', *Q. J. R. Meteorol. Soc.*, 1963, **89**, pp. 376–380
- [50] MOORE, C.B., and VONNEGUT, B.: 'The thundercloud', in GOLDE, R.H. (Ed.): *Lightning, vol. 1: Physics of Lightning* (Academic Press, San Diego, CA, 1977) pp. 51–98
- [51] MOORE, C.B., VONNEGUT, B., STEIN, B.A., and SURVILAS, H.J.: 'Observations of electrification and lightning in warm clouds', *J. Geophys. Res.*, 1960, **65**, pp. 1907–1910
- [52] MUHLER-HILLEBRAND, D.: 'Charge generation in thunderclouds by collision of ice crystals with graupel falling through a vertical electric field', *Tellus*, 1954, **6**, pp. 367–381
- [53] PALUCH, I.R., and SARTOR, J.D.: 'Thunderstorm electrification by the inductive charging mechanism: I. Particle charges and electric fields', *J. Atmos. Sci.*, 1973, **30**, pp. 1166–1173
- [54] PIETROWSKI, E.L.: 'An observation of lightning in warm clouds', *J. Meteorol.*, 1960, **17**, pp. 562–563
- [55] PRUPPACHER, H.R., and KLETT, J.D.: *Microphysics of Clouds and Precipitation* (D. Reidel, Dordrecht, Holland, 1997)
- [56] REYNOLDS, S.E., BROOK, M., and GOURLEY, M.F.: 'Thunderstorm charge separation', *J. Meteorol.*, 1957, **14**, pp. 426–436
- [57] SARTOR, J.D.: 'The role of particle interactions in the distribution of electricity in thunderstorms', *J. Atmos. Sci.*, 1967, **24**, pp. 601–615

- [58] SAUNDERS, C.P.R., and PECK, S.L.: 'Laboratory studies of the influence of rime accretion rate on charge transfer during crystal/graupel collisions', *J. Geophys. Res.*, 1998, **103**, pp. 13949–13956
- [59] SAUNDERS, C.P.R., AVILA, E.E., PECK, S.L., CASTELLANO, N.E., and AGUIRRE VARELA, G.G.: 'Vapour and heat supply to riming graupel: Effect on charging'. *Proceedings of the 11th International Conference on Atmospheric Electricity*, Guntersville, AL, USA, 1999, pp. 268–271
- [60] SAUNDERS, C.P.R., KEITH, W.D., and MITZEVA, R.P.: 'The effect of liquid water on thunderstorm charging', *J. Geophys. Res.*, 1991, **96**, pp. 11007–11017
- [61] SCOTT, W.D., and LEVIN, Z.: 'A stochastic electrical model of an infinite cloud: Charge generation and precipitation development', *J. Atmos. Sci.*, 1975, **32**, pp. 1814–1828
- [62] SHEPHERD, T.R., RUST, W.D., and MARSHALL, T.C.: 'Electric fields and charges near 0°C in stratiform clouds', *Mon. Weather Rev.*, 1996, **124**, pp. 919–938
- [63] SIMPSON, G.C., and SCRASE, F.J.: 'The distribution of electricity in thunderclouds', *Proc. R. Soc., Ser. A*, 1937, **161**, pp. 309–352
- [64] STANDLER, R.B., and WINN, W.P.: 'Effects of coronae on electric fields beneath thunderstorms', *Q. J. R. Meteorol. Soc.*, 1979, **105**, pp. 285–302
- [65] STOLZENBURG, M., RUST, W.D., and MARSHALL, T.C.: 'Electrical structure in thunderstorm convective regions 2: Isolated storms', *J. Geophys. Res.*, 1998, **103**, pp. 14079–14096
- [66] TAKAHASHI, T.: 'Electric potential of a rubbed ice surface', *J. Atmos. Sci.*, 1969, **26**, pp. 1259–1265
- [67] TAKAHASHI, T.: 'Electric potential of liquid water on an ice surface', *J. Atmos. Sci.*, 1969, **26**, pp. 1253–1258
- [68] TAKAHASHI, T.: 'Electrification of growing ice crystals', *J. Atmos. Sci.*, 1973, **30**, pp. 1220–1224
- [69] TAKAHASHI, T.: 'Riming electrification as a charge generation mechanism in thunderstorms', *J. Atmos. Sci.*, 1978, **35**, pp. 1536–1548
- [70] VONNEGUT, B.: 'Possible mechanism for the formation of thunderstorm electricity', *Bull. Am. Meteorol. Soc.*, 1953, **34**, pp. 378–381
- [71] VONNEGUT, B.: 'Some facts and speculations concerning the origin and role of thunderstorm electricity', *Meteorol. Monogr.*, 1963, **5**, pp. 224–241
- [72] WILLIAMS, E.R.: 'The role of ice in the electrification and dynamics of thunderstorms'. Conference on *Cloud physics*, American Meteorological Society, San Francisco, USA, 1990
- [73] WILSON, C.T.R.: 'Some thundercloud problems', *J. Franklin Inst.*, 1929, **208**, pp. 1–12
- [74] WINN, W.P., and BYERLEY, L.G.: 'Electric field growth in thunderclouds', *Q. J. R. Meteorol. Soc.*, 1975, **101**, pp. 979–994
- [75] WORKMAN, E.J., and REYNOLDS, S.E.: 'Electrical phenomena occurring during the freezing of dilute aqueous solutions and their possible relationship to thunderstorm electricity', *Phys. Rev.*, 1950, **78**, pp. 254–259
- [76] WORMELL, T.W.: 'Atmospheric electricity: Some recent trends and problems', *Q. J. R. Meteorol. Soc.*, 1953, **79**, p. 3
- [77] ZIV, A., and LEVIN, Z.: 'Thundercloud electrification: Cloud growth and electrical development', *J. Atmos. Sci.*, 1974, **31**, pp. 1652–1661



---

*Chapter 3*

**Mechanism of electrical discharges**

*Vernon Cooray*

---

### **3.1 Introduction**

The experiments performed by researchers in different countries, notably South Africa, England, Switzerland and the United States, during the last 60 years have greatly advanced our knowledge concerning the mechanism of lightning flashes. However, many pieces of the puzzle pertinent to the mechanism of lightning flashes are still missing and many of the theories put forth as explanation of its mechanism are mainly of qualitative nature. The reason for this slow progress is the impossibility of studying lightning flashes under controlled laboratory conditions. On the other hand, the mechanism of the electric spark, which could be studied under controlled conditions, may guide the researchers in their quest for understanding the mechanism of lightning flashes and creating more advanced theories of the phenomena. After all, it is the observed similarities between the small laboratory sparks and lightning discharges that forced Benjamin Franklin to conclude that lightning flash is a manifestation of electricity. This chapter is devoted to a description of the mechanism of laboratory sparks.

### **3.2 Basic definitions**

#### *3.2.1 Mean free path and cross section*

An electron moving in a medium consisting of other atoms can make either elastic or inelastic collisions. An elastic collision is one in which the total kinetic energy of the colliding particles is conserved during the collision. An inelastic collision is a collision in which part or all of the kinetic energy of the colliding particles is converted to potential energy of one or more colliding particles. An inelastic collision between an electron and an atom could lead to the attachment of the electron to the atom, to the excitation of the atom or to the ionisation of the atom. The atomic excitations could be electronic, vibrational or rotational.

The distance an electron travels between elastic collisions is called the free path for elastic collision. Similarly, one can define the free paths for excitation and ionisation collisions. The average values of these free paths are defined as mean free paths for respective collisions (i.e. elastic, excitation, ionisation etc.).

The mean free path for a given type of collision can be described by the equation

$$\lambda = \frac{1}{n\sigma} \tag{3.1}$$

where  $n$  is the atomic or molecular number density of gas and  $\sigma$ , which has the dimension of area, is known as the microscopic collision cross section, and the quantity  $n\sigma$  is known as macroscopic collision cross section of the process under consideration.

One can define a collision cross section for elastic collisions, excitation collisions or ionisation collisions. Let  $\sigma_t$  and  $Q_t$  be, respectively, the gross (total) *microscopic* and gross (total) *macroscopic* cross sections for an electron to undergo some reaction regardless of type in traversing a gaseous medium. Then one can write

$$\sigma_t = \sigma_e + \sigma_{ex} + \sigma_{ion} + \sigma_a + \sigma_{oth} \quad (3.2)$$

and the gross (total) *macroscopic* cross section is given by

$$Q_t = Q_e + Q_{ex} + Q_{ion} + Q_a + Q_{oth} \quad (3.3)$$

where the subscripts stand as follows: *e*: elastic, *ex*: excitation, *ion*: ionisation, *a*: attachment and *oth*: other processes. Note that  $Q_{ex}$  refers to electronic excitations, vibrational excitations or rotational excitations.

If  $p_x$  is the probability that a collision will result in the process  $x$  then

$$p_x = Q_x/Q_t \quad (3.4)$$

where the subscript  $x$  stands for either *e*, *ex*, *ion*, *a*, or *oth*. Then (3.3) can also be written as

$$Q_t = (p_e + p_{ex} + p_{ion} + p_a + p_{oth})Q_t \quad (3.5)$$

### 3.2.2 *Drift velocity and mobility*

If given sufficient time two types of particles in a medium will reach thermal equilibrium and their motion can be described by the Boltzmann equation [1]. However, in the case of charged particles immersed in a background electric field the situation may become much more complicated. The electric field exerts a force on the charged particles in a direction parallel to the electric field. As a result, in addition to the random motion the charge particles will drift either in the direction of the electric field or opposite to it depending on the sign of their charge. In a vacuum the charged particles will continue to accelerate under the influence of the electric field, but in a medium full of gas atoms the charged particles will make collisions with the atoms resulting in a loss of energy gained from the electric field. This energy dissipation to the gas atoms increases with increasing drift speed of the charged particles and as a result the charged particles will attain a certain constant speed within a certain time called the relaxation time. This constant speed is known as the drift velocity. The drift velocity depends on the applied electric field, the charge and the mass of the particle among other parameters. The ratio of the drift velocity to the electric field is known as the mobility of the charged particles. Table 3.1 gives the mobility of common ions in air [2, 3].

Table 3.1 Mobility of singly charged positive ( $K^+$ ) and negative ( $K^-$ ) gaseous ions at  $0^\circ\text{C}$  and 760 Hg (in  $\text{cm}^2/\text{V}\cdot\text{cm}$ )

Gas	$K^-$	$K^+$
Air (dry)	2.1	1.36
Air (very pure)	2.5	1.8
A	1.7	1.37
A (very pure)	206.0	1.31
$\text{Cl}_2$	0.74	0.74
$\text{CCl}_4$	0.31	0.30
$\text{C}_2\text{H}_2$	0.83	0.78
$\text{C}_2\text{H}_5\text{Cl}$	0.38	0.36
$\text{C}_2\text{H}_5\text{OH}$	0.37	0.36
CO	1.14	1.10
$\text{CO}_2$	0.98	0.84
$\text{H}_2$	8.15	5.9
$\text{H}_2$ (very pure)	7900.0	
HCl	0.95	1.1
$\text{H}_2\text{S}$	0.56	0.62
He	6.3	5.09
He (very pure)	500.0	5.09
$\text{N}_2$	1.84	1.27
$\text{N}_2$ (very pure)	145.0	1.28
$\text{NH}_3$	0.66	0.56
$\text{N}_2\text{O}$	0.90	0.82
Ne		9.9
$\text{O}_2$	1.80	1.31
$\text{SO}_2$	0.41	0.41

The drift velocity of electrons,  $v_e$ , as a function of electric field,  $E$ , in air can be calculated from the following empirical equations<sup>1</sup> [4]:

$$v_e = 1.0 \times 10^6 (E/p)^{0.075} \quad E/p \leq 100 \text{ (V/cm-torr)} \quad (3.6)$$

$$v_e = 1.55 \times 10^6 (E/p)^{0.62} \quad E/p \geq 100 \text{ (V/cm-torr)} \quad (3.7)$$

where  $p$  is the pressure in torr and the drift velocity is given in  $\text{cm/s}$ .

Another expression which is frequently used in the recent literature for the drift velocity as a function of the electric field is given by [5, 6]

$$v_e = 5.747 \times 10^{16} (E/N)^{0.6064} \text{ m/s} \quad (3.8)$$

where  $N$  is the gas density (in  $\text{cm}^{-3}$ ) and  $E$  is the background electric field (in  $\text{V/cm}$ ).

### 3.2.3 Thermal equilibrium and local thermal equilibrium

For a given type of particles in an ensemble, the concept of temperature is defined in terms of the average kinetic energy of the particles. Thus ascribing a certain temperature to a species presupposes that their velocity distribution conforms to a

<sup>1</sup> In many of the empirical equations pertinent to electrical discharges the electric field is given in  $\text{V/cm}$  and the pressure is given in torr ( $1 \text{ torr (mm Hg)} = 1.333 \cdot 10^2 \text{ Pa}$ ).



definite distribution function. For example, the velocity distribution of the atoms or molecules in a gas follows the Maxwellian distribution. The requirement that the particle velocities should conform to a certain distribution imposes some restrictions on the system. For example, the mean free path of the particle must be much less compared to the dimension of the enclosure containing the particles and the time between collisions should be short in comparison to other characteristic times of the system. These are the time spent by a particle within the enclosure before being lost and the time taken for a new particle to reach the energies characteristic of the ensemble. The energy of an ensemble is also present in the form of radiation and if the mean free path for the absorption of the radiation is much less than plasma dimensions a radiation equilibrium is established. In this case the plasma characteristics approaches those of a black body. When all the species in the plasma including the radiation are in thermodynamic equilibrium with each other one can say that the system is in thermal equilibrium.

Under thermal equilibrium all the particles including the radiation has the same temperature. However, in laboratory plasmas, the optical mean free path is usually longer than the dimensions of the plasma, so complete radiation equilibrium is not reached. In this situation there is a possibility for the collisional process to be in complete thermodynamic equilibrium excluding the radiation processes which are assumed to cause insignificant energy exchange and losses. In this case the system is said to be in local thermodynamic equilibrium. It is important to note that in some situations all the species may not be in thermodynamic equilibrium but the reactions that takes place in the ensemble are dominated by one species. In this case the temperature which describes the local thermodynamic equilibrium is that which describes the distribution function of the species that dominates the reaction rates. In dense laboratory plasmas, this is the electron temperature, since their cross section for collisions tend to be higher than for all other reactants.

Whenever a system is in thermal equilibrium, the system is devoid of temperature and density gradients. However, in reality they exist and the condition for the thermodynamic equilibrium in such cases can be written as [7]

$$\lambda \frac{\partial T_g}{\partial r} \ll T_g \quad (3.9)$$

$$\lambda \frac{\partial n}{\partial r} \ll n \quad (3.10)$$

$$Ee\lambda_e \ll \frac{mc^2}{2} \quad (3.11)$$

where  $E$  is the electric field,  $e$  is the electronic charge,  $\lambda_e$  and  $\lambda$  are the mean free path of electrons and gas atoms, respectively,  $mc^2/2$  is the mean electron kinetic energy,  $T_g$  is the temperature of gas,  $n$  is its concentration and  $r$  is the distance. The first two conditions impose small temperature and density variation and the third condition restricts the energy fed to the electrons from the electric field. If this condition is not satisfied the behaviour of electrons would not be able to be described using an average temperature because the energy fed from the electric field will upset the thermodynamic equilibrium.

In the presence of an electric field the energy gained by the electrons from the electric field is randomised by the collisions between electrons and gas particles. Thus one can speak of an electron temperature. However, it is important to note

that the energy exchange between the electrons and gas particles is an inefficient process since in elastic collisions an electron loses only a small fraction of its energy. Thus, in the presence of an electric field the electron temperature would be higher than that of the gas.

### 3.3 Ionisation processes

The electrical breakdown of air takes place when the air changes from an insulator to a conductor. This process is mediated by an increase in the electron concentration in air. The processes that lead to the increase in electron concentration in air are called ionisation processes. There are many ionisation processes in air and following is a description of them.

#### 3.3.1 Ionisation due to electron impact

In an electric field an electron continues to gain energy but it can transfer only a quantum of its energy to atoms in the medium during an inelastic collision. Thus when the electron energy increases more than the excitation energy of the colliding atom a quantum of energy is transferred during collisions leaving the atom in an excited state. If the electron energy is larger than the ionisation energy of the atom a collision may result in the ionisation of the atom. The ionisation energy of common gases are tabulated in Table 3.2 [8].

The process of ionisation due to electrons can be quantified in terms of an ionisation cross section, coefficient of ionisation or the probability of ionisation. The coefficient of ionisation (also known as the Townsend's primary ionisation coefficient) is defined as the number of ionisation collisions made by an electron in moving a unit distance along the direction of the electric field. Usually this is denoted by the symbol  $\alpha$ . The probability of ionisation is defined as the ratio of the number of ionisation collisions to the total number of collisions. These quantities can be related to each other as follows. The mean free path for the ionisation collisions,  $\lambda_{ion}$ , is given by

$$\lambda_{ion} = \frac{1}{n\sigma_{ion}} \quad (3.12)$$

Table 3.2 Some excitation and ionisation energies of atomic and molecular forms of some gases

Gas		Excitation energy ( $W_e$ ), eV	Ionisation energy ( $W_i$ ), eV
Oxygen	O <sub>2</sub>	7.9	12.5
	O	1.97, 9.15	13.61
Nitrogen	N <sub>2</sub>	6.3	15.6
	N	2.38, 10.33	14.54
Hydrogen	H <sub>2</sub>	7.0	15.4
	H	10.16	13.59
Mercury	Hg	4.89	10.43
	Hg <sub>2</sub>		9.6
Water	H <sub>2</sub> O	7.6	12.62
Nitrogenoxide	NO	5.4	9.26
	NO <sub>2</sub>		9.59

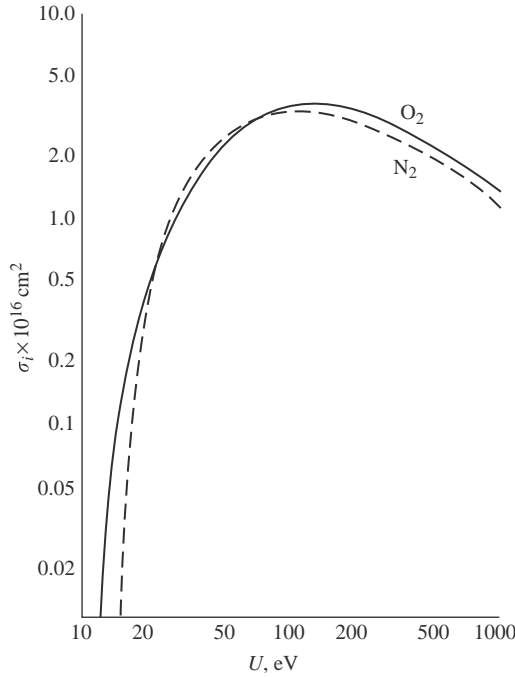


Figure 3.1 Ionisation cross section,  $\sigma_i$ , for electrons colliding with  $O_2$  and  $N_2$  molecules as a function of electron energy,  $U$  (eV) [4]

where  $n$  is the concentration of gas atoms and  $\sigma_{ion}$  is the microscopic cross section for ionisation. Thus the number of ionisation collisions made by an electron in moving a unit length,  $\alpha$ , is given by

$$\alpha = n\sigma_{ion} \quad (3.13)$$

The probability of ionisation is given by

$$P_{ion} = \frac{\sigma_{ion}n}{\sigma n} = \frac{\sigma_{ion}}{\sigma} \quad (3.14)$$

where  $\sigma$  is the total collision cross section.

The ionisation cross section of electrons in nitrogen and oxygen as a function of the electron energy is shown in Figure 3.1. It has been mentioned earlier that the electrons will ionise when their energy is larger than the ionisation energy of the atoms. However, the curve in this figure in combination with the data tabulated in Table 3.2 show that the ionisation starts even before this threshold is reached. The reason for this is the stepwise ionisation of the atoms. The first collision of the atom with an electron may cause an excitation of the atom and the next collision may remove the excited electron from the atom. This process can take place with electrons having energies less than the ionisation threshold. Note also that even though the electron energy is larger than the ionisation energy, this does not mean that the electron will ionise every time it collides with an atom. During each collision the electron has a certain probability of ionisation. This probability (which is proportional to the ionisation cross section) increases with increasing electron energy and, in  $N_2$  and  $O_2$ , reaches its peak value around 100 eV and then starts to

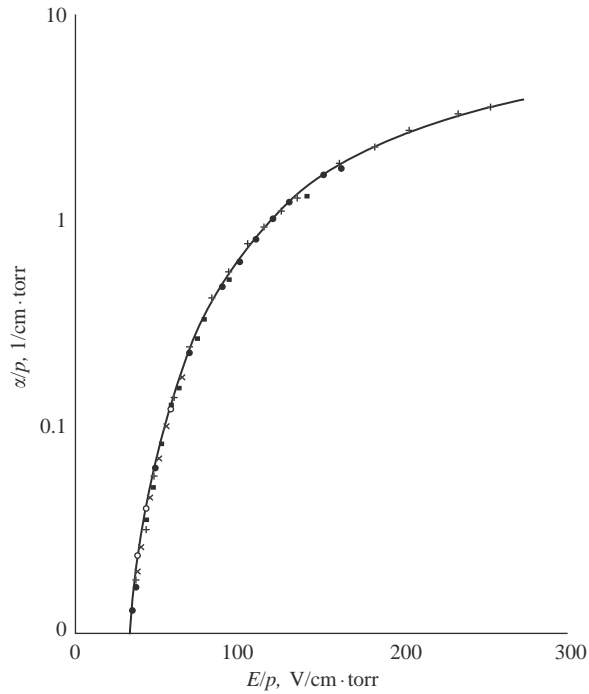


Figure 3.2 Measured ionisation coefficient  $\alpha$  as a function of the reduced electric field  $E/p$ . Data of a number of authors are shown. The solid line represents (3.16) [4]

decrease. The decline is probably caused by the fact that the time available for the interaction between a high energetic electron and an atom is small and the electron may pass near the atom without ejecting an electron from it.

The way in which the coefficient of ionisation in air vary as a function of the electric field is shown in Figure 3.2. Townsend had derived an expression for the coefficient of ionisation,  $\alpha$ , in air as a function of the electric field and it is given by

$$\frac{\alpha}{p} = Ae^{-B/(E/p)} \quad (3.15)$$

where  $p$  is the atmospheric pressure,  $E$  is the electric field and  $A$  and  $B$  are constants. The constants  $A$  and  $B$  depend on the gas under consideration and the atmospheric conditions. Even though the predictions of this equation are confirmed by experimental observation [9], this equation is not used in practice to evaluate the ionisation coefficient in air. It is customary to use the following set of empirical equations based on experimental observations [4].

$$\frac{\alpha}{p} = \exp\left(\frac{E/p - 58.2}{4.95}\right) \quad E/p \leq 35 \text{ V/cm/torr} \quad (3.16)$$

$$\frac{\alpha}{p} = \exp\left(\sum_{n=0}^9 a_n \{E/p\}^n\right) \quad 35 \leq E/p \leq 250 \text{ V/cm/torr} \quad (3.17)$$

$$\frac{\alpha}{p} = 14.5 \exp(-356E/p) \quad E/p \geq 250 \text{ V/cm/torr} \quad (3.18)$$

Table 3.3 Coefficients corresponding to (3.16)

---

$a_0 = -0.64927 \times 10^2$
$a_1 = 0.52642 \times 10^1$
$a_2 = -0.20238 \times 10^0$
$a_3 = 0.45178 \times 10^{-2}$
$a_4 = -0.63081 \times 10^{-4}$
$a_5 = 0.56724 \times 10^{-6}$
$a_6 = -0.32780 \times 10^{-8}$
$a_7 = 0.11739 \times 10^{-10}$
$a_8 = -0.23661 \times 10^{-13}$
$a_9 = 0.20479 \times 10^{-16}$

---

where  $E$  is in V/cm,  $p$  is in torr and  $\alpha$  is in  $\text{cm}^{-1}$ . The values of coefficients  $a_n$  are given in Table 3.3.

Another expression which is frequently used in the recent literature for the variation of  $\alpha$  as a function of the electric field is given by

$$\frac{\alpha}{N} = 2.0 \times 10^{-16} \exp[(-7.248 \times 10^{-15})/(E/N)] \text{cm}^2$$

for  $E/N > 1.5 \times 10^{-15} \text{ V}\cdot\text{cm}^2$  (3.19)

$$\frac{\alpha}{N} = 6.619 \times 10^{-17} \exp[(-5.593 \times 10^{-15})/(E/N)] \text{cm}^2$$

for  $E/N \leq 1.5 \times 10^{-15} \text{ V}\cdot\text{cm}^2$  (3.20)

where  $N$  is the gas density (in  $\text{cm}^{-3}$ ) and  $E$  is the background electric field (in V/cm) [5, 6].

### 3.3.2 Photoionisation

Ionisation of an atom can be caused not only by energetic material particles but also by photons if the photon energy is larger than the ionisation energy of the atom. The process can be represented by the equation

$$A + h\nu = A^+ + e \quad (3.21)$$

where  $A$  is the target atom,  $h$  is the Plank constant and  $h\nu$  is the energy of the incident photon. The escaping electron,  $e$ , has the energy  $h\nu - hv_n$  where  $hv_n$  is the ionisation energy and  $\nu_n$  is the minimum frequency at which photoionisation occurs. This threshold frequency for ionisation is given by

$$\nu_n = V_i/h \quad (3.22)$$

where  $V_i$  is the ionisation energy of the atom. Experiments show, however, that ionisation occurs even if the frequency of the incident photons is below this threshold [10]. The reason for this is the stepwise ionisation of the atoms where many photons act on the atom simultaneously. Stepwise ionisation caused by many photons is important in ionisation of gases by lasers where in many cases the energy of individual photons is less than the ionisation energy of the target atom.

### 3.3.3 Thermal ionisation

If a gas is heated the input heat energy will increase the translational or kinetic energy of the atoms in the gas. The velocities of the atoms are distributed according

to the Boltzmann distribution, and with increasing energy the atoms in the tail of the distribution may reach first energies sufficient to cause ionisation through collisions. With increasing temperature the number of atoms that have energies sufficient to cause ionisation increases and so does the number of ionisation collisions. However, in analysing the thermal ionisation it is not possible to confine only to collisions between neutral atoms because once the ionisation sets in it will change the particle concentrations and the type of particles which in turn may take part in the ionisation process. For example the ionisation in a gas at high pressure is caused by (1) ionisation by collision of atoms with atoms, (2) photoionisation resulting from the thermal emissions and (3) the collision of high energetic electrons produced by the above two processes. The first scientist to analyse this process in detail is Saha [11]. In a gas volume heated to a high temperature there are electrons, neutral atoms, excited atoms, ions and radiation. In the mathematical development Saha assumed that all these species are in thermal equilibrium at the temperature of the gas volume. Then the Maxwell–Boltzmann distribution laws apply to the various components of the discharge. Using this procedure, Saha evaluated the concentration of different species in the discharge in terms of the gas temperature. For example according to Saha the number of ionised particles in a volume of gas which is in thermodynamic equilibrium is given by

$$\frac{\beta^2}{1 - \beta^2} = \frac{2.4 \times 10^{-4}}{p} T^{2.5} e^{-V_i/kT} \quad (3.23)$$

with  $\beta = n_i/n$  where  $n$  is the total number of particles and  $n_i$  is the number of ionised particles in the volume of gas under consideration,  $p$  is the pressure in torr,  $T$  is the temperature in kelvins,  $V_i$  is the ionisation energy of atoms in electron volts and  $k$  is the Boltzmann constant given in units of eV/K. This expression is plotted in Figure 3.3 for several values of ionisation potentials. The data show that the thermal ionisation in air is significant only at temperatures above about 4000 K.

It is important to note that the derivation of the Saha equation does not depend on any particular ionisation process, although the thermal equilibrium implies thermal ionisation as opposed to ionisation created by the acceleration of charged

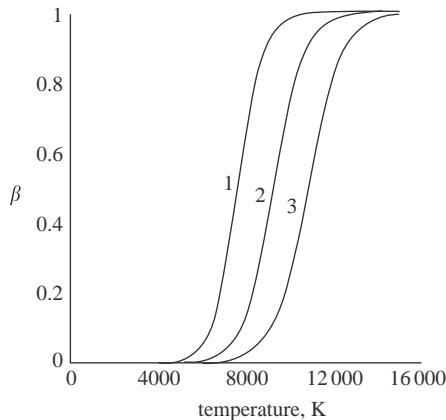


Figure 3.3 The fraction of ionisation,  $\beta$ , as a function of temperature as predicted by the Saha equation (3.20): (1)  $V_i = 10$  eV; (2)  $V_i = 12.5$  eV; (3)  $V_i = 15$  eV

particles. However, the above equation is sometimes used in situations where the ionisation is known to occur through electron impacts with the temperature of the electrons at a higher level than the gas atoms. Then the temperature appearing in the equation is actually the electron temperature and the assumption is that the ionisation is the same if the process takes place thermally at that temperature.

### 3.3.4 Ionisation caused by meta-stable excited atoms

Usually, an excited atom in a gas returns from its excited state to the ground state within about  $10^{-8}$  s, releasing the energy as one or more quanta of radiation. These are called normal excited states of the atom. The meta-stable excited states of an atom differs from these normal states in the following manner. Owing to quantum mechanical selection rule restrictions, the meta-stable level of an atom can be excited only by a direct electron impact and it can come back to its ground state only by transferring its extra energy to a third body. Thus the duration of the meta-stable excited state could last 10–100 ms; however in the presence of other particles the lifetime of these states are much shorter than these times due to de-excitation by various collision processes [3]. If the meta-stable excited state has energy equal or slightly higher than the ionisation energy of atoms in the ensemble the process leads to enhanced ionisation. This process is sometimes called the Penning ionisation. A typical collision process of this kind is given by [12]



where  $\text{Ne}_m$  is a meta-stable neon atom. For example Figure 3.4 shows the breakdown voltage of neon and argon mixtures as a function of the Argon content. Note the reduction of breakdown voltage of the mixture in comparison to the virgin gases. The reduction in the breakdown voltage is caused by the Penning ionisation.

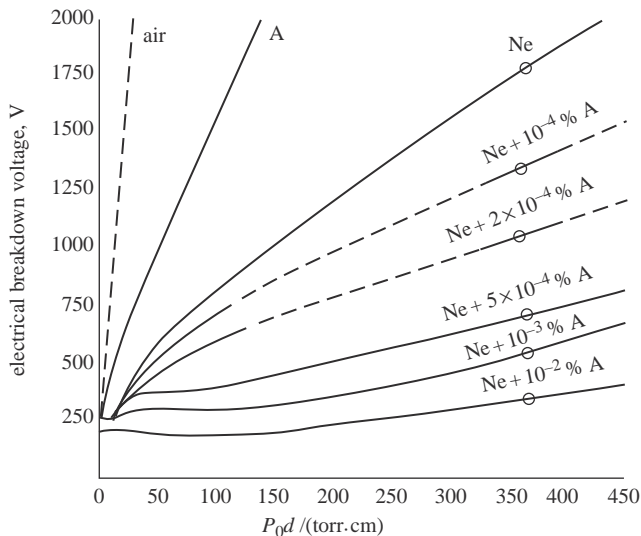


Figure 3.4 Electrical breakdown voltage, V, as a function of  $pd$  (pressure  $\times$  gap length) in neon–argon mixtures between parallel plates at 2 cm spacing at  $0^\circ\text{C}$  (from [2])

Normal excited states cannot take part in a similar process because, due to the short lifetime of the excited state, the atom suffers only a few collisions except when the gas pressure is very high before returning to the ground state.

It is important to note that common molecular gases have ionisation potentials below the meta-stable levels of He and Ne. Thus small traces of (1 ppm) common molecular gases can drastically affect the electrical breakdown characteristics of inert gases.

### 3.3.5 Ionisation due to positive ions

Any charged particle can gain energy from an electric field and one can expect that if raised to sufficient energies through the application of an electric field, positive ions can also contribute to the ionisation process through collisions. Using basic laws of mechanics one can easily show that a positive ion needs twice the energy needed by an electron to ionise an atom. However, the experimental data indicate that positive ions need more energy than this threshold before ionisation from them could be detected [13, 14]. The reason for this could be that the collision between the ion and the atom is not so rapid that the system can gradually adjust itself throughout the collision, thus preventing kinetic to potential energy transfer leading to an elastic collision. This may also depend on the fact that the collision is not point like, as in the case of electrons, and the collision energy is distributed in the electron cloud so that it is not concentrated on a single electron.

In considering the collision between the ions and molecules it is necessary to consider the collisions in which only charge transfer occurs between the colliding particles. One example is the collision of an argon atom, A, with singly ionised neon,  $\text{Ne}^+$ , where after the collision the argon is ionised leaving behind an energetic and neutral neon atom. This can be represented by



Such a process can produce fast neutral atoms at the expense of the kinetic energy of the ions. This is the reason why it is difficult to produce a homogeneous beam of high-speed positive ions in a gas.

## 3.4 De-ionisation processes

### 3.4.1 Electron-ion recombination

In a volume of gas in which an electrical discharge takes place there is a high concentration of electrons and positive ions. Whenever these oppositely charged particles come closer in collisions they have a tendency to recombine. The recombination between an electron and an ion can take place in several modes depending on the way the extra kinetic energy of the electron is removed.

#### 3.4.1.1 Radiative recombination

In radiative recombination, as the electron combines with the ion,  $X^+$ , the extra energy of the electron is released as a quantum of radiation. During recombination the electron may be captured into a vacant orbit and the recombination energy is released as a photon,  $h\nu$ . The resulting neutral atom could be in an excited state



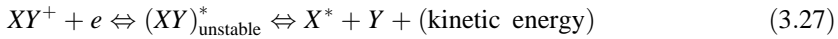
which may come back to the ground state by releasing another photon. The process can be described by the following reaction:



where  $X^*$  denotes an excited state of  $X$ .

### 3.4.1.2 Dissociative recombination

In this mode of neutralisation the extra energy of the electron is spent in dissociating the ion,  $XY^+$  to which it gets attached to. In general the dissociation process takes place in two steps. In the first step a negative, unstable and vibrationally excited ion  $XY^*$  is formed. Subsequently, the relaxation of the vibrational energy causes the molecule to dissociate. This process can be visualised as follows:



In the case of dissociative recombination the removal of energy to vibrational levels can be done very quickly (order of a vibrational period) and, therefore, high rates of recombination are realised. Due to the absence of dissociative recombination, the recombination process in monoatomic gases is one or two orders of magnitude slower than in molecular gases [15].

### 3.4.1.3 Three-body recombination

In this mode the extra energy of the reaction is transferred to a third body. At low pressures, however, the probability of finding a third body is rather small and three-body recombination mostly occurs at the walls of the discharge chamber, the latter acting as the third body. Thus the probability of three-body recombination is rather low at low gas pressures and it increases with increasing pressure.

## 3.5 Other processes that can influence the process of ionisation

### 3.5.1 Electron attachment and detachment

Some molecules and atoms have an affinity to form negative ions. The ground state energy of the negative ions in these cases are slightly lower than the energy of the ground state of the neutral molecules. The difference in energy, which is released during the formation of negative ions, is called the electron affinity of the atoms or molecules. The stability of the negative ion increases with increasing electron affinity.

When electronegative molecules are present in a gas discharge they tend to attach to free electrons. This process will remove fast-moving free electrons and replace them with slow-moving molecules. Even though no charge is destroyed during the process it can impede the development of the discharge. Thus the addition of electronegative gases into a discharge chamber may lead to the stabilisation of the medium against electrical breakdown.

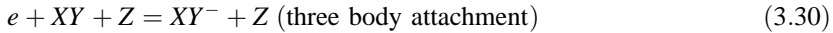
The electron affinity of different molecules of interest is given in Table 3.4. Observe that oxygen molecule is electronegative with an electron affinity of about 0.5 eV. The electron affinity of  $\text{SF}_6$  is 1.0–1.5 eV and this large affinity makes this gas a suitable candidate in increasing the breakdown voltage in high-voltage equipment.

The process of electron attachment can be divided into different types depending on the way in which the extra energy is released in the process. As in the case of electron recombination the process can be divided into radiative attachment,

Table 3.4 Electron affinities of some atoms and molecules

Atom or molecule	Electron affinity, eV
O	1.461
O <sub>2</sub>	0.451
O <sub>3</sub>	2.103
NO <sub>2</sub>	2.273
NO	0.026
SF <sub>6</sub>	1.05–1.5
H	0.714

dissociative attachment or three-body attachment. The three processes can be described mathematically as



where  $XY$  is a molecular species,  $h\nu$  is the energy released as radiation and  $Z$  is an atom or molecule that acts as a third body.

The process of attachment can be defined in terms of an attachment coefficient or by an attachment frequency. The attachment coefficient  $\eta$  denotes the number of attachment events per electron per unit length of travel. The attachment frequency is a measure of how fast free electrons are disappearing in a given medium due to attachment. This can be represented by the equation

$$n_e = n_0 \exp(-\nu_a t) \quad (3.31)$$

where  $n_0$  is the density of free electrons at  $t = 0$  and  $n_e$  is the density of free electrons at time  $t$ . For thermalised electrons at  $T = 300$  K the value of  $\nu_a = 0.9 \times 10^8 \text{ s}^{-1}$  [16]. That is, the lifetime of a free electron in air is about  $10^{-8}$  s.

The attachment coefficient of electrons is a function of the electric field and the pressure. Its value in air can be calculated from the empirical equation [4]

$$\frac{\eta}{p} = 1.95 \frac{e^{-60p/E}}{E/p} \quad (3.32)$$

where  $p$  is in Torr,  $\eta$  is in  $\text{cm}^{-1}$  and  $E/p$  is expressed in units of  $\text{V}/\text{cm}\cdot\text{torr}$ . Another expression which is frequently used in the recent literature for the attachment coefficient of electrons as a function of the electric field is given by [5, 6]

$$\frac{\eta}{N} = 8.889 \times 10^{-5} (E/N) + 2.567 \times 10^{-19} \text{ cm}^2 \quad (3.33)$$

for  $E/N > 1.05 \times 10^{-15} \text{ V}\cdot\text{cm}^2$

$$\frac{\eta}{N} = 6.089 \times 10^{-4} (E/N) - 2.893 \times 10^{-19} \text{ cm}^2 \quad (3.34)$$

for  $E/N \leq 1.05 \times 10^{-15} \text{ V}\cdot\text{cm}^2$

where  $N$  is the gas density (in  $\text{cm}^{-3}$ ) and  $E$  is the background electric field (in  $\text{V}/\text{cm}$ ).

Electron detachment is the opposite of the electron attachment. Once an electron is attached to an atom or molecule it is necessary to provide the negative ion with a certain amount of energy to remove the attached electron. This amount of energy is equal to the electron affinity in the case of atoms but need not be the same as electron affinity in the case of molecular ions. Depending on the way this energy is supplied the detachment process can be divided into three categories.

The first process is called photo detachment. In this case the extra electron of a negative ion can be detached by the energy of incident photon. The process can be described by the equation



where  $h\nu$  is the energy of the photon.

The second one is the associative detachment process. This is the inverse process of dissociative attachment and can be represented by



If the electron affinity of  $X^-$  is less than the dissociative energy of  $XY$  the reaction is possible for zero relative kinetic energy of  $X^-$  and  $Y$  and the process can therefore be important under electrical discharge conditions.

The third process is the collisional detachment. In this case the energy necessary to release the electron from the ion is obtained from the energy released during the collision of negative ion,  $XY^-$ , with another atom or molecule,  $Z$ . This is actually the reverse of the three body attachment. This can be represented by



This process is important under discharge conditions and most probably the first seeding electrons necessary for the initiation of an electrical discharge in air are produced by this process. For example, the negative  $O_2^-$  ions are decomposed by collisions with molecules possessing an energy high enough to detach an electron. Especially effective in this are the excited nitrogen molecules [15, 16].

The situation is little bit more complicated in the case of humid air. The detachment of electrons from negative oxygen atoms in humid air is much slower than in dry air because the negative ions become hydrated by attaching it to a cluster of water molecules, i.e.  $O_2^-(H_2O)_n$  ( $n = 1, 2, 3, \dots$ ). The most probable cluster type in atmospheric pressure is  $O_2^-(H_2O)_3$  [16]. The detachment energy increases with cluster number and, therefore, it is more difficult to remove an electron from a hydrated ion. In order to detach an electron from a hydrated ion the latter has to be declustered first and then the electron should be removed from the negative ion.

### 3.5.2 *Excitation of molecular vibrations*

Low-energy electrons can actively excite molecular vibrations and this is one of the most important processes that removes energy from free electrons in air. In nitrogen, molecular vibrations are excited by electrons in the range of energies 1.8–3.3 eV. Electrons can also excite rotational levels, but the process is not that important as an energy-draining source. In moderate values of  $E/p$  about  $3\text{--}30 \text{ V}\cdot\text{cm}^{-1}\cdot\text{torr}^{-1}$ , electrons spend about 90–95 per cent of the gained energy in exciting molecular vibrations in air and nitrogen [15]. At higher values of  $E/p$  excitation of electronic levels and ionisation are the main energy-draining processes.

Once a molecule is excited vibrationally it will take some time for this energy to convert back to translational or kinetic energy. This process is called vibrational–translational (VT) relaxation and is denoted by the relaxation time  $\tau$ . In dry air at atmospheric pressure  $\tau = 1.7 \times 10^{-2}$  s. In air containing  $0.8 \times 10^{-5}$  g·cm<sup>-3</sup> of water the relaxation time decreases to  $\tau = 7 \times 10^{-4}$  s. That is, water molecules can deactivate the molecular vibrations. In hot humid air  $\tau = 8 \times 10^{-5}$  s at 1000 K and it will decrease to  $10^{-5}$  s at 2000 K [15]. This shows that the VT relaxation process is ‘self-accelerated’, that is the relaxation produces heat resulting in an increase of temperature of the gas, which in turn decreases the relaxation time, thus accelerating the relaxation process.

### 3.5.3 Diffusion

Diffusion is the process in which gases move from the regions of high concentration to lower concentrations. Diffusion plays an important role during the initiation and decay of discharge channels because diffusion causes charged particles to move from regions of high concentrations, where they are created, to regions of low concentrations. This reduces the charge density in the source region thus impeding the discharge development.

A given volume of an electrical discharge contains both electrons and positive ions. Electrons being smaller than the positive ions diffuse faster than the positives from region of high concentrations. This will lead to a charge separation and the result will be the creation of an electric field. This electric field will accelerate the drift of positive ions but retard the drift of electrons. However, at equilibrium, there will be an equilibrium electric field and both electrons and positive ions diffuse at the same rate. Diffusion taking place under these circumstances is called ambipolar diffusion.

Let us consider a situation in one dimension where the concentration of particles vary in the  $x$  direction. The number of particles crossing a unit area of thickness  $dx$  placed perpendicular to the direction of  $x$  per unit time (i.e. the particle flux in  $x$  direction),  $p_f$ , is given by

$$p_f = -D \frac{dn}{dx} \quad (3.38)$$

where  $D$  is the coefficient of diffusion and  $n$  is the concentration of particles (i.e. number of particles per unit length). The rate of increase of the number of particles in the element  $dx$  is

$$\frac{\partial n}{\partial t} \cdot dx = p_f(x) - p_f(x + dx) \quad (3.39)$$

This can be written as

$$\frac{\partial n}{\partial t} \cdot dx = p_f(x) - \left[ p_f(x) + \frac{\partial p_f(x)}{\partial x} dx \right] \quad (3.40)$$

or

$$\frac{\partial n}{\partial t} = - \frac{\partial p_f(x)}{\partial x} \quad (3.41)$$

Combining (3.38) and (3.41) one obtains the rate of change of concentration of charged particles due to diffusion as

$$\frac{\partial n}{\partial t} = D \frac{\partial^2 n}{\partial x^2} \quad (3.42)$$

In three dimension this can be written as

$$\frac{\partial n}{\partial t} = D \nabla^2 n \quad (3.43)$$

The diffusion coefficient of electrons is related to their mobility through the equation

$$\frac{\mu}{D} = \frac{2.4 \times 10^{19} e}{\epsilon_e} \quad (3.44)$$

where  $\mu$  is the mobility (in  $\text{cm}^2 \cdot \text{V}^{-1} \cdot \text{s}^{-1}$ ),  $e$  is the electronic charge (in C) and  $\epsilon_e$  is the mean energy of the electrons (in eV) and  $D$  is given in  $\text{cm}^2 \cdot \text{s}^{-1}$ . The electronic mobility is a function of the electric field and for air it can be obtained from the equations for the drift velocity ((3.6), (3.7) or (3.8)). The mean energy of the electrons is also a function of the background electric field. The relationship between the two parameters in air can be described by the equation [4]

$$\eta_m = 17(E/p)^{0.71} \quad E/p \leq 3 \text{ (V/cm} \cdot \text{torr)} \quad (3.45)$$

$$\eta_m = 21(E/p)^{0.49} \quad E/p \geq 3 \text{ (V/cm} \cdot \text{torr)} \quad (3.46)$$

with

$$\eta_m = \epsilon_e / \epsilon_{gas} \quad (3.47)$$

where  $\epsilon_{gas}$  is the mean thermal energy of the gas molecules given by  $3kT/2$ ,  $T$  is the gas temperature in kelvins and  $k$  is the Boltzmann constant. In the above equation  $E$  is given in V/cm, and  $p$  in torr. Using these equations one can calculate the coefficient of diffusion of electrons in air for a given value of  $E/p$ .

### 3.6 Cathode processes

In general laboratory discharges are created between electrodes and these electrodes can supply the discharge with electrons through various physical processes. Under normal conditions electrons in a metal are prevented from leaving the metal by electrostatic forces between the electrons and the ions in the metal lattice. As shown in Figure 3.5a the electrons in the metal are trapped in a potential well. The energy necessary to remove an electron from the top of the Fermi energy levels is known as the work function of the metal. This is denoted by  $\phi$  in Figure 3.5a. The work function of typical metals are tabulated in Table 3.5 [17].

Table 3.5 *Work function for typical elements*

Element	Ag	Al	Cu	Fe	W
$W_a$ (eV)	4.74	2.98–4.43	4.07–4.7	3.91–4.6	4.35–4.6

Electrons can be removed from the metal either by giving the electrons sufficient kinetic energy to surmount the potential barrier, or the work function, at the surface, by reducing the height of the barrier so that the electrons can overcome it or by reducing the thickness of the barrier so that the electrons can tunnel through it. The first can be achieved by the application of heat to the electrode, through impact of photons on the surface of the electrode or by the incidence of particles such as other electrons, positive ions, neutral molecules and meta-stable atoms on the electrode. The reduction in the potential barrier height or its thickness can be achieved by the application of an electric field in the correct direction so that the electrons will experience a force directed out of the metal surface (see Figure 3.5b). Let us consider different physical processes that can cause emission of electrons from metals.

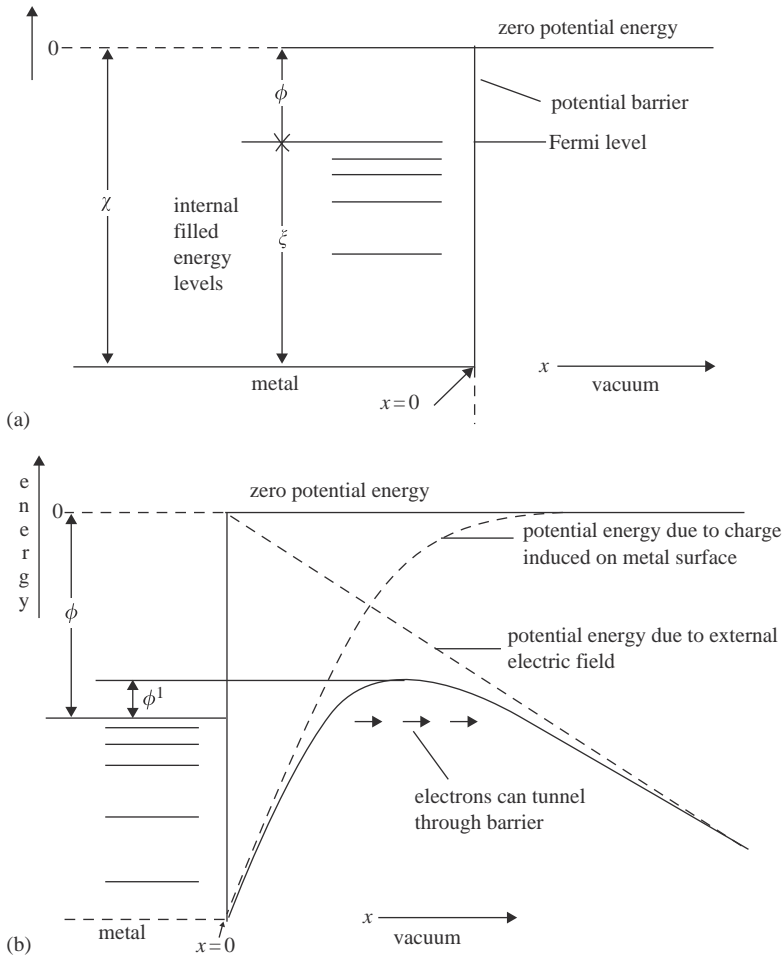


Figure 3.5 Energy diagrams: (a) electrons in a metal; (b) when an electric field is applied. Note that the electric field reduces not only the height of the barrier but also the thickness of the barrier. This makes it easier for the energetic electrons to jump over the barrier (Schottky effect) and a certain percentage of the electrons to tunnel through the barrier

### 3.6.1 Photoelectric emission

When a photon is incident on a metal it can transfer all its energy to an electron in the metal so that the latter can surmount the potential barrier at the surface of the metal. Thus an electron at the Fermi level after absorbing the energy of the quanta can escape with energy  $E_e$  given by

$$E_e = h\nu - \phi \quad (3.48)$$

where  $h\nu$  is the energy of the photon. For clean Ag surface  $\phi = 4.74$  eV (Table 3.5) and the threshold frequency corresponds to a wavelength of 2616 Å.

### 3.6.2 Thermionic emission

In metals at room temperature the energy of the conduction electrons is not sufficient for them to surmount the potential barrier at the surface of metals. However, heating a metal will increase the kinetic energy of the electrons in the metal. With increasing temperature of the electrode the energy of the electrons increases and one may expect the number of electrons surmounting the barrier to increase. Since this process is caused by the heating of the electrode it is called thermionic emission. The thermionic current density,  $J_t$ , is given by the following equation [18]:

$$J_t = AT^2 \exp(-\phi/kT) \quad (3.49)$$

where  $k$  is the Boltzmann constant,  $\phi$  is the work function of the metal,  $T$  is the absolute temperature and  $A$  is a constant equal to  $120 \text{ A}\cdot\text{cm}^{-2}\cdot\text{deg}^{-2}$ . Actually the experimentally obtained current densities are smaller than those predicted by this equation because this equation does not take into account the wave nature of electrons and the possibility that some of the electrons will be reflected at the barrier even if it has enough energy to overcome it.

### 3.6.3 Schottky effect

As one can see from the equation given in the previous section, the thermionic current depends on the height of the barrier that the electrons have to surmount to come out of the metal. The height of this barrier can be decreased by the application of an electric field in such a way the electrons in the metal experience a force out of the metal if they are exposed to this electric field. This is illustrated in Figure 3.5b. In the presence of such an electric field the work function is effectively reduced to [19]

$$\phi_1 = \phi - \sqrt{\frac{e^3 E}{4\pi\epsilon_0}} \quad (3.50)$$

This reduction in the barrier height will lead to a change in the thermionic emission current. Thus if  $J_0$  is the thermionic emission current density for zero electric field at temperature  $T$  then the current density at the same temperature in the presence of an electric field  $E$  is given by

$$J_s = J_0 \exp(4.4\sqrt{E}/T) \quad (3.51)$$

where the electric field  $E$  is given in V/cm and  $T$  in kelvins. This was shown to be valid for electric fields up to about  $10^6$  V/cm. This process of enhancement of the

thermionic emission current due to the reduction in the barrier height is called Schottky emission.

### 3.6.4 Field emission

Calculations done with the Schottky equation show that the thermionic emission current at  $T=293$  K for values of  $\phi$  about 4.5 eV is negligible even when the electric field reaches values as high as  $10^6$  V/cm. However, experiments show that electrodes in vacuum do emit appreciable currents, in the range of  $\mu\text{A}$ , at such electric fields. The reason for this is the quantum nature of the elementary particles. The illustration in Figure 3.5b shows that the application of the electric field not only reduces the height of the barrier but will also decrease the thickness of the barrier. In the absence of the electric field the barrier is infinitely thick but its thickness decreases with increasing electric field.

Electrons incident on the barrier can be represented by a wave; during the interaction part of the wave will be reflected and the other part of the wave will be transmitted. The transmitted wave attenuate rapidly when moving into the barrier. But, if the thickness of the barrier is not large a small fraction of the wave may be able to penetrate the barrier. Of course in the case of electrons the reflection and transmission coefficients have to be regarded as probability functions. So there is a certain probability that an electron incident on the barrier will penetrate it. If the number of electrons incident on the barrier per unit time is known quantum mechanical calculations can be performed to evaluate the number of electrons coming out of the barrier. Fowler and Norheim [20] analysed this process in details and obtained the following expression for the field emission current density,  $J_f$ , for pure metallic surfaces in vacuum:

$$J_f = 61.6 \times 10^{-7} \frac{\zeta^{\frac{1}{2}} E^2}{(\zeta + \phi) \phi^{\frac{1}{2}}} \exp(-6.8 \times 10^7 \phi^{\frac{3}{2}} / 3E) \quad (3.52)$$

where  $\zeta = 5$  eV (typical value for metals),  $\phi$  is the work function in eV,  $E$  is the electric field in V/cm and the current density is given in  $\text{A}/\text{cm}^2$ . This equation indicates that measurable currents should be obtained for electric fields of the order of  $10^7$  V/cm. This has been found to be valid for very clean surfaces. Experiments show, however, that an appreciable electric field dependent emission current can be obtained for electric fields one to two orders of magnitude smaller than this in the presence of surface contamination. The reason for this is that surface contamination causes a reduction in the width of the barrier thus enhancing the field emission process. Moreover, if there are protrusions on the surface the electric field at the tip of these protrusions can reach very high values leading to field emission from them. The field emission process is very important in providing initiatory electrons in the creation of electrical discharges.

### 3.6.5 Incidence of positive ions

It was mentioned previously that photons incident on a metal can supply electrons with energy sufficient to surmount the barrier. Indeed, not only photons but also elementary particles incident on the surface can cause electrons to be ejected from the surface. This is a common situation at the surface of the cathode of an electrical discharge where positive ions, having sufficient energy to support an electron to overcome the potential barrier, are incident on the cathode and liberate electrons from it.



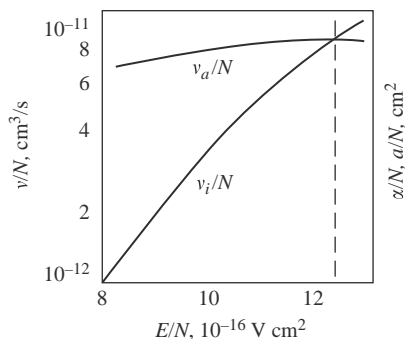


Figure 3.6 The electron ionisation frequency (per unit air density),  $v_i/N$ , and the electron attachment frequency (per unit air density),  $v_a/N$ , as a function of reduced electric field in air [21].  $N$  is the density of air. At  $T = 273$  K and  $p = 760$  torr the value  $N = 2.69 \times 10^{19} \text{ cm}^{-3}$

### 3.7 Electrical breakdown

In a given environment with a background electric field there is a competition between the ionisation and deionisation processes. The ionisation processes attempt to increase the number of electrons in the environment, whereas the deionisation processes attempt to reduce their number. The relative efficiency of the two competing processes depends on the magnitude of the background electric field. Figure 3.6 shows how the frequency of ionisation,  $v_i$ , and the frequency of attachment,  $v_a$ , vary as a function of the reduced electric field. Since  $\alpha = v_i/v_e$  and  $\eta = v_a/v_e$ , where  $v_e$  is the electron drift velocity, one can also infer from the data how the ionisation coefficient and the electron attachment coefficient in air at atmospheric pressure vary as a function of the background electric field [21]. Note that there is a critical electric field above which the frequency of ionisation becomes large than the attachment frequency (i.e.  $\alpha = \eta$ ). Probably due to uncertainties in the input parameters used in the calculations presented in Figure 3.6 the electric field at which  $\alpha = \eta$  became  $4.1 \times 10^4$  V/cm. The correct value is about  $2.6 \times 10^4$  V/cm.

Figure 3.7 illustrates how the background electric field necessary to cause electrical breakdown in a plane parallel gap (i.e. the electric field is uniform) varies with the plate separation [22]. Note that for small gap separations the breakdown electric field is larger than the critical field given above. However, the breakdown electric field approaches this critical electric field with increasing gap distance. The data show that in order to create electrical breakdown two conditions should be satisfied. First the electric field in the gap should exceed a critical value. Second, depending on the magnitude of the electric field there is a certain critical length over which the electric field should extend. This critical length decreases with increasing electric field.

The physical processes that take place during the formation of an electric discharge can be summarised as follows: The electrical breakdown in a gas starts with a single electron which will lead to an avalanche of electrons created through the electron collision ionisation. As the avalanche grows the electric field created by charges concentrated at the avalanche head starts to modify the electric field in the vicinity of the head of the avalanche. When this space charge electric field

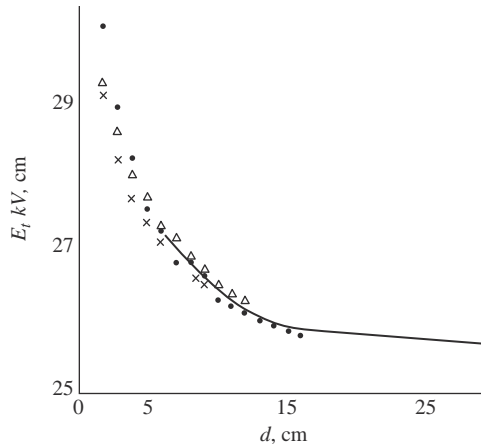


Figure 3.7 Threshold electric field,  $E_t$ , for the breakdown of air ( $p = 760$  torr, water vapour pressure = 20 torr, temperature =  $20^\circ\text{C}$ ) as a function of the gap length,  $d$ . Data of a number of authors are shown by different symbols in the figure (from [22])

reaches a critical value the avalanche will convert itself to a *streamer discharge*. If the gap is short then the streamer discharge may bridge the gap and, after *streamer to spark transition*, the complete breakdown of the gap may take place. If the gap is long many streamers may start from the electrode having their origin at a common streamer stem. The heat generated by the streamer currents will increase the temperature of the streamer stem and when the temperature reaches a critical value the thermal ionisation sets in the stem, the conductivity of the stem increases and it will convert itself to a *leader discharge*. Since the leader channel is a good conductor the potential of the electrode is now transferred to the head of the leader channel and the resulting high electric field will cause streamers to grow from the head of the leader channel. The leader elongates in the gap through the action of streamers that forge further and further into the gap. When the leader discharge reaches the grounded electrode the current in the channel increases, and the applied voltage collapses, leading to the formation of a spark. In the following sections these processes that take place in the formation of electric sparks are described.

### 3.7.1 Electron avalanche

Consider a free electron originated at  $x=0$  in space and moving under the influence of a background electric field directed in the negative  $x$  direction. If the background electric field is larger than the critical value necessary for cumulative ionisation the electron may produce another electron through ionisation collisions and these two electrons in turn will give rise to two more electrons. In this way the number of electrons increases with increasing  $x$ . Assume that the number of electrons at a distance  $x$  from the origin is  $n_x$ . Let  $\alpha$  be the number of ionising collisions per unit length made by an electron travelling in the direction of the electric field and  $\eta$  be the number of attachments over the same length. As discussed previously  $\alpha$  is the Townsend's ionisation coefficient and  $\eta$  is the attachment coefficient. Consider an elementary length of width  $dx$  located at a distance

$x$  from the origin. In travelling across the length  $dx$ ,  $n_x$  number of electrons will give rise to  $dn$  additional electrons:

$$dn = n_x(\alpha - \eta)dx \quad (3.53)$$

The solution of this equation is

$$n_x = e^{(\alpha-\eta)x} \quad (3.54)$$

This equation shows that the number of electrons increases exponentially with distance. This exponential growth of electrons with distance is called an electron avalanche. Figure 3.8 shows a photograph of an electron avalanche obtained in a cloud chamber [23]. The equation also shows that cumulative ionisation is possible only if  $(\alpha - \eta) > 0$ . The quantity  $(\alpha - \eta)$  is known as the effective ionisation coefficient and denoted by  $\bar{\alpha}$ .

It is important to note however that the value of  $n_x$  given in (3.54) is a mean value and it is subjected to considerable variations due to the statistical nature of the collision process. The probability that one electron at the origin results in an avalanche of total number  $n$  at a distance  $x$  is given by

$$P(n, x) = \frac{1}{n_{mean}} \left[ 1 + \frac{1}{n_{mean}} \right]^{n-1} \quad (3.55)$$

with a standard deviation given by

$$\sigma = n_{mean} \left[ 1 - \frac{1}{n_{mean}} \right]^{\frac{1}{2}} \quad (3.56)$$



Figure 3.8 *Cloud chamber photograph of a single electron avalanche (from [23])*

where

$$n_{mean} = e^{(\alpha-\eta)x} \quad (3.57)$$

For large values of  $n$  this becomes

$$P(n, x) = \frac{1}{n_{mean}} e^{-n/n_{mean}} \quad (3.58)$$

with  $\sigma = n_{mean}$ . That is, the size of an electron avalanche originating from a single electron follows an exponential distribution. It is important to note that this result is based on the assumptions that (a) the space charge of the avalanche does not have significant influence on the background electric field and (b) the probability of an electron ionising a gas molecule is constant and is independent of the distance it has travelled in the electric field direction since the last ionising collision.

### 3.7.2 The space charge electric field due to an avalanche

It has been shown in previous sections that as an avalanche initiated by a single electron grows the number of electrons in the avalanche head increases according to the formula

$$n = e^{\bar{\alpha}x} \quad (3.59)$$

where  $\bar{\alpha}$  is the effective ionisation coefficient. Let us assume that these electrons at the head of the avalanche is confined to a spherical region of radius  $r$ . Then the electric field at the head of the avalanche is given by

$$E_r = \frac{ee^{\bar{\alpha}x}}{4\pi\epsilon_0 r^2} \quad (3.60)$$

where  $e$  is the electronic charge (not to be confused with the exponential). In fact as the electron avalanche advances, its tip is spreading laterally by the random diffusion of the electrons. The average radial distance of diffusion can be calculated from the equation  $r = \sqrt{4Dt}$  where  $t = x/v_d$  is the time of advance of the avalanche,  $D$  is the coefficient of diffusion and  $v_d$  is the drift velocity of the electrons. Substituting this in (3.60) one obtains

$$E_r = \frac{ee^{\bar{\alpha}x}}{4\pi\epsilon_0} \left( \frac{v_d}{4Dx} \right) \quad (3.61)$$

This equation shows that with increasing avalanche length the electric field created by the space charge increases and at a certain critical length the electric field generated by the space charge becomes comparable to the background electric field. At this stage an electron avalanche will convert itself to a streamer discharge.

Numerical evaluation of (3.61) requires a value for the electron diffusion coefficient. This parameter is given by [5, 6]

$$D = \left[ 0.3341 \times 10^9 (E/N)^{0.54069} \right] |W_e/E| \text{ cm}^2 \cdot \text{s}^{-1} \quad (3.62)$$

$$W_e = - \left[ 7.4 \times 10^{21} (E/N) + 7.1 \times 10^6 \right] \text{ cm} \cdot \text{s}^{-1} \quad (3.63)$$

for  $E/N > 2.0 \times 10^{-15} \text{ V} \cdot \text{cm}^2$

$$W_e = -[1.03 \times 10^{22}(E/N) + 1.3 \times 10^6] \text{ cm} \cdot \text{s}^{-1}$$

for  $10^{-16} < E/N < 2.0 \times 10^{-15} \text{ V} \cdot \text{cm}^2$

(3.64)

$$W_e = -[7.2973 \times 10^{21}(E/N) + 1.63 \times 10^6] \text{ cm} \cdot \text{s}^{-1}$$

for  $2.6 \times 10^{-17} < E/N \leq 10^{-16} \text{ V} \cdot \text{cm}^2$

(3.65)

$$W_e = -[6.87 \times 10^{22}(E/N) + 3.38 \times 10^4] \text{ cm} \cdot \text{s}^{-1}$$

for  $E/N \leq 2.6 \times 10^{-17} \text{ V} \cdot \text{cm}^2$

(3.66)

where  $N$  is the gas density (in  $\text{cm}^{-3}$ ) and  $E$  is the background electric field (in  $\text{V/cm}$ ).

### 3.7.3 *Formation of a streamer*

A schematic description of the formation of a positive streamer is shown in Figure 3.9 [24]. As the electron avalanche propagates towards the anode low mobile positive space charge accumulates at the avalanche head. When the avalanche reaches the anode, the electrons will be absorbed into it leaving behind the net positive space charge. Due to the recombination of positive ions and electrons, avalanche head is a strong source of high energetic photons. These photons will create other avalanches in the vicinity of the positive space charge. If the number of positive ions in the avalanche head is larger than a critical value the electric field created by the space charge becomes comparable to the background electric field and the secondary avalanches created by the photons will be attracted towards the positive space charge. The electrons in the secondary avalanches will be neutralised by the positive space charge of the primary avalanche leaving behind a new positive space charge, little bit closer to the cathode. The process repeats itself and the positive space charge head travels towards the cathode as a consequence. This discharge that travels towards the cathode from the anode is called a cathode directed streamer or a positive streamer. Cloud chamber photographs of the creation and propagation of streamer discharges are shown in Figure 3.10 [22].

The formation of a negative streamer or an anode directed streamer is shown in Figure 3.11. The electrons of the avalanche move into the gap leaving behind positive charge close to the cathode. When the avalanche reaches the critical size the secondary avalanches extend the positive space charge towards the cathode (as in a cathode directed streamer). When the positive channel reaches the cathode both the field enhancement associated with the proximity of positive space charge to the cathode and the collision of positive ions on the cathode lead to the emission of electrons from the latter. These electrons will neutralise the positive space charge creating a weakly conducting channel that connects the negative head of the electron avalanche to the cathode. The high electric field at the head of the avalanche pushes the negative space charge further into the gap while the positive space charge left behind is neutralised by the electrons supplied by the cathode and travelling along the weakly conducting channel connecting the streamer head and the cathode.

If the background electric field is very high the positive space charge of the avalanche may reach the critical size necessary for streamer formation before reaching the anode. This may lead to the formation of a bidirectional discharge the two ends of which travel towards the anode and the cathode, former as a negative streamer

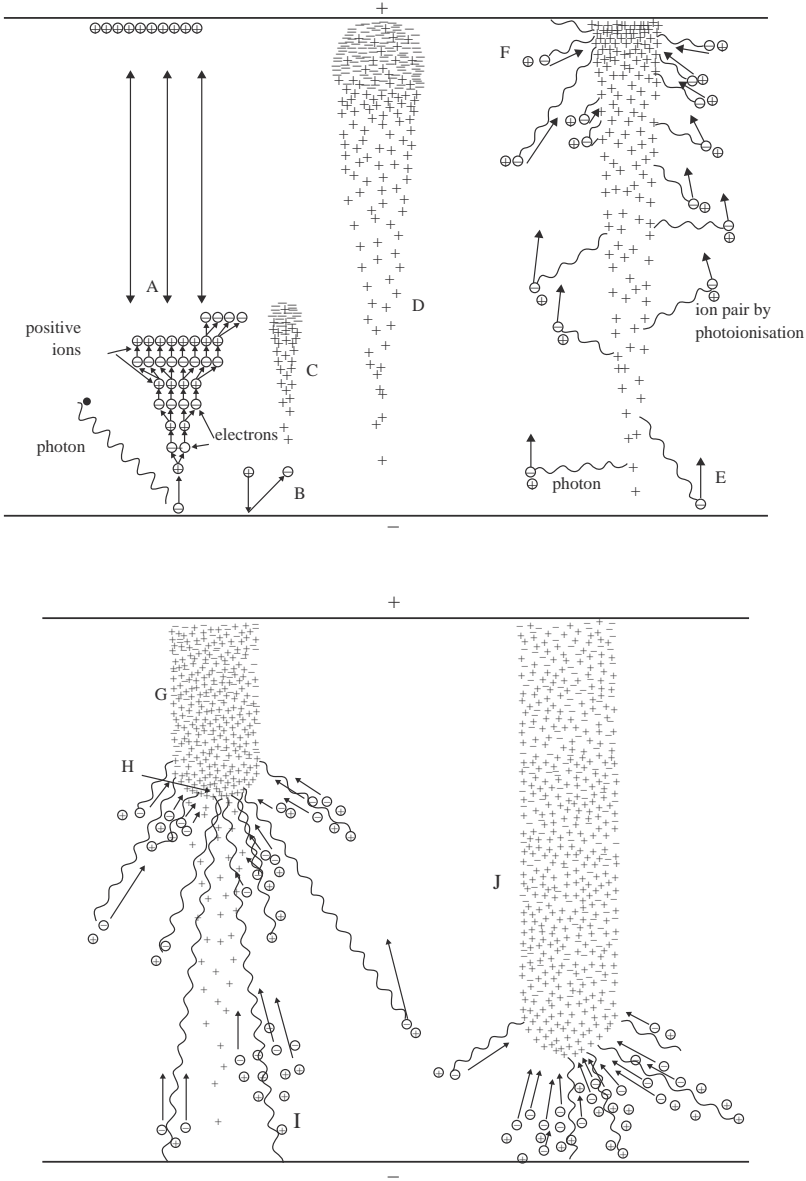
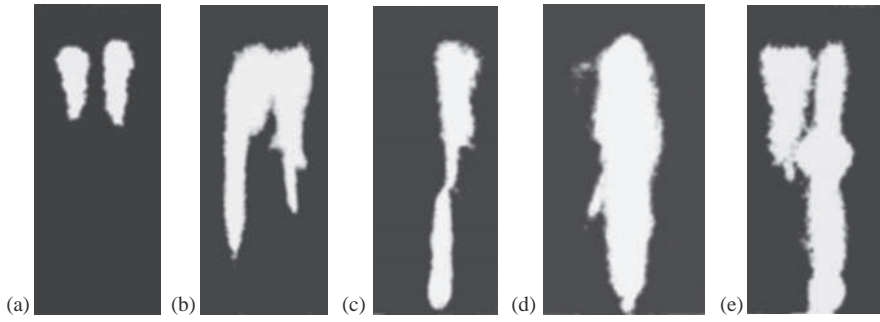
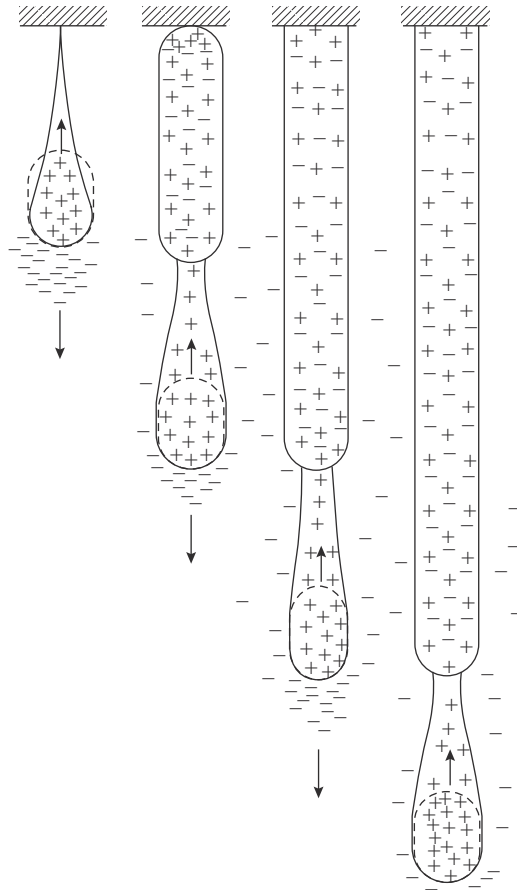


Figure 3.9 Schematic diagram showing the formation of a positive streamer – A, an external photon triggers an avalanche; B, a positive ion strikes the cathode and starts an avalanche C; D, the avalanche tip reaches the anode; E, photons originating from the avalanche produce free electrons both from the cathode and in the gas; F, the positive space charge close to the anode increases the electric field and a streamer is just about to be formed; G, plasma of positive ions and electrons forms the streamer channel; H, streamer tip; I, production of free electrons by photons; J, streamer close to the cathode (from [24])



*Figure 3.10* Cloud chamber photograph showing the development of positive streamers – (a) avalanche near the anode; (b and c) positive streamer starts; (d and e) the streamer bridges the gap (from [26])



*Figure 3.11* Schematic representation of the formation of a negative streamer and the physical processes taking place at the streamer head (adapted from [25])

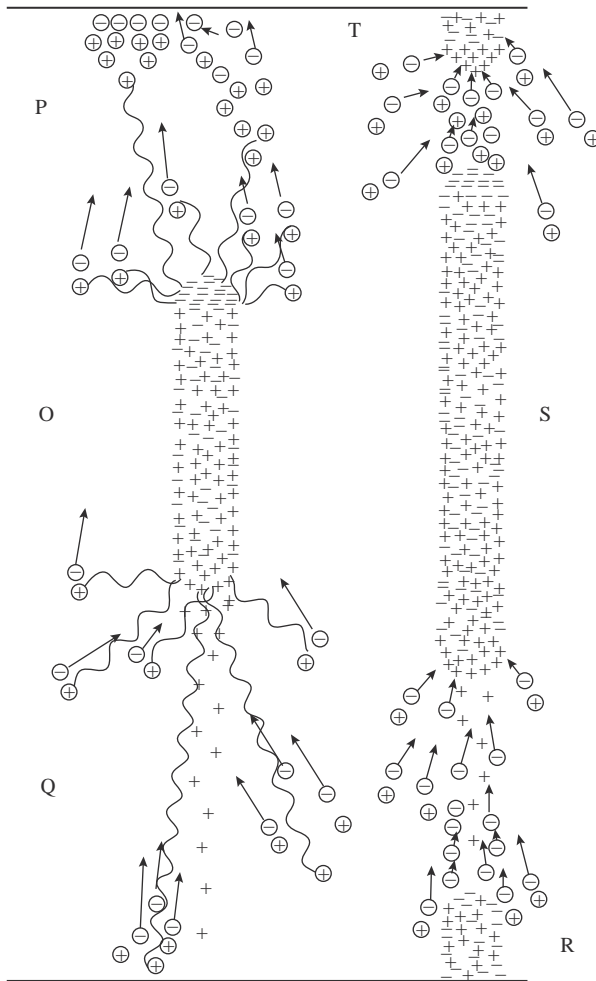


Figure 3.12 Schematic diagram showing the formation of a mid-gap streamer. The electron avalanche converts itself to a streamer when it has advanced two thirds of the gap (O). This may lead to the formation of a bidirectional discharge, the two ends of which travel towards the anode and the cathode, former as a negative streamer and the latter as a positive streamer. As the streamer heads approach the electrodes the electric field at the electrodes is enhanced leading to the formation of avalanches (P and Q) which may even lead to the formation of streamers from the electrodes (T and R) (from [24])

and the latter as a positive streamer. Such a discharge is called a mid-gap streamer. This is illustrated in Figure 3.12.

As the streamer propagates it may lead to the formation of branches. The mechanism of streamer branching is illustrated in Figure 3.13.

The avalanche to streamer transition takes place when the number of charged particles at the avalanche head exceeds a critical value,  $N_c$ . From cloud chamber photographs of the avalanches and streamers, Raether [26] estimated that an



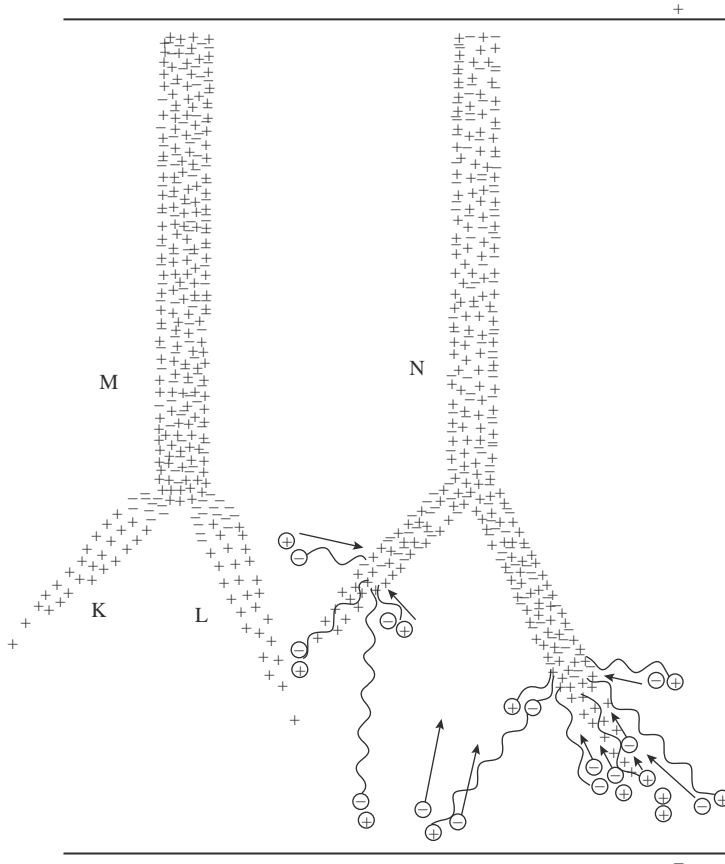


*Figure 3.13 Schematic diagram showing the branching of the streamer. The streamer channel M attracts two avalanches K and L towards its tip simultaneously leading to the formation of a branch (from [24])*

avalanche will convert to a streamer when the number of positive ions in the avalanche head reaches a critical value of about  $10^8$ . A similar conclusion is also reached independently by Meek [27]. Thus the critical avalanche length for transition to a streamer is given by

$$e^{\bar{\alpha}x_c} = 10^8 \quad (3.67)$$

or

$$\bar{\alpha}x_c \approx 18 \quad (3.68)$$

Figure 3.14 shows the critical avalanche length at which an electron avalanche transforms itself to a streamer discharge as a function of the background electric field which is assumed to be uniform [28]. Note that the critical avalanche length decreases with increasing electric field.

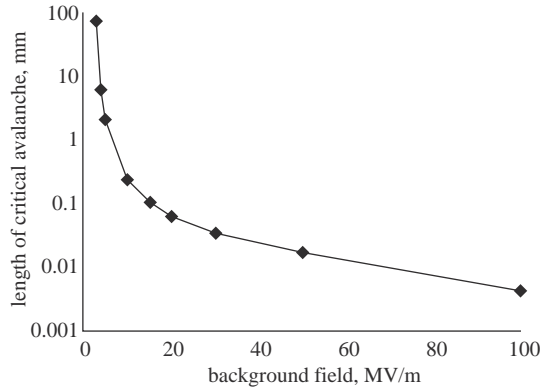


Figure 3.14 The length of the avalanche at the avalanche to streamer transition for different values of the uniform background electric field (from [28])

### 3.7.4 Characteristics of the streamers

#### 3.7.4.1 Physical processes taking place at the streamer head and its propagation

The advancement of the streamer in a given background electric field is based on the distortion of the electric field at and the enhanced production of the photons from the head. The photons create secondary electrons in front of the streamer head and these secondary electrons give rise to secondary avalanches that will move, in the case of positive streamers, towards the streamer head. Once initiated, the streamers have been observed to travel in background electric fields that itself cannot support avalanche formation. Thus, the secondary avalanche formation in the streamer is confined to a very small region around the streamer head where the electric field exceeds  $2.6 \times 10^4$  V/cm, which is the minimum field required for the cumulative ionisation in air at atmospheric pressure. This region is called the active region. A schematic representation of the streamer tip and the active region is shown in Figure 3.15.

If the number of positive charges at the streamer head of radius  $R_s$  is  $Q_c$  then, assuming spherical charge distribution, the electric field at a distance  $r$  from the centre of the charge distribution is given by

$$E(r) = \frac{Q_c}{4\pi\epsilon_0 r^2} \quad \text{for } r > R_s \quad (3.69)$$

With the number of charges at the head equal to  $10^8$  (i.e.  $Q_c = 10^8 e$ , where  $e$  is the electronic charge), the electric field will be higher than  $2.6 \times 10^4$  V/cm for a radius of 0.23 mm. This shows that the radius of the active region is about 200  $\mu\text{m}$ . The average electron energy in the active region is about 10–15 eV and this corresponds to an average electric field of about  $1\text{--}1.5 \times 10^5$  V/cm [29].

#### 3.7.4.2 Propagation of streamer discharges

A schematic representation of the propagation of a positive streamer is shown in Figure 3.16. The local but strong electric field resulting from the concentration of positive charge at the streamer head attract the secondary avalanches towards it.

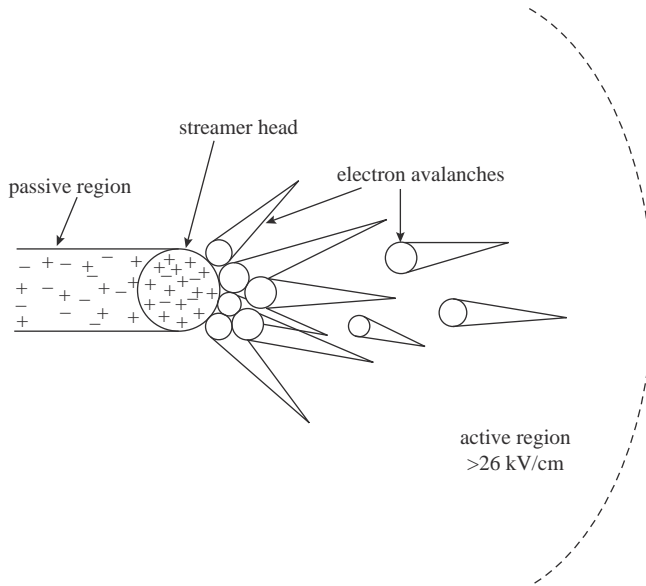


Figure 3.15 *Schematic presentation of the active region of the streamer (adapted from [16])*

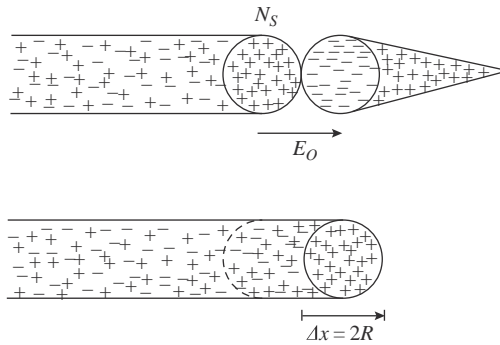


Figure 3.16 *Schematic presentation of the propagation of positive streamers (from [30])*

These avalanches neutralise the positive space charge of the original streamer head leaving behind an equal amount of positive space charge at a location slightly ahead of the previous head. The repetition of the process leads to an effective forward propagation of the streamer head which is connected to the anode by a weakly conducting channel.

Since the electron multiplication in the active region is supported by the space charge electric field of the streamer head, the streamer can propagate in electric fields which are much smaller than the critical electric field necessary for cumulative electron ionisation. Indeed Dawson and Winn have shown that a spherical space charge containing  $10^8$  electrons confined within a radius of  $30 \mu\text{m}$  can propagate in zero electric field for a short time [31].

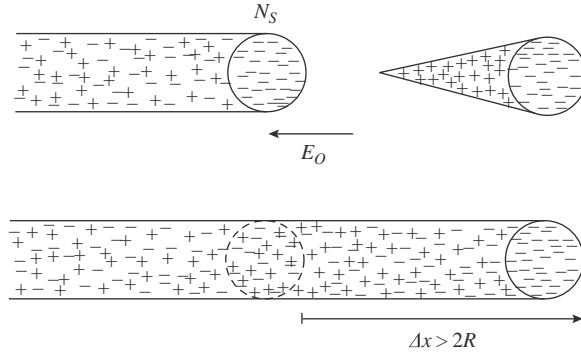


Figure 3.17 Schematic presentation of the propagation of negative streamers (from [30])

The mechanism of propagation of negative streamers are a little bit more complicated than the positive streamers. This is shown in Figure 3.17. Note that there are two main differences between the negative and positive streamers. In the negative streamer, the electrode has to supply the electrons necessary for the neutralisation of the positive space charge left behind by the avalanches, whereas in the positive streamers the anode absorbs the extra electrons generated by the secondary streamers. The latter is a much easier process than the former. Second, in the positive streamers the electrons propagate towards the positive charge head of the streamer and therefore into an increasing electric field. In the case of negative streamers the electrons move into the low electric field region and some of them will be captured by electronegative atoms which create an immobile negative space charge region that will impede the streamer propagation. Both these features make the propagation of positive streamers easier than that of negative streamers. This is reflected in the minimum background electric fields necessary for the propagation of streamers as will be described in section 3.7.4.4.

We have seen before that for the inception of a streamer the number of charged particles at the avalanche head should reach a critical value. Similarly for the continuous propagation of a streamer the number of charged particles in the streamer head has to be larger than a critical number,  $N_{stab}$ . The value of  $N_{stab}$  partly depends on the background electric field,  $E_b$ , and can be calculated from the following equation [16]:

$$N_{stab} = 0.558 \times 10^8 - 0.231 \times 10^3 E_b \quad \text{for } E_b \leq 2 \times 10^5 \text{ V/cm} \quad (3.70)$$

$$N_{stab} = 3.34 \times 10^8 e^{-1.614 \times 10^{-5} E_b} \quad \text{for } E_b \geq 2 \times 10^5 \text{ V/cm} \quad (3.71)$$

### 3.7.4.3 Physical properties of the positive streamer channel

The streamer channel, though weakly ionised, provides a path for the electrons to propagate from the head of the streamer to the anode in the case of positive streamers or from the anode to the head of the streamer in the case of negative streamers. The streamer channel consists of a quasi-neutral plasma with an excess of positive charge and based on rotation temperature measurements [29], one can conclude that the gas in the streamer channel is at ambient temperature.

The streamer radius was found to be on the order of 10–50  $\mu\text{m}$  [32, 33]. This value however may correspond to short streamers. The radius of long streamers could be larger than these values because of the channel expansion due to diffusion. Streamer length in principle has no limits. It may grow as long as the gap and the voltage source permits. In laboratory conditions, cathode directed streamers as long as 10 m were observed in air at gap voltages of 5 MV. This may be even longer in the stepped leaders of lightning discharge. However, this length has not yet been measured in them.

The net positive charge in the streamer channel is about  $0.6\text{--}3 \times 10^9$  ions/cm. The free electron density per unit length of the streamer channel lies in the range of  $0.7\text{--}6 \times 10^{12}$ /cm [34]. Thus the streamer can be regarded as a quasi-neutral plasma filament.

#### 3.7.4.4 Critical background electric field necessary for streamer propagation

In air, the background electric field necessary for positive streamer propagation lies in the range of  $4\text{--}6 \times 10^3$  V/cm [35–37]. For negative streamers it lies in the range of  $1\text{--}2 \times 10^4$  V/cm. Any variation in the electron loss processes can change this electric field. For example, when air is saturated with water vapour, the critical electric field for positive streamer propagation grows from about  $4.3 \times 10^3$  V/cm at humidity of  $3/\text{g}\text{m}^3$  to about  $5.6 \times 10^3$  V/cm at  $18 \text{ g}/\text{cm}^3$  [37–39]. The critical electric field necessary for streamer propagation not only varies with gas composition and humidity but also changes with the temperature and density. For example, Figure 3.18 shows how this critical electric field varies both with humidity and with pressure. Note that the critical electric field decreases with decreasing pressure.

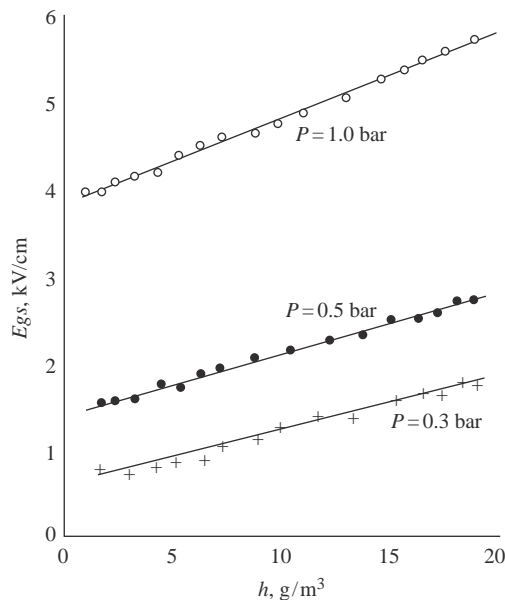


Figure 3.18 *The critical streamer propagation fields as a function of absolute humidity for three values of pressure (from [38], see also [39])*

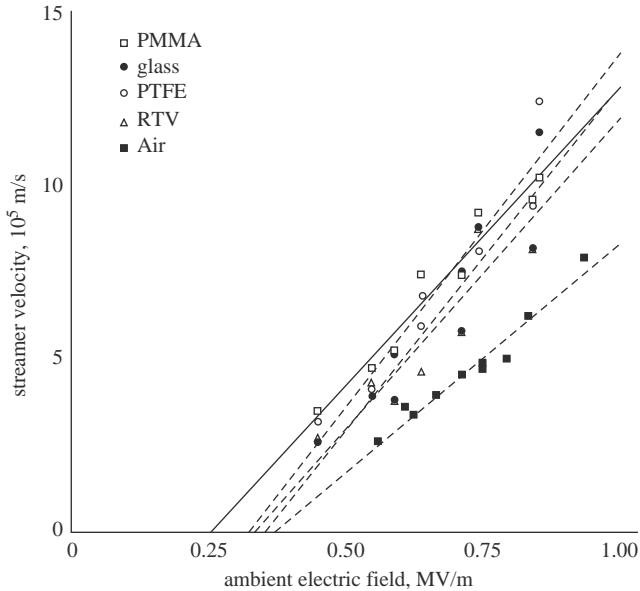


Figure 3.19 Speed of streamers propagating along different insulator surfaces and in air as a function of the ambient electric field [40]

### 3.7.4.5 Streamer speed

Experimental data on positive streamer speed both in air and along insulating surfaces are shown in Figure 3.19 [40]. The results show that the streamer speed increases with increasing background electric field. When the background electric field is close to the critical electric field necessary for streamer propagation the streamer speed is close to  $2 \times 10^7$  cm/s. For a given background electric field the speed of a streamer propagating along an insulating surface may be higher than that of the streamers propagating in air.

The minimum or critical streamer velocity seems to increase when electro-negative components are removed from gas. In technical nitrogen (about 1 per cent oxygen) long-lived steady streamers could be observed propagating at  $5 \times 10^8$  cm/s and in pure argon at  $2 \times 10^8$  cm/s [41, 42].

### 3.7.4.6 Current in the streamer

The current flowing along the streamer channel is essentially an electron conduction current supported by the background electric field. An example of a current generated at the initiation of a streamer is shown in Figure 3.20 [37]. The peak current of the streamer may depend on the background electric field and whether or not the streamer is propagating along an insulating surface. The streamer current has a risetime of about 10–50 ns and the tail duration of about 200–500 ns [16, 37]. Experiments show that the duration of the tail depends on the concentration of electronegative  $O_2$  molecules because this will change the lifetime of free electrons due to attachment [33].

### 3.7.4.7 Potential gradient of the streamer channel

No direct measurements are available today on the potential gradient of the streamer channels. Experiments conducted with long sparks show that the average

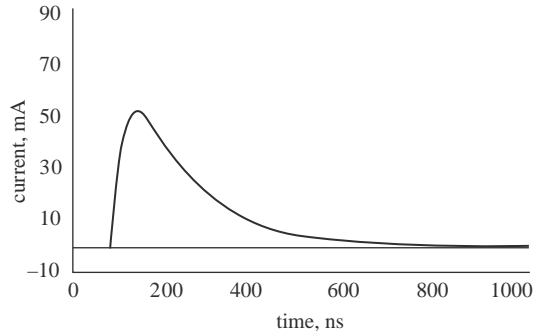


*Figure 3.20 Typical example of a streamer current measured at the point of inception. In the experiment the streamer is initiated by applying a 15 kV impulse to a needle of length 2 mm and 0.35 mm diameter located in a background electric field of 430 kV/m [44]*

potential gradient of the electrode gap when the positive streamers bridge the gap between the two electrodes is about  $5 \times 10^3$  V/cm [43]. This indicates that the potential gradient of the positive streamer channels in air at atmospheric pressure is close to this value. Note that this value is approximately the same as the critical electric field necessary for the propagation of positive streamers.

#### **3.7.4.8 Charge distribution along the streamer channel**

The charge incorporated into a streamer channel can be evaluated from the current oscillograms, and the linear charge density along the channel can be evaluated by dividing this number by the length. However, this procedure is not very informative because the streamer charge need not be distributed uniformly along the channel. The charge distribution along the streamer channel can be evaluated theoretically but the distributions obtained so depend on the assumptions made in the theory. Actually, there is no consensus among scientists on the distribution of the charge along the streamer channel. Some scientists assume that the charge distribution in the streamer channel is such that the potential gradient is constant and equal to about  $5 \times 10^3$  V/cm in the channel [44]. Some scientists assume that the charge of the streamer channel is concentrated at the head and the streamer channel is neutral [16, 31]. One can also treat the streamer channel as a perfect conductor in estimating the charge distribution of the streamer in a given background field [45]. This treatment neglects the fact that the streamer channel is a weakly conducting channel and there is a potential gradient along it. The present author believes that the first assumption is the most reasonable one.

#### **3.7.5 Streamer to spark transition and thermalisation**

In the previous sections we have considered the conditions necessary for the initiation of streamer discharges in a given electric field configuration but not the formation of electrical breakdown in the gap. As mentioned previously, the streamer is a cold discharge (i.e. the gas temperature in the channel is close to ambient) and the conductivity of the streamer channel is rather small. Thus, the propagation of the streamer from one electrode to another is not a guarantee that it will result in electrical breakdown. Before the electrical breakdown of the gap is realised the streamer channel has to be converted to a highly conducting channel by heating.

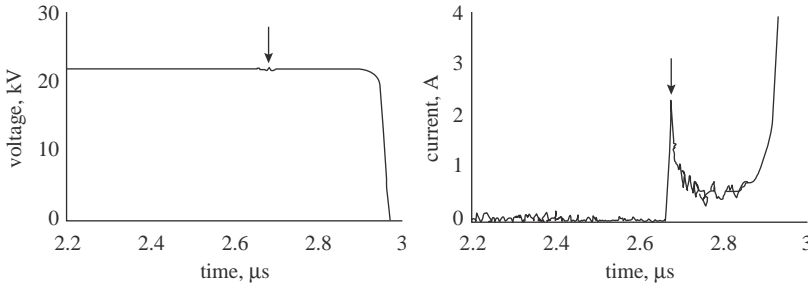


Figure 3.21 The voltage (left) and current (right) oscillogram corresponding to the streamer inception and streamer to spark transition. Data obtained for a 10 mm gap at atmospheric pressure [46]

This process is called streamer to spark transition and it is achieved by the heating of the channel through the process of thermalisation.

In small electrode gaps, the streamer channel can convert itself to a highly conducting spark channel leading to direct streamer to spark transition. Figure 3.21 shows the current and the gap voltage associated with the formation of the streamer and the subsequent increase in the current due to the streamer to spark transition in a 10 mm gap [46]. Observe that the streamer inception (at the time marked with the arrow) and its subsequent crossing of the gap (streamer may take about 50 ns to cross the gap) do not lead to the collapse of the voltage. The streamer channel has to be heated up before full breakdown materialises in the gap. According to Marode [33] the streamer to spark transition takes place as follows. The streamer creates an ionised track which finally bridges the gap with the formation of a cathode fall region at the cathode (see section 3.10). At all stages of its development streamer channel behaves like a glow discharge with a local high electric field region (i.e. at the head) followed by a filamentary positive column. Within this positive column the small value of the electric field leads to an attachment rate higher than the ionisation rate so that the discharge current decreases. In spite of the inefficient transfer of energy from the electrons to neutrals, a weak but non-negligible increase of the temperature of the neutrals can occur which raises the pressure in the channel. The resulting dynamics of the neutral species will lead to a reduction of this pressure causing the neutral density within the discharge channel to decrease. In turn, the ratio of electric field strength to neutral density increases, and if it reaches a critical value, where the ionisation coefficient begins to surpass the apparent attachment coefficient, a final growth of ionisation will occur leading to thermalisation and spark formation. Let us now consider how thermalisation is achieved in the discharge.

In the streamer phase of the discharge many free electrons are lost due to attachment to electronegative oxygen. Furthermore, a considerable amount of energy gained by electrons from the electric field is used in exciting molecular vibrations. Since the electrons can transfer only a small fraction of their energy to neutral atoms during elastic collisions the electrons have a higher temperature than the neutrals. That is, the gas and the electrons are not in thermal equilibrium. As the gas temperature rises to about 1600–2000 K rapid detachment of the electrons from oxygen negative ions supplies the discharge with a copious amount of electrons thus enhancing the ionisation [16]. As the temperature rises the VT relaxation time (see section 3.5.2) decreases and the vibrational energy converts back to



translational energy thus accelerating the heating process. As the ionisation process continues the electron density in the channel continues to increase. When the electron density increases to about  $10^{17} \text{ cm}^{-3}$  a new process starts in the discharge channel. This is the strong interaction of electrons with positive ions through long-range Coulomb forces [16]. This leads to a rapid transfer of the energy of electrons to positive ions causing the electron temperature to decrease. The positive ions, having the same mass as the neutrals, transfer their energy very quickly, in a time on the order of  $10^{-8} \text{ s}$ , to neutrals. This results in a rapid heating of the gas. At this stage the thermal ionisation sets in causing a rapid increase in the ionisation and the conductivity of the channel. This process is called thermalisation. During thermalisation as the electron temperature decreases the gas temperature increases and very quickly all the components of the discharge namely electrons, ions and neutrals will achieve the same temperature and the discharge will reach local thermodynamic equilibrium. The rapid increase in the conductivity of the channel during thermalisation leads to an increase in the current in the discharge channel and the collapse of the applied voltage leading to a spark.

### 3.7.6 *Electrical breakdown criterion in the presence of streamer discharges*

As discussed in the previous section creation of a streamer in a discharge gap does not necessarily mean that it will always lead to electrical breakdown of the gap. However, if electrical breakdown does not materialise after the streamers has bridged the gap only a slight increase in the voltage will lead to final breakdown. Thus, the voltage necessary for the inception of a streamer and the subsequent propagation across the gap can be used as a criterion for electrical breakdown.

#### 3.7.6.1 **Plane uniform gap**

Consider a plane uniform gap of separation  $d$ . In order for a streamer to be incepted in the gap the electric field in the gap (and hence the applied voltage) should be such that the critical avalanche length  $x_c$  is less than or equal to the gap length. This is illustrated in Figure 3.22. Thus the electrical breakdown criterion could be stated as

$$x_c = d \quad (3.72)$$

If we use the Raether and Meek criterion for streamer inception, the electrical breakdown criterion in the gap would be

$$\bar{\alpha}d \approx 18 \quad (3.73)$$

Note that in order for a streamer to be initiated in the gap the electric field should increase beyond  $2.6 \times 10^6 \text{ V/m}$ . Since this electric field is larger than the critical background electric field necessary for the propagation of streamers, once a streamer is initiated in the gap the conditions necessary for its propagation is already fulfilled in the space between the two electrodes.

#### 3.7.6.2 **Non-uniform gap**

The geometry under consideration is shown in Figure 3.23. For a streamer to be initiated at the high-voltage electrode and for it to bridge the gap two conditions,

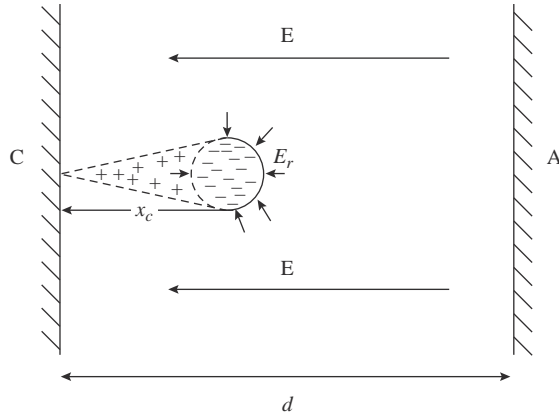


Figure 3.22 Geometry pertinent to the derivation of streamer breakdown criterion in a plane parallel gap

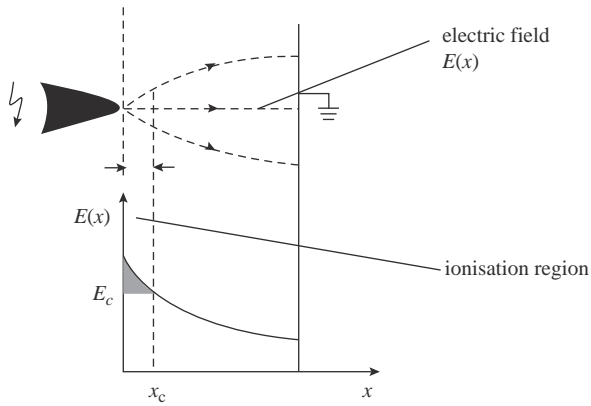


Figure 3.23 Geometry pertinent to the derivation of streamer breakdown criterion in a non-uniform gap

one for the streamer inception and the other for the streamer propagation, have to be satisfied.

- (i) *Inception criterion*: The criterion for the inception of the streamer can be written as

$$\exp \left\{ \int_0^{x_c} \bar{\alpha}(x) dx \right\} \geq 10^8 \quad (3.74a)$$

or

$$\int_0^{x_c} \bar{\alpha}(x) dx \geq 18 \quad (3.74b)$$

where  $x_c$  is the axial length of the region within which the electric field is higher than  $2.6 \times 10^4$  V/cm). The coordinate at the tip of the electrode is assumed to be  $x = 0$ . Note that this is identical to the Raether and Meek streamer inception criterion, the only difference being that the electric field is not uniform and hence  $\bar{\alpha}$  is not a constant but a function of  $x$ .

- (ii) *Propagation criterion:* Once the streamer is created, the background electric field must be able to sustain the streamer propagation. If the background electric field beyond the point  $x_c$  decreases below about  $0.5 \times 10^4$  V/cm then neither positive nor negative streamers will reach the grounded electrode (in reality one has to consider the fact that streamers can propagate short distances in electric fields less than this critical value). If this background electric field is greater than about  $0.5 \times 10^4$  V/cm but it is less than about  $1.0\text{--}2 \times 10^4$  V/cm then positive streamers will cross the gap and reach the cathode while the negative streamers may die out before reaching the anode. This last fact explains the reason why it is easier to cause breakdown in a rod-plane gap when the rod is at a positive polarity than when it is at a negative polarity.

### 3.8 Electrical breakdown in very small gaps: Townsend's breakdown mechanism

As described previously, avalanche to streamer transition requires that the avalanche grows to about  $10^8$  electrons and the space charge in the avalanche tip creates an electric field that significantly adds to the background electric field in the vicinity of the avalanche tip. This avalanche to streamer transition has been observed when the product of the pressure and the electrode spacing in plane uniform gaps exceeds about 0.5 bar·cm. Below this limit the space charge of the avalanche is not large enough to change the background field significantly. This will inhibit the avalanche to streamer transition. Under such conditions the breakdown takes place according to the Townsend's mechanism.

#### 3.8.1 Townsend's experiment

In the Townsend's experiment (Figure 3.24) a plane parallel electrode gap was located in a cell, the gas pressure of which was on the order of a few torr [47]. The cathode was illuminated with a steady beam of ultraviolet radiation which led to a steady stream of electrons from it. The current flowing across the gap is measured as a function of the voltage. Townsend found that the voltage and the current vary in a manner shown in Figure 3.25.

Let us investigate the features of this curve in details. Initially, the current in the gap increases with increasing voltage. The reason for this is that some of the electrons emitted by the cathode diffuse back into it and some of the electrons are lost to the walls. This diffusion and losses to the walls of the tube decrease with increasing voltage. When the voltage increases to a certain level almost all the electrons emitted by the cathode are collected by the anode thus producing the saturation in current. In reality, however, the current will only approach but not sustain a saturation level. The reason for this is that even though the back diffusion decreases with increasing voltage not all the emitted electrons will reach the anode even when the voltage is close to the sparking potential. As the voltage increases further, Townsend found that the current starts to increase exponentially with the

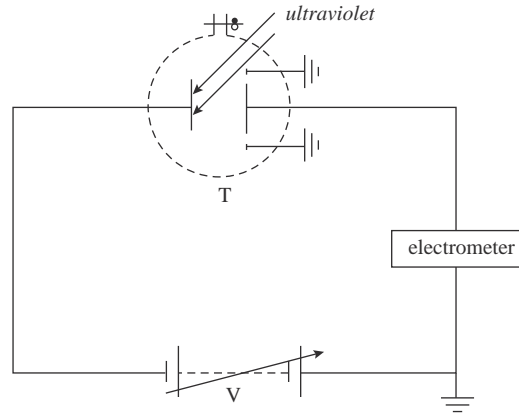


Figure 3.24 Schematic representation of the apparatus used by Townsend in his experiment.  $V$  is the voltage source and  $T$  is the vacuum tube. The discharge gap is located in the vacuum tube and the cathode is illuminated by ultraviolet radiation

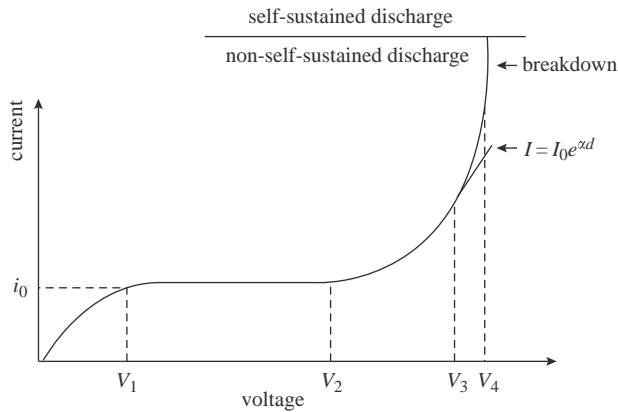


Figure 3.25 Variation of the current flowing across the discharge tube of Townsend's experiment as a function of the applied voltage

applied voltage. This exponential growth of the current was sustained over a certain range of applied voltage but with further increase in voltage the current started to increase faster than the exponential growth. Further increase in voltage resulted in the electrical breakdown of the gap.

### 3.8.2 Townsend's theory of electrical breakdown

Townsend assumed that the initial exponential growth of the current in the discharge tube is caused by the production of secondary electrons through the collision of primary electrons, generated from the cathode, with gas atoms. The second phase of the discharge in which the current grows faster than exponential is assumed to be caused by the ionisation of the atoms through the collision of ions. However, today we know that the correct explanation is the additional production of electrons by the collision of positive ions with the cathode. Let us consider the

mathematical treatment of the discharge process taking place in the Townsend's experiment and come up with an equation that matches the experimental data.

### 3.8.2.1 Primary ionisation stage

If  $n_0$  is the number of electrons emitted by the cathode per second then in steady state, neglecting the electron attachment, the number of electrons reaching the anode per second,  $n_d$ , is given by

$$n_d = n_0 e^{\alpha d} \quad (3.75)$$

Consequently, the current inside the tube is given by

$$i_d = i_0 e^{\alpha d} \quad (3.76)$$

where  $d$  is the gap length,  $i_d = n_d e$ ,  $i_0 = n_0 e$ ,  $\alpha$  is the Townsend's first ionisation coefficient and  $e$  is the electronic charge. This equation explains the exponential growth of current with increasing voltage. Note that even though the voltage does not appear explicitly in this equation it indirectly appears in  $\alpha$  which increases with increasing electric field (and hence with increasing voltage when  $d$  is constant). Note that  $i_0$  is the current generated by the ultraviolet radiation at the cathode. Consequently, if the source of ultraviolet radiation is removed (i.e.  $i_0 = 0$ ) then the current in the discharge tube will go to zero. Thus the discharge is not self-sustained. That is, it needs the support of the external agency for its continuation.

### 3.8.2.2 Secondary ionisation stage

Townsend observed that with increasing voltage the current in the discharge tube begins to increase with voltage at a rate faster than that predicted by (3.76). This departure from (3.76) is shown in Figure 3.26 where  $\log(I)$  is plotted as a function of the gap spacing,  $d$ . The upcurving occurs when the current departs from this equation. Townsend assumed that the cause of this departure of the experimental data from that predicted by (3.76) is the ionisation of the gas atoms due to the collision of positive ions. But, in reality, the energy gained by the positive ions at electric fields encountered in the Townsend's experiment is not sufficient enough

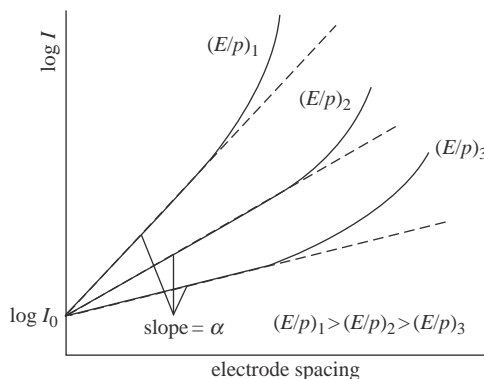


Figure 3.26 Variation of the logarithm of the current flowing across the discharge tube in Townsend's experiment as a function of the logarithm of the electrode spacing for different values of  $(E/p)$  where  $E$  is the electric field in the gap and  $p$  is the pressure

to create significant ionisation. However, one process that may cause this departure from (3.76) is the generation of electrons from the cathode by positive ion bombardment. As the voltage increases the positive ions gain more and more energy and this energy is released at the cathode. With increasing energy a stage will be reached in which these positive ions will start liberating electrons from the electrode. In order to explain the variation of current with voltage one has to take this effect into account. Let us now derive a mathematical expression for the current in the discharge tube taking into account the electron current created by the bombardment of positive ions on the cathode.

Let  $n_0$  be the number of electrons emitted by the cathode per second due to ultraviolet illumination and  $n_+$  be the number of electrons released from the cathode per second due to bombardment of positive ions. Then the number of electrons reaching the anode at steady state per second,  $n$ , is equal to

$$n = (n_0 + n_+)e^{ad} \quad (3.77)$$

The number of positive ions created by the electrons reaching the anode per second is equal to  $n - (n_0 - n_+)$  and at steady state the number of positive ions reaching the cathode per second is equal to this number. Consequently, the number of electrons released by the positive ion bombardment at the cathode per second is given by

$$n_+ = \{n - (n_0 - n_+)\}\gamma \quad (3.78)$$

where  $\gamma$  is the average number of electrons released by each positive ion striking the cathode. This parameter is called the Townsend's secondary ionisation coefficient. Substituting this expression in (3.77) one obtains

$$n = \frac{n_0 e^{ad}}{1 - \gamma(e^{ad} - 1)} \quad (3.79)$$

The current in the discharge tube is given by

$$I = \frac{I_0 e^{ad}}{1 - \gamma(e^{ad} - 1)} \quad (3.80)$$

This equation predicts a faster current growth than (3.76) with increasing electric field (or voltage) providing an explanation for the Townsend's experimental results.

In deriving the above equation we have considered the bombardment of positive ions on the cathode as the only secondary ionisation process. Let us now consider the other secondary ionisation processes.

- (i) *Ionisation of gas by positive ions*: Townsend in his original derivation assumed that the secondary ionisation mechanism is due to the ionisation in the gas by positive ions. However, as mentioned above positive ions cannot produce significant ionisation at electric fields at which electrical breakdown is observed in Townsend's experiment. Nevertheless, if we assume that the ions will contribute to the ionisation the resulting equation for the current will take the form [47]

$$i = i_0 \frac{e^{(\alpha-\beta)d}}{\left(\frac{\alpha}{\alpha-\beta}\right) - \left(\frac{\beta}{\alpha-\beta}\right)e^{(\alpha-\beta)d}} \quad (3.81)$$

where  $\beta$  is the ionisation coefficient of positive ions. Since electrons ionise more readily than positive ions one can replace  $(\alpha - \beta)$  by  $\alpha$  and the equation will reduce to

$$i = i_0 \frac{e^{(\alpha)d}}{1 - \left(\frac{\beta}{\alpha}\right) e^{(\alpha)d}} \quad (3.82)$$

This equation has the same form as that of the expression obtained for positive ion bombardment at the cathode (i.e. (3.80)).

- (ii) *Photo emission from the electrode*: Another secondary emission process that one may take into account is the interaction of photons in the discharge with the electrodes. If the incident photon has an energy larger than the work function of the electrode then the interaction may lead to a liberation of an electron. If this process is taken into account as a secondary mechanism then the expression for the current will take the form [23]

$$i = i_0 \frac{e^{(\alpha)d}}{1 - \left(\frac{\Delta g \theta}{\alpha - \mu}\right) [e^{(\alpha-\mu)d} - 1]} \quad (3.83)$$

where  $g$  is the fraction of photons emitted in the gas that are headed towards the cathode,  $\mu$  is the coefficient of absorption of photons in the gas,  $\Delta$  is the probability of photoelectric emission from the photons incident on the electrode (note that only a fraction of the incident photons will have sufficient energy to cause photoionisation) and  $\theta$  is the number of excited states or photons created per unit path in the electric field direction per electron.

In general  $\alpha \gg \mu$  and the equation will reduce to

$$i = i_0 \frac{e^{(\alpha)d}}{1 - \left(\frac{\Delta g \theta}{\alpha}\right) [e^{(\alpha)d} - 1]} \quad (3.84)$$

This again has the same form as that of (3.80).

- (iii) *Collision of meta-stable ions on the cathode*: Collision of meta-stable atoms on the cathode can also liberate electrons from the cathode. If the meta-stable level has a higher energy than the work function of the metal such an interaction can lead to the emission of electrons. If this is taken into account [14]

$$i = i_0 \frac{e^{(\alpha)d}}{1 - (\gamma_m) [e^{(\alpha)d} - 1]} \quad (3.85)$$

where  $\gamma_m$  is the number of electrons liberated by the collision of a meta-stable atom on the cathode.

- (iv) *Ionisation of the gas by photons*: Another process that may contribute to the electron production in the gas is the ionisation of the gas by photons. If this is

taken into account, one can show that the resulting equation will have the form [14]

$$i = i_0 \frac{e^{(\alpha)d}}{1 - \left(\frac{\zeta g f \mu}{\alpha - \mu}\right) [e^{(\alpha-\mu)d} - 1]} \quad (3.86)$$

where  $\mu$  is the coefficient of absorption of photons,  $\zeta$  is the fraction of absorbed photons that will cause ionisation,  $f = \theta/\alpha$  where  $\theta$  is the number of excited states or photons created per unit path in the electric field direction per electron and  $g$  is a geometrical factor that will describe the fraction of photons directed in a given direction.

- (v) *Final expression for the current in the presence of secondary processes:* The results presented above show that irrespective of the secondary ionisation process under consideration the final expression for the current has the same form. Indeed one can include all of them in a single formula as follows:

$$i = i_0 \frac{e^{(\alpha)d}}{1 - (\gamma_i)[e^{(\alpha)d} - 1]} \quad (3.87)$$

where

$$\gamma_i = \gamma + (\alpha/\beta) + (\Delta g \theta/\alpha) + \gamma_m + \left(\frac{\zeta g f \mu}{\alpha - \mu}\right) \quad (3.88)$$

### 3.8.2.3 Townsend's electrical breakdown criterion

The final expression for the current given in (3.87) shows that the discharge is still non-self-sustained. That is, the discharge current goes to zero if the ultraviolet illumination on the cathode is removed (i.e. as  $I_0 \rightarrow 0$ ). However, as the voltage is continued to increase a stage will be reached at which the discharge will transform itself from a non-self-sustained discharge to a self-sustained discharge. At this stage the discharge will continue to burn between electrodes even after removing the background ultraviolet radiation (i.e. when  $I_0 = 0$ ). This change of state of the discharge is accompanied by a several orders of magnitude increase in the current (provided that the voltage supply can sustain such an increase in the current) in the discharge gap. This is the stage of electrical breakdown in the gap. Townsend defined the electrical breakdown condition as the condition which makes the current in the discharge gap goes to infinity. From (3.87) one can see that  $I_0 \rightarrow \infty$  when the denominator of the expression for the current goes to zero. That is when

$$1 - \gamma_i [e^{\alpha d} - 1] = 0 \quad (3.89)$$

This condition is known as Townsend's breakdown criterion.

One can indeed show that this criterion has a physical significance. Assume that is the  $\gamma$  dominant secondary ionisation process. Also assume that  $n_0$  denotes the primary electrons leaving the cathode per second. These electrons will give rise to  $n_0(e^{\alpha d} - 1)$  positive ions in the gap, and these positive ions on incidence on the cathode produce  $\gamma n_0(e^{\alpha d} - 1)$  secondary electrons. When the Townsend's breakdown criterion is satisfied the number of secondary electrons is equal to the original number of electrons which has been drawn away from the cathode and later passed into the anode. Consequently, each avalanche will give rise to another avalanche



through secondary processes and so causes a repetition of the avalanche process. That is, the discharge process becomes self-sustained.

An alternative expression for the Townsend's breakdown criterion can be obtained by rewriting the above equation as

$$\alpha d = \ln\left(1 + \frac{1}{\gamma_i}\right) \quad (3.90)$$

The value of  $\gamma_i$  is greatly affected by the cathode surface and gas pressure. However,  $\gamma_i$  is a very small number ( $< 10^{-2} - 10^{-3}$ ) so  $1/\gamma_i$  is very large. Therefore,  $\ln\left(1 + \frac{1}{\gamma_i}\right)$  does not change too much and is on the order of 8–10 in a Townsend's discharge.

### 3.8.2.4 Townsend's mechanism in the presence of electron attachment

In the experiments conducted by Townsend the gases under investigation were Noble gases. In this case electron attachment to atoms can be neglected. However, in air, one cannot neglect the electron attachment. Let us consider the effect of electron attachment in the Townsend's equation. In the presence of attachment, the number of electrons reaching the cathode per second is given by

$$n_d = n_0 e^{(\alpha - \eta)d} \quad (3.91)$$

Consider an elementary length  $dx$  located at distance  $x$  from the cathode. Let  $n_x$  be the number of electrons reaching  $x$  in a unit time. In travelling across  $dx$  these electrons will generate  $dn_-$  number of negative ions per second. Then

$$dn_- = n_x \eta dx \quad (3.92)$$

substituting for  $n_x$  one obtains

$$dn_- = \eta n_0 e^{(\alpha - \eta)x} dx \quad (3.93)$$

Since the number of negative ions at the cathode is equal to zero, the solution of this equation is given by

$$n_- = \frac{\eta n_0}{\alpha - \eta} [e^{(\alpha - \eta)x} - 1] \quad (3.94)$$

where  $n_-$  is the number of negative ions crossing a plane at a distance  $x$  from the cathode per second. Thus the number of negative ions reaching the anode per second,  $n_{-d}$ , is given by

$$n_{-d} = \frac{\eta n_0}{\alpha - \eta} [e^{(\alpha - \eta)d} - 1] \quad (3.95)$$

The total current reaching the anode, both due to the electrons and negative ions, is given by

$$i = \frac{i_0}{\alpha - \eta} [\alpha e^{(\alpha - \eta)d} - \eta] \quad (3.96)$$

In the presence of secondary ionisation due to bombardment of positive ions on the cathode one can show using the procedure outlined in section 3.8.2.2

$$i = i_0 \frac{[\alpha e^{(\alpha - \eta)d} - \eta]}{\alpha - \eta - \alpha \gamma \{e^{(\alpha - \eta)d} - 1\}} \quad (3.97)$$

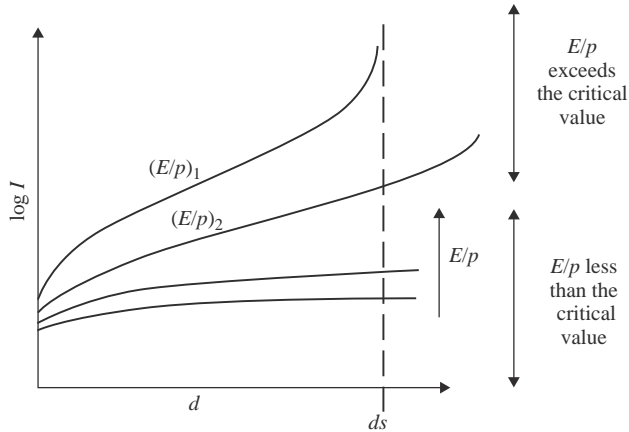


Figure 3.27 Variation of the logarithm of the current flowing across the discharge tube in Townsend's experiment as a function of the logarithm of the electrode spacing for different values of  $(E/p)$  for electronegative gases

This reduces to (3.80) in the absence of attachment (i.e.  $\eta = 0$ ). From this equation the breakdown condition in the presence of electron attachment is given by

$$1 - \left\{ \frac{\gamma\alpha}{(\alpha - \eta)} \right\} [(e^{(\alpha - \eta)d} - 1)] = 0 \quad (3.98)$$

This criterion shows that if  $\alpha > \eta$  then electrical breakdown is possible irrespective of the values of  $\alpha$ ,  $\eta$  and  $\gamma$  provided that  $d$  is large enough. That is, for a given electric field there is a particular value of  $d$  at which the gap breaks down. For  $\alpha < \eta$ , with increasing  $d$  the above equation approaches an asymptotic form

$$\frac{\gamma\alpha}{(\alpha - \eta)} = -1 \quad \text{or} \quad \alpha = \frac{\eta}{(1 + \gamma)} \quad (3.99)$$

This defines the limiting condition at which electrical breakdown is possible in an electronegative gas. This condition depends only on  $E/p$ . Noting that the value of  $\gamma \ll 1$ , the limiting value of  $E/p$  which can cause electrical breakdown in electronegative gases can be obtained from the relationship  $\alpha = \eta$  (see section 3.7). This point is illustrated in the plot given in Figure 3.27.

### 3.9 Paschen's law

If a slowly increasing voltage is applied across two plane parallel electrodes the electrical breakdown of the gap occurs at a certain critical voltage. The experimental data show that the breakdown voltage,  $V_s$ , is only a function of the gas pressure,  $p$  (or gas density), multiplied by the gap length,  $d$ . That is

$$V_s = f(pd) \quad (3.100)$$

This is known as the Paschen's law. The Paschen curve for air is shown in Figure 3.28 [48]. In this figure the results are given in terms of  $pd$  corresponding to a temperature of 293 K. The data points correspond to measurements by

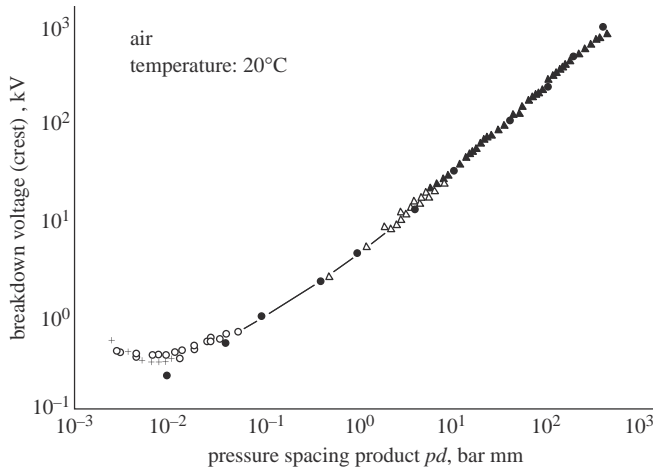


Figure 3.28 Paschen curve for air in log–log scale at temperature 20°C (from [48])

several scientists and the solid black dots are generated from the equation  $V_s = 6.72\sqrt{pd} + 24.4(pd)$  ( $p$  in bar and  $d$  in mm). Note that the sparking potential is high both in the case of low and high values of  $pd$  but there is a minimum at a certain value of  $pd$ . This minimum is called the Paschen minimum. The Paschen minimum in air is about  $pd = 10^{-2}$  bar·mm.

One can show that the breakdown voltage estimated using either the Townsend's or the Raether and Meek's criterion adhere to the Paschen's law. The electrical breakdown criterion of a uniform gap of length  $d$  is given by

$$ad = K \quad (3.101)$$

where  $K$  is a constant. Depending on the value of  $K$  this equation represent both Townsend's breakdown criterion and the streamer breakdown criterion. Substituting the expression for  $\alpha$  given in (3.15) we obtain

$$K = Ape^{-Bpd/V_s} \quad (3.102)$$

where  $V_s$  is the voltage at which electrical breakdown is observed. Note that in deriving this equation we have used  $E = V_s/d$ . Rearranging the above equation we find that

$$V_s = \frac{Bpd}{\ln\left\{\frac{Apd}{K}\right\}} \quad (3.103)$$

This equation shows that  $V_s$  is a function of  $pd$ . The general shape of this equation is in agreement with the Paschen curve.

### 3.9.1 Physical interpretation of the shape of the Paschen curve

In order to give a physical interpretation for the shape of the Paschen curve let us rewrite (3.103) as follows:

$$E_s = \frac{B_1(d/\lambda)}{\ln\left\{\frac{A_1(d/\lambda)}{K}\right\}} \quad (3.104)$$

where  $A_1$  and  $B_1$  are constants,  $\lambda$  is the mean free path of the electrons,  $E_s = V_s/d$  and we have used the relationship that the mean free path is inversely proportional to the pressure. This equation has the same form as (3.103) except that  $pd$  is now replaced by  $d/\lambda$ . It thus predicts that the breakdown electric field has a minimum corresponding to a certain value of  $d/\lambda$ , say  $(d/\lambda)_{\min}$ , and it increases when the value of  $d/\lambda$  moves away from this minimum. The reason for the existence of this minimum can be explained qualitatively as follows: Let  $E_m$  be the electric field in the gap corresponding to  $(d/\lambda)_{\min}$ . At  $(d/\lambda)_{\min}$  an electron crossing the gap will make a certain number of ionisation collisions. Consider the case  $(d/\lambda) > (d/\lambda)_{\min}$ . Now, the number of collisions made by an electron in crossing the gap, and hence the energy lost in collisions in crossing the gap, is higher than at  $(d/\lambda)_{\min}$ . If the background electric field remained at  $E_m$  the total number of ionisation collisions made by an electron crossing the gap would be less than the corresponding value at  $(d/\lambda)_{\min}$ . Consequently, the electric field should be increased in order to compensate for the losses and to increase the probability of ionisation. For  $d/\lambda < (d/\lambda)_{\min}$  the number of collisions, and hence the number of ionisation collisions, made by an electron in crossing the gap is less than the corresponding value at  $(d/\lambda)_{\min}$ . In this case the only way to increase the number of ionisation collisions is to increase the probability of ionisation in each collision. This can be achieved only by increasing the energy gained by electrons within a mean free path. This requires a higher electric field than the one corresponds to  $(d/\lambda)_{\min}$ .

### 3.9.2 Validity of Paschen's law

In section 3.9 it was shown that the Paschen's law follows directly if the dominant collision processes, as is often the case, are such that the coefficients representing them, for example  $\alpha$ , are directly proportional to  $p$  at a given value of  $E/p$ . When this is the case the processes are said to obey similarity.

In general, the experimental data obey the Paschen's law and any deviations are relatively small and arise from the existence of collision processes in the gas which do not conform to similarity. The deviations from Paschen's law can occur at high pressures and at temperatures above about 3000–4000 K. At high pressures exceeding a few atmospheres the processes such as field emission may play a significant role in the breakdown process. The role of field emission at high pressures and its influence on the Paschen's law is clearly demonstrated by the observation that when very clean molybdenum electrodes are used the Paschen's law is held up to very high pressures. The clean electrodes do not have oxide layers that generate field emission at low electric fields. At high temperatures experimental data depart from Paschen's law partly due to the dominant role of thermal ionisation and partly due to the gradual change of chemical composition of the gas, for example, by dissociation. The Paschen's law may also break down at low pressures because the breakdown process is governed by pre-ionisation processes caused by electrodes such as thermionic emission and the breakdown phenomena has to be described by vacuum breakdown processes.

### 3.10 Voltage and current (V–I) characteristics and the post breakdown stage (low pressures)

The type of discharge that appears in the gap after breakdown depends on the gas, gap length, the applied voltage and the parameters of the electric circuit. If the

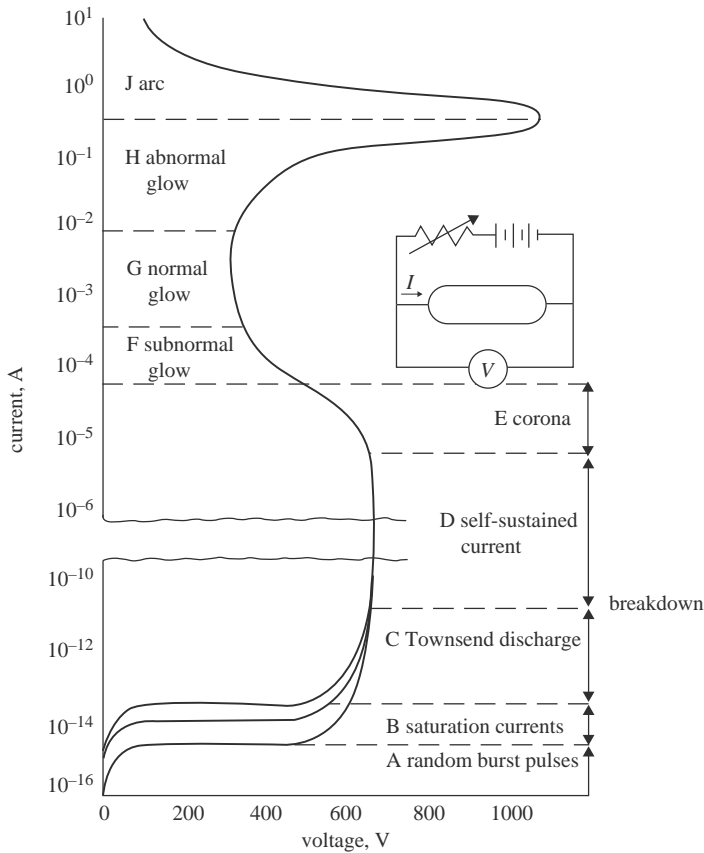


Figure 3.29 Typical voltage–current relation of a gaseous gap. The curve given is for neon at 1 torr with disk electrodes of 2 cm diameter and 50 cm separation (from [14])

breakdown occurs at a pressure on the order of 1–100 torr between electrodes supplied from a DC source, and if the current is carefully controlled then the V–I characteristics as shown in the Figure 3.29 can be obtained [14]. The example shown in this figure corresponds to neon gas at 1 torr. It is important to remember that what is shown is the static characteristics, and the dynamic characteristics could be very different from this one. The regions marked B and C in the diagram correspond to the Townsend discharge. During electrical breakdown, the region marked D, the current in the gap increases by several orders of magnitude and the rate of change of current with voltage is very high. The region marked G is called the normal glow discharge. Here as the current increases the voltage remains at a constant value. As the current reaches a critical value the voltage starts to increase with increasing current and this region, marked H in the diagram, is called the abnormal glow. A further increase in current leads to a sudden change from abnormal glow to an arc discharge with a rapid drop in voltage as the current rises.

### 3.10.1 The glow discharge

The physical appearance of the glow discharge and the different parameters of interest as a function of length along the discharge tube are shown in Figure 3.30.

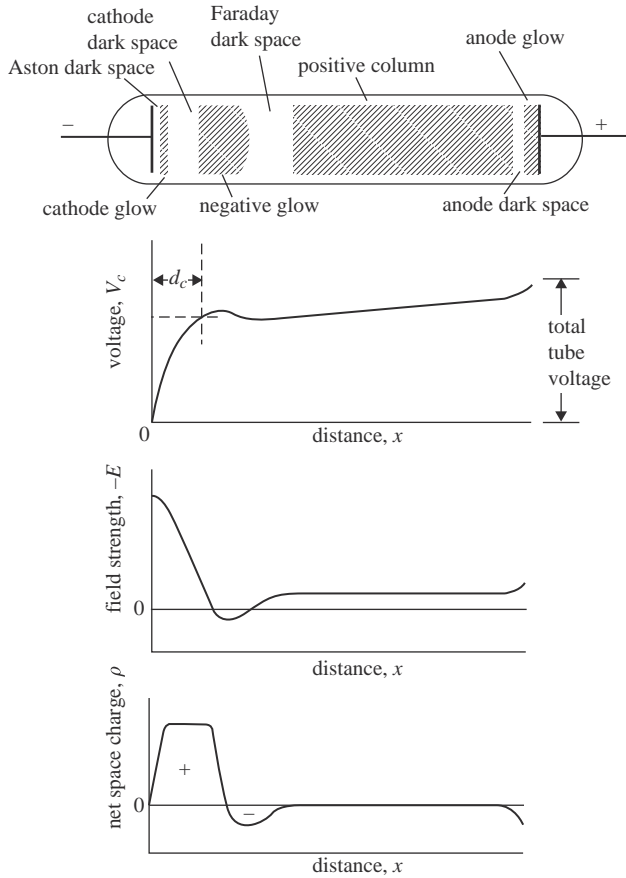


Figure 3.30 Schematic representation of the glow discharge at low pressure together with the variation of the voltage, field strength and the space charge density along the discharge channel (from [7])

It is important to point out that ‘dark’ spaces marked in the diagram are not completely dark. They give less visible radiation than the other regions. One can observe that the distance marked  $d_c$  from the cathode accounts for most of the applied voltage. This rapid drop in voltage is caused by the excessive positive charge located in the vicinity of the negative glow. This voltage drop is known as the cathode drop. Its magnitude, on the order of hundreds of volts, depends mainly on the type of gas and the material of the cathode. In the positive column there is a uniform but slow increase in the voltage and the voltage rises sharply very close to the anode. This is known as the anode fall.

### 3.10.1.1 Physical explanation

Electrons are emitted by positive ion bombardment and incident radiation at the cathode. Before these electrons gain appreciable velocity, they form a negative space charge very close to the cathode. The space charge becomes positive a short distance from the cathode and remains positive throughout the cathode dark space. The cathode glow is caused by the release of ionisation energy as photons by the recombination of slow electrons with the incoming positive ions for which the

recombination coefficient is high. As the electrons are accelerated in the electric field and gain energy the probability of recombination is reduced giving rise to the cathode dark space. At the end of the cathode dark space the high energetic electrons produce intense excitation and ionisation giving rise to the brightest section of the discharge, namely, the negative glow. Indeed since the excitation and ionisation cross sections decrease at very high electron energies the maximum excitation and ionisation takes place after the electrons are slowed down somewhat. Thus the brightest part of the negative glow occurs a short distance away from the leading edge of the negative glow. As the electrons are slowed down the negative space charge reaches a maximum; the energy available for excitation and ionisation is exhausted and the Faraday dark space begins. The negative space charge increases in the Faraday dark space in comparison to the positives because only a few ions are produced here. As a result, the electric field attains a small value and electrons can gain very little energy in this region. At the end of the Faraday dark space the electric field starts to increase again leading to the acceleration of electrons. The electric field stabilises over a small distance, however, at the beginning of the positive column.

The typical values of the electric field in the positive column range from about a fraction of a V/cm to about a few tens of V/cm depending on the gas type, its pressure and the current flowing in the tube. The luminosity of the positive column is created by the excited particles and not from recombination. The colour of the positive column is characteristic of the gas in the discharge. The gas in the positive column is ionised with equal positive and negative charge densities. The length and diameter of the positive column depend on the geometry of the discharge tube. As the pressure increases the positive column contracts radially. One interesting fact is that if the length of the tube is reduced the total reduction in length is taken completely by the positive column leaving the other features of the discharge and the current the same (the voltage may fault slightly in the process). This will continue until the anode is in the negative glow region at which point the voltage required begins to rise. The conclusion is that positive column is unimportant and unnecessary for the operation of the discharge.

One interesting fact pertinent to the discharge is that the product  $pd_c$  (where  $p$  is the pressure) is approximately equal to the Paschen minimum corresponding to the gas in the discharge tube. That is, discharge optimises itself by creating an effective anode at a distance  $d_c$  from the cathode.

### **3.10.1.2 The effect of changing the pressure**

If the pressure in the discharge tube is increased the negative glow and the two dark spaces that surround it will shrink towards the cathode. The positive column will occupy much of the tube length that is available to it. With increasing pressure the voltage gradient of the positive column increases. The opposite happens with decreasing pressure. At pressures so low that the cathode dark space fills the entire tube, the discharge is becoming more like an electron beam.

### *3.10.2 Abnormal glow*

If the discharge is operating within the glow region it is observed that the cathode glow covers only part of the cathode surface. The area of the cathode glow may increase or decrease apparently in proportion to the current flowing. As the current increases the area of the cathode glow increases. It appears that the current density

at the cathode remains constant during the normal glow and therefore the voltage also remain constant. This continues until the glow covers the whole area of the cathode. A further increase in current will lead to an increase in the voltage. This is the beginning of the abnormal glow.

### 3.10.3 The glow to arc transition

The glow to arc transition of the discharge takes place when the abnormal glow has acquired a critical voltage and when the power supply is capable of supplying a high current with a low internal resistance. The arc voltage is an order of magnitude lower than the glow discharge. This transition requires an important change in the electron emission process at the cathode. As we have seen in the case of Townsend's mechanism a self-sustained discharge is created in the gap only after the secondary processes (i.e. positive ion bombardment on the cathode etc.) generated a steady stream of electrons from the cathode by positive ion bombardment. However, these secondary processes alone are not sufficient to maintain an arc. In order to maintain an arc the supply of electrons from the cathode should be increased. This can be realised in three ways: (1) the cathode is heated by an external agent to increase the electron supply; (2) the cathode is heated by the arc itself resulting in an increase in supply of electrons (hot spots created in this way are called cathode spots); (3) an increase in the electron supply caused by the field emission resulting from the very high electric fields caused by the space charge located in the vicinity of the cathode. Such arcs are called field emission arcs.

If the pressure is close to one atmosphere the formation of an arc takes place through a transient spark. All the features shown in Figure 3.29 will then be compressed into a very small time span, and the current voltage characteristics shown in Figure 3.31 is observed [49].

In an arc the current density is much higher than that of the glow discharge. At atmospheric pressure the arc seems to have a very bright core surrounded by a less luminous region. The particle density of the arc may range from  $10^{14}$  to  $10^{18}$  electrons/cm<sup>3</sup> depending on the pressure.

The longitudinal voltage distribution of an arc is shown in Figure 3.32. Note that except at the vicinity of the cathode and the anode the potential gradient is constant. Between pressures  $10^{-3}$  torr to about 10 torr the potential gradient of the arc remains close to a few V/cm and it increases very rapidly to about 10–20 V/cm

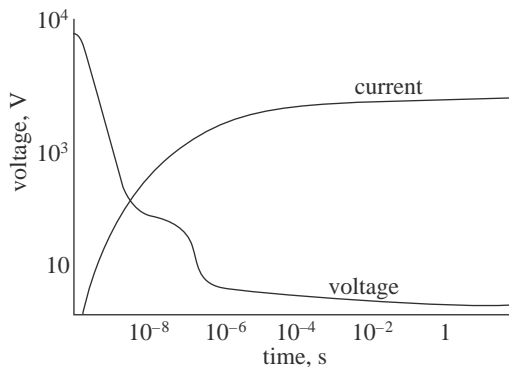


Figure 3.31 The time variation of current and voltage at the initiation of an arc at atmospheric pressure (from [49])



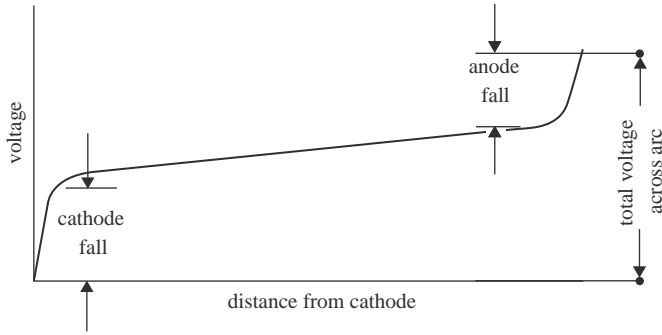


Figure 3.32 Potential distribution along the arc channel (from [49])

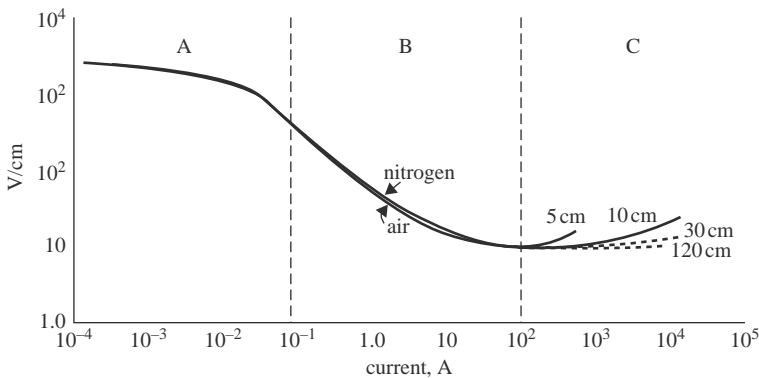


Figure 3.33 Potential gradient-current characteristics of free burning arcs of different lengths in nitrogen and in air at atmospheric pressure (from [50])

at atmospheric pressure. There is a sharp drop in the arc voltage at both the cathode (cathode fall) and the anode (anode fall), and the cathode fall is larger than the anode fall. The cathode fall, being of the order of the ionisation potential of the gas atoms i.e. about 10 V, takes place over a very small fraction of a millimetre. Recall that in the case of glow discharge the cathode fall is on the order of hundreds of volts. Usually the cathode and anode falls remain constant and independent of the arc length. Thus one requires more voltage in order to increase the arc length. This is the case since the extension of the arc leads to the extension of the linear portion of the voltage drop without affecting the end regions.

The potential gradient of atmospheric arcs as a function of current is shown in Figure 3.33 [50]. The potential gradient is on the order of 10–20 V/cm over a large range of current amplitudes. The potential gradient of the high pressure arc column is considerably higher than for the low pressure arc column, but the ratio of potential gradient to the gas pressure is much less at high pressure.

The neutral gas temperature of the arc depends on the pressure of the discharge. It may vary from about 200 K at  $10^{-3}$  torr to about 5000–10 000 K (axial temperature) at atmospheric pressure. The radial distribution of the temperature of a high pressure arc is shown in Figure 3.34. Note that the temperature of the arc has a maximum at the centre and it decreases with increasing radius.

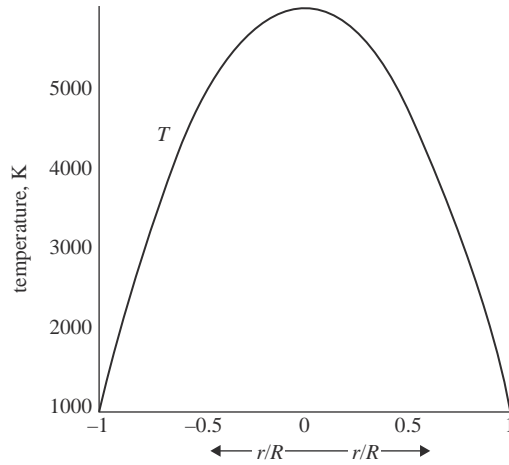


Figure 3.34 The radial temperature distribution of a high-pressure arc (from [49])

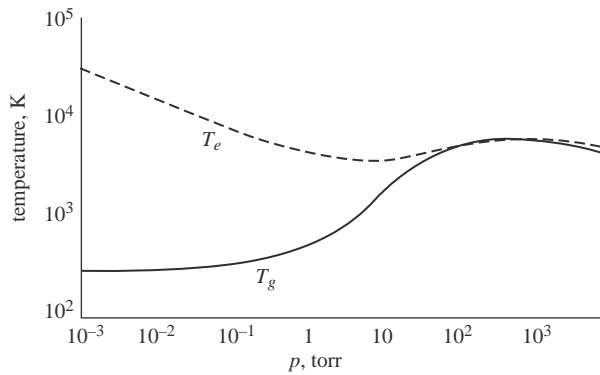


Figure 3.35 The gas temperature  $T_g$  and the electron temperature  $T_e$  in arcs as a function of pressure (adapted from [49])

In low-pressure arcs even though the gas temperature is low the electron temperature is very high. Figure 3.35 shows how the arc temperature and the electron temperature vary as a function of pressure. Observe that at low pressures the electron temperature is much higher than the gas temperature and the two approach each other with increasing pressure. The ion temperature is about the same as that of the neutrals. At low pressures the electron density is not large enough for the thermalisation to occur and as a result the gas and the electrons have different temperatures. With increasing pressures the electron temperature comes closer to the gas temperature partly due to the increased frequency of elastic collisions between electrons and gas atoms and partly due to the increased importance of the coulomb interactions (see section 3.7.5).

### 3.11 Resistance of spark channels

After the streamer to spark transition the thermal ionisation increases the conductivity of the channel leading to a rapid drop in the channel resistance as the

current in the channel increases. There are several theoretical as well as empirical formulas that describe the time-dependent resistance of the spark channel in atmospheric pressure after the streamer to spark transition has taken place. The formula which is used frequently by electrical engineers is the Toepler's formula [51]. According to this the resistance per unit length of the spark channel varies as

$$R(t) = \frac{k_t}{\int_0^t i(t) dt} \quad (3.105)$$

where  $k_t$  is a constant and equal to  $0.005 \pm 20\% \text{ Vsm}^{-1}$ . Observe, however, that according to this equation irrespective of the shape of the spark current the resistance of the spark channel decreases monotonically with time. In reality, the resistance of the channel decreases with increasing current in the discharge channel but it will recover as the current in the spark channel decreases and finally goes to zero.

Engel *et al.* [52] compared the Toepler's equation and several other published equations that predict the temporal variation of the spark resistance. According to them the equation that predicts the resistance per unit length of the spark channel over the entire length of the current pulse is the one published by Kushner *et al.* [53] and it is given by

$$R(t) = k_k \left\{ \frac{P_0^3}{A^2 i(t)^6} \right\}^{1/5} \quad (3.106)$$

where  $k_k$  is a constant equal to 24.7,  $A$  is the cross-sectional area of the discharge in  $\text{m}^2$ ,  $p_0$  is the pressure in Pa and  $i(t)$  is the current in the discharge in A. The cross section of the discharge channel varies with the current and it can be obtained from the following formula, derived by Braginskii [54], which shows how the time-dependent radius of the discharge channel,  $r(t)$  varies with time:

$$r(t) = 0.93 \times 10^{-3} \rho_0^{-1/6} i^{1/3} t^{1/2} \quad (3.107)$$

where  $r(t)$  is given in metres,  $t$  is the time in microseconds,  $i$  is the instantaneous current in kiloamperes and  $\rho_0$  is the air density at atmospheric pressure ( $1.29 \times 10^{-3} \text{ g/cm}^3$ ). It is important to note that Braginskii's derivation is valid for a linearly increasing current. That means that the results may be applicable in the rising part of the discharge current which can be approximated by a linear ramp. On the other hand, the current in a discharge increases initially and then continues to decay. Braginskii [54] warned that the constant in the above equation may have to be modified in order for this equation to describe the variation of the resistance of a spark channel. After comparing the measurements of discharge channel radii available in the literature Cooray *et al.* [55] suggested that in order to apply (3.107) for spark channels the constant  $0.93 \times 10^{-3}$  should be replaced with  $0.328 \times 10^{-3}$ .

### 3.12 Corona discharges

In many situations the electric field in air in the vicinity of objects at higher voltages or exposed to high external electric fields may overwhelm the critical electric

field necessary for the formation of electron avalanches in air. Moreover, the extent of the volume in which this high electric field exist may confine to a very small region around the object (i.e. the electric field is strongly non-uniform) so that it would not lead to any electrical breakdown between the object under consideration and another one in its vicinity. In this case the electrical activity will be concentrated and confined to a small volume around the object. These types of discharge activity are called corona discharges. During corona discharges ionic space charges of both polarities accumulate near the highly stressed electrode, thus modifying the electric field distribution. The equilibrium between accumulation and removal of space charge causes several modes of corona discharges. Moreover, the physical nature of these corona discharges are affected by the electronegativity of the gas under consideration.

In general the conditions necessary for the inception of negative corona discharge do not differ from the Townsend's breakdown condition generalised to include the non-uniformity of the electric field. This is given by

$$1 - \gamma \left\{ \exp \left( \int_0^{x_c} (\alpha - \eta) dx \right) - 1 \right\} = 0 \quad (3.108)$$

where the integral is performed over the region in which  $(\alpha - \eta) > 0$ . The streamer criterion, generalised to take into account the electric field non-uniformity, can be chosen as the inception criterion for positive corona. That is

$$\int_0^{x_c} (\alpha - \eta) dx \approx 18 \quad (3.109)$$

Trinch [56] has given an excellent review of DC corona modes in air. We are indebted to this work for the following brief account.

### 3.12.1 Negative corona modes

In negative corona, the electron avalanches are initiated at the cathode and develop towards anode in a decreasing electric field. The situation is illustrated in Figure 3.36. Due to their high mobility electrons will move rapidly away from the cathode into the low electric field region leaving behind the positive space charge close to the cathode. The electron avalanche will stop at the surface  $S_0$  where the electric field is below the critical electric field necessary for ionisation. Here, the electrons are rapidly captured by the electronegative oxygen atoms creating a negative space charge. These two space charge regions, one positive and the other negative, will modify the electric field configuration in the gap in such a manner that the electric field increases near the cathode while reducing it near the anode. As one can see the avalanches that develop later will develop in a higher electric field but propagate to a shorter distance than their predecessors. The influence of this space charge will lead to three forms of corona modes. They are, according to the order of appearance with increasing voltage, trichel streamers, negative pulseless glow and negative streamer. The appearance of these corona modes are shown in Figure 3.37.

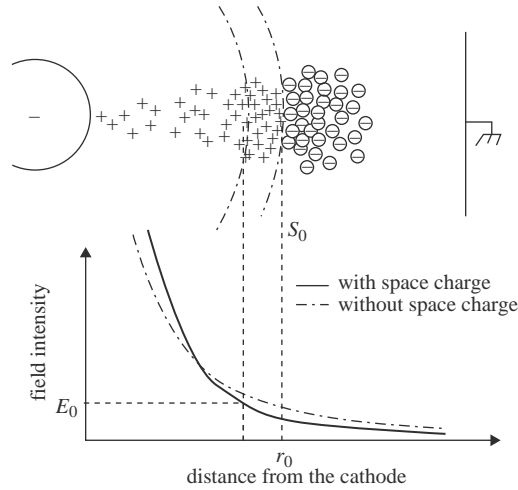


Figure 3.36 *Space charge and the electric field distribution in the gap during the formation of negative corona (from [56])*

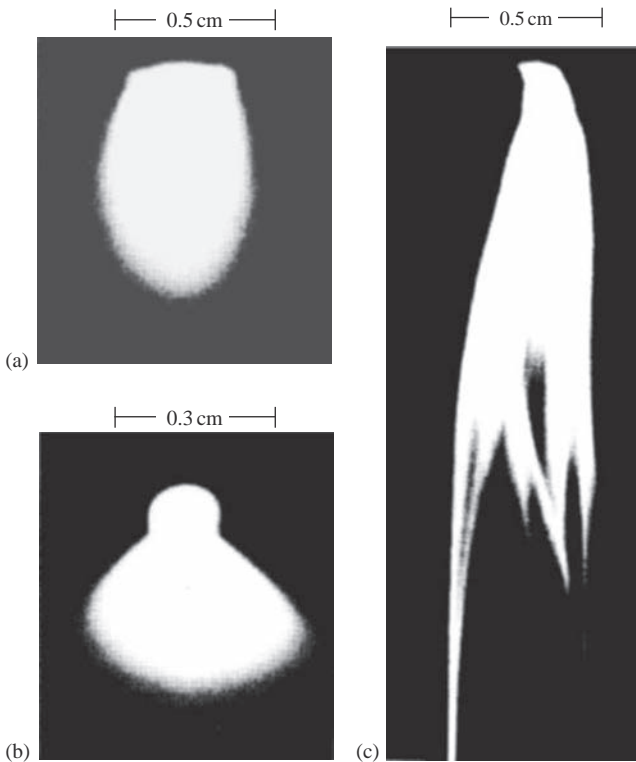


Figure 3.37 *Negative corona modes: (a) trichel streamers; (b) negative glow; (c) negative streamers. Cathode: spherical boss ( $d=0.8$  cm) on a sphere ( $D=7$  cm); gap length 19 cm; time exposure: 0.25 s (from [56])*

### 3.12.1.1 Trichel streamers

In this mode the discharge activity takes place in very regular pulses with a well-defined repetition frequency. The current waveform associated with a single pulse has a duration of a few tens of nanoseconds. In each event a streamer-like discharge is initiated, develops, and finally suppressed. The pulse frequency, which depends on the geometry of the electrode and pressure, increases with increasing voltage. The dead time between the pulses may vary from a few microseconds to hundreds of microseconds. The reason for the pulsation of the discharge is the following. As the discharge develops it will give rise to a negative space charge that will reduce the electric field at the cathode leading to the choking off of the discharge. During the dead time between pulses, the space charge is removed by the electric field and this will increase the electric field at the cathode leading to the creation of another streamer.

### 3.12.1.2 Negative pulseless glow

This stage is characterised by a more or less uniform discharge activity without pulse bursts. The absence of the pulses indicates that electric field is high enough to quickly transport away the negative space charge so that it will not choke the discharge activity. Moreover, positive ions gain enough energy from the electric field so that they generate a copious supply of electrons to the discharge when they collide with the cathode. The discharge behaves as a miniature glow discharge.

### 3.12.1.3 Negative streamer

In this regime the removal of the space charge is so efficient that the avalanches develop into streamer discharges. These streamer discharges extend far into the low electric field region of the gap with their extension increasing with increasing voltage. The streamers generate low-frequency pulses in the discharge current.

## 3.12.2 Positive corona modes

The important features of the positive corona are the following: (a) The primary electrons initiate avalanches which grow towards the anode within the volume of gas in which the electric field is higher than the critical value necessary for electrical breakdown (see Figure 3.38). (b) Since the avalanches grow in the direction of increasing electric field the drift velocity of electrons increases as the avalanche grows thus diminishing the probability of attachment to electronegative gases and giving rise to negative ions. (c) The electrons reaching the anode have a high kinetic energy and they have to dispose of their energy before they can be absorbed into the anode. Thus they spend their energy in ionisation collisions leading to discharge activity at the anode surface. (d) The incoming avalanches and the electrical activity at the anode leave behind a positive space charge in front of the anode. If the number density of the positive space charge within a volume of about  $50 \mu\text{m}$  radius exceeds  $10^8$  ions the streamer inception criterion is satisfied and streamers that propagate towards the anode are generated. The interplay between these processes give rise to different modes of corona. The visual appearance of the positive corona modes is shown in Figure 3.39.

### 3.12.2.1 Burst corona

The avalanches generate fast electrons which initiate ionisation and excitation at the surface of the anode as they spend their energy before they are being absorbed by the anode. This discharge activity, which appears as a thin luminous sheath

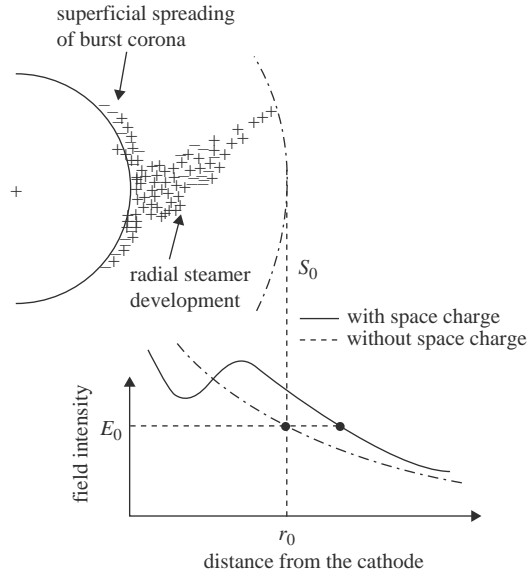


Figure 3.38 *Space charge and the electric field distribution in the gap during the formation of positive corona (from [56])*

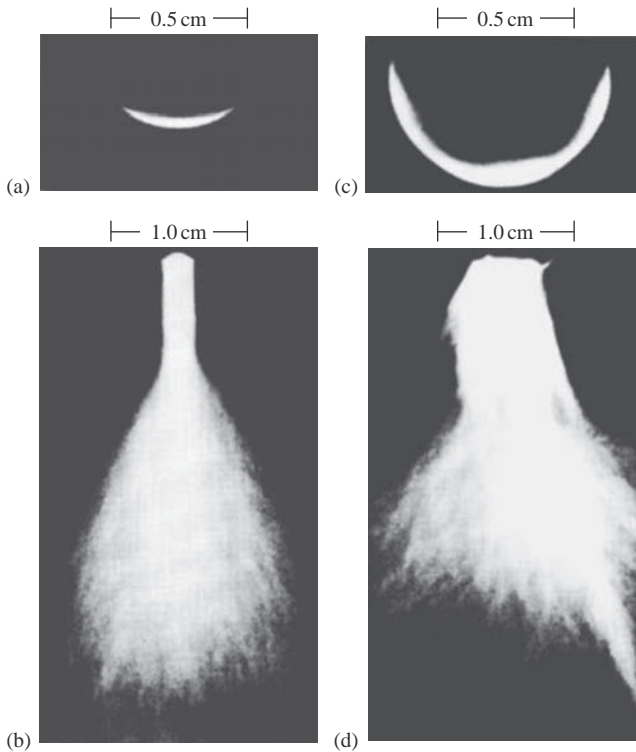


Figure 3.39 *Positive corona modes: (a) burst corona; (b) onset streamer; (c) positive (or anode) glow; (d) breakdown streamers. Cathode: spherical boss ( $d=0.8$  cm) on a sphere ( $D=7$  cm); gap length 35 cm; time exposure: 0.25 s (from [56])*

attached to the anode, gives rise to positive ions. As the concentration of the positive ions grow it will choke the discharge and the latter moves to a new location on the anode. The discharge current consists of small pulses resulting from the movement of discharge activity on the surface of the anode.

### **3.12.2.2 Onset streamer**

As the voltage builds up the positive space charge of the avalanches reaching the anode exceeds the critical value necessary for the inception of streamers. The streamers thus generated extend into the gap. However, the streamers are short because the positive space charge of the streamers will reduce the electric field at the anode thus impeding the rapid removal of electrons from the streamer channels and choking off the streamer. A dead time is required to remove the ionic space charge and restore the electric field for the formation of another streamer-like discharge. Even in this stage the electrons continue their electrical activity close to the anode so that burst corona activity occurs simultaneously with the streamer development. Some of the electrons travelling towards the anode along the streamer channels will be captured by electronegative atoms. However, when reaching the anode they shed their electrons which contribute to the electron activity at the anode. As the voltage is raised even higher, the burst corona is enhanced. The positive space charge generated by the burst corona moves away from the anode surface and forms a stable positive ionic space charge around the anode which prevents the radial development of the streamer discharge into the gap. With increasing voltage the burst corona intensifies at the expense of the onset streamers. Finally, it will completely choke off the streamer activity giving rise to a new corona mode called positive or Hermitian glow.

### **3.12.2.3 Positive glow**

The discharge activity, which appears as a luminous layer, adheres to the surface of the anode and as in the burst corona moves around the anode from one place to another giving rise to the pulsation of the current.

### **3.12.2.4 Breakdown streamers**

If the applied voltage is further increased, the electric field will be able to remove quickly the positive space charge that has blocked the streamer activity leading again to the development of radial streamers. Usually the streamers develop from local 'hot spots' with intense ionisation activity. As the voltage increases the streamers become more and more vigorous and extend further and further away from the anode surface.

## *3.12.3 Electrical breakdown and corona*

Figures 3.40 and 3.41 show the threshold voltage for different corona modes of positive and negative polarity, respectively, in a rod-plane gap as a function of the gap spacing in atmospheric air. Note that at very small gap spacing where the electric field is uniform direct breakdown is possible without corona inception. With increasing gap spacing the electric field in the gap becomes non-uniform and different forms of corona appear at different voltages.

## **3.13 Dependence of electrical breakdown conditions on atmospheric conditions**

As discussed previously, the ionisation and attachment coefficients are not constants but depend on pressure and temperature of the gas or the density of the gas.



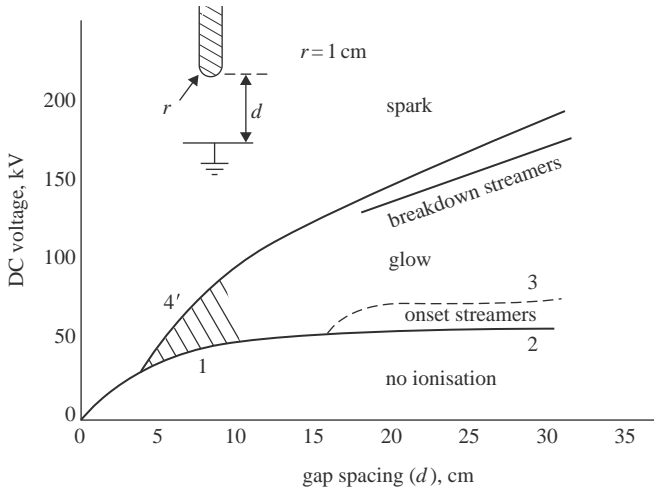


Figure 3.40 *Threshold curves in atmospheric air for various modes of positive corona and for spark breakdown for a spherically capped anode and plate cathode (from [2])*

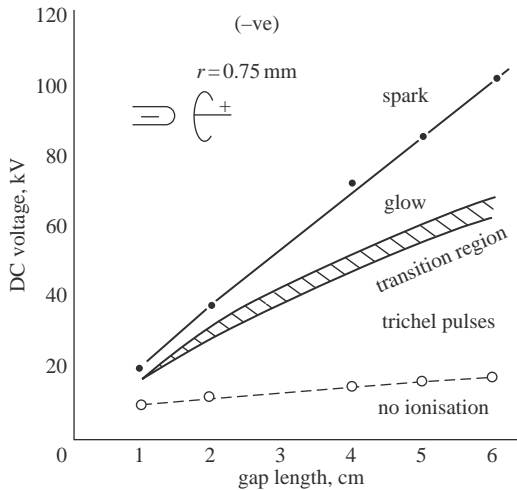


Figure 3.41 *Threshold curves in atmospheric air for various modes of negative corona and for spark breakdown for a spherically capped anode and plate cathode (from [2])*

For this reason these parameters are usually expressed as  $\alpha/n$  or  $\eta/n$  where  $n$  is the density of the gas. For the same reason the critical electric field necessary for cumulative ionisation in air, and hence the breakdown voltage of air gaps, also depends on the density of air. Let  $E_c$  ( $= 2.6 \times 10^4$  V/cm) be the critical electric field in air for cumulative ionisation at standard atmospheric conditions (i.e.  $p_0 = 1.013$  bar,  $T_0 = 293$  K). The corresponding critical electric field,  $E_x$ , at non-standard atmospheric conditions corresponding to  $p$  and  $T$  can be obtained from

$$E = E_c \delta \tag{3.110}$$

where  $\delta$  is the relative density correction factor given by

$$\delta = \left( \frac{pT_0}{p_0T} \right) \quad (3.111)$$

with  $T$  given in kelvins. Observe that for a given gap length this linear form of correction is valid only over a certain range of pressures. The reason for this limitation is apparent from the Paschen curve which is linear only over a certain range of pressures for a given gap length.

The atmospheric conditions influence not only the electrical breakdown electric fields but also the critical electric field necessary for corona inception. For example the corona inception voltage in air between coaxial cylinders is given by [57]

$$E_c = 3.15 \times 10^4 \delta (1 + 0.305/\sqrt{\delta r}) \quad (3.112)$$

where  $E_c$  is given in V/cm and the radius of the inner conductor,  $r$ , is given in cm. This equation is known as the Peek's formula.

### 3.14 Statistical nature of electrical breakdown

Consider the situation in which a 'step voltage' is applied to a plane parallel gap (Figure 3.42). Since the electric field in the gap should be larger than the critical value of  $2.6 \times 10^6$  V/m for electrical breakdown, electrical breakdown will not be observed until the applied voltage increases beyond a critical value  $V_s$ , given by  $V_s = d \times 2.6 \times 10^6$  where  $d$  is the gap length. However, to achieve electrical breakdown two conditions should be satisfied. First, a free electron that is capable of generating an electron avalanche should be available in the gap. Usually free electrons in air are generated by the background cosmic radiation or by the radioactivity of the ground. In general, a free electron may not be available at the instant of the application of the voltage in the volume of air under consideration. That is, there is a certain time lag between the application of the voltage and the time of creation of a free electron in the gas volume. This time lag is known as the

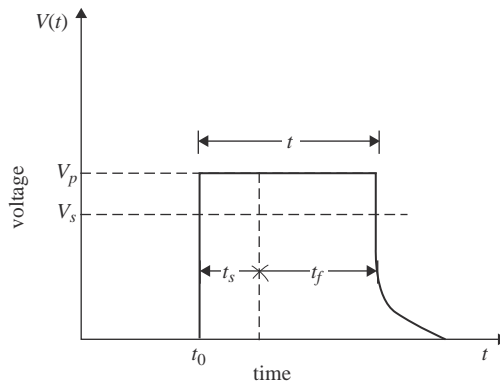


Figure 3.42 Time lag components under a step voltage. The voltage is applied at  $t = t_0$ .  $V_s$ , minimum static breakdown voltage;  $V_p$ , peak voltage;  $t_s$ , statistical time lag;  $t_f$ , formative time lag. The total time lag is denoted by  $t$

statistical time lag. The statistical time lag could be decreased by illuminating the electrodes with ultraviolet radiation which will cause the electrode to emit free electrons. The statistical time lag decreases also with increasing applied voltage. One reason could be (in the case of negative high-voltage electrode) the increasing probability of field emission from cathode with increasing surface electric field. The other reason is the increase in the critical volume of gas (see section 3.15.2.3 for the definition of critical volume) with increasing applied voltage. Once an electron is found it should first generate a streamer and then the streamer should be converted to a spark. This process will also take some time to be completed. This time is called the formative time lag. The total time between the application of the voltage and the final breakdown is called the time lag.

### 3.14.1 *Electrical breakdown under the application of impulse voltages*

The situation is more complicated when an impulse voltage (i.e. a voltage that reaches a peak value and then decay to zero after a certain time) is applied to a plane parallel gap (Figure 3.43). In this case two conditions have to be satisfied in order to achieve complete breakdown of the gap:

- (i) The applied voltage (and hence the electric field in the gap) has to exceed the critical value  $V_s$  where cumulative ionisation is possible.
- (ii) The applied voltage must remain over this critical value until the formation of the discharge is completed, which means that the voltage must remain over this critical value for a duration larger than the total time lag. Observe that since the statistical time lag and the formative time lag may change from one voltage application to another, the same voltage waveform may or may not cause breakdown in the gap depending on the length of the time lag. That is, the electrical breakdown of a gap becomes a probabilistic event.

It is important to note that for a given peak amplitude the duration over which the applied voltage exceeds the critical value depends on the shape or the time variation of the applied voltage. The narrower the impulse voltage the shorter the duration over which the voltage exceeds the critical value. Thus the breakdown voltage of a gap depends on the shape of the applied impulse voltage. The narrower

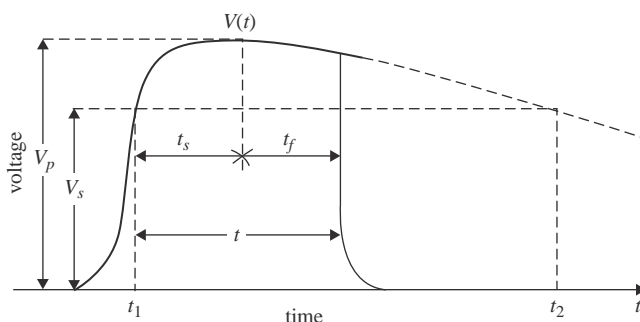


Figure 3.43 *Breakdown under impulse voltage,  $V(t)$ .  $V_s$ , minimum static breakdown voltage;  $V_p$ , peak voltage;  $t_s$ , statistical time lag;  $t_f$ , formative time lag. The total time lag is denoted by  $t$*

the impulse voltage the higher is the peak value necessary to cause electrical breakdown.

### 3.14.2 Statistical nature of the electrical breakdown

Due to the statistical nature of the time lags, when a given number of identical voltage impulses with magnitude exceeding the static breakdown voltage  $V_s$  is applied to a gap only a certain percentage will lead to breakdown. Thus, for a given voltage impulse there is a certain probability that the gap will breakdown.

The breakdown probability for a given impulse voltage is obtained by applying a large number of identical impulses and taking the ratio of the number of impulses that lead to breakdown to the total number. Conventionally,  $V_{b-100}$  represents 100 per cent breakdown voltage. That is, each voltage application of this magnitude leads to breakdown.  $V_{b-50}$  represents the peak voltage in which one half of the applied voltage impulses at this level leads to breakdown.  $V_{b-0}$  represents the largest peak impulse voltage that does not lead to breakdown. It is known as the impulse withstand level of the gap.

## 3.15 The long spark

In small gaps the transformation of the streamer to spark channel takes place directly after the streamer has crossed the gap and reached the grounded electrode. In the case of long gaps the processes that lead to the electrical breakdown are a little bit more complicated. The first phase of the discharge development is a corona discharge (called first corona) which takes the form of a burst of filamentary channels from the high-voltage electrode. The next stage is the development of a highly conducting discharge channel called the leader from the high-voltage electrode. In the third phase the leader extends, with the aid of corona discharges emanating from its head, towards the grounded electrode. The final jump is the last stage of the leader before final breakdown. The final jump starts when the corona streamers emanating from the leader head reaches the grounded electrode.

### 3.15.1 Streamer to leader transition and the initiation of the leader

Many of the streamers in the first corona have their origin in a common channel called the streamer stem. The streamers stop when the electric field decreases below the critical value necessary for their propagation. Each individual streamer is a cold discharge and the current associated with this cannot heat the air sufficiently to make it conducting. However, the combined current of all streamers flowing through the stem causes this common region to heat up increasing the conductivity of the stem. When the temperature of the stem increases to about 1000–1500 K, the rate of negative ion destruction greatly increases, retarding the drop in conductivity [16]. Furthermore, during the initial current flow through cold air, about 95 per cent of the energy gained by electrons from the electric field is transferred to vibrations of nitrogen molecules [15]. The vibrational relaxation time decreases with increasing temperature. Around 1500–2500 K, the VT relaxation of nitrogen molecules is accelerated, and the energy stored in the vibrational states of the molecules transfers to the translational energy thus raising the temperature (see also section 3.16). The increase in the temperature causes the gas to expand making the  $E/n$  ( $E$  is the

electric field and  $n$  is the gas density) ratio to increase leading to an increase in ionisation and electron production. Thus the current will be concentrated into a thin channel and this in turn will produce more heating and accelerate the ionisation. Through this process the stem will be transformed into a hot and conducting channel called the leader.

Owing to its high conductivity the most of the applied voltage will be transferred to the head of the leader channel resulting in a high electric field there. The production of streamer discharges now takes place from a common stem located at the head of the leader channel. With the aid of cumulative streamer currents the new stem gradually transforms itself to a newly created leader section with the streamer process now repeating at the new leader head. The streamer system located in front of the leader is the source of current which heats the air and make possible the elongation of the leader. As the leader progresses forward through the space originally traversed by streamers, the charge of the latter forms a space charge or corona sheath around the leader channel.

The ability of the leader to propagate in the gap is determined by the electric field around the leader head and the streamer zone in front of it. At constant voltage, as the leader elongates the electric field at the leader head decreases. There are two reasons for this decrease in the electric field. One is the voltage drop along the elongated leader channel. The other is the growth of charge of opposite sign induced in the leader head by space charge in the gap, namely the streamer zone and the corona sheath. Thus in order for the leader to propagate continuously, the voltage applied to the gap must be initially high enough or be raised during the leader development.

The leader supports a current of about 1 A at a relatively low longitudinal electric field of about  $10^3$  V/cm. The spectroscopic measurements show that the air in the leader channel is heated to about 5000 K [35, 36].

### *3.15.2 General characteristics of impulse breakdown in rod-plane gaps*

Extensive amount of work on the electrical breakdown characteristics of long gaps under the application of impulse voltages was conducted by the Renardiers group [35, 36]. The summary given here is based mainly on the results obtained by this group (see also [58]).

#### **3.15.2.1 Positive breakdown**

The breakdown voltage of a rod-plane gap depends on the risetime of the applied voltage impulse. Experiments show that there is a critical rise time at which the breakdown voltage is a minimum. This risetime is called the critical risetime or critical time to crest. The basic physical phenomena that happen when a voltage impulse of critical time to crest is applied to a rod-plane gap are shown in Figure 3.44. At time  $t_i$ , when the voltage reaches a value  $U_i$ , depending on the gap geometry, the first phase of the discharge occurs. This is a corona (or streamer) burst which takes the form of filamentary discharges. This corona burst is called the first corona. The corona streamers are emanating from a short bright channel located at the electrode and is called the stem (Figure 3.45). At this stage the current measured at the high-voltage electrode shows an impulse with a duration of some hundreds of nanoseconds. The space charge injected into the gap during the first corona reduces the electric field. This electric field recovers at a rate which depends on the rate of increase of the applied voltage and the dissipation of the space charge. No ionisation

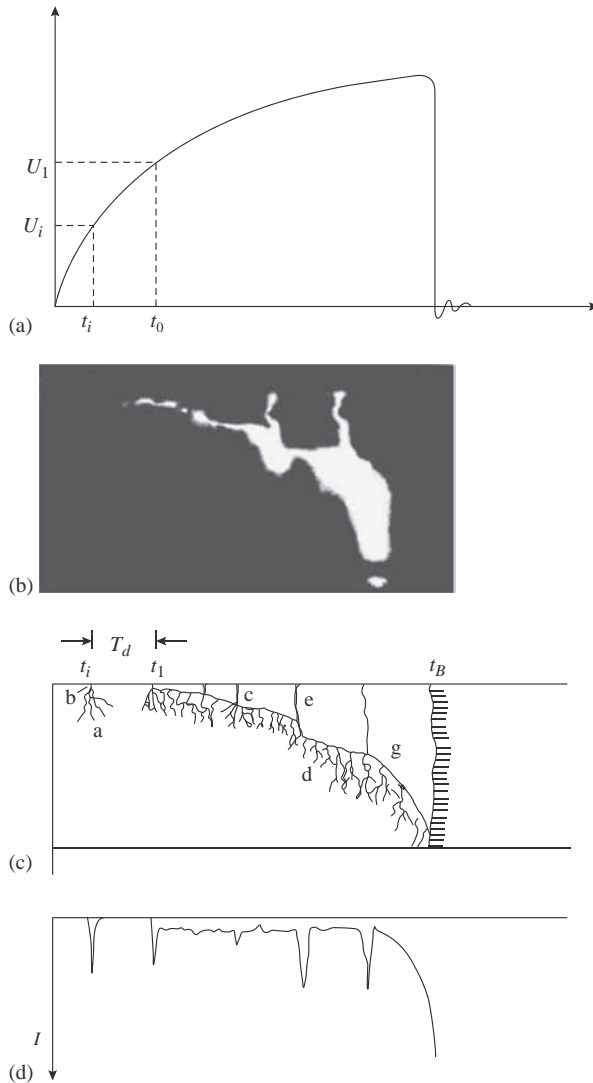


Figure 3.44 Development of long positive spark in air. (a) Applied voltage; (b) Streak photograph; (c) Schematic representation of the discharge development; (d) the current associated with the discharge. The first corona occurs at time  $t_i$  when the voltage reaches the value  $U_i$ . The corona takes place in the form of filamentary channels (b and d). The stem is observed at the root of the corona streamers (b). After the dark period  $T_d$  the leader is initiated at time  $t_1$  preceded by a secondary corona discharge. The leader propagates forward with the aid of corona discharges from the head (d). The leader channel luminosity is quite low except in the case of sudden elongation of the leader called restrikes (c and e). The final jump starts when the leader corona reaches the plane electrode (g). The final breakdown takes place at  $t_B$  (adapted from [35])

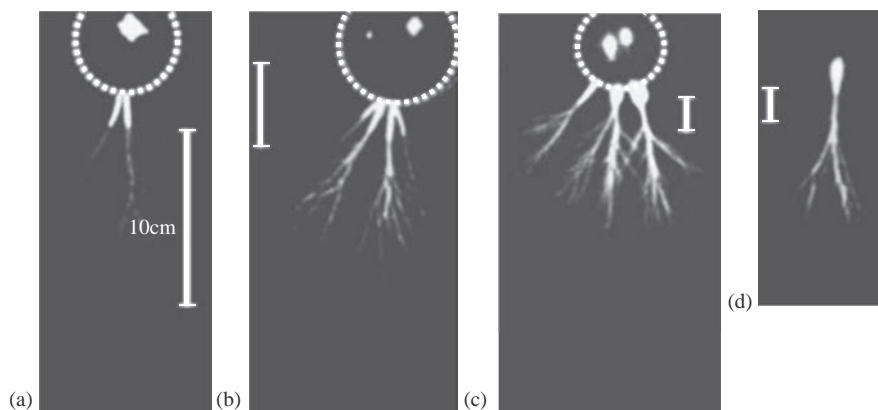


Figure 3.45 Streamer discharges from electrodes of different dimensions: (a) 6.2 cm; (b) 15 cm; (c) 25 cm; (d) 50 cm (adapted from [59])



Figure 3.46 Successive frames of image converter picture in a 10 m gap showing the development of streamer discharges from the head of the leader channel [60]

activity can be detectable during this period, marked  $T_d$  in the diagram. This time is called the dark period. Depending on the geometry and the rate of rise of the applied voltage, a leader channel develops from the stem preceded by a secondary corona discharge after the dark period. If the radius of curvature of the electrode is large enough the dark period can be reduced to zero and the leader may start immediately with the first corona. The minimum radius of the electrode at which the dark period becomes zero is called the critical radius (see section 3.15.2.7).

Once initiated the leader channel propagates along a tortuous path with a corona discharge developing from its tip (Figure 3.46). Usually the leader travels

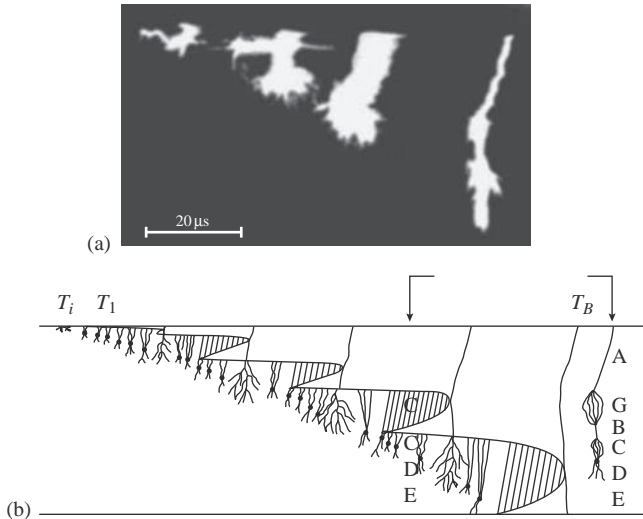


Figure 3.47 Development of long negative spark in air. (a) Streak photograph. (b) Schematic representation of the discharge development. The gap length was 7 m. A, negative leader; B, space leader; C, positive streamers, D, space stem; E, negative streamers; G, positive streamers (adapted from [36])

more or less continuously. However, if the rate of increase of the applied voltage is too low then sudden elongations or brightening of the leader occurs. These are called restrikes. When the streamers of the leader reaches the ground plane, the final jump begins (see section 3.15.2.6). At this stage the arrest of the leader is not possible and breakdown of the gap is inevitable. The leader velocity increases almost exponentially and when the leader head reaches the plane a conducting channel bridges the electrodes and the return stroke begins.

### 3.15.2.2 Negative breakdown

The development of the negative leader discharge is depicted schematically in Figure 3.47. The first corona and the dark period are similar to that of the positive breakdown. However, after the dark period a unique feature, namely, a pilot system, that does not exist in the positive breakdown is manifest in the system. The pilot system consists of a bright spot called space stem (marked by dark spots in the figure) of short duration, from which streamers of both polarity develop in opposite directions. The positive streamers propagate towards the high-voltage system and the negative streamers in the opposite direction. The interaction of the positive streamers generated by the space stem and the streamers of the first corona leads to the initiation of the negative leader from the cathode. During the propagation of the leader, a space stem appears in front of it at regular intervals generating positive streamers towards the leader head. The positive streamers of the space stem propagate in the region previously covered by negative streamers connecting the space stem with the tip of the leader by a dense net work of streamer channels. Once the connection is made between the positive streamers and the leader head, another section ahead of the leader head is thermalised leading to the extension of the leader. As the leader channel grows the whole system of positive and negative streamers including the space stem repeats itself in a more advanced position in the gap.



The space stem in some cases gives rise to a space leader and it starts to elongate in both directions from the space stem. The space leader lengthens with a high velocity towards the cathode (3 cm/ $\mu$ s) than towards the anode (1 cm/ $\mu$ s). As the space leader approaches the main leader, the velocity of both increases exponentially. The connection of the two leaders is accompanied by a simultaneous illumination of the whole channel starting from the meeting point. When this happens, the negative leader length increases by an amount equal to the length of the space leader. This generates an intense source of corona streamers propagating towards the ground plane ahead, at least as far as and some times exceeding the most advanced position of the space stem. The process may lead to the creation of new space stems. The space leaders may have lengths 30–50 cm before the acceleration phase and the elongation of the negative leader after the connection between the space leader and the negative leader could be about 1 m.

### 3.15.2.3 Inception and characteristics of first corona

The inception electric field for the corona can be calculated by using the streamer inception criterion. That is

$$\int_{r_a}^{r_c} (\alpha - \eta) dx = K \quad (3.113)$$

where  $x$  is the co-ordinate parallel to the electric field and directed away from the high-voltage electrode with its origin at the centre of the spherical tip of the electrode with radius  $r_a$ ,  $r_c$  is the value of  $x$  at which  $E = 2.6 \times 10^4$  V/cm, and  $K = 10^8$ . It is important to note that the inception electric field does not depend on the gap length the reason being that it is controlled more by the local electric field at the electrode surface which is not much influenced by the gap length. However, it is strongly influenced by the electric field inhomogeneity close to the electrode. The minimum electric field necessary for the inception of corona,  $E_i$ , is given by

$$E_i = 6.77 \log(1.75 \times 10^3 d_f) \quad 0.05 < d_f < 5 \text{ cm}^{-1} \quad (3.114)$$

where

$$d_f = \left[ -\frac{dE_b}{dx} \cdot \frac{1}{E_b} \right]_{\text{at the electrode surface}} \quad (3.115)$$

is the electric field divergency factor with  $E_b$  being the background electric field. In the above equation  $d_f$  is given in  $\text{cm}^{-1}$  and the electric field is given in kV/cm.

For the initiation of the corona two conditions have to be satisfied. The first one is the availability of a free electron and the second requirement is that the free electron should be found in a volume of gas located in such a way that the electron can give rise to an avalanche that will lead to a streamer discharge. The natural production rate of electrons in air due to background radiation (both cosmic and terrestrial) is about 10 electrons/ $\text{cm}^3/\text{s}$ . These electrons will get attached to electronegative oxygen atoms forming negative ions. Since in the case of impulse voltages the times involved are in the range of microseconds the background radiation may not contribute significantly in providing the initiatory electrons. However, this radiation leads to a copious supply of negative ions. The electrons

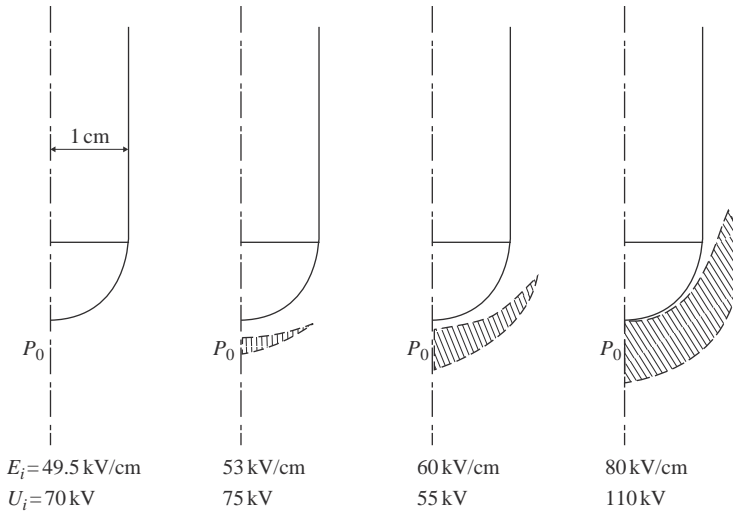


Figure 3.48 The critical volume for different applied voltages in a rod–plane gap of 30 cm.  $U_i$  is the applied voltage and  $E_i$  is the electric field at the electrode (from [61])

may detach from these ions due to the influence of the electric field and this is the dominant process that provides initiatory electrons. Due to the statistical time lag involved with finding an initiatory electron there is a spread in the time of inception of first corona after the application of the impulse voltage. This time can be reduced using ultraviolet illumination of the electrode.

In order to create an avalanche that will subsequently lead to a streamer the initiatory electrons should appear in the gap in a volume of gas in which the electric field is above the critical electric field necessary for breakdown. Moreover, the location of the electron in the volume should be such that the electron can give rise to a streamer discharge. For example, if the electron is located too close to the electrode it will collide with the electrode before forming a critical avalanche. This volume is known as the critical volume. With increasing voltage the volume in which the electric field increases above the critical electric field increases. Since the probability of finding an electron in a given volume increases with its size, the probability of finding an electron that will initiate the breakdown process increases with increasing applied voltage. Figure 3.48 shows how the critical volume increases in rod–plane geometry with increasing applied voltage.

### 3.15.2.4 Leader velocity

The leader velocity is actually a function of the leader current. The velocity of a 1 A current leader is about 1 cm/ $\mu$ s. The average leader velocity may increase during the final jump. The speed of the leader may be equal to about 2–5 cm/ $\mu$ s at the initiation of the final jump. During the final jump its speed may increase to about 100 cm/ $\mu$ s.

The experimental data suggest a relationship between the leader speed,  $v$ , and the current measured at the base of the leader channel,  $i$ . The results can be approximated by the empirical equation [62]

$$v = k_v i^a \quad (3.116)$$

with  $a = 0.66$  and

$$k_v = 0.858 \text{ cm } (\mu\text{SA}^a)^{-1} \quad \text{for } 1 < i < 22.6 \text{ A} \quad (3.117)$$

$$k_v = 2.65 \text{ cm } (\mu\text{SA}^a)^{-1} \quad \text{for } 85 < i < 1100 \text{ A} \quad (3.118)$$

In the above equation the leader speed is given in cm/ $\mu\text{s}$ . On the other hand, Bazelyan [63] suggests the relationship

$$v = kI_l^{0.5}, \quad k = 4 \text{ cm}/\mu\text{SA}^{0.5} \quad (3.119)$$

### 3.15.2.5 The potential gradient of the leader channel

Even though the potential gradient of the leader channel cannot be measured directly, Gallimberti [16] made several calculations using a thermodynamic model of the leader. The results show that the leader potential gradient decreases with increasing length and approaches about  $10^3$  V/cm for lengths larger than about 10 m.

### 3.15.2.6 The final jump

As mentioned previously, the final jump is initiated when the leader corona reaches the anode. During the final jump the brightness and the velocity of the leader channel increase. The speed may increase to several metres per microsecond. The instantaneous velocity is an inverse exponential function of the length of the gap remaining unabridged by the leader channel. In the case of negative leader, when the negative streamers reach the anode a positive upward going leader is initiated from the anode. Both the downward coming negative leader and the positive upward going leader approach each other with an exponentially increasing velocity. When the two leaders meet the return stroke is initiated at the junction point.

### 3.15.2.7 The critical radius

As described in section 3.15.2.1, the critical radius is the minimum radius of a spherical electrode in a given gap length which will produce leader inception immediately with the inception of first corona. In sphere–plane geometry the critical radius,  $R_c$  in cm, is given by [35, 36]

$$R_c = 38 \left( 1 - e^{-D/500} \right) \quad (3.120)$$

where  $D$  is the gap length in cm. In the case of conductor–plane geometry it is given by

$$R_c = 37 \ln(1 + D/100) \quad (3.121)$$

The critical radius concept is commonly applied in lightning research in the evaluation of the background electric field necessary for the generation of a continuous leader from a grounded structure. This is done by assuming that a connecting leader is incepted when the electric field at the surface of a hypothetical metal sphere of critical radius (i.e. 38 cm) at ground potential located at the tip of the structure exceeds the breakdown electric field in air.

Observe that the critical radius is different in sphere–plane gaps and conductor–plane gaps. However, experiments show that the length of the corona streamers at the critical radius is about 3 m and that this length is the same in both geometries (Figure 3.49) [35, 36]. In other words, irrespective of the geometry the length of the

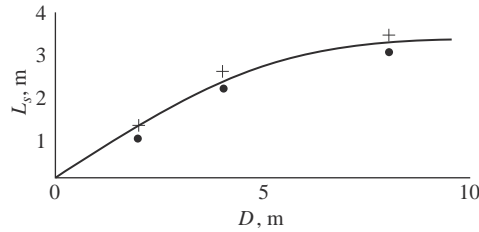


Figure 3.49 The length of streamers at the leader inception from electrodes of critical radius as a function of the gap length. The solid dots correspond to spherical geometry and the crosses correspond to cylindrical geometry [35]

streamers should exceed this critical value before the inception of the leader. Akyuz and Cooray [64] have used the critical streamer length as the criterion, instead of the critical radius, in evaluating the inception of connecting leaders from grounded structures under the influence of the downward coming stepped leader. One advantage of the critical streamer length criterion over the critical radius criterion is that the former is independent of geometry. The second advantage is that the former can be easily implemented in any complicated structure that one may encounter in practice. In the next section we will describe a physically reasonable procedure to evaluate the inception and propagation of a positive leader paying special attention to the inception of positive connecting leaders from grounded structures under the influence of downward coming negative stepped leaders.

### 3.15.3 Some features of mathematical modelling of positive leader discharges

Consider a grounded object which is exposed to electric field. An example being a Franklin rod exposed to the electric field generated by a downward moving negative stepped leader. The goal is to simulate the initiation and propagation of the connecting leader, which is a positive leader discharge from the Franklin rod. A brief description of how this could be achieved is given below. The description is based on the work published previously by Becerra and Cooray [65–67].

Assume that the electric field at ground level as a function of time generated by the downward coming stepped leader is known. This can be calculated for example by using the leader charge distribution as extracted by Cooray *et al.* [68]. The simulation consists of several main steps; let us take them one by one:

- (i) The first step is to extract the time or the height of the stepped leader when streamers are incepted from the grounded rod. Since the background electric field is known the electric field at the tip of the grounded rod can be calculated, for example, by using charge simulation method. This field is used together with the avalanche to streamer conversion criterion given by (3.74a) or (3.74b) to investigate whether the electric field at the conductor tip is large enough to convert avalanches to streamers. The simulation continues using the time-varying electric field of the stepped leader until the streamer inception criterion is satisfied.
- (ii) The moment the streamer inception criterion is satisfied a burst of streamers will be generated by the tip of the rod. The next task is to calculate the charge in this streamer burst. The charge associated with these streamer bursts are

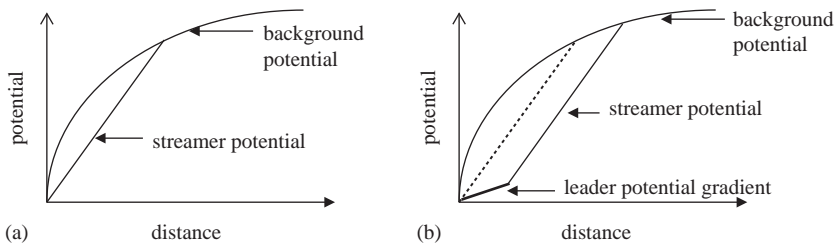


*Figure 3.50 The use of distance–voltage diagrams to calculate the streamer charge. (a) The charge in the first streamer burst is given by the area between the two curves representing the background potential and the streamer potential gradient. (b) To calculate the charge in subsequent streamer burst one has to include both the leader and the streamer region in a distance–voltage diagram*

calculated using a distance–voltage diagram with the origin at the tip of the grounded conductor as follows. The streamer zone is assumed to maintain a constant potential gradient  $E_{str}$ . In the distance–voltage diagram this is represented by a straight line (Figure 3.50a). On the same diagram the background potential produced by the thundercloud and the downward coming stepped leader at the current time is depicted. If the area between the two curves up to the point where they cross is  $A$ , the charge in the streamer zone is given by

$$Q_o \approx K_Q A \quad (3.122)$$

where  $K_Q$  is a geometrical factor. Becerra and Cooray [66] estimated its value to be about  $3.5 \times 10^{-11} \text{ C/V}\cdot\text{m}$ .

- (iii) The next task is to investigate whether this streamer burst is capable of generating a leader. This decision is based on the fact that in order to generate a leader a minimum of  $1 \mu\text{C}$  is required in the charge generated by the streamers. If the charge in the streamer zone is less than this value then the procedure is repeated for a small time interval later. Note that with increasing time the electric field generated by the stepped leader increases and, consequently, the charge in the streamer bursts increases.
- (iv) Assume that at time  $t$  the condition necessary for leader inception is satisfied. The next task is to estimate the length and the radius of this initial leader section. In doing this it is assumed that the amount of charge you need to create a unit length of positive leader is  $q_1$ . The value of  $q_1$  is about  $40\text{--}60 \mu\text{C/m}$ . With this the initial length of the leader section  $L_1$  is given by  $Q_o/q_1$ . The initial radius of the leader,  $a_{L1}(t)$ , is assumed to be  $10^{-3} \text{ m}$  and the initial potential gradient of the leader section,  $E_{L1}(t)$ , is assumed to be equal to the potential gradient of the streamer region, i.e.  $5.0 \times 10^3 \text{ V/cm}$ . Now we proceed to the next time step, i.e.  $t = t + \Delta t$ .
- (v) During the time interval  $\Delta t$  the background potential changes and we also have a small leader section of length  $L_1$ . Now the new charge in the streamer zone generated from the head of the new leader section is calculated as before but now including both the leader and its streamer zone in the distance–voltage diagram (Figure 3.50b). The leader is represented by a line with a potential gradient  $E_{L1}(t)$ . The charge generated in the current time step

is obtained by subtracting from this the total charge obtained in the previous time step. Let the charge obtained thus be  $Q_1$ . This charge is used to evaluate the length of the new leader section  $L_2$ . Moreover, the flow of this charge through the leader channel changes the potential gradient and the radius of the older leader section  $L_1$ . The new potential gradient and the radius of  $L_1$  are given by  $E_{L_1}(t + \Delta t)$  and  $a_{L_1}(t + \Delta t)$ .

- (vi) Now let us consider the  $n$ th time step. There are  $n$  leader sections and they have there respective potential gradients and radii. The radius and the potential gradient of the  $i$ th leader section are obtained from

$$\pi \cdot a_{L_i}^2(t + \Delta t) = \pi \cdot a_{L_i}^2(t) + \frac{\gamma - 1}{\gamma \cdot p_0} E_{L_i}(t) \cdot I_{L_i}(t) \cdot \Delta t \tag{3.123}$$

$$E_{L_i}(t + \Delta t) = \frac{a_{L_i}^2(t)}{a_{L_i}^2(t + \Delta t)} E_{L_i}(t) \tag{3.124}$$

In the above equations  $E_{L_i}(t)$  is the internal electric field and  $I_{L_i}(t)$  is the current of the leader section  $L_i$  at time  $t$ . With these, it is possible to calculate the time evolution of the internal electric field for each segment and the potential drop along the leader channel (at a given time) as follows:

$$\Delta U_L = \sum_{i=1}^k E_{L_i}(t) \cdot L_i \tag{3.125}$$

The steps described above can be used to simulate the inception and propagation of positive leaders. Figure 3.51 describes the basics of the process schematically.

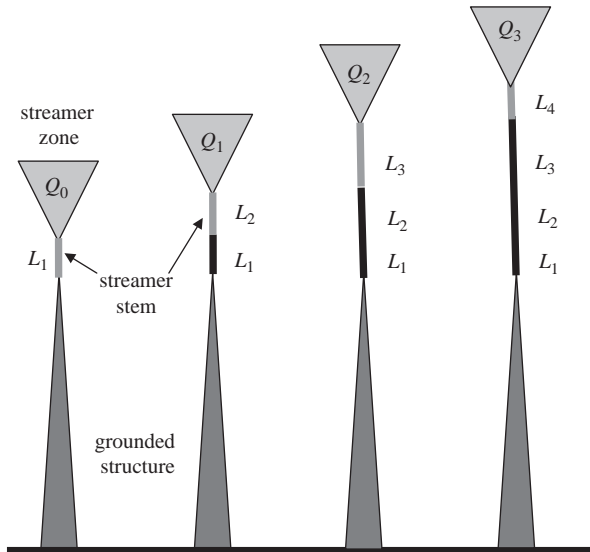


Figure 3.51 Pictorial definition of the parameters used in the mathematical modelling of positive leader discharges as described in section 3.8. Note that  $Q_1, Q_2$  etc. are the charges in the streamer zones. The flow of charge across the streamer stem makes it conducting and converts it to a leader section

The calculation can be simplified if, instead of calculating the time evolution of leader potential gradient in each segment as above, one uses the expression derived by Rizk [69] for the potential of the tip of the leader channel which is given by

$$U_{tip}^{(i)} = l_L^{(i)} E_\infty + x_0 E_\infty \ln \left[ \frac{E_{str}}{E_\infty} - \frac{E_{str} - E_\infty}{E_\infty} e^{-\{l_L^{(i)}/x_0\}} \right] \quad (3.126)$$

In the above equation  $l_L^{(i)}$  is the total leader length at the current simulation step,  $E_\infty$  is the final quasi-stationary leader gradient,  $E_{str}$  is the potential gradient of streamer channels and  $x_0$  is a constant parameter given by the product  $v\theta$ , where  $v$  is the ascending positive leader speed and  $\theta$  is the leader time constant.

### 3.16 Humidity effects

The increase in humidity causes an increase in the attachment coefficient and a decrease of the photoionisation efficiency. The reason for the former is the high affinity of water molecules to electrons. Thus in a given electric field the rate of ionisation decreases with increasing humidity. The reason for the latter is the reduction in the ultraviolet absorption length by humidity. Moreover, with increasing humidity the probability of finding a free electron in the critical volume decreases. The reason for the reduction of this probability is caused by the increased difficulty of electron detachment from hydrated negative ions. Consequently the electron detachment rate decreases with increasing humidity. Another interesting effect of humidity is its influence on the relaxation time of vibrational energy into translational energy. As mentioned before, in the preliminary stages of electrical discharges a large fraction of the energy of electrons goes into vibrational excitation of the molecules. The VT relaxation time is the time within which this energy is converted to thermal energy. This relaxation time,  $\tau_{vt}$ , depends on the temperature and the water vapour content. At  $T=910$  K,  $\tau_{vt}$  varies from 32  $\mu\text{s}$  with humidity 12  $\text{g}/\text{m}^3$  to about 100  $\mu\text{s}$  with 4  $\text{g}/\text{m}^3$ . These effects can influence the characteristics of electrical discharges in several ways [16].

#### 3.16.1 Critical electric field necessary for streamer propagation

The propagation characteristics of streamers depend on the energy balance in the active region: between the energy input from the space charge and applied electric fields and losses in electron avalanche production. The decrease in ionisation rate caused by the increased humidity in the streamer requires an increase in the minimum charge at the head which is necessary to sustain streamer propagation. Thus the stable streamer propagation electric field increases linearly with humidity from about  $4 \times 10^3$  V/cm in dry air to about  $6 \times 10^3$  V/cm at 20  $\text{g}/\text{m}^3$  (see Figure 3.18).

#### 3.16.2 Influence on the corona development at the initiation of long sparks

The amount of corona produced at the initiation of the long sparks depends on the humidity. The charge associated with the first corona and the extension of the corona streamers into the gap decreases with increasing humidity. This is the case since the rate of ionisation decreases with increasing humidity [16, 35, 36].

The duration of the dark period between the first corona and the second corona decreases with humidity. The reason for this is the following. The first corona

injects a space charge into the gap and it causes a reduction in the electric field in the gap. Restart of the ionisation after the dark period is determined by the recovery of the electric field in the stem region. The recovery of the electric field depends on the rate of increase of the applied voltage and how fast the space charge is removed from the stem region. Since the space charge injected by the first corona decreases with increasing humidity a smaller increase in voltage is needed for second corona inception [16, 35, 36].

### 3.16.3 Influence on leader propagation

At high humidity, a situation can be reached in which the streamer activity is so low that the leader current is practically reduced to zero. However, since the channel behaves like a resistive conductor, the leader tip potential approaches that of the high-voltage electrode. The local electric field is increased and vigorous new corona can start from the leader tip. This leads to the sudden elongation of the leader channel called restrikes. Another important effect of the increased humidity is that, in spite of the large current pulses associated with the restrikes, the charge per unit length of the leader decreases strongly with increasing humidity [16, 35, 36].

## References

- [1] Loeb, L.B., *The Kinetic Theory of Gases*, Wiley, New York, NY, 1963.
- [2] Kuffel, E. and Zaengl, W.S., *High Voltage Engineering Fundamentals*, Pergamon Press, 1984.
- [3] Cobine, J.D., *Gaseous Conductors: Theory and Engineering Applications*, Dover Publications, New York, NY, 1958.
- [4] Badaloni, S. and Gallimberti, I., University Di Padova, Istituto Di Elettrotecnica E Di Elettronica, Upee-72/05, 1972.
- [5] Morrow, R., *Physical Rev. A*, 32, 1799–1809, 1985.
- [6] Morrow, R. and Lowke, J.J., *J. Phys. D: Appl. Phys.*, 30, 614–627, 1997.
- [7] Howatson, A.M., *An Introduction to Gas Discharges*, Pergamon Press, 1965.
- [8] Knoll, M., Ollendorff, F. and Rompe, R., *Gasentladungstabellen*, p. 63. *Handbuch der Physik*, Bd.23/1, pp. 141, 142, 1933.
- [9] von Angel, A. *Ionised Gases*, 2nd ed., p. 181. Clarendon Press, 1965.
- [10] Tozer, B.A., *Phys. Rev.*, 137, A1665, 1965.
- [11] Saha, M.H., *Phil. Mag.*, 40, p. 472, 1920.
- [12] Penning, F.M., *Physica*, 1, p. 1028, 1934.
- [13] Thomson, J.J., *Phil. Mag.*, 23, 449, 1912.
- [14] Nasser, E., *Fundamentals of Gaseous Ionization and Plasma Electronics*, Wiley-Interscience, 1971.
- [15] Bazelyan, E.M. and Raizer, Y.P., *Spark Discharge*, CRC Press, 1998.
- [16] Gallimberti, I., *J. Phys. – Paris*, 40(7), pp. C7-193–250, 1979.
- [17] Weissler, G.L., *Encyclopedia of Physics*, vol. 16, p. 445, Springer, Berlin, 1956.
- [18] Richardson, O.W., *The Emission of Electricity from Hot Bodies*, Longmans Green, London, 1921.
- [19] Schottky, W.Z., *Phys.*, 14, 63, 1923.
- [20] Fowle, R.H. and Nordheim, L.W., *Proc. Roy. Soc. London*, 119(1928), 173;124(1929), 699.



- [21] Bortnik, I.M., Kushko, A.N., and Lobanov, A.N., 'Physics of electrical breakdown of gases', *Proceedings of the Second All-Union Conference*, Tartu, p. 270, 1984.
- [22] Raether, H., *Electron Avalanches and Breakdown in Gases*, Butterworths, London, 1964.
- [23] Loeb, L.B., *Basic Processes of Gaseous Electronics*, University of California Press, 1955.
- [24] Loeb, L.B. and Meek, J.M., *The Mechanism of the Electric Spark*, Stanford University Press, 1940.
- [25] Loeb, L.B., *Electrical Coronas: Their Basic Physical Mechanisms*, University of California Press, 1965.
- [26] Raether, H., *Z. Phys.*, 112, p.464, 1939.
- [27] Meek, J.M., *Phys. Rev.*, 57, p. 722, 1940.
- [28] Cooray, V. et al. *Proceedings of the 24th International Conference on Lightning Protection*, Birmingham, Paper 1c.10, pp. 128–133, United Kingdom, 1998.
- [29] Hartmann, G., *Doctorat d'Etat Thesis*, University of Paris-Sud, France, 1977.
- [30] Bacchiega, G.L., Gazzani, A., Bernadi, M., Gallimberti, I., and Bondiou, A., *Proceedings of the 1994 International Aerospace and Ground Conference on Lightning and Static Electricity*, p. 23, Manheim, Germany, 1994.
- [31] Dawson, G.A. and Winn, W.P., *Z. Phys.*, 183, 159, 1965.
- [32] Marode, E., 'The glow to arc transition', in *Electrical Breakdown and Discharges in Gases* (E. Kunhardt and L. Larssen, eds.), Plenum Press, New York, NY, 1983.
- [33] Marode, E., *J. Appl. Phys.*, 46, 2005–2020, 1975.
- [34] Suzuki, T., *J. Appl. Phys.*, 42, 3766–3777, 1971.
- [35] Les Renardières Group, *Electra*, 53, 31–153, 1977.
- [36] Les Renardières Group, *Electra*, 74, 67–216, 1981.
- [37] Gao, L., Larsson, A., Cooray, V., and Scuka, V., *IEEE Trans. Dielect. Elect. Insul.*, 7(3), 458–460, 2000.
- [38] Griffiths, R.F. and Phelps, C.T., *Q. J. R. Meteorol. Soc.*, 102, 419–426, 1976.
- [39] Phelps, C.T., *J. Atmos. Terr. Phys.*, 15, 169, 1974.
- [40] Windmar, D., *Water Drop Initiated Discharges in Air*, Acta Universitatis Upsaliensis, Uppsala, 1994.
- [41] Bazelyan, E.M., Goncharov, V.A., and Gorjunov, A.Y., *Izv. Akad. Nauk SSSR, Energetika transp.*, 2, 154, 1985.
- [42] Bazelyan, E. M. and Gorjunov A.Y., *Izv. Akad. Nauk SSSR, Energetika transp.*, 4, 75, 1982.
- [43] Paris, L. and Cortina, R., *IEEE Trans. PAS-98*, 947–957, 1968.
- [44] Gao, L., Larsson, A., Cooray, V., and Scuka, V., *IEEE Trans. Dielect. Elect. Insul.*, 6(1), February 1999.
- [45] Akyus, M., Larsson, A., Cooray, V., and Strandberg, G., *UURIE 286–02*, Division for Electricity and Lightning Research, University of Uppsala, Sweden, 2002.
- [46] Larsson, A., 'Ph.D. thesis', *Acta Universitatis Upsaliensis*, 12, Uppsala, 1997.
- [47] Townsend, J.S., *Electricity in Gases*, Oxford, 1914.
- [48] Dakin, T.W. et al. *Electra*, 32, 61–82, 1974.

- [49] Brown, S.C., *Introduction to Electrical Discharges in Gases*, John Wiley & Sons, 1966.
- [50] King, L.A., *Proceedings of the 5th International Conference on Ionisation Phenomena in Gases*, Munich, 1961.
- [51] Toepfer, M., *Ann. Phys. D*, 4(21), pp. 193–222, 1906.
- [52] Engel, T. G., Donaldson, A. L., Kristiansen, M., *IEEE Trans. Plasma Sci.*, 17(2), April 1989.
- [53] Kushner, M. J. *et al.*, *J. Appl. Phys.*, 58, 1744–1751, September 1985.
- [54] Braginskii, S.I., *Sov. Phys. – JETP*, 34(7), 1068–1074, December 1958.
- [55] Cooray, V., Rahman, M., Rakov, V., and Atmos, J., *Solar Terres. Phys.*, 71, 1877–1889, 2009.
- [56] Trinh, N.G., *IEEE Trans. Elect. Insul.*, 11(2), March 1995.
- [57] Peek, F.W., *Dielectric Phenomena in High Voltage Engineering*, 2nd ed. McGraw-Hill, New York, NY, 1920.
- [58] Baldo, G., in *Electrical Breakdown and Discharges in Gases* (E. Kunhardt and L. Luessen, eds.), Plenum Press, 1983.
- [59] Salka, O., *En översikt över urladdningar i långa gap vid stötspänningar*, Internal Report of the Institute of High Voltage Research, 1966.
- [60] Leroy, G., Simon, M.F., and Liao, T.W., *Proceedings of the IEE Summer Power Meeting*, Paper 74 CH 0910-0 PWR, 1974.
- [61] Badaloni, S. and Galimberti, I., *Padua University Report*, Upee 72/03, 1972.
- [62] Kekez, M. and P. Savich, *Proceedings of the Fourth International Symposium on High Voltage Engineering*, Athens, 1983.
- [63] Bazelyan, E.M., *Zh. Tekh. Fiz.*, 36, 365, 1966.
- [64] Akyuz, M. and Cooray, V., *J. Electrostatics*, 51 and 52, 319–325, 2001.
- [65] Becerra, M. and Cooray, V., *J. Phys. D: Appl. Phys.*, 39, 3708–3715, 2006.
- [66] Becerra, M. and Cooray, V., *IEEE Trans. Power Deliver.*, 21(2), 897–908, 2006.
- [67] Becerra, M. and Cooray, V., *J. Phys. D: Appl. Phys.*, 39, 4695–4702, 2006.
- [68] Cooray, V., Rakov, V., and Theethayi, N., *J. Electrostatics*, 65(5, 6), 296–306, 2007.
- [69] Rizk, F., *IEEE Trans. Power Deliver.*, 4(1), 596–603, 1989.



---

*Chapter 4*

## **Mechanism of the lightning flash**

*Vernon Cooray*

---

### **4.1 Introduction**

Experimental observations of the optical and electromagnetic fields generated by lightning flashes during the last 50 years have significantly advanced our knowledge concerning the mechanism of the lightning flash. Nevertheless, this knowledge is not as exhaustive as that of long laboratory sparks due to our inability to observe lightning flashes under controlled conditions. Thus, the mathematical description of the mechanism of the lightning flash is relatively poor at present even though the main features of the lightning flashes themselves are well known. The main goal of this chapter is to provide the reader with the important features of the mechanism of the lightning flash. No attempt is made to provide an exhaustive list of the literature since this can be found elsewhere. The chapter is organised as follows. First a basic description of the mechanism of lightning flashes is given to introduce the reader to the terminology used in lightning research. After that, each event associated with the lightning flash is described in detail with particular attention being paid to the electromagnetic fields generated by these events.

*Nomenclature:* In this chapter a positive discharge is defined in such a way that the direction of motion of electrons in such a discharge is opposite to that of the discharge itself; a negative discharge is defined as one in the opposite sense. According to this definition a ‘negative return stroke’ is a positive discharge and a ‘positive return stroke’ is a negative discharge.

A positive field change is defined to be in the sense of negative charge being lowered to ground or positive charge being raised. According to this definition a lightning flash that transports negative charge to ground gives rise to a positive field change.

### **4.2 Ground flash**

As outlined in Chapter 1, a thundercloud generally contains two main charge centres, one positive and the other negative, and a small positive charge pocket (PCP) located at the base of the cloud. A ground flash occurs between the charge centres of the cloud and the ground. When a ground flash brings positive charge down to earth it is called a positive ground flash and when it brings negative charge it is called a negative ground flash. Time-resolved luminous features of a lightning flash as would be recorded by a streak camera are shown in Figure 4.1.

Electromagnetic field measurements show that a ground flash is initiated by an electrical breakdown process in the cloud called the preliminary breakdown.

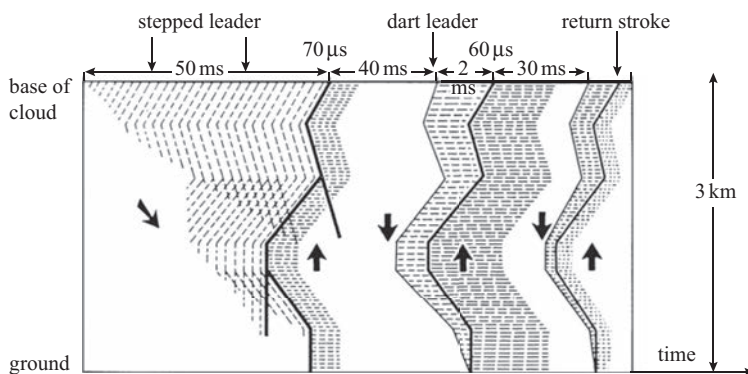


*Figure 4.1 Time-resolved luminous features of a lightning flash as would be recorded by a streak camera. The time increases from left to right. The time scale has been distorted for clarity (adapted from [208])*

This process leads to the creation of a column of charge called the stepped leader that travels from cloud to ground in a stepped manner. Some researchers use the term ‘preliminary breakdown’ to refer to both the initial electrical activity inside the cloud and the subsequent stepped leader stage.

On its way towards the ground a stepped leader may give rise to several branches. As the stepped leader approaches the ground the electric field at ground level increases steadily. When the stepped leader reaches to a height of about a few hundred or less metres from ground the electric field at the tip of grounded structures increases to such a level that electrical discharges are initiated from them. These discharges, called connecting leaders, travel towards the down-coming stepped leader. One of the connecting leaders may successfully bridge the gap between the ground and the down-coming stepped leader. The object that initiated the successful connecting leader is the one that will be struck by lightning. Once the connection is made between the stepped leader and ground, a wave of near ground potential travels along the channel towards the cloud and the associated luminosity event that travels upwards with a speed close to that of light is called the return stroke.

Whenever the upward-moving return stroke front encounters a branch, there is an immediate increase in the luminosity of the channel; such events are called branch components. Although the current associated with the return stroke tends to last for a few hundred microseconds, in certain instances the return stroke current may not go to zero within this time, but may continue to flow at a low level for a few tens to a few hundreds of milliseconds. Such long duration currents are called continuing currents.

The arrival of the first return stroke front at the cloud end of the return stroke channel leads to a change of potential in the vicinity of this point. This change in potential may initiate a positive discharge that travels away from the end of the return stroke channel. Occasionally, a negative *recoil streamer* may be initiated at the outer extremity of this positive discharge channel and propagates along it towards the end of the return stroke channel. Sometimes, discharges originate at a point several kilometres away from the end of the return stroke channel and travel towards it. On some occasions these discharges may die out before they make contact with the end of the return stroke channel. Such events are called K changes.

If these discharges make contact with the previous return stroke channel, the events that follow may depend on the physical state of the return stroke channel. If the return stroke channel happens to be carrying a continuing current at the time of the encounter, it will result in a discharge that travels towards the ground. These are called M-components. When the M-components reach the ground no return strokes are initiated, but recent analyses of the electric fields generated by M-components show that the current wave associated with them may reflect from the ground. If the return stroke channel happens to be in a *partially conducting stage* with no current flow during the encounter, it may initiate a *dart leader* that travels towards the ground. Sometimes the lower part of the channel has decayed to such an extent that the dart leader stops *before actually reaching the ground*. These are termed 'attempted leaders'. In other instances, the dart leader may encounter a channel section whose ionisation has decayed to such an extent that it cannot support the continuous propagation of the dart leader. In this case the dart leader may start to propagate towards the ground as a stepped leader. Such a leader is called a dart stepped leader. If these leaders travel all the way to ground then another return stroke, called the subsequent return stroke is initiated. In general, dart leaders travel along the residual channel of the first return strokes but it is not uncommon that the dart leader takes a different path than the first stroke. In this case it ceases to be a dart leader and travel towards the ground as a stepped leader. The point at which this leader terminates may be different from that of the original first leader. The separation between such subsequent channels was observed to be about a few kilometres on average.

Electrical activity similar to that which occurs after the first return strokes may also take place after the subsequent return strokes. Note, however, that branch components occur mainly in the first return strokes and occasionally in the first subsequent stroke. This is the case because in general dart leader do not give rise to branches. In the literature on lightning, the electrical activity in the cloud that takes place between the strokes and after the final stroke are called collectively, junction processes or J processes. A typical ground flash may last for about 0.5 s with a mean number of strokes between four and five.

The description given above is based on the observations of negative ground flashes. Not much information is available today concerning the mechanism of positive ground flashes but their mechanism is qualitatively similar to the negatives with differences in the details. For example, the scanty evidence indicates that positive leaders propagate more or less continuously and many positive ground flashes contain only one return stroke. In addition to these typical ground flashes, lightning flashes can also be initiated by tall structures. In this case a connecting leader is initiated at the top of a tower, for example, and propagates into the cloud. Dart leaders travel along this channel and initiate return strokes. As a consequence these flashes do not contain first return strokes initiated by stepped leaders.

### 4.3 Cloud flash

Cloud flashes normally occur between the main negative and upper positive charge of the cloud. Most of the information available today on the mechanism of the cloud flash is based on electric field measurements. More recently, Proctor [1–3] and Krehbiel and co-workers [4–6] made important discoveries utilising VHF radio

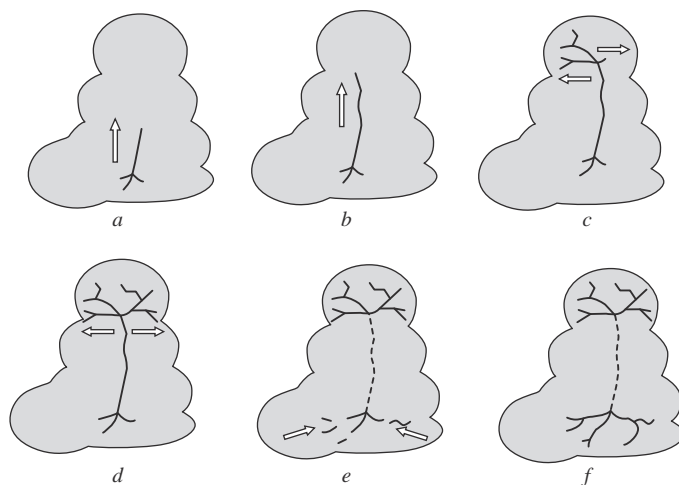


*Figure 4.2 Mechanism of a cloud flash. The cloud flash commences with a movement of negative discharges from the negative charge centre towards the positive one in a more or less vertical direction. This is the initial stage (a and b). This stage is followed by an active stage in which horizontal extension of the upper level channels takes place while charge is being transported from the lower level to the upper level along the vertical channel (c and d). In the latter part of this active stage significant extensions of the lower level channels take place but the extensions take place retrogressively (e). In the final stage the conductivity of the vertical channel decreases and the upper level channels will be cut off from the low-level channels (f). The arrows indicate the general direction of the discharge development*

imaging techniques (see section 4.11). The following picture of the cloud flash is based on the observations of Krehbiel and his co-workers (Figure 4.2).

1. The cloud flash commences with a movement of negative discharges from the negative charge centre towards the positive one in a more or less vertical direction. The vertical channel develops within the first 10–20 ms from the beginning of the flash. This channel is a few kilometres in length and it develops with a speed of about  $1.5 \times 10^5$  m/s. Even after the vertical channel was formed, the authors could detect an increase in the electrostatic field indicative of negative charge transfer to the upper levels along the vertical channel.
2. The main activity after the development of the vertical channel is the horizontal extension of the channels in the upper level (i.e. the channels in the positive charge centre). These horizontal extensions of the upper level channels are correlated to the brief breakdowns at the lower levels, followed by discharges propagating from the lower level to the upper level along the vertical channel. Thus, the upper level breakdown events are probably initiated by the electric field changes caused by the transfer of charge from the lower levels. For about 20–140 ms of the cloud flash, repeated breakdowns occur between the lower and upper levels along the vertical channel. These discharges transported negative charges to the upper levels. Breakdown events of this type can be categorised as K changes. In general, the vertical channels through which these discharges

propagate do not generate any radiation in the radio frequency (RF) range, indicating that they are conducting. This is so because, in general, conducting channels do not generate RFs as discharges propagate along them. Occasionally, however, a discharge makes the vertical channel visible at RFs and then the speed of propagation can be observed to be about  $(5-7) \times 10^6$  m/s, typical of K changes. This active stage of the discharge may continue to about 200 ms.

3. In the latter part of this active stage (140–200 ms), significant extensions of the lower level channels (i.e. the channel in the negative charge centre) take place, but they occur retrogressively. That is, successive discharges, or K changes, often start just beyond the outer extremities of the existing channels and then move into and along these channels, thereby extending them further. These K changes transport negative charge from successively longer distances to the origin of the flash, and sometimes even to the upper level of the cloud flash as inferred from RF emissions from the vertical channel. Sometimes, these K changes give rise to discharges that start at the origin of the flash and move away from it towards the origin of the K changes. Such discharges can be interpreted as positive recoil events that transport positive charge away from the flash origin and towards the point of initiation of the K change.
4. At the final part of the discharge the vertical channel and the upper level channels were cut off from the lower level channels. This is probably caused by the decrease in the conductivity of the vertical channel.

#### 4.4 Frequency of lightning discharges

The number of lightning flashes occurring in a given region is of interest to both power engineers and lightning protection engineers. Historically, the lightning activity was measured in terms of the number of thunder days for each region. A thunder day is a day in which thunder is heard by meteorological observers. On the basis of this data, World Meteorological Organisation has published a thunder-day map covering the whole world (see Chapter 1). More recently, information on lightning activity has been obtained by counting the number of lightning flashes occurring over a given region by (1) using satellites to capture the optical signals generated by lightning flashes [7, 8], (2) using lightning flash counters [9], (3) employing magnetic direction finding systems [10] and (4) employing VHF lightning mapping techniques [1–6] (see section 4.11 for a detailed description of some of these techniques). Some attempts have also been made to evaluate the number of lightning flashes occurring in the atmosphere by measuring the radio noise with an ionospheric sounding satellite [11]. Recently, advances have been made to relate the global lightning activity to the Schumann resonance [12, 13]. Schumann resonances are caused by the lightning induced excitation of the Earth ionospheric waveguide. The resonance frequencies are located at 8 Hz, 16 Hz, 32 Hz etc. Various estimates making use of these different techniques indicate that at a given time there are about 1000–2000 thunderstorms active around the globe. An isolated thundercloud may produce lightning at a rate of a few lightning flashes in a minute, but severe storms can produce lightning at a rate of several tens of flashes per minute, the maximum number recorded being about 85 flashes per minute [14]. At any one time the thunderstorms active around the globe produce lightning flashes at a rate of about  $20-120 \text{ s}^{-1}$ . The lightning activity over the oceans is about a factor of 3 smaller than over land.



#### 4.4.1 *Cloud to ground flash ratio*

A study conducted by Prentice and Mackerras [15] has summarised much of the available data on the cloud to ground flash ratio. According to them

$$\frac{N_c}{N_g} = 1.0 + 0.063T_d \quad 10 \leq T_d \leq 84 \quad (4.1)$$

where,  $N_c$  is the number of cloud flashes,  $N_g$  is the number of ground flashes and  $T_d$  is the number of thunderstorm days per year. They have also developed an empirical relationship between the cloud to ground flash ratio and the latitude. That relationship is given by

$$\frac{N_c}{N_g} = (4.11 + 2.11\cos 3\lambda) \quad 0 \leq \lambda \leq 60^\circ \quad (4.2)$$

where  $\lambda$  is the latitude. This equation indicates that the cloud to ground flash ratio is highest in the tropics and that it decreases with increasing latitude.

#### 4.4.2 *Ground flash density*

Until the late 1970s, the ground flash density, that is the number of lightning flashes striking one square kilometre on the Earth in a year, was obtained by lightning flash counters. More recently it has been determined by lightning localisation systems either using the principle of magnetic direction finding or the time of arrival technique, and sometimes both (see section 4.11). It is important to note that the sensitivity of these systems is not 100 per cent and that the sensitivity may vary in space, depending on the location of the detectors. Thus, the exact values of the ground flash density may be higher than the figures estimated from the data obtained from lightning localisation systems. Moreover, the ground flash density may vary from one geographical region to another and from one location to another within the same geographical region. In general the ground flash density will range between fewer than one ground flash per square kilometre per year to about 10 flashes/km<sup>2</sup>/yr. In analysing the ground flash density it is important to consider that some lightning flashes may have more than one termination to ground. The studies conducted by Rakov *et al.* [16] show that more than 20 per cent of the lightning flashes evidently have multiple terminations and the average separation between individual channel terminations varied from 0.3 to 7.3 km, with a geometric mean of 1.7 km.

The lightning ground flash density,  $N_g$  (in flashes/km<sup>2</sup>/yr) can be obtained from the thunder days  $T_d$  by using the empirical equation

$$N_g = 0.04T_d^{1.25} \quad (4.3)$$

This equation was derived by Andersson *et al.* [17] by comparing the ground flash density measured using CIGRE 10 kHz lightning flash counters with the thunder days measured in meteorological stations. As proposed by MacGorman *et al.* [18] one can also use the annual thunder hours  $T_h$  in the equation

$$N_g = 0.05T_h^{1.1} \quad (4.4)$$

to obtain the ground flash density.

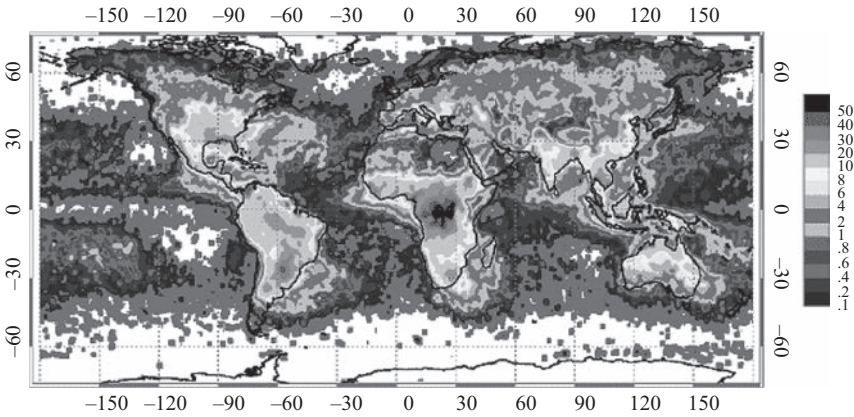


Figure 4.3 Global distribution of lightning flashes (in flashes/km<sup>2</sup>/yr) as observed by the optical transient detector (image courtesy of NASA)

#### 4.4.3 Total lightning activity

The total flash density in different regions of the world has been analysed by Mackerras and Darvaniza [19] who used the data from specially designed lightning flash counters located in 14 countries. They have found a clear tendency for the lightning flash activity to be a maximum at the equator and to decrease with increasing latitude. They have summarised their results through the equation

$$N = \exp(3.7 - 0.07\lambda) \text{ km}^{-2} \cdot \text{yr}^{-1} \quad (4.5)$$

where  $\lambda$  is the magnitude of the latitude in degrees. The satellite observations of lightning flash density shown in Figure 4.3 is in qualitative agreement with this general tendency.

### 4.5 Inception of lightning discharges in clouds

Lightning flashes are initiated in the mixed phase region of the cloud where water drops, ice crystals, graupel and water vapour co-exist. To unravel the physical processes in which these various phases of water interact with electric fields to initiate lightning flashes is one of the main challenges in atmospheric electricity. Several measurements conducted inside electrically active clouds show that they harbour electric fields of strengths typically in the range of 100–200 kV/m; the fields may occasionally reach values as high as 400 kV/m [20–25]. Let us consider the conditions necessary for the initiation of electrical discharges in the cloud.

#### 4.5.1 The particle interaction or classical mechanism

The discussion given here is based on a publication of Cooray *et al.* [26].

##### 4.5.1.1 Initiation of streamer discharges from a single water drop

Since the streamer discharges are a precursor to the electrical breakdown process at atmospheric pressures which are of interest in this study, the initiation of such discharges is a necessary condition for the generation of lightning flashes.

A spherical water drop enhances the background electric field by a factor of 3. Thus, the strength of the background field has to be higher than 500 kV/m so that the maximum electric field at the surface of the water drop becomes higher than about 1.5 MV/m, the electrical breakdown field at  $0.5 \times 10^5$  Pa (i.e. about half the atmospheric pressure) and at 273 K. In general, the negative charge centre of the cloud is located close to the 263 K ( $-10^\circ\text{C}$ ) isotherm, but this decrease in temperature will increase the breakdown electric field only by about 4 per cent. Since the electric field decreases rapidly with increasing distance from the surface of the drop, raising the surface field to 1.5 MV/m is not a sufficient condition for the generation of a streamer. The reason for this is the following: For the creation of a streamer an electric field of strength equal to or higher than the electrical breakdown value should exist over a critical volume in space. This necessarily requires an electric field higher than the breakdown field at the surface of the drop to create a streamer. Since the way in which the electric field decreases as a function of distance, measured from the surface of the drop, varies with its radius, the critical background field necessary for the creation of a streamer also varies with the drop radius. Table 4.1 summarises the background electric field necessary for the creation of streamers from different drop sizes.

Note that, although the field decreases with increasing drop radius, spherical drops need to be large, more than 3 mm in radius, to initiate streamers in background fields less than the electrical breakdown field. This means that it is not likely that single spherical drops will create streamers. So far we have not included the effects of deformation of the drop due to electrical forces. According to the results of Taylor [27], a drop will form a conical structure with an apex angle of 98.6 degrees just before it goes into corona. The results given in Table 4.1 show that the background electric field necessary for streamer inception does not change significantly even when this change in shape is introduced into the calculations except in the case of very large drop radii. The reason for this is that, even though the field enhancement at the drop surface is drastically increased due to the conical shape, it decreases rapidly as one moves away from the surface, approaching the field strengths

*Table 4.1 Background electric field necessary to create streamers from single water drops, both spherical ( $R_p/R_e = 1$ ) and deformed ( $R_p/R_e < 1$ ) according to Taylor's observations (from [27])*

<b>Equivalent drop radius, mm</b>	<b>Roundness, <math>R_p/R_e</math></b>	<b>Background field, MV/m</b>
1	1	1.41
1	1/32	1.41
2	1	1.41
2	1/32	1.27
3	1	1.41
3	1/32	1.07
4	1	1.35
4	1/32	0.95
5	1	1.29
5	1/32	0.86
6	1	1.24
6	1/32	0.80

$R_p$ , polar radius;  $R_e$ , equatorial radius.

identical to that of spherical drops within a fraction of drop radius. The conclusion is that only very large and very deformed drops may create streamers on their own.

#### 4.5.1.2 Initiation of streamer discharges by a chain of water drops

Crabb and Latham [28] analysed the generation of corona when two water drops collide and give rise to an elongated body. Cooray *et al.* [26] analysed the situation in which two water drops come close to each other in an electric field leading to an electric discharge between them. In the calculations it was assumed that the discharge takes place when the minimum electric field in the space between the drops surpasses the breakdown electric field. This is justified since the separation between the water drops just before the discharge is such that the electric field is approximately uniform in the space between them. During the discharge, the two drops will be connected by a conducting channel and this will create a complex body with a dumbbell shape. The situation just before and after the discharge is shown Figure 4.4 together with the corresponding electric fields. In this example the background electric field was assumed to be 200 kV/m. Furthermore, in their calculations it was assumed that the electrical relaxation time of the water in the cloud is so fast that it will not impede the redistribution of charge during the discharge event. These results show that the connection of the two drops by a discharge channel enhances the electric field at the outer periphery of the two drops much more than the field enhancement caused by a single drop or two drops without the connecting discharge. This situation, therefore, favours the creation of

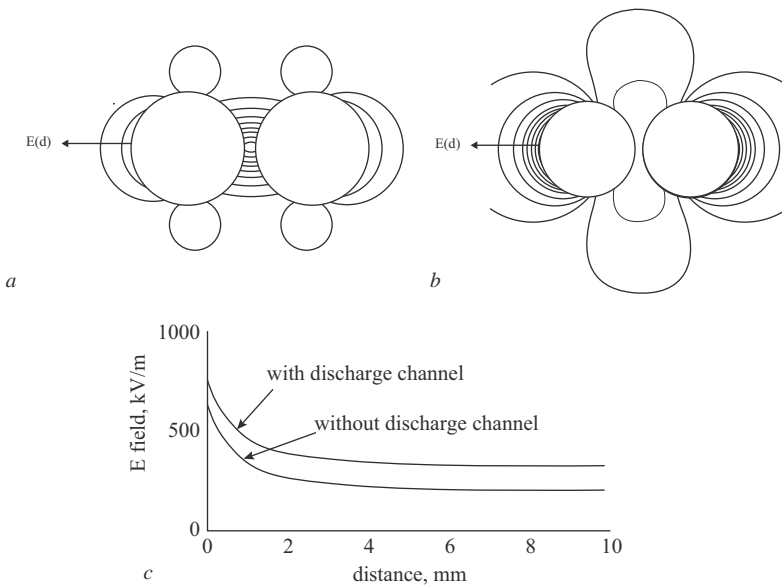


Figure 4.4 Surfaces of constant electric field (equipotential lines) for two water drops (a) before and (b) after discharge. Observe that in (b) there is a channel connecting the two drops. (c) The Electric field as a function of distance from the outer ends of the water drops. Background electric field is 200 kV/m; drop radius is 2 mm; separation between the drops is 0.39 mm (adapted from [26])

*Table 4.2 Background electric field necessary to create streamers from pairs of spherical water drops with a connecting discharge channel in between (see Figure 4.4)*

<b>Drop radius, mm</b>	<b>Background field, MV/m</b>	<b>Gap between drops, mm</b>
0.1	1.41	0.62
0.5	1.20	1.52
1	1.14	2.67
2	0.97	3.83
3	0.89	4.88
4	0.83	5.94

streamers more than a single drop. The results in Table 4.2 show the background electric fields necessary for the creation of streamers from such an encounter.

The electric fields given in Table 4.2 are lower than those given in Table 4.1 for single drops. Of course, a similar situation may occur in the transitory region of two drops coalescing to form a complex body. In this case the two drops will be connected by a liquid column instead of a discharge channel. But, the field enhancement would be more or less similar. Note that the electric discharge between the two water drops is a transitory event, but the field enhancement achieved during the discharge phase would remain the same even after the decay of the discharge channel. However, if a streamer is created from the outer periphery of the water drops, the resulting charge redistribution may provide sufficient current to maintain the discharge channel between the two drops.

As the electric field at the outer periphery of two interacting water drops increases, an electric discharge may take place to a third drop if the latter is located at a suitable distance. Because of the field enhancement, the distance to the third water drop need not be as small as the separation between the first two water drops. If a chain of drops is available, this process may continue along the drop chain and, with each succeeding discharge, the electric field at the outer periphery of the drop chain connected by the discharge channel may achieve a value higher than the one that existed during the previous discharge. If a sufficient amount of drops are available, this field enhancement associated with the elongation of the drop chain may proceed until a streamer is initiated from the drops at the terminations. A mechanism somewhat similar to this is also proposed by Nguyen and Mishnowski [29]. The data in Table 4.3 gives the length of the drop chain that is required to produce a streamer in a given background electric field. Calculations show that the field enhancement at the outer edge of the drop chain can be obtained without much error by replacing the drop chain with a conducting channel of hemispherical ends with radius identical to that of the water drops. This similarity was used in obtaining the data in Table 4.3. The data in this table can also be interpreted as the minimum length of the discharge channel needed to create sufficient field enhancement at the channel ends to generate a streamer in the background electric field.

The analysis presented above shows that sufficiently long drop chains can give rise to streamer discharges in the cloud in background fields as low as 100 kV/m. However, the number of closely spaced water drops needed to create streamer discharges in such low fields is large, and the chances of finding such a collection of closely spaced drops in the cloud is very remote. For example, according to

Table 4.3 Number of drops and total length of drop chain that is required to produce a streamer for a given drop radius and background electric field

Drop radius, mm	Background field, kV/m	Length of drop chain, mm
0.1	100	65
0.1	200	29
0.1	600	7
1	100	179
1	200	78
1	600	18
2	100	269
2	200	114
2	600	26
3	100	344
3	200	146
3	600	32

Latham and Dye [30], the ice particle (crystal and graupel) size distributions could be expressed roughly by the equations

$$N(D) = N_0 \exp(-\lambda d) \quad (4.6a)$$

where  $N(D)$ , the relative number of particles whose diameter (measured in mm) exceed the value  $d$ , is measured in  $\text{m}^{-3} \cdot \text{mm}^{-1}$ . Thus, the number of particles in a unit volume having diameters between  $d_1$  and  $d_2$ ,  $N_{d_1 d_2}$  (in  $\text{m}^{-3}$ ), is given by

$$N_{d_1 d_2} = \int_{d_1}^{d_2} N(D) dD \quad (4.6b)$$

Early in the electrical development of the storm,  $N_0 = 10^4 \text{ m}^{-3}$ ,  $\lambda = 2.0 \text{ mm}^{-1}$ . Towards the end of the electrical life of the cloud,  $N_0 = 10^5 \text{ m}^{-3}$ ,  $\lambda = 2.76 \text{ mm}^{-1}$ . According to this distribution, the number of particles with 0.5 mm or larger radii in an electrically active cloud is about 2000 per cubic metre. Thus, the relative distance between the large (i.e. radii in the mm range) precipitation particles can be as long as a decimetre. On the other hand, cloud droplets with radii in the range of a few micrometres to a few tens of micrometres are abundant in the cloud and the number of such cloud droplets in a  $1 \text{ m}^3$  of thundercloud air is about  $100 \times 10^6$  [31]. Consequently, the space between large precipitation particles is densely populated by cloud droplets, and the electric discharges may propagate in between these small droplets in exactly the same way as outlined earlier. Furthermore, under turbulent conditions the precipitation particle density may exceed the average values given above, at least in small volumes, and conditions favourable for discharge initiation may arise in there.

The calculations presented earlier also show that the length of the conducting channel necessary for the creation of streamer discharges in electric fields as low as 100 kV/m is in the range of a few decimetres. If the cloud has hot spots where the electric field is large enough to create electrical discharges frequently, whenever the length of these discharges exceeds a few decimetres they may act as sources of streamer discharges in the low background electric field. The volume of the hot spot need not be larger than a few cubic metres for this to happen.

### 4.5.1.3 Conditions necessary for the streamer propagation and streamer to leader transition

If clouds have hot spots where streamer discharges are frequently generated, they will culminate in lightning only if the background electric field exceeds the critical electric fields necessary for the propagation of streamers. This critical electric field decreases with decreasing pressure and increases with increasing humidity. At sea level the critical electric field necessary for streamer propagation is about 450–500 kV/m and at the altitude of 6 km where the atmospheric pressure is about  $0.5 \times 10^5$  Pa this field decreases to about 200 kV/m. However, the cloud environment is saturated with water vapour and the stable streamer propagation requires about 250–300 kV/m.

Before a streamer system can lead to a lightning discharge it has to be converted to a leader. A system of streamers may give rise to a leader whenever the length of the streamer system exceeds about 3 m (see Chapter 3). Thus, if the background electric field exceeds the critical field necessary for streamer propagation in a region whose dimensions are a few metres the streamer system may lead to the inception of a leader.

### 4.5.1.4 Conditions necessary for the propagation of the leader

The potential gradient of the leader in laboratory discharges is about 100 kV/m. Thus, lightning leaders immediately after inception may require electric fields of this order of magnitude for stable propagation. This indicates that immediately in the vicinity of the region of leader inception the background electric field has to be on the order of 100 kV/m for the newly created leaders to propagate out of the region of inception. However, as the leader extends in space the potential gradient of the older leader channel sections may decrease to values on the order of 1 kV/m which are the values corresponding to arc channels in air. Consequently, long leaders may propagate in background electric fields much less than 100 kV/m.

The way in which the critical electric field necessary for leader propagation changes with atmospheric pressure and relative humidity is not available in the literature, but judging from the characteristic of streamer discharges one may expect the critical electric field to decrease with decreasing pressure. The humidity may increase this critical field but the effect of pressure may overwhelm that due to humidity.

### 4.5.1.5 Conditions necessary for lightning initiation based on particle interaction or classical mechanism – a summary

The results presented above show that the lightning can be initiated through the interaction of water drops if (a) the electric field in a volume of about  $1 \text{ m}^3$  exceeds about 300–400 kV/m (for streamer inception), (b) the background electric field exceeds about 200 kV/m over length of about a few metres (for leader inception) and (c) the background electric field remains around 100 kV/m in bulk of the cloud (for leader propagation). Available experimental data demonstrate that the lightning is initiated in the cloud when the bulk field is about 100 kV/m. Unfortunately, the present day experimental techniques may not be able to detect the high field regions if they are confined to volumes of few metres in radius. For example, an instrumented balloon, being several metres in diameter, could disrupt highly localised regions of strong electric fields and may not detect them even if the balloon passes right through them.

#### 4.5.2 The runaway electron hypothesis

Another mechanism that may lead to the initiation of lightning flashes in the cloud is the acceleration of cosmic-ray-generated high energetic electrons in thunderstorm electric fields to produce an avalanche of MeV electrons [32]. A brief description of the electron runaway mechanism is the following: A free electron located in a gaseous medium when exposed to an electric field will experience a force equal to  $-eE$  where  $E$  is the applied electric field. Under the influence of this force and governed by the Lorentz force and Newton's second law the electron continues to accelerate. As the electron accelerates through the gaseous medium it collides with atoms and molecules and this causes the electron to lose energy. Thus, this interaction of the electron with atoms and molecules will generate a 'frictional force' that will oppose the force applied on the electron by the electric field. Let us denote the energy lost by an electron moving a unit length due to this frictional force as  $F_d$ . The unit of this parameter is eV/m. Figure 4.5, adapted from Moss *et al.* [33], shows how this frictional force varies as a function of the energy of the electron. The electric field in the figure corresponds to values pertinent to standard atmospheric pressure and temperature. Note that the maximum value of this frictional force corresponds to electron energy of about 100 eV. After reaching a peak at this electron energy the frictional force continues to decrease with increasing electron energy and reaches a minimum when the electron energy is about  $10^6$  eV. It is interesting to note that the frictional force can be expressed as an electric field that opposes the motion of the electron caused by the applied field. For example,

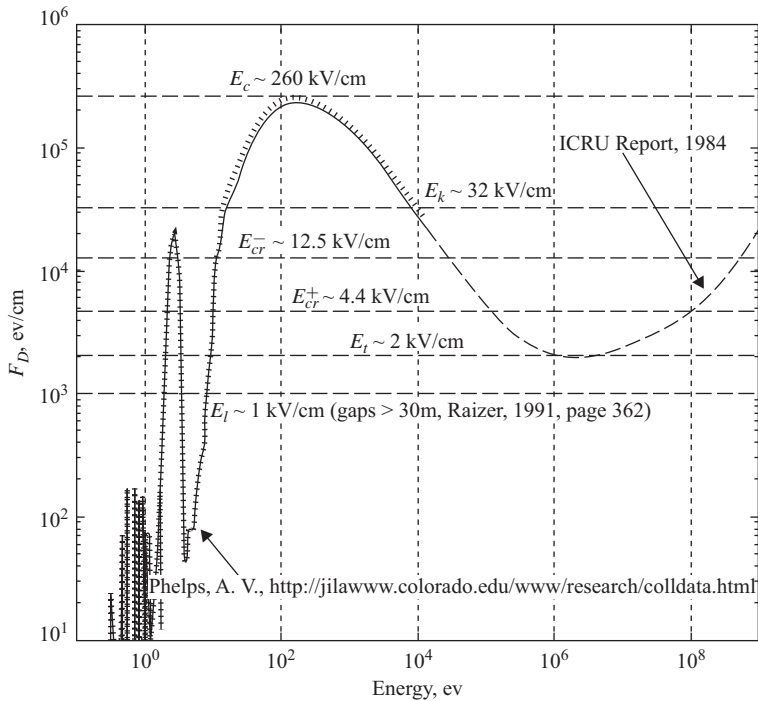


Figure 4.5 Magnitude of the 'drag force' as a function of electron energy. The data in the diagram corresponds to normal atmospheric density (adapted from [33])



the peak frictional force experience by an electron having energy 100 eV can be translated to an opposing electric field of magnitude  $26.0 \times 10^3$  kV/m (at standard atmospheric pressure). If the magnitude of the background electric field that accelerates the electron is larger than this value, in moving a unit length the gain in the energy of the electron will be larger than the losses and the electron will continue to gain energy and become a runaway. As one can see from this figure once the electron passes over the threshold energy of about 100 eV, the background electric field necessary to push the electron to runaway status decreases. For example, a  $10^4$  eV electron will become a runaway in a background electric field of about  $3.2 \times 10^3$  kV/m. One can see from this figure that the minimum frictional force of 200 kV/m is experienced by MeV electrons. This diagram is for atmospheric pressure and if it is scaled down to the pressure at cloud level which is about a factor of 2 less than atmospheric pressure at ground level the minimum frictional force will be about 100 kV/m. This field is similar in magnitude to the typical electric fields measured in active thunderclouds. Marshall *et al.* [25] suggested that whenever the electric field in the cloud exceeds about 100 kV/m initiatory MeV electron, generated by a high energetic X-ray from cosmic radiation, may give rise to an avalanche of MeV electrons which will initiate the electric breakdown process in the cloud. Marshall *et al.* [25] presented experimental data to show that whenever the electric field exceeds about 100 kV/m the probability of lightning initiation is enhanced significantly.

Recall that the 100 kV/m threshold for lightning initiation could also be explained using conventional method described in the previous section because it is the limiting field necessary for the propagation of leaders. It is also possible that lightning initiation in the cloud is caused by a combination of both runaway mechanism and the classical mechanism. For example, the runaway mechanism could change the electric field configuration in a small region of the cloud by generating a copious amount of negative and positive charges that trigger the particle interaction breakdown mechanism.

## 4.6 Physical processes and the electromagnetic fields of ground flashes

### 4.6.1 Preliminary breakdown process

Experiments conducted in long gaps with metal electrodes under atmospheric conditions show the occurrence of several corona bursts before a self-propagating leader discharge is launched from the high-voltage electrode to the earthed one (see also Chapter 3). On the basis of this experience one may expect some form of electrical activity inside the cloud before the stepped leader is launched. This electrical activity in the cloud can be much more complicated than that in the laboratory studies mainly for the following two reasons: First, in contrast with the case of metal electrodes, the electrical charges involved in thunderclouds reside on cloud droplets and precipitation particles and an efficient mechanism is needed to accumulate the charge necessary for the initiation of the stepped leader. Second, discharges are of several hundreds of metres to several kilometres in length and they occur within a complex environment of cloud particles and reduced pressure. The best means available today to deduce the breakdown mechanism inside the cloud is to make measurements of the electromagnetic fields generated by the processes inside the cloud at several stations and to combine the information

gathered such as with the data from VHF time of arrival and VHF imaging techniques [1–6; see also section 4.11].

#### 4.6.1.1 Electromagnetic fields at ground level generated by the preliminary breakdown process

##### *Slow electric fields*

The electromagnetic fields at ground level generated by the preliminary breakdown processes have been recorded and characterised by many researchers [34–39]. A typical electric field generated by the preliminary breakdown process is shown in Figure 4.6. Even though the main features of the electromagnetic fields obtained in different studies are similar, there are differences on a more detailed level caused probably by the meteorological conditions and the differences in the experimental techniques used in different studies. The main features of the slow electric fields generated by the preliminary breakdown process are the following. The electrostatic field starts to increase slowly and this increase may continue for some several tens to several hundred milliseconds. This initial phase is called the preliminary variation and it ends with a burst of pulses. This pulse burst is called the characteristic pulses or the preliminary breakdown pulses. The duration of the pulse burst is of the order of a millisecond. Sometimes this stage is followed immediately by a rapid increase in the electrostatic field and it culminates in a return stroke. However sometimes the electric field may level off and continue to increase at a reduced rate before the onset of the rapid electric field change leading to the return stroke. Measurements conducted in different geographical regions may contain some or all of these features. For example, measurements conducted in Sweden consistently showed that in Swedish lightning flashes the first detectable activity before the first return stroke is the occurrence of preliminary breakdown or characteristic pulses [39]. The static field starts to increase together with the onset of preliminary pulses and it culminates in the first return stroke. One such example is shown in Figure 4.7. The behaviour of the field after the occurrence of characteristic pulses could also be governed to a large extent by the path taken by the downward-moving stepped leader in its journey towards ground.

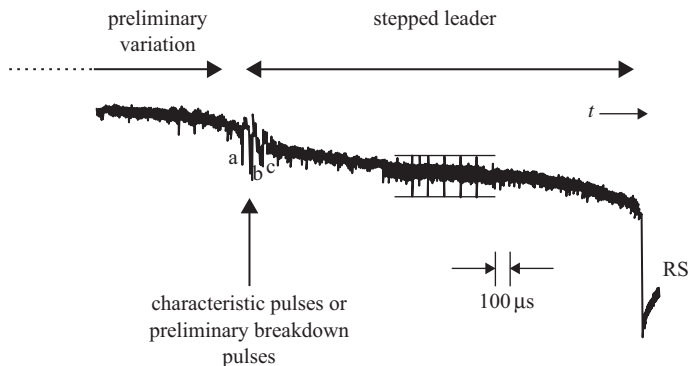


Figure 4.6 A typical electric field preceding a cloud to ground flash at a distance of 11 km. *a*, *b*, *c* are the individual characteristic pulses and *RS* is the return stroke. A positive field corresponds to a downward deflection (adapted from [34])

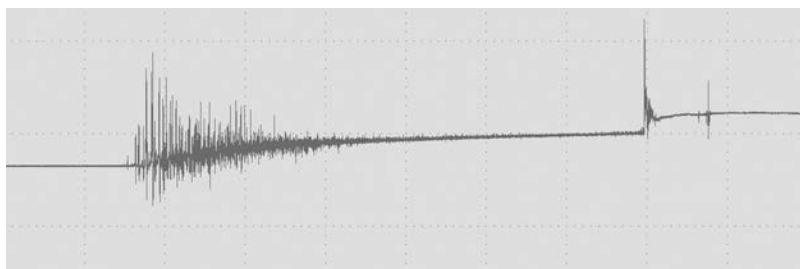


Figure 4.7 *Electric field generated by the preliminary breakdown process preceding the first return stroke (obtained from the study conducted in [39])*

### *Characteristic pulses*

According to Beasley *et al.* [34] the characteristic pulses signal the initiation of the stepped leader in the cloud. Measurements conducted in Sweden show that the HF radiation (at 3 MHz) associated with the leader stage starts immediately or with the occurrence of characteristic pulse burst, supporting this proposition [38, 40].

Beasley *et al.* [34] state that in many of the electric field records obtained in Florida, USA, the characteristic pulses could not be clearly identified except in 6 of their 79 recordings. On the other hand, the experimental data obtained from land based thunderstorms in Sweden over the years show very pronounced characteristic pulses and rarely can one see a return stroke without them [38–40]. However, measurements carried out in Sri Lanka in the tropics using an identical experimental set up show that the characteristic pulses are weak and barely discernible in these tropical storms [38, 40]. It is noteworthy that the ratio of the peak of the largest characteristic pulse to the peak of the first return stroke radiation field in Sri Lanka is about 0.1 whereas in Sweden the ratio is about ten times larger. Measurements of HF radiation at 3 MHz conducted simultaneously with these broadband measurements show that as in Sweden the onset of HF radiation takes place simultaneously with the onset of characteristic pulses in Sri Lanka. In some cases where characteristic pulses were barely detectable, one can still observe the onset of the HF radiation. It may be reasonable to assume that characteristic pulses are present, if not in all, in many of the preliminary breakdown stages, the only difference being that their amplitudes differ under different meteorological conditions.

#### **4.6.1.2 Duration of the preliminary breakdown process**

The total duration of the preliminary breakdown process can be defined as the time interval between the first detectable static field change and the return stroke. For several reasons, however, it is not easy to measure exactly the point at which the change in the static field associated with the preliminary breakdown occurs. First, inside a mature thundercloud electrical activity may take place almost continuously and any activity in the cloud that has no connection to the ground flash under study may contaminate the static field of the preliminary breakdown leading to erroneously long durations. Second, the onset of the preliminary breakdown may produce only a small static field which is difficult to detect in the background noise. Third, if the decay time constant of the measuring equipment is not long enough the equipment may not be able to reproduce the slowly increasing static field faithfully (see section 4.10). Measurements indicate that the duration of the preliminary

breakdown process may range from several tens of milliseconds to several hundreds of milliseconds [34, 38]. However, for the reasons mentioned above the measured durations of the preliminary breakdown process should be accepted with caution. As mentioned previously, in Sweden any field change could not be detected before characteristic pulses even though the digitising system (working at 12 bit resolution) and the antenna set up (with a decay time constant of 10 s) are capable of detecting any such field change if existed. The similar feature was also observed in lightning flashes in Malaysia [39].

#### **4.6.1.3 Location of the preliminary breakdown stage in the cloud**

The location of the preliminary breakdown in the cloud can be determined by using one of three methods. The first method involves making multi-station electric field measurements [41, 42]. The preliminary breakdown is an intracloud process and the neutralisation and rearrangement of charge during this process can be modelled as a dipole. Seven variables (six space variables and the charge) describe the magnitude and location of the charge distribution and, therefore, measurements of the change in the electric field are required from at least seven stations in separate locations to estimate the unknowns. Once these are estimated the location of the preliminary breakdown process in the cloud can be obtained. The second method is based on single station measurements and utilises the fact that at ground level the vertical electric field of a dipole reverses its sign at a certain horizontal distance from the dipole. This distance depends on the height of the dipole. Thus, if the charge neutralisation or rearrangement during the preliminary breakdown stage can be represented as a dipole, the field reversal distance can provide information concerning the height of the breakdown process. This technique requires the measurement of electric field change of preliminary breakdown process from a number of ground flashes located at different distances from the measuring station. The method will give only a rough estimation of the height of the preliminary breakdown process in a given storm. This method was used by Clarence and Malan [35] to extract the height of the preliminary breakdown process. The third method is based on the VHF radio imaging technique [2, 5, 42; see also section 4.11]. These three kinds of measurements indicate that the preliminary breakdown process takes place at the same height from which the negative charge is eventually lowered to ground by the return stroke. On the basis of these measurements, one may conclude that, in general, the preliminary breakdown takes place at an altitude corresponding to an ambient temperature of about  $-10^{\circ}\text{C}$  to  $-20^{\circ}\text{C}$ .

#### **4.6.1.4 Physical nature of the characteristic pulses**

Clarence and Malan [35] suggested that the characteristic pulse in the preliminary breakdown process is produced by an electrical breakdown between the negative charge centre and the Positive Charge Pocket (PCP) located below it. Ogawa [43] suggests that the preliminary breakdown starts with the positive leaders travelling from the PCP towards the negative charge centre. When the contact is established, rapid neutralisation of the positive charge by the negative charge coming down from the negative charge centre generates the characteristic pulses. This process charges the vertical channel with negative charge leading to the initiation of the stepped leader. However, the suggestion that the preliminary breakdown process involves a PCP is not accepted by all researchers. The main argument against this theory being that the heights at which the preliminary breakdown takes place appear to be somewhat larger than the base level of the cloud where the PCP is expected to be located [41].

The recent laboratory experiments and the inferences based on them show that the collision of graupel with ice crystals in the presence of super-cooled liquid water could be the dominant process in charge generation inside the cloud [44, 45; see also Chapter 2]. The graupel and ice crystals obtain charges of opposite polarity during the collision. The graupel particles are heavier and fall towards the base of the cloud while the miniscule ice crystals move upwards creating two charge centres. The experimental data show that at temperatures below  $-10^{\circ}\text{C}$  (according to Takahashi, [46]) or  $-20^{\circ}\text{C}$  (according to Jayaratne *et al.* [47]) the graupel will receive a net negative charge during the collision but above this temperature they will be charged positively. Thus, the PCP in the cloud may occur at regions in the cloud in which the temperature is higher than about  $-20^{\circ}\text{C}$  or  $-10^{\circ}\text{C}$ , explaining why the preliminary breakdown process takes place at significantly larger heights than the height at which the cloud base is located.

The observations of Jacobson and Krider [48] provide support for the involvement of a lower positive charge in the initiation of cloud to ground flashes. Analyses of multi-station electric field data, and the field-changes produced by lightning, show that ground flashes often require the presence of positive charge below the main negative charge centre to obtain a satisfactory description of the field pattern. This is further supported by the observations of Murphy and Krider [49] and Krider *et al.* [50] which show that more than 80 per cent of the cloud-to-ground flashes were initiated by RF sources that began just below the negative charge centre and propagated downward towards what was inferred to be a region of positive charge at lower altitude.

As described previously, in Sweden the electric field pulses generated by the preliminary breakdown process at distances of 5–10 km have peak amplitudes comparable to those of the return stroke radiation fields [38]. It is difficult to understand how the preliminary breakdown process can generate electric field pulses of that magnitude if the breakdown is not associated with a neutralisation process.

Cooray and Jayaratne [40] argue that since the electric field enhancements at cloud heights attributable to the presence of the ground could not influence breakdown processes taking place in the cloud, the necessary condition for the creation of a lightning ground flash is the generation of a vertical conducting channel below the main negative charge centre. When the electric field between the main negative charge centre and the PCP leads to electrical breakdown, one end of the discharge channel advances towards the negative charge centre while the other extends towards the PCP. The orientation of this channel will be determined by the relative location of the two charged regions. If the PCP is located below the negative charge centre, the channel will grow in a more or less vertical direction. When this channel reaches the PCP, the charge in it is neutralised. After the neutralisation of the PCP, the conducting channel may continue to grow along the direction of the ambient electric field produced by the negative charge centre. If the positive charge was originally located below the negative charge centre, the channel grows downwards towards the ground leading to a ground flash.

The probability of ground flashes increases if electric breakdown events take place frequently between the negative charge centre and the PCP. Cooray and Jayaratne attribute the characteristic pulses to an electrical breakdown event between the negative charge centre and PCP and, based on the observation that the characteristic pulses are more intense in Sweden than in Sri Lanka, argue that

meteorological conditions which favour the production of strong PCPs are more likely to be found at mid and high latitudes than in the tropics, thereby explaining why there is a greater probability of lightning flashes striking the ground in these regions.

If this argument is correct then any process that increases the positive charge in the cloud below the negative charge centre should promote the creation of ground flashes. One such process is the ground corona, the positive charge generated by which is transported into the base of the cloud by updrafts [51]. In this respect it is of interest to investigate whether the topographical conditions that favour corona generation, such as the presence of thick vegetation, can lead to high ground flash densities.

## 4.6.2 Stepped leader

### 4.6.2.1 Structure of the stepped leader

It is general consensus that the stepped leader channel consists of a hot core surrounded by a cold, charged region called the corona sheath. Based on the results obtained from the spectral emissions of the stepped leader, Orville [52] estimated the radius of the hot core to be between 0.1 m and 0.5 m. The corona sheath is formed partly by the charge deposited by streamers propagating ahead of the leader channel and partly by the lateral corona discharges from the hot core.

A rough estimation of the diameter of the corona sheath can be obtained by assuming that the space charge spreads out radially until the electric field at the outer boundary of the corona sheath is equal to the breakdown electric field in air. For example, if the charge per unit length on the stepped leader channel is  $\rho$  then under the assumptions that the stepped leader channel is long and the electric field is directed radially from it, the radius of the corona sheath of the stepped leader channel is given by

$$R = \frac{\rho}{2\pi\epsilon_0 E_b} \quad (4.7)$$

In the above equation  $E_b$  is the breakdown electric field in air at a pressure corresponding to the height of the leader channel section of interest. At standard atmospheric pressure and temperature the breakdown electric field of air is about  $3.0 \times 10^6$  V/m and it decreases with decreasing pressure. A typical stepped leader may deposit about 0.0005 C/m to 0.001 C/m of charge in channel sections close to ground. Thus, the diameter of the corona sheath of a typical leader close to ground would be about 3–6 m.

### 4.6.2.2 Optically determined properties of the stepped leader

#### *The stepping process*

On photographs the stepped leader appears to advance in a series of rapid and discontinuous steps [36]. During their formation leader steps appear bright, whereas the channel remains dark in between the step formation. A new step generally starts a little way back up the track formed by the previous step. Usually, the leader gives rise to several branches and therefore at a given instant the stepping process may proceed in several branches simultaneously. The length of the steps ranges from 10 to –100 m. The average length of the steps in the upper portion of the channel (close to the cloud base) is about 50 m and close to ground it reduces to about 10 m. The formation of a step takes place in about a microsecond. The interval between

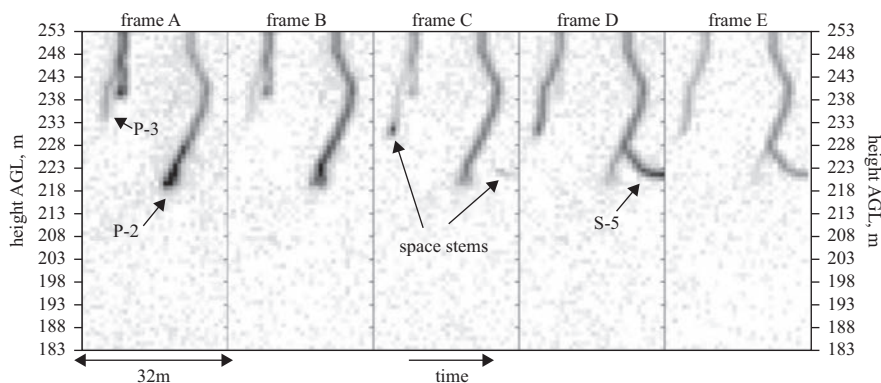


Figure 4.8 Several examples of space stems associated with negative lightning stepped leaders (adapted from [56])

the steps is about  $50 \mu\text{s}$  at upper levels and decreases to about  $10 \mu\text{s}$  close to ground [36, 53–55]. The available data indicate that the step length increases with increasing time interval between the steps [36].

Laboratory experiments show that it is not only the negative lightning leaders but also the negative leaders in long laboratory sparks that exhibit the stepping behaviour. A detailed description of the mechanism of formation of steps in negative laboratory leaders is given in Chapter 3. Recent observations show that a similar mechanism is active also in lightning stepped leaders (Figure 4.8) [56]. The mechanism described in brief is the following. First, a space leader that extends in two directions (one towards the tip of the leader and the other in the opposite direction) is created at the extremity of the streamer region of the stepped leader. When the tip of the space leader meets the tip of the stepped leader, the whole length of the space leader is converted to a part of the stepped leader channel. The sudden brightening of the space leader during this transformation appears as the formation of a new step. During this event a new streamer burst is generated in front of the new tip of the stepped leader (i.e. the tip of the space leader moving in the opposite direction). The sudden change in the potential and the resulting rearrangement of charge generate a current not only in the space leader but also along the rest of the stepped leader. This upward discharge appears as a luminous phenomenon propagating towards the cloud. Observations of Chen *et al.* [53] indicate that the luminosity travels upward without much degradation within the first several tens of metres to 200 m from the leader step but with severe attenuation above. The upward speed of propagation is estimated to be about  $10^8 \text{ m/s}$ . The speed at which the luminosity of the negative discharge surges forward (i.e. the speed of the step development) has not yet been measured. However, the signature of the optical pulse generated by this process has been measured. It has a rise time of about  $1.5 \mu\text{s}$  and its duration is about  $3 \mu\text{s}$  [53, 57]. Since the length of the step is a few tens of metres and the formation of the step is over in a few microseconds a speed of about  $10^8 \text{ m/s}$  appears to be reasonable.

According to observations made by Berger [58], one could observe faint traces of impulse corona at the tip of the newly made step. The impulse corona appears simultaneously with the step formation and the corona region extends forward by a distance of about one step length. This observation adds support to the above theory and experimental data.

### *Speed of the stepped leader*

The average speed at which the stepped leader propagates differs from the speed of the step development because there is a gap in time or a pause time between the steps. Schonland [59] divided the stepped leaders into two categories. The  $\alpha$  type leaders have a more or less continuous speed of  $10^5$  m/s and have a steps length and luminosity that does not vary appreciably along the channel. The  $\beta$  type leaders, on the other hand, are heavily branched near the cloud base, are very bright and make long steps and travel towards the ground with a speed of the order of  $10^6$  m/s. As they approach the ground they take on the characteristics of  $\alpha$  leaders. It is debatable whether  $\alpha$  and  $\beta$  leaders are two different phenomena or whether they are attributable to the same process manifested in different ways because of the presence of space charge below the cloud base. More recent measurements show that the average stepped leader speed is about  $0.5 \times 10^6$  m/s with individual values falling in between  $10^5$  and  $10^6$  m/s [53, 58, 60, 61]. Combining the results from electric field measurements with theory, Thomson [62] estimated the stepped leader speeds along the 0.6–2 km of the channel to be between  $1.3 \times 10^5$  and  $19 \times 10^5$  m/s with a mean value of  $5.7 \times 10^5$  m/s. Latest measurements conducted by Saba *et al.* [61] using high speed video cameras show that the average stepped leader speed is about  $3 \times 10^5$  m/s.

### *The temperature of the stepped leader*

The measurements made by Orville [52] showed that the formation of the step increases the channel temperature to about 30 000 K. The channel section associated with a particular step is illuminated again and again due to the upward-moving waves of current associated with the successive steps below it. Orville suggests that the temperature of the channel between these illuminations does not fall much below 15 000 K.

## **4.6.2.3 The electric field generated by the stepped leader**

### *Duration of the stepped leader electric fields*

One major problem in evaluating the duration of the stepped leader field is caused by the difficulty to pinpoint its exact beginning. Researchers have used different techniques to identify the beginning of the stepped leader field [34, 37, 38]. Some have utilised the occurrence of the characteristic pulses or the beginning of the HF radiation to identify the initiation of the stepped leader. Others, guided to some extent by the simulation of the stepped leader as a column of charge travelling towards the ground, have utilised the rate of change of the electric field to pinpoint the beginning of the stepped leader. Based on the work carried out in Sweden, the best procedure to use in evaluating the duration of the stepped leader is to measure the separation between the characteristic pulses and the return stroke. Since the beginning of 3 MHz radiation also coincides with the occurrence of characteristic pulses one can also get the leader duration by measuring the time interval between the return stroke and the origin of the 3 MHz radiation. The duration of stepped leader fields, summarised in Table 4.4, is based on the methods described above.

### *Signature of the static electric fields generated by the leader*

The static fields generated by stepped leaders at different distances are shown in Figure 4.9. The signature of these fields can be characterised and its main features can be described by simulating the stepped leader as a uniform line charge with one end fixed at cloud height and the other end approaching the ground with a



Table 4.4 *Duration of the stepped leader (adapted from Beasley et al.[34])*

Reference	No. of flashes	Distance, km	Minimum, ms	Maximum, ms	Mode, ms	Frequency system
Schonland <i>et al.</i> [59]	69	0–24	0–3	66	9–12	30 Hz to 20 kHz
Pierce [63]	340	40–100	0–20	525–550	20–40	1 Hz to 4 kHz
Clarence and Malan [35]	234	0–80	6	442	–	0 Hz to 300 kHz
Kitagawa [65]	41	0–15	8	89	20–30	0 Hz to 300 kHz
Kitagawa and Brook [64]	290	–	0–10	210	10–30	1 Hz to 1 MHz
Thomson [37]	53	6–40	4	36	–	0.1 Hz to 7.2 kHz
Beasley <i>et al.</i> [34]	79	0–20	2.8	120	6–20	0.03 Hz to 1.5 MHz
Gomes <i>et al.</i> [38]	41	10–100	2.0	70	8.7	1 kHz to 5 MHz

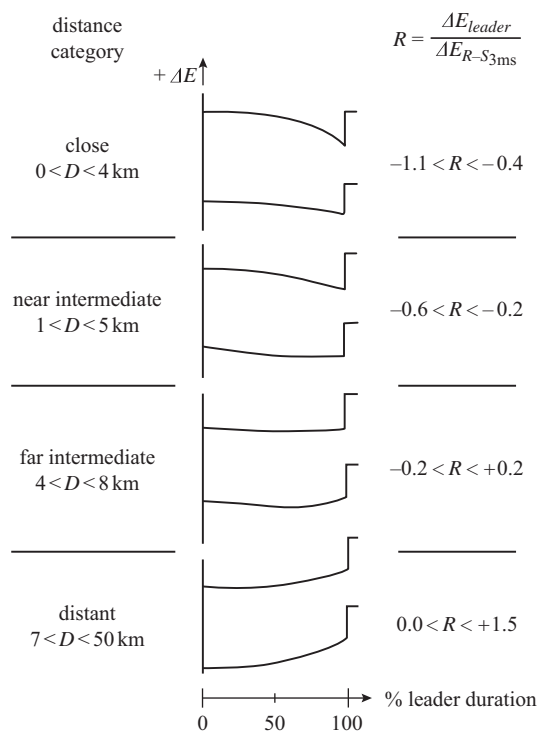


Figure 4.9 *Representative shapes of stepped leader fields in four distant categories. The ratio, R, of the leader field to the return stroke field is also given in the diagram. D denotes the distance. A positive field corresponds to an upward deflection (adapted from [34])*

uniform speed. Such model simulations can be compared with measurements to evaluate the approximate charge and the charge per unit length on the leader.

Thomson [62] showed that the time derivative of the static electric field generated by the stepped leader can be used to derive the properties of the leader. For example, he showed that the derivative of the leader field is a function of the speed of the leader tip and the measured field derivatives can be used to estimate the leader speeds. However, such an interpretation is valid only if the linear charge density at a given point on the leader does not vary as the leader extends towards the ground. However, a leader moving in a background electric field produces a charge density that increases with increasing time. For example, a leader moving in a constant background electric field acquires a charge that increases linearly with its length except at the very tip of the leader where the charge increases nearly exponentially. This also generates a charge distribution that varies as a function of time. This is the case since the charge density at a given point starts with a high value when the leader tip is at that point and it relaxes to a smaller value as the leader tip extends forward. More details on this are given in section 4.6.2.4.

*Signature of the radiation fields generated by the stepped leader*

Broad band measurements of leader fields indicate that small field pulses with an amplitude in the range of about 0.5–1 V/m at 100 km occur in the electric fields preceding the return strokes (see Figure 4.10a) [54, 55, 65, 66]. Several examples of

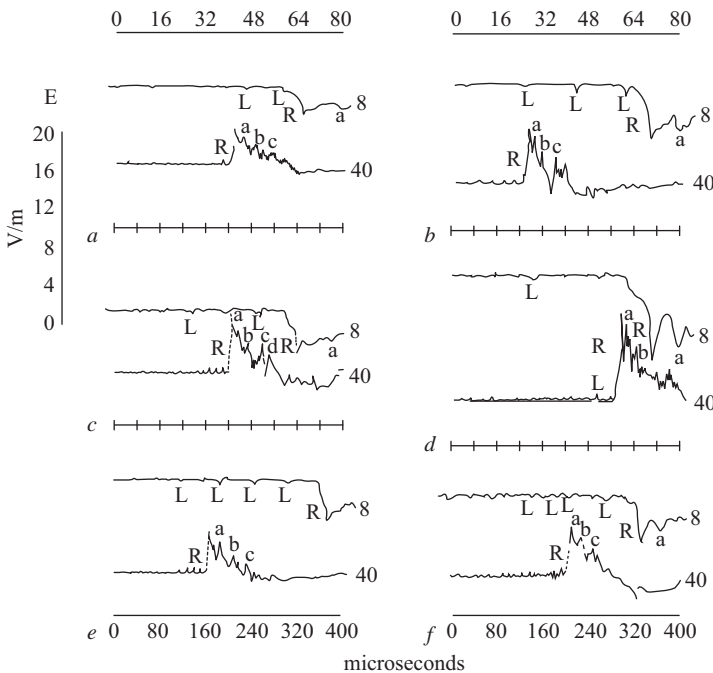
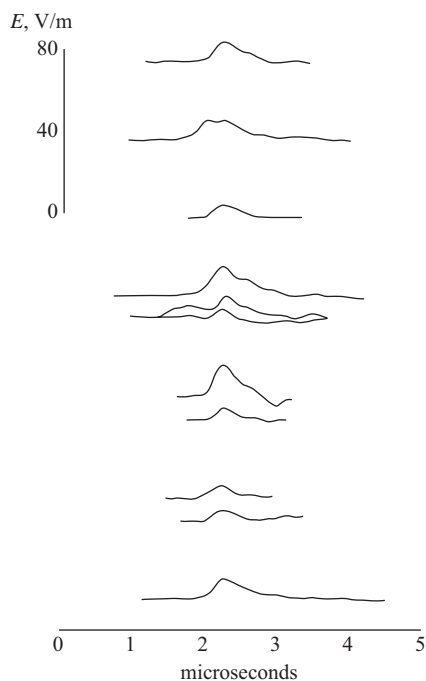


Figure 4.10a Electric fields produced by first return strokes at distances of 100–200 km over salt water. Each record contains an abrupt return stroke transition R preceded by small pulses characteristics of leader steps. The same waveform is shown on both a slow (40  $\mu\text{s}/\text{div}$ ) and a fast (8  $\mu\text{s}/\text{div}$ ) time scale. A positive field corresponds to an upward deflection (adapted from [146])



*Figure 4.10b Time-resolved electric fields produced by the stepping process of stepped leaders at distances of 20–30 km or less over salt water. A positive field corresponds to an upward deflection (adapted from [55])*

such pulses are shown in Figure 4.10b. Simultaneous optical and electric field measurements show that these radiation field pulses are produced by the processes taking place during the formation of leader steps [57]. The separation between these pulses immediately before the return stroke is about 10–15  $\mu\text{s}$ . When the propagation path of the electromagnetic fields is over salt water, which is highly conducting, one can observe that the rise time of the electric field pulses is about 0.1  $\mu\text{s}$  and their duration is about a microsecond [55, 67]. The leader pulses immediately preceding the return stroke are almost unipolar and their electric field derivative normalised to 100 km is about 22  $\text{V/m}/\mu\text{s}$ , which is comparable to that of return strokes [68, 69].

The amplitude of the last leader pulse,  $E_l$ , is about 0.1 of the return stroke amplitude,  $E_r$ , and Cooray and Lundquist [66] found that these amplitudes are correlated through the relationship

$$E_r = kE_l^\nu \quad (4.8)$$

where  $\nu = 0.64$  and  $k = 10.5$ . Since the amplitudes of the radiation fields are correlated to the respective peak currents, (4.8) implies a relationship between the charge on the leader channel and the return stroke peak current.

The amplitude spectrum of leader pulses is shown in Figure 4.11. The high-frequency end of this spectrum is almost identical to that of the return strokes. This indicates that the stepped leader pulses could play an important role in creating disturbances in telecommunication systems and low-voltage power installations.

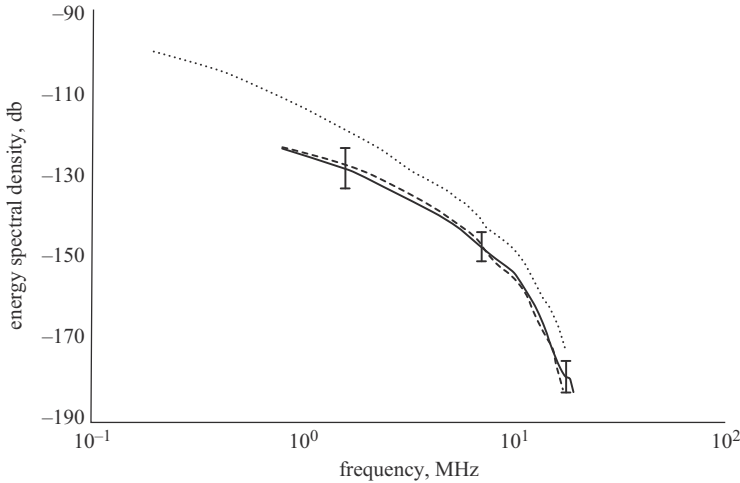


Figure 4.11 Average frequency spectrum of stepped leader steps (solid line) and dart stepped leader steps (dashed line). The average spectrum of first return strokes is shown by a dotted line for comparison (adapted from [67])

#### 4.6.2.4 Linear charge density and the total charge of the leader channel

From electric field measurements Schonland [70] estimated the charge density of the leader channel to be typically about 0.001 C/m. By combining theory with experiment Thomson *et al.* [62] estimated the linear charge density of a stepped leader to vary between  $0.7 \times 10^{-3}$  and  $32 \times 10^{-3}$  C/m with a mean of  $3.4 \times 10^{-3}$  C/m. One should keep in mind however that the leader is branched and the charge density estimated through electrostatic fields is an effective value.

An estimate of the total charge on the leader channel can be obtained either by analysing the electric fields created by stepped leaders [71] or by integrating the return stroke current measured at the channel base [58]. In the first case the geometry and the assumed charge distribution in interpreting the measured data may influence the results and in the latter case one has to make an assumption concerning the mechanism of charge deposition by the return stroke on the leader channel. Moreover, in integrating the currents measured at the channel base one must make a judgement, which may very well be subjective, concerning the time at which the current generated by the return stroke (arising from the neutralisation of the leader) ends and the continuing currents begin.

In a recent study, Cooray *et al.* [72] measured the charge brought to ground by the first 100  $\mu$ s of the return stroke. The measured charge as a function of peak return stroke current is shown in Figure 4.12. They found a strong correlation between the first return stroke peak current  $I_p$  and the measured charge  $Q$ . This correlation could be written as

$$Q = 0.062 \times I_p \quad (4.9)$$

Combining this information with the bidirectional leader model they have investigated how this charge was distributed along the stepped leader channel. In their analysis they have assumed that the stepped leader channel is vertical. It is not

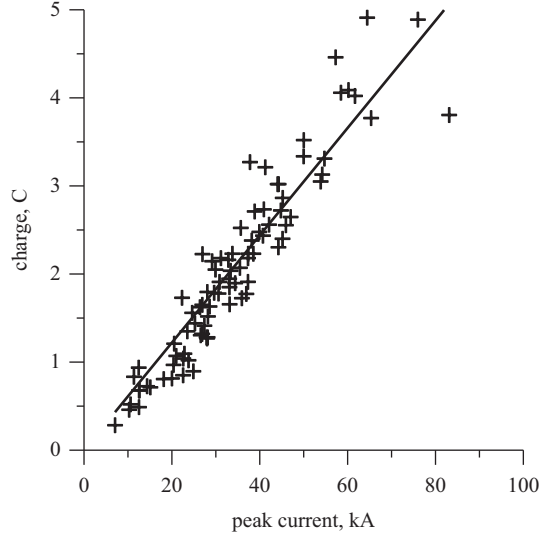


Figure 4.12 *The relationship between the first return stroke current peak and the charge brought to ground by the first return stroke in the first 100  $\mu$ s (adapted from [72])*

that difficult to modify the analytical expression they have obtained for a vertical stepped leader channel to an inclined one. Let us assume that the height of the tip of the stepped leader at a given instant of time is located at a height  $z_0$ . Let  $\zeta$  represent the distance from the tip of the leader channel, measured along the stepped leader channel, to the point on the leader channel, say P, where the charge density is required. The linear charge density at this point on the stepped leader channel can be represented analytically by

$$\rho(l) = a_0 \left( 1 - \frac{\zeta}{L - z_0} \right) G(z_0) I_p + \frac{I_p (a + b\zeta)}{1 + c\zeta + d\zeta^2} J(z_0) \tag{4.10}$$

$$\zeta = (z - z_0) \quad z > z_0 \tag{4.11}$$

$$G(z_0) = 1 - \frac{z_0}{L} \tag{4.12}$$

$$J(z_0) = 0.3\alpha + 0.7\beta \tag{4.13}$$

$$\alpha = e^{-(z_0-10)}/75 \tag{4.14}$$

$$\beta = \left( 1 - \frac{z_0}{L} \right) \tag{4.15}$$

where  $z_0$  is the height of the leader tip above ground in metres,  $z$  is the vertical height of the point P,  $L$  is the height of origin of the leader channel from ground level,  $\rho(z)$  is the charge per unit length (in C/m) of a leader section located at height  $z$ ,  $I_p$  is the return stroke peak current in kA,  $a_0 = 1.476 \times 10^{-5}$  s/m,  $a = 4.857 \times 10^{-5}$  s/m,  $b = 3.9097 \times 10^{-6}$  s/m<sup>2</sup>,  $c = 0.522$  m<sup>-1</sup> and  $d = 3.73 \times 10^{-3}$  m<sup>-2</sup>. Note that the above equation is valid for  $z_0 \geq 10$  m. This charge distribution is plotted in Figure 4.13 for a stepped leader with a prospective return stroke current of 30 kA. Note that the charge distribution is linear at

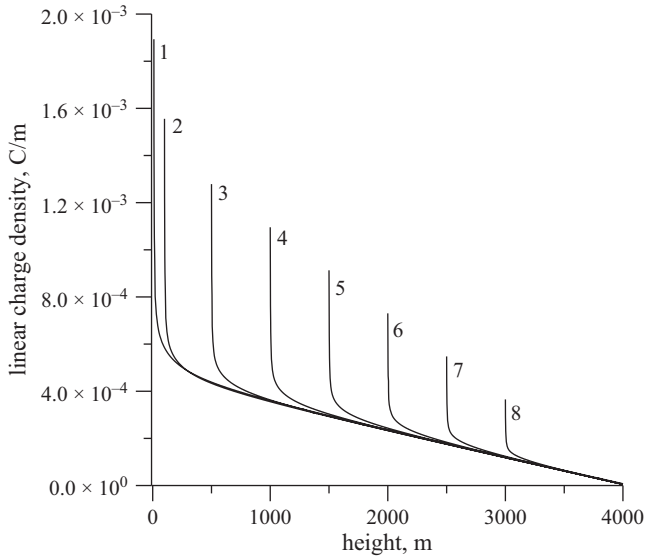


Figure 4.13 Charge distribution along a stepped leader channel with a prospective return stroke current of 30 kA. The height of the leader tip above ground is (1) 10 m, (2) 100 m (3) 500 m, (4) 1000 m, (5) 1500 m, (6) 2000 m, (7) 2500 m and (8) 3000 m

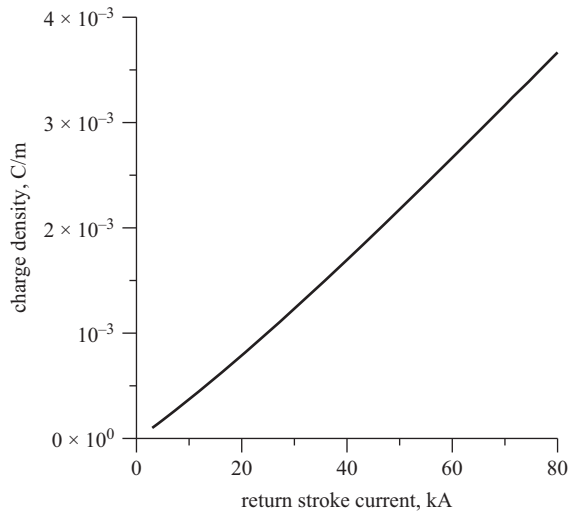


Figure 4.14 The average linear charge density (in C/m) over the first 100 m of a stepped leader with a prospective return stroke current of 30 kA

points far away from the tip but increases almost exponentially as one approaches the tip. The average charge over the first 100 m obtained in the analysis is shown in Figure 4.14. Note that a stepped leader associated with a typical return stroke carries a charge density of about 0.001 C/m over the last hundred metres of the channel.

### 4.6.2.5 Leader current

There are two forms of currents associated with a stepped leader. The first one is the time averaged current and the second one is the impulse current associated with the formation of steps.

#### *Average leader current*

Since the duration of the leader is around a few tens of milliseconds and the charge on the stepped leader ranges from a few coulombs to about 20 C, the average current of the stepped leader should be of the order of a few hundred amperes. Several researchers have estimated the leader current by analysing the remote electric and magnetic fields. Williams and Brook [73] estimated the leader currents of 50 and 65 A. However, much larger currents are obtained by Krehbiel [74] and Thomson *et al.* [62]. Krehbiel found that the average leader current over the last several milliseconds of the leader to be 0.2–3.8 kA for seven leaders. For 62 leaders Thomson *et al.* found leader currents within the few hundred microseconds of the return stroke in the range of 0.1–5 kA with an average current of 1.3 kA. One can also utilise the estimated leader charge distributions to obtain the leader current. Let us see how this can be achieved and under which assumptions. In the analysis let us represent the linear charge density of an element on the leader channel at any height  $z$  at any time  $t$  by  $\rho(z, t)$ . The current per unit length associated with the charging process of the leader at the same element is denoted by  $I_{ch}(z, t)$ . The geometry relevant to the calculation is shown in Figure 4.15. Consider a channel element  $d\xi$  located at height  $\xi$ . The charging of this current element starts at time  $(H - \xi)/v$  when the tip of the stepped leader reaches this channel element. In this expression  $v$  is the speed of the leader and  $H$  is the height or origin of the leader channel. We assume that this current travels with the speed of light towards the cloud. Thus, the current at level  $z$  due to the current generated at the leader element  $d\xi$  is given by

$$dI_l(z, t) = I_{ch} \left( \xi, t - \frac{(H - \xi)}{v} - \frac{(z - \xi)}{c} \right) d\xi \quad (4.16)$$

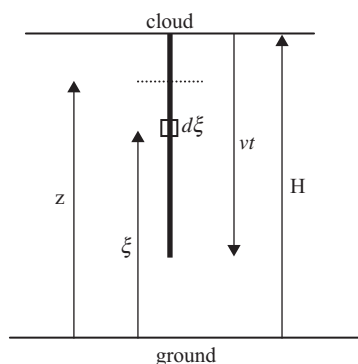


Figure 4.15 *The geometry relevant to the calculation of the current associated with a stepped leader. The stepped leader starts in the cloud and moves towards ground with uniform speed  $v$*

The total current at level  $z$  at time  $t$  can be obtained by integrating the above from  $(H - vt)$  to  $z$ . That is

$$I_l(z, t) = \int_{H-vt}^z I_{ch} \left( \xi, t - \frac{(H - \xi)}{v} - \frac{(z - \xi)}{c} \right) d\xi \quad (4.17)$$

Noting that the charge at any time on a leader element is given by

$$I_{ch}(z, t) = \frac{\partial \rho(z, t)}{\partial t} \quad (4.18)$$

one can solve the above equation to obtain the leader charge for any given charge density  $\rho(z, t)$ . The above equation can be simplified greatly if one makes the assumption  $v \ll c$ . This is a reasonable assumption since the speed of propagation of the stepped leader is around  $10^5$ – $10^6$  m/s. With this assumption the terms associated with the speed of light can be neglected compared to other terms and we obtain

$$I_l(z, t) = \int_{H-vt}^z I_{ch} \left( \xi, t - \frac{(H - \xi)}{v} \right) d\xi \quad (4.19)$$

Now, if one assumes that the charge at any given point is deposited instantaneously and the total charge deposited is  $\rho(z)$  then the above equation can be reduced to

$$I_l(z, t) = \int_{H-vt}^z \rho(\xi) \delta \left( \xi, t - \frac{(H - \xi)}{v} \right) d\xi \quad (4.20)$$

This can be easily integrated to obtain

$$I_l(z, t) = v\rho(H - vt) \quad (4.21)$$

That means the current at any level is the same at any given time and it is related to the charge deposited by the leader at its tip. This is the equation frequently used in estimating the leader current. However, this is not correct if the charge deposited by the leader varies with time. In that case one has to solve (4.19) to obtain the leader current. Figure 4.16 shows the leader current flowing at the origin of the stepped leader (i.e. at height  $H$ ) as a function of time obtained using the charge distribution given by (4.10) corresponding to a prospective return stroke current of 30 kA.

#### *Leader current associated with the steps*

A rough estimation of the peak of the impulse current associated with the stepping process can be obtained from the amplitude of the electromagnetic field pulses generated by leader steps using the transmission line model [55; see Chapter 9]. Since the radiation field amplitude of the stepped leader pulses is about 10 per cent of that of the return stroke, if similar speeds are assumed for the return stroke and leader step development, a peak current of about 3 kA is involved in the formation of a step in a stepped leader that gives rise to a 30 kA return stroke current. In reality, the step speed could be less than that of the return stroke and hence the step current would be larger than the 3 kA given. Using the same theory, Krider *et al.* [55] estimated the leader step current to be about 2–8 kA and the charge transported by the stepping process to be about  $1$ – $4 \times 10^{-3}$  C/m. If this estimation is correct then the step process is responsible for the bulk of charge transfer down



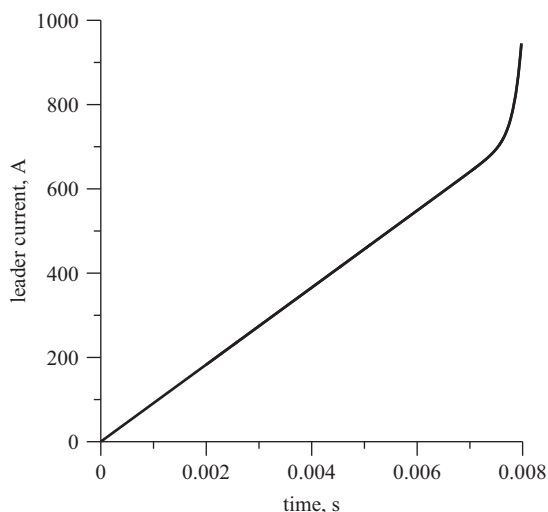


*Figure 4.16 The leader current flowing at the origin of the stepped leader (i.e. at height  $H$ ) as a function of time obtained using the charge distribution given by (4.10) corresponding to a prospective return stroke current of 30 kA*

the leader channel. This is the case since the estimated linear charge densities of the leader channel lie in this range. This is in contrast to the inferences made by Schonland [75]. According to Schonland's measurements, the electrostatic field change caused by the stepping process is less than one tenth of the static field change that takes place during the step interval. From this observation he concluded that the stepping process does not transport much charge but the bulk of it is transported by other processes such as negative streamers that travel continuously ahead of the stepped leader channel – the pilot leader of Schonland. Uman and McLain [76] question the validity of this observation since, if the bandwidth of the measuring system were large enough to resolve electrostatic field change taking place in a few microseconds, then such a measurement would be obscured by the presence of radiation fields. However, since the durations of the step fields are about  $1 \mu\text{s}$  and the intervals between the steps are about  $10\text{--}50 \mu\text{s}$ , one should be able to see the static fields generated by the steps even in the presence of radiation fields.

#### **4.6.2.6 Bidirectional and unidirectional leader concept**

The bidirectional leader concept was first introduced by Sopor [77] and then independently by Kasemir [78, 79]. The concept was supported and developed further by Mazur [80, 81], Mazur and Ruhnke [82], Kawasaki and Mazur [83] and Heckman and Williams [84]. The bidirectional leader concept is as follows: From the point from which the leader is initiated – probably the outer periphery of the negative charge centre – a negatively charged channel propagates downwards while a positively charged channel penetrates the negative charge centre. The net charge on the leader channel is zero with negative charges being concentrated on the lower end and positive charges on the upper branches. All the mobile charges are created in the channel and no movement of the cloud charge takes place during the leader progression. However, the positive end of the bidirectional leader brings positive charge into the charge centre, thus effectively removing negative charge from it.

Laboratory experiments that support the bidirectional leader concept were performed and reported by Laroche *et al.* [85], Bondiou *et al.* [86] and Mazur [80]. On the other hand, the VHF observations of Shao *et al.* [5] did not show any bidirectional leader activity in the cloud. However, Mazur [80] argued that the positive leaders do not produce strong VHF radiation and therefore the VLF mapping technique of Shao *et al.* is not sensitive to positive streamer activity (see section 4.11). However, observations of the latter show that at least some positive discharge activity could be detected using the VHF techniques. It is possible, however, that the detected radiation is associated with negative recoil leaders propagating along the positive leader channel.

The unidirectional leader model, which is frequently utilised in the calculation of leader fields, treats the leader as a charged cylindrical column extending out from the charge centre. It does not specify, however, any mechanism for the generation and transfer of charge from the main negative charge centre onto the leader channel. Nevertheless, it assumes that charge is depleted from the charge centre as the leader progresses. The two concepts are illustrated in Figure 4.17. If we assume that the upper branches of the leader channel form a dendritic network of channels, then, as far as the fields generated at ground level by the leader are concerned, there is not much difference in the two concepts. The upward-moving branches of the bidirectional leader bring positive charge into the charge centre, the net effect being that the

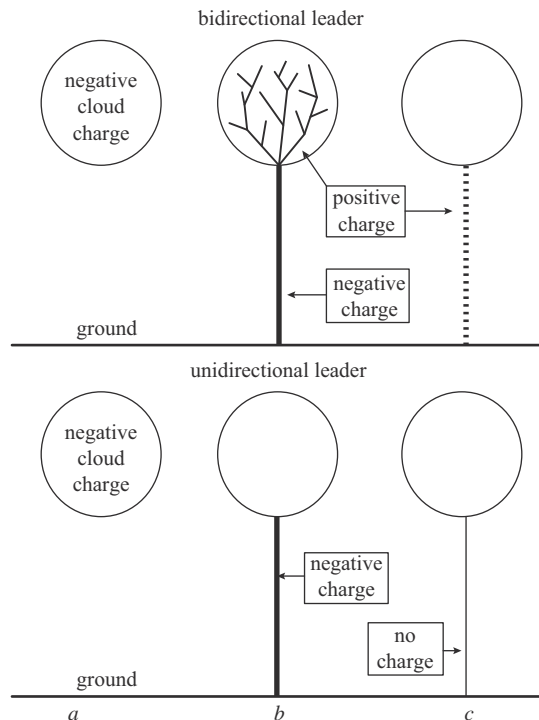


Figure 4.17 The concept of bidirectional and unidirectional leader. The unidirectional leader does not specify any mechanism for the transfer of charge from the cloud to the leader channel. Note that in the bidirectional leader model the channel is positively charged after the return stroke (adapted from [245])

net negative charge in the charge centre decreases and the negative column of charge extends towards ground. In unidirectional leader model too, one assumes that cloud charge is effectively removed and deposited on the down-coming leader channel. In this respect, the only difference between the two models is that the bidirectional leader specifies what happens and unidirectional leader concept does not.

#### **4.6.2.7 Stepped leader as a source of disturbance**

Usually, the return strokes are responsible for the largest overvoltages in electrical networks and, for this reason, the majority of the studies dealing with overvoltages in electrical systems have concentrated on the effects of return strokes. The rapid development of low-voltage electronic devices and their incorporation in modern day decision-making apparatus, however, make it necessary for engineers to consider the threats imposed by lightning events other than return strokes – for example stepped leaders.

As described previously, each step of a stepped leader gives rise to a fast electromagnetic radiation pulse, the duration of which is about a microsecond. A stepped leader can create a long train of such pulses with a time interval between individual pulses of some 10–200  $\mu\text{s}$ . Given the low tolerance of modern day electronic devices there is little doubt that these bursts of pulses can create significant disturbances in digital electronic systems.

In order to characterise the features of voltages and currents induced in electrical networks by stepped leaders, it is necessary to have a mathematical model that can describe this phenomena so that the electromagnetic fields generated by them can be calculated at any distance, especially where it is difficult to make experimental observations. Such a model was introduced recently by Cooray and Galvan [87]. The model is an engineering model but is based to some extent on the observed features of the negative leaders in long sparks. The model parameters were selected to give a fit to the electric field pulses of stepped leaders observed in reality. The model was used to evaluate the induced voltages caused by stepped leaders in low-voltage power installations. It is shown that the stepping process of the stepped leader could be an important source of disturbance in them.

#### **4.6.2.8 Interception of the stepped leader and grounded structures**

As the stepped leader approaches the ground, the electric field at the extremities of the grounded objects increases to such a level that they launch connecting leaders towards the down-coming stepped leader. There is direct and indirect evidence for the occurrence of connecting leaders to meet the down-coming stepped leader. A time-resolved picture of the down-coming leader and the upward-moving connecting leader is shown in Figure 4.18.

The majority of the speeds of upward-moving leaders reported in the literature are for those in either rocket-triggered lightning or upward-initiated lightning flashes from tall structures. In both these cases the leaders move under the influence of a more or less static background electric field generated by an overhead thundercloud.

The reported values of upward leader speeds vary between  $1 \times 10^4$  and  $1.4 \times 10^5$  m/s [58, 88–91]. However, in studies related to lightning attachment what is needed is the speed of upward-moving connecting leaders propagated under the influence of the electric field created by down-coming stepped leaders. Yokoyama *et al.* [91] studied lightning attachment to an 80 m tall tower and managed to obtain

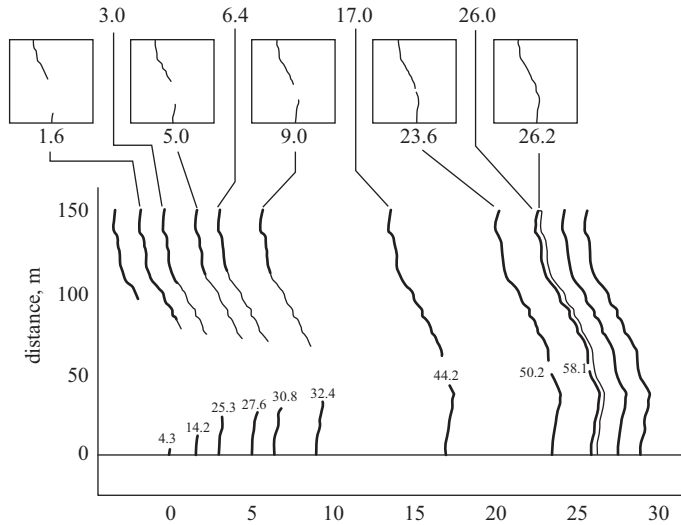


Figure 4.18 Time-resolved photograph of a down-coming leader and the upward-connecting leader. The time is given in microseconds and the time zero corresponds to the instant at which a connecting leader is initiated. The height of the connecting leader at different times is indicated in the figure. The numbers on the horizontal axis and at the boxes show the time in microseconds (courtesy of Prof. S. Yokoyama)

a few samples of the speed of upward-moving connecting leaders propagated in this way. In the four examples presented by Yokoyama *et al.* [91], the speed of stepped leaders and connecting leaders at the moment of connection was estimated as  $5.9 \times 10^6$  and  $1.3 \times 10^6$  m/s,  $2.7 \times 10^5$  and  $14 \times 10^5$  m/s,  $2.7 \times 10^6$  and  $2.9 \times 10^6$  m/s, and  $6.9 \times 10^5$  and  $5 \times 10^5$  m/s, respectively. The average propagation speed of the upward-connecting leaders ranged from  $0.8 \times 10^5$  to  $2.7 \times 10^5$  m/s. Unfortunately, it is not possible to distinguish between the positive and negative upward-connecting leaders in this experiment because neither the polarity nor the return stroke peak current was reported.

Direct measurement of currents in upward-connecting leaders of natural lightning flashes is complicated because, in addition to the current measurements, we need to have simultaneous time-resolved records of the development of the discharge to separate the measured current into contributions from the connecting leader and the return stroke. However, a triggered-lightning technique at altitude has provided a possible way to measure the currents associated with the development of upward-connecting leaders in the presence of a down-coming negative leader. Using this technique Lalande *et al.* [92] managed to record the currents in upward leaders. Results show that the current can reach values as large as 100 A before the connection is made.

The first return stroke is initiated at the instant contact is made between the down-coming stepped leader and one of the connecting leaders. The strike point of the lightning flash is the place from which the connecting leader that made the successful connection to the stepped leader was initiated. With the knowledge available at present, derived mainly from laboratory experiments, one can specify the conditions necessary for the launch of a successful connecting leader from a

grounded object such as a Franklin conductor. These conditions are the following: (i) inception of streamers at the tip of the Franklin conductor; (ii) inception of a connecting leader; (iii) propagation of the connecting leader; (iv) final attachment of the connecting leader and the stepped leader. A detailed description of the theory and the procedure that can be used to simulate these four steps are given in Chapter 3. More details on the process of interception and the models used to simulate it can be found in Chapter 14.

### 4.6.3 *Return stroke*

#### 4.6.3.1 **Origin of the return stroke**

The front of the leader channel consists of a system of streamers and the return stroke is initiated when this streamer front makes a connection either with the ground or with the streamer front of a connecting leader that rises to meet it. It is reasonable to assume that, starting from the meeting point between the stepped leader and the connecting leader, the neutralisation process will progress in opposite directions, one towards the ground and the other towards the cloud. Direct evidence for the existence of such two fronts is not available in the literature for first return strokes. However, for subsequent return strokes in triggered lightning Wang *et al.* [93] found that the return stroke is initiated at a height above the tip of the grounded structure. All the 14 subsequent return strokes contained in 4 rocket-triggered lightning flashes are found to be initiated at a height ranging from 2.3 to 26.0 m above the lightning termination point. A return stroke with a larger peak current tends to initiate higher.

#### 4.6.3.2 **Optically determined properties**

##### *Return stroke speed*

Pioneering work on the development of return strokes was done by Schonland and co-workers in South Africa and McEachron in the United States. They obtained time-resolved pictures of the return stroke development using Boys camera or streak cameras [36, 94, 95]. More recent speed measurements have been carried out using either streak cameras [96] or detectors consisting of a series of photomultipliers [97]. The most important results from a number of studies are summarised in Table 4.5. The data obtained from these studies indicate that (1) the return stroke speed decreases with height in both first and subsequent return strokes; (2) the average speed of subsequent return strokes over the first few hundred metres close to ground is greater than that of the first return strokes; (3) the return stroke speed in the vicinity of the ground may, in some cases, reach values close to the speed of light in free space; (4) the average speed of both first (positive and negative) and subsequent return strokes over the first kilometre is about  $1.0 \times 10^8$  m/s. The return stroke speed is an important parameter both in extracting the physical mechanism behind the return stroke development and as an input to the mathematical return stroke models (see Chapter 9 for a description of the return stroke models). A description of various models developed to predict the return stroke speed is given in Chapter 10.

It is important to note, however, that the optically measured speeds may differ considerably from the speed of the onset of the return stroke current along the channel for several reasons. First, the limited resolution of the optical measuring systems may make it almost impossible to obtain the exact time of the onset of the optical radiation. The situation is further complicated by the fact that the channel

Table 4.5 Velocity of return strokes as obtained in different studies

Reference	Type of return stroke	Average speed, m/s	Standard deviation, m/s	Comments
Mach and Rust [97]	Positive	$0.8 \times 10^8$	$0.4 \times 10^8$	Short channel segments close to ground (average 370 m)
Mach and Rust [97]	Positive	$0.9 \times 10^8$	$0.3 \times 10^8$	Long channel segments (average length 1120 m)
Mach and Rust [98]	Negative (first)	$1.7 \times 10^8$	$0.7 \times 10^8$	Short channel segments (average length less than 500 m near ground)
Mach and Rust [98]	Negative (first)	$1.2 \times 10^8$	$0.6 \times 10^8$	Long channel segments (average length greater than 500 m near ground)
Mach and Rust [98]	Negative (subsequent)	$1.9 \times 10^8$	$0.7 \times 10^8$	Short channel segments (average length less than 500 m near ground)
Mach and Rust [98]	Negative (subsequent)	$1.3 \times 10^8$	$0.5 \times 10^8$	Long channel segments (average length greater than 500 m near ground)
Mach and Rust [98]	Negative (triggered)	$1.4 \times 10^8$	$0.4 \times 10^8$	Short channel segments (average length less than 500 m near ground)
Mach and Rust [98]	Negative (triggered)	$1.2 \times 10^8$	$0.2 \times 10^8$	Long channel segments (average length greater than 500 m near ground)
Idone and Orville [96]	Negative (first and subsequent)	$1.4 \times 10^8$	–	Velocity near ground (<1.3 km)
Idone and Orville [96]	Negative (first and subsequent)	$1.1 \times 10^8$	–	Over longer channel segments (at least 0.7 km in length)
McEachron [95]	Negative (subsequent)	$6.1 \times 10^7$	–	
Schonland and Collens [94]		$4.6 \times 10^7$	–	

may remain slightly luminous, either continuously or intermittently, after the passage of the leader. Second, it is difficult to locate the same relative point on the optical signature at two different heights; this is further complicated by the fact that the optical pulse changes its shape and amplitude along the channel. Third, there can be a delay in the onset of optical radiation with respect to the onset of the current and this delay might vary depending on the rise time of the current waveform. Fourth, there could be a significant difference in the signatures of the optical pulse and the current waveform at a given height. The optical speed, therefore, may differ considerably from that of the speed of the onset of the return stroke current along the channel. The latter is the speed which is needed in return stroke models. On the other hand the measured optical speed provides information concerning the speed of propagation of bulk of the current and using this speed in return stroke models may lead to the correct general features of return stroke electromagnetic fields.

At present there is scanty evidence concerning the spatial variation of the first return stroke speed at the onset of the discharge. The data available is for the

subsequent strokes in triggered lightning. This data show that the subsequent return stroke speed increases initially over the first hundred metres or so of the return stroke, reaches a peak and then continues to decay. The return stroke model introduced by Cooray and Rakov [99] make a similar prediction. In the case of first return strokes it is reasonable to assume that the first contact between the stepped leader and the grounded object is established by the streamer region of the former. Thus, the early stage of the first return stroke involves the neutralisation of the streamer region of the stepped leader. The streamers, being cold discharges, are not good conductors like the thermalised and hot portion of the stepped leader channel. One would expect, therefore, the front of the return stroke to accelerate initially as it propagates towards the hot tip of the stepped leader channel, reaches its peak at the meeting point and then continues to decay. A first return stroke model based on this concept is introduced by Cooray *et al.* [100]. A detailed description of this model is given in Chapter 9.

#### **4.6.3.3 Characteristics of the optical radiation generated by the return stroke**

##### *Variation of the broadband optical pulse along the return stroke channel*

Information about the variation of the return stroke current as a function of height is important in the construction and validation of return stroke models. The behaviour of the current signature along the channel can be inferred to some extent by analysing the way in which the broadband optical radiation generated by the return stroke varies as a function of height. Using a measuring system capable of 0.5  $\mu\text{s}$  resolution, Jordan and Uman [101] and Jordan *et al.* [102] found that the light signal produced by a small channel section of subsequent strokes has a fast rise to peak followed by a slower decrease to a relatively constant value. The 20–80 per cent rise time of the light signal near ground is about 1.5  $\mu\text{s}$ . This rise time increased to about 4.0  $\mu\text{s}$  by the time the return stroke peak reached the cloud base at about 1.4 km. The amplitude of the initial peak decreased exponentially with height with a decay height constant of about 0.6–0.8 km. The photomultiplier measurements of Mack and Rust [97] show that the rise time (10–90 per cent) of the optical pulse generated by a channel segment with an average length of about 3 m and located within 100 m of the ground is 3.5  $\mu\text{s}$  for negative first strokes and 9.4  $\mu\text{s}$  for positive first strokes. According to their observations the rise time of the optical pulse increased with increasing height.

The experimental data of long laboratory sparks show that the rise time of the current in the discharge channel is approximately equal to the rise time of the optical pulse, and the peak amplitude of the optical pulse is linearly correlated to the peak current [103]. Interestingly, Idone and Orville [104] found a strong linear correlation between the peak current and the peak optical radiation. It is reasonable to assume, therefore, that the rising part of the return stroke optical pulse follows the rising part of the current waveform, at least approximately. If this is the case, the data given earlier indicate that (1) the rise time of the return stroke current waveform increases with height, (2) the peak return stroke current decreases with height and (3) the rise time of the current in positive return strokes is longer than that of the negative return strokes. It is important to mention here that Idone and Orville [104] found that the 20–80 per cent rise time of the optical radiation from a channel section 50 m above the point of strike of triggered lightning flashes had an average value of 2  $\mu\text{s}$ , whereas the current measured at the channel base had a rise

time of about 0.5  $\mu\text{s}$ . The reason for this difference could be the rapid elongation of the front of the current waveform during the first few tens of metres (see Chapter 9).

#### *Energy and power released in the optical signal*

The energy and power released in the optical signals of return strokes are important in the evaluation of the total energy dissipated in them. For example, the ratio between the electrical energy and the optical energy in long sparks can be obtained from experiments conducted in the laboratory. The electrical energy dissipated in lightning discharges can thus be obtained by assuming the same energy conversion ratio as in the laboratory discharges and measuring the optical energy generated by lightning flashes [105].

The most extensive investigation made to date on optical signals generated by return strokes was that conducted by Guo and Krider [106, 107]. They recorded the optical signals radiated by return strokes in the 0.4–1.1  $\mu\text{m}$  wavelength interval. The peak optical power radiated by the first return strokes in the range 5–35 km had a mean and standard deviation of  $2.3 \pm 1.8 \times 10^9$  W. Normal subsequent strokes (i.e. those preceded by dart leaders) generated  $4.8 \pm 3.6 \times 10^8$  W and subsequent strokes preceded by dart stepped leaders produced  $5.4 \pm 2.2 \times 10^8$  W. From the data they estimated the average radiance over space and time to be  $1.0 \pm 0.9 \times 10^6$  W/m for first return strokes,  $2.5 \pm 1.8 \times 10^5$  W/m for subsequent strokes preceded by dart leaders and  $4.3 \pm 3.1 \times 10^5$  W/m for subsequent strokes preceded by dart stepped leaders. The values of peak optical powers obtained by Guo and Krider are in general agreement with the results obtained by other researchers [108, 109]. From this data Guo and Krider estimated the average peak radiance of subsequent strokes near the ground to be in the range of  $6 \times 10^5$  W/m to  $1 \times 10^6$  W/m. By integrating the optical power they arrived at the figures of  $3.7 \times 10^5$ ,  $7.7 \times 10^4$  and  $8.7 \times 10^4$  J for the mean radiant energies of first return strokes, normal subsequent strokes and subsequent strokes preceded by dart leaders respectively. Note that this energy is produced mainly by the visible channel section, which may be about 1–2 km, located below the cloud.

#### *Estimation of the channel temperature, electron density and pressure from the lightning spectrum*

The measured spectral data of return strokes can be used to determine physical properties of the lightning channel such as the temperature, pressure and particle densities. For example, the ratio between two spectral lines can be related to the channel temperature through theory, provided that the following assumptions are valid: (1) the lightning discharge is optically thin for the two wavelengths under consideration; (2) the temperature is constant across the cross-section of the stroke; (3) the discrete atomic levels responsible for the spectral lines used to determine the temperature must be populated according to Boltzmann statistics and (4) the lightning channel is in local thermodynamic equilibrium, and this is achieved within a time short compared to the time over which the temperature is evaluated (see Chapter 3). If the last assumption is not satisfied, the temperature determined is the electron temperature. Using the theory and the measured relative intensities of NII emissions at 5680 and 5942 Å, Orville [110] determined the temperature of the lightning channel as a function of time. The results are shown in Figure 4.19a. Using the experimentally observed stark broadening of the H-alpha line, Orville estimated the electron density in the channel as a function of time. The results



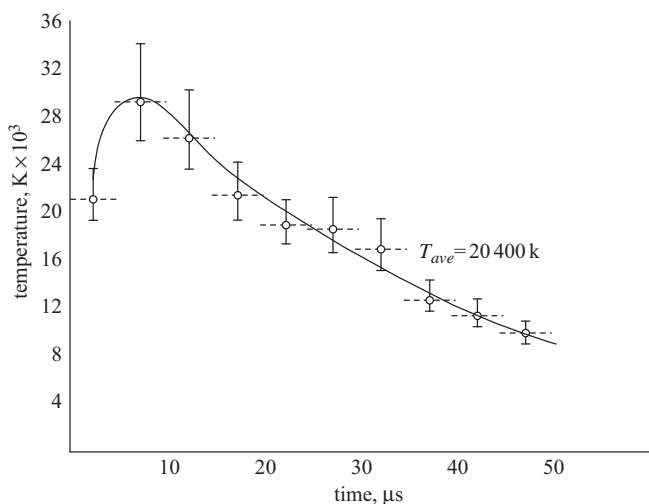


Figure 4.19a Return stroke temperature as a function of time obtained from the analysis of NII spectral emissions. The dashed lines show the time interval over which the data points are averaged (adapted from [110])

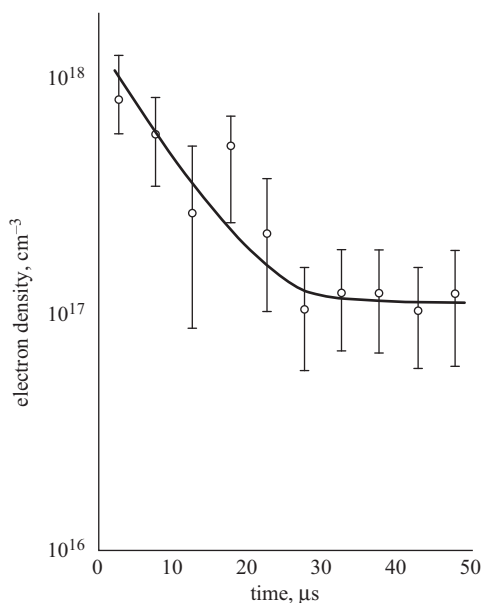


Figure 4.19b Return stroke electron density as a function of time obtained from the analysis of H-alpha line widths. Each data point is averaged over  $5 \mu s$  (adapted from [110])

obtained are shown in Figure 4.19b. Once the temperature and the electron density in the channel have been determined it is possible to use the data to obtain the other physical characteristics of the channel. For example, from the data, Orville [110] estimated that the channel pressure within the first  $5 \mu s$  of the initiation of the return stroke is about 8 atmospheres and that it decreased to atmospheric pressure within about  $30 \mu s$ .

*Lateral propagation of the optical radiation from return strokes*

There is a general consensus that the bulk of the charge in the stepped leader channel resides in the corona sheath, which has a diameter in the range of several metres to several tens of metres (see section 4.6.2.1). The return stroke neutralises this charge and one may expect some luminosity variations in the radial direction to be associated with this process. Recently Takagi *et al.* [111] measured the radial variation in the light intensity of the return stroke as a function of time. They found that, at a height of about 200–300 m from ground, the luminous region of the return stroke channel expands with a speed of  $10^5$  m/s during the initial stage and reaches a maximum diameter of several tens of metres about 100  $\mu$ s after the initiation of the return stroke. The speed given above is similar to that of positive streamers and, therefore, the observations lend support to the idea of Cooray [112] that the neutralisation of the corona sheath takes place by positive streamers that travel out from the central core.

*Thickness of the lightning channel*

The lightning channel diameter can be measured by photographic observations [113–115], by measuring the diameters of fulgarites in sand and fulgamites [116, 117], by measuring the dimension of holes made by lightning flashes in metal [118] or fibre glass plates [119], by analysing the lightning damage [120] and finally by using theoretical analysis [121–125]. The results obtained with these techniques are summarised in Table 4.6. In describing the lightning channel diameter, it is important to note that the temperature of the lightning channel varies in the radial direction. At the very centre there is a high temperature core and even within this core the temperature may decrease radially outwards. Outside this core there could be a streamer region which is at ambient temperature and very weakly luminous. Thus, it is more reasonable to discuss the radius of the lightning channel above a certain temperature. The measuring techniques used in gathering the data in Table 4.6 may provide a reasonable estimation of the high temperature core of the return strokes.

#### 4.6.3.4 The properties of return stroke currents measured at the base of the channel

The return stroke current at the channel base can be measured in two ways. The first is to use the fact that tall structures are struck frequently by lightning flashes.

Table 4.6 Diameter of the lightning return stroke (adapted from Orville *et al.* [115])

Reference	Diameter, cm	Method of determination
Schonland [113]	15–23	Photographic
Schonland [116]	<5	Fulgarites in sand
Evans and Walker [114]	3–12	Photographic
Hill [117]	0.03–0.52	Fulgamites
Uman [119]	0.2–0.5; 2–3.5	Holes in fibreglass Bonnets
Taylor [120]	0.05–0.3, 1–8	Tree trunk damage
Jones [118]	0.1–0.3	Discharge craters in aluminium
Orville [115]	6–7	Photographic
Braginskii [121]	0.3–2	Spark discharge model
Oetzel [122]	0.1–8	Electrical circuit model
Plooster [123]	0.33–1.76	Spark discharge model

Relatively tall structures, such as high towers can be equipped with current measuring equipment that can record the current signatures at the channel base of lightning flashes. Since the frequency of lightning strikes to a given object increases with increasing height, a reasonable amount of information can be obtained over a time span of a few years using this technique [58, 126]. The second method is to use the lightning triggering technique. In this technique a small rocket trailing a thin metal wire attached to ground through a coaxial shunt is launched towards a mature thundercloud. As the rocket travels upwards, the field at its tip increases and, when this field reaches a certain critical value, a connecting leader is initiated that travels towards the cloud. Lightning flashes initiated by this upward-moving leader follow the trailing wire to ground. In this case, the lightning channel intercepts the instrumented launching pad and the current is measured directly to an accuracy better than 10 per cent as it passes through the resistive shunt [127–133]. A summary of the parameters of lightning currents of engineering interest obtained from both tower measurements and triggered lightning techniques is presented in Tables 4.7 and 4.8. These parameters are of interest from an engineering viewpoint because: the knowledge of the peak current distribution in lightning flashes is necessary to estimate the voltages developed across resistive devices during lightning strikes and the number and the strength of lightning strikes that a given structure will intercept over a given time interval. The available data indicate that the peak current distribution can be approximated by a log-normal distribution.

*Table 4.7 Parameters of the currents measured at the tower at San Salvarore, Switzerland [134]*

	Units	<i>N</i>	Percentage of cases exceeding the tabulated value		
			95%	50%	5%
Peak current	kA				
Negative first strokes		101	14	30	80
Negative subsequent strokes		135	4.6	12	30
Positive first strokes		20	4.6	35	250
Impulse charge	C				
Negative first strokes		90	1.1	4.5	20
Negative subsequent strokes		117	0.22	0.95	4.0
Positive strokes		25	2.0	16	150
Maximum current derivative	kA/μs				
Negative first strokes		92	5.5	12	32
Negative subsequent strokes		122	12	40	120
Positive first strokes		21	0.2	2.4	32
Action integral	A <sup>2</sup> s				
Negative first strokes		91	$6.0 \times 10^3$	$5.5 \times 10^4$	$5.5 \times 10^5$
Negative subsequent strokes		88	$5.5 \times 10^2$	$5.5 \times 10^3$	$5.2 \times 10^4$
Positive first strokes		26	$2.5 \times 10^4$	$6.5 \times 10^5$	$1.5 \times 10^7$
Total charge	C				
Negative first strokes			1.1	5.2	24
Negative subsequent strokes			0.2	1.4	11
Negative flashes			1.3	7.5	40
Positive flashes			20	80	350

*N*, number of observations.

Table 4.8 Triggered lightning current parameters (adapted from Rakov [133])

	Units	N	GM	Percentage of cases exceeding the tabulated value		
				95%	50%	5%
Peak current (Fort McClellan, Alabama, USA)	kA	45	12	4.7	13	29
Peak current (Kennedy Space Center)	kA	305	12.1	4.7	12.1	31.3
Peak current (Saint-Privat d'Allier, France)	kA	54	9.8	4.5	9.8	21.5
Peak current derivative (Kennedy Space Center)	kA/ $\mu$ s	134	91.4	28.1	91.4	297.7
Peak current derivative (Saint-Privat d'Allier, France)	kA/ $\mu$ s	47	36.8	14.9	36.8	90.9
Stroke charge (Fort McClellan, Alabama, USA)	C	65	2.5	0.38	2.1	15
Action integral <sup>a</sup> (Fort McClellan, Alabama, USA)	A <sup>2</sup> s	65	3500	400	3800	20 000

<sup>a</sup>The charge and action integrals are underestimates because part of the waveforms are saturated. GM, geometric mean; N, number of observations.

The distribution of the peak current derivative is necessary to evaluate the inductive voltage drop developed across conductors as the lightning current travels along them. The action integral provides a measure of the total energy that will be dissipated when the current passes through resistive materials or protective devices such as varistors. The total charge provides an estimation of the heat generated, and hence any melting, when lightning strikes a metal object. In this case a constant voltage drop is maintained between the plasma and the metal transition and the total heat energy generated is given by the charge times this voltage drop.

#### *Modification to the current parameters introduced by the experimental technique*

It is important to note that the experimental technique used to measure the current can, itself, introduce errors into the measurements. Let us consider the tower measurements first. The theory shows (see Chapter 14) that the distance from which a stepped leader is attracted to a given structure increases with increasing charge of the stepped leader and hence with the peak first return stroke current. It also increases with increasing height of the structure. One can presume, therefore, that tall structures (typically the ones used to measure lightning currents) receive a high proportion of large currents and the current distribution is somewhat biased towards the higher end. However, as of today there is no experimental evidence that the peak current distributions measured are affected by the presence of the tower.

The second problem with the tower measurements is the following. The current waveform injected by the return stroke at the top of the tower travels along the body of the tower and will be reflected at the ground end, due to the impedance mismatch, with the reflection coefficient being determined by the grounding conditions. These reflections may travel along the tower producing errors in the measured currents. Guerrieri *et al.* [135], showed that the error resulting from this could be significant even for a tower of 55 m height, similar to that of Berger's experiment.

The error depends on the reflection coefficient and for higher reflection coefficients it can increase the measured current amplitude by about 30–50 per cent. However, Guerrieri and co-authors point out that the effect might be minor in the case of Berger's measurements [58] since the towers were built on dry terrain with a low conductivity. In addition to these uncertainties, the field enhancements caused by the tower can lead to connecting leaders that are longer than their counterparts in open terrain. The length of the connecting leader may change the current parameters to some extent, but exactly how and to what degree is not known at present.

The main difference between the triggered and natural lightning flashes is the absence in the former of first return strokes initiated by stepped leaders. Furthermore, in the triggering process a leader is launched into a cloud which may not yet be ripe enough to launch a natural lightning flash to ground. This may affect the characteristics of lightning flashes, such as the time interval between strokes and the percentage of continuing current strokes. Moreover, the last few hundred metres of the lightning channel is polluted by the vapour of the metal wire used in the triggering process; this may to some extent influence the measured current parameters such as the peak current derivatives.

Whatever technique is used to measure the current parameters, the fast features of the current waveforms will be distorted if the recording system does not have a sufficiently high resolution to record them faithfully. This could very well be the case in the Berger's measurements, where the measured current derivatives may have been affected by the low time resolution of the measuring equipment, thereby leading to lower measured values than the values actually present. However, it is difficult to believe that the current derivatives of first strokes obtained in that study are significantly distorted by the measuring system because the measured values lie much below the values measured for subsequent strokes using the same measuring equipment. On the basis of the results of theoretical simulations Cooray *et al.* [100, 136, 137] suggest that Berger's first return stroke current derivatives have not been significantly distorted by the frequency response of the current measuring system (see also Chapter 9). This is confirmed by the recent measurements of first return stroke currents conducted by Visacro *et al.* [138] and Takami and Okabe [139].

#### *Experimentally observed correlation between different current parameters*

Various relationships and correlations observed between different current parameters are of interest both in return stroke modelling and in improving the understanding of the physical mechanism behind lightning return strokes. The available experimental data indicate that there is a weak correlation between the peak current,  $I_p$ , and the peak current derivatives,  $(dI/dt)_p$ , of return strokes. This relationship can be described by the equation

$$(dI/dt)_p = a(I_p)^b \quad (4.22)$$

where  $a = 3.9$  and  $b = 0.55$  for first strokes and  $a = 3.8$  and  $b = 0.93$  for subsequent strokes [140]. In this relationship the peak current is in kA and the peak current derivative in kA/ $\mu$ s. A similar relationship is also observed in triggered lightning currents (pertinent to subsequent return strokes) with constants  $a = 2.6$  and  $b = 1.34$  for Florida, USA, and  $a = 2.0$  and  $b = 1.28$  for Saint-Privat d'Allier, France [141].

The tower measurements of Garbagnati and Pipero [126] show that the peak current is correlated to the action integral,  $A_c$ , calculated over the first 500  $\mu\text{s}$  through the equation

$$A_c = a(I_p)^b \quad (4.23)$$

where  $a = 12.0$  and  $b = 2.4$  for first strokes and  $a = 26.9$  and  $b = 2.13$  for subsequent strokes. In triggered subsequent strokes  $a = 50.0$  and  $b = 1.89$  [141]. In the above relationship peak current is in kA and the action integral is in  $\text{A}^2\cdot\text{s}$ .

Both Berger [58, 142] and Garbagnati and Pipero [126] found a strong correlation between the peak current and the impulse charge (the charge associated with the return stroke excluding the contribution from continuing currents),  $Q_{im}$ , dissipated in the first return stroke. Both relationships can be written as

$$Q_{im} = a(I_p)^b \quad (4.24)$$

where Garbagnati and Pipero found  $a = 3.16 \times 10^{-2}$  and  $b = 1.3$  for the charge dissipated over the first 500  $\mu\text{s}$  and Berger found,  $a = 3.43 \times 10^{-2}$  and  $b = 1.43$  for the charge dissipated over the first 2 ms. In these relationships peak current is in kA and the charge in coulombs. In the case of subsequent strokes in triggered lightning  $a = 0.09$  and  $b = 0.89$  [141]. At first glance it is difficult to understand the existence of such a correlation. For example, the peak current is determined by the charge on the first few hundred metres of the leader channel, whereas the impulse charge is the charge located on a channel section of about 3–7 km. But, if there is a strong correlation between the linear charge density of the lower sections of the channel and the peak return stroke current (which could very well be the case), one would obtain a correlation between the peak current and the total charge if the way in which the charge density varies along the channel is more or less similar in first return strokes with different current amplitudes. As described in section 4.6.2.4, Cooray *et al.* [72] observed a strong linear correlation between the charge brought to ground by the first return stroke over the first 100  $\mu\text{s}$  and the peak return stroke current. This relationship is given in (4.9). They have also observed a strong correlation between the charge brought to ground by subsequent return strokes and the corresponding return stroke current (see (4.26)). Sheoene *et al.* [143] have shown that for triggered subsequent strokes the relationship between the charge brought to ground over the first 1 ms and the return stroke peak current can be represented by the regression equation

$$I_p = 12.3Q^{0.54} \quad (4.25)$$

In the above equation  $I_p$  is in kA and  $Q$  is in coulombs.

#### 4.6.3.5 Electromagnetic fields generated by return strokes

##### *General features*

The overall features of the electric and magnetic fields of first and subsequent strokes at different distances are shown in Figure 4.20 [144]. The qualitative features of these waveforms are similar to those generated by a dipole excited by a non-uniform current waveform (see Chapter 9). The far fields, around 100 km, being radiation, are bipolar and electric and magnetic fields have identical signatures. As the distance to the return stroke decreases, the electrostatic and induction fields become dominant. The near magnetic field is mainly induction (magnetostatic) and

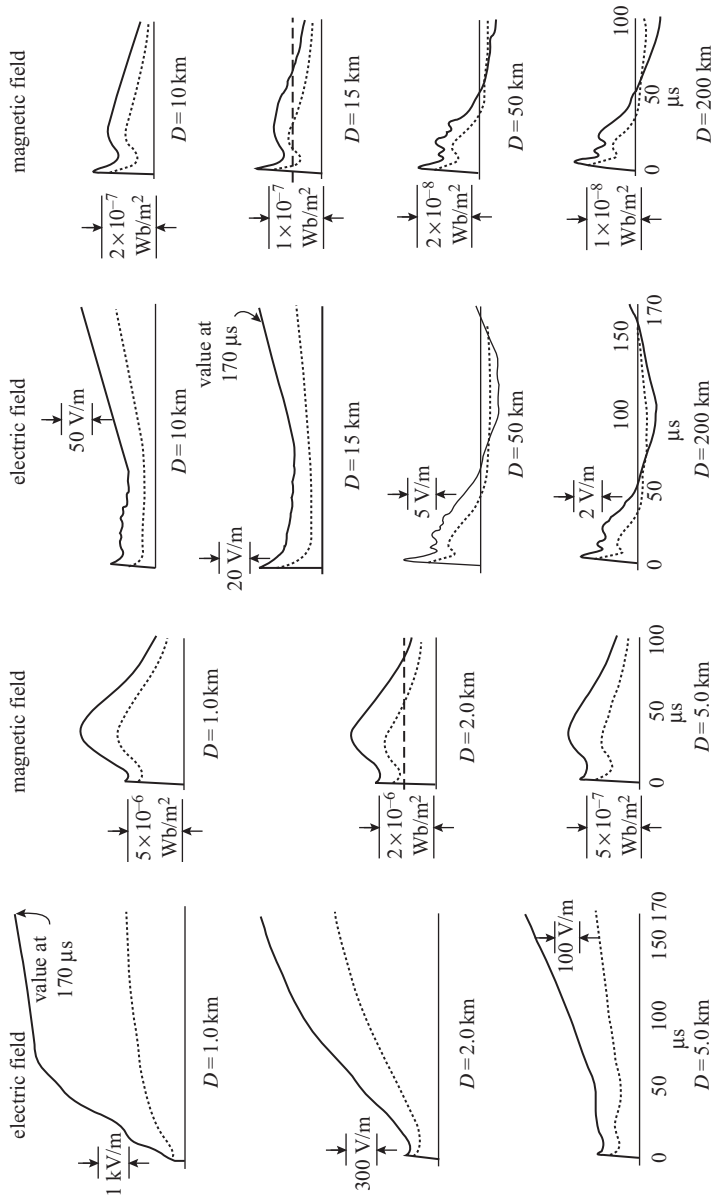
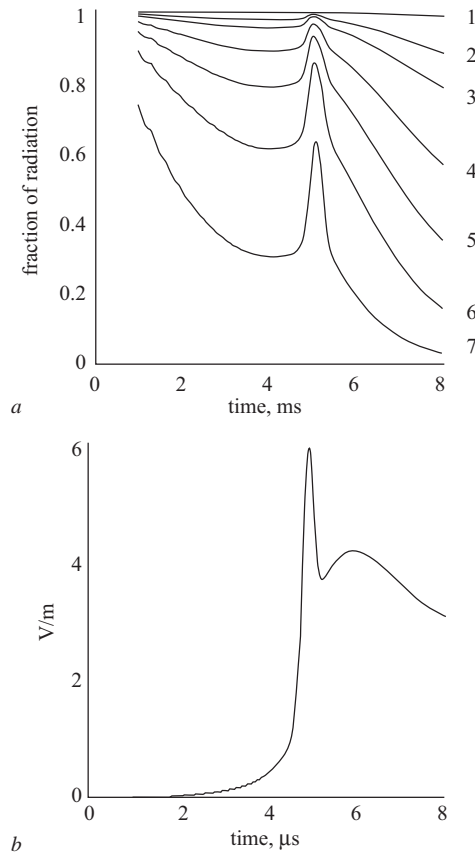


Figure 4.20 Typical electric field intensity and magnetic flux density for first (solid line) and subsequent (dotted line) return strokes at different distances. A positive field corresponds to an upward deflection (adapted from [144])

shows a pronounced hump. It is important to observe that whether the electric field at a given point on the waveform is radiation or not depends on the distance to the return stroke, the location of the point of interest on the waveform and on the shape of the waveform. Figure 4.21a, based on the first return stroke model described in section 9.6.5 of Chapter 9, shows the relative contributions of the radiation field to the total field as a function of distance. As a reference the model-predicted radiation field at 100 km is given in Figure 4.21b. Note that at a given distance the contribution of the radiation field increases as the point of interest comes closer to the beginning of the waveform. Observe also how the radiation field is enhanced at the fast transition that occurs at  $5 \mu\text{s}$  (see also the section ‘Characteristics of radiation fields’). The reason for this is the enhancement of the high frequencies by the fast transition in the waveform.

Experimental data on electromagnetic fields very close to the channel (within about 100 m) are not available for natural lightning, but some data obtained from



*Figure 4.21 (a) The time variation of the electric radiation field as a fraction of the total field at different distances from the return stroke. (1) 100 km, (2) 10 km, (3) 5 km, (4) 2 km, (5) 1 km, (6) 500 m and (7) 200 m. The results are obtained from the negative first return stroke model described in section 9.6.5 of Chapter 9. (b) The model predicted electric field at 100 km. A positive field corresponds to an upward deflection*



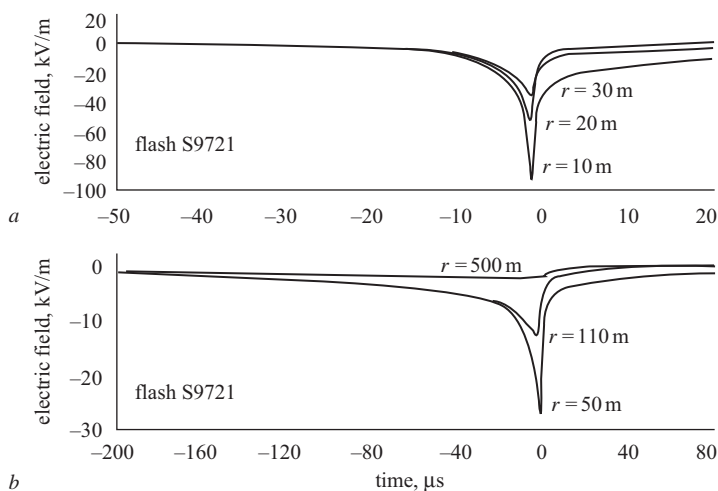


*Figure 4.22 Electric field waveforms of the dart leader/return stroke sequence as recorded at different distances, at Camp Blanding Florida. The electric field to the left of the minimum is produced by the dart leader and the rapid recovery of the field from the minimum is produced by the return stroke. A positive field corresponds to an upward deflection (adapted from [133])*

triggered subsequent strokes do exist. An example from such a measurement carried out in the vicinity of the return stroke channel is shown in Figure 4.22. The field is ‘U’ shaped with the left arm of the U being produced by the down-coming dart leader. The return stroke neutralises the charge on the dart leader which will cause a field change opposite to that of the dart leader. Note that the return stroke field saturates within a few microseconds. Measurements show that the signature of the magnetic field at these distances approaches that of the current waveform at the channel base. There does not appear to be any experimental data in the literature showing how the electric fields from positive return strokes vary with distance. Model simulations of the positive return stroke fields at different distances, based on the models introduced by Cooray [145] and Cooray *et al.* [100], are given in Chapter 9.

#### *Characteristics of radiation fields*

The fine structure of the radiation fields generated by return strokes has been analysed by many researchers [68, 69, 144, 146–151]. The main features of the radiation fields generated by return strokes are shown in Figure 4.23. Several examples of the first 10  $\mu\text{s}$  or so of the radiation fields from positive return strokes measured in such a way to minimise propagation effects (see Chapter 11) are shown in Figure 4.24.

*Slow front and the fast transition:* The initial rising part of the radiation field contains a slow front followed by a fast transition. The duration of the slow front is about 5  $\mu\text{s}$  in negative first return strokes, about 10  $\mu\text{s}$  in positive first return strokes and about 0.5  $\mu\text{s}$  in the subsequent return strokes. The slow front is followed by a fast transition. The amplitude of the breakpoint is about 50 per cent of the total peak in first return strokes (both positive and negative) and is about 20 per cent in the subsequent strokes. The 10–90 per cent rise time of the fast transition is similar in

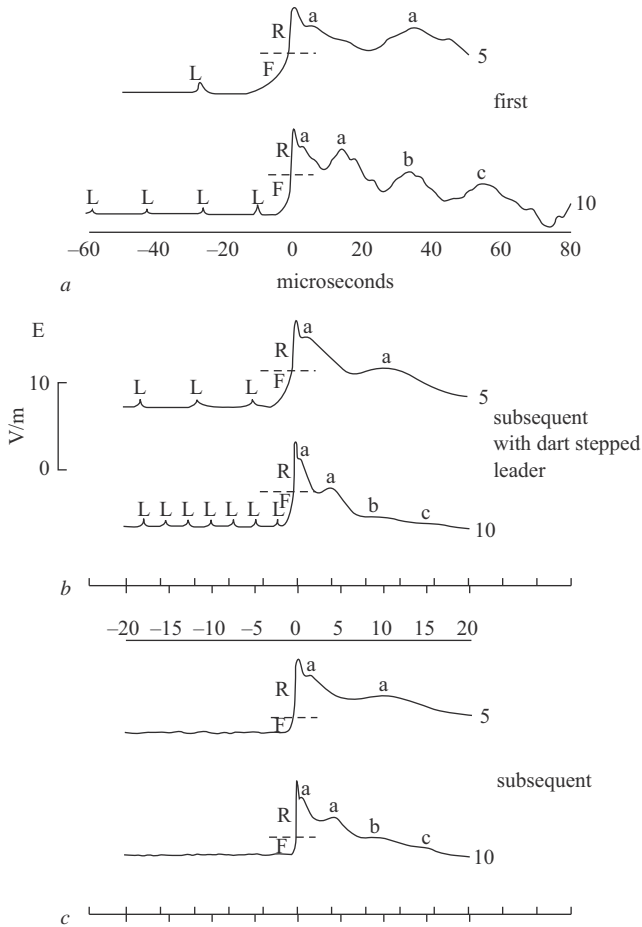


Figure 4.23 Sketches of the shapes of the electric radiation fields produced by (a) the first return stroke, (b) a subsequent return stroke preceded by a dart stepped leader, and (c) a subsequent stroke preceded by a dart leader. The small pulses characteristic of leader steps L are followed by a slow front F and an abrupt transition to peak R. The peak amplitudes are normalised to a distance of 100 km. A positive field corresponds to an upward deflection (adapted from [146])

negative first and subsequent strokes and the average value is about  $0.1 \mu\text{s}$ . In positives the corresponding rise time is about  $0.25 \mu\text{s}$ .

Weidman and Krider [146] investigated the possibility that the slow front of return stroke radiation fields is generated by the connecting leader that rises up to meet the down-coming leader just before the connection between the leader and the ground is established. Their calculations show that, in order to produce field magnitudes comparable to those in slow fronts, the connecting leader has to carry a current of the order of 10 kA. However, as pointed out by Weidman and Krider, connecting leaders are quite faint and difficult to photograph, which is not consistent with currents of the order of 10 kA. Cooray *et al.* [100] (see Chapter 9) suggested a scenario that will overcome this problem. According to this, the slow front is generated by the almost exponential increase in the current in the connecting leader as it

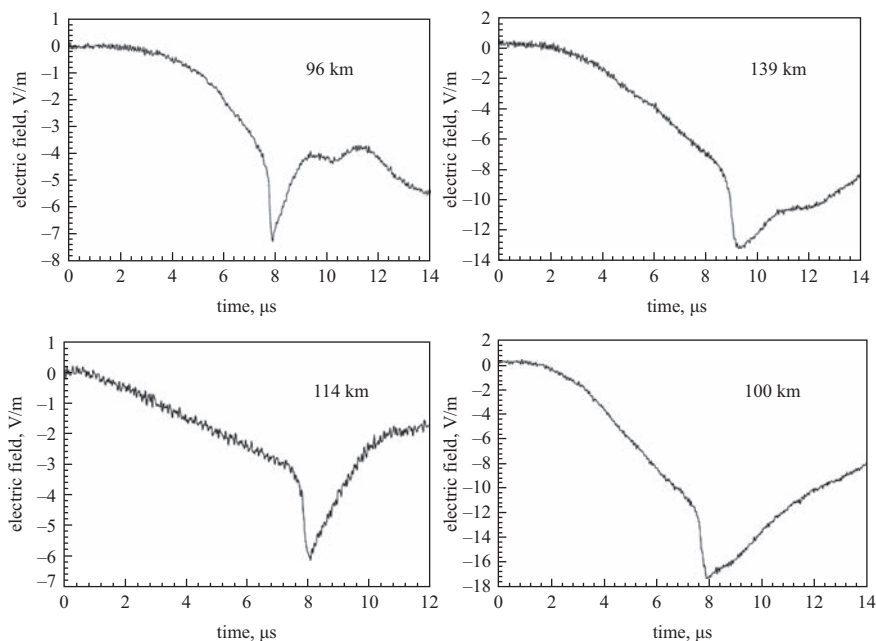


Figure 4.24 Several examples of the first 10–14 μs of positive return stroke radiation field measured in such a way to minimise propagation effects (adapted from [149])

moves through the streamer region of the stepped leader, that is after the interception of the connecting leader with the stepped leader. This stage can also be interpreted as the initial stage of the return stroke. The fast transition of the field is caused by the rapid increase in the current that results when the connecting leader meets the hot core of the leader channel. Cooray *et al.* [100] suggested that the longer duration of the slow front in positive first return strokes is caused by the longer streamer portion associated with the positive downward leaders.

It is not clear, however, whether a streamer region can produce the conductivity gradient necessary for the creation of slow fronts in subsequent return stroke fields. The dart leader travels along a channel whose temperature may be higher than 1500–3000 K. It is not known at present whether streamer discharges in the conventional sense exist at these temperatures. However, optical observations show that the rise time (zero to peak) of the optical radiation associated with the dart leader is about 2–3 μs [102, 152, 153]. This indicates that the build-up of the ionisation process takes a finite time in the case of the dart leader. It is reasonable to assume, therefore, that there is a conductivity gradient along the dart leader channel with the region of lowest conductivity located at the forward end of the leader. As shown by Cooray [154], such a conductivity gradient could give rise to the slow front in the subsequent return stroke fields.

*Subsidiary peaks:* After the initial peak, both negative first and subsequent strokes exhibit a shoulder within about 1 μs from the initial peak. The decaying part of the first return stroke radiation field contains several subsidiary peaks whose separations are in the range of tens of microseconds. The subsequent strokes do not usually show these subsidiary peaks except in the cases in which the preceding

stroke is the first stroke. Weidman and Krider [146] suggest that these subsidiary peaks are caused by the rapid changes in the current and the speed when the return stroke front encounters branches of the stepped leader channel. Calculation of Cooray and Fernando [155] also demonstrates that the channel branches can be the source of subsidiary peaks in the radiation fields.

*Zero crossing time:* The negative first return stroke waveform crosses the zero line in about 50–100  $\mu\text{s}$ , whereas the corresponding values for the subsequent return strokes are 30–50  $\mu\text{s}$ . In positive first strokes without slow tails (see the next section) the zero crossing time is distributed over the range of 50–130  $\mu\text{s}$ .

The zero crossing time of the radiation fields depends mainly on two parameters [156]. First, it depends on the rapidity at which the current generated by the neutralisation process decreases along the channel. If the current decays rapidly with height the zero crossing time will be shorter, and vice versa. The way in which the current decreases along the channel is governed to some extent by the charge distribution along the leader channel that initiated the discharge. Second, the zero crossing time depends on the vertical length of the channel. The vertical length of the channel is approximately equal to the height of the negative charge centre in the cloud. Inside the charge centre the channel may extend horizontally. A longer vertical channel can produce a longer zero crossing time and the opposite is true for shorter channels. Furthermore, even if the current does not decay along the channel, a shorter channel cannot sustain a longer radiation field because the field will decay rapidly when the return stroke front reaches the end of the vertical channel section. Thus, the zero crossing time is to some extent controlled by the speed of the return stroke front. Some evidence for this conjecture is the observation that the zero crossing time of the radiation fields is significantly higher in the tropics than in temperate regions [66]. The height of the negative charge centre and hence the length of the vertical section of the return stroke channel are higher on average in the tropics than in temperate regions.

*The tail of the waveforms – difference between the negative and positive return strokes:* After a comparative study of electromagnetic fields generated by positive and negative return strokes, Cooray [148] discovered that in many cases the tail of the electromagnetic radiation fields of positive return strokes, that is the section of the field beyond about 30  $\mu\text{s}$ , varies in a manner different to that of negative return strokes. After the zero crossing the negative fields continue to decrease, form a peak of opposite polarity and come back to the zero level at about 100–150  $\mu\text{s}$  of the beginning of the waveform. The positive waveforms exhibit the following behaviour: After an initial peak, they also continue to decay and reach or momentarily cross the zero line at about 30–80  $\mu\text{s}$ . However, at later times, instead of continuing to decrease – as does their negative counterpart – the field starts to increase again and reaches a second peak between 100 and 400  $\mu\text{s}$  (see Figure 4.25). Analysis of the electric radiation fields from distant (400 km or more) positive return strokes shows that the field continues to decrease after this second peak, crossing the zero line at about 1 ms [148, 157]. Several such examples measured 450 km from the return stroke channel are shown in Figure 4.26. Numerous examples show that this slowly varying phase of the positive return stroke field is associated with a burst of leader-like pulse activity.

Cooray [145, 148] suggested the following physical process as an explanation for the difference in the tail of the positive and negative return stroke radiation fields. The initial peak and the subsequent decay of the electric radiation field of both negative and positive return stroke fields within the first few tens of

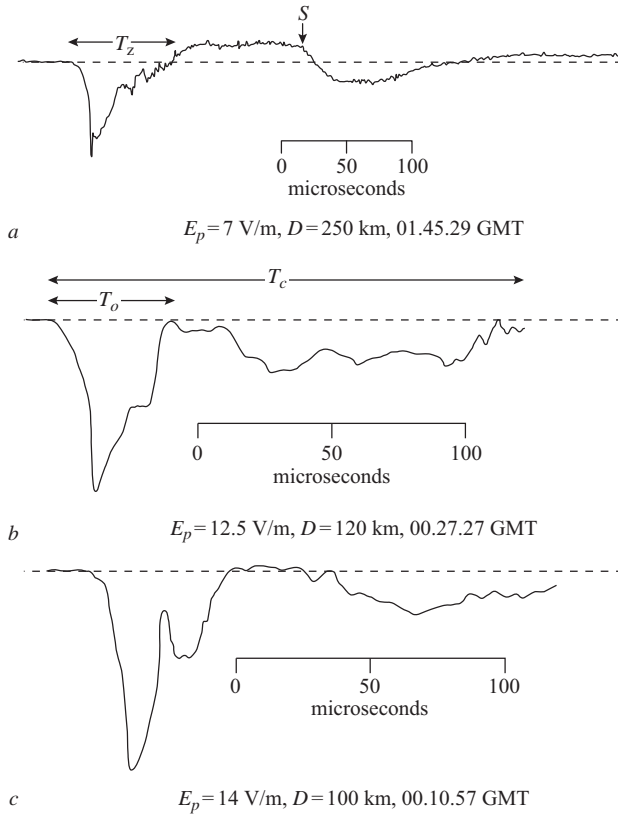


*Figure 4.25 Electric radiation fields of positive return strokes observed in Sweden. The initial peak value ( $E_p$ ) and the range ( $D$ ) is given below each diagram. A positive field corresponds to an upward deflection (adapted from [148])*

microseconds are features associated with the neutralisation of the leader channel as the return stroke surges upwards through it. Since there is no qualitative difference in the distribution of the leader charge and the way in which this charge is neutralised in negative and positive return strokes, there is not much difference in the electric radiation fields generated by them during this time. But what happens when the return stroke front reaches the cloud differs between negative and positive return strokes. When the front of the negative return stroke reaches the cloud end of the leader, the current flowing into the vertical channel of the negative return stroke is quenched and, as a result, the radiation field makes an excursion to the other side of the zero-field line, returning to the line at a rate which is determined by the rapidity at which the current is quenched in the channel. On the other hand, when the positive return stroke front reaches the cloud end of the leader channel, it encounters a large source of positive charge, probably located on an extensive dendritic pattern of mainly horizontal branches in the cloud. Some of the recent observations do indeed show extensive horizontal branching in the cloud portion of the positive return strokes [158]. This source of charge enhances the current flowing into the vertical channel, thereby producing a second surge in the electromagnetic radiation. The high-frequency activity superimposed on the tail of the

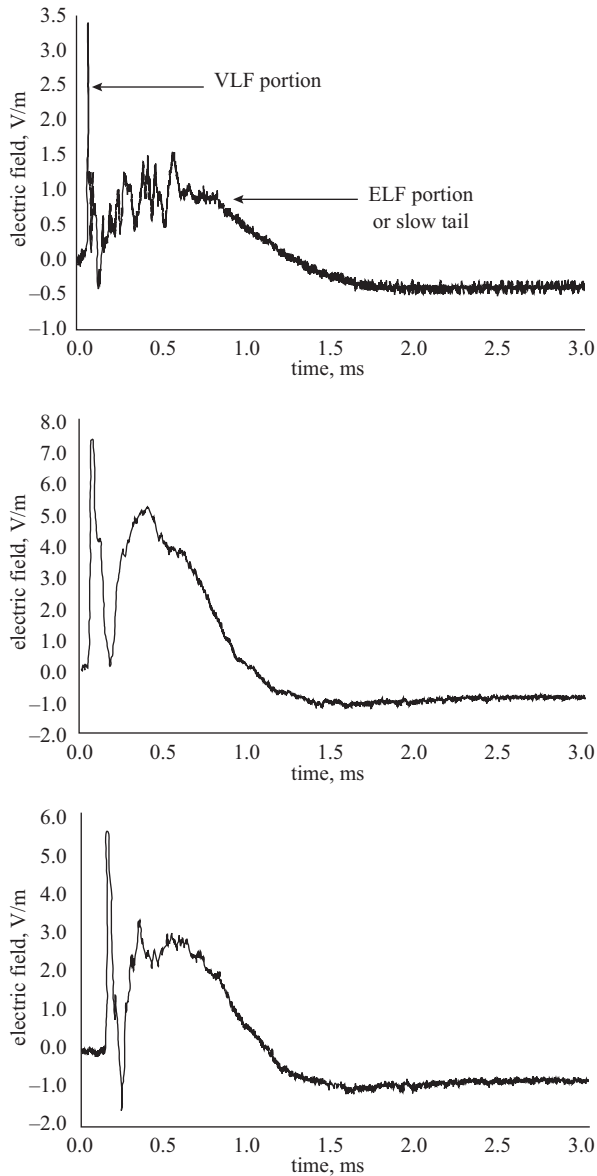


Figure 4.26 Examples of electric radiation fields from positive return strokes measured at 450 km from the flash origin. A positive field corresponds to a downward deflection (adapted from [157])

fields, as observed by Cooray [148], is probably connected with the processes that make this charge available to the return stroke. In fact, the experimental data available on negative and positive return stroke currents strengthen the above hypothesis. In the first 50–100  $\mu\text{s}$ , the temporal variation of the positive return stroke current is qualitatively similar to that of the negative one. After this time, however, while the negative current continues to decay, the positive current starts to increase again, reaches a second peak and then decays to zero level within about a millisecond.

*Distribution of the peak radiation fields of return strokes:* Several studies in which an estimation of the initial peak of the radiation field is made are available in the literature [144, 147, 149, 159–161]. The peak of the radiation field of negative first return strokes normalised to 100 km lies in the range of 3–30 V/m, with a mean value lying somewhere between 5 and 10 V/m. The mean of the initial peak of positive return strokes is about a factor of 2 larger than that of negative first return strokes. The initial peak of the subsequent return strokes normalised to 100 km lies in the range of 2–15 V/m with a mean value around 3–4 V/m. Many of the observations of peak electric fields are made over land and, therefore, depending on the conductivity, these peak values could to some extent be distorted by propagation effects (see Chapter 11).

Experimental data gathered from lightning direction finders show that the peak radiation fields of first return strokes striking the sea are larger by about 25 per cent than the radiation fields of first return strokes striking land. One might explain this difference as due to propagation effects but the fact that such differences do not exist in subsequent return stroke fields make it possible to rule out the propagation effect. A possible explanation for this difference is provided in [162].

Some of the most recent data on the initial peak amplitudes are summarised in Table 4.9. Since the peak of the radiation field occurs within a few microseconds of the beginning of the electric field and since the first microseconds of the electric field are approximately radiation down to about 1 km, it is possible to extrapolate these values to calculate the peak fields at any other distance by using the fact that the radiation field decreases inversely with distance (see the section ‘General features’ under ‘Electromagnetic fields generated by return strokes’).

*Time derivative of the radiation field:* The radiation field time derivative is a parameter which is difficult to measure accurately in land based measurements owing to the strong impact propagation has on it (see Chapter 11). In order to obtain accurate results, the fields have to be measured very close to the lightning channel, or the propagation path should be over the sea so that the propagation effects are negligible. The data available today on the characteristics of the time derivatives of the radiation field are obtained from measurements conducted with the latter

Table 4.9 *Peak radiation fields in V/m, normalised to 100 km assuming inverse distance dependence, generated by return strokes*

Author	First strokes			Subsequent strokes		
	Number of observations	Mean	SD	Number of observations	Mean	SD
Master <i>et al.</i> [159]	112	6.2	3.4	237	3.8	2.2
Guo and Krider [106]	69	11.2	5.6	84	4.6	2.6
Lin <i>et al.</i> [144] (KSC)	51	6.7	3.8	83	5.0	2.2
Lin <i>et al.</i> [144] (Ocala)	29	5.8	2.5	59	4.3	1.5
Willett <i>et al.</i> [160]	125	8.6	4.4			
Rakov and Uman [161]	76	5.9 (GM)		270	2.9 (GM)	
Cooray and Lundquist [147]						
(positive)	58	11.5	4.5			
(negative)	553	5.3	2.7			
Cooray <i>et al.</i> [149] <sup>a</sup>	46	15.7	6.7			

<sup>a</sup>Lightning flashes striking the sea.

GM, geometric mean; SD, standard deviation.

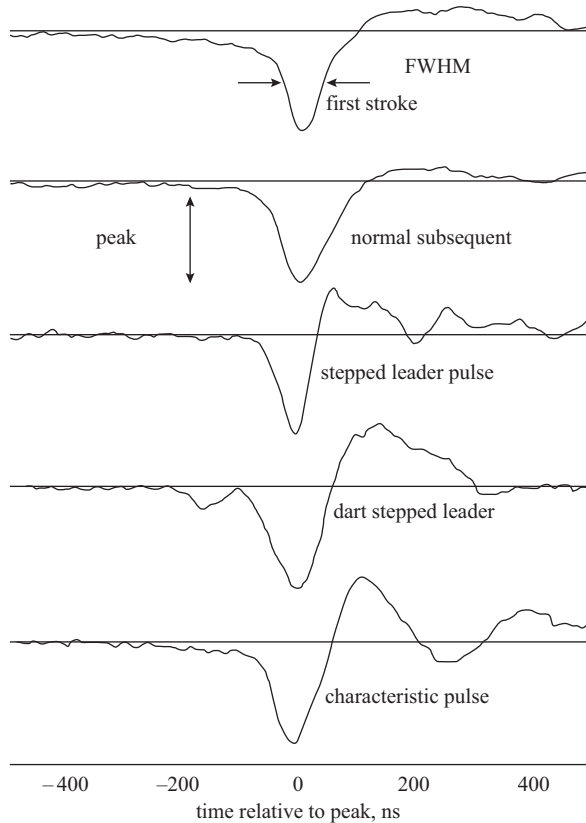


Figure 4.27 Examples of observed  $dE/dt$  signatures from first and subsequent return strokes, stepped and dart stepped leader steps, and pulses from cloud flashes (marked characteristic pulses). The FWHM is marked on the first return stroke field. The vertical scale is arbitrary. A positive field corresponds to a downward deflection (adapted from [151])

approach [149, 68, 160, 69]. The typical shape of the time derivatives of the radiation fields of several processes is shown in Figure 4.27 with parameters of interest marked on it. Note that the signature of the time derivative is similar in all the cases. Tables 4.10 and 4.11 provide a summary of the various parameters of the time derivative of the electric field as observed by different researchers.

#### *Radio frequency radiation generated by first return strokes*

Radio frequency emission from return strokes have been analysed by several researchers [163–168]. Brook and Kitagawa [164] observed that the onset of the RF radiation during the first return stroke stage is delayed by 60–100  $\mu\text{s}$  from the beginning of the return stroke. Since the observed delay in the RF radiation from the onset of the return stroke is larger than the time necessary for the return stroke front to reach the cloud, Brook and Kitagawa concluded that the return stroke is not a strong source of RF radiation. LeVine and Krider [165] also observed a delay in the onset of RF radiation, but the delay they measured was about 10–30  $\mu\text{s}$ . However, since this delay is not large enough to let the return stroke reach the cloud end



Table 4.10 *Full width at half maximum (FWHM) of the radiation field derivative of lightning return strokes*

Reference	Number of observations ( <i>N</i> )	Mean (ns)	SD (ns)	Comments
Willett and Krider [151]	133	77	20	First strokes
Willett and Krider [151]	85	79	20	Subsequent strokes
Krider <i>et al.</i> [68]	61	75	15	First strokes
Weidman and Krider [67]	18	73		First and subsequent
Cooray <i>et al.</i> [149]	39	170	90	Positive

Table 4.11 *Peak values of electric field derivative*

Reference	Number of observations ( <i>N</i> )	Mean (V/m/ $\mu$ s)	SD (V/m/ $\mu$ s)	Comments
Willett <i>et al.</i> [160]	131	37 (42) <sup>a</sup>	12	First
Krider <i>et al.</i> [68]	63	39 (46) <sup>a</sup>	11(13) <sup>a</sup>	First
Weidman and Krider [69]	97	29	12	First and subsequent
Cooray <i>et al.</i> [149]	40	25	11.6	Positive

<sup>a</sup>After correction for propagation effects.

of the leader before the commencement of the RF, this observation indicates that the first return stroke itself is a source of RF radiation. This inference is also supported by the observations of Shao *et al.* [6] who found that the strength of the RF radiation increases several fold upon the initiation of the first return stroke. They could also detect RF radiation sources travelling upwards during the first return stroke phase. Cooray [168] and LeVine *et al.* [169] suggest that the delay in the onset of RF radiation following the first return strokes is probably caused by propagation effects. Furthermore, Cooray [168] could not detect any delay in 3 MHz radiation when the electromagnetic fields are propagating over the sea.

Cooray and Perez [166] and Jayaratne and Cooray [170] measured the HF radiation associated with first return strokes. According to their observations, the duration of the burst of RF radiation at 3 MHz associated with the first return stroke is about 130 and 170  $\mu$ s in Sweden and Sri Lanka respectively.

Shao *et al.* [6] have found that the dart leader is a strong source of RF radiation and the radiation intensity decreases at the onset of the subsequent return stroke and remains at a low level until the return stroke front reaches the cloud end of the leader. Bursts of RF pulses may appear after the return stroke front has travelled into the cloud. This also agrees with the findings of Brook and Kitagawa [164] and LeVine and Krider [165] who also observed that the subsequent return strokes are not strong sources of RF. The latter study found that the HF starts about 265  $\mu$ s prior to the onset of the subsequent return strokes and ceases before the onset of the return strokes. However, the 3 MHz radiation frequently persists up to and during the return stroke. Examples of the broadband electric fields are shown in Figure 4.28 together with the HF radiation at several frequencies [171]. Note the increased intensity, for example in the 10 MHz, during the leader stage of first

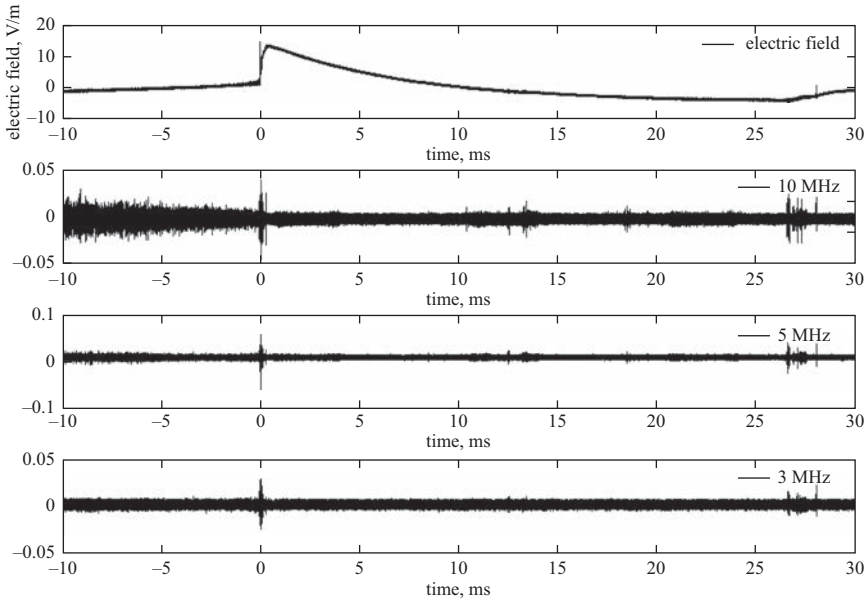


Figure 4.28 The broadband electric field together with the HF radiation at 10, 5 and 3 MHz (adapted from [171])

return stroke (occurred at 0 time mark) and the subsequent return stroke (occurred around 28 ms time mark).

The data available concerning the RF generation by positive return strokes are scanty. Kawasaki and Mazur [167] observed UHF (at 327 MHz) radiation during the return stroke stage, but the resolution given in the data plots is not high enough to conclude whether the radiation starts immediately at the onset of the return strokes (i.e. within microseconds) or if it is delayed (and starts within tens of microseconds). Their data show that the UHF radiation peaks at a time close to the initiation of the return stroke and tail off within about 10 or 20 ms. The observations of Cooray and Perez [166] show that there is an enhancement of the HF at 3 MHz immediately after the onset of the positive return stroke and the radiation continues for at least several milliseconds.

The mechanism whereby lightning produces HF, VHF and UHF radiation is not completely understood [172, 173]. Cooray and Cooray [174] estimated the electric radiation fields generated by electron avalanches. Based on the results they suggested that the UHF radiation in the region of 1 GHz is probably generated by the electron avalanches active both in the leader and the return stroke stage of lightning flashes. LeVine and Krider [165] suggested that branched breakdown processes could be an important source of HF, and LeVine and Meneghini [175] showed that the effects of channel tortuosity could produce HF radiation during return strokes. However, the channel tortuosity may not be solely responsible for the HF radiation for the following reason: The available photographic observations show that many of the subsequent strokes in a lightning flash also travel along the path traversed by the first return stroke. If channel tortuosity is mainly responsible for the HF radiation, one can expect comparable HF radiation from both the first and subsequent return strokes. However, the data available at present show that subsequent strokes generate much less HF radiation than do first return strokes [165]. This shows that

channel tortuosity is not the main source of HF radiation associated with return strokes. The negative return strokes are capable of generating HF radiation almost immediately with the onset of the return strokes. Usually the lower portion of the leader channel is free of branches and therefore it is doubtful that the branches alone are responsible for the HF emission just after the return stroke.

The observations of Shao *et al.* [6] indicate that the VHF radiation from the stepped leader is mainly generated by the downward propagating tip of the leader. The source of the VHF radiation could be the streamer system of the stepped leader. Streamers could also be responsible for the generation of RF radiation during the first return stroke stage. The charge on the leader channel resides mainly on the corona sheath, whose radius is of the order of several metres to several tens of metres. On the other hand, the radius of the highly conducting return stroke channel is of the order of a few centimetres. During the return stroke stage the funnelling of the corona charge into the highly conducting return stroke channel may be accompanied by the ionisation of virgin air or the reionisation of old channels that have decayed to a non-conducting stage. As mentioned previously, Takagi *et al.* [111] have observed luminous discharge phenomena propagating radially from the central channel during the return stroke stage. The speed of propagation of the discharges is similar to that of streamer discharges observed in long laboratory sparks. This neutralisation process could be a source of RF radiation.

As mentioned in section 4.6.2.1 the corona sheath is created partly by the charge deposited in space by the corona streamers travelling ahead of the stepped leader channel. This charge may not be distributed uniformly along the leader channel because the streamers are created mainly in bursts from the tip of the newly created leader steps. This non-uniform charge distribution in the corona sheath may give rise to an amplitude modulation of the return stroke current leading to the generation of RF radiation. Indeed, Cooray and Fernando [155] analysed this problem in detail and showed that the irregularities in the charge distribution of the stepped leader can generate HF radiation during the return stroke stage. This fact may also explain why subsequent return strokes do not radiate strongly in the RF region. The dart leader propagates continuously down the defunct return stroke channel and, therefore, one may presume the charge distribution on the corona sheath is more or less uniform leading to a diminishing of the RF radiation during the neutralisation. Moreover, it is also possible that the corona sheath produced by the dart leader remains conducting until the charge on it is neutralised by the return stroke.

#### *Frequency spectrum of lightning-generated electromagnetic fields*

Frequency spectra of the electromagnetic fields generated by lightning flashes have been made either by monitoring the power received at individual frequencies using narrow-band recording systems [176] or by recording the transient with a broad-band device and performing the Fourier transformation [177]. The problem with narrow-band systems is the difficulty of identifying the radiation produced by different components of the lightning flash. The problem is the conflict between two desirable attributes. The first of these is to have a narrow bandwidth so the measurements are truly representative of a particular frequency and the second one is to have a large bandwidth so that the individual events can be distinguished. However, as pointed out by LeVine [178], both techniques have yielded similar spectra; these spectra agree reasonably well below 1 MHz, but even at high frequencies there is an overlap of data points.

The return stroke spectrum in the VLF region was studied, among others, by Taylor [179] and Serhan *et al.* [180]. The spectrum that extends from the VLF to the HF region was analysed by Weidman and Krider [181], Weidman *et al.* [182] and Willett *et al.* [177]. The spectrum of first and subsequent return strokes, which actually is a combination of the results from several of these studies, is shown in Figure 4.29. Note that the shape of the subsequent return stroke spectrum is identical to that of the first return strokes, with the exception that its amplitude is somewhat lower in the low-frequency region. The fact that the high-frequency ends of the two spectra are identical indicates that the sub-microsecond structures of the first and subsequent return strokes are identical. It is important to note here that the spectrum of the return stroke at the high-frequency end is remarkably similar to those obtained for stepped leaders and cloud pulses. LeVine [178] suggests that this could be because there is some physical process which is common to all these events.

In the spectrum shown in Figure 4.29, the spectral amplitudes decrease like  $1/f^2$  over the range from 1 to about 10 MHz. Beyond that frequency the spectral amplitudes decay much faster. Ye and Cooray [183] show that this rapid decrease in spectral amplitudes is probably caused by impact of propagation on the radiation fields as they travel over a rough ocean surface. They point out that the return stroke spectrum measured at high altitudes, where the propagation effects are not involved, shows  $1/f^2$  dependency in the region of 10 MHz and above. The spectrum obtained by applying narrow-band techniques does not show this rapid decrease at high frequencies. Recall, however, that the narrow-band spectrum is generated by the composite event including the activities inside the cloud. If the lightning flashes are located within about 20 km of the point of observation, the cloud portion of the ground flash can produce signals that do not attenuate significantly by propagation effects [184].

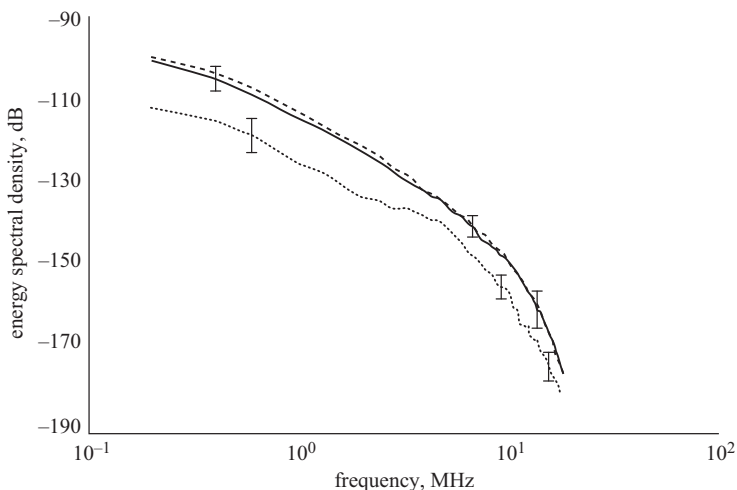
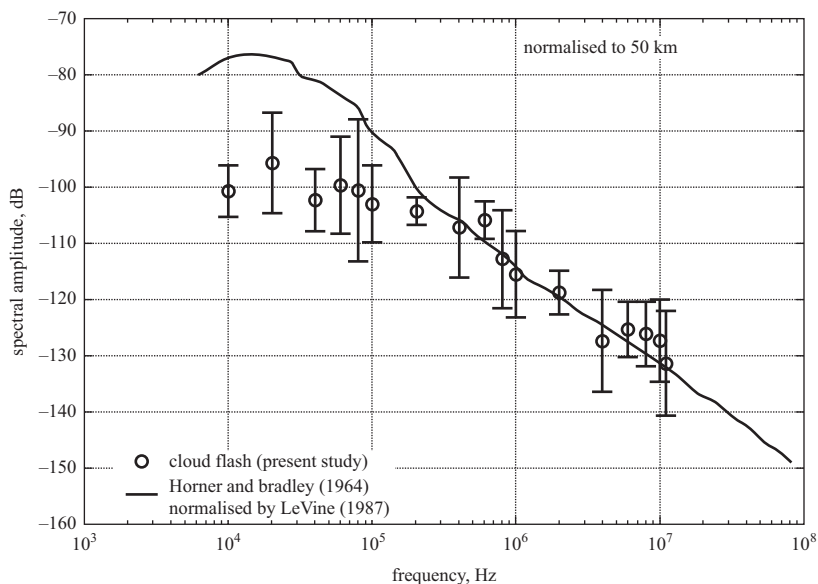


Figure 4.29 Average spectra of 74 first return strokes (solid line) and 55 subsequent strokes (dashed line). The dotted line shows the average spectrum of 18 pulses generated by cloud flashes (adapted from [177])



*Figure 4.30* The average spectral amplitude of cloud flashes (open circles) obtained by Fourier transforming the radiation fields of the first 100 ms of the cloud flashes. The vertical bars show the standard deviation. The solid line shows the spectrum of lightning flashes obtained by Horner and Bradley [176] using narrow-band receivers

In order to calculate the spectrum from measured electromagnetic fields it is necessary to Fourier transform the measured electric or the magnetic field. Since the computation time and the required memory to perform the operation over a very long waveforms are very large it is usually the return stroke fields or the single pulses from cloud flashes that were Fourier transformed to obtain the spectrum. On the other hand in the narrow-band studies depending on the bandwidth of the system larger portion of the activity associated with a lightning flash contributes to the spectrum. Fortunately, the latest developments in recording systems and computer facilities made it possible to analyse and Fourier transform longer and longer signals. In a study conducted by Sonnadara *et al.* [185] the first 10 ms of the cloud flash was Fourier transformed to obtain the spectrum. In a more recent study conducted by Ahmed *et al.* [186] the first 100 ms of the cloud flash was used to obtain the spectrum. The spectrum obtained is shown in Figure 4.30. One can see that as one uses longer and longer waveforms to obtain the spectrum the content of the upper frequency level increases. The reason is the added contribution of all the pulses that were missed when the spectrum was calculated using short waveforms. Moreover, one can see a tendency for the tail of the spectrum to approach the spectrum obtained from narrow-band measurements.

Cooray and Cooray [174] showed that electromagnetic radiation from electron avalanches and streamers may contribute to the tail of the spectrum in the region of GHz. Using the charge transferred as a measure of the amount of electron avalanche created by a lightning flash they made an estimation of the contribution of electron avalanches to the spectrum. Their results are shown together with the narrow band spectrum in Figure 4.31.

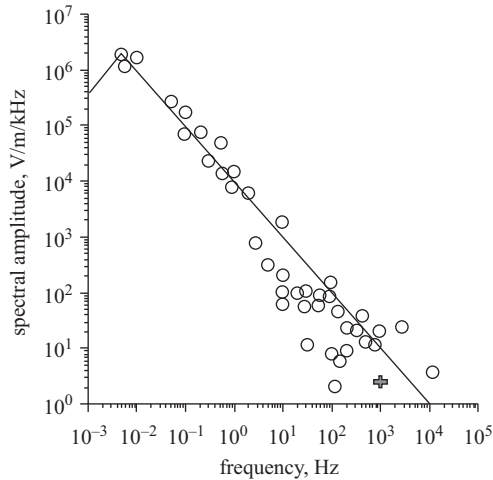


Figure 4.31 The spectral characteristics of close lightning flashes normalised to a common distance of 10 km. The data points correspond to different measurements and the solid line shows the overall behaviour. The cross represents the predicted contribution from electron avalanches (adapted from [174])

#### 4.6.4 Continuing current

Even though the currents associated with return strokes usually come to zero in several hundred microseconds, there are some return strokes in which the current amplitude decreases to about 100 A within this time but then, instead of going down to zero, may maintain this amplitude for a few milliseconds to a few hundreds of milliseconds. Such currents are known in the literature as continuing currents.

The existence and the duration of continuing currents can be identified by the close electric fields produced by lightning flashes [161]. Based on the results obtained from such records, the continuing current can be divided into several categories. Kitagawa *et al.* [187] and Brook *et al.* [71] defined continuing currents longer than 40 ms as long continuing currents, whereas Shindo and Uman [188] defined the continuing currents of duration between 10 and 40 ms as short continuing currents. They also found examples where the continuing current duration was 1–10 ms. Saba *et al.* [189] defined them as very short continuing currents. However, it is important to mention that this division, while helping the bookkeeping, does not have a physical basis. That is, the physical process that gives rise to continuing currents irrespective of their duration could be the same.

Heidler and Hopf [190] studied the presence of continuing currents in lightning flashes in Germany using electric field records. The mean, maximum and minimum durations observed in that study are tabulated in Table 4.12. According to Heidler and Hopf [190] 48 per cent of negative flashes were hybrid flashes containing at least one continuing current (these are long continuing currents). In a study conducted by Thompson [191] it was found that in 34 multiple stroke flashes 47 per cent had at least one continuing current. In a study conducted by Schonland [36] this was 20 per cent. According to the observations of Livingston and Krider [192] the frequency of flashes having continuing currents ranges from 29 to 46 per cent.

Table 4.12 *Parameters of M-components (adapted from [197])*

	Units	N	GM	Percentage of cases exceeding the tabulated value		
				95%	50%	5%
Peak current	A	124	117	20	121	757
Risetime	$\mu$ s	124	422	102	415	1785
Duration	ms	114	2.1	0.6	2.0	7.6
Half peak width	$\mu$ s	113	816	192	800	3580
Charge	mC	104	129	33	131	377

GM, geometric mean; N, number of observations.

In a study conducted by Shindo and Uman [188] 22 out of 90 negative flashes contained long continuing currents and 11 contained short continuing currents.

Saba *et al.* [189] using high speed video cameras managed to obtain statistics concerning continuing currents in lightning flashes in Brazil. Analysing 233 negative ground flashes containing 608 strokes, they found that 50 per cent of strokes support continuing currents longer than about 1 ms and 35.6 per cent of the strokes were followed by short or long continuing currents. The distribution of the duration of continuing currents observed in the study is shown in Figure 4.32. After analysing the continuing currents in negative and positive ground flashes Saba *et al.* [193] concluded that the combination of stroke amplitudes greater than 20 kA and continuing currents longer than 40 ms is highly unlikely to occur. This is shown in Figure 4.33. However in the case of positive ground flashes such a restriction was not observed. They also observed that the peak currents of the strokes (estimated from electric field records) supporting long continuing currents are smaller on average than those of other strokes. This observation is similar to the observations made by Rakov and Uman [194]. Ballarotti *et al.*, [195] analysing 890 strokes of 233 negative ground flashes, found that the geometric mean duration of continuing currents was 5.3 ms. The histogram of very short continuing current durations observed by Ballarotti *et al.* [195], is shown in Figure 4.34. According to the study, about 28 per cent of all negative strokes observed were followed by continuing currents longer than 3 ms.

#### 4.6.5 *M-Components*

Malan and Collens [196] coined the term ‘M-components’ to refer to the temporal increase in luminosity of the channel observed after some ground return strokes. For example the sudden increases in the current in Figure 4.35 are caused by M-components. The wealth of information available today on the M-components was derived by analysing the channel base currents and the luminosity changes in triggered lightning flashes [131, 197]. The M-component is a current impulse that initially travels from cloud to ground with a speed of about  $10^7$ – $10^8$  m/s [6,198] and occurs during the continuing current phase of the return stroke. The light pulse associated with the M-component exhibits a more or less symmetrical waveshape with a total duration of several hundreds of microseconds. The shape of the light pulse does not change much within the bottom 1 km or so of the channel, whereas its amplitude varies somewhat with height. The statistics on M-components are given in Table 4.12.

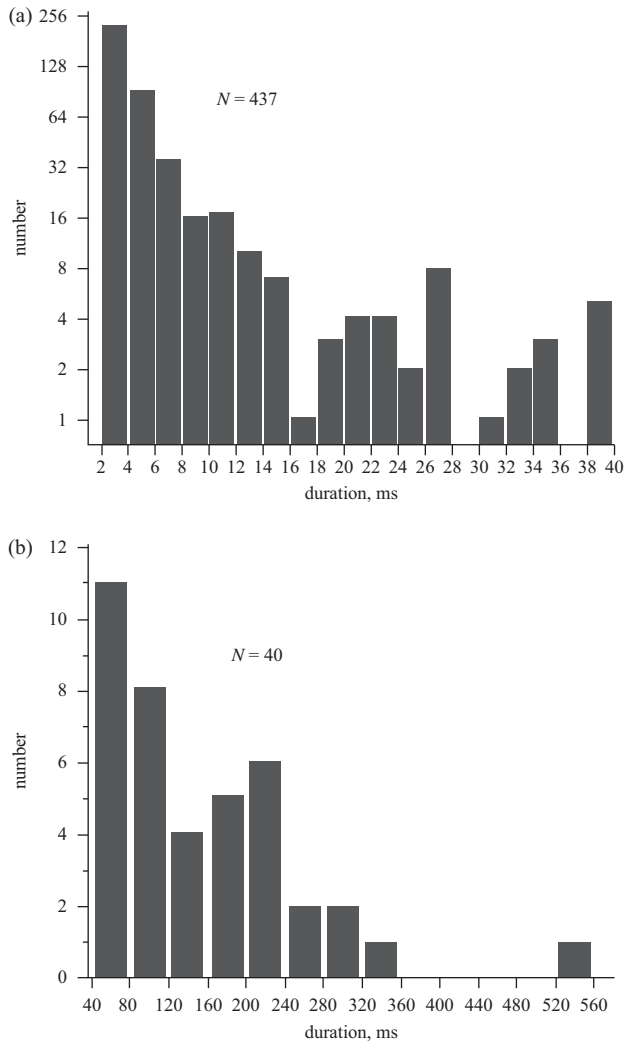


Figure 4.32 The histogram of continuing current durations observed by Saba *et al.* [189]. (a) Histogram corresponding to continuing current durations below 40 ms. (b) Histogram corresponding to continuing current durations longer than 40 ms

An example of the electric field change generated by an M-component is shown in Figure 4.36. Note that the M-component generates a hook shape change in an otherwise ramp-like electric field change caused by the continuing current. By analysing the way in which the electric fields of M-components vary with distance, Rakov *et al.* [199] established that the M-component involves a downward progressing incident current wave followed by an upward progressing reflected wave. This provides an explanation for why the M-component was sometimes observed to travel down and sometimes travel up [196]. Rakov *et al.* [199] treated the M-component as a current wave travelling along a transmission line that is short-circuited at the ground end. They explained that the observed uniformity of the pulse shape along the channel was the result of two opposing effects. The first one



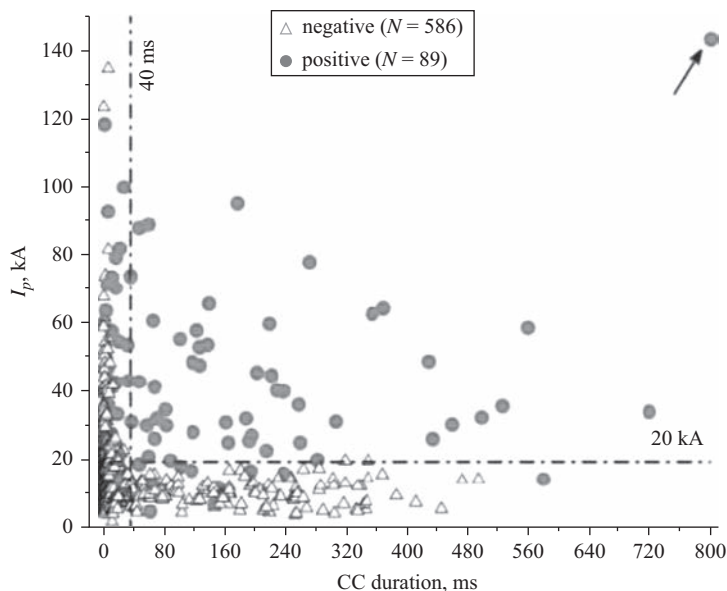


Figure 4.33 Peak current versus continuing current duration for 586 negative strokes and 89 positive strokes (adapted from [193])

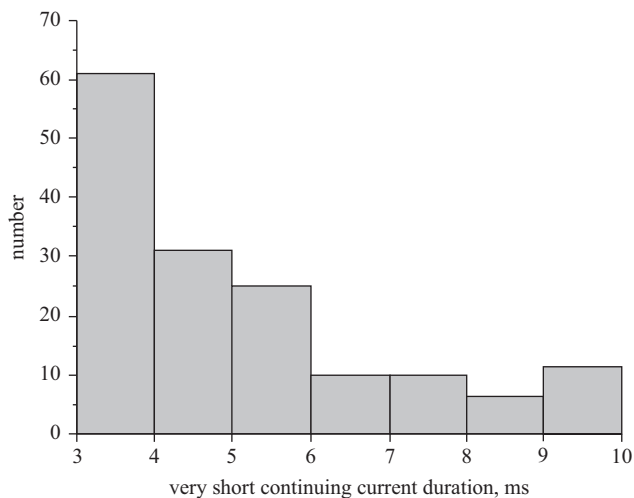


Figure 4.34 Histogram of very short continuing current durations as observed in the study conducted by Ballarotti *et al.* [195]

being that the high-frequency components travel faster than the slow ones due to the inherent nature of the R–C line. The second one being that the M-current pulse heats the channel so that the pulse tail encounters a lower resistance, thus accelerating the low-frequency components.

#### 4.6.5.1 Origin inside the cloud

The observations of Shao *et al.* [6] show that M-components are initiated inside the cloud in two ways. Some of the M-components are initiated by a negative

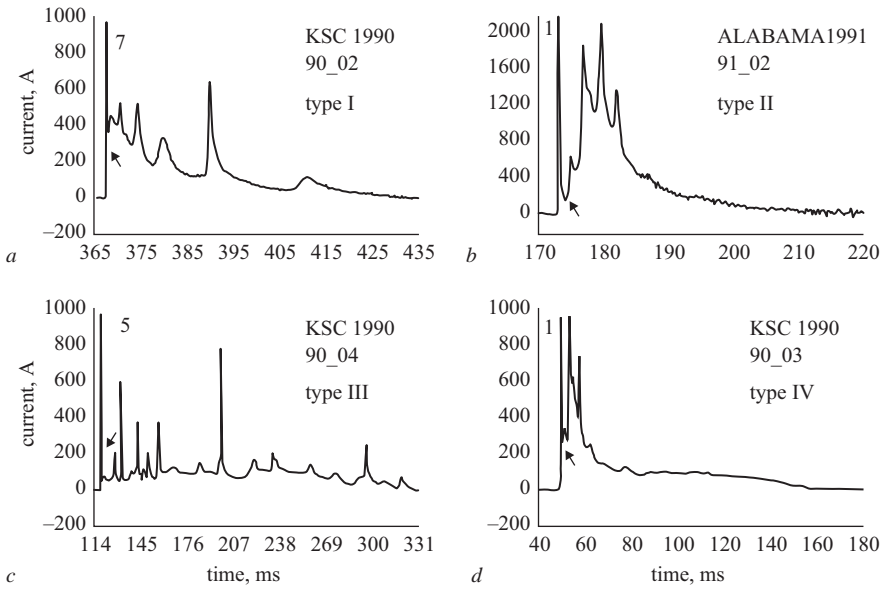


Figure 4.35 Typical examples of continuing current wave shapes measured in triggered lightning flashes. The arrow indicates the assumed beginning of the continuing current. The subsidiary peaks in the current waveform are generated by M-components (adapted from [131])

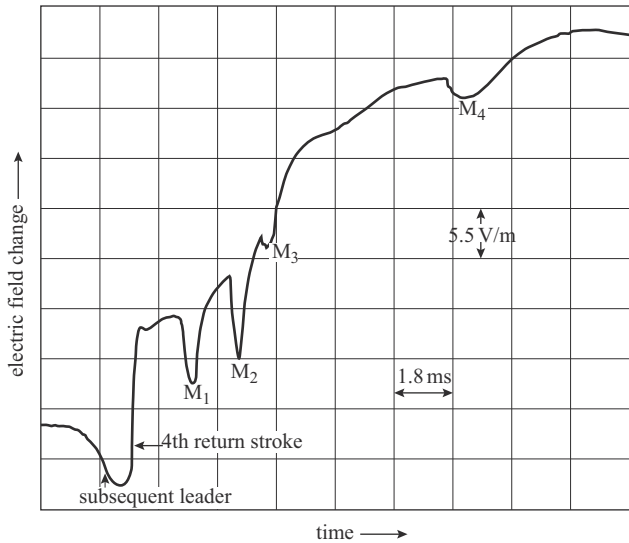


Figure 4.36 Hooked shape M-field changes (marked  $M_1$ ,  $M_2$ ,  $M_3$  and  $M_4$ ) in the continuing current phase generated by the fourth return stroke in the electric field record of a lightning flash. A positive field corresponds to an upward deflection (adapted from [200])

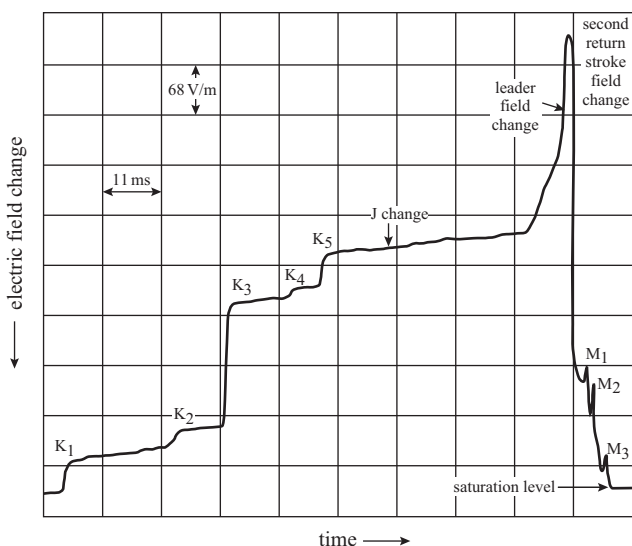


Figure 4.37 Portion of an electric field record of a lightning flash showing the electric field changes created by K changes. A positive field corresponds to a downward deflection (adapted from [202])

breakdown starting some distance from the cloud end of the return stroke channel (or the flash origin) and propagating towards it. When this discharge makes contact with the return stroke channel carrying the continuing current, an M-component is initiated. The other M-components are initiated as follows: Immediately after the return stroke front has reached the end of the channel, a positive breakdown event propagates away from it. This generates a negative recoil event (i.e. in effect, like a return stroke travelling along the leader channel) which travels along it and towards the end of the return stroke channel. When it arrives there and makes contact with the return stroke channel it gives rise to an M-component. The first type of initiation usually happens in the later stages of the continuing current phase, whereas the latter is initiated immediately after the return stroke. M-components do not usually radiate in the VHF range when they are travelling along the return stroke channel.

#### 4.6.6 K changes

K changes refer to small, millisecond duration electric field changes that occur during the inter-stroke intervals of cloud to ground flashes and also during intra-cloud flashes [64, 200]. Actually, the step-like field changes occurring between return strokes were first observed by Malan and Schonland [201] who interpreted them as being attributable to a leader not being able to reach ground that, instead of producing a return stroke, gave rise to a small adjustment of the charge in the cloud.

When K changes are measured with instruments having a long decay time constant (say 100 ms or more), they appear as electrostatic steps in the electric field [200, 202]. Examples of K changes are shown in Figure 4.37. The polarity of the K pulses is observed to be the same as the polarity of the slow field change that occurs in between return strokes. The duration of the K pulses is distributed approximately log-normally with a geometric mean of about 0.7 ms. It is important to note that, if K pulses are measured with an antenna system with a fast decay time constant, the original step may appear as an exponentially decaying pulse [200; see section 4.10].

The radiation field pulses associated with the K changes were analysed by Rakov *et al.* [200]. In about 23 per cent of the K changes they could detect microsecond scale pulse activity with an amplitude exceeding 50 per cent of the noise level. The beginning of the pulse activity was delayed by more than about 100  $\mu\text{s}$  from the beginning of the K change. In some K changes, the initial polarity of the microsecond scale pulses was opposite to that of the K change.

#### 4.6.6.1 Origin

Kitagawa and Brook [64] suggested that K change is a recoil event that occurs when a positive leader meets a concentration of negative charge (i.e. an event like a return stroke). This picture of a K discharge as a recoil event was disputed recently by the observations of Shao *et al.* [5, 6]. According to these observations, K changes are negative breakdown events which often start from a point just beyond the far end of a previously active channel and move into it, thereby extending the original channel. Once the connection is made with the previously active channel, they continue to move towards the origin of the flash along this channel, but usually cease before reaching it. In some cases, when the K discharge was on its way a burst of radiation occurred at its starting point. This was accompanied by a fast electric field change of relatively large amplitude at ground level which signals a rapid increase in current along the channel. This breakdown appears to be a process that rejuvenates the K channel at its origin, leading to an increase in the current in the channel.

The mechanism of the K change appears to be similar to that of M-components, except that the latter connects to a conducting channel and transports negative charge to ground. On the basis of the differences in the distribution of time intervals between K changes and M-components, Thottappillil *et al.* [202] argue that different mechanisms are responsible. Note, however, that the continuing currents, which are present during M-components, may change the local conditions inside the cloud, giving rise to changes in the distribution of time interval between events.

### 4.6.7 Subsequent strokes

#### 4.6.7.1 General properties

A typical ground flash may contain about four to five return strokes on average and, as mentioned previously, the return strokes that occur after the first return strokes are called subsequent strokes. The average separation between the subsequent strokes lies in the range of 30–60 ms.

Thomson [203] investigated the characteristics of lightning flashes measured in different geographical regions to determine whether there is any systematic variation in the number of strokes per flash and the inter-stroke time intervals with latitude. He concluded that large differences reported in the value of the parameters in different regions are caused by the use of different measuring techniques.

A comparison between the features of return strokes in lightning flashes using the same equipment in the temperate and tropical region was conducted by Cooray and Perez [204] and Cooray and Jayaratne [205]. A summary of the statistics obtained in these studies and those obtained in Florida by Thottappillil *et al.* [206] are given in Tables 4.13 and 4.14.

In general the peak current in the subsequent strokes is smaller than that of first return strokes. However, the tower measurements conducted by Berger [58, 142] show that in about 15 per cent of the flashes at least one subsequent stroke may

Table 4.13 *Summary of interstroke interval statistics (adapted from [205])*

Reference	Total number of flashes	Total number of subsequent strokes	Arithmetic mean (ms)	Geometric mean (ms)
Cooray and Jayaratne [205], Sri Lanka	81	284	82.8	56.5
Cooray and Pérez [204], Sweden	271	568	65	48
Thottappillil <i>et al.</i> [206], Florida	46	199	–	57

Table 4.14 *Summary of strokes per flash and percentage of single stroke flashes (adapted from [205])*

Reference	Total number of flashes	Single stroke flashes, %	Mean number of strokes per flash
Cooray and Jayaratne [205], Sri Lanka	81	21	4.5
Cooray and Pérez [204], Sweden	137	18	3.4
Rakov and Uman [206], Florida	76	17	4.6

Table 4.15 *Ratio of subsequent stroke field peak to that of the first return stroke (adapted from [205])*

Reference	Number of subsequent strokes	Arithmetic mean	Geometric mean
Cooray and Jayaratne [205], Sri Lanka	284	0.55	0.43
Cooray and Pérez [204], Sweden	314	0.63	0.51
Thottappillil <i>et al.</i> [206], Florida	199	–	0.42

carry a peak current which is larger than that of the first stroke [206]. This fact is strengthened further by the observation that in about 30 per cent of the lightning flashes at least one subsequent stroke may generate an electric radiation field peak which is larger than the first. Statistics relevant to this are presented in Tables 4.15 and 4.16. Note, however, that the peak of the radiation field is governed not only by the peak current in the channel but also by the speed of the return strokes. Thus, some of the field peaks which are larger than the peak of the first return stroke are probably caused by high return stroke velocities and not by high peak currents.

#### 4.6.8 *Dart leaders*

Dart leaders, which initiate subsequent return strokes, were first identified in data obtained from a series of experiments performed in South Africa in the 1930s by Schonland and co-workers [36]. The dart leader deposits negative charge along the defunct first return stroke channel and sets the stage for the subsequent return strokes. Dart leaders usually travel along the main channel of the previous return stroke and do not give rise to branches, but if the previous return stroke is the first

Table 4.16 Summary of multiple-stroke flash characteristics (adapted from [205])

Reference	Total number of flashes	Percentage of flashes with at least one subsequent stroke field peak larger than the first, %	Total number of subsequent strokes	Percentage of subsequent strokes with field peak larger than the first, %
Cooray and Jayaratne [205], Sri Lanka	81	35	284	12.3
Cooray and Pérez [204], Sweden	276	24	479	15
Thottappillil <i>et al.</i> [206], Florida	46	33	199	13

Table 4.17 Speed of dart leaders

Reference	Mean speed, $10^6$ m/s
Schonland <i>et al.</i> [94]	5.5(natural)
McEachron [95]	
Brook and Kitagawa [Winn, 271]	11(natural)
Berger [58]	
Hubert and Mouget [272]	9.7(natural)
Orville and Idone [60]	9.0(natural)
Idone <i>et al.</i> [209]	11(triggered)
Jordan <i>et al.</i> [215]	11(natural and triggered)
Shao <i>et al.</i> [6]	20(triggered)
Mach and Rust [152]	14(natural)
Mach and Rust [152]	10(natural)
Wang <i>et al.</i> [273]	13(triggered)
Wang <i>et al.</i> [274]	19(natural)
	30–40(triggered)
	14(natural)

one then it may re-energise one or two branches. In addition to photographic techniques, the propagation path of the dart leader can be detected from VHF radiation that originates at the lower tip of the descending leader [6].

#### 4.6.8.1 Optically determined properties

##### *Dart leader length and speed*

In optical records, the dart leader appears as a faintly luminous discharge with a bright tip of a few tens of metres long (i.e. the ‘dart’), which travels continuously along the trail of the previous return stroke. The main body of the data available concerning the speed of the dart leaders are summarised in Table 4.17. The dart leaders radiate significantly in the wavelength region 400–510 nm [207]. Thus, in evaluating the dart length it is important to take into consideration the spectral sensitivity of the film and any other filters used. For example, Orville and Idone [60] show examples where the differences in the measured dart leader lengths,

Table 4.18 *Rise time of dart leader optical radiation*

Reference	Optical risetime, $\mu\text{s}$
Cooray <i>et al.</i> [153]	2.9 (0 to peak rise time) (triggered) 1.5 (20–80% rise time) (triggered)
Mach and Rust [152]	2.6 (10–90% rise time) (natural) 1.4 (10–90% rise time) (triggered)
Wang <i>et al.</i> [273]	0.6 – 0.7 (10–90% rise time) (triggered)
Wang <i>et al.</i> [275]	0.5 (dart stepped leaders) (triggered)
Jordan <i>et al.</i> [102]	0.5–1 (20–80% rise time) (natural)

15 m in Florida and 42 m in New Mexico could have been caused by the use of a red filter in the Florida measurements which excluded wavelengths below about 620 nm thereby giving a weaker image of the dart leader.

Orville and Idone found that the dart leader length and the speed are correlated with dart leader length increasing with increasing speed.

#### *Spectrum and temperature of the dart leader*

Orville [207] recorded the spectrum of the dart leader in the range of 390–510 nm. All spectral lines recorded in the dart leader have been identified as singly ionised emissions which are also observed in the return stroke spectra. Combining theory with the relative intensity of NII lines at 4447 and 4630 Å, he estimated the temperature of the dart leader to be around 20 000 K, somewhat lower than the average observed for return strokes. He also estimated that the channel temperature remains around 20 000 K, at least in the channel section below the cloud base, until the arrival of the return stroke.

#### *Optical signature of the dart leader*

The optical signature generated by the dart leader rises to its peak value in about a microsecond [102, 152, 153]. After reaching a maximum, the pulse decays in a few microseconds to a more or less constant level. The plateau continues until it is overridden by the light waveform of the return stroke. The shape of the optical pulse of the dart leader does not change significantly with height, although the pulse amplitude may increase as the leader approaches the ground. In Table 4.18 the important parameters obtained for the optical signature of the dart leader in different studies are tabulated. Since the optical radiation from long sparks shows that the rising part of the optical pulse is approximately the same as the current rise time [103], the above results indicate that the current rise time in the dart leader remains constant at around 1  $\mu\text{s}$  along the channel, but the peak current may increase as the dart propagates towards the ground.

A typical dart leader is intrinsically a factor of 10 less intense than return strokes [102, 104]. Measurements made by Orville [207] indicate that the brighter the dart leader, the shorter the time interval between the passage of the dart leader and the return stroke, indicating that the brighter the leader, the higher the speed with which it (and also probably the ensuing return stroke) travels along the lightning channel. Idone *et al.* [209] observed a strong correlation between the dart leader speed and the peak current of the return stroke in the experiments using triggered lightning. Moreover, the light intensity of the dart leader was positively correlated with the light intensity of the return stroke. That is brighter dart leaders have brighter return strokes. The brightness of the dart leader is a measure of

the peak of the associated current. Thus, one can infer that dart leaders carrying large currents have larger speeds and that they generate return strokes with larger currents.

#### 4.6.8.2 Origin of the dart leader in the cloud

Using VHF radiation as a tool, Shao *et al.* [6] reported that successive dart leaders in the cloud to ground flash tend to start further and further away from the origin of the flash. The exception was that sometimes successive leaders started from the same location. According to these authors, the origin of the dart leader in the cloud is no different to that of K changes and M-components. The only difference in the three processes is that the dart leader makes a connection to a partially conducting return stroke channel, the M-component connects to a return stroke channel which is conducting and carrying a continuing current and the K change stops short of reaching the return stroke channel. Sometimes the propagation of the dart leader may stop before reaching the ground; Shao *et al.* termed such events 'attempted leaders'. They claimed that it would be difficult to distinguish such an event from a K change solely from the electric field record.

#### 4.6.8.3 Current and charge of dart leaders

The charge deposited on the dart leader channel has been determined by Brook *et al.* [71] to be a minimum of 0.2 C with the most frequent value between 0.5 and 1C. These values also agree with the charge brought to ground by subsequent strokes [142]. The dart traverses the return stroke channel with a length of about 5 km in about a millisecond; the total charge of 0.5 C then corresponds to a current of about 1 kA. By using the observed correlation between the dart leader speed and the return stroke current, both Idone and Orville [104] and Cooray *et al.* [153] have estimated the dart leader current to be about a kilo ampere on average.

The charge per unit length on the dart leader channel located very close to the ground can be estimated from the electric field changes produced by dart leaders within about 200 m. Results obtained in this manner indicate that the charge per unit length close to the ground has a strong linear correlation to the peak current of the ensuing return stroke [133]. When interpreted using a uniformly charged leader channel, these results indicate that the value of the linear charge density of the dart leader channel lies in the range of 7–12  $\mu\text{C}/\text{m}$  for each kA of the peak current of the return stroke at the channel base.

As in the case of first return stroke described in section 4.6.3.4 Cooray *et al.* [72] utilised the charge brought to ground in the first 50  $\mu\text{s}$  of subsequent return strokes to estimate the charge distribution along the dart leader channel. The measured charge as a function of peak return stroke current is shown in Figure 4.38 They found a strong correlation between the subsequent return stroke peak current  $I_p$  and the measured charge  $Q$ . This correlation could be written as

$$Q = 0.028 \times I_p \quad (4.26)$$

Combining this information with the bidirectional leader model they have investigated how this charge was distributed along the dart leader channel. Their results show that the charge distribution can be described by an equation identical to 4.10 but with the following parameters:  $a_0 = 1.476 \times 10^{-5} \text{ s/m}$ ,  $a = 4.857 \times 10^{-5} \text{ s/m}$ ,  $b = 3.9097 \times 10^{-6} \text{ s/m}^2$ ,  $c = 0.522 \text{ m}^{-1}$  and  $d = 3.73 \times 10^{-3} \text{ m}^{-2}$ . The predicted charge distribution for a 12 kA current is depicted in Figure 4.39. In order to test the validity of this charge distribution Cooray *et al.* [72] calculated the electric field



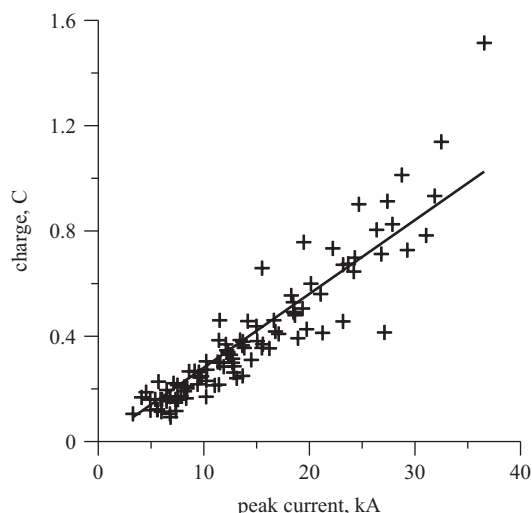


Figure 4.38 *The relationship between the subsequent return stroke current peak and the charge brought to ground by the first return stroke in the first 100  $\mu$ s (adapted from [72])*

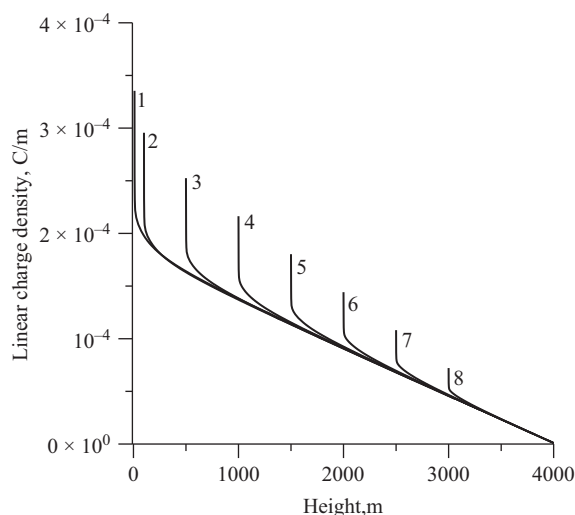


Figure 4.39 *Charge distribution along a dart leader channel with a prospective return stroke current of 12 kA. The height of the leader tip above ground is (1) 10 m, (2) 100 m, (3) 500 m, (4) 1000 m, (5) 1500 m, (6) 2000 m, (7) 2500 m and (8) 3000 m*

generated by the dart leader in the vicinity of the channel. The results compared well with the experimental observations obtained from triggered lightning [133].

#### 4.6.8.4 Static fields generated by dart leaders

The features of slow fields produced by dart leaders in lightning flashes were originally described by Malan and Schonland [201] and, more recently, electric fields generated by dart leaders in triggered lightning flashes have been described by

Rubinstein *et al.* [210], Rakov [133] and Crawford *et al.* [211]. An example has already been shown in Figure 4.22. The qualitative features of the near fields produced by dart leaders can be simulated by assuming the dart leader to be a uniformly charged channel which propagates towards ground with a constant speed.

#### 4.6.8.5 RF radiation from dart leaders

Dart leaders produce considerable radiation in the HF, VHF and microwave regions. Shao *et al.* [6] show that the VHF radiation pulses associated with the dart leader propagate downward along the defunct return stroke channel indicating that the dart leader head is a strong source of RF radiation. The RF radiation starts 100–1000  $\mu\text{s}$  before the return stroke and in some cases it ceases 50–100  $\mu\text{s}$  before the return stroke, whereas in other cases it may continue up to the return stroke. The cessation of the RF radiation just before the return stroke could be partly attributable to propagation effects. The studies conducted by Mäkelä *et al.* [212] at 10 MHz radiation show that a significant increase in HF radiation generated by dart leaders takes place if the dart leaders are associated with a chaotic pulse bursts (or chaotic dart leaders; see section 4.6.8.9).

#### 4.6.8.6 The parameters that control the dart leader speed

Cooray [213] and Cooray and Rakov [214] modelled the dart leader as a self-propagating discharge that carries a high electric field at the front which is strong enough to cause electrical breakdown in the defunct return stroke channel. The electric field at the front of the dart leader depends on both the current flowing behind it (and hence on the charge being stored on the dart leader) and the speed of the dart leader. Thus, by equating this field to the critical electric field necessary to cause electric breakdown in the defunct return stroke channel, a relationship was derived by Cooray [213] between the dart leader speed, its current and the temperature of the defunct return stroke channel through which it propagates. The results show that the speed of the dart leader increases with increasing current amplitude (and hence with increasing charge on the leader), with decreasing current rise time and with increasing temperature of the defunct return stroke channel.

If the charge on the dart leader increases as it propagates towards the ground, then its speed may also increase as it approaches the ground provided that the temperature of the defunct return stroke channel and the rise time of the dart leader current do not vary with height. The measurements show that the rise time of the optical signature generated by the dart leader does not vary significantly as the dart leader propagates towards the ground. This indicates that the rise time of the dart leader current does not vary as a function of height. On the other hand, the channel temperature may not remain constant as a function of height. If the channel sections close to ground decay faster than the rest of the channel, the dart speed may decrease as it approaches the ground, in case the charge on the dart leader remains unchanged. Depending on the way in which the dart leader charge and the channel temperature vary with height some dart leaders may show a tendency to increase their speed as they propagate towards the ground and the others may show the opposite tendency.

If the charge and the current rise time of dart leaders are independent of the inter-stroke time interval one may observe a tendency for the dart leader speeds to decrease with increasing time interval between return strokes. This is the case since the temperature of the defunct return stroke channel decreases with increasing

inter-stroke time interval. However, one cannot rule out the possibility of the charge on the dart leader to increase with increasing time interval between strokes. Thus, it is difficult to predict the dependence of the dart leader speed on inter-stroke time interval. Depending on the amount of charge transported down, some dart leaders may show a tendency to increase their speed with increasing inter stroke interval and others may show the opposite tendency.

Unfortunately, all of the parameters that control the dart leader speed could change both spatially and temporally in an – as yet – undefined manner, and it is not easy to relate the speed of the dart leader to any one of these parameters. These facts should be kept in mind in the interpretation of the information given in the next section.

#### **4.6.8.7 Correlation between parameters of dart leaders and return strokes**

##### *Dart speed and the inter-stroke interval*

Schonland [36] reports that the higher dart leader speeds in natural lightning occur when the leaders follow the previous stroke with little delay and that low speeds are associated with longer time intervals. Such a relationship, though weak, is also found by Jordan *et al.* [215] for natural lightning. The triggered lightning data apparently exhibited the opposite tendency [215]; however, there was a clear trend for the maximum leader speed to decrease with an increasing previous return stroke interval. For successive inter-stroke interval ranges of 0–30, 30–70 and 70–140 ms, the maximum dart leader speed observed was  $49 \times 10^6$ ,  $34 \times 10^6$  and  $12 \times 10^6$  m/s. According to the experimental data of Campos *et al.* [216] the minimum, the maximum and the mean dart leader speeds were  $3.33 \times 10^5$  m/s,  $2.9 \times 10^7$  m/s and  $4.6 \times 10^6$  m/s respectively.

Schonland *et al.* [217] never found that the speed of the dart leader increased as the leader approached the ground, while Orville and Idone [60] found that in 4 cases out of 26 it did. Orville and Idone [60] report that the best recorded data set in their study did show not only an increase in speed but also the light output increased by a factor of 2 from cloud base to ground. In agreement with the observations of Schonland *et al.* [217], Orville and Idone also observed dart leaders decreasing in speed near the ground. Experimental observations of Campos *et al.* [216] show that 32.1 per cent of the 53 negative dart-leaders accelerated as they approach the ground, 54.7 per cent decelerated, and 13.2 per cent oscillated around an average speed. Orville and Idone [60] warned, however, of the possibility that the speeds determined are two dimensional and some variations could arise because of channel geometry, which cannot be identified in two dimensional photographs.

Possible reasons for the dart leaders to show either a tendency to accelerate or decelerate as they approach the ground are given in the previous section.

##### *Dart speed and the dart length*

Orville and Idone [60] found that the length of the dart leader increases with increasing speed of the dart. This correlation is shown in Figure 4.40. The correlation coefficient was 0.72. If the duration of the luminosity of a given point on the channel caused by the current of the dart leader is  $\tau$  then the length of the dart is given by  $\tau v$ , where  $v$  is the speed of the dart leader. The laboratory experiments show that the duration of the channel luminosity of long sparks having identical current waveshapes became longer with increasing peak current [103]. This observation suggests that the duration of the luminosity may also increase with

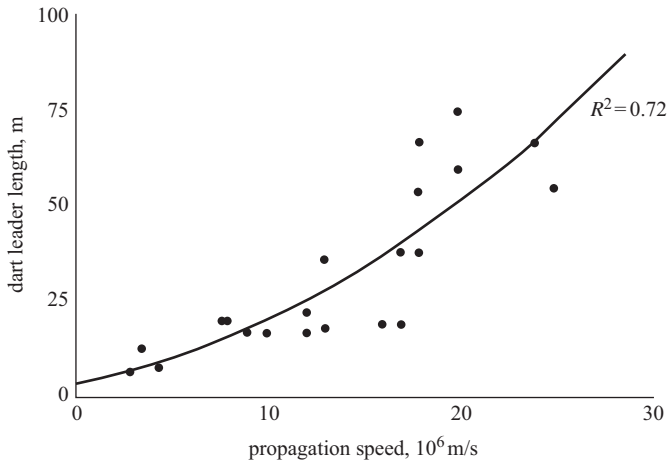


Figure 4.40 Dart leader length versus speed of propagation along the channel (adapted from [60])

increasing current and hence with the speed of the dart leader. The latter is likely since the experimental data hint that the larger dart speeds are associated with larger currents [104, 209]. This makes the dart leader length increase more rapidly than linearly with increasing speed.

#### *Dart speed and the return stroke current*

As mentioned previously, Idone *et al.* [209] found a strong correlation between the speed of the dart leader and the peak return stroke current. This relationship can be understood easily if the speed of the dart leader and the return stroke is controlled by the charge density deposited by the dart leader along the lightning channel. Larger amounts of deposited charge will give rise to dart leaders with higher speeds and return strokes with larger currents. Indeed, the field measurements conducted very close to the triggered return strokes show that the peak return stroke current increases approximately linearly with increasing leader charge [133] – hence the connection between the dart leader speed and the return stroke current.

#### **4.6.8.8 Dart stepped leaders**

Schonland *et al.* [36] were the first to report that if the time interval to the previous return stroke is large, some of the dart leaders resume the stepping process when they approach the ground. In the literature such leaders are called dart stepped leaders. The steps in the dart stepped leaders are relatively short, about 10 m, and the time interval between the steps is about 5–10  $\mu$ s. Data that confirm these observations pertinent to dart stepped leaders were obtained recently by Orville and Idone [60]. The average downward speed of dart stepped leaders, about  $0.5 \times 10^6$  to  $1.7 \times 10^6$  m/s is somewhat slower than for dart leaders. Wang *et al.* [218] found the rise time of the optical pulse created during the formation of a dart stepped leader step to be about 0.5  $\mu$ s and the half peak width (width of the peak at half maximum) to be about 1.3  $\mu$ s. Moreover, they found that the formation of the step gives rise to an optical signature that travels upwards along the leader channel at a speed of about  $(0.2\text{--}1) \times 10^8$  m/s for a distance from several tens of metres to more than 200 m, beyond which it becomes undetectable.

In the records on electric radiation fields, one can identify the electric field pulses produced by the dart stepped leaders. Krider *et al.* [55] found that the mean time interval between the pulses of the radiation field produced by the dart stepped leaders immediately before the subsequent return strokes is about 6–8  $\mu\text{s}$ , which is shorter than 10–15  $\mu\text{s}$  observed for the stepped leader pulses immediately preceding the first return strokes.

#### 4.6.8.9 Chaotic leaders

Weidman [219] reported that some of the electric fields of subsequent return strokes were preceded by a train of pulses irregular in shape, width and separation. He named these return strokes ‘chaotic subsequent strokes’ or subsequent strokes preceded by ‘chaotic leaders’. Bailey and Willett [220] illustrated one such subsequent stroke recorded about 25 km from the place of impact. Gomes *et al.* [221] analysed the characteristics of these chaotic pulse trains (CPT) in detail. One example from their study is shown in Figure 4.41. Gomes *et al.* reported that the width of the individual pulses of these pulse trains is in the range of a few microseconds, the lower limit of which may, however, extend into the sub-microsecond region. The pulse separation lies in the range of 2–20  $\mu\text{s}$ . The most probable duration of the CPT is 400–500  $\mu\text{s}$ . Eighty four (about 25 per cent) of the CPT that these authors have observed preceded subsequent return strokes. Among these CPT, 65 immediately preceded a subsequent stroke and continued up to the return stroke. The rest had a delay between the end of the CPT and the return stroke. This delay varied from 0.35 to 73 ms. Gomes *et al.* [221] observed such CPT in ground flashes, but without any association with return strokes; they also observed them in cloud flashes. The fact that CPT occur before subsequent return strokes indicates

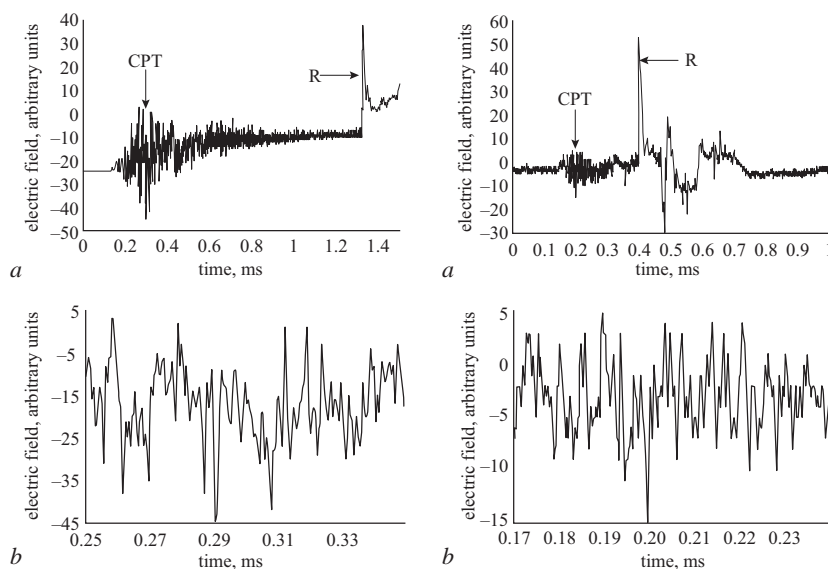


Figure 4.41 Two examples (figures marked a) of chaotic pulse trains (marked CPT) preceding subsequent return strokes (marked R). The lower traces (marked b) show a portion of the pulse train in a faster time scale. A positive field corresponds to an upward deflection (adapted from [221])

that they are probably connected with the initiation of dart leaders. Recent data gathered in Sri Lanka [277] show that most of the K changes in the electric field records were associated with CPT. Since the mechanism of creation of dart leaders, K changes and M-components are the same it is possible that even M-components are also associated with CPT.

As mentioned previously, the studies conducted by Mäkelä *et al.* [212] at 10 MHz radiation show that a significant increase in HF radiation generated by dart leaders takes place if the dart leaders are associated with a chaotic pulse bursts. This shows that the mechanism which is responsible for the chaotic pulse burst (most probably the mechanism responsible for the initiation of dart leaders, K changes and M-components) is a strong source of HF radiation.

## 4.7. Electromagnetic fields generated by cloud flashes

### 4.7.1 General features

General features of the electromagnetic fields of cloud flashes were reported by Brook and Ogawa [172] and Ogawa and Brook [222]. Typical slow electric fields generated by cloud flashes within about 10 km are shown in Figure 4.42. Note that the fields can be either unipolar or bipolar. The average duration of the cloud flashes as measured from records of electric field changes can range from about 200 ms to about 500 ms. The average charge neutralised by a cloud flash is about  $33 \pm 27$  C and the average charge moment change associated with a cloud flash is about  $87 \pm 62$  km C. This sets the average vertical length of a cloud flash to be about 3 km.

One of the most extensive studies of the electric fields generated by cloud flashes was conducted by Kitagawa and Brook [64]. According to these authors, the

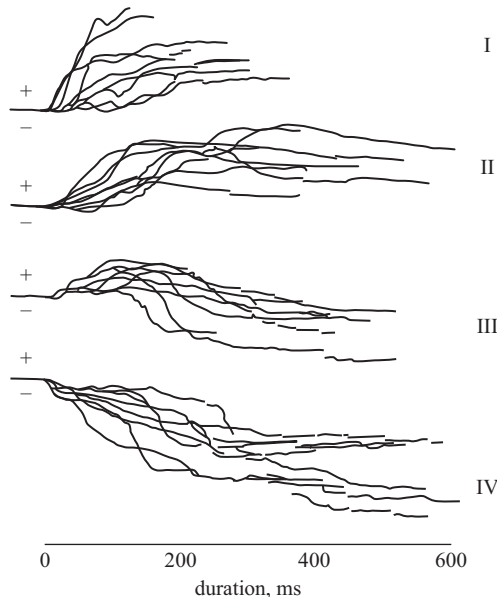
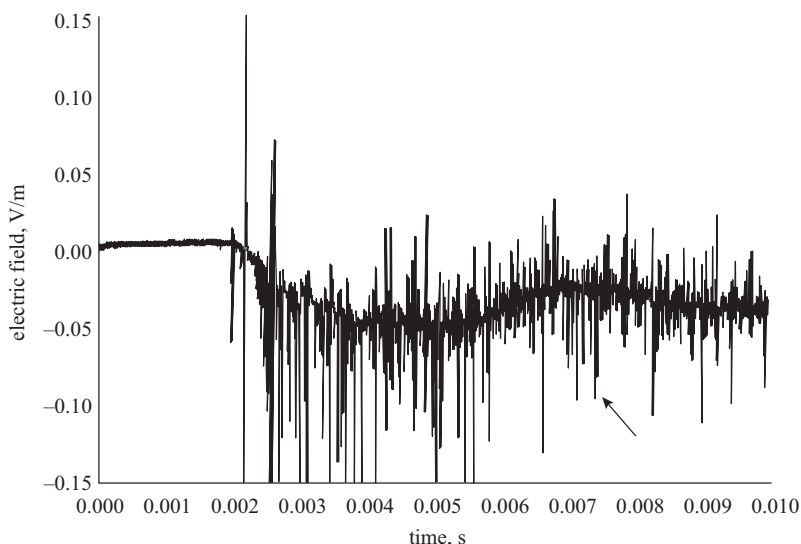


Figure 4.42 Different types of slow electric field changes produced by cloud flashes (adapted from [172])



*Figure 4.43 Radiation field pulses generated by a cloud flashes within the first 10 ms from its beginning. The distance to the flash is about 10 km. The arrow indicates the location of the pulse shown in Figure 4.44d. A positive field corresponds to an upward deflection (see [237] for the details of the experiment). The vertical scale should be multiplied by 100 to get the amplitude in V/m*

electric field signature of cloud flashes consists of three portions which they classified as initial, very active and the final stage. The initial portion is characterised by small microsecond scale pulses. During the very active portion, pulse activity is accentuated and is characterised by the pulses with the highest amplitudes in the flash. The final stage is composed of relatively small step-like electrostatic field changes generated by the K changes. Out of about 1400 cloud discharge studies, 50 per cent contained all the three categories of electric field signature, 40 per cent exhibited very active and final stage, while in 10 per cent the final portion was not identified, but they did have either the initial or active phases or both. In contrast, Bils *et al.* [223] and Villanueva *et al.* [224] show that the largest microsecond scale pulses occur predominantly in the initial part of the cloud flash, typically in the first 20 ms. However, in agreement with Kitagawa and Brook, they find that the final portion of the flash consists of sequences of K changes. Figure 4.43 shows an example of the radiation field pulses generated by cloud flashes within the first 10 ms of flashes recorded in Sweden. The arrow indicates the location of the pulse shown in Figure 4.44d. Note, that in agreement with the work presented by Bils *et al.* and Villanueva *et al.*, the largest pulse amplitudes are generated within the first few milliseconds of the flash.

#### 4.7.2 *Radiation field pulse characteristics*

Four categories of radiation field pulses have been observed in cloud flashes. These are (1) large bipolar pulses with several structures superimposed on the initial half cycle, (2) bursts of pulses similar to the dart stepped leader pulses, (3) narrow bipolar pulses, (4) microsecond scale pulses with a smooth rise to peak and

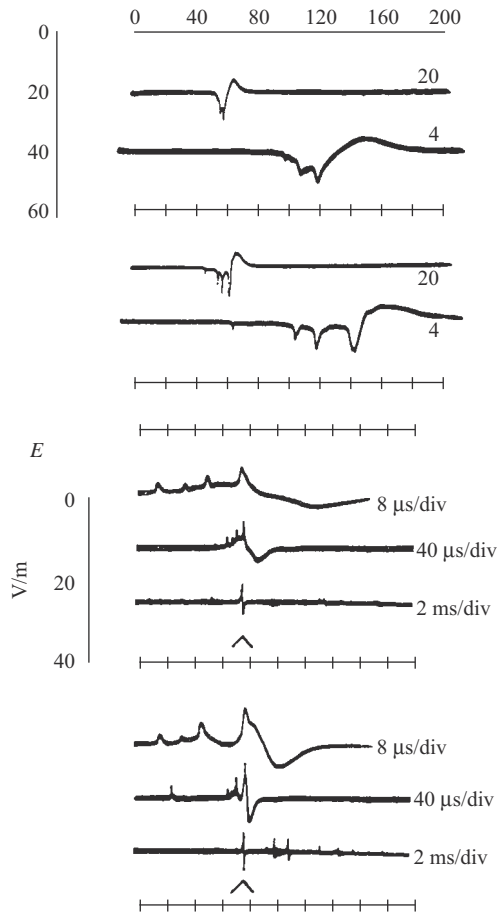


Figure 4.44a Large bipolar pulses with positive and negative initial polarities generated by electrical activity in the cloud. Note the pulses superimposed on the initial rising part of the waveform. Each waveform is shown on two ( $20 \mu\text{s}/\text{div}$  or  $4 \mu\text{s}/\text{div}$ ) or three ( $8 \mu\text{s}/\text{div}$ ,  $40 \mu\text{s}/\text{div}$  and  $2 \text{ms}/\text{div}$ ) time scales. A positive field corresponds to a downward deflection. Adapted from [225]

(5) chaotic pulses as described in an earlier section. Different types of radiation fields generated by cloud flashes is shown in Figure 4.44a to 4.44d.

#### 4.7.2.1 Large bipolar pulses

According to Weidman and Krider [225] cloud flashes generate large bipolar pulses with both positive (according to the definition of polarity adopted in this chapter) and negative initial polarity (Figure 4.44a). The pulses of positive initial polarity are very similar to the characteristic pulses in the preliminary breakdown stage of return strokes. The bipolar pulse bursts with positive initial polarity analysed by these authors did not lead to return strokes and thus could be characterised as cloud flashes. Their polarity indicated that the breakdown process transferred negative charge towards the ground. This kind of pulse activity should be distinguished from 'typical' cloud flashes in which the initial pulse polarity tends to be negative.



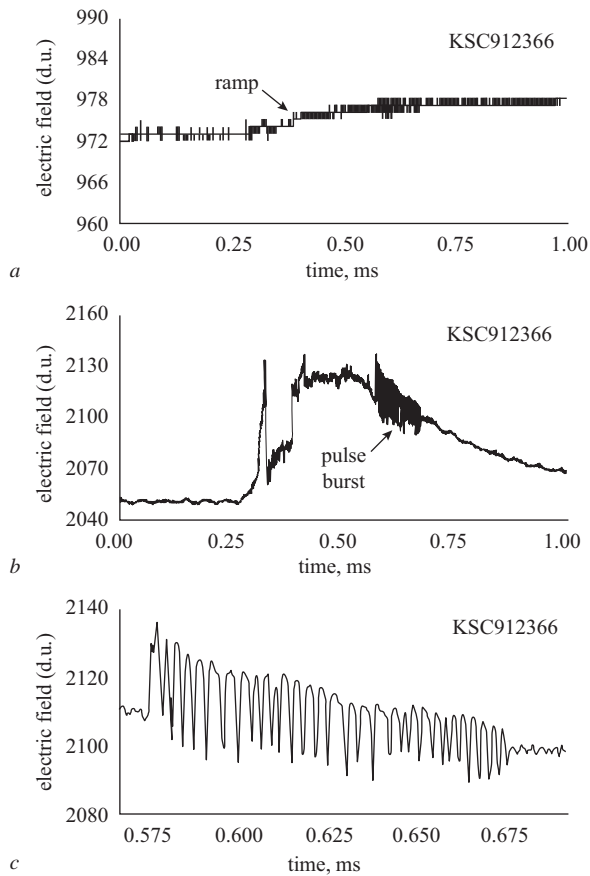


**Figure 4.44b** Bursts of pulses similar to the dart stepped leader pulses generated by electrical activity in the cloud. (a) The location of the pulse burst in a ramp-like field change produced by the cloud flash. The pulse burst is shown in two time scales in (b) and (c). A positive field corresponds to a downward deflection (adapted from [227])

The shape of the large pulses tends to be bipolar, with almost always two or three fast pulses, with sub-microsecond rise times and microsecond widths, superimposed on the rising part. The time interval between these fast unipolar pulses that are superimposed on the initial portion of the bipolar waveforms averaged  $7.8 \pm 5.7 \mu\text{s}$  for 66 positive and  $15 \pm 14 \mu\text{s}$  for 78 negative waveforms. The intervals tend to increase with increasing width of the pulses.

The time interval between the bipolar pulses with positive initial polarity is about  $130 \mu\text{s}$  and for negative initial polarity the pulse separation is  $780 \mu\text{s}$  on average. For a total of 137 negative pulses Weidman and Krider [225] report a mean total pulse duration of  $63 \mu\text{s}$ , and a ratio of initial peak to overshoot peak of 3.6. The corresponding value for positive pulses was 2.1. The average duration they found for positive pulses was  $41 \mu\text{s}$  for 117 pulses.

The spectrum of these pulses obtained by Weidman *et al.* [182] and Willett *et al.* [177] matched the return stroke spectra above 2–3 MHz. The time derivatives of the electric field associated with the pulses were analysed by Weidman and

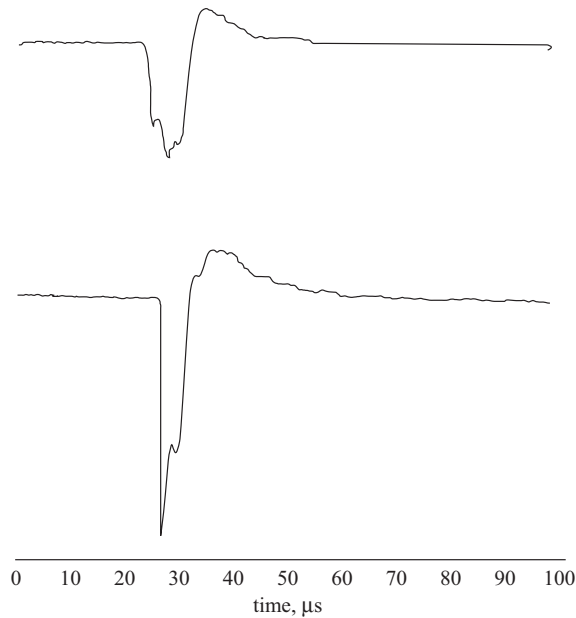


*Figure 4.44c* Narrow bipolar pulses generated by electrical activity in the cloud. Observations indicate that these pulses are generated by cloud activity in the growing stage of the thundercloud. The vertical scale is linear in V/m but uncalibrated. A positive field corresponds to an upward deflection (adapted from [228])

Krider [67] and an average value normalised to 100 km of about 20 V/m/ $\mu$ s was found. This value is slightly less but of the same order of magnitude as derivatives of the return stroke field. It is important to note that the normalisation to 100 km using the inverse distance dependence is only valid if the channel is vertical, whereas some of the cloud pulses are definitely generated by channel sections which are far from vertical.

#### 4.7.2.2 Bursts of pulses similar to the dart stepped leader pulses

Krider *et al.* [226] observed regular sequences or bursts of microsecond scale pulses with an amplitude about an order of magnitude smaller than the return stroke pulses. Each burst had a typical duration of 100–400  $\mu$ s with a mean time interval between individual pulses of about 5–6  $\mu$ s. The total duration of a single pulse was typically 1–2  $\mu$ s with the zero crossing time at about 0.75  $\mu$ s. The spectrum of the typical pulse sequence peaked around 100 kHz. The pulse bursts tend to occur towards the end of intracloud discharges and the authors suggest that the pulse burst could be due to an intracloud dart stepped leader process. Similar pulse bursts have been observed by Rakov *et al.* [227] both in cloud flashes and in cloud activity taking place between return strokes in ground flashes (Figure 4.44b). In the latter case, the amplitudes of the individual pulses were two orders of magnitude smaller than the initial peaks of the return stroke in the same flash. There is a tendency for these bursts to occur in the latter stages of the discharge and positive and negative polarity pulses are equally probable. Many bursts were found to be associated with the latter part of K changes.

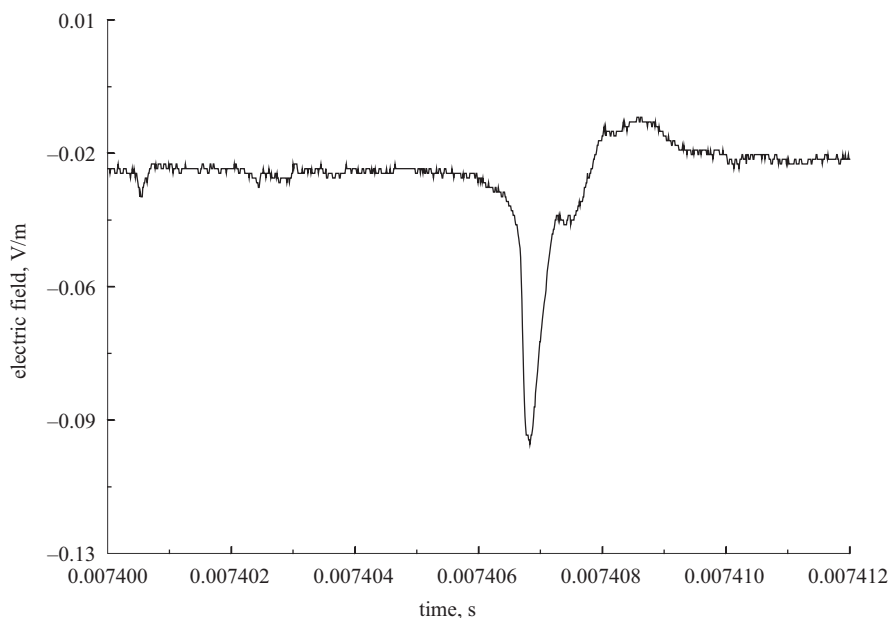


*Figure 4.44d* An example of microsecond scale pulses with a smooth rise to peak embedded in the electrical activity of a cloud flash. Note the slow front followed by the fast transition. The location of this pulse in the pulse burst generated by the cloud flash within the first 10 ms is shown by an arrow in Figure 4.43. A positive field corresponds to an upward deflection (see [237] for the details of the experiment). The vertical scale should be multiplied by 100 to get the amplitude in V/m

#### 4.7.2.3 Narrow bipolar pulses (or electric fields from compact cloud discharges)

Weidman and Krider [225] report that the first signals radiated by developing storms are single fast negative pulses with an initial half cycle of about 10  $\mu\text{s}$  (judging from the waveform reproduced in their paper). Interestingly, LeVine [228] found that the source of the strongest RF radiation at 3, 139 and 259 MHz generated by lightning flashes is a short duration bipolar pulse with negative initial polarity. Most probably these pulses are identical to those reported by Weidman and Krider. Since then pulses similar to these are described by several other researchers [66, 223, 229, 230–233, 234]. The discharge responsible for the narrow bipolar pulses is given the name ‘compact cloud discharges’ (CID) by Smith *et al.* [233]. According to Ahmed *et al.* [234] the initial rising portion of these pulses contain narrow pulses indicating that the process that generated this pulse is more complex than the mechanism of a return stroke.

Nag and Rakov [230, 231] suggested that the narrow bipolar pulses are generated by a current pulse that bounces between the two ends of a discharge channel of several hundreds of metres length. Watson and Marshall [235] modelled the source of the narrow bipolar pulse or the CID as a current pulse that increases its amplitude as it propagates along the discharge channel. Cooray *et al.* [236] showed that the source of narrow bipolar pulses can be modelled either as a single or as a multiple of relativistic avalanches in the cloud. All the three models mentioned

above managed to predict the correct electric field signatures of narrow bipolar pulses at close and far distances. The model of Cooray *et al.* [236] managed to predict the correct signature for the derivatives of the narrow bipolar pulses and the HF and VHF bursts associated with them.

Two examples of these pulses are shown in Figure 4.44c. The average duration of the negative half cycle or zero crossing of these pulses was 10  $\mu$ s or less. According to LeVine [228] the peak amplitude of these pulses is of the order of one third of the peak of the return stroke fields recorded from the same thunderstorm. Recent data show that the peak amplitude of these pulses are comparable or even larger than the peak amplitudes of return stroke fields originated at the same distances [230–234]. In the VLF range the peak of the spectrum of the pulses occurred at 10–24 kHz with 16 kHz as the average. These pulses had a higher spectral content above 1 MHz than the return stroke spectral amplitudes. However, it is possible that the difference is caused by the different propagation characteristics of these pulses and return stroke fields. Most of these pulses occurred in isolation without detectable electrical activity before or after the pulse. Recent experimental data show that they sometimes occur just before or within the activity of the lightning flashes.

#### 4.7.2.4 Microsecond scale pulses with a smooth rise to peak

Fernando and Cooray [237] discovered that, in addition to the bipolar pulses described previously, the pulses generated by cloud flashes within the first 10 ms (the length of their record) of its initiation contain microsecond scale pulses with a smooth rise to peak (Figure 4.44d). The location of the pulse shown in Figure 4.44d is marked by an arrow in Figure 4.43. Most of these pulses begin with a slow front which rises slowly for 0.05–4  $\mu$ s to about 20 per cent of the peak field amplitude. At the end of the slow front the field rises rapidly to its peak value in about 0.1–0.2  $\mu$ s. Even though the average duration of these pulses was more than an order of magnitude shorter than the duration of return stroke radiation fields, the characteristics of the initial rising portion of the cloud pulses show a remarkable similarity to those of the radiation fields generated by subsequent return strokes.

## 4.8 Difference between the ground flashes and cloud flashes

The main difference between the ground flashes and cloud flashes is that the ground flashes neutralise the charge centre in an intermittent manner in a number of high current events, i.e. subsequent strokes, whereas in a cloud flash a continuous current may flow from one charge centre to the other during the initial and active part of the cloud flash. Only in the later part of the cloud flash do intermittent breakdowns transfer charge from the negative to the positive. This difference is probably caused by the fact that in ground flashes the presence of the ground will lead to a rapid neutralisation of the leader channel, giving rise to return strokes, whereas no good conductor is involved in cloud flashes and the neutralisation process should take place slowly in comparison to the return strokes. An interesting comparison can be made between the lightning flashes and laboratory discharges. Discharge between two metal electrodes takes place in one burst of ‘return stroke’, whereas a discharge between two non-conducting materials takes place intermittently in a series of discharges with low current amplitude [238]. The reason for this is that, in the case of non-conducting ‘electrodes’, the charges transported along the discharge channel will accumulate at its extremities, thereby reducing the

electric field and choking the discharge. As the charges dissipate slowly, the electric field recovers and reignites the discharge channel. In ground flashes the problem of charge dissipation is encountered only at the cloud end of the leader, whereas in cloud flashes the difficulty exists at both ends. Another difference is that in ground flashes the channels extend downward to high pressure region, whereas the vertical channel of cloud flashes extends into the low pressure region [41]. Owing to high pressure close to the ground level the ground end of the channel decays first and it will continue progressively into the upper reaches of the cloud. In the meantime negative charge continues to flow down the still conducting part of the channel. This would have the effect of filling the decaying channel with negative charge making it more difficult for the next discharge to occur. In the case of cloud flashes, the channel would be cut off first at the negative charge centre and as a result no negative charge will accumulate along the channel. Since most of the discharge events in a cloud flash travel upward from the negative to positive charge centre, this will make it easier for the subsequent discharges to reignite the upward path and maintain its conductivity.

One interesting question that can be raised concerning ground and cloud flashes is the following: Are both ground and cloud flashes initiated by the same mechanism? In order to find an answer to this question Ahmed *et al.* [239] analysed the details of the very first pulse generated by cloud and ground flashes at their initiation. They found that the first pulse in both cloud and ground flashes has identical features indicating a similar origin for these two types of lightning flashes.

#### **4.9 Energy dissipation in return strokes and lightning flashes and cloud potential**

The amount of energy dissipated during lightning flashes is an important parameter in many investigations involving lightning. It must be considered when characterising lightning flashes using their optical radiation from geostationary satellites and when quantifying the atmospheric production of ozone and nitrogen oxides, etc. For example, the uncertainty involved in estimating the amount of  $\text{NO}_x$  produced by lightning flashes can be attributed mainly to our poor knowledge about energy dissipation in lightning flashes. Unfortunately, it is not possible to measure the energy dissipated in a lightning flash directly. Consequently, researchers have employed indirect methods for this task. These methods can be divided into four categories. In the first category the amount of energy dissipated in lightning flashes is calculated on the basis of electrostatic energy considerations [208, 240–245]. The energy dissipation is calculated by assuming that a known amount of charge is transferred across a known potential difference during the lightning flash. The potential of the thundercloud with respect to the Earth is estimated by using familiar electrostatics principles. In the study conducted by Cooray [245] the size of the charge centres and the presence of leaders in lightning flashes were taken into account in the energy estimates. Table 4.19 summarises the results obtained by this method. In the second category the energy dissipation in lightning flashes is derived from the measured optical radiation [107–109, 242, 243, 246]. In the analysis, experimentally obtained relationships between the electrical and optical energy in spark discharges were extrapolated to obtain the electrical energy dissipation in lightning flashes on the basis of the measured optical radiation. Table 4.20 summarises the results obtained. In the third category the energy

Table 4.19 Estimates of energy in lightning derived from electrical measurements

Reference	Cloud potential assumed in the calculation, MV	Channel height, km	Charge dissipated, C	Energy, J	Comment
Wilson [240]	500	2	20	$10^{10}$	Leader + Return stroke
Malan [241]	500		0.6	$3 \times 10^8$	Leader + Return stroke
Krider et al. [242]	300		4.6	$7 \times 10^8$	Leader + Return stroke
Connor [243]		1.8	9.3	$1.5 \times 10^8$	Return stroke
Berger [244]	30	5	5	$1.5 \times 10^8$	Leader + Return stroke
Uman [208]	100	3	5	$5 \times 10^8$	Leader + Return stroke
Cooray [245]		5–7	variable (0.5–9)	$3.5 \times 10^8$	Energy given is for the return stroke stage with 5 C of charge dissipation

Table 4.20 Estimates of energy in lightning derived from optical measurements (adapted from [249])

Reference	Optical band, Å	Radiant energy per unit length, J/m	Mean peak radiant power, W	Energy dissipation per unit length, J/m
Connor [243]	3800–7000	580		
Barasch [246]	Visible	400	$4 \times 10^9$ (stroke)	
Krider <i>et al.</i> [242]	4000–11 000	870	$1.1 \times 10^{10}$ (stroke)	$2.3 \times 10^5$
Turman [8]	4000–11 000		$10^9$ (first stroke)	

Table 4.21 Estimates of energy in lightning derived from acoustic measurements (adapted from [249])

Reference	Energy estimate, J/m
Zhivlyuk and Mandel'shtam [247]	$10^3$
Newman [127]	$10^2$
Hill and Robb [276]	$5 \times 10^4$ – $10^5$
Few [248]	$10^5$

dissipation in lightning flashes is estimated by measuring the spectrum of thunder and relating it to the energy dissipation by applying the theory of shock waves [247, 248]. Table 4.21 summarises the results obtained. In the fourth category the shape and amplitude of the return stroke current are assumed, and the energy dissipated in the channel is calculated by analysing the temporal development of the channel properties as a function of time [123–125]. Table 4.22 summarises the results obtained using this technique.

The electrostatic estimations of energy dissipation during lightning flashes assume a certain potential of the cloud and then estimate the energy dissipation by

Table 4.22 *Estimates of energy in lightning derived from the theoretical analysis of the temporal development of channel properties (adapted from [249])*

Reference	Energy dissipation, J/m
Plooster [123]	$2.5 \times 10^3$
Hill [124]	$1.5 \times 10^4$

assuming the charge brought to ground during the lightning flash transferred across this potential. This raises the question: What is the potential of the cloud? Let us try to provide an answer to this question.

#### 4.9.1 *Potential of the cloud*

As mentioned in sections 4.6.2.4 and 4.6.8.3 Cooray *et al.* [72] evaluated the distribution of the charge along the stepped leader and dart leader channels from the charge transported to ground by first and subsequent return strokes. Since the background electric field below thunderclouds is approximately uniform, in their analysis Cooray *et al.* [72] have replaced the cloud with a charged sheet raised to a certain potential, say  $V$ . Then the electric field below the artificial cloud is  $V/H$  where  $H$  is the height to the charge centre. They also assumed that the stepped and the dart leader channels are good conductor and therefore maintain the cloud potential along their length. Utilising these assumptions and appealing to the bidirectional leader concept they managed to estimate the total charge dissipated by a return stroke as a function of the background electric field. Since the charge dissipated by the return strokes as a function of the peak currents were measured from the records of currents obtained by Berger [58] at mount San Salvatore, they could derive a relationship between the return stroke peak current and the way in which the charge dissipated by the return stroke is distributed along the leader channel. Since the charge dissipated by a return stroke as a function of the background electric field (or the cloud potential) is available one can combine it with the measured relationship between the charge and the peak return stroke current to derive a relationship between the return stroke peak current and the cloud potential. The results of that exercise are presented below.

##### 4.9.1.1 **Cloud potential and energy dissipation in first return strokes**

Based on the procedure described in the previous section one can show that the potential of the cloud (in volts) is connected to the first return stroke current peak (in kA) by the equation

$$V = 5.86 \times 10^6 + 1.569 \times 10^6 I_p - 3.279 \times 10^3 I_p^2 \quad (4.27)$$

This can be described approximately by reducing the accuracy at low currents by the equation

$$V = 3.0 \times 10^6 I_p^{0.813} \quad (4.28)$$

The above equation shows that a stepped leader that generates a typical current of 30 kA is associated with a cloud potential of 50 MV. This also shows that as the cloud potential decreases the current generated by the corresponding stepped leader decreases.

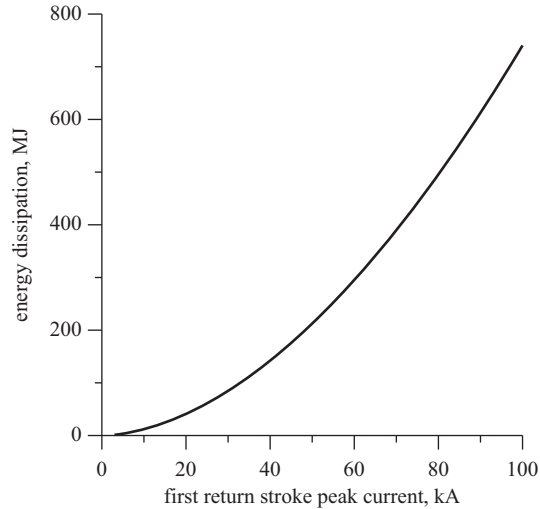


Figure 4.45 Energy dissipation in first return strokes as a function of return stroke peak current as calculated using (4.29)

Another interesting exercise that one can do with the above equation is to estimate the total energy dissipated by a return stroke. Now, the charge removed during a first return stroke is given by (4.9). This charge is transported across potential difference given by (4.28). Thus, the energy dissipated is just the charge times the potential difference, and the energy dissipated during a first return stroke of current  $I_p$  is given by

$$E = 1.86 \times 10^5 I_p^{1.8} \quad (4.29)$$

This equation is plotted in Figure 4.45. Thus, a typical return stroke of 30 kA dissipates about  $8.5 \times 10^7$  J. About one half of this will dissipate as the leader brings the charge, brought to ground during the return stroke, towards the ground and the other one half is generated by the return stroke. Thus, the energy dissipated by the return stroke is about  $4 \times 10^7$  J. Now, since the length of the channel assumed in the analysis is 4 km, a typical return stroke having a current of 30 kA dissipates about  $10^4$  J/m.

#### 4.9.1.2 Cloud potential and energy dissipation in subsequent return strokes

In the case of subsequent return strokes one can show that the potential of the cloud (in volts) is connected to the subsequent return stroke current peak (in kA) by the equation

$$V = 5.86 \times 10^6 + 0.72 \times 10^6 I_p - 0.691 \times 10^3 I_p^2 \quad (4.30)$$

Now, the charge removed during a first return stroke is given by (4.26). This charge is transported across potential difference given by (4.30). Thus, the energy dissipated is just the charge times the potential difference, and the energy dissipated during a subsequent stroke of current  $I_p$  is given by

$$E = 0.164 \times 10^6 \times I_p + 0.02 \times 10^6 I_p^2 - 0.019 \times 10^3 I_p^3 \quad (4.31)$$



This shows that a typical subsequent return stroke of 12 kA of current will release an energy of 4.7 MJ. For a 4 km channel this generates about 1 kJ/m.

#### 4.10 Measuring lightning-generated electric and magnetic fields

The electric fields generated by lightning flashes can be measured using either a field mill [250] or a flat plate (or a vertical whip) antenna [64, 66], each method having its advantages and disadvantages. The conventional method used to measure the magnetic field is the crossed loop antenna [10, 251]. The following is a brief description of these techniques.

##### 4.10.1 Electric field mill or generating voltmeter

The principle of operation of the field mill is illustrated in Figure 4.46. The plate marked *S* is the detector which is placed in a background electric field assumed for the moment to be uniform and steady. The plate marked *M* is a movable electrode which is at ground potential. This electrode can be moved back and forth in front of the sensing plate either exposing it to or screening it from the background electric field. Consider the situation shown in Figure 4.46 in which the sensing plate is completely exposed to the electric field. The electric field lines end on the plate and the total charge induced on the sensing plate is  $A\epsilon_0 E$  where *A* is the area of the plate. Assume that the plate *M* is moved back and forth in front of the sensing plate. This will change the exposed area of the sensing plate as a function of time and since the charge induced on the plate is a function of the exposed area of the sensing plate a current will flow between the sensing plate and ground. This current is given by

$$i(t) = \frac{da(t)}{dt} \epsilon_0 E \quad (4.32)$$

where  $a(t)$  is the instantaneous exposed area of the sensing plate. Thus, knowing the way in which the exposed area of the sensing plate vary in time, the background electric field can be obtained by measuring the current flowing between the sensing plate and ground.

Assume that *M* moves periodically back and forth over the sensing plate thus alternatively shielding and unshielding the sensing plate from the background electric field. If *M* moves back and forth *n* times per second then the output current oscillates with a period  $T_p$  equal to  $1/n$  and the peak amplitude proportional to the

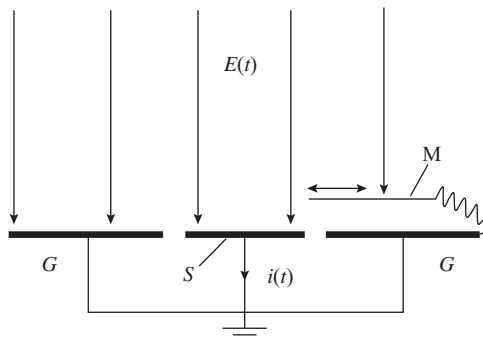


Figure 4.46 Principle of the electric field mill

background electric field. If the background field vary with the time then the envelope of the oscillating output voltage follows the background electric field. However, any rapid variation in the background electric field faster than the period  $T_p$  cannot be measured using the field mill. In other words the time resolution of the field mill is on the order of  $T_p$ . Thus, the rate of the periodic motion of  $M$  gives an upper limit to the resolution of the field that can be measured by a field mill. In modern field mills the time resolution is increased by utilising a rotating vaned wheel which alternatively shields or unshields the sensing electrode from the electric field as each vane rotates over it. If the rotational speed of the metal vane is  $n$  revolutions per second, and if it has  $m$  vanes, then the time resolution of the field mill will decrease to  $1/mn$ . Such field mills can measure faster variations in the background electric field than the one described above. In general the upper frequency limit of the modern field mills may range from 1 to 10 kHz. The main advantage of the field mill is that it can be used to measure the absolute value of the background field.

#### 4.10.2 Plate or whip antenna

The physical configuration of the plate (or whip) antenna is shown in Figure 4.47. In principle, the antenna is a metal object connected to ground through an electric circuitry. As the background electric field vary in time, the charge induced on the antenna also varies in time generating a current in the electrical circuitry.

If the dimension of the antenna is much smaller than the minimum wavelength of interest in the time varying electric field, the antenna will act as a capacitive voltage source with the voltage proportional to the background electric field  $e(t)$ .

The equivalent circuit of the antenna shown in Figure 4.47 is depicted in Figure 4.48 where  $C_a$  is the capacitance of the antenna to ground and  $C_c$  is the capacitance of the cable connected to the antenna. The effective height  $h_e$  of the antenna can be either calculated from theory or measured by applying a known electric field to the antenna and measuring the output voltage.

The electronic circuitry that can be used to obtain the background electric field from a plate or whip antenna is given in Figure 4.49a. The equivalent circuit of the electronic circuitry when connected to the antenna is given in Figure 4.49b.

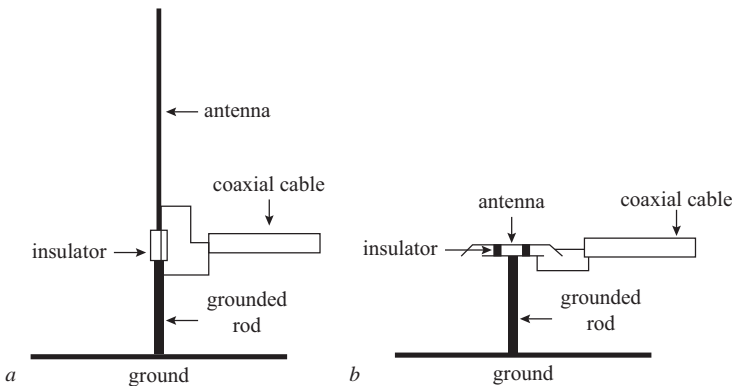


Figure 4.47 Antennas for the measurement lightning generated electric fields: (a) whip antenna; (b) plate antenna. The end of the cable is connected to the electronic circuit shown in Figure 4.41

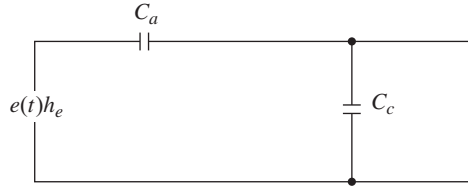


Figure 4.48 Equivalent circuit of the electric field measuring antenna.  $e(t)$  is the background electric field,  $h_e$  is the effective height of the antenna,  $C_a$  is the capacitance of the antenna and  $C_c$  is the capacitance of the cable

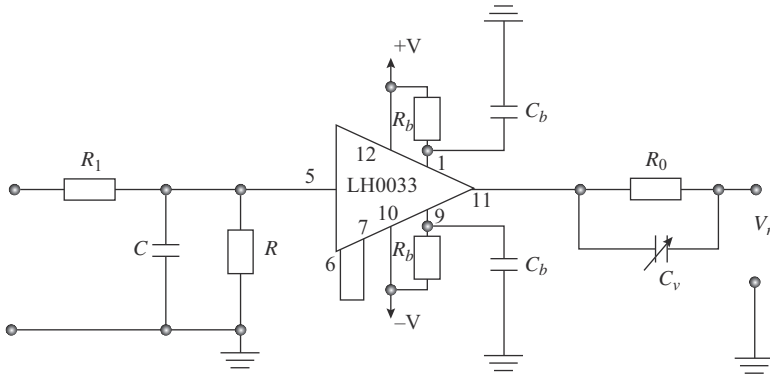


Figure 4.49a Electronic circuit used by Uppsala researchers in the measurement of electric fields using plate antenna.  $R_1 = 50\Omega$ ,  $R = 99M\Omega$ ,  $C = 15$  pF to nF,  $R_b = 100\Omega$ ,  $R_0 = 43\Omega$ ,  $C_b = 0.1 \mu F$  and  $C_v = 91$  pF. LH0033 is an operational amplifier with an input impedance of  $10^{13}\Omega$

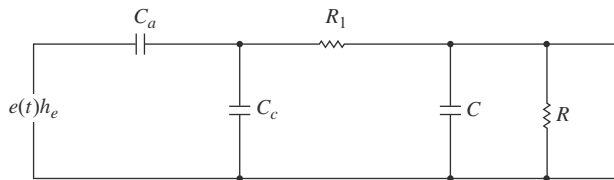


Figure 4.49b Equivalent circuit of the electric field measuring system

The relationship between the output signal  $V_m$  of the circuit and the electric field incident on the antenna is given in frequency domain by

$$V_m = E(s)h_e \frac{sC_a R}{1 + sF_1 + s(R_1 + R)(C_a + C_c)} \quad (4.33)$$

with

$$F_1 = RC[1 + sR_1(C_a + C_c)] \quad (4.34)$$

where  $s$  is the Laplace variable and  $E(s)$  is the Laplace transform of the background electric field  $e(t)$ . In general the resistance  $R_1$  (equal to the cable impedance) can be neglected and the above equation can be simplified to

$$V_m = E(s)h_e \frac{s}{s + \frac{1}{R(C_a + C_c + C)}} \frac{C_a}{C_a + C_c + C} \tag{4.35}$$

Assume for the moment that the background field incident on the antenna is a Heaviside step function of amplitude  $E_0$ . The output of the circuit in time domain  $v_m(t)$  can be obtained by taking the inverse Laplace transformation of the above equation. The result is

$$v_m = E_0 h_e \frac{C_a}{C_a + C_c + C} e^{-\{t/\tau_d\}} \tag{4.36}$$

where

$$\tau_d = R(C_a + C_c + C) \tag{4.37}$$

This shows that the output voltage decays exponentially with a time constant  $\tau_d$ . Since the applied field is a step the above results show that  $\tau_d$  controls the ability of the circuit to faithfully represent the low-frequency contents of the background electric field to be measured. In other words,  $\tau_d$  determines the low-frequency limit of the bandwidth of the measuring system. The lower 3 dB frequency limit of the bandwidth is given by  $1/2\pi\tau_d$ . To obtain an accurate measurement of the time varying background electric field the time constant of the antenna system should be much longer than the total duration of the time varying field. This point is illustrated further in the waveforms shown in Figure 4.50 where the effect of the time constant

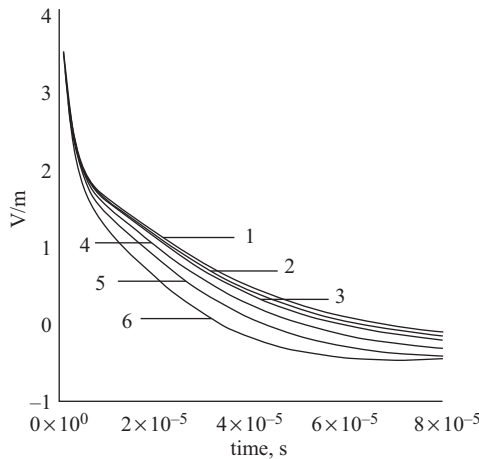
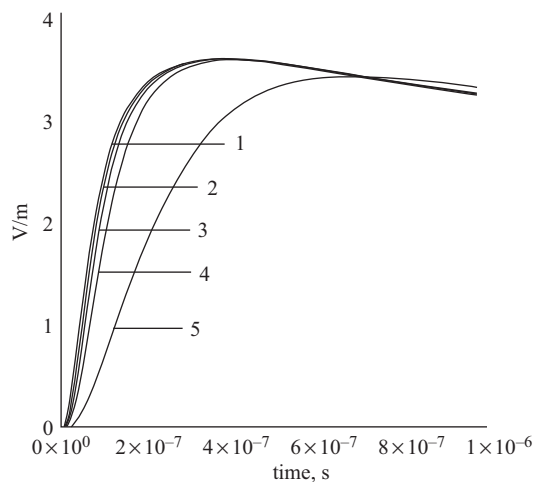


Figure 4.50 Curve 1 shows the electric radiation field at 100 km over perfectly conducting ground as simulated by the subsequent return stroke model described in section 9.6.3.4 Chapter 9. The rest of the curves show the effect of the decay time constant,  $\tau$ , on the output of the electric field measuring system when excited by this electric field. (2)  $\tau = 1$  ms, (3)  $\tau = 500$   $\mu$ s, (4)  $\tau = 200$   $\mu$ s, (5)  $\tau = 100$   $\mu$ s and (6)  $\tau = 50$   $\mu$ s. A positive field corresponds to an upward deflection

on the measurement of distant radiation field generated by a subsequent return stroke is illustrated. The data show that in order to obtain an accurate measurement of the radiation field, the duration of which is about 100  $\mu\text{s}$ , the decay time constant of the measuring system should be about 1 ms.

The upper frequency limit of the bandwidth of the measuring system is determined by the physical dimension of the antenna, the electronics components used in the circuitry and the recording system used to record the output of the measuring system. If  $l$  is the length or the diameter of the antenna, it is necessary that  $l \ll \lambda_m/4$  where  $\lambda_m$  is the minimum wavelength of interest in the electric field measurements. If this condition is not satisfied the current induced in different parts of the antenna will reach the electronic circuitry at different times thus invalidating the theory presented above. However, in many practical applications  $l$  may not exceed a few metres in the case of whip antenna and a few tens of centimetres in the case of plate antenna. Thus, the upper frequency limit of the bandwidth is determined mainly by the electronics circuitry and the recording system. The waveforms in Figures 4.51 and 4.52 show how the upper frequency limit (3 dB limit) of the bandwidth of the measuring system affects the measurements of subsequent stroke radiation field and its derivative. This data show that in order to perform an accurate measurement of the peak radiation field the upper limit of the bandwidth should exceed about 5 MHz. To make an accurate measurement of the peak radiation field derivative it has to exceed about 20 MHz.

This antenna system has an advantage over the field mill in providing a higher time resolution in the measurements. However, the disadvantage of this system is that, since there is a limit to which the decay time constant could be increased, it cannot measure the low-frequency components of the electric fields including DC.



*Figure 4.51* Curve 1 shows the electric radiation field at 100 km over perfectly conducting ground as simulated by the subsequent return stroke model described in section 9.6.3.4 of Chapter 9. The rest of the curves show the effect of the upper frequency limit (3 dB point),  $f_m$ , on the output of the electric field measuring system when excited by this electric field. (2)  $f_m = 20$  MHz, (3)  $f_m = 10$  MHz, (4)  $f_m = 5$  MHz, and (5)  $f_m = 1$  MHz. A positive field corresponds to an upward deflection

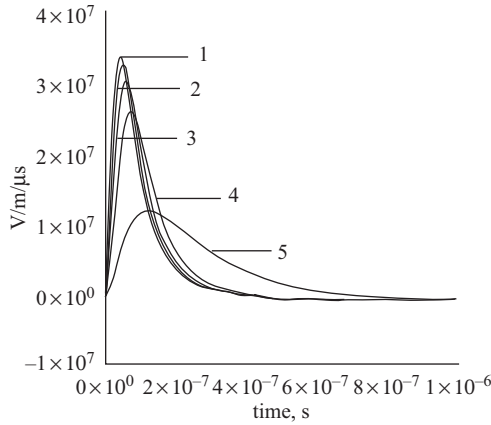


Figure 4.52 Curve 1 shows the derivative of the electric field depicted in curve 1 of Figure 4.51. The rest of the curves show the effect of the upper frequency limit (3 dB point),  $f_m$ , on the derivative of the output of the electric field measuring system when excited by this electric field. (2)  $f_m = 20$  MHz, (3)  $f_m = 10$  MHz, (4)  $f_m = 5$  MHz and (5)  $f_m = 1$  MHz. A positive field corresponds to an upward deflection

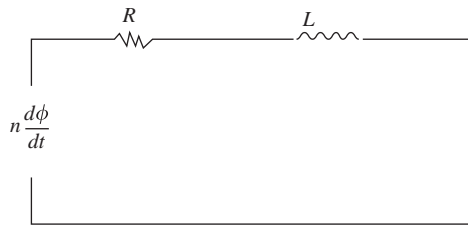


Figure 4.53 Equivalent circuit of the magnetic loop

### 4.10.3 Crossed loop antennas to measure the magnetic field

The voltage induced in a loop antenna due to an incoming magnetic field is proportional to the area of the loop multiplied by the derivative of the magnetic field component perpendicular to the loop. By measuring the voltage induced in two magnetic loops placed orthogonal to each other the component of the magnetic field parallel to the plane containing the two axes of the loops can be obtained. The magnetic field generated by a vertical lightning channel is parallel to the ground plane and is directed perpendicular to the line joining the point of observation and the lightning channel. Therefore, the direction of the lightning flash from a given point can be obtained by measuring the ratio of the voltages induced in two orthogonal magnetic loops.

The equivalent circuit of the loop antenna is shown in Figure 4.53. Here  $L$  is the inductance of the loop and  $R$  is its resistance. In practice the resistance of the loop can be neglected. The voltage,  $V$ , induced in the loop, assumed to be electrically small, is given by

$$V = -n \frac{d\phi}{dt} \tag{4.38}$$

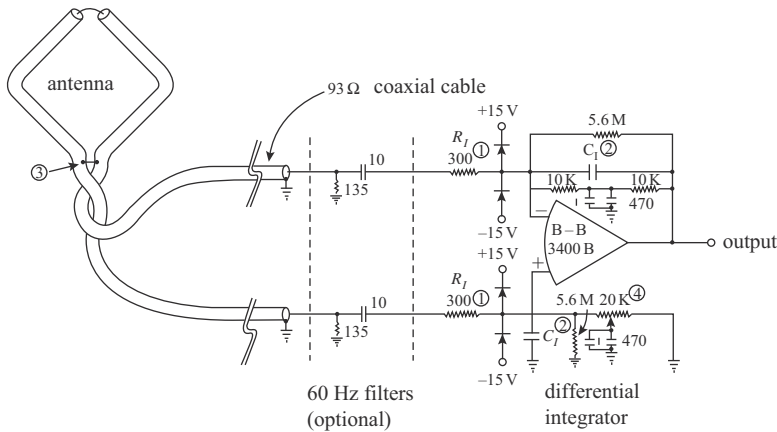


Figure 4.54 A magnetic field antenna formed from a single loop of 93  $\Omega$  coaxial cable and associated electronics to obtain an output proportional to the field (adapted [251])

where  $n$  is the number of turns in the loop and  $\phi$  is the magnetic flux threading the loop. The flux is given by

$$\phi = B(t)A\cos\theta \quad (4.39)$$

where  $B(t)$  is the time varying magnetic field,  $A$  is the area of the loop and  $\theta$  is the angle between the axis of the loop and the magnetic vector. Since the output of the antenna is proportional to the derivative of the magnetic field it has to be integrated to obtain a signal which is proportional to the magnetic field. An antenna and the corresponding electronics suitable for this purpose, as developed by Krider and Noggle [251], are shown in Figure 4.54.

The lower limit of the bandwidth of the magnetic field measuring system is determined by the integration time constant of the integrator. Thus, the integration time constant of the system should be much longer than the duration of the waveforms of interest. In the circuit shown in Figure 4.54, with  $C_1 = 1000$  pF the time constant of the integrator was 4 ms without the 60 Hz filters and 1.3 ms when they were included. As in the electric field measuring system the upper limit of the bandwidth is determined by the electronic circuitry and the recording system.

In measuring magnetic fields it is also necessary to avoid any contamination of the measurements due to the electric fields. In the measuring system shown in the Figure 4.54 this is achieved (a) by shielding the magnetic field sensor with an outer screen which is broken at the top to avoid any circulating currents and (b) by measuring the difference in the voltages induced at the two ends of the antenna thus cancelling out any contribution from the electric field.

## 4.11 Detection of lightning flashes

The lightning detection and location systems can be divided into two categories. If the detection systems belong to the first category the number of lightning flashes striking a given area is obtained without any specific knowledge concerning actual location of the lightning flashes. The lightning flash counters fall into this category. Detection systems that could pinpoint the point of strike or the detailed geometry of

the lightning channel fall into the second category. Examples are the magnetic direction finding systems, time of arrival systems and radio interferometric systems.

#### 4.11.1 Lightning flash counters

In lightning flash counters the lightning-generated electric field is received by a standardised electric field sensor (a vertical or a horizontal antenna) and the resulting current is passed through an electronic circuit. When the output voltage of the electronic circuit exceeds a threshold a counter is triggered. In order to avoid multiple counts due to subsequent strokes the trigger circuit has a dead time of about 1 s.

The first standard lightning flash counter was the one approved by the International Radio Consultative Committee (CCIR) [252]. This counter is fitted with a 7 m long vertical antenna that acts as the field sensor. The bandwidth of the electronic circuitry of this counter has 3 dB points at 3 kHz and 50 kHz with the peak at 10 kHz. CCIR counter-responds mainly to the radiation field of the lightning return strokes and Pierce [253] suggested the advantages of having a counter that responds to the electrostatic field of the lightning discharges. After several modifications such a counter was adopted by CIGRE as a standard and it is called CIGRE 500 Hz counter. This counter has a bandwidth of 100 Hz to 2.5 kHz with a peak at 500 Hz. It was fitted with a horizontal antenna located 5 m above ground. Tests conducted with this counter showed that a considerable fraction of its counts are due to cloud flashes and in order to achieve a better discrimination between ground and cloud flashes Anderson *et al.* [254] modified this counter to a frequency response peaked on 10 kHz with a bandwidth of 2.5–50 kHz. This modified counter is called CIGRE 10 kHz counter.

The ability of a lightning flash to trigger the counter depends on the strength of the electric field produced by that flash at the location of the counter. Thus, strong lightning flashes could trigger a counter at long range and weak lightning flashes can do that only if they are located close to it. Thus, the receiving range of a counter has to be defined in a statistical manner. The effective range of a lightning flash counter is defined as

$$R_e = \sqrt{2 \int_0^{\infty} P(r) r dr} \quad (4.40)$$

where  $P(r)$  is the probability that a lightning flash located at a distance  $r$  will be detected by the counter. In general, flash counters are designed to respond to ground flashes, but triggers due to cloud flashes cannot be avoided. Before one can obtain the ground flash density from the data it is necessary to correct it for triggers due to cloud flashes. If  $N$  is the total number of flashes registered by a counter within a given period of time then the total counts due to ground flashes within the same period is given by  $K \cdot N$  where  $K$  is the correction factor. Then the ground flash density  $N_g$  over that period of time at the location of the lightning flash counter is given by

$$N_g = \frac{K \cdot N}{\pi R_e^2} \quad (4.41)$$

The effective range of a counter for ground and cloud flashes can be obtained by long-term observations by different methods [254] or through calculations based



on the features of lightning-generated electromagnetic fields [255]. More recently, Mackerras [256] has developed an advanced lightning flash counter that can separate cloud flashes, negative ground flashes and positive ground flashes. This counter is in operation in several countries.

#### 4.11.2 *Magnetic direction finding*

In this technique the direction of the horizontal component of the magnetic field generated by the lightning flash is obtained at two spatially separated stations using crossed magnetic loops. Since the horizontal component of the magnetic field at a given point is perpendicular to the direction of the lightning strike as observed from that point, information obtained from two stations can be used through triangulation to obtain the point of strike of the lightning flash. Apparently, the possibility of locating lightning flashes through magnetic direction finding was first described by Watson-Watt and Herd [257] in 1926. Since then, both narrowband [258] and wide-band [259] direction finding systems have been utilised. The narrow-band systems were tuned to a frequency of about 5 kHz. At this frequency the attenuation of the signals propagating along the Earth ionospheric waveguide is minimum where the lightning signal is maximum.

If the lightning channel is vertical and the signal received by the loops is free of ionospheric reflections then the direction finder provides an accurate direction to the point of strike. However, in general the lightning channel is not vertical and the signal received by the direction finder may partly be due to the reflections of the lightning-generated magnetic field from the ionosphere. Both these facts can cause errors in the direction finding systems. The early magnetic direction finders had a low accuracy because of these errors. The modern broadband magnetic direction finders solve this problem by utilising the initial few microseconds of the return stroke signal which is free from ionospheric reflections [259]. Moreover, the first few microseconds of the return stroke signal is generated by the first few hundred metres of the lightning channel which is more or less straight and vertical.

The location accuracy of a direction finding system with two stations is reduced significantly when lightning flashes are located close to the baseline of the two stations and the system cannot provide a fix when a lightning flash is located on the baseline. This problem can be solved by increasing the number of direction finding stations. With a crossed loop direction finder it is impossible to determine whether a signal received by it is due to a negative ground flash in one direction or a positive ground flash in the opposite direction. This ambiguity in direction can be removed by measuring the polarity of the electric field simultaneously with the magnetic field and determining the polarity of the flash.

Thanks to the development of decision making electronics, the modern day direction finders can discriminate between cloud and ground flashes by utilising the characteristic features of the signals generated by respective lightning flashes [259]. Today, such systems are installed world-wide.

#### 4.11.3 *Time of arrival technique: VLF range*

The electromagnetic fields generated by lightning flashes propagate over the surface of the Earth with the speed of light, and the time of arrival of a particular feature of the electromagnetic radiation field (e.g. the peak of the radiation field) at several spatially separated stations can be utilised to obtain the location of the lightning flashes. Apparently Lewis *et al.* [260] are the first to describe such a

lightning locating system. The time difference between the arrival of the pulse at two stations will define a hyperbola on the surface of the Earth. The data from three stations define three hyperbolas, the intersection of which provides the location of the lightning flash. This method is sometimes defined as hyperbolic direction finding. With three stations, two points of intersection may appear in some regions and these ambiguities can be removed by having more than three stations.

The method will work without errors if (a) the time synchronisation between different stations can be achieved with a high resolution, (b) the bandwidth of the sensing elements at different stations are identical and (c) the radiation field of the lightning flash does not change its shape in propagating from the source to the sensing stations (i.e. there are no propagation effects). Points (a) and (b) can be solved without difficulties, but it is nearly impossible to realise (c). The reason for the latter is the finite ground conductivity which causes the peak of the radiation field to shift in time as it propagates from the source to the sensor. Since the length of the path of propagation and the ground conductivity may vary from one station to another the propagation effects may introduce a time delay of more than several microseconds between stations (see Chapter 11). This causes an error in the calculated point of strike.

Today, one can find lightning location systems that utilise both magnetic direction finding and time of arrival principle, thus increasing the accuracy of lightning location.

#### 4.11.4 Time of arrival technique: VHF range

During a lightning flash a large number of pulses whose rise times and durations are so short that they can excite systems tuned to HF and VHF ranges are generated. When excited by an impulse a receiving system tuned to a central frequency  $f_0$  and bandwidth  $B$  generates an oscillating output that decays in a time which is given approximately by  $1/B$ . If such an antenna system is used to tag the time of arrival of the impulsive events at several spatially separated stations the information can be utilised to obtain the location of the discharge events that gave rise to these impulses. The possibility was first suggested by Oetzel and Pierce [261]. Electrical breakdown process in air gives rise to impulses that can excite systems tuned to VHF, and by mapping the position of a large number of such pulses generated by lightning flashes an image of the lightning flash in three dimension can be obtained.

The VHF time of arrival systems can be divided into two categories, namely long baseline systems [1–3, 262, 263] and short baseline systems [264–266]. In the long baseline systems the antennas are separated by distances of several kilometres. From the measured time of arrival of the same pulse at different stations hyperbolic geometry should be used to obtain the position. In short baseline systems the incoming signal can be treated as a plane wave and straight-line geometry can be applied. One difficulty with the long baseline systems is the difficulty of identifying the same pulse feature in different antennas. Moreover, the number of impulsive events that excites the receiving systems at all the stations is limited. Some of these problems can be avoided by utilising short baseline systems. However, notwithstanding these difficulties, the pioneering work of Proctor [1, 3] demonstrated the feasibility of the technique as a tool of studying the physics and mechanism of the lightning flash. Proctor's system was tuned to a frequency of 355 MHz and the separation between stations was about 10–30 km. Today several systems that utilise this technique are in operation.

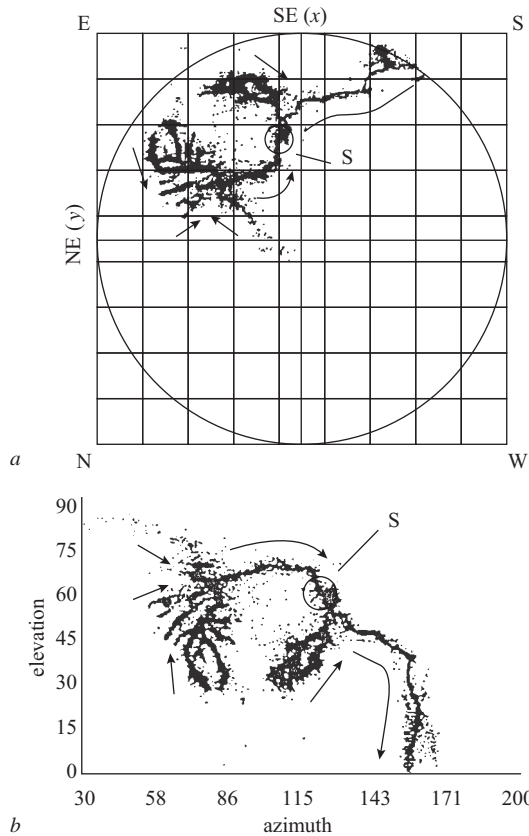


Figure 4.55 *The location of the radiation sources of a ground flash in both (a) projection plane and (b) azimuth-elevation format as located by the VHF interferometer technique. The discharge started in the region marked by a circle (adapted from [4])*

#### 4.11.5 VHF radio interferometry

VHF radio interferometry was first used for lightning studies by Hayanga and Warwik [267, 268]. The technique was further developed and improved by ONERA in France [269], by New Mexico Tech in the United States [4–6] and by Osaka University in Japan [270].

The general principle of the VHF interferometry is the following. Assume that a plane sinusoidal wave is incident on two antennas separated by a distance  $d$ . The direction of incidence of the plane wave can be characterised by azimuth angle  $\theta$  and elevation angle  $\phi$ . The phase difference  $\phi$  of the output signal of the two antennas will be related to the direction of arrival of the wave by

$$\phi = 2\pi d \sin\theta \cos\phi / \lambda \tag{4.42a}$$

where  $\lambda$  is the wavelength. The distance  $d$  may have values ranging from a few metres to a few tens of metres depending on the frequency or the wavelength of the

signal. If the system contains two sets of such antennas with orthogonal baselines then the phase difference between the outputs of the set of antennas is given by

$$\phi_1 = 2\pi d \sin\theta \cos\phi/\lambda \quad (4.42b)$$

$$\phi_2 = 2\pi d \cos\theta \cos\phi/\lambda \quad (4.42c)$$

By measuring the phase difference of the output of two independent pairs one can estimate the azimuth and the elevation of the incoming plane wave. Note however that in order to obtain a phase measurement it is necessary that the distance between the two antennas or baseline,  $d$ , should satisfy the criterion  $d/c \leq 1/B$  where  $c$  is the speed of light and  $B$  is the bandwidth of the antenna system. In order to locate the source two or more such antenna systems located at distances on the order of 10 km are needed. The development of a cloud to ground flash as observed by this technique is shown in Figure 4.55 [4–6].

The central frequency of the antenna system used by the New Mexico group is 274 MHz with a bandwidth of 6 MHz. The system that is in operation in France has a central frequency of 114 MHz with a bandwidth of 1 MHz. The Osaka group utilise a broad band system having a bandwidth of 10–200 MHz.

## References

- [1] Proctor, D. E., A radio study of lightning, Ph.D. thesis, University of Witwatersrand, Johannesburg, South Africa, 1976
- [2] Proctor, D. E., Lightning and precipitation in a small multi-cellular thunderstorm, *J. Geophys. Res.*, 88, 5421–5440, 1983
- [3] Proctor, D. E., VHF pictures of cloud flashes, *J. Geophys. Res.*, 86, 4041–4071, 1981
- [4] Shao, X. M., The development and structure of lightning discharges observed by VHF radio interferometer, Ph.D. thesis, New Mexico Institute of Mining and Technology, Socorro, 1993
- [5] Shao, X. M. and P. R. Krehbiel, The spatial and temporal development of intracloud lightning, *J. Geophys. Res.*, 101, 26641–26668, 1996
- [6] Shao, X. M., P. R. Krehbiel, R. J. Thomas, and W. Rison, Radio interferometric observations of cloud-to-ground lightning phenomena in Florida, *J. Geophys. Res.*, 100, 2749–2783, 1995
- [7] Orville, R. E., Global distribution of midnight lightning September to November 1977, *Mon. Weather Rev.*, 109, 391–395, 1981
- [8] Turman, B. N. and B. C. Edgar, Global lightning distributions at dawn and dusk, *J. Geophys. Res.*, 87, 1191–1206, 1982
- [9] Prentice, S. A., Frequencies of lightning discharges, in *Physics of Lightning*, R. H. Golde, ed., Academic Press, New York, NY, pp. 465–496, 1977
- [10] Krider, E. P., R. C. Noggle, A. E. Pifer, and D. L. Vance, Lightning direction-finding system for forest fire detection, *Bull. Am. Meteor. Soc.*, 61(9), 980–986, 1980
- [11] Kotaki, M., I. Kuriki, C. Katoh, and H. Sugiuchij, Global distribution of thunderstorm activity observed with ISS-b, *J. Radio Res. Labs. Japan*, 28, 49–71, 1981
- [12] Schumann, W. O. Über die strahlungslosen Eigenschwingungen einer leitenden Kugel, die von einer Luftschicht und einer Ionosphärenhülle umgeben ist, *Z. Naturf.*, 72, 149–154, 1952

- [13] Williams, E. R., Schumann resonance: A global tropical thermometer, *Science*, 256, 1184–1187, 1992
- [14] Orville, R. E., Cloud-to-ground lightning in the blizzard of '93, *Geophys. Res. Lett.*, 20(13), 1367–1370, July 9, 1993
- [15] Prentice, S. A. and D. Mackerras, The ratio of cloud to cloud ground lightning flashes in thunderstorms, *J. Appl. Meteor.*, 16, 545–549, 1977
- [16] Rakov, V. A., M. A. Uman, and R. Thottappillil, Review of lightning properties from electric field and TV observations, *J. Geophys. Res.*, 99, 10745–10750, May 20, 1994
- [17] Anderson, R. B., A. J. Eriksson, H. Kroninger, D. V. Meal, and M. A. Smith, Lightning and thunderstorm parameters. In *Lightning and Power Systems*, IEE Conference Publication No. 236, 5 pp., London, 1984
- [18] MacGorman, D. R., M. W. Maier, and W. D. Rust. Lightning strike density for the contiguous United States from thunderstorm duration records, NUREG/CR-3759, Office of Nuclear Regulatory Research, U.S. Nuclear Regulatory Commission, Washington, DC, 44 pp., 1984
- [19] Mackerras, D. and M. Darveniza, Latitudinal variation of lightning occurrence characteristics, *J. Geophys. Res.*, 99(D5), 10813–10821, May 20, 1994
- [20] Gunn, R., Electric field intensity inside of natural cloud, *J. Appl. Phys.*, 19, 481–484, 1948.
- [21] Winn, W. P., G. W. Schwede, and C. B. Moore, Measurements of electric fields in thunderclouds, *J. Geophys. Res.*, 79, 1761–1767, 1974
- [22] Winn, W. P., C. B. Moore, and C. R. Holmes, Electric field structure in an active part of a small, isolated thundercloud, *J. Geophys. Res.*, 86, 1187–1193, 1981
- [23] Marshall, T. C. and W. D. Rust, Electric field soundings through thunderstorms, *J. Geophys. Res.*, 96, 22297–22306, 1991
- [24] Marshall, T. C., M. P. McCarthy, and W. D. Rust, Electric field magnitudes and lightning initiation in thunderstorms, 3rd International Workshop on Physics of Lightning, France, 1997
- [25] Marshall, T. C., M. P. McCarthy, and W. D. Rust, Electric field magnitudes and lightning initiation in thunderstorms, *J. Geophys. Res.*, 100, 7097–7103, 1995
- [26] Cooray, V. *et al.* Initiation of ground flashes: Some microscopic electrical processes associated with precipitation particles, *24th International Conference on Lightning Protection*, Birmingham, United Kingdom, 1998
- [27] Taylor, G. I., Disintegration of water drops in an electric field, *Proc. Roy. Soc. A*, 280, 383–397, 1964
- [28] Crabb, J. A. and J. Latham, Corona from colliding drops as a possible mechanism for the triggering of lightning, *Q. J. R. Meteor. Soc.*, 100, 191–202, 1974
- [29] Nguyen M. D. and S. Michnowski, On the initiation of lightning discharge in a cloud 2. The lightning initiation on precipitation particles, *J. Geophys. Res.*, 101, 26675–26680, 1996
- [30] Latham, J. and J. E. Dye, Calculations on the electrical development of a small thunderstorm, *J. Geophys. Res.*, 94, 13141–13144, 1989
- [31] Mason, B. J., *The Physics of Clouds*, Clarendon Press, Oxford, 1971

- [32] Gurevich, A. V., Y. V. Medvedev, and K. P. Zybin, New type discharge generated in thunderclouds by joint action of runaway breakdown and extensive atmospheric shower, *Phys. Lett. A*, 329, 348–361, 2004
- [33] Moss, G. D., V. P. Pasko, N. Liu, and G. Veronis, Monte Carlo model for analysis of thermal runaway electrons in streamer tips in transient luminous events and streamer zones of lightning leaders, *J. Geophys. Res.*, 111, A02307, 2006
- [34] Beasley, W. H, M. A. Uman, and P. L. Rustan, Electric fields preceding cloud to ground lightning flashes, *J. Geophys. Res.*, 87, 4883–4902, 1982
- [35] Clarence, N. D. and D. J. Malan, Preliminary discharge processes in lightning flashes to ground, *Q. J. R. Meteor. Soc.*, 83, 161–172, 1957
- [36] Schonland, B. F. J., The lightning discharge, *Handb. Phys.*, 22, 576–628, 1956
- [37] Thomson, E. M., Characteristics of Port Moresby ground flashes, *J. Geophys. Res.*, 85, 1027–1036, 1980
- [38] Gomes, C., V. Cooray, and C. Jayaratne, Comparison of preliminary breakdown pulses observed in Sweden and in Sri Lanka, *J. Atmos. Terr. Phys.*, 60, 975–979, 1998
- [39] Baharudin, Z. A. *et al.* Electric field changes generated by the preliminary breakdown for the negative cloud-to-ground lightning flashes in Malaysia and Sweden, *J. Atmos. Sol.-Terr. Phys.*, 84–85, 15–24, 2012, doi:10.1016/j.jastp.2012.04.009
- [40] Cooray, V. and R. Jayaratne, What directs a lightning flash towards the ground?, *Sri Lankan J. Phys.*, 1, 1–10, 2000
- [41] Krehbiel, P. R., M. Brook, and R. McCrory, An analysis of the charge structure of lightning discharges to the ground, *J. Geophys. Res.*, 84, 2432–2456, 1979
- [42] Rustan, P. L., M. A. Uman, D. G. Childers, W. H. Beasley, and C. L. Lennon, Lightning source locations from VHF radiation data for a flash at Kennedy Space Center, *J. Geophys. Res.*, 85, 4893–4903, 1980
- [43] Ogawa, T., Initiation of lightning in clouds, *J. Atmos. Elec.*, 13, 121–132, 1993
- [44] Saunders, C. P. R., Thunderstorm electrification laboratory experiments and charging mechanisms, *J. Geophys. Res.*, 99, 10773–10779, 1994
- [45] Williams, E. R., Large scale charge separation in thunderclouds, *J. Geophys. Res.*, 6013–6025, 1985
- [46] Takahashi, T., Electrification of growing ice crystals, *J. Atmos. Sci.*, 35, 1220–1224, 1973
- [47] Jayaratne, E. R., C. P. R. Saunders, and J. Hallett, Laboratory studies of the charging of soft hail during ice crystal interactions, *Q. J. Roy. Meteor. Soc.*, 109, 609–630, 1985
- [48] Jacobson, E. A. and E. P. Krider, Electrostatic field changes produced by Florida lightning, *J. Atmos. Sci.*, 33, 103–117, 1976
- [49] Murphy, M. J. and E. P. Krider, Lightning charge analyses in small convection and precipitation electrification (CaPE) experiment storms. *J. Geophys. Res.*, 101(D23), 29615–29626, 1996
- [50] Krider, E. P., L. M. Maier, M. J. Murphy, and D. J. Schiber, The onset of electrification in Florida thunderstorms, 1998 Fall Meeting, AGU, San Francisco, CA, December 6–10, 1998

- [51] Chauzy, S., and S. Soula, Contribution of the ground corona ions to the convective charging mechanism. *Atmospheric Research*, 51, 279–300, 1999
- [52] Orville, R. E., Spectrum of the stepped leader, *J. Geophys. Res.*, 73, 6999–7008, 1968
- [53] Chen, M. *et al.* Spatial and temporal properties of optical radiation produced by stepped leaders, *J. Geophys. Res.*, 104, 27573–27584, 1999
- [54] Krider, E. P. and G. J. Radda, Radiation field waveforms produced by lightning stepped leaders, *J. Geophys. Res.*, 80, 2653–2657, 1975
- [55] Krider, E. P., C. D. Weidman, and R. C. Noggle, The electric fields produced by lightning stepped leaders, *J. Geophys. Res.*, 82, 951–960, 1977
- [56] Hill, J. D., M. A. Uman, and D. M. Jordan, High speed video observations of a lightning stepped leader, *J. Geophys. Res.*, 116, D16117, 2011, doi:10.1029/2011JD015818
- [57] Beasley, W. H., M. A. Uman, D. M. Jordan, and C. Ganesh, Simultaneous pulses in light and electric field from stepped leaders near ground level, *J. Geophys. Res.*, 88, 8617–8619, 1983
- [58] Berger, K., Novel observations on lightning discharges: Results of research on mount San Salvatore, *J. Franklin Inst.*, 283, 478–525, 1967
- [59] Schonland, B. F. J., Progressive lightning, IV, The discharge mechanism, *Proc. Roy. Soc. London Ser. A*, 164, 132–150, 1938
- [60] Orville, R. E. and V. P. Idone, Lightning leader characteristics in the thunderstorm research international program (TRIP), *J. Geophys. Res.*, 87, 11172–11192, 1982
- [61] Saba, M. M. F., M. G. Ballarotti, and O. Pinto Jr., Negative cloud-to-ground lightning properties from high-speed video observations. *J. Geophys. Res.*, 111, D03101, 2006, doi:10.1029/2005JD006415
- [62] Thomson, E. M., M. A. Uman, and W. H. Beasley, Speed and current for lightning stepped leaders near ground as determined from electric field records, *J. Geophys. Res.*, 90, 8136–8142, 1985
- [63] Pierce, E. T., Electrostatic field changes due to lightning discharges, *Q. J. Roy. Meteor. Soc.*, 81, 211–228, 1955
- [64] Kitagawa, N. and M. Brook, A comparison of intracloud and cloud-to-ground lightning discharges, *J. Geophys. Res.*, 65, 1189–1201, 1960
- [65] Kitagawa, N., On the electric field changes due to the leader processes and some of their discharge mechanism, *Pap. Meteorol. Geophys. (Tokyo)*, 7, 400–414, 1957
- [66] Cooray, V. and S. Lundquist, Characteristics of the radiation fields from lightning in Sri Lanka in the tropics, *J. Geophys. Res.*, 90, 6099–6109, 1985
- [67] Weidman, C. and E. P. Krider, Variations à l'échelle submicroseconde des champs électro-magnétiques rayonnés par la foudre, *Ann. Telecommun.*, 39, 165–174, 1984
- [68] E. P. Krider, C. Letenturier, and J. C. Willett, Submicrosecond field radiated during the onset of first return strokes in cloud-to-ground lightning, *J. Geophys. Res.*, 101(D1), 1589–1597, 1996
- [69] Weidman, C. and E. P. Krider, Submicrosecond risetimes in lightning return stroke fields, *Geophys. Res. Lett.*, 7, 955–958, 1980
- [70] Shonland, B. F. J., The pilot streamer in the lightning and the long spark, *Proc. Roy. Soc. London Ser. A*, 220, 25–38, 1953

- [71] Brook, M., N. Kitagawa, and E. J. Workman, Quantitative study of strokes and continuing currents lightning discharges to ground, *J. Geophys. Res.*, 67, 649–659, 1962
- [72] Cooray, V., V. Rakov, and N. Theethayi. The lightning striking distance – revisited, *J. Electrostat.*, 65(5–6), 296–306, 2007
- [73] Williams, D. P. and M. Brook, Magnetic measurement of thunderstorm currents, I. Continuing currents in lightning, *J. Geophys. Res.*, 68, 3243–3247, 1963
- [74] Krehbiel, P. R., An analysis of the electric field change produced by lightning, Ph.D. thesis, UMIST, Manchester, England, 1981
- [75] Schonland, B. F. J., Lightning and the long electric spark, *Adv. Sci.*, 19, 306–313, 1962
- [76] Uman, M. A. and D. K. McLain, Radiation field and the current of the lightning stepped leader, *J. Geophys. Res.*, 75, 1058–1066, 1970
- [77] Sopor, S., Review of the relaxation theory of the stepped leader, *Acta Geophys. Pol.*, 18, 73–77, 1970
- [78] Kasemir, H. W., A contribution to the electrostatic theory of a lightning discharge, *J. Geophys. Res.*, 65, 1873–1878, 1960
- [79] Kasemir, H. W., Static discharge and triggered lightning, *Proceedings of the 8th International Aerospace and Ground Conference on Lightning and Static Electricity*, 21–23, Fort Worth, Texas, June 1983
- [80] Mazur, V., Triggered lightning strikes to aircraft and natural intracloud discharges, *J. Geophys. Res.*, 94, 3311–3325, 1989
- [81] Mazur, V., Physical model of lightning initiation in aircrafts in thunderstorms, *J. Geophys. Res.*, 94, 3326–3340, 1989
- [82] Mazur, V. and L. H. Ruhnke, Common physical processes in natural and artificially triggered lightning, *J. Geophys. Res.*, 98, 12913–12930, 1993
- [83] Kawasaki, Z-I., and V. Mazur, Common physical processes in natural and triggered lightning in winter storms in Japan, 97, 12935–12945, 1992
- [84] Heckman, S. J. and E. R. Williams, Corona envelopes and lightning currents, *J. Geophys. Res.*, 94, 13287–13294, 1989
- [85] Laroche, P., V. Idone, A. Eybert-Berard, and L. Barret, Observations of bidirectional leader development in triggered lightning flashes, *Proceedings of the 1991 International Aerospace and Ground Conference on Lightning and Static Electricity*, 57.1–57.10, Cocoa Beach, FL, April 1991
- [86] Bondiou-Clergerie, A. *et al.* Experimental and theoretical study of bidirectional leader process, Part I: Experimental Investigation, *Proceedings of the 10th International Conference on Atmospheric Electricity*, Osaka, Japan, 1996
- [87] Cooray, V. and A. Galvan, The stepped leader as a source interference in electrical installations, *Proceedings of the 25th International Conference on Lightning Protection (ICLP)*, Rhodos, Greece, 2000
- [88] Kito, Y., K. Horii, Y. Higashiyama, K. Nakamura, Optical aspects of winter lightning discharges triggered by the rocket-wire technique in Hokuriku District of Japan. *J. Geophys. Res.*, 90(D4), 6147–6157, 1985
- [89] Asakawa, A. *et al.* Two types of lightning discharges to a high stack on the coast of the sea of Japan in winter, *IEEE Trans. Power Delivery*, 12(3), 1222–1231, 1997



- [90] Wada, A., A. T. Asakawa, A. Shindo, S. Yokoyama, Leader and return stroke speed of upward-initiated lightning. *Proceedings of the 12th International Conference on Atmospheric Electricity*, pp. 553–556.
- [91] Yokoyama, S., K. Miyake, T. Suzuki, S. Kanao, Winter lightning on Japan Sea coast – development of measuring system on progressing feature of lightning discharge. *IEEE Trans. Power Delivery*, 5(3), 1418, 1990
- [92] Lalande, P., *et al.*, Leader properties determined with triggered lightning techniques, *J. Geophys. Res.*, 103(D12), 14109–14115, 1998
- [93] Wang, D. *et al.* Attachment process in rocket triggered lightning, *J. Geophys. Res.*, 104, 2143–2150, 1999
- [94] Schonland, B. F. J. and H. Collens, Progressive lightning, *Proc. Roy. Soc. London Ser. A*, 143, 654–674, 1934
- [95] McEachron, K. B., Lightning to the empire state building, *J. Franklin Inst.*, 227, 149–217, 1939
- [96] Idone, V. P. and R. Orville, Lightning return stroke velocities in the thunderstorm research program, *J. Geophys. Res.*, 87, 4903–4916, 1982
- [97] Mach, D. M. and W. D. Rust, Two-dimensional velocity, optical risetime, and peak current estimates for natural positive lightning return strokes, *J. Geophys. Res.*, 98, 2635–2638, 1993
- [98] Mach, D. M. and W. D. Rust, Photoelectric return stroke velocity and peak current estimates in natural and triggered lightning, 94, 13237–13247, 1989
- [99] Cooray, V. and V. Rakov, Engineering lightning return stroke models incorporating current reflection from ground and finitely conducting ground effects, *IEEE Trans. Electromagn. Compat.*, 53, 773–781, 2011
- [100] Cooray, V., R. Montano and V. Rakov, A model to represent first return strokes with connecting leaders, *J. Electrostat.*, 40, 97–109, 2004
- [101] Jordan, D. M. and M. A. Uman, Variation in light intensity with height and time from subsequent lightning return strokes, *J. Geophys. Res.*, 88, 6555–6562, 1983
- [102] Jordan, D. M., V. A. Rakov, W. H. Beasley, and M. A. Uman, Luminosity characteristics of dart leaders and return strokes in natural lightning, *J. Geophys. Res.*, 102, 22025–22032, 1997
- [103] Gomes, C. and V. Cooray, Correlation between the optical signatures and current waveforms of long sparks: Application in lightning research, *J. Electrostat.*, 43, 267–274, 1998
- [104] Idone, V. P. and R. E. Orville, Correlated peak relative light intensity and peak current in triggered lightning subsequent strokes, *J. Geophys. Res.*, 90, 6159–6164, 1985
- [105] Krider, E. P., G. A. Dawson, and M. A. Uman, Peak power and energy dissipation in a single lightning flash, *J. Geophys. Res.*, 73, 3335–3339, 1968
- [106] Guo, C. and E. P. Krider, The optical radiation field signatures produced by lightning return strokes, *J. Geophys. Res.*, 87, 8913–8922, 1982
- [107] Guo, C. and E. P. Krider, The optical power radiated by lightning return strokes, *J. Geophys. Res.*, 88, 8621–8622, 1983
- [108] Maccerras, D., Photoelectric observations of the light emitted by lightning flashes, *J. Atmos. Terr. Phys.*, 35, 521–535, 1973
- [109] Turman, B. N., Analysis of lightning data from the DMSP satellite, *J. Geophys. Res.*, 83, 5019–5024, 1978

- [110] Orville, R. E., A high speed time-resolved spectroscopic study of the lightning return stroke, Parts 1, 2, 3, *J. Atmos. Sci.*, 25, 827–856, 1968
- [111] Takagi, N. *et al.* Expansion of the luminous region of the return stroke channel, *J. Geophys. Res.*, 103, 14131–14134, 1998
- [112] Cooray, V., A model for subsequent return strokes, *J. Electrostat.*, 30, 343–354, 1993
- [113] Schonland, B. F. J., The diameter of the lightning channel, *Phil. Mag.*, 37, 503–508, 1937
- [114] Evans, W. H. and R. L. Walker, High-speed photographs of lightning at close range, *J. Geophys. Res.*, 68, 4455–4461, 1963
- [115] Orville, R. E., Quantitative analysis of a lightning return stroke for diameter and luminosity changes as a function of space and time, *J. Geophys. Res.*, 79, 4059–4067, 1974
- [116] Schonland, B. F. J., *The Flight of Thunderbolts*, p. 63, Oxford University Press, New York, NY, 1950
- [117] Hill, R. D., Determination of charges conducted in lightning strokes, *J. Geophys. Res.*, 68, 1365–1375, 1963
- [118] Jones, R. D., Return stroke core diameter, *J. Geophys. Res.*, 73, 809–814, 1968
- [119] Uman, M. A., The diameter of lightning, *J. Geophys. Res.*, 69, 583–585, 1964
- [120] Taylor, A. R., Diameter of lightning as indicated by tree scars, *J. Geophys. Res.*, 70, 5693–5695, 1965
- [121] Braginskii, S. I., Theory of the development of spark channel, *Sov. Phys. – JETP (Engl. Trans.)*, 34, 1068–1074, 1958
- [122] Oetzel, G. N., Computation of the diameter of a lightning return stroke, *J. Geophys. Res.*, 73, 1889–1896, 1968
- [123] Plooster, M. N., Numerical model of the return stroke of the lightning channel, *Phys. Fluids*, 14, 2124–2133, 1971
- [124] Hill, R. D., Channel heating in return stroke lightning, *J. Geophys. Res.*, 76, 637–645, 1971
- [125] Paxton, A. H., R. L. Gardner, and L. Baker, Lightning return stroke: A numerical calculation of the optical radiation, *Phys. Fluids*, 29, 2736–2742, 1986
- [126] Garbagnati, E. and G. B. Lo Piparo, Parameter von Blitzströmen, *Elektrotech. Z. etz-a*, 103, 61–65, 1982
- [127] Newman, M. M., *Problems of Atmospheric and Space Electricity*, pp. 482–490, Elsevier, New York, NY, 1965
- [128] Fieux, R., C. Gary, and P. Hubert, Artificially triggered lightning above land, *Nature*, 257, 212–214, 1975
- [129] Liu, X.-S. *et al.* *J. Geophys. Res.*, 99(10), 727–731, 1994
- [130] Horii, K. and M. Nakano, Artificially Triggered Lightning, in *Handbook of Atmospheric Electrodynamics*, vol. 1. H. Volland, ed., pp. 151–166, CRC Press, Boca Raton, FL
- [131] Fisher, R. J., *et al.* Parameters of triggered lightning flashes in Florida and Alabama, *J. Geophys. Res.*, 98(22), 887–902, 1993
- [132] Leitenturier, C., J. H. Hamelin, and A. Eybert-Berard, Sub-microsecond characteristics of lightning return stroke currents, *IEEE Trans. Electromagn. Compat.*, 33, 351–357, 1991
- [133] Rakov, V., Lightning discharges triggered using rocket and wire techniques, *Recent Res. Dev. Geophys.*, 2, 141–171, 1999

- [134] Berger, K., R. B. Anderson, and H. Kroninger, Parameters of lightning flashes. *Electra*, 80, 23–37, 1975
- [135] Guerrieri, S., C. A. Nucci, F. Rachidi, and M. Rubinstein, On the influence of elevated strike objects on directly measured and indirectly estimated lightning current, *IEEE Trans. Power Delivery*, 33, 1543–1551, 1998
- [136] Cooray, V., A model for negative first return strokes in lightning flashes, *Phys. Scr.*, 55, 119–128, 1997
- [137] Cooray, V. and A. Galvan, A negative return stroke model for engineering applications, *Proceedings of the 25th International Conference on Lightning Protection (ICLP)*, Rhodes, Greece, 2000
- [138] Visacro, S., A. Soares Jr., M. A. O. Schroeder, L. C. L. Cherchiglia, and V. J. de Sousa. Statistical analysis of lightning current parameters: Measurements at Morro do Cachimbo Station, *J. Geophys. Res.*, 109, D01105, 2004, doi:10.1029/2003JD003662
- [139] Takami, J. and S. Okabe, Observational results of lightning current on transmission towers, *IEEE Trans. Power Delivery*, 22, 547–556, 2007
- [140] Anderson, R. B. and A. J. Eriksson, Lightning parameters for engineering application, *Electra*, 170, 65–102, 1979
- [141] P. Depasse, Statistics on artificially triggered lightning, *J. Geophys. Res.*, 99, 18515–18522, 1994
- [142] Berger, K., Methoden und Resultate der Blitzforschung auf dem Monte San Salvador bei Lugano in den Jahren 1963–1971, *Bull. Schweiz. Elektrotech. Ver.*, 63, 1403–1422, 1972
- [143] Schoene, J., M. A. Uman, and V. R. Rakov, Return stroke peak current versus charge transfer in rocket-triggered lightning. *J. Geophys. Res.*, 115, D12107, 2010, doi:10.1029/2009JD013066
- [144] Lin, Y. T. *et al.* Characterization of lightning return stroke electric and magnetic fields from simultaneous two-station measurements, *J. Geophys. Res.*, 84, 6307–6314, 1979
- [145] Cooray, V., The modelling of positive return strokes in lightning flashes, *J. Atmos. Sol.-Terr. Phys.*, 62, 169–187, 2000
- [146] Weidman, C. and E. P. Krider, The fine structure of lightning return stroke wave forms, *J. Geophys. Res.*, 83, 6239–6247, 1978
- [147] Cooray, V., and S. Lundquist, On the characteristics of some radiation fields from lightning and their possible origin in positive ground flashes, *J. Geophys. Res.*, 87, 11203–11214, 1982
- [148] Cooray, V., Further characteristics of positive radiation fields from lightning in Sweden, *J. Geophys. Res.*, 84, 11807–11815, 1984
- [149] Cooray, V., M. Fernando., C. Gomes, and T. Sorensen., The fine structure of positive lightning return-stroke radiation fields, *IEEE Trans. Electromagn. Compat.*, 46, 87–95, 2004
- [150] Ishii, M. and J. Hojo, Statistics of fine structure of cloud-to-ground lightning field waveforms, *J. Geophys. Res.*, 94, 13272–13274, 1989
- [151] Willett, J. C. and P. E. Krider, Rise times of impulsive high-current processes in cloud-to-ground lightning, *IEEE Trans. Antennas Propag.*, 48, 1442–1451, September 2000
- [152] Mach, D. M. and W. D. Rust, Two-dimensional speed and optical risetime estimates for natural and triggered dart leaders, *J. Geophys. Res.*, 102(D12), 13673–13684, June 27, 1997

- [153] Cooray, V., P. Idone, and R. E. Orville, Velocity of a self-propagating discharge as a function of current parameters with special attention to return strokes and dart leaders, papers presented at the 1989 *International Conference on Lightning and Static Electricity*, pp. 1A.3.1–1A.3.9, University of Bath, England, September 26–28, 1989
- [154] Cooray, V., Variation of return stroke velocity over the first few hundred meters and its relationship to the slow front in return stroke radiation fields, *Inst. Phys. Conf. Ser.*, 143, 235–240, 1995
- [155] Cooray, V. and M. Fernando, Effects of branches, charge irregularities and tortuosity of the stepped leader channel on the current, electromagnetic fields and HF radiation of return strokes, *Proceedings of the International Conference on Lightning Protection*, Uppsala, 2008
- [156] Cooray, V. and R. E. Orville, The effects of variation of current amplitude, current risetime and return stroke velocity along the return stroke channel on the electromagnetic fields generated by return strokes, *J. Geophys. Res.*, 95(D11), 18617–18630, October 1990
- [157] Gomes, C. and V. Cooray., Long impulse currents associated with positive return strokes, *J. Atmos. Sol.-Terr. Phys.*, 60, 693–699, 1998
- [158] Boccippio, D. J. *et al.* Sprites, Q-bursts and positive ground flashes, *Science*, 269, 1078–1091, 1995
- [159] Master, M. J., M. A. Uman, W. H. Beasley, and M. Darveniza, Lightning induced voltages on power lines: Experiment. *IEEE Trans. Power Appar. Syst.*, PAS-103, 2519–2529, 1984
- [160] Willett, J. C., E. P. Krider, and C. Leteinturier, Submicrosecond field variations during the onset of first return strokes in cloud-to-ground lightning, *J. Geophys. Res.*, 103, 9027–9034, 1998
- [161] Rakov, V. and M. Uman, Long continuing current in negative lightning ground flashes, *J. Geophys. Res.*, 95, 5455–5470, April 20, 1990
- [162] Cooray, V., R. Jayaratne, and K. L. Cummins, On the peak amplitude of lightning return stroke currents striking the sea, *Atmos. Res.*, <http://dx.doi.org.ezproxy.its.uu.se/10.1016/j.atmosres.2013.07.012>, 2013
- [163] Takagi, M., VHF radiation from ground discharges, *Proceedings of the Research Institute on Atmospheric*, Nagoya University, Japan, pp. 163–168, 1969
- [164] Brook, M. and N. Kitagawa, Radiation from lightning discharges in the frequency range 400–1000 Mc/s, *J. Geophys. Res.*, 69, 2431–2434, 1964
- [165] LeVine, D. M. and E. P. Krider, The temporal structure of HF and VHF radiations during Florida lightning return strokes, *Geophys. Res. Lett.*, 4, 13–16, January 1977
- [166] Cooray, V. and H. Pérez, HF radiation at 3 MHz associated with positive and negative return strokes, *J. Geophys. Res.*, 99, 10633–10640, May 20, 1994
- [167] Kawasaki, Z. and V. Mazur, Common physical processes in natural and triggered lightning in winter storms in Japan, *J. Geophys. Res.*, 97, 12935–12945, 1992
- [168] Cooray, V., Temporal behaviour of lightning HF radiation at 3 MHz near the time of first return strokes, *J. Atmos. Terr. Phys.*, 48, 73–78, 1986
- [169] LeVine, D. M., L. Gesell, and M. Kao, Radiation from lightning return strokes over finitely conducting Earth, *J. Geophys. Res.*, 91, 11897–11908, 1986

- [170] Jayaratne, K. P. S. C. and V. Cooray, The lightning HF radiation at 3 MHz during leader and return stroke processes, *J. Atmos. Terres. Phys.*, 56, 493–501, 1994
- [171] Edirisinghe, M. and V. Cooray, Fine structure signatures in ground flashes as a source of HF radiation, *International Letters of Chemistry, Physics and Astronomy* (ILCPA), 1, 91–104, 2014
- [172] Brook, M. and T. Ogawa, The cloud discharge, in *Lightning, vol. 1, Physics of Lightning*, R. H. Golde, ed., Academic, San Diego, CA, 1977
- [173] Pierce, E. T., Atmospheric and radio noise, in *Lightning, vol. 1, Physics of Lightning*, R. H. Golde, ed., Academic, San Diego, CA, 1977
- [174] Cooray, V. and G. Cooray, Electromagnetic radiation field of an electron avalanche, *Atmos. Res.*, 117, 18–27, November 1, 2012, doi:10.1016/j.atmosres.2011.06.004
- [175] LeVine, D. M. and R. Meneghini, Simulation of radiation from lightning return strokes: The effects of tortuosity, *Radio Sci.*, 13, 801–809, 1978
- [176] Horner, F. and P. A. Bradley, The spectra of atmospheric sferics from near lightning discharges, *J. Atmos. Terr. Phys.*, 26, 1155–1166, 1964
- [177] Willett, J. C., J. C. Bailey, C. Letenturier, and E. P. Krider, Lightning electromagnetic radiation field spectra in the interval from 0.2 to 20 MHz, *J. Geophys. Res.*, 95, 20367–20387, November 20, 1990
- [178] LeVine, D. M., Review of measurements of the RF Spectrum of radiation from lightning, *Meteor. Atmos. Phys.*, 37, 195–204, 1987
- [179] Taylor, C. D., External interaction of the nuclear EMP with aircraft and missiles, *IEEE Trans. Electromagn. Compat.*, 20, 64–76, 1978
- [180] Serhan, G. I., M. A. Uman., D. G. Childers, and Y. T. Lin, The RF spectra of first and subsequent lightning return strokes in the 1- to 200-km range, *Radio Sci.*, 15, 1089–1094, 1980
- [181] Weidman, C. D. and E. P. Krider, The amplitude spectra of lightning radiation fields in the interval from 1 to 20 MHz, *Radio Sci.*, 21, 964–970, 1986
- [182] Weidman, C. D., E. P. Krider, and M. A. Uman, Lightning amplitude spectra in the interval from 100 kHz to 20MHz, *Geophys. Res. Lett.*, 8, 931–934, 1981
- [183] Ye, M. and V. Cooray, Propagation effects caused by a rough ocean surface on the electromagnetic fields generated by lightning return strokes, *Radio Sci.*, 29, 73–85, 1994
- [184] Cooray, V., Interaction of electromagnetic fields produced by lightning flashes with electrical networks: The influence of propagation effects, *Proceedings of the International Conference on Lightning Protection*, Birmingham, England, 1998
- [185] Sonnadara, U., V. Cooray, and M. Fernando, The lightning radiation field spectra of cloud flashes in the interval from 20 kHz to 20 MHz, *IEEE Trans. Electromagn. Compat.*, 48(1), 234–239, 2006
- [186] Ahmad, N. A., Z. Baharudin, M. Fernando, and V. Cooray, Radiation field spectra of long duration cloud flashes, in *Broadband and HF Radiation from Cloud Flashes and Narrow Bipolar Pulses*, Ph.D. thesis of N. A. Ahmad, University of Uppsala, Uppsala, 2011
- [187] Kitagawa, N., M. Brook, and E. J. Workman, Continuing currents in cloud-to-ground lightning discharges, *J. Geophys. Res.*, 67, 637–647, 1962
- [188] Shindo, T. and M. A. Uman, Continuing current in negative cloud-to-ground lightning, *J. Geophys. Res.*, 94(D4), 5189–5198, 1989

- [189] Saba, M. M. F., M. G. Ballarotti, and O. Pinto Jr., Negative cloud-to-ground lightning properties from high-speed video observations, *J. Geophys. Res.*, 111, D03101, 2006
- [190] Heidler, F. and C. Hofp, Measurement results of the electric fields in cloud to ground lightning in nearby Munich, Germany, *IEEE Trans. Electromagn. Compat.*, 40, 436–443, 1998
- [191] Thomson E. M., Characteristics of Port Moresby ground flashes, *J. Geophys. Res.*, 85(C2), 1027–1036, February 20, 1980
- [192] Livingston, J. M. and E. P. Krider, Electric fields produced by Florida thunderstorms, *J. Geophys. Res.*, 83(C1), 385–401, 1978
- [193] Saba, M. M. F. *et al.* High-speed video observations of positive lightning flashes to ground, *J. Geophys. Res.*, 115, D24201, 2010, doi:10.1029/2010JD014330
- [194] Rakov, V. A. and M. A. Uman, Some properties of negative cloud-to-ground lightning flashes versus stroke order, *J. Geophys. Res.*, 95, 5447–5453, 1990
- [195] Ballarotti, M. G., M. M. F. Saba, and O. Pinto Jr., High-speed camera observations of negative ground flashes on a millisecond-scale, *Geophys. Res. Lett.*, 32, L23802, 2005, doi:10.1029/2005GL023889
- [196] Malan, D. J. and H. Collens, Progressive lightning, III, The fine structure of return lightning strokes, *Proc. Roy. Soc. London Ser. A*, 162, 175–203, 1937
- [197] Thottappillil, R. *et al.* Properties of M components from currents measured at triggered lightning channel base, *J. Geophys. Res.*, 100, 25711–25720, December 20, 1995
- [198] Jordan, D. M., V. P. Idone, R. E. Orville, V. A. Rakov, and M. A. Uman, Luminosity characteristics of lightning M components, *J. Geophys. Res.*, 100, 25695–25700, 1995
- [199] Rakov, V. A., R. Thottappillil, M. A. Uman, and P. Barker, Mechanism of the lightning M component, *J. Geophys. Res.*, 100, 25701–25710, December 20, 1995
- [200] Rakov, V. A., R. Thottappillil, and M. A. Uman, Electric field pulses in K and M changes of lightning ground flashes, *J. Geophys. Res.*, 97, 9935–9950, June 20, 1992
- [201] Malan, D. J. and B. F. J. Schonland, The electrical processes in the intervals between the strokes of a lightning discharge, *Proc. Roy. Soc. London Ser. A*, 206, 145–163, 1951
- [202] Thottappillil, R., V. A. Rakov, and M. A. Uman, K and M changes in close lightning ground flashes in Florida, *J. Geophys. Res.*, 95, 18631–18640, 1990
- [203] Thomson, E. M., The dependence of lightning return stroke characteristics on latitude, *J. Geophys. Res.*, 85, 1050–1056, February 20, 1980
- [204] Cooray, V. and H. Pérez, Some features of lightning flashes observed in Sweden, *J. Geophys. Res.*, 99, 10683–10688, May 20, 1994
- [205] Cooray, V. and K. P. S. C. Jayaratne, Characteristics of lightning flashes observed in Sri Lanka in the tropics, *J. Geophys. Res.*, 99, 21051–21056, October 20, 1994
- [206] Thottappillil, R. *et al.* Lightning subsequent-stroke electric field peak greater than the first stroke peak and multiple ground terminations, *J. Geophys. Res.*, 97, 7503–7509, 1992

- [207] Orville, R. E., Spectrum of the lightning dart leader, *J. Atmos. Sci.*, 32, 1829–1837, 1975
- [208] Uman, M. A., *Lightning*, McGraw-Hill, New York, NY, 1969
- [209] Idone, V. P., R. E. Orville, P. Hubert, L. Barret, and A. Eybert-Berard, Correlated observations of three triggered lightning flashes, *J. Geophys. Res.*, 89, 1385–1394, 1984
- [210] Rubinstein, M. *et al.* Characterization of vertical electric fields 500 m and 30 m from triggered lightning, *J. Geophys. Res.*, 100, 8863–8872, 1995
- [211] Crawford, D. E. *et al.* The close lightning electromagnetic environment: dart leader electric field change versus distance, *J. Geophys. Res.*, 106, 14909–14917, 2001
- [212] Mäkelä, J. S., M. Edirisinghe, M. Fernando, R. Montaña, and V. Cooray, HF radiation emitted by chaotic leader processes, *J. Atmos. Sol.-Terr. Phys.*, 69(6), 707–720, 2007
- [213] Cooray, V., A Model for dart leaders in lightning flashes, *J. Atmos. Elec.*, 16, 145–159, 1996
- [214] Cooray, V., M. Becerra and V. Rakov, On the electric field at the tip of dart leaders in lightning flashes, *J. Atmos. Terr. Phys.*, 71, 1397–1404, 2009
- [215] Jordan, D. M. *et al.* Observed dart leader speed in natural and triggered lightning, *J. Geophys. Res.*, 97, 9951–9957, June 20, 1992
- [216] Campos, L. Z. S. *et al.* Does the average speed of a lightning leader change as it approaches the ground? – an observational approach, *21st International Lightning Detection Conference*, Orlando, FL, 2010
- [217] Schonland, B. F. J., D. J. Malan, and H. Collens, Progressive lightning, Pt.2. *Proc.Roy.Soc. London Ser. A*, 152, 595–625, 1935
- [218] Wang, D. *et al.* Attachment process in rocket-triggered lightning strokes, *J. Geophys. Res.*, 104, 2143–2150, January 27, 1999
- [219] Weidman, C. D., The submicrosecond structure of lightning radiation fields, Ph.D. dissertation, University of Arizona, 1982
- [220] Bailey, J. C. and J. C. Willett, *Catalog of Absolutely Calibrated Range Normalized Wideband Electric Field Waveforms from Located Lightning Flashes in Florida: July 24 and August 14, 1985 Data*, NRL Memorandum Report No. 6497, 1989
- [221] Gomes, C., V. Cooray, M. Fernando, and C. Jayaratne, Chaotic pulse trains associated with negative subsequent strokes, *Proceedings of the International Conference on Lightning Protection*, Birmingham, England, 1998
- [222] Ogawa, T. and M. Brook, Charge distribution in thunder clouds, *Q. J. R. Meteor. Soc.*, 95, 513–525, 1969
- [223] Bils, J. R., E. M. Thompson, M. A. Uman, and D. Mackerras, Electric field pulses in close lightning cloud flashes, *J. Geophys. Res.*, 93, 15933–15940, 1988
- [224] Villanueva, Y., V. A. Rakov, M. A. Uman, and M. Brook, Microsecond-scale electric field pulses in cloud lightning discharges, *J. Geophys. Res.*, 99, 14353–14360, 1994
- [225] Weidman, C. D. and E. P. Krider, The radiation field wave forms produced by intracloud lightning discharge processes, *J. Geophys. Res.*, 84, 3159–3164, June 20, 1979
- [226] Krider, E. P., G. J. Radda, and R. C. Noggle, Regular radiation field pulses produced by intracloud lightning discharges, *J. Geophys. Res.*, 80, 3801–3804, 1975

- [227] Rakov, V. A., M. A. Uman, G. R. Hoffman, M. W. Masters, and M. Brook, Bursts of pulses in lightning electromagnetic radiation: Observations and implications for lightning test standards, *IEEE Trans. Electromagn. Compat.*, 38(2), 156–164, May 1996
- [228] LeVine, D. M., Sources of the strongest RF radiation from lightning, *J. Geophys. Res.*, 85, 4091–4095, 1980
- [229] Willett, J. C., J. C. Bailey, and E. P. Krider, A class of unusual lightning electric field waveforms with very strong high-frequency radiation, *J. Geophys. Res.*, 94, 16255–16267, November 20, 1989
- [230] Nag, A. and V. A. Rakov, Compact intracloud lightning discharges: 1. Mechanism of electromagnetic radiation and modeling, *J. Geophys. Res.*, 115, D20102, 2010, doi:10.1029/2010JD014235
- [231] Nag, A. and V. A. Rakov, Compact Intracloud lightning discharges: 2. Estimation of electrical parameters, *J. Geophys. Res.*, 115, D20103, 2010, doi:10.1029/2010JD014237
- [232] Eack, K. B., Electrical characteristics of narrow bipolar events, *Geophys. Res. Lett.*, 31, L20102, 2004, doi: 10.1029/2005GL023975
- [233] Smith, D. A. *et al.* A distinct class of isolated intracloud discharges and their associated radio emissions, *J. Geophys. Res.*, 104(D4), 4189–4212, 1999, doi:10.1029/1998JD200045
- [234] Ahmad, N. A. *et al.* The characteristics of narrow bipolar pulses in Malaysia. *J. Atmos. Sol.-Terr. Phys.*, 72, 534–540, 2010
- [235] Watson, S. S. and T. C. Marshall, Current propagation model for a narrow bipolar pulse, *Geophys. Res. Lett.*, 34, L04816, 2007, doi: 10.1029/2006GL027426
- [236] Cooray, V. *et al.* Electromagnetic fields of a relativistic electron avalanche with special attention to the origin of lightning signatures known as Narrow Bipolar Pulses, *Atmos. Res.*, <http://dx.doi.org.ezproxy.its.uu.se/10.1016/j.atmosres.2013.12.011>, 2013
- [237] Fernando, M. and V. Cooray, Sub-microsecond structure of electric field pulses generated by cloud flashes, *Proceedings of the International Conference on Lightning Protection*, Birmingham, England, 1998
- [238] Bendjamine, J., Characteristics of electrostatic discharges (ESD) based on current, optical and magnetic radiation fields, doctoral thesis, University of Uppsala, Uppsala, 2000
- [239] Ahmad, N. A. *et al.* (The first electric field pulse of cloud and cloud-to-ground lightning discharges. *J. Atmos. Sol.-Terr. Phys.*, 72, 143–150, 2010
- [240] Wilson, C. T. R., Investigations on lightning discharges and on the electric field of thunderstorms, *Philos. Trans. Roy. Soc. London. Ser. A*, 221, 73–115, 1920
- [241] Malan, D. J., *Physics of Lightning*, English University Press, London, 1963
- [242] Krider, E. P., G. A. Dawson, and M. A. Uman, Peak power and energy dissipation in a single stroke lightning flash, *J. Geophys. Res.*, 73, 3335–3339, 1968
- [243] Conner, T. R., *The 1967 APRA-AEC Joint Lightning Study at Los Alamos, vol. 1, LA-3754*, Los Alamos Scientific Laboratory, Los Alamos, NM, 1967
- [244] Berger, K., The earth flash, in *Lightning*, R. H. Golde, ed., pp. 119–190, Academic, San Diego, CA, 1977
- [245] Cooray, V., Energy dissipation in lightning flashes, *J. Geophys. Res.*, 102, 21401–21410, 1997



- [246] Barasch, G. E., Spectral intensities emitted by lightning discharges, *J. Geophys. Res.*, 75, 1049–1057, 1970
- [247] Zhivlyuk, Y. N. and S. L. Mandel'shtam, On the temperature of lightning and force of thunder, *Sov. Phys. – JEPT (Engl. Trans.)*, 13, 338–340, 1961
- [248] Few, A. A., Power spectrum of thunder, *J. Geophys. Res.*, 74, 6926–6934, 1969
- [249] Hill, R. D., A survey of lightning energy estimates, *Rev. Geophys. and Space Phys.*, 17, 155–164, 1979
- [250] Malan, D. J. and B. F. J. Schonland, An electrostatic Fluxmeter of short response time for use in studies of transient field changes, *Proc. Phys. Soc. London Ser. B*, 63, 402–408, 1950.
- [251] Krider, E. P. and R. C. Noggle, Broadband antenna systems for lightning magnetic fields, *J. Appl. Meteor.*, 14, 252–256, 1975
- [252] Horner, F., The design and use of instruments for counting local lightning flashes, *Proc. Inst. Elec. Engrs.*, 107B, 321–330, 1960
- [253] Pierce, E. T., The influence of individual variations in field change due to lightning discharges upon design and performance of lightning flash counters, *Archiv. Meteor. Geophys. Bioklim. Ser.*, A9, 78–86, 1956.
- [254] Anderson, R. B., H. R. Van Niekerk, S. A. Prentice, and D. Mackerras, Improved lightning flash counters, *Electra*, 66, 85–98, 1979
- [255] Cooray, V., Response of CIGRE and CCIR lightning flash counters to the electric field changes from lightning: A theoretical study, *J. Geophys. Res.*, 91, 2835–2842, 1986
- [256] Mackerras, D., Automatic short range measurement of the cloud flash to ground flash ratio in thunderstorms, *J. Geophys. Res.*, 90, 6195–6201, 1985
- [257] Watson-Watt, R. A. and J. F. Herd, An instantaneous direct-reading radiogoniometer, *J. Inst. Elec. Engrs.*, 64, 611–622, 1926
- [258] Horner, F., Very low frequency propagation and direction finding, *Proc. IEEE*, 101B, 73–80, 1957
- [259] Krider, E. P., R. C. Noggle, and M. A. Uman, A gated wide band direction finder for lightning return strokes, *J. Appl. Meteor.*, 15, 301–306, 1976
- [260] Lewis, E. A., R. B. Harvey, and J. E. Rasmussen, Hyperbolic direction finding with sferics of transatlantic origin, *J. Geophys. Res.*, 65, 1879–1905, 1960
- [261] Oetzel, G. N. and E. T. Pierce, VHF technique for locating lightning, *Radio Sci.*, 4, 199–201, 1969
- [262] Lennon, C. L., LDAR – a new lightning detection and ranging system (abstract), *Eos Trans. AGU*, 56(12), 991, 1975
- [263] Rustan, P. L., Properties of lightning derived from time series analysis of VHF radiation data, Ph.D. thesis, University of Florida, Gainesville, FL, 1979
- [264] Cianos, N., G. N. Oetzel, and E. T. Pierce, A technique for accurately locating lightning at close range, *J. Appl. Meteor.*, 11, 1120–1127, 1972
- [265] Murty, R. C. and W. D. MacClement, VHF direction finder for lightning location, *J. Appl. Meteorol.*, 12, 1401–1405, 1973
- [266] Taylor, W. L., A VHF technique for space time mapping of lightning discharge processes, *J. Geophys. Res.*, 83, 3575–3583, 1978
- [267] Hayanga, C. O., Positions and movement of VHF lightning sources determined with microsecond resolution by interferometry, Ph.D. thesis, University of Colorado, Boulder, CO, 1979

- [268] Hayanga, C. O. and J. W. Warwik, Two-dimensional interferometric positions of VHF lightning sources, *J. Geophys. Res.*, 86, 7451–7462, 1981
- [269] Richard, P. and G. Auffray, VHF-UHF interferometric measurements, application to lightning discharge mapping, *Radio Sci.*, 20, 171–192, 1985
- [270] Ushio, T., Z. Kawasaki, Y. Ohta, and K. Matsuura, Broadband interferometric measurement of rocket triggered lightning in Japan, *Geophys. Res. Lett.*, 24, 2769–2772, 1997
- [271] Winn, W. P., A laboratory analog to the dart leader and return stroke of lightning, *J. Geophys. Res.*, 70, 3265–3270, 1965
- [272] Hubert, P. and G. Mouget, Return stroke velocity measurements in two triggered lightning flashes, *J. Geophys. Res.*, 86, 5253–5261, 1981
- [273] Wang, D. *et al.* Attachment process in rocket triggered lightning, *J. Geophys. Res.*, 104, 2143–2150, 1999
- [274] Wang, D. *et al.* Luminous propagation of lightning attachment to CN tower, *J. Geophys. Res.*, 100, 11661–11667, 1995
- [275] Wang, D., N. Takagi, T. Watanabe, V. A. Rakov, and M. A. Uman, Observed leader and return stroke propagation characteristics in the bottom 400 m of a rocket triggered lightning channel, *J. Geophys. Res.*, 104, 14369–14376, 1999
- [276] Hill, E. L. and J. D. Robb, Pressure pulse from a lightning stroke, *J. Geophys. Res.*, 73, 1883–1888, 1968
- [277] Nanayakkara, S., M. Fernando, T. A. L. N. Gunasekera, S.P.A. Vayanganie, and V. Cooray, K changes: Is it a static field of a chaotic pulse burst?, *Proceedings of the International Conference in Lightning Protection (ICLP)*, Shanghai, China, 2014



---

## Chapter 5

# Features of lightning flashes obtained from high-speed video recordings

*Marcelo M. F. Saba, Tom A. Warner  
and Carina Schumann*

---

### 5.1 Introduction

Most of what is known about the structure and time evolution of lightning was determined by high-speed photography. The first measurements were obtained using a two-lens streak camera, named Boys camera after its inventor [1]. In a streak camera, a relative movement between the lens and the film is used to record the phases of a lightning discharge. Subsequent improvements of Boys camera allowed measurements of several lightning parameters [2–5].

In 1978, Waldteufel *et al.* [6] used a 16-mm high-speed film movie camera to observe a rocket-triggered lightning flash at 730 images per second (ips). The camera shutter was however open only 2.5 per cent of the time and some of the lightning return strokes were missed.

Film-based cameras produced the best resolving capability, however, film development time, chemical disposal, recurring media cost, and faster digital analysis were factors that influenced the desire for digital high-speed cameras. Some of the last lightning measurements using this technique were reported by Jordan *et al.* [7].

Winn *et al.* [8] and Brantley *et al.* [9] studies are among the first that used standard (30 ips) TV video tape recordings to analyse the characteristics of cloud-to-ground (CG) lightning flashes. Biases that are introduced by finite video resolution of standard video tape recordings have been discussed by several publications (e.g. [10]). For example, if two different strokes occur within a 1/30-s interval they will appear to be a single stroke unless they follow different paths.

The advent of high-speed motion digital video cameras allowed the use of temporal high-resolution video images of lightning flashes. As far as we know, Moreau *et al.* [11] pioneered the use of high-speed video to observe lightning at 200 ips with vertical resolution of 262 lines and horizontal resolution of 200 pixels. With higher temporal resolution, processes that occur during a lightning flash can be visualized with detail and missing of strokes that occur at relatively short-time intervals is practically excluded.

Currently robust and portable high-speed video cameras offer a wide range of frame rate and exposure options ranging from 1000 to over 3 00 000 ips. Images can be displayed on the computer monitor and each sequence of images can be stored in a computer file, retrieved and replayed at various speeds to analyse a motion sequence in detail. Image processing (e.g. brightness, gain) is also easily performed with dedicated software for these cameras.

Most high-speed cameras have a trigger system that detects a signal from an external source (e.g. optical, current or electric field sensor input). Pre- and post-trigger recording durations can be set to ensure the desired components of the flash are recorded relative to the trigger signal. Alternatively, a camera operator can make a manual trigger input via a hand-held switch or keyboard entry.

The optimum recording length required to capture an entire lightning flash is 1.5–2 s; previously, Ballarotti *et al.* [12] based on high-speed videos of negative cloud-to-ground (–CG) flashes, reported a maximum flash duration of 1.43 s with approximately 97 per cent of 736 multistroke flashes lasting less than 1 s. For 85 positive CG lightning, the maximum duration observed by Saba *et al.* [13] was 912 ms. If the recording trigger system is manually initiated, one must take in consideration the response time of the operator which is approximately 0.3 s.

A frame rate of 1000 ips is capable of visualizing most of the phases of CG lightning: stepped leaders, return strokes, and continuing currents. Other lightning processes require a higher frame rate. The observation of dart leaders, upward connecting leaders or recoil leaders may require 10 000 ips or more. Some studies of lightning processes have already been accomplished at 240 000 ips [14].

For a given sensor size (e.g.  $1280 \times 800$  pixels) and fixed focal length lens combination, the number of active sensor photosites (i.e. pixels) decrease as the recording speed is increased. Therefore, the field of view also decreases as recording speed is increased. One must consider the desired field of view and recording speed before selecting the appropriate lens. Even though sensor ISO sensitivity is high relative to digital still camera and standard speed video sensors, lenses with a large aperture are necessary to record faint lightning components especially as higher recording speeds.

It is advisable to use a red filter in front of the lens in order to increase the contrast between the lightning channel and the background during daytime recordings. It is also highly recommended that the video frames of the high-speed camera are GPS time-stamped with a timing accuracy greater than the duration of the individual frame. For example, if a camera records at 10 000 ips, the GPS timing accuracy should be at least 100  $\mu$ s. This synchronization allows the correlation of each flash recorded with the ones detected by the lightning locating system (LLS) or other auxiliary measurements (e.g. electric-field measurements, lightning mapping arrays [LMA] or interferometers). The temporal correlated analysis is usually extremely useful to identify the polarity of the discharges imaged.

Sometimes when observing distant lightning, heavy rain can obscure the lightning channel and what is a CG flash may be interpreted as an intracloud (IC) discharge. Simultaneous data from electric-field measurements will help to identify the polarity of the lightning and classify it as CG or IC.

Data from the lightning locating systems can be used complement lightning studies with high-speed cameras. LLS may give the stroke polarity, an estimate of the peak current near the ground, and the location of the ground strike point. Conversely, data from high-speed cameras can be used to monitor the performance of LLS. The analysis of the images may provide the detection efficiency of the LLS (see section 5.2.7.4). For flashes containing strokes following the same channel to ground, some indication of location accuracy can also be provided. High-speed video recordings can also be used as a ground truth to check the classification of the lightning discharge given by LLS (e.g. IC or CG).

## 5.2 Negative and positive cloud-to-ground flashes

The analysis of lightning parameters with digital high-speed videos started with Moreau *et al.* [11] and Mazur *et al.* [15]. Moreau *et al.* [11] observed 9 lightning strikes to an aircraft with a video camera with a recording speed of 200 ips and Mazur *et al.* [15] observed a six-stroke CG flash with a high-speed video at 1000 ips. In 2003, a systematic and continuous study of lightning parameters with high-speed videos started. Based on hundreds of high-speed video recordings at 1000 ips in Brazil, three studies reported some characteristics of negative CG flashes [16–18]. In subsequent years, similar studies in Brazil and in the United States were done for negative and positive flashes [12, 13, 19–26]. With exception to the components of a CG lightning flash that occur inside an opaque thundercloud, all the components that occur at or below cloud base such as stepped leaders, upward connecting discharges, return strokes, continuing current, M-components and subsequent return strokes have been studied. The main results of these studies will be the basis for the parameters of CG lightning presented in the next sections.

### 5.2.1 Leaders

Lightning initiation involves electrical breakdown processes usually in the cloud. They may be seen by high-speed cameras as diffuse luminous pulses in the cloud. This process may initiate a leader that travels from the cloud to the ground producing a CG lightning flash. Some of the leader characteristics obtained from high-speed video recordings are described in the following sections.

#### 5.2.1.1 General properties

The tip of the leader is usually brighter and leaves behind a channel that is faintly illuminated by a continuing current. When the leader tip approaches ground, the luminosity of the channel increases (Figure 5.1).

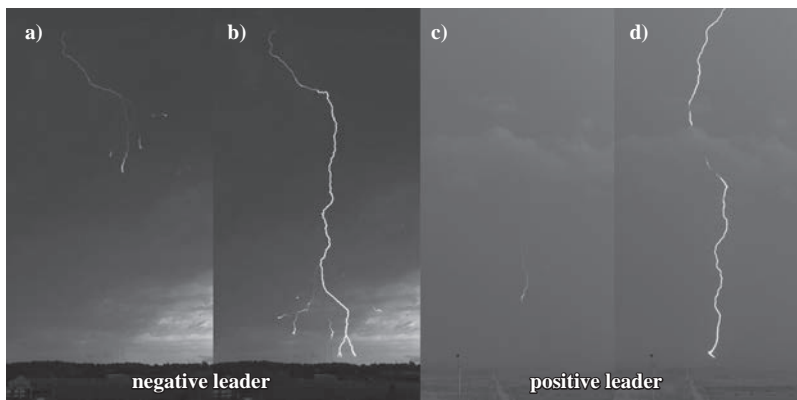


Figure 5.1 High-speed image showing (a) downward propagating negative leader with bright tip and dim trailing channel, (b) the same negative leader with the channel brightened as it approaches the ground, (c) downward propagating positive leader with a bright tip and dim trailing channel and (d) the same positive leader with the entire channel brightened prior to connection with the ground

Figure 5.2 shows a sequence of video frames of the leader propagation to ground in a negative and positive flash. Note that the branching of the positive leader appears to be much less profuse than in negative leaders. Also, contrary to what typically happens to the negative leader, the positive leader may move horizontally and thus produce very extensive channels before connecting with ground.

Leader stepping was observed with streak camera photography in the past [27]. However, in digital high-speed video recordings, leaders show a continuous progression towards ground, and no discrete steps can be resolved unless a very high frame rate is used. Biagi *et al.* [14, 28] using digital high-speed video camera running at 50 000 and 240 000 ips found evidences of stepping in negative leaders similar to what was found in streak photographs for laboratory sparks by Gallimberti *et al.* [29]. At recording speeds above 50 000 ips, bright non-branched positive leaders can exhibit periodic pulsing originating at the leader tip. However, unlike negative leader stepping, there appears to be no clear spatially separated bidirectional leader stem that forms ahead of the positive leader like that seen with negative leaders.

Positive cloud-to-ground (+CG) flashes can be initiated by leaders emanating from IC leader development that was at or close to the cloud base as shown in Figure 5.3. The initial IC leaders can be either positive or negative. In the case of

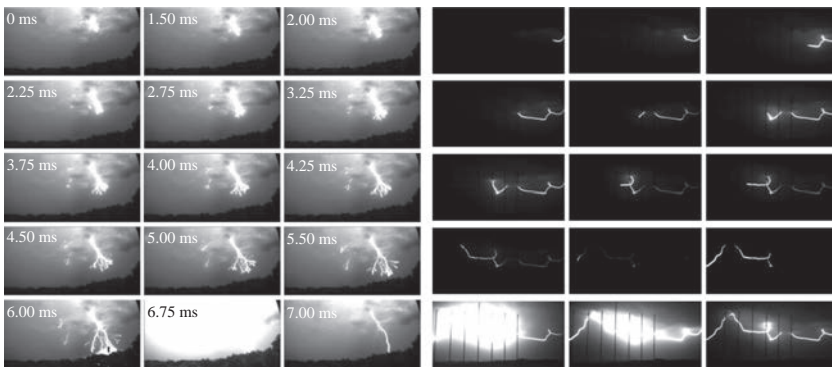


Figure 5.2 *Example of a negative (left) and a positive (right) cloud-to-ground leader observation at 4000 ips (some weakly luminous frames are omitted)*



Figure 5.3 *Image of a positive leader developing and propagating downward from a previous horizontal channel. The dashed arrows show the directions of progression of the horizontal and vertical leaders (Saba *et al.* [20])*

Table 5.1 Average 2-D speed of negative and positive leaders

	Average 2-D speed ( $\times 10^5 \text{ m}\cdot\text{s}^{-1}$ )					
	Sample	Min	Max	AM	Median	GM
Negative	62	0.90	19.8	3.30	2.24	2.68
Positive	29	0.24	11.8	2.76	1.80	1.81

Min stands for minimum value, Max for maximum value, AM for arithmetic mean and GM for geometric mean.

positive IC leaders, a branch at the tip of the leader can form and travel to ground causing a +CG return stroke. Positive leaders have also been observed to develop downward from previously formed horizontally-oriented negative leaders while the channel segment is still luminous or after trailing segment of the negative leader decays. These observations help to explain why extensive IC lightning commonly precedes positive CG flashes [21].

### 5.2.1.2 Leader speed

The two-dimensional speed of a leader can be measured if the distance between the camera and the lightning flash and the geometric characteristics of the camera and lens used are known. The distance can be calculated if flash is detected and located by an LLS or estimated using sound ranging.

Using high-speed video recordings of leaders that preceded CG lightning, it is possible to show that negative stepped and positive leaders present average speeds within a similar range of values, with the latter presenting a tendency towards lower speeds (Table 5.1).

The majority of positive leaders increase their propagation speed as they get closer to ground, while negative-stepped leaders present either a more modest acceleration or speeds that oscillate around an average value [20, 30]. Figure 5.4 presents the average speed value at each range of heights for both negative and positive leaders. While the averages for the negative-stepped leaders oscillate between  $2$  and  $3 \times 10^5 \text{ m}\cdot\text{s}^{-1}$  the positive leaders present a steady increase by one order of magnitude (i.e. from  $10^4$  to  $10^5 \text{ m}\cdot\text{s}^{-1}$ ). Note, however, that throughout the majority of their development the positive leaders present inferior speeds when compared to negative stepped leaders [30].

With study by high-speed cameras, it was possible to register events related to each of the polarities of leader propagation. Negative leaders present stepped propagation as defined in this section and positive flashes present continuous propagation and recoil leaders towards ground as described in the following topic.

### 5.2.1.3 Recoil leaders

During the progression of some positive leaders towards ground, high-speed video recording may observe very short duration ( $<135\text{--}250 \mu\text{s}$ ) and short extension discharges near the path of the downward-propagating leader. These short extension discharges are recoil leaders (RLs) occurring below the cloud base. They were observed for the first time with high-speed video cameras recording 4000 ips in 2007 (more details in Saba *et al.* [20]).

Figure 5.5 shows the integrated luminous development produced by the RLs during the descent of a positive leader. The retracing of the positive leaders by RLs reveals an abundant fine structure that is not usually seen or is very faint. Note that



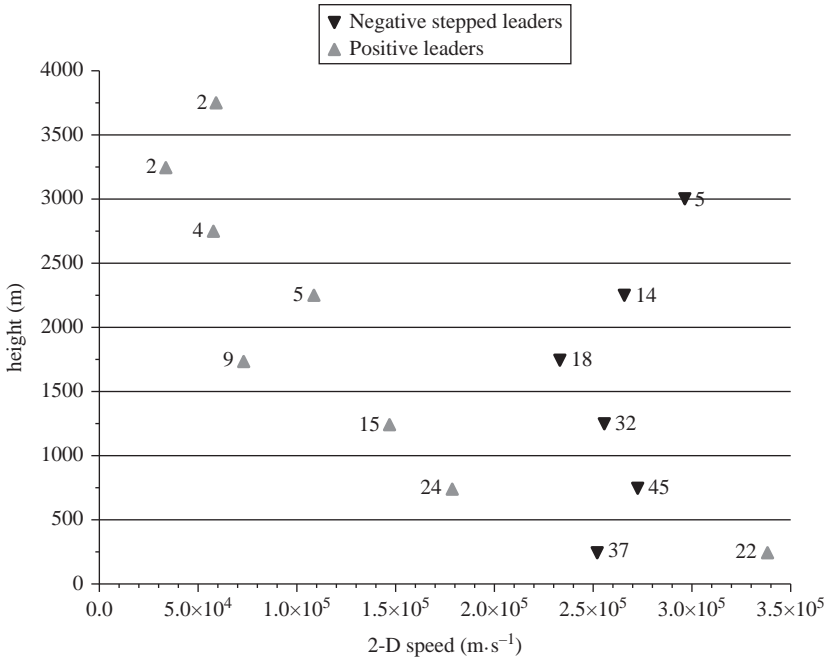


Figure 5.4 Comparison of the average leader speed change by range of heights for negative stepped and positive leaders. The number near each point represents the quantity of measurements available at each range of heights (Campos et al. [30])

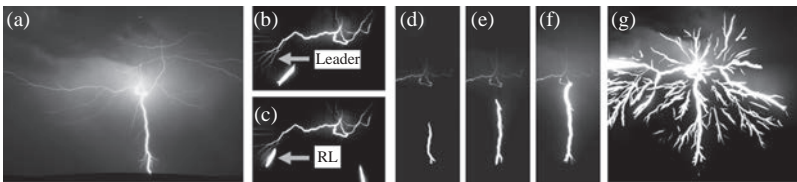


Figure 5.5 Still image and video frames of a positive CG flash in South Dakota that struck 16 km from the camera. (a) Photograph of the flash showing extensive horizontal channel and discrete branching along the vertical channel; (b and c) an example of a RL retracing a faint but visible positive leader path; (d, e and f) the retrograde movement of the RL; (g) time-integrated image of all video frames during the descent of a positive leader (Saba et al. [20])

the fine structures observed with high-speed video do not appear in the still photograph of the flash that is associated with these positive leaders (Figure 5.5a). This is probably due to the extremely short duration of these RLs and due to the fact that the sensitivity difference between the still camera and high-speed camera can be of about a factor of 10.

The present knowledge of recoil leaders is that they are leaders that form on a positive leader branch that has become cutoff from the main positive leader channel from which it branched. RLs initiate in trail of the positive leader branch tip and develop in a bipolar/bidirectional manner in an attempt to reionise and reconnect the

cutoff branch. The negative end of the RL propagates in a retrograde direction away from the advancing positive leader branch tip and towards the branch point [31, 32].

In +CG flashes RLs may be seen either during the propagation of the positive leader before the return stroke or retracing some horizontal channels close to the cloud base after the return stroke. In -CG flashes the RLs retrace positive leaders that propagate inside the cloud, therefore they are not seen by video cameras due to the opacity of the cloud. Sometimes IC discharges also may have some RLs exposed and captured by video cameras.

### 5.2.1.4 Upward connecting leader

Sometimes it is possible to see leaders propagate upward from the tip of nearby tall structures and connect with downward propagating leaders. Depending on the proximity of the flash and the frame rate used, it is possible to calculate the speed of these upward leaders. Figure 5.6 shows two examples of connecting leaders propagating towards the descending leader. The average speed of the connecting leader from the 143-m-tall tower on the left ranged from  $0.27 \times 10^5$  to  $2.9 \times 10^5 \text{ m}\cdot\text{s}^{-1}$  before connecting the downward leader. The average speed of the leader (recorded at 7200 ips) was  $1.2 \times 10^5 \text{ m}\cdot\text{s}^{-1}$ .

### 5.2.2 Return stroke

The return stroke (RS) is the most luminous processes in a lightning flash. The extremely large current and resulting luminosity involved in this process may easily saturate a significant portion of, if not the entire, sensor. In Figure 5.7, a sequence



Figure 5.6 Examples of connecting leaders propagating upward towards the descending leader

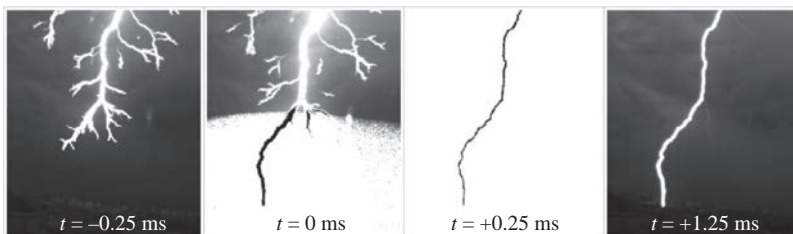


Figure 5.7 Sequence of images showing the leader propagation before the RS, the RS and some continuing current following the RS. The saturation of the pixels along the channel makes their colour reversed to black. This video was recorded with 4000 ips.

of video images show the stepped leader approaching ground, the bright illumination caused by the initiation of the RS and continuing current following the RS. Sometimes the upward propagation of the luminosity generated by the RS can be progressively registered in one or more frames (Figure 5.7;  $t = 0$  ms).

### 5.2.3 *Number of return strokes per flash*

A lightning flash may be composed by several return strokes. In order to calculate the average number of strokes per flash (multiplicity) with high-speed cameras, a special care has to be taken with two situations that could reduce the accuracy of stroke counting: (a) multiple channel flash occurring too close, and out of view of the camera and (b) strokes with channels obscured by rain. In the first case, channels occurring outside the field of the view of the camera would be lost; in the second case, CG strokes could be mistaken by an IC stroke. Most of these relatively difficult cases can be solved using a wide-angle standard video camera, and auxiliary data from an electric field sensor or from a lightning detection network.

Saba *et al.* [17] presented a histogram for the number of strokes per flash in 233 negative CG flashes recorded with a high-speed camera at 1000 ips. Of these 233 flashes, 186 had two or more strokes and the average number of strokes per flash observed was 3.8. Later, Ballarotti *et al.* [12] expanded the number of flashes to 833 with frame rates ranging from 1000 to 8000 ips (Figure 5.8) and found a little higher average number of strokes per flash (4.6). This higher value in this later study can be attributed to two factors: (a) only CG flashes within 30 km from the observing point were selected, thus avoiding the missing of RS obscured by rain in distant flashes and (b) the requirement that all flashes analysed had at least one stroke detected as a  $-CG$  stroke by the LLS. This last requirement prevented the inclusion on any positive CG flash in the data base. However, it may have excluded some single-stroke negative CG flashes which are usually less intense and therefore less detected by LLS. In fact, the percentage of single-strokes flashes in Ballarotti *et al.* [12] (16 per cent) is less than the usual reported value, which is around 20 per

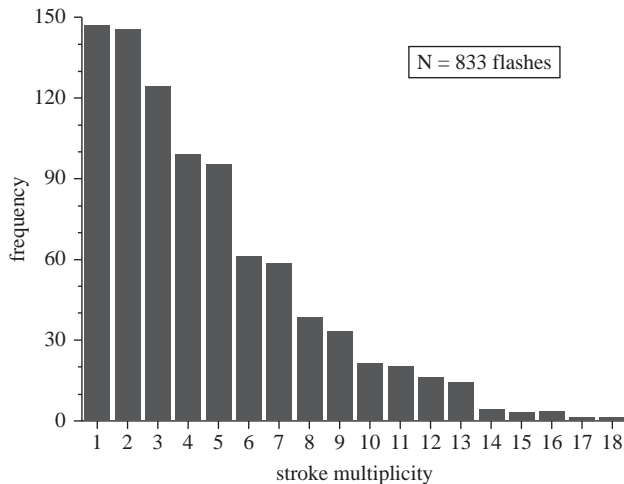


Figure 5.8 *Histogram of stroke multiplicity for the 883 negative cloud-to-ground flashes observed in Vale do Paraíba, Brazil (Ballarotti *et al.*, [12])*

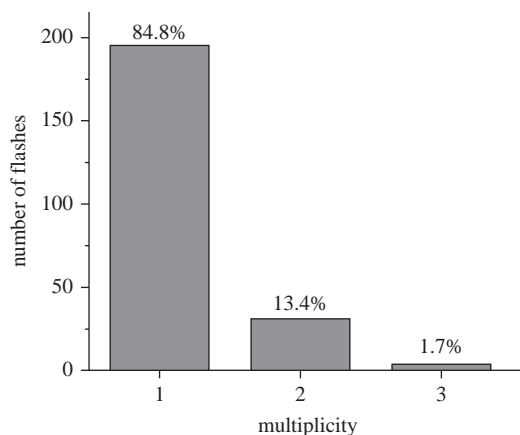


Figure 5.9 Number of positive flashes that contained the given number of strokes (Schumann [26])

cent [17, 24]. This value is fairly similar to other accurate stroke counting studies confirming that, when the possibility of missing strokes is practically excluded, the overwhelming majority (about 80 per cent or more) of negative CG flashes contains more than one stroke [33].

Figure 5.9 shows a histogram of the number of strokes per flash for 231 +CG flashes. In this sample, 31 flashes had two strokes and 4 had three strokes. The average number of positive strokes per flash is only 1.17. Contrary to –CGs, the percentage of single-stroke flashes in +CG flashes is high, 84 per cent [26].

#### 5.2.4 Flash duration

Flash duration is here defined as the time interval between the occurrence of the first return stroke and the end of the continuing current following the last return stroke, if present.

The median duration of 233 –CG flashes recorded by high-speed video by Saba *et al.* [17] was 163 ms. The maximum duration value (1356 ms) was observed in a flash that produced 16 strokes. This flash had also the maximum number of strokes per flash. Figure 5.10 shows the flash duration distribution.

A minimum flash duration per number of strokes was previously presented by Saba *et al.* [17]. There is a clear threshold establishing a minimum value of flash duration for a given number of strokes per flash. This minimum value seems to indicate that processes in the channel and in the cloud do not permit multiple strokes occur under a certain minimum duration. A good correlation between the mean flash duration and the number of strokes per flash for 724 multistroke –CG flashes was found by Ballarotti *et al.* [12] (Figure 5.11).

Figure 5.12 shows a histogram of the total flash duration of 196 +CG flashes. Here, the geometric and arithmetic means are 97 and 176 ms, respectively. The maximum duration (912 ms) was observed for a flash that produced three strokes, and the last stroke was followed by a continuing current (CC) that lasted 165 ms [26].

Although most of the positive flashes are single, the median value of the duration of positive flashes (125 ms) is not considerably smaller than the median value for negative ones (163 ms). This may be explained by the fact that nearly 70 per cent of positive flashes contain at least one long continuing current (longer

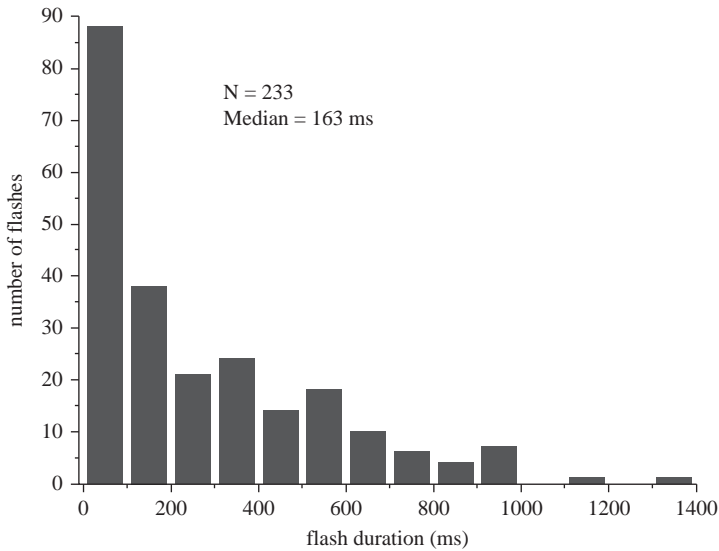


Figure 5.10 Histogram of number of  $-CG$  flashes having a given flash duration (Saba et al. [17])

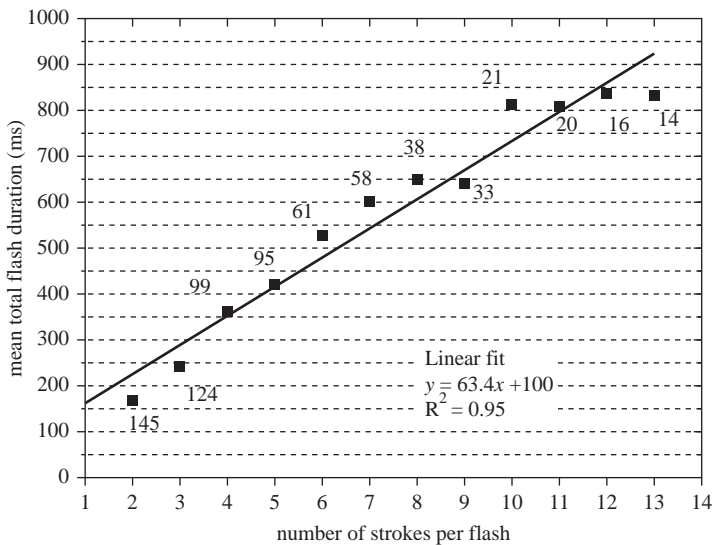


Figure 5.11 Mean total flash duration versus number of strokes per flash based on the 724 multiple-stroke flashes observed in Vale do Paraiba, Brazil. Sample sizes are indicated (Ballarotti et al. [12])

than 40 ms) and also because interstroke intervals are slightly longer in positive flashes.

### 5.2.5 Multigrounded lightning flashes

Previous studies using high-speed cameras have shown that 50 per cent of the  $-CG$  flashes strike the ground in two or more places. Up to 5 different contact points has

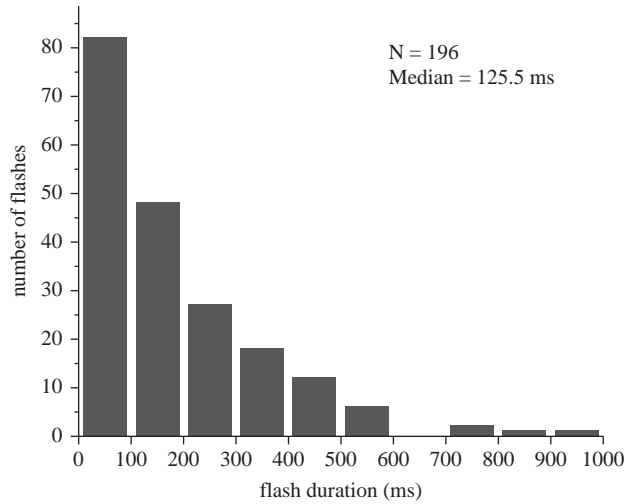


Figure 5.12 Histogram of number of +CG flashes having a given flash duration (Schumann [26])

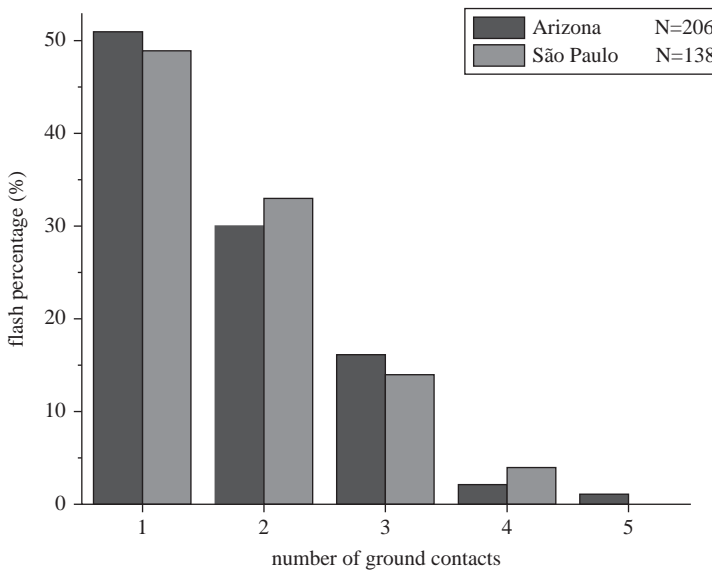
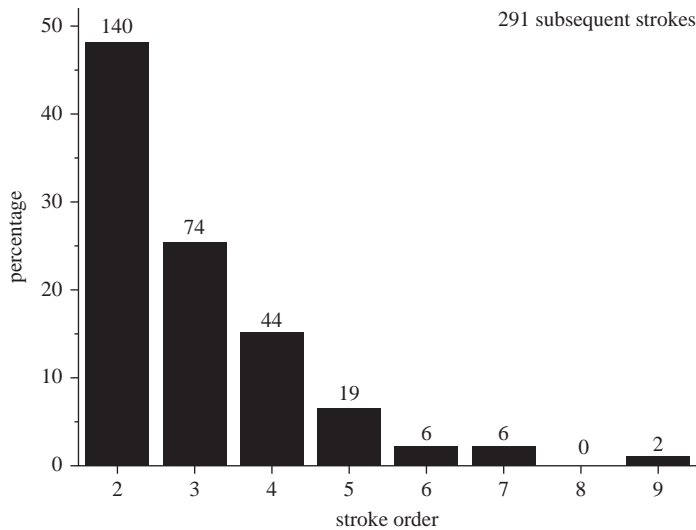


Figure 5.13 Percentage of flashes that produced a given number of ground contacts in Arizona, US and São Paulo, Brazil (Saraiva et al. [24]).

been observed in the same flash. The average of ground strike points per –CG flash is around 1.7, which means that the average number of lightning strike points is 70 per cent higher than the number of flashes [17, 24, 33].

Figure 5.13 shows the distributions of the number of ground contacts per flash in Arizona, US and São Paulo, Brazil. Both distributions were obtained using the same high-speed camera. Note that no flash exceeded five ground contacts in both data sets and that the percentage of flashes with more than three ground contacts is very low (only 2.6 per cent of the cases) [24].



*Figure 5.14* Distribution of new channel strokes according to their stroke order. The numbers on the bars represent the number of strokes (Ferro *et al.* [25])

Although most of the subsequent strokes in –CG flashes tend to follow the previously formed channel, this tendency is not observed in the second stroke (i.e. the first subsequent stroke). Around 50 per cent of the new channels occur in the second stroke (Figure 5.14) [17, 25].

According to Ferro *et al.* [25], 83 per cent of new channels occur following the first stroke down a given channel. Thus, after only one stroke an unalterable path to ground is not usually established. Only 17 per cent of the 291 new channels studied by Ferro *et al.* [25] occur when more than one return stroke goes down the same channel. For the remaining 17 per cent of new channel events, a longer preceding interval (about 3.5 times greater than the average interval between previous strokes that follow the same channel in the same data subset) is an important factor in new channel formation.

Therefore, contrary to what it was generally assumed in some past studies [4, 8, 34–36], the formation of a new channel stroke in a –CG flash is not clearly dependent on the interstroke interval that precedes it. In general, most of the new channels occur after a single usage of the channel and in these cases the previous interstroke time interval is not an important parameter. However, when the channel is used more than once, a new channel occurs mostly after a long interstroke interval [25].

Considering that the missing of strokes in high-speed videos is practically negligible, we can say from the average multiplicity (approximately 4) and from the average number of strike points per flash (1.7), that each ground contact point is, in average, struck approximately 2.5 times [17]. Knowledge of this parameter, as of the relative occurrence of single- and multiple-stroke is useful in estimating the probability of successful circuit-breaker reclosure following a lightning-caused outage of the power line [33, 37].

While only half of the –CG flashes have more than one termination on ground, almost all +CG flashes do have them. Less than 1 per cent of 231 +CG

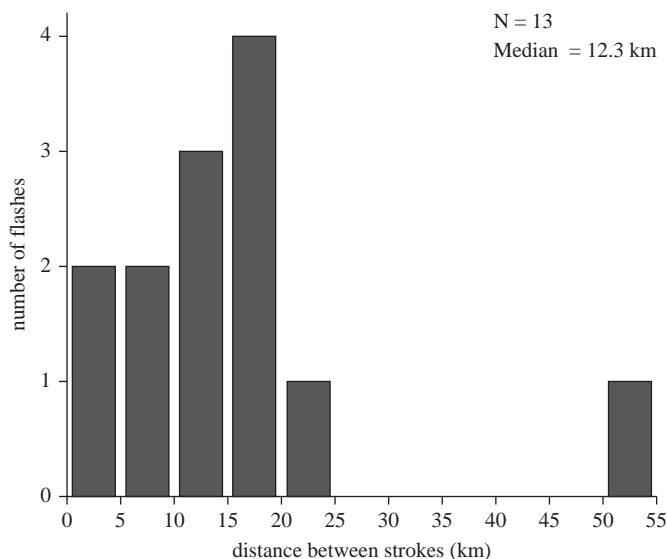


Figure 5.15 Histogram of the horizontal distances between the different ground contacts in multiple-stroke +CG flashes (Schumann [26])

flashes observed by high-speed video recordings by Schumann [26] presented 2 strokes following the same channel to ground. That is, positive subsequent RS almost always create a new termination on the ground [13, 26].

As seen before, positive leaders may travel long horizontal distances before moving towards ground. Also, +CG flashes can be initiated by IC leaders of either polarity, that is downward positive leader can emanate from pre-existing IC discharges [21, 38]. Both characteristics contribute to the fact that +CG flashes are commonly associated with extensive horizontal channel development.

Schumann [26] estimated the horizontal distances between the different ground strike points for the multiple-stroke +CG flashes where each stroke was located by an LLS (Figure 5.15). Note that the distances in Figure 5.15 range from 2 to 53 km and that most (70 per cent) are greater than 10 km, the default range used by the LLSs to group strokes into flashes [39]. For the 22 and 59 –CG flashes that were analysed by Thottappillil *et al.* [40] and Stall *et al.* [41], respectively, all distances between the different ground strike points were found to be less than 10 km [13].

The temporal and spatial criteria that are commonly used in lightning locating systems to group negative strokes into flashes may not be valid for +CG flashes. The use of the same grouping criteria may also contribute to the low positive stroke multiplicities that are often reported by LLSs (e.g. [42]).

Also, the fact that in +CG flashes: (a) almost all the subsequent strokes in multiple-stroke create a new ground termination; (b) subsequent strokes can make a new ground contact even during the continuing current of the previous stroke; and (c) the large distances between the different ground contacts in +CG flashes, leads to the conclusion that there is a very low interdependence between positive strokes. Moreover, the very concept of a lightning ‘flash’ being a group of strokes that are co-located in space (and time) should be reconsidered for positive flashes to ground.



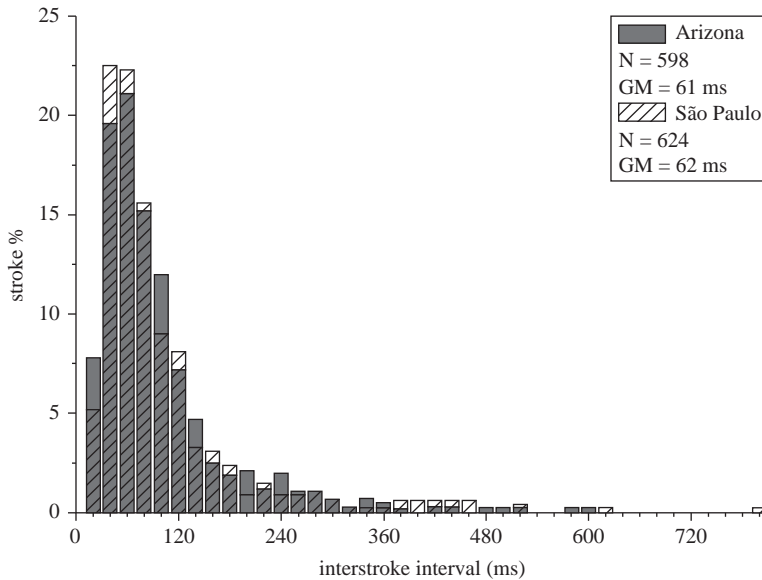


Figure 5.16 *Distributions of interstroke intervals in Arizona and São Paulo (Saraiva et al. [24])*

### 5.2.6 *Interstroke time intervals*

High-speed video measurements of interstroke intervals range from hundreds of microseconds to almost 800 ms. The extremely long intervals are associated with the presence of long continuing currents [17]. Less than 1 per cent of all interstroke intervals lasts more than 500 ms. This reinforces the criterion of maximum 500 ms between strokes largely used by lightning detection networks (see, e.g. [43]).

The geometric mean interval for  $-CG$  flashes is almost always around 60 ms [14, 17]. Figure 5.16 shows the distributions of interstroke intervals measured in two different places (Arizona, US and São Paulo, Brazil) with the same high-speed video camera. Note that both distributions have almost the same lognormal shape with values that are almost the same. Two hundred and thirty-three (19 per cent) out of the 1222 interstroke intervals analysed by Saraiva *et al.* [24] (Figure 5.16) were less than 33 ms, the resolving time of a standard video camera, but considering the percentage of strokes that create a new path to ground, approximately 15 per cent of the total number of strokes would have been missed in standard (30 ips) video recordings, even using deinterlaced fields of frames (60 ips) (e.g. [10, 17, 44]).

Figure 5.17 shows the distribution of interstroke intervals for  $+CG$  flashes [26]. The arithmetic mean (AM) and geometric mean (GM) of 39 time intervals between strokes in the 36 multiple-stroke  $+CG$  flashes are 113 ms and 68 ms, respectively. The smallest and the largest intervals in Figure 5.17 are 2.3 ms and 439 ms, respectively [26].

### 5.2.7 *Continuing current*

Most of the continuing current (CC) characteristics presented in this section come from observations of natural CG flashes with high-speed cameras obtained over the last decade [13, 16–18, 23, 24, 26, 45, 46].

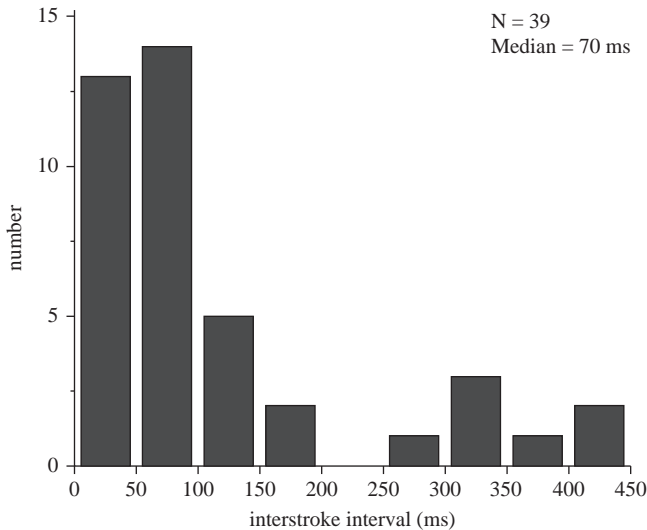


Figure 5.17 Distribution of 39 interstroke intervals in 35 multiple-stroke +CG flashes (Schumann [26])

In using high-speed cameras, the presence and the duration estimates of CC are based on the assumption that the luminosity of the channel is due to the electric current that flows through it. In fact, Diendorfer *et al.* [47] found a strong linear correlation (determination coefficient  $R^2 = 0.96$ ) between brightness and current of the initial continuous current (ICC) in upward initiated flashes to the Gaisberg tower (the range of 10–250 A). Based on the fact that continuing current values in CG flashes are usually in this range, it is generally assumed that the variations observed in the brightness of the channel are proportional to variations in the current that flows along the channel.

High-speed cameras can estimate the duration of CC that is as short as a few milliseconds. However, CC durations may be underestimated at large observation distances or in the presence of rain [17]. In order to minimize underestimation, only flashes occurring at distances less than 50 km were included in the review presented here. The data presented here are for strokes with visible channels, where it is possible to identify the presence of the CC.

### 5.2.7.1 Presence of continuing currents

CC can last from a few to hundreds of milliseconds, and it can be classified as long (duration  $>40$  ms) [4, 5], short (between 10 and 40 ms) [48], and very short (between 3 and 10 ms) [16]. In order to avoid contamination by what could be just return-stroke pulse tails, the observation of CG channels with luminosity duration less than 3 ms is not considered to be a CC event.

Long CC (duration  $>40$  ms) are responsible for most serious lightning damage associated with thermal effects, such as burned-through ground wires and optical fibre ground wires (OPGW) of overhead power lines, initiating forest fires, as well as blowing fuses used to protect distribution transformers, holes in the metal skins of aircraft, etc. (e.g. [49–51]).

In the following we present a review of statistics on the occurrence of long CC in –CG flashes and in +CG flashes based on observations done with high-speed video cameras.

A study of the characteristics of a large number of  $-CG$  flashes from 124 different storms based on high-speed video records was recently done in Brazil. A number of 2459 out of 4495 negative strokes (55 per cent) were followed by some CC (very-short, short or long), and 759 out of 971 negative flashes (78 per cent) contained at least one stroke followed by some CC. The percentage of flashes containing at least one stroke followed by a long CC was 27 per cent [45].

The presence of long CC (lasting more than 40 ms) after first strokes is very rare in  $-CG$  flashes. Ballarotti *et al.* [12] observed that only 2.4 per cent (19/809) of first strokes in multistroke flashes were followed by long CC. This percentage is in agreement with the one found by Rakov and Uman [50] (2 per cent) using broadband E-field and TV recordings. For single-stroke flashes, however, long CC was present in 14 per cent of the 162 flashes in the study by Medeiros and Saba [45].

Medeiros and Saba [45] also found that in 43 per cent of the cases ( $N = 328$ ) a  $-CG$  flash ends after the occurrence of a long CC. If the flash does not end and a subsequent return stroke occurs, it will in 50 per cent of the cases follow the same channel of the preceding RS. Only 4 per cent of the subsequent RS will create a new termination to ground.

The presence of CC in  $+CG$  flashes is very common. Beasley [52], in his review of observations of positive CG flashes, reports that in some past studies [53–55] there were large electric field changes that could be interpreted as CC in positive CG flashes. In fact, high-speed video observations of  $+CG$  flashes [26] indicate that, 166 out of 171 positive strokes (97 per cent) were followed by some CC (very short, short or long). The percentage of flashes containing at least one long CC was 68 per cent (100 out of 148). Further, relatively high percentages were observed in different geographical locations: 87 per cent (46 out of 53) in southeast Brazil, 73 per cent (24 out of 33) in south Brazil, 66 per cent (40 out of 61) in South Dakota, and 53 per cent (24 out of 45) in Vienna, Austria [26].

Table 5.2 summarizes the overall percentage of CC present in negative and positive strokes and flashes derived from recent studies based on high-speed video records mentioned above. Note that the percentages of positive flashes or strokes containing CC are much higher than in negative flashes/strokes. The percentages for positive flashes and positive strokes are very similar due to the fact that a large fraction of the positive flashes (around 80 per cent) produces just a single stroke [13, 26].

### 5.2.7.2 Continuing current duration

The cumulative probability distributions of CC duration for negative and positive flashes are presented in Figure 5.18. Note that the probability to exceed any given duration of CC in  $+CG$  flashes is much higher than in  $-CG$  flashes.

Table 5.2 *Summary of the occurrence of CC in negative and positive strokes and flashes [26, 46]*

Polarity	Number	% with some CC ( $\geq 3$ ms)	% with long CC ( $> 40$ ms)
Negative flashes	971	78% (759)	27% (259)
Negative strokes	4495	55% (2459)	7% (328)
Positive flashes	201	97% (196)	68% (137)
Positive strokes	235	96% (226)	61% (143)

Sample sizes are given in the parentheses.

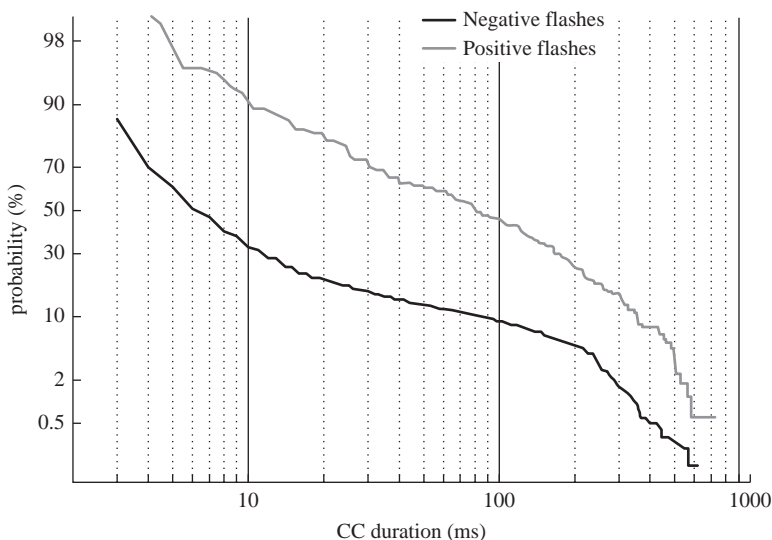


Figure 5.18 Cumulative probability distributions of CC durations greater than or equal to 3 ms in negative and positive strokes (CIGRE [46])

Table 5.3 Summary of CC duration for positive and negative CG flashes

Continuing current duration (ms)	Location	No. of storms	No. of events	Arithmetic mean	Percentage <sup>a</sup> exceeding tabulated value		
					95%	50%	5%
<b>Negative CG flashes</b>							
All CC ( 3 ms) Ballarotti et al. [12]	S. Paulo, Brazil	102	2180	31	2 <sup>b</sup>	6	204
Long CC (>40 ms) Ballarotti et al. [12]	S. Paulo, Brazil	102	304	173	45	145	366
Long CC (>40 ms) Kitagawa et al. [4]	New Mexico, US	1	40	206	48	188	435
<b>Positive CG flashes</b>							
All CC ( 3 ms) CIGRE [46]	Brazil/Austria/US	46	166	142	7	81	484
Long CC (>40 ms) CIGRE [46]	Brazil/Austria/US	46	106	212	55	165	519

<sup>a</sup>Based on values taken from the cumulative probability distribution curves.

<sup>b</sup>Extrapolated value.

Table 5.3 shows 5, 50 and 95 per cent values for all CC (3 ms) and for long CC (>40 ms) for both positive and negative CG flashes. Values obtained by Kitagawa et al. [4] for long CC in negative CG flashes distribution are also shown.

Although there is a significant difference between the 5, 50 and 95 per cent values in Table 5.3 for negative and positive CC when all CC durations are considered, these values are similar if only long CC duration is considered.

According to Ballarotti et al. [12], the maximum measured CC duration value for a negative flash found in the literature is 714 ms. They observed only six cases

of continuing current longer than 500 ms, representing 0.28 per cent of the 2180 CC events (or 0.68 per cent of the 883 flashes). However, the percentage of CC longer than 500 ms in positive CG flashes is much higher, 3.1 per cent of the 228 CC events (or 3.5 per cent of the 201 flashes) [26].

### 5.2.7.3 Return stroke peak current and following continuing current

In this section, we summarize the results of studies of the relationship between peak current (estimated by LLS) and the duration of CC (from high-speed videos) in ground flashes [18, 24]. Similar studies were done comparing electric field peak and charge values for strokes initiating CC with those not initiating CC (e.g. [5, 48, 50, 56]), with generally similar findings but with smaller datasets. Figure 5.19 shows a scatterplot of the peak current ( $I_p$ ) of negative strokes versus the duration of the CC that followed it. Note that this scatterplot shows a so-called ‘exclusion zone’ for negative strokes, discussed by Saba *et al.* [18]. That is, negative strokes that produce estimated peak currents greater than 20 kA are never followed by a CC longer than 40 ms, while negative strokes that produce peak currents less than 20 kA can be followed by CC of any duration.

Figure 5.19 also includes data for 141 positive strokes for comparison. Note that positive strokes can produce both a high peak current ( $I_p > 20$  kA) and a long CC ( $> 40$  ms), a feature that has not been found in any negative stroke. Note also in Figure 5.19 (upper right corner of the plot), that the positive stroke followed by the longest (800 ms) CC had one of the largest estimated peak current values (142 kA).

A pattern in the initiation of long CC was first suggested by Rakov and Uman [50]. According to their suggestion, this pattern has the following characteristics: (i) strokes initiating long CC tend to have a smaller initial electric field peak than regular strokes, the latter defined as neither initiating long CC nor preceding those doing so nor following a long CC interval; (ii) strokes that precede those initiating a long CC are more likely to have a relatively large electric field peak than regular

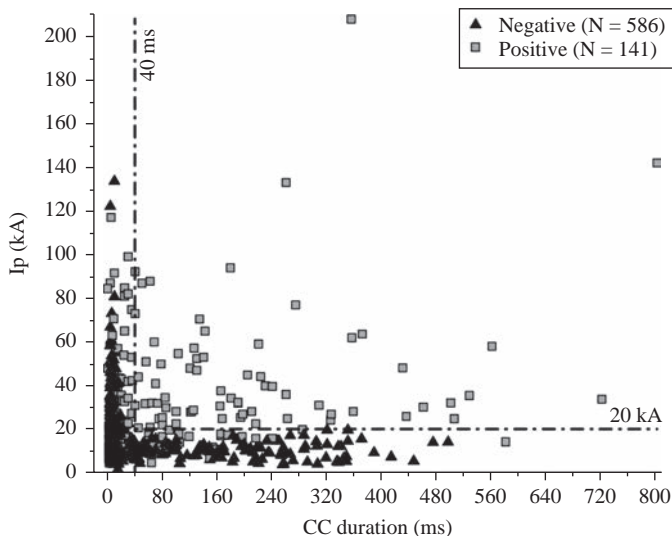


Figure 5.19 Peak current ( $I_p$ ) versus CC duration for 586 negative strokes and 141 positive strokes (Schumann [26])

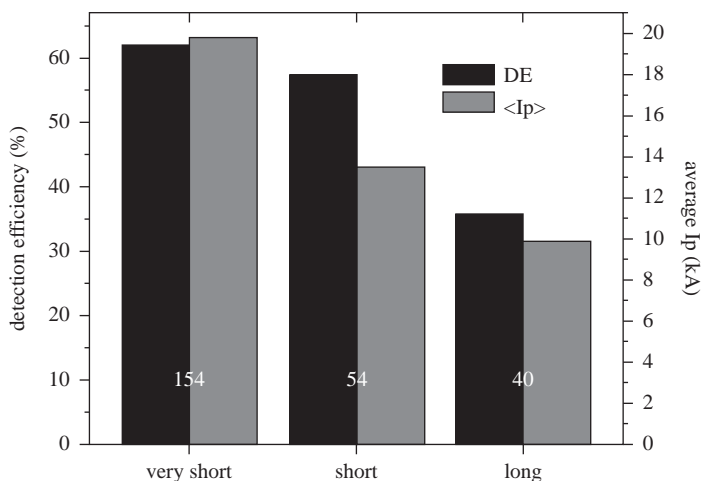


Figure 5.20 Detection efficiency and average peak current  $I_p$  for negative strokes with different ranges of CC. The numbers in white represent the number of strokes detected and used for calculating the average peak current (Saba *et al.* [18])

strokes and (iii) strokes that initiate long CC are usually preceded by a relatively short interstroke interval. This pattern in the initiation of long CC is also valid for the long CC initiated by a stroke that follows a new channel [23].

#### 5.2.7.4 Detection of strokes followed by continuing currents

As the detection efficiency of most of the existing lightning detection networks depends on the intensity of the return stroke, the smaller negative strokes followed by long CC are usually less detectable. Consequently, thunderstorms with a high percentage of negative strokes followed by long CC probably have a lower average  $I_p$  and lower percentage of detected strokes. Since positive strokes followed by long CC do not exhibit lower peak current, their detection is, in principle, not affected.

Figure 5.20 shows the average detection efficiency and average  $I_p$  for 454 negative strokes with different ranges of CC. Saba *et al.* [18] carried out this study using the BrazilDat LLS in southern Brazil. The average  $I_p$  for strokes initiating very-short CC (20 kA) is larger than the average  $I_p$  for strokes initiating short CC (14 kA) and long CC (10 kA). The detection efficiency values for negative strokes followed by very-short, short and long continuing currents were respectively 62 per cent (154 out of 248), 57 per cent (54 out of 94) and 36 per cent (40 out of 112). It is clear that the longer the CC, the lower the average  $I_p$  and, consequently, the lower the stroke detection efficiency.

Clearly, more sensitive systems or methods should be used in order to better detect negative strokes followed by this deleterious mode of discharge.

#### 5.2.7.5 Continuing current waveshapes and M-components

Although CCs are usually assumed in lightning protection standards to have a constant current value (e.g. IEC [57]), the CC intensity exhibits significant variations with time. These current variations can be either M-components

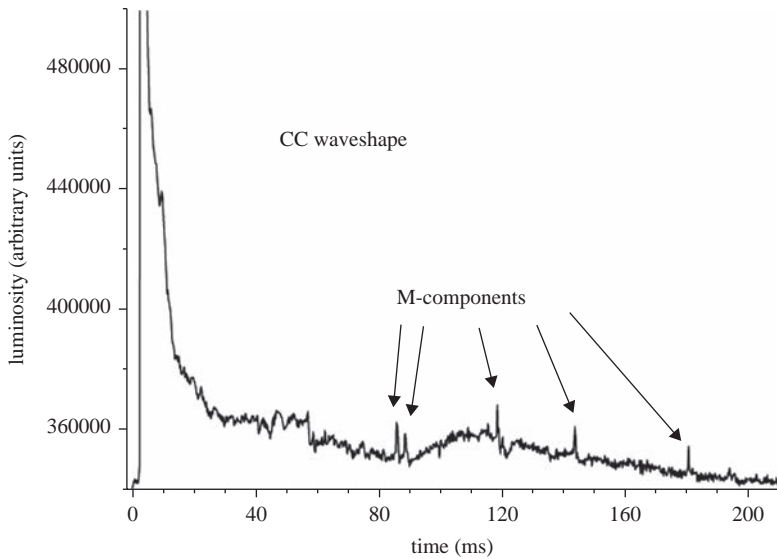


Figure 5.21 *Example of continuing current with M-components. The M-components are indicated by arrows*

(approximately symmetrical relatively short duration current pulses superimposed on the background steady current) [58] or long duration variations that define the overall CC waveshape (Figure 5.21). Both were first studied through direct current measurements by Fisher *et al.* [59] for negative triggered lightning. They have grouped the current-versus-time graphs into four waveshape types.

More recently, high-speed video data have made it possible to study waveshapes of CC and M-components in both negative and positive natural cloud-to-ground lightning [19, 22]. The high-speed video records were used to examine the luminosity variation with time for specific pixels on each frame. Assuming that the luminosity is directly proportional to the channel current [47], the results were interpreted in terms of CC variation with time.

Video observations of a lightning flash may differentiate M-components from subsequent return strokes (RS) by the luminosity level preceding them. If a luminosity pulse occurs after the cessation of any luminosity in the channel it is an indicative of a subsequent RS, but if the pulse enhances the brightness of an already luminous channel, it is an indicative of an M-component. In the following, the classification of the discharges as being either M-components or subsequent RS will be based on this luminosity criterion.

Findings from Campos *et al.* [19, 22] indicate that natural CG flashes exhibit two more waveshape types, in addition to those suggested by Fisher *et al.* [59]. More than 30 M-components was observed in one extremely long negative CC. Furthermore, the average number of M-components per CC is very different for different polarities: while for negative flashes Campos *et al.* [19] observed 5.5 M-components per CC, Campos *et al.* [22] observed 9.0 for positive flashes.

Table 5.4 summarizes some parameters for negative and positive CG flashes obtained from high-speed video recordings reported in the recent studies cited above.

Table 5.4 Negative and positive CG flashes parameters from high-speed videos

	<i>N</i>	Min.	Max.	Mean	Median	GM
<b>Negative CG flashes</b>						
Negative leader speed ( $\times 10^5$ m·s <sup>-1</sup> ) Campos <i>et al.</i> [30]	62	0.90	19.8	3.30	2.24	2.68
Flash multiplicity Saba <i>et al.</i> [17]	233	1	16	3.8	3.0	3.0
Flash duration (ms) Saba <i>et al.</i> [17]	233	1	1356	–	163	–
Number of strike points per flash Saba <i>et al.</i> [17]	138	1	5	1.7	2.0	1.6
Interstroke intervals (ms) Saraiva <i>et al.</i> [24]	624	–	800	–	–	62
Continuing current duration (ms) Ballarotti <i>et al.</i> [12]	2180	3	714	31	6	–
<b>Positive CG flashes</b>						
Positive leader speed ( $\times 10^5$ m·s <sup>-1</sup> ) Campos <i>et al.</i> [30]	29	0.24	11.8	2.76	1.80	1.81
Flash multiplicity Schumann [26]	231	1	3	1.17	1	1.12
Flash duration (ms) Schumann [26]	196	2.3	912	176	125.5	97
Interstroke intervals (ms) Schumann [26]	39	2.3	439	113	70	68
Continuing current duration (ms) CIGRE [46]	166	3	800	142	81	68

### 5.3 Bipolar cloud-to-ground flashes

A lightning discharge is usually defined as bipolar lightning if it sequentially lowers both positive and negative charge to ground. Most reported bipolar flashes are associated with upward lightning (see section 5.4). Natural bipolar cloud-to-ground flashes are not as common and very few events have been documented to date. These downward bipolar flashes can be divided into those that have return strokes of opposite polarity that occur in different channels (i.e. different termination points) and those that have return strokes of opposite polarity in the same channel. When strokes of different polarities occur in different channels, one could argue that they do not belong to the same flash but are two different flashes occurring close in time and space. This is not the case when strokes of different polarities use the same channel as will be discussed here [62].

There are very few cases of CG bipolar flashes using only one channel reported in literature. Reports on this type of bipolar flashes are not common due to the fact that in order to confirm that currents of both polarities follow the same channel to the ground one needs video records and simultaneous electric field measurements or lightning location systems that give reliable polarity identification as well as a reliable IC/CG discrimination.

Eight cases of single channel CG bipolar flashes were reported in the literature, three with standard video camera [60, 61] and five with high-speed video



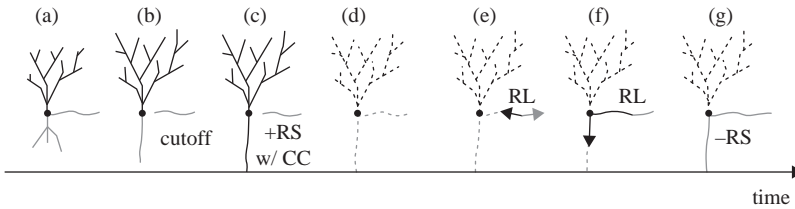


**Figure 5.22** Sequence of events that could explain the occurrence of a bipolar single channel flash: (a) bidirectional leader propagation (positive leaders in gray, negative leaders in black); (b) cutoffs may occur before the return stroke leaving segments of the positive leader disconnected; (c) return stroke and continuing current occur; (d) channel decay; (e–f) recoil leader retraces the decayed channel and propagates to ground; (g) negative return stroke (Saba *et al.* [62])

camera [62]. All bipolar flashes had very similar characteristics, the most important one being that they all initiated with a positive CG return stroke.

Based on the video images obtained and based on previous observations of positive CG flashes with high-speed cameras, Saba *et al.* [62] suggest a common process that may explain how return strokes of different polarity traverse the same channel. Specifically, a positive leader branch develops from the main downward propagating positive leader prior to the first positive return stroke. This positive leader branch travels horizontally near cloud base, becomes cut off from the downward leader, and does not participate in the return stroke (Figure 5.22a–c). Following the decay of the positive return stroke, an RL forms on the horizontal branch and the negative end of the RL travels back to the branch point and down to the ground following the previous return stroke channel path (Figure 5.22d–f). When the RL connects with the ground a negative return stroke occurs (Figure 5.22g). In all cases observed with high-speed cameras, the horizontal branch retraced by the RL is present before the positive return stroke.

The cutoff of the horizontal positive leader branch (Figure 5.22b) makes possible the occurrence of the recoil leader that retraces it. And, it is not uncommon to see recoil leaders retracing horizontal channels after a positive return stroke, as shown in Figure 5.23d, but, in order for this flash to become bipolar, the negative end of the RL must find a way down to ground. In high-speed videos we see that sometimes RLs fade before reaching the positive leader branch point from the main channel or may, upon reaching the branch point, go upward into the upper portion of the decayed flash. So, the negative end of the RL must reach the main channel and move towards ground to form a subsequent negative CG return stroke. Furthermore, the RL must occur before the residual conductivity in the return stroke channel decays beyond the point that it provides a favourable path to ground.

In Figure 5.23, a sequence of video images shows the initiation and development of an RL that formed on a previously established horizontal positive leader branch travelled back to the branch point (Figure 5.23b–e) and then propagated downward to ground using the same channel path of the previous positive return stroke (Figure 5.23e–g). Upon reaching the ground, the negative end of the RL caused a negative return stroke (Figure 5.23h).

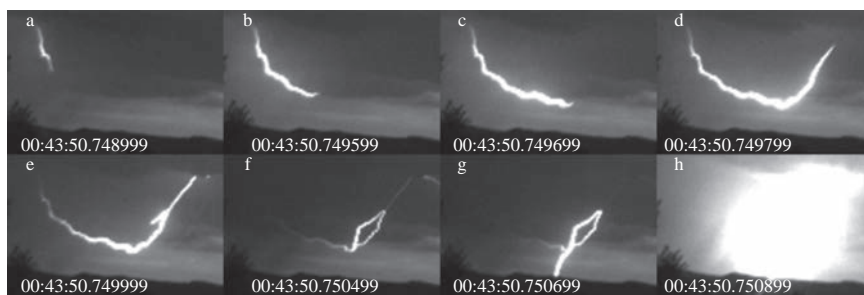


*Figure 5.23 Sequence of high-speed video images of a bipolar CG showing the initiation and development of an RL along the path of a previously formed positive leader branch. The negative end of the RL travels to the right and upon reaching the branch point, travels down the previous return stroke channel path and connects with ground forming a negative return stroke (from Saba et al. [62])*

As far as we know, there is no report in the literature of a single-channel CG bipolar flash having a first return stroke of negative polarity. There are some reasons that may require a bipolar flash to be initiated by positive discharges:

- Contrary to what is usually observed in negative CG discharges, positive CG flashes often involve long, horizontal channels, up to tens of kilometres in length (e.g. [13, 20, 21, 38, 54]). Frequently these channels are formed by positive leaders that propagate horizontally at or near the cloud base instead of propagating downward and connecting with ground.
- According to Heckman [63] these long horizontal channels are unstable and contribute to the current cutoff. This current cutoff and resulting floating conductor can result in the development of recoil leaders [32, 64].
- The negative subsequent return stroke has its origin in RLs that retrace the paths of previously formed horizontal positive leader branches. An opposite situation, that is a positive subsequent return stroke following a negative return stroke, is likely not viable given that RLs would be required to retrace the horizontal channels created by negative leaders. To date, RLs forming on decayed negative leader branches have not been reported [32, 65].

The reason why bipolar single channel flashes are rare is probably due to the combination of factors that are needed for its occurrence. The horizontal branch formed by the positive leader branch must cutoff from the main positive leader channel before the positive return stroke. This keeps the horizontal branch from participating in the positive return stroke (Figure 5.22c).

## 5.4 Upward lightning flashes

Observations of upward lightning from tall objects have been reported since 1939. Interest in this subject has grown recently, some of it because of the rapid expansion of wind power generation. Also, with the increasing number of tall buildings and towers, there will be a corresponding increase in the number of upward lightning flashes from these structures. Reports from recent high-speed video observations are beginning to address the nature of upward lightning initiation, but much still needs to be learned [31, 66].

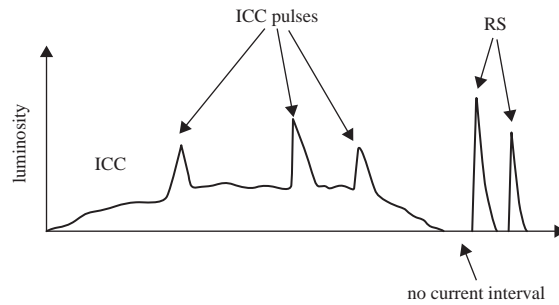


Figure 5.24 Schematic channel luminosity variation for an upward-initiated flash. The ICC is followed by two RS after a time interval of no current flow

Upward lightning discharges always starts as an upward leader (UL) characterized by a sustained propagation and that may or may not be followed by one or more dart leader-return stroke sequences. The propagation of UL produces an ICC with a duration of some hundreds of milliseconds and an amplitude of some tens to some thousands of amperes [67]. In many cases the ICC contains current pulses superimposed on the slowly varying continuous current referred to as ICC pulses (see Figure 5.24). The ICC can be followed, after a no current interval, by one or more dart leader-return stroke sequences. The dart leader-return stroke sequences in upward lightning are similar to subsequent leader-return-stroke in natural downward lightning and in rocket-triggered lightning. Figure 5.24 shows a schematic of overall current waveform of upward-initiated lightning with three pulses superimposed on the ICC and two return strokes following the ICC after a period of no current flow [65, 67].

In this section, the information presented is based on the analysis of high-speed observations and correlated electric field data of upward positive leaders (UPLs) that developed in South Dakota, US and in S. Paulo, Brazil [31, 66, 68]. To date, no upward negative leaders have been observed.

#### 5.4.1 Upward leader initiation characteristics

The initiation of a UPL can be either triggered by another lightning discharge (IC or CG) or be self-initiated [69].

Based on high-speed optical observations, lightning mapping array, LLS data and electric field records, Saba *et al.* [66] and Warner *et al.* [31] reported that in São Paulo, Brazil and in South Dakota, US, almost all upward flashes initiated by UPLs had optically observed preceding nearby flash activity suggesting the UPLs were triggered (i.e. lightning-triggered upward lightning).

The UPLs were triggered by either (1) the approach of horizontally propagating negative stepped leaders associated with either IC development or following a +CG return stroke or (2) a +CG return stroke as it propagated through a previously formed leader network that was near the towers.

In some cases, it is possible to record high-speed imagery of horizontally propagating in-cloud brightness following the occurrence of a +CG return stroke. Figure 5.25 shows propagating in-cloud brightness due to leader activity following a +CG RS. The tips of the leaders causing the in-cloud brightness are visible in the

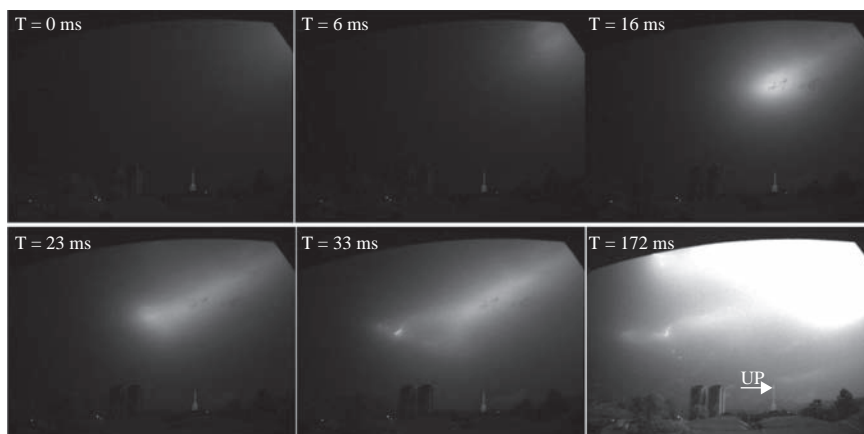


Figure 5.25 Sequence of images showing the approach of negative leaders following a +CG return stroke that occurred at 6 km from the tower

last two images, and based on supporting electric field data, this leader activity was negative polarity.

The approach of negative leaders near or over the tower following +CG RS in São Paulo, Brazil, was confirmed by lightning mapping array plots as the one shown in Figure 5.26 [66]. The +CG RS (indicated as a red cross in Figure 5.26) occurred at a distance of 36 km north-west from the tower that developed an UPL (letter “T” in Figure 5.26). Note that negative leaders (represented by blue and then greenish dots), moved towards the tower at a height of about 5 km after the occurrence of the +CG RS.

In South Dakota, the time from the first indication of in-cloud visual brightness increase to upward leader initiation was determined for 80 flashes [70]. The resulting mean, GM, median, maximum and minimum time between the first visual sign of flash activity and upward leader initiation was 181, 112, 109, 918 and less than 1 ms, respectively. Note that the maximum delay observed was almost an entire second. For the 37 cases (46 per cent) in which there was a preceding visible ground stroke, the mean, GM, median, maximum and minimum time between the visible ground stroke and upward leader initiation was 50, 32, 36, 267 and less than 1 ms, respectively. The most common triggering flash type was the +CG flash, which preceded the initiation of upward leaders in 67 per cent of the cases.

#### 5.4.2 Upward leader characteristics

Short duration (and length) attempted leaders occasionally preceded sustained UL development. Sustained ULs would develop initially with weak luminosity that was sometimes below the optical threshold of the high-speed cameras. Those that did not branch shortly after initiation typically developed luminosity pulses/steps (when observed at 54 000 ips, 18  $\mu$ s exposures or faster) that would originate at or near the tip of the leader, with an increased luminosity front that travelled down the leader towards the tower tip. When compared to negative leader stepping observed at the same temporal resolution, the pulsing of the positive leader (PL) appeared more irregular with wider luminosity variation. This pulsing would continue until the full length of the UL brightened significantly at which point the pulsing

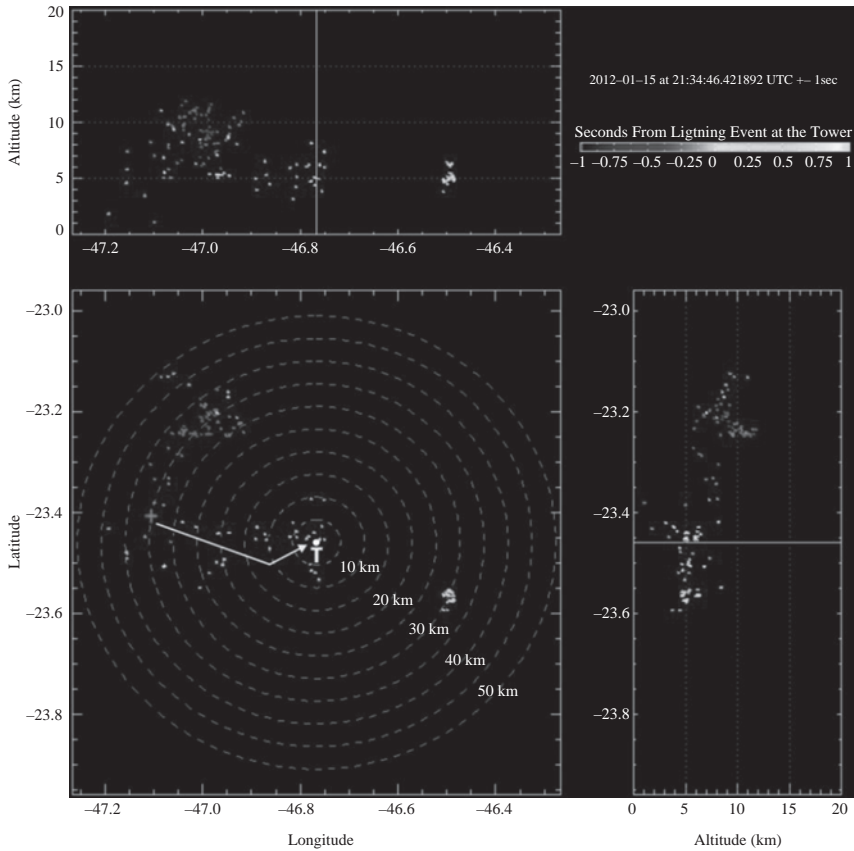


*Figure 5.26 LMA plot showing negative leader that approached a tower and triggered an UPL. The time scale is centred on the +CG return stroke which preceded the UPL. The tower is located at the centre of the image and the arrow shows the progression of the negative leaders following the +CG RS*

frequency would diminish and the leader would continue in a nearly continuous manner. On average, the pulsing terminated within 8 ms of UL initiation and within 600 m of the tower tip. Similar initial pulsing/stepping has been observed with UPLs in rocket-triggered lightning (e.g. [71, 72]). Biagi *et al.* [72] suggest that the transition to a more continuous development is likely due to increasing channel resistance as the leader grows longer. Irregular luminosity variations lasting either 10s of microseconds or 1s of milliseconds frequently followed this transition to a more continuous propagation. The luminosity increase associated with short duration variations initiated at the UPL tip whereas the channel luminosity along the entire UPL length appeared to increase uniformly during the longer lasting variations. A sequence of images of a UPL obtained from a high-speed video is shown in Figure 5.27.

For those leaders that branched shortly after initial development (within 300 m), the branching tended to become prolific with the branched leader network luminosity remaining very low in the newly formed branches. The branch

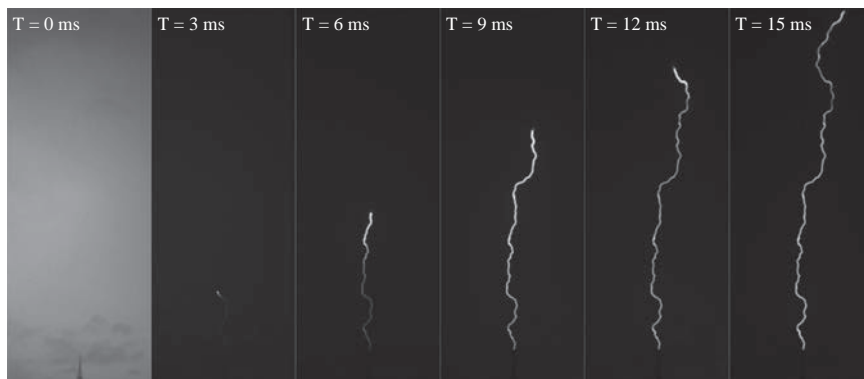


Figure 5.27 A sequence of images showing the development of a UPL. The time stamp in each image indicates the time elapsed from the leader initiation at the tip of a 130-m tower in Brazil (structure shown at the bottom of the image)



Figure 5.28 A composite image of three upward flashes photographed with a digital still camera (20 s exposure)

luminosity would frequently remain below detection thresholds of the faster high-speed cameras (e.g. greater than 20 000 ips). Pulsing similar to that seen with the non-branched ULs was not apparent in these cases.

Most of the ULs transition to horizontal propagation just below cloud base. This region also appeared favourable for branching as half of the ULs observed in South Dakota exhibited further (and sometimes intensified) branching coincident with or immediately following the transition to horizontal propagation.

Typically, the behaviour and geometry of all the ULs that occurred during the same storm were similar. If the first upward flash had an UL that did not branch until approaching cloud base, ULs from following flashes usually did not branch until cloud base as well. Figure 5.28 shows a composite image of three upward flashes that occurred within a 12-minute period. All three non-branched UPLs initiated from the same tower, and all grew vertically without branching before transitioning to horizontal propagation below cloud base.

### 5.4.3 *Corona brush and leader branching*

Non-branched positive leaders tended to be brighter than those that branched and frequently a corona brush was visible at the tip of a non-branched bright leader as it propagated. A similar corona brush was seen with a bright non-branched downward propagating PL associated with a +CG flash as well. The corona brush would change angle width and direction as the leader followed a tortuous path and would split prior to an unsuccessful (or successful) branch attempt. On a few occasions, a corona brush was visible at the tip of multiple bright branches for those UPLs that branched only a few times. Figure 5.29 shows the corona brush at three different times along a UPL's travel. Interestingly, Berger *et al.* [73] reported that corona brush was visible in one upward negative leader filmed with a streak camera, but not with any of the observed UPLs.

Often, when a corona brush was visible, bright and very short length leader segments that extended outward at an upward angle from the leader channel in trail of the leader tip would pulse without growing in length (see Figure 5.30). The

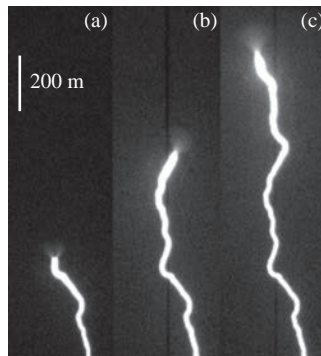


*Figure 5.29* A corona brush is visible at the tip of an upward propagating PL. In (a) the brush splits during an unsuccessful branch attempt. The brush grows in length and brightness as it propagates. The corona brush length at (b) is 83 m and 121 m at (c) (from Warner *et al.* [31])

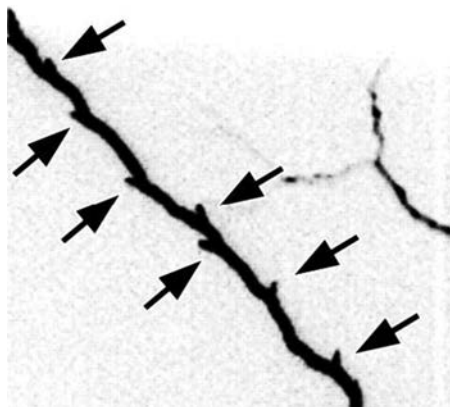


*Figure 5.30* Time-integrated image from high-speed camera (9000 ips, 110  $\mu$ s exposure) showing short attempted leader segments that pulse repeatedly as the leader continues to grow (from Warner *et al.* [31])

shape of these short pulsing segments were descriptively similar in appearance to thorns on a rose stem. Close inspection of the location of these short pulsing leader segments showed that they formed at unsuccessful branches as indicated by corona brush splitting. On one occasion, a short-lived leader branch developed from one of these ‘thorns’ after multiple previous pulses.

When a bright leader channel branched, the two new leader segments would each exhibit luminosity pulsing/stepping similar to that seen during initial development. However, the pulse brightening would alternate between the two new branches. One of the new branch segments would brighten via a luminosity pulse that originated at or near the tip of the leader branch. As the pulse luminosity decayed, the other branch would develop a similar pulse, which would then decay before the first branch would again produce another pulse. As the leader branches grew, the pulsing frequency would diminish and the apparent interdependence between the two branches would also decrease. The branches would then continue to develop independently in a near continuous fashion.

#### *5.4.4 Recoil leaders in upward lightning flashes*

Recoil leaders developed on weakly luminous PL branches that became cutoff from the main upward channel from which they branched [20, 62, 64, 65]. They are particularly easy to observe during the propagation of the PL in upward lightning flashes.

RL development seemed proportional to the amount of branching. Weakly luminous PLs branched much more than bright PLs, and RLs formed on the weakly luminous branches that became cutoff from their branch point. Therefore, widely branched ULs usually produced numerous RLs. In some cases, numerous weak branches were not initially seen by the faster high-speed cameras, however, the subsequent and prolific development of bright RLs along the cutoff branch paths clearly showed where the branches had formed (see Figure 5.31).

Initially, a weakly luminous branch would grow from the branch point with luminosity visible from the branch point to the growing branch tip. As the branch extended further, the luminosity beginning from the branch point outward would

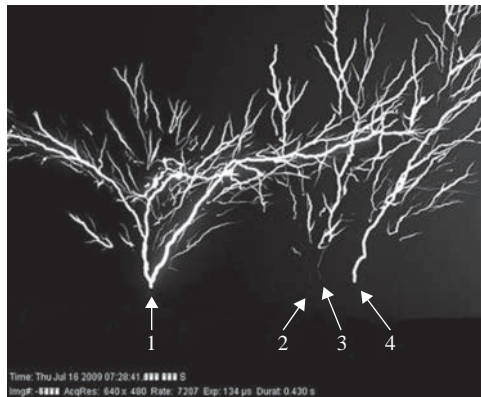


*Figure 5.31 Time-integrated video segment from a high-speed camera (7207 ips, 134  $\mu$ s exposure) showing the prolific development of bright RLs on the weakly luminous branches of four UPLs. Many of the RLs faded prior to connecting to the main stem (from Warner et al. [31])*



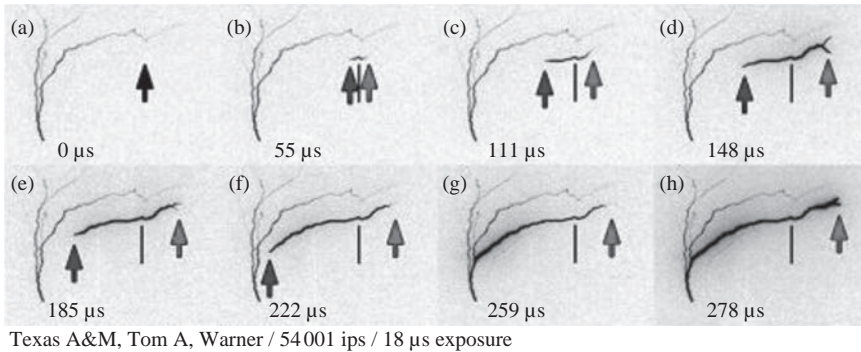


**Figure 5.32** *High-speed camera image sequence (54 001 ips, 18 μs exposure) showing the bidirectional development of an RL. (a) arrow shows the initiation point. (b) RL develops bidirectionally with gray (right) arrow indicating the RLPE and the black (left) indicating the RLNE. Black line remains at the initiation point. (d) RLPE reaches the PL branch tip and illuminates short forked segment. (g) The RLNE reaches the branch point on the main channel and the branch brightens towards the branch tip. Main channel stem between the branch point and tower tip begins brightening. (h) Luminosity increase reaches the positive branch tip and branch extends with new forks visible (from Warner et al. [31])*

fade below the camera-sensing threshold even though the growing tip was still visible.

A bright bidirectional leader (recoil leader) would initiate at a point that lagged behind the tip of the advancing PL branch. The RL would expand bidirectionally with the negative end propagating towards the branch point and the positive end towards the branch tip. Most of the time, the RL would decay before the positive end reached the branch tip or the negative end reached the branch point.

For those that did not fade, the recoil leader positive end (RLPE) would typically reach the tip of the leader branch before the recoil leader negative end (RLNE) reached the branch point. The RLPE arrival at the PL tip many times caused the illumination of a short, forked leader segment. It is unclear if this forked segment was already formed and illuminated by the RLPE or a new forked segment formed due to (and therefore following) the arrival of the RLPE.

When the RLNE connected with a bright main luminous channel at the branch point, the branch luminosity would rapidly increase from the branch point outward towards the branch tip. When the luminosity front reached the branch tip, the forked tip would rebrighten, and frequently additional forks or short branches near the branch tip would illuminate within 250 μs following the front's arrival (Figure 5.32).

#### 5.4.5 *M-components, dart leaders and return strokes in upward lightning flashes*

The behaviour of the main channel stem (branch point to tower tip) following the RLNE arrival at the branch point varied. At recording speeds up to 67 000 ips (14 μs exposure), an RLNE connection at the branch point appeared to cause a bright main channel to brighten evenly along the entire segment no matter how

high the connection. This process was similar to an M-component that happens during the continuing current phase of CG flashes.

However, the luminosity increase rate (rise time) for the main channel was slower with higher connections. In some cases, the brightness increase in the stem was negligible, even when the reconnecting branch experienced a very bright pulse that far exceeded the main channel's luminosity.

As the brightness of the main channel decreased during the course of the flash, there was a point at which the connection of a RLNE at the branch point would fail to produce a luminosity increase. Instead, the RLNE would travel from the branch point down towards the tower tip along the weaker, but still luminous main channel. The RLNE luminosity front would lengthen and travel faster on the more conductive main channel, and a bright luminosity increase would occur when the front reached the tower tip. The luminosity increase would travel back up the path traversed by the RL. This process was similar to a dart leader/return stroke sequence except that the main channel was still luminous and therefore current was not completely cutoff. McEachron [74] described a similar observation after filming upward lightning from the Empire State Building using Boys cameras.

In all our observed cases, the luminous main channel segment from the branch point upward (i.e. the main leader segment above the branch point and not part of the cutoff branch) did not brighten and appeared to not participate in nor be affected by the connections.

Frequently, the reilluminated/reconnected branch would quickly lose its luminosity following an RL connection, and additional RL connections would occur along the same branch in a repeating cycle. The repeated RL connections gave the appearance that the branch was unstable and that the RL connections were trying to establish stable leader growth. On a few occasions, a leader branch would remain luminous following a connection and would then grow continuously without additional RLs forming.

Figure 5.32 shows the initiation and development of an RL that formed along a cutoff PL branch as captured by a high-speed camera (54 001 ips, 18  $\mu$ s exposure) in South Dakota. The RL developed bidirectionally and the RLNE connected with the main luminous channel causing a brightness increase from the branch point out the PL branch upon which the RL formed. The luminous main channel stem (between the branch point and tower tip) brightened more slowly and reached a lower peak luminosity value than the branch.

This connection would, therefore, result in a current pulse exceeding the slowly varying current resulting from the developing UL (e.g. [67, 75]). If the impulsive electric field change resulting from these connections exceeds the LLS's sensing threshold, a negative polarity event ( $-CG$  or negative IC) would be recorded. This was in fact the case for those connections exhibiting the brightest pulse luminosity as seen by the high-speed cameras [31].

There were some cases when the connections occur in a completely dark channel producing the classic dart leader/return stroke sequence that is well known in  $-CG$  flashes. Although the towers struck by lightning in South Dakota and in São Paulo, Brazil, were not instrumented to measure current, based on the sensitivity of the high-speed cameras and on some electric field measurements, it is plausible to assume that these RLs in upward lightning flashes occurred after a complete cutoff, being therefore, similar to subsequent strokes in  $-CG$  flashes and more easily detected by LLS [70].

## References

- [1] BOYS, C. V.: 'Progressive lightning', *Nature*, 1926, **118**, pp. 749–750
- [2] SCHONLAND, B. F. J. and COLLINS, H.: 'Progressive lightning', *Proc. Roy. Soc. Lond.*, 1934, **A143**, pp. 654–674
- [3] SCHONLAND, B. F. J.: 'The lightning discharge', *Hand. Phys.*, 1956, **22**, pp. 576–628
- [4] KITAGAWA, N., BROOK, M. and WORKMAN E. J.: 'Continuing current in cloud-to-ground lightning discharges', *J. Geophys. Res.*, 1962, **67**, pp. 637–647
- [5] BROOK, M., KITAGAWA, N. and WORKMAN, E. J.: 'Quantitative study of strokes and continuing currents in lightning discharges to ground', *J. Geophys. Res.*, 1962, **67**, pp. 649–659
- [6] WALDTEUFEL, P., METZGER, P., BOULAY, J. L., LAROCHE, P. and HUBERT, P.: 'Triggered lightning strokes originating in clear air', *J. Geophys. Res.*, 1980, **85**, pp. 2861–2868
- [7] JORDAN, D. M., RAKOV, V. A., BESLEY, W. H. and UMAN, M. A.: 'Luminosity characteristics of dart leaders and return strokes in natural lightning', *J. Geophys. Res.*, 1997, **102**, pp. 22,025–22,032
- [8] WINN, W. P., ALDRIDGE, T. V. and MOORE, C. B.: 'Video tape recordings of lightning flashes', *J. Geophys. Res.*, 1973, **78**, pp. 4515–4519
- [9] BRANTLEY, R. D., TILLER, J. A. and UMAN, M. A.: 'Lightning properties in Florida thunderstorms from video tape records', *J. Geophys. Res.*, 1975, **80**, pp. 3402–3406
- [10] THOMSON, E. M., GALIB, M. A., UMAN, M. A., BEASLEY, W. H. and MASTER, M. J.: 'Some features of stroke occurrence in Florida lightning flashes', *J. Geophys. Res.*, 1984, **89**, pp. 4910–4916
- [11] MOREAU, J., ALLIOT, J. and MAZUR, V.: 'Aircraft lightning initiation and interception from in situ electric measurements and fast video observations', *J Geophys Res.*, 1992, doi: 10.1029/92JD01077. issn: 0148-0227
- [12] BALLAROTTI, M. G., MEDEIROS, C., SABA, M. M. F., SCHULZ, W. and PINTO JR., O.: 'Frequency distributions of some parameters of negative downward lightning flashes based on accurate-stroke-count studies', *J. Geophys. Res.*, 2012, doi:10.1029/2011JD017135
- [13] SABA M. M. F., *et al.*: 'High-speed video observations of positive lightning flashes to ground', *J. Geophys. Res.*, 2010, **115**, doi:10.1029/2010JD014330
- [14] BIAGI, C. J., *et al.*: 'Observations of stepping mechanisms in a rocket-and-wire triggered lightning flash', *J. Geophys. Res.*, 2010, **115**, D23215, doi:10.1029/2010JD014616
- [15] MAZUR, V., RUHNKE, L. H. and LAROCHE, P.: 'The relationship of leader and return stroke processes in cloud-to-ground lightning', *Geophys. Res. Lett.*, 1995, **22**, doi:10.1029/95GL02348. issn: 0094-8276
- [16] BALLAROTTI, M. G., SABA, M. M. F. and PINTO JR., O.: 'High-speed camera observations of negative ground flashes on a millisecond-scale', *Geophys. Res. Lett.*, 2005, **32**, L23802, doi:10.1029/2005GL023889
- [17] SABA, M. M. F., BALLAROTTI, M. G. and PINTO JR. O.: 'Negative cloud-to-ground lightning properties from high-speed video observations', *J. Geophys. Res.*, 2006, **111**, D03101, doi:10.1029/2005JD006415

- [18] SABA, M. M. F., PINTO JR., O. and BALLAROTTI, M. G.: 'Relation between lightning return stroke peak current and following continuing current', *Geophys. Res. Lett.*, 2006, **33**, L23807, doi:10.1029/2006GL027455
- [19] CAMPOS, L. Z. S., SABA, M. M. F., PINTO JR., O. and BALLAROTTI, M. G.: 'Waveshapes of continuing currents and properties of M-components in natural negative cloud-to-ground lightning from high-speed video observations', *Atmos. Res.*, 2007, **84**, pp. 302–310, doi:10.1016/j.atmosres.2006.09.002
- [20] SABA M. M. F., *et al.*: 'Positive leader characteristics from high-speed video observations', *Geophys. Res. Lett.*, 2008, **35**, L07802, doi:10.1029/2007GL033000
- [21] SABA M. M. F., CAMPOS, L. Z. S, KRIDER, E. P. and PINTO JR., O.: 'High-speed video observations of positive ground flashes produced by intracloud lightning', *Geophys. Res. Lett.*, 2009, **36**, L12811, doi:10.1029/2009GL038791
- [22] CAMPOS, L. Z. S., SABA, M. M. F., PINTO JR., O. and BALLAROTTI, M. G.: 'Waveshapes of continuing currents and properties of M-components in natural positive cloud-to-ground', *Lightning, Atmos. Res.*, 2009, **91**, pp. 416–424, doi:10.1016/j.atmosres.2008.02.020
- [23] FERRO, M. A., SABA, M. M. F. and PINTO JR., O.: 'Continuing current in multiple channel cloud-to-ground lightning', *Atmos. Res.*, 2009, **91**, pp. 399–403
- [24] SARAIVA, A. C. V., *et al.*: 'A comparative study of negative cloud-to-ground lightning characteristics in São Paulo (Brazil) and Arizona (United States) based on high-speed video observations', *J. Geophys. Res.*, 2010, **115**, D11102, doi:10.1029/2009JD012604
- [25] FERRO, M. A. S., SABA, M. M. F. and PINTO JR., O.: 'Time-intervals between negative lightning strokes and the creation of new ground terminations', *Atmos. Res.*, 2012, **116**, pp. 130–133
- [26] SCHUMANN, C., 'Caracterização dos raios positivos através de câmeras de alta velocidade e sensores de campo elétrico', Master dissertation, Department of Space Geophysic, Atmospheric Electricity Group, National Institute for Space Research, São José dos Campos, 2012, Brazil, <http://urlib.net/rep/8JMKD3MGP7W/3BPDNCS?languagebutton=pt-BR>
- [27] BERGER, K. and VOGELSANGER, E.: 'Photographische Blitzuntersuchungen der Jahre 1955–1965 auf dem Monte San Salvatore', *Bull. Schweiz. Elektrotech.*, 1966, Ver., **57**, pp. 599–620.
- [28] BIAGI, C. J., *et al.*: 'High-speed video observations of rocket-and-wire initiated lightning', *Geophys. Res. Lett.*, 2009, **36**, L15801, doi:10.1029/2009GL038525
- [29] GALLIMBERTI, I., BACCHIEGA, G., BONDIOU-CLERGERIE, A. and LALANDE P.: 'Fundamental processes in long air gap discharges', *Comptes Rendus-Physique*, 2002, **3**(10), 1335–1359
- [30] CAMPOS, L. Z. S., *et al.*: 'High-speed video observations of natural cloud-to-ground lightning leaders – a statistical analysis', *Atmos. Res.*, 2013, <http://dx.doi.org/10.1016/j.atmosres.2012.12.011>
- [31] WARNER, T. A., *et al.*: 'Lightning-triggered upward lightning from towers in Rapid City', South Dakota, paper presented at the 2012 International Lightning Detection Conference, 2012, Apr. 2–3, Boulder, Colorado

- [32] MAZUR, V., RUHNKE, L. H., WARNER, T. A. and ORVILLE, R. E.: 'Recoil leader formation and development', *J. Electrostatics*, 2013, **71**(4), pp. 763–768
- [33] RAKOV, V. A. and HUFFINES, G. R.: 'Return-stroke multiplicity of negative cloud-to-ground lightning flashes', *J. Appl. Meteor.*, 2003, **42**, pp. 1455–1462
- [34] MALAN, D. J., 'The relation between the number of strokes intervals and the total durations of lightning discharges', *Geofis. Pura Appl.*, 1956, **34**, pp. 224–230
- [35] RAKOV, V. A. and UMAN, M. A.: 'Some properties of negative cloud-to-ground lightning versus stroke order', *J. Geophys. Res.*, 1990, **95**, pp. 5447–5453
- [36] RAKOV, V. A., UMAN, M. A. and THOTTAPPILLIL, R., 'Review of lightning properties from electric field and TV observations', *J. Geophys. Res.*, 1994, **99**, 10,745–10,750
- [37] ANDERSON R. B. and ERIKSSON A. J.: 'Lightning parameters for engineering application', *Electra*, 1980, **69**, pp. 65–102
- [38] KONG, X., QIE, X. and ZHAO, Y.: 'Characteristics of downward leader in a positive cloud-to-ground lightning flash observed by high-speed video camera and electric field changes', *Geophys. Res. Lett.*, 2008, **35**, p. L05816.
- [39] CUMMINS, K. L. and MURPHY, M. J.: 'An overview of lightning locating systems: History, techniques, and data uses, with an in-depth look at the U.S. NLDN', *IEEE Trans. Electromagn. Compat.*, 2009, **51**, pp. 499–518, doi:10.1109/TEMC.2009.2023450
- [40] THOTTAPPILLIL, R., *et al.*: 'Lightning subsequent stroke electric field peak greater than the first stroke peak and multiple ground terminations', *J. Geophys. Res.*, 1992, **97**, pp. 77,503–77,509
- [41] STALL, C. A., CUMMINS, K. L., KRIDER, E. P. and CRAMER, J. A.: 'Detecting multiple ground contacts in cloud-to-ground lightning flashes', *J. Atmos. Oceanic Technol.*, 2009, **26**, pp. 2392–2402, doi:10.1175/2009JTECHA1278.1
- [42] ORVILLE, R. A. and HUFFINES, G. R.: 'Cloud-to-ground lightning in the United States: NLDN results in the first decade', 1989–1998. *Mon. Wea. Rev.*, 2001, **129**, pp. 1179–1193
- [43] CUMMINS, K. L., *et al.*: 'A combined TOA/MDF Technology Upgrade of the U.S. National Lightning Detection Network', *J. Geophys. Res.*, 1998, **103**, pp. 9035–9044
- [44] BIAGI, C. J., CUMMINS, K. L., KEHOE, K. E. and KRIDER, E. P.: 'National Lightning Detection Network (NLDN) performance in southern Arizona, Texas, and Oklahoma in 2003–2004', *J. Geophys. Res.*, 2007, **112**(D5)
- [45] MEDEIROS, C. and SABA, M. M. F., 'Presence of continuing currents in negative cloud-to-ground flashes', *International Conf. on Lightning Detection*, 2012, Denver.
- [46] RAKOV, V. A., *et al.*: 'Lightning parameters for engineering applications', CIGRE WG C4.407 Technical Brochure 549, 2013, 117 p., Aug.
- [47] DIENDORFER, G., VIEHBERGER, M., MAIR, M., and SCHULZ, W.: 'An attempt to determine currents in lightning channels branches from optical

- data of a high-speed video system', International Conference on Lightning and Static Electricity 2003, Blackpool, Inglaterra.
- [48] SHINDO, T. and UMAN, M. A.: 'Continuing current in negative cloud-to-ground lightning', *J. Geophys. Res.*, 1989, **94**, pp. 5189–5198
- [49] FISHER, F. A. and PLUMER, J. A.: 'Lightning protection of aircraft', NASA, 1977, *Ref. Publ.*, NASA-RP-1008
- [50] RAKOV, V. A., and UMAN, M. A.: 'Long continuing current in negative lightning ground flashes', *J. Geophys. Res.*, 1990, **95**, pp. 5455–5470
- [51] CHISHOLM, W. A., LEVINE, J. P. and CHOWDHURI, P.: 'Lightning arc damage to optical fiber ground wires (OPGW): Parameters and test methods', in 2001 *Power Engineering Society Summer Meeting. Conference Proceedings*, 2001, **1**, pp. 88–93, Vancouver, BC, Canada, 15–19 Jul. 2001
- [52] BEASLEY, W.: 'Positive cloud-to-ground lightning observations', *J. Geophys. Res.*, 1985, **90**(D4), pp. 6131–6138
- [53] RUST, W. D., MACGORMAN, D. R. and ARNOLD, R. T.: 'Positive cloud to ground lightning flashes in severe storms', *Geophys. Res. Lett.*, 1981, **8**, pp. 791–794.
- [54] FUQUAY M. D.: 'Positive cloud-to-ground lightning in summer thunderstorms', *J. Geophys. Res.*, 1982, **87**, pp. 7131–7140
- [55] BEASLEY, W. H., UMAN, M. A., JORDAN, D. M. and GANESH, C.: 'Positive cloud to ground lightning return strokes', *J. Geophys. Res.*, 1983, **88**, pp. 8475–8482
- [56] LIVINGSTON, J. M. and KRIDER, E. P.: 'Electric fields produced by Florida thunderstorms', *J. Geophys. Res.*, 1978, **83**, pp. 385–401
- [57] IEC 62305–1: 'Protection Against Lightning, Part 1: General Principles', 2006
- [58] RAKOV, V. A. and UMAN, M. A.: 'Lightning: Physics and effects', pp. 687, Cambridge Univ. Press, 2003 New York
- [59] FISHER, R. J., *et al.*: 'Parameters of triggered-lightning flashes in Florida and Alabama', *J. Geophys. Res.*, 1993, **98**, 22887–22908
- [60] JERAULD J. E., *et al.*: 'Measured electric and magnetic fields from an unusual cloud-to-ground lightning flash containing two positive strokes followed by four negative strokes', *J. Geophys. Res.*, 2009, pp. 114, D19115, doi:10.1029/2008JD011660
- [61] FLEENOR, S. A., BIAGI, C. J., CUMMINS, K. L., KRIDER, E. P. and SHAO, X. M.: 'Characteristics of cloud-to-ground lightning in warm-season thunderstorms in the Central Great Plains', *Atmos. Res.*, 2009, **91**, doi:10.1016/j.atmosres.2008.08.011, 333–352
- [62] SABA, M. M. F., *et al.*: 'Bipolar cloud-to-ground lightning flash observations', *J. Geophys. Res. Atmos.*, 2013, **118**, doi:10.1002/jgrd.50804
- [63] HECKMAN, S., 'Why does a lightning flash have multiple strokes?' PhD thesis, Department of Earth, Atmospheric and Planetary Sciences, Massachusetts Institute of Technology, Cambridge, MA, June, 1992, pp. 134
- [64] MAZUR, V.: 'Physical processes during the development of lightning flashes', *C. R. Acad. Sci.*, 2002, R. Physique, Ser. IV, **3**, pp. 1393–1409

- [65] MAZUR, V. and RUHNKE, L. H.: 'Physical processes during development of upward leaders from tall structures', *J. Electrostatics*, 2011, **69**, pp. 97–110
- [66] SABA, MARCELO M. F., *et al.* 'Upward lightning in Brazil First results', In: Ground 2012 International Conference on Grounding and Earthing & 5th International Conference on Lightning Physics and Effects, 2012, Bonito-MS. Ground 2012 International Conference on Grounding and Earthing & 5th International Conference on Lightning Physics and Effects, 2012
- [67] DIENDORFER, G., PICHLER, H. and MAIR, M.: 'Some parameters of negative upward-initiated lightning to the Gaisberg Tower (2000–2007)', *IEEE Trans. Electromagnetic Compatibility*, 2009, **51**, p. 3
- [68] WARNER, T. A., HELSDON JR., J. H., BUNKERS, M. J., SABA, M. M. F., and ORVILLE, R. E.: 'UPLIGHTS – upward lightning triggering study', *Bull. Amer. Meteor. Soc.*, 2013, **94**(5), pp. 631–635
- [69] WANG, D., TAKAGI, N., WATANABE, T., SAKURANO, H. and HASHIMOTO, M.: 'Observed characteristics of upward leaders that are initiated from a windmill and its lightning protection tower', *Geophys. Res. Lett.*, 2008, **35**, L02803, doi:10.1029/2007GL032136
- [70] WARNER T. A., CUMMINS, K. L. and ORVILLE, R. E.: 'Upward lightning observations from towers in Rapid City, South Dakota and comparison with National Lightning Detection Network data 2004–2010', *J. Geophys. Res.*, 2012, **117**, D19109, doi:10.1029/2012JD018346
- [71] IDONE, V. P.: 'The luminous development of Florida triggered lightning', *Res. Lett. Atmos. Electr.*, 1992, **122**, pp. 23–28
- [72] BIAGI, C. J., UMAN, M. A., HILL, J. D. and JORDAN, D. M.: 'Observations of the initial, upward-propagating, positive leader steps in a rocket-and-wire triggered lightning discharge', *Geophys. Res. Lett.*, 2011, **38**, doi: 10.1029/2011GL049944. issn: 0094-8276
- [73] BERGER, K.: 'Novel observations on lightning discharges: Results of research on Mount San Salvatore', *J. Franklin Inst.*, 1967, **283**, pp. 478–525
- [74] MCEACHRON, K. B.: 'Lightning to the Empire State Building', *J. Franklin Inst.*, 1939, **227**, pp. 149–217
- [75] FLACHE, D., RAKOV, V. A., HEIDLER, F., ZISCHANK, W. and THOTTAPPILLIL, R.: 'Initial-stage pulses in upward lightning: Leader/return stroke versus M-component mode of charge transfer to ground', *Geophys. Res. Lett.*, 2008, **35**, L13812, doi:10.1029/2008GL034148

---

## Chapter 6

# Rocket-and-wire triggered lightning experiments

Vladimir A. Rakov

---

### 6.1 Introduction

An understanding of the physical properties and deleterious effects of lightning is critical to the adequate protection of power and communication lines, aircraft, spacecraft, and other objects and systems. Many aspects of lightning are not yet well understood and are in need of research that often requires the termination of lightning channel on an instrumented object or in the immediate vicinity of various sensors. The probability for a natural lightning to strike a given point on the Earth's surface or an object of interest is very low, even in areas of relatively high lightning activity. Simulation of the lightning channel in a high-voltage laboratory has very limited application, since it does not allow the reproduction of many lightning features important for lightning protection and it does not allow the testing of large distributed systems such as overhead power lines. One promising tool for studying both the direct and the induced effects of lightning is an artificially initiated (or triggered) lightning discharge from a thunderstorm cloud to a designated point on ground. In most respects, the triggered lightning is a controllable analog of natural lightning. The most effective technique for artificial lightning initiation is the so-called rocket-and-wire technique. This technique involves the launching of a small rocket extending a thin wire (either grounded or ungrounded) into the gap between the ground and a charged cloud overhead.

The possibility of artificially initiating lightning by ground-based activity was apparently first discussed by Newman (1958) and by Brook *et al.* (1961). Brook *et al.* (1961) showed that, in the laboratory, a spark discharge could be triggered by the rapid introduction of a thin wire into an electric field, while the steady presence of the wire did not result in a spark. They suggested that the corona discharge from a stationary conductor acts to shield this conductor so that the high fields necessary to initiate electrical breakdown are not obtained, whereas the field enhancement due to the rapid introduction of a conductor is not significantly reduced by corona, since there is insufficient time for its development.

The first triggered lightning discharges were produced in 1960 by launching small rockets trailing thin grounded wires from a research vessel off the west coast of Florida (Newman 1965; Newman *et al.* 1967; Newman and Robb 1977). The first triggering over land was accomplished in 1973, at Saint-Privat d'Allier in France (Fieux *et al.* 1975, 1978). In the following decades, a number of triggered-lightning programs have been developed in different countries, as summarized in Table 6.1. As of this writing, there are four operating lightning-triggering facilities, two in the United States (in New Mexico and in Florida) and



Table 6.1 An overview of major triggered-lightning programs

Experimental site	Height above sea level, m	Years of operation <sup>a</sup>	Wire material	Location of wire spool	Selected references
Saint Privat d'Allier, France	1100	1973–1996	Steel or copper	Ground or rocket	Fioux <i>et al.</i> (1978), SPARG (1982)
Kahokugata, Hokuriku coast, Japan	0	1977–1985	Steel	Ground	Horii (1982), Kito <i>et al.</i> (1985)
Langmuir Laboratory, New Mexico	3230	1979–present	Steel	Ground	Hubert <i>et al.</i> (1984), Idone <i>et al.</i> (1984)
KSC, Florida (south of Melbourne, Florida in 1983)	0	1983–1991	Copper	Rocket	Eybert-Berard <i>et al.</i> (1986, 1988), Willett (1992)
Okushishiku, Japan	930	1986–1998	Steel	Ground or rocket	Nakamura <i>et al.</i> (1991, 1992)
Seven different sites in China <sup>b</sup>	Various	1989–present	Steel or copper	Ground or rocket	Liu <i>et al.</i> (1994), Qie <i>et al.</i> (2009), Zhang <i>et al.</i> (2013)
Fort McClellan, Alabama	190	1991–1995	Copper	Rocket	Fisher <i>et al.</i> (1993), Morris <i>et al.</i> (1994)
Camp Blanding, Florida	20–25	1993–present	Copper	Rocket	Uman <i>et al.</i> (1997), Rakov <i>et al.</i> (1998, 2005)
Cachoeira Paulista, Brazil	570	1999–2007	Copper	Rocket	Saba <i>et al.</i> (2000, 2005), Pinto <i>et al.</i> (2005)

<sup>a</sup>As of this writing and not necessarily continuous.

<sup>b</sup>As of this writing, experiments are conducted at two sites, one in Shandong province, eastern China (since 2005) and the other in Guangdong province, southern China (since 2006). Additionally, triggered-lightning experiments have been conducted in Germany (Hierl 1981), in Indonesia (Horii *et al.* 1990), and in Russia (Beituganov and Zashakuev 1992).

two in China (in Guangdong and Shandong provinces). Rocket-triggered lightning experiments in France have been reviewed by Fieux *et al.* (1978); in Japan by Horii (1982), Kito *et al.* (1985), Nakamura *et al.* (1991, 1992), and Horii *et al.* (2006); in New Mexico by Hubert *et al.* (1984); at the Kennedy Space Center, Florida, by Willett (1992); at Camp Blanding, Florida, by Uman *et al.* (1997) and Rakov *et al.* (1998, 2005a); in China by Liu and Zhang (1998), Qie *et al.* (2009), and Zhang *et al.* (2013); and in Brazil by Pinto *et al.* (2005). Triggered-lightning experiments conducted in different countries have been reviewed by Uman (1987), Horii and Nakano (1995), Rakov (1999b, 2009, 2010), Rakov and Uman (2003, Ch. 7), and Qie *et al.* (2012).

In all published experiments, the triggering wires were made of either steel or copper with a diameter of typically about 0.2 mm, wound on a spool located either on the ground or on the rocket. Various rockets made of plastic and of steel have been used, with the rocket length being typically about 1 m. Most of the experiments in Japan were conducted in the winter, the several attempts made to trigger in the summer months being unsuccessful. At Camp Blanding, Florida, lightning has been triggered in both summer and winter storms. All other triggering sites have apparently been operated only during the summer. The results from these programs have made possible a number of new insights into the various lightning processes and effects.

Descriptions of the classical and altitude rocket-and wire triggering techniques are given in sections 6.2.1 and 6.2.2, respectively. More than a thousand lightning discharges have been triggered using these techniques to date. An overview of lightning-triggering facilities is found in Table 6.1, with a description of Camp Blanding facility being given in section 6.2.3. Over 400 lightning flashes were triggered to date at the Camp Blanding site. Properties of rocket-triggered lightning (including its close electromagnetic environment) are reviewed in sections 6.3 through 6.6. The use of rocket-triggered lightning for testing various objects and systems (which can be viewed as the primary focus of this chapter) is described in section 6.7.

## 6.2 Triggering techniques

Two techniques for triggering lightning with a small rocket that extends a thin wire in the gap between a thundercloud and the ground are discussed here. “Classical” triggering is described in section 6.2.1 and “altitude” triggering in section 6.2.2. These descriptions primarily apply to triggering negative lightning.

### 6.2.1 Classical triggering

This triggering method involves the launching of a small rocket trailing a thin grounded wire toward a charged cloud overhead, as illustrated in Figure 6.1. Still photographs of classical triggered lightning flashes are shown in Figure 6.2. To decide when to launch a triggering rocket, the cloud charge is indirectly sensed by measuring the electric field at ground, with absolute values of 4–10 kV·m<sup>-1</sup> generally being good indicators of favorable conditions for negative lightning initiation in Florida, as seen in Figure 6.3. However, other factors, such as the general trend of the electric field and the frequency of occurrence of natural lightning discharges, are usually taken into account in making the decision to

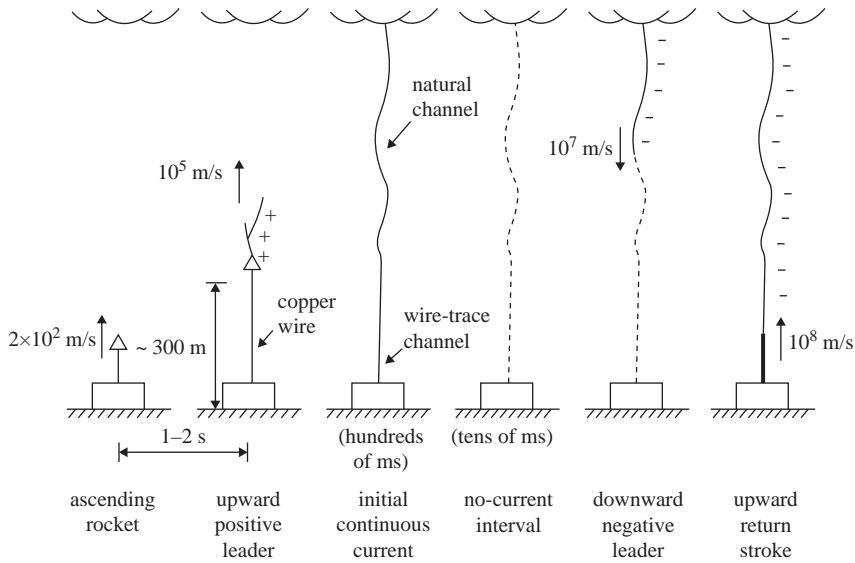


*Figure 6.1* Sequence of events (except for precursors and the attachment process) in classical triggered lightning. The upward positive leader (UPL) and initial continuous current (ICC) constitute the initial stage (IS) (adapted from Rakov *et al.* 1998)

launch a rocket. The triggering success rate is generally relatively low during very active periods of thunderstorms, one reason being that during such periods the electric field is more likely to be reduced by a natural lightning discharge before the rocket rises to a height sufficient for triggering.

When the rocket, ascending at about  $150\text{--}200\text{ m s}^{-1}$ , is about  $200\text{--}300\text{ m}$  high, the field enhancement near the rocket tip launches a positively charged leader that propagates upward toward the cloud. This upward positive leader (UPL) vaporizes the trailing wire, bridges the gap between the cloud charge source and ground, and establishes an initial continuous current (ICC) with a duration of some hundreds of milliseconds that transports negative charge from cloud charge source to the triggering facility. The ICC can be viewed as a continuation of the UPL when the latter has reached the main negative charge region in the cloud. At that time, the upper extremity of the UPL is likely to become heavily branched. The UPL and ICC constitute the initial stage (IS) of a classical triggered lightning discharge. After the cessation of the initial continuous current, one or more downward dart leader/upward return stroke sequences may traverse the same path to the triggering facility. It is important to stress that by the time of initiation of dart leader the triggering wire is long gone, so that the leader has to propagate all the way to the ground (triggering facility). Only one leader/return stroke sequence is depicted in Figure 6.1, with possible upward connecting leader being not shown to simplify the drawing. Further, not shown in Figure 6.1, are the so-called precursors (Willett *et al.* 1999; Biagi *et al.* 2012) that occur prior to the onset of sustained UPL and can be viewed as aborted UPLs.

The dart leaders and the following return strokes in triggered lightning are similar to dart leader/return stroke sequences in natural lightning, although the initial processes in natural downward and classical triggered lightning are distinctly different.

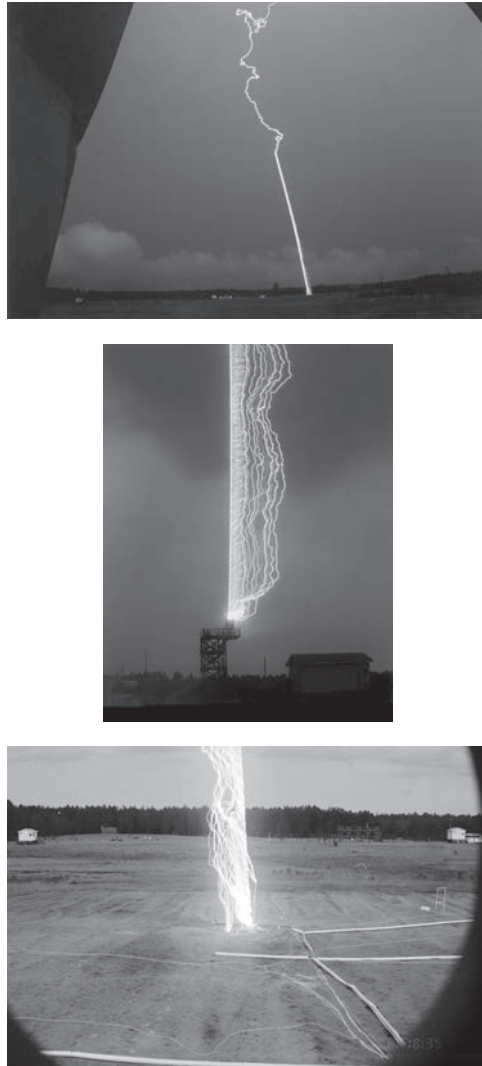
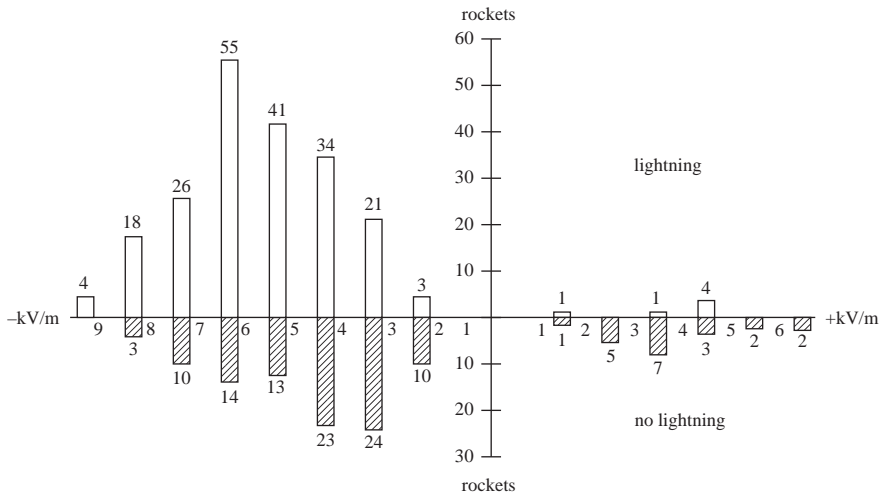


Figure 6.2 Photographs of lightning flashes triggered at Camp Blanding, Florida. Top – a distant view of a strike to the test runway; middle, a strike to the test power system initiated from the tower launcher; bottom – a strike initiated from the underground launcher at the center of a  $70 \times 70 \text{ m}^2$  buried metallic grid

In summer, the triggering success rate for positive lightning is apparently lower than for negative lightning (e.g., Fieux *et al.* 1978), one known exception being the triggered lightning experiment in northern China (Liu *et al.* 1994; Liu and Zhang 1998), although all discharges triggered there were composed of an initial stage only, that is, no leader/return stroke sequences occurred.

There is contradictory information regarding whether the height  $H$  of the rocket at the time of lightning triggering depends on the electric field intensity  $E$  at ground at the time of launching the rocket. Hubert *et al.* (1984) found a strong correlation between  $H$  and  $E$  ( $H$  decreasing with increasing  $E$ ) for triggered



242 Rockets Triggered Lightning (Readings Not Available For 34)  
 167 Rockets Did Not Trigger Lightning (Readings Not Available For 50)

Figure 6.3 Histograms of successful (above the horizontal axis) and unsuccessful (below the horizontal axis) classical triggering attempts in 1983–1991 at the NASA Kennedy Space Center. Individual histogram bins correspond to different positive and negative values of surface electric field at the time of rocket launch. Upward-directed field is considered negative (atmospheric electricity sign convention) (adapted from Jafferis 1995)

lightning in New Mexico. They gave the following equation between  $H$  (in meters) and  $E$  (in  $\text{kV}\cdot\text{m}^{-1}$ )

$$H = 3900E^{-1.33} \tag{6.1}$$

In Hubert *et al.*'s (1984) study,  $E$  varied from about 5 to 13  $\text{kV}\cdot\text{m}^{-1}$  and  $H$  from about 100 to 600 m, with a mean value of 216 m. On the other hand, in winter triggered-lightning studies at the Kahokugata site in Japan (Table 6.1), no clear relation was observed between  $H$  and  $E$  for either sign of  $E$  (Horii and Nakano 1995; Figure 6.2.3). Biagi *et al.* (2011) reported a strong linear relationship between  $H$  and  $E$  ( $H$  decreasing with increasing  $E$ ) for triggered lightning in Florida.

Willett *et al.* (1999), who used electric field sounding rockets in Florida, studied ambient-field conditions that are sufficient to initiate and sustain the propagation of upward positive leaders in triggered lightning. It was found that lightning can be initiated with grounded triggering wires approximately 400 m long when the ambient fields aloft are as small as 13  $\text{kV}\cdot\text{m}^{-1}$ . When lightning occurred, ambient potentials with respect to Earth at the triggering-rocket altitude were 3.6 MV (negative with respect to Earth). These potentials were referred to as triggering potentials by Willett *et al.* (1999).

### 6.2.2 Altitude triggering

A stepped leader followed by a first return stroke in natural downward lightning can be reproduced to some degree by triggering lightning via a metallic wire that is

not attached to the ground. This ungrounded-wire technique is usually called altitude triggering and is illustrated in Figure 6.4 which shows that a bidirectional (positive charge up and negative charge down) leader process is involved in the initiation of the first return stroke from ground. Note that the “gap” (in this case, the length of the insulating kevlar cable) between the bottom end of the upper (triggering) wire and the top end of the grounded (intercepting) wire is some hundreds of meters. Altitude triggering can also be accomplished without using an intercepting wire whose only function is to increase the probability of lightning attachment to the instrumented rocket-launching facility. In some triggered-lightning experiments, the bottom end of the triggering wire has been attached to an air gap of up to 10 m in length (e.g., Nakamura *et al.* 1992). Such triggering is not considered as being of the altitude type, since it was not intended to simulate the downward stepped leader (discussed below in this section) from the bottom of the triggering wire. On the other hand, altitude triggering may also occur as a result of the accidental breakage of the wire during classical triggering, so that the wire connection to ground is unintentionally lost. Additionally, altitude triggering has been accomplished using a two-stage rocket system in which the two rockets separated in the air with the triggering wire extending between them (e.g., Nakamura *et al.* 1992). The properties of altitude triggered lightning are discussed by Laroche *et al.* (1991),

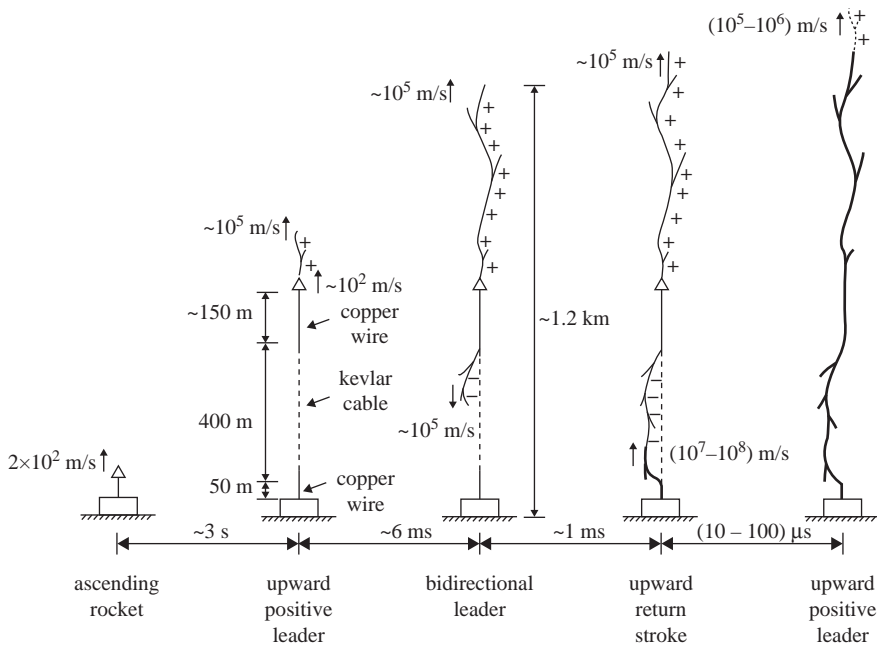


**Figure 6.4** Sequence of events (except for the attachment process) in altitude triggered lightning leading to the establishment of a relatively low-resistance connection between the upward-moving positive leader tip and the ground, based on the event described by Laroche *et al.* (1991). The processes that follow the sequence of events shown, the initial continuous current and downward leader/upward return-stroke sequences, are similar to their counterparts in classical triggered lightning (see Figure 6.1) (adapted from Rakov *et al.* 1998)

Lalande *et al.* (1996, 1998), Uman *et al.* (1996), Rakov *et al.* (1996, 1998), Wang *et al.* (1999d), Chen *et al.* (2003), Saba *et al.* (2005), and Lu *et al.* (2009).

In the following, we briefly discuss the sequence of processes involved in altitude triggered lightning, as illustrated in Figure 6.4. A downward negative leader is usually launched from the lower end of the elevated triggering wire some milliseconds after the initiation of UPL from the upper end of the wire (Lalande *et al.* 1998; Figure 6). The downward negative leader shown in Figure 6 of Lalande *et al.* (1998) was apparently initiated after two unsuccessful attempts. As the negative downward leader approaches the triggering facility, an upward connecting leader (not shown in Figure 6.4) is initiated from the grounded intercepting wire. Once the attachment between the two leaders is made, the return stroke is initiated. Since (1) the length of the channel available for the propagation of the first return stroke in altitude triggered lightning is relatively small (of the order of 1 km) and (2) the return-stroke speed is two to three orders of magnitude higher than that of the leader, the return stroke catches up with the tip of the upward leader within 10  $\mu$ s or so. As a result, the upward leader becomes strongly intensified. The processes that follow, the initial continuous current and downward leader/upward return-stroke sequences, are probably similar to those in classical triggered lightning (see Figure 6.1). Thus the downward-moving negative leader of the bidirectional leader system and the resulting return stroke in altitude triggered lightning serve to provide a relatively low-resistance connection between the upward-moving positive leader tip and the ground. The initial stage of altitude triggered lightning can be viewed as composed of an initial upward leader, a bidirectional leader (part of which is a continuation of the initial upward leader), an attachment process, an initial-stage return stroke, an intensified upward leader, and an initial continuous current.

Wang *et al.* (1999d) reported on a positive flash that was initiated using the altitude triggering technique from a summer thunderstorm in China. This is the first documented triggering of a positive lightning using the altitude triggering technique. For this flash, the length of grounded intercepting wire was 35 m and the length of insulating cable was 86 m. The flash was apparently initiated when the rocket was at an altitude of 550 m, so that the length of the ungrounded triggering wire was 429 m.

### 6.2.3 *Triggering facility at Camp Blanding, Florida*

The lightning-triggering facility at Camp Blanding, Florida was established in 1993 by the Electric Power Research Institute (EPRI) and Power Technologies, Inc. (PTI). In September 1994, operation of the facility was transferred to the University of Florida (UF). Over 50 researchers (excluding UF faculty, students, and staff) from 15 countries representing 4 continents have performed experiments at Camp Blanding concerned with various aspects of atmospheric electricity, lightning, and lightning protection. Since 1995, the Camp Blanding facility has been referred to as the International Center for Lightning Research and Testing (ICLRT) at Camp Blanding, Florida. Presently, the ICLRT is jointly operated by UF and Florida Institute of Technology (FIT) and additionally includes the Lightning Observatory in Gainesville (LOG) (Rakov *et al.* 2012). A summary of the lightning triggering operations at Camp Blanding conducted for various experiments from 1993 to 2012 is presented in Table 6.2. Over the 20-year period, the total number of triggered flashes was 409, that is, on average about 20 per year (although there was no

Table 6.2 Summary of 1993–2012 triggered-lightning experiments at Camp Blanding, Florida

Year(s)	Rocket launchers used	Total flashes triggered	Flashes with return strokes	Positive or bipolar flashes	Time period
1993	1	32	22	–	Jun. 7–Sep. 21
1994	2	15	11	–	Aug. 4–Sep.
1995	2	14	13	–	Jun. 25–Aug. 19
1996	2	30	25	–	Jun. 20–Sep. 11
1997	4	48	28	1	May 24–Sep. 26
1998	3	34	27	–	May 15, Jul. 24–Sep. 30
1999	2	30	22	1	Jan. 23, Jun. 26–Sep. 27
2000	2	30	27	–	Jun. 12–Sep. 6
2001	2	23	11	–	Jul. 13–Sep. 5
2002	2	19	14	–	Jul. 9–Sep. 13
2003	2	24	12	1	Jun. 30–Aug. 15
2004	1	5	3	–	Jun. 23–Jul. 24
2005	2	11	8	–	Jul. 2–Aug. 5
2006 <sup>a</sup>	–	–	–	–	–
2007	1	2	1	–	Jul. 13–Jul. 31
2008	1	11	7	1	May 16–Oct. 9
2009	1	26	18	2	Feb. 19–Aug. 18
2010	2	13	12	–	Jun. 5–Sep. 27
2011	1	16	12	1	Jan. 25–Aug. 18
2012	1	26	19	1	May 15–Aug. 21
1993–2012		409	292 (71%)	8 (2.0%)	

<sup>a</sup>There was no lightning triggering in 2006.

triggering in 2006), with about 14 (71%) of them containing return strokes. Out of the total of 409 flashes in Table 6.2, 401 transported negative charge and 8 either positive or both negative and positive charge to ground.

The principal results obtained from 1993 through 2012 at the ICLRT include

- identification of the M-component mode of charge transfer to ground (Rakov *et al.* 1995a, 1998, 2001);
- new insights into the lightning stepping mechanism (Rakov *et al.* 1998; Wang *et al.* 1999a; Biagi *et al.* 2010);
- characterization of the close lightning electromagnetic environment (Rakov *et al.* 1998, 2001; Uman *et al.* 2000, 2002; Crawford *et al.* 2001; Schoene *et al.* 2003a);
- inferences on the interaction of lightning with ground and with grounding electrodes (Rakov *et al.* 1998, 2002, 2003a; Bejleri *et al.* 2004; DeCarlo *et al.* 2008);
- first lightning return-stroke speed profiles within 400 m of ground (Wang *et al.* 1999a; Olsen *et al.* 2004);
- observations of upward connecting leaders in triggered-lightning strokes (Wang *et al.* 1999c; Biagi *et al.* 2009);
- electric fields in the immediate vicinity of the lightning channel core, inside the corona sheath (Miki *et al.* 2002);
- discovery and characterization of X-rays produced by triggered-lightning strokes (Dwyer *et al.* 2003, 2004a, 2005; Saleh *et al.* 2009; Schaal *et al.* 2012; Howard *et al.* 2008, 2010; Hill *et al.* 2012);



- new insights into the mechanism of cutoff and reestablishment of current in the lightning channel (Rakov *et al.* 2003b; Olsen *et al.* 2006);
- ground-based observations of gamma-ray bursts, similar to terrestrial gamma-ray flashes (TGFs) recorded by satellite detectors (Dwyer *et al.* 2004b, 2012);
- ground-truth evaluation of the performance characteristics of the U.S. National Lightning Detection Network (NLDN) (Jerauld *et al.* 2005; Nag *et al.* 2011);
- direct estimates of lightning input energy (Jayakumar *et al.* 2006);
- first direct measurements of NO<sub>x</sub> production by lightning (Rahman *et al.* 2007);
- characterization of currents induced by lightning in a buried loop conductor and in a grounded vertical conductor (Schoene *et al.* 2008);
- first VHF images of UPLs in triggered lightning (Yoshida *et al.* 2010).

Some of these results are discussed in more detail in the following sections.

### 6.3 Overall current waveforms

In this section, we discuss currents measured at the rocket launcher. For both classical and altitude triggered lightning, the emphasis will be placed on the initial stage, with the characterization of current waveforms due to return strokes (primarily from classical triggered lightning) being presented in section 6.4. Initial-stage return strokes in altitude triggered lightning are discussed in section 6.3.2. For classical triggered lightning, initial-stage current initially flows through the triggering wire until the wire is destroyed and replaced by a plasma channel, as described by Rakov *et al.* (2003b) and Olsen *et al.* (2006). Gamerota *et al.* (2013) reported on an “anomalous” flash in which the explosion of triggering wire was followed by a downward stepped leader (apparently from the bottom of the floating UPL channel, 282 m above ground level) that attached to a grounded utility pole 117 m from the launching facility. For altitude triggered lightning, current exceeding some amperes is first measured when an upward connecting leader (not shown in Figure 6.4) emanates from the launcher (or from a grounded intercepting wire) in response to the approaching downward-extending, negative part of the bidirectional leader system.

#### 6.3.1 Classical triggering

The overall current record for a typical negative classical triggered lightning flash is presented in Figure 6.5a, and portions of this record are shown on expanded time scales in Figure 6.5b and c. The record is intentionally clipped at the 2-kA level in order to accentuate the current components in the hundreds of amperes range. Other researchers (e.g., Eybert-Berard *et al.* 1986, 1988) used recorders with a logarithmic vertical scale in order to be able to view both small currents and large currents on the same record. Median values of the overall flash duration from triggered lightning experiments in France and New Mexico are 350 and 470 ms (Hubert 1984), respectively. The median flash charges from the same studies are 50 and 35 C, respectively. Both the flash duration and charge transferred are comparable, within a factor of 2–4, to their counterparts in object-initiated lightning and in natural downward lightning.

We first consider the overall characteristics, that is, the duration, the charge transfer, and the average current, of the initial stage (IS), and then discuss (1) the current variation at the beginning of the IS, termed the initial current variation

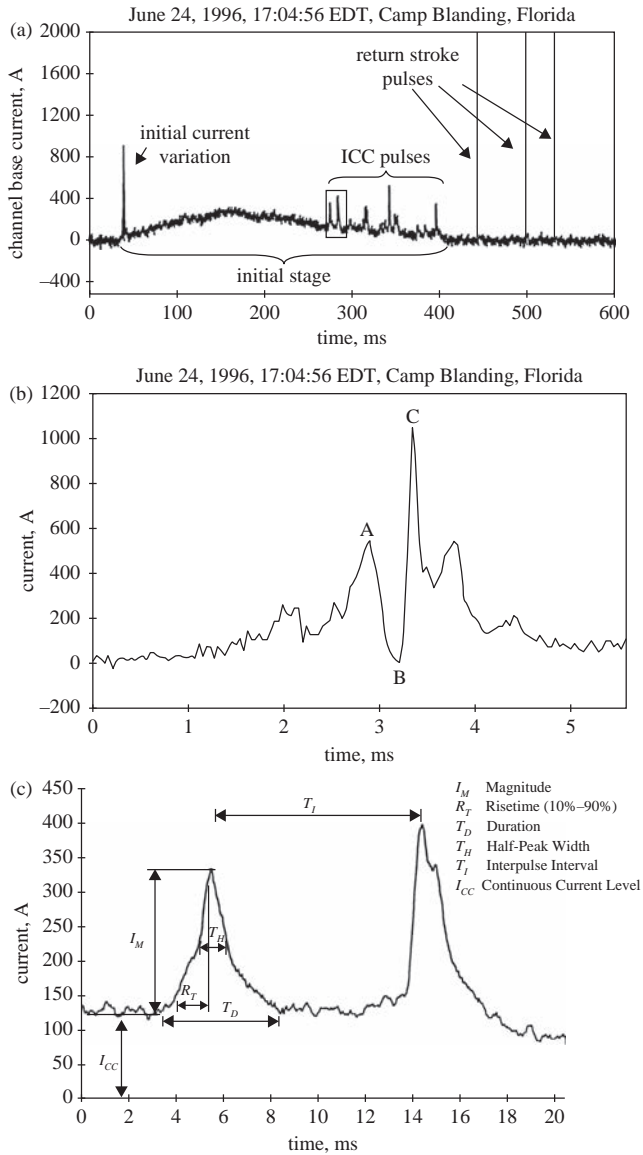


Figure 6.5 (a) Example of the overall current record of a triggered lightning at Camp Blanding, Florida, containing an initial stage (IS) and three return strokes. The initial tens of milliseconds of IS are due to the upward positive leader (UPL), while the rest of IS is due to the initial continuous current (ICC). The record is intentionally clipped at about 2 kA (adapted from Wang et al. 1999b). (b) Initial current variation (ICV) shown in Figure 6.5a but on an expanded time scale (adapted from Wang et al. 1999b). (c) First two initial continuous current (ICC) pulses of Figure 6.5a on an expanded time scale. This figure illustrates the definitions of the ICC pulse magnitude  $I_M$ , 10–90 per cent risetime  $R_T$ , duration  $T_D$ , half-peak width  $T_H$ , interpulse interval  $T_I$ , and preceding continuous current level  $I_{CC}$ . All these parameters have been found to be similar to the corresponding parameters of M-component current pulses analyzed by Thottappillil et al. (1995) (adapted from Wang et al. 1999b)

(ICV), and (2) the current pulses superimposed on the later part of the IS current, referred to as initial continuous current (ICC) pulses. Parameters of the return-stroke current pulses (three pulses are shown in Figure 6.5a) that often follow the initial stage current are discussed in section 6.4.

Miki *et al.* (2005), based on data from Camp Blanding, Florida, reported that the initial stage had a geometric mean (GM) duration of 305 ms and lowered to ground a GM charge of 30 C. The average initial stage current in an individual lightning discharge had a GM value of 100 A.

In many cases the initial current variation includes (1) a current drop, probably associated with the disintegration of the copper triggering wire (abrupt current decrease from A to B in Figure 6.5b), and (2) the following current reestablishment (abrupt current increase from B to C in Figure 6.5b). The processes of current cutoff and reestablishment were studied in detail by Rakov *et al.* (2003b) and Olsen *et al.* (2006).

The initial continuous current usually includes impulsive processes, illustrated in Figure 6.5c, that resemble the M processes observed during the continuing currents that often follow return strokes in both natural and triggered lightning (Rakov *et al.* 1995a, 2001). Wang *et al.* (1999b), from a comparison of various characteristics of the initial continuous current pulses with the characteristics of the M-component current pulses analyzed by Thottappillil *et al.* (1995), concluded that these two types of pulses are similar and hence likely due to similar lightning processes. Like M-component pulses, the initial continuous current pulses sometimes have amplitudes in the kiloamperes range.

### 6.3.2 *Altitude triggering*

As noted in section 6.2.2, the initial stage of altitude triggered lightning includes an initial upward leader, a bidirectional leader (which includes a continuation of the initial upward leader), an attachment process, an initial-stage return stroke, an intensified upward leader, and an initial continuous current. Since the triggering wire is ungrounded, no current can be directly measured at ground during the initial upward leader and bidirectional leader stages. Shown in Figure 6.6b is the current associated with an upward positive connecting leader initiated in response to the approaching downward negative leader of the bidirectional leader system (Figure 6.4), with the corresponding electric field measured on ground 50 m from the lightning attachment point being shown in Figure 6.6a. This current record, reported by Lalande *et al.* (1998), suggests that the upward positive connecting leader is stepped (possibly in response to the stepping of the approaching negative leader), with the interstep interval being 20  $\mu$ s or so. When contact is established between the downward leader and the upward connecting leader, the initial-stage return stroke begins. The current waveform of this return stroke differs appreciably from a typical return-stroke current waveform in that the former appears to be chopped soon after reaching its peak value. As a result, the width of the current waveform produced by the initial-stage return stroke is appreciably smaller than that of the following return strokes in the same flash. As discussed in section 6.2.2, the initial-stage return stroke front catches up with the upward-moving leader tip after 10  $\mu$ s or so. This is likely to produce an opposite polarity downward-moving reflected current wave that is presumably responsible for the chopped shape of both the channel-base current and the close magnetic field waveforms. Examples of the latter are shown, along with waveforms produced by “normal” return strokes, in Figure 6.7. The initial stage

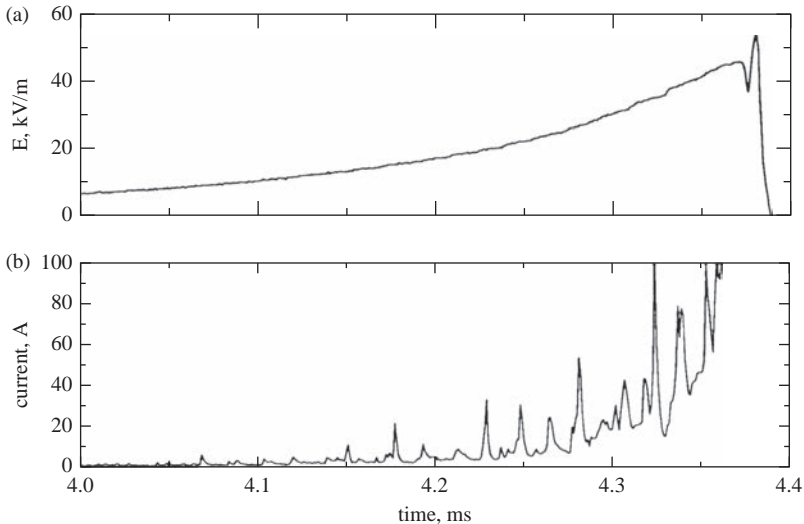


Figure 6.6 (a) Electric field measured 50 m from the lightning attachment point and (b) current produced by the upward connecting positive leader from the grounded 50 m wire in altitude triggered lightning 9516 at Camp Blanding, Florida (adapted from Lalande *et al.* 1998)

characteristics of altitude triggered lightning, after the return stroke has established a relatively low-resistance connection between the upward-moving positive leader tip and ground (see Figure 6.4), are apparently similar to their counterparts in classical triggered lightning. Further, the downward leader/upward return-stroke sequences that follow the initial stage in altitude triggered lightning are thought to be similar to those in classical triggered lightning (see Figure 6.1).

#### 6.4 Parameters of return-stroke current waveforms

In this section, we discuss return-stroke current peak and current waveform parameters such as risetime, rate of rise (steepness), and half-peak width. We will additionally consider interstroke intervals and characteristics that may involve both the return-stroke current component and the following continuing current component, such as the total stroke duration, the total stroke charge,  $\int I(t) dt$ , and the total stroke action integral,  $\int I^2(t) dt$ . The action integral is measured in  $A \cdot s^2$ , which is the same as  $J \cdot \Omega^{-1}$ , and represents the joule or ohmic heating energy dissipated per unit resistance at the lightning attachment point. The action integral is also called the specific energy. We will additionally discuss correlations among the various parameters listed above. The characterization of the return-stroke current waveforms presented in this section is based primarily on data for classical triggered lightning. It is possible that some of the samples on which the statistics presented here are based contain a small number of initial-stage return strokes from altitude triggered lightning, but their exclusion would have essentially no effect on the statistics.

Some researchers (e.g., Hubert *et al.* 1984; Horii and Ikeda 1985), in presenting statistics on triggered lightning currents, do not distinguish between current pulses associated with return strokes and those produced by other lightning processes such as M-components and processes giving rise to the initial current

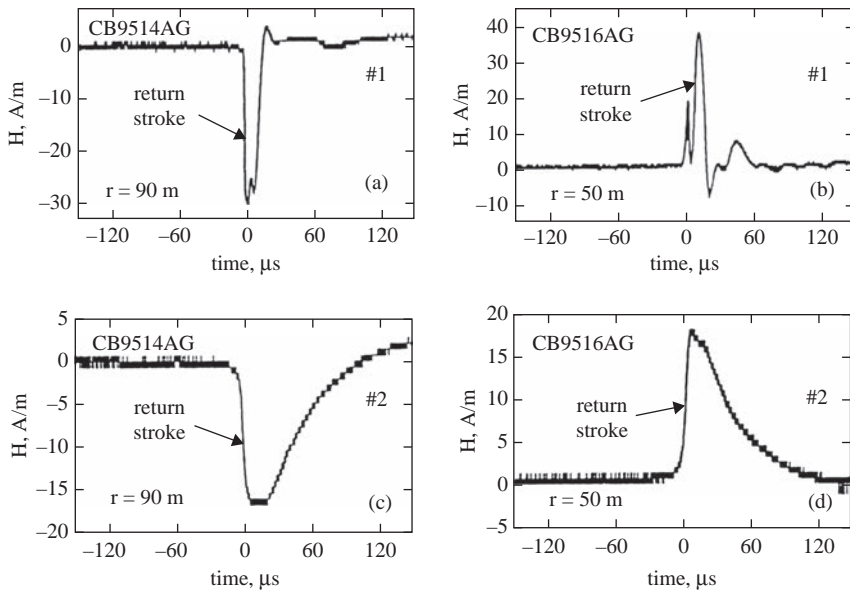


*Figure 6.7* The magnetic fields produced by the first two strokes of the Camp Blanding altitude triggered lightning flashes 9514 (a, first stroke; c, second stroke; four strokes total) and 9516 (b, first stroke; d, second stroke; four strokes total). In each case, the waveshapes of all the higher-order strokes are similar to the second-stroke waveshape. The measuring system's decay time constant was about  $120\ \mu\text{s}$ . The difference in polarity of the waveforms is due to different positions of the lightning channel with respect to the magnetic field antenna, all strokes lowering negative charge to ground. Note that the first-stroke magnetic field pulses in (a) and (b) are appreciably shorter than the corresponding second-stroke magnetic field pulses in (c) and (d), respectively (adapted from Rakov *et al.* 1998)

variation and initial continuous current pulses described in section 6.3.1. In this section, we consider only return-stroke current pulses. These can usually be distinguished from other types of pulses by the absence of an appreciable steady current immediately prior to a pulse (Fisher *et al.* 1993). Further, we do not consider here three unusual New Mexico triggered lightning flashes, each of which contained 24 return strokes (Idone *et al.* 1984). For these three flashes, the geometric means of the return-stroke current peak and interstroke interval are 5.6 kA and 8.5 ms, respectively, each considerably smaller than its counterpart in either natural lightning or other triggered lightning discussed below.

We first review measurements of the peak values of current and current derivative. Summaries of the statistical characteristics of measured return-stroke currents,  $I$ , and derivatives of current with respect to time,  $dI/dt$ , are given in Tables 6.3 and 6.4, respectively. As seen in Table 6.3, the geometric mean values of current peak range from about 12–16 kA. These values are comparable to the median value of 12 kA reported by Anderson and Eriksson (1980) for subsequent strokes in natural lightning. The geometric mean values of  $dI/dt$  peak based on data from two Camp Blanding studies presented in Table 6.4 are 73 and  $97\ \text{kA}\cdot\mu\text{s}^{-1}$ .

Table 6.3 Current waveform parameters for negative strokes in rocket-triggered lightning flashes

Experimental site	$n$	Min.	Max.	Arithmetic mean	$\sigma$	Geometric mean	$\sigma_{\log}$ (base 10)	References
<i>Peak current (kA)</i>								
KSC, Florida, 1985-1991	305	2.5	60.0	14.3	9.0	—	—	Depasse (1994)
Saint-Privat d'Allier, France, 1986, 1990-1991	54	4.5	49.9	11.0	5.6	—	—	Depasse (1994)
KSC, Florida, 1990; Alabama, 1991	45	—	—	—	—	12.0	0.28	Fisher <i>et al.</i> (1993)
Camp Blanding, Florida, 1993	37	5.3	44.4	15.1	—	13.3	0.23	Rakov <i>et al.</i> (1998)
Camp Blanding, Florida, 1997	11	5.3	22.6	12.8	5.6	11.7	0.20	Crawford (1998)
Camp Blanding, Florida, 1998	25	5.9	33.2	14.8	7.0	13.5	0.19	Uman <i>et al.</i> (2000)
Camp Blanding, Florida, 1999-2004	165	2.8	42.3	13.9	6.9	12.2	0.22	Schoene <i>et al.</i> (2009)
Shandong, China, 2005-2011	36	4.4	41.6	14.3	9.2	12.1	0.23	Qie <i>et al.</i> (2013)
Guangdong, China, 2006-2011	28	6.7	31.9	17.2	7.0	15.9	0.18	Zhang <i>et al.</i> (2013)
<i>Current 10-90% risetime (<math>\mu</math>s)</i>								
Saint-Privat d'Allier, France, 1990-1991	37	0.25	4.9	1.14	1.1	—	—	Depasse (1994)
KSC, Florida, 1990; Alabama 1991	43	—	2.9	—	—	0.37	0.29	Fisher <i>et al.</i> (1993)
Camp Blanding, Florida, 1997	11	0.3	4.0	0.9	1.2	0.6	0.39	Crawford (1998)
Camp Blanding, Florida, 1999-2004	81	0.2	5.7	1.2	0.8	0.9	0.32	Schoene <i>et al.</i> (2009)
Shandong, China, 2005-2011	36	0.2	8.4	2.0	2.1	1.9	0.47	Qie <i>et al.</i> (2013)
Guangdong, China, 2006-2011	28	0.22	2.3	0.52	0.42	0.43	0.24	Zhang <i>et al.</i> (2013)
<i>Current half-peak width (<math>\mu</math>s)</i>								
Saint-Privat d'Allier, France, 1990-1991	24	14.7	103.2	49.8	22.4	—	—	Depasse (1994)
KSC, Florida, 1990; Alabama 1991	41	—	—	—	—	18	0.30	Fisher <i>et al.</i> (1993)
Camp Blanding, Florida, 1997	11	6.5	100	35.7	24.6	29.4	0.29	Crawford (1998)
Camp Blanding, Florida, 1999-2004	142	4	93	23	17	19	0.30	Schoene <i>et al.</i> (2009)
Shandong, China, 2005-2011	36	1	68	23.7	17.1	14.8	0.52	Qie <i>et al.</i> (2013)
Guangdong, China, 2006-2011	28	6.2	74.2	23.8	16.7	19.1	0.30	Zhang <i>et al.</i> (2013)
<i>Return-stroke charge transfer within 1 ms (C)</i>								
Camp Blanding, Florida, 1999-2004	151	0.3	8.3	1.4	1.4	1.0	0.35	Schoene <i>et al.</i> (2009)
Shandong, China, 2005-2011	36	0.18	4.2	1.1	0.76	0.86	0.31	Qie <i>et al.</i> (2013)
Guangdong, China, 2006-2011	28	0.44	4.2	1.8	1.3	1.3	0.33	Zhang <i>et al.</i> (2013)

KSC = Kennedy Space Center

Table 6.4 *Current derivative waveform parameters for negative return strokes in rocket-triggered lightning<sup>a</sup> (adapted from Schoene et al. 2003a)*

Location/year	<i>n</i>	Min.	Max.	Arithmetic mean	$\sigma$	Geometric mean	$\sigma_{\log}(\text{base } 10)$
<i>dl/dt Peak, kA/<math>\mu</math>s</i>							
Kennedy Space Center, Florida; 1985–1991 <sup>b</sup>	134	5	411	118	97	–	–
Saint-Privat d'Allier, France; 1986, 1990–1991 <sup>b</sup>	47	13	139	43	25	–	–
Camp Blanding, Florida; 1998 <sup>c</sup>	15	45	152	80	35	73	0.17
Camp Blanding, Florida; 1999–2000 <sup>d</sup>	64	8	292	117	65	97	0.31
<i>dl/dt 30–90% Risetime, ns</i>							
Camp Blanding, Florida; 1999–2000	29	17	69	32	13	30	0.16
<i>dl/dt 10–10% Width, ns</i>							
Saint-Privat d'Allier, France; 1990–1991 <sup>b</sup>	17	70	2010	400	210	–	–
<i>dl/dt Half-Peak Width, ns</i>							
Camp Blanding, Florida; 1999–2000	29	49	149	92	25	89	0.12

<sup>a</sup>The polarity of the peak values is ignored.

<sup>b</sup>Depasse (1994).

<sup>c</sup>Uman *et al.* (2000).

<sup>d</sup>Fifteen *dl/dt* peaks obtained by differentiating *I*.

Scatter plots of *dl/dt* peak versus *I* peak from the triggered lightning experiments in Florida (1985, 1987, and 1988) and in France (1986) are shown in Figure 6.8. Correlation coefficients are 0.87, 0.80, and 0.70 for the 1985, 1987, and 1988 Florida data, respectively, and 0.78 for the 1986 data from France. The largest measured value of *dl/dt* is 411 kA· $\mu$ s<sup>-1</sup>, as reported from Florida (KSC) studies by Leteinturier *et al.* (1991). The corresponding measured peak current is greater than 60 kA, the largest value of this parameter reported for summer triggered lightning to date. Also shown in Figure 6.8 are the linear regression line and the regression equation for each of the four subsets of the data. Note that the correlation coefficients between the logarithms of *dl/dt* and *I* for the same data were found to be lower: 0.79, 0.56, and 0.60 for the 1985, 1987, and 1988 Florida data, respectively, and 0.71 for the 1986 data from France (Depasse 1994; Table 10).

Fisher *et al.* (1993) compared a number of return-stroke current parameters for classical triggered-lightning strokes from Florida and Alabama with the corresponding parameters for natural lightning in Switzerland reported by Berger *et al.* (1975) and Anderson and Eriksson (1980). This comparison is given in Figures 6.9 through 6.17. Recall that triggered-lightning strokes are considered to be similar to subsequent strokes in natural lightning. Therefore, the comparison in Figures 6.9 through 6.17 applies only to subsequent strokes that are usually initiated by leaders that follow the path of the previous stroke. Both Berger *et al.* (1975) and Anderson and Eriksson (1980) fitted a straight line representing a lognormal approximation to the experimental statistical distribution in order to determine the percentages (95, 50, and 5%) of cases exceeding the tabulated values, while Fisher *et al.* (1993) used

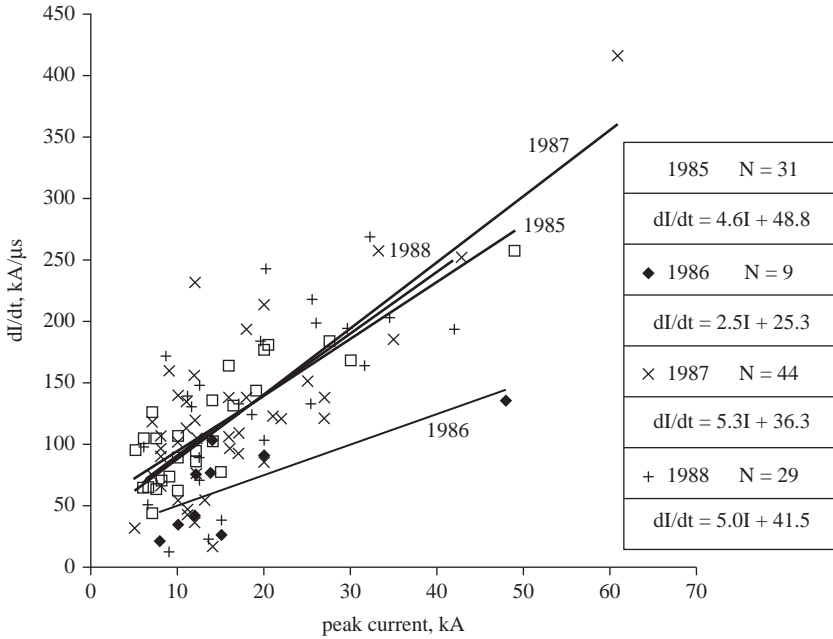
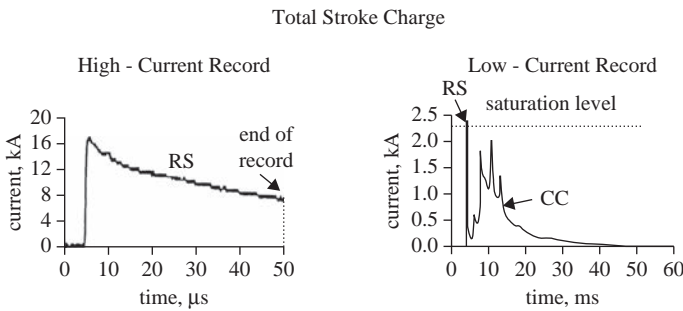


Figure 6.8 Relation between peak current rate of rise,  $dI/dt$ , and peak current  $I$ , from triggered-lightning experiments conducted at the NASA Kennedy Space Center, Florida, in 1985, 1987, and 1988 and in France in 1986. The regression line for each year is shown, and the sample size and the regression equation are given (adapted from Leteinturier et al. 1991)

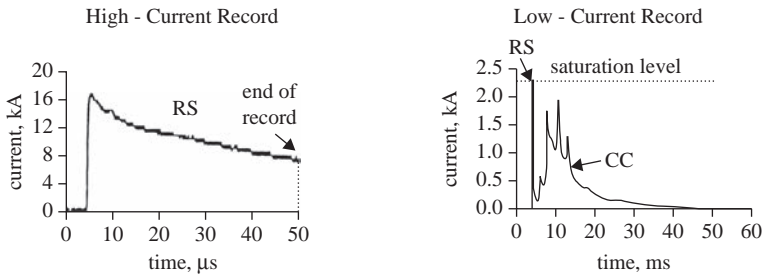


Reference	Sample Size	Unit	GM	SD $\log_{10}(x)$	Percent Cases Exceeding the Tabulated Value		
					95%	50%	5%
Fisher et al. (1993)	65	C	2.5	0.55	0.38	2.1	15
Berger et al. (1975)	122	C	-	-	0.2	1.4	11

Figure 6.9 Total stroke charge. RS is the return stroke, CC is the continuing current, GM is the geometric mean, and SD is the standard deviation of the logarithm (base 10) of the parameter (adapted from Fisher et al. 1993)

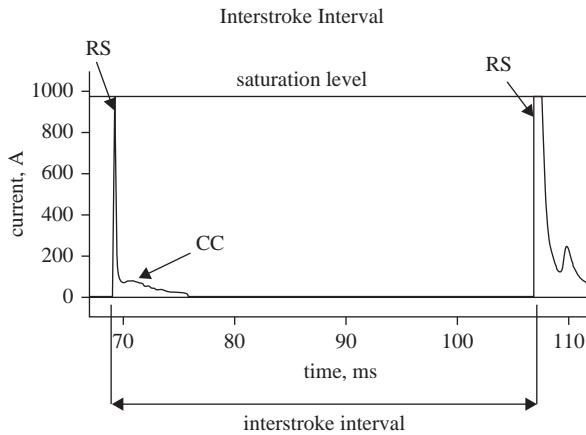


Total Stroke Action Integral



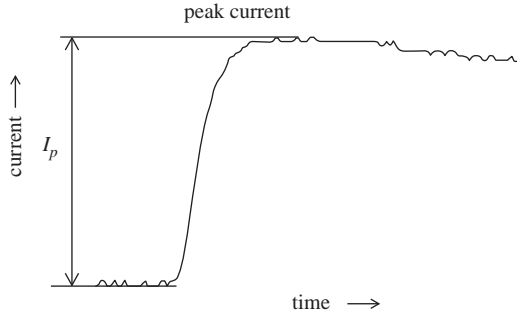
Reference	Sample Size	Unit	GM	SD $\log_{10}(x)$	Percent Cases Exceeding the Tabulated Value		
					95%	50%	5%
Fisher et al. (1993)	65	A <sup>2</sup> s	$3.5 \times 10^3$	0.54	$0.4 \times 10^3$	$3.8 \times 10^3$	$20 \times 10^3$
Berger et al. (1975)	88	A <sup>2</sup> s	-	-	$0.55 \times 10^3$	$6.0 \times 10^3$	$52 \times 10^3$

Figure 6.10 Total stroke action integral. RS is the return stroke, CC is the continuing current, GM is the geometric mean, and SD is the standard deviation of the logarithm (base 10) of the parameter (adapted from Fisher et al. 1993)



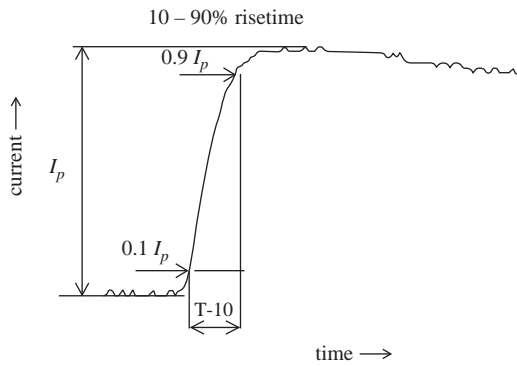
Reference	Sample Size	Unit	GM	SD $\log_{10}(x)$	Percent Cases Exceeding the Tabulated Value		
					95%	50%	5%
Fisher et al. (1993)	52	ms	47	0.48	5.0	48	215
Berger et al. (1975)	133	ms	-	-	7.0	33	150

Figure 6.11 Interstroke interval. RS is the return stroke, CC is the continuing current, GM is the geometric mean, and SD is the standard deviation of the logarithm (base 10) of the parameter (adapted from Fisher et al. 1993)



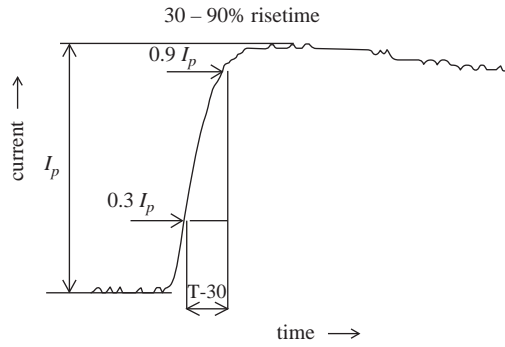
Symbol	Reference	Sample Size	Unit	GM	SD $\log_{10}(x)$	Percent Cases Exceeding the Tabulated Value		
						95%	50%	5%
$I_p$	Fisher <i>et al.</i> (1993)	45	kA	12	0.28	4.7	13	29
	Anderson and Eriksson (1980)	114	kA	-	-	4.9	12	29

Figure 6.12 Peak current. GM is the geometric mean and SD is the standard deviation of the logarithm (base 10) of the parameter (adapted from Fisher *et al.* 1993)



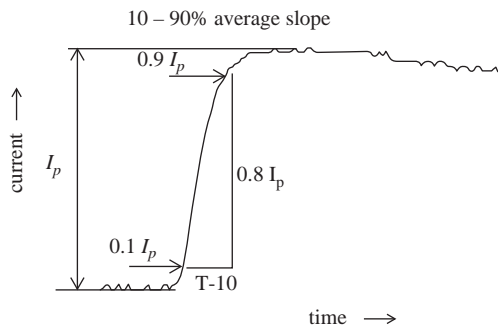
Symbol	Reference	Sample Size	Unit	GM	SD $\log_{10}(x)$	Percent Cases Exceeding the Tabulated Value		
						95%	50%	5%
T-10	Fisher <i>et al.</i> (1993)	43	$\mu\text{s}$	0.37	0.29	0.20	0.32	1.1
	Anderson and Eriksson (1980)	114	$\mu\text{s}$	-	-	0.1	0.6	2.8

Figure 6.13 The 10–90% risetime. GM is the geometric mean and SD is the standard deviation of the logarithm (base 10) of the parameter (adapted from Fisher *et al.* 1993)



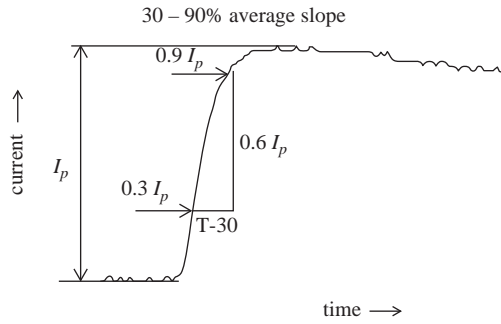
Symbol	Reference	Sample Size	Unit	GM	SD $\log_{10}(x)$	Percent Cases Exceeding the Tabulated Value		
						95%	50%	5%
T-30	Fisher <i>et al.</i> (1993)	43	$\mu\text{s}$	0.28	0.28	0.14	0.24	0.96
	Anderson and Eriksson (1980)	114	$\mu\text{s}$	-	-	0.1	0.4	1.8

Figure 6.14 The 30–90% risetime. GM is the geometric mean and SD is the standard deviation of the logarithm (base 10) of the parameter (adapted from Fisher *et al.* 1993)



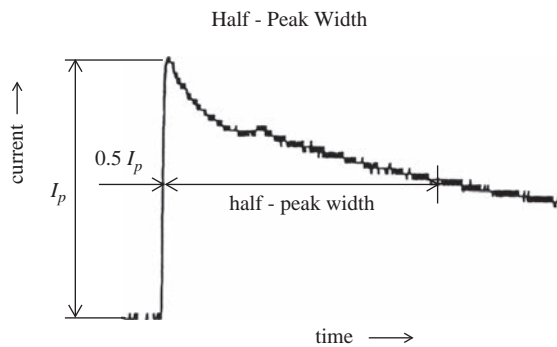
Symbol	Reference	Sample Size	Unit	GM	SD $\log_{10}(x)$	Percent Cases Exceeding the Tabulated Value		
						95%	50%	5%
S-10	Fisher <i>et al.</i> (1993)	43	$\text{kA}/\mu\text{s}$	28	0.37	5.4	34	83
	Anderson and Eriksson (1980)	114	$\text{kA}/\mu\text{s}$	-	-	3.3	15	72

Figure 6.15 The 10–90% average slope (steepness). GM is the geometric mean and SD is the standard deviation of the logarithm (base 10) of the parameter.  $S-10 = 0.8I_p/T-10$  (adapted from Fisher *et al.* 1993)



Symbol	Reference	Sample Size	Unit	GM	SD log <sub>10</sub> (x)	Percent Cases Exceeding the Tabulated Value		
						95%	50%	5%
S-30	Fisher <i>et al.</i> (1993)	43	kA/μs	28	0.36	4.6	31	91
	Anderson and Eriksson (1980)	114	kA/μs	-	-	4.1	20	99

Figure 6.16 The 30–90% average slope (steepness). GM is the geometric mean and SD is the standard deviation of the logarithm (base 10) of the parameter.  $S-30 = 0.6I_p/T-30$  (adapted from Fisher *et al.* 1993)



Reference	Sample Size	Unit	GM	SD log <sub>10</sub> (x)	Percent Cases Exceeding the Tabulated Value		
					95%	50%	5%
Fisher <i>et al.</i> (1993)	41	μs	18	0.30	5.0	20	40
Anderson and Eriksson (1980)	115	μs	-	-	6.5	32	140

Figure 6.17 Half-peak width. GM is the geometric mean and SD is the standard deviation of the logarithm (base 10) of the parameter (adapted from Fisher *et al.* 1993)

the nearest experimental point instead. Distributions of peak currents are very similar, with median values being 13 and 12 kA for triggered and natural lightning, respectively. On the other hand, there appear to be appreciable differences between the triggered-lightning data of Fisher *et al.* (1993) and the natural-lightning data of Berger *et al.* (1975) and Anderson and Eriksson (1980) in terms of current wave-front parameters, half-peak width, and stroke charge. The shorter risetime and higher average slope (steepness) in the triggered-lightning data may be explained by the better time resolution of the measuring systems used in the triggered-lightning studies. The Swiss data were recorded as oscilloscopic traces with the smallest measurable time being  $0.5 \mu\text{s}$  (Berger and Garbagnati 1984).

Fisher *et al.* (1993) also studied relations among some return-stroke parameters, the results being shown in Figure 6.18. They found a relatively strong positive correlation between 10–90 per cent average steepness (S-10) and current peak (correlation coefficient = 0.71) and between 30–90 per cent average steepness (S-30) and current peak (correlation coefficient = 0.74). As seen in Figure 6.18a,

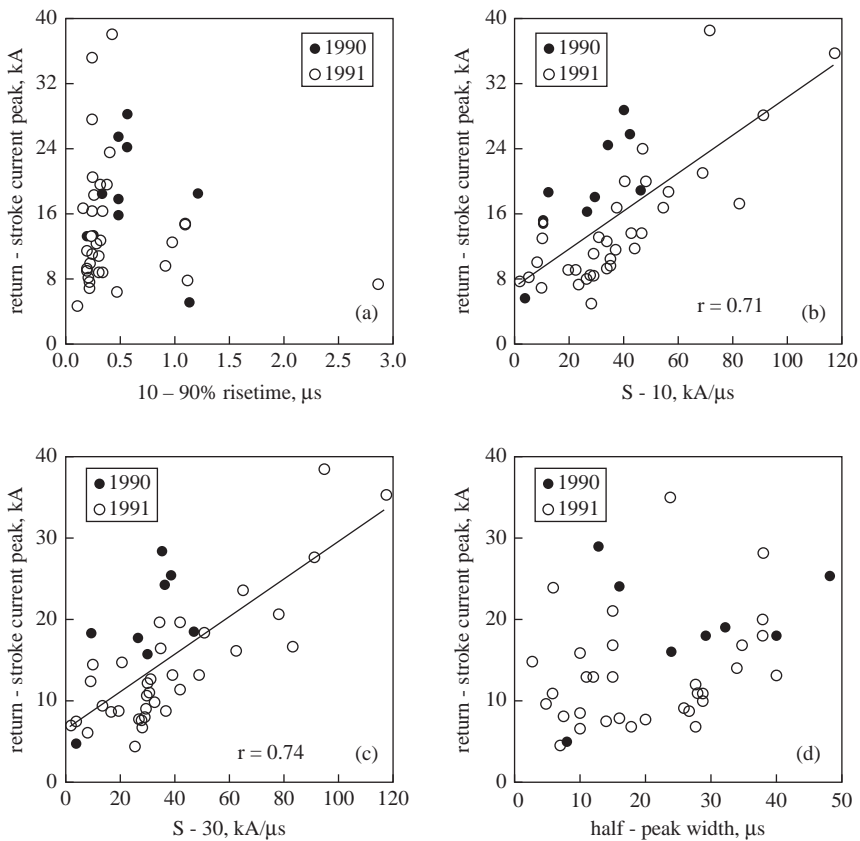


*Figure 6.18 Scatterplots relating various return-stroke parameters. Solid circles represent 1990 data from KSC, Florida, and open circles represent 1991 data from Fort McClellan, Alabama. (a) Current peak versus 10–90% risetime; (b) current peak versus S-10; (c) current peak versus S-30; (d) current peak versus half-peak width. Need to show the regression lines in (b) and (c) and correlation coefficients ( $r$ ) are given in (b) and (c) (adapted from Fisher *et al.* 1993)*

there is essentially no linear correlation between current peak and 10–90 per cent risetime.

Schoene *et al.* (2009) have shown that for Camp Blanding triggered-lightning strokes (which, as noted above, are similar to natural-lightning subsequent strokes) the scatter-plot of return stroke peak current versus charge transfer to 1 ms is surprisingly similar to the 1 ms natural-lightning first stroke data of Berger (1972). The regression equation for 143 triggered-lightning strokes as given by Schoene *et al.* (2009) is  $I = 12.3 Q^{0.54}$  ( $R^2 = 0.76$ ) and the regression equation for Berger's 89 natural-lightning first strokes is  $I = 10.6 Q^{0.7}$  ( $R^2 = 0.59$ ). Qie *et al.* (2007) reported that  $I = 18.5 Q^{0.65}$  for ten triggered-lightning strokes in China.

Schoene *et al.* (2010) examined data on 117 return strokes in 31 triggered lightning flashes acquired during experiments conducted from 1999 through 2004 at Camp Blanding, in order to compare the peak currents of the lightning return strokes with the corresponding charges transferred during various time intervals within 1 ms after return stroke initiation. They found that the determination coefficient ( $R^2$ ) for lightning return-stroke peak current versus the corresponding charge transfer decreases with increasing the duration of the charge transfer starting from return-stroke onset. For example,  $R^2 = 0.91$  for a charge transfer duration of 50  $\mu\text{s}$  after return stroke onset,  $R^2 = 0.83$  for a charge transfer duration of 400  $\mu\text{s}$ , and  $R^2 = 0.77$  for a charge transfer duration of 1 ms. Their results support the view that (1) the charge deposited on the lower portion of the leader channel determines the current peak and that (2) the charge transferred at later times is increasingly unrelated to both the current peak and the charge deposited on the lower channel section. Additionally, they found that the relation between the return-stroke peak current and charge transfer to 50  $\mu\text{s}$  for triggered lightning in Florida is essentially the same as that for subsequent strokes in natural lightning in Switzerland, further confirming the view that triggered-lightning strokes are very similar to subsequent strokes in natural lightning.

## 6.5 Return-stroke current peak versus grounding conditions

In examining the lightning current flowing from the bottom of the channel into the ground, it is convenient to approximate lightning by a Norton equivalent circuit (e.g., Baba and Rakov 2005), that is, by a current source equal to the lightning current that would be injected into the ground if that ground were perfectly conducting (a short-circuit current) in parallel with a lightning-channel equivalent impedance  $Z_{ch}$  assumed to be constant. The lightning grounding impedance  $Z_{gr}$  is a load connected in parallel with the lightning Norton equivalent. Thus the “short-circuit” lightning current  $I$  effectively splits between  $Z_{gr}$  and  $Z_{ch}$  so that the current measured at the lightning-channel base is found as  $I_{meas} = I Z_{ch} / (Z_{ch} + Z_{gr})$ . Both source characteristics,  $I$  and  $Z_{ch}$ , vary from stroke to stroke, and  $Z_{ch}$  is a function of channel current, the latter nonlinearity being in violation of the linearity requirement necessary for obtaining the Norton equivalent circuit. Nevertheless, if we are concerned only with the peak value of current and assume that for a large number of strokes the average peak value of  $I$  and the average value of  $Z_{ch}$  at current peak are each more or less constant, the Norton equivalent becomes a useful tool for studying the relation between lightning current peak and the corresponding values of  $Z_{ch}$  and  $Z_{gr}$ . For instance, if the measured channel-base current peak statistics are similar under a variety of grounding conditions, then  $Z_{ch}$  must always be much

larger than  $Z_{gr}$  at the time of the current peak. In the following, we will compare the geometric mean current peaks from triggered lightning experiments in which similar rocket launchers having a relatively small height of 4–5 m were used, but grounding conditions differed considerably. All the information needed for this comparison is given in Table 6.5.

As seen in Table 6.5, Camp Blanding measurements of lightning currents that entered sandy soil with a relatively poor conductivity of  $2.5 \times 10^{-4} \text{ S}\cdot\text{m}^{-1}$  without any grounding electrode resulted in a value of the geometric mean return-stroke current peak, 13 kA, that is similar to the geometric mean value, 14 kA, estimated from measurements at KSC made in 1987 using a launcher of the same geometry which was much better grounded into salt water with a conductivity of 3–6  $\text{S}\cdot\text{m}^{-1}$  via underwater braided metallic cables. Additionally, fairly similar geometric mean values were found from the Fort McClellan, Alabama, measurements using a poorly grounded launcher (10 kA) and the same launcher well grounded (11 kA) in 1993 and 1991, respectively. Also, Ben Rhouma *et al.* (1995) give arithmetic mean values of return stroke current peaks in the range from 15 to 16 kA for the Florida triggered-lightning experiments at Camp Blanding in 1993 and at KSC in 1987, 1989, and 1991.

The values of grounding resistance (probably the dominant component of  $Z_{gr}$ ) given in Table 6.5 should be understood as the initial values encountered by a lightning downward leader before the onset of any breakdown processes in the soil or along the ground surface associated with the return stroke. Note from Table 6.5 that the grounding resistance varies from 0.1  $\Omega$  to 64 k $\Omega$ , while  $Z_{ch}$ , assumed to be a real number, was estimated from the analysis of the current waves traveling along the 540-m high tower to be in the range from hundreds of ohms to some kilohms (Gorin *et al.* 1977; Gorin and Shkilev 1984). The observation that the average return-stroke current is not much influenced by the level of man-made grounding, ranging from excellent to none, implies that lightning is capable of lowering the grounding impedance it initially encounters (Table 6.5) to a value that is always much lower than the equivalent impedance of the main channel. On the basis of (1) the evidence of the formation of plasma channels (fulgurites) in the sandy soil at Camp Blanding (Uman *et al.* 1994b, 1997; Rakov 1999a; Jones *et al.* 2005) and (2) optical records showing arcing along the ground surface at both Camp Blanding and Fort McClellan (Fisher *et al.* 1994; Rakov *et al.* 1998), it can be inferred that surface and underground plasma channels are important means of lowering the lightning grounding impedance, at least for the types of soil at the lightning triggering sites in Florida and Alabama (sand and clay, respectively). Bazelyan and Raizer (2000a) found from their laboratory experiments and modeling that surface arcs developing at a speed of  $10^6$  to  $10^7 \text{ m}\cdot\text{s}^{-1}$  is the most likely mechanism of grounding impedance reduction by lightning current. They stated that a voltage as low as 135 kV was required to bridge a 5-m-long gap by such an arc. Since the arcs develop at a speed of 1–10  $\text{m}\cdot\mu\text{s}^{-1}$  (see above), some reduction of grounding impedance should occur before the current peak, particularly when the current risetime is greater than 1  $\mu\text{s}$ .

A photograph of surface arcing during a triggered-lightning flash from Fort McClellan, Alabama, is shown in Figure 6.19, and evidence of surface arcing in natural lightning is presented in Figure 6.20. Injection of laboratory currents up to 20 kA into loamy sand in the presence of water sprays simulating rain resulted in surface arcing that significantly reduced the grounding resistance at the current peak (M. Darveniza, personal communication, 1995). The fulgurites (glassy tubes produced by lightning in sand; Figures 6.21 and 6.22) found at Camp Blanding usually show that the in-soil plasma channels tend to develop toward the better

Table 6.5 Geometric mean peak current versus grounding conditions from different triggered-lightning experiments (adapted from Rakov *et al.* 1998)

Experiment	Reference	Trigger threshold, kA	Sample size	GM peak current, kA	Soil	Artificial grounding	Grounding resistance, $\Omega$
KSC, Florida, 1987	Eybert-Berard <i>et al.</i> (1988), Leteinturier <i>et al.</i> (1991), as reported by Fisher <i>et al.</i> (1993)	5	36	14	0.5-m deep salt water ( $3-6 \text{ S}\cdot\text{m}^{-1}$ )	$1.2 \times 1.2 \text{ m}$ square metal plane connected through three 0.5 m long wires at the four corners to salt water	0.1
Fort McClellan, Alabama, 1991	Fisher <i>et al.</i> (1993)	2 (two strokes below 2 kA from continuous tape record included)	37	11	Clay ( $3 \times 10^{-3} \text{ S}\cdot\text{m}^{-1}$ )	Rebar framework of the munition storage bunker inter-connected with lightning protection system including air terminals, down conductors and buried counterpoise	Presumably low
Camp Blanding, Florida, 1993	Uman <i>et al.</i> (1994a, 1997)	3.3 and 4.2	37	13	Sand ( $2.5 \times 10^{-4} \text{ S}\cdot\text{m}^{-1}$ )	None; launcher was based on two parallel 15-m long, 2 m apart concrete slabs above three unenergized power cables buried 1 m deep and 5 m apart	$64 \times 10^3$ (assuming that the contact surface between the channel and the ground was a hemisphere with 1-cm radius)
Fort McClellan, Alabama, 1993	Fisher <i>et al.</i> (1994)	$\sim 4$	31	10	Heavy red clay ( $1.8 \times 10^{-3} \text{ S}\cdot\text{m}^{-1}$ )	Single 0.3-m or 1.3-m-long vertical grounding rod	260

KSC = Kennedy Space Center. The values of grounding resistance are determined by the geometry of the grounding electrode (or the geometry of the contact surface between the channel and the ground in the absence of grounding electrode) and soil conductivity. They are measured under low-frequency, low-current conditions and should be understood as the initial values of resistance encountered by lightning before the onset of any breakdown processes in the soil or along the ground surface.





*Figure 6.19 Photograph of surface arcing associated with the second stroke (current peak of 30 kA) of flash 9312 triggered at Fort McClellan, Alabama. Lightning channel is outside of field of view. One of the surface arcs approached the right edge of the photograph, a distance of 10 m from the rocket launcher (adapted from Fisher et al. 1994)*



*Figure 6.20 Evidence of surface arcing on a golf course green in Arizona (courtesy of E.P. Krider)*

conducting layers of soil or toward buried metallic objects that, when contacted, serve to further lower the grounding resistance. The percentages of return strokes producing optically detectable surface arcing versus return stroke peak current, from the 1993 and 1995 Fort McClellan experiments, are shown in Figure 6.23. The surface arcing appears to be random in direction and often leaves little if any evidence on the ground. Even within the same flash, individual strokes can produce

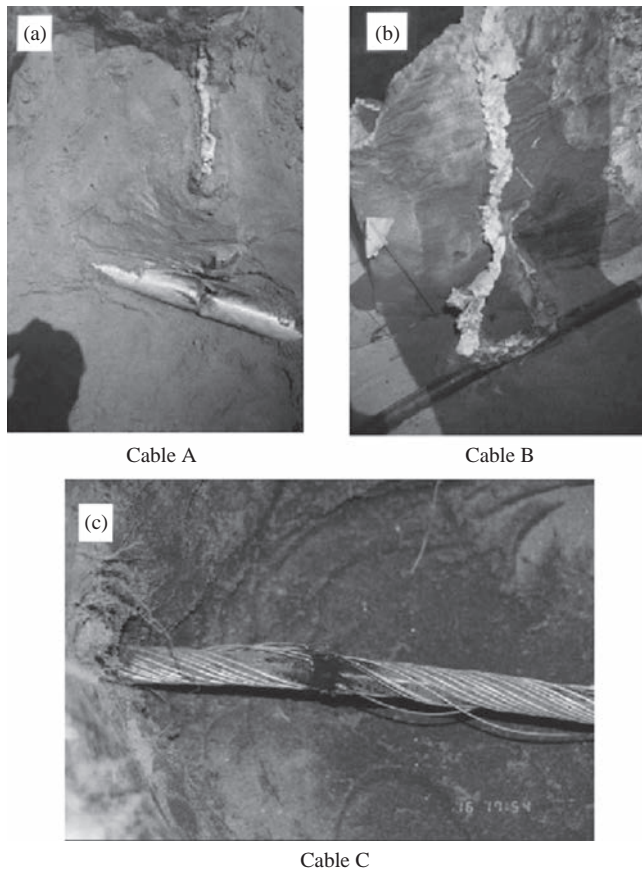


*Figure 6.21 Lightning damage to underground power cables. (a) coaxial cable in an insulating jacket inside a PVC conduit; note the section of vertical fulgurite in the upper part of the picture (the lower portion of this fulgurite was destroyed during excavation) and the hole melted through the PVC conduit, (b) coaxial cable in an insulating jacket, directly buried; note the fulgurite attached to the cable, (c) coaxial cable whose concentric neutral was in contact with earth; note that many strands of the neutral are melted through. The cables were tested at Camp Blanding, Florida in 1993 (photos in (a) and (b) were taken by V.A. Rakov and in (c) by P.P. Barker)*

arcs developing in different directions. In one case, it was possible to estimate the current carried by one arc branch which contacted the instrumentation. That current was approximately 1 kA, or 5 per cent of the total current peak in that stroke. The observed horizontal extent of surface arcs was up to 20 m, which was the limit of the photographic coverage during the 1993 Fort McClellan experiment. No fulgurites were found in the soil (red clay) at Fort McClellan, only concentrated current exit points at several spots along the 0.3- or 1.3-m steel earthing rod (Table 6.5). It is likely that the uniform ionization of soil, usually postulated in studies of the behavior of grounding electrodes subjected to lightning surges, is not an adequate assumption, at least not in the southeastern United States, where



*Figure 6.22 A Florida fulgurite of about 5 m length produced by triggered lightning at Camp Blanding, Florida*

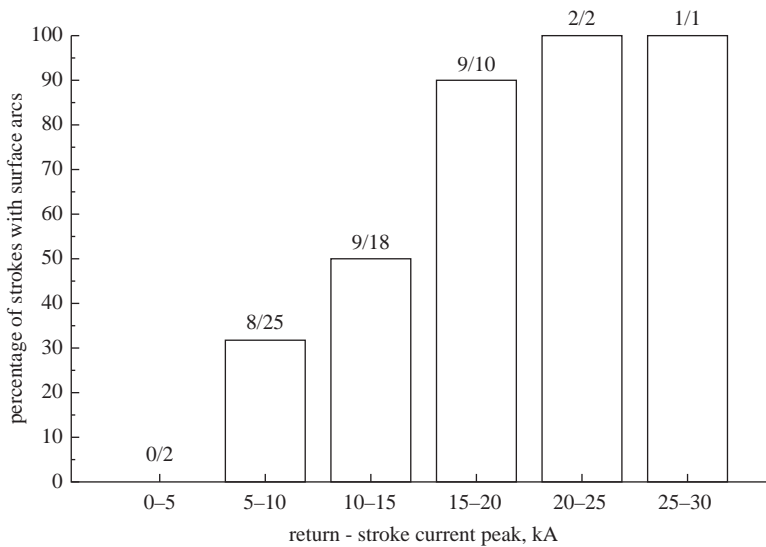


*Figure 6.23 Percentages of return strokes producing optically detectable surface arcing as a function of return-stroke current peak (Fort McClellan, Alabama, 1993 and 1995). Numbers above each histogram column indicate the number of strokes producing optically detectable arcing (numerator) and the total number of strokes in that current peak range (denominator) (adapted from Rakov et al. 1998)*

distinct plasma channels in the soil and on the ground surface appear to contribute considerably to lowering the grounding resistance.

## 6.6 Characterization of the close lightning electromagnetic environment

A knowledge of close lightning electric and magnetic fields is needed for the evaluation of lightning-induced effects in various electric circuits and systems (e.g., Nucci and Rachidi 1995) and for the testing of the validity of lightning models (e.g., Rakov and Uman 1998; Schoene *et al.* 2003b). The close (within tens to hundreds of meters) lightning electromagnetic environment is most easily studied using rocket-triggered lightning for which the termination point on ground is known (Leteinturier *et al.* 1990; Depasse 1994; Rubinstein *et al.* 1995; Rakov *et al.* 1995b, 1998, 2001, 2005b; Uman *et al.* 2000, 2002; Crawford *et al.* 2001; Schoene *et al.* 2003a; Jerauld *et al.* 2004, 2007).

Rubinstein *et al.* (1992, 1995) measured and analyzed electric field waveforms at 500 m for 31 leader/return stroke sequences and at 30 m for two leader/return stroke sequences in lightning flashes triggered at the Kennedy Space Center, Florida, in 1986 and 1991, respectively. They found that, at tens to hundreds of meters from the lightning channel, leader/return-stroke vertical electric field waveforms appear as asymmetrical V-shaped pulses, the negative slope of the leading edge being lower than the positive slope of the trailing edge. The bottom of the V is associated with the transition from the leader (the leading edge of the pulse) to the return stroke (the trailing edge of the pulse). The first multiple-station electric field measurements within a few hundred meters of the triggered-lightning channel were performed in 1993 at Camp Blanding, Florida (Uman *et al.* 1994a) and at Fort McClellan, Alabama (Fisher *et al.* 1994). Detailed analyses of these data have been presented by Rakov *et al.* (1998). From the 1993 experiment, the geometric mean width of the V at half of peak value is 3.2  $\mu\text{s}$  at 30 m, 7.3  $\mu\text{s}$  at 50 m, and 13  $\mu\text{s}$  at 110 m, a distance dependence close to linear.

In 1997, the multiple-station field measuring experiment at Camp Blanding, Florida, was extended to include seven stations at distances of 5, 10, 20, 30, 50, 110, and 500 m from the triggered-lightning channel (Crawford *et al.* 1999). Most of the data obtained at 5 m appeared to be corrupted, possibly due to ground surface arcs (see section 6.5) and are not considered here. Leader/return-stroke electric field waveforms in one flash (S9721) simultaneously measured at 10, 20, 30, 50, 110, and 500 m are shown in Figure 6.24. The evolution of the leader/return-stroke electric field waveform as distance increases is consistent with previous measurements (Rubinstein *et al.* 1995; Rakov *et al.* 1998) and reflects an increasing contribution to the field from progressively higher channel sections.

Crawford *et al.* (2001) analyzed net electric field changes due to dart leaders in triggered lightning from experiments conducted in 1993, 1997, 1998, and 1999 at Camp Blanding, Florida and in 1993 at Fort McClellan, Alabama. In 1997–1999, the fields were measured at 2–10 stations with distances from the lightning channel ranging from 10 to 621 m, while in 1993 the fields were measured at three distances, 30, 50, and 110 m, in Florida, and at two distances, about 10 and 20 m, in Alabama. The data on the leader electric field change as a function of distance for Florida are presented in Table 6.6. With a few exceptions, the 1997–1999 data indicate that the distance dependence of the leader electric field change is close to an inverse proportionality ( $r^{-1}$ ), in contrast with the 1993 data (from both Florida,

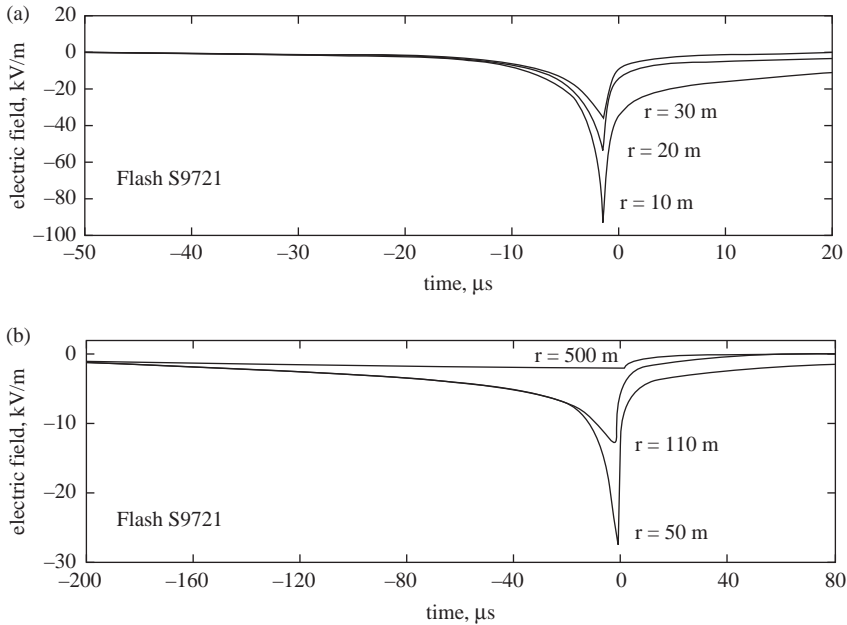


**Figure 6.24** *Electric field waveforms of the first leader/return-stroke sequence of flash S9721 as recorded in 1997 at distances (a) 10, 20, and 30 m and (b) 50, 110, and 500 m at Camp Blanding, Florida. The initial downward-going portion of the waveform is due to the dart leader, and the upward-going portion is due to the return stroke (adapted from Crawford *et al.* 1999)*

shown in Table 6.6, and Alabama, not shown) in which a somewhat weaker distance dependence was observed. The typically observed  $r^{-1}$  dependence is consistent with a uniform distribution of leader charge along the bottom kilometer or so of the channel. This observation simply indicates that for such a relatively short channel section a nonuniform charge density distribution will appear approximately uniform. Cooray *et al.* (2004) compared Crawford *et al.*'s (2001) experimental results with theoretical predictions for a vertical conductor in an external electric field and found a fairly good agreement. A variation of  $\Delta E_L$  with distance slower than  $r^{-1}$  dependence implies a decrease of leader charge density with decreasing height.

## 6.7 Studies of interaction of lightning with various objects and systems

In sections 6.7.1, 6.7.2, and 6.7.3, we consider the triggered-lightning testing of overhead power distribution lines, underground cables, and power transmission lines, respectively. Lightning interaction with lightning protective systems of a residential building and an airport runway lighting system is discussed in sections 6.7.4 and 6.7.5, respectively. In section 6.7.6, we briefly review the use of triggered lightning for testing components of power systems, different types of lightning rods, and other objects, and also for measuring step voltages and for making fulgurites.

Table 6.6 Dart-leader electric field change as a function of distance from the lightning channel for events recorded at Camp Blanding, Florida, in 1993–1999 (adapted from Crawford et al. 2001)

Year	Flash	Stroke	Number of stations	$I_p$ (kA)	$\Delta E_L = f(r)$ (kV/m)	Distances (m)
1993	9313	2	3	9.7	$61r^{-0.28}$	30/50/110
		3	3	11	$69r^{-0.30}$	30/50/110
		4	3	13	$76r^{-0.30}$	30/50/110
		5	3	11	$56r^{-0.25}$	30/50/110
	9320	1	3	9.6	$1.7 \times 10^2 r^{-0.51}$	30/50/110
		2	3	8.4	$1.0 \times 10^2 r^{-0.42}$	30/50/110
1997	S9711	1	3	6.5	$1.6 \times 10^3 r^{-1.1}$	50/110/500
	S9712	1	3	5.3	$1.4 \times 10^2 r^{-0.59}$	10/20/30
	S9718	1	5	12	$2.1 \times 10^3 r^{-1.1}$	20 – 500
			3	$1.4 \times 10^3 r^{-1.0}$	30/50/110	
	S9720	1	4	21	$2.6 \times 10^3 r^{-1.1}$	30–500
			3	$1.7 \times 10^3 r^{-0.99}$	30/50/110	
	S9721	1	6	11	$1.3 \times 10^3 r^{-1.0}$	10 – 500
			3	$9.9 \times 10^2 r^{-0.93}$	30/50/110	
3			$7.1 \times 10^2 r^{-0.84}$	10/20/30		
1998	U9801	1	10	8.7	$2.8 \times 10^3 r^{-1.2}$	102–410
	U9822	1	10	11	$2.6 \times 10^3 r^{-1.1}$	92–380
	U9824	1	10	17	$5.1 \times 10^3 r^{-1.2}$	102–410
	U9825	1	10	NR	$5.8 \times 10^3 r^{-1.2}$	102–410
	U9827	1	9	41	$7.1 \times 10^3 r^{-1.2}$	92–380
	S9806	1	10	9.1	$1.5 \times 10^3 r^{-0.96}$	67–619
1999	U9901	1	10	8.2	$3.3 \times 10^3 r^{-1.2}$	91–380
	U9902	1	10	12	$2.1 \times 10^3 r^{-1.1}$	91–380
	S9915	1	9	11	$1.0 \times 10^3 r^{-0.98}$	15–621
	S9918	1	9	26§	$5.3 \times 10^3 r^{-1.2}$	15–621
	S9930	1	3	39	$4.0 \times 10^3 r^{-1.0}$	15–507
	S9932	1	4	19	$3.6 \times 10^3 r^{-1.1}$	15–507
	S9934	1	4	30	$3.0 \times 10^3 r^{-1.0}$	15–507
	S9935	1	3	21§	$2.1 \times 10^3 r^{-1.0}$	15–507

NR = not recorded.  $I_p$  = return-stroke peak current. § = peak current estimated from peak magnetic field recorded at 15 m from the channel using Ampere’s law for magnetostatics.

### 6.7.1 Overhead power distribution lines

Most of the published studies concerned with the responses of power distribution lines to direct and nearby triggered-lightning strikes have been conducted in Japan and in Florida.

#### 6.7.1.1 Nearby strikes

From 1977 to 1985, a test power distribution line at the Kahokugata site in Japan (see Table 6.1) was used for studying the induced effects of close triggered-lightning strikes to ground (Horii 1982). Both negative and positive polarity flashes were triggered. The wire simulating the phase conductor was 9 m above ground, and the minimum distance between the test line and the rocket launcher was 77 m. The peak value of induced voltage was found to be linearly related to the peak value of lightning current, with 25–30 kV corresponding to a 10-kA stroke. Installation of a grounded wire 1 m above the phase conductor resulted in a reduction of the induced voltage peak by about 40 per cent. Horii and Nakano (1995) show a photograph (their Figure 6.4.2)

of the test distribution line being struck directly during the induced-effect experiments. All triggered-lightning experiments in Japan were performed in winter.

In 1986, the University of Florida lightning research group studied the interaction of triggered lightning with an unenergized, three-phase 448-m overhead test line at the NASA Kennedy Space Center. Lightning was triggered 20 m from one end of the line, and acquired data included induced voltages on the top phase (10 m above ground) and fields at a distance of 500 m from the lightning channel (Rubinstein *et al.* 1994). Two types of induced-voltage waveforms were recorded: oscillatory and impulsive. The former exhibit peak values that range from tens of kilovolts to about 100 kV, while the latter show peak voltages nearly an order of magnitude larger. The oscillatory nature of the waveforms is due to multiple reflections at the ends of the line. Both types of voltage waveforms were observed to occur for different strokes within a single flash. The time domain technique of Agrawal *et al.* (1980) as adopted by Master and Uman (1984), Rubinstein *et al.* (1989), and Georgiadis *et al.* (1992) was used to model the observed voltages. Some success was achieved in the modeling of the oscillatory voltage waveforms, whereas all attempts to model the impulsive waveforms failed, probably because these measurements had been affected by a flashover in the measuring system. Rubinstein *et al.* (1994) used only the return-stroke electric field as the source in their modeling, assuming that the contribution from the leader was negligible. In a later analysis of the same data, Rachidi *et al.* (1997) found that the overall agreement between calculated and measured voltages of the oscillatory type was appreciably improved by taking into account the electric field of the dart leader.

From 1993 to 2004, studies of the interaction of triggered and natural lightning with power distribution systems were conducted at Camp Blanding, Florida. An overview of the Camp Blanding facility in 1997 is given in Figure 6.25.

During the 1993 experiment at Camp Blanding, the voltages induced on the overhead distribution line shown in Figure 6.25 were measured at poles 1, 9, and 15.

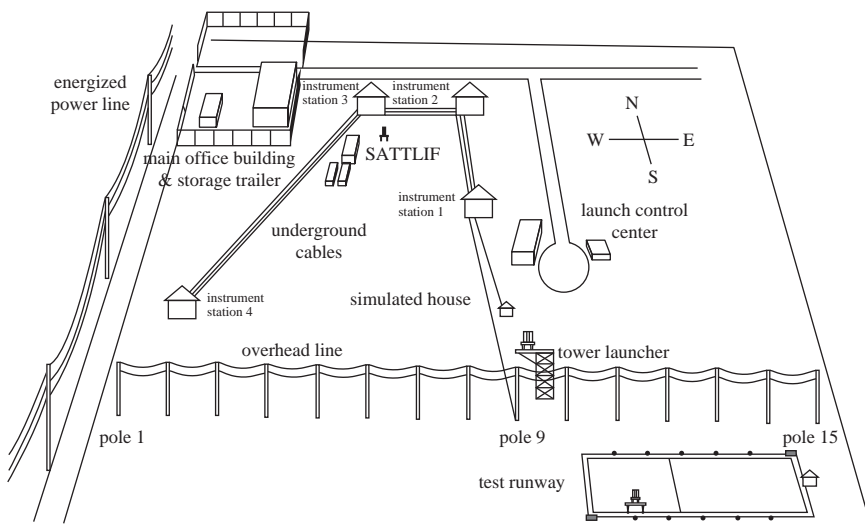


Figure 6.25 Overview of the International Center for Lightning Research and Testing (ICLRT) at Camp Blanding, Florida, 1997 (artwork by C.T. Mata)

The line had a length of about 730 m. The distance between the line and the triggered lightning strikes was 145 m. The line was terminated at both ends with a resistance of  $500 \Omega$ , and its neutral (the bottom conductor; see Figure 6.25) was grounded at poles 1, 9, and 15. The results of this experiment have been reported by Barker *et al.* (1996) and are briefly reviewed next. Waveforms of the induced voltage and of the total lightning current were obtained for 63 return strokes in 30 triggered flashes. Typical induced current voltage waveform at pole 9 and corresponding lightning return stroke current waveform are shown in Figure 6.26. A strong correlation was observed between the peak values of the return-stroke current, ranging from 4 to 44 kA, and the voltage, ranging from 8 to 100 kV, induced at pole 9, with a correlation coefficient of 0.97 (see Figure 6.27). Voltages induced at the terminal poles were typically half the value of the voltage induced at pole 9.

In 1994–1997, the test distribution system at Camp Blanding shown in Figure 6.25 was subjected to both direct (see section 6.7.1.2) and nearby triggered-lightning strikes. A large number of system configurations were tested, and several important results were obtained. It was observed, for example, that when lightning strikes earth at tens of meters from the system's grounds, an appreciable fraction of the total lightning current enters the system from earth (Fernandez 1997; Fernandez

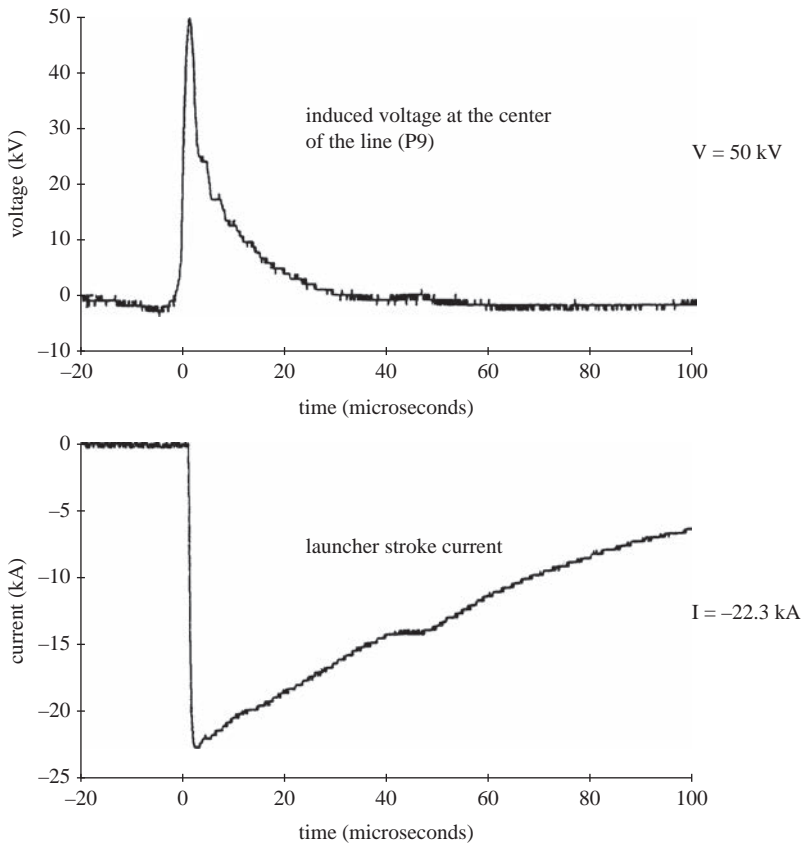


Figure 6.26 Typical induced voltage at pole 9 and corresponding lightning return stroke current (flash 93-05) reported by Barker *et al.* (1996)



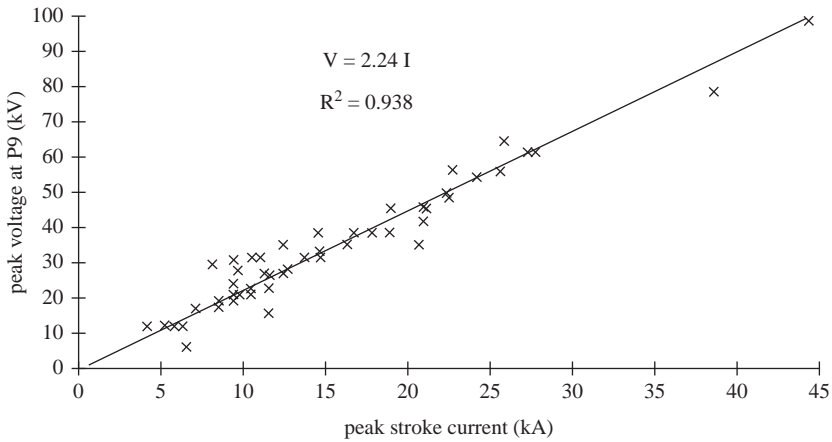


Figure 6.27 Peak induced voltage (8–100 kV) at pole 9 versus return-stroke peak current (4–44 kA),  $N = 63$ , reported by Barker *et al.* (1996)

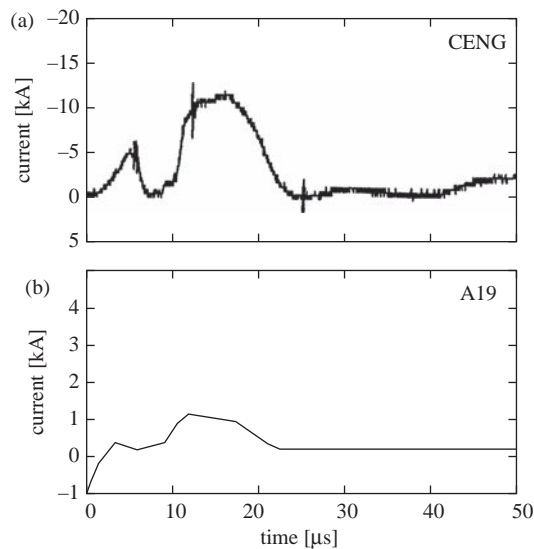


Figure 6.28 Current versus time waveforms for Camp Blanding flash 9516, displayed on a 50- $\mu$ s scale, illustrating injection of lightning current into the system from earth. (a) Total lightning current at the CENG launcher; (b) ground-rod current, A19, measured 60 m from the lightning strike point (adapted from Rakov *et al.* 2003a)

*et al.* 1998a, b). The observed peak values of current entering the system from earth, in percent of the total lightning current peak, were (for three different events) 10 per cent at 60 m (see Figure 6.28), 5 per cent at 40 m, and 18 per cent at 19 m from the ground strike point. These observations have important implications for modeling of lightning-induced effects on power lines.

Additional, more detailed data on lightning currents entering the system from earth, obtained at Camp Blanding in 2003, are presented by Schoene *et al.* (2009).

Triggered-lightning current was injected into the earth a distance of 11 m from one of the termination poles of an unenergized three-phase, 15-pole test power distribution line (see Vertical Configuration Distribution Line in Figure 6.29). The line was 812 m long, was equipped with four arrester stations, at poles 2, 6, 10, and 14, and was terminated in its characteristic impedance at poles 1 and 15. The neutral conductor of the line was grounded at each arrester station and at both line terminations. All pole grounds were instrumented. Measurements suggest that a significant fraction of the lightning current injected into the earth a distance of 11 m from pole 15 entered the line through the grounding system of pole 15. The peak value of the microsecond-scale return stroke current entering the line through the pole 15 line ground was 7 per cent of the peak value of the return stroke current injected into the earth. The peak value of the millisecond-scale triggered lightning initial stage current and the millisecond-scale return-stroke and initial-stage charge transfer to the line through the pole 15 line ground was between 12 and 19 per cent of the lightning peak current/charge transfer. This indicates that the percentage values for the injected peak currents are dependent on the current waveshape: for microsecond-scale return stroke currents, possibly due to electromagnetic coupling effects, a smaller fraction of the current peak enters the line via the grounding system compared to millisecond-scale initial stage currents. In the latter case, any influence of electromagnetic coupling to the line on ground currents is expected to be negligible.

### 6.7.1.2 Direct strikes

As noted above, various configurations of distribution system at Camp Blanding (see Figure 6.25) were tested in 1994–1997. In 1996, the responses of MOV arresters in the system, composed of an overhead line, underground cable, and padmount transformer with a resistive load, were measured during direct lightning strikes to the overhead line. Arresters were installed on the overhead line at two locations 50 m apart (on either side of the strike point) and at the primary of the padmount transformer which was connected to the line via the underground cable. Simultaneously-recorded arrester discharge current and voltage waveforms were obtained. Additionally, the energy absorbed by an arrester on the line as a function of time for the first 4 ms for one lightning event was estimated. The total energy absorbed by the arrester was 25 kJ (about 60 per cent of its maximum energy capability). The energy absorbed during the initial 200  $\mu$ s was about 8 kJ.

More details on findings from the 1994–1997 experiments at Camp Blanding are found in Uman *et al.* (1997), Fernandez (1997), Fernandez *et al.* (1998c, 1999), and Mata *et al.* (2000).

Presented below are results of triggered-lightning experiments conducted in 2000, 2001, and 2002 at the ICLRT at Camp Blanding, Florida, to study the responses of four-conductor (three-phase plus neutral) overhead distribution lines (see Figure 6.29) to direct lightning strikes. Presented first are direct-strike results for the line with horizontally configured phase conductors obtained in 2000 and then for the line with vertically configured phase conductors obtained in 2001 and 2002.

#### *Horizontal configuration distribution line*

The horizontal configuration, 856-m line was subjected to eight lightning flashes containing return strokes between July 11 and August 6, 2000 (Mata *et al.* 2003). The line was additionally subjected to two flashes without return strokes that are not considered here. The lightning current was injected into the phase C conductor

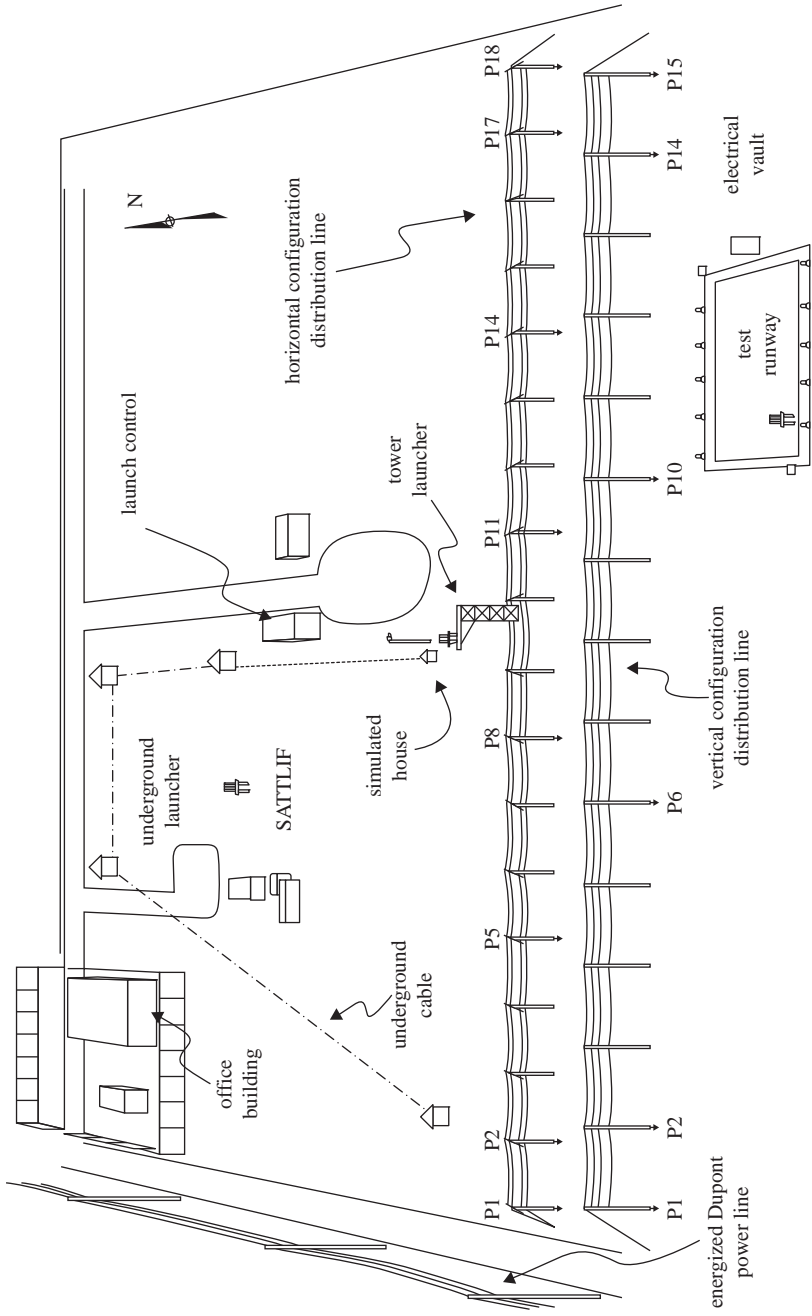


Figure 6.29 Overview of the ICLRT at Camp Blanding, Florida, 2000–2003

in the middle of the line. Six of the eight flashes with return strokes produced damage to the phase C arrester at pole 8. Of the two that did not, one had a triggering wire over the line and the other produced a flashover at the current injection point. The eight triggered flashes contained 34 recorded return strokes. These return strokes were characterized by submicrosecond current risetimes and by peak currents having geometric and arithmetic means between 15 and 20 kA with a maximum peak current of 57 kA. Each triggered flash also contained an initial continuous current of the order of hundreds of amperes, which flowed for a time of the order of hundreds of milliseconds, and some flashes contained a similar continuing current after subsequent strokes. A total of six 3-phase sets of arresters were installed on the line, at poles 2, 5, 8, 11, 14, and 17, the arresters being connected between the phase conductors and the neutral conductor. The neutral of the line was grounded at these poles and at the two line-terminating poles, 1 and 18. The 856-m three-phase line was terminated at each end in an impedance of about 500  $\Omega$ . The distance between poles of the line varied from 47 to 73 m.

The focus of the study was on the paths of return stroke current and charge transfer from the current injection point on one phase, C, between poles 9 and 10, to the eight grounds. This current division was examined in detail only for flash 0036, for which an initial continuous current and currents of 5 return strokes were injected into phase C between poles 9 and 10 prior to the arrester failure at pole 8. As an example, Figure 6.30 shows a drawing depicting the division of the incident current for the first stroke of flash 0036. This stroke had a peak current of about 26 kA. Note that the arrester current at pole 8 was lost due to instrumentation (fiber optic link) malfunction, but it likely was similar to the arrester current at pole 11, given the symmetry of the other currents on the line. Also, current through the terminating resistor at pole 18 was not measured.

Figure 6.31a shows the arrester and terminating-resistor peak currents recorded for all five strokes of flash 0036, while Figure 6.31b gives the peak currents entering all eight pole grounds for the five return strokes. It is evident from Figures 6.30 and 6.31 that the bulk of the peak current injected into phase C passed through the arrester at pole 11, and by inference at pole 8, and also went to ground mostly at poles 8 and 11.

Figure 6.30 shows current waveforms only to 100  $\mu$ s, although the total duration of current records is 10 ms. Figure 6.32a shows percentages of charge transfer through arresters and terminating resistor at pole 1, and Figure 6.32b percentages of charge transfer through ground rods, at 100, 500  $\mu$ s, and 1 ms.

It is clear from Figure 6.30, an observation also illustrated in Figure 6.32b, that after 25  $\mu$ s or so the current from the neutral to ground no longer flows primarily through the grounds closest to the strike point but is more uniformly distributed among the eight grounds. In fact, the currents after 25  $\mu$ s are distributed roughly inversely to the measured low-frequency, low-current grounding resistance. Figure 6.32b shows that the percentage of charge transferred to a given ground rod in the first 100  $\mu$ s is not much different from that transferred in the first millisecond.

As seen in Figure 6.30, there are considerable differences among the wave-shapes of currents measured in different parts of the test system. As a result, the division of peak current to ground (Figure 6.31b) is very different from the division of associated charge transfer (Figure 6.32b). It appears that the higher-frequency current components that are associated with the formation of initial current peak tend to flow from the struck phase to ground through the arresters and ground rods at the two poles closest to the current injection point. The low-frequency,

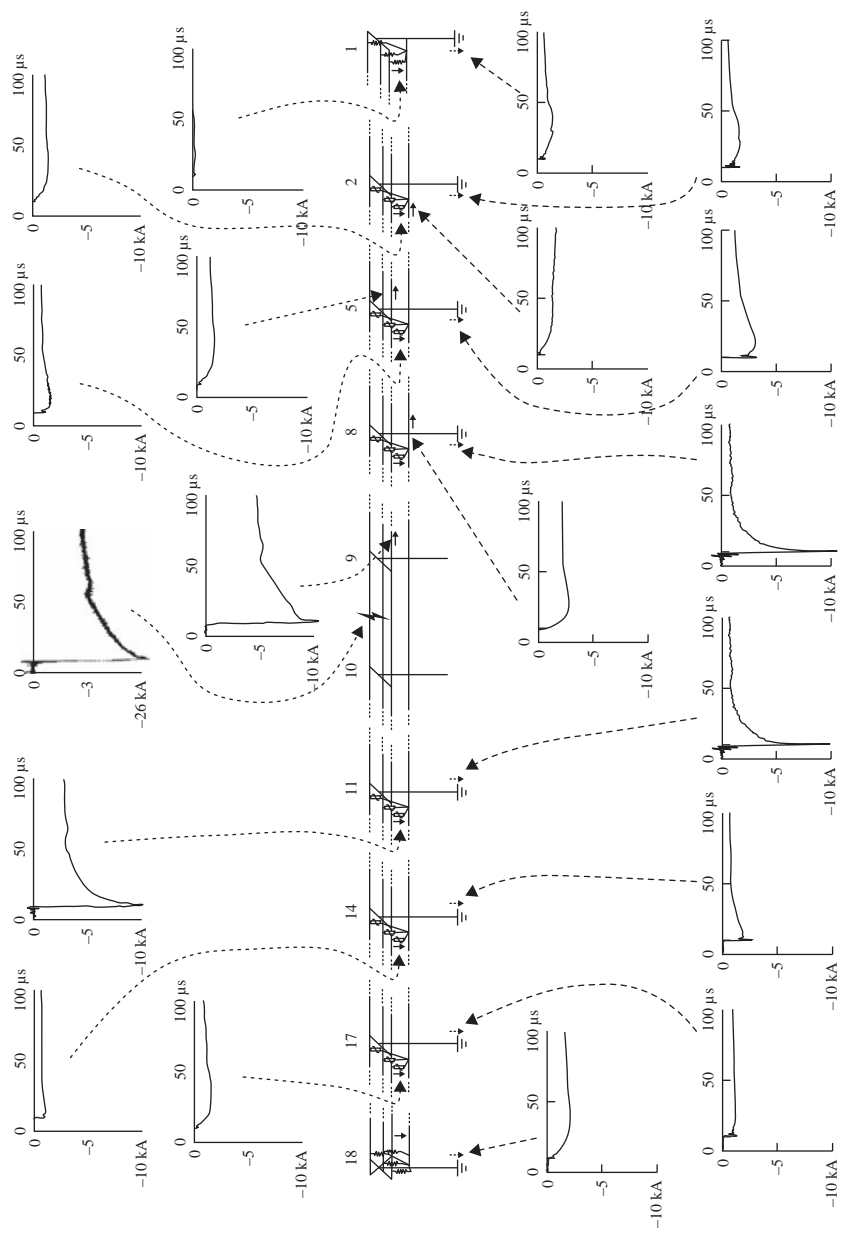


Figure 6.30 Horizontal configuration distribution line experiment. Current distribution for flash 0036, stroke 1, reported by Mata et al. (2003)

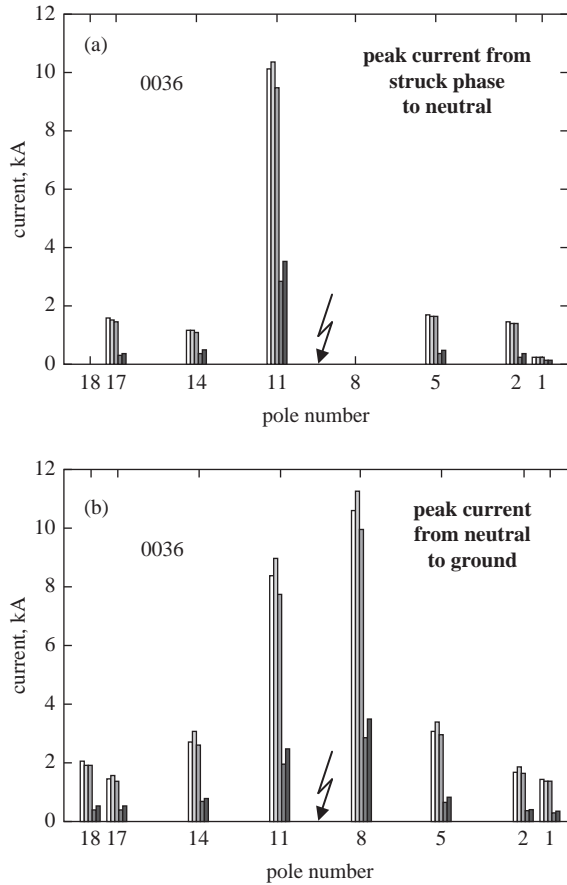


Figure 6.31 Horizontal configuration distribution line experiment. (a) Measured peak currents through arresters and terminating resistor at pole 1 for strokes 1 through 5 (in ascending order from left to right) of flash 0036. Arrester currents at pole 8 were lost due to instrumentation malfunction. Currents through the terminating resistor at pole 18 were not measured. (b) Measured peak currents to ground for strokes 1 through 5 (in ascending order from left to right) of flash 0036 (adapted from Mata et al. 2003)

low-current grounding resistances of the ground rods apparently have little or no effect on determining the paths for these current components. The lower-frequency current components that are associated with the tail of current waveforms are distributed more evenly among the multiple ground rods of the test system and appear to be significantly influenced by the low-frequency, low-current grounding resistances of the ground rods. In fact, the distribution of charge transfer in Figure 6.32b is very similar to the distribution of the inverse of the low-frequency, low-current grounding resistances of the ground rods, with poles 5 and 18 having the largest charge transfer and the lowest grounding resistances. Since the current waveshapes may differ considerably throughout the system, charge transfer is apparently a better quantity than the peak current for studying the division of lightning current among the various paths in the system.

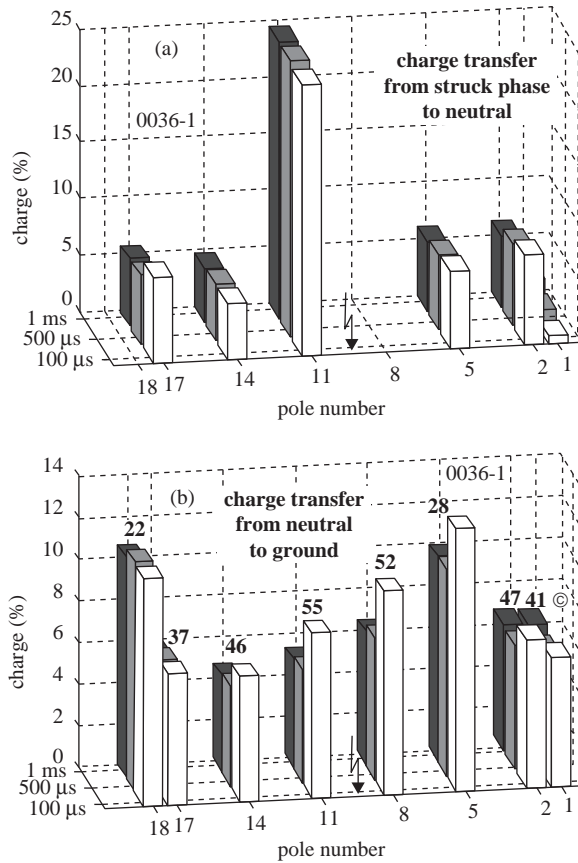


Figure 6.32 Horizontal configuration distribution line experiment. (a) Percentage of total charge transferred through phase C arresters at different poles and terminating resistor at pole 1, calculated at three different instants of time (100, 500 μs, and 1 ms from the beginning of the return stroke) for stroke 1 of flash 0036. No measurements are available at pole 8 and pole 18. (b) Percentage of total charge transferred to ground at different poles, calculated at three different instants of time (100, 500 μs, and 1 ms from the beginning of the return stroke) for stroke 1 of flash 0036. Low-frequency, low-current grounding resistance values of the poles are indicated in (b) (adapted from Mata *et al.* 2003)

*Vertical configuration distribution line*

The vertical configuration, 812-m line was subjected to four lightning flashes containing return strokes (also to four flashes without return strokes) between July 26 and September 5, 2001 and to ten flashes with return strokes between June 27 and September 13, 2002 (Mata *et al.* 2001, 2002). In 2001, return-stroke peak currents ranged from 6 to 28 kA and in 2002 from 6 to 34 kA. Arresters were installed at poles 2, 6, 10, and 14. Lightning current was injected into the top conductor near the center of the line.

In 2001, for one of the flashes having return strokes, an arrester failed early in the flash, probably during the initial stage. The three other flashes with return strokes were triggered with failed arresters already on the line. Two flashes without return

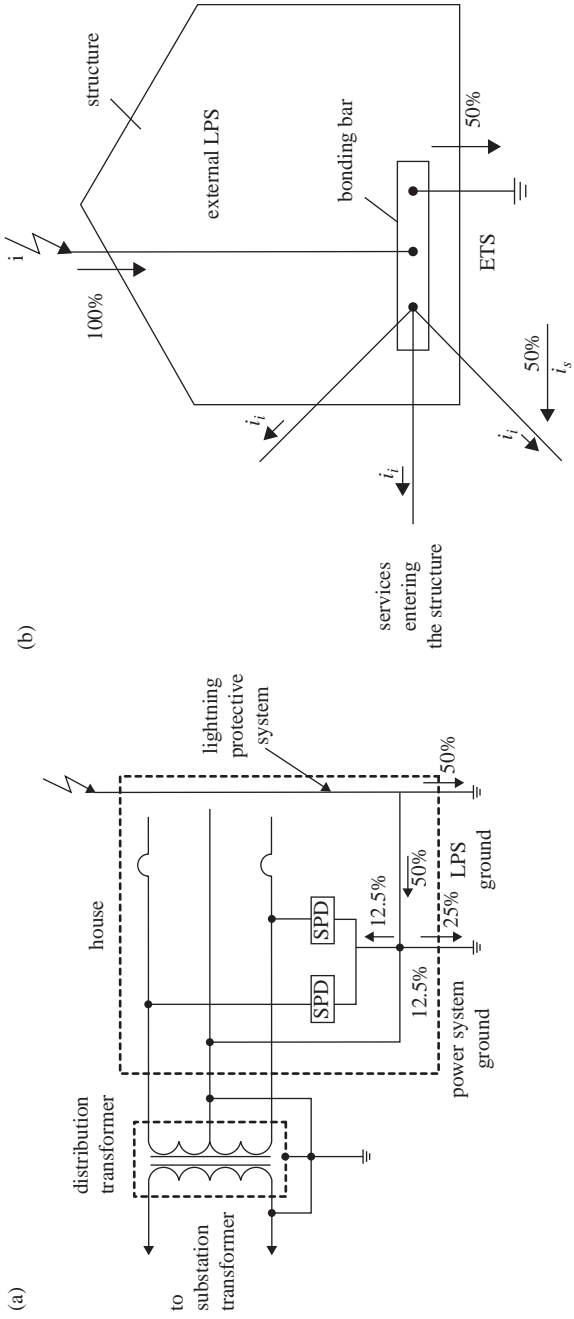


Figure 6.33 (a) Currents in different parts of the electrical circuit of a house when it is struck by lightning, in percent of the injected lightning current, as hypothesized by the International Electrotechnical Commission (J. L. Koepfinger, personal communication, 1998). SPD = surge protective device; LPS = lightning protective system. (b) Division of lightning current between the structure's earth termination (grounding) system, ETS, and services entering the structure, as assumed by IEC 61 312-1 (1995). LPS = lightning protective system



strokes did not damage arresters. One flash with return strokes was triggered when the line contained two damaged arresters, resulting in the failure of a third arrester.

In 2002, in order to reduce arrester damage during the initial stage of rocket-triggered lightning, a different configuration of the tower launching system was used. This new configuration allowed the diversion of most of the initial-stage current to ground at the tower base. Additionally, two arresters were installed in parallel on the struck (top) phase conductor. In 2002, arresters failed on three storm days out of a total of five (60 per cent), compared with two out of three storm days (67 per cent) in 2001. Flashovers on the line were very frequent during the direct strike tests. Significant currents were detected in phase B, which was not directly struck by lightning, with the waveshape of phase B currents being similar to that of the corresponding current in phase A that was directly struck.

Overall, the results presented in this section suggest that many direct lightning strikes to power distribution lines are capable of damaging MOV arresters, unless alternative current paths (flashovers, transformers, underground cable connections, etc.) are available to allow the lightning current to bypass the arrester.

In 2003, the vertical configuration line was equipped with a pole-mounted transformer. With the transformer on the line, the bulk of the return-stroke current injected into the line after about 1 ms flowed from the struck phase to the neutral through the transformer primary protected by an MOV arrester. Very little lightning current was passing through the transformer primary during the first few hundred microseconds.

### 6.7.2 *Underground cables*

In 1993, an experiment was conducted at Camp Blanding to study the effects of lightning on underground power distribution systems. All three cables shown in Figure 6.25 were used in this experiment. The cables were 15-kV coaxial cables with polyethylene insulation between the center conductor and the outer concentric neutral. One of the cables (Cable A) had an insulating jacket and was placed in PVC conduit, another one (Cable B) had an insulating jacket and was directly buried, and the third one (Cable C) had no jacket and was directly buried. The three cables were buried 5 m apart at a depth of 1 m. Thirty lightning flashes were triggered, and lightning current was injected into the ground directly above the cables, with the current injection point being approximately equidistant from instrument stations 1 and 2 (see Figure 6.25), but at different positions with respect to the cables. The cables were unenergized. Transformers at instrument stations 1, 2, 3, and 4 were connected to Cable A. More details on this test system configuration are found in Fernandez *et al.* (1998c).

Barker and Short (1996a, b, c) reported the following results from the underground power cables experiment. After lightning attachment to ground, a substantial fraction of the lightning current flowed into the neutral conductor of the cable with approximately 15–25 per cent of the total lightning current (measured at the rocket launcher) being detected 70 m in either direction from the strike point at instrument stations 1 and 2. The largest voltage measured between the center conductor and the concentric neutral of the cable was 17 kV, which is below the cable's basic insulation level (BIL) rating. Voltages measured at the transformer secondary were up to 4 kV. These could pose a threat to residential appliances. The underground power cables were excavated in 1994 (next year after the experiment). Lightning damage to these three cables is illustrated in Figure 6.21.

Paolone *et al.* (2005) measured, also at Camp Blanding, currents induced by triggered (and natural) lightning events at the end of a buried coaxial cable, both in the concentric neutral and in the inner conductor. The horizontal magnetic field above the ground surface was also measured. The obtained experimental data have been used to test the theoretical models and the developed time-domain and frequency-domain computer codes. In general, a reasonably good agreement has been found between numerical simulations and experimentally recorded waveforms.

### 6.7.3 Power transmission lines

Extensive studies of the interaction of triggered lightning with an unenergized power transmission line, the Okushishiku test line, were performed in Japan. The line was designed to operate at a voltage of 275 kV and had six conductors and one ground wire suspended on seven steel 60-m towers. The total length of the test line was 2 km. All experiments were conducted in winter, primarily using the altitude triggering technique (see section 6.2.2).

The distribution of triggered lightning current injected into the tower top among the four tower legs and the overhead ground wire was studied. The currents through the four legs were not equal, presumably because of the differences among the grounding impedances of the individual legs. It was observed that the higher-frequency components of current tended to flow to ground through the struck tower while the lower-frequency components appeared to travel to other towers along the ground wire. Currents in the phase conductors and voltages between each phase conductor and the tower were also measured.

### 6.7.4 Residential building

In 1997, the grounding system of a test house (labeled “Simulated house” in Figure 6.25) at Camp Blanding was subjected to triggered-lightning discharges for three different configurations, with the house’s electrical circuit being connected to the secondary of a transformer in Instrument Station 1, about 50 m distant. The primary of the transformer was connected to the underground cable which was open-circuited at Instrument Station 4. The cable’s neutral was grounded at Instrument Stations 1 and 4. The test system was unenergized. The division of lightning current injected into the grounding system of the test house among the various paths in the overall test system was analyzed. The waveshapes of currents in the ground rods of the test house differed markedly from the current waveshapes in other parts of the overall system. The ground rods at the test house appeared to filter out the higher frequency components of the lightning current, allowing the lower frequency components to enter the house’s electrical circuit. In other words, the ground rods exhibited a capacitive rather than the often expected and usually modeled resistive behavior. This effect was observed for dc resistances of the ground rods ranging from more than a thousand of ohms to some tens of ohms. The peak value of the current entering the test house’s electrical circuit was found to be over 80 per cent of the injected lightning current peak, in contrast with the 25 or 50 per cent assumed in two IEC-suggested scenarios, illustrated in Figure 6.33. Similarly, the percentages of current flowing (a) to the transformer secondary neutral and (b) through the SPDs were observed to be approximately a factor of 2–4 greater than those expected in the IEC hypothetical scenario shown in Figure 6.33a. Selected current waveforms for one of the configurations tested are presented in Figure 6.34. Since the current waveshapes may differ

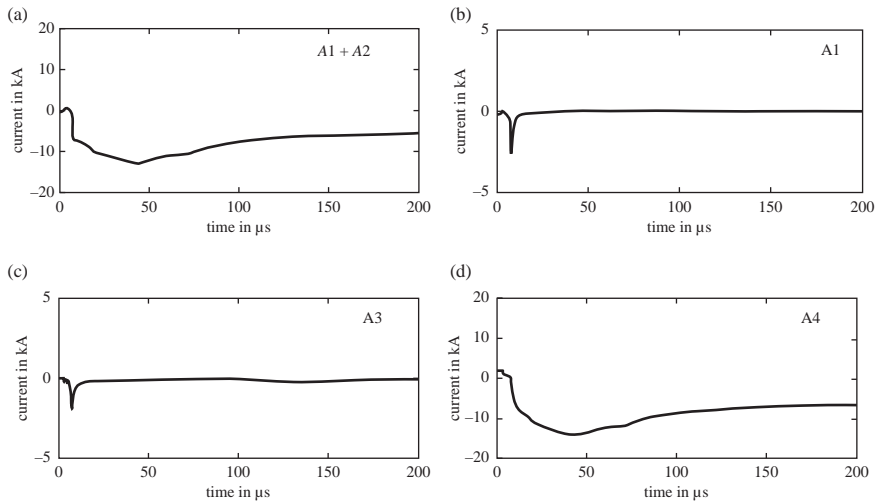


**Figure 6.34** *Simulated house experiment. Current versus time waveforms for Flash 9706, displayed on a 200- $\mu$ s scale. (a) Injected lightning current. (b) Current to ground at node A (lightning protective system ground, 1550  $\Omega$ ). (c) Current to ground at node B (power system ground, 590  $\Omega$ ). (d) Current entering the test house's electrical circuit (adapted from Rakov *et al.* 2002)*

considerably throughout the system, charge transfer is apparently a better quantity than the peak current for studying the division of lightning current among the various paths in the system (as already noted, based on results of a different experiment, in section 6.7.1.2).

In 2004 and 2005, structural lightning protective system (LPS) studies were conducted using a different test house at Camp Blanding. Triggered-lightning current was directly injected into the LPS. The test configurations in 2004 and 2005 differed in the lightning current injection point, number of down conductors (downloads), grounding system at the test house, and the use of SPDs. The primary objective was to examine the division of the injected lightning current between the grounding system of the test house and remote ground accessible via the neutral of the power-supply cable. The results are presented by DeCarlo *et al.* (2008). In 2004 (two pairs of interconnected LPS ground rods plus a bonded power-supply system rod), the mean value of the peak current entering the electrical circuit neutral was about 22 per cent of the injected lightning current peak, while in 2005 (four LPS ground rods plus power-supply system rod, all interconnected by a buried loop conductor), it was about 59 per cent. For comparison, more than 80 per cent of the injected peak current was observed to enter the electrical circuit neutral in the 1997 tests (one LPS ground rod interconnected with a power-supply system rod) described above. The 1997, grounding system was clearly poorer than in either 2004 or 2005, which is consistent with the observed poorer LPS performance (lower peak current dissipated by the LPS grounding system) in 1997. However, the apparently poorer LPS performance in 2005, compared to 2004, seems to be inconsistent with the notion that a buried loop conductor (employed in 2005) represents a superior grounding system relative to short radials (employed in 2004).

### 6.7.5 Airport runway lighting system

In 1997–1998, the University of Florida studied the interaction of lightning with an airport lighting system, shown in Figure 6.35. The experiment was conducted at Camp Blanding lightning triggering facility (see Figure 6.25). The test airport lighting system, was subjected to a total of 16 lightning strikes, 12 of which contained one or more return strokes. The total number of return strokes was 47 (24 in 1997 and 23 in 1998). Lightning current injection points were (1) the pavement, (2) one of the stake-mounted lights, (3) the counterpoise, and (4) the ground directly above the counterpoise or between the counterpoise and the edge of pavement. The system was energized using a generator and a current regulator for some of the tests and unenergized for others. The total lightning current and the currents and voltages at various points on the lighting system were measured.

The results of these experiments are presented by Bejleri *et al.* (2004). They include the first measurements of the responses of an underground bare conductor (counterpoise) to direct lightning strikes. These measurements can serve as ground truth for the testing of the validity of various counterpoise models. Overall results of the experiments can be summarized as follows.

#### 6.7.5.1 Current decay along the counterpoise

When lightning struck a stake-mounted light or directly struck the counterpoise, 10–30 per cent of the total lightning current was dissipated locally, within 3 m of the strike point (from measurements made at a distance of 3 m on either side of the strike point), while 70–90 per cent was carried by the counterpoise further away from the

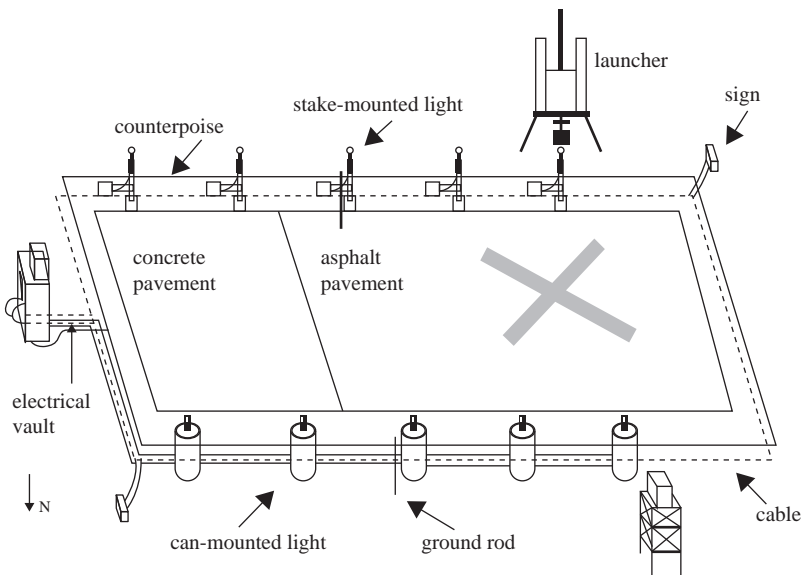


Figure 6.35 Schematic representation of the Camp Blanding test runway and its lighting system. The horizontal dimensions of the lighting system are about  $106 \times 31$  m. The cable is buried at a depth of 0.4 m with the counterpoise placed in the same trench 0.1 m or so above the cable. The counterpoise was connected to the light stakes and cans (adapted from Bejleri *et al.* 2004)

strike point. Measurements of the counterpoise current at four different locations (two on each side of the strike point) made it possible to estimate that about 63 per cent of the current detected 3 m from the strike point was dissipated in the ground after propagating along 50 m of the counterpoise, and about 73 per cent of the current detected 3 m on the other side from the strike point was dissipated in the ground after propagating along 67 m of the counterpoise. The average percent current decay rate is about 1 per cent per meter, independent of the peak current at the origin (peak current measured 3 m from the strike point). The current waveshape changes as the current wave propagates along the counterpoise: while the risetime remains more or less the same, a plateau or a broad maximum, not seen in the total lightning current waveform, is observed at distances of 50 and 67 m. The plateau duration is approximately between 10 and 50  $\mu\text{s}$ . In some cases, when the lightning current is smaller than 10 kA, current waveforms do not exhibit the plateau.

### 6.7.5.2 Currents in vertical ground rods

During experiments with configurations 1 and 2 (a total of four configurations were tested) the entry point of current in the counterpoise was about 12 m from the north ground rod (see Figure 6.35). In this case, the current through the ground rod was as high as 1–2 kA, accounting for 10–15 percent of the total lightning current.

During experiments with configurations 3 and 4 the entry point of current in the counterpoise was about 36 m from the south ground rod. Shown in Figure 6.36 are the waveforms of the injected lightning current and the current through the ground rod for the first stroke of triggered lightning flash U9841. In this particular

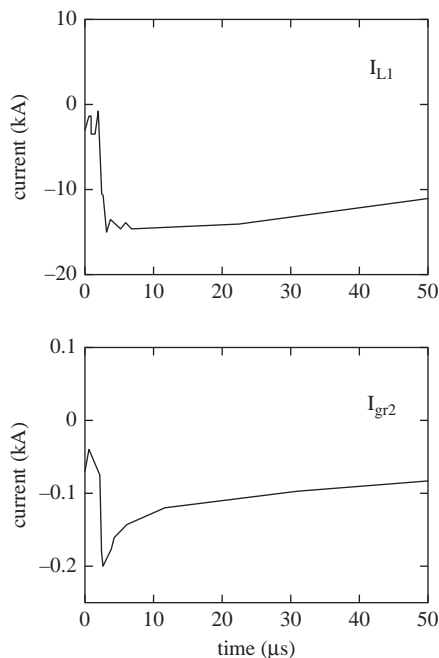


Figure 6.36 Runway experiment. Lightning channel current,  $I_{L1}$ , and ground rod current,  $I_{gr2}$ , for Flash U9841, first return stroke (adapted from Bejleri et al. 2004)

case the current through the ground rod accounted for approximately 1.3 percent of the lightning channel current (peak values). For all the lightning strikes 36 m from the south ground rod, the maximum value of current leaving the system through this ground rod was about 300 A, which was less than 5 percent of the total lightning current. The ground rod current waveform had approximately the same rise-time as the lightning current but shorter duration. This suggests that the ground rod is a better path than the counterpoise for the higher-frequency current components.

### 6.7.5.3 Cable currents

From the data recorded, it appears that the current flowing in the counterpoise induced current in the cable. The largest currents in the cable were observed near the current injection point. No evidence of direct lightning current injection into the cable or flashover to the cable from the counterpoise was found, but they definitely cannot be ruled out. Voltage pulses between the cable and the counterpoise had very short durations, ranging from a few hundred nanoseconds to a few microseconds, and magnitudes of some tens of kilovolts (likely underestimated due to insufficiently short sampling interval of 50 ns).

### 6.7.5.4 Lightning damage to the system

Several elements of the test airport runway lighting system sustained damage caused by one or more lightning strikes. The damage includes (1) failure of one of the electronic boards of the current regulator (CCR), (2) minor damage to the light fixture and to the glass cover of the light bulb of the stake-mounted light under the launcher, (3) multiple burn marks on the surface of the secondary cable of the current transformers (at the strike point and at distance of 36 m from it), (4) pin-holes on the secondary cable of the current transformer, and (5) melting of the counterpoise conductor at the point where the lightning attached to the system.

### 6.7.6 Miscellaneous experiments

Besides the tests described above, triggered-lightning experiments were performed in order to study the interaction of lightning with a number of miscellaneous objects and systems and for a variety of other reasons. Some of those studies are briefly reviewed below. Triggered lightning has been used to test power transformers (e.g., Horii 1982), lightning arresters (e.g., Horii and Nakano 1995; Kobayashi *et al.* 1997; Barker *et al.* 1998), overhead ground wires (e.g., Horii and Nakano 1995), lightning rods including so-called early-streamer-emission rods (e.g., Eybert-Berard *et al.* 1998) and high-resistance (tens to hundreds of kilohm), current-limiting rods (e.g., Teramoto *et al.* 1996), explosive materials (e.g., Fieux *et al.* 1978), and explosives storage facilities (Morris *et al.* 1994). Various aspects of lightning safety have been studied using a mannequin with a hairpin on the top of its head and a metal-roof car with a live rabbit inside (e.g., Horii 1982; Horii *et al.* 2006). The car was confirmed to be a lightning-safe enclosure. Step voltages have been measured within a few tens of meters of the triggered-lightning strike point (Horii 1982; Fisher *et al.* 1994; Schnetzer and Fisher 1998). Voltages have been measured across a single overhead power line tower and between the tower footing and remote ground (over a distance of 60 m), along with the lightning current injected into the tower (Gary *et al.* 1975). Additionally, triggered lightning has been used to make fulgurites (Kumazaki *et al.* 1993; Davis *et al.* 1993; Uman *et al.* 1994b; Rakov 1999a). Photographs of fulgurites are found in Figures 6.21 and 6.22.

Oxide reduction during triggered-lightning fulgurite formation has been examined by Jones *et al.* (2005).

## 6.8 Concluding remarks

The rocket-and-wire technique has been routinely used since the 1970s to artificially initiate (trigger) lightning from natural thunderclouds for purposes of research and testing. Leader/return stroke sequences in triggered lightning are similar in most (if not all) respects to subsequent leader/return stroke sequences in natural downward lightning and to all such sequences in upward (object-initiated) lightning. The initial processes in triggered lightning are similar to those in object-initiated lightning and are distinctly different from the first leader/return stroke sequence in natural downward lightning. The results of triggered-lightning experiments have provided considerable insight into natural lightning processes that would not have been possible from studies of natural lightning due to its random occurrence in space and time. Among such findings are the observation of an upward connecting leader in a dart leader/return stroke sequence, identification of the M-component mode of charge transfer to ground, the observation of a lack of dependence of return stroke current peak on grounding conditions, discovery of X-rays produced by lightning subsequent-stroke leaders, new insights into the mechanism of cutoff and reestablishment of current in the lightning channel, direct measurements of NO<sub>x</sub> production by an isolated lightning channel section, and the characterization of the electromagnetic environment within tens to hundreds of meters of the lightning channel. Triggered-lightning experiments have contributed significantly to testing the validity of various lightning models and to providing ground-truth data for the U.S. National Lightning Detection Network (NLDN). Triggered lightning has proved to be a very useful tool to study the interaction of lightning with various objects and systems.

## Acknowledgment

This work was supported in part by NSF (grant ATM-0852869), DARPA (grant HR0011-10-1-0061), and GRF (grant No. 14.B25.31.0023). Yongfu Li helped with editing the text.

## References

- Agrawal, A.K., Price, H.J., and Gurbaxani, S.H. 1980. 'Transient response of multiconductor transmission lines excited by a nonuniform electromagnetic field.' *IEEE Trans. Electromagn. Compat.* 22: 119–29
- Anderson, R.B., and Eriksson, A.J. 1980. 'Lightning parameters for engineering application.' *Electra.* 69: 65–102
- Baba, Y., and Rakov, V. A. 2005. 'On the use of lumped sources in lightning return stroke models.' *J. Geophys. Res.: Atmos.*, 110, D03101, doi:10.1029/2004JD005202
- Barker, P.P., and Short, T.A. 1996a. 'Lightning effects studied: The underground cable program.' In *Transmission and Distribution World*, May 1996, pp. 24–33
- Barker, P.P., and Short, T.A. 1996b. 'Lightning measurements lead to an improved understanding of lightning problems on utility power systems.' In *Proc. 11 CEPSI*, vol. 2, Kuala Lumpur, Malaysia, pp. 74–83

- Barker, P., and Short, T. 1996c. 'Findings of recent experiments involving natural and triggered lightning.' Panel Session Paper presented at 1996 Transmission and Distribution Conference, Los Angeles, California, September 16–20, 1996
- Barker, P.P., Short, T.A., Eybert-Berard, A.R., and Berlandis, J.P. 1996. 'Induced voltage measurements on an experimental distribution line during nearby rocket triggered lightning flashes.' *IEEE Trans. Pow. Del.* 11: 980–95
- Barker, P., Short, T., Mercure, H., Cyr, S., and O'Brien, J. 1998. 'Surge arrester energy duty considerations following from triggered lightning experiments.' *IEEE PES*, 1998 Winter Meeting, Panel Session on Transmission Line Surge Arrester Application Experience, p. 19
- Bazelyan, E.M., and Raizer, Yu. P. 2000a. *Lightning Physics and Lightning Protection*, Bristol: IOP Publishing, 325 p.
- Beituganov, M.N., and Zashakuev, T.Z. 1992. 'The experience of initiation of lightning and spark discharges.' In *Proc. 9th Int. Conf. on Atmospheric Electricity*, St. Petersburg, Russia, pp. 283–6
- Bejleri, M. *et al.* 2004. 'Triggered lightning testing of an airport runway lighting system.' *IEEE Trans. on EMC*, 46(1): 96–101
- Ben Rhouma, A., Auriol, A.P., Eybert-Berard, A., Berlandis, J.-P., and Bador, B. 1995. 'Nearby lightning electromagnetic fields.' In *Proc. 11th Int. Zurich Symp. on Electromagn. Compat.*, Zurich, Switzerland, pp. 423–28
- Berger, K. 1972. 'Methoden und Resultate der Blitzforschung auf dem Monte San Salvatore bei Lugano in den Jahren 1963–1971.' *Bull. Schweiz. Elektrotech.* 63: 1403–22
- Berger, K., Anderson, R.B., and Knoninger, H. 1975. 'Parameters of lightning flashes.' *Electra*, 41: 23–37
- Berger, K., and Garabagnati, E. 1984. 'Lightning current parameters.' Results obtained in Switzerland and in Italy. URSI Conf., Florence, Italy, 13 p.
- Biagi, C.J. *et al.* 2009. 'High-speed video observations of rocket-and-wire initiated lightning.' *Geophys. Res. Lett.*, 36: L15801, doi:10.1029/2009GL038525
- Biagi, C.J. *et al.* 2010. 'Observations of stepping mechanisms in a rocket-and-wire triggered lightning flash.' *J. Geophys. Res.*, 115: D23215, doi:10.1029/2010JD014616
- Biagi, C.J. *et al.* 2011. 'Determination of the electric field intensity and space charge density versus height prior to triggered lightning.' *J. Geophys. Res.*, 116: D15201, doi:10.1029/2011JD015710
- Biagi, C.J., Uman, M.A., Hill, J.D., Rakov, V.A., and Jordan, D. M. 2012. 'Transient current pulses in rocket-extended wires used to trigger lightning.' *J. Geophys. Res.*, 117: D07205, doi:10.1029/2011JD016161
- Brook, M., Armstrong, G., Winder, R.P.H., Vonnegut, B., and Moore, C.B. 1961. 'Artificial initiation of lightning discharges.' *J. Geophys. Res.* 66: 3967–9
- Chen, M. *et al.* 2003. 'Simultaneous observations of optical and electrical signals in altitude-triggered negative lightning flashes.' *J. Geophys. Res.*, 108(D8): 4240, doi:10.1029/2002JD002676
- Cooray, V., Montano, R., and Rakov, V. 2004. 'A model to represent negative and positive lightning first return strokes with connecting leaders.' *J. Electrostatics*, 60: 97–109
- Crawford, D.E. 1998. 'Multiple-station measurements of triggered lightning electric and magnetic fields.' M.S. Thesis, Univ. Florida, Gainesville, 282 pp.



- Crawford, D.E. *et al.* 1999. Multiple-station measurements of triggered-lightning electric and magnetic fields. In *Proc. 11th Int. Conf. on Atmospheric Electricity*, Guntersville, Alabama, pp. 154–7
- Crawford, D.E. *et al.* 2001. ‘The close lightning electromagnetic environment: Dart-leader electric field change versus distance.’ *J. Geophys. Res.* 106: 14,909–17
- Davis, D.A. *et al.* 1993. ‘Fulgurites from triggered lightning.’ *Eos Trans. AGU*, 74(43), Fall Meet. Suppl., 165
- DeCarlo, B.A. *et al.* 2008. ‘Distribution of currents in the lightning protective system of a residential building—Part I: Triggered-lightning experiments.’ *IEEE Trans. Power Delivery*, 23(4): 2439–46
- Depasse, P. 1994. ‘Statistics on artificially triggered lightning.’ *J. Geophys. Res.* 99: 18,515–22
- Dwyer, J.R. *et al.* 2003. ‘Energetic radiation produced by rocket-triggered lightning.’ *Science*, 299: 694–7
- Dwyer, J.R. *et al.* 2004a. ‘Measurements of x-ray emission from rocket-triggered lightning.’ *Geophys. Res. Lett.*, 31: L05118, doi: 10.1029/2003GL018770, p. 4
- Dwyer, J.R. *et al.* 2004b. ‘A ground level gamma-ray burst observed in association with rocket-triggered lightning.’ *Geophys. Res. Lett.*, 31: L05119, doi: 10.1029/2003GL018771, p. 4
- Dwyer, J.R. *et al.* 2005. ‘X-ray bursts associated with leader steps in cloud-to-ground lightning.’ *Geophys. Res. Lett.*, 32(1): L01803, doi:10.1029/2004GL021782
- Dwyer, J.R. *et al.* 2012. ‘Observation of a gamma-ray flash at ground level in association with a cloud-to-ground lightning return stroke.’ *J. Geophys. Res.: Space Physics*, 117, A10303, doi:1029/2012JA017810
- Eybert-Berard, A., Barret, L., and Berlandis, J.P. 1986. ‘Campagne foudre aux ETATS-UNIS.’ Kennedy Space Center (Florida), Programme RTLP 85\* (in French). STT/ASP 86-01, Cent. D’Etud. Nucl. de Grenoble, Grenoble, France
- Eybert-Berard, A., Barret, L., and Berlandis, J.P. 1988. ‘Campagne d’experimentations foudre RTLP 87.’ NASA Kennedy Space Center, Florida, USA (in French). STT/LASP 88-21/AEB/JPB-pD, Cent. D’Etud. Nucl. de Grenoble, Grenoble, France
- Eybert-Berard, A., Lefort, A., and Thirion, B. 1998. ‘On-site tests.’ In *Proc. 24th Int. Conf. on Lightning Protection*, Birmingham, United Kingdom, pp. 425–35
- Fernandez, M.I. 1997. ‘Responses of an unenergized test power distribution system to direct and nearby lightning strikes.’ M.S. Thesis, Univ. Florida, Gainesville, p. 249
- Fernandez, M.I., Rambo, K.J., Rakov, V.A., and Uman, M.A. 1999. ‘Performance of MOV arresters during very close, direct lightning strikes to a power distribution system.’ *IEEE Trans. Pow. Del.* 14(2): 411–8
- Fernandez, M.I., Rambo, K.J., Stapleton, M.V., Rakov, V.A., and Uman, M.A. 1998a. ‘Review of triggered lightning experiments performed on a power distribution system at Camp Blanding, Florida, during 1996 and 1997.’ In *Proc. 24th Int. Conf. on Lightning Protection*, Birmingham, United Kingdom, pp. 29–35

- Fernandez, M.I. *et al.* 1998c. 'Improved lightning arrester protection results, final results.' Technical Report, TR-109670-R1, (Addendum AD-109670-R1), EPRI, 3412 Hillview Avenue, Palo Alto, California 94304
- Fernandez, M.I., Rakov, V.A., and Uman, M.A. 1998b. 'Transient currents and voltages in a power distribution system due to natural lightning.' In *Proc. 24th Int. Conf. on Lightning Protection*, Birmingham, United Kingdom, pp. 622–629
- Fieux, R., Gary, C., and Hubert, P. 1975. 'Artificially triggered lightning above land.' *Nature*, 257: 212–4
- Fieux, R.P. *et al.* 1978. 'Research on artificially triggered lightning in France.' *IEEE Trans. Pow. Appar. Syst.*, PAS-97: 725–33
- Fisher, R.J., Schnetzer, G.H., and Morris, M.E. 1994. 'Measured fields and earth potentials at 10 and 20 meters from the base of triggered-lightning channels.' In *Proc. 22nd Int. Conf. on Lightning Protection*, Budapest, Hungary, Paper R 1c-10, p. 6
- Fisher, R.J. *et al.* 1993. 'Parameters of triggered-lightning flashes in Florida and Alabama.' *J. Geophys. Res.*, 98: 22,887–902
- Gamerota, W.R. *et al.* 2013. 'An "anomalous" triggered lightning flash in Florida.' *J. Geophys. Res. Atmos.*, 118: 3402–14, doi:10.1002/jgrd.50261
- Gary, C., Cimador, A., and Fieux, R. 1975. 'La foudre: Étude du phénomène. Applications à la protection des lignes de transport.' *Revue Générale de l'Électricité*, 84: 24–62
- Georgiadis, N., Rubinstein, M., Uman, M.A., Medelius, P.J., and Thomson, E.M. 1992. 'Lightning-induced voltages at both ends of a 450-m distribution line.' *IEEE Trans. Electromagn. Compat.*, 34: 451–460
- Gorin, B.N., Levitov, V.I., and Shkilev, A.V. 1977. 'Lightning strikes to the Ostankino tower.' *Elektrichestvo*, 8: 19–23
- Gorin, B.N., and Shkilev, A.V. 1984. 'Measurements of lightning currents at the Ostankino tower.' *Elektrichestvo*, 8: 64–5
- Hierl, A. 1981. 'Strommessungen der Blitztriggerstation Steingaden.' In *Proc. 16th Int. Conf. on Lightning Protection*, Szeged, Hungary, Paper R-1.04, p. 10
- Hill, J.D., Uman, M.A., Jordan, D.M., Dwyer, J.R., and Rassoul, H. 2012. "'Chaotic" dart leaders in triggered lightning: Electric fields, X-rays, and source locations.' *J. Geophys. Res.: Atmos.*, (1984–2012), 117(D3)
- Horii, K. 1982. 'Experiment of artificial lightning triggered with rocket.' *Memoirs of the Faculty of Engineering, Nagoya Univ.* Japan 34: 77–112
- Horii, K., and Ikeda, G. 1985. 'A consideration on success conditions of triggered lightning.' In *Proc. 18th Int. Conf. on Lightning Protection*, Munich, Germany, paper 1–3, p. 6
- Horii, K., Nakamura, K., and Sumi, S.I. 2006. 'Review of the experiment of triggered lightning by rocket in Japan.' In *Proc. 28th Int. Conf. on Lightning Protection*, Kanazawa, Japan
- Horii, K., and Nakano, M. 1995. 'Artificially triggered lightning.' In *Handbook of Atmospheric Electrodynamics*, vol. 1, H. Volland, ed., Boca Raton, Florida: CRC Press, pp. 151–66
- Horii, K. *et al.* 1990. 'Experiment of rocket-triggered lightning in Indonesia.' *Trans. IEE Japan*, 110-B: 1068–9
- Howard, J. *et al.* 2010. 'RF and X-ray source locations during the lightning attachment process.' *J. Geophys. Res.*, 115: D06204, doi:10.1029/2009JD012055

- Howard, J. *et al.* 2008. 'Co-location of lightning leader x-ray and electric field change sources.' *Geophys. Res. Lett.*, 35: L13817, doi:10.1029/2008GL034134
- Hubert, P. 1984. 'Triggered lightning in France and New Mexico.' *Endeavour*, 8: 85–9
- Hubert, P., Laroche, P., Eybert-Berard, A., and Barret, L. 1984. 'Triggered lightning in New Mexico.' *J. Geophys. Res.*, 89: 2511–21
- Idone, V.P., Orville, R.E. Hubert, P. Barret, L., and Eybert-Berard, A. 1984. 'Correlated observations of three triggered lightning flashes.' *J. Geophys. Res.*, 89: 1385–94
- IEC 61312-1. 1995. 'Protection against lightning electromagnetic impulse – Part 1: General principles
- Jafferis, W. 1995. 'Rocket triggered lightning – Kennedy Space Center and beyond.' In *Proc. 1995 Int. Conf. on Lightning and Static Electricity*, Williamsburg, Virginia, pp. 57/1–57/20
- Jayakumar, V. *et al.* 2006. 'Estimation of input energy in rocket-triggered lightning.' *Geophys. Res. Lett.*, 33: L05702, doi:10.1029/2005GL025141
- Jerauld, J. *et al.* 2005. 'An evaluation of the performance characteristics of the U.S. National Lightning Detection Network in Florida using rocket-triggered lightning.' *J. Geophys. Res.*, 110: D19106, doi:10.1029/2005JD005924
- Jerauld, J., Uman, M.A., Rakov, V.A., Rambo, K.J., and Jordan, D.M. 2004. 'A triggered lightning flash containing both negative and positive strokes.' *Geophys. Res. Lett.*, 31: L08104, doi:10.1029/2004GL019457
- Jerauld, J., Uman, M.A., Rakov, V.A., Rambo, K.J., and Schnetzer, G.H. 2007. 'Insights into the ground attachment process of natural lightning gained from an unusual triggered-lightning stroke.' *J. Geophys. Res.*, 112: D13113, doi:10.1029/2006JD007682
- Jones, B.E. *et al.* 2005. 'Oxide reduction during triggered-lightning fulgurite formation.' *J. Atmos. Solar-Terrestrial Physics*, 67: 427–8
- Kito, Y., Horii, K., Higashiyama, Y., and Nakamura, K. 1985. 'Optical aspects of winter lightning discharges triggered by the rocket-wire technique in Hokuriku district of Japan.' *J. Geophys. Res.*, 90: 6147–57
- Kobayashi, M., Sasaki, H., and Nakamura, K. 1997. 'Rocket-triggered lightning experiment and consideration for metal oxide surge arresters.' In *Proc. 10th Int. Symp. on High Voltage Engineering*, Montreal, Quebec, Canada, p. 4
- Kumazaki, K., Nakamura, K., Naito, K., and Horii, K. 1993. 'Production of artificial fulgurite by utilizing rocket triggered lightning.' In *Proc. 8th Int. Symp. on High Voltage Engineering*, Yokohama, Japan, pp. 269–72
- Lalande, P. *et al.* 1996. 'Connection to ground of an artificially triggered negative downward stepped leader.' In *Proc. 10th Int. Conf. on Atmospheric Electricity*, Osaka, Japan, pp. 668–71
- Lalande, P. *et al.* 1998. 'Leader properties determined with triggered lightning techniques.' *J. Geophys. Res.*, 103: 14,109–15
- Laroche, P., Idone, V., Eybert-Berard, A., and Barret, L. 1991. 'Observations of bi-directional leader development in a triggered lightning flash.' In *Proc. 1991 Int. Conf. on Lightning and Static Electricity*, Cocoa Beach, Florida, pp. 57/1–57/10
- Leteinturier, C., Hamelin, J.H., and Eybert-Berard, A. 1991. 'Submicrosecond characteristics of lightning return-stroke currents.' *IEEE Trans. Electromagn. Compat.*, 33: 351–7

- Leteinturier, C., Weidman, C., and Hamelin, J. 1990. 'Current and electric field derivatives in triggered lightning return strokes.' *J. Geophys. Res.*, 95: 811–28
- Liu, X., and Zhang, Y. 1998. 'Review of artificially triggered lightning study in China.' *Trans. IEE Japan*, 118-B(2): 170–5
- Liu, X.-S. *et al.* 1994. 'Experiment of artificially triggering lightning in China.' *J. Geophys. Res.*, 99: 10,727–31
- Lu, W. *et al.* 2009. 'Simultaneous optical and electrical observations on the initial processes of altitude-triggered negative lightning.' *Atmos. Res.*, 91(2): 353–9
- Master, M.J., and Uman, M.A. 1984. 'Lightning induced voltages on power lines: Theory.' *IEEE Trans. Pow. App. Syst.*, 103: 2505–17
- Mata, A.G., Rakov, V.A., Rambo, K.J., Stapleton, M.V., and Uman, M.A. December 2001. 'UF/FPL study of triggered lightning strikes to FPL distribution lines: 2001 experiments.' Phase III Report. University of Florida, p. 25
- Mata, A.G. *et al.* December 2002. 'Study of triggered lightning strikes to FPL distribution lines.' Phase IV Report. University of Florida, p. 258
- Mata, C.T. 2000. 'Interaction of lightning with power distribution lines.' Ph.D. Dissertation, Univ. Florida, Gainesville, p. 388
- Mata, C.T., Fernandez, M.I., Rakov, V.A., and Uman, M.A. 2000. 'EMTP modeling of a triggered-lightning strike to the phase conductor of an overhead distribution line.' *IEEE Trans. Pow. Del.*, 15(4): 1175–81
- Mata, C.T. *et al.* 2003. 'Measurement of the division of lightning return stroke current among the multiple arresters and grounds of a power distribution line.' *IEEE Trans. on Power Delivery*, 18(4): 1203–8
- Miki, M., Rakov, V.A., Rambo, K.J., Schnetzer, G.H., and Uman, M.A. 2002. 'Electric fields near triggered lightning channels measured with Pockels sensors.' *J. Geophys. Res.*, 107(D16): 4277, doi: 10.1029/2001JD001087
- Miki, M. *et al.* 2005. 'Initial stage in lightning initiated from tall objects and in rocket-triggered lightning.' *J. Geophys. Res.*, 110: D02109, doi:10.1029/2003JD004474
- Morris, M.E., Fisher, R.J., Schnetzer, G.H., Merewether, K.O., and Jorgenson, R.E. 1994. 'Rocket-triggered lightning studies for the protection of critical assets.' *IEEE Trans. Ind. Appl.*, 30: 791–804
- Nag, A. *et al.* 2011. 'Evaluation of U.S. National Lightning Detection Network performance characteristics using rocket-triggered lightning data acquired in 2004–2009.' *J. Geophys. Res.*, 116: D02123, doi:10.1029/2010JD014929
- Nakamura, K., Horii, K., Nakano, M., and Sumi, S. 1992. 'Experiments on rocket triggered lightning.' *Res. Lett. Atmos. Electr.*, 12: 29–35
- Nakamura, K. *et al.* 1991. 'Artificially triggered lightning experiments to an EHV transmission line.' *IEEE Trans. Pow. Del.*, 6: 1311–8
- Newman, M.M. 1958. 'Lightning discharge channel characteristics and related atmospherics.' In *Recent Advances in Atmospheric Electricity*, L.G. Smith, ed., New York: Pergamon Press, pp. 475–84
- Newman, M.M. 1965. 'Use of triggered lightning to study the discharge channel.' In *Problems of Atmospheric and Space Electricity*, New York: Elsevier, pp. 482–90
- Newman, M.M., and Robb, J.D. 1977. 'Protection of aircraft.' In *Lightning, vol. 2: Lightning Protection*, R.H. Golde, ed., London: Academic Press, pp. 659–96
- Newman, M.M. *et al.* 1967. 'Triggered lightning strokes at very close range.' *J. Geophys. Res.*, 72: 4761–4

- Nucci, C.A., and Rachidi, F. 1995. 'On the contribution of the electromagnetic field components in field-to-transmission line interaction.' *IEEE Trans. Electromagn. Compat.*, 37: 505–8
- Olsen, R.C., Jordan, D.M., Rakov, V.A., Uman, M.A., and Grimes, N. 2004. 'Observed one-dimensional return stroke propagation speeds in the bottom 170 m of a rocket-triggered lightning channel.' *Geophys. Res. Lett.*, 31: L16107, doi:10.1029/2004GL020187
- Olsen, R.C. *et al.* 2006. 'Leader/return-stroke-like processes in the initial stage of rocket-triggered lightning.' *J. Geophys. Res.*, 111: D13202, doi:10.1029/2005JD006790, p. 11
- Paolone, M. *et al.* 2005. 'Lightning induced disturbances in buried cables – part 2: Experiment and model validation, *IEEE Trans. on Electromagnetic Compatibility*, 47(3): 509–20
- Pinto, O., Jr., Pinto, I.R.C.A., Saba, M.M.F., Solorzano, N.N., Guedes, D. 2005. 'Return stroke peak current observations of negative natural and triggered lightning in Brazil.' *Atmos. Res.*, 76: 493–502
- Qie, X., Jiang, R., and Laroche, P. 2012. 'Triggering lightning experiments: An effective approach to the research of lightning physics.' *Aerospace Lab*, issue 5, AL05-05, p. 12
- Qie X.S., Yang, J., and Jiang, R.B. 2013. 'Characteristics of current pulses in rocket-triggered lightning.' *Atmos. Res.*, dx.doi.org/10.1016/j.atmosres.2012.11.012
- Qie, X.S. *et al.* 2007. 'Artificially triggered lightning and its characteristic discharge parameters in two severe thunderstorms.' *Sci. China, Ser. D: Earth Sci.*, 50: 1241–50, doi:10.1007/s11430-007-0064-2
- Qie, X. *et al.* 2009. 'Characteristics of triggered lightning during Shandong artificial triggering lightning experiment (SHATLE).' *Atmos. Res.*, 91(2): 310–5
- Rachidi, F., Rubinstein, M., Guerrieri, S., and Nucci, C.A. 1997. 'Voltages induced on overhead lines by dart leaders and subsequent return strokes in natural and rocket-triggered lightning.' *IEEE Trans. Electromagn. Compat.*, 39(2): 160–6
- Rahman, M. *et al.* 2007. 'Measurements of NO<sub>x</sub> produced by rocket-triggered lightning.' *Geophys. Res. Lett.*, 34: L03816. doi:10.1029/2006GL027956. p. 5
- Rakov, V.A. 1999a. 'Lightning makes glass.' *J. Glass Art Society*, pp. 45–50
- Rakov, V.A. 1999b. 'Lightning discharges triggered using rocket-and-wire techniques.' In *Recent Res. Devel. Geophysics*, vol. 2, Research Signpost, India, pp. 141–71
- Rakov, V.A. 2009. 'Triggered lightning.' In *Lightning: Principles, Instruments and Applications*, H.D. Betz, U. Schumann, and P. Laroche, eds., Springer, 691 p. ISBN 978-1-4020-9078-3, pp. 23–56
- Rakov, V.A. 2010. 'Rocket-triggered lightning and new insights into lightning protection gained from triggered-lightning experiments.' In *Lightning Protection*, V. Cooray, ed., IEE, London, 1036 p., ISBN 978-0-86341-744-3, pp. 97–164
- Rakov, V.A., Mallick, S., and Nag, A. 2012. 'Lightning observatory in Gainesville (LOG), Florida: A review of recent results.' 31st International Conference on Lightning Protection, Vienna, Austria, Paper 275, p. 8
- Rakov, V.A., Mata, C.T., Uman, M.A., Rambo, K.J., and Mata, A.G. 2003a. 'Review of triggered-lightning experiments at the ICLRT at Camp Blanding, Florida.' In *Proc. of 5th IEEE Power Tech Conference*, Bologna, Italy, Paper 381, p. 8

- Rakov, V.A., Thottappillil, R., Uman, M.A., and Barker, P.P. 1995a. 'Mechanism of the lightning M component.' *J. Geophys. Res.*, 100: 25,701–10
- Rakov, V.A., and Uman, M.A. 1998. 'Review and evaluation of lightning return stroke models including some aspects of their application.' *IEEE Trans. on Electromagn. Compat.*, 40: 403–26
- Rakov, V.A., and Uman, M.A. 2003. *Lightning: Physics and effects*. Cambridge University Press, p. 687, ISBN 0521583276
- Rakov, V.A., Uman, M.A., Rambo, K.J. 2005a. 'A review of ten years of triggered-lightning experiments at Camp Blanding, Florida.' *Atmos. Res.*, 76(1–4): 504–18
- Rakov, V.A., Uman, M.A., and Thottappillil, R. 1995b. 'Review of recent lightning research at the University of Florida.' *Electrotechnik und Informationstechnik*, 112: 262–5
- Rakov, V.A. *et al.* 1998. 'New insights into lightning processes gained from triggered-lightning experiments in Florida and Alabama.' *J. Geophys. Res.*, 103: 14,117–30
- Rakov, V.A. *et al.* 1996. 'Observed electromagnetic environment close to the lightning channel.' In *Proc. 23rd Int. Conf. on Lightning Protection*, Florence, Italy, pp. 30–35
- Rakov, V.A. *et al.* 1999b. 'Some results from recent experiments at the International Center for Lightning Research and Testing at Camp Blanding, Florida.' (Abstract), *Eos Trans. Suppl., AGU*, 80(46): F203
- Rakov, V.A. *et al.* 2001. 'M-component mode of charge transfer to ground in lightning discharges.' *J. Geophys. Res.*, 106: 22,817–31
- Rakov, V.A. *et al.* 2002. 'Direct lightning strikes to the lightning protective system of a residential building: Triggered-lightning experiments.' *IEEE Trans. on Power Delivery*, 17(2): 575–86
- Rakov, V.A. *et al.* 2003b. 'Cutoff and re-establishment of current in rocket-triggered lightning.' *J. Geophys. Res.*, 108(D23): 4747, doi:10.1029/2003JD003694
- Rakov, V.A. *et al.* 2005b. 'Close electric field signatures of dart leader/return stroke sequences in rocket-triggered lightning showing residual fields.' *J. Geophys. Res.*, 110: D07205, doi:10.1029/2004JD0054
- Rubinstein, M., Tzeng, A.Y., Uman, M.A., Medelius, P.J., and Thomson, E.M. 1989. 'An experimental test of a theory of lightning-induced voltages on an overhead wire.' *IEEE Trans. Electromagn. Compat.* 31: 376–83
- Rubinstein, M., Uman, M.A., Medelius, P.J., and Thomson, E.M. 1994. 'Measurements of the voltage induced on an overhead power line 20 m from triggered lightning.' *IEEE Trans. Electromagn. Compat.*, 36(2): 134–40
- Rubinstein, M., Uman, M.A., Thomson, E.M., Medelius, P., and Rachidi, F. 1992. 'Measurements and characterization of ground level vertical electric fields 500 m and 30 m from triggered-lightning.' In *Proc. 9th Int. Conf. on Atmospheric Electricity*, St. Petersburg, Russia, pp. 276–8
- Rubinstein, M. *et al.* 1995. 'Characterization of vertical electric fields 500 m and 30 m from triggered lightning.' *J. Geophys. Res.*, 100: 8863–72
- Saba, M.M.F., Pinto Jr., O., Solorzano, N.N., and Eybert-Berard, A. 2005. 'Lightning current observation of an altitude-triggered flash.' *Atmos. Res.*, 76: 402–411
- Saba, M.M.F. *et al.* 2000. 'An international center for triggered and natural lightning research in Brazil.' In *Proc. 2000 Int. Lightning Detection Conf.*, GAI, 2705 East Medina Road, Tucson, Arizona 85706-7155, paper 40, p. 7

- Saleh, Z. *et al.* 2009. 'Properties of the X-ray emission from rocket-triggered lightning as measured by the Thunderstorm Energetic Radiation Array (TERA).' *J. Geophys. Res.*, 114: D17210, doi:10.1029/2008JD011618
- Schaal, M.M. *et al.* 2012. 'Spatial and energy distributions of X-ray emissions from leaders in natural and rocket triggered lightning.' *J. Geophys. Res.*, 117: D15201, doi:10.1029/2012JD017897
- Schnetzer, G.H., and Fisher, R.J. 1998. 'Earth potential distributions within 20 m of triggered lightning strike points.' In *Proc. 24th Int. Conf. on Lightning Protection*, Birmingham, United Kingdom, pp. 501–505
- Schoene, J., Uman, M.A., and Rakov, V.A. 2010. 'Return stroke peak current versus charge transfer in rocket-triggered lightning.' *J. Geophys. Res.* 115: D12107, doi:10.1029/2009JD013066
- Schoene, J. *et al.* 2008. 'Experimental study of lightning-induced currents in a buried loop conductor and a grounded vertical conductor.' *IEEE Trans. on Electromagnetic Compatibility*, 50(1): 110–7
- Schoene, J. *et al.* 2009. 'Lightning currents flowing in the soil and entering a test power distribution line via its grounding.' *IEEE Trans. on Power Delivery*, 24(3): 1095–1103
- Schoene, J. *et al.* 2003a. 'Statistical characteristics of the electric and magnetic fields and their time derivatives 15 m and 30 m from triggered lightning.' *J. Geophys. Res.*, 108(D6): 4192, doi:10.1029/2002JD002698
- Schoene, J. *et al.* 2003b. 'Test of the transmission line model and the traveling current source model with triggered lightning return strokes at very close range.' *J. Geophys. Res.*, 108(D23): 4737, doi:10.1029/2003JD003683
- Schoene, J. *et al.* 2009. 'Characterization of return-stroke currents in rocket-triggered lightning.' *J. Geophys. Res.*, 114: D03106, doi:10.1029/2008JD009873
- SPARG (Saint-Privat-d'Allier Research Group). 1982. 'Eight years of lightning experiments at Saint-Privat-d'Allier.' *Extrait de la Revue Générale de l'Electricité*, Septembre, Paris
- Teramoto, M. *et al.* 1996. 'Triggered lightning to a new type lightning rod with high resistance.' In *Proc. 10th Int. Conf. on Atmospheric Electricity*, Osaka, Japan, pp. 341–4
- Thottappillil, R., Goldberg, J.D., Rakov, V.A., and Uman, M.A. 1995. 'Properties of M components from currents measured at triggered lightning channel base.' *J. Geophys. Res.*, 100: 25,711–20
- Uman, M.A. 1987. *The Lightning Discharge*. San Diego, California: Academic Press, p. 377
- Uman, M.A., Schoene, J., Rakov, V.A., Rambo, K.J., and Schnetzer, G.H. 2002. 'Correlated time derivatives of current, electric field intensity, and magnetic flux density for triggered lightning at 15 m.' *J. Geophys. Res.*, 107(D13), 10.1029/2000JD000249, p. 11
- Uman, M.A. *et al.* 1994a. 'Electric fields close to triggered lightning.' In *Proc. Int. Symp. on Electromagn. Compat. (EMC'94 ROMA)*, Rome, Italy, pp. 33–37
- Uman, M.A. *et al.* 1994b. 'Fulgurites produced by triggered lightning.' *Eos Trans. AGU*, 75(44), Fall Meet. Suppl., 99
- Uman, M.A. *et al.* 1996. '1995 triggered lightning experiment in Florida.' In *Proc. 10th Int. Conf. on Atmospheric Electricity*, Osaka, Japan, pp. 644–7

- Uman, M.A. *et al.* 1997. 'Triggered-lightning experiments at Camp Blanding, Florida (1993–1995).' *Trans. IEE Japan*, 117-B: 446–52
- Uman, M.A. *et al.* 2000. 'Time derivative of the electric field 10, 14, and 30 m from triggered lightning strokes.' *J. Geophys. Res.*, 105: 15,577–95
- Wang, D., Takagi, N., Watanabe, T., Rakov, V.A., and Uman, M.A. 1999a. 'Observed leader and return-stroke propagation characteristics in the bottom 400 m of the rocket triggered lightning channel.' *J. Geophys. Res.*, 104: 14,369–76
- Wang, D. *et al.* 1999b. 'Characterization of the initial stage of negative rocket-triggered lightning.' *J. Geophys. Res.*, 104: 4213–22
- Wang, D. *et al.* 1999a. 'Attachment process in rocket-triggered lightning strokes.' *J. Geophys. Res.* 104: 2141–50
- Wang, C. *et al.* 1999d. 'Bidirectional propagation of lightning leader.' *Chinese Sci. Bull.*, 44(2): 163–6
- Willett, J.C. 1992. 'Rocket-triggered-lightning experiments in Florida.' *Res. Lett. Atmos. Electr.*, 12: 37–45
- Willett, J.C., Davis, D.A., and Laroche, P. 1999. 'An experimental study of positive leaders initiating rocket-triggered lightning.' *Atmos. Res.*, 51: 189–219
- Yoshida, S. *et al.* 2010. 'Three-dimensional imaging of upward positive leaders in triggered lightning using VHF broadband digital interferometers,' *Geophys. Res. Lett.*, 37: L05805, doi:10.1029/2009GL042065
- Zhang, Y. *et al.* 2013. 'Experiments of artificially triggered lightning and its application in Conghua, Guangdong, China.' *Atmos. Res.*, <http://dx.doi.org/10.1016/j.atmosres.2013.02.010> (in press)





---

## Chapter 7

# Tower initiated lightning discharges

*Gerhard Diendorfer*

---

### 7.1 Introduction

Upward lightning has gained increasing interest in recent years, some of it due to the observation of upward lightning triggered by wind turbine exceeding total heights of 200 m and more. Lightning initiated from tall objects, especially during winter thunderstorms in Japan, but also at other places around the world, has become subject of different studies in order to understand the mechanism of lightning initiation as well as to determine the electrical parameters of this type of discharges (peak current, transferred charge, action integral, etc.). These parameters are essential in order to allow the design of proper lightning protection systems for objects triggering upward lightning (Figure 7.1).

In general, grounded vertical objects produce relatively large electric field enhancement near their upper extremities when they are exposed to the electric field of a downward propagating leader. As a consequence upward-moving connecting leaders from these objects start earlier than from the surrounding ground and, therefore, serve to make the object a preferential lightning attachment point for the downward propagating leaders. Thus an elevated tower is basically more attractive for downward propagating leaders and it is therefore struck by larger peak current cloud to ground lightning (see Borghetti *et al.*, 2003).

On the other hand, tower initiated lightning, the topic of this chapter, is characterized by an upward propagating leader that is initiated from the high and grounded object and that propagates toward overhead charged clouds. Contrary to downward lightning, upward lightning is triggered by tall objects and would not occur if these objects were not present. It is usually assumed that structures of heights of less than 100 m are struck only by downward lightning, whereas structures of heights of 500 m and more solely experience upward lightning.

A still open question is the actual mechanism of how the upward leader is finally initiated at the top of a tall object. Is it (1) due to the slow built up of charge in the cloud above the object or, (2) due to a rapid field change caused by nearby in-cloud lightning activity?

With increasing height of an object an increase in the number of lightning discharges is observed with an increasing percentage of upward initiated flashes. Objects with heights ranging from 100 to 500 m experience both types of flashes, upward and downward. Objects with heights greater than 500 m will experience upward discharges only. The relatively high number of lightning events to tall towers (several tens of discharges per year are not unusual) makes those objects also preferential to perform direct lightning current measurements.



Figure 7.1 *Upward lightning from an electric power plant chimney in June 2013 (photo: OVE-ALDIS)*

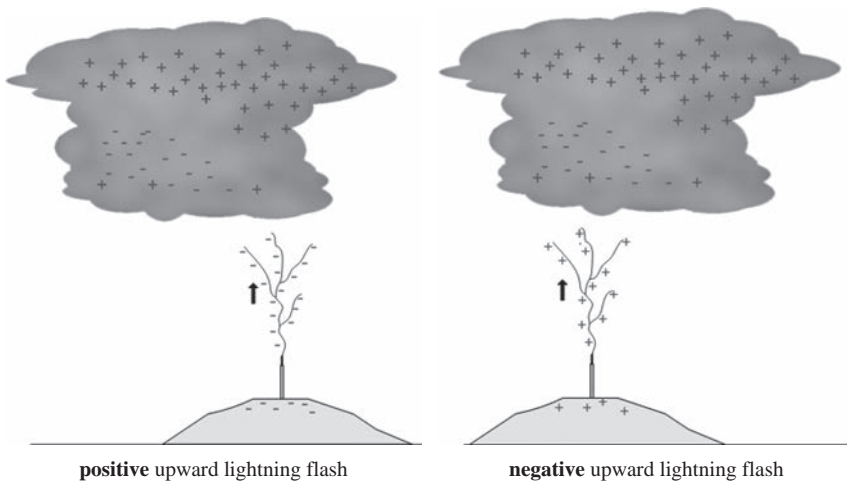


Figure 7.2 *Positive and negative upward lightning. Arrows indicate direction of leader propagation. Note: As the polarity of the flash is defined by the charge transferred from the cloud, a positive upward lightning has a negative leader and vice versa*

Depending on the polarity of charge transferred from the cloud to ground, positive and negative upward initiated discharges are observed, where a positive upward discharge is initiated by a negatively charged leader and a negative upward discharge is initiated by a positive leader (Figure 7.2).

## 7.2 Concept of effective height of tall objects

To account for the observation of an increased amount of upward lightning from towers of moderate height (less than 100 m) on top of high mountains a “effective height”

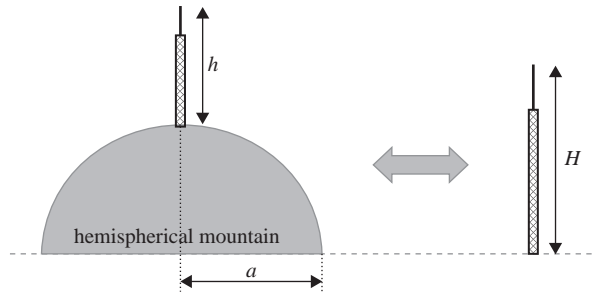


Figure 7.3 Concept of “effective height  $H$ .” The structure with the effective height  $H$  on the flat ground will experience the same number of lightning incidences as a real structure of height  $h$  on the mountain of height  $a$  (idealized as a hemispherical mountain) (adapted from Zhou *et al.*, 2010)

that is larger than the physical height of the object is assigned to the structure. The effective height accounts for the additional field enhancement at the tower top due to the presence of the mountain. A structure with the effective height  $H$  on flat ground will experience the same number of lightning incidences as a real structure of height  $h$  on the mountain (Figure 7.3).

Based on experimental observations of lightning incidences to towers, Pierce (1972) and Eriksson and Meal (1984) proposed two statistical and empirical methods to estimate the effective height of tall objects. According to Eriksson (1987), the total number of flashes  $N_{all}$  to a tall structure, including both downward and upward, is given by

$$N_{all} = N_g \cdot 24 \cdot H^{2.05} \cdot 10^{-6} \quad (7.1)$$

where  $H$  is the height of the structure in meters and  $N_g$  is the local ground flash density (average number of flashes per  $\text{km}^2$  per year) in the region where the object is situated.

An expression for the percentage of upward flashes  $P_u$  as a function of structure height  $H$  was proposed by Eriksson and Meal (1984) as

$$P_u = 52,8 \cdot \ln(H) - 230 \quad (7.2)$$

In derivation of empirical formulas (7.1) and (7.2), an effective height of 350 m was used for Berger’s towers at Mount San Salvatore in Switzerland, instead of their physical height of 70 m. In accordance to (7.2) all structures with effective heights below 78 m will not experience any upward flashes, while structures having effective heights greater than 518 m will experience only upward flashes.

Zhou *et al.* (2010) proposed a different method to estimate the effective height of elevated objects based on a model taking into account the overall geometry of the tall structure and the mountain, the electric field distribution around the top of the mountain, and the upward flash inception criterion proposed by Rizk (1990). Hence, this new method is called the Rizk-model method. Variations of the assumed upward positive leader speed and the mountain base radius have been identified as the most influencing parameters in estimating the effective height of a given tower based on this Rizk-model method.

Table 7.1 summarizes the effective heights of some structures estimated by Pierce (1972) and Eriksson (1978) together with the effective height calculated

Table 7.1 An overview of lightning studies conducted at instrumented tall objects, including effective height estimates (adapted from Rakov, 2011)

Object	Location	Height (m)	Terrain	Effective height (m)	Selected references
Empire State Building	New York City, U.S.	410	Flat	410	McEachron (1941a) McEachron (1941b) Hagenguth and Anderson, (1952)
Two towers 400 m apart <sup>a</sup>	Mount San Salvatore, Lugano, Switzerland	70	Mountain 640 m above Lake Lugano, 912 m above sea level	270 (Pierce, 1972) 350 (Eriksson, 1979) 198 (Zhou <i>et al.</i> , 2010)	Berger and Vogelsanger (1965), Berger and Vogelsanger (1966), Berger (1967), Berger (1972), Berger (1977), Berger (1978), Berger <i>et al.</i> (1975)
Ostankino TV Tower	Moscow, Russia	540	Flat	540	Gorin and Shkilev (1984)
Two TV towers <sup>b</sup>	Sasso di Pale, and Monte Orsa	40	Mountains 980 and 993 m above sea level	500 (Eriksson, 1979) 120 (Zhou <i>et al.</i> , 2010)	Garbagnati and Lo Piparo (1982), Garbagnati <i>et al.</i> (1981)
CSIR research mast	Pretoria, South Africa	60	Hill 80 m above surrounding terrain, 1400 m above sea level	148 (Eriksson, 1979) 113 (Zhou <i>et al.</i> , 2010)	Eriksson (1979), Eriksson (1982)
CN Tower	Toronto, Canada	553	Flat	553	Hussein <i>et al.</i> (1995), Janischewskyj <i>et al.</i> (1997)
Peissenberg Tower	Hoher Peissenberg, Munich, Germany	160	Mountain about 288 m above surrounding terrain, 988 m above sea level <sup>c</sup>	324 (Zhou <i>et al.</i> , 2010)	Beierl (1992), Fuchs <i>et al.</i> (1998), Flache <i>et al.</i> (2008)

(Continues)

Table 7.1 (Continued)

Object	Location	Height (m)	Terrain	Effective height (m)	Selected references
St. Chrischona Tower	Basel, Switzerland	248	Mountain 493 m above sea level	468 (Zhou <i>et al.</i> , 2010)	Montandon (1992), Montandon (1995)
Cachimbo Tower	Brazil	60	Mountain 200 m above surrounding terrain, 1600 m above sea level	145 (Zhou <i>et al.</i> , 2010)	Schroeder <i>et al.</i> (2002), Visacro (2004)
Gaisberg Tower (GBT)	Salzburg, Austria	100	Mountain 1287 m above sea level	274 (Zhou <i>et al.</i> , 2010)	Diendorfer <i>et al.</i> (2000), Diendorfer <i>et al.</i> (2009), Zhou <i>et al.</i> (2010), Zhou <i>et al.</i> (2011a), Zhou <i>et al.</i> (2012)
Fukui chimney	Fukui, Japan	200	Flat	200	Miyake <i>et al.</i> (1992), Asakawa <i>et al.</i> (1997)
Meteorological tower	Maki, Japan	150	Flat	150	Goto and Narita (1995)
Säntis Tower	Switzerland	124	Mountain 2505 m above sea level	Unknown ( $P_u \rightarrow 100\%$ )	Romero <i>et al.</i> (2012b), Romero <i>et al.</i> (2013)
Windmill and its protection tower (45 m apart)	Uchinada, Japan	100 and 105	Hill 40 m above sea level	Unknown ( $P_u = 96\%$ )	Wang <i>et al.</i> (2008), Wang and Takagi (2012), Lu <i>et al.</i> (2009)

<sup>a</sup>The first tower, made of wood and equipped with a grounded lightning rod, was erected in 1943. The second tower, made of steel was erected in 1950. In 1958, the wooden tower was replaced by a tower made of steel.

<sup>b</sup>Most data have been obtained on Monte Orsa, which is only 10 km from Mount San Salvatore.

<sup>c</sup>The tower is located below the mountain top, at about 937 m above sea level (F. Heidler, personal communication, 1999).

using the Rizk-model method proposed by Zhou *et al.* (2010). As seen from Table 7.1, the effective heights differ significantly based on the applied method and depend on both mountain height and the tower height but in any case the effective height is always larger than the physical height of the tower.

More recently new approaches based on the analysis of the data provided by lightning locating systems (LLS) were suggested by Smorgonskiy *et al.* (2013) and Ishii *et al.* (2011) in order to estimate the number of upward flashes from tall structures. Smorgonskiy *et al.* (2013) analyzed the proportion of upward flashes obtained at the towers on Mount San Salvatore (Switzerland) and the Gaisberg Tower (GBT) in Austria, respectively. Direct measurements of lightning currents at these towers have revealed a major difference in terms of the ratio of upward and downward flashes, although their physical heights are comparable. While Berger and coworkers obtained a significant number of downward flashes, more recent observations of lightning on the GBT were essentially composed of upward flashes only. An independent method, based on the data from LLS was applied by Smorgonskiy *et al.* (2013) in order to determine the number of upward flashes initiated from these towers and the results were in agreement with the observed differences in the percentage of upward and downward flashes at the two towers. Their analysis revealed that in the evaluation of the percentage of upward flashes initiated from a tall structure, different parameters should be carefully examined, namely (1) the value of the ground flash density, (2) the topographical conditions, and (3) the presence of other tall structures in the region from which upward flashes might be initiated.

Ishii *et al.* (2011) analyzed hot spots of lightning activity present in LLS data during winter time (December and January in the years 2000–2009) along the east coast of Japan. They found that artificial structures existed at all these hot spots, and wind turbines are common at these spots. They could show a significant increase rate of upward lightning after the construction of the wind turbines at given locations. It is worth noting that a significant fraction of upward flashes from tall objects is not detected by most of the today's commercial LLS when no return strokes are following the initial continuing current (see paragraph 7.9).

### **7.3 Initiation of upward lightning**

It is generally assumed that an object-initiated discharge (upward leader) begins when the electric field intensity over some critical distance from the top of the object exceeds the breakdown value. Based on the analysis of the electric field changes resulting from 14 upward lightning flashes initiated from a windmill and its lightning protection tower in Japan, Wang *et al.* (2008) suggested to classify upward lightning discharges into the two types “self-triggered” (initiated without any preceding nearby lightning activity) and “other-triggered” (triggered by nearby lightning activity). Zhou *et al.* (2012) used the terms “self-initiated” and “nearby-lightning-triggered” flashes, respectively, to classify the same two categories of upward lightning.

Wang and Takagi (2012) classified 53 per cent (28/53) of the flashes from a wind turbine and its neighboring lightning protection tower as self-triggered and 47 per cent (25/53) as triggered by in-cloud or nearby CG lightning. During summer seasons in Rapid City, South Dakota, USA, almost 100 per cent (80 out of 81) of upward lightning flashes were triggered by a nearby flash, with a positive

CG return stroke being the dominant triggering event (Warner *et al.* 2011). In contrast, Zhou *et al.* (2012) report that 87 per cent (179/205) of the upward flashes from the GBT were initiated without any preceding nearby discharge activity, whereas 13 per cent (26/205) were initiated from the tower top with immediately preceding nearby lightning activity. The majority (85 per cent) of those nearby-lightning-triggered upward flashes occurred during convective season (April–August). Similar results are reported by Heidler *et al.* (2013) for 35 negative upward flashes from the Peissenberg Tower in Germany. All 34 flashes that occurred during winter time were self-initiated, whereas the only one flash in their dataset that occurred during summer time was initiated by a nearby discharge.

The above observations indicate that there are strong regional and seasonal dependencies of the mechanism of initiation of upward lightning, with strong indication of a dominance of self-initiation during winter time (cold season) and initiation by nearby lightning during convective season. This could also be a reason why none of the presently available methods to estimate the expected number of upward flashes from a tall structure provides satisfactory results.

#### 7.4 Seasonal occurrence of upward lightning

Seasonal occurrence of upward lightning is observed to be completely different from the seasonal occurrence of downward lightning. Upward lightning to the GBT in Austria was reported by Diendorfer *et al.* (2009) to be more or less uniformly distributed over the year (Figure 7.4b) and independent of the overall lightning activity in Austria, which shows a pronounced lightning season in summer (Figure 7.4a). During an eight-year period (2000–2007) 56 per cent of negative upward lightning from the GBT were recorded during the cold season (September–March) compared to 44 per cent recorded during the warm season (April–August). Note that in other geographical regions the seasonal occurrence of upward lightning initiated from tall structures can be quite different from observations at the GBT.

Also in Japan Ishii *et al.*, (2011) observed higher frequencies of lightning caused outages of transmission lines and wind turbines in winter time, despite the much smaller number of lightning strokes observed by lightning location systems

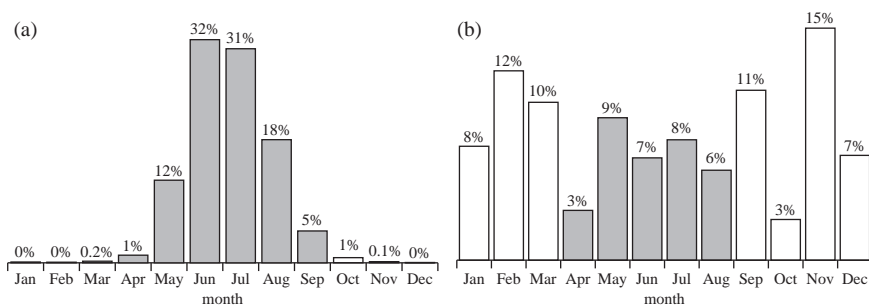


Figure 7.4 Monthly lightning activity observed in (a) country of Austria and (b) at the Gaisberg Tower from 2000 to 2007. Shaded diagram bars represent the warm (convective) season from April to August and unshaded bars represent the cold (nonconvective) season from September to March (adapted from Diendorfer *et al.*, 2009)



(LLS) in winter. Ishii and Saito (2009) performed a study of transmission-line faults in Japan during winter time and concluded that the vast majority of lightning discharges causing transmission-line faults in winter were initiated by upward leaders from transmission lines, and injected high pulse currents into transmission towers resulting in back flashovers. This observation also confirms that tall structures, such as wind turbines or transmission line towers, are struck by lightning much more frequently than predicted from conventional estimation methods based on experiences of summer lightning.

Polarity of upward lightning can be negative, positive, or bipolar. *Diendorfer et al.* (2009) analyzed a total of 489 lightning upward initiated flashes from the GBT during an eight-year period from 2000 to 2007. Negative upward lightning, which is initiated by a positive leader, clearly dominates and out of the 489 flashes 457 (93 per cent) lowered negative charge to ground, 19 (4 per cent) positive charge, and 13 (3 per cent) records exhibited bipolar current waveforms. Similar values are reported by *Wada et al.* (2004) for lightning measured at the 200-m-high Fukui Chimney in Japan, where about 90 per cent of the discharges were negative and about 10 per cent of the upward lightning was positive.

## 7.5 General characterization of upward negative lightning

Upward negative discharges are initiated by upward positive leaders from the tops of elevated objects (Figure 7.5). Object-initiated negative lightning discharges always involve an initial stage (IS) that may or may not be followed by downward dart leader (DL)/upward return stroke (RS) sequences as depicted in Figure 7.5 and

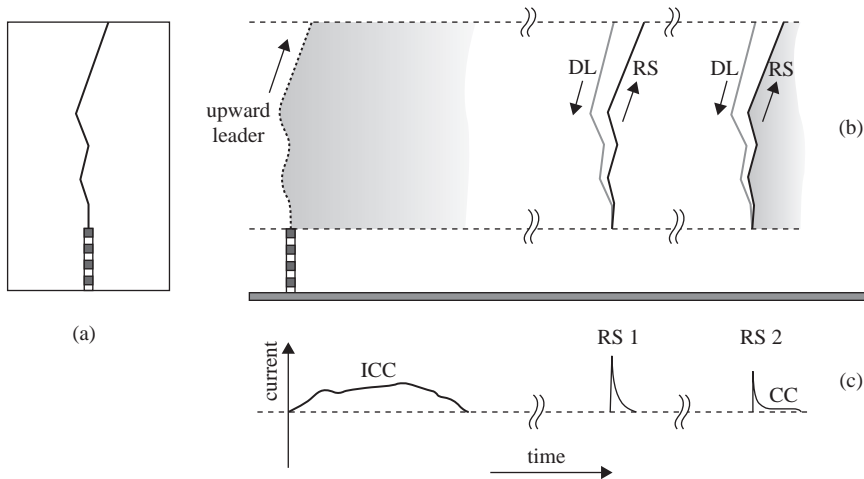


*Figure 7.5 Drawing showing the luminosity of a typical negative upward flash and the corresponding current at the channel base, (a) still-camera image, (b) streak-camera image, (c) current record. The flash is composed of an upward positive leader followed by an initial continuous current, ICC, and two downward dart leaders (DL)/upward return stroke (RS) sequences. RS2 is followed by a continuing current (CC) (adapted from Rakov and Uman, 2003)*

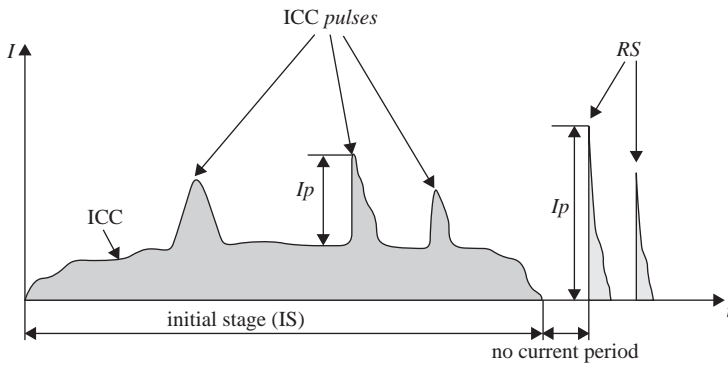


Figure 7.6 Schematic current record of upward-initiated flash. Labeled are the initial continuous current (ICC) with three superimposed ICC pulses, a period of no current flow, and two return strokes (RS). Note: Return stroke amplitudes and durations are not in scale (adapted from Diendorfer *et al.*, 2009)

Figure 7.6. The latter are generally assumed to be similar to downward leader/upward return stroke sequences in rocket-triggered lightning and even more important similar to subsequent leader/return stroke sequences in natural downward lightning. Consequently the obtained lightning parameters of return strokes in upward initiated flashes can be used for lightning protection standards representing only subsequent strokes. Upward lightning, as well as triggered lightning, does not have a first stroke, and their current parameters can only be determined from rare cases of downward lightning to instrumented towers.

The percentage of upward flashes with return strokes was found to be 50 per cent for the Empire State Building (Hagenguth and Anderson, 1952), 20–25 per cent for the two towers on Mount San Salvatore (Berger, 1978), 27 per cent for the Ostankino Tower (Gorin and Shkilev, 1984), and 30 per cent for the Gaisberg Tower (Diendorfer *et al.*, 2009). Interestingly, the percentage of rocket-triggered flashes with return strokes is significantly higher, 70–75 per cent (Wang *et al.*, 1999; Rakov, 2009). On the other hand, about 50 per cent of 457 flashes recorded at the GBT from 2000 to 2009 did not contain any pulses with peaks greater than 2 kA, neither superimposed on the ICC, nor following the ICC. The initial stage in object-initiated lightning is similar to the initial stage in rocket-triggered lightning. The initial stage, in a sense, replaces in both cases the downward stepped leader/upward return stroke sequence (first stroke) characteristic of natural downward lightning.

Overall characteristics of the initial stage for both object-initiated and rocket-triggered negative lightning are summarized in Table 7.2.

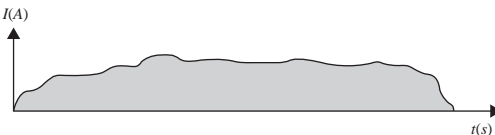
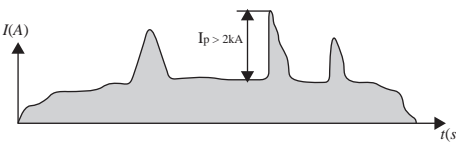
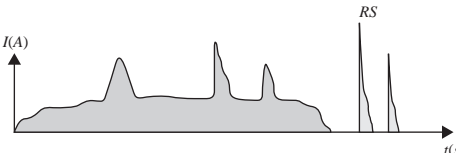
Diendorfer *et al.* (2009) identified and analyzed three basic categories of upward negative flashes, namely  $ICC_{RS}$  (ICC is followed by one or more RS),  $ICC_P$  (ICC is not followed by any RS but with one or more current pulses  $>2$  kA superimposed on the ICC), and  $ICC_{Only}$  (ICC is not followed by any RS and no ICC pulse  $>2$  kA occurred) (Table 7.3).

Table 7.2 Overall characteristics (geometric mean values) of the initial stage of natural upward and rocket-triggered negative lightning (adapted from Miki et al. (2005), Diendorfer et al. (2009), and Diendorfer et al. (2011))

Data set	Sample size	Duration (ms)	Charge transfer (C)	Average current (A)	Action integral ( $10^3 \text{ A}^2 \text{ s}$ )
Peissenberg Tower, Germany	21	290	38.5	133	3.5
Fukui Chimney, Japan <sup>a</sup>	36	>82.5	>38.3 (>36.8)	465	40 (34)
Gaisberg Tower, Austria (2000–2007)	457	266 (N = 431)	33	113 (N = 431)	7.0
Rocket-triggered lightning, Florida	45	305	30.4	99.6	8.5

<sup>a</sup>Values in the parentheses were calculated from the current data limited to 2 kA in order to make the Fukui data (upper current measurement limit of 13 kA) comparable to the other data sets (upper current measurement limit of 2–2.1 kA).

Table 7.3 The three basic current waveforms observed in tower initiated negative lightning

Type	Typical current wave form	Comment
ICC <sub>Only</sub>	 <p>The graph shows current I(A) on the y-axis and time t(s) on the x-axis. A single, broad, low-amplitude pulse is shown, representing the initial current (ICC) without any return strokes.</p>	ICC is not followed by any return strokes and no ICC pulse >2 kA are superimposed on the ICC. This type of upward initiated flash is typically not detected by LLS.
ICC <sub>P</sub>	 <p>The graph shows current I(A) on the y-axis and time t(s) on the x-axis. A broad current pulse is shown with several sharp, high-amplitude peaks superimposed on it. One peak is labeled with a vertical double-headed arrow and the text 'I<sub>p</sub> &gt; 2kA'.</p>	ICC not followed by any return strokes but one or more ICC pulses >2 kA are superimposed on the ICC. Sometimes detected by LLS, when superimposed pulses are similar to return strokes in their current waveform.
ICC <sub>RS</sub>	 <p>The graph shows current I(A) on the y-axis and time t(s) on the x-axis. A broad current pulse is shown, followed by several sharp, high-amplitude peaks labeled 'RS' (return strokes).</p>	ICC is followed by one or more return strokes (RS). Typically detected by LLS. Note: Return stroke amplitude and duration are not in scale.

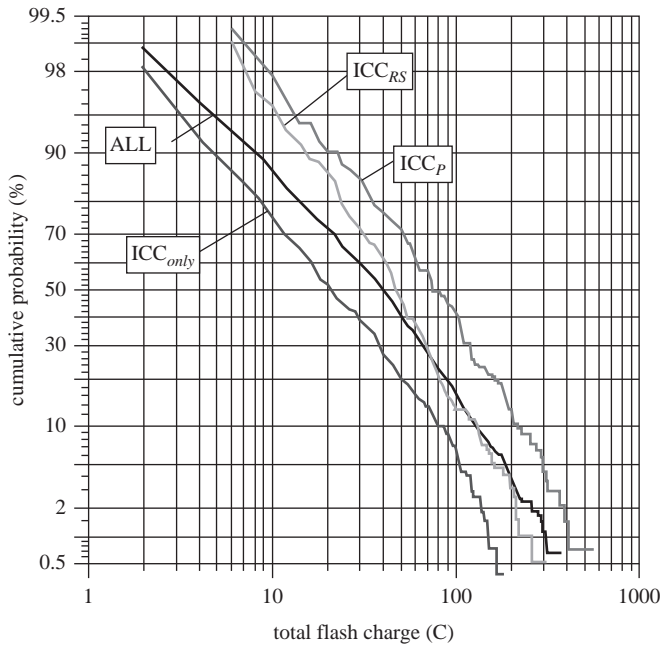


Figure 7.7 Cumulative frequency distribution of total charge transfer for all negative upward flashes and the three categories  $ICC_{RS}$ ,  $ICC_P$ , and  $ICC_{Only}$  at the Gaisberg Tower (2000–2007) (from Diendorfer *et al.*, 2009)

According to Figure 7.7 the geometric mean transferred charge of 69 C for the  $ICC_P$  type discharges is more than three times larger than the 21 C determined for  $ICC_{Only}$  type flashes.

Since the year 2000, the highest amount of transferred charge measured in a single flash to the GBT was 783 C recorded on 15.10.2012. It was in a negative flash and the current waveform is shown in Figure 7.8. Overall about 1.5 per cent (10/625) of the flashes initiated by the GBT transferred a charge exceeding 300 C, and interestingly all these events occurred during cold season (Diendorfer *et al.*, 2011). Contrary to winter lightning in Japan, where upward initiated flashes with large charge transfer are predominantly bipolar (Ishii *et al.*, 2012), at the GBT seven out of the ten flashes exceeding 300 C were negative, two positive and one bipolar.

When local conditions are favorable for the initiation of upward flashes from a tall object it is not uncommon that a number of flashes is triggered within a short period of some tens of minutes. On March 1, 2008, at the GBT 22 upward flashes were recorded within a period of 25 minutes and those 22 flashes transferred an accumulated charge of 3.735 C to ground (Diendorfer *et al.*, 2010). In case of wind turbines the accumulated charge transfer decides the wear (melting) of materials and therefore influences the need for maintenance of air termination systems. More frequent maintenance cycles for the air termination system could be required for wind turbines installed at exposed sites with such high accumulated charge transfers.

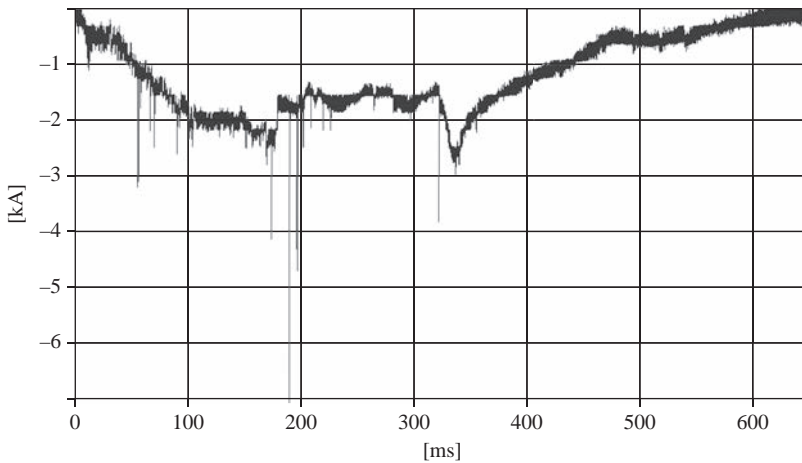


Figure 7.8 Current waveform of negative upward lightning from the GBT (#878 at 15.10.2012) with a transferred total charge of 783 C within a time period of about 600 ms

## 7.6 Characteristics of impulsive current components in negative upward lightning

### 7.6.1 Parameters of ICC pulses

High-speed video records of upward lightning frequently show several branches of the lightning channel carrying current simultaneously and/or consecutively in time. This superposition of different current components is assumed to be the reason for the rather complex current waveforms measured in upward lightning from tall towers. In many cases the initial stage contains current pulses (ICC pulses) superimposed on the slowly varying continuous current (see Figure 7.6). Some of these pulses have peaks in the kilo amperes range, comparable to current peaks of smaller return strokes. A statistical comparison between the initial-stage pulses and the M-component pulses following return strokes in rocket-triggered lightning indicated that both types of pulses are due to similar physical processes (Wang *et al.*, 1999). On the other hand, Miki *et al.* (2005) observed that the initial stage pulses in object-initiated lightning exhibit larger peaks, shorter rise times, and shorter half-peak widths than do the initial-stage pulses in rocket-triggered lightning (Table 7.4). This observed difference is most likely a result of the more pronounced branching of tower initiated lightning compared to rocket-triggered lightning.

Flache *et al.* (2008) analyzed high-speed video images of upward flashes initiated from the Peissenberg Tower in Germany and found that six (86 per cent) of seven ICC pulses with shorter risetimes developed in a newly illuminated branch, whereas 25 (96 per cent) of 26 ICC pulses with longer risetimes occurred in already luminous channels. These results support the hypothesis that longer risetimes are indicative of the M-component mode of charge transfer to ground, while shorter risetimes are associated with (dominated by) the leader/RS mode. An example of an M-component type ICC pulse with relatively high peak current ( $-16$  kA) is shown in Figure 7.9. In this case, the ICC current level at the time when the pulse occurred was about  $-300$  A.

Table 7.4 Parameters (geometric mean values) of initial-stage current pulses in upward-initiated lightning (adapted from Miki *et al.*, 2005)

Data set	Sample size	Magnitude (A)	Duration ( $\mu$ s)	Risetime ( $\mu$ s)	Half-peak width ( $\mu$ s)
Fukui Chimney, Japan	231	781	514	44.2	141
Peissenberg Tower, Germany	124	512	833	60.9	153
Gaisberg Tower, Austria	348–377	>377 ( $N=351$ )	1199 ( $N=377$ )	< 110 ( $N=344$ )	276 ( $N=348$ )

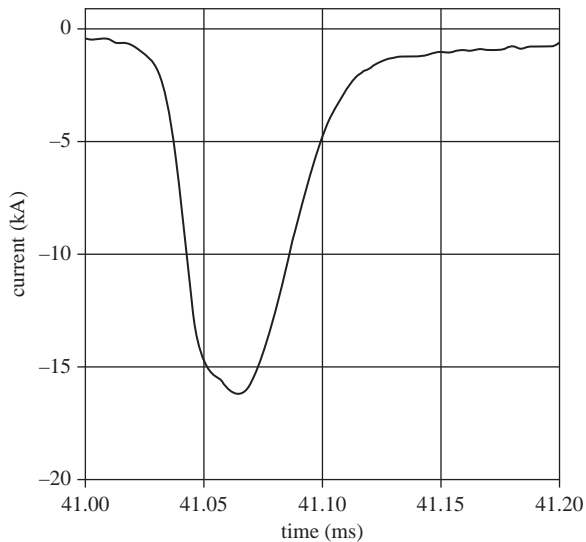


Figure 7.9 *M*-component type ICC pulse of GBT flash #542

For comparison a return stroke type ICC pulse is depicted in Figure 7.10. The current pulse shows the fast rising front to a peak current of about  $-11$  kA followed by decay to half value at about  $50 \mu$ s. ICC background current at time of occurrence of this pulse was  $-195$  A.

More recently, Zhou *et al.* (2011b) proposed the term “mixed mode” of charge transfer to ground for the ICC pulses previously referred to as the “leader/RS mode” by Flache *et al.* (2008). In the “mixed mode,” a leader/RS sequence in one channel occurs simultaneously with the continuous current flowing to ground in another channel. The mixed mode is usually associated with relatively low-level upward branching that is common in object-initiated lightning, but not in rocket-triggered lightning in Florida. Thus, the mixed-mode concept can explain the occurrence of ICC pulses like the one shown in Figure 7.10 in object-initiated lightning with larger peaks, shorter risetimes, and shorter half-peak widths than those in rocket-triggered lightning, as reported by Miki *et al.* (2005).

### 7.6.2 Parameters of return strokes following the ICC

Return strokes in upward lightning that follow the ICC after a period of no current flow are assumed to be similar to subsequent strokes in natural cloud-to-ground

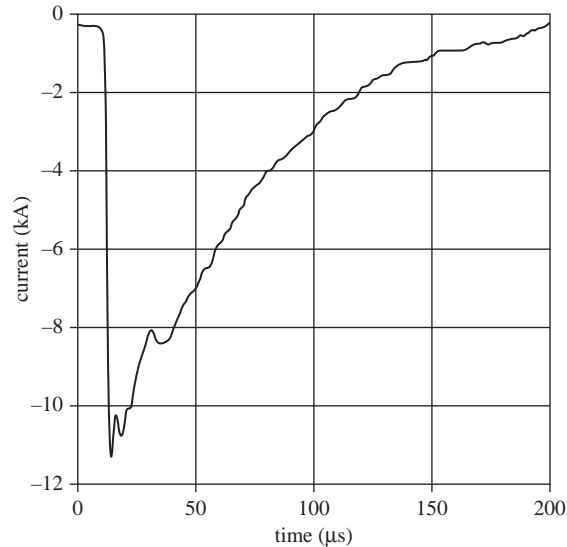


Figure 7.10 Return stroke type ICC pulse in GBT flash #759

lightning and subsequent strokes in triggered lightning. Therefore, this type of discharge is of great interest in lightning research. Data from direct current measurements at instrumented towers are used to collect larger datasets of subsequent strokes than available from the typically much more limited number of available current records of downward lightning to instrumented objects. These datasets are used to determine the current parameters of subsequent strokes for lightning protection applications or they are also used as ground truth data to validate the performance of lightning location systems (see paragraph 7.9) in terms of their ability to estimate the stroke peak currents from measured peak fields.

Table 7.5 shows a comparison of return-stroke current peaks (in kA) and transferred stroke charge (in coulombs) in natural upward (object-initiated), natural downward, and rocket-triggered lightning.

Since 2010, direct current measurements are also performed on the 124 m Sântis Tower in Switzerland (Romero *et al.*, 2012a; Romero *et al.*, 2012b; Romero *et al.*, 2013). More than 200 flashes (about 30 of which were positive) were recorded during the first 2 years of operation, and apparently all of them were upward initiated. For 2034 negative current pulses (some of them superimposed on the ICC) with peaks greater than 2 kA and risetimes shorter than 8  $\mu$ s, the median peak current was found to be 6 kA.

In any measuring campaign of lightning to tall objects, correct classification of ICC pulses versus return strokes is a critical task. This classification is possibly affected by the method used to measure the lightning current at the tall object, especially when a current pulse is superimposed on an ICC of relatively small amplitude (a few tens of amperes). Due to their limitations in measuring low-frequency current components Rogowski coils or other inductive current probes may have some problems to correctly reproduce such a low amplitude ICC. In case of a long lasting, small amplitude ICC current there could be uncertainties in defining the end of the ICC current flow, which is also the beginning of the no current period ahead of a return stroke, and then actual ICC pulses are possibly misclassified as

Table 7.5 Peak current and charge transfer (median values) of return strokes in natural upward, natural downward, and rocket-triggered lightning flashes

Reference	Location	Sample size	Peak current (kA)	Stroke charge Line Feed (C)
<b>Return strokes in upward initiated flashes</b>				
Diendorfer <i>et al.</i> (2009)	Austria, Gaisberg Tower	615	9.2	0.51
Fuchs <i>et al.</i> (1998)	Germany, Peissenberg Tower	35	8.5	
Gorin and Shkilev (1984)	Russia	58	9	
Berger (1978)	Switzerland, Mount San Salvatore	76	18 <sup>a</sup>	0.77 ( <i>N</i> = 579)
Hagenguth and Anderson (1952)	New York, Empire State Building	176	10	0.15 ( <i>N</i> = 83) <sup>c</sup>
<b>Return strokes in natural downward flashes</b>				
Anderson and Eriksson (1980)	Switzerland	114	12	
Berger <i>et al.</i> (1975)	Switzerland	135	12	0.95 ( <i>N</i> = 117)
<b>Return strokes in rocket-triggered lightning</b>				
Schoene <i>et al.</i> (2009)	Florida, Camp Blanding	144	12.4 <sup>d</sup>	1.1 <sup>e</sup> ( <i>N</i> = 122)
Fisher <i>et al.</i> (1993)	Florida (KSC) and Alabama	45	13	
Depasse (1994)	Florida	305	12.1	–
	France	54	9.8	0.59 ( <i>N</i> = 24)

<sup>a</sup>Overestimates due to a transient process in the tower.

<sup>b</sup>Two events out of 84 were of positive polarity.

<sup>c</sup>Sample includes one or two events of positive polarity. Charge was determined only up to half-peak value on the tail of the current waveform.

<sup>d</sup>Geometric mean value.

<sup>e</sup>Geometric mean value of charge transfer within 1 ms.

return strokes. Also, the minimum measurable current in the lightning channel affects the quality of pulse classification when the current waveform is the only source for this classification. High-speed videos or corresponding E-field measurements can provide additional, useful information to perform this classification.

## 7.7 Characteristics of upward positive lightning

Upward positive lightning usually involves an upward negative leader initiated from the top of a tall structure (see Figure 7.2). Berger and coworkers were the researchers who first presented a comprehensive study of positive discharges including both upward positive and downward positive flashes (Berger *et al.*, 1975; Berger, 1978). Very few systematic studies of upward positive lightning have been



Table 7.6 *Lightning current parameters (median values) of upward positive flashes (the sample size is given in the parenthesis)*

References	Location	Peak current (kA)	Flash duration (ms)	Charge transfer (C)	Action integral ( $\times 10^3 \text{ A}^2\text{s}$ )
Berger (1978)	Berger's Tower, Switzerland	1.5 (132)	72 (138)	26 (137)	–
Miki <i>et al.</i> (2010)	Nikaho Kougen Wind Farm, Japan	6.5 (16)	40 (16)	30.2 (16)	–
Zhou <i>et al.</i> (2012)	Gaisberg Tower, Austria	5.2 (26)	82 (26)	58 (26)	160 <sup>a</sup> (26)
Romero <i>et al.</i> (2012c)	Säntis Tower, Switzerland	11 (30)	80 (30)	169 (30)	390 (30)

<sup>a</sup>The value of action integral of  $0.16 \times 10^3 \text{ A}^2\text{s}$  given by Zhou *et al.* (2012) is a misprint.

reported since Berger's work (Garbagnati and Lo Piparo, 1982; Fuchs *et al.*, 1998; Heidler *et al.*, 2000). Miki (2006) presented simultaneous current and optical observations of upward positive flashes at the Fukui chimney in Japan and, more recently, Miki *et al.* (2010) observed 16 upward positive discharges, initiated from wind turbines at Nikaho Kougen Wind Farm in the coastal area of the Sea of Japan. At the GBT in Austria, positive upward lightning accounted for 4 per cent (26/652) of the total flashes recorded from 2000 to 2009 (Zhou *et al.*, 2012) and 19 (73 per cent) out of these 26 upward positive flashes occurred during cold season. At the Säntis Tower, in the period from June 2010 to January 2012, about 15 per cent of the recorded flashes (30 out of 201) were of positive polarity (Romero *et al.*, 2012c) and most of the positive flashes were recorded in summer months. Ishii and Natsuno (2011) measured 304 current waveforms at wind turbines at 25 different sites in Japan during 2008–2011 (no data were recorded during May–September). They found that 21 per cent of the currents were positive. Wang and Takagi (2012) reported that 11 per cent of 36 upward flashes striking a windmill or its lightning protection tower in winter in Japan were of positive polarity.

A comparison of lightning parameters of upward positive flashes reported from different studies is given in Table 7.6.

Both Miki *et al.* (2012) and Zhou *et al.* (2012) have shown that the estimated channel charge density in upward negative stepped leaders is on the order of several mC/m and more. These estimated values are significantly larger than charge densities typically used in leader progression models with a charge density of, e.g., 0.1 mC/m in Dellera and Garbagnati (1990).

In case of upward positive flashes, observed current pulses of high repetition rate and superimposed on the initial portion of initial continuous current shown in Figure 7.11 were inferred by Zhou *et al.* (2012) to be associated with the upward negative stepped leader process. This is also in agreement with high-speed camera observations reported by Miki *et al.* (2012).

From comparison of Tables 7.2 and 7.6, median charge transfers for upward positive flashes are comparable (except for that for the Säntis Tower flashes) to their counterparts for the initial stage of upward negative flashes, while upward positive flashes have shorter durations. This implies a higher average current for

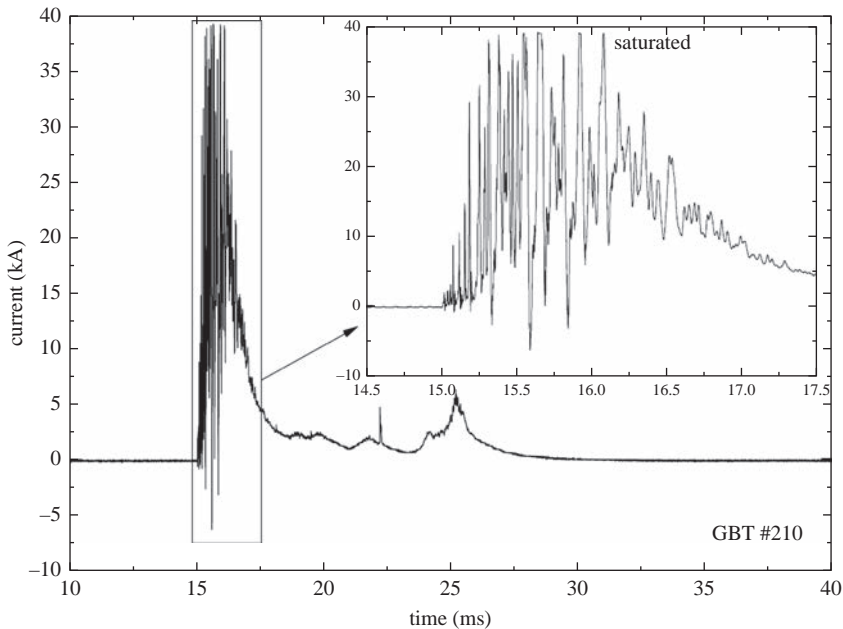


Figure 7.11 Overall current record for the positive flash GBT #210 with large impulsive current components saturated at 40 kA. The inset shows the high frequency characteristics of current pulses on a 3-ms time scale

upward positive flashes. Note also that median action integrals in Table 7.6 are considerably larger than for the initial stage of upward negative flashes (see Table 7.2).

## 7.8 Characteristics of upward bipolar lightning

Bipolar lightning is defined as a lightning discharge in which the current waveform measured at the channel-base exhibits a polarity reversal within the same flash. McEachron (1941a) first reported this kind of flashes from his measurements at the Empire State Building in New York, and later Hagenguth and Anderson (1952) presented a total of 11 bipolar flashes for a 10-year observation period. Berger (1978) observed 68 upward bipolar flashes (6 per cent) out of 1196 discharges at Mount San Salvatore in Switzerland between 1963 and 1973. Gorin and Shkilev (1984) reported six (6.7 per cent) of 90 upward discharges initiated from the Ostankino Tower in Moscow to be bipolar, and two bipolar flashes were observed on the Peissenberg Tower in Germany by Heidler *et al.* (2000). Miki *et al.* (2004) observed 43 (20 per cent) bipolar flashes of 213 upward flashes observed at the Fukui chimney in Japan. Wang and Takagi (2008) reported three upward bipolar lightning flashes observed from a windmill and its lightning protection tower. Ishii *et al.* (2011) measured 304 current waveforms at wind turbines at 25 sites in Japan during 2008–2011 (no data were recorded during May–September). They found that 6 per cent of the currents were bipolar. Wang and Takagi (2012) reported that 25 per cent of 36 upward flashes striking a windmill or/and its lightning protection tower in winter in Japan were bipolar.

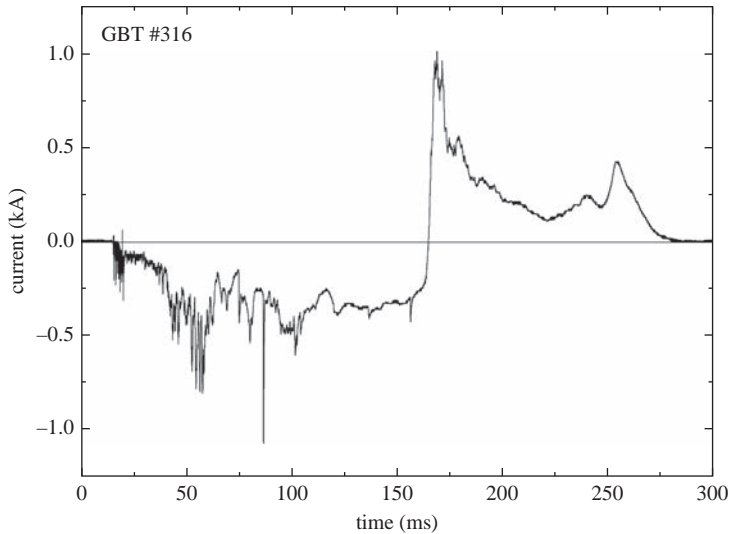


Figure 7.12 Overall current record of a Type 1 bipolar lightning measured at the GBT (flash #316), starting with initial current of negative polarity (from Zhou *et al.*, 2011a)

Zhou *et al.* (2011a) analyzed 21 upward-initiated bipolar lightning flashes observed at the Gaisberg Tower in 2000–2009. At this tower, bipolar lightning flashes constitute 3 per cent (21/652), and 13 (62 per cent) of the 21 bipolar flashes occurred in cold season (September–March). Based on the classification suggested by Rakov and Uman (2003), 13 (62 per cent) of the 21 bipolar flashes belong to Type 1 associated with a polarity reversal during the initial stage current, five belong to Type 2 associated with different polarities of the IS current and the following return strokes, one belongs to Type 3 associated with return strokes of opposite polarity following the initial stage (IS), and two were not assigned to any of the above types. In agreement with observations in other studies, the initial polarity reversal from negative to positive occurred more often (76 per cent or 16/21) than from positive to negative. At the Gaisberg Tower the geometric mean (GM) and arithmetic mean (AM) of the total absolute charge transfer are 99.5 C and 125 C, with the GM and AM total flash durations being 320 ms and 396 ms, respectively. An example of a Type 1 bipolar lightning with polarity reversal during the initial stage current after about 160 ms is shown in Figure 7.12.

Bipolar upward-initiated flashes are different from downward bipolar lightning flashes reported by Fleenor *et al.* (2009) and Jerauld *et al.* (2009). To date, the knowledge of the physics of bipolar lightning is still poorer than that of negative or positive lightning, although continuing measurements of lightning currents on tall towers should provide more insights in the near future. At least when tall structures are involved, bipolar lightning flash occurrence is similar to that of positive lightning (Rakov, 2005). It is generally assumed that the pronounced branching of upward initiated lightning is one of the main reasons for the relatively frequent observation of this type of discharges on tall objects. Different branches of the upward discharge may ascend into charged regions of opposite polarity in the cloud above the tall object.

## 7.9 Detection of upward lightning

Today lightning location systems (LLS) are operated in many countries of the world in order to monitor the overall lightning activity, mainly the cloud-to-ground (CG) discharges. Most popular and widely used networks operate in the frequency range of some hundreds of kilohertz up to megahertz. When high amplitude transient current pulses propagate in long, previously established channels, such as those that occur in CG return strokes and some of the cloud pulses, the most powerful electromagnetic emissions are in the LF and VLF frequency ranges. In the VLF band, the radiation is dominated by return strokes. On the other hand, cloud discharges produce tens to hundreds of small pulses with most of their energy in the upper LF range and higher. Vertically polarized transient pulses in the LF and VLF frequency range propagate along the surface of the earth and have been used to detect and locate return strokes in CG flashes for many years. Sensors that operate in the LF and VLF range can also be used to detect and locate the larger pulses produced by cloud flashes.

There are many networks worldwide that employ instrumentation operating in the VLF/LF frequency range. Detection of lightning discharges with such systems requires fast rising current pulses in the lightning channel in order to radiate electromagnetic field pulses of amplitudes that are high enough to be detected by sensors at distances of upto several hundreds of kilometers. In tower initiated lightning only return strokes and some of the superimposed ICC pulses, like the return stroke type ICC pulses shown in Figure 7.10, are detected by LLS. As a consequence only  $ICC_{RS}$  type discharges initiated from tall objects are typically detected with a high detection efficiency (DE) in the same range as for natural CG lightning. A fraction of the tower initiated discharges of  $ICC_P$  type is also detected, whereas the  $ICC_{Only}$  type discharges are typically not detected by LLS at all.

Overall about 32 per cent (206 out of 652) of the flashes recorded at the GBT from 2000 to 2009 exhibited one or more return strokes ( $ICC_{RS}$ ), 21 per cent (135/652) of the tower flashes were ICCs with superimposed pulses, and 47 per cent of the flashes were categorized as  $ICC_{Only}$ . The Austrian Lightning Detection & Information System ALDIS detected 286 (44 per cent) out of the total of 652 flashes triggered by the Gaisberg Tower. Flash detection efficiency for the  $ICC_{RS}$  type flashes was 96 per cent (198/206) and this is also assumed to be a lower limit of the flash detection efficiency for natural downward lightning. Given that natural first strokes typically have higher peak currents than subsequent strokes in existing channels in upward initiated lightning, the overall flash DE for natural lightning should be higher. The detection efficiency for  $ICC_P$  type flashes to the Gaisberg Tower is 65 per cent (88/135) and as expected none of the  $ICC_{Only}$  type flashes was located by the Austrian LLS. The relatively low overall flash DE of LLS for upward initiated lightning of less than 50 per cent needs to be considered in any application of LLS data regarding lightning to tall objects.

## 7.10 Summary

Tall objects (higher than 100 m or so) located on flat terrain and objects of moderate height (some tens of meters) located on mountain tops experience primarily upward lightning discharges initiated by upward-propagating leaders. Upward (object-initiated) lightning discharges always involve an initial stage that may or

may not be followed by downward-leader/upward-return-stroke sequences. The initial-stage current often exhibits superimposed pulses whose peaks range from tens of amperes to several kilo amperes (occasionally a few tens of kilo-amperes).

Object-initiated lightning events often occur relatively independent from natural downward lightning activity during the cold season and it has been observed that frequently several flashes were initiated from a tall object within a short period. Diendorfer *et al.* (2010) reported on 22 negative flashes to the Gaisberg Tower during one night in March 2008 (winter season) transferring a total charge of more than 3735 C to ground.

At tall objects, the probability of occurrence of bipolar lightning is about the same as for positive lightning. Possible reasons for the observed differences from downward lightning and the high complexity of upward lightning are the multiple upward branches of leaders initiated from the tower tip and the relatively short upward leader channels approaching charged regions above the object.

The scientific community is still facing a number of open questions regarding tower initiated lightning, such as the observation of significant regional differences in the occurrence of self-initiated versus nearby lightning-triggered discharges. Hopefully future research employing modern experimental technology such as high-speed cameras, lightning mapping arrays, etc., will support a better understanding of this very complex type of lightning discharge.

## References

- Anderson, R. B., and A. J. Eriksson (1980), Lightning parameters for engineering application, *Electra*, (69), 65–102
- Asakawa, A. *et al.* (1997), Two types of lightning discharges to a high stack on the coast of the sea of Japan in winter, *Power Delivery, IEEE Transactions on*, 12(3), 1222–1231, doi:10.1109/61.636953
- Beierl, O. (1992), Front shape parameters of negative subsequent strokes measured at the Peissenberg tower, in *Lightning Protection (ICLP), 1992 International Conference on*, Berlin, Germany
- Berger, K. (1967), Novel observations on lightning discharges: Results of research on Mount San Salvatore, *Journal of the Franklin Institute*, 283(6), 478–525, doi:http://dx.doi.org/10.1016/0016-0032(67)90598-4
- Berger, K. (1972), Methoden und Resultate der Blitzforschung auf dem Monte San Salvatore bei Lugano in den Jahren 1963–1971, *SEV*, 63(A 971)
- Berger, K. (1977), The earth flash, in *Lightning: Physics of Lightning, Volume 1*, edited by R. H. Golde, pp. 119–190, Academic Press, New York
- Berger, K. (1978), Blitzstrom-Parameter von Aufwärtsblitzen, *Bull des SEV/VSE*, 69(8), 353
- Berger, K., and E. Vogelsanger (1965), Messungen und Resultate der Blitzforschung der Jahre 1955–1963 auf dem Monte San Salvatore, *Schweizer Elektrotechnischer Verein (SEV)*, 56(1), 2–22
- Berger, K., and E. Vogelsanger (1966), Photographische Blitzuntersuchungen der Jahre 1955–1965 auf dem Monte San Salvatore, *Schweizer Elektrotechnischer Verein (SEV)*, 57(14), 599–620
- Berger, K., R. B. Anderson, and H. Kroeninger (1975), Parameters of lightning flashes, *Electra*, 41, 23–37

- Borghetti, A., C. A. Nucci, and M. Paolone (2003), Effect of tall instrumented towers on the statistical distributions of lightning current parameters and its influence on the power system lightning performance assessment, *European Transactions on Electrical Power*, 13(6), 365–372, doi:10.1002/etep.4450130605
- Dellera, L., and E. Garbagnati (1990), Lightning stroke simulation by means of the leader progression model. I. Description of the model and evaluation of exposure of free-standing structures, *Power Delivery, IEEE Transactions on*, 5(4), 2009–2022, doi:10.1109/61.103696
- Depasse, P. (1994), Statistics on artificially triggered lightning, *Journal of Geophysical Research: Atmospheres*, 99(D9), 18515–18522, doi:10.1029/94JD00912
- Diendorfer, G., R. Kaltenböck, M. Mair, and H. Pichler (2006), Characteristics of tower lightning flashes in a winter thunderstorm and related meteorological observations, in *International Lightning Detection Conference (ILDC)*, pp. 1–6
- Diendorfer, G., M. Mair, W. Schulz, and W. Hadrian (2000), Lightning current measurements in Austria – Experimental setup and first results, in *Lightning Protection (ICLP), 2000 International Conference on*, Rhodes, Greece
- Diendorfer, G., H. Pichler, and M. Mair (2009), Some parameters of negative upward-initiated lightning to the Gaisberg Tower (2000–2007), *Electromagnetic Compatibility, IEEE Transactions on*, 51(3), 443–452, doi:10.1109/TEMC.2009.2021616
- Diendorfer, G., H. Pichler, and M. Mair (2010), Cumulative charge transfer by upward lightning to the Gaisberg tower, in *International Conference on Grounding and Earthing (GROUND' 2010) & International Conference on Lightning Physics and Effects (4th LPE)*, Salvador, Brazil
- Diendorfer, G., H. Zhou, and H. Pichler (2011), Review of 10 years of lightning measurement at the Gaisberg Tower in Austria, in *International Symposium on Winter Lightning (ISWL)*, Sapporo, Japan, pp. 185–190
- Eriksson, A., and D. Meal (1984), The incidence of direct lightning strikes to structures and overhead lines, *IEE-Conference on Lightning and Power Systems. IEE-Conference Publications*, Vol. 236, pp. 67–71
- Eriksson, A. J. (1978), Lightning and tall structures. *Trans. SAIEE*, Vol. 69, August 1978, pp. 238–252
- Eriksson, A. J. (1982), *The CSIR lightning research mast-data for 1972–1982*, Pretoria, South Africa
- Eriksson, A. J. (1987), The incidence of lightning strikes to power lines, *Power Delivery, IEEE Transactions on*, 2(3), 859–870, doi:10.1109/TPWRD.1987.4308191
- Fisher, R. J. *et al.* (1993), Parameters of triggered-lightning flashes in Florida and Alabama, *Journal of Geophysical Research: Atmospheres*, 98(D12), 22887–22902, doi:10.1029/93JD02293
- Flache, D., V. A. Rakov, F. Heidler, W. J. Zischank, and R. Thottappillil (2008), Initial-stage pulses in upward lightning: Leader/return stroke versus M-component mode of charge transfer to ground, *Geophysical Research Letters*, 35(13), L13812, doi:10.1029/2008GL034148
- Fleenor, S. A., C. J. Biagi, K. L. Cummins, E. P. Krider, and X.-M. Shao (2009), Characteristics of cloud-to-ground lightning in warm-season thunderstorms

- in the Central Great Plains, *Atmospheric Research*, 91(2-4), 333–352, doi:10.1016/j.atmosres.2008.08.011
- Fuchs, F., E. U. Landers, R. Schmid, and J. Wiesinger (1998), Lightning current and magnetic field parameters caused by lightning strikes to tall structures relating to interference of electronic systems, *Electromagnetic Compatibility, IEEE Transactions on*, 40(4), 444–451, doi:10.1109/15.736205
- Garbagnati, E., and G. B. Lo Piparo (1982), Parameter von Blitzströmen, *Elektrotechnische Zeitung (ETZ)*, 103, 61–65
- Garbagnati, E., F. Marinoni, and G. B. Lo Piparo (1981), Parameters of lightning currents. Interpretation of the results obtained in Italy, in *Lightning Protection (ICLP), 1981 International Conference on*, Seged, Hungary
- Gorin, B. N., and A. V. Shkilev (1984), Measurements of lightning currents at the Ostankino tower (in Russian), *Elektrichestvo*, 8, 64–65
- Goto, Y., and K. Narita (1995), Electrical characteristics of winter lightning, *Journal of Atmospheric and Terrestrial Physics*, 57(5), 449–458, doi:http://dx.doi.org/10.1016/0021-9169(94)00072-V
- Hagenguth, J. H., and J. G. Anderson (1952), Lightning to the Empire State Building-Part III, *Power Apparatus and Systems, Part III. Transactions of the American Institute of Electrical Engineers*, 71(1), 641–649, doi:10.1109/AIEEPAS.1952.4498521
- Heidler, F. H., M. Manhardt, and K. Stimper (2013), The slow-varying electric field of negative upward lightning initiated by the Peissenberg Tower, Germany, *Electromagnetic Compatibility, IEEE Transactions on*, 55(2), 353–361, doi:10.1109/TEMC.2012.2209121
- Heidler, F., W. J. Zischank, and J. Wiesinger (2000), Statistics of lightning current parameters and related nearby magnetic fields measured at the Peissenberg tower, in *Lightning Protection (ICLP), 2000 International Conference on*, Rhodes, Greece
- Hussein, A. M. *et al.* (1995), Simultaneous measurement of lightning parameters for strokes to the Toronto Canadian National Tower, *Journal of Geophysical Research: Atmospheres*, 100(D5), 8853–8861, doi:10.1029/95JD00543
- Ishii, M., and D. Natsuno (2011), Statistics of recent lightning current observations at wind turbines in Japan—preliminary report presented at CIGRE WG C4.407, June 2011, Sapporo, Japan
- Ishii, M., and M. Saito (2009), Lightning electric field characteristics associated with transmission-line faults in winter, *Electromagnetic Compatibility, IEEE Transactions on*, 51(3), 459–465, doi:10.1109/TEMC.2009.2025496
- Ishii, M., M. Saito, M. Chihara, and D. Natsuno (2012), Transferred charge and specific energy associated with lightning hitting wind turbines in Japan, *IEEE Transactions on Power and Energy*, 132(3), 294–295
- Ishii, M., M. Saito, F. Fujii, M. Matsui, and D. Natsuno (2011), Frequency of upward lightning from tall structures in winter in Japan, in *Lightning (APL), 2011 7th Asia-Pacific International Conference on*, pp. 933–936
- Janischewskij, W. *et al.* (1997), Statistics of lightning strikes to the Toronto Canadian National Tower (1978–1995), *Power Delivery, IEEE Transactions on*, 12(3), 1210–1221, doi:10.1109/61.636949
- Jerauld, J. E. *et al.* (2009), Measured electric and magnetic fields from an unusual cloud-to-ground lightning flash containing two positive strokes followed by

- four negative strokes, *Journal of Geophysical Research: Atmospheres*, 114 (D19), D19115, doi:10.1029/2008JD011660
- Lu, W., D. Wang, Y. Zhang, and N. Takagi (2009), Two associated upward lightning flashes that produced opposite polarity electric field changes, *Geophysical Research Letters*, 36(5), L05801, doi:10.1029/2008GL036598
- McEachron, K. B. (1941a), Lightning to the Empire State Building, *Journal of Franklin Institute*, 227(September), 149–217, doi:http://dx.doi.org/10.1016/S0016-0032(39)90397-2
- McEachron, K. B. (1941b), Lightning to the Empire State Building, *IEEE*, 60(September), 885–890, doi:http://dx.doi.org/10.1016/S0016-0032(39)90397-2
- Miki, M. (2006), Observation of current and leader development characteristics of winter lightning, in *Lightning Protection (ICLP), 2006 International Conference on*, Kanazawa, Japan
- Miki, M., Miki, T., and Asakawa, A. (2012), Characteristics of upward leaders of winter lightning in the coastal area of the Sea of Japan. *IEEE Transactions on Power and Energy*, 132(6), 560–567. DOI:10.1451/ieejpes.132.560
- Miki, M. et al. (2010), Observation of lightning flashes to wind turbines, in *Lightning Protection (ICLP), 2010 International Conference on*, pp. 1–7, Cagliari, Italy
- Miki, M. et al. (2005), Initial stage in lightning initiated from tall objects and in rocket-triggered lightning, *Journal of Geophysical Research: Atmospheres*, 110(D2), D02109, doi:10.1029/2003JD004474
- Miki, M., A. Wada, and A. Asakawa (2004), Observation of upward lightning in winter at the coast of Japan Sea with a high-speed video camera, in *Lightning Protection (ICLP), 2004 International Conference on*, Avignon, France
- Miyake, K., T. Suzuki, and K. Shinjou (1992), Characteristics of winter lightning current on Japan Sea Coast, *Power Delivery, IEEE Transactions on*, 7(3), 1450–1457, doi:10.1109/61.141864
- Montandon, E. (1992), Lightning positioning and lightning parameter determination experiences and results of the Swiss “PTT” research project, in *Lightning Protection (ICLP), 1992 International Conference on*, Berlin, Germany
- Montandon, E. (1995), Messung und Ortung von Blitzeinschlägen und ihren Auswirkungen am Fernmeldeturm “St. Chrischona” bei Basel der schweizerischen Telecom PTT, *Elektrotechnik und Informationstechnik (e&i)*
- Pierce, E. T. (1972), Triggered lightning and some unsuspected lightning hazards, *Stanford Research Institute Menlo Park CA*, (January), 20
- Rakov, V. A. (2005), Lightning flashes transporting both negative and positive charges to ground, *Research Signpost*, 661(2), 9–21
- Rakov, V. (2009), Triggered lightning, in *Lightning: Principles, Instruments and Applications SE-2*, edited by H. Betz, U. Schumann, and P. Laroche, pp. 23–56, Springer Netherlands
- Rakov, V. A., and M. A. Uman (2003), *Lightning – Physics and Effects*, Cambridge University Press
- Rizk, F. A. M. (1990), Modeling of transmission line exposure to direct lightning strokes, *Power Delivery, IEEE Transactions on*, 5(4), 1983–1997, doi:10.1109/61.103694
- Romero, C. et al. (2012a), A statistical analysis on the risetime of lightning current pulses in negative upward flashes measured at Säntis Tower, in *Lightning Protection (ICLP), 2012 International Conference on*, Vienna, Austria



- Romero, C. *et al.* (2012b), A system for the measurements of lightning currents at the Sántis Tower, *Electric Power Systems Research*, 82(1), 34–43, doi:10.1016/j.epr.2011.08.011
- Romero, C., F. Rachidi, M. Paolone, and M. Rubinstein (2013), Statistical distributions of lightning currents associated with upward negative flashes based on the data collected at the Sántis (EMC) tower in 2010 and 2011, *Power Delivery, IEEE Transactions on*, 28(3), 1804–1812, doi:10.1109/TPWRD.2013.2254727
- Romero, C. *et al.* (2012c), Some characteristics of positive and bipolar lightning flashes recorded on the Sántis Tower in 2010 and 2011, in *Lightning Protection (ICLP), 2012 International Conference on*, Vienna, Austria
- Schoene, J. *et al.* (2009), Characterization of return-stroke currents in rocket-triggered lightning, *Journal of Geophysical Research: Atmospheres*, 114(D3), D03106, doi:10.1029/2008JD009873
- Schroeder, M. A. O., A. Soares, S. Visacro, L. Cherchiglia, and V. J. Souza (2002), Lightning current statistical analysis: measurements of Morro do Cachimbo station – Brazil, in *Lightning Protection (ICLP), 2002 International Conference on*, Cracow, Poland
- Smorgonskiy, A., F. Rachidi, M. Rubinstein, G. Diendorfer, and W. Schulz (2013), On the proportion of upward flashes to lightning research towers, *Atmospheric Research*, 129–130(0), 110–116, doi:10.1016/j.atmosres.2012.08.014
- Visacro, S. (2004), A representative curve for lightning current waveshape of first negative stroke, *Geophysical Research Letters*, 31(7), L07112, doi:10.1029/2004GL019642
- Wada, A., M. Miki, and A. Asakawa (2004), Upward lightning flashes observed at the 200-m Fukui Chimney in winter, *AGU Fall Meeting Abstracts*, -1, 06
- Wang, D., and N. Takagi (2008), Characteristics of upward bipolar lightning derived from simultaneous recording of electric current and electric field change, *Union of Radio Sci., Chicago, Ill.*
- Wang, D., and N. Takagi (2012), Characteristics of winter lightning that occurred on a windmill and its lightning protection tower in Japan, *IEEE Transactions on Power and Energy*, 132(6), 568–572, doi:10.1541/ieejpes.132.568
- Wang, D., N. Takagi, T. Watanabe, H. Sakurano, and M. Hashimoto (2008), Observed characteristics of upward leaders that are initiated from a windmill and its lightning protection tower, *Geophysical Research Letters*, 35(2), L02803, doi:10.1029/2007GL032136
- Wang, D. *et al.* (1999), Characterization of the initial stage of negative rocket-triggered lightning, *Journal of Geophysical Research: Atmospheres*, 104 (D4), 4213–4222, doi:10.1029/1998JD200087
- Warner, T. A., K. L. Cummins, and R. E. Orville (2011), Comparison of upward lightning observations from towers in Rapid City, South Dakota with National Lightning Detection Network Data – Preliminary Findings, in *International Symposium on Winter Lightning (ISWL)*, Sapporo, Japan
- Zhou, H., G. Diendorfer, R. Thottappillil, H. Pichler, and M. Mair (2011a), Characteristics of upward bipolar lightning flashes observed at the Gaisberg Tower, *Journal of Geophysical Research: Atmospheres*, 116(D13), D13106, doi:10.1029/2011JD015634
- Zhou, H., G. Diendorfer, R. Thottappillil, H. Pichler, and M. Mair (2011b), Mixed mode of charge transfer to ground for initial continuous current pulses in

upward lightning, in *Lightning (APL), 2011 7th Asia-Pacific International Conference on*, pp. 677–681

Zhou, H., G. Diendorfer, R. Thottappillil, H. Pichler, and M. Mair (2012), Characteristics of upward positive lightning flashes initiated from the Gaisberg Tower, *Journal of Geophysical Research: Atmospheres*, 117(D6), D06110, doi:10.1029/2011JD016903

Zhou, H., N. Theethayi, G. Diendorfer, R. Thottappillil, and V. A. Rakov (2010), On estimation of the effective height of towers on mountaintops in lightning incidence studies, *Journal of Electrostatics*, 68(5), 415–418, doi:http://dx.doi.org/10.1016/j.elstat.2010.05.014



---

*Chapter 8*

**Computation of electromagnetic fields  
from lightning discharge**

*Rajeev Thottappillil*

---

Electromagnetic fields from lightning can couple to electrical systems and produce transient overvoltages, which can cause power and telecommunication outages and destruction of electronics. Knowledge of electromagnetic fields at high altitudes produced by return strokes in cloud-to-ground (CG) lightning are required in the study of transient luminous events in the mesosphere. Electric and magnetic field pulses from various electrical breakdown events in the lightning are used in detecting and locating lightning flashes. Therefore, calculation of the electric and magnetic fields from different lightning processes has several practical applications. In this chapter, expressions for electric and magnetic fields are derived for charge and current configurations applicable to lightning. In general lightning currents and charges vary with time. First, simple expressions for non-time varying cases are presented. Then, electric and magnetic field expressions from time-varying lightning sources are presented.

## **8.1 Electrostatics and magnetostatics**

### *8.1.1 Electrostatic field from a dipole*

Measurements indicate that thunderclouds have a bipolar structure with a lower negative charge region and an upper positive charge region. Therefore, as far as the slowly varying fields at ground level are concerned, the thundercloud can be approximately modelled as a dipole. Charge structure of thunderclouds has been dealt with in Chapter 1. For simplicity, we can assume spherically symmetric distribution of charges for negatively and positively charged regions of the thundercloud, even though charge distribution is more extended horizontally than vertically. The charge centres are separated by a distance  $\Delta h$ . The Earth is assumed to be flat and a perfect conductor. We will now see how the static electric field at ground level will look like as a function of distance from the thundercloud. The geometry of the problem is shown in Figure 8.1. The influence of the conducting ground on the fields is taken into account by the image charges.

The electric field at ground from charge  $+Q$  at height  $H_2$  is given by

$$E_{2+} = \frac{Q}{4\pi\epsilon_0 R_2^2} \text{V/m} \quad (8.1)$$

where  $R_2 = \sqrt{H_2^2 + r^2}$ . The direction of  $E_{2+}$  is as shown in Figure 8.1. The direction of fields from other point charges is shown. From the geometry of the

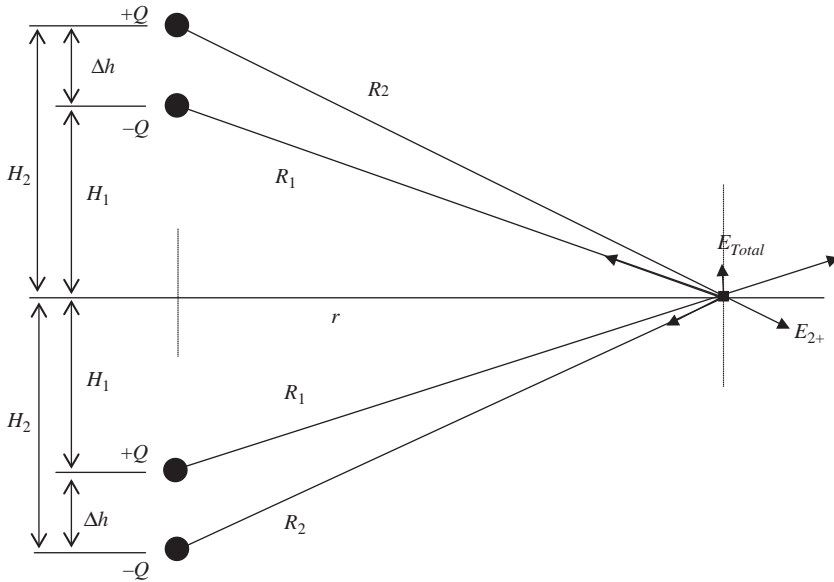


Figure 8.1 Diagram for the calculation of electrostatic fields from a dipole above ground

problem (Figure 8.1) it is clear that there is no net horizontal component for the electric field at ground level. We define a net vertical component  $E_{Total}$  as shown in Figure 8.1. The contribution of  $E_{2+}$  in the direction of  $E_{Total}$  is given by multiplying (8.1) by  $-H_2/R_2$ , the cosine of the angle between the vectors  $E_{Total}$  and  $E_{2+}$ . Adding up the contribution to  $E_{Total}$  from the two point charges and their images we get an expression for the total field as

$$E_{Total} = \frac{2Q}{4\pi\epsilon_0} \left[ \frac{H_1}{R_1^3} - \frac{H_2}{R_2^3} \right] \tag{8.2}$$

where  $R_1 = \sqrt{H_1^2 + r^2}$ .

The distance between the point charges is  $\Delta h$  and  $H_2 = H_1 + \Delta h$ . As the value of the horizontal distance  $r$  is increased,  $E_{Total}$  changes its polarity from positive value (the same direction shown in Figure 8.1) when  $r \ll H_1$  to negative value when  $r \gg H_1$ . In between these extremes there is a certain distance  $r$  at which the net field  $E_{Total}$  become zero, which can be found by setting (8.2) equal to zero. It has been noticed that the field at ground created by a thunderstorm reverses its sign as the thunderstorm approaches the observing station from far away.

The fine weather electric field vector is directed downward towards the Earth and by convention, in atmospheric electricity studies, this field is considered to be the positive field. The sign convention adopted in this chapter is opposite to this convention.

### 8.1.2 Magnetostatic field from a line current

During a CG lightning, the leader and the return stroke channels are predominantly vertical and carry a current. For most part of its existence this current varies rapidly

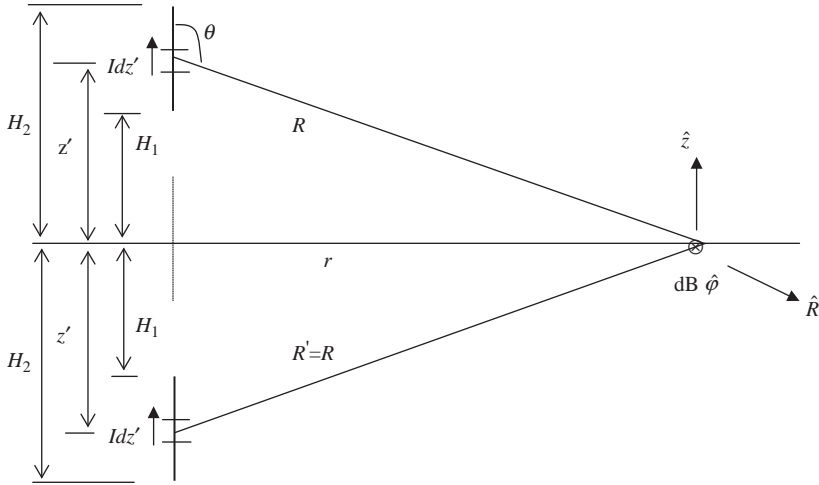


Figure 8.2 Diagram for the calculation of magnetostatic fields from a line current above ground

with time. However, for simplicity, let us first consider a line current above the ground whose current is directed upward and is steady or only slowly varying with time. The effect of the conducting ground on the magnetic field is taken into account by considering an image channel carrying an equal current and also in the upward direction (Figure 8.2).

Magnetic flux density at any distance  $R$  from a current element  $Idz'$  is given by

$$d\vec{B} = \frac{\mu_0 Idz'}{4\pi R^2} (\hat{z} \times \hat{R}) \tag{8.3}$$

where  $\hat{z}$  is a unit vector in the direction of current and  $\hat{R}$  is a unit vector directed towards the field point from the current element  $dz'$ . Now,

$$\hat{z} \times \hat{R} = \sin \theta \hat{\phi} = \frac{r}{R} \hat{\phi} \tag{8.4}$$

where  $R = \sqrt{z'^2 + r^2}$  and  $\hat{\phi}$  is the unit vector in the direction of the magnetic field flux density.

Total magnetic flux density is obtained by integrating (8.3) over the length of the channel. The image channel also creates an equal magnetic flux density at a horizontal distance  $r$  on the ground and in the same direction. Therefore the contribution from the image channel is included by multiplying (8.3) by 2. The total magnetic field is given by

$$\begin{aligned} \vec{B} &= \frac{\mu_0 I}{2\pi} \int_{H_1}^{H_2} \frac{r}{(z'^2 + r^2)^{3/2}} dz' \hat{\phi} \\ &= \frac{\mu_0 I}{2\pi r} \left[ \frac{H_2}{\sqrt{H_2^2 + r^2}} - \frac{H_1}{\sqrt{H_1^2 + r^2}} \right] \hat{\phi} \end{aligned} \tag{8.5}$$

If a steady current flows between the ground ( $H_1 = 0$ ) and the charge centre at height  $H$  ( $H_2 = H$ ), then (8.4) becomes

$$\bar{B} = \frac{\mu_0 I}{2\pi r} \left[ \frac{H}{\sqrt{H^2 + r^2}} \right] \hat{\phi} \quad (8.6)$$

Very close to the channel ( $r \ll H$ ) the magnetic flux density becomes

$$\bar{B} = \frac{\mu_0 I}{2\pi r} \hat{\phi} \quad (8.7)$$

That is, the magnetic flux density varies as  $1/r$  very near to the finite length current carrying channel.

Very far away from the channel ( $r \gg H$ ) the magnetic flux density becomes

$$\bar{B} = \frac{\mu_0 IH}{2\pi r^2} \hat{\phi} \quad (8.8)$$

That is, the magnetic flux density varies as  $1/r^2$  far away from the finite length channel.

### 8.1.3 *Electrostatic and magnetostatic fields from a semi-infinite vertical thin-wire antenna above a conducting plane*

Lightning return stroke channel is often considered as a vertical thin-wire antenna above a conducting ground plane. The thin-wire antenna is assumed to have a radius that approaches zero.

In this section, we will derive the electrostatic and magnetostatic fields from a semi-infinite vertical thin-wire antenna above a conducting plane, for uniform charge density and uniform current distribution. Later in this chapter we will show how these static solutions are in the same form as the dynamic solution in which a current pulse from ground travels up the antenna with speed of light.

#### 8.1.3.1 **Electrostatic field from a semi-infinite uniform line charge vertical to a conducting plane**

Consider a uniform vertical line charge having a charge density  $\rho$  above a conducting plane. It has been shown previously that the equilibrium charge distribution on finite-length conducting wires tends to uniform as the wire radius approaches zero [1, 2]. The line charge is along the positive  $z$ -axis and the conducting plane is on the  $x$ - $y$  plane passing through the origin. The effect of the conducting plane on the electric field can be taken into account by replacing the plane by an image line charge of opposite polarity along the negative  $z$ -axis. Let  $P$  be an arbitrary point in space. The problem is worked out in spherical coordinates  $r, \theta, \phi$ , and the geometry is shown in Figure 8.3. The problem has rotational symmetry about the  $z$ -axis, and therefore the potential and fields are independent of angle  $\phi$ . The scalar potential and electric field from this charge configuration in Figure 8.3 can be derived as shown below [3].

#### *Scalar potential*

The scalar potential at  $P$  due to an elemental charge  $\rho dz'$  is

$$V_1(r, \theta) = \int_0^L \frac{\rho dz'}{4\pi\epsilon_0 R} \quad (8.9)$$

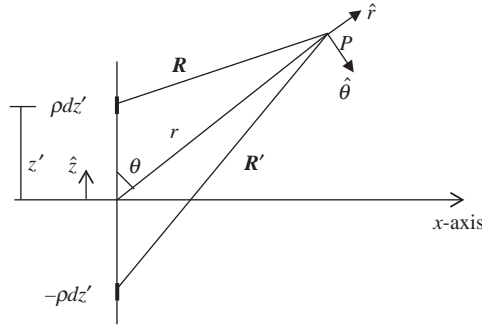


Figure 8.3 The geometry for the calculation showing the line charge and its image

where  $R = \sqrt{r^2 + z'^2 - 2z'r \cos \theta}$ , and  $L$  is the length of the line charge.

Integrating (8.9), we find

$$\begin{aligned} V_1(r, \theta) &= \frac{\rho}{4\pi\epsilon_0} \left[ \sinh^{-1} \frac{2z' - 2r \cos \theta}{\sqrt{4r^2(1 - \cos^2 \theta)}} \right]_0^L \\ &= \frac{\rho}{4\pi\epsilon_0} \left[ \sinh^{-1} \frac{L - r \cos \theta}{r \sin \theta} + \sinh^{-1} \frac{\cos \theta}{\sin \theta} \right] \end{aligned} \quad (8.10)$$

The influence of perfectly conducting ground plane can be taken into account by considering an image line charge of equal magnitude, but opposite polarity. The scalar potential from the image line charge is given by

$$V_2(r, \theta) = \int_0^L \frac{-\rho dz'}{4\pi\epsilon_0 R'} \quad (8.11)$$

where  $R' = \sqrt{r^2 + z'^2 - 2z'r \cos(\pi - \theta)}$ .

Integrating (8.11), and adding to (8.10), we obtain the total scalar potential as

$$\begin{aligned} V(r, \theta) &= \frac{\rho}{4\pi\epsilon_0} \left[ \sinh^{-1} \frac{L - r \cos \theta}{r \sin \theta} - \sinh^{-1} \frac{L + r \cos \theta}{r \sin \theta} \right] \\ &\quad + \frac{\rho}{4\pi\epsilon_0} \left[ \sinh^{-1} \frac{\cos \theta}{\sin \theta} + \sinh^{-1} \frac{\cos \theta}{\sin \theta} \right] \end{aligned} \quad (8.12)$$

Applying the relation  $\text{Sinh}^{-1} x = \ln(x + \sqrt{x^2 + 1})$ ,  $-\infty < x < \infty$  to (8.12) and simplifying, we find

$$V(r, \theta) = \frac{\rho}{4\pi\epsilon_0} \left[ \ln \frac{L - r \cos \theta + \sqrt{L^2 + r^2 - 2Lr \cos \theta}}{L + r \cos \theta + \sqrt{L^2 + r^2 + 2Lr \cos \theta}} \right] + \frac{\rho}{2\pi\epsilon_0} \left[ \ln \frac{1 + \cos \theta}{\sin \theta} \right] \quad (8.13)$$



In the limit that  $L$  approaches infinity, it can be shown that the first term of (8.13) becomes zero ( $\ln 1 = 0$ ). Therefore, for an infinite line charge (8.13) reduces to

$$V(\theta) = \frac{\rho}{2\pi\epsilon_0} \left[ \ln \frac{1 + \cos \theta}{\sin \theta} \right] \tag{8.14}$$

Alternatively, (8.14) can also be written as

$$V(\theta) = \frac{\rho}{4\pi\epsilon_0} \left[ \ln \frac{1 + \cos \theta}{1 - \cos \theta} \right] \tag{8.15}$$

From (8.15) it is clear that the scalar potential is dependent only on the angle  $\theta$ , and is independent of the distance  $r$  from the origin. The equipotential surfaces are surfaces of cones whose apex is at the origin and whose axis is along the line charge. This is illustrated in Figure 8.4. The magnitude of the potential is zero at the conducting plane ( $\theta = 90^\circ$ ), increases with decreasing angle, and become infinite on the line charge ( $\theta = 0$ ).

*Electrostatic field*

The electrostatic field at  $P$  due to the semi-infinite line charge above the conducting plane is given by

$$\begin{aligned} \vec{E} &= -\nabla V \\ &= -\hat{\theta} \frac{1}{r} \frac{\partial V}{\partial \theta} \end{aligned} \tag{8.16}$$

since  $V$  is not a function of  $r$  or  $\phi$ .

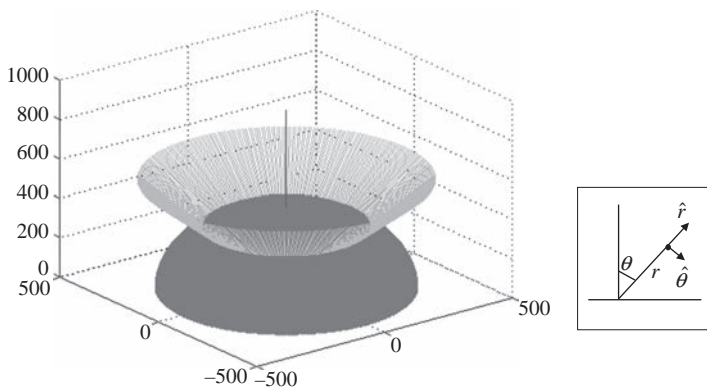


*Figure 8.4 Illustration of electrostatic potential and electrostatic field structure from a semi-infinite line charge above a perfectly conducting ground plane. The potential is equal at the surface of the cone (constant apex angle  $\theta$ ) and the electric field vectors are tangential to the hemispherical surface (constant radius  $r$ ). The cone and hemispherical surface intersect at right angles and the electric field vector is constant on the circle formed at the junction of these two surfaces (constant  $\theta$  and  $r$ ). Moreover, the electric field vector normal to the ground plane has constant magnitude on the hemispherical surface (adapted from [3])*

Evaluating (8.16) and simplifying, we find

$$\bar{E}(r, \theta) = \hat{\theta} \frac{\rho}{2\pi\epsilon_0 r \sin \theta} \quad (8.17)$$

From (8.17) it is apparent that the electrostatic field has only a  $\theta$ -component and is tangential to a semi-spherical shell of radius  $r$  (see Figure 8.4). On the conducting plane, the electric field is perpendicular, as expected, and is a minimum. The electric field vector in the  $\theta$ -direction on the semi-spherical shell increases with decreasing  $\theta$  and becomes infinite on the line charge. The cone and hemispherical surface intersect at right angles and the electric field vector is constant on the circle formed at the junction of these two surfaces. Also, it can be easily shown that the vertical component of the electric field anywhere on the semi-spherical shell is a constant and is given by

$$\bar{E}_z(r) = -\hat{z} \frac{\rho}{2\pi\epsilon_0 r} \quad (8.18)$$

except at the wire itself corresponding to  $\theta = 0$ .

### *Magnetostatic field*

Let us now replace the line charge by a line current  $I$ , directed vertically upward ( $z$ -direction). The effect of the conducting plane on the magnetic field can be obtained by replacing the ground plane by an image line current. The direction of the image line current is the same as that of the original line current. As the length of the line current is made infinite, the problem is reduced to an infinite line current  $I$ . From Ampere's law, the magnetic field at  $P$  in cylindrical or rectangular co-ordinates is given by several text books, and in spherical co-ordinates it can be written as

$$\bar{B}(r, \theta) = \hat{\phi} \frac{\mu_0 I}{2\pi r \sin \theta} = \hat{\phi} \frac{I}{2\pi\epsilon_0 c^2 r \sin \theta} \quad (8.19)$$

where  $r \sin \theta$  is the distance from the line current to the point  $P$ .

## **8.2 Time varying fields from lightning**

### *8.2.1 Introduction*

Lightning discharge is a thin channel when compared to its overall length. Usually we are interested in the electromagnetic fields created by lightning several tens of meters or kilometres away. Therefore, to calculate electric and magnetic fields from lightning, it is modelled as a linear antenna, which has some current distribution or which has certain line charge density distribution that changes with time. Besides lightning discharge is self-propagating and its length extends at great speeds, sometimes at significant fraction of the speed of light. Therefore, field calculation requires careful consideration of the retardation phenomenon due to finite travel time of the signals at speed of light. In this chapter, the analytical expressions for calculating the electric and magnetic fields from lightning are presented. These are general expressions applicable to any line source distribution that varies with time.

### *Three approaches for calculating the electric fields*

Expressions for electric and magnetic fields from an electric dipole in frequency domain can be found in most books on electromagnetics. However, time domain expressions are the most suitable for lightning discharge since it is a transient event

that changes its current and charge distribution in space and time in a non-periodic manner. Besides, the lightning discharge propagates and hence the linear dimensions of the discharge increase with time, often at speeds one-third to one-half the speed of light.

The problem of calculating the electric and magnetic fields from a known source distribution is discussed extensively in literature. Usually the fields are calculated by using scalar and vector potentials. These potentials are directly related to the source distribution.

There are three equivalent approaches to calculating the electric fields produced by a specified source. Two of these equivalent approaches are discussed in [4–6], and the third equivalent approach in [5, 7]. The first approach, the so-called dipole technique or Lorentz condition technique, involves

1. the specification of current density  $\vec{J}$ ;
2. the use of  $\vec{J}$  to find the vector potential  $\vec{A}$ ;
3. the use of  $\vec{A}$  and the Lorentz condition to find the scalar potential  $\phi$ ;
4. the computation of electric field  $\vec{E}$  using  $\vec{A}$  and  $\phi$ ;
5. the computation of magnetic field  $\vec{B}$  using  $\vec{A}$ .

In this technique, the source is described only in terms of current density, and the field equations are expressed only in terms of current. The use of the Lorentz condition eliminates the need for the specification of the line charge density along with the current density and assures that the current continuity equation, which is not explicitly used in this technique, is satisfied.

The second approach, the so-called monopole technique or the continuity equation technique, involves

1. the specification of current density  $\vec{J}$ ;
2. the use of  $\vec{J}$  and the continuity equation relating charge density and current density to find  $\rho$ ;
3. the use of  $\vec{J}$  to find  $\vec{A}$  and  $\rho$  to find  $\phi$ ;
4. the computation of electric field  $\vec{E}$  using  $\vec{A}$  and  $\phi$ ;
5. the computation of magnetic field  $\vec{B}$  using  $\vec{A}$ .

In this technique, the source is described in terms of both current density and line charge density, and the electric field equations are expressed in terms of both charge density and current. The current continuity equation is needed to relate the current density and charge density. There is no need for the explicit use of the Lorentz condition in this technique, although properly specified scalar and vector potentials do satisfy the Lorentz condition.

In the third approach, the electric fields are expressed in terms of the apparent charge density, that is, the charge density that would be ‘seen’ on the lightning channel by an observer at the field point. The difference between this apparent charge density and the charge density in the second approach above will be explained later in this chapter. Field equations obtained in either of the first two approaches can be converted into this third form.

In the first approach electric fields are completely expressed in terms of the current, in the second approach in terms of both current and charge, and in the third approach completely in terms of apparent charge. Magnetic fields are expressed completely in terms of current in the first two approaches and completely in terms of apparent charge in the third approach.

*Some special situations*

In certain situations the evolution of currents in the lightning channel is assumed to be a travelling wave or combination of travelling waves with certain speed. In that case the solution available for electric and magnetic fields from an accelerating point charge can be adapted to find the electric and magnetic fields from the lightning channel [8]. If the current in the channel is travelling at speed of light, then simplified expressions relating the current and electromagnetic fields can be derived from the general expressions [9, 10].

*Organisation of this section*

This section is organised in the following way. Section 8.2 discusses the treatment of the retardation effects in calculating the electromagnetic fields when the source region is extending at considerable speeds. Section 8.3 discusses the derivation of expressions for electric and magnetic fields from a propagating lightning discharge using the Lorentz condition approach [5, 6]. In Section 8.4, electric and magnetic field expressions using the continuity equation approach are discussed [5]. The electric field expressions from both approaches look different, even though they are analytically equivalent. Also, individual components of the field, such as static component, induction component, and radiation component are different in these two approaches even though the total field is the same. In Section 8.5, the non-uniqueness of the individual components of the field are discussed and some numerical calculations are presented [5, 11]. Section 8.6 discusses two different forms of continuity equation, one as viewed by the observer at the source location and other as viewed by the observer at remote location away from the source [5]. In Section 8.7, expressions for electric and magnetic fields from the lightning channel completely in terms of the apparent charge distribution is presented and discussed [5, 7]. Section 8.8 discusses the calculation of lightning electromagnetic fields using the expressions derived in sections 8.3, 8.4 and 8.7, with numerical examples. Section 8.9 treats a special case of a return stroke model in which the solution for the electric and magnetic fields reduces to a simple expression. Section 8.10 shows how electromagnetic field equations of moving and accelerating charges can be used to generate electromagnetic fields from lightning return strokes, assuming travelling waves with certain speed  $v$  in the channel.

**8.3 Treatment of retardation effects**

Lightning return stroke wavefront extends typically at speeds one-third to one-half the speed of light. The return stroke current above the extending wavefront is considered to be zero and the current below the extending wavefront is rapidly changing with time. The finite travel time from the source at the return stroke to the point where the field is measured can not be ignored. At any given time the observer at the field point ‘sees’ the current on the return stroke channel from an earlier time. Similarly, the observer do not see the true length of the channel, that is, only some portion of the actual lightning channel contribute to the field at a given time. Therefore retarded sources and retarded channel lengths are to be used in the calculation of return stroke fields. An extensive treatment of retardation effects in calculating the electromagnetic fields from the lightning discharge is given in [12]. The apparent length  $L'(t)$  of the return stroke channel, to be used in the expressions for the fields in later sections of this chapter, are derived in this section.

Consider a return-stroke channel with one end fixed at  $A$  as shown in Figure 8.5. It takes a time  $r/c$  for the information from  $Q$  to reach the observer at  $P$  and hence the observer ‘sees’ the channel emerging from  $A$  at time  $r/c$ . The actual length  $L(t)$  of the channel at a time  $t$  is given by  $L(t) = v \cdot t$ , where  $v$  is the speed of the return stroke wavefront. The apparent length of the channel at time  $t$  ‘seen’ by the observer at  $P$  is different from  $L(t)$ . This length,  $L'(t)$ , can also be called the retarded length.

If we define the time  $t$  such that it is the sum of the time required for the return-stroke wavefront to reach a height  $L'(t)$  and the time required for a signal to travel from the wavefront at  $L'(t)$  and the time required for a signal to travel from the wavefront at  $L'(t)$  to the observer at  $P$ ,  $t$  can be written as

$$t = \frac{L'(t)}{v} + \frac{R(L')}{c} \tag{8.20}$$

where

$$R(L') = \sqrt{r^2 + L'^2(t) - 2L'(t)r \cos \theta} \tag{8.21}$$

The retarded length  $L'(t)$  can be obtained by solving (8.20) and (8.21), and is given by

$$L'(t) = \frac{r}{1 - (v^2/c^2)} \left( -\frac{v^2}{c^2} \cos \theta + \frac{vt}{r} - \frac{v}{c} \sqrt{\left(1 - \frac{v^2}{c^2}\right) + \frac{v^2 t^2}{r^2} + \frac{v^2}{c^2} \cos^2 \theta - \frac{2vt}{r} \cos \theta} \right) \tag{8.22}$$

If the ground is treated as perfectly conducting, (8.22) can also be used, with  $\theta$  replaced by  $(180 - \theta)$  to find the apparent length  $L''(t)$  of the channel image ‘seen’ by the observer.

If all the channel sections were equidistant from the observer, that is, if the discharge were to extend in a circular arc of radius  $r$  with the observer at the centre, the length of the discharge seen by the observer would be  $L'(t) = v \cdot (t - r/c)$ . For  $\theta = 0$ , that is, for the observer straight ahead of the propagating discharge, the apparent channel length is obtained from (8.22) as

$$L'(t) = \frac{v}{1 - v/c} \cdot (t - r/c) \tag{8.23}$$

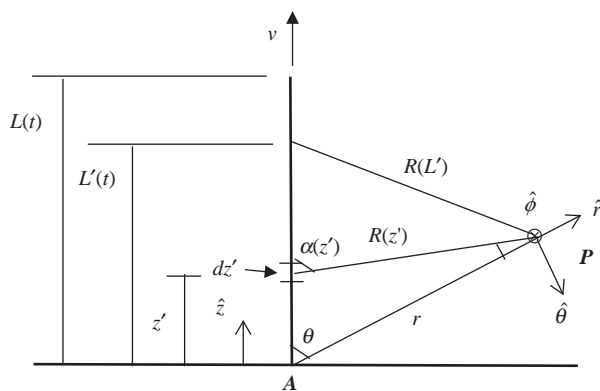


Figure 8.5 *Geometry of the problem in the treatment of retardation effects*

and the image channel length is obtained from (8.22) by replacing  $\theta$  by  $180^\circ$  as

$$L''(t) = \frac{v}{1 + v/c} \cdot (t - r/c) \tag{8.24}$$

If the channel is very small compared to the distance to the observer, that is, if  $L'(t) \ll r$ , then  $R(L')$  can be approximated as  $R(L') = r - L'(t)\cos \theta$ , substitution of which in (8.22) gives

$$L'(t) = \frac{v}{1 - \frac{v}{c}\cos \theta} \cdot (t - r/c) \tag{8.25}$$

### 8.4 Fields in terms of current (the Lorentz condition approach)

The lightning return-stroke channel can be modelled as a straight line fixed at one end  $A$ , with the other end extending with speed  $v$ . The geometry of the problem is shown in Figure 8.6. The current on the lightning channel is represented by  $i(z', t)$ , where  $z'$  indicate the position along the  $z$ -axis with origin at the base of the channel and  $t$  indicate the time. At time  $t=0$  the return stroke starts to propagate from origin  $A$ . The observer at the fixed field point  $P$  ‘sees’ the return stroke starting to propagate from the origin at time  $t = r/c$ , where  $c$  is the speed of light. The retarded current at any elemental channel section  $dz'$  is given by  $i(z', t - R(z')/c)$ , where  $z'$  is less than or equal to  $L'(t)$ , the length of the return stroke channel ‘seen’ by the observer at  $P$  at time  $t$ . Note that the assumption of constant return-stroke speed is not required in the derivations presented here.

In fact, the lightning channel can be considered composed of many electric dipoles of length  $dz'$ . An electric dipole is a linear current element whose length is vanishingly small compared to the distance at which the fields are to be calculated. Also, the current is assumed to be a constant over the length of the dipole. Field expressions in time domain, with specific application to lightning, are popularised by the paper [6] in 1975, and later developed by others [4, 5, 7, 12–14]. The treatment presented here closely follows that of [5].

The vector potential at  $P$  due to the entire extending channel is given by (equation 9 of [12])

$$\bar{A}(r, \theta, \tau) = \frac{1}{4\pi\epsilon_0 c^2} \int_0^{L'(\tau)} \frac{i(z', \tau - R(z')/c)}{R(z')} \hat{z} dz' \tag{8.26}$$

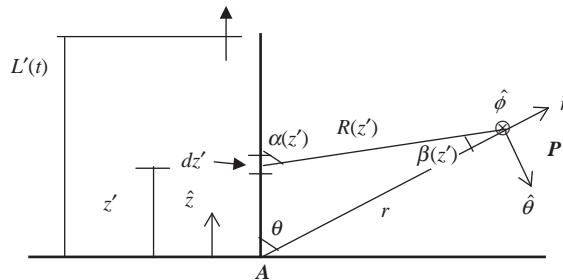


Figure 8.6 Geometry of the problem

where  $\tau$  is a time less than or equal to time  $t$ . At time  $\tau$ , return-stroke wavefront is 'seen' at a height  $L'(\tau)$  by the observer at  $P$  and  $L'(\tau)$  is less than or equal to  $L'(t)$ . Note that in (8.26) we have not considered the presence of ground, usually assumed to be perfectly conducting and replaced by the channel image.

The total electric field can be calculated using the relation

$$\bar{E} = -\nabla\phi - \frac{\partial\bar{A}}{\partial t} \quad (8.27)$$

where  $\phi$  can be obtained from the Lorentz condition  $\nabla \bullet \bar{A} + \frac{1}{c^2} \frac{\partial\phi}{\partial t} = 0$ , as

$$\phi(r, \theta, t) = -c^2 \int_{r/c}^t \nabla \bullet \bar{A} d\tau \quad (8.28)$$

Taking the divergence of (8.26) it can be shown that

$$\begin{aligned} \nabla \bullet \bar{A}(r, \theta, \tau) = & + \frac{1}{4\pi\epsilon_0 c^2} \int_0^{L'(\tau)} \left[ \frac{z' - r \cos \theta}{R^3(z')} i(z', \tau - R(z')/c) \right. \\ & \left. + \frac{z' - r \cos \theta}{cR^2(z')} \frac{\partial i(z', \tau - R(z')/c)}{\partial \tau} \right] dz' \\ & + \frac{1}{4\pi\epsilon_0 c^2} \frac{L'(\tau) - r \cos \theta}{cR^2(L')} i(L', \tau - R(L')/c) \frac{dL'(\tau)}{d\tau} \end{aligned} \quad (8.29)$$

Substituting (8.29) into (8.28) and interchanging the order of integration, an expression for the scalar potential completely in terms of current can be obtained. As time increases from  $r/c$  to  $t$ , the channel length  $L'(\tau)$  increases monotonically from 0 to  $L'(t)$ . Therefore, the order of integration can be changed as follows according to the standard rule.

$$\int_{r/c}^t \int_0^{L'(\tau)} \Rightarrow \int_0^{L'(t)} \int_{\tau}^t \quad (8.30)$$

where the lower limit  $\tau = t_b$  is the time at which the observer at the field point 'sees' the return-stroke front at height  $z'$  for the first time. For a constant return-stroke speed  $v$ ,

$$\tau = \frac{L'(\tau)}{v} + \frac{R(L'(\tau))}{c} = \frac{z'}{v} + \frac{R(z')}{c}$$

Performing the operations explained above and after some reductions, we get an expression for scalar potential as

$$\begin{aligned} \phi(r, \theta, t) = & - \frac{1}{4\pi\epsilon_0} \int_0^{L'(t)} \left[ \frac{z' - r \cos \theta}{R^3(z')} \int_{z'/v + R(z')/c}^t i(z', t - R(z')/c) d\tau \right. \\ & \left. + \frac{z' - r \cos \theta}{cR^2(z')} i(z', t - R(z')/c) \right] dz' \end{aligned} \quad (8.31)$$

Taking the gradient of (8.31),  $\nabla\phi$ , and the time derivative of (8.26),  $\partial\bar{A}/\partial t$ , we get an expression for electric field according to (8.27) as given below:

$$\bar{E}(r, \theta, t) = -\frac{1}{4\pi\epsilon_0} \hat{r} \int_0^{L'(t)} \frac{\cos\theta - 3\cos\alpha(z')\cos\beta(z')}{R^3(z')} \int_{t_b}^t i\left(z', \tau - \frac{R(z')}{c}\right) d\tau dz' \quad (8.32a)$$

$$-\frac{1}{4\pi\epsilon_0} \hat{r} \int_0^{L'(t)} \frac{\cos\theta - 3\cos\alpha(z')\cos\beta(z')}{cR^2(z')} i\left(z', t - \frac{R(z')}{c}\right) dz' \quad (8.32b)$$

$$-\frac{1}{4\pi\epsilon_0} \hat{r} \int_0^{L'(t)} \frac{\cos\theta - \cos\alpha(z')\cos\beta(z')}{c^2R(z')} \frac{\partial i(z', t - R(z')/c)}{\partial t} dz' \quad (8.32c)$$

$$+\frac{1}{4\pi\epsilon_0} \hat{\theta} \int_0^{L'(t)} \frac{\sin\theta + 3\cos\alpha(z')\sin\beta(z')}{R^3(z')} \int_{t_b}^t i\left(z', \tau - \frac{R(z')}{c}\right) d\tau dz' \quad (8.32d)$$

$$+\frac{1}{4\pi\epsilon_0} \hat{\theta} \int_0^{L'(t)} \frac{\sin\theta + 3\cos\alpha(z')\sin\beta(z')}{cR^2(z')} i\left(z', t - \frac{R(z')}{c}\right) dz' \quad (8.32e)$$

$$+\frac{1}{4\pi\epsilon_0} \hat{\theta} \int_0^{L'(t)} \frac{\sin\theta + \cos\alpha(z')\sin\beta(z')}{c^2R(z')} \frac{\partial i(z', t - R(z')/c)}{\partial t} dz' \quad (8.32f)$$

$$-\frac{1}{4\pi\epsilon_0} \hat{r} \frac{\cos\theta - \cos\alpha(L')\cos\beta(L')}{c^2R(L')} i\left(L', t - \frac{R(L')}{c}\right) \frac{dL'}{dt} \quad (8.32g)$$

$$+\frac{1}{4\pi\epsilon_0} \hat{\theta} \frac{\sin\theta + \cos\alpha(L')\sin\beta(L')}{c^2R(L')} i\left(L', t - \frac{R(L')}{c}\right) \frac{dL'}{dt} \quad (8.32h)$$

$$(8.32)$$

In (8.32),  $dL'/dt$  is the speed of the current wavefront as 'seen' by the observer at  $P$ , which is different from the real speed  $v$ . Also, from Figure 8.6 we get  $\cos\alpha(z') = -(z' - r\cos\theta)/R(z')$ ,  $\cos\beta(z') = (r - z'\cos\theta)/R(z')$ , and  $\sin\beta(z') = z'\sin\theta/R(z')$ . In the electric field expression (8.32) terms containing the factors  $R^{-3}$ ,  $c^{-1}R^{-2}$  and  $c^{-2}R^{-1}$  are called the static component, the induction component, and the radiation component, respectively. The last two terms of the expression (8.32) containing  $dL'/dt$  will have non-zero values only if there is a current discontinuity (non-zero current) at the wavefront.



### 8.4.1 Magnetic field

The magnetic field is given by  $\vec{B} = \nabla \times \vec{A}$ . For a vertical channel, the magnetic field has only a horizontal component and it is given by (taking the curl of (8.26))

$$\begin{aligned}
 B(r, t) = & + \frac{1}{4\pi\epsilon_0 c^2} \hat{\phi} \int_0^{L'(t)} \left[ \frac{\sin \alpha(z')}{R^2(z')} i \left( z', t - \frac{R(z')}{c} \right) \right. \\
 & \left. + \frac{\sin \alpha(z')}{cR(z')} \frac{\partial i(z', t - R(z')/c)}{\partial t} \right] dz' \\
 & + \frac{1}{4\pi\epsilon_0 c^2} \hat{\phi} \frac{\sin \alpha(L')}{cR(L')} i \left( L', t - \frac{R(L')}{c} \right) \frac{dL'}{dt}
 \end{aligned} \tag{8.33}$$

where  $\sin \alpha(z') = r \sin \theta / R(z')$ .

Equations (8.32) and (8.33) are valid for any return-stroke model, that is, for all time varying current and charge distributions on the channel. In the electric field expression (8.32) terms containing the factors  $R^{-3}$ ,  $c^{-1}R^{-2}$  and  $c^{-2}R^{-1}$  constitute what is called the static component, the induction component, and the radiation component, respectively.

### 8.4.2 Image channel

A perfectly conducting plane at  $z' = 0$  is introduced to simulate the effect of earth. Using the image theory, we can replace this plane by an image channel carrying current in the same direction as the actual channel. The expression for the image channel can be easily obtained from (8.32) and (8.33) by replacing  $z'$  by  $-z'$  wherever it appears. Note that the upper limit of integration for the image channel is  $L''$ , which is less than  $L'$  for a field point above ground. Expression for  $L''$  can be obtained from the expression for  $L'$  in (8.22) by replacing  $\theta$  by  $(180^\circ - \theta)$ .

### 8.4.3 Fields at ground level

A common problem in lightning is to find the electric and magnetic fields at ground level from a lightning return-stroke, which is considered as straight and vertical above ground. Under this case,  $\theta = 90^\circ$  and  $\hat{\theta} = -\hat{z}$ . The ground is assumed to be infinitely conducting. The effect of ground plane can be included by considering an image channel carrying an image current. The magnitude and direction of this image current are identical to the current in the channel at any given position and time, for an observer at ground level. The field expression corresponding to the image channel have their  $\hat{r}$ -directed components same as in magnitude, but opposite in sign to the  $\hat{r}$ -directed components in (8.32). However, the field expression corresponding to the image channel has its  $\hat{\theta}$ -directed components the same both in magnitude and sign to that in (8.32). Therefore, adding the contribution of the image channel to (8.32), we get the complete field expression as

$$\begin{aligned}
 E_V(r, t) = & \frac{1}{2\pi\epsilon_0} \int_0^{L'(t)} \frac{2 - 3 \sin^2 \alpha(z')}{R^3(z')} \int_{t_b}^t i(z', \tau - R(z')/c) d\tau dz' \\
 & + \frac{1}{2\pi\epsilon_0} \int_0^{L'(t)} \frac{2 - 3 \sin^2 \alpha(z')}{cR^2(z')} i(z', t - R(z')/c) dz'
 \end{aligned}$$

$$\frac{-1}{2\pi\epsilon_0} \int_0^{L(t)} \frac{\sin^2\alpha(z')}{c^2 R(z')} \frac{\partial i(z', t - R(z')/c)}{\partial t} dz' \tag{8.34}$$

$$\frac{-1}{2\pi\epsilon_0} \frac{\sin^2\alpha(L')}{c^2 R(L')} i(L', t - R(L')/c) \frac{dL'}{dt}$$

Adding the contribution of image channel to (8.33), the magnetic field at ground level is given by

$$B_\phi(r, t) = \frac{1}{2\pi\epsilon_0 c^2} \int_0^{L(t)} \left( \frac{\sin\alpha(z')}{R^2(z')} i(z', t - R(z')/c) + \frac{\sin\alpha(z')}{cR(z')} \frac{\partial i(z', t - R(z')/c)}{\partial t} \right) dz' + \frac{1}{2\pi\epsilon_0 c^2} \frac{\sin\alpha(L')}{cR(L')} i(L', t - R(L')/c) \frac{dL'}{dt} \tag{8.35}$$

Equations (8.34) and (8.35) are valid for any return-stroke model, that is, for any time varying current distribution along the channel. The last term in (8.34) and the last term in (8.35) become zero if there is no current discontinuity at the propagating wavefront, i.e. if  $i(L', t - R(L')/c) = 0$ .

### 8.5 Fields in terms of current and charge (the continuity equation approach)

The purpose here is to find an expression for electric field using both scalar potential and vector potential related by the continuity equation that define the relationship between the charge density and current locally. The continuity equation that relate the charge density and current locally, but at retarded time is given by [14, 15]

$$\frac{\partial \rho^*(z', t - R(z')/c)}{\partial t} = - \frac{\partial i(z', t - R(z')/c)}{\partial z'} \Big|_{t - R(z')/c = \text{const.}} \tag{8.36}$$

In (8.36), the partial differentiation of retarded current with respect to the source coordinate  $z'$  is carried out keeping the retarded time constant. That is, the dependence of  $R(z')$  on  $z'$  is ignored while taking the partial derivative. Note that as viewed by an observer at a remote point  $P$ , the relationship between the charge density and current could be different from that given in (8.36) [5, 7]. We will come to this point later in Section 8.6.

The return-stroke starts from the ground level ( $z' = 0$ ). To satisfy the continuity equation (8.36) at  $z' = 0$ , a point charge  $Q(t - r/c)$  is required at  $z' = 0$  as the source for the current emerging from  $z' = 0$ . This stationary point charge is given by

$$Q(t - r/c) = - \int_{r/c}^t i(0, \tau - r/c) d\tau \tag{8.37}$$

The scalar potential from the whole lightning channel is given by

$$\phi(r, t) = \frac{1}{4\pi\epsilon_0} \frac{Q(t - r/c)}{r} + \frac{1}{4\pi\epsilon_0} \int_0^{L(t)} \frac{1}{R(z')} \rho^*(z', t - R(z')/c) dz' \quad (8.38)$$

The electric field can be obtained from (8.27). Using the spherical coordinate system centred at the starting point of the return stroke at ground (Figure 8.6) and ignoring the presence of ground for the moment, the negative gradient of the scalar potential  $-\nabla\phi$  and the negative time derivative of the vector potential  $-\partial A/\partial t$  can be found as described below. For  $-\nabla\phi$  we have

$$\begin{aligned} -4\pi\epsilon_0 \nabla\phi = & -\hat{r} \frac{\partial}{\partial r} \frac{Q(t - r/c)}{r} - \hat{r} \frac{\partial}{\partial r} \int_0^{L(t)} \frac{\rho^*(z', t - R(z')/c)}{R(z')} dz' \\ & - \hat{\theta} \frac{1}{r} \frac{\partial}{\partial \theta} \int_0^{L(t)} \frac{\rho^*(z', t - R(z')/c)}{R(z')} dz' \end{aligned} \quad (8.39)$$

Note that the first term of (8.37) is independent of the spatial coordinate  $\theta$ . The maximum length of the channel  $L(t)$ , as seen from the field point, is a function of  $r$ ,  $\theta$  and  $t$ . The distance to the field point from the differential channel segment  $R(z')$  is a function of both  $r$  and  $\theta$ , as given by (8.40).

$$\begin{aligned} R(z') &= \sqrt{r^2 + z'^2 - 2rz' \cos \theta} \\ \frac{dR(z')}{dr} &= \frac{r - z' \cos \theta}{R(z')} \\ \frac{dR(z')}{d\theta} &= \frac{rz' \sin \theta}{R(z')} \end{aligned} \quad (8.40)$$

Carrying out the differentiation of the second and third terms in (8.39) and using (8.40), we obtain the following expression

$$\begin{aligned} -4\pi\epsilon_0 \nabla\phi = & + \hat{r} \int_0^{L(t)} \left[ \frac{r - z' \cos \theta}{R^3(z')} \rho^*(z', t - R(z')/c) + \frac{r - z' \cos \theta}{cR^2(z')} \frac{\partial \rho^*(z', t - R(z')/c)}{\partial t} \right] dz' \\ & + \hat{\theta} \int_0^{L(t)} \left[ \frac{z' \sin \theta}{R^3(z')} \rho^*(z', t - R(z')/c) + \frac{z' \sin \theta}{cR^2(z')} \frac{\partial \rho^*(z', t - R(z')/c)}{\partial t} \right] dz' \\ & - \hat{r} \frac{\rho^*(L', t - R(L')/c)}{R(L')} \frac{\partial L'}{\partial r} - \hat{\theta} \frac{\rho^*(L', t - R(L')/c)}{rR(L')} \frac{\partial L'}{\partial \theta} - \hat{r} \frac{\partial}{\partial r} \frac{Q(t - r/c)}{r} \end{aligned} \quad (8.41)$$

The time derivative of vector potential (8.26) is given by

$$-4\pi\epsilon_0 \frac{\partial \bar{A}}{\partial t} = -\hat{z} \int_0^{L(t)} \frac{1}{c^2 R(z')} \frac{\partial i(z', t - R(z')/c)}{\partial t} dz' - \hat{z} \frac{i(L', t - R(L')/c)}{c^2 R(L')} \frac{dL'}{dt} \quad (8.42)$$

where

$$\hat{z} = \hat{r} \cos \theta - \hat{\theta} \sin \theta \quad (8.43)$$

The general expression for electric field at a field point can be found by combining (8.41), (8.42) and (8.43), and is given below.

$$\begin{aligned} \bar{E}(r, \theta, t) = & + \frac{1}{4\pi\epsilon_0} \hat{r} \int_0^{L'(t)} \frac{\cos \beta(z')}{R^2(z')} \rho^*(z', t - R(z')/c) dz' \\ & + \frac{1}{4\pi\epsilon_0} \hat{r} \int_0^{L'(t)} \frac{\cos \beta(z')}{cR(z')} \frac{\partial \rho^*(z', t - R(z')/c)}{\partial t} dz' \\ & - \frac{1}{4\pi\epsilon_0} \hat{r} \int_0^{L'(t)} \frac{\cos \theta}{c^2 R(z')} \frac{\partial i(z', t - R(z')/c)}{\partial t} dz' \\ & + \frac{1}{4\pi\epsilon_0} \hat{\theta} \int_0^{L'(t)} \frac{\sin \beta(z')}{R^2(z')} \rho^*(z', t - R(z')/c) dz' \\ & + \frac{1}{4\pi\epsilon_0} \hat{\theta} \int_0^{L'(t)} \frac{\sin \beta(z')}{cR(z')} \frac{\partial \rho^*(z', t - R(z')/c)}{\partial t} dz' \\ & + \frac{1}{4\pi\epsilon_0} \hat{\theta} \int_0^{L'(t)} \frac{\sin \theta}{c^2 R(z')} \frac{\partial i(z', t - R(z')/c)}{\partial t} dz' \\ & + \frac{1}{4\pi\epsilon_0} \hat{r} \frac{\cos \beta(L')}{cR(L')} \rho^*(L', t - R(L')/c) \frac{dL'(t)}{dt} \\ & - \frac{1}{4\pi\epsilon_0} \hat{r} \frac{\cos \theta}{c^2 R(L')} i(L', t - R(L')/c) \frac{dL'(t)}{dt} \\ & + \frac{1}{4\pi\epsilon_0} \hat{\theta} \frac{\sin \beta(L')}{cR(L')} \rho^*(L', t - R(L')/c) \frac{dL'(t)}{dt} \\ & + \frac{1}{4\pi\epsilon_0} \hat{\theta} \frac{\sin \theta}{c^2 R(L')} i(L', t - R(L')/c) \frac{dL'(t)}{dt} \\ & + \frac{1}{4\pi\epsilon_0} \hat{r} \left[ \frac{1}{r^2} Q(t - r/c) + \frac{1}{rc} \frac{dQ(t - r/c)}{dt} \right] \end{aligned} \quad (8.44)$$

where  $\cos \beta(z') = (r - z' \cos \theta)/R(z')$ ,  $\sin \beta(z') = z' \sin \theta/R(z')$ , and  $Q$  is given by (8.37).

The magnetic field expression using this approach is identical to (8.35) since it is completely determined by the vector potential.

### 8.5.1 Image channel

A perfectly conducting plane at  $z' = 0$  is introduced to simulate the effect of earth. Using the image theory, we can replace this plane by an image channel carrying current in the same direction as the actual channel. The expression for the image channel can be easily obtained from (8.44) by replacing  $z'$  by  $-z'$ ,  $\rho$  by  $-\rho$ , and  $Q$  by  $-Q$ , wherever they appear. Note that the upper limit of integration for the image channel is  $L''$ , which is less than  $L'$  for a field point above ground. As discussed before, expression for  $L''$  can be obtained from the expression for  $L'$  given by (8.22) by replacing  $\theta$  by  $(180^\circ - \theta)$ .

### 8.5.2 Fields at ground level

We are interested in the return stroke field at ground level. For this case,  $\theta = 90^\circ$ , and therefore  $\cos \theta = 0$ ,  $\sin \theta = 1$  and  $\hat{\theta} = -\hat{z}$ . The unit vector  $\hat{r}$  is now horizontal, pointing away from the channel. A perfectly conducting plane at  $z' = 0$  is introduced to simulate the effect of earth. Using the image theory, we can replace this plane by an image channel carrying current in the same direction as the actual channel. Writing out the equations for image channel and adding them to (8.44) for the case  $\theta = 90^\circ$ , we get the expression for E-field, as below.

$$\begin{aligned}
 E_V(r, t) = & \frac{-1}{2\pi\epsilon_0} \int_0^{L'(t)} \frac{z'}{R^3(z')} \rho^*(z', t - R(z')/c) dz' \\
 & \frac{-1}{2\pi\epsilon_0} \int_0^{L'(t)} \frac{z'}{cR^2(z')} \frac{\partial \rho^*(z', t - R(z')/c)}{\partial t} dz' \\
 & \frac{-1}{2\pi\epsilon_0} \int_0^{L'(t)} \frac{1}{c^2 R(z')} \frac{\partial i(z', t - R(z')/c)}{\partial t} dz' \\
 & \frac{-1}{2\pi\epsilon_0} \frac{L'(t)}{cR^2(L')} \rho^*(L', t - R(L')/c) \frac{dL'}{dt} \\
 & \frac{-1}{2\pi\epsilon_0} \frac{1}{c^2 R(L')} i(L', t - R(L')/c) \frac{dL'}{dt} \tag{8.45}
 \end{aligned}$$

Note that by definition, the current and charge density in (8.45) are related by the local continuity (8.36). Equation (8.45) contains both current and charge density, while (8.34) contains only current. The first three terms of (8.45) are similar to the corresponding terms of the expression for E-field derived in the book of Jefimenko [16] for a volume charge and current distribution whose boundary is fixed in space. The first term of (8.45) can be considered as representing the electrostatic field ( $R^{-3}$  dependence), the sum of second and fourth terms as representing the induction field ( $c^{-1}R^{-2}$  dependence), and the sum of third and last terms as representing the radiation field ( $c^{-2}R^{-1}$  dependence). It appears that the electrostatic, induction, and radiation terms (except for the last two terms associated with the wavefront) in (8.45) can also be identified as containing  $z'$  times line charge density (charge),  $z'$  times time derivative of line charge density (time derivative of charge) or current, and derivative of current, respectively. If there is no current or charge discontinuity at the wavefront, the last two terms become zero.

### 8.6 Non-uniqueness of electrostatic, induction, and radiation field components

Fields calculated using the Lorentz condition approach and the continuity equation approach, given by (8.34) and (8.45), respectively, should be identical since both are derived by rigorous application of electromagnetic principles and use the same basic assumptions. However, in appearance the expressions look different. Therefore, it would be interesting to compare the fields from (8.34) and (8.45) due to a known current distribution. It will be shown that while the total fields given by (8.34) and (8.35) are identical, the individual field components (electrostatic, induction, and radiation terms identified by their dependence on  $R$ ) in these two equations are different. Take the following numerical example. Imagine the return stroke as a current wave that starts from the ground, and travels up with a constant speed  $v$ . In that case the current at any height  $z$  at time  $t$  is equal to the current at ground at an earlier time  $t - z'/v$ , where  $z'/v$  is the travel time between ground and the height  $z'$ . This is the so-called transmission line (TL) model and the current at any height is related to the current at ground by the relation

$$i(z', t) = i(0, t - z'/v) \tag{8.46}$$

Since there is no discontinuity at the wavefront for the TL model, the last term of (8.34) and the last two terms of (8.45) drop out of the equations. The charge density in (8.45) is calculated using the local continuity equation (8.36), which for the transmission line model can be rewritten as [7]

$$\rho^*(z', t - R(z')/c) = \frac{i(0, t - z'/v - R(z')/c)}{v} \tag{8.47}$$

where  $v$  is the return stroke speed.

Computed electric fields at distances 50 m, 1 km and 100 km are shown in Figures 8.7, 8.8 and 8.9, respectively. In the curve labels in Figures 8.7, 8.8 and 8.9,

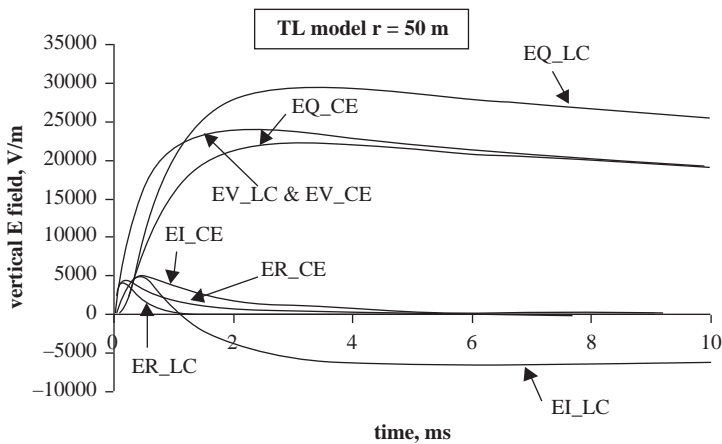


Figure 8.7 Comparison of the total electric field and its components at a distance of 50 m predicted by the TL model and field expressions (8.34) and (8.45). “LC” (Lorentz condition) at the end of the label corresponds to (8.34), and “CE” (Continuity equation) to (8.45)

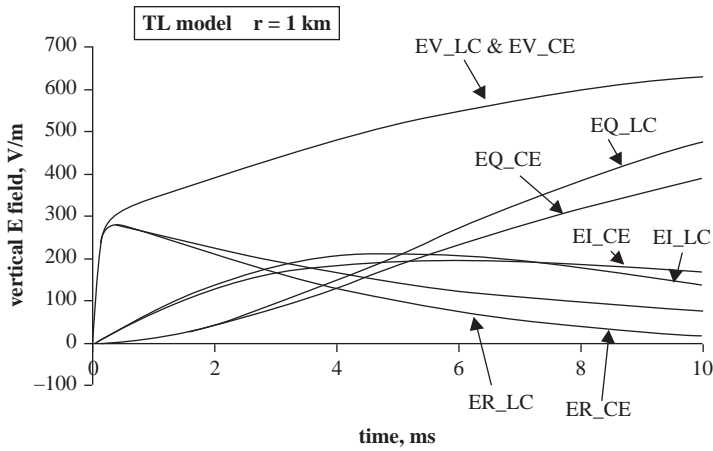


Figure 8.8 Same as Figure 8.7, but at a distance of 1 km

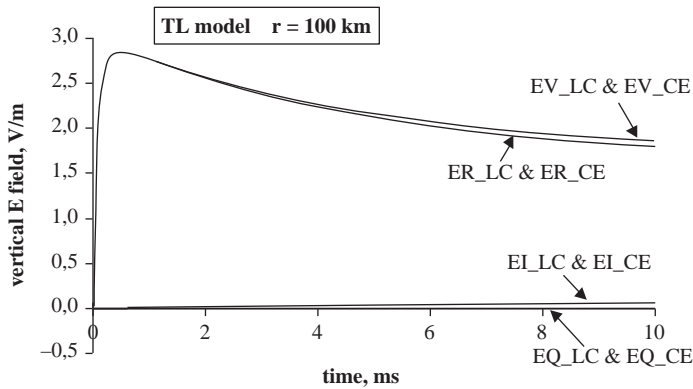


Figure 8.9 Same as Figure 8.7, but at a distance of 100 km

LC indicates the terms in (8.34), and CE indicates the terms in (8.45). The labels EQ, EI, and ER indicate the electrostatic ( $R^{-3}$  dependence), induction ( $c^{-1}R^{-2}$  dependence), and radiation ( $c^{-2}R^{-1}$  dependence) field components. The current waveform and return stroke speed used in the calculations are given in [5]. The following can be observed from Figures 8.7, 8.8 and 8.9 and from (8.34) and (8.45).

1. The total fields given by (8.34) and (8.45) are identical (for up to several decimal places when numbers are compared).
2. In (8.45), the electrostatic and induction terms are given completely by the gradient of the scalar potential, while the radiation term is completely given by the time derivative of the vector potential. In contrast, in (8.34), both the gradient of the scalar potential and the time derivative of the vector potential contribute to the radiation field term.
3. The electrostatic ( $R^{-3}$  dependence), induction ( $c^{-1}R^{-2}$  dependence), and radiation ( $c^{-2}R^{-1}$  dependence) terms in (8.34) are different from the corresponding terms in (8.45). The difference is considerable at 50 m (very close to the channel) and almost negligible at 100 km (far away from the channel).

- At 50 m (very close to the channel), the electrostatic term ( $R^{-3}$  dependence) in (8.34) is larger than its counterpart in (8.45) (compare curves EQ\_LC and EQ\_CE in Figure 8.7).

The above analysis clearly shows that, even though the total electric field from a current or charge distribution is unique, the division of total electric field in the time domain into the so-called electrostatic ( $R^{-3}$  dependence), induction ( $c^{-1}R^{-2}$  dependence), and radiation ( $c^{-2}R^{-1}$  dependence) components is not unique. This was further verified by calculating the individual field components and the total fields using six different return stroke models (BG, TCS, MTLE, MTL and DU models described by [17]). Of these models, the BG and TCS models have current discontinuity at the wavefront, whereas other models do not have wavefront current discontinuity.

Note that in the Lorentz condition technique all field components are expressed in terms of current, while in the continuity equation technique both current and charge density are involved. In the Lorentz condition technique the gradient of scalar potential contributes to all the three field components, whereas in the continuity equation technique, it contributes only to the electrostatic and induction field components. In either case, the expression for magnetic field at ground level is the same, (8.35), since it depends only on the vector potential. We get the same Poynting vector whether we calculate it from equation pairs (8.34) and (8.35) or (8.45) and (8.35), since the total electric fields given by (8.34) and (8.45) are the same. In fact, (8.34) can be analytically derived from (8.45), as shown in [5].

### 8.7 The continuity equation

Continuity equation expresses the principle of charge conservation and is a fundamental law. Let us inspect this with an example of a linear element having only one spatial dimension.

Consider a current-carrying channel segment of length  $\Delta z'$  whose centre (midpoint)  $M$  is at a height  $z'$  (Figure 8.10). Let  $q^*(z', t^*)$  be the charge contained in the segment at time  $t^*$ . Associated with  $q^*(z', t^*)$  is a line charge density which is defined as  $\rho^*(z', t^*) = \lim_{\Delta z' \rightarrow 0} \frac{q^*(z', t^*)}{\Delta z'}$ . Charge conservation principle requires that a positive rate of change of charge in segment  $\Delta z'$  is equal to a negative net outflow of current

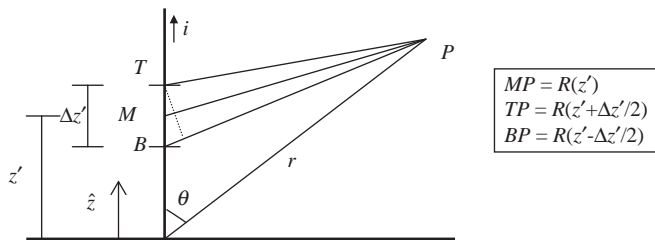


Figure 8.10 Geometry for explaining the physical meaning of two formulations of the continuity equation, which differ in how retardation effects are accounted for



from the segment. That is,  $\frac{\partial q^*(z', t^*)}{\partial t^*} = -(i(z' + \Delta z'/2, t^*) - i(z' - \Delta z'/2, t^*))$ . Note that currents at the top and bottom boundaries ( $T$  and  $B$ ) of the segment are specified at the same local time  $t^*$ . Dividing through by  $\Delta z'$  and letting  $\Delta z' \rightarrow 0$  we can obtain the continuity equation  $\frac{\partial \rho^*(z', t^*)}{\partial t^*} = -\frac{\partial i(z', t^*)}{\partial z'}$ , with  $t^*$  kept constant while carrying out the partial differentiation with respect to  $z'$ . The local time  $t^*$  could as well be  $t - R(z')/c$ , where  $t$  is the time measured at a remote observation point  $P$  at a distance  $R(z')$  from the midpoint of the segment, as shown in Figure 8.6. Then we can write the continuity equation as

$$\frac{\partial \rho^*(z', t - R(z')/c)}{\partial t} = -\frac{\partial i(z', t - R(z')/c)}{\partial z'} \Bigg|_{t - R(z')/c = \text{const.}} \tag{8.48}$$

Note that keeping the time  $t - R(z')/c$  a constant in (8.48) implies that the current crossing the boundary of the element  $\Delta z'$  is measured *simultaneously* at time  $t - R(z')/c$ . If the currents crossing the ends  $T$  and  $B$ , sends a signal to the observer at a certain time then these signals arrive at a remote point simultaneously only if the remote point is equidistant from the ends  $T$  and  $B$ . An observer on a line passing through the mid-point  $M$  of the segment and perpendicular to the segment can receive the signals from the end points simultaneously. Any observer away from this line, such as  $P$  in Figure 8.10 can not receive the signal simultaneously from the end points because of different travel times for the signals. Now let us see the relationship between the charge and current in segment  $\Delta z'$  as viewed from point  $P$ .

An observer at  $P$  does not ‘see’ the currents at the top ( $T$ ) and bottom ( $B$ ) of the segment at the same time. The current at  $T$  that observer ‘sees’ at a given time  $t$  is from an earlier time  $t - R(z' + \Delta z'/2)/c$  and the current at  $B$  is from a different earlier time  $t - R(z' - \Delta z'/2)/c$ . If the difference in the current from the endpoints is interpreted as the rate of change of charge in the segment, then the rate of change of charge in the channel segment as ‘seen’ by the observer at  $P$  is  $\frac{\partial q(z', t - R(z')/c)}{\partial t} = -(i(z' + \Delta z'/2, t - R(z' + \Delta z'/2)/c) - i(z' - \Delta z'/2, t - R(z' - \Delta z'/2)/c))$ . Dividing through by  $\Delta z'$  and letting  $\Delta z' \rightarrow 0$ , we can get equation

$$\frac{\partial \rho(z', t - R(z')/c)}{\partial t} = -\frac{\partial i(z', t - R(z')/c)}{\partial z'} \tag{8.49}$$

that relate charge density and current in the channel as ‘seen’ by observer at  $P$ .

The line charge densities in (8.48) ( $\rho^*$ ) and in (8.49) ( $\rho$ ) are different. In (8.47), the partial differentiation of retarded current with respect to the source co-ordinate  $z'$  is carried out without keeping the retarded time constant; that is, the ‘total’ partial derivative of retarded current is taken. Equation (8.48) gives the local charge density or ‘real charge density’ at retarded time, while (8.49) gives the ‘apparent charge density’ or charge density as ‘seen’ by the remote observer. Both charge densities can be used in calculating electric fields. In Section 8.5, we saw how the local charge density  $\rho^*$  can be used in finding an expression for electric field (8.45) and we found that in this expression both current and charge appears explicitly. Besides, in Section 8.6 we found that the division of terms into electrostatic, induction, and radiation field is different in (8.45) when compared to the electric field expression (8.34) completely in terms of current. It is possible to derive an electric field expression completely in terms of ‘apparent charge density’ or charge density as ‘seen’ by the remote observer. This derivation is done in Section 8.8.

We can now find a relationship between the two charge densities  $\rho^*$  and  $\rho$ , corresponding to (8.48) and (8.49), respectively. The total partial derivative of retarded current with respect to  $z'$  can be written as

$$\begin{aligned} \frac{\partial i(z', t - R(z')/c)}{\partial z'} &= \left. \frac{\partial i(z', t - R(z')/c)}{\partial z'} \right|_{t-R/c=\text{const.}} \\ &+ \frac{\partial i(z', t - R(z')/c)}{\partial(t - R(z')/c)} \frac{\partial(t - R(z')/c)}{\partial z'} \end{aligned} \quad (8.50)$$

From (8.40),

$$\frac{\partial(t - R(z')/c)}{\partial z'} = - \frac{z' - r \cos \theta}{cR(z')} \quad (8.51)$$

and

$$\frac{\partial i(z', t - R(z')/c)}{\partial(t - R(z')/c)} = \frac{\partial i(z', t - R(z')/c)}{\partial t} \quad (8.52)$$

Substituting (8.51) and (8.52) in (8.50) and rearranging the terms we obtain

$$\begin{aligned} \left. \frac{\partial i(z', t - R(z')/c)}{\partial z'} \right|_{t-R/c=\text{const.}} &= \frac{\partial i(z', t - R(z')/c)}{\partial z'} \\ &+ \frac{z' - r \cos \theta}{cR(z')} \frac{\partial i(z', t - R(z')/c)}{\partial t} \end{aligned} \quad (8.53)$$

Applying (8.48) and (8.49) in (8.53), we get the relationship between the two charge densities as

$$\frac{\partial \rho(z', t - R(z')/c)}{\partial t} = \frac{\partial \rho^*(z', t - R(z')/c)}{\partial t} + \frac{z' - r \cos \theta}{cR(z')} \frac{\partial i(z', t - R(z')/c)}{\partial t} \quad (8.54)$$

where the second term on the right-hand side can be viewed as an adjustment term for the time rate of change of local charge density. Integration of both sides of (8.54) over time yields

$$\rho(z', t - R(z')/c) = \rho^*(z', t - R(z')/c) + \frac{z' - r \cos \theta}{cR(z')} i(z', t - R(z')/c) \quad (8.55)$$

The factor  $\frac{z' - r \cos \theta}{cR(z')} = - \frac{\partial(R/c)}{\partial z'}$  is the negative rate of change of time retardation with respect to  $z'$ .

In short, (8.48) and (8.49) are two forms of the continuity equation, the former can be viewed as the local continuity equation in retarded time relating real charges and current on the channel and the later can be viewed as the retarded form of the continuity equation in retarded time relating apparent charges (or charges as seen by observer) and the current.

The scalar potential in terms of current is given by (8.31) and in terms of charge by (8.38). It is possible to show that (8.31) and (8.38) are analytically equivalent [5]. A third equivalent expression for scalar potential in terms of apparent charge density can be derived from (8.38) using (8.55).

## 8.8 Fields in terms of apparent charge distribution

In this section, exact time domain expressions for remote electric and magnetic fields as a function of the spatial and temporal distribution of the charge density on the lightning channel are derived for the return-stroke process, and leader process. In Section 8.4, we saw how the local charge density  $\rho^*$  can be used in finding an expression for electric field (8.45) and we found that in this expression both current and charge density appears explicitly. Besides, in Section 8.6 we found that the division of terms into electrostatic, induction, and radiation field is different in (8.45) when compared to the electric field expression (8.34) completely in terms of current. However, it is possible to derive an electric field expression completely in terms of apparent charge density or charge density as ‘seen’ by the remote observer. This derivation is done in this section. The relationship between apparent charge density and the local charge density in retarded time are established earlier in Section 8.6. To illustrate the method, at first the field expressions are derived for the special case of observer at ground, following [7]. Then a general expression for electric field at any arbitrary point is presented.

### 8.8.1 Theory

#### 8.8.1.1 General

The remote differential electric field  $dE_z$  and magnetic field  $dB_\phi$  at ground due to a small, vertical, current carrying element  $dz'$  above a perfectly conducting Earth is given by (e.g. [18])

$$dE_z(r, t) = \frac{dz'}{2\pi\epsilon_0} \left[ \frac{2z'^2 - r^2}{R^5(z')} \int_{t_b(z')}^t i(z', \tau^*) d\tau + \frac{2z'^2 - r^2}{cR^4(z')} i(z', t^*) - \frac{r^2}{c^2R^3(z')} \frac{\partial i(z', t^*)}{\partial t} \right] \tag{8.56}$$

$$dB_\phi(r, t) = \frac{dz'}{2\pi\epsilon_0 c^2} \left[ \frac{r}{R^3(z')} i(z', t^*) + \frac{r}{cR^2(z')} \frac{\partial i(z', t^*)}{\partial t} \right] \tag{8.57}$$

where  $t^* = t - R(z')/c$  is the retarded time,  $t_b(z')$  is the time at which the current is ‘seen’ to begin in the channel section at  $z'$  by the observer at  $P$ ,  $c$  is the speed of light in vacuum,  $R(z') = (z'^2 + r^2)^{1/2}$  as shown in Figure 8.11. The right-hand side of

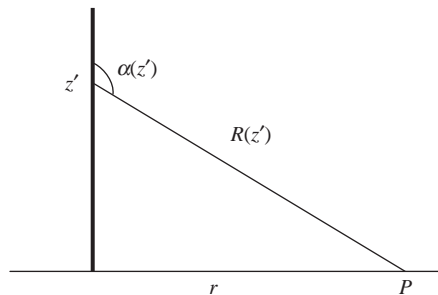


Figure 8.11 *Geometry used in deriving the expressions for electric and magnetic fields at a point P on earth a horizontal distance r from the vertical lightning return-stroke channel extending upward*

(8.56) and (8.57) are the same as the integrands of (8.34) and (8.35), respectively. Using the continuity equation relating the current and apparent charge, presented in (8.49), the electric and magnetic fields given by (8.56) and (8.57) in terms of channel current distribution, can be rewritten in terms of apparent channel charge density  $\rho(z', t^*)$  distribution, as shown in the following sections.

### 8.8.1.2 Relation between apparent charge density and retarded current

Consider a section of the current carrying channel at an arbitrary height  $z'$  (Figure 8.11). The travel time of the electromagnetic signal from the channel segment at  $z'$  to an observer at ground, at  $P$ , is  $R(z')/c$ . The continuity equation relating the retarded charge density as 'seen' by the observer (apparent charge density) and retarded current at an arbitrary time  $t$  is given by (8.47) and reproduced below.

$$\frac{\partial \rho^*(z', t^*)}{\partial t} = - \frac{\partial i(z', t^*)}{\partial z'} \quad (8.58)$$

where  $t^*$  is the retarded time as given earlier. The physical meaning of (8.58) is discussed earlier in Section 8.5. The return-stroke front is assumed to start from ground level ( $z' = 0$ ) and to propagate upward with a constant speed  $v$ , reaching a height  $z'$  in a time  $z'/v$ . Taking the time integral from  $z'/v + R(z')/c$  to  $t$  on both sides of (8.58), noting that  $z'$  and  $t$  are independent variables, we obtain an expression for apparent charge density

$$\rho(z', t^*) = \frac{i(z', z'/v)}{v_a(z')} - \int_{z'/v + R(z')/c}^t \frac{\partial i(z', \tau^*)}{\partial z'} d\tau \quad (8.59)$$

where  $v_a(z')$  is the apparent speed of the front at  $z'$  as seen by a stationary observer at a distance  $r$  from the base of the channel and is given by

$$\begin{aligned} \frac{1}{v_a(z')} &= - \frac{\partial}{\partial z'} \left( t - \frac{R(z')}{c} - \frac{z'}{v} \right) \\ &= \frac{1}{v} \cdot \left( 1 - \frac{v}{c} \cos \alpha(z') \right) \end{aligned} \quad (8.60)$$

Angle  $\alpha(z')$  is defined in Figure 8.11, with observer at ground, and in Figure 8.6, with observer at an elevation. Note that the first term of (8.59) represents the apparent charge density at the wavefront when it has reached  $z'$  and is due to the extension of the front. Equation (8.59) defines the charge density distribution along the channel at any given time  $t$  as 'seen' by a stationary observer at  $P$  at a distance  $r$  from the base of the channel (see Figure 8.11).

Equation (8.59) can be rewritten as

$$\rho^*(z', t^*) = - \frac{d}{d'z} \int_{z'/v + R(z')/c}^t i(z', \tau^*) d\tau \quad (8.61)$$

From (8.61), we find

$$\rho_L(z', t^*) dz' = -d \left[ \int_{z'/v + R(z')/c}^t i(z', \tau^*) d\tau \right] \quad (8.62)$$

Further, multiplying both sides of (8.58) by  $dz'$ , we find

$$\begin{aligned} \frac{\partial \rho(z', t^*)}{\partial t} dz' &= - \frac{\partial i(z', t^*)}{\partial z'} dz' \\ &= -di(z', t^*) \end{aligned} \tag{8.63}$$

Finally, taking the partial derivative with respect to time of (8.63), we obtain

$$\frac{\partial^2 \rho(z', t^*)}{\partial t^2} dz' = -d \left( \frac{\partial i(z', t^*)}{\partial t} \right) \tag{8.64}$$

Note that for a leader beginning from a height  $H_m$  at time  $t=0$  and travelling downward at a speed  $v$  the lower limit of the integral in (8.61) and (8.62) will be the travel time to  $z'$  and from  $z'$  to the observer, that is,  $(H_m - z')/v + R(z')/c$ . In general, the lower limit of the integral in (8.61) and (8.62) is the time,  $t_b(z')$ , at which the current is ‘seen’ to begin in the channel at  $z'$  by the observer and with this modification equation (8.62), along with (8.63) and (8.64) are valid for any lightning process. It is not necessary for the return-stroke speed to be constant if the lower limit of (8.62) is written as  $t_b(z')$ .

### 8.8.1.3 General expressions for differential electric and magnetic fields

The remote differential electric field at ground due to a vertical, current carrying element  $dz'$  above a perfectly conducting earth is given by (8.56). In the following (8.56) will be written in terms of charge density using (8.62), (8.63) and (8.64). Each term of (8.56) can be represented, omitting  $1/(2\pi\epsilon_0)$ , by

$$df_1(z')f_2(z', t) = d[f_1(z')f_2(z', t)] - f_1(z')df_2(z', t) \tag{8.65}$$

where  $f_2(z', t)$  is the current integral, current or the current derivative and the total differential  $df_1(z')$  is  $(2z'^2 - r^2)/R^5(z')dz'$ ,  $(2z'^2 - r^2)/cR^4(z')dz'$ , or  $-r^2/c^2R(z')dz'$ . Using (8.65) the first (electrostatic) term of (8.56) can be expanded as follows

$$2\pi\epsilon_0 dE_s(r, t) = d \left( \frac{-z'}{R^3(z')} \int_{t_b(z')}^t i(z', \tau^*) d\tau \right) - \frac{-z'}{R^3(z')} d \left( \int_{t_b(z')}^t i(z', \tau^*) d\tau \right) \tag{8.66}$$

Similarly, the second (induction) term of (8.56) can be written as

$$\begin{aligned} 2\pi\epsilon_0 dE_i(r, t) &= d \left( \left[ -\frac{3}{2} \frac{z'}{cR^2(z')} + \frac{1}{2} \frac{\tan^{-1}(z'/r)}{cr} \right] i(z', t^*) \right) \\ &\quad - \left[ -\frac{3}{2} \frac{z'}{cR^2(z')} + \frac{1}{2} \frac{\tan^{-1}(z'/r)}{cr} \right] di(z', t^*) \end{aligned} \tag{8.67}$$

Also, the third (radiation) term of (F1) can be written as

$$2\pi\epsilon_0 dE_r(r, t) = d \left( \frac{-z'}{c^2R(z')} \frac{\partial i(z', t^*)}{\partial t} \right) - \frac{-z'}{c^2R(z')} d \left( \frac{\partial i(z', t^*)}{\partial t} \right) \tag{8.68}$$

Applying (8.62), (8.63) and (8.64) to the second term of (8.66), (8.67) and (8.68), respectively, and adding the resulting equations we get the expression (8.69) for differential electric field, equivalent to (8.56).

$$\begin{aligned}
 dE_z(r, t) = & -\frac{1}{2\pi\epsilon_0} \frac{z'}{R^3(z')} \rho(z', t^*) dz' \\
 & - \frac{1}{2\pi\epsilon_0} \left[ \frac{3}{2} \frac{z'}{cR^2(z')} - \frac{1}{2} \frac{\tan^{-1}(z'/r)}{cr} \right] \cdot \frac{\partial \rho(z', t^*)}{\partial t} dz' \\
 & - \frac{1}{2\pi\epsilon_0} \frac{z'}{c^2 R^2(z')} \frac{\partial^2 \rho_L(z', t^*)}{\partial t^2} dz' + \frac{1}{2\pi\epsilon_0} d \left[ \frac{-z'}{R^3(z')} \int_{t_b(z')}^t i(z', \tau^*) d\tau \right] \\
 & + \frac{1}{2\pi\epsilon_0} d \left[ \left( -\frac{3}{2} \frac{z'}{cR^2(z')} + \frac{1}{2} \frac{\tan^{-1}(z'/r)}{cr} \right) i(z', t^*) \right] + \frac{1}{2\pi\epsilon_0} d \left[ \frac{-z'}{c^2 R^2(z')} \frac{\partial i(z', t^*)}{\partial t} \right]
 \end{aligned} \tag{8.69}$$

In a similar manner the differential magnetic field given by (8.57) can be rewritten as

$$\begin{aligned}
 dB_\phi(r, t) = & \frac{1}{2\pi\epsilon_0 c^2} \frac{1}{r} \frac{z'}{R(z')} \frac{\partial \rho(z', t^*)}{\partial t} dz' + \frac{1}{2\pi\epsilon_0 c^2} \frac{1}{c} \tan^{-1} \left( \frac{z'}{r} \right) \frac{\partial^2 \rho(z', t^*)}{\partial t^2} dz' \\
 & + \frac{1}{2\pi\epsilon_0 c^2} d \left( \frac{1}{r} \frac{z'}{R(z')} i(z', t^*) \right) + \frac{1}{2\pi\epsilon_0 c^2} d \left( \frac{1}{c} \tan^{-1} \left( \frac{z'}{r} \right) \frac{\partial i(z', t^*)}{\partial t} \right)
 \end{aligned} \tag{8.70}$$

Note that (8.69) and (8.70) are general and applicable to any lightning process in a vertical channel above a perfectly conducting ground. In the following (8.69) and (8.70) will be integrated for return strokes with the result being expressed in terms of charge density only.

## 8.8.2 Return stroke electric and magnetic fields

### 8.8.2.1 Exact expressions

As mentioned earlier, the return stroke is assumed to be an extending discharge with a discharge front speed  $v$ , assumed to be a constant and the observer at  $P$  'sees' the discharge front passing a height  $z'$  at time  $t_b(z') = z'/v + R(z')/c$ . The height of the channel  $L(t)$  'seen' at time  $t$  by the observer is given by the solution of the following equation

$$t = \frac{L'(t)}{v} + \frac{(L'^2(t) + r^2)^{1/2}}{c} \tag{8.71}$$

If  $L(t)$  is the height of the discharge front 'seen' by the observer, then the total electric field at  $P$  at time  $t$  is given by integrating (8.69) from 0 to  $L(t)$ . Also, from (8.59) the current at the wavefront, as 'seen' by the observer at  $P$  is given by

$$i \left( L'(t), \frac{L'(t)}{v} \right) = \rho_L \left( L'(t), \frac{L'(t)}{v} \right) v_a(L'(t)) \tag{8.72}$$

where

$$v_a(L') = \frac{dL'(t)}{dt} = v \left[ 1 - \frac{v}{c} \cos \alpha(L') \right]^{-1} \tag{8.73}$$

is the apparent speed of the return-stroke wavefront; that is, the front speed 'seen' by the observer at  $P$  (see Figure 8.11). Differentiating both sides of (8.72) with respect to time we get,

$$\frac{\partial}{\partial t} i \left( L(t), \frac{L'(t)}{v} \right) = \frac{\partial}{\partial t} \left[ \rho_L \left( L'(t), \frac{L'(t)}{v} \right) v_a(L') \right] \quad (8.74)$$

Performing the integration of (8.69) from height 0 to  $L(t)$ , using (8.71), (8.72) and (8.74), we can obtain the relation expressing the total electric field from a return-stroke channel in terms of the charge distribution on the channel. To this the radiation field term due to current discontinuity at the wavefront, that is a term equivalent to the last term of (8.34), has to be added to get the complete field expression at ground level. The expression is given below.

$$\begin{aligned} E_z(r, t) = & -\frac{1}{2\pi\epsilon_0} \int_0^{L'(t)} \frac{z'}{R^3(z')} \rho(z', t^*) dz' \\ & -\frac{1}{2\pi\epsilon_0} \int_0^{L'(t)} \left( \frac{3}{2} \frac{z'}{cR^2(z')} - \frac{1}{2} \frac{\tan^{-1}(z'/r)}{cr} \right) \frac{\partial \rho(z', t^*)}{\partial t} dz' \\ & -\frac{1}{2\pi\epsilon_0} \int_0^{L'(t)} \frac{z'}{c^2 R(z')} \frac{\partial^2 \rho(z', t^*)}{\partial t^2} dz' \\ & -\frac{1}{2\pi\epsilon_0} \left( \frac{3}{2} \frac{L'(t)}{cR^2(L')} - \frac{1}{2} \frac{\tan^{-1}(L'(t)/r)}{cr} \right) \rho \left( L', \frac{L'(t)}{v} \right) \frac{dL'(t)}{dt} \\ & -\frac{1}{2\pi\epsilon_0} \frac{L'(t)}{c^2 R(L')} \frac{\partial}{\partial t} \left[ \rho \left( L'(t), \frac{L'(t)}{v} \right) \frac{dL'(t)}{dt} \right] \\ & -\frac{1}{2\pi\epsilon_0} \frac{r^2}{c^2 R^3(L')} \rho \left( L', \frac{L'(t)}{v} \right) \left( \frac{dL'}{dt} \right)^2 \end{aligned} \quad (8.75)$$

To get the last term of (8.75), we have used the relationship (8.72). Adopting a procedure similar to that used for obtaining (8.75), we can show that the horizontal component of the magnetic field at ground is given by

$$\begin{aligned} B_\phi(r, t) = & \frac{1}{2\pi\epsilon_0 c^2} \int_0^{L'(t)} \frac{1}{r} \frac{z'}{R(z')} \frac{\partial \rho(z', t^*)}{\partial t} dz' \\ & + \frac{1}{2\pi\epsilon_0 c^2} \int_0^{L'(t)} \frac{1}{c} \tan^{-1} \left( \frac{z'}{r} \right) \frac{\partial^2 \rho(z', t^*)}{\partial t^2} dz' \\ & + \frac{1}{2\pi\epsilon_0 c^2} \frac{1}{r} \frac{L'(t)}{R(L')} \rho \left( L'(t), \frac{L'(t)}{v} \right) \frac{dL'(t)}{dt} \\ & + \frac{1}{2\pi\epsilon_0 c^2} \frac{1}{c} \tan^{-1} \left( \frac{L'(t)}{r} \right) \frac{\partial}{\partial t} \left[ \rho \left( L'(t), \frac{L'(t)}{v} \right) \frac{dL'(t)}{dt} \right] \\ & + \frac{1}{2\pi\epsilon_0 c^2} \frac{r}{cR^2(L')} \rho \left( L', \frac{L'(t)}{v} \right) \left( \frac{dL'(t)}{dt} \right)^2 \end{aligned} \quad (8.76)$$

The requirement that speed  $v$  be a constant can be relaxed to allow any arbitrary function of height if  $v$  is replaced by an ‘average’ speed  $V_{av}$ ,

$$V_{av}(z') = \frac{z'}{\int_0^{z'} \frac{dz''}{v(z'')}} \quad (8.77)$$

as defined by [19].

### 8.8.2.2 Numerical illustration

It is possible to show the analytical equivalence between the three different expressions for electric field at ground level due to a propagating lightning return stroke, that is between (8.34), (8.45) and (8.75) and was done in [5]. The numerical equivalence between (8.34) and (8.45), for the case of the Transmission Line model for the return stroke, is shown in Figures 8.7, 8.8 and 8.9. For the TL model the current and charge density in (8.35) is related by the continuity equation (8.26), giving a charge density given by (8.48). However, the apparent charge density to be used in (8.75) and (8.76) is given by (8.49), giving a charge density as follows [5]

$$\rho(z', t - R(z')/c) = \frac{i(0, t - z'/v - R(z')/c)}{v \cdot F_{TL}} \quad (8.78)$$

where  $F_{TL} = \frac{1}{1 + v \frac{z'}{cR(z')}}$

Calculation of electric fields at ground for TL model using (8.75) and (8.78) yielded exactly the same curves as that for EQ\_LC, EI\_LC, ER\_LC and EV\_LC in Figures 8.7, 8.8 and 8.9, as shown in [5].

### 8.8.2.3 Expression for electric field at an elevation

Often, it is necessary to calculate electric fields at an elevation above ground. Equation (8.75) gives electric field only at ground level. It is possible to derive a general expression for electric field at an elevation in terms of the ‘apparent charge density’. The general expression (8.32) in terms of current can be taken as a starting point. The procedure is the same as that outlined earlier in this section. In addition to (8.62), (8.63) and (8.64), we also use the following relations to convert each terms of (8.32) into terms expressed in apparent charge density.

$$\frac{d}{dz'} \left( \frac{r - z' \cos \theta}{R^3(z')} \right) = - \left( \frac{\cos \theta - 3 \cos \alpha(z') \cos \beta(z')}{R^3(z')} \right) \quad (8.79)$$

$$\frac{d}{dz'} \left( \frac{3r - z' \cos \theta}{2cR^2(z')} + \frac{1}{2} \frac{\cot \theta}{cr} \tan^{-1} \frac{z' - r \cos \theta}{r \sin \theta} \right) = - \left( \frac{\cos \theta - 3 \cos \alpha(z') \cos \beta(z')}{cR^2(z')} \right) \quad (8.80)$$

$$\frac{d}{dz'} \left( \frac{r - z' \cos \theta}{c^2 R(z')} \right) = - \left( \frac{\cos \theta - \cos \alpha(z') \cos \beta(z')}{c^2 R(z')} \right) \quad (8.81)$$

$$\frac{d}{dz'} \left( \frac{z' \sin \theta}{R^3(z')} \right) = \frac{\sin \theta + 3 \cos \alpha(z') \sin \beta(z')}{R^3(z')} \quad (8.82)$$



$$\frac{d}{dz'} \left( \frac{3}{2} \frac{z' \sin \theta}{cR^2(z')} - \frac{1}{2} \frac{1}{cr} \tan^{-1} \frac{z' - r \cos \theta}{r \sin \theta} \right) = \frac{\sin \theta + 3 \cos \alpha(z') \sin \beta(z')}{cR^2(z')} \quad (8.83)$$

$$\frac{d}{dz'} \left( \frac{z' \sin \theta}{c^2 R(z')} \right) = \frac{\sin \theta + \cos \alpha(z') \sin \beta(z')}{c^2 R(z')} \quad (8.84)$$

The general expression for electric field at an elevation in terms of apparent charge is given by

$$\bar{E}(r, \theta, t) = + \frac{1}{4\pi\epsilon_0} \hat{r} \int_0^{L'(t)} \frac{\cos \beta(z')}{R^2(z')} \rho(z', t - R(z')/c) dz' \quad (8.85a)$$

$$+ \frac{1}{4\pi\epsilon_0} \hat{r} \int_0^{L'(t)} \left[ \frac{3 \cos \beta(z')}{2 cR(z')} + \frac{1}{2} \frac{\cot \theta}{cr} \tan^{-1}(-\cot \alpha(z')) \right] \frac{\partial \rho(z', t - R(z')/c)}{\partial t} dz' \quad (8.85b)$$

$$+ \frac{1}{4\pi\epsilon_0} \hat{r} \int_0^{L'(t)} \frac{\cos \beta(z')}{c^2} \frac{\partial^2 \rho(z', t - R(z')/c)}{\partial t^2} dz' \quad (8.85c)$$

$$+ \frac{1}{4\pi\epsilon_0} \hat{r} \frac{1}{r^2} Q(t - r/c) \quad (8.85d)$$

$$+ \frac{1}{4\pi\epsilon_0} \hat{r} \left[ \frac{3}{2} \frac{1}{cr} + \frac{1}{2} \cot \theta \frac{\tan^{-1}(-\cot \theta)}{cr} \right] \frac{\partial Q(t - r/c)}{\partial t} \quad (8.85e)$$

$$+ \frac{1}{4\pi\epsilon_0} \hat{r} \frac{1}{c^2} \frac{\partial^2 Q(t - r/c)}{\partial t^2} \quad (8.85f)$$

$$+ \frac{1}{4\pi\epsilon_0} \hat{r} \left[ \frac{3 \cos \beta(L')}{2 cR(L')} + \frac{1}{2} \frac{\cot \theta}{cr} \tan^{-1}(-\cot \alpha(L')) \right] \rho(L', t - R(L')/c) \frac{dL'(t)}{dt} \quad (8.85g)$$

$$+ \frac{1}{4\pi\epsilon_0} \hat{r} \frac{\cos \beta(L')}{c^2} \frac{\partial}{\partial t} \left[ \rho(L', t - R(L')/c) \frac{dL'(t)}{dt} \right] \quad (8.85h)$$

$$+ \frac{1}{4\pi\epsilon_0} \hat{\theta} \int_0^{L'(t)} \frac{\sin \beta(L')}{R^2(z')} \rho(z', t - R(z')/c) dz' \quad (8.85i)$$

$$+ \frac{1}{4\pi\epsilon_0} \hat{\theta} \int_0^{L'(t)} \left[ \frac{3 \sin \beta(L')}{2 cR(z')} - \frac{1}{2} \frac{1}{cr} \tan^{-1}(-\cot \alpha(z')) \right] \frac{\partial \rho(z', t - R(z')/c)}{\partial t} dz' \quad (8.85j)$$

$$+ \frac{1}{4\pi\epsilon_0} \hat{\theta} \int_0^{L'(t)} \frac{\sin \beta(z')}{c^2} \frac{\partial^2 \rho(z', t - R(z')/c)}{\partial t^2} dz' \quad (8.85k)$$

$$-\frac{1}{4\pi\epsilon_0}\hat{\theta}\frac{1}{2}\frac{\tan^{-1}(-\cot\theta)}{cr}\frac{\partial Q(t-r/c)}{\partial t} \quad (8.85l)$$

$$+\frac{1}{4\pi\epsilon_0}\hat{\theta}\left[\frac{3\sin\beta(L')}{2}\frac{1}{cR(L')}-\frac{1}{2cr}\tan^{-1}(-\cot\alpha(L'))\right]\rho(L',t-R(L')/c)\frac{dL'(t)}{dt} \quad (8.85m)$$

$$+\frac{1}{4\pi\epsilon_0}\hat{\theta}\frac{\sin\beta(L')}{c^2}\frac{\partial}{\partial t}\left[\rho(L',t-R(L')/c)\frac{dL'(t)}{dt}\right] \quad (8.85n)$$

$$-\frac{1}{4\pi\epsilon_0}\hat{r}\frac{\cos\theta-\cos\alpha(L')\cos\beta(L')}{c^2R(L')}\rho\left(L',t-\frac{R(L')}{c}\right)\left(\frac{dL'}{dt}\right)^2 \quad (8.85o)$$

$$+\frac{1}{4\pi\epsilon_0}\hat{\theta}\frac{\sin\theta+\cos\alpha(L')\sin\beta(L')}{c^2R(L')}\rho\left(L',t-\frac{R(L')}{c}\right)\left(\frac{dL'}{dt}\right)^2 \quad (8.85p)$$

(8.85)

where,  $\cos\alpha(z') = -(z' - r\cos\theta)/R(z')$ ,  $\sin\alpha(z') = r\sin\theta/R(z')$ ,  $\cos\beta(z') = (r - z'\cos\theta)/R(z')$ ,  $\sin\beta(z') = z'\sin\theta/R(z')$  and  $Q$  is given by (8.64). Note also that,  $\tan^{-1}(-\cot(\alpha(z'))) = \pi/2 + \alpha(z')$ . Expression (8.85) do not include the effect of the perfectly conducting ground plane.

### 8.8.3 Magnetic field

It is also possible to derive a general expression for magnetic field in terms of apparent charge, starting from (8.33). As before, each term of integrand of (8.33) can be represented, omitting  $1/(4\pi\epsilon_0c^2)$ , by (8.65), where  $f_2(z', t)$  is the current or the current derivative and the total differential  $df_1(z')$  is any one of the remaining factors and is given by (8.86) and (8.87).

$$d\left(\frac{1}{c}\tan^{-1}\left(\frac{z' - r\cos\theta}{r\sin\theta}\right)\right) = \frac{r\sin\theta}{cR^2(z')}dz' \quad (8.86)$$

$$d\left(\frac{z' - r\cos\theta}{r\sin\theta}\frac{1}{R(z')}\right) = \frac{r\sin\theta}{R^3(z')}dz' \quad (8.87)$$

Function  $df_2(z')$  can be written in terms of charge density using (8.63) and (8.64). Using (8.63) and (8.64), and (8.86) and (8.87) in (8.33), and carrying out the integration between the limits 0 and  $L'(t)$ , we get the general expression for magnetic field at an elevation as in (8.88).

$$B(r, \theta, t) = \frac{1}{4\pi\epsilon_0c^2}\hat{\phi}\int_0^{L'(t)}\left[\frac{\frac{1}{r\sin\theta}\frac{z' - r\cos\theta}{R(z')}}{\frac{\partial\rho(z', t - R(z')/c)}{\partial t}}\right]dz' \quad (8.88a)$$

$$+\frac{1}{4\pi\epsilon_0c^2}\hat{\phi}\int_0^{L'(t)}\left[\frac{\frac{1}{c}\tan^{-1}\left(\frac{z' - r\cos\theta}{r\sin\theta}\right)}{\frac{\partial\rho^2(z', t - R(z')/c)}{\partial t^2}}\right]dz' \quad (8.88b)$$

$$+ \frac{1}{4\pi\epsilon_0 c^2} \hat{\phi} \frac{1}{r \sin \theta} \frac{L'(t) - r \cos \theta}{R(L')} \cdot \rho(L', t - R(L')/c) \frac{dL'(t)}{dt} \quad (8.88c)$$

$$+ \frac{1}{4\pi\epsilon_0 c^2} \hat{\phi} \frac{\cot \theta}{r} \frac{\partial Q(t - r/c)}{\partial t} \quad (8.88d)$$

$$+ \frac{1}{4\pi\epsilon_0 c^2} \hat{\phi} \frac{1}{c} \tan^{-1} \frac{L'(t) - r \cos \theta}{r \sin \theta} \cdot \frac{\partial}{\partial t} \left[ \rho \left( L', t - \frac{R(z')}{c} \right) \frac{dL'(t)}{dt} \right] \quad (8.88e)$$

$$+ \frac{1}{4\pi\epsilon_0 c^2} \hat{\phi} \frac{1}{c} \tan^{-1} (-\cot \theta) \frac{\partial^2 Q(t - r/c)}{\partial t^2} \quad (8.88f)$$

$$+ \frac{1}{4\pi\epsilon_0 c^2} \hat{\phi} \frac{\sin \alpha(L')}{cR(L')} \rho \left( L', t - \frac{R(L')}{c} \right) \left( \frac{dL'}{dt} \right)^2 \quad (8.88g)$$

(8.88)

In (8.88), sum of the terms marked as (a), (c) and (d) corresponds to magnetostatic field component, which is analytically equivalent to the magnetostatic term (first term) of (8.33), sum of the terms marked as (b), (e) and (f) corresponds to the radiation term, which is analytically equivalent to the radiation term (second term) of (8.33), and term marked as (g) is the radiation term corresponding to current discontinuity at the propagating wavefront which is analytically equivalent to the last term of (8.33). Equation (8.88) is new (not found in previous literature). In field (8.85) and (8.88), the apparent charge density is related to the current by (8.59).

### 8.8.4 Image channel

A perfectly conducting plane at  $z' = 0$  can be introduced to simulate the effect of earth. Using the image theory, we can replace this plane by an image channel carrying current in the same direction as the actual channel. The expression for the image channel can be easily obtained from (8.90) and (8.93) by replacing  $z'$  by  $-z'$ ,  $\rho$  by  $-\rho$ , and  $Q$  by  $-Q$ , wherever they appear. Note that the upper limit of integration for the image channel is  $L''$ , which is less than  $L'$  for a field point above ground. As discussed before, expression for  $L''$  can be obtained from the expression for  $L'$  in (8.22) by replacing  $\theta$  by  $(180 - \theta)$ .

Equations (8.85) and (8.32) are analytically equivalent, and the terms analytically equivalent in these equations are shown in Table 8.1.

Table 8.1. Terms analytically equivalent in the electric field expressions (8.85) and (8.32)

Terms in (8.85)	Equivalent terms in (8.32)	Comments
(a) + (d)	(a)	static component along $\hat{r}$
(b) + (e) + (g)	(b)	induction component along $\hat{r}$
(c) + (f) + (h)	(c)	radiation component along $\hat{r}$
(i)	(d)	static component along $\hat{\theta}$
(j) + (l) + (m)	(e)	induction component along $\hat{\theta}$
(k) + (n)	(f)	radiation component along $\hat{\theta}$
(o)	(g)	radiation component along $\hat{r}$ due to source discontinuity at return-stroke wave front
(p)	(h)	radiation component along $\hat{\theta}$ due to source discontinuity at return-stroke wave front

### 8.8.4.1 The moment approximation

Far from the channel, that is, for  $L'(t) \ll r$ , the integral terms of (8.75) and (8.76) readily reduce to the familiar charge-moment approximation (e.g. [20]) given by

$$E_z(r, t) = \frac{-1}{4\pi\epsilon_0} \left[ \frac{M(t)}{r^3} + \frac{1}{cr^2} \frac{dM(t)}{dt} + \frac{1}{c^2r} \frac{d^2M(t)}{dt^2} \right] \quad (8.89)$$

$$B_\phi(r, t) = \frac{1}{4\pi\epsilon_0c^2} \left[ \frac{1}{r} \frac{dM(t)}{dt} + \frac{1}{cr} \frac{d^2M(t)}{dt^2} \right] \quad (8.90)$$

where

$$M(t) = 2 \int_0^H z' \rho_L \left( z', t - \frac{r}{c} \right) dz' \quad (8.91)$$

Note that in (8.75) and (8.76) for  $z' \ll r$ ,  $\tan^{-1}(z'/r) \approx z'/r$  (in radians) and this result is used to arrive at (8.89) and (8.90) from those equations, respectively.

### 8.8.5 Leader electric fields

In the following, electric field change at ground level due to a vertically descending leader from a concentrated charge source in the cloud is derived in terms of ‘apparent charge density.’

#### 8.8.5.1 Exact expressions

The electric field at ground level due to a descending leader can also be obtained from (8.69). The leader is assumed to be an extending discharge propagating down from a charge centre at height  $H_m$  (Figure 8.12). The observer ‘sees’ the lower end of the leader at a height  $h(t)$  given by the solution of

$$t = \frac{H_m - h(t)}{v} + \frac{\sqrt{h^2(t) + r^2}}{c} \quad (8.92)$$

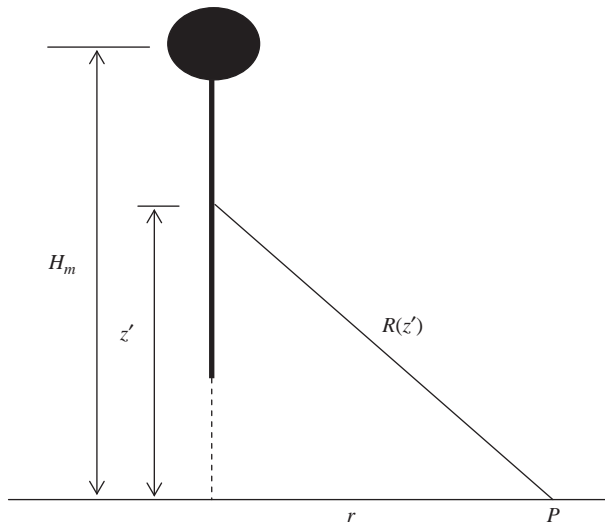


Figure 8.12 Geometry used in deriving the expressions for electric fields at a point P on earth a horizontal distance  $r$  from the vertical lightning leader channel extending downward

The total leader electric field is given by integrating (8.69) along the channel from  $h(t)$  to  $H_m$  and is given by where  $t^* = t - R(z')/c$ .

$$\begin{aligned}
 E_z(r, t) = & + \frac{1}{2\pi\epsilon_0} \int_{h(t)}^{H_m} \frac{z'}{R^3(z')} \rho(z', t^*) dz' \\
 & + \frac{1}{2\pi\epsilon_0} \int_{h(t)}^{H_m} \left( \frac{3}{2} \frac{z'}{cR^2(z')} - \frac{1}{2} \frac{\tan^{-1}(z'/r)}{cr} \right) \frac{\partial \rho(z', t^*)}{\partial t} dz' \\
 & + \frac{1}{2\pi\epsilon_0} \int_{h(t)}^{H_m} \frac{z'}{c^2 R(z')} \frac{\partial^2 \rho(z', t^*)}{\partial t^2} dz' - \frac{1}{2\pi\epsilon_0} \frac{H_m}{R^3(H_m)} \int_{h(t)}^{H_m} \rho(z', t^*) dz' \\
 & - \frac{1}{2\pi\epsilon_0} \left( \frac{3}{2} \frac{H_m}{cR^2(H_m)} - \frac{1}{2} \frac{\tan^{-1}(H_m/r)}{cr} \right) \cdot \frac{d}{dt} \int_{h(t)}^{H_m} \rho(z', t^*) dz' \\
 & - \frac{1}{2\pi\epsilon_0} \left( \frac{3}{2} \frac{h(t)}{cR^2(h)} - \frac{1}{2} \frac{\tan^{-1}(h(t)/r)}{cr} \right) \rho \left( h(t), \frac{h(t)}{v} \right) \frac{dh(t)}{dt} \\
 & - \frac{1}{2\pi\epsilon_0} \frac{H_m}{c^2 R(H_m)} \frac{d^2}{dt^2} \int_{h(t)}^{H_m} \rho(z', t^*) dz' - \frac{1}{2\pi\epsilon_0} \frac{h(t)}{c^2 R(h)} \frac{\partial}{\partial t} \left[ \rho \left( h(t), \frac{h(t)}{v} \right) \frac{dh(t)}{dt} \right]
 \end{aligned} \tag{8.93}$$

### 8.8.5.2 Electrostatic approximation

As an example of the application of the leader field expression in terms of charge density, consider the electrostatic approximation for the leader electric field, expected to be applicable to close lightning. The first and fourth term of (8.90) represent the static terms, the first term represents the field change at ground due to apparent charge on the leader channel, and the fourth term represents the field change due to the depletion of the charge at the charge source as it is drained by the extending leader. The total charge on the leader channel at any time is equal to the total charge drained from the charge source in the cloud up to that time. The time retardation effects can be neglected if the difference in travel times between sources on the channel and the remote observer is much less than the time required for significant variation in the sources. In that case the charge and the apparent charge, defined by (8.48) and (8.49), become identical. Neglecting retardation effects we can combine the first and fourth terms of (8.90) as

$$E_z(r, t) = \frac{-1}{2\pi\epsilon_0} \int_{H_m}^{z_t} \left[ \frac{z'}{R^3(z')} - \frac{H_m}{R^3(H_m)} \right] \rho(z', t) dz' \tag{8.94}$$

where  $z_t = H - vt$  is the height of the leader tip at time  $t$  and  $v$  is the leader speed assumed to be a constant.

### 8.9 Calculation of fields from lightning return stroke

The commonly used engineering models of the return stroke gives the spatial and temporal variation of the current along the return stroke channel. Once the source distribution is specified, the remote electric fields and magnetic fields can be calculated from any one of the three different, but equivalent and exact, methods presented in this chapter. The electric field is expressed in terms of the current in (8.32), in terms of both the current and local charge density in (8.44), and in terms of apparent charge density in (8.85). The magnetic field is expressed in (8.55) in terms of current, and in (8.88) in terms of apparent charge density. Expressions (8.32), (8.33), (8.44), (8.85) and (8.88) do not take into account the presence of the conducting ground. The effect of the ground plane, assumed to be perfectly conducting, on the fields can be modelled by replacing the ground plane by an image channel. It has been explained before how the expressions for the fields from the image channel can be readily written from (8.32), (8.33), (8.44), (8.85) and (8.88).

A number of measurements of the return stroke current waveform  $i(0, t)$  at the base of the channel and the speed  $v$  of the return stroke wavefront are available. Therefore in calculating the electromagnetic fields from the return stroke the channel-base current and speed are used as inputs. The current, local charge, and the apparent charge along the channel for different return stroke models, for use in (8.32), (8.44) and (8.85) are summarised below. In addition to the known channel base current and return stroke speed some additional parameters such as discharge time constant  $\tau$ , current attenuation constant  $\lambda$ , and cloud charge centre height  $H$  are required for some of the models.

*Bruce-Golde model (BG):*

$$i(z', t - R(z')/c) = i(0, t - R(z')/c) \tag{8.95}$$

$$\rho^*(z', t - R(z')/c) = \frac{i(0, z'/v)}{v} \tag{8.96}$$

$$\rho(z', t - R(z')/c) = i(0, z'/v) \cdot \left[ \frac{1}{v \cdot F(z')} + \frac{1}{c \cdot F_{BG}(z')} \right] - \frac{i(0, t - R(z')/c)}{c \cdot F_{BG}(z')} \tag{8.97}$$

where

$$F(z') = \frac{1}{1 - \frac{v}{c} \cos \alpha(z')} \quad \text{and} \quad F_{BG}(z') = \frac{1}{\cos \alpha(z')} \tag{8.98}$$

*Travelling current source model (TCS):*

$$i(z', t - R(z')/c) = i(0, t + z'/c - R(z')/c) \tag{8.99}$$

$$\rho^*(z', t - R(z')/c) = \frac{i(0, z'/v^*)}{v^*} - \frac{i(0, t + z'/c - R(z')/c)}{c} \tag{8.100}$$

$$\rho(z', t - R(z')/c) = i(0, z'/v^*) \cdot \left[ \frac{1}{v \cdot F(z')} + \frac{1}{c \cdot F_{TCS}(z')} \right] - \frac{i(0, t + z'/c - R(z')/c)}{c \cdot F_{TCS}(z')} \tag{8.101}$$

where

$$v^* = \frac{v}{1 + v/c} \quad (8.102)$$

$$F_{TCS}(z') = \frac{1}{1 + \cos \alpha(z')} \quad (8.103)$$

and  $F(z')$  is given by (G4).

*Diendorfer-Uman model (DU):*

$$i(z', t - R(z')/c) = i(0, t + z'/c - R(z')/c) - i(0, z'/v^*) \cdot e^{-(t - \frac{z'}{v} - \frac{R(z')}{c})/\tau_D} \quad (8.104)$$

$$\begin{aligned} \rho^*(z', t - R(z')/c) &= \frac{i(0, z'/v^*)}{v^*} + \frac{\tau_D}{v^*} \frac{di(0, z'/v^*)}{dt} - \frac{i(0, t + z'/c - R(z')/c)}{c} \\ &\quad - e^{-(t - \frac{z'}{v} - \frac{R(z')}{c})/\tau_D} \cdot \left[ \frac{\tau_D}{v^*} \frac{di(0, z'/v^*)}{dt} + \frac{i(0, z'/v^*)}{v} \right] \end{aligned} \quad (8.105)$$

$$\begin{aligned} \rho(z', t - R(z')/c) &= i(0, z'/v^*) \cdot \left[ \frac{1}{v \cdot F(z')} + \frac{1}{c \cdot F_{TCS}(z')} \right] \\ &\quad + \frac{\tau_D}{v^*} \frac{di(0, z'/v^*)}{dt} - \frac{i(0, t + z'/c - R(z')/c)}{c \cdot F_{TCS}(z')} \\ &\quad - e^{-(t - \frac{z'}{v} - \frac{R(z')}{c})/\tau_D} \cdot \left[ \frac{\tau_D}{v^*} \frac{di(0, z'/v^*)}{dt} + \frac{i(0, z'/v^*)}{v \cdot F(z')} \right] \end{aligned} \quad (8.106)$$

where  $v^*$ ,  $F_{TCS}(z')$  and  $F(z')$  are given by (8.102), (8.103) and (8.98), respectively.

*Transmission Line (TL) model:*

$$i(z', t - R(z')/c) = i(0, t - z'/v - R(z')/c) \quad (8.107)$$

$$\rho^*(z', t - R(z')/c) = \frac{i(0, t - z'/v - R(z')/c)}{v} \quad (8.108)$$

$$\rho(z', t - R(z')/c) = \frac{i(0, t - z'/v - R(z')/c)}{v \cdot F(z')} \quad (8.109)$$

where  $F(z')$  is given by (8.98).

*Modified Transmission Line Model-Linear (MTLL):*

$$i(z', t - R(z')/c) = i(0, t - z'/v - R(z')/c) \cdot (1 - z'/H) \quad (8.110)$$

$$\rho^*(z', t - R(z')/c) = (1 - z'/H) \cdot \frac{i(0, t - z'/v - R(z')/c)}{v} + \frac{Q(z', t - R(z')/c)}{H} \quad (8.111)$$

$$\rho(z', t - R(z')/c) = (1 - z'/H) \cdot \frac{i(0, t - z'/v - R(z')/c)}{v \cdot F(z')} + \frac{Q(z', t - R(z')/c)}{H} \quad (8.112)$$

where

$$Q(z', t - R(z')/c) = \int_{z'/v + R(z')/c}^t i(0, \tau - z'/v - R(z')/c) d\tau$$

Modified Transmission Line Model-Exponential (MTLE):

$$i(z', t - R(z')/c) = i(0, t - z'/v - R(z')/c) \cdot e^{-z'/\lambda} \tag{8.113}$$

$$\rho^*(z', t - R(z')/c) = e^{-z'/\lambda} \cdot \frac{i(0, t - z'/v - R(z')/c)}{v} + e^{-z'/\lambda} \cdot \frac{Q(z', t - R(z')/c)}{\lambda} \tag{8.114}$$

$$\rho(z', t - R(z')/c) = e^{-z'/\lambda} \cdot \frac{i(0, t - z'/v - R(z')/c)}{v \cdot F(z')} + e^{-z'/\lambda} \cdot \frac{Q(z', t - R(z')/c)}{\lambda} \tag{8.115}$$

### 8.9.1 Numerical calculation of fields at different elevations and distances from the lightning return stroke

Numerical calculation of fields at different elevation and distance from the lightning return stroke is presented in this section. The equivalence between the electric field expressions derived using the Lorentz condition technique (dipole technique) and the continuity equation technique (monopole technique) has been numerically established in [5, 11]. Verification of the equivalence between the general field expressions at an elevation using the current formulation and apparent charge formulation is also presented in this section. Electric fields at different angles from the vertical, at different distances from channel-base and for different return stroke speeds are calculated using (8.32) and (8.85), including the images to take into account the effect of a perfectly conducting ground. Similarly, magnetic fields at different angles from the vertical, different distances from channel-base and different return stroke speeds are calculated using (8.33) and (8.88), including the images to take into account the effect of a perfectly conducting ground. The transmission line (TL) model of the return stroke is used for computations. A spherical coordinate system, with origin at the base of the channel, is used for defining the field components in the  $\hat{r}$ ,  $\hat{\theta}$ , and  $\hat{\phi}$  direction (Figure 8.6).

### 8.9.2 Electric fields

Figures 8.13–8.19 show the electric fields above a perfectly conducting ground at distances 100 m, 1000 m, and 100 km from the channel base of the return stroke for various angles 10°, 30°, 60° and 90° (ground level) with respect to vertical. Assumed return stroke speed is  $1.5 \times 10^8$  m/s for results presented in Figures 8.13–8.15,  $2.7 \times 10^8$  m/s for results in Figures 8.16–8.18, and  $3 \times 10^8$  m/s (speed of light; the upper-bound case) for results in Figure 8.19. Electric fields for the speed of light were calculated using the simple exact expression derived in Thottappillil *et al.* [3, 9] given by

$$\bar{E}(r, \theta, t) = \hat{\theta} \frac{1}{2\pi\epsilon_0 cr \sin \theta} i(0, t - r/c) \tag{8.116}$$



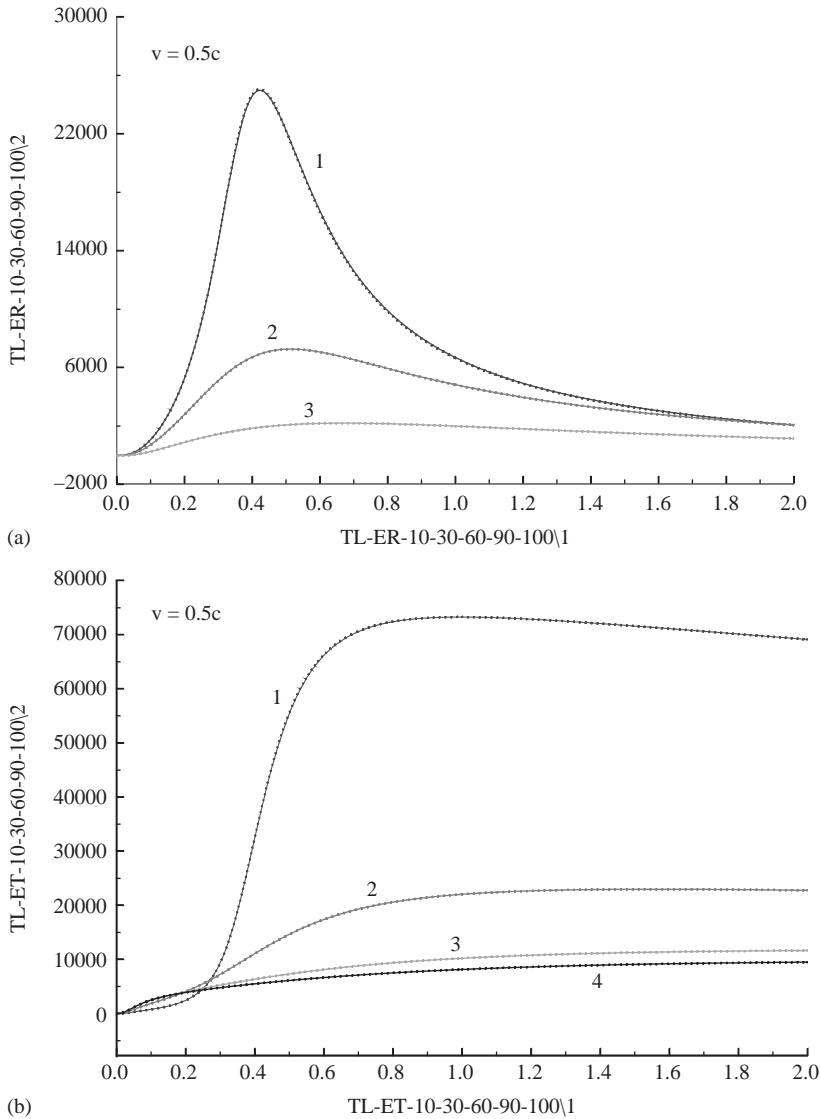


Figure 8.13 *E*-field predicted by the TL model for return stroke speed  $v = 0.5c$ , above perfectly conducting ground at a distance of 100 m from channel-base. Solid line – current formulation, dotted line – apparent charge formulation. The two types of lines (fields for two formulations) are indistinguishable in the plot. 1 –  $10^\circ$ , 2 –  $30^\circ$ , 3 –  $60^\circ$ , 4 –  $90^\circ$ . Angle is measured with respect to vertical (Figure 8.6). Time in  $\mu\text{s}$  on the x-axis and *E*-field in  $\text{V/m}$  on the y-axis. (a) The *r*-component of *E*-field. The *r*-component is zero at  $90^\circ$  and hence not shown. (b) The  $\theta$ -component of *E*-field

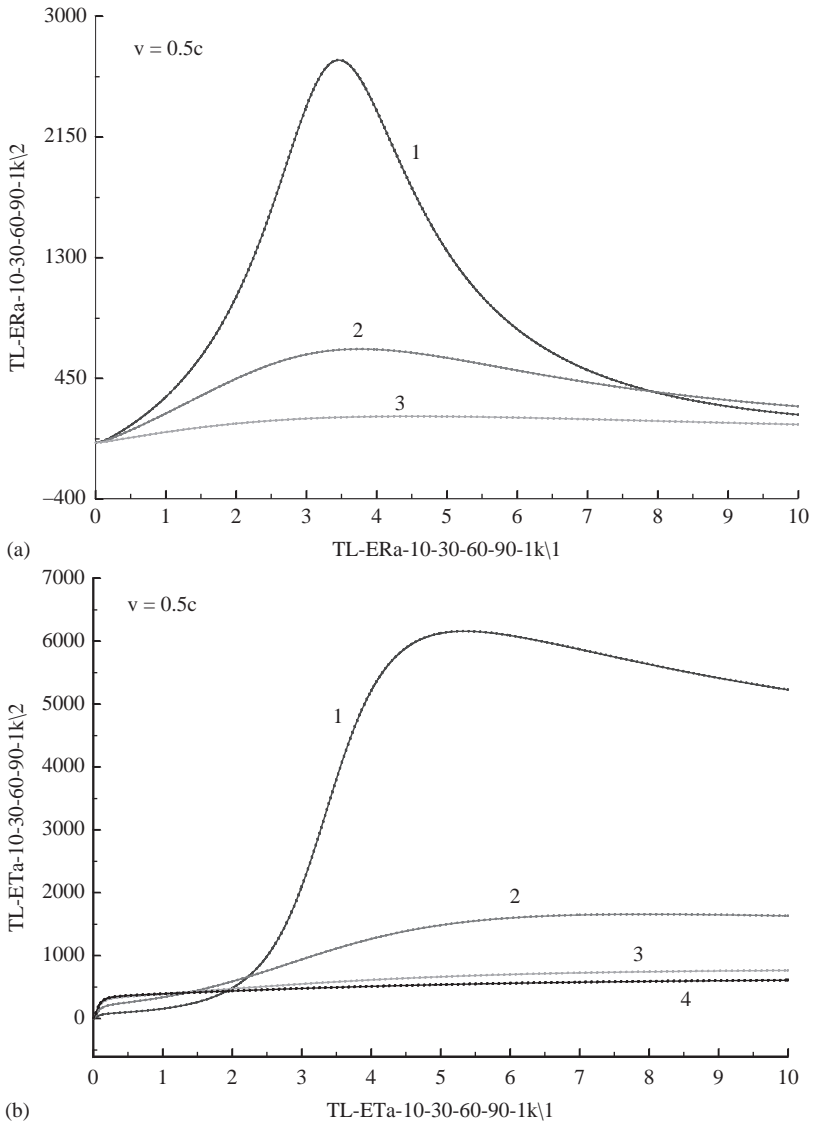


Figure 8.14 *E*-field predicted by the TL model for return stroke speed  $v = 0.5c$ , above perfectly conducting ground at a distance of 1000 m from channel-base. Solid line – current formulation, dotted line – apparent charge formulation. The two types of lines (fields for two formulations) are indistinguishable in the plot. 1 – 10°, 2 – 30°, 3 – 60°, 4 – 90°. Angle is measured with respect to vertical (Figure 8.6). Time in  $\mu\text{s}$  on the x-axis and *E*-field in  $\text{V/m}$  on the y-axis. (a) The  $r$ -component of *E*-field. The  $r$ -component is zero at 90° and hence not shown. (b) The  $\theta$ -component of *E*-field

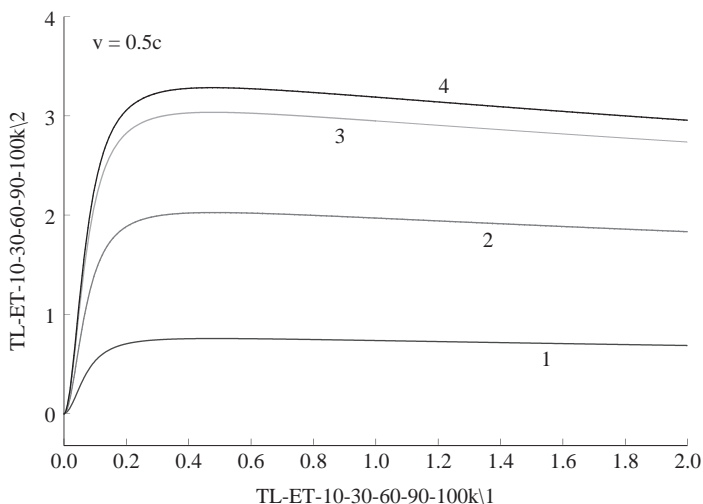


Figure 8.15 The  $\theta$ -component of  $E$ -field predicted by the TL model for return stroke speed  $v = 0.5c$ , above perfectly conducting ground at a distance of 100 km from channel-base. Solid line – current formulation, dotted line – apparent charge formulation. The two types of lines (fields for two formulations) are indistinguishable in the plot. 1 –  $10^\circ$ , 2 –  $30^\circ$ , 3 –  $60^\circ$ , 4 –  $90^\circ$ . Angle is measured with respect to vertical (Figure 8.6). Time in  $\mu\text{s}$  on the  $x$ -axis and  $E$ -field in  $\text{V/m}$  on the  $y$ -axis

For the case of TL model, (8.116) is equivalent to the sum of (8.32) and similar equation applicable for the image channel. The channel-base current used in all the calculations presented in this paper are that given by Nucci *et al.* [21], which has a peak of about 11 kA and maximum current rate of rise of  $110 \text{ kA}/\mu\text{s}$ , which are thought to be representative of subsequent return strokes. The  $r$ -component of the electric field at a distance of 100 km is very small or zero and hence not presented. The vertical and horizontal  $E$ -fields ( $E_v$  and  $E_H$ , respectively) can be obtained from the calculated  $r$ -component and  $\theta$ -component of the  $E$ -fields ( $E_r$  and  $E_\theta$ , respectively) as

$$\begin{aligned} E_v &= E_r \cos \theta - E_\theta \sin \theta \\ E_H &= E_r \sin \theta + E_\theta \cos \theta \end{aligned} \quad (8.117)$$

In Figures 8.13–8.18, fields calculated using the current formulation (solid line) is the same as that calculated using the apparent charge formulation (dotted line), verifying the equivalence between (8.32) and (8.85). Table 8.2 summarises the peak electric fields as a function of angle from the vertical, return stroke speed, and distance from channel-base. At close distances (100 and 1000 m), both the  $r$ -component and  $\theta$ -component have the largest peak value at small angles for all return stroke speeds. However, at a far distance of 100 km, where the field is almost entirely due to radiation, the  $r$ -component is negligible and the  $\theta$ -component has the largest peak value at  $90^\circ$  at lower speeds ( $v = 1.5 \times 10^8 \text{ m/s}$ ) and the smallest peak value at  $90^\circ$  for the limiting speed equal to the speed of light. At a speed of

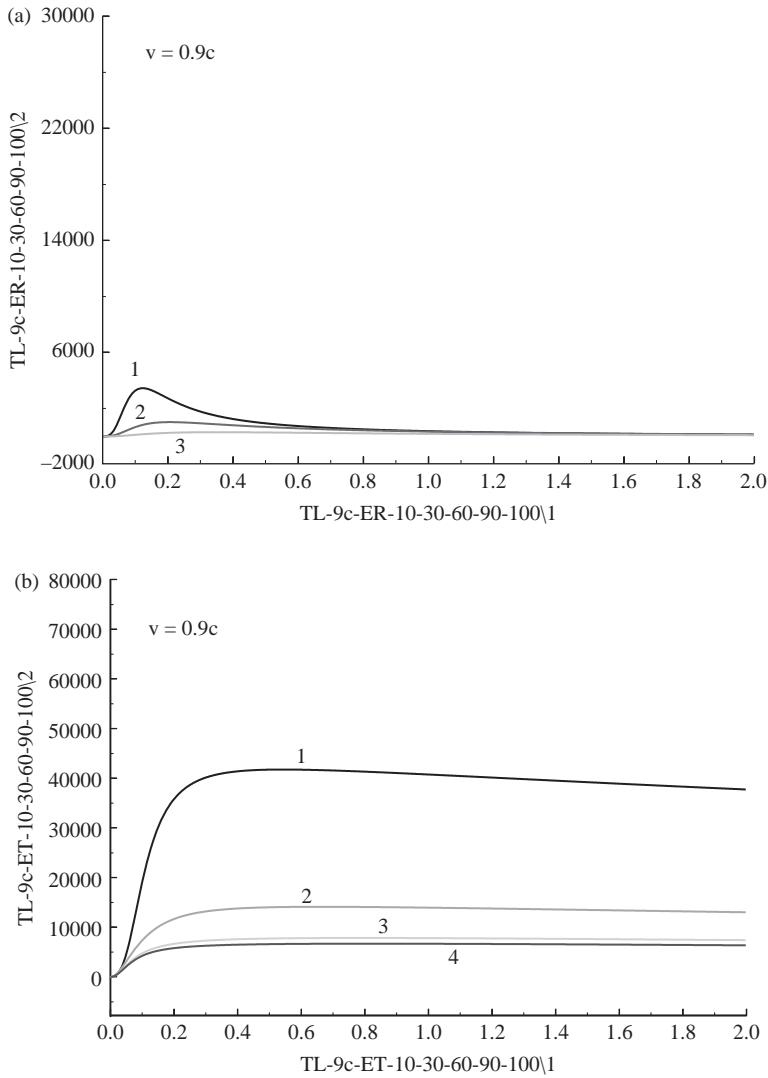


Figure 8.16  $E$ -field predicted by the TL model for return stroke speed  $v = 0.9c$ , above perfectly conducting ground at a distance of 100 m from channel-base. Other details are as in the caption of Figure 8.13. (a) The  $r$ -component of the  $E$ -field. Note the substantial reduction in the  $r$ -component field with increased speed. (b) The  $\theta$ -component of  $E$ -field

$2.7 \times 10^8$  m/s, the maximum radiation is at an angle between  $10^\circ$  and  $90^\circ$ . The existence of a critical angle lower than  $90^\circ$  at which the far radiated field attains a maximum has been discussed in Krider [22], Thottappillil *et al.* [9] and Rakov and Tuni [23]. Also, at closer distances (100 and 1000 m), the peak electric fields decreases with increasing return stroke speed whereas at far distance there is an opposite trend in which the far fields increase dramatically with increasing speed. The linear dependence of the far field peak on the speed of the return stroke is valid

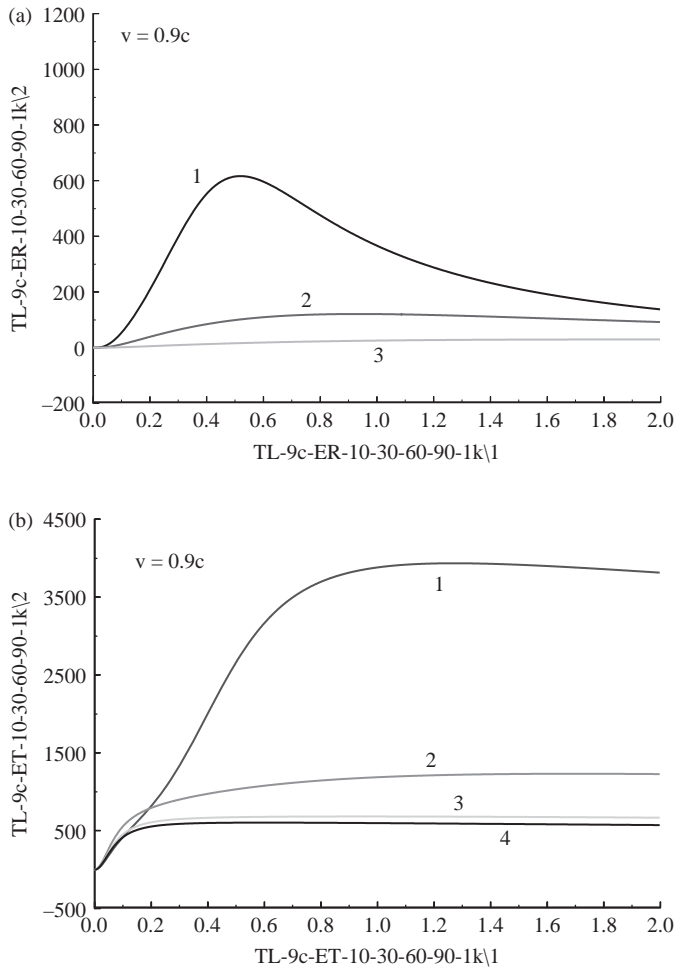


Figure 8.17 *E*-field predicted by the TL model for return stroke speed  $v = 0.9c$ , above perfectly conducting ground at a distance of 1000 m from channel-base. Other details are as in the caption of Figure 8.14. (a) The  $r$ -component of *E*-field. (b) The  $\theta$ -component of *E*-field

only for  $\theta = 90^\circ$ . At other angles, the dependence of the far field peak on the speed is complicated and much stronger than the linear dependence would suggest. For example, at  $10^\circ$ , changing the speed from  $v = 0.5c$  to  $v = c$  increases the field peak by a factor of 50.

### 8.9.3 Magnetic fields

Magnetic fields are calculated using (8.33) expressed completely in terms of current and (8.88) expressed completely in terms of apparent charge density. As before the TL model of return stroke is assumed. The effect of a perfectly conducting ground plane is added in all calculations. Figures 8.20–8.25 show the complete

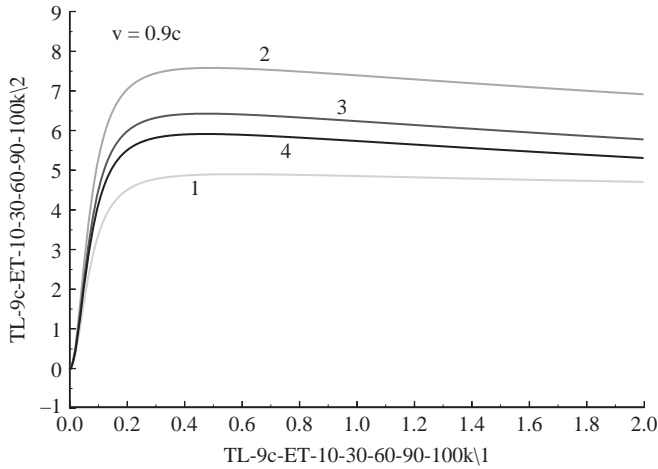


Figure 8.18 The  $\theta$ -component of E-field predicted by the TL model for return stroke speed  $v = 0.9c$ , above perfectly conducting ground at a distance of 100 km from channel-base. Other details are as in the caption of Figure 8.15

Table 8.2a Peak electric fields in V/m as a function of angle and return stroke speed at a distance of 100 m from channel-base as predicted by TL model

Angle from vertical	$E_\theta$ at 100 m			$E_r$ at 100 m		
	$v = 0.5c$ Figure 8.14b	$v = 0.9c$ Figure 8.17b	$v = c$ Figure 8.20	$v = 0.5c$ Figure 8.14a	$v = 0.9c$ Figure 8.17a	$v = c$
10°	73 300	41 800	37 828	25 000	3500	0
30°	23 000	14 100	13 137	7280	1030	0
60°	11 700	7800	7585	2220	306	0
90°	9500	6700	6569	0	0	0

Table 8.2b Peak electric fields in V/m as a function of angle and return stroke speed at a distance of 1000 m from channel-base as predicted by TL model

Angle from vertical	$E_\theta$ at 1000 m			$E_r$ at 1000 m		
	$v = 0.5c$ Figure 8.15	$v = 0.9c$ Figure 8.18	$v = c$ Figure 8.20	$v = 0.5c$ Figure 8.15	$v = 0.9c$ Figure 8.18	$v = c$
10°	6160	3900	3783	2690	617	0
30°	1656	1230	1314	657	121	0
60°	760	684	758	184	30	0
90°	603	605	657	0	0	0

Table 8.2c Peak electric fields in V/m as a function of angle and return stroke speed at a distance of 100 km from channel-base as predicted by TL model

Angle from vertical	$E_\theta$ at 100 km			$E_r$ at 100 km		
	$v = 0.5c$ Figure 8.16	$v = 0.9c$ Figure 8.19	$v = c$ Figure 8.20c	$v = 0.5c$	$v = 0.9c$	$v = c$
10°	0.76	4.9	38	—	—	0
30°	2.0	7.6	13	—	—	0
60°	3.0	6.4	7.6	—	—	0
90°	3.3	5.9	6.6	0	0	0

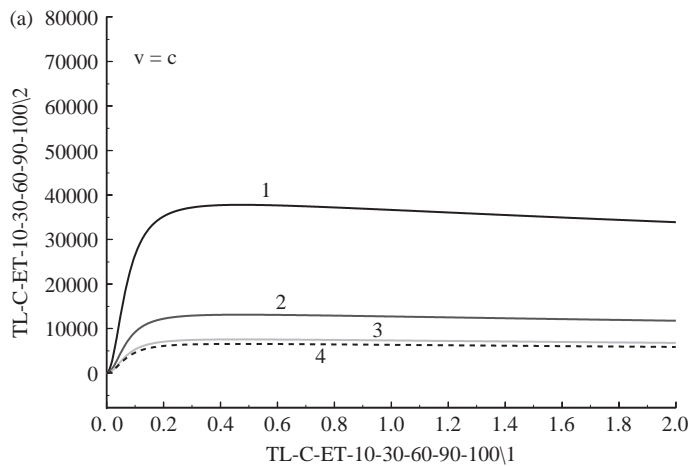


Figure 8.19 The  $\theta$ -component of the E-field predicted by the TL model for return stroke speed  $v = c$  (the upper-bound case), above perfectly conducting ground. The  $r$ -components are identically zero at all angles. (a) At a distance of 100 m from channel-base. (b) At a distance of 1000 m from channel-base. (c) At a distance of 100 km from channel-base

agreement between the current formulation (solid line) and apparent charge formulation (dashed line). Magnetic fields at a return stroke speed equal the speed of light (the upper-bound case), and assuming the TL model, can be calculated using an exact simplified expression given by Thottappillil *et al.* [3, 8] as in (8.118).

$$\bar{B} = \hat{\phi} \frac{1}{2\pi\epsilon_0 c^2 r \sin \theta} i(0, t - r/c) \tag{8.118}$$

Equation (8.118) is equivalent to the sum of (8.32) and similar equation for the image channel. Comparing (8.116) and (8.118) it can be seen that ratio of  $E/B$  is equal to the speed of light at all angles and distances. Therefore, magnetic fields for

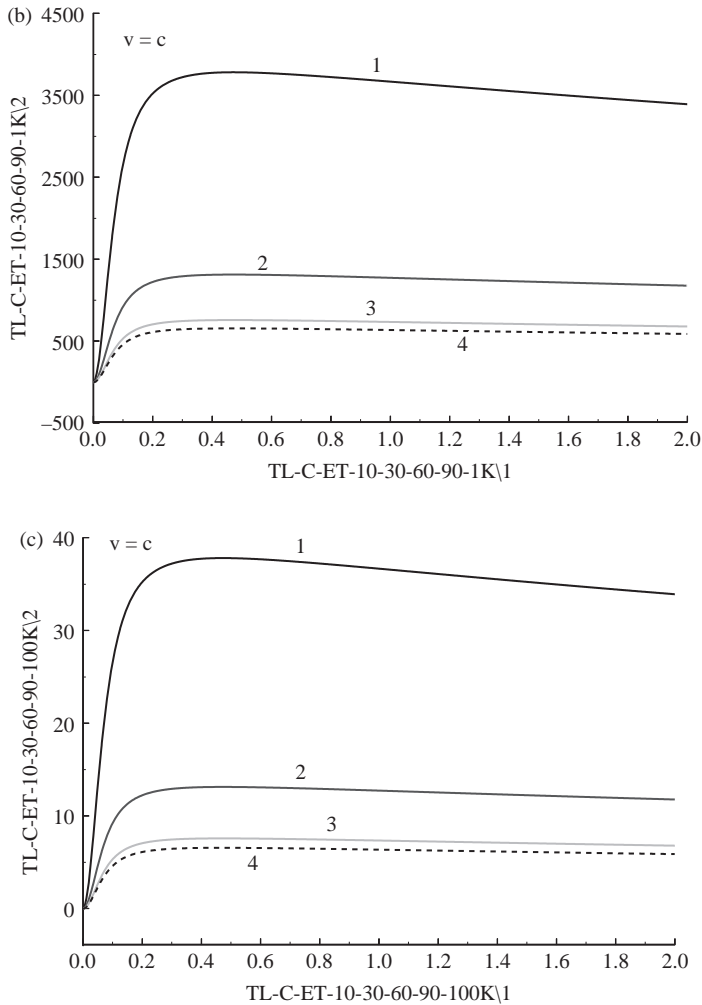


Figure 8.19 (Continues)

return stroke speed equal to the speed of light are similar in shape to the electric fields shown in Figure 8.19 and also to the channel-base current, provided TL model of return stroke is assumed.

At close distances (100 and 1000 m) magnetic field has the largest peak value at small angles for all return stroke speeds. However, at a far distance of 100 km, where the field is almost entirely due to radiation, the magnetic field has the largest peak value at 90° at lower speeds ( $v = 1.5 \times 10^8$  m/s) and the smallest peak value at 90° for the limiting value of speed equal to the speed of light. At a speed of  $2.7 \times 10^8$  m/s, the maximum radiation is at an angle between 10° and 90°.

As mentioned earlier, the TL model is used for the numerical calculations for the fields at an elevation presented in Figures 8.13–8.25 for the current formulation and the apparent charge formulation. The authors have also compared the numerical calculations for the two formulations using other types of return stroke models, namely, the modified transmission line model with exponential decay (MTLE) as



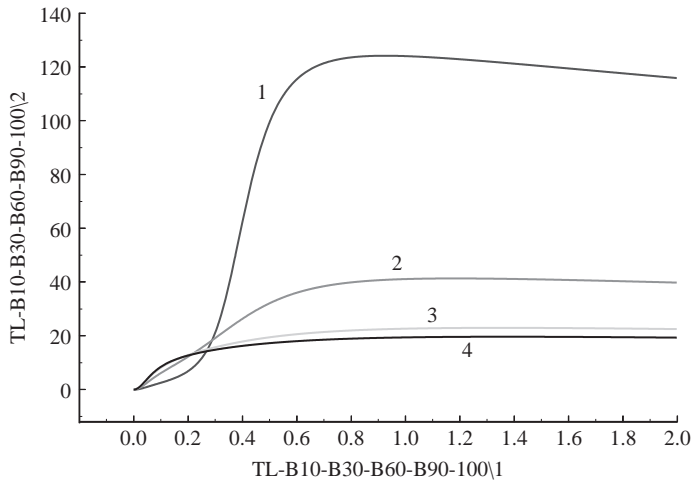


Figure 8.20 The magnetic field predicted by the TL model for return stroke speed  $v = 0.5c$ , above perfectly conducting ground at a distance of 100 m from channel-base. Solid line – current formulation, dotted line – apparent charge formulation. The two types of lines (fields for two formulations) are indistinguishable in the plot. 1 – 10°, 2 – 30°, 3 – 60°, 4 – 90°. Angle is measured with respect to vertical (Figure 8.6). Time in  $\mu\text{s}$  on the x-axis and E-field in V/m on the y-axis

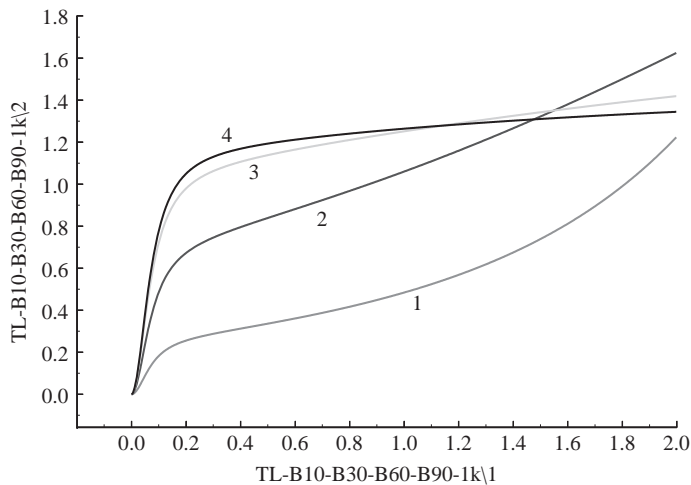


Figure 8.21 The magnetic field predicted by the TL model for return stroke speed  $v = 0.5c$ , above perfectly conducting ground at a distance of 1000 m from channel-base. Solid line – current formulation, dotted line – apparent charge formulation. The two types of lines (fields for two formulations) are indistinguishable in the plot. 1 – 10°, 2 – 30°, 3 – 60°, 4 – 90°. Angle is measured with respect to vertical (Figure 8.6). Time in  $\mu\text{s}$  on the x-axis and E-field in V/m on the y-axis

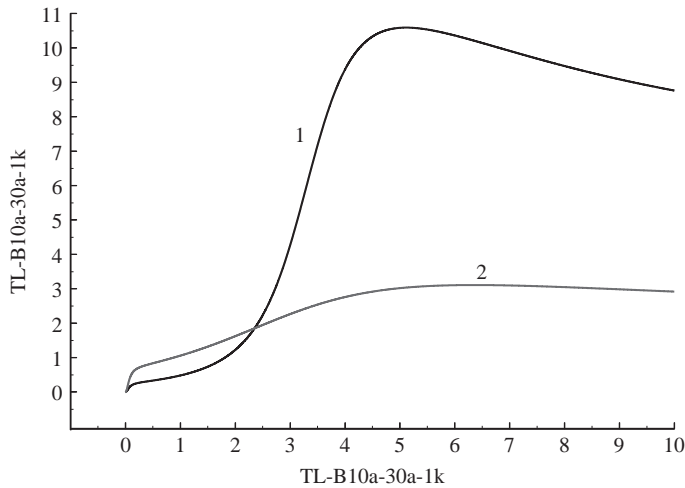


Figure 8.22 Same as in Figure 8.21, but  $\theta = 10^\circ$  and  $\theta = 30^\circ$  shown on a time scale of  $10 \mu\text{s}$

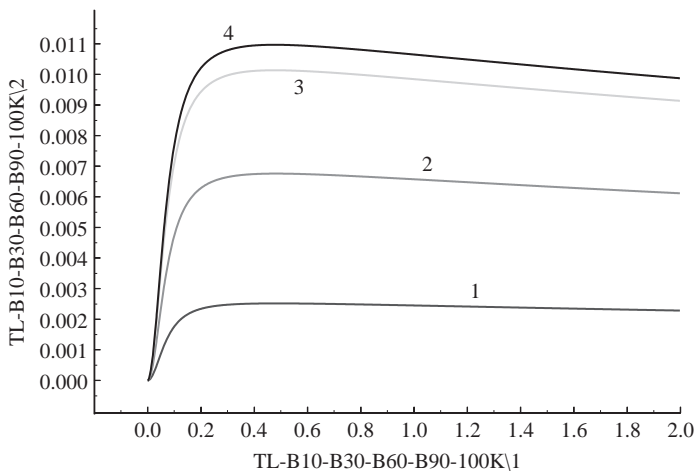


Figure 8.23 The magnetic field predicted by the TL model for return stroke speed  $v = 0.5c$ , above perfectly conducting ground at a distance of 100 km from channel-base. Solid line – current formulation, dotted line – apparent charge formulation. The two types of lines (fields for two formulations) are indistinguishable in the plot. 1 –  $10^\circ$ , 2 –  $30^\circ$ , 3 –  $60^\circ$ , 4 –  $90^\circ$ . Angle is measured with respect to vertical (Figure 8.6). Time in  $\mu\text{s}$  on the x-axis and E-field in V/m on the y-axis

well as linear decay (MTLL), and the Travelling Current Source (TCS) model. Excellent agreement was obtained for the fields from the two formulations in those cases also. Thus, the equivalence between (8.32) and (8.85), and also between (8.33) and (8.88) is shown both analytically and numerically.

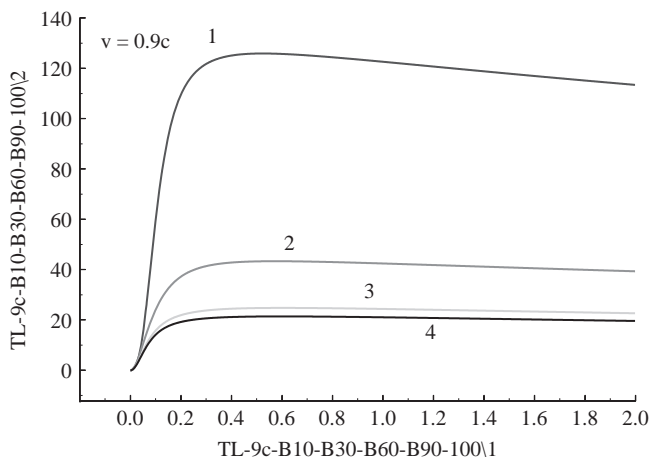


Figure 8.24 *The magnetic field predicted by the TL model for return stroke speed  $v = 0.9c$ , above perfectly conducting ground at a distance of 100 m from channel-base. Other details are as in the caption of Figure 8.20*

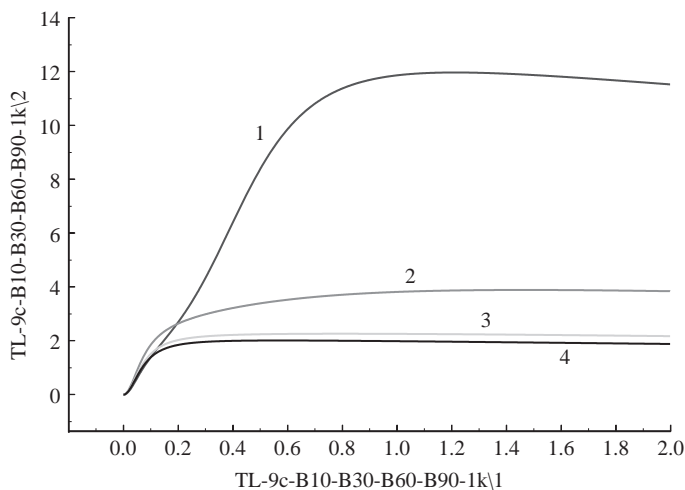


Figure 8.25 *The magnetic field predicted by the TL model for return stroke speed  $v = 0.9c$ , above perfectly conducting ground at a distance of 1000 m from channel-base. Other details are as in the caption of Figure 8.21*

### 8.10 Transmission line model of the return stroke

The transmission line (TL) model of the lightning return stroke [24], has been widely used to calculate return stroke currents and current derivatives from measured electric fields and electric field derivatives (e.g. [6, 25]). This model is interesting because many kilometres from the return stroke where the radiation field term of (8.34) and (8.45) are dominant, the measured fields and field derivatives were directly proportional to the current and current derivative, respectively, of the return stroke current at the base of the channel. The TL model is characterised by a non-attenuating travelling current on the channel described by

(8.107). The approximate relationship between remote fields at ground ( $\theta = \pi/2$  in Figure 8.6) and currents are given by

$$i(0, t) \approx -\frac{2\pi\epsilon_0 c^2 r}{v} E_{far}(r, t + r/c) \quad (8.119)$$

and

$$\frac{\partial i(0, t)}{\partial t} \approx -\frac{2\pi\epsilon_0 c^2 r}{v} \frac{\partial E_{far}(r, t + r/c)}{\partial t} \quad (8.120)$$

Equations (8.119) and (8.120) are good approximations in the far field and at ground where the static and induction terms of the total field are negligible and if (8.119) and (8.120) are only used up to the peak value of the field/current waveform. These equations are the basis of the estimation of peak lightning return stroke currents by remote detection of electric and magnetic field by the lightning location system. The validity of (8.119) and (8.120) has been tested by several authors (e.g. [26–28]). However, there are several drawbacks for the above simple equations. First, the return stroke speed  $v$  is generally not known for a given return stroke. Second, the attenuation due to finite conductivity of the earth is not taken into account. Third, these equations are not considered to be valid near to the lightning channel where the static and induction terms can not be neglected.

Krider [22] has shown that for the transmission line model of the return stroke with a speed  $v$  and with the presence of ground taken into account, the far field at an elevation angle  $\theta$  from vertical is given by

$$\bar{E}(r, \theta, t) = \frac{v \sin \theta}{2\pi\epsilon_0 c^2 r \left(1 - \frac{v^2}{c^2} \cos^2 \theta\right)} i(0, t - r/c) \hat{\theta} \quad (8.121)$$

Krider [22] also showed (8.121) implies that for speeds less than  $2.1 \times 10^8$  m/s, the maximum field is radiated along the ground surface (corresponding to  $\theta = 90^\circ$ ), and for speeds in excess the maximum field is radiated at an angle between  $90^\circ$  and  $0^\circ$ , closer to  $0$  as the speed approaches the speed of light.

### 8.10.1 Pulse propagation on a vertical wire antenna above a conducting plane: exact formulation

The exact expression for the electric and magnetic fields (8.32) and (8.33) from a time-varying current or charge density distribution behind an upward travelling lightning return stroke wavefront is derived in earlier sections of this chapter. It can be shown that if the source is a current pulse that travels upward with the speed of light and without any attenuation and dispersion, then the exact expressions for electric field and magnetic field, from that part of the antenna above the ground plane (not including the effects of the ground plane) reduces to simple expressions [3] given by

$$\bar{E}(r, t) = \frac{-1}{4\pi\epsilon_0 r^2} \int_{r/c}^t i(0, \tau - r/c) d\tau \hat{r} + \frac{(1 + \cos \theta)}{4\pi\epsilon_0 c r \sin \theta} i(0, t - r/c) \hat{\theta}, \quad \theta \neq 0 \quad (8.122)$$

$$B_\phi(r, \theta, t) = \frac{1 + \cos \theta}{4\pi\epsilon_0 c^2 r \sin \theta} i(0, t - r/c), \quad \theta \neq 0 \quad (8.123)$$

Equations (8.122) and (8.123) can be derived from (8.32) and (8.33), respectively, by applying (8.107) for a travelling current pulse with speed  $v = c$ , the speed of light. The first term in (8.122) is independent of the angle  $\theta$  and can be viewed as the field created due to the depletion of a point charge at the base of the channel. If the vertical line is above a perfectly conducting ground plane, then the effect of the ground plane on the fields above can be taken into account by replacing the ground plane by an image line perpendicular to the ground plane and beneath it carrying an equal current in the same direction. Adding to the fields in (8.122) and (8.123), the contributions from the image channel, we obtain the expressions for total electric and magnetic fields [8] as

$$\bar{E}(r, \theta, t) = \frac{1}{2\pi\epsilon_0 cr \sin \theta} i(0, t - r/c) \hat{\theta}, \quad \theta \neq 0 \quad (8.124)$$

$$\bar{B}(r, \theta, t) = \frac{1}{2\pi\epsilon_0 c^2 r \sin \theta} i(0, t - r/c) \hat{\phi}, \quad \theta \neq 0 \quad (8.125)$$

These expressions (8.124) and (8.125) is consistent with a TEM wave structure as it is evident by comparing (8.124) and (8.125) to their respective static cases (8.17) and (8.19) and Figure 8.4.

The unique and exact solution above ((8.124) and (8.125)) for a current pulse travelling up a vertical antenna above a conducting plane, all conductors being perfect, can also be obtained from the solution of the wave equation between two concentric conical surfaces of infinite conductivity with common cone apexes [30], the case of a vertical antenna above a ground plane being viewed as the limiting case in which the polar angle of one of the cones goes to zero (the vertical wire) and the polar angle of the other cone goes to  $90^\circ$  (the ground plane). If the only charge/current injection point in the problem space is a point source located at the base of the vertical conductor of vanishing radius, then the electromagnetic field created between the conductor and ground can only have a spherical TEM (transverse electromagnetic) structure originating at the charge source and expanding outwards in the  $r$ -direction with the speed of light.

The ratio between E and B, from (8.124) and (8.125) is  $c$ , the speed of light, consistent with a TEM wave. The wave impedance is the free-space impedance at all distances from the antenna.

The Poynting vector, the cross product of (8.124) and (8.125), is in the  $r$ -direction, which indicate energy flow in the radial direction from the source at the bottom of the antenna. That is, in this ideal case the only source of radiation is the point source at the bottom of the antenna and the vertical antenna itself does not radiate. However, the situation is different if the pulse reaches and reflects from the top of a finite antenna. That case is not considered here.

With a return stroke speed equal the speed of light  $c$ , the waveshapes of the electric field, the magnetic field, and the current are identical at any distance, whereas this is not the case for speeds less than  $c$ , as seen in the previous section.

The ideal and exact solution for a vertical wire antenna of infinite length and vanishing radius above a ground plane excited at the bottom, all conductors being perfect, is spherical TEM. Spherical TEM solution of the wave equation between two concentric conical surfaces of infinite conductivity and length with common cone apexes has been suggested in [30]. The case of a vertical antenna above a ground plane can be viewed as the limiting case in which the polar angle of one of

the cones goes to zero (the vertical wire) and the polar angle of the other cone goes to  $90^\circ$  (the ground plane) [9]. Currents along such an antenna do not suffer from attenuation and dispersion. All the energy lost due to radiation from such an antenna comes from the source at the bottom. In reality, lightning return stroke is different from this ideal case and therefore (8.122) to (8.125) are only applicable in some special cases.

### 8.10.2 Pulse propagation along a vertical lightning channel above conducting ground at certain speed $v$ : exact expressions using electromagnetic fields of accelerating charges

A current pulse moving with constant velocity  $v$  from ground to cloud along the vertical lightning return stroke channel ( $z$ -axis), without any attenuation and distortion represents a special case of current distribution along the lightning channel, i.e. the transmission line model. The equivalent linear charge density of the return stroke is given by  $\rho(z, t) = i(0, t - z/v)/v$ , where  $i(0, t)$  is the current at the point of the initiation of the return stroke. The electric and magnetic field equations of moving charges that can be found readily in textbooks [31] can be used to calculate the electromagnetic fields from return strokes for the case of transmission line model, as shown in Cooray and Cooray [8]. They present the total vertical and horizontal field components at any point in space. They also showed that the same technique can also be used conveniently to get the field expressions for other types of return stroke models that could be expressed in the form of equivalent current/charge propagation along the channel [29]. Calculation of electromagnetic fields from return stroke and comparison of different return strokes are subject of another chapter and hence not treated here.

## References

- [1] Jackson, J.D., Charge density on thin straight wire, revisited, *Am. J. Phys.*, **68**, 789–799, 2000
- [2] Jackson, J.D., Charge density on a thin straight wire: The first visit, *Am. J. Phys.*, **70**, 409–410, 2002
- [3] Thottappillil, R., M.A. Uman and N. Theethayi, Electric and magnetic fields from a semi-infinite antenna above a conducting plane, *J. Electrostatics*, **61**, 209–221, 2004
- [4] Rubinstein, M. and M.A. Uman, Methods for calculating the electromagnetic fields from a known source distribution: Application to lightning, *IEEE Trans. Electromagn. Comp.*, **31**, 183–189, 1989
- [5] Thottappillil, R. and V.A. Rakov, On different approaches to calculating lightning electric fields, *J. Geophys. Res.*, **106**, 14191–14205, 2001
- [6] Uman, M. A., D.K. McLain and E.P. Krider, The electromagnetic radiation from a finite antenna, *Am. J. Phys.*, **43**, 33–38, 1975
- [7] Thottappillil, R., V.A. Rakov and M.A. Uman, Distribution of charge along the lightning channel: Relation to remote electric and magnetic fields and to return-stroke models, *J. Geophys. Res.*, **102**, 6987–7006, 1997
- [8] Cooray, V. and G. Cooray, Electromagnetic fields of an accelerating charge: Applications in lightning return stroke models, *Trans. IEEE (EMC)*, **52**(4), 944–955, 2010

- [9] Thottappillil, R., J. Schoene and M.A. Uman, Return stroke transmission line model for stroke speed near and equal that of light, *Geophys. Res. Lett.*, **28**, 3593–3596, 2001
- [10] Thottappillil, R., V.A. Rakov and N. Theethayi, Expressions for far electric fields produced at an arbitrary altitude by lightning return strokes, *J. Geophys. Res.*, **112**, D16102, doi:10.1029/2007 JD008559, 2007
- [11] Thottappillil, R. and V.A. Rakov, On the computation of electric fields from a lightning discharge in time domain, *2001 IEEE EMC International Symposium*, Montreal, Canada, Aug. 13–17, 2001
- [12] Thottappillil, R., M.A. Uman and V.A. Rakov, Treatment of retardation effects in calculating the radiated electromagnetic fields from the lightning discharge, *J. Geophys. Res.*, **103**, 9003–9013, 1998
- [13] Rubinstein, M. and M.A. Uman, On the radiation field turn-on term associated with travelling current discontinuities in lightning, *J. Geophys. Res.*, **95**, 3711–3713, 1990
- [14] Thomson, E.M. Exact expressions for electric and magnetic fields from a propagating lightning channel with arbitrary orientation, *J. Geophys. Res.*, **104**, 22,293–22,300, 1999
- [15] Stratton, J.A., *Electromagnetic Theory*, McGraw-Hill, Inc., 1941
- [16] Jefimenko, O.D., *Electricity and Magnetism*, 2nd edn., Electret Scientific Company, Star City, USA, 1989
- [17] Rakov, V.A. and M.A. Uman, Review and evaluation of lightning return stroke models including some aspects of their application, *IEEE Trans. Electromagn. Comp.*, **40**, 403–426, 1998
- [18] Uman, M.A., *The Lightning Discharge*, Academic Press, San Diego, Calif., 1987
- [19] Thottappillil, R., D.K. McLain, M.A. Uman and G. Diendorfer, Extension of Diendorfer-Uman lightning return stroke model to the case of a variable upward return stroke speed and a variable downward discharge current speed, *J. Geophys. Res.*, **96**, 17143–17150, 1991
- [20] McLain, D.K. and M.A. Uman, Exact expression and moment approximation for the electric field intensity of the lightning return stroke, *J. Geophys. Res.*, **76**, 2101–2105, 1971
- [21] Nucci, C.A., *et al.*, Lightning return stroke current models with specified channel-base current: A review and comparison, *J. Geophys. Res.* **95**, 20,395–20,408, 1990
- [22] Krider, E.P., On the peak electromagnetic fields radiated by lightning return strokes toward the middle-atmosphere, *J. Atmos. Electr.*, **14**, 17–24, 1994
- [23] Rakov, V.A. and W.G. Tuni, Lightning electric field intensity at high altitudes: Inferences for production of Elves, *J. Geophys. Res.*, **108**(D20), 4639, doi: 10.1029/2003JD003618, 2003
- [24] Uman, M.A. and D.K. McLain, The magnetic field of the lightning return stroke, *J. Geophys. Res.*, **74**, 6899–6910, 1969
- [25] Willet, J.C., E.P. Krider and C. Leteinturier, Submicrosecond field variations during the onset of first return strokes in cloud-to-ground lightning, *J. Geophys. Res.*, **103**, 9027–9034, 1998
- [26] Willett, J.C., J.C. Bailey, V.P. Idone, A. Eybert-Berard and L. Barret, Submicrosecond intercomparison of radiation fields and currents in triggered

- lightning return strokes based on the transmission line model, *J. Geophys. Res.*, **94**, 13275–13286, 1989
- [27] Willett, J.C. *et al.*, An experimental test of the ‘transmission line model’ of electromagnetic radiation from triggered lightning return strokes, *J. Geophys. Res.*, **93**, 3867–3878, 1988
- [28] Thottappillil, R. and M.A. Uman, Comparison of lightning return stroke models, *J. Geophys. Res.*, **98**, 22903–22914, 1993
- [29] Cooray, V., On the concepts used in return stroke models applied in engineering practice, *Trans. IEEE (EMC)*, **45**, 101–108, 2003
- [30] Schelkunoff, S.A., *Antennas, Theory and Practice*, John Wiley and Sons, New York, 1952, p. 104
- [31] Pannofsky, W.K.H. and M. Phillips, *Classical Electricity and Magnetism*, Addison-Wesley, Reading, Mass., 1962





---

## Chapter 9

# Return stroke models with special attention to engineering applications<sup>1</sup>

Vernon Cooray

---

### 9.1 Introduction

A lightning flash is initiated by electrical breakdown of air in a cloud. This process, commonly known as the preliminary breakdown, signifies the initiation of a stepped leader. Such a stepped leader propagates towards the Earth in a succession of nearly discontinuous surges or steps. The stepped leader leaves a charged, conducting channel in its wake. When the leader reaches the ground, the current flowing in the channel increases abruptly, marking the beginning of the return stroke. After the first return stroke, several subsequent return strokes may occur, each of which is preceded by a fast, continuously moving dart leaders propagating from cloud to the Earth down the channel made by the stepped leader. This chapter is concerned with the mathematical modelling of first and subsequent return strokes.

### 9.2 Modelling of return strokes

From the point of view of an electrical engineer, the return stroke is the most important event in a lightning flash; it is the return stroke that causes most of the destruction and disturbance in electrical and telecommunication networks. In their attempts to provide protection, engineers seek the aid of return stroke models for three reasons: First, they would like to characterise and quantify the electromagnetic fields produced by return strokes at various distances to provide them with the input for mathematical routines that analyse the transient voltages and currents induced in electrical networks by these fields. This calls for return stroke models that are capable of generating electromagnetic fields similar to those created by natural return strokes. Second, their profession demands detailed knowledge of the effects of direct injection of lightning current into electrical installations, electronic equipment and structures. In a real situation this direct injection of lightning current will be superimposed on currents and voltages induced by electromagnetic fields in various electrical networks. This necessitates the use of return stroke models that are capable of generating channel base currents similar to those in nature. Finally, in order to evaluate the level of threat posed by lightning, engineers require statistical distributions of peak currents and peak

<sup>1</sup>Part of this chapter was published previously in *Lightning Protection* (V. Cooray, Ed.), IET publishers, 2010 [57]. Author thanks Dr. Alberto Di Conti for his input in the section 9.4 dealing with transmission line models.

current derivatives in lightning flashes. Even though the characteristics of return stroke currents can be obtained through measurements at towers equipped with current measuring devices, gathering statistically significant data samples in different regions and under different weather conditions is an exceptionally difficult enterprise. Accurate return stroke models can simplify this task to a large extent by providing the connection between the electromagnetic fields and the currents so that the latter can be extracted from the measured fields. Having outlined the importance of return stroke models in the engineering profession, let us consider the attributes of a *model* in general and a *return stroke model* in particular.

A model, by definition, is a mathematical construct which, with the addition of certain verbal interpretations, describes observed phenomena. The justification of such a mathematical construct solely and precisely is that it is expected to be representative of a given situation. If the mechanism behind all the fundamental processes leading to an observed phenomenon is known, it is not necessary to construct a model to describe it. A model is needed when all or some of the basic principles governing the observed phenomenon are not completely understood. Thus, a model may contain hypotheses that have yet to be proved and variables whose values are selected *a priori* to fit the experimental observations. However, irrespective of the way it was constructed, a model should be able to explain at least some of the experimental observations concerning the physical process under consideration and should be able to make predictions so that its validity can be tested through further experimental investigations.

In the case of return strokes, a model is a mathematical formulation that is capable of predicting the temporal and spatial variation of the return stroke current, the variation of return stroke speed, the temporal spatial characteristics of optical radiation, the features of electromagnetic fields at different distances and the signature of thunder. From the point of view of an engineer, the lightning parameters of particular interest are the return stroke current and its electromagnetic fields, whence most of the return stroke models available today are constructed to predict either one or both of these features. On the other hand, the physicist is mostly concerned with the lightning-generated optical radiation and the shock waves. This is the case because they provide the physicist with information concerning the thermal, electrical and thermodynamic behaviour of air heated very rapidly by the discharge. Unfortunately, no single model available at present is capable of predicting all the facets of the return stroke that are of interest to both engineers and physicists. The reason for this is not only the complexity of the return stroke itself, but also that it encompasses various processes the understanding of which requires expertise in several branches of physics, such as electromagnetic field theory, discharge physics, thermodynamics and hydrodynamics. As a consequence, those modelling the return stroke may be compelled to keep within the subject matter of their own field of expertise. However, with the proper combination of different solutions available in the literature, it may be possible to construct an *all inclusive* return stroke model.

Unfortunately, researchers encounter problems not only in the construction stage of models, but also in making a comparison of model predictions with experimental data. For example, one may not be able to provide an unequivocal answer to simple questions such as ‘What is the speed of propagation of return strokes?’ or ‘What is the signature of the current generated at the base of the return stroke channel?’. The reason is that the lightning return stroke, as with any other

discharge process for that matter, can only be described in statistical terms. The characteristics of return strokes may differ from one example to another and it may not be an easy task to find a ‘typical return stroke’. This fact makes it difficult to compare model predictions with the available experimental observations. For instance, the predictions of a model that is capable of generating a ‘typical channel base current’ and ‘typical electromagnetic fields’ may fall wide of the mark when the observations are confined to a single return stroke. Indeed, an appropriate comparison of model predictions with experimental observations requires simultaneous measurements of current at the channel base and at different heights, remote electromagnetic fields, and the optical and thunder signature of a *single* return stroke. Even though we still do not have proper techniques to quantify how the current signature varies as a function of height, all the other features mentioned above can be measured from a single stroke if both the time and the point of strike can be predetermined. This indeed is the case with triggered lightning flashes (the reader is referred to Chapter 6 for a discussion on triggered lightning). Simultaneous experimental data on various return stroke features gathered from such lightning flashes can provide enough information to validate return stroke models, but not beyond reasonable doubt though. The triggering technique itself can introduce physical constraints and initial conditions that are very different to the natural conditions. Thus, even if a good agreement is observed between the experiment and theory, there will always be unknown parameters which may tip the balance between a good model and a bad one. Keeping these facts and warnings in mind, let us consider the principles behind various return stroke models.

On the basis of the concepts and aims of return stroke models, they can be separated into four main groups, namely, (1) the electro-thermodynamic models, (2) the transmission line or LCR models, (3) electromagnetic models and (4) the semi-physical and engineering models. In this chapter basic concepts associated with each of these model types are presented together with a detailed description of engineering models.

### 9.3 Electro-thermodynamic models

These models were originally motivated by the need to understand the shock waves from line disturbances; some examples are long explosive charges, exploding wires, supersonic projectiles, sparks and lightning. Models of this kind describe the relationship between the observable parameters of the discharge, such as current–voltage characteristics, acoustic and radiative effects, plasma temperature, plasma composition and the plasma column dimensions. Most of these models make the following three simplifying assumptions: (1) The discharge column is straight and cylindrically symmetric so all the events are functions of a radial co-ordinate  $r$  and time  $t$  only. This assumption requires that the current in the channel be uniform along the length of the column so that there is no dependence on  $z$  co-ordinate. (2) The conducting portion of the plasma is electrically neutral and (3) local thermodynamic equilibrium (LTE) exists at all times so that the state of the medium at a given point can be computed from a knowledge of the temperature and pressure. The driving force of these models is the resistive heating of the plasma channel by a prescribed flow of electric current coupled with the computation of the electrical conductivity of the plasma. The model then describes the properties of the plasma

column and its surroundings through numerical integration of three conservation equations (the conservation of mass, momentum and energy) and two state equations (the thermal equation of state and caloric equation of state). According to Hill [1], the conservation equations can be written as

$$\frac{1}{\rho} = \frac{1}{2} \frac{\partial r^2}{\partial m} \quad (\text{Conservation of mass}) \quad (9.1)$$

$$\frac{\partial u}{\partial t} = -r^2 \frac{\partial}{\partial m} (P + Q) \quad (\text{Conservation of momentum}) \quad (9.2)$$

$$\frac{\partial E}{\partial t} + P \frac{\partial V}{\partial t} + Q \frac{\partial V}{\partial t} + \frac{\partial L}{\partial m} + D = 0 \quad (\text{Conservation of energy}) \quad (9.3)$$

In these equations  $m$  which equals  $\int \rho r \, dr$  is the particle mass (the mass per radian per unit length of channel),  $\rho$  is the density of air,  $V$  is the specific volume,  $r$  is the radial distance,  $u$  is the particle velocity,  $t$  is the time,  $P$  is the pressure,  $Q$  is the artificial viscosity pressure,  $E$  is the specific internal energy,  $D$  is the specific energy source rate and  $L$  is the luminosity (i.e. the radiant flux per radian per unit length of channel). The two state equations are given by

$$P = \rho RT \quad (\text{Thermal equation of state}) \quad (9.4)$$

$$E = \frac{RT}{(\gamma - 1)} \quad (\text{Caloric equation of state}) \quad (9.5)$$

where  $R$  is the gas constant per unit mass,  $T$  is the temperature and  $\gamma$  is the constant specific heat ratio. The evaluation of the equations of state requires information concerning the state of ionisation of air at a given temperature and pressure. This information is usually obtained through Saha's [2] equation by assuming local thermodynamic equilibrium. The initial boundary conditions imposed on the model are the temperature, pressure and the radius of the conducting channel formed by the processes subsequent to the initiation of the return stroke current. The outputs of the model are the radial variation of pressure, electron density, temperature, optical radiation and parameters of the shock wave.

One of the first models of this kind applicable to spark discharges was introduced by Drabkina [3]. However, the theory she advanced is not complete. The electrical conductivity and the temperature in the channel are not computed in her theory. It only relates the hydrodynamic conditions to the energy released in the channel, which must be determined experimentally. Braginskii [4] extended this theory by removing the simplifying assumption. He considered the channel conductivity and temperature to be uniform within the plasma channel, and outside this the temperature is taken to be ambient temperature. He also made the simplifying assumption that the conductivity of the plasma channel takes a constant value (i.e. it is independent of time  $t$ ). For a spark current increasing linearly with time, he then gives the following expression for the spark channel radius  $a$ :

$$a = 0.93 \times 10^{-3} \rho_0^{-\frac{1}{6}} I^{\frac{1}{3}} t^{\frac{1}{2}} \quad (9.6)$$

where  $a$  is in metres,  $\rho_0 = 1.29 \times 10^{-3} \text{ g/cm}^3$  is the density of the air at atmospheric pressure,  $I$  is in kiloamperes and  $t$  is in microseconds. Even though Braginskii's treatment allows calculation of the energy input from the current waveform,

both his and Drabkina's theory use the strong shock approximation – which assumes that the channel pressure is much greater than the ambient pressure – and therefore applicable to the initial stages of the spark. Plooster [5–7] extended the work of Brode [8], which is valid for spherical sources, to describe spark and lightning discharges. The work of Hill [1] is also an extension of Brode's work to cylindrical symmetries. Indeed, there is a qualitative agreement between the calculations of Hill and Plooster. More recently, Paxton *et al.* [9] improved the calculations made by Plooster by introducing a better radiative transfer algorithm.

These models have to overcome several problems in obtaining the correct initial conditions. Lightning discharges exhibit a great variation in observed parameters so that it is difficult to have a unique set of initial conditions that is valid for the majority of the return strokes. The models do not account for the processes occurring before the onset of high current and, therefore, the mechanism that leads to the generation of the return stroke current is not taken into account. As a consequence, the temporal variation of the return stroke current is used as an input parameter. But, there is no general consensus as to the temporal profile of the current waveform that should be used in the calculations. Moreover, in addition to it being a function of altitude, the current waveform at a given height may differ significantly from one stroke to another. The situation is made even more complicated by the fact that the initial conditions of the breakdown channel may differ from one point on the channel to another. In general the initial conditions can be split up into two categories – those in which the gas density in the channel equals that in the surrounding atmosphere, and those in which the pressures are equal. The constant density condition corresponds to that portion of the return stroke channel close to the surface of the Earth. Here, the time elapsed between the passage of the leader and the onset of the return stroke is usually short and the gas heated by the leader will not have sufficient time for the pressure to equilibrate with the surrounding atmosphere. The initial density of the channel under these circumstances will be that of the surrounding atmosphere. The constant pressure condition applies in channel sections which are well above the Earth. Here, a considerable time may elapse between the passage of the leader and the onset of the return stroke and there is enough time for the channel to achieve pressure equilibrium with the surrounding atmosphere. Notwithstanding, throughout most of the channel length the initial conditions may fall in between these two extremes. In addition, the initial plasma temperature and the channel radius may also change from one location on the channel to another. However, the calculations of Plooster [6] show that the initial conditions only affect the channel properties at times immediately after the current onset.

The existence of a local thermodynamic equilibrium (LTE), which is one of the presumptions of these models, may be justified a few microseconds after the onset of the return stroke phase, but whether LTE prevails during the rising portion of the current waveform where the electric field driving the current is sufficiently high is doubtful. If this assumption is not valid immediately after the onset, any relationship between the peak return stroke current and the optical output over the first few microseconds as derived by these models may be in error. Besides, these models do not take into account the consequences associated with the neutralisation of the corona sheath surrounding the central core of the leader channel during the return stroke. Available evidence suggests that this neutralisation is accompanied by streamer-like discharges progressing into the corona sheath [10, 11]. Even though the streamers are cold discharges, their stems may acquire conditions favourable

for thermalisation – a rapid increase in temperature caused by thermal ionisation. In principle, this can be considered to be an expansion of the hot central core, a process not taken into account by the present electro-thermodynamic models.

Due to these various assumptions and simplifying approximations, the results obtained from the electro-thermodynamic models may be quantitatively in error, but they do show qualitatively the importance and effects of various processes in lightning discharges. Plooster [6–7] compared the results of his computations with those obtained from laboratory sparks by Orville *et al.* [12]. The model-simulated temporal growth of channel temperature, channel pressure and electron density are in reasonable agreement with the measurements. Plooster [6–7] also extended his theory to describe the return strokes. His results show a reasonable agreement with the experimental data gathered by Orville [13–15]. Recently, a rigorous and one-to-one comparison of the optical radiation predicted by the electro-thermodynamic model of Paxton *et al.* [9] with measured lightning data was made by Baker *et al.* [16]. In the experiment, simultaneously with the channel base current, the light output of a small length of a triggered lightning channel was measured. The theory was used to make numerical predictions of the optical output for the measured current. The calculated and the measured waveforms are qualitatively similar, but there are differences in the details. Authors claim that these discrepancies are probably caused by the initial conditions selected for the simulations.

As indicated earlier, electro-thermodynamic models are capable of qualitatively describing the thermodynamic and electrical properties of air in a lightning channel heated by the return stroke current. The main disadvantage of these models is their inability to predict the temporal and spatial variation of the lightning current. Due to this deficiency, these models cannot be manipulated to predict the electromagnetic fields and channel base current, the parameters which are of prime interest to engineers. Nevertheless, the potential of these models can be enhanced by combining them with LCR or semi-physical models, which have the ability to predict the spatio-temporal characteristics of the return stroke current.

## 9.4 Transmission line or LCR models

The most simple model of a lightning return stroke is a lumped circuit model. This can be represented by a capacitor connected across a switch to an inductor in series with a resistor. The inductor and resistor represent the return stroke, and the capacitor the charge stored in the cloud. This model inherently assumes that the current in the return stroke channel at any given time is the same at any point on the channel. It also neglects the finite speed of propagation of the information along the channel. Such a simple model was used by Oetzel [17] to calculate the diameter of the lightning channel. He assumed that the current in the return stroke channel is given by a double exponential function, enabling him to determine the value of the resistor that is consistent with this current waveform. Once the resistance is known, assuming that the channel is cylindrical and filled with a finitely conducting plasma, he obtained the diameter of the channel. Even though the lumped circuit description of the lightning channel is an oversimplification, it provided reasonable values for the diameter of the channel. But, a transmission line is a better analogy to the physical reality (Figure 9.1). The initial charge on the transmission line is analogous to the charge stored on the channel of the leader. The speed of waves on the line can be adjusted to fit the observed speed of propagation of the return stroke

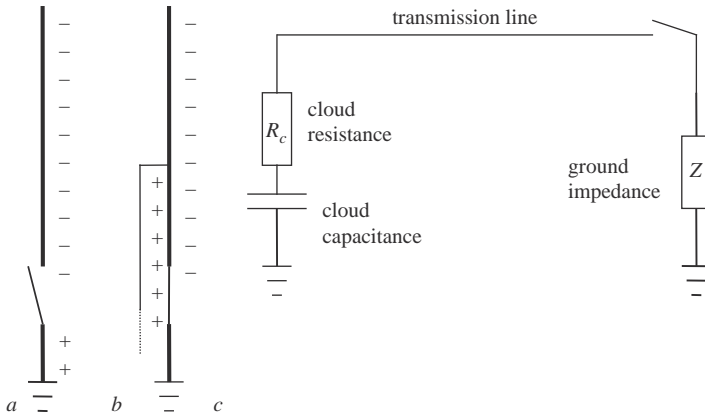


Figure 9.1 Schematic representation of the similarity between a return stroke and a transmission line model: (a) leader channel; (b) return stroke; (c) transmission line model

front. This representation also makes it possible to evaluate the current at different points along the channel, a prerequisite for the calculation of the electromagnetic fields. This procedure also provides a satisfactory approach to the extrapolation of the current measurements made at the bottom of the channel to other points along the channel. Oetzel [17] also considered a finite, lossy, uniform transmission line as a model for return strokes. He found that the double exponential form for the current at the base of the channel – used frequently in the existing literature – can be generated by a reasonably non-uniform initial charge distribution. As pointed out by Price and Pierce [18], however, such a charge distribution on a uniform transmission line implies a complex dynamic state just before the initiation of the return stroke. But, since the stepped leader speed is on the order of  $10^6$  m/s, there is ample time for the channel to reach equilibrium conditions.

Price and Pierce [18] considered an infinite, lossy, uniform transmission line with a given initial charge distribution to represent the return stroke. The line was characterised by its series resistance  $R$ , shunt capacitance  $C$  and series inductance  $L$  per unit length. At  $t = 0$ , the line was linked to ground through a resistance equal to the characteristic impedance. The main purpose of this study was to obtain a general picture of the current signature as a function of height along the channel. Thus, no attempt was made to evaluate values of  $L$ ,  $C$  or  $R$  suitable for a lightning channel. Using this representation and assuming that the charge distribution at  $t = 0$  is uniform along the line, they calculated the temporal and spatial variation of the current along the channel. The results produced a current at ground level which rose to its peak value instantaneously (i.e. a step-like rise), but the subsequent decay was more realistic than that of an exponential function. They employed the model to evaluate the signatures of remote electric and magnetic fields at 1, 10 and 100 km. The agreement with the measured fields was only qualitative.

A more general LCR representation of the return stroke was introduced by Little [19]. He assumed both the inductance per unit length  $L$  and the capacitance per unit length  $C$  to vary with height. The value of  $C$  as a function of height was obtained by first calculating the charge distribution on the leader channel supposing it to be a good conductor extending down from either a spherical or a plane charge centre, and then converting the estimated charge per unit length  $q$  into  $C$  through



the equation  $q = VC$ , where  $V$  is the line potential. The magnitude of  $L$  was calculated by means of the following concept: When the current flows from any channel segment to ground, the displacement current flows in the space between that segment and the ground, and along the electric field lines. These electric field lines were obtained from the calculated charge distribution along the transmission line and the inductance associated with the line segment was found from the area under the electric field lines. Little [19] was also aware of the fact that the value of  $R$  is a complex function of time and height. Notwithstanding this, he assumed a constant resistance that is capable of generating a unidirectional current pulse without oscillations. These considerations led him to decide upon a resistance of 1 ohm/m which he used throughout the calculations. The ground end of the line was terminated by a resistance equivalent to a hemispherical earth conductor buried in soil of specific conductivity  $\sigma$ . In the simulations, the potential of the cloud and the channel were both set at 100 MV and the cloud was represented by a 1  $\mu\text{F}$  capacitor. The simulations show that the current pulse amplitude decreases with height while its rise time increases. The speed of the return stroke front  $v$  as estimated by the time of travel of the current peak was  $1.5 \times 10^8$  m/s over the first 1000 m. Little [19] did not make any attempt to evaluate the remote electromagnetic fields.

A non-uniform transmission line model in which both the inductance and capacitance per unit length vary exponentially as a function of height was introduced by Amoruso and Lattarulo [20]. The return stroke was simulated by an injection of current of a given waveshape into this transmission line. The inductance and capacitance per unit length of the line were given by

$$L = L_0 e^{kh} \quad C = C_0 e^{-kh} \quad (9.7)$$

where  $C_0$  and  $L_0$  are unspecified quantities,  $h$  is the height and  $k$  is a suitable constant. The basis for the preference for an exponentially decreasing  $C$  is the following. The modellers assumed that the charge per unit length  $q$  on the leader channel decreases exponentially with height. If the potential of the leader channel is uniform throughout and equal to  $V$ , the capacitance  $C$  per unit length will also decrease exponentially with height (note that  $C = q/V$ ). The impedance of the line  $Z$  and the propagation speed  $v$  of the waves travelling along this line were given by

$$v = \sqrt{(L_0 C_0)^{-1}} \quad Z = \sqrt{(L_0 C_0)} e^{kh} \quad (9.8)$$

Thus, the impedance of the line increases with increasing height while the speed of propagation remains constant. As the current pulse propagates along this transmission line, an overall change in the current waveshape takes place. The higher frequency components, and hence the initial part of the current waveform, decrease almost exponentially along the channel with a decay height constant of  $(k)^{-1}$ . The lower harmonic components, and hence the tail of the current waveform are reduced much more. In the simulations the authors assumed  $v = c/3$ , where  $c$  is the speed of light in free space. The authors used the model to calculate the remote electromagnetic fields and the results obtained are in reasonable agreement with the measured fields.

The LCR models discussed so far treated the line parameters as being time independent. However, the channel may expand in diameter by over an order of magnitude during the initial 100  $\mu\text{s}$  [7] so that time independent values of line

parameters cannot adequately represent the entire phase of the return stroke. However, the variation of  $L$  and  $C$  with time is weak due to the logarithmic nature of the expressions for these parameters. The variation of  $R$  with time, however, may significantly alter the model predictions. The temporal variation of  $R$ , of the lightning channel, is governed by the discharge and plasma physics – disciplines which are not within the realm of transmission line theory. Fortunately, the electro-thermodynamic models can correct for this deficiency in the LCR models. Even though they are neither complete nor completely self-consistent, the electro-thermodynamic models offer the possibility of incorporating discharge physics into the transmission line models. Moreover, the benefits of combining LCR and electro-thermodynamic models are not only limited to the LCR models but also contribute to the further development of electro-thermodynamic models. For example, in these models the current is assumed to be independent of the properties of the plasma channel. In reality though, there is a complex interaction between the channel properties and the return stroke current making it difficult to consider the latter as a parameter that is independent of the state of the channel. This complex interaction, manifested mainly through the channel resistance, can be understood by combining the electro-thermodynamic models with LCR models. A model with such a blend was first proposed by Strawe [21].

In the model of Strawe [21], the lightning channel was represented by an LCR network (unfortunately he neither gave the values of  $L$  and  $C$  used in the simulation nor a discussion of how they were evaluated) in which the resistance of the channel was simulated with the help of Braginskii's [4] model. Strawe also took into account the presence of a connecting leader by simulating it with a short section of transmission line which was terminated by a 50 ohm resistance at ground level. The discharge was supposed to start when the downward leader got attached to the connecting leader. This attachment was represented by a switch placed between the short and long sections of the transmission line. At each time step in the simulation, a model subroutine calculated the channel resistance for each section of the transmission line from the past current history and fed it into the next time step. Consequently, the model-simulated return stroke current is influenced by the variation of the channel resistance and vice versa. Strawe mainly confined his simulations to the extraction of the current signature as a function of height and did not evaluate the remote electromagnetic fields. The most significant result obtained from the simulations is the rapid decline of the rate at which the current rises with elevation.

A model similar to Strawe's in which the resistance of the channel was simulated by means of an electro-thermodynamic model was presented recently by Mattos and Christopoulos [22], who also incorporated a time-dependent resistance, that Braginskii [4] anticipated should exist in spark channels, into LCR models. The conductivity of the channel was obtained from the Spitzer and Härm [23] conductivity formula assuming the electron temperature to be 30 000 K. Moreover, the capacitance and inductive elements of the channel were obtained in a manner identical to that of Little [19]. The cloud was represented by a resistance in series with a capacitor and the earth termination was represented by a linear resistance. The cloud resistor represents the resistance of the path from the outer boundary to the middle of the charge centre. This was estimated by first calculating the radius of the charge centre by accepting that the electric field at the outer boundary of the charge centre is about  $10^6$  V/m and assuming the resistance per unit length of the

path to be about 3 ohms. The results obtained by Mattos and Christopoulos are qualitatively similar to those obtained by Strawe.

The LCR models examined so far took no account of the physical structure of the leader channel. The leader channel consists of a central hot core surrounded by a corona sheath. In fact, most of the leader charge which is neutralised by the return stroke resides on the corona sheath. Baum and Baker [24] presented an LCR model which acknowledged the presence of the corona sheath. In this model, the return stroke was represented as a wave propagating along a conical transmission line. The modellers visualised the leader tip as a circular cone at the centre of which there is a conducting core carrying most of the current. The leader charge was assumed to reside primarily on the conical surface. As pointed out by Baum [25], although it seems overly simplified, this approximation has its physical merits. As the leader propagates through the air, the corona near the leader tip has only a short time in which to disperse outwards, while further down the tip the corona has more time to propagate outwards. Accordingly, the radius of the corona sheath increases as one moves down the leader tip – hence the approximation of a conical shape for the corona sheath. Note, however, that this approximation is only valid adjacent to the tip of the leader and therefore the conical model is only appropriate for times close to the initiation of the return stroke. By the time the return stroke has propagated a few tens of metres, it will encounter a fully developed corona sheath and hence the conical model has to be replaced by a cylindrical one. In the model Baum and Baker [24] neglected the dissipative effects and that made it possible for them to solve the model equations analytically. One significant prediction of the conical model is that the speed of propagation of the return stroke front is initially close to the speed of light, but after the front has propagated a few tens of metres it decreases to about one third the speed of light. The reason for this is the increase in capacitance per unit length of the channel with increasing height. Subsequently, Baker [26] expanded the model by introducing dissipative effects through a channel resistance which was allowed to vary as a function of time. The resistance at a given time was computed by using an electro-thermodynamic model similar to that developed by Paxton *et al.* [9]. The model differs from that of Strawe [21] which had the simplifying approximation that the shock wave does not separate from the edge of the hot channel. Moreover, it incorporated improved treatments of the equation of state, radiative losses and shock wave propagation. The equivalent circuit (per unit length) of Baker's model is shown in Figure 9.2. In the simulations, however, Baker chose to neglect the conductance,  $G$ , per unit length. To calculate the capacitance and the inductance per unit length of the model it is necessary to have a value for the *return current radius*, which was assumed to be a fixed parameter. With this assumption, the per-unit-parameters were calculated from the equations

$$L = \frac{\mu_0}{2\pi} \ln \left[ \frac{r_{\text{return}}}{r_{\text{channel}}} \right]; \quad C_c = \frac{2\pi\epsilon_0}{\ln \left[ \frac{r_{\text{corona}}}{r_{\text{channel}}} \right]}; \quad C = \frac{2\pi\epsilon_0}{\ln \left[ \frac{r_{\text{return}}}{r_{\text{corona}}} \right]} \quad (9.9)$$

where  $r_{\text{channel}}$  is the radius of the return stroke core through which the return stroke current flows,  $r_{\text{corona}}$  is the radius of the corona sheath which is a function of height and  $r_{\text{return}}$  is the *return current radius* – the radius of a hypothetical conductor along which the current returns to ground. The radius of the corona sheath is calculated by assuming that the electric field at the outer boundary of the channel is

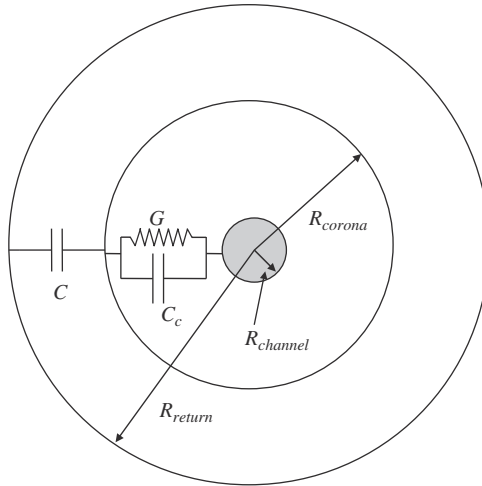


Figure 9.2 Sketch of the assumed transmission line geometry of Baker [26] model. Observe that  $R_{channel}$  is the radius of the central core of the return stroke, which carries essentially all the current and  $R_{corona}$  is the outer radius of the corona sheath.  $R_{return}$  is the radius of the conductor along which the return stroke current returns to ground. In the analysis, the leakage capacitance  $C_c$  was neglected, i.e. the resistor was assumed to be of negligible resistance or large conductance  $G$ , so that the time constant  $C_c/G$  is small compared to times of interest

equal to 3 MV/m. The boundary conditions are the fixed impedances at the cloud and ground terminations. The starting parameters for the calculations are zero current flow everywhere and the voltage of the line. The latter is set to an initial value along the line as far down to as an ‘initiation point’ above the ground, below which it decreases linearly to zero. Baker utilised the model first to understand how the return stroke current alters as a function of height and then to evaluate the remote electromagnetic fields. The simulations revealed that the front of the current waveform spreads out as it advances along the channel and its amplitude decreases. The model-simulated vertical electric field at 50 km decayed rather rapidly after about 7  $\mu$ s. This was probably due to the fixing of the channel length at 1.5 km. The initial ascent of the field does resemble the measured one whereas the decaying part of the electric field does not.

In the last decade or so there has been a renewed interest in return stroke models based on transmission line theory. The newly proposed models generally assume a lightning channel with zero initial condition that is excited by a lumped current or voltage source inserted between the bottom of the channel and the ground. The presence of branches and tortuosity of the channel is usually neglected, in which case the problem reduces to the modelling of a vertical wire above a ground plane. The resulting transmission line is clearly a non-uniform one because the capacitance and inductance of the vertical wire intended to represent the channel vary with position. Different procedures have been used to calculate the channel parameters in this case. Rondón *et al.* [27] used a quasi-static approximation for the inductance of a vertical wire of finite length to derive the channel characteristic impedance. Theethayi and Cooray [28] based their capacitance and

inductance calculations on the application of the charge simulation method to a vertical wire positioned above a perfectly conducting ground plane. Visacro and De Conti [29] and De Conti *et al.* [30] used Jordan's equation in its revised form as proposed by De Conti *et al.* [31] to calculate the channel characteristic impedance. More recently, De Conti *et al.* [32] calculated the channel inductance and capacitance per unit length by representing the lightning channel as a conical antenna whose cone angle is very small. In all cases above, the values of inductance and capacitance calculated with the different methods present differences in their nominal values. However, they all vary logarithmically with increasing height, in which case the spatial and temporal distribution of the channel current can be shown to be nearly model independent if a lumped current source is assumed to excite the channel base.

Some of the newly proposed models also consider the variation of the channel parameters with time in order to accommodate the dynamic behaviour of the lightning channel, which is highly resistive ahead of the return stroke front (leader channel) and present a relatively lower resistance behind the return stroke front (return stroke channel). Theethayi and Cooray [28] and Visacro and De Conti [29] assumed the channel resistance to decay exponentially at each channel section. In this simplified approach, the arrival of the return stroke current serves only as a trigger to initiate the resistance decay, which is assumed to be independent of the shape of the impinging current. A more thorough discussion on the modelling of a time-varying channel resistance in the context of a return stroke model of transmission line type was later presented by De Conti *et al.* [30], who analysed and compared the representation of the channel resistance provided by different arc-resistance models. In particular, it was shown that the strong-shock approximation proposed by Braginskii [4] is able to lead to an overall more realistic variation of the channel resistance than the assumption of a simple exponential decay for this parameter. This conclusion comes from the fact that in Braginskii's formulation the rate of decay of the channel resistance depends on the rate of rise of the current calculated at each channel section, which in principle is not the case if the resistance is assumed to decay exponentially upon the arrival of the return stroke front. De Conti *et al.* [30] also have shown that results qualitatively equivalent to those given by the strong-shock approximation can be obtained with the application of any of the following simplified approaches: (i) direct use of the arc resistance models of Toepler [33] and Barannik *et al.* [34], with a judicious choice of constants and (ii) consideration of a channel resistance exponentially decaying with time, with decay time constants linearly increasing with height (in the evaluated cases, from about 0.3  $\mu\text{s}$  at the channel base to a few microseconds at 3000 m). Such linear variation of the time constants with height compensates the lack of actual dependence between the propagating current and the channel resistance when the exponential approach is used to simulate the time variation of the channel resistance.

The nonlinear return stroke model of De Conti *et al.* [30], which considers the time variation of the channel resistance in accordance with Braginskii [4] model, was later extended by De Conti and Visacro [35] to account for the interaction of lightning with tall grounded structures.

Another topic of interest in the newly proposed return stroke models of transmission line type is how to include the effects of corona generation from the central core of the return stroke channel. In Rondón *et al.* [27], the presence of a corona sheath surrounding the channel core was incorporated in the model by

assuming an increased radius for calculating the per-unit-length capacitance, while a reduced radius was used for calculating the per-unit-length inductance. Visacro and De Conti [29] used a similar procedure for considering corona, but assumed the radius of the corona sheath to decay exponentially with time. Cooray and Theethayi [36] presented a thorough discussion on the effect of corona on the propagation of the return stroke current in a lossless channel and proposed a rigorous approach to incorporate corona currents in telegrapher's equations. The obtained results indicate that corona currents leaving the channel can be equivalently modelled as the result of a time-varying channel capacitance and a time-varying channel conductance. A similar approach was later used by De Conti *et al.* [32] to incorporate corona in their model, which also considered a nonlinear channel resistance.

Perhaps the main feature of the return stroke models of transmission line type proposed in the last decade or so consists in their ability to consistently reproduce many of the observable characteristics of lightning return strokes, namely the increase in the front time of the return stroke current and the reduction in its amplitude with increasing height [37], the reduction of return stroke speed with increasing height [38], and the overall behaviour of electromagnetic fields measured at different distances from the channel [39]. In particular, the ability to reproduce the latter feature is in clear contrast with most of the return stroke models based on transmission line theory proposed in the past, which either remained not completely validated because of the lack of comparison between predicted and measured lightning electromagnetic fields, or presented predicted electromagnetic fields that are largely inconsistent with measured data [39, 40]. A recent review and discussion on return stroke models based on transmission line theory can be found in [32].

Utilisation of the transmission line as a vehicle to probe the return stroke has improved our knowledge about the possible behaviour of the lightning return stroke current along the channel. All the models that incorporated dissipative effects show a spreading out of the return stroke front as it propagates along the channel. This model prediction is in agreement with the results inferred from optical radiation. Some of the latest models also predict electromagnetic fields similar to those measured. On the other hand, using transmission line concepts to describe return strokes is not without its share of difficulties. The first problem is the representation of the thin vertical lightning channel located over the ground plane as a transmission line. Sometimes it is claimed that the lightning channel represents a bi-conical transmission line with the apex angle approaching zero. Unfortunately, the equations pertinent to bi-conical transmission line are not valid in the extreme case where the apex angle becomes zero. A second problem is the following: The transmission line models constrain the speed of propagation of the return stroke front to  $\sqrt{(LC)^{-1}}$ . This, of course, is correct in a conventional transmission line, but in the case of the return stroke the speed of the front is probably governed to a large extent by the plasma properties and discharge physics and, to a lesser degree, by the apparent capacitance and inductance. It may be more correct to represent the return stroke as a transmission line extending upwards from ground level in the background electric field created by the stepped leader. The speed of extension of the transmission line is equal to the return stroke speed. A third problem is associated with the line terminations. In a transmission line the current signature at different locations is significantly

altered by the conditions at the line terminations. In many LCR models, it is imagined that the ground end is terminated with the characteristic impedance. Unfortunately researchers have not yet fathomed the nature of ground terminations of return strokes. In addition to soil ionisation – which creates a time-dependent impedance – the surface flashover may confuse the situation still further. A fourth problem is that the transmission line theory requires TEM propagation of waves. But, in the vicinity of the return stroke front where the longitudinal electric fields are strong, significant deviations from the TEM mode can be anticipated. A fifth problem is that all the transmission line models assume instantaneous charge depletion from the charged capacitor on the line. In reality, leader charge resides on the corona sheath so that the dimension and conductivity of the corona sheath could impose limitations on how rapidly the charge can be drained from it, limiting the current rise and fall times. In fact, some of the semi-physical and engineering models to be described later do attempt to take this fact into consideration. Finally, the *return current radius*, the value of which determines the inductance, and hence the wave speed, is an *ad hoc* parameter. The models do not provide any indication as to how one should choose this radius. In reality, a current pulse on a lightning channel is not accompanied by a return current pulse, hence there is actually no return current conductor for a lightning channel. A better representation of the return stroke is to designate it as a TM wave propagating along a single conductor. Such an analysis was presented by Borovsky [41].

Borovsky's is *not* a transmission line model, so there is little or no justification to discuss his model here in a section allocated to the description of transmission line models. Yet, in principle, waves guided along both transmission lines and single conductors are characterised through Maxwell's equations, hence the reason for discussing this model here. Borovsky [41] made a detailed examination of the guided wave propagation along a single conductor with finite electrical conductivity. The input parameters required to obtain a solution are the radius of the channel and its electrical conductivity, which were both assumed to be uniform in space and constant in time. Since the constituent of the lightning channel is a plasma, the channel temperature determines the electrical conductivity. The conductivity corresponding to a certain temperature was obtained from empirical expressions, derived from experimental data. The model simulations show that the nature of the waves guided along the conductor depends on the relative size of the channel radius  $r_{ch}$  and the electromagnetic skin depth  $\delta$ . If  $r_{ch} \geq \delta$ , the speed of the wavemode is approximately equal to the speed of light and there is little dispersion. If  $\delta \gg r_{ch}$ , the speed is less than that of light and the mode is strongly dissipative. Defining,  $dt = 1/\omega$  where  $\omega$  is the frequency of the wavemode, Borovsky's calculations disclosed that the group velocity of the wavemode is increased if (1) the channel radius is increased, (2) the channel temperature is increased or (3) the rise time,  $dt$ , of the wavemode is decreased. Additionally, the damping of the wave is decreased if (1) the channel radius is increased, (2) the channel temperature is increased or (3) the rise time  $dt$  of the wavemode is increased. For  $dt = 500$  ns (a number which lies in the range of values measured for current rise times) and for  $T = 15\,000$  K, the calculated group velocities are in the range of  $10^7 - 10^8$  m/s, the correct range of observed return stroke speeds. The speed was found to decrease with declining channel temperature (i.e. with decreasing conductivity) or with growing wavemode rise times. Borovsky [41] pointed out that the observed drop in the return stroke speed with height is probably

caused by the decrease in channel conductivity or the increase in the rise time of the current. Borovsky applied the model to take out information regarding the power dissipation and came up with values of the order of  $10^9$  W/m. Another interesting parameter extracted through this labour is the electric field at the front of the wavemode corresponding to rise times and temperatures close to return strokes. The estimated peak field was  $3.0 \times 10^5$  V/m.

Even though the model of Borovsky is a step forward in the endeavour to understand return strokes, it does have several weaknesses. First, the simulations are valid for a single conductor in free space which may not be a suitable approximation at times close to the initiation of the return stroke due to the close proximity to ground. Second, the conductivity of the return stroke channel may change as a function of time in general, and close to the return stroke front in particular. As a consequence, the assumption of constant conductivity may fail in the vicinity of the return stroke front. Finally, as mentioned earlier, most of the charge on the leader resides on the corona sheath and the model does not take this fact into consideration.

There is no doubt that the results gained through the manipulation of LCR models have contributed a great deal to our understanding of the return stroke. However, the present author believes that one of the main contributions was the provision of a framework and vision on which the semi-physical and engineering models – the most successful in terms of their predictions from an engineering point of view – were built.

## **9.5 Electromagnetic models**

In electromagnetic models the lightning channel is represented by a perfectly conducting wire of finite radius located (vertically) over a ground plane. The current or the voltage at the ground end of the wire is given as boundary conditions and Maxwell's equations are solved for the particular geometry and boundary conditions using either the method of moments or the finite difference technique to obtain the distribution of the current along the conductor. Since the speed of propagation of electromagnetic signals along the conductor located in air is equal to the speed of light, the medium in which the conductor (or the return stroke) is located is modified in different ways to obtain a wave speed comparable to that of the return stroke. The techniques employed for this purpose are (1) a resistive wire in air above ground [42] (2) replacing air above the conducting boundary (i.e. ground) by a dielectric medium [43] (3) coating the wire with a dielectric material [44] (4) loading the wire with additional distributed series inductances [45] and (5) two parallel wires having additional distributed capacitances between them [46].

It is doubtful whether the return stroke properties can be derived purely using Maxwell's equations because the return stroke gives rise to considerable heating of the channel accompanied by channel expansion in the shock wave mode. In order to get a correct physical representation the electrodynamics should be combined with both thermodynamic and hydrodynamic. This deficiency is probably the reason why the return stroke speed had to be reduced by artificial means in the electromagnetic models.

A good review of electromagnetic models is provided by Baba and Rakov [47] and Moini and Sadeghi [48].



## 9.6 Engineering models

From a historical point of view two basic approaches have been utilised in creating engineering models. In the first approach, a spatial and temporal variation is assumed for return stroke current and then used to calculate the remote electromagnetic fields – the sole prediction of these models that can be compared with the measurements. Some of the models go one step further by invoking physical processes as the cause of the temporal and spatial variation of the return stroke current and speed. These models are capable of predicting at least two or more of the following return stroke features: (1) the channel base current, (2) the temporal and spatial variation of current along the channel, (3) the variation of the return stroke speed with height and (4) the remote electromagnetic fields. In general engineering return stroke models can be divided into three categories. They are (1) current propagation models (2) current generation models and (3) current dissipation models. In fact, current propagation models are a special case of current dissipation models and in principle only two categories of engineering models exist. However, in order to appreciate the historical development of engineering return stroke models they are described within the three categories mentioned above. A survey of the historical development of engineering models is sketched in Figure 9.3.

### 9.6.1 *Current propagation models (CP models)*

#### 9.6.1.1 **Basic concept**

Consider a uniform and lossless transmission line. A current pulse injected into this line will propagate along the line with uniform speed without any change in the amplitude of the waveshape. The transmission line does not interfere with the current (of course this is not true in the case of a transmission line going into corona). It will only provide a path for the propagation of the current pulse from one location to another. This is the basis of the current propagation models. In these models it is assumed that the return stroke is a current pulse originating at ground level and propagating from ground to cloud along the transmission line created by the leader. The engineering models using this postulate as a base were constructed by Norinder [49], Bruce and Golde [50], Lundholm [51], Dennis and Pierce [52], Uman and McLain [53], Nucci *et al.* [54], Rakov and Dulzon [55] and Cooray and Orville [56]. The models differ from each other by the way they prescribe how the return stroke current varies as it propagates along the leader channel. For example, in the model introduced by Uman and McLain [53], popularly known as the transmission line model, the current is assumed to propagate along the channel without attenuation and constant speed. In the model introduced by Nucci *et al.* [54] (MTLE – modified transmission line model with exponential current decay), the current amplitude decreases exponentially and in the one introduced by Rakov and Dulzon [55] (MTLL – modified transmission line model with linear current decay) the current amplitude decreases linearly. Cooray and Orville [56] introduced both current attenuation and dispersion while allowing the return stroke speed to vary along the channel.

#### 9.6.1.2 **Most general description**

In order to generalise the description of the model let us assume that the return stroke process consists of two waves. The first one travelling with speed  $u$  (which

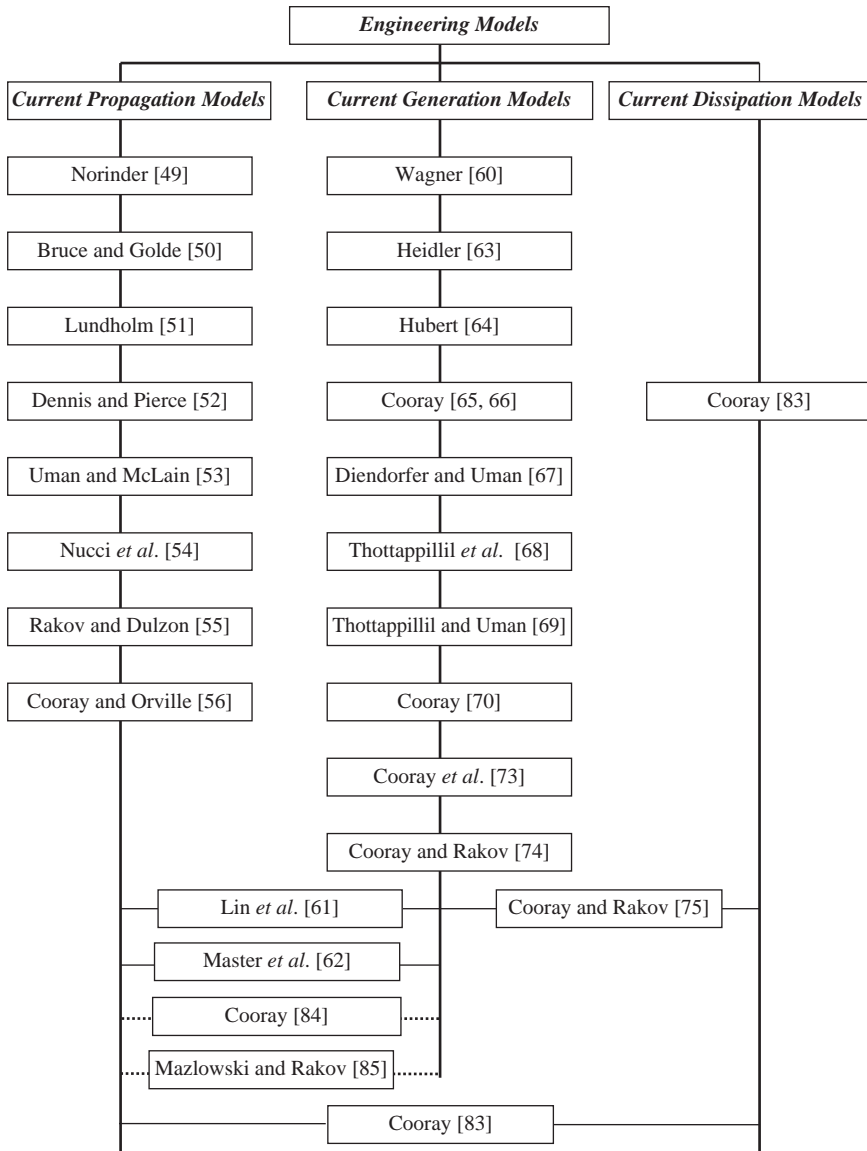


Figure 9.3 Historical development of engineering return stroke models. Note that papers by Cooray [84] and Maslowski and Rakov [85] discuss the relationship between current generation and current propagation models. Cooray [83] also showed that current propagation models are a special case of current dissipation model

very well could be a function of height) is preparing the channel for the transport of charge and current. The second one is the current wave and the associated charge which is travelling upwards with average speed  $v$ , depending again on the height. The current wave cannot penetrate the propagating plasma front and therefore the current is zero ahead of the plasma front which prepares the channel for conduction. If  $u < v$  then the upward moving current waveform encounters a barrier at the plasma front and the charges that is being carried up by the current waveform will

be deposited at the plasma front. There will be a current discontinuity at the return stroke front. In this case the return stroke front speed is equal to  $u$ . On the other hand, if  $u \geq v$  then the return stroke front speed is equal to  $v$  and there will be no current discontinuity at the return stroke front. Thus, the current at level  $z$  is given by

$$I(z, t) = A(z)F(z, t - z/v) \quad t > z/u \quad \text{if } u < v \quad (9.10a)$$

$$I(z, t) = A(z)F(z, t - z/v) \quad t > z/v \quad \text{if } u \geq v \quad (9.10b)$$

In the above equations  $A(z)$  is a function that represents the attenuation of the peak current and  $F(z, t)$  describes the waveshape of the current at height  $z$ . Note also that  $F(z, t) = 0$  for  $t < 0$ . One can define the function  $F(z, t)$  as follows:

$$F(z, t) = \int_0^t I_b(\tau)R(z, t - \tau)d\tau \quad (9.11)$$

where  $I_b(t)$  is the channel base current and  $R(z, t)$  is a function that describes how the shape of the current waveform is being modified with height. However, this operation itself leads to the attenuation of the current and if we would like to represent the attenuation only by the factor  $A(z)$ , then we have to normalise this function to unity. Let  $t_p$  be the time at which the peak of the function defined in (9.11) is reached. Then the normalisation can be done as follows:

$$F(z, t) = I_p \frac{\int_0^t I_b(\tau)R(z, t - \tau)d\tau}{\int_0^{t_p} I_b(\tau)R(z, t - \tau)d\tau} \quad (9.12)$$

where  $I_p$  is the peak current at channel base. If the speeds of propagation of the pulses depend on  $z$  then  $u$  and  $v$  in (9.10) have to be replaced by the average speeds. In Table 9.1 the expressions for the parameters of (9.10)–(9.12) pertinent to different return stroke models are presented. Note that the parameter description given in Table 9.1 for the Bruce and Golde [50] model is based on the general description involving two speeds as described above. The original formulation of the model however is based on just one speed.

In analysing these models using the parameters given in Table 9.1 the following points should be kept in mind.

1. The numerical values of the parameters given in Table 9.1 are only of historical value. The important point is the way in which different scientists attempted to incorporate the observed facts into the models.
2. In all the models the channel base current is given as an input parameter. It varies from one return stroke model to another but these variations are mainly due to the lack of information available in the literature concerning the return stroke current at the time of the creation of the model. Thus, one can replace it with analytical forms created recently by scientists to represent the return stroke current. Several such examples are given in the latter part of this chapter. One

Table 9.1 Basic features of current propagation models

The model	$v$	$u$	$A(z)$	$R(z, t)$
Norinder [49] Lundholm [51]	$\infty$ $v$ varies as a function of peak current. The value of $v$ is evaluated as a function of peak current using the theory of Wagner (see Chapter 10)	$\infty$ $u = v$	1.0 1.0	$\delta(t)$ $\delta(t)$
Bruce and Golde [50] <sup>a</sup> Dennis and Pierce [52] <sup>a</sup>	$\infty$ Case 1: $v = u$ Case 2: $v = c$ For first: $v = v_d e^{-\gamma t}$ For subsequent: $v = v_u$	$u(z) = u_p e^{-\gamma t}$ $u = u_d e^{-\gamma t}$ $u = v$	1.0 1.0 For first: $A(z) = I_p \frac{v}{v_d}$ For subsequent: $A(z) = 1.0$	$\delta(t)$ $\delta(t)$ $\delta(t)$
Uman and McLain [53]				
Rakov and Dulzon [55]	$v = v_r$ , Authors have also considered exponentially decaying speeds	$u = v$	$A(z) = \left(1 - \frac{z}{H}\right)$ $A(z) = \left(1 - \frac{z}{H}\right)^2$	$\delta(t)$
Nucci <i>et al.</i> [54]	$v = v_n$	$u = v$	$A(z) = e^{-z/\lambda}$	$\delta(t)$ $R(z, t) = \frac{e^{-t/\tau(z)}}{\tau(z)}$
Cooray and Orville [56]	$v = v_1 \left\{ \begin{array}{l} ae^{-z/\lambda_1} \\ +be^{-z/\lambda_2} \end{array} \right\}$	$u = v$	$A(z) = \left\{ \begin{array}{l} c_0 e^{-z/\lambda_3} \\ +d e^{-z/\lambda_4} \end{array} \right\}$	$\tau(z) = \eta z$ $\tau(z) = 1 - e^{-z/\lambda_5}$ $\tau(z) = 1 - e^{-(z/\lambda_6)^2}$

Parameters:  $u_p = 8.0 \times 10^7$  m/s,  $v_d = 8.0 \times 10^7$  m/s,  $v_r = 2 \times 10^4$  s<sup>-1</sup>,  $v_u = 8.0 \times 10^7$  m/s,  $I_p = 1.5 \times 10^8$  m/s,  $H = 7.5$  km,  $v_n = 1.1 \times 10^8$  m/s,  $\lambda = 2000$  m,  $v_1 = 2.2 \times 10^8$ ,  $a = 0.5$ ,  $b = 0.5$ ,  $\lambda_1 = 100.0$  m,  $\lambda_2 = 5000$  m,  $c_0 = 0.3$ ,  $d = 0.7$ ,  $\lambda_3 = 100$  m,  $\lambda_4 = 3000$  m,  $\lambda_5 = 500$  m,  $\eta = 7 \times 10^{-10}$  s m<sup>-1</sup>,  $\lambda_6 = 500 - 250$  m and  $c$  is the speed of light.

<sup>a</sup>In reference [57] the  $u$  and  $v$  were interchanged by mistake.

exception to this is the Lundholm model [51] in which, for the reasons of mathematical simplicity, the channel base current is assumed to be a step.

3. The return stroke speed is another input parameter of these models. In some models the return stroke speed is assumed to be uniform whereas in others it is assumed to decrease exponentially. Cooray and Orville [56] assumed a more complicated function containing two exponential to represent the variation of return stroke speed with height. However, recent information shows that the speed can actually increase initially, reach a peak and then continue to decay [58].
4. Note that Cooray and Orville [56] changed the rise time of the current directly with height without first defining the function  $R(z, t)$ . The functions given in Table 9.1 are the ones which approximate this variation in the standard form written above. However, use of this function in the model will not only change the rise time but also change the shape of the current waveform with height. On the other hand, any physically reasonable dispersion process will affect not only the rise time but also the fast variations in any other part of the current.

Figures 9.4–9.9 depict the return stroke current at several heights as predicted by the Bruce and Golde model, Dennis and Pierce model, transmission line model, MTLE model, MTLL model and Cooray and Orville model, respectively. In all the examples the same current waveform that is being proposed by Nucci *et al.* [59] for

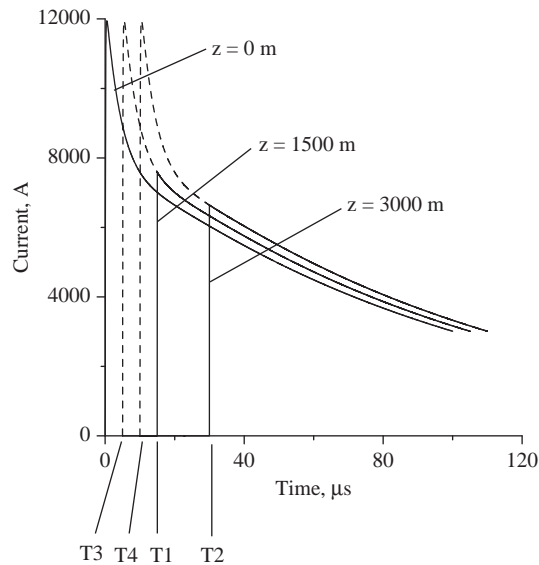


*Figure 9.4 Return stroke current at several locations along the channel according to Bruce and Golde [50] model. In the calculation the channel base current is represented by the analytical waveform created for subsequent return strokes by Nucci *et al.* [59] and the speed of the plasma front that prepares the channel for current propagation  $u$  is kept constant at  $10^8$  m/s. The speed of the current wave according to the physics of the model is equal to infinity. In the figure  $T1$  and  $T2$  are the times at which the current at heights 1500 and 3000 m are initiated (i.e.  $T1 = 1500/v$ ,  $T2 = 3000/v$ ) with the passage of the plasma front*

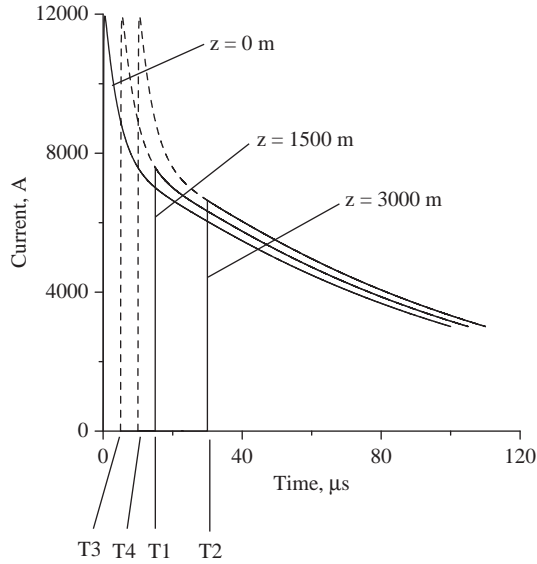


*Figure 9.5 Return stroke current at several locations along the channel according to Dennis and Pierce [52] model. In the calculation the channel base current is represented by the analytical waveform created for subsequent return strokes by Nucci et al. [59]. In the calculation the speed of propagation of the current pulse  $v$  is assumed to be  $3 \times 10^8$  m/s and the speed of propagation of the plasma front that prepares the channel for current conduction  $u$  is assumed to be  $10^8$  m/s. In the figure  $T1$  and  $T2$  are the times at which the plasma front reaches the heights 1500 and 3000 m respectively. The times  $T3$  and  $T4$  correspond to the hypothetical arrival times of the current pulse if its propagation is not restricted by the propagation of the plasma front. Note that if  $v = u$ ,  $T1 = T3$  and  $T2 = T4$  and the model reduces to the transmission line model. If  $v = \infty$  then  $T3 = T4 = 0$  and the model reduces to the Bruce and Golde model*

subsequent return strokes is used at the base of the channel and the return stroke front speed  $v$  is kept constant at  $10^8$  m/s. Observe that when  $v = \infty$  the Dennis and Pierce model reduced to the Bruce and Golde model and when  $u = v$  the Dennis and Pierce model reduces to the transmission line model. Observe also that in the case of Cooray and Orville model the current rise time increases as it propagates along the channel.

## 9.6.2 Current generation models (CG models)

### 9.6.2.1 Basic concept

If a transmission line goes into corona, the corona currents released at each line element will give rise to currents propagating along the line and an observer will be able to measure a current appearing at the base of the line [36]. A similar scenario is used in the current generation models to describe the creation of the return stroke current. In these models the leader channel is treated as a charged transmission line and the return stroke current is generated by a wave of ground potential that travels

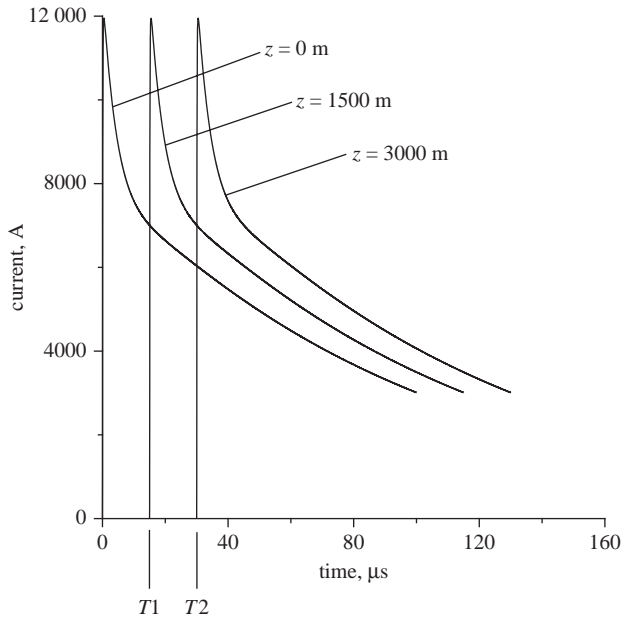


*Figure 9.6* Return stroke current at several locations along the channel according to the transmission line model [53]. In the calculation the channel base current is represented by the analytical waveform created for subsequent return strokes by Nucci *et al.* [59] and the return stroke speed  $v$  is kept constant at  $10^8$  m/s. In the figure  $T_1$  and  $T_2$  are the times at which the current at heights 1500 and 3000 m are initiated (i.e.  $T_1 = 1500/v$ ,  $T_2 = 3000/v$ )

along it from ground to cloud. The arrival of the wavefront (i.e. return stroke front) at a given point on the leader channel changes its potential from cloud potential to ground potential causing the release of bound charge on the central core and the corona sheath giving rise to the current in the channel (this is called the corona current in the literature). These models postulate that as the return stroke front propagates upwards the charge stored on the leader channel collapses into the highly conducting core of the return stroke channel. Accordingly, each point on the leader channel can be treated as a current source which is turned on by the arrival of the return stroke front at that point. The corona current injected by these sources into the highly conducting return stroke channel core travels to ground with a speed denoted by  $v_c$ . As we will see later, in most of the return stroke models it is assumed that  $v_c = c$  where  $c$  is the speed of light.

The basic concept of CG models was first introduced by Wagner [60]. He assumed that the neutralisation of the corona sheath takes a finite time and therefore the corona current can be represented by a decaying exponential function. The decay time constant associated with this function is called the *corona decay time constant*. Wagner assumed, however, that the speed of propagation of the corona current down the return stroke channel is infinite. Lin *et al.* [61] introduced a model in which both CG and CP concepts are incorporated in the same model. In the portion of the current described by CG concept, the corona current is represented by a double exponential function. The speed of propagation of corona current down

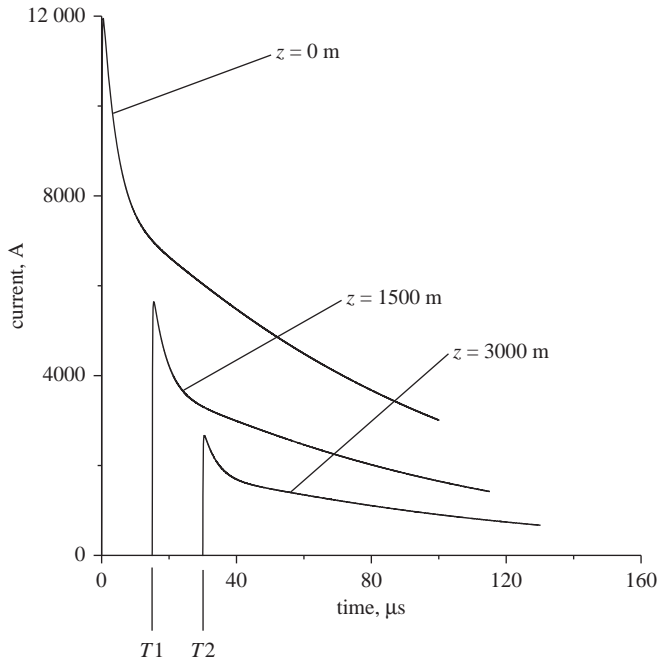
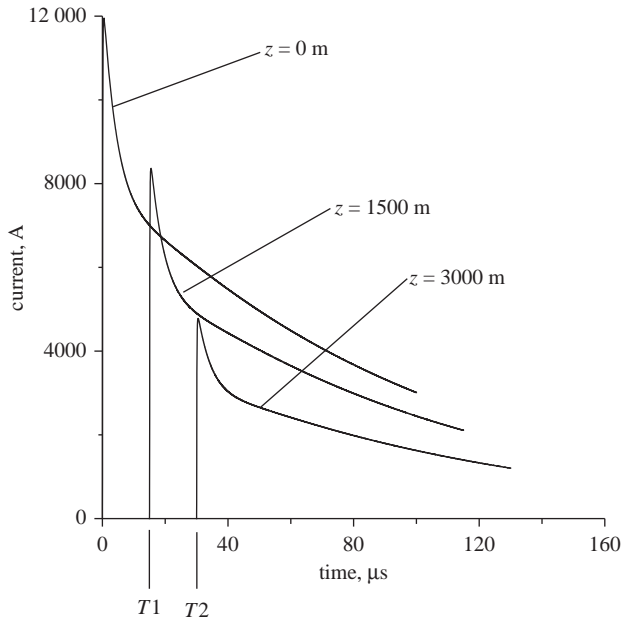


Figure 9.7 Return stroke current at several locations along the channel according to the MTLE [54]. In the calculation the channel base current is represented by the analytical waveform created for subsequent return strokes by Nucci *et al.* [59] and the return stroke speed  $v$  is kept constant at  $10^8$  m/s. In the figure  $T1$  and  $T2$  are the times at which the current at heights 1500 and 3000 m are initiated (i.e.  $T1 = 1500/v$ ,  $T2 = 3000/v$ )

the channel is assumed to be the same as the speed of light. A modified form of this model is introduced by Master *et al.* [62] but in this modification the CG description remained intact. Heidler [63] constructed a model based on this principle in which the channel base current and the return stroke speed are assumed as input parameters. Furthermore, it was assumed that the neutralisation of the corona sheath is instantaneous and hence the corona current generated by a given channel section can be represented by a Dirac delta function. The speed of propagation of the corona current down the return stroke channel is assumed to be equal to the speed of light. This model gives rise to a current discontinuity at the return stroke front which, according to the author's understanding is not physically reasonable. Hubert [64] constructed a current generation model rather similar to that of the Wagner's model with the exception that the downward speed of propagation of the corona current is equal to the speed of light. He utilised this model to reproduce experimental data (both current and electromagnetic fields) obtained from triggered lightning. Cooray [65, 66] introduced a model in which the distribution of the charge deposited by the return stroke (i.e. sum of the positive charge necessary to neutralise the negative charge on the leader and the positive charge induced on the channel due to the action of the background electric field) and the decay time constant of the corona current are taken as input parameters with the model





**Figure 9.8** Return stroke current at several locations along the channel according to the MTL [55]. In the calculation the channel base current is represented by the analytical waveform created for subsequent return strokes by Nucci *et al.* [59] and the return stroke speed  $v$  is kept constant at  $10^8$  m/s. In the figure  $T_1$  and  $T_2$  are the times at which the current at heights 1500 and 3000 m are initiated (i.e.  $T_1 = 1500/v$ ,  $T_2 = 3000/v$ )

predicting the channel base current and return stroke speed. Moreover, he took into consideration that the process of neutralisation of the corona sheath takes a finite time in reality and, as a consequence, the corona current was represented by an exponential function with a finite duration. This is the first model in which the decay time constant of the corona current (and hence the duration of the corona current) is assumed to increase with height. Since the leader channel contains a hot core surrounded by a corona sheath, he also divided the corona current into two parts, one fast and the other slow. The fast one was associated with the neutralisation of the core and the slow one with the neutralisation of the corona sheath. Furthermore, by treating the dart leader as an arc and assuming that the electric field at the return stroke front is equal to the electric field that exists in this arc channel, he manages to derive the speed of the return stroke. Diendorfer and Uman [67] introduced a model in which the channel base current, return stroke speed and the corona decay time constant were assumed as input parameters. They also divided the corona current into two parts one fast and the other slow. Thottappillil *et al.* [68] and Thottappillil and Uman [69] modified this model to include variable return stroke speed and a corona decay time constant that varies with height. Cooray [70] developed the ideas introduced in [65] and [66] to create a CG model with channel base current as an input. Cooray [71], Cooray and Galvan [72] and Cooray *et al.* [73] extended the concept to include first return strokes with connecting leaders.

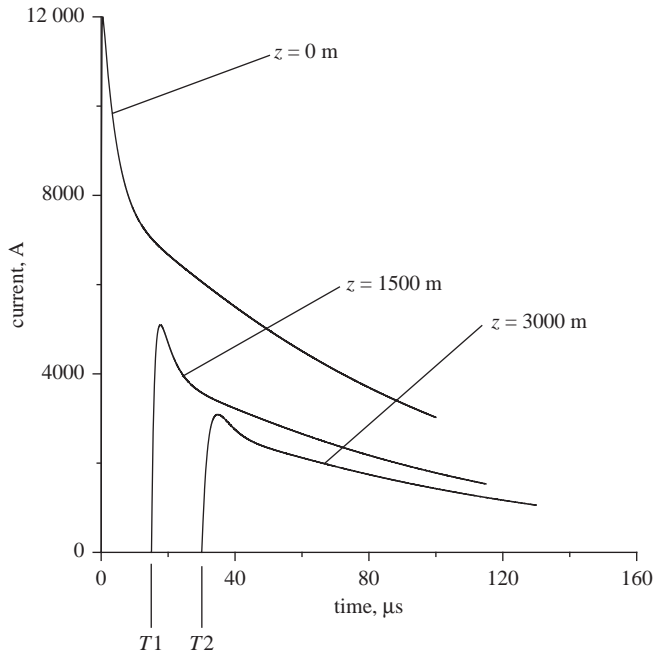


Figure 9.9 Return stroke current at several locations along the channel according to Cooray and Orville [56] model. In the calculation the channel base current is represented by the analytical waveform created for subsequent return strokes by Nucci *et al.* [59] and the return stroke speed  $v$  is kept constant at  $10^8$  m/s. Moreover in the calculation  $\eta = 7 \times 10^{-10}$  S/m. In the figure  $T1$  and  $T2$  are the times at which the current at heights 1500 and 3000 m are initiated (i.e.  $T1 = 1500/v$ ,  $T2 = 3000/v$ ). Note that the rise time of the current waveform increases with height

In CG models one has the choice of selecting the channel base current,  $I_b(t)$ , the distribution of the charge deposited by the return stroke along the channel,  $\rho(z)$ , the return stroke speed,  $v(z)$ , and the magnitude and variation of the corona discharge time constant with height,  $\tau(z)$  as input parameters. Any set of three of these four input parameters will provide a complete description of the temporal and spatial variation of the return stroke current. Most of the CG models use  $v(z)$  and either the  $\rho(z)$  or  $\tau(z)$  in combination with  $I_b(t)$  as input parameters. Recently, Cooray and Rakov [74] developed a model in which  $\rho(z)$ ,  $\tau(z)$  and  $I_b(t)$  are selected as input parameters. The model could generate  $v(z)$  as a model output.

### 9.6.2.2 Mathematical background

As mentioned above, a current generation model needs three input parameters which can be selected from a set of four parameters, i.e.  $\rho(z)$ ,  $\tau(z)$ ,  $I_b(t)$  and  $v(z)$ . Once three of these parameters are specified the fourth can be evaluated either analytically or numerically. Let us now consider the mathematics necessary to do this.

*Evaluate  $I_b(t)$  given  $\rho(z)$ ,  $\tau(z)$  and  $v(z)$*

Since the current at any given level on the channel is the cumulative effect of corona currents associated with channel elements located above that level, the

return stroke current at any height in the return stroke channel  $I(z,t)$  can be written as

$$I(z,t) = \int_z^{h_e} I_{cor}(t - \xi/v_{av}(\xi) - (\xi - z)/v_c) d\xi \quad t > z/v_{av}(z) \quad (9.13)$$

$$I_{cor}(z) = \frac{\rho(z)}{\tau(z)} \exp\{-(t - z/v_{av}(z))\} \quad t > z/v_{av}(z) \quad (9.14)$$

Note that  $I_{cor}(z)$  is the corona current per unit length associated with a channel element at height  $z$  and  $v_{av}(z)$  is the average return stroke speed over the channel section of length  $z$  with one end at ground level. The latter is given by

$$v_{av}(z) = z / \int_0^z \frac{1}{v(z)} dz \quad (9.15)$$

The value of  $h_e$  can be obtained from the solution of the following equation:

$$t = \frac{h_e}{v_{av}(h_e)} + \frac{h_e - z}{v_c} \quad (9.16)$$

The current at the channel base is given by

$$I_b(0,t) = \int_0^{h_0} I_{cor}(t - \xi/v_{av}(\xi) - \xi/v_c) d\xi \quad (9.17)$$

$$t = \frac{h_0}{v_{av}(h_0)} + \frac{h_0}{v_c} \quad (9.18)$$

*Evaluate  $\tau(z)$  given  $I_b(t)$ ,  $\rho(z)$  and  $v(z)$*

In most of the return stroke models corona current is represented by a single exponential function. An exponential function gives an instantaneous rise time to the corona current which is not physically reasonable. For this reason in a few models it is represented by a double exponential function. In the analysis to be given below we assume that the corona current is represented by a double exponential function. The corona current in this case is given by

$$I_{cor}(z) = \frac{\rho(z)}{\tau(z) - \tau_r} [\exp\{-(t - z/v_{av}(z))/\tau(z)\} - \exp\{-(t - z/v_{av}(z))/\tau_r\}] \quad t > z/v_{av}(z) \quad (9.19)$$

where both  $\rho(z)$ ,  $\tau_r$  are known but  $\tau(z)$  is unknown. Results pertinent to a corona current with a single exponential function can be obtained by letting  $\tau_r = 0$ . With this corona current the return stroke current at ground level is given by

$$I_b(0,t) = \int_0^{h_0} \frac{\rho(z) dz}{\tau(z) - \tau_r} [\exp\{-(t - z/v_{av}(z) - z/v_c)/\tau(z)\} - \exp\{-(t - z/v_{av}(z) - z/v_c)/\tau_r\}] \quad (9.20)$$

where  $h_0$  can be extracted by the solution of the (9.18). If we divide the channel into a large number of segments of equal length  $dz$ , the above integral can be written as a summation as follows:

$$I_b(t_m) = \sum_{n=1}^m \frac{\rho_n}{\tau_n - \tau_r} \exp\left\{-\left(t_m - \frac{(n-1)dz}{v_{av,n}} - \frac{(n-1)dz}{v_c}\right)/\tau_n\right\} - \sum_{n=1}^m \frac{\rho_n}{\tau_n - \tau_r} \exp\left\{-\left(t_m - \frac{(n-1)dz}{v_{av,n}} - \frac{(n-1)dz}{v_c}\right)/\tau_r\right\} \quad (9.21)$$

where  $\rho_n$  is the charge deposited per unit length on the  $n^{\text{th}}$  segment,  $\tau_n$  is the decay time constant of the corona current of the  $n^{\text{th}}$  segment and  $v_{av,n}$  is the average return stroke speed over the channel section connecting the ground and the  $n^{\text{th}}$  segment. In this equation  $t_m$  is the time for the corona current released from the  $m^{\text{th}}$  segment to reach the ground. This is given by the equation

$$t_m = \frac{m}{v_{av,m}} + \frac{m}{v_c} \quad (9.22)$$

If the return stroke speed and the current at the channel base is known, then the value of the discharge time constant at different heights can be estimated progressively by moving from  $m = 1$ . For example when  $m = 1$  the only unknown is the  $\tau_1$ . Once this is found one can consider the case  $m = 2$ . In the resulting equation the only unknown is the value of  $\tau_2$  and it can be obtained by solving that equation. In this way the values of discharge time constants up to the  $m^{\text{th}}$  element can be obtained sequentially [68, 70].

*Evaluate  $\rho(z)$  given  $I_b(t)$ ,  $\tau(z)$  and  $v(z)$*

Equations (9.21) and (9.22) can also be used to evaluate the charge density  $\rho(z)$  when the other parameters are given as inputs. For example in this case when  $m = 1$  the only unknown is the  $\rho_1$ . Once this is found one can consider the case  $m = 2$ . In the resulting equation the only unknown is the value of  $\rho_2$  and it can be obtained by solving that equation. In this way the values of charge densities up to any  $m^{\text{th}}$  element can be obtained sequentially.

*Evaluate  $v(z)$ , given  $\rho(z)$ ,  $I_b(t)$  and  $\tau(z)$*

As before, we start with (9.21). Since  $I_b(t)$ ,  $\rho(z)$  and  $\tau(z)$  are given the only unknown parameter in these equations is  $v_{av,m}$ , the average speed along the  $n^{\text{th}}$  channel segment. Solving the equations as before one can observe that when  $m = 1$  the only unknown is  $v_{av,1}$ , the average speed over the first channel segment. Once this is found the value of  $v_{av,2}$  can be obtained by considering the situation of  $m = 2$ . In this way the average return stroke speed as a function of height can be obtained. It is important to point out that in this evaluation the value of  $dz$  in (9.21) and (9.22) should be selected in such a manner that it is reasonable to assume constant return stroke speed along the channel element. Once the average return stroke speed as a function of height is known the return stroke speed as a function of height can be obtained directly from it.

**9.6.3 CG models in practice**

As mentioned in the introduction, several current generation models are available in the literature and they differ from each other by the way in which input

parameters are selected. In the sections to follow information necessary to use CG models to calculate the spatial and temporal variation of the return stroke current is given.

### 9.6.3.1 Model of Wagner [60]

This is the first CG model to be introduced in the literature and therefore the credit for the creation of current generation models goes to Wagner. He is the first scientist to come up with the concept of corona current and to treat the return stroke current as a sum of corona currents generated by channel elements located along the channel. The input parameters of the Wagner's model are the distribution of the charge deposited by the return stroke, corona decay time constant and the return stroke speed. In the model Wagner assumed that the speed of propagation of the corona current down the return stroke channel is infinite. The parameters of Wagner's model are the following:

*Channel base current:*

The channel base current can be calculated using the parameters given below in (9.17).

*Corona current per unit length:*

$$I_c(t, z) = \frac{\rho(z)}{\tau} e^{-t/\tau} \text{ with } \tau = 6.66 \times 10^{-6} \text{ s.}$$

*Speed of the corona current:*

$$v_c = \infty$$

*Linear density of the charge deposited by the return stroke:*

$\rho(z) = \rho_0 e^{-z/\lambda}$ . The peak current at ground level varies with  $\rho_0$  and the latter can be selected to get the desired current peak at ground level,  $\lambda = 10^3$  m.

*Return stroke speed:*

$v(z) = v_0 e^{-\gamma t}$  where  $\gamma = 3 \times 10^4 \text{ s}^{-1}$  and  $v_0$ , which is a constant, is assumed to vary between  $0.1c$  and  $0.5c$  where  $c$  is the speed of light.

*Comment:* Note that the predicted current at ground level has a double exponential shape. The rise time of the current is determined by  $\tau$  and the decay time by  $\lambda$  and  $\gamma$ .

### 9.6.3.2 Model of Heidler [63]

Heidler is the first scientist to introduce the channel base current as an input parameter in CG models and to connect the other parameters of the model to the channel base current. The input parameters of the model in addition to the channel base current are the return stroke speed and the corona discharge time constant. In the model Heidler assumed that the discharge time constant of the corona current is zero, i.e. the discharge process takes place instantaneously. With these parameters the model can predict the distribution of the charge deposited by the return stroke along the channel. The parameters of the model are given below. Observe that the linear density of the charge deposited by the return stroke can be derived analytically.

*Channel base current:*

$I_b(0, t) = \frac{I_p}{\eta} \frac{k^n}{1+k^n} e^{-t/\tau_2}$  with  $k = t/\tau_1$ ,  $n = 10$ ,  $\tau_1 = 1.68 \text{ } \mu\text{s}$ ,  $\tau_2 = 20\text{--}150 \text{ } \mu\text{s}$ ,  $\eta$  is the factor that has to be adjusted to get the exact current peak value.

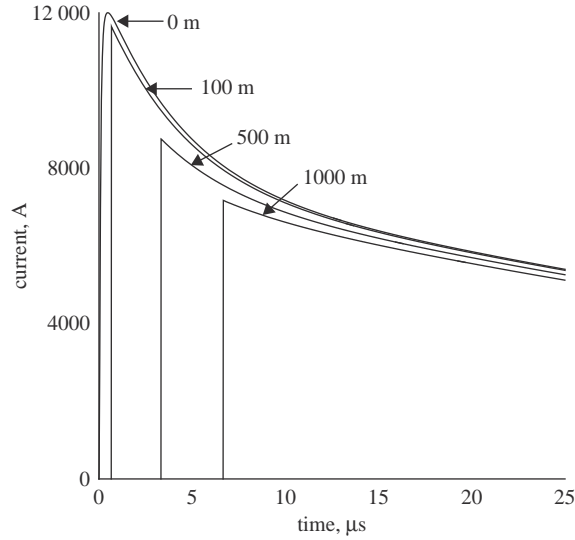


Figure 9.10 The current waveform at different heights as predicted by the Heidler [63] model

Corona current per unit length:

$$I_c(t, z) = \rho(z)\delta(t)$$

In the above equation  $\delta(t)$  is the Dirac impulse function.

Speed of the corona current:

$$v_c = c$$

Linear density of the charge deposited by the return stroke:

$$\rho(z) = \frac{I_b(0, z/v + z/v_c)}{v^*} \quad \text{with} \quad \frac{1}{v^*} = \frac{1}{v} + \frac{1}{v_c}$$

Return stroke speed:

In the model  $v$  is assumed to be a constant.

The return stroke current at several heights along the return stroke channel as predicted by this model is shown in Figure 9.10. Note that the current at the return stroke front at elevated points on the return stroke channel contains a step current rise (i.e. an instantaneous current rise).

### 9.6.3.3 Model of Hubert [64]

Hubert utilised a model based on CG concept to generate a fit to the measured currents and electromagnetic fields of triggered lightning flashes. The values of various model parameters were selected so that the predictions agree with experiment. The input parameters of the model are the distribution of the charge deposited by the return stroke, return stroke speed and the corona decay time constant. The parameters of the model are the following:

Channel base current:

The channel base current can be calculated using the parameters given in (9.17).

*Corona current per unit length:*

$$I_c(t, z) = \frac{\rho(z)}{\tau} e^{-t/\tau} \quad \tau = 10^{-7} \text{ s}$$

*Speed of the corona current:*

$$v_c = c$$

*Linear density of the charge deposited by the return stroke:*

$\rho(z) = \rho_0 e^{-z/\lambda}$  where  $\lambda = 15 \times 10^3$  m and the value of  $\rho_0$  is selected to provide the required peak current at ground level.

*Return stroke speed:*

In the model  $v$  is assumed to be a constant equal to  $1.0 \times 10^8$  m/s.

### 9.6.3.4 Model of Cooray [65, 66]

Cooray introduced a CG model where for the first time the discharge time constant is assumed to increase with height. He also assumed that the neutralisation process can be divided into two parts: one fast and the other slow. The fast one is assumed to be generated by the neutralisation of the charge on the central core of the leader channel and the slow one by the neutralisation of the cold corona sheath. The input parameters of the model are the corona discharge time constant and the distribution of the charge deposited by the return stroke on the channel. Cooray also attempted to evaluate the return stroke speed by connecting the electric field at the return stroke front to the potential gradient of the leader channel. The results showed that the return stroke speed increases initially, reaches a peak and then continue to decrease with increasing height. However, in using this model in engineering studies one can skip this iterative calculation and use it as a normal CG model by plugging in a speed profile similar to that predicted by the full model as an input parameter. An approximate for this speed profile is given by

$$v(z) = v_1 + (v_2/2) [2 - e^{-(z-1)/a} - e^{-(z-1)/b}] \quad 1.0 \leq z \leq 50 \text{ m} \quad (9.23a)$$

$$v(z) = v_3 e^{-(z-50)/a1} + v_4 e^{-(z-50)/b1} \quad z \geq 50 \text{ m} \quad (9.23b)$$

with  $v_1 = 1.02 \times 10^8$  m/s,  $v_2 = 1.35 \times 10^8$  m/s,  $v_3 = 7.11 \times 10^7$  m/s,  $v_4 = 1.66 \times 10^8$  m/s,  $a = 1.4$  m,  $b = 7.4$  m,  $a1 = 400$  m,  $b1 = 2100$  m. The other model parameters are summarised below:

*Channel base current:*

Inserting the parameters given below in (9.13) one can calculate the return stroke current at any level along the channel.

*Corona current per unit length of the hot corona sheath:*

$$I_{hc}(t, z) = \frac{\rho_h(z)}{\tau_h - \tau_b} [e^{-t/\tau_h} - e^{-t/\tau_b}] \quad \text{with } \tau_h \approx 50 - 100 \text{ ns} \quad \tau_b = 5 \text{ ns}$$

*Corona current per unit length of the cold corona sheath:*

$$I_{cc}(t, z) = \frac{\rho_c(z)}{\tau_s - \tau_h} [e^{-t/\tau_s} - e^{-t/\tau_h}] \quad \text{where } \tau_s = \tau_{so} [1 - e^{-z/\lambda_s}] \quad \text{and } \tau_{so} = 1 \text{ } \mu\text{s}, \lambda_s = 200 \text{ m.}$$

Corona current per unit length:

$$I_c(t, z) = I_{hc}(t, z) + I_{cc}(t, z)$$

Speed of corona current:

$$v_c = c$$

Total linear density of the charge deposited by the return stroke on the leader channel:

$$\rho(z) = \rho_0[0.3e^{-z/\lambda_1} + 0.7e^{-z/\lambda_2}] \text{ with } \rho_0 = 0.0001 \text{ C/m (for a typical subsequent stroke), } \lambda_1 = 600 \text{ m, } \lambda_2 = 5000 \text{ m}$$

Linear density of charge deposited by the return stroke on the hot core:

$$\rho_h(z) = \rho_0 e^{-z/\lambda_c} \text{ with } \lambda_c = 50 \text{ m.}$$

Linear density of charge deposited by the return stroke on the corona sheath:

$$\rho_c(z) = \rho(z) - \rho_h(z)$$

Return stroke speed:

Predicted by the model; speed profile given by (9.23a) and (9.23b) can also be used as an input parameter in order to simplify the calculations.

*Comment:* Observe that the peak value of the current at ground level varies linearly with  $\rho_0$ .

### 9.6.3.5 Model of Diendorfer and Uman [67]

Diendorfer and Uman introduced a return stroke model where, similar to the model of Cooray [65, 66] described above, the corona current is separated into two parts, one fast and the other slow. The fast corona current is assumed to be generated by the neutralisation of the leader core and the slow one by the corona sheath. However, in contrast to Cooray model they utilised the channel base current as one of the input parameters. In the model, this current was separated into two parts. One part was assumed to be generated by the cumulative effects of the fast corona current and the other part by the cumulative effects of the slow corona currents. In addition to the channel base current the input parameters of the model are the return stroke speed and the discharge time constants. The input parameters of this model are the following:

Channel base current:

$$I_b(0, t) = i_h(t) + i_c(t)$$

Channel base current component associated with the leader core:

$$i_h(t) = \frac{I_{01}}{\eta_1} \frac{(t/\tau_{11})^2}{(t/\tau_{11})^2 + 1} e^{-t/\tau_{21}} \text{ with } I_{01} = 13 \text{ kA, } \eta_1 = 0.73, \tau_{11} = 0.15 \text{ } \mu\text{s, } \tau_{21} = 3.0 \text{ } \mu\text{s for typical subsequent strokes and } I_{01} = 28 \text{ kA, } \eta_1 = 0.73, \tau_{11} = 0.3 \text{ } \mu\text{s, } \tau_{21} = 6.0 \text{ } \mu\text{s for typical first strokes.}$$

Channel base current component associated with the corona sheath:

$$i_c(t) = \frac{I_{02}}{\eta_2} \frac{(t/\tau_{12})^2}{(t/\tau_{12})^2 + 1} e^{-t/\tau_{22}} \text{ with } I_{02} = 7 \text{ kA, } \eta_2 = 0.64, \tau_{12} = 5 \text{ } \mu\text{s, } \tau_{22} = 50 \text{ } \mu\text{s for typical subsequent strokes and } I_{02} = 16 \text{ kA, } \eta_2 = 0.53, \tau_{12} = 10 \text{ } \mu\text{s, } \tau_{22} = 50 \text{ } \mu\text{s for typical first strokes.}$$



Corona current per unit length from the leader core:

$$I_h(t, z) = \frac{\rho_h(z)}{\tau_h} e^{-t/\tau_h} \quad \text{with } \tau_h = 0.6 \text{ } \mu\text{s.}$$

Corona current per unit length from the corona sheath:

$$I_c(t, z) = \frac{\rho_c(z)}{\tau_c} e^{-t/\tau_c} \quad \text{with } \tau_c = 5 \text{ } \mu\text{s.}$$

Total corona current:

$$I_c(t, z) = I_h(t, z) + I_c(t, z)$$

Linear density of charge deposited by the return stroke on the leader core:

$$\rho_h(z) = \frac{i_h(0, z/v^*) + \tau_h \frac{di_h(0, z/v^*)}{dt}}{v^*} \quad \text{with } \frac{1}{v^*} = \frac{1}{v} + \frac{1}{v_c}$$

Linear density of charge deposited by the return stroke on the corona sheath:

$$\rho_c(z) = \frac{i_c(0, z/v^*) + \tau_c \frac{di_c(0, z/v^*)}{dt}}{v^*} \quad \text{with } \frac{1}{v^*} = \frac{1}{v} + \frac{1}{v_c}$$

Total linear charge density deposited by the return stroke:

$$\rho(z) = \rho_h(z) + \rho_c(z)$$

Speed of corona current:

$$v_c = c$$

Return stroke speed:

In the model  $v$  is assumed to be a constant equal to  $1.3 \times 10^8$  m/s.

*Comment:* Note that the charge densities are not input parameters but could be derived once the channel base current, return stroke speed and the corona decay time constants are given.

The return stroke current at several heights along the return stroke channel as predicted by this model is shown in Figure 9.11.

### 9.6.3.6 First modification of the Diendorfer and Uman model by Thottappillil *et al.* [68]

Thottappillil *et al.* modified the Diendorfer and Uman model to introduce a return stroke speed that varies with height. The parameters are tabulated below:

Channel base current:

$$I_b(0, t) = i_h(t) + i_c(t)$$

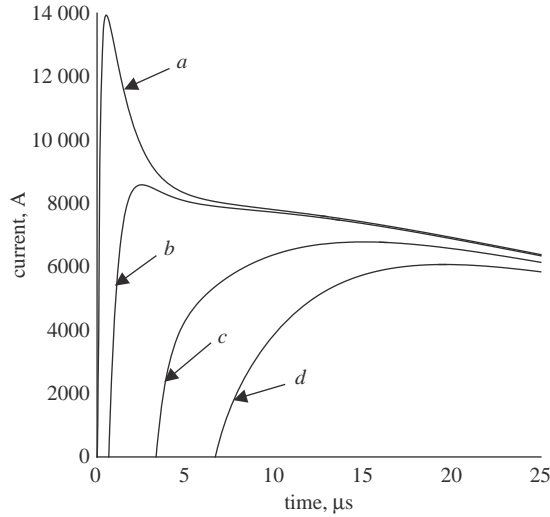


Figure 9.11 The current waveform at different heights as predicted by the Diendorfer and Uman [67] model

Channel base current component associated with the leader core:

$i_h(t) = \frac{I_{01}}{\eta_1} \frac{(t/\tau_{11})^2}{(t/\tau_{11})^2 + 1} e^{-t/\tau_{21}}$  with  $I_{01} = 13$  kA,  $\eta_1 = 0.73$ ,  $\tau_{11} = 0.15$   $\mu$ s,  $\tau_{21} = 3.0$   $\mu$ s for typical subsequent strokes and  $I_{01} = 28$  kA,  $\eta_1 = 0.73$ ,  $\tau_{11} = 0.3$   $\mu$ s,  $\tau_{21} = 6.0$   $\mu$ s for typical first strokes.

Channel base current component associated with the corona sheath:

$i_c(t) = \frac{I_{02}}{\eta_2} \frac{(t/\tau_{12})^2}{(t/\tau_{12})^2 + 1} e^{-t/\tau_{22}}$  with  $I_{02} = 7$  kA,  $\eta_2 = 0.64$ ,  $\tau_{12} = 5$   $\mu$ s,  $\tau_{22} = 50$   $\mu$ s for typical subsequent strokes and  $I_{02} = 16$  kA,  $\eta_2 = 0.53$ ,  $\tau_{12} = 10$   $\mu$ s,  $\tau_{22} = 50$   $\mu$ s for typical first strokes.

Corona current per unit length from the leader core:

$$I_h(t, z) = \frac{\rho_h(z)}{\tau_h} e^{-t/\tau_h} \quad \text{with } \tau_h = 0.6 \mu\text{s.}$$

Corona current per unit length from the corona sheath:

$$I_c(t, z) = \frac{\rho_c(z)}{\tau_c} e^{-t/\tau_c} \quad \text{with } \tau_c = 5 \mu\text{s.}$$

Total corona current:

$$I_c(t, z) = I_h(t, z) + I_c(t, z)$$

Linear density of charge deposited by the return stroke on the leader core:

$$\rho_h(z) = \frac{i_h(0, z/v_{av}(z) + z/v_c) + \tau_h \frac{di_h(0, z/v_{av}(z) + z/v_c)}{dt}}{\Gamma}$$

$$\frac{1}{\Gamma} = \frac{v_{av}(z) - z \frac{dv_{av}(z)}{dz}}{(v_{av}(z))^2} + \frac{1}{v_c}$$

*Linear density of charge deposited by the return stroke on the corona sheath:*

$$\rho_c(z) = \frac{i_c(0, z/v_{av}(z) + z/v_c) + \tau_c \frac{di_c(0, z/v_{av}(z) + z/v_c)}{dt}}{\Gamma}$$

*Total linear charge density deposited by the return stroke:*

$$\rho(z) = \rho_h(z) + \rho_c(z)$$

*Speed of corona current:*

$$v_c = c$$

*Return stroke speed:*

$v = v_0 e^{-z/\lambda}$  with  $v_0 = 1.3 \times 10^8$  m/s and  $\lambda$  varying between 1000 and 3000 m.

### 9.6.3.7 Second modification of the Diendorfer and Uman model by Thottappillil and Uman [69]

In a subsequent publication Thottappillil and Uman modified the Diendorfer and Uman model to include a discharge time constant that increases with height. The input parameters of the model are the charge density, return stroke speed and the channel base current. These input parameters are tabulated below.

*Channel base current:*

$$I_b(0, t) = i_h(t) + i_c(t)$$

$i_h(t) = \frac{I_{01}}{\eta_1} \frac{(t/\tau_{11})^2}{(t/\tau_{11})^2 + 1} e^{-t/\tau_{21}}$   $I_{01} = 13$  kA,  $\eta_1 = 0.73$ ,  $\tau_{11} = 0.15$   $\mu$ s,  $\tau_{21} = 3.0$   $\mu$ s for typical subsequent strokes and  $I_{01} = 28$  kA,  $\eta_1 = 0.73$ ,  $\tau_{11} = 0.3$   $\mu$ s,  $\tau_{21} = 6.0$   $\mu$ s for typical first strokes  $i_c(t) = \frac{I_{02}}{\eta_2} \frac{(t/\tau_{12})^2}{(t/\tau_{12})^2 + 1} e^{-t/\tau_{22}}$  with  $I_{02} = 7$  kA,  $\eta_2 = 0.64$ ,  $\tau_{12} = 5$   $\mu$ s,  $\tau_{22} = 50$   $\mu$ s for typical subsequent strokes and  $I_{02} = 16$  kA,  $\eta_2 = 0.53$ ,  $\tau_{12} = 10$   $\mu$ s,  $\tau_{22} = 50$   $\mu$ s for typical first strokes.

*Corona current per unit length:*

$I_{cor}(t, z) = \frac{\rho(z)}{\tau(z)} e^{-t/\tau(z)}$ ;  $\tau_z$  has to be evaluated from (9.21).

*Linear density of charge deposited by the return stroke on the leader channel:*

$$\rho(z) = \frac{i_h(0, z/v^*) + \tau_h \frac{di_h(0, z/v^*)}{dt}}{v^*} + \frac{i_c(0, z/v^*) + \tau_c \frac{di_c(0, z/v^*)}{dt}}{v^*}$$

where  $\frac{1}{v^*} = \frac{1}{v} + \frac{1}{v_c}$ . The values of  $\tau_h$  and  $\tau_c$  are given in section 9.6.3.5.

*Speed of corona current:*

$$v_c = c$$

*Return stroke speed:*

In the model  $v$  is assumed to be a constant equal to  $1.3 \times 10^8$  m/s.

*Comment:* Note that the charge distribution used as an input to the model is identical to that obtained in the original Diendorfer and Uman model.

### 9.6.3.8 Model of Cooray [70]

In constructing the model, Cooray utilised the same principles as the ones used in his original model but utilised the channel base current as one of the input parameters. The other input parameter is the distribution of the charge deposited by the return stroke. Both the variation of the corona discharge time constant with height and the return stroke speed were extracted from the model. In order to obtain the return stroke speed he assumed that the electric field at the front of the return stroke is equal to the potential gradient of the leader channel. Again it is observed that the return stroke speed increases initially, reaches a peak and then continues to decrease. However, one can skip the additional numerical procedures by treating the return stroke speed as an input parameter. Then the model can be used as a normal CG model. The parameters of the model are given below:

*Channel base current:*

$I_b(0, t) = \frac{I_{01}}{\eta} \frac{(t/\tau_1)^2}{(t/\tau_1)^2 + 1} e^{-t/\tau_2} + I_{02}(e^{-t/\tau_3} + e^{-t/\tau_4})$ ; for a typical subsequent return stroke  $I_{01} = 9.9$  kA,  $\eta = 0.845$ ,  $\tau_1 = 0.072$   $\mu$ s,  $\tau_2 = 5$   $\mu$ s,  $I_{02} = 7.5$  kA,  $\tau_3 = 100$   $\mu$ s and  $\tau_4 = 6$   $\mu$ s.

*Corona current per unit length:*

$I_{cor}(t, z) = \frac{\rho(z)}{\tau(z) - \tau_b} [e^{-t/\tau(z)} - e^{-t/\tau_b}]$ ,  $\tau_b = 5$  ns,  $\tau(z)$  has to be evaluated from (9.21).

*Linear charge density deposited by the return stroke:*

$\rho(z) = \rho_0 [1 - \frac{z}{H}]$ ; the value of  $\rho_0$  scales linearly with peak current with 100  $\mu$ C/m for a 10 kA current.  $H$  is the height of the return stroke channel (assumed to be 9 km in the model).

*Speed of corona current:*

$$v_c = c$$

*Return stroke speed:*

Predicted by the model. But one can use the model as a normal CG model by using the return stroke speed as an input parameter.

The return stroke current at several heights along the return stroke channel as predicted by this model is shown in Figure 9.12.

### 9.6.3.9 Models of Cooray and Rakov – Version I [75]

In a paper published by Cooray and Rakov [75] several possibilities that could be used to model return strokes were explored. One of the possibilities explored by Cooray and Rakov is presented here.

Since the return stroke speed is one of the possible input parameters of CG models, Cooray and Rakov realised that if the charge deposited by the return stroke, corona decay time constant and channel base current are given as input parameters, one can utilise the return stroke model itself to predict the return stroke speed profile without any additional mathematics. A model that can do that is introduced by Cooray and Rakov. The model showed again that the return stroke speed increases initially, reaches a peak and then continue to decay. The input parameters of the model are tabulated below:

*Channel base current:*

$I_b(0, t) = \frac{I_{01}}{\eta} \frac{(t/\tau_1)^2}{(t/\tau_1)^2 + 1} e^{-t/\tau_2} + I_{02}(e^{-t/\tau_3} + e^{-t/\tau_4})$ ; for a typical subsequent return stroke  $I_{01} = 9.9$  kA,  $\eta = 0.845$ ,  $\tau_1 = 0.072$   $\mu$ s,  $\tau_2 = 5$   $\mu$ s,  $I_{02} = 7.5$  kA,  $\tau_3 = 100$   $\mu$ s and  $\tau_4 = 6$   $\mu$ s.

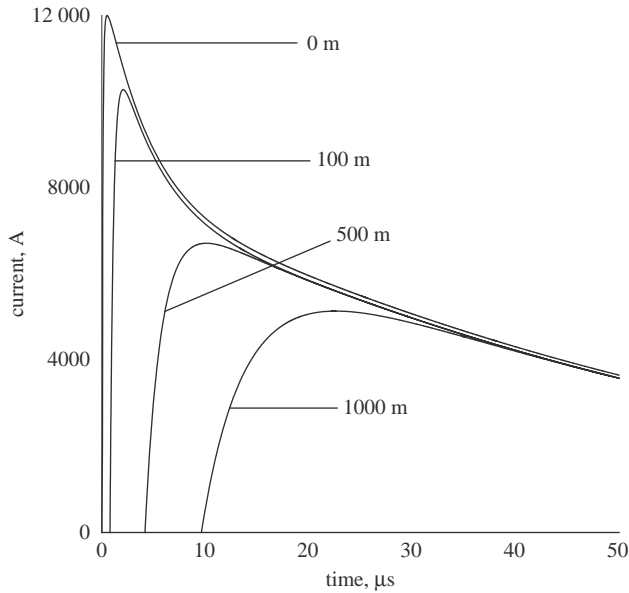


Figure 9.12 The current waveform at different heights as predicted by the Cooray [70] model

Corona current per unit length:

$$I_{cor}(t, z) = \frac{\rho(z)}{\tau(z)} e^{-t/\tau(z)}; \tau(z) = \tau_i + \mu z \text{ with } \tau_i = 10^{-8} \text{ s, and } \mu = 10^{-9} \text{ s/m.}$$

Linear charge density of the charge deposited by the return stroke on the leader channel:

$$\rho(z) = a_0 I_p + I_p \frac{(a+bz)}{1+cz+dz^2}; I_p \text{ is the peak return stroke current, } a_0 = 5.09 \times 10^{-6} \text{ s/m, } a = 1.325 \times 10^{-5} \text{ (s/m), } b = 7.06 \times 10^{-6} \text{ (s/m}^2\text{), } c = 2.089 \text{ m}^{-1}, d = 1.492 \times 10^2 \text{ (m}^{-2}\text{). This is based on the results obtained in [76].}$$

Speed of corona current:

$$v_c = c$$

Return stroke speed:

Evaluated from the model using (9.21).

#### 9.6.4 Inadequacy of the CG models used in practice to represent first return strokes

One of the input parameters that is frequently used in current generation type return stroke models is the channel base current. Experimental data show that there is a significant difference in the first return stroke current waveform in comparison to that of subsequent return strokes. The main difference is the presence of a slow front in the rising edge of the first return stroke current waveforms. Cooray *et al.* [73] showed that a channel base current waveform having a slow front is not compatible with the current generation type return stroke models available in the literature. For example their calculations show that when a typical first return stroke current with a slow front is used in either Diendorfer and Uman model [67] or the Heidler model [63] the close fields become negative and the distant radiation fields become very large and narrow. These features are not in agreement with

measured electromagnetic fields. Cooray *et al.* [73] showed that the only way to accommodate a current waveform with a slow front in a CG model is to make the assumption that the slow front is generated by a connecting leader rising up to meet the down-coming stepped leader. Cooray and Galvan [72] and Cooray *et al.* [73] created a first return stroke model belonging to CG type that treats the slow front in the channel base current waveform as the current generated by the connecting leader as it surges forward through the streamer region of the stepped leader. This model is presented in the next section.

## 9.6.5 A CG model to represent first return strokes

### 9.6.5.1 Basic features

The main difference between the first return stroke and the subsequent return strokes is the nature of the leader that initiates the discharge. The stepped leader propagates in an un-ionised media, whereas the dart leader propagates along a medium at elevated temperature. The leading edge of the leader channel consists of two parts: a cold streamer region attached to the hot leader channel. It is doubtful whether such a streamer region exists in dart leaders given the fact that the dart leader is propagating continuously at speeds on the order of  $10^6$ – $10^7$  m/s. In any model that attempts to simulate first return strokes the presence of the streamer region should be considered. Cooray and Galvan [72] and Cooray *et al.* [73] have constructed a first return stroke model that takes into account the presence of the streamer region.

The basic features of the model are depicted in Figure 9.13. The leader channel surges forward through the action of the negative streamers originating from the highly conducting or the arc portion of the leader channel. When the tip of the negative streamer region makes contact with ground (Figure 9.13a), the neutralisation process proceeds upwards along the path taken by the streamers. This neutralisation process, which occurs before the beginning of the return stroke proper, can be interpreted as a connecting discharge moving towards the highly conducting region of the stepped leader. The return stroke proper is initiated when this connecting leader makes contact with the arc portion of the stepped leader channel (Figure 9.13c). The model calculations show that the meeting of the connecting leader with the hot stepped leader generates two fast current waveforms that travel in opposite directions, one towards the cloud and the other towards the ground (Figure 9.13d). The results of this study show that the slow front in the first return stroke current waveforms is generated by the connecting leader when it is moving through the streamer region of the down-coming stepped leader. Let us now consider the details of the model.

#### *Input parameters of the model*

1. Channel base current
2. Charge per unit length at the ground end of the stepped leader channel
3. Return stroke speed

#### *Assumptions of the model*

1. The charge density per unit length,  $\rho_0$ , deposited by the return stroke along the channel is independent of the height (the model can accommodate any other charge profile too without difficulty).
2. The leading edge of the stepped leader supports a streamer system and a connecting leader is initiated from the ground at the instant these streamers touches the ground.

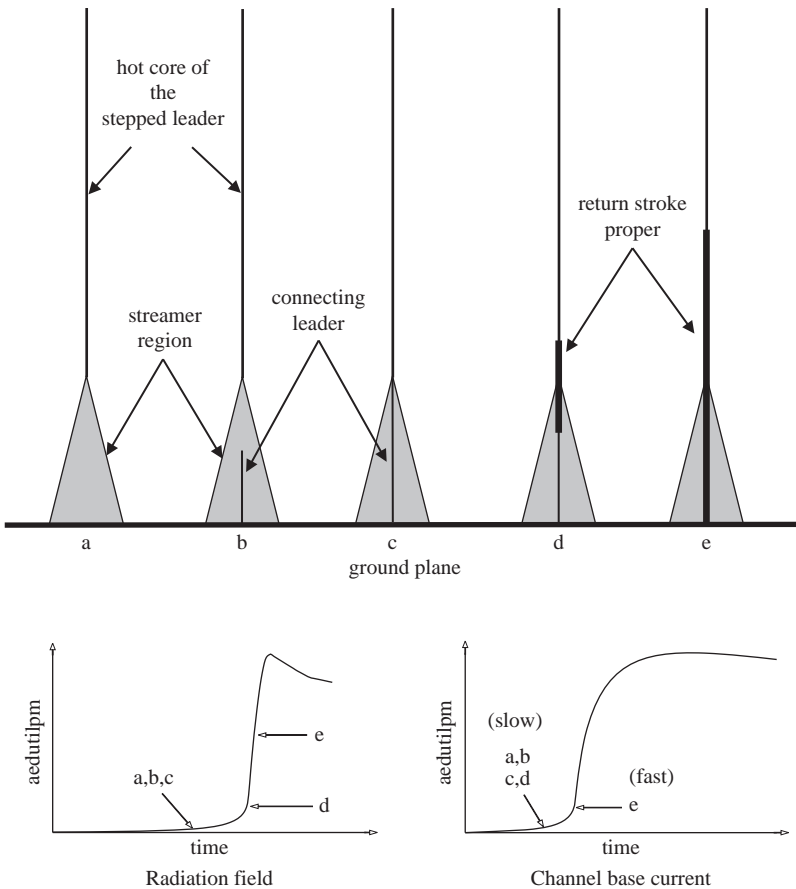


**Figure 9.13** *A schematic representation of the mechanism of the first return stroke and the possible events in the first return stroke that lead to the various features observed in the channel base current and the distant radiation field. The temporal growth of the channel base current and the radiation field at various stages of the development of the return stroke are also shown in the figure*

*The leader channel surges forward through the action of the negative streamers originating from the highly conducting or the arc portion of the leader channel. When the tip of the negative streamer region makes contact with ground (diagram a), the neutralisation process proceeds upwards along the path taken by the streamers. This neutralisation process, which occurs before the beginning of the return stroke proper, can be interpreted as a connecting discharge moving towards the highly conducting region of the stepped leader. The return stroke proper is initiated when this connecting leader makes contact with the arc portion of the stepped leader channel (diagram c). The model calculations show that the meeting of the connecting leader with the hot stepped leader generates two fast current waveforms that travel in opposite directions, one towards the cloud and the other towards the ground (diagram d). When the fast front reaches the ground a rapid increase in the channel base current takes place. The slow front in the first return stroke current waveforms is generated by the connecting leader when it is moving through the streamer region of the down-coming stepped leader*

3. The slow front of the current waveform is produced by the connecting leader as it moves through the streamer region of the stepped leader.
4. The connecting leader moves upwards with an exponentially increasing speed and it merges into the return stroke proper when it encounters the hot region of the stepped leader channel.
5. The corona current injected into the channel at a given point decays exponentially with time.

*Mathematical representation*

Based on the above assumptions one can develop the necessary equations as follows. The speed of the connecting leader,  $v_c(z)$ , is given by

$$v_c(z) = v_0 \exp(z/\lambda_c) \tag{9.24}$$

where  $v_0$  and  $\lambda_c$  are constant to be determined. Since the connecting leader merges into the return stroke proper at a height  $l_c$

$$v_c(l_c) = v_0 \exp(l_c/\lambda_c) = v_i \tag{9.25}$$

where  $v_i$  is the initial speed of the return stroke proper and  $l_c$  is the length of the connecting leader. Note that  $l_c$  is the same as the length of the streamer region in the ‘final jump’ and hence is equal to the striking distance of the return stroke over flat ground (see Chapter 14). Since the model belongs to the CG class of models, the duration of the slow front in the channel base current waveform,  $t_s$ , and the length of the connecting leader,  $l_c$ , are related through the equation

$$t_s = [\lambda_c(1 - \exp(-l_c/\lambda_c))/v_0] + l_c/c \tag{9.26}$$

where  $c$  is the speed of light in free space. Since the current waveform and the return stroke speed profile are given, both  $t_s$  and  $v_c$  are known quantities. Thus (9.24)–(9.26) can be solved to obtain  $v_0$  and  $\lambda_c$  provided  $l_c$  is known. Once the charge distribution on the leader channel is assumed the extension of the streamer region in front of the stepped leader tip can be easily calculated by assuming that the negative streamers maintain a potential gradient of about  $(1 - 2) \times 10^6$  V/m (see Chapter 3 for a discussion on how to calculate the extension of the streamer region in front of the stepped leader channel). For a uniform linear charge density of about 0.001 C/m the value of  $l_c$  is about 70 m.

In the model the speed of the return stroke,  $v_r$ , is assumed to decrease exponentially with height; one can write

$$v_r = v_i \exp(-(z - l_c)/\lambda_r) \tag{9.27}$$

where  $\lambda_r$  is the decay height constant. The corona current injected into the channel at a given point can be represented by

$$I_c(z, t) = I_0(z)[e^{-t/\tau(z)}] \tag{9.28}$$

where  $\tau(z)$ , which is a function of height, is the discharge time constant and hence the duration of the corona current. Owing to charge conservation,  $I_0(z)$  and  $I_c(z, t)$  are related to each other through the equation

$$\rho_0 = \int_0^\infty I_c(z, t) dt \tag{9.29}$$

This gives a value for  $I_0$  of

$$I_0(z) = \rho_0/[\tau(z)] \tag{9.30}$$



By substituting this expression into the above equation, it can be seen that the corona current can be written as

$$I_c(z, t) = \frac{\rho_0}{[\tau(z)]} [e^{-t/\tau(z)}] \quad (9.31)$$

Since the speed of the upward moving discharge (both the connecting leader and the return stroke) and the channel base current are given, the function  $\tau(z)$  can be estimated without difficulty using equations given in section 9.6.22.

### 9.6.5.2 Channel base current

An analytical expression for a waveform that can represent the first return stroke current was presented by the working group 01 (Lightning) of the CIGRE Study Committee 33 [77]. This current waveform is used to represent the channel base current in the paper presented by Cooray and Galvan [72] (a different current waveform is used in [73]). The current waveform suggested in [77] is the following:

$$I(t) = At + Bt^n \quad \text{for } t \leq t_n \quad (9.32)$$

$$I(t) = I_1 e^{-(t-t_n)/t_1} + I_2 e^{-(t-t_n)/t_2} \quad \text{for } t \geq t_n \quad (9.33)$$

with

$$n = 1 + 2(S_n - 1) \left( 2 + \frac{1}{S_n} \right) \quad (9.34)$$

$$t_n = 0.6 t_f \frac{3S_n^2}{(1 + S_n^2)} \quad (9.35)$$

$$S_n = S_m t_f / I_p \quad (9.36)$$

$$t_1 = (t_h - t_n) / \ln(2) \quad (9.37)$$

$$t_2 = 0.1 I_p / S_m \quad (9.38)$$

$$I_1 = \frac{t_1 t_2}{t_1 - t_2} \left( S_m + 0.9 \frac{I_p}{t_2} \right), A = \frac{1}{n - 1} \left( 0.9 \frac{I_p}{t_n} n - S_m \right) \quad (9.39)$$

$$I_2 = \frac{t_1 t_2}{t_1 - t_2} \left( S_m + 0.9 \frac{I_p}{t_1} \right), B = \frac{1}{t_n^n (n - 1)} (S_m t_n - 0.9 I_p) \quad (9.40)$$

In these equations  $I_p$  is the peak current,  $S_m$  is the peak current derivative,  $t_f$  is the 30–90 per cent front time and  $t_n$  is the time to half value. For an average return stroke current the recommended values are  $I_p = 30$  kA,  $S_m = 26$  kA/ $\mu$ s,  $t_f = 3$   $\mu$ s and  $t_n = 75$   $\mu$ s. This current waveform has a slow front of 5  $\mu$ s and the impulse charge associated with this current waveform is 3 C. The charge associated with this current waveform over the first 100  $\mu$ s is 1.8 C. In the calculations presented here the value of  $S_m$  was increased to 37 kA/ $\mu$ s, which is slightly higher than the recommended value for negative first strokes. This current waveform is shown in Figure 9.14.

### 9.6.5.3 Values of model parameters

On the basis of the available data on the charge distribution in the stepped leader,  $\rho_0 = 0.001$  C/m can be used to represent typical first return strokes. The available experimental observations indicate that the first return stroke speeds averaged

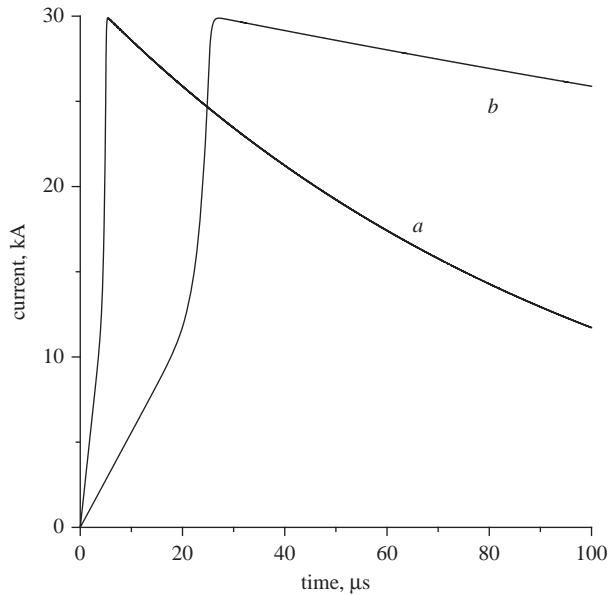


Figure 9.14 (a) Current waveform recommended by CIGRE study committee 33 (overvoltages and insulation co-ordination) to represent the channel base current of negative first return strokes. (b) Same current waveform shown in a five times faster time scale

over channel lengths of about 300 m and 1000 m are about  $1.7 \times 10^8$  m/s and  $1.4 \times 10^8$  m/s respectively (see Chapter 4). Both these observations could be satisfied by assuming  $v_i = 2.0 \times 10^8$  m/s and  $\lambda_r = 1500$  m. For the charge of 0.001 C/m the calculated length of the streamer region (i.e.  $l_c$ ) is about 70 m. Calculations show that the length of the streamer region is approximately equal to  $(6-8) \times 10^4 \rho_0$ . Substituting this and  $t_s = 5 \times 10^{-6}$  s in (9.24)–(9.26) one finds that  $v_0 = 3.5 \times 10^6$  m/s. This value is not far from the values obtained from direct measurements [78]. Let us consider some of the results obtained from this model.

#### 9.6.5.4 Predictions of the model

##### *Return stroke current*

The temporal variation of the return stroke current as a function of height is depicted in Figure 9.15a. The way in which the peak and the rise time (0 to peak) of the current vary with height is depicted in Figures 9.15b and 9.15c respectively. First, note how the slow front decreases with height and finally disappears around 70 m, the height at which the connecting leader met the stepped leader. Second, observe that the peak current decreases and the current rise time increases with height. This is an important prediction of the model and it agrees with the indirect inferences made from the optical observations. Figure 9.16a shows how the peak current derivative varies with height. Note that the current derivative increases initially, reaches a peak around 70 m and decreases rapidly with further increase in height. Figure 9.16b shows the time at which the peak current derivative occurs as a function of height. Note that the maximum derivative first occurs not at ground level but at the meeting point of the connecting leader and the stepped leader. The current derivative reaches a peak at later times at points located below and above

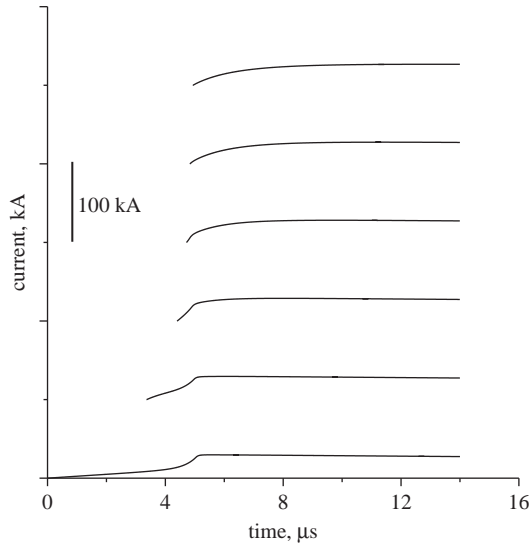


*Figure 9.15a* Temporal variation of the first return stroke current as a function of height (0, 20, 40, 60, 80 and 100 m) along the return stroke as predicted by the negative first return stroke model. Note how the slow front disappears gradually as the height increases

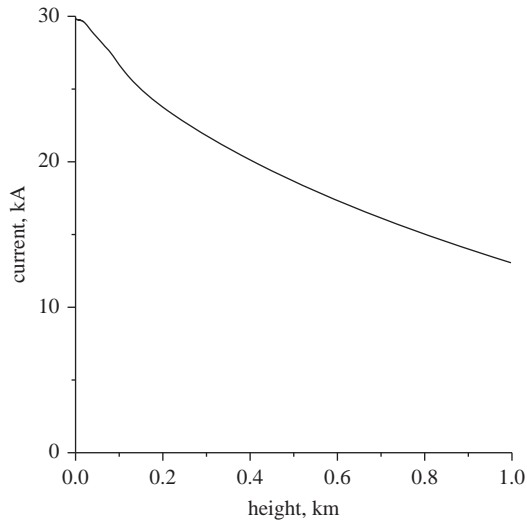


*Figure 9.15b* Variation of the first return stroke peak current as a function of height along the channel

this critical point. This shows that the encounter between the connecting leader and the stepped leader gives rise to two fast current waveforms, one travelling towards the cloud and the other travelling towards the ground. This is one of the important predictions of the model.

*Electromagnetic fields*

The model-simulated electric and magnetic fields at distances of 50 m, 1 km, 2 km, 5 km, 10 km and 200 km are shown in Figure 9.17 for a 30 kA current at the

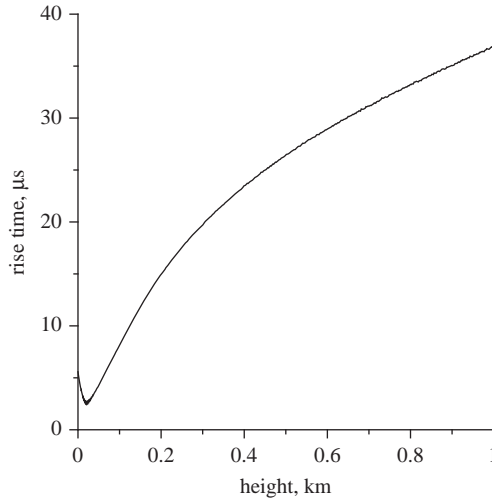


Figure 9.15c Variation of the rise time (0 to peak) of the first return stroke current as a function of height along the channel

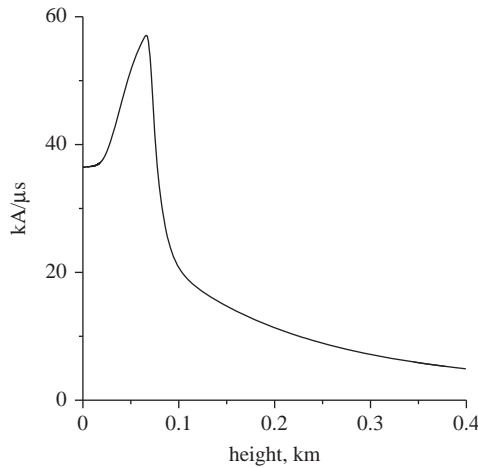
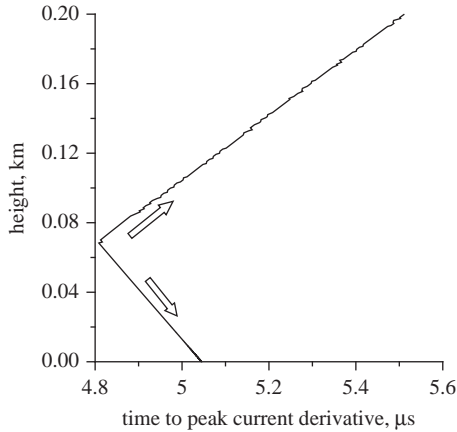


Figure 9.16a Variation of the return stroke peak current derivative as a function of height along the channel

channel base. At 100 km, the fields are pure radiation and they show a slow front followed by a fast transition. This is a common feature in the first return stroke fields. After attaining a peak value, the field crosses the zero line around  $60 \mu\text{s}$ . The electric field within about 2–10 km exhibits a ramp-like increase and the magnetic field has a hump. The electric field within 50 m of the strike shows a rapid saturation within a few tens of microseconds. Both of these features are observed in the subsequent strokes of triggered lightning flashes. However, data is not available yet to find out whether this is a feature common to first return stroke fields.

#### *Connection between the field and current parameters*

It is common practice today to extract the peak return stroke currents from the measured fields by using the equations from the transmission line model. However, there is no general consensus on the value of the effective speed that should be used



*Figure 9.16b* The time (measured from the beginning of the return stroke) at which the peak of the return stroke current derivative occurs as a function of height along the channel. Note that this represents two fast current waveforms originating at height 70 m (the point of contact of the connecting leader and the stepped leader) and travelling in opposite directions

in such studies. Let us consider the predictions of the present model on this subject. The peak radiation field corresponding to the 30 kA current is about 6.5 V/m.

It is common practice to use the relationship between the peak return stroke current and the peak electric field as predicted by the transmission line model (see section 9.6.1) to estimate peak current and the peak current derivatives from the measured peak electric radiation field and peak electric radiation field derivative. According to the prediction of the transmission line model, the peak electric field  $E_p$  is connected to the peak current  $I_p$  at the channel base by  $E_p = \mu_0 v I_p / 2\pi d$  where  $d$  is the distance where the electric field is measured. When the two numbers mentioned in the previous paragraph are used in this transmission line equation one obtains  $10^8$  m/s as the effective transmission line speed. Observe that this value is less than the assumed initial speed,  $2.0 \times 10^8$  m/s, in the model simulations. Since the return stroke speed used in the model is based on the average return stroke speeds obtained from experiments, the model results show that an effective return stroke speed of  $10^8$  m/s may be used in converting the measured peak values of the first return strokes to peak currents using transmission line equation.

Let us consider the relationship between the peak current derivative and the peak electric field derivative. According to the model, a current derivative of 37 kA/ $\mu$ s generates a peak electric field derivative of about 30 V/m/s at 100 km. According to the transmission line model, the peak electric field derivative and the peak current derivative are connected by the equation  $E'_p = \mu_0 v I'_p / 2\pi d$  where  $E'_p$  and  $I'_p$  are the peak derivatives of the electric radiation field and the channel base current. When these two numbers mentioned above are used in this equation the effective transmission line speed will become  $4 \times 10^8$  m/s, which indeed is larger than the speed of light. The reason for this high value of the effective transmission line speed is the two current waveforms propagating in opposite directions at the initiation of the return stroke. These two current waveforms boost the amplitude of the radiation field peak derivatives making the effective speed needed in the transmission line model to

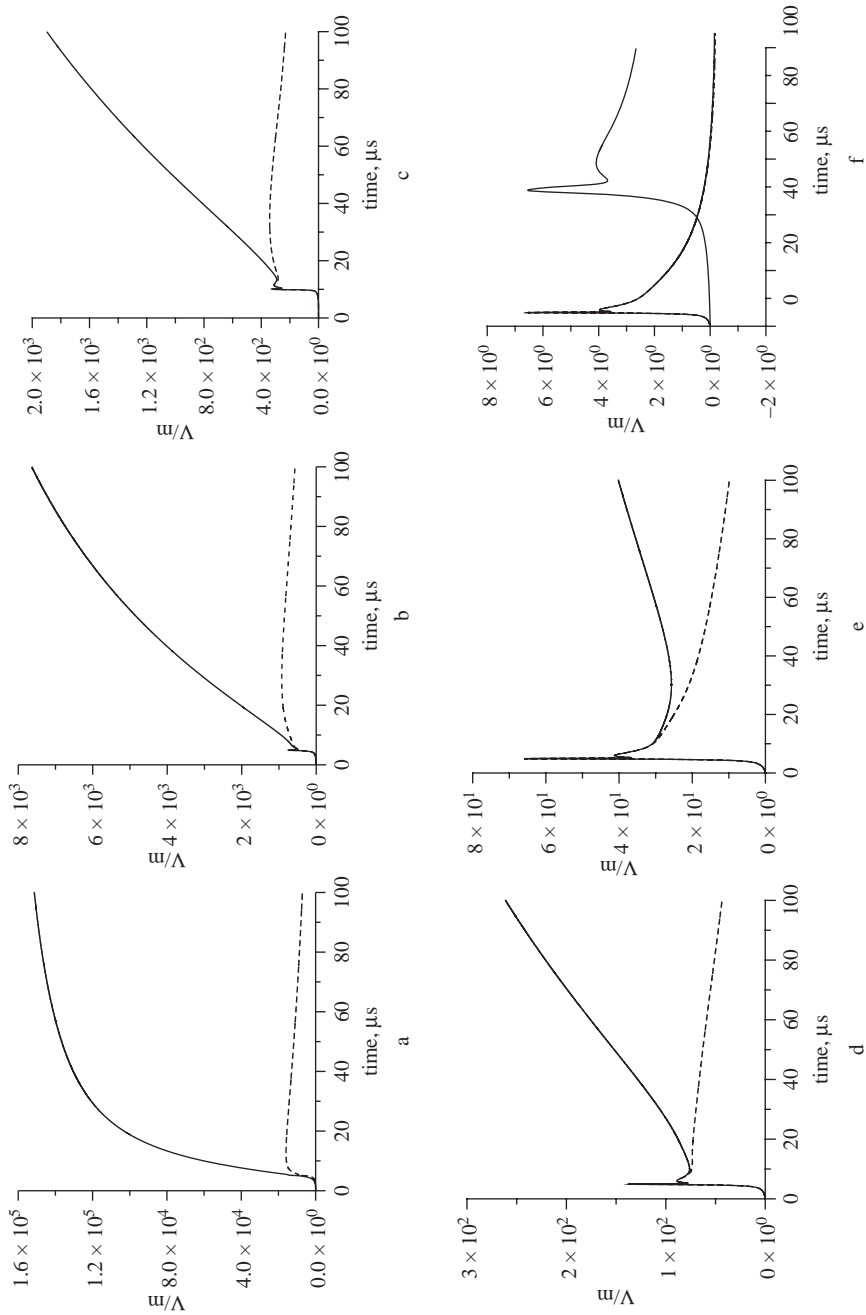


Figure 9.17 The electromagnetic fields (electric field: solid line, magnetic field  $\times c$ : dashed line) at different distances as predicted by the first return stroke model: (a) 50 m; (b) 1 km; (c) 2 km; (d) 5 km; (e) 10 km; (f) 100 km. Note that  $c$  is the speed of light in free space. The electric field at 100 km is also given in a ten times faster time scale

obtain the correct current derivatives larger than the speed of light. The calculated effective transmission line speed may depend to some extent on the shape of the current waveform and the initial speed of the return stroke used in the calculations. Based on the results obtained from this model, one can recommend an effective transmission line speed of  $4\text{--}5 \times 10^8$  m/s in converting the measured first return stroke peak electric field derivatives to peak current derivatives using the transmission line equation. In other words, using an effective transmission line speed of about  $1\text{--}1.5 \times 10^8$  m/s in converting the peak electric field derivatives to peak current derivatives, which indeed is the common practice today, may overestimate the peak current derivatives of first return strokes by a factor of about 3–4.

### *Connecting leader and the slow front*

The new concept incorporated in the first return stroke model described in the previous section is the identification of the slow front in the channel base current waveform as the current signature generated by the connecting leader. This idea is mathematically incorporated into the model as a modification of the speed profile of the discharge.

It is not new for attempts to be made to connect the slow front in electromagnetic fields and currents in first return strokes to the connecting leader. One such attempt was made by Weidman and Krider [82] when they studied this problem and came to the conclusion that the measured currents in connecting leaders are not large enough to give rise to the slow front in electromagnetic fields. Recall, however, that the current measurements from connecting leaders that are available in the literature are from those initiated at the top of high towers and which did not succeed in making a connection to a stepped leader. The scenario presented here is that the slow front is generated by the connecting leader when it enters into the streamer zone of the stepped leader (see Figure 9.13), that is at the ‘final jump’ stage (to borrow jargon from laboratory work on sparks, see Chapter 3). At this stage the return stroke is inevitable and the growth of the connecting leader within the streamer zone can be treated as the ‘initiation phase’ of the return stroke. The slow front in the current waveform is indeed a manifestation of the return stroke.

### **9.6.5.5 Extension of the model to include positive return strokes**

Experimental observations based on both electric field and direct current measurements indicate that the main difference between the positive and negative return stroke currents is the presence of a long current tail in the former. The electric field measurements indicate that the first few tens of microseconds of the positive return stroke current is qualitatively similar to that of the negative first strokes. After this initial stage the negative current continues to decay, whereas the positive current starts to increase again, reach a second peak within about 100–300  $\mu$ s and decay within a few milliseconds [86, 87].

The current waveform shown in Figure 9.18 has these features and can be used to represent a typical positive first return stroke current. This current waveform can be represented analytically by the equation

$$\begin{aligned}
 I(t) &= At + Bt^n \quad \text{for } t \leq t_n \\
 I(t) &= I_1 e^{-(t-t_n)/t_1} + I_2 e^{-(t-t_n)/t_2} + \left\{ I_3 \frac{[(t-t_n)/\tau_4]^5}{1 + [(t-t_n)/\tau_4]^5} \exp[-(t-t_n)/\tau_5] \right\} \quad \text{for } t \geq t_n
 \end{aligned}
 \tag{9.41}$$

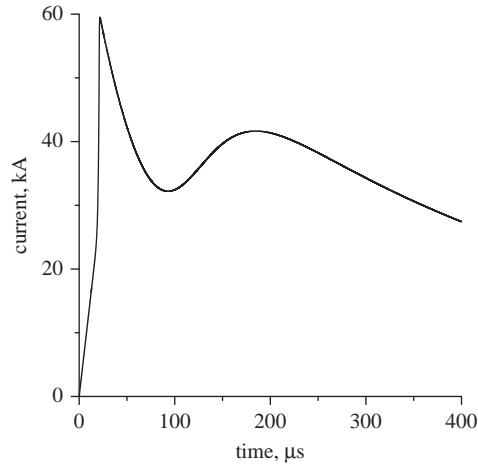


Figure 9.18 The channel base current of a typical positive return stroke used in the simulation. The waveform is based on the inferences made from the measured currents and the electromagnetic fields of positive return strokes (see Chapter 4)

where  $I_3 = 69 \times 10^3$  A,  $\tau_4 = 150 \times 10^{-6}$  s and  $\tau_5 = 480 \times 10^{-6}$  s. The values of A, B, n,  $I_1$ ,  $I_2$ ,  $t_n$ ,  $t_1$  and  $t_2$  are estimated from (9.34) to (9.40) using  $I_p = 60$  kA,  $S_m = 30$  kA/ $\mu$ s,  $t_f = 12$   $\mu$ s and  $t_h = 75$   $\mu$ s.

The slow front duration,  $t_s$ , of this current waveform is 21  $\mu$ s and the rise time of this current waveform is 22  $\mu$ s. This rise time is close to the corresponding median values of positive return stroke currents [86, 87]. The peak value of the current waveform is 60 kA. This is larger than the median positive current of 35 kA. This choice is based on the experimentally observed fact that, on average, the peak radiation fields of positives are two times larger than those of negative first strokes. Since the positive return stroke speeds do not differ significantly from those of negatives, the only plausible explanation for this experimental observation is the two times higher median current in positives than in the negatives. The derivative of the current waveform is 30 kA/ $\mu$ s. This is also higher than the median value measured in positives, but it will lead to electric field derivatives similar to those measured. The impulse charge associated with it is 28 C which is close to the experimentally measured value for a 60 kA positive current.

The speed profile used in calculating electromagnetic fields is similar to that used earlier for negative return strokes. Since the peak current is twice that of the negative the value  $\rho_0$  is assumed to be 0.002 C/m. This leads to a connecting leader of length 130 m which is longer than the corresponding length obtained for a typical negative first stroke.

#### *Electromagnetic fields of positive return strokes*

The electromagnetic fields generated by the model at several distances are given in Figures 9.19a and 19b. Note the long slow front and the slow tail of the radiation field. These signatures are similar to those observed in measured fields [79, 80]; see also Chapter 4. The peak radiation field and the peak radiation field derivative at 100 km are about 14 V/m and 26 V/m/ $\mu$ s, respectively. These values also agree with the typical values observed for positive strokes [81].



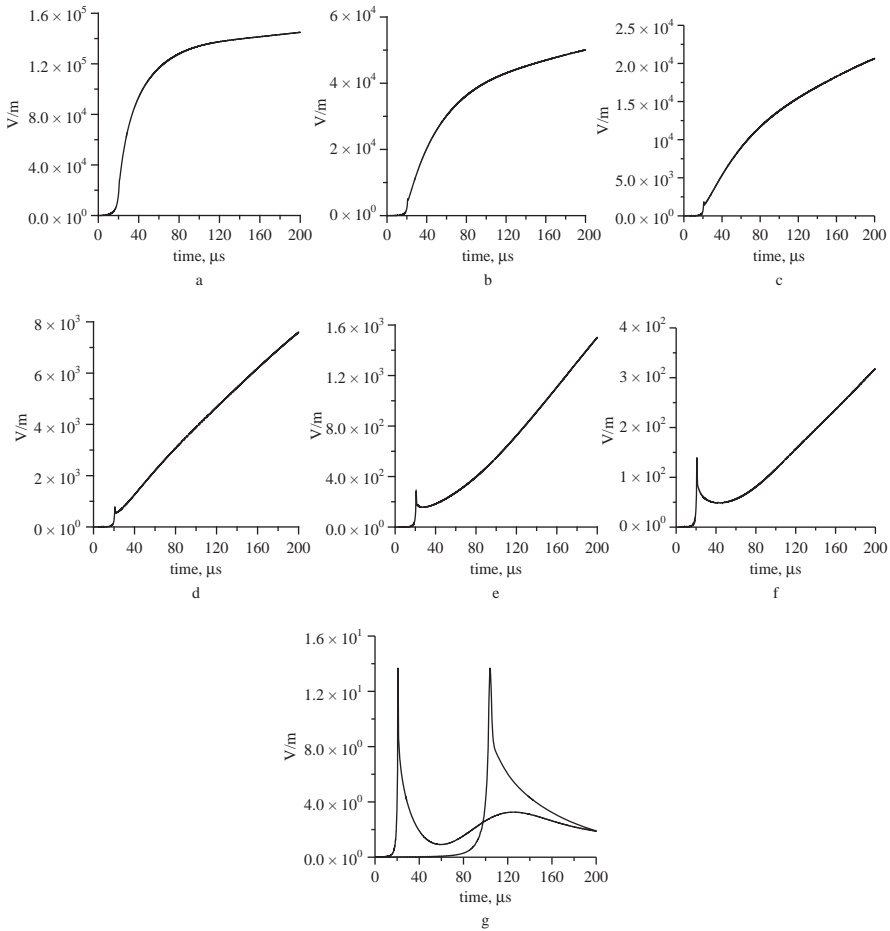


Figure 9.19a The electric field at different distances as predicted by the positive first return stroke model: (a) 200 m; (b) 500 m; (c) 1 km; (d) 2 km; (e) 5 km; (f) 10 km; (g) 100 km. The electric field at 100 km is also given in a five times faster time scale. Note that the polarity of the field is inverted with respect to the electric fields of negative first return stroke shown in Figure 9.17 for clarity

## 9.7 Current dissipation models (CD models)

### 9.7.1 General description

As mentioned previously, if a current pulse is propagating without corona along a transmission line, it will travel along the line without any attenuation and modification of the current waveshape. This concept is used as a base in creating current propagation models. When the current amplitude is larger than the threshold current necessary for corona generation, each element of the transmission line acts as a corona current source. Half of the corona current generated by the sources travels downwards and the other half travels upwards. The upward moving corona currents interact with the front of the injected current pulse in such a way that the speed of the upward moving current pulse is reduced, and for a transmission line in air, to a

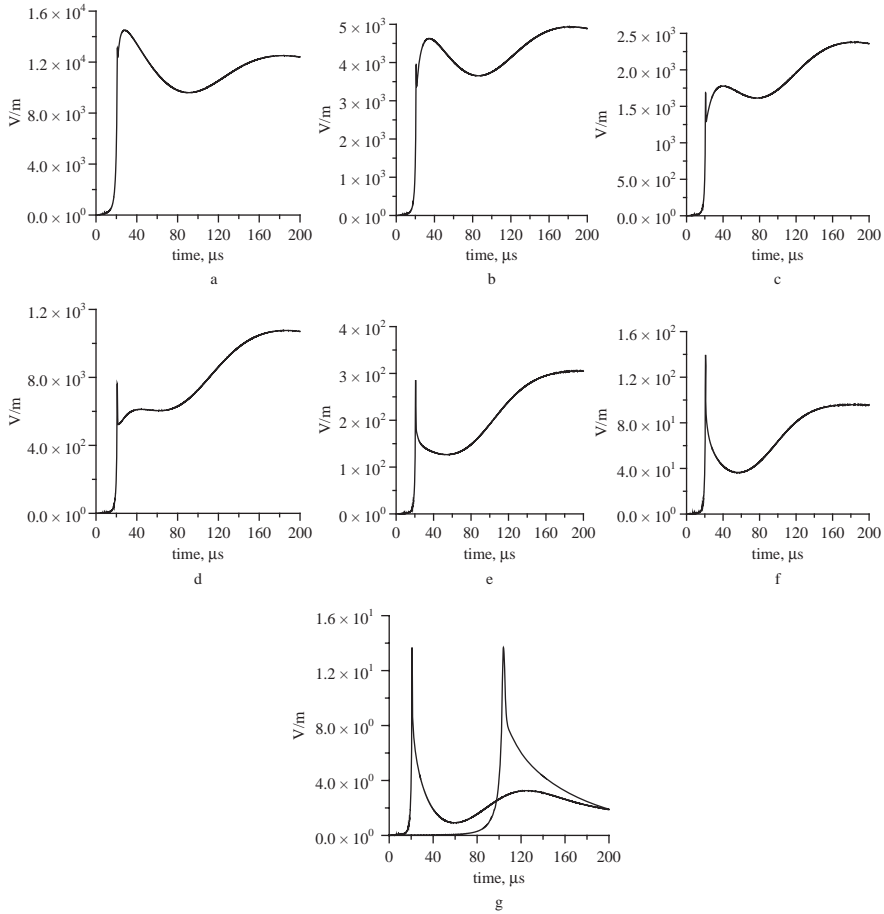
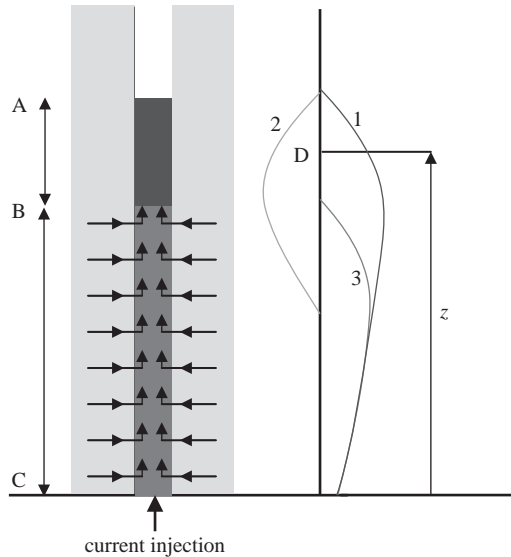


Figure 9.19b The magnetic field ( $\times c$ ) at different distances as predicted by the positive first return stroke model: (a) 200 m; (b) 500 m; (c) 1 km; (d) 2 km; (e) 5 km; (f) 10 km; (g) 100 km. The magnetic field at 100 km is also shown in a five times faster time scale. Note that  $c$  is the speed of light in free space

value less than the speed of light [36]. In a recent publication Cooray [83] showed that the upward moving corona current concept can also be used to create return stroke models. He coined the term ‘current dissipation models’ for the same. The basic features of the current dissipation models are depicted in Figure 9.20. The main assumptions of the current dissipation models are the following: The return stroke is initiated by a current pulse injected into the leader channel from the grounded end. The arrival of the return stroke front at a given channel element will turn on a current source that will inject a corona current into the central core. It is important to stress here that by the statement *the arrival of the return stroke front at a given channel element* it is meant the onset of the return stroke current in that channel element (i.e. point  $B$  in Figure 9.20). Once in the core this corona current will travel upwards along the channel. In the case of negative return strokes the polarity of the corona current is such that it will deposit positive charge on the



*Figure 9.20 Pictorial description of the processes associated with a current dissipation model at a given time  $t$ . The injected current (waveform 1 to the right) and the sum of corona currents (waveform 2 to the right) travel upwards with the speed  $v_c$ . Point A is the front of these current waveforms. In the region A–B these two currents cancel each other making the current above point B equal to zero. The cancellation is not complete below point B and therefore the net current below point B is finite (waveform 3 to the right). Thus, point B is the front of the net current (i.e. return stroke front) moving upwards. Distance AC is equal to  $v_c t$  and the distance BC is  $vt$  where  $v$  is the average speed of propagation of the net current front (i.e. return stroke front). Note that the current waveforms are not drawn to scale (adapted from [83])*

corona sheath and transport negative charge along the central core. Let us now incorporate mathematics into this physical scenario.

Assume that the return stroke is initiated by a current pulse injected into the leader channel at ground level. This current pulse propagates upwards along the channel with speed  $v_c$ . When the return stroke front (i.e. the net current front) reaches a given channel element a corona source is turned on. This source will generate a corona current that will travel upwards along the central core with the same speed as the current pulse injected at the channel base (i.e.  $v_c$ ). Note that the polarity of the upward moving corona current is opposite to that of the upward moving current injected at the channel base. For example, in the case of negative return stroke the current injected at the channel base carry positive charge upwards, whereas the corona current transports negative charge upwards. According to this model, the total current at a given point of the channel consists of two parts – upward moving current pulse injected at the channel base and the total contribution of the upward moving corona currents. The upward moving corona current being of opposite polarity leads to the dissipation of the current pulse injected at the channel base.

### 9.7.2 Mathematical background

Consider the diagram to the right in Figure 9.20. This depicts a situation at any given time  $t$ . At this time the tip of the injected current is located at point  $A$  and the return stroke front is located at point  $B$ . The net current at any point above the return stroke front is zero. This is the case since the injected current and the cumulative effects of the corona current cancel each other above the return stroke front. Now, let us consider a point  $D$  located above the return stroke front. The height of this point from ground level is  $z$ . The net corona current at that point is given by (note that since the corona current is defined as positive here it has to be subtracted from the injected current)

$$I_{cor,total}(z, t) = \int_0^{h_d} I_c(\xi, t - \xi/v_{av}(z) - (z - \xi)/v_c) d\xi \tag{9.42}$$

the value of  $h_d$ , the highest point on the channel whose corona current can reach point  $z$  at time  $t$ , can be obtained by solving the equation

$$t - \frac{h_d}{v_{av}(h_d)} - \frac{(z - h_d)}{v_c} = 0 \tag{9.43}$$

The injected current at point  $z$  at time  $t$  is given by

$$I_m(z, t) = I_b(0, t - z/v_c) \tag{9.44}$$

Since the corona current annihilate the injected current at all points above the return stroke front we have

$$I_b(0, t - z/v_c) = \int_0^{h_d} I_c(\xi, t - \xi/v_{av}(\xi) - (z - \xi)/v_c) d\xi \tag{9.45}$$

Changing the variable we can write

$$I_b(0, t') = \int_0^{h_s} I_c(\xi, t' - \xi/v_{av}(\xi) + \xi/v_c) d\xi \tag{9.46}$$

with  $h_s$  given by

$$t' - \frac{h_s}{v_{av}(h_d)} + \frac{h_s}{v_c} = 0 \tag{9.47}$$

Now, a comparison of (9.46) and (9.47) with (9.17) and (9.18) shows that the only difference in the equations when moving from current generation concept to current dissipation concept is that  $v_c$  is replaced by  $-v_c$ . Moreover, as in the case of current generation models, the input parameters of current dissipation models are the charge deposited on the channel by the return stroke, corona decay time constant, return stroke speed and the channel base current. When three of these parameters are given the fourth one can be obtained in the same manner as it was done in the case of current generation models. But in (9.13)–(9.22),  $v_c$  has to be replaced by  $-v_c$  when using the equations in connection with current dissipation models [83].

An application of this principle to represent the reflected current component at ground level in a return stroke is introduced by Cooray and Rakov [75]. This model is presented in the next section.

### 9.7.3 *Current dissipation concept in practice – introducing current reflection from ground level into return stroke models*

In current generation models the corona current generated by current sources located along the return stroke channel travel downwards with a speed equal to the speed of light (i.e.  $v_c = c$ ). In general, it is assumed that this current waveform travelling down the channel will be completely absorbed by the ground. However, it is more correct to assume that the incident current would be reflected completely at ground level. A model that takes into account the reflected current component is introduced by Cooray and Rakov [75] (note that in this paper two return stroke models were introduced: one that takes into account the current reflection and the other to take into account the finite conductivity of the ground. The latter is described in section 9.12). If the current is reflected at ground level, it will propagate up with the speed of light similar to the injected current in the current dissipation models. In the model the incident current at ground level is represented by current generation model principles and the propagation of the reflected current along the channel is represented by current dissipation principles. Since the incident current is assumed to be completely reflected at ground level, the incident current component contributes to half of the channel base current, and the other half is caused by the reflected current component.

In treating the incident current at ground level, Cooray and Rakov [75] used the channel base current (i.e. half of the total channel base current), corona current and the return stroke speed as the input parameters. Since the return stroke speed and the discharge time constant are common for both current components (i.e. there is only one return stroke front), these together with the channel base current (i.e. half of the total channel base current) are used as the input parameters of the current dissipation model that simulated the reflected wave. By representing the reflected current wave using the CG concepts these authors managed to avoid any current discontinuity at the return stroke front even though the reflected current is assumed to move upwards along the channel with the speed of light, a speed higher than the speed of the return stroke front. The main features of the model are given below:

*Channel base current:*

$$I_b(0, t) = i_i(t) + i_r(t)$$

*Incident component of the channel base current:*

$$i_i(t) = \frac{1}{2} \left\{ \frac{I_{01}}{\eta} \frac{(t/\tau_1)^2}{(t/\tau_1)^2 + 1} e^{-t/\tau_2} + I_{02}(e^{-t/\tau_3} + e^{-t/\tau_4}) \right\}; \text{ for a typical subsequent return stroke } I_0 = 9.9 \text{ kA}, \eta = 0.845, \tau_1 = 0.072 \text{ } \mu\text{s}, \tau_2 = 5 \text{ } \mu\text{s}, I_{02} = 7.5 \text{ kA}, \tau_3 = 100 \text{ } \mu\text{s} \text{ and } \tau_4 = 6 \text{ } \mu\text{s}.$$

*Corona current per unit length associated with the incident current:*

$$I_i(t, z) = \frac{\rho_i(z)}{\tau} e^{-t/\tau}, \tau = 0.1 \text{ } \mu\text{s}$$

*Linear density of charge deposited by the incident current [83]:*

$$\rho_i(z) = \frac{i_i(0, z/v^*) + \tau \frac{di_i(0, z/v^*)}{dt}}{v^*} \quad \text{where} \quad \frac{1}{v^*} = \frac{1}{v} + \frac{1}{v_c}$$

Reflected component of the channel base current:

$i_r(t) = \frac{1}{2} \left\{ \frac{I_{01}}{\eta} \frac{(t/\tau_1)^2}{(t/\tau_1)^2 + 1} e^{-t/\tau_2} + I_{02} (e^{-t/\tau_3} + e^{-t/\tau_4}) \right\}$ ; for a typical subsequent return stroke  $I_{01} = 9.9$  kA,  $\eta = 0.845$ ,  $\tau_1 = 0.072$   $\mu$ s,  $\tau_2 = 5$   $\mu$ s,  $I_{02} = 7.5$  kA,  $\tau_3 = 100$   $\mu$ s and  $\tau_4 = 6$   $\mu$ s.

Corona current per unit length associated with the reflected current:

$$I_r(t, z) = \frac{\rho_r(z)}{\tau} e^{-t/\tau}, \tau = 0.1 \mu\text{s}$$

Linear density of charge deposited by the reflected current:

$$\rho_r(z) = \frac{i_r(0, z/v^{**}) + \tau \frac{di_r(0, z/v^{**})}{dt}}{v^{**}} \quad \text{where} \quad \frac{1}{v^{**}} = \frac{1}{v} - \frac{1}{v_c}$$

Speed of corona current:

$$v_c = c$$

Speed of the return stroke:

In the model  $v$  is assumed to be a constant equal to  $1.3 \times 10^8$  m/s.

### 9.7.3.1 Predictions of the model

Figure 9.21 shows how the return stroke current varies along the return stroke channel. The electric and magnetic fields generated by the model at different

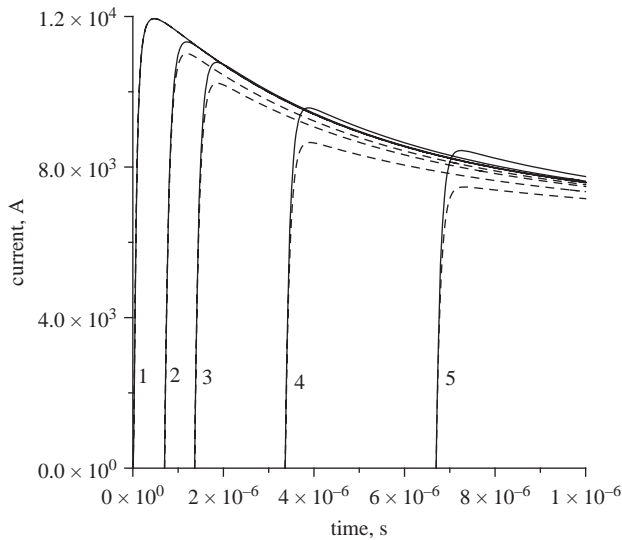


Figure 9.21 Current waveforms at different heights along the return stroke channel as predicted by the model of Cooray and Rakov [75] that was developed to take into account the current reflection at ground level: (1) 0 m; (2) 100 m; (3) 200 m; (4) 500 m; (5) 1000 m. The solid line curves include reflection from ground. The dashed line corresponds to the current distribution that will be present along the channel if one removes the current reflection at ground level and assumes that the total current at ground level is equal to the incident current

distances are shown in Figure 9.22. The dashed lines in each diagram represent the current, electric and magnetic fields that would be generated by the model if the reflection coefficient at ground level is zero and the total current at ground level is allocated to the incident current. Observe that the effect of the reflected current component is to clamp the tail of the current waveform. Observe also that, even

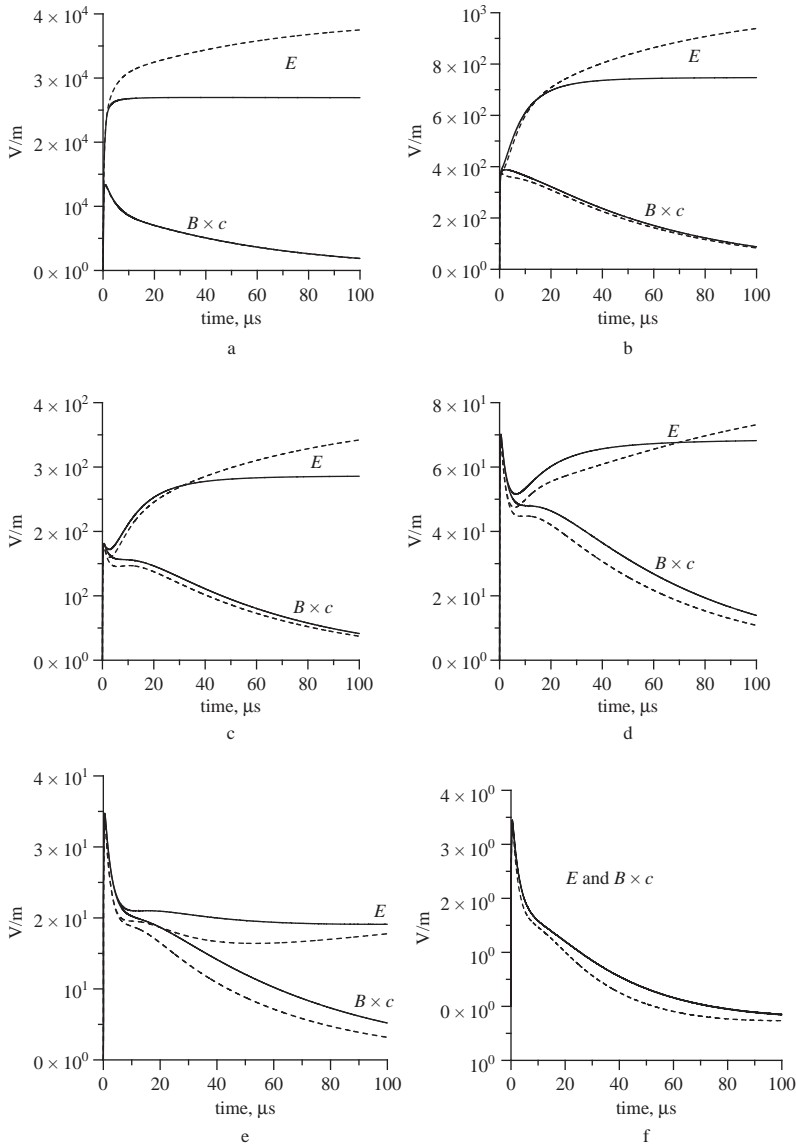


Figure 9.22 Electric and magnetic field (multiplied by the speed of light) predicted by Cooray and Rakov [75] model that was developed to take into account the current reflection at ground level. The solid lines correspond to results with current reflection and the dashed lines correspond to results without current reflection: (a) 50 m; (b) 1 km; (c) 2 km; (d) 5 km; (e) 10 km; (f) 100 km

though the number of model parameters used in the model in addition to the channel base current is two, the predictions of the model are not far from the features of the measured fields.

### 9.8 Generalisation of any model to current generation type

Cooray [84] showed that any return stroke model can be converted to a current generation model by introducing an effective corona current. Here we will illustrate the mathematical analysis that led to that conclusion.

Consider a channel element of length  $dz$  at height  $z$  and let  $I(z,t)$  represent the temporal variation of the total return stroke current at that height. In the case of CG models, this current is generated by the action of corona current sources located above this height. Assume for the moment that the channel element does not generate any corona current. In this case the channel element will behave as a passive element that will just transport the current that is being fed from the top. In this case one can write

$$I(z + dz, t) = I(z, t + dz/v_c) \tag{9.48}$$

That is, the current injected at the top of the element will appear without any change at the bottom of the channel element after a time  $dz/v_c$  which is the time taken by the current to travel from the top of the channel element to the bottom.

Now let us consider the real situation in which the channel element  $dz$  will also generate a corona current. As the current injected at the top passes through the channel element the corona sources will add their contribution resulting in a larger current appearing at the bottom than the amount injected at the top. The difference in these two quantities will give the corona current injected by the channel element. Thus, the average corona current generated by the element  $dz$  is given by

$$I_{cg}(z, t)dz = I(z, t + dz/v_c) - I(z + dz, t) \tag{9.49}$$

Using the Taylor's expansion, the above equation can be rewritten as

$$I_{cg}(z, t)dz = I(z, t) - I(z + dz, t) + \frac{dz}{v_c} \frac{\partial I(z, t)}{\partial t} \tag{9.50}$$

Dividing both sides by  $dz$  and taking the limit  $dz \rightarrow 0$ , the corona current per unit length,  $I_{cg}(z, t)$ , injected into the return stroke channel at height  $z$  is given by

$$I_{cg}(z, t) = -\frac{\partial I(z, t)}{\partial z} + \frac{1}{v_c} \frac{\partial I(z, t)}{\partial t} \tag{9.51}$$

This equation can be utilised to transfer any return stroke model to a current generation model with an equivalent corona current. It is important to stress here that even though the distribution of the return stroke current as a function of height remains the same during this conversion, there is a radical change in the corona current. If one attempts to extract the physics of the leader charge neutralisation process using the temporal variation of the corona current as predicted by a return stroke model, the information one gathers will depend strongly on the way in which the return stroke model is formulated. This can easily be illustrated using the transmission line model [53]. In the current propagation scenario of the



transmission line model, the upward propagating current will not give rise to any corona and therefore the corona current is zero. On the other hand, if the same model is converted to a current generation model then the equivalent corona current associated with the converted model (obtained from (9.51)) becomes bipolar [84]. The physics of the neutralisation process pertinent to this equivalent corona current is the following: As the rising part of the upward moving current passes through a given channel element the corona sheath located around that channel element will be neutralised by injection of positive charge into it. During the decaying part of the upward moving current all the deposited positive charge will be removed bringing the corona sheath back to its original state. Thus, the physics of corona dynamics in the two scenarios is completely different even though the longitudinal distribution of current and the charge along the channel at any given time is the same in the two formulations. This shows that conversion of a model from one type to another will change the underlying physics even though both descriptions are identical from a point of view of the total current as a function of height. Thus, one has to apply caution in deriving the physics of corona neutralisation process using these models because the information extracted concerning it will be model dependent.

### 9.9 Generalisation of any model to a current dissipation type model

An analysis similar to the one presented in section 9.8 was conducted by Cooray [83] for current dissipation type models. That analysis is presented below.

Consider a channel element of length  $dz$  at height  $z$  and let  $I(z,t)$  represent the temporal variation of the total return stroke current at that height. Assume for the moment that the channel element does not generate any corona current. In this case the channel element will behave as a passive element that will just transport the current that is being fed from the top. In this case one can write

$$I(z + dz, t) = I(z, t - dz/v_c) \quad (9.52)$$

That is, the current injected at the bottom of the channel element will appear without any change at the top of the channel element after a time  $dz/v_c$  which is the time taken by the current to travel from the bottom of the channel element to the top.

Now let us consider the real situation in which the channel element  $dz$  will also generate a corona current. As the current injected at the bottom passes through the channel element the corona sources will add their contribution, and since the polarity of the corona current is opposite to that of the injected current, resulting in a smaller current appearing at the top than the amount of current injected at the bottom. The difference in these two quantities will give the corona current injected by the channel element. Thus, the average corona current generated by the element  $dz$  is given by

$$I_{cd}(z, t)dz = I(z, t - dz/v_c) - I(z + dz, t) \quad (9.53)$$

Using the Taylor's expansion, the above equation can be rewritten as

$$I_{cd}(z, t)dz = I(z, t) - I(z + dz, t) - \frac{dz}{v_c} \frac{\partial I(z, t)}{\partial t} \quad (9.54)$$

Dividing both sides by  $dz$  and taking the limit  $dz \rightarrow 0$ , the corona current per unit length,  $I_{cd}(z,t)$ , injected into the return stroke channel at height  $z$  is given by

$$I_{cd}(z,t) = -\frac{\partial I(z,t)}{\partial z} - \frac{1}{v_c} \frac{\partial I(z,t)}{\partial t} \quad (9.55)$$

Note that this equation is completely symmetrical to the one derived for the current generation model (i.e. (9.51)) except that second term has a negative sign. This equation can be utilised to transfer any return stroke model to a current dissipation model with an equivalent corona current. The discussion given at the end of section 9.8 is also applicable here.

### 9.10 Current propagation models as a special case of current dissipation models

In the introduction of this chapter we have pointed out that current propagation models available in the literature are special cases of the current dissipation models. Let us now demonstrate this fact.

In current dissipation models both the injected current and the corona current propagate up with speed  $v_c$ . However, due to the interaction of these two current waveforms (i.e. injected current and the sum of corona currents) the net current front or the return stroke front propagates upwards with a speed less than the speed  $v_c$ . However, there is one special situation in which the return stroke front also travels upwards with the same speed as the injected and corona currents. In this special situation the current dissipation models reduce to current propagation models. This special situation can be realised by selecting the corona current in a particular manner. This can be illustrated mathematically as follows: Let us represent the injected current at the channel base as  $I_b(0,t)$ . The injected current at height  $z$ ,  $I_i(z,t)$ , is given by

$$I_i(z,t) = I_b(0,t - z/v_c) \quad (9.56)$$

Assume that the corona current per unit length at level  $z$  is given by

$$I_{cd}(z,t) = I_b(0,t - z/v_c)A(z) \quad (9.57)$$

where  $A(z)$  is some function of  $z$ . According to this equation the corona current at a given height is proportional to the injected current at that height. Substituting this expression in (9.55) one finds that

$$I_b(0,t - z/v_c)A(z) = -\frac{\partial I(z,t)}{\partial z} - \frac{1}{v_c} \frac{\partial I(z,t)}{\partial t} \quad (9.58)$$

One can easily show by substitution that the solution of this equation is given by

$$I(z,t) = A'(z)I_b(0,t - z/v_c) \quad (9.59)$$

with

$$A'(z) = -\int A(z)dz \quad (9.60)$$

Note that  $I(z,t)$  in the above equation is the total current, i.e. sum of the corona current and the injected current. According to (9.59), the total current propagates

upwards with the same speed as that of the injected current and corona current. Moreover, it propagates upwards without any distortion while its amplitude varies with height according to the function  $A'(z)$ . Indeed, (9.59) describes a current propagation model. In this special case (9.55) reduces to

$$I_c(z, t) = -\frac{\partial I(z, t)}{\partial z} - \frac{1}{v} \frac{\partial I(z, t)}{\partial t} \quad (9.61)$$

where  $v$  is the speed of the return stroke front. This equation is identical to the expression for the corona current in current propagation models derived by Maslowski and Rakov [85].

### 9.11 Advantage of utilising current dissipation concept in constructing models in comparison to current propagation concept

There are several advantages in modelling the return stroke using current dissipation concept as compared to current propagation concept. They are the following:

1. In current propagation models it is assumed that the current injected at ground level propagates upwards along the conducting leader channel at a speed which is considerably less than the speed of light in free space. However, since the speed of propagation of electromagnetic fields in air is equal to the speed of light, the speed of propagation of current pulses along conductors in air is equal to the speed of light. Of course, as the current pulse propagates along the conductors it may disperse and change its shape, but the speed of propagation of the tip of the current pulse cannot be less than the speed of light. Due to dispersion of course the bulk of the current pulse may appear to propagate with a speed less than the speed of light. Thus, the current propagation models describe the apparent behaviour of currents along conductors in air. On the other hand, the current dissipation concept assumes that both the injected current and the corona currents are propagating with the speed of light along the conducting lightning channel. It also shows that the interaction of the two current waveforms generates an apparent movement of a current pulse with a speed less than the speed of light. Thus, the assumption of current dissipation model does not violate the basic principle that the propagation of electromagnetic fields in air is equal to the speed of light. Moreover, as illustrated earlier, all the current propagation models are indeed special cases of current dissipation model where the corona currents satisfy a special relationship with the channel base current as given by (9.57)–(9.60).
2. In current propagation models one has to select the way in which the current amplitude and the current waveform change as a function of height. These have to be selected without much consideration as to why such a variation is adopted in the model. That means the model parameters have to be selected without much consideration on the physics of the lightning return stroke process. These parameters selected somewhat arbitrary will fix the most important physical parameter of the model, namely the temporal and spatial variation of the corona current [85]. Moreover, the model cannot be used directly to study how the dynamics of the corona current will give rise to the various parameters of the return stroke electromagnetic fields. On the other hand, in the current

dissipation models the corona current itself is the input parameter. The way in which the return stroke current varies along the channel, i.e. the way in which its amplitude and waveshape change with height, is decided by the nature of the corona current selected. This gives the possibility to incorporate physical processes associated with the neutralisation of the leader charge directly into the current propagation models. This is what was lacking in current propagation models in comparison to the current generation models. Thus, the current dissipation concepts lift up the current propagation models to the same status as that of current generation models.

### 9.12 Introducing ground conductivity in CG type return stroke models

The way in which the ground conductivity can be incorporated into CG type return stroke models and the effect of ground conductivity on the return stroke current have been described by Cooray and Rakov [75]. The procedure they have used to incorporate ground conductivity into return stroke models is described below.

Consider the physical process that leads to the formation of the corona current through the neutralisation process. The neutralisation process takes place when the channel core changes its potential from cloud to ground value. If this change is instantaneous, then in principle the corona decay time constant could be very small and the shape of the corona current can be replaced by a Dirac delta function. However, when the ground is finitely conducting, the ground potential cannot be transferred to the channel faster than the relaxation time of the finitely conducting ground. Thus, the relaxation time limits the rapidity at which the channel potential could be changed. In other words, the neutralisation time and hence the corona decay time constant depend on the ground conductivity. Assume that the ground is perfectly conducting. Then the ground potential cannot be transferred at a time less than about 10 ns which is the time necessary for the heating and transfer of electron energy to the ions and neutrals in the central core. This sets a lower limit to the value of corona decay time constant. When the ground is finitely conducting and the relaxation time is larger than the thermalisation time then the minimum value of the corona decay time constant,  $\tau_0$ , is determined by the relaxation time. Thus one can write

$$\tau_0 = \tau_t \quad \tau_r \leq \tau_t \tag{9.62}$$

$$\tau_0 = \tau_r \quad \tau_r \geq \tau_t \tag{9.63}$$

$$\tau_r = \varepsilon \varepsilon_0 / \sigma \tag{9.64}$$

In the above equations  $\varepsilon$  is the relative permittivity of the ground,  $\varepsilon_0$  is the permittivity of air,  $\sigma$  is the conductivity of soil and  $\tau_r$  is the relaxation time of soil. The value of  $\tau_t$  (thermalisation time) is 10 ns. Let us now consider how this idea was incorporated into the return stroke models by Cooray and Rakov [75]. The main features of the model which belongs to CG category are the following:

*Linear charge density deposited by the return stroke along the leader channel:*

$\rho(z) = a_0 I_p + I_p \frac{(a+bz)}{1+c\tau+d\tau^2}$ ;  $I_p$  is the peak return stroke current,  $a_0 = 5.09 \times 10^{-6}$ ,  $a = 1.325 \times 10^{-5}$ ,  $b = 7.06 \times 10^{-6}$ ,  $c = 2.089$  and  $d = 1.492 \times 10^{-2}$ . This is based on the results obtained in [76] (see also section 9.13).

*Corona current per unit length:*

$$I_{cor}(t, z) = \frac{\rho(z)}{\tau(z)} e^{-t/\tau(z)}$$

$$\tau(z) = \tau_0 + \eta z \quad \text{with} \quad \eta = 10^{-9} \text{ s/m}$$

$$\tau_0 = \tau_t \quad \tau_r \leq \tau_t$$

$$\tau_0 = \tau_r \quad \tau_r \geq \tau_t$$

$$\tau_r = \varepsilon \varepsilon_0 / \sigma; \tau_t = 10^{-8} \text{ s}$$

*Speed of the downward moving corona current:*

$$v_c = c$$

*Return stroke speed:*

$$v = 1.5 \times 10^8 \text{ m/s}$$

*Channel base current:*

Predicted by the model.

### 9.12.1 *Model predictions*

According to the model both the return stroke current and the electric fields are affected by the ground conductivity at the point of strike. However, these effects are negligible for ground conductivities higher than about 0.01 S/m. That is, the results obtained for 0.01 S/m ground conductivity is almost identical to the ones obtained when the ground is assumed to be perfectly conducting.

The model-predicted return stroke current at the channel base and its time derivative for different values of ground conductivities are shown in Figure 9.23. Note that the decrease in the peak current when the conductivity changes from 0.01 to 0.001 S/m is negligible for all practical purposes. Thus, for ground conductivities higher than about 0.001 S/m one may not be able to discern any change in peak current in experimental observations. Nevertheless, the peak current continues to decrease with decreasing ground conductivity, and it decreases by about 20 per cent for 0.0001 S/m. The effect of ground conductivity on the peak current derivative is much more significant than on the peak current. The peak current time derivative decreases by about 40 per cent when the conductivity decreases from 0.01 (or perfect conductivity) to 0.001 S/m. For  $\sigma = 0.0001$  S/m, it becomes as low as 17 per cent of the value for perfectly conducting ground.

Figure 9.24 depicts the electric and magnetic fields predicted by this model at different distances for a ground conductivity of 0.01 S/m. Since the idea of this presentation is to illustrate the effect of ground conductivity on model predictions, the electric and magnetic fields were assumed to propagate over perfectly conducting ground. In other words what is presented here are the electric and magnetic fields as generated by the return stroke before they were distorted by propagation effects. First, note that the electromagnetic fields predicted by the model have all the correct features of the measured fields qualifying the model as a reasonable model to simulate the electromagnetic fields from return strokes. In order to qualify as a good return stroke model the predicted electromagnetic fields have to satisfy the following criteria:

1. Sharp initial peak at 5 and 100 km
2. Slow ramp after the initial peak in electric fields at 5 km

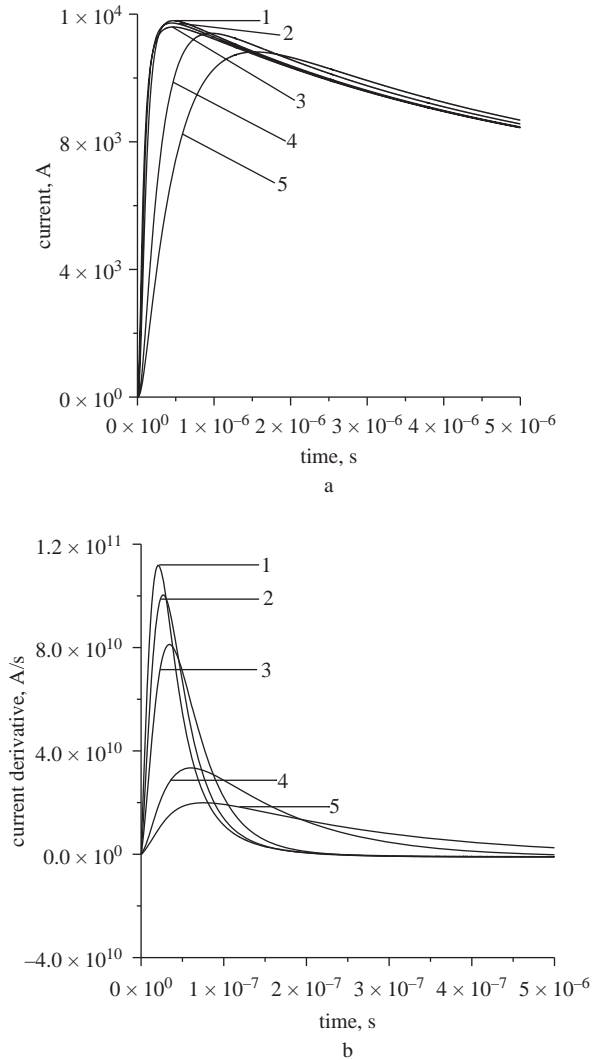
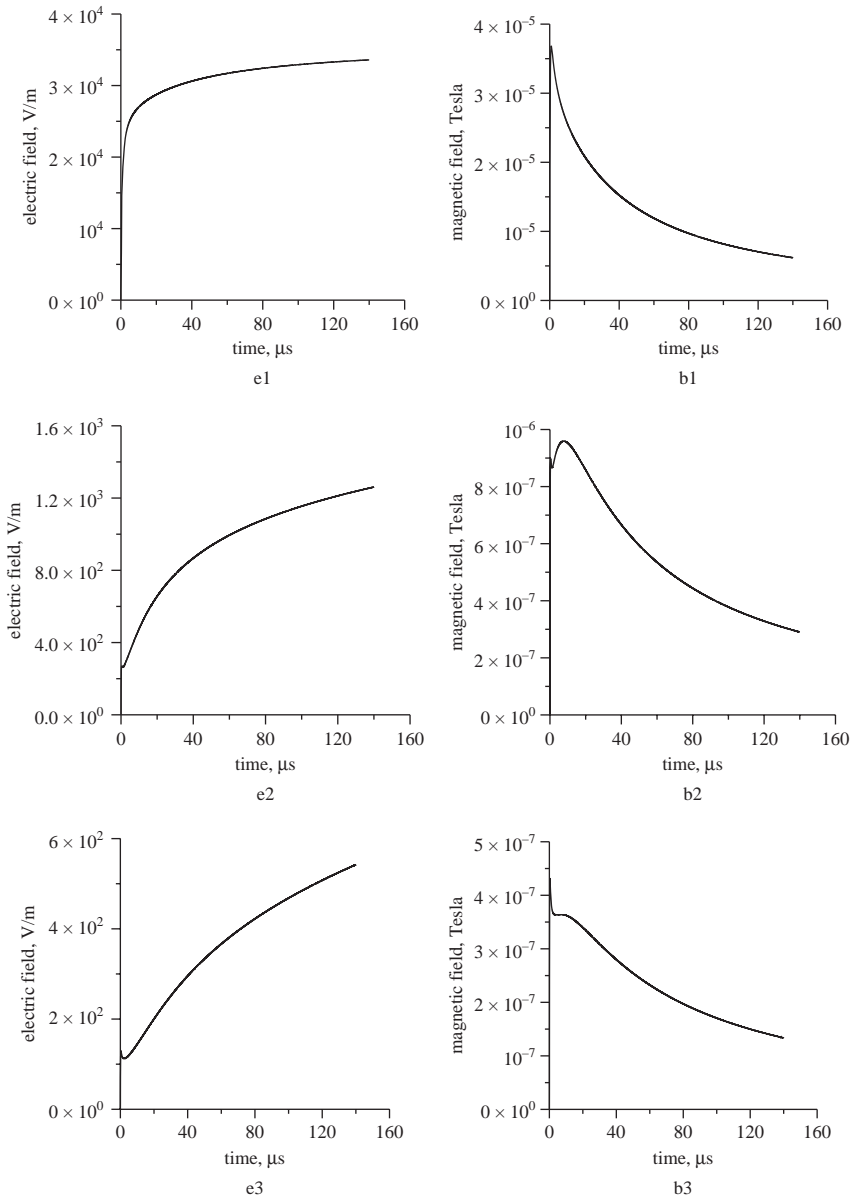


Figure 9.23 The channel base current waveform (a) and its derivative (b) as a function of ground conductivity as predicted by the model of Cooray and Rakov [75] that was developed to incorporate ground conductivity into the return stroke models: (1) 0.01 S/m; (2) 0.002 S/m; (3) 0.001 S/m; (4) 0.0002 S/m; (5) 0.0001 S/m

3. Hump after the initial peak in the magnetic field at 5 km
4. Zero crossing of the tail of the waveform at 100 km
5. Flattening of the electric field at 50 m

As mentioned earlier, the results shown are for a ground conductivity of 0.01 S/m at the strike point. Now let us investigate the effect of this conductivity on the electric and magnetic fields. The electric field at 100 km as generated by the source (i.e. without propagation effects) for different ground conductivities at the strike point are shown in Figure 9.25a. The corresponding electric field derivatives



*Figure 9.24 Electric field (waveforms marked e) and magnetic field (waveforms marked b) as predicted by the Cooray and Rakov [75] model that was developed to take into account the effect of ground conductivity into return stroke models. The electromagnetic fields shown in the figure correspond to a ground conductivity of 0.01 S/m. Note that fields shown are the source fields, i.e. those calculated without taking into account the effects of finitely conducting ground on the electric fields: (e1, b1) 50 m; (e2, b2) 1 km; (e3, b3) 2 km; (e4, b4) 5 km; (e5, b5) 10 km; (e6, b6) 100 km*

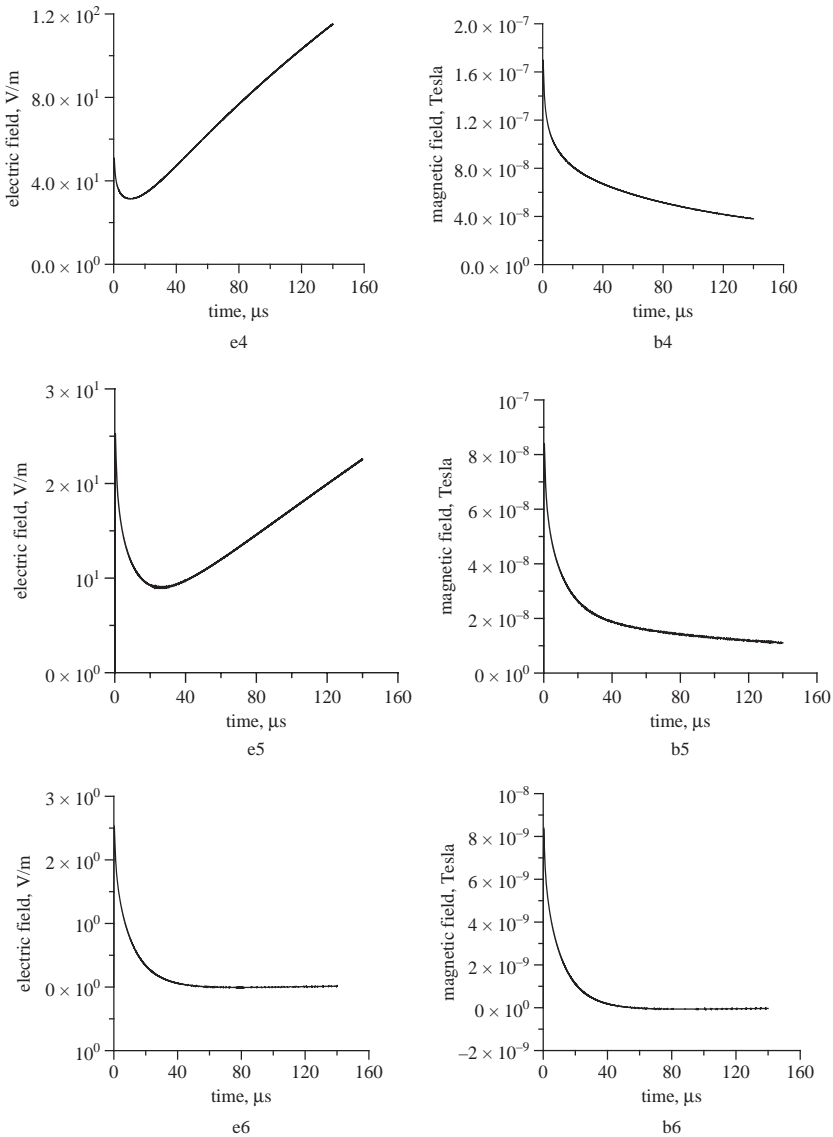


Figure 9.24 (Continued)

are shown in Figure 9.25b. Observe that the reduction in the electric field peak becomes noticeable for conductivities smaller than about 0.001 S/m. The reduction in the peak electric field derivative is more significant. The field derivative decreases by about 20 per cent when the conductivity changes from 0.01 to 0.001 S/m. The reduction is nearly 80 per cent when the conductivity is reduced to 0.0001 S/m. This also shows that in regions where the ground conductivity is low the electric field time derivatives generated by return strokes will be low even when the fields are measured in such a way that the propagation effects are minimal.



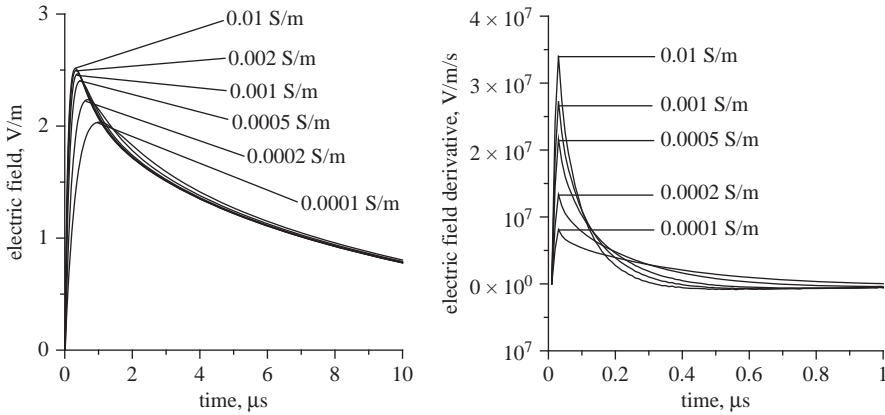


Figure 9.25 (a) The electric field at 100 km and (b) the electric field time derivative as generated by the return stroke model of Cooray and Rakov [75] that was developed to incorporate ground conductivity into return stroke models. The results corresponding to several ground conductivities are shown in the figure. Observe that the electric fields shown are the source fields (i.e. the fields calculated at 100 km without taking into account the propagation effects)

### 9.13 Linear charge density deposited by the first return stroke along the leader channel

Recently, Cooray *et al.* [76] evaluated the charge distribution along the stepped leader channel and the dart leader channel by combining the bidirectional leader model and the charge lowered to ground by first and subsequent return strokes as measured by Berger [86, 87]. Using the results presented in that study one can show that the distribution of the positive charge deposited along the leader channel,  $\rho(z)$ , by a return stroke is given by

$$\rho(z) = a_0 k I_p + \frac{k I_p (a + bz)}{1 + cz + dz^2} \quad (9.65)$$

where  $z$  is the co-ordinate directed along the channel with the origin at ground level and  $I_{pm}$  is the measured return stroke peak current in kA. In the case of first return strokes  $a_0 = 1.476 \times 10^{-5}$ ,  $a = 4.857 \times 10^{-5}$ ,  $b = 3.909 \times 10^{-6}$ ,  $c = 0.522$  and  $d = 3.73 \times 10^{-3}$ . For subsequent return strokes the corresponding parameters are  $a_0 = 5.09 \times 10^{-6}$ ,  $a = 1.325 \times 10^{-5}$ ,  $b = 7.06 \times 10^{-6}$ ,  $c = 2.089$  and  $d = 1.492 \times 10^{-2}$ . The parameter  $k$  is introduced into this equation to take care of the scatter in the measured relationship between the return stroke peak current and the charge lowered to ground. The measured values of peak current versus charge have a scatter of about 25–30 per cent around the mean value. This scatter can be taken into account by setting  $k = 1.0 \pm 0.3$ . This charge distributions corresponding to 30 kA first return stroke and 12 kA subsequent return stroke are shown in Figures 9.26 and 9.27, respectively.

Note that the charge distribution given above can be utilised in return stroke models where the positive charge deposited by the return stroke is one of the input parameters. If the channel base current is one of the predicted parameters then the

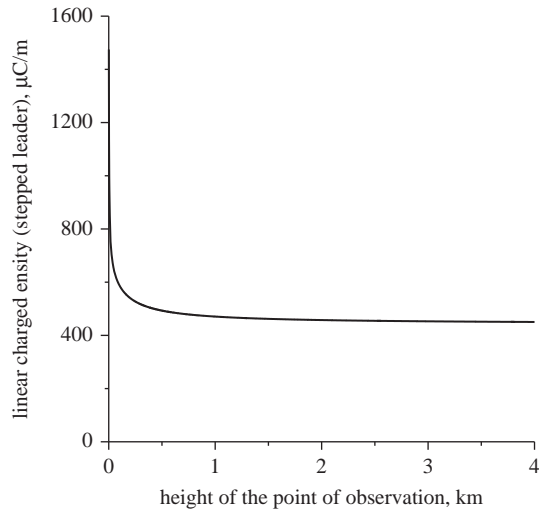


Figure 9.26 The positive charge deposited by a negative first return stroke of 30 kA on the stepped leader channel as given by (9.65)

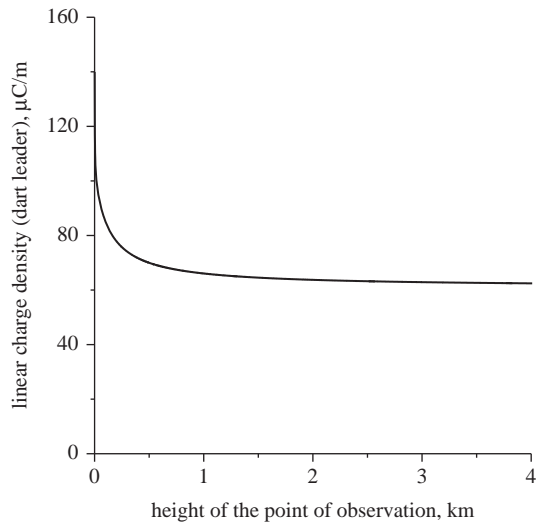


Figure 9.27 The positive charge deposited by a negative subsequent return stroke of 12 kA on the dart leader channel as given by (9.65)

use of this charge distribution with  $I_p = 12$  kA may not necessarily result in a 12 kA peak channel base current in the model. However, if the model is physically reasonable the predicted peak current should lie within a factor of 0.7–1.3. For example, in the model presented in section 9.23 the above equation is used with  $I_p = 12$  kA for a subsequent return stroke. As one can notice from Figure 9.15 the model-generated channel base current had a peak of 11 kA. However, this value of  $k$  is still within the allowable limits based on the scatter of the experimental data points reported in [76].

## 9.14 Future of return stroke models

The engineering models play down the physics and performed a game of trial and error to extract the correct electromagnetic fields. However, the introduction of CG and CD type models is a step forward in our endeavour to understand the physical principles behind the return stroke process. These models promise to be as revolutionary as the model of Bruce and Golde [50] was nearly half a century ago. The new understanding gained through these models shows how the leader and the Earth interact to create spectacular return strokes, and the computer simulations adopted within these models have proved very successful in reproducing the features of return strokes. It is clear, however, that there is ample room for both theoretical and experimental studies on several aspects.

1. The current generation and current dissipation models, though much closer to physical reality than the current propagation models, are not yet self-consistent. What is needed is a theory for the neutralisation process of the leader corona and more experimental data on the radial discharge processes that may take place during the return stroke stage. In this respect, experiments of the kind performed by Takagi *et al.* [11] should be mentioned. More stringent tests of return stroke models may emerge from such observations.
2. Many return stroke models make predictions as to the way in which the peak and the rise time of the return stroke current vary as a function of height. Within this subject there is an urgent need to develop remote sensing techniques to 'feel' the signature of return stroke currents at different altitudes. One possible course of action is to find the correlation between the optical radiation and the current waveforms and then use this information to infer the way in which the return stroke current varies with height.
3. Theories should be developed concerning the speed of the return stroke front. On the experimental side, simultaneous measurements of the leader temperature, the return stroke speed and the temporal variation of the optical radiation may provide valuable clues to guide the efforts of the theorists.
4. A few return stroke models predict the spatial variation of the return stroke speed close to the point of initiation. This calls for experimental studies of the luminous features associated with the development of the return stroke within about 100 m of the point of initiation. In addition to providing a rigorous test of the existing models, the data will serve as the foundation on which the next stage of return stroke models will be built on.

Even though our knowledge about the mechanism of the return stroke is still far from complete, the modellers have built up theories and syntheses to fill in the gaps. Ultimately, it may be found that the final consensus will depend to a large extent on the diligent work of experimentalists, which will eventually weed out the bad theories from the good ones.

## References

- [1] Hill, H. L., 'Channel heating in return stroke lightning', *J. Geophys. Res.*, 76, 637–645, 1971.
- [2] Saha, M. H., 'Ionization in the solar chromosphere', *Phil. Mag.*, 40, 472, 1920.

- [3] Drabkina, S. I., 'On the theory of development of the channel of a spark discharge', *J. Exp. Theoret. Phys. (USSR)*, 21, 473, 1951.
- [4] Braginskii, S. I., 'Theory of the development of a spark channel', *Sov. Phys. - JETP*, 34, 1068–1074, 1958.
- [5] Plooster, M. N., 'Shock waves from line sources: Numerical solutions and experimental measurements', *Phys. Fluids*, 13, 2665, 1970.
- [6] Plooster, M. N., 'Numerical simulation of spark discharges in air', *Phys. Fluids*, 14(10), 2111–2123, 1971.
- [7] Plooster, M. N., 'Numerical model of the return stroke of the lightning discharge', *Phys. Fluids*, 14(10), 2124–2133, 1971.
- [8] Brode, H. L., 'Blast wave from a spherical charge', *Phys. Fluids*, 2, 217–229, 1959.
- [9] Paxton, A. H., Gardine, R. L., and Baker L., 'Lightning return stroke a numerical calculation of the optical radiation', *Phys. Fluids*, 29, 2736–2741, 1986.
- [10] Cabrera, V., and V. Cooray, 'On the mechanism of space charge generation and neutralization in a coaxial cylindrical configuration', *J. Electrostat.*, 28, 187, 1992.
- [11] Takagi N. *et al.*, 'Expansion of the luminous region of the lightning return stroke channel', *J. Geophys. Res.*, 103, D12, 14131–14134, 1998.
- [12] Orville, R. E., M. A. Uman, and A. M. Sletten, 'Temperature and electron density in long air sparks', *J. Appl. Phys.*, 38, 895, 1967.
- [13] Orville, R. E., 'A high-speed time-resolved spectroscopic study of the lightning return stroke: Part I. A quantitative analysis', *J. Atmos. Sci.*, 25, 827–838, 1968.
- [14] Orville, R. E., 'A high-speed time-resolved spectroscopic study of the lightning return stroke: Part II. A quantitative analysis', *J. Atmos. Sci.*, 25, 839–851, 1968.
- [15] Orville, R. E., 'A high-speed time-resolved spectroscopic study of the lightning return stroke: Part III. A time dependent model', *J. Atmos. Sci.*, 25, 852–856, 1968.
- [16] Baker, L., L. Gardner, A. H. Paxton, C. E. Baum, and W. Rison, 'Simultaneous measurement of current, electromagnetic fields, and optical emission from a lightning stroke', in *Lightning Electromagnetics* (R. L. Gardner, Ed.), Hemisphere, New York, NY, p. 365, 1990.
- [17] Oetzel, G. N., 'Computation of the diameter of a lightning return stroke', *J. Geophys. Res.*, 73, 1889–1896, 1968.
- [18] Price, G. H., and Pierce, E. T., 'The modeling of channel current in the lightning return stroke', *Radio Sci.*, 12, 381–388, 1977.
- [19] Little, P. F., 'Transmission line representation of a lightning return stroke', *J. Phys. D: Appl. Phys.*, 11, 1893–1910, 1978.
- [20] Amoruso, V., and F. Lattarulo, 'The electromagnetic field of an improved lightning return stroke representation', *IEEE Trans. Electromagn. Compat.*, 35, 317–328, 1993.
- [21] Strawe, D. F., 'Non-linear modeling of lightning return stroke', in *Proc. Fed. Aviation Admin./Florida Inst. Technol. Workshop Grounding Lightning Technol.*, Melbourne, FL, 1979, Rep. FAA-RD-79-6, pp. 9–15.
- [22] Mattos, M. A. F., and C. Christopoulos, 'A non-linear transmission line model of the lightning return stroke', *IEEE Trans. Electromagn. Compat.*, 30, 40–406, 1988.

- [23] Spitzer, L., and R. Härm, 'Transport phenomena in a completely ionized gas', *Phys. Rev.*, 89, 977, 1953.
- [24] Baum, C., and L. Baker, 'Analytical return stroke transmission line model', in *Lightning Electromagnetics* (R. L. Gardner, Ed.), Hemisphere, New York, NY, p. 17, 1990.
- [25] Baum, C. E., 'Return stroke initiation', in *Lightning Electromagnetics* (R. L. Gardner, Ed.), Hemisphere, New York, NY, p. 101, 1990.
- [26] Baker, L., 'Return stroke transmission line model', in *Lightning Electromagnetics* (R. L. Gardner, Ed.), Hemisphere, New York, NY, p. 63, 1990.
- [27] Rondón, D. A., F. H. Silveira, and S. Visacro, 'A varying surge impedance transmission line model for simulation of lightning return current in time domain', in *Proceedings of the International Conference on Grounding and Earthing*, Rio De Janeiro, Brazil, 2002.
- [28] Theethayi, N., and V. Cooray, 'On the representation of the lightning return stroke as a current pulse propagating along a transmission line', *IEEE Trans. Power Del.*, 20(2), 823–837, 2005.
- [29] Visacro, S., and A. De Conti, 'A distributed-circuit return-stroke model allowing time and height parameter variation to match lightning electromagnetic field waveform signatures', *Geophys. Res. Lett.*, 32(L23805), doi:10.1029/2005GL024336, 2005.
- [30] De Conti, A., S. Visacro, A. Soares J., and M. A. O. Schroeder, 'Revision, extension and validation of Jordan's formula to calculate the surge impedance of vertical conductors', *IEEE Trans. Electromagn. Compat.*, 48(3), 530–536, 2006.
- [31] De Conti, A., S. Visacro, N. Theethayi, and V. Cooray, 'A comparison of different approaches to simulate a nonlinear channel resistance in lightning return stroke models', *J. Geophys. Res.*, 113(D14129), doi: 10.1029/2007JD009395, 2008.
- [32] De Conti, A., F. H. Silveira, and S. Visacro, Transmission line models of lightning return stroke, in *Lightning Electromagnetics*, Edited by Vernon Cooray, The Institution of Engineering and Technology (IET), London, UK, 2012.
- [33] Toepler, M., 'Zur kenntnis der gesetz der gleitfunkenbildung', *Ann. Phys. D.*, 4(21), 193–222, 1906.
- [34] Barannik, S. I., S. B. Vasserman, and A. N. Lukin, 'Resistance and inductance of a gas arc', *Sov. Phys. Tech. Phys.*, 19(11), 1449–1453, 1975.
- [35] De Conti, A., and S. Visacro, 'On the use of lumped sources in a nonlinear lightning return stroke model and extension for evaluating strikes to tall objects', *J. Geophys. Res.*, 114(D11115), doi: 10.1029/2008JD011120, 2009.
- [36] Cooray, V., and N. Theethayi, 'Pulse propagation along transmission lines in the presence of corona an their implication to lightning return strokes', *IEEE Trans. Antenn Propag.*, 56(7), 1948–1959, 2008.
- [37] Jordan, D. M., and M. A. Uman, 'Variation in light intensity with height and time from subsequent lightning return strokes', *J. Geophys. Res.*, 88(C11), 6555–6562, 1983.
- [38] Mach, D. M., and W. D. Rust, Photoelectric return stroke velocity and peak current estimates in natural and triggered lightning, *J. Geophys. Res.*, 94, 13237–13247, 1989.

- [39] Rakov, V. A., and M. A. Uman, 'Review and evaluation of lightning return stroke models including some aspects of their application', *IEEE Trans. Electromagn. Compat.*, 40(4), 403–426, 1989.
- [40] Gomes, C., and V. Cooray, 'Concepts of lightning return stroke models', *IEEE Trans. on Electromagn. Compat.*, 42, 82–96, 2000.
- [41] Borovsky, J. E., 'An electrodynamic description of lightning return strokes and dart leaders', *J. Geophys. Res.*, 100, 2697–2726, 1995.
- [42] Podgorski, A. S., and J. A. Landt, 'Three dimensional time domain modeling of lightning', *IEEE Trans. Power Deliv.*, PWRD-2(3), 931–938, 1987.
- [43] Moini, R., B. Kordi, and M. Abedi, 'Evaluation of LEMP effects on complex wire structures located above a perfectly conducting ground using electric field integral equation in time domain', *IEEE Trans. Electromagn. Compat.*, 40(2), 154–162, 1998.
- [44] Kato, S., T. Narita, T. Yamada, and E. Zaima, 'Simulation of electromagnetic field in lightning to tall tower', paper presented at *11th International Symposium on High Voltage Engineering*, London, UK, p. 467, 1999.
- [45] Kato, S., T. Takinami, T. Hirai, and S. Okabe, 'A study of lightning channel model in numerical electromagnetic field computation', paper presented at 2001 IEEJ National Convention, Nagoya, Japan, pp. 7–140 (in Japanese), 2001.
- [46] Bonyadi-ram, S., R. Moini, S. H. H. Sadeghi, and V. A. Rakov, 'Incorporation of distributed capacitive loads in the antenna theory model of lightning return stroke', paper presented at *16th International Zurich Symposium and Technical Exhibition on Electromagnetic Compatibility*, Swiss Federal Institute of Technology, Zurich, Switzerland, pp. 213–218, 2005.
- [47] Baba, Y., and V. Rakov, 'Electromagnetic models of lightning return strokes', in *Lightning Electromagnetics*, Edited by Vernon Cooray, The Institution of Engineering and Technology (IET), London, UK, 2012.
- [48] Moini, R. and S. H. H. Sadeghi, Antenna models of lightning return stroke: an integral approach based on the method of moments, in *Lightning Electromagnetics*, Edited by Vernon Cooray, The Institution of Engineering and Technology (IET), London, UK, 2012.
- [49] Norinder, H., 'Quelques essais recents relatifs á la determination des surtensions indirectes', CIGRE session 1939, 29 June–8 July, Paris, p. 303, 1939.
- [50] Bruce, C. E. R., and Golde, R. H., 'The lightning discharge', *J. Inst. Elect. Eng.*, 88, 487–520, 1941.
- [51] R. Lundholm, Ph. D. dissertation, KTH, Stockholm, Sweden, 1957.
- [52] Dennis, A. S., and E. T. Pierce, 'The return stroke of the lightning flash to earth as a source of atmospherics', *Radio Sci.*, vol. 68D, 777–794, 1964.
- [53] Uman, M. A., and McLain, D. K., 'Magnetic field of lightning return stroke', *J. Geophys. Res.*, 74, 6899–6910, 1969.
- [54] Nucci, C. A., C. Mazzetti, F. Rachidi, and M. Ianoz, 'On lightning return stroke models for LEMP calculations', in *19th International Conference on Lightning Protection*, Graz, Austria, 1988.
- [55] Rakov, V. A., and A. A. Dulzon, 'A modified transmission line model for lightning return stroke field calculation', in *Proc. 9th International Symposium on Electromagnetic Compatibility*, Zurich, Switzerland, 44H1, pp. 229–235, 1991.
- [56] Cooray, V., and R. E. Orville, 'The effects of variation of current amplitude, current risetime and return stroke velocity along the return stroke channel on

- the electromagnetic fields generated by return strokes', *J. Geophys. Res.*, 95, D11, October 1990, 18617–18630.
- [57] Cooray, V., 'Return stroke models for engineering applications', in *Lightning Protection* (V. Cooray, Ed.), Institute of Engineering and Technology, London, UK, 2010.
- [58] Olsen, R. C., D. M. Jordan, V. A. Rakov, M. A. Uman, and N. Grimes, 'Observed one—Dimensional return stroke propagation speeds in the bottom 170 m of a rocket-triggered lightning channel', *Geophys. Res. Lett.*, 31, L16107–L16104, 2004.
- [59] Nucci, C. A. *et al.*, 'Lightning return stroke current models with specific channel base current: A review and comparison', *J. Geophys. Res.*, 95, 20395–20408, 1990.
- [60] Wagner, C. F., 'Calculating lightning performance of transmission lines', *AIEE Trans.*, 1232, 1985, 1956.
- [61] Lin, Y. T., M. A. Uman, R. B. Standler, 'Lightning return stroke models', *J. Geophys. Res.*, 85, 1571–1583, 1980.
- [62] Master, M. J., M. A. Uman, Y. T. Lin, R. B. Standler, 'Calculation of lightning return stroke electric and magnetic fields above ground', *J. Geophys. Res.*, 86, 12127–12132, 1981.
- [63] Heidler, F., 'Travelling current source model for LEMP calculation', in *Proceedings of the 6th International Symposium on Electromagnetic Compatibility*, Zurich, Switzerland, vol. 29F2, pp. 157–162, 1985.
- [64] Hubert, P. 'New model of lightning return stroke – Confrontation with triggered lightning observations', *Proceedings of the 10th International Aerospace and Ground Conference on Lightning and Static Electricity*, Paris, pp. 211–215, 1985.
- [65] Cooray, V., 'A return stroke model', in *Proceedings of the International Conference on Lightning and Static Electricity*, UK, pp. 6B.4.1–6B.4.6., 1989.
- [66] Cooray, V., 'A model for subsequent return stroke', *J. Elect.*, 30, 343–354, 1993.
- [67] Diendorfer, G., and M. A. Uman, 'An improved return stroke model with specified channel base current', *J. Geophys. Res.*, 95, 13621–13644, 1990.
- [68] Thottappillil, R., D. K. McLain, M. A. Uman, and G. Diendorfer, 'Extension of Diendorfer–Uman lightning return stroke model to the case of a variable upward return stroke speed and a variable downward discharge current speed', *J. Geophys. Res.*, 96, 17143–17150, 1991.
- [69] Thottappillil, R., and M. A. Uman, 'Lightning return stroke model with height-variable discharge time constant', *J. Geophys. Res.*, 99, 22773–22780, 1994.
- [70] Cooray, V., 'Predicting the spatial and temporal variation of the electromagnetic fields, currents, and speeds of subsequent return strokes', *IEEE Trans. Electromagn. Compat.*, 40, 427–435, 1998.
- [71] Cooray, V., 'A model for first return strokes in lightning flashes', *Physica Scripta*, 55, 119–128, 1996.
- [72] Cooray, V., and A. Galvan, 'A negative first return stroke model for engineering application', *Proceedings of the 25th International Conference on Lightning Protection (ICLP)*, Rhodos, Greece, 2000.
- [73] Cooray, V., R. Montano, and V. Rakov, 'A model to represent first return strokes with connecting leaders', *J. Electrostat.*, 40, 97–109, 2004.

- [74] Cooray, V., and V. Rakov, 'A current generation type return stroke model that predicts the return stroke velocity', *J. Lightning Res.*, 1, 32–39, 2007.
- [75] Cooray, V., and V. Rakov, 'Engineering lightning return stroke models incorporating current reflection from ground and finitely conducting ground effects', *Proceedings of the IEEE on Electromagnetic Compatibility*, 53, 773–781, 2011.
- [76] Cooray, V., V. Rakov, and N. Theethayi, 'The lightning striking distance revisited', *J. Electrostat.*, 65(5–6), 296–306, 2007.
- [77] CIGRE, paper 63, report of the working group 01 (Lightning) of Study Committee 33, 1991.
- [78] Yokoyama, S., paper presented at CIGRE SC 33 (WG 01) meeting, Milano, 1995.
- [79] Cooray, V., 'Further characteristics of positive radiation fields from lightning in Sweden'. *J. Geophys. Res.*, 84(11), 807–811, 815, 1984.
- [80] Gomes, C., and V. Cooray., 'Long impulse currents associated with positive return strokes', *J. Atmos. Terrest. Phys.*, 60, pp. 693–699
- [81] Cooray, V., M. Fernando., C. Gomes, and T. Sorensen, 'The fine structure of positive return stroke radiation fields', *Proceedings of the IEEE on Electromagnetic Compatibility*, vol. 46, 87–95, 2004.
- [82] Weidman, C. D., and E. P. Krider, 'The fine structure of lightning return stroke wave forms', *J. Geophys. Res.*, 83(C12), 6239–6247, 1978.
- [83] Cooray, V., 'A novel procedure to represent lightning strokes – current dissipation return stroke models', *IEEE Trans. Electromagn. Compat.*, 51, 748–755, 2009.
- [84] Cooray, V., 'On the concepts used in return stroke models applied in engineering practice', *IEEE Trans. Electromagn. Compat.*, 45, 101–108, 2003.
- [85] Maslowski, G., and V. A. Rakov, 'Equivalency of lightning return stroke models employing lumped and distributed current sources', *IEEE Trans. Electromagn. Compat.*, 49, 123–132, 2007.
- [86] Berger, K., and E. Vogelsanger, 'Measurement and results of lightning records at Monte San Salvatore from 1955–1963', *Bull. Schweiz. Elektrotech.*, 56, 2–22 (in German), 1965.
- [87] Berger, K., 'Methods and results of lightning records at Monte San Salvatore from 1963–1971', *Bull. Schweiz. Elektrotech.*, 63, 21403–21422 (in German), 1972.





---

## *Chapter 10*

# **Return stroke speed models**

*Vernon Cooray*

---

### **10.1 Introduction**

The return stroke speed is one of the main parameters in the modelling of return strokes. The available experimental observations show that the return stroke speed decreases with height, both in the first and the subsequent return strokes [1, 2]. The experimental data also seem to indicate that there is no relationship between the return stroke current and the return stroke speed [3]. This observation is somewhat against the theoretical intuition where a larger electric field at the return stroke front associated with a larger return stroke current is expected to expedite the neutralisation process giving rise to a larger return stroke speed.

What parameters of the lightning channel that control the return stroke speed is one of the most important questions in lightning research. A current pulse propagating along a perfect conductor located above the ground will move at a speed equal to the speed of light in air. Since the speed of propagation of the return stroke front is significantly less than the speed of light one may hypothesise that the process of electrical breakdown that converts the partially ionised leader channel to a highly conducting return stroke channel decides the speed at which the return stroke is propagating. The lower the conductivity of the leader channel the lower the speed of propagation of the return stroke front. In this chapter, we will consider some of the models that have attempted to take this point into consideration and predict the return stroke speed as a function of other current parameters. The specific models that we will consider are the ones due to Lundholm [4], Wagner [5], Rai [6], Cooray [7] and Cooray [8]. However, before doing that let us perform a simple exercise with engineering return stroke models (see Chapter 9) and see whether the results can tell us something about the variation of the return stroke front speed as it surges through the leader channel.

### **10.2 Subsequent return stroke speed profile as predicted by current generation type engineering return stroke models**

Let us first give a quick summary of the concepts underlining engineering return stroke models. One can find the details in Chapter 9. As described in Chapter 9 (see also [9]) engineering models can be divided into three categories, namely, current propagation, current generation and current dissipation. Here we utilize a model based on current generation concept. In the current generation (CG) models, the neutralisation of the leader charge during the return stroke phase gives rise to the

return stroke current. According to these models, as the return stroke front passes through a given point on the leader channel, the collapse of the corona sheath results in the injection of a corona current into the central core of the return stroke. In all the CG models found in the current literature it is assumed that the temporal variation of the corona current can be represented by an exponential function which decays with a certain time constant called the corona discharge time constant. The total return stroke current is the sum of such elementary current components generated by corona sources distributed along the channel. Once in the core, the corona current is assumed to travel to ground at the speed of light.

In current generation models, one has the choice of selecting the channel base current, the return stroke speed, the distribution of the charge deposited by the return stroke on the leader channel, and the variation of corona discharge time constant along the channel as input parameters. Any set of three of these four input parameters will provide a complete description of the temporal and spatial variation of the return stroke current. In general, the input parameters of the current generation type return stroke models are the return stroke speed, channel base current and either the charge distribution or the corona discharge time constant. However, Cooray and Rakov [10] were the first to suggest that by using the channel base current, charge distribution and the discharge time constant as input parameters one can obtain the return stroke speed profile as a model output.

Let us represent the corona current per unit length  $I_c(z, t)$ , injected into the channel element located at height  $z$  as

$$I_c(z, t) = I_o(z)e^{-(t-z/v_a(z))/\tau(z)} \quad t \geq z/v_a(z) \quad (10.1)$$

where  $t$  is the time,  $v_a(z)$  is the average speed of the return stroke over the channel segment extending from ground to height  $z$ , and  $\tau(z)$  is the corona discharge time constant. If  $\rho(z)$  is the distribution of charge per unit length deposited by the return stroke along the leader channel, then  $\rho(z)$  and  $I_o(z)$  are related to each other through the following equation:

$$I_o(z) = \rho(z)/\tau(z) \quad (10.2)$$

Let us assume that the return stroke speed is a function of height and is given by  $v(z)$ . Then the average speed  $v_a(z)$  of the return stroke over the channel section from ground level to  $z$  is given by

$$v_a(z) = z / \int_0^z \frac{dz}{v(z)} \quad (10.3)$$

The current at ground level,  $I(t)$  is given by (see Chapter 9 for a general description)

$$I(t) = \int_0^{h_e} \left( \frac{\rho(z)}{\tau(z)} \right) \exp \frac{-\left( t - \frac{z}{v_a(z)} - \frac{z}{c} \right)}{\tau(z)} dz \quad (10.4)$$

where  $h_e$  can be found as the solution of the following equation

$$t - \frac{h_e}{v_a(h_e)} - \frac{h_e}{c} = 0 \quad (10.5)$$

In the equations given above, all the parameters are known (recall that the channel base current is also given), except for  $v_a(z)$ . The function  $v_a(z)$  can be extracted from (10.4) by first converting the integral into a summation and then solving the resulting equation consecutively for  $t = n\Delta t$ , where  $n$  is an integer with the smallest value equal to 1 (see Chapter 9). The value of  $\Delta t$  should be selected in such a way that the return stroke speed does not change appreciably over that time interval. Now let us input some reasonable parameters into the above equations.

Based on the data gathered from triggered lightning experiments Cooray and Rakov [10] suggested using  $120 \mu\text{C}/\text{m}$  as a representative value for the charge density at the lower end of a dart leader that will give rise to a 12-kA return stroke current. Following Cooray and Rakov [10], assume that the linear density of the charge deposited by the return stroke on the dart leader channel is uniform. Assume also that the discharge time constant is uniform along the return stroke channel. The channel base current was simulated by a 12-kA peak current the wave shape of which is represented by the analytical function published by Nucci *et al.* [11]. Once the value of the discharge time constant is given the equations presented previously could be used to estimate the return stroke speed profile. In Figure 10.1, the calculated speed profile for  $\rho_0 = 120 \mu\text{C}/\text{m}$  and  $\tau = 50 \text{ ns}$  is depicted. Note that the speed increases initially, reaches a peak and then continues to decay. Cooray and Rakov [10] showed that even in the case in which the charge density and the discharge time constant vary along the channel the model generated speed always follow the spatial variation described above. Interestingly, Olsen *et al.* [12] who measured the speed profile of subsequent return strokes in the bottom hundred meters or so of the channel observed a speed profiles that increased initially with height.

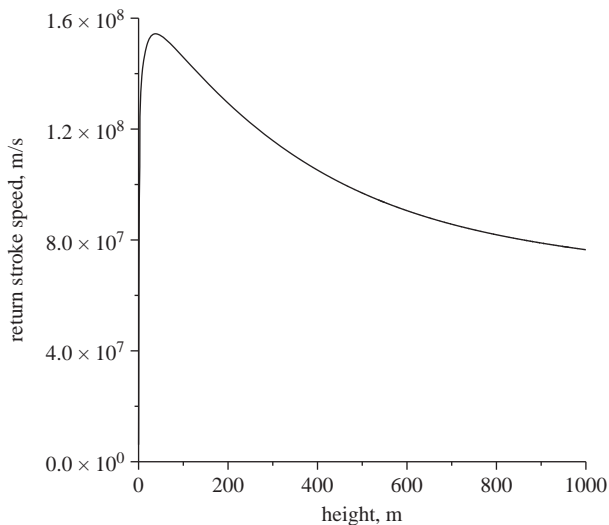


Figure 10.1 The speed profile of a subsequent return stroke calculated using the model of Cooray and Rakov [10]. The channel base current was simulated using the analytical function published by Nucci *et al.* [11]. In the calculation  $\rho_0 = 0.00012 \text{ C}/\text{m}$  and  $\tau = 50 \text{ ns}$

Unfortunately, this procedure cannot be extended further to evaluate how the return stroke speed varies as a function of return stroke peak current and its rise time because the exact connection between these parameters and the dart leader charge density and the corona discharge time constant are unknown at present. A more physically reasonable approach to derive the return stroke speed requires appealing to the details of the processes taking place at the tip of the return stroke. In the next section we will describe such models.

### 10.3 Return stroke speed as predicted by models taking into consideration the processes taking place at the return stroke front

#### 10.3.1 *Lundholm and Wagner*

Both Lundholm [4] and Wagner [5] visualised the return stroke as a step current pulse propagating along the leader channel with a constant speed  $v$ . This model, which of course is a gross simplification of the return stroke, was launched in an attempt to discover the relationship between the return stroke current and its speed. The treatment of Lundholm was as follows: The upward moving current pulse generates an electric field at the surface of the current carrying conductor (in this case the core of the return stroke channel). The component of this field parallel to the surface of the return stroke core and at a point just below the return stroke front is given approximately by

$$E_z = \frac{I_p}{4\pi\epsilon_0 c} \left[ \frac{c^2 - v^2}{cv^2 \left(t - \frac{z}{v}\right)} \right] = I_p R \quad t > z/v \quad (10.6)$$

where  $I_p$  is the peak current and,  $R$  is the resistance per unit length of the return stroke channel. Assume the validity of Toepler's law [13], which describes the resistance of a spark channel by the equation

$$R(z) = \frac{k}{Q(z)} \quad (10.7)$$

where  $R(z)$  is the resistance per unit length of the spark channel at  $z$ ,  $Q(z)$  is the charge that has passed through the point  $z$  and  $k$  is the Toepler's spark constant. Since  $Q(z) = I_p \times (t - z/v)$  for the situation under consideration, the combination of (10.6) and (10.7) provides a relationship between  $I_p$  and  $v$ , namely,

$$v = \frac{c}{\sqrt{1 + \frac{4\pi\epsilon_0 c^2 k}{I_p}}} \quad (10.8)$$

The basics of the Wagner [5] treatment can be described in the following manner. Consider the return stroke as a transmission line with inner and outer conductor radii  $a$  and  $b$ . A charge per unit length  $\rho$  is deposited on this transmission line during the leader stage. The energy of the system is electrostatic. As the return stroke surges up through the transmission line releasing the bound charge, the

energy of the system changes from electrostatic to magnetic energy. Consequently, the energy  $E_u$  released per unit length of the return stroke channel is

$$E_u = \frac{\rho^2}{2C} - \frac{LI_p^2}{2} \quad (10.9)$$

where  $L$  and  $C$  are the inductance and capacitance per unit length, respectively. Observe that if the speed of propagation  $v$  of the return stroke is equal to the speed of light  $c$ , then  $E_u = 0$ . This is the case since  $c = \sqrt{(LC)^{-1}}$  and  $I_p = \rho v$ . When  $v \neq c$ , the above equation gives the power that must be absorbed by the front of the return stroke. From experiments conducted in the laboratory, it was observed that an energy of 0.2 J/m/A is required to raise a spark to a conducting state. Then the energy  $E_u$  per unit length that must be absorbed by the front of the wave to bring the channel to a conductivity which will support a current of  $I_p$  A is equal to 0.2  $I_p$ . Substituting this into (10.9) and after some mathematical manipulations one arrives at the equation

$$v = \frac{c}{\sqrt{1 + \frac{0.4}{LI_p}}} \quad (10.10)$$

The value of the inductance per unit length was calculated by assuming  $a$  (the radius of the inner core) = 0.03 m and  $b$  (the radius of the current return conductor) = 180 m. No discussion or justification was given for the value assumed for the latter parameter.

The derivations of Lundholm and of Wagner could be criticised on several points. Both have assumed the current to be a step function, which is an oversimplification. Furthermore, due to the assumption of an instantaneous rise in the current at the front, any relationship between the risetime of the return stroke current and the speed is lost. The validity of Lundholm's derivation is based on the assumed validity of Toepler's law. This law characterises the temporal variation of the channel resistance in the early stages of a discharge and may not be applicable to return strokes since they propagate along moderately conducting channels already thermalised by leaders. Wagner's simulations depend on the radius of the return current conductor which does not exist in practice. These simplifications cast doubt on the quantitative validity of both Lundholm's and Wagner's results. Nonetheless, the expressions derived may still provide a qualitative description of the relationship between the return stroke current and the speed.

### 10.3.2 Rai

Rai [6] incorporated discharge physics into Bruce and Golde's model [14] (see Chapter 9) in an attempt to couple the return stroke current to its speed. He envisaged the return stroke front as an upward moving equipotential surface which separates a highly ionised gas region below and a neutral gas region with low temperature (virgin air) above. Albright and Tidman [15] derived the following expression to connect the speed  $v$  and the electric field  $E$  at the wavefront of such an ionising potential wave

$$E = \frac{vm\chi}{e \left\{ 1 + \frac{T_o}{\eta} \right\}} \quad (10.11)$$

where  $m$  and  $e$  are the electronic mass and charge,  $\chi$  is the elastic scattering frequency of electrons,  $T_o$  is the electron temperature of the channel, and  $\eta$  is the ionisation potential of the constituent gas. In addition to the assumption that the above equation can describe the processes at the return stroke front, Rai [6] also supposed that the conductivity in the vicinity of the return stroke tip can be described by an equation of the form

$$\sigma(t) = \sigma_o e^{-pt} \quad (10.12)$$

where  $\sigma_o$  and  $p$  are constants. A combination of (10.11) and (10.12) through the identity  $J = E\sigma$  where  $J$  is the current density at the return stroke front, led to the relationship

$$v(t) = \frac{e \left\{ 1 + \frac{T_o}{\eta} \right\} J(t)}{m\chi\sigma(t)} \quad (10.13)$$

According to Bruce and Golde [14], the current at the return stroke front at any instant of time is equal to the current at the channel base at the same instant. Thus, it was possible to replace  $J(t)$  in the above expression with the double exponential expression used by Bruce and Golde to describe the channel base current. The resulting mathematical identity

$$v(t) = \frac{eI_o \left\{ 1 + \frac{T_o}{\eta} \right\} \{ e^{-(\alpha-p)t} - e^{-(\beta-p)t} \}}{m\chi\sigma_o A} \quad (10.14)$$

expresses how the return stroke speed varies as a function of time and current. Note that in the above equation,  $A$  is the cross-sectional area of the return stroke channel. This relationship shows that the return stroke speed has the same mathematical form as that of the return stroke current at the channel base; provided of course the assumptions used in the derivation are justified. Unfortunately, the actual situation may differ from the ideal circumstances assumed in the derivation in several ways. First, (10.11) is valid as long as the medium ahead of the front is virgin air. In reality, the return stroke propagates through the core of the leader channel which is highly conducting due to its elevated temperature. Second, the theory is only applicable if there is a current discontinuity at the return stroke front; such a discontinuity is not physically possible. Third, the validity of the final result depends on the assumptions of Bruce and Golde who assumed that the current along the return stroke channel changes instantaneously from one moment to another. This assumption violates the basic laws of physics.

### 10.3.3 *Cooray – first model*

The procedure used by Cooray [7] to calculate the return stroke speed is based on the following facts. Return strokes either propagate along the channels of the stepped or the dart leaders. Cooray [7] assumed that, with the exception of the very tip, these leader channels can be treated as arc channels in air with an axial potential gradient of the order of 2–10 kV/m. Thus, to induce a significant change in the current in the leader channel, the minimum field required is of the same order of magnitude as this axial electric field. During the return stroke phase the current in the leader channel starts to increase, and the first significant change in the current

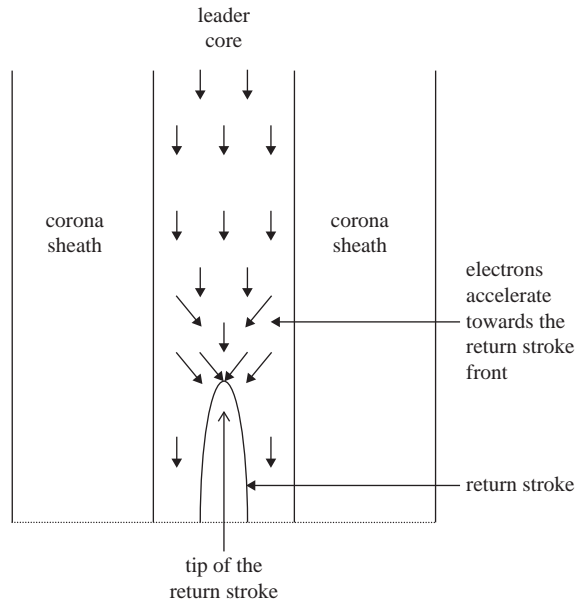


*Figure 10.2 Pictorial depiction of the concept used by Cooray [7] to connect the return stroke speed to the return stroke current. In the model it is assumed that the electric field at the tip of the return stroke is of the order of the external field that exists along the core of the leader channel. When this condition is satisfied electrons will be accelerated towards the return stroke front, enhancing ionisation and leading to an increase in the current at the tip of the return stroke*

takes place at the tip of the return stroke. Thus, the return stroke should maintain a field at the tip which is of the order of the axial field along the leader channels. When this condition is satisfied, electrons will be accelerated towards the tip of the return stroke, causing an increase in the current (Figure 10.2). On the basis of this reasoning Cooray [7] assumed that the field at the tip of the return stroke is equal to the potential gradient of the leader channel.

Let us consider how this assumption can be used to evaluate the return stroke speed as a function of height. First, it is necessary to calculate the electric field at the front of the return stroke. The electric field at the return stroke front can be calculated using the classical dipole method used frequently by lightning researchers or by appealing to the electromagnetic fields of accelerating charges as introduced recently by Cooray and Cooray [16] and applied by Cooray [8] in solving the problem that we have at hand, i.e. calculating the electric field in the return stroke channel. Both methods give identical results for the value of the field even though the final expressions for the field are completely different. Both methods are presented here for comparison.

### 10.3.3.1 Classical dipole method of electric field calculation

Consider the situation at time  $t$  when the return stroke front is at a distance  $Z_0$  from ground. If  $v(z)$  is the speed of the return stroke (which is a function of  $z$ ), then  $Z_0$  and  $t$  are connected by the equation



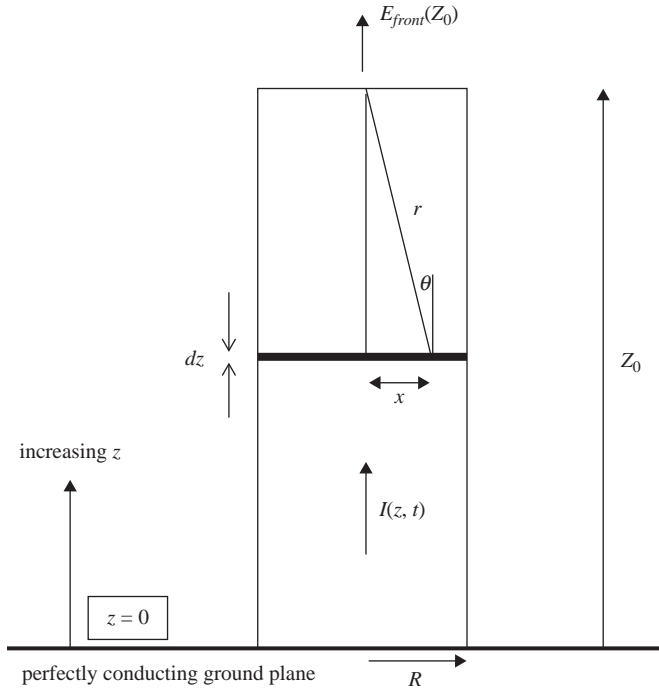


Figure 10.3 The geometry relevant to the calculation of the electric field at the front of the return stroke

$$t = \int_0^{Z_0} \frac{dz}{v(z)} \tag{10.15}$$

Assume that the current in the return stroke is uniformly distributed along its cross section and the current density is given by  $j(z, t)$ . The radius of the return stroke is taken to be  $R$ . The geometry of the situation is shown in Figure 10.3. The problem is to find the field at  $z = Z_0$  at time  $t$ , which is the field at the front of the return stroke. This can be done by dividing the channel into elementary sections and treating each element as an electric dipole. The total field at the front can be obtained by summing the contribution from each dipole. This will result in the following expression for the electric field at the front of the return stroke:

$$E_{real}(Z_0) = -\frac{1}{2\epsilon} \int_0^{Z_0} dz \int_0^R \left\{ \cos^2\theta \left[ \frac{2}{r^3} \int_{\zeta}^{t-r/c} j(z, \tau - \zeta) d\tau + \frac{2}{cr^2} j(z, t - \zeta - r/c) \right] \right. \\ \left. + \sin^2\theta \left[ \frac{1}{r^3} \int_{\zeta}^{t-r/c} j(z, \tau - \zeta) d\tau + \frac{1}{cr^2} j(z, t - \zeta - r/c) \right] \right. \\ \left. + \frac{1}{cr^2} \frac{d}{dt} j(z, t - \zeta - r/c) \right\} x dx \tag{10.16}$$

where  $\zeta$  is the time, measured from the beginning of the discharge, at which the current in the element at  $z$  is turned on. We assume that it is turned on when the front reaches the height  $z$ . With that assumption

$$\zeta = \int_0^z \frac{dz}{v(z)} \quad (10.17)$$

So far we have calculated the field at the front owing to the actual channel section being considered. Now it is necessary to include the image contribution for an assumed perfectly conducting ground plane. This can easily be obtained by changing the limits of the integration of variable  $z$  in (10.16) from  $(0, Z_0)$  to  $(Z_0, 2Z_0)$ . Performing this change in (10.16), the image field at the front is given by

$$\begin{aligned} E_{image}(Z_0) = & -\frac{1}{2\epsilon} \int_Z^{2Z_0} dz \left\{ \cos^2 \theta \left[ \frac{2}{r^3} \int_{\zeta}^{t-r/c} j(z, \tau - \zeta) d\tau + \frac{2}{cr^2} j(z, t - \zeta - r/c) \right] \right. \\ & + \sin^2 \theta \left[ \frac{1}{r^3} \int_{\zeta}^{t-r/c} j(z, \tau - \zeta) d\tau + \frac{1}{cr^2} j(z, t - \zeta - r/c) \right. \\ & \left. \left. + \frac{1}{cr^2} \frac{d}{dt} j(z, t - \zeta - r/c) \right] \right\} x dx \quad (10.18) \end{aligned}$$

The total electric field at the return stroke front is then given by

$$E_{front}(Z_0) = E_{image}(Z_0) + E_{real}(Z_0) \quad (10.19)$$

### 10.3.3.2 Calculation of electric fields using electromagnetic fields of accelerating charges

Cooray [8] utilised the electromagnetic fields of accelerating charges in evaluating the electric field at any point on the axis of the return stroke channel. In writing down the equations he assumed that the return stroke can be represented by a current generation type model concept. Since any return stroke model can be reformulated as a current generation model this choice does not in any way compromise the generality of the derived equations. According to this picture as the return stroke front surges forward each channel element behaves as a current source which is being triggered by the arrival of the return stroke front at that element. The current generated by the source travels to ground with the speed of light. When treating this problem using the accelerating charge concept the total electric field at any point can be divided into four terms. They are (i) the static field generated by the accumulation of charge on a given channel element as the corona current takes away negative charge from that channel element, (ii) the radiation field generated by charge acceleration during the initiation of the corona current in a given channel element, (iii) the radiation field generated during the

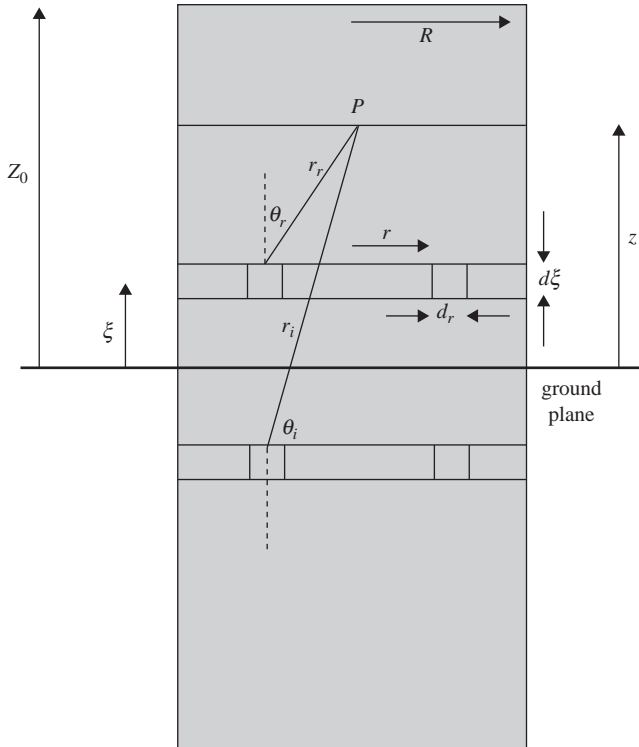


*Figure 10.4 Geometry relevant to the calculation of the static field and the radiation field generated by the corona current at the point of observation  $P$ . In order to calculate the electric field at point  $P$ , the channel is divided into circular discs of width  $d\xi$  and each disc is divided into rings of width  $dr$ . The charge deposited in and the current flowing through the ring when the return stroke front is at height  $Z_0$  (i.e. corresponding to time  $t$ ) is used to calculate the electric field at point  $P$  at time  $t$  attributable to the ring, and the electric field produced by the disc at point  $P$  is obtained by integrating the result from  $r = 0$  to  $r = R$ . The total electric field at point  $P$  is determined by summing the contribution from all the elementary discs located along the channel*

deceleration of charges associated with the corona current when the downward moving corona current is terminated at ground end and (iv) the velocity field generated by the uniform downward movement of corona current along the return stroke channel. Since the speed of propagation of the corona current along the return stroke channel is equal to the speed of light, the velocity term associated with this current flow is equal to zero.

Let us refer to the geometry given in Figures 10.4 and 10.5. Mathematical expressions for the electric field components at any point along the return stroke channel are derived by Cooray [8, 17] and the results are as follows:

- (i) The total radiation field in the positive  $z$  direction (geometry is given in Figure 10.1) at the point of observation  $P$  attributable to the generation of corona current is

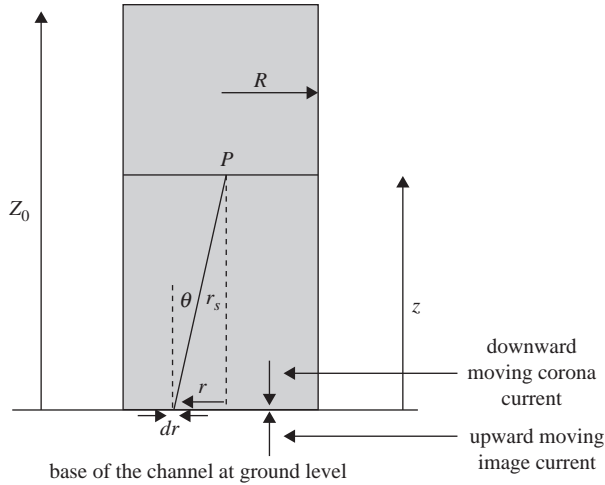


Figure 10.5 Geometry relevant to the calculation of the radiation field generated by the deceleration of electric charges at the channel base. Note that the electric field at point  $P$  has two contributions, one from the downward moving corona current and the other caused by the image current of opposite polarity (representing the effect of perfectly conducting ground plane) which neutralises the charge deposited by the downward moving corona current at the channel base

$$E_{cor}(t, z) = - \int_0^{Z_0} \int_0^R \frac{I_{cor}(t - \xi/v_{av} - r_r/c)}{2\pi\epsilon_0 c R^2} \frac{r \sin^2 \theta_r d\xi dr}{r_r(1 - \cos \theta_r)} \quad (10.20a)$$

$$+ \int_0^{Z_0} \int_0^R \frac{I_{cor}(t - \xi/v_{av} - r_i/c)}{2\pi\epsilon_0 c R^2} \frac{r \sin^2 \theta_i d\xi dr}{r_i(1 - \cos \theta_i)}$$

with

$$v_{av} = \frac{\xi}{\int_0^{\xi} \frac{1}{v(z)} dz} \quad (10.20b)$$

In the above equation,  $v_{av}$  is the average speed of the return stroke over the channel from ground level to height  $\xi$ .

(ii) The total static electric field in the positive  $z$  direction (for the geometry given in Figure 10.1) at the point of observation is

$$E_{stat}(t, z) = \int_0^{Z_0} \int_0^R \left[ \frac{\rho_v r}{2\epsilon_0 r_r^2} \cos \theta_r - \frac{\rho_v r}{2\epsilon_0 r_i^2} \cos \theta_i \right] d\xi dr \quad (10.21)$$

$$\rho_v = \frac{dq}{\pi R^2} \quad (10.22)$$

$$dq = \int_{\xi/v}^{Z_0/v} I_{cor}(t - \xi/v_{av} - r_r/c) dt \quad (10.23)$$

- (iii) The total electric radiation field in the positive  $z$  direction (geometry is given in Figure 10.2) generated by the deceleration of charges during the termination of the corona current at the channel base at ground level is given by

$$E_g(t, z) = \int_0^R \frac{J(t - r/c) \sin^2 \theta r dr}{2\epsilon_0 c r_s (1 + \cos \theta)} + \int_0^R \frac{J(t - r/c) \sin^2 \theta r dr}{2\epsilon_0 c r_s (1 - \cos \theta)} \quad (10.24)$$

The down-coming corona current will deposit its charge at the channel base in accordance with the charge continuity equation. Since the effect of perfectly conducting ground on the electric field is represented by an image current, the charge deposited by the downward moving corona current at ground end of the channel is neutralised by the opposite charge associated with the image current (i.e. the ground potential is assumed to remain zero during the process). Thus, the contribution to the radiation field consists of two terms, one from the termination of the real current (the first term) and the other attributable to the termination of the image current [16]. In the above equations  $I_{cor}(t, z)$  is the corona current at any given height  $z$  along the channel,  $J(t)$  is the current density at the base of the channel,  $dq$  is the charge that will be accumulated in a disc of unit thickness located at height  $\xi$  when the return stroke front is at height  $Z_0$ ,  $\rho_v$  is the corresponding volume charge density of the element,  $v$  is the return stroke speed and  $c$  is the speed of light in free space. The above equations completely define the electric field at any point on the axis of the return stroke. The total electric field at any point on the axis of the return stroke channel generated purely by the neutralisation process of the return stroke (i.e. neglecting the existing electric field in the leader channel) is then given by

$$E_t(t, z) = E_{cor}(t, z) + E_{stat}(t, z) + E_g(t, z) \quad (10.25)$$

The electric field at the return stroke front can be obtained by replacing  $z$  by  $Z_0$  and by replacing  $t$  by  $\int_0^{Z_0} \{1/v(z)\} dz$ .

In the components of both (10.19) and (10.25) the return stroke channel radius appears as a parameter. It is important to note that the value of the return stroke radius does not affect significantly the electric field at the return stroke front. The reason for this is the following: The electric field at the front is determined by the charge on the section of the channel located below the return front. In the case of channel elements located at distances larger than the radius of the channel

(which is only a few centimetres) from the return stroke front the charge on the channel elements can be assumed to be concentrated at the centre of the return stroke channel. Thus, irrespective of whether the value of  $R$  is 0.001 m or 0.1 m, the field at the front would be more or less the same.

Once the electric field at the front of the return stroke is obtained the return stroke speed can be obtained by using the condition that this field is equal to the electric field  $E_{arc}$  in the leader channel. That is

$$E_{front}(Z_0) = E_{arc} \quad (10.26)$$

All the parameters in this equation are specified through (10.15–10.19) or (10.20–10.25). The only unknown parameter in this equation is  $v(z)$ , the speed of the return stroke at height  $z$ . This can be determined by numerically solving this equation. The numerical procedure adopted in this calculation is the following: Let us refer to the diagram displayed in Figure 10.6. This shows an intermediate step in the calculation in which the speed of the return stroke over the section labelled  $L$  is known, and we would like to know the speed of the return stroke over the section labelled  $l$ . One can make the section  $l$  as small as possible so that one can assume that the return stroke speed is constant along this section of the channel. An iterative method can be used to find the value of the speed that satisfies (10.26). Once this has been obtained, the channel is extended again, and the same procedure is applied to obtain the speed over the new channel section.

According to the results obtained through this procedure, the main conclusion that one can make is that the return stroke speed is determined primarily by three parameters: The risetime of the return stroke current, its peak value and the potential gradient of the leader channel. The return stroke speed decreases with increasing risetime and with decreasing peak of the current. Moreover, the return stroke speed increases as the potential gradient of the channel decreases. Since the potential gradient of the channel decreases with increasing conductivity the model predicts higher speed in highly conducting channels. One disadvantage of this

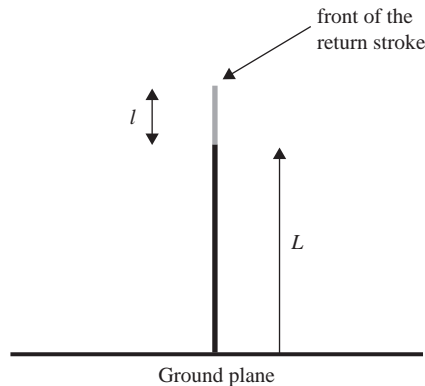


*Figure 10.6 Intermediate stage in the calculation of the return stroke velocity. The return stroke velocity over the section labelled 'L' is known and the task is to obtain the return stroke velocity over the section 'l'. The length of the section 'l' is selected in such a way that the return stroke speed over that section can be considered constant*

model is that it is of empirical in nature and it does not appeal to the physics of the breakdown process at the tip of the channel. Irrespective of these shortcomings the theory can be used to make some qualitative conclusions concerning the return stroke speed. Let us assume that the return stroke current is a ramp function and it propagates along the return stroke channel with constant speed  $v$ . Consider a situation where the location of the return stroke front is several tens of meters above the ground so that the contribution to the electric field at the return stroke front by the image current is negligible. The main contribution to the electric field at the front of the return stroke is coming from the static field (10.21) and one can show that electric field at the return stroke front  $E_f$  is given approximately given by

$$E_f = \frac{1}{4\pi\epsilon_0} \left( \frac{1}{v^2} - \frac{1}{c^2} \right) G \ln \left[ \frac{Z_0}{R} \right] \quad (10.27)$$

In the above equation  $G$  is the gradient of the ramp (i.e. A/s) and  $R$  is the radius of the return stroke channel. In deriving this equation it was assumed that a major portion of the contribution to the electric field at the return stroke front is coming from the section of the channel between  $z=0$  and  $z=Z_0 - R$ . In the case of real lightning currents the equivalent gradient can be obtained from the ratio  $I_p/t_r$ , where  $I_p$  is the peak current and  $t_r$  is the risetime of the current. Thus, the above equation can be written as

$$v = \frac{1}{\sqrt{\frac{4\pi\epsilon_0 E_f}{\left\{ \frac{I_p}{t_r} \right\} \ln \left[ \frac{Z_0}{R} \right]} + \frac{1}{c^2}}} \quad (10.28)$$

This equation shows that the speed of propagation of the current pulse is determined by the ratio  $I_p/t_r$ . Only if the risetime of the current is kept constant while changing the return stroke peak current one would find the return stroke speed to increase with return stroke current. Since the average derivative of the current depends only very weakly on return stroke peak current (see the next section) any dependence on return stroke speed on return stroke peak current has to be weak. Any experimental scatter in the data can thus make the relationship between the peak current and the return stroke speed random.

Cooray [18] applied a similar procedure to calculate the speed of dart leaders as a function of the dart leader current peak, dart leader current risetime and the temperature of the defunct return stroke channel. In that calculation the assumption is made that the electric field at the tip of the dart leader is equal to the breakdown electric field of the low density defunct return stroke channel.

### 10.3.4 Cooray – second model

Observe that the theories of Lundholm and Wagner even though they attempt to take into account the physics of the breakdown process at the return stroke front assume that the current at the return stroke front rises to its peak value instantaneously. In other words, these theories do not allow for a return stroke current that rises from zero to its peak value over a finite time at the front of the return stroke. For this reason any connection between the return stroke speed and the return stroke current risetime is lost in the theory. This could be the reason why these theories cannot account for the apparent absence of a relationship between the return stroke peak

current and the return stroke speed. On the other hand, the theory of Cooray [7] can take into account the finite risetime of the return stroke current but it tacitly avoids incorporating the electrical breakdown process at the return stroke front.

In order to remove this disadvantage of the above theories, Cooray [8] developed a theory in which the slow development of the current at the return stroke front can be taken into account in evaluating the return stroke speed. The basic foundation of the theory is the following. As shown in the previous section, if the spatial and temporal variation of the return stroke current and the channel radius are given as inputs one can calculate the temporal variation of the electric field at any point along the axis of the return stroke. For example, the electric field calculated at a point located at 100 m in a subsequent return stroke for three current waveforms is shown in Figure 10.7. The corresponding current waveforms are shown in Figure 10.8. Note that as the return stroke front approaches the point of observation the electric field rises rapidly and reaches a peak a fraction of a microsecond after the passage of the return stroke front. After that the electric field continues to decrease with time. This electric field depends both on the risetime of the current and the return stroke speed. Note that the peak electric field decreases as speed of the return stroke and the current risetime increase. Since the current flowing at that point is given as an input one can calculate the energy released per unit length during the return stroke at any given point on the channel. The energy calculated thus depends on the return stroke speed and the rise time of the return stroke current. For example, Figure 10.9 shows the energy released over the first 70  $\mu\text{s}$  of the return stroke for three current waveforms. In the calculation the return stroke speed is kept constant at  $1.5 \times 10^8$  m/s. One can use this technique for example to calculate the total energy released in any given section of the channel below the return stroke front.

Now, it is reasonable to think that the return stroke speed is controlled by the electric field at the front of the return stroke. This field is controlled by the charge distribution below the return stroke front. However, calculations show that a significant contribution to this field is coming only from the first 100 m or so of the channel section below the return stroke front. In other words, the return stroke speed is controlled by the physical processes taking place in the first 100 m of the channel below the front. So far all the results and conclusions are purely based on the Maxwell's equations. Let us summarise the results by the following equation: Let  $U$  represents the energy released in the first 100 m of the channel below the return stroke front. Since this is the section of the channel which controls the return stroke speed the physical processes taking place here with the aid of released energy  $U$  should provide the correct conditions for the return stroke front to propagate at a specified speed. Since this energy is a function of peak current, current rise time and return stroke speed let us write it as

$$U = f(I_p, t_r, v) \quad (10.29)$$

In the above equation  $I_p$  is the return stroke peak current,  $t_r$  is the current rise time and  $v$  is the return stroke speed. The next step is to combine the above equation with the fluid dynamics and thermodynamics of the electric discharges.

In order to make the analysis simple, we assume that the first return stroke current can be represented by a ramp function that rises to a peak value of  $I_p$  in a time  $t_r$ . After reaching the peak the current remains constant with time. Of course, this is a crude approximation but it is a better approximation than a step function.



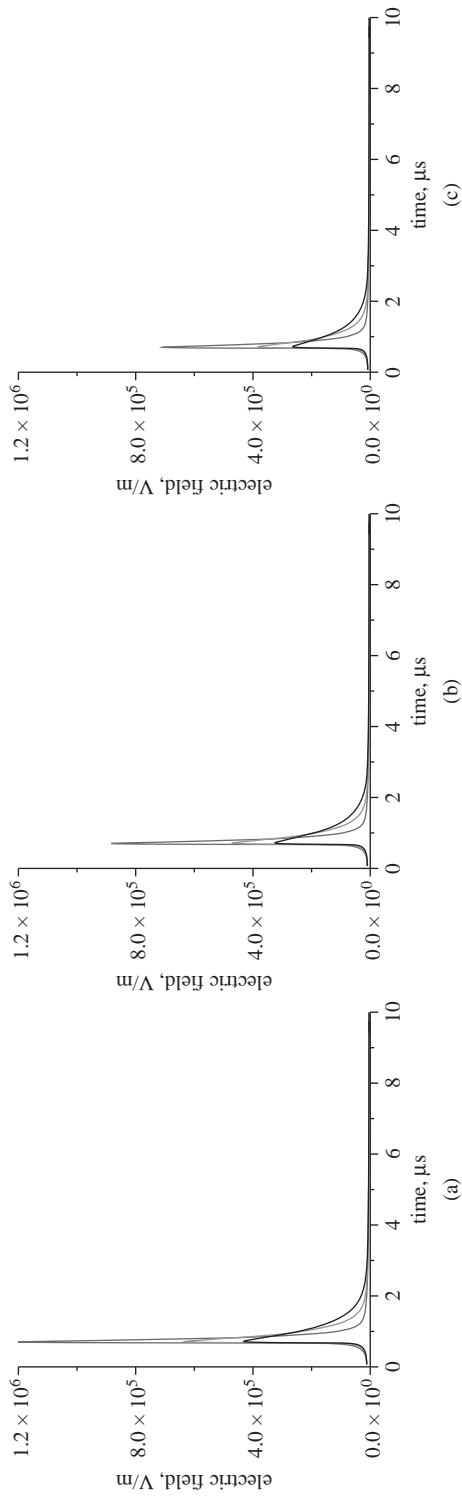


**Figure 10.7** Electric field at a point located 100 m above ground as a function of time; in each figure, the current risetimes used were  $0.5 \mu\text{s}$  (curve corresponding to the highest peak),  $1.0 \mu\text{s}$  (curve corresponding to the intermediate peak) and  $1.5 \mu\text{s}$  (the curve corresponding to the lowest peak). (a) Electric fields corresponding to  $v = 1.0 \times 10^8$  m/s; (b) electric fields corresponding to  $v = 1.5 \times 10^8$  m/s; and (c) electric fields corresponding to  $v = 2.0 \times 10^8$  m/s. In the calculations, the peak current at 100 m was kept constant at 12 kA

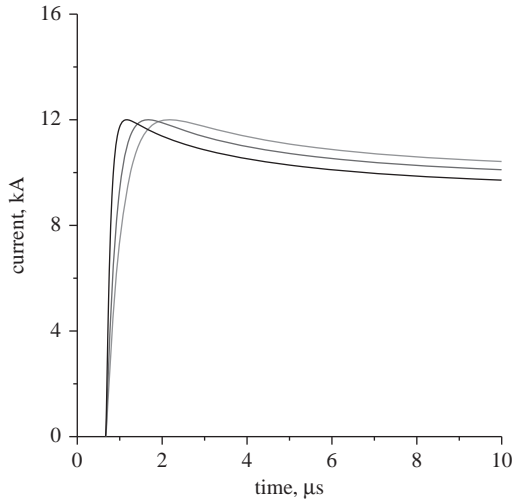


Figure 10.8 The model-predicted current at 100 m for discharge time constants of  $1.03 \times 10^{-7}$  s (curve with the shortest risetime),  $2.47 \times 10^{-7}$  s (curve with the intermediate risetime), and  $3.9 \times 10^{-7}$  s (curve with the longest risetime). The risetimes of the corresponding currents are 0.5, 1.0 and 1.5  $\mu$ s, respectively. In the three calculations, the speed of the return stroke was fixed at  $1.5 \times 10^8$  m/s

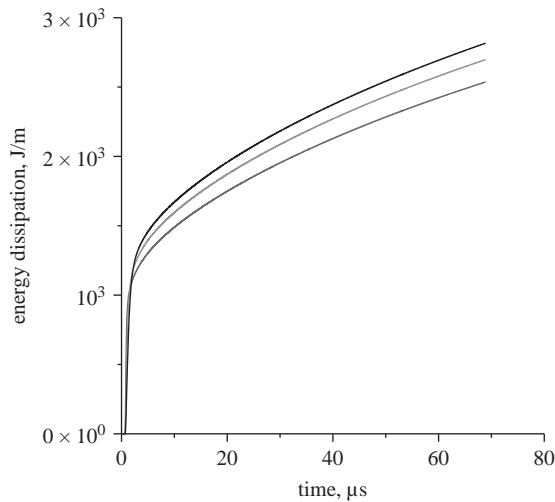


Figure 10.9 The energy dissipated over the first 70  $\mu$ s at a point located 100 m above ground as a function of time for three different current risetimes: (i) 0.5  $\mu$ s (corresponds to the lowest energy); (ii) 1.0  $\mu$ s (corresponds to the intermediate energy); (iii) 1.5  $\mu$ s (corresponds to the highest energy). In each case,  $I_p = 12$  kA,  $v = 1.5 \times 10^8$  m/s

With this approximation the current along the channel can be represented by a ramp function. The gradient of the ramp varies with return stroke peak current and rise time (i.e. the gradient is given by  $I_p/t_r$ ). Now, the energy that will be dissipated in the creation of a discharge channel of unit length that supports a ramp current can be calculated using the theory developed by Braginski [19]. According to the theory, the radius of a spark channel transporting a ramp current is given by

$$r(t) = 0.93 \times 10^{-3} \rho_0^{-1/6} i^{1/3} t^{1/2} \quad (10.30)$$

In the above equation  $r(t)$  is the radius of the channel at time  $t$  in meters,  $t$  is the time in microseconds and  $i$  is the current in the channel at that instant in kA, and  $\rho_0$  is the density of air at atmospheric pressure ( $1.29 \times 10^{-3} \text{ g/cm}^3$ ). Since Braginski [19] assumed that the conductivity of the high-temperature channel remains more or less constant around  $10^4 \text{ S/m}$ , one can calculate the channel resistance and hence the energy dissipation in the channel as a function of time. In the study conducted by Cooray [9], the energy released over the 100 m of channel below the front (through which a ramp current is propagating) is obtained. Let us denote this calculated energy by  $U_B$ . Since it is also a function of peak current, current rise time and return stroke speed let us write it as

$$U_B = f_B(I_p, t_r, v) \quad (10.31)$$

Note that the above parameter depends only indirectly on the return stroke speed because the integration time to calculate the energy dissipation over the first 100 m of the channel below the return stroke front depends on the speed of propagation of the return stroke front. Cooray [9] equated  $f(I_p, t_r, v)$  to  $f_B(I_p, t_r, v)$  and that gave rise to an expression for the return stroke speed as a function of its peak current. The results obtained thus show that the front speed is related to the height of the front, return stroke peak current, and return stroke rise time. Figure 10.10 shows how the return stroke speed varies as a function of the height of the return stroke front, peak current and the current rise time. First, observe that the return stroke speed increases as the return stroke front surges upwards through the channel. The speed at a given height increases with increasing return stroke current and with decreasing return stroke rise time. Of course, recall that the return stroke current rise time may also vary along the channel and this will also add another variable to the return stroke speed. These results still show that the return stroke speed is a strong function of the return stroke current. But, how can one explain the apparent lack of relationship between these two parameters? According to Cooray, the reason for this is that the previous models did not take into account the variation of return stroke current rise time with return stroke current peak. By measuring the rise time of first return stroke currents recorded by Berger on San Salvatore [20], Cooray [8] showed that the return stroke peak current and return stroke current rise time are correlated to each other and that the return stroke current rise time increases with increasing peak current. The relationship obtained by Cooray [8] is shown in Figure 10.11. When this variation was included in the model the return stroke speed remains more or less the same with increasing current. The results are shown in Figure 10.12. Thus the theory managed to explain the experimentally observed lack of correlation between the return stroke speed and return stroke peak current.

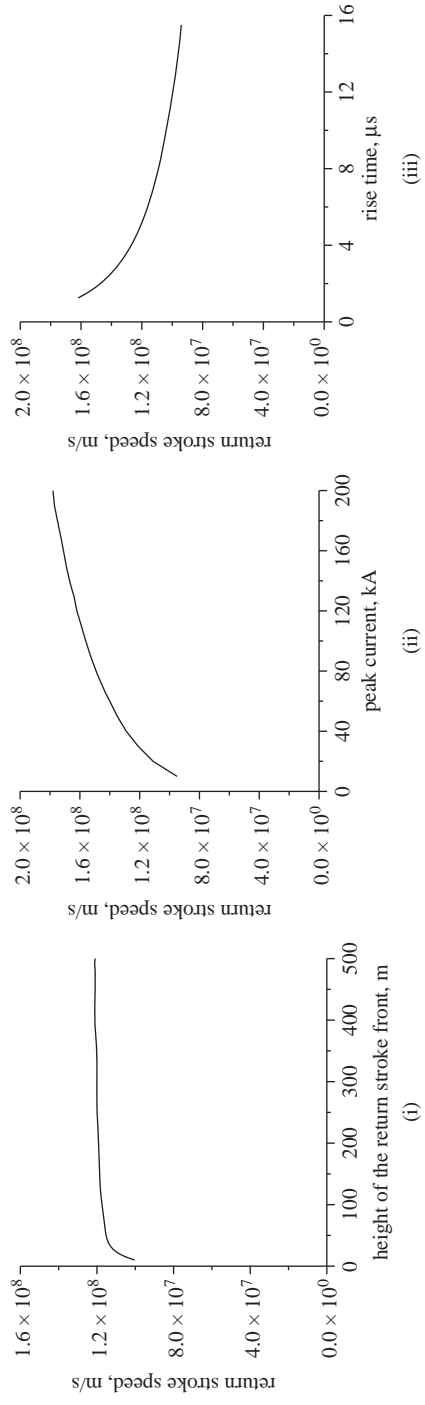


Figure 10.10 Variation of return stroke speed as a function of (i) height of the return stroke front, (ii) return stroke peak current and (iii) return stroke current risetime. In (i) risetime =  $0.5 \mu$ s and  $I_p = 30$  kA. In (ii) risetime =  $0.5 \mu$ s. In (iii)  $I_p = 30$  kA

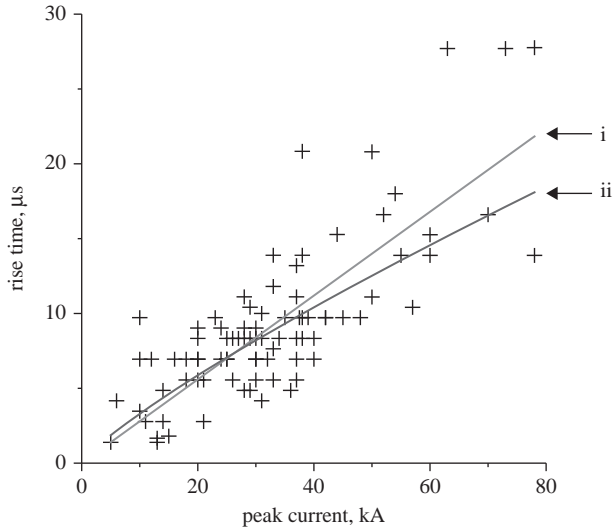


Figure 10.11 *The peak current and the corresponding risetime of the first return stroke waveforms measured by Berger [20]. The lines for the best fit obtained with a linear fit (line marked i) and a power (line marked ii) regression are depicted in the figure*

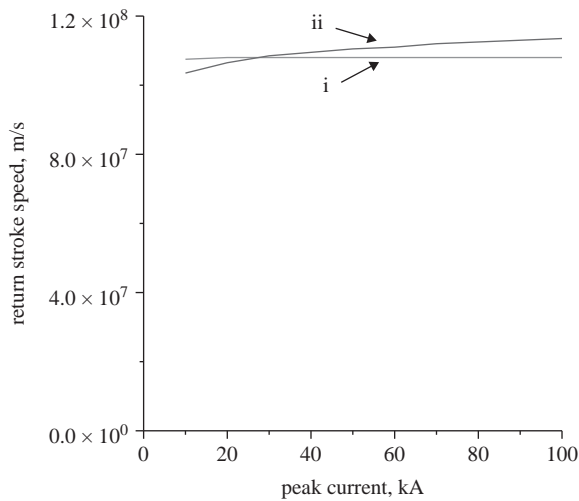


Figure 10.12 *The variation of first return stroke speed as a function of peak current if the return stroke current risetime is assumed to increase according to curve i in Figure 10.11- linear fit (line marked i) and according to curve ii in Figure 10.11- power fit (line marked ii). Since the data in Figure 10.11 are valid for first return strokes the results given in the figure are also valid for first return strokes*

## References

- [1] Idone, V. P. and R. Orville, Lightning return stroke velocities in the thunderstorm research program, *J. Geophys. Res.*, **87**, 4903–4916, 1982.
- [2] Mach, D. M. and W. D. Rust, Two-dimensional velocity, optical risetime, and peak current estimates for natural positive lightning return strokes, *J. Geophys. Res.*, **98**, 2635–2638, 1993
- [3] Rakov, V., Lightning return stroke speed, *J. Lightning Res.*, **1**, 2007, pp. 80–89
- [4] Lundholm, R., Induced overvoltage-surges on transmission lines and their bearing on the lightning performance at medium voltage networks, Ph.D. Dissertation, Royal Institute of Technology (KTH), Sweden, 1957
- [5] Wagner, C. F., Relationship between return stroke current and velocity of the return stroke, *AIEE Trans.*, **80**, 609–617, 1963
- [6] Rai, J., Current and velocity of the return lightning stroke, *J. Atmos. Terr. Phys.* **40**, 1275–1285, 1978
- [7] Cooray, V., Predicting the spatial and temporal variation of the current, the speed and electromagnetic fields of subsequent return strokes, *IEEE Trans. Electromagnetic Compatibility*, **40**, 427–435, 1998
- [8] Cooray, V., Power and energy dissipation in negative lightning return strokes, *Atmospheric Res.*, <http://dx.doi.org/10.1016/j.atmosres.2013.10.017>, 2013
- [9] Cooray, V., On the concepts used in return stroke models applied in engineering practice, *Trans. IEEE (EMC)*, **45**, 101–108, 2003
- [10] Cooray, V. and V. Rakov, A current generation type return stroke model that predicts the return stroke velocity, *J. Lightning Res.*, **1**, 32–39, 2007
- [11] Nucci, C. A. *et al.* Lightning return stroke current model with specified channel-base current: A review and comparison, *J. Geophys. Res.*, **95**, 20,395–20,408, 1990
- [12] Olsen, R.C., D. M. Jordan, V. A. Rakov, M. A. Uman, and N. Grimes, Observed one dimensional return stroke propagation speeds in the bottom 170 m of a rocket-triggered lightning channel, *Geophys. Res. Lett.*, **31**, L16107–L16104, 2004
- [13] Toepler, M., Zur kenntnis der gesetz der gleitfunkenbildung, *Ann. Phys. D*, 4 folge, bd. 21, 193–222, 1906
- [14] Bruce, C. E. R., and R. H. Golde, The lightning discharge, *J. Inst. Elect. Eng.*, **88**, 487–520, 1941
- [15] Albright, N. W., and D. A. Tidman, Ionizing potential waves and high voltage break down streamers, *Phys. Fluid*, **15**, 86, 1972
- [16] Cooray, V. and G. Cooray, The electromagnetic fields of an accelerating charge: Applications in lightning return-stroke models, *IEEE Trans. Electromagnetic Compatibility*, **52**(4), 944–955, 2010
- [17] Cooray, V., Electric field of the return stroke channel, *Proc. International Conf. Lightning Protection*, Vienna, Austria, 2012
- [18] Cooray, V., A model for dart leaders in lightning flashes, *J. Atmos. Elec.*, **16**, 145–159, 1996
- [19] Braginski, S. I., Theory of development of a spark channel, *Soviet Physics JEPT*, **34**(7), 1068–1074, 1958
- [20] K. Berger, Methods and results of lightning records at Monte San Salvatore from 1963–1971, *Bull. Schweiz. Elektrotech. ver.* **63**, 21403–21422, 1972



---

## Chapter 11

# On the various approximations to calculate lightning return stroke-generated electric and magnetic fields over finitely conducting ground

Vernon Cooray

---

### 11.1 Introduction

The knowledge concerning the characteristics of electromagnetic fields generated by lightning flashes is of importance in evaluating the interaction of these electromagnetic fields with electrical networks and in the remote sensing of lightning current parameters from the measured fields. However, electromagnetic fields generated by lightning flashes change their character as they propagate over the ground surface due to selective attenuation of the high frequency signals by finitely conducting ground (i.e. propagation effects). Thus, depending on the distance of propagation and the conductivity of ground, the peak and the rise time of the lightning-generated electromagnetic fields and their time derivatives measured at a given distance from the lightning channel may deviate more or less from the values that would be present over perfectly conducting ground.

Propagation effects on lightning return stroke-generated electromagnetic fields have been studied experimentally by Uman *et al.* [1] and Cooray *et al.* [2]. Theoretical evaluation of propagation effects on lightning flashes has been conducted by Cooray *et al.* [2], Gardner [3], Cooray and Lundquist [4], Le Vine *et al.* [5], Cooray [6], Ming and Cooray [7], Cooray and Ming [8], Cooray [9, 10], Cooray and Cummins [11, 12], Shoory *et al.* [13, 14] and Delfino *et al.* [15, 16].

Theoretical quantification of propagation effects on lightning return stroke-generated electromagnetic fields requires knowledge concerning the electromagnetic fields of electrical dipoles located over finitely conducting ground. Once the electromagnetic fields due to a dipole are known, the corresponding fields due to lightning return strokes can be calculated by representing the lightning channel as a series of infinitesimal dipoles.

The exact solution to the electromagnetic fields generated by electric dipoles located above a finitely conducting ground plane was obtained by Sommerfeld [17]. He presented his results in the form of a set of integrals. Since the numerical solutions of these integrals are time consuming, attempts have been made to find approximate solutions to these integrals [10, 18, 19]. In this chapter, various approximate solutions and procedures that have been used to calculate electromagnetic fields of return strokes over finitely conducting ground are presented together with their limits of validity.



## 11.2 Exact expressions for the electromagnetic fields of a dipole located over finitely conducting ground and their extension to return stroke fields

### 11.2.1 Exact expressions for the vector potential of a dipole over finitely conducting ground

The geometry under consideration is shown in Figure 11.1. The finitely conducting ground plane is represented by the surface  $\zeta=0$ , and the lightning channel is located at the origin of the coordinate system. The lightning channel is assumed to be straight, vertical and without any branches. Medium  $\zeta > 0$  is free space with dielectric constant  $\epsilon_0$  and magnetic permeability  $\mu_0$ . The region  $\zeta < 0$  consists of finitely conducting ground of conductivity  $\sigma$  and dielectric constant  $\epsilon = \epsilon_0 \epsilon_r$ , where  $\epsilon_r$  is the relative dielectric constant. The point of observation is located at a horizontal distance  $\rho$  from the lightning channel. Note that, for points of observations located above ground  $\zeta > 0$  and for points located below the ground  $\zeta < 0$ . Consider a vertical electrical dipole (a channel element) of length  $dz$  located at a height  $z$  from ground level, i.e. at the point  $(0, 0, z)$ . The vertical component of the magnetic vector potential at a point  $(\rho, 0, \zeta)$  (i.e. point  $W$  in Figure 11.1) located above ground due to the dipole is given by [20]

$$A_z = \frac{\mu_0 I(j\omega) dz}{4\pi} \left( \frac{\exp(-jk_0 R_0)}{R_0} - \frac{\exp(-jk_0 R_1)}{R_1} \right) + \frac{\mu_0 I(j\omega) dz}{4\pi} \left( 2k_1^2 \int_0^\infty \frac{J_0(\lambda\rho) \exp\left(- (z + \zeta) \sqrt{(\lambda^2 - k_0^2)}\right)}{k_1^2 \sqrt{(\lambda^2 - k_0^2)} + k_0^2 \sqrt{(\lambda^2 - k_1^2)}} \lambda d\lambda \right) \quad (11.1a)$$

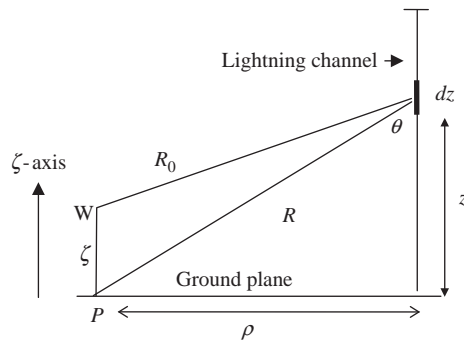


Figure 11.1 The geometry relevant to the problem under consideration. The dipole (or a channel element of the return stroke channel) is located at height  $z$  above ground. The region  $\zeta > 0$  is air and the region  $\zeta < 0$  is finitely conducting homogeneous ground of conductivity  $\sigma$  and relative dielectric constant  $\epsilon_r$ . Point  $P$  is located at the finitely conducting surface at a horizontal distance  $\rho$  from the dipole

The above expression can also be written as [20]

$$A_z = \frac{\mu_0 I(j\omega) dz}{4\pi} \left( \frac{\exp(-jk_0 R_0)}{R_0} + \frac{\exp(-jk_0 R_1)}{R_1} \right) - \frac{\mu_0 I(j\omega) dz}{4\pi} \left( 2k_0^2 \int_0^\infty \frac{J_0(\lambda\rho)(\lambda^2 - k_1^2) \exp\left(- (z + \zeta) \sqrt{(\lambda^2 - k_0^2)}\right)}{k_1^2 \sqrt{(\lambda^2 - k_0^2)} + k_0^2 \sqrt{(\lambda^2 - k_1^2)}} \frac{\lambda}{\sqrt{\lambda^2 - k_0^2}} d\lambda \right) \quad (11.1b)$$

The corresponding vertical component of the magnetic vector potential inside the ground is given by

$$A_{z1} = \left[ \frac{\mu_0 I(j\omega) dz}{4\pi} \int_0^\infty \frac{2k_1^2}{k_1^2 \sqrt{(\lambda^2 - k_0^2)} + k_0^2 \sqrt{(\lambda^2 - k_1^2)}} J_0(\lambda\rho) \exp\left(-z\sqrt{(\lambda^2 - k_0^2)} + \zeta\sqrt{(\lambda^2 - k_1^2)}\right) \lambda d\lambda \right] \quad (11.2)$$

$$k_0^2 = \omega^2 \mu_0 \epsilon_0 \quad (11.3)$$

$$k_1^2 = -j\omega\mu_0(\sigma + j\omega\epsilon_0\epsilon_r) \quad (11.4)$$

$$R_0 = \sqrt{\rho^2 + (\zeta - z)^2}, R_1 = \sqrt{\rho^2 + (\zeta + z)^2} \quad (11.5)$$

In the above equations,  $I(j\omega)$  is the current in the dipole in the frequency domain,  $\omega$  is the angular frequency,  $J_0$  represents the Bessel function of the first kind of order zero and  $j = \sqrt{-1}$ .

## 11.2.2 The exact expressions for the electromagnetic fields of a dipole over finitely conducting ground

### 11.2.2.1 Vertical electric field in air and underground

The vertical component of the electric field in the frequency domain in air due to the dipole can be obtained from the magnetic vector potential by

$$de_z(j\omega) = \frac{-j\omega}{k_0^2} \left( \frac{\partial^2 A_z}{\partial \zeta^2} + k_0^2 A_z \right) \quad (11.6)$$

Performing this operation on (11.1a), one obtains the vertical electric field in the frequency domain at point  $P$  at ground level, i.e. at the point  $(\rho, 0, 0)$ , as

$$de_z(z, j\omega, \rho) = \frac{I(j\omega) dz}{4\pi j\omega\epsilon_0} \left( 2k_1^2 \int_0^\infty \frac{J_0(\lambda\rho) \exp\left(-z\sqrt{(\lambda^2 - k_0^2)}\right)}{k_1^2 \sqrt{(\lambda^2 - k_0^2)} + k_0^2 \sqrt{(\lambda^2 - k_1^2)}} \lambda^3 d\lambda \right) \quad (11.7)$$

The vertical electric field underground can be obtained from

$$de_{z,under}(z, j\omega, \rho) = \frac{-j\omega}{k_1^2} \left( \frac{\partial^2 A_{z1}}{\partial \xi^2} + k_1^2 A_{z1} \right) \quad (11.8)$$

After performing this operation one obtains the vertical electric field underground as

$$de_{z,under}(z, j\omega, \rho) = \left[ -\frac{\mu_0 I(j\omega) dz}{4\pi k_1^2} \int_0^\infty \frac{2k_1^2}{k_1^2 \sqrt{(\lambda^2 - k_0^2)} + k_0^2 \sqrt{(\lambda^2 - k_1^2)}} J_0(\lambda\rho) \exp\left(-z\sqrt{(\lambda^2 - k_0^2)} + \zeta\sqrt{(\lambda^2 - k_1^2)}\right) \lambda^3 d\lambda \right] \quad (11.9)$$

### 11.2.2.2 The azimuthal magnetic field in air and underground

The azimuthal component of the magnetic field in the frequency domain due to the dipole can be obtained from the magnetic vector potential by

$$db_\varphi(z, j\omega, \rho) = -\frac{\partial A_z}{\partial \rho} \quad (11.10)$$

Performing this operation on (11.1a), one obtains the azimuthal magnetic field in the frequency domain at point  $P$  at ground level, i.e. at the point  $(\rho, 0, 0)$ , as

$$db_\varphi(z, j\omega, \rho) = \frac{\mu_0 I(j\omega) dz}{4\pi} \left( 2k_1^2 \int_0^\infty \frac{J_1(\lambda\rho) \exp\left(-z\sqrt{(\lambda^2 - k_0^2)}\right)}{k_1^2 \sqrt{(\lambda^2 - k_0^2)} + k_0^2 \sqrt{(\lambda^2 - k_1^2)}} \lambda^2 d\lambda \right) \quad (11.11)$$

where  $J_1$  represents the Bessel function of the first kind of order one. The magnetic field underground can be obtained by performing the operation given in (11.10) on  $A_{z1}$ . The resulting field is given by

$$db_{\varphi,under}(z, j\omega, \rho) = \left[ \frac{\mu_0 I(j\omega) dz}{4\pi} \int_0^\infty \frac{2k_1^2}{k_1^2 \sqrt{(\lambda^2 - k_0^2)} + k_0^2 \sqrt{(\lambda^2 - k_1^2)}} J_1(\lambda\rho) \exp\left(-z\sqrt{(\lambda^2 - k_0^2)} + \zeta\sqrt{(\lambda^2 - k_1^2)}\right) \lambda^2 d\lambda \right] \quad (11.12)$$

### 11.2.2.3 Horizontal electric field in air and underground

The horizontal component of the electric field in air in the frequency domain due to the dipole can be obtained from the magnetic vector potential by

$$de_\rho(z, j\omega, \rho) = \frac{-j\omega}{k_0^2} \frac{\partial^2 A_z}{\partial \rho \partial \xi} \quad (11.13)$$

Performing this operation on (11.1b), one obtains the horizontal field in the frequency domain for  $\zeta > 0$  as

$$de_{\rho}(z, j\omega, \rho) = \left[ -\frac{\mu_0 I(j\omega) dz j\omega}{4\pi k_0^2} \frac{\partial^2}{\partial \rho \partial \zeta} \left\{ \frac{e^{-jk_0 R_0}}{R_0} + \frac{e^{-jk_0 R_1}}{R_1} \right\} \right. \\ \left. + \frac{\mu_0 I(j\omega) dz j\omega}{4\pi} \int_0^{\infty} \frac{2\sqrt{(\lambda^2 - k_1^2)}}{k_1^2 \sqrt{(\lambda^2 - k_0^2)} + k_0^2 \sqrt{(\lambda^2 - k_1^2)}} J_1(\lambda \rho) \right. \\ \left. \exp\left(-z\sqrt{(\lambda^2 - k_0^2)} - \zeta\sqrt{(\lambda^2 - k_0^2)}\right) \lambda^2 d\lambda \right] \quad (11.14)$$

When the point of observation is at ground level (i.e.  $\zeta = 0$ ), this equation reduces to

$$de_{\rho}(z, j\omega, \rho) = \left[ \frac{\mu_0 I(j\omega) dz j\omega}{4\pi} \int_0^{\infty} \frac{2\sqrt{(\lambda^2 - k_1^2)}}{k_1^2 \sqrt{(\lambda^2 - k_0^2)} + k_0^2 \sqrt{(\lambda^2 - k_1^2)}} J_1(\lambda \rho) \right. \\ \left. \exp\left(-z\sqrt{(\lambda^2 - k_0^2)}\right) \lambda^2 d\lambda \right] \quad (11.15)$$

The horizontal electric field at a given depth below the ground surface (i.e.  $\zeta < 0$ ) can be obtained from the magnetic vector potential from

$$de_{\rho, \text{under}}(z, j\omega, \rho) = \frac{-j\omega}{k_1^2} \frac{\partial^2 A_{z1}}{\partial \rho \partial \zeta} \quad (11.16)$$

Performing this operation one finds

$$de_{\rho, \text{under}}(z, j\omega, \rho) = \left[ \frac{\mu_0 I(j\omega) dz j\omega}{4\pi} \int_0^{\infty} \frac{2\sqrt{(\lambda^2 - k_1^2)}}{k_1^2 \sqrt{(\lambda^2 - k_0^2)} + k_0^2 \sqrt{(\lambda^2 - k_1^2)}} J_1(\lambda \rho) \right. \\ \left. \exp\left(-z\sqrt{(\lambda^2 - k_0^2)} + \zeta\sqrt{(\lambda^2 - k_1^2)}\right) \lambda^2 d\lambda \right] \quad (11.17)$$

where, as indicated earlier,  $J_1$  represents the Bessel function of the first kind of order one.

### 11.2.3 Electromagnetic fields of return strokes

The electromagnetic fields in time domain generated by a dipole over finitely conducting ground can be obtained by inverse Fourier transformation of the frequency domain results presented in the earlier sections, and the corresponding electromagnetic fields due to the lightning flash can be obtained by dividing the lightning channel into a series of infinitesimal dipoles and integrating the dipole fields from

$z=0$  to  $z=H$ , where  $H$  is the height of the return stroke. For example, the time domain vertical electric field at the surface of the ground,  $E_z(t, \rho)$  is given by

$$E_z(t, \rho) = \int_0^H dE_z(z, t, \rho) \quad (11.18)$$

where  $dE_z(z, t, \rho)$  is the inverse Fourier transformation of  $de_z(z, j\omega, \rho)$ .

### 11.3 Return stroke models utilised in testing the approximate expressions

In order to calculate the electric fields from return strokes, an expression for  $I(z, t)$  – the spatial and temporal variation of the return stroke current – is required. Since no direct experimental data are available today to quantify the way in which the return stroke current signature varies as a function of height, it is necessary to rely on return stroke models to obtain an expression for  $I(z, t)$ . There are a number of return stroke models that predict the spatial and temporal variation of the return stroke current ([21]; see also Chapter 9 of this book). Any one of these models could be utilised for the purpose at hand. However, the published studies whose results are presented in this chapter had utilised the Modified Transmission Line Model (MTLE) for this purpose. According to the MTLE model, the temporal and spatial variation of the return stroke current is given by [22]

$$I(z, t) = P(z)I_b(0, t - z/v) \quad (11.19)$$

with

$$P(z) = \exp(-z/\lambda_e) \quad (11.20)$$

In this equation  $\lambda_e$  is the current decay height constant,  $P(z)$  is the current attenuation factor,  $v$  is the return stroke speed assumed to be uniform and  $I_b(0, t)$  is the current at the base of the channel. The two analytical expressions for the channel base current that have been used frequently in the literature and especially in the literature related to propagation effects are the following: The first expression that represents the channel base current of a subsequent stroke is given by [23]

$$I_b(t, 0) = \frac{I_1}{\eta} \left( \frac{t}{\tau_1} \right)^2 \frac{e^{-t/\tau_2}}{1 + \left( \frac{t}{\tau_1} \right)^2} + I_2 \{ \exp(-t/\tau_3) - \exp(-t/\tau_4) \} \quad (11.21)$$

where  $I_1 = 10.8$  kA,  $I_2 = 8.2$  kA,  $\eta = 0.845$ ,  $\tau_1 = 7.2 \times 10^{-8}$  s,  $\tau_2 = 5.0 \times 10^{-6}$  s,  $\tau_3 = 100.0 \times 10^{-6}$  s and  $\tau_4 = 6.0 \times 10^{-6}$  s. This current exhibits a peak value of 12 kA and a maximum time derivative of 115 kA/ $\mu$ s. Expression (11.21) is constructed by adding a Heidler function [24] to a double exponential function.

The other expression, which consists of the sum of two Heidler functions, used to describe both the first and subsequent return strokes is given by [16]

$$I_b(0, t) = \frac{I_1}{\eta_1} \left( \frac{t}{\tau_{11}} \right)^{n_1} \frac{e^{-t/\tau_{12}}}{1 + \left( \frac{t}{\tau_{11}} \right)^{n_1}} + \frac{I_2}{\eta_2} \left( \frac{t}{\tau_{21}} \right)^{n_2} \frac{e^{-t/\tau_{22}}}{1 + \left( \frac{t}{\tau_{21}} \right)^{n_2}} \quad (11.22)$$

$$\eta_m = \exp \left\{ -(\tau_{m1}/\tau_{m2})(n_m \tau_{m2}/\tau_{m1})^{1/n_m} \right\} \quad (11.23)$$

Table 11.1 Parameters of the first (FS) and subsequent (SS) return stroke currents

	$I_1$ (kA)	$\tau_{11}$ ( $\mu$ s)	$\tau_{12}$ ( $\mu$ s)	$n_1$	$I_2$ (kA)	$\tau_{21}$ ( $\mu$ s)	$\tau_{22}$ ( $\mu$ s)	$n_2$
FS	28	1.8	95	2				
SS	10.7	0.25	2.5	2	6.5	2	280	2

The parameters used to represent the first and subsequent stroke currents are given in Table 11.1.

#### 11.4 Summary of exact propagation effects in the vicinity of the channel

Many of the approximate expressions that account for the effects of finitely conducting ground (to be described later) fail when the distance to the point of observation is close to the channel. Thus it is important to describe the extent of propagation effects close to the channel so that the reader can himself or herself decide whether the propagation effects could be neglected or whether it is necessary to use full expressions given earlier to calculate the electromagnetic fields.

Let us first consider the return stroke vertical electric fields at ground level evaluated by the numerical integration of the Sommerfeld's integrals. Several such examples corresponding to distances between 10 m and 1 km from the lightning channel for ground conductivities of 0.01 and 0.001 S/m are presented by Cooray [9, 10]. In the calculation the effective dielectric constant was kept at 5. The calculated electric fields and electric field derivatives at several distances from the lightning channel are shown in Figures 11.2 and 11.3, respectively. In each diagram the vertical electric field that would be present at the same distance over perfectly conducting ground is also shown by a dotted line for comparison purposes.

The results presented in Figure 11.2 show that as far as the vertical electric field is concerned the propagation effects will not cause any significant changes, except for a slight change in the slope of the rising part, for distances within about 1000 m from the lightning channel and for conductivities greater than about 0.001 S/m. Similar conclusions concerning the non-significant propagation effects on the electric field in the vicinity of the channel have also been arrived at previously by Baba and Rakov [25] and Mimouni *et al.* [26]. In the study conducted by Mimouni *et al.* [26], the electromagnetic field was calculated at a height of 10 m. It is important to mention here that the propagation effects on the field at higher elevations are slightly less than those on the ones at ground level. The possibility to neglect the propagation effects on the magnetic field in the vicinity of the lightning channel can also be inferred from the research work of Caligaris *et al.* [27] and Rubinstein [28]. On the other hand, the calculations of Cooray [10] show that the derivative of the electric field is much more sensitive to the propagation effects and it could be significantly distorted by propagation effects even within about 1 km from the channel (see Figure 11.3). The peak amplitude of the time derivative of the vertical electric field will decrease by about 30%, 40% and 70% in propagating 100, 200 and 1000 m, respectively, over finitely conducting ground of 0.001 S/m of conductivity. The corresponding results for 0.01 S/m conductivity are 4%, 8% and 27%. The calculations of Cooray [10] show that very close to the channel, i.e. within about 20 m, the propagation effects lead to a

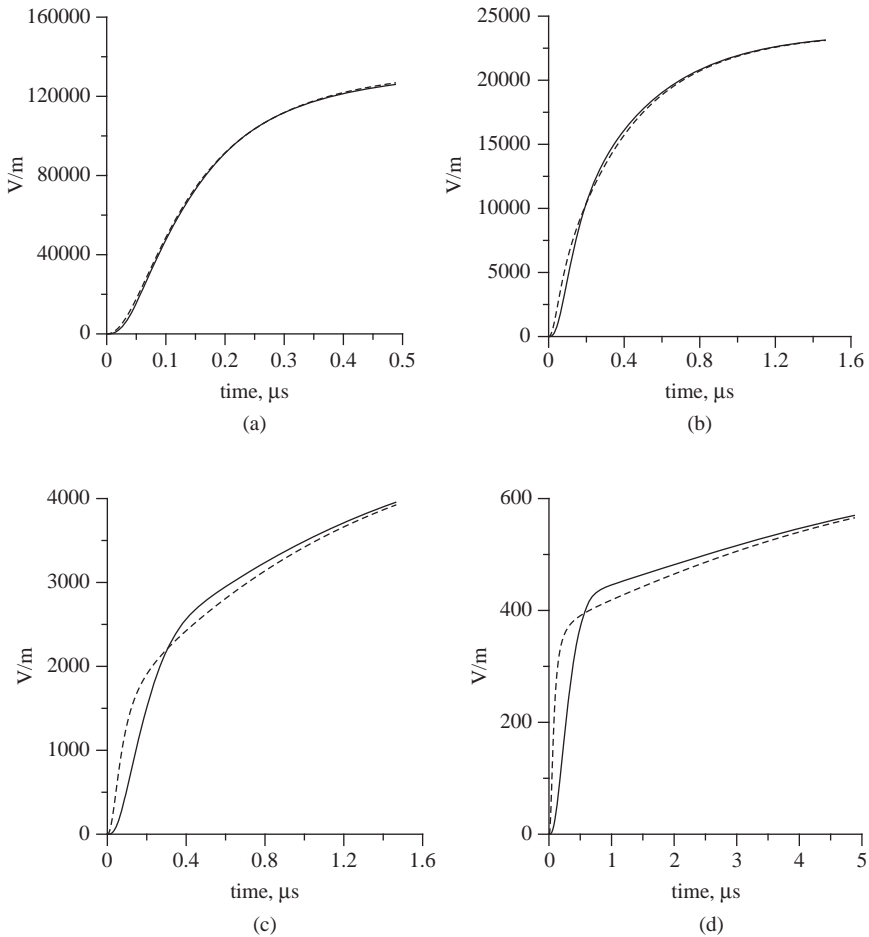


**Figure 11.2** Vertical electric field at ground level at (a) 10 m, (b) 50 m, (c) 200 m and (d) 1000 m from the lightning channel. The solid line shows the field over finitely conducting ground calculated using Sommerfeld's integrals and the dotted line shows the corresponding one over perfectly conducting ground. The conductivity of the ground is 0.001 S/m and the relative dielectric constant is 5. In the calculations, the return stroke is modelled by using the MTLE model with a current decay height constant  $\lambda_e$  equal to 2 km. The return stroke speed is kept at  $1.5 \times 10^8$  m/s. The current waveform at ground level is simulated by the analytical expression given by (11.21). Adapted from [10]

slight increase in the peak of the time derivative. The reason for this is that a significant fraction of the electric field time derivative very close to the lightning channel comes from the induction and static terms. The peak of the time derivative of the induction and static terms occurs at a time slightly longer than the time at which the peak of the time derivative of the radiation field takes place. The propagation effects will not only decrease the peak amplitude of the radiation field time derivative but it will also increase the time at which the peak occurs. This propagation delay will shift the peak of the radiation field time derivative closer to the peak of the time derivative of the static field component, making their sum to contribute more efficiently to the

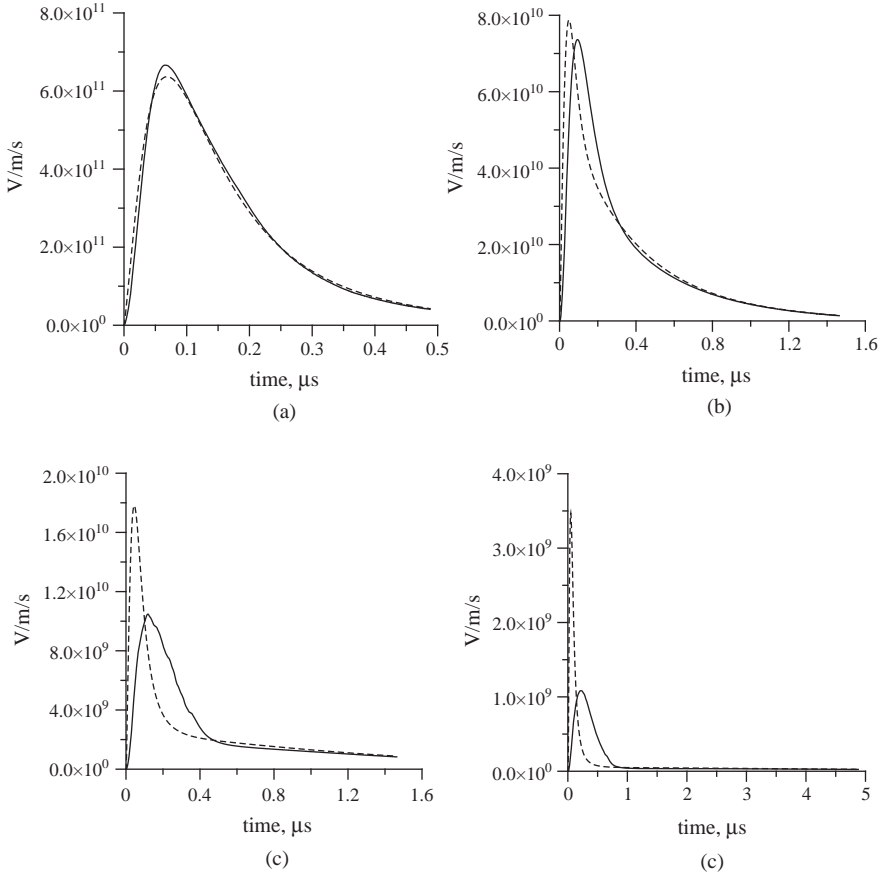


**Figure 11.3** Time derivative of the vertical electric field at ground level at (a) 10 m, (b) 50 m, (c) 200 m and (d) 1000 m from the lightning channel. The solid line shows the time derivative of the electric field over finitely conducting ground and the dotted line shows the corresponding one over perfectly conducting ground. The conductivity of the ground is 0.001 S/m and the relative dielectric constant is 5. In the calculations, the return stroke is modelled by using the MTL model with a current decay height constant  $\lambda_e$  equal to 2 km. The return stroke speed is kept at  $1.5 \times 10^8$  m/s. The current waveform at ground level is simulated by the analytical expression given by (11.21). Adapted from [10]

peak of the time derivative of the total electric field. This effect will compensate for the decrease in the total field component due to the attenuation of the radiation field. At distances larger than about 20 m the latter effect will take over, making the peak of the derivative of the electric field to decrease.

Now, let us consider the magnetic fields. The calculations by Cooray [9] show that, similar to the electric fields within about 1 km from the lightning channel, the propagation effects on the magnetic fields can be neglected as far as the rise time and the peak of these fields are concerned. For larger distances the approximate expressions to be described later can provide reasonable results. However, this is not the case for the magnetic field derivative. Similar to the electric field time derivative,



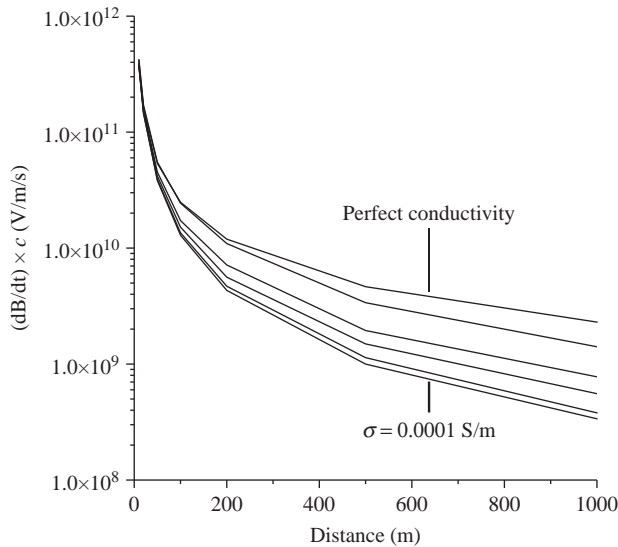


Figure 11.4 The peak amplitude of the magnetic field time derivative multiplied by the speed of light in free space as a function of distance for several conductivities. The results are shown for perfectly conducting ground,  $\sigma = 0.01 \text{ S/m}$ ,  $\sigma = 0.001 \text{ S/m}$ ,  $\sigma = 0.0005 \text{ S/m}$ ,  $\sigma = 0.0002 \text{ S/m}$  and  $\sigma = 0.0001 \text{ S/m}$ . Note that the peak amplitude at a given distance decreases as the conductivity decreases from infinity (perfect conductivity) to  $0.0001 \text{ S/m}$ . In the calculations, the return stroke is modelled by using the MTLE model with a current decay height constant  $\lambda_e$  equal to  $2 \text{ km}$ . The return stroke speed is kept at  $1.5 \times 10^8 \text{ m/s}$ . The current waveform at ground level is simulated by the analytical expression given by (11.21). Adapted from [9]

the magnetic field time derivative also attenuates significantly even within  $1 \text{ km}$  from the lightning channel. Figure 11.4 depicts how the peak magnetic field time derivative varies with distance over finitely conducting ground for conductivities in the range of  $0.01\text{--}0.0001 \text{ S/m}$ . Since the temporal behaviour of magnetic and electric field time derivatives are almost identical up to about a few tens of metres from the lightning channel, propagation effects on them are almost identical.

## 11.5 Simplified procedures to calculate electric and magnetic fields over finitely conducting ground

### 11.5.1 Norton's and Bannister's approximations

According to the analysis presented by Norton [18], the vertical electric field at ground level at point  $P$  due to a dipole located at height  $z$  is given by

$$\begin{aligned}
 de_z(z, j\omega, \rho) = & \frac{I(j\omega)dz}{2\pi \epsilon_0} \left( \frac{2 - 3\sin^2\theta}{j\omega R^3} + \frac{2 - 3\sin^2\theta}{cR^2} \right. \\
 & \left. + \Delta_0 \frac{\cos\theta}{cR^2} + j\omega \frac{\sin^2\theta}{c^2R} a(z, j\omega, \rho) \right) e^{-j\omega R/c}
 \end{aligned}
 \tag{11.24}$$

Bannister had presented expressions for the vertical electric field, horizontal electric field and the magnetic field in both air and underground. According to Bannister [19], the vertical electric field at ground level is given by

$$de_z(z, j\omega, \rho) = \frac{I(j\omega)dz}{2\pi \epsilon_0} \left( \frac{2 - 3\sin^2\theta}{j\omega R^3} + \frac{2 - 3\sin^2\theta}{cR^2} + j\omega \frac{\sin^2\theta}{c^2R} a(z, j\omega, \rho) \right) e^{-j\omega R/c} \quad (11.25)$$

In equations 11.24 and 11.25

$$a(z, j\omega, \rho) = \frac{1}{2} [(1 + R_v) + (1 - R_v) w_{1-1}(\rho)] \quad (11.26)$$

$$R = \sqrt{\rho^2 + z^2}, \cos \theta = z/R \quad (11.27)$$

$$R_v = \frac{\cos \theta - \Delta_1}{\cos \theta + \Delta_1} \quad (11.28)$$

$$\Delta_1 = \frac{k_0}{k_1} \left( 1 - \frac{k_0^2}{k_1^2} \sin^2\theta \right)^{1/2} \quad (11.29)$$

$$\eta = -\frac{j\omega R}{2 c \sin^2\theta} [\cos \theta + \Delta_1]^2 \quad (11.30)$$

$$w_{1-1}(\rho) = 1 - j(\pi\eta)^{1/2} e^{-\eta} \operatorname{erfc}(j\eta^{1/2}) \quad (11.31)$$

In these equations *erfc* stands for the complementary error function. The function  $a(z, \omega, \rho)$  is the attenuation function corresponding to a dipole at height  $z$  over homogeneous and finitely conducting ground of surface impedance  $\Delta_1$ . With  $\cos \theta = 0$  the function  $w_{1-1}(\rho)$  becomes the attenuation function corresponding to a dipole at ground level over homogeneous ground of surface impedance  $\Delta_1$ .

Note that the expression for the electric field at ground level derived by Norton [18] contains an additional term that is not present in Bannister's derivation. However, as shown by Cooray [10], this additional term will make only a very small contribution in the case of lightning electromagnetic fields, making the results obtained by Norton [18] almost identical to that obtained by Bannister [19].

### 11.5.1.1 Comparison of Norton's and Bannister's approximate expressions for the vertical electric field with exact calculations

Cooray [10] compared the results obtained from Norton's and Bannister's expressions for the vertical electric field with those obtained from Sommerfeld's integrals. Figure 11.5 depicts the exact vertical electric fields together with the electric fields obtained with Norton's and Bannister's approximations. Figure 11.6 shows the time derivative of the vertical electric fields. The solid line (black) in each diagram shows the exact vertical electric field. The short-dashed line shows the Bannister approximation and the long-dashed line shows the Norton approximation. First, note that the difference between Norton's and Banister's

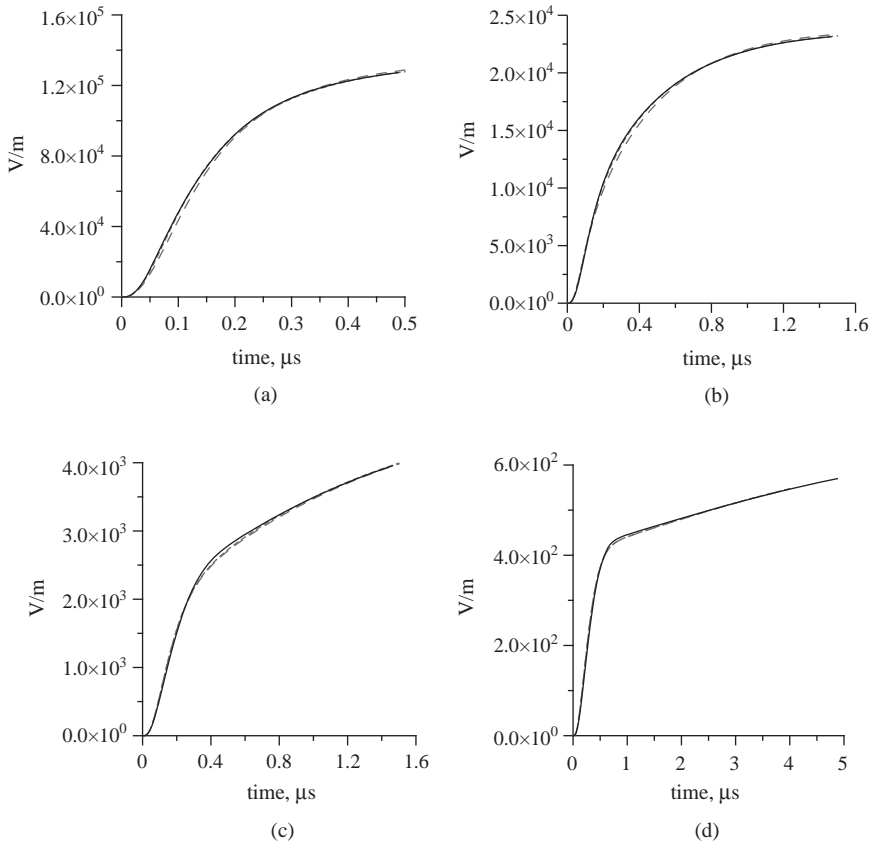


**Figure 11.5** Vertical electric field at ground level at (a) 10 m, (b) 50 m, (c) 200 m and (d) 1000 m from the lightning channel. The solid line shows the field obtained from Sommerfeld's equation, the short-dashed line the Bannister approximation and the long-dashed line the Norton approximation. The conductivity of the ground is 0.001 S/m and the relative dielectric constant is 5. In the calculations, the return stroke is modelled by using the MTLE model with a current decay height constant  $\lambda_e$  equal to 2 km. The return stroke speed is kept at  $1.5 \times 10^8$  m/s. The current waveform at ground level is simulated by the analytical expression given by (11.21). Adapted from [10]

approximations is very small, and for distances larger than about 200 m both Norton's and Bannister's approximations generate identical results. This shows that the third term inside the bracket of Norton's equation (11.24) does not contribute significantly to the electric field at ground level. The results also show that except for a difference of no more than a few per cent both Norton's and Bannister's approximations provide a good fit to the results based on the exact theory. The results are shown only for the conductivity of 0.001 S/m because the agreement is even better when the conductivity is 0.01 S/m. One can conclude, therefore, that in calculating propagation effects on the lightning-generated vertical electric field at ground level one can use either the Norton's or Bannister's equations without resorting to integration of the cumbersome Sommerfeld's equations.

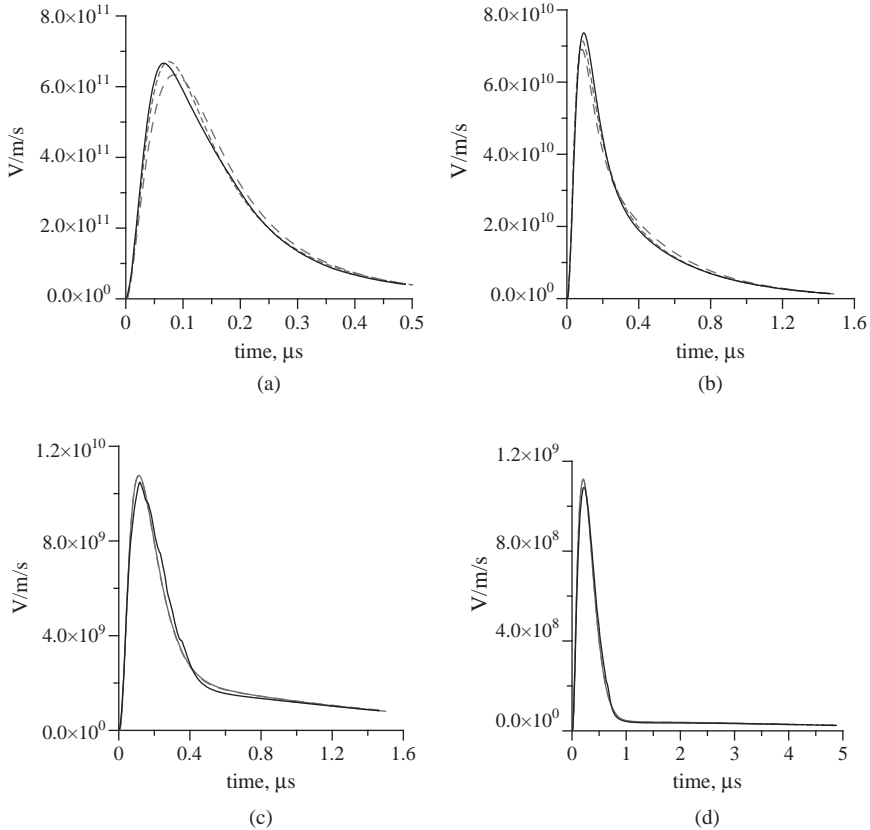


**Figure 11.6** The time derivative of the vertical electric field at ground level at (a) 10 m, (b) 50 m, (c) 200 m and (d) 1000 m from the lightning channel. The solid line shows the field obtained from Sommerfeld's equation, the short-dashed line the Bannister approximation and the long-dashed line the Norton approximation. The conductivity of the ground is 0.001 S/m and the relative dielectric constant is 5. In the calculations, the return stroke is modelled by using the MTLE model with a current decay height constant  $\lambda_c$  equal to 2 km. The return stroke speed is kept at  $1.5 \times 10^8$  m/s. The current waveform at ground level is simulated by the analytical expression given by (11.21). Adapted from [10]

In order to estimate the errors associated with the predictions of Norton's and Bannister's theories, the peak time derivatives of the magnetic field predicted by these theories were calculated by Cooray [9] and the errors associated with the predicted values were obtained by comparing them with the values obtained using Sommerfeld's integrals. The peak magnetic field derivative was used for this purpose because it is more sensitive to propagation effects than the peak magnetic field. The results obtained by Cooray [9] are tabulated in Table 11.2. Note that the mean error (estimated from seven data points corresponding to 10, 20, 50, 100, 200, 500 and 1000 m) associated with these formulations increases with decreasing conductivity and it can reach about 20% for conductivity of 0.0001 S/m. For

Table 11.2 *The mean error and the standard deviation, based on the peak magnetic field derivative, associated with the predictions of Bannister's and Norton's approximations (adapted from Cooray [9])*

$\sigma$ (S/m)	Mean error	Standard deviation
0.01	4.1	4.0
0.001	5.8	4.0
0.0005	8.5	4.1
0.0002	14.8	3.7
0.0001	17.4	8.6

conductivity less than about 0.001 the approximations generate results with errors less than about 5% and for all practical purposes these approximations can be used instead of the numerical solution of Sommerfeld's equations.

### 11.5.2 *Simplified expressions to calculate vertical electric field and horizontal magnetic field over finitely conducting ground*

Cooray and Lundquist [4] and Cooray [6] simplified the calculation of the vertical electric field and horizontal magnetic field from lightning return strokes over finitely conducting ground using two simplifying approximations. Let us consider these approximations one at a time.

#### 11.5.2.1 **Approximation 1**

According to Bannister's approximation, the total electric field due to a lightning flash over finitely conducting ground at a horizontal distance  $\rho$  is given by

$$e_z(j\omega, \rho) = \int_0^H \frac{I(j\omega) dz}{2\pi \epsilon_0} \left( \frac{2 - 3 \sin^2 \theta}{j\omega R^3} + \frac{2 - 3 \sin^2 \theta}{cR^2} + j\omega \frac{\sin^2 \theta}{c^2 R} a(z, j\omega, \rho) \right) e^{-j\omega R/c} dz \quad (11.32)$$

where  $R = \sqrt{z^2 + \rho^2}$ . The same result is obtained if one neglects the third term inside the bracket of Norton's equation (i.e. (11.24)). Note that this equation is nothing but the integration (or summing up) of the dipole fields generated by elementary dipoles into which the channel is divided, taking into account the proper time delays.

Cooray and Lundquist [4] and Cooray [6] simplified this equation by using the following arguments. As far as the propagation effects are concerned, the section of the waveform which is of interest is that occurring within the first few microseconds. If the speed of propagation of the return stroke front is about  $10^8$  m/s, the length of the channel that contributes to the radiation field during this time would not be larger than a few hundred metres. Thus, in (11.32), the attenuation function  $a(z, j\omega, \rho)$  can be replaced by  $a(0, j\omega, \rho)$  (i.e.  $w_{1-1}(\rho)$ ), which is the attenuation

function corresponding to a dipole located at ground level. With this approximation (11.32) can be transformed into time domain to find an expression for the vertical electric field over finitely conducting ground. The result is

$$E_{z,app1}(t, \rho) = E_{z,s}(t, \rho) + E_{z,i}(t, \rho) + \int_0^t E_{z,r}(t - \tau, \rho) W_{1-1}(\rho) d\tau \tag{11.33}$$

where  $w_{1-1}(\rho)$  is the inverse Fourier transformation of  $w_{1-1}(\rho)$ . In this equation  $E_{z,s}(t, \rho)$ ,  $E_{z,i}(t, \rho)$  and  $E_{z,r}(t, \rho)$  are the static, induction and radiation field components, respectively, of the electric fields generated by the return stroke over perfectly conducting ground. These field components are given by

$$E_{z,s}(t, \rho) = \int_0^H \frac{dz}{2\pi\epsilon_0} \left\{ \frac{2 - 3\sin^2\theta}{R^3} \int_0^t i(z, \tau - R/c) d\tau \right\} \tag{11.34}$$

$$E_{z,i}(t, \rho) = \int_0^H \frac{dz}{2\pi\epsilon_0} \frac{2 - 3\sin^2\theta}{cR^2} i(z, t - R/c) \tag{11.35}$$

$$E_{z,r}(t, \rho) = \int_0^H \frac{dz}{2\pi\epsilon_0} \frac{\sin^2\theta}{c^2R} \frac{\partial i(z, t - R/c)}{\partial t} \tag{11.36}$$

According to these equations only the radiation field term is disturbed by propagation effects while the static and induction terms remain intact. One has to remember that (11.33) is an approximation and it should not be used to justify the claim that electrostatic fields are not disturbed by propagation effects. However, as we will show in the next section, this equation provides a reasonable approximation to the exact fields obtained by Sommerfeld's equations, demonstrating that the propagation effects on the static fields are not very significant.

*Comparison between exact theory and the predictions of approximation 1*  
 Calculations presented by Cooray [10] show that the difference in the electric field and the time derivative of the electric field as predicted by the exact theory and (11.33) is no more than a few per cent in the distant range of 10 m to 1 km. For example, Figure 11.7 depicts the electric field derivative at several distances as predicted by exact theory (solid line) and approximation 1 (dashed line) for ground conductivity of 0.001 S/m. The agreement becomes even better with increasing distance and increasing conductivity. Thus, one can conclude that (11.33) provides an accurate description of the propagation effects on lightning-generated electromagnetic fields.

### 11.5.2.2 Approximation 2

In (11.33)  $W_{1-1}(\rho)$  is the inverse Fourier transformation of  $w_{1-1}(\rho)$ . Use of this equation to calculate the vertical electric field requires performing the inverse

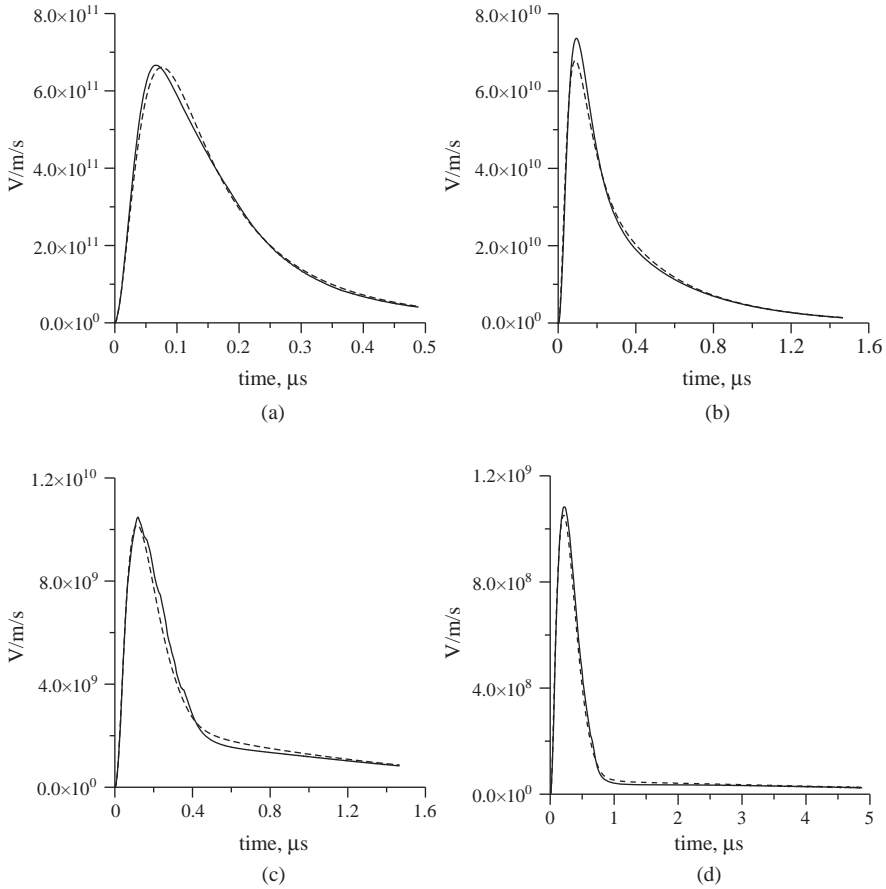


*Figure 11.7 The time derivative of the vertical electric field at ground level at (a) 10 m, (b) 50 m, (c) 200 m and (d) 1000 m from the lightning channel. The solid line shows the time derivative of the field obtained from Sommerfeld's equation and the dotted line shows the data obtained using approximation 1 outlined in section 11.5.2.1. The conductivity of the ground is 0.001 S/m and the relative dielectric constant is 5. In the calculations, the return stroke is modelled by using the MTL model with a current decay height constant  $\lambda_e$  equal to 2 km. The return stroke speed is kept at  $1.5 \times 10^8$  m/s. The current waveform at ground level is simulated by the analytical expression given by (11.21). Adapted from [10]*

Fourier transformation at every distance of interest. On the other hand, Wait [29] has derived an analytical approximation for  $W_{1-1}(\rho)$ , which can be used in (11.33) to reduce the computational time. The analytical approximation to  $W_{1-1}(\rho)$  derived by Wait [29] is given by

$$W_{1-1}(\rho)_{wait} = \frac{d}{dt} \left( 1 - \exp\left(-\frac{t^2}{4\xi^2}\right) + 2\beta(\epsilon_r + 1) \frac{Q(t/2\xi)}{t} \right) \quad (11.37)$$

with

$$Q(x) = x^2(1 - x^2)\exp(-x^2) \tag{11.38}$$

$$\beta = 1/\mu_0\sigma c^2 \tag{11.39}$$

$$\zeta^2 = \rho/2\mu_0\sigma c^3 \tag{11.40}$$

The third term inside the bracket of (11.37) is a term that takes into account approximately the displacement current in the ground. If one neglects this term the equation can be written as

$$W_{1-1}(\rho)_{wait} = \frac{d}{dt} \left( 1 - \exp\left(-\frac{t^2}{4\zeta^2}\right) \right) \tag{11.41}$$

Using this analytical expression instead of the Fourier transform of  $w_{1-1}(\rho)$  in (11.33) one obtains

$$E_{z,app2}(t, \rho) = E_{z,s}(t, \rho) + E_{z,i}(t, \rho) + \int_0^t E_{z,r}(t - \tau, \rho) W_{1-1}(\rho)_{wait} d\tau \tag{11.42}$$

Cooray and Lundquist [4] and Cooray [6] used the third term of (11.42) to calculate the propagation effects on return stroke radiation fields. Note that if the expression given in (11.41) is substituted for  $W_{1-1}(\rho)_{wait}$  then the predicted propagation effects depend only on the parameter  $\rho/\sigma$ .

*Comparison between exact theory and the predictions of approximation 2*  
 Cooray [10] had compared the predictions of (11.42) with the exact results obtained using Sommerfeld's equations. The results pertinent to the electric field derivative are presented here. First, let us consider (11.42) with the attenuation function as given by (11.37). The results obtained from this equation are depicted in Figure 11.8 (dashed line) together with the results corresponding to the Sommerfeld's equations (solid line). Note that the shape of the electric field derivative calculated using the approximation 2 differs from that obtained from Sommerfeld's equations. Analysis done by Cooray [10] showed that this difference is caused by the first order approximation for the displacement current (third term in (11.37)). Now, let us consider (11.42) with the attenuation function given by (11.41). The results of Cooray's calculations are shown in Figure 11.9. Note that the predicted electric field time derivatives are in better agreement with the Sommerfeld's results. Cooray [10] has also studied the effect of the displacement current term carefully and realised that slight change in the displacement current term can make the predictions of this simple theory agree rather well with the Sommerfeld's over the whole range of distances spanning from 10 to 1000 m and for ground conductivities equal to or less than 0.001 S/m. The agreement becomes even better with increasing distance. The slight modification to the attenuation function that Cooray [10] has come up with is given by the following formula:

$$W_{1-1}(\rho)_{wait-mod} = \frac{d}{dt} \left( 1 - \exp\left(-\frac{t^2}{4\zeta^2}\right) + \beta \sqrt{\frac{\sigma}{\sigma_0}} \frac{(\epsilon_r + 1)}{\epsilon_r} \frac{Q(t/2\zeta)}{t} \right) \tag{11.43}$$



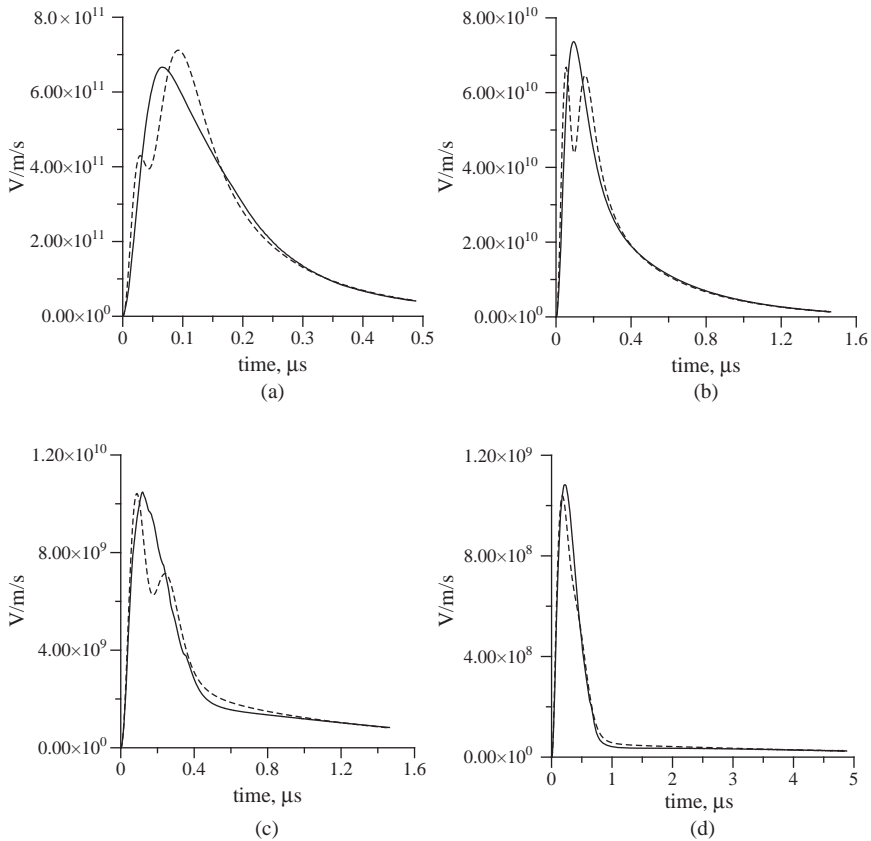


**Figure 11.8** *The time derivative of the vertical electric field at ground level at (a) 10 m, (b) 50 m, (c) 200 m and (d) 1000 m from the lightning channel. The solid line shows the time derivative of the field obtained from Sommerfeld's equation and the dotted line shows the results obtained using approximation 2 outlined in section 11.5.2.2, with attenuation function given by (11.37). The conductivity of the ground is 0.001 S/m and the relative dielectric constant is 5. In the calculations, the return stroke is modelled by using the MTLE model with a current decay height constant  $\lambda_e$  equal to 2 km. The return stroke speed is kept at  $1.5 \times 10^8$  m/s. The current waveform at ground level is simulated by the analytical expression given by (11.21). Adapted from [10]*

where  $\sigma_0 = 10^{-4}$  S/m. The results obtained by using attenuation function given by (11.43) in (11.42) are depicted in Figure 11.10 together with the Sommerfeld's results. Note that this equation provides a good fit to the Sommerfeld's results in the distance range of 10 m to 1 km. The agreement between the two theories becomes better with increasing distance. The conclusion to be reached from this study is that (11.42) together with the attenuation function given in (11.43) can be used to calculate propagation effects within 1 km from the lightning channel to an accuracy better than 10%. For larger distances the simple formula provides a better accuracy.

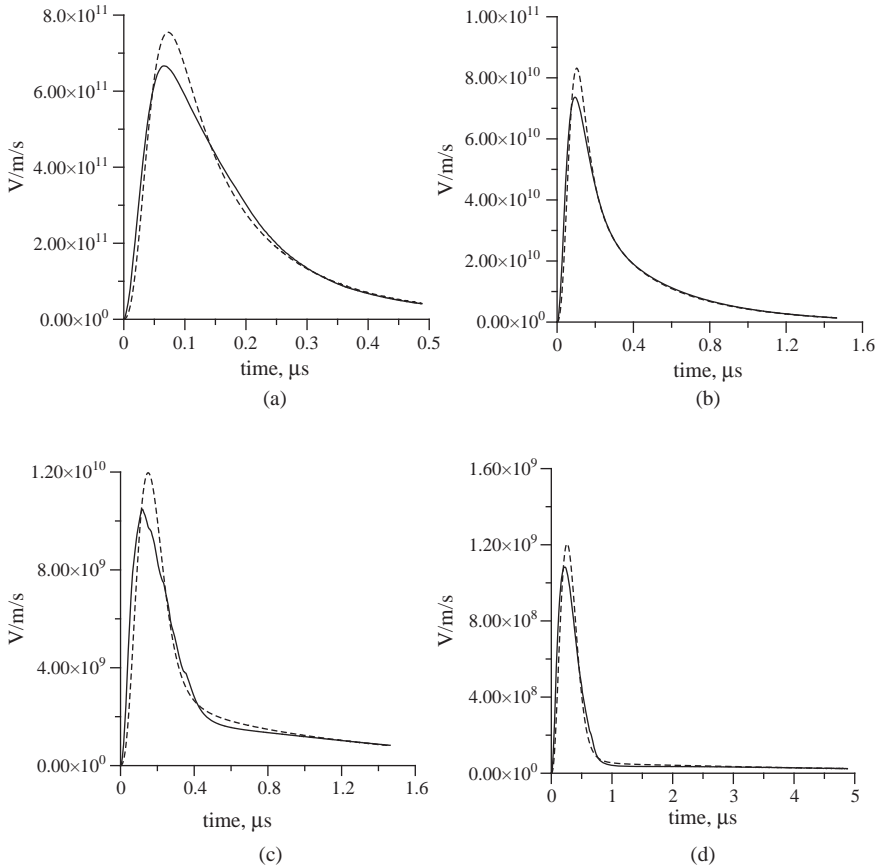
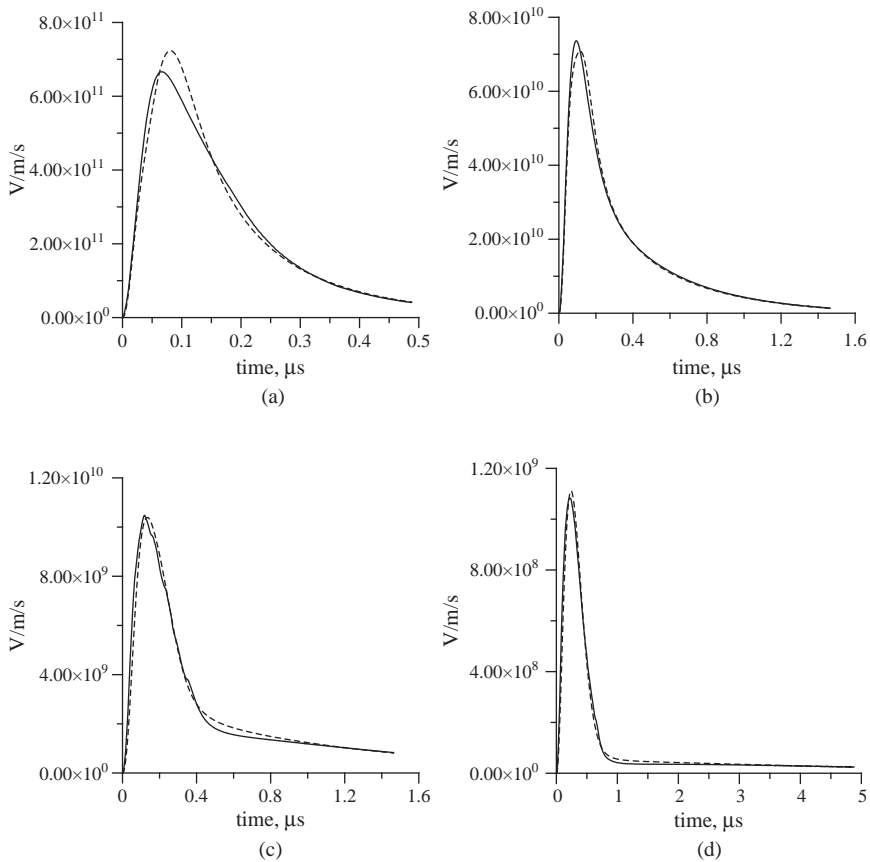


Figure 11.9 Same as that in Figure 11.8 except that the dotted line shows the results obtained using approximation 2 outlined in section 11.5.2.2, with attenuation function given by (11.41). The conductivity of the ground is  $0.001 \text{ S/m}$  and the relative dielectric constant is 5. In the calculations, the return stroke is modelled by using the MTLE model with a current decay height constant  $\lambda_e$  equal to 2 km. The return stroke speed is kept at  $1.5 \times 10^8 \text{ m/s}$ . The current waveform at ground level is simulated by the analytical expression given by (11.21). Adapted from [10]

Cooray [10] had presented calculations also to illustrate the effect of dielectric constant on the calculated results. The results showed that for values of dielectric constants lying within the range of 3–15, which is typical of many soils, the dielectric constant does not influence the propagation effects significantly.

### 11.5.3 Propagation effects on radiation fields of the first return strokes of negative and positive lightning flashes

For the reasons described in the next section, propagation effects may vary from one return stroke electromagnetic field to another. In order to quantify the propagation effects it is necessary to calculate them for a large number of return stroke electromagnetic fields and obtain the average values. This exercise requires



*Figure 11.10 Same as that in Figure 11.8 except that the dotted line shows the results obtained using approximation 2 outlined in section 11.5.2.2, with attenuation function given by (11.43). The conductivity of the ground is 0.001 S/m and the relative dielectric constant is 5. In the calculations, the return stroke is modelled by using the MTLE model with a current decay height constant  $\lambda_e$  equal to 2 km. The return stroke speed is kept at  $1.5 \times 10^8$  m/s. The current waveform at ground level is simulated by the analytical expression given by (11.21). Adapted from [10]*

electromagnetic radiation fields from a large number of lightning return strokes undistorted by propagation effects as an input.

There are several ways to avoid or reduce the propagation effects. For example, propagation effects can be reduced by measuring the electromagnetic fields from lightning flashes striking the sea, so that the path of propagation of the electromagnetic fields is over sea water [6, 30–33]. Even though sea water is a good conductor, with a conductivity of about 4 S/m, the roughness of the sea surface, caused by the presence of strong winds, may enhance the attenuation and scattering of high frequencies in the lightning-generated electromagnetic fields [7]. Furthermore, it is not an easy task to avoid the presence of a small strip of land between the high water mark of the ocean and the measuring station [6, 34, 35]. The presence of this strip of land in the path of propagation can enhance the propagation effects [8]. However,

these propagation effects are negligible when compared to those introduced by finitely conducting ground. Consequently, electromagnetic fields from lightning flashes measured such could be used as inputs in calculating propagation effects.

Cooray *et al.* [2] analysed the propagation effects on both negative and positive return strokes by using a sample of electromagnetic fields from lightning flashes striking the sea. In analysing the propagation effects, these electric field waveforms were used in (11.42) to calculate the signature of the fields at different distances over finitely conducting ground. By comparing these signatures with the original undistorted ones the effects of propagation were evaluated.

Since the interest of Cooray *et al.* [2] was in understanding propagation effects over large distances, they have utilised (11.42) to calculate the propagation effects. According to this equation, the propagation effects depend only on the ratio of  $D/\sigma$ , where  $\sigma$  is the ground conductivity and  $D$  is the distance of propagation. Let us denote this ratio by  $\gamma$ . In order to make the presentation easier, Cooray *et al.* [2] defined the coefficient of attenuation,  $A$ , as  $A = E_\sigma/E_\infty$ , where  $E_\sigma$  is the peak of the radiation field at a given distance corresponding to a certain  $\gamma$ , and  $E_\infty$  is the radiation field at that distance over perfectly conducting ground. With this definition of  $A$ , the quantity  $(1 - A)$  gives the amount of attenuation of the radiation field peak due to propagation over finitely conducting ground. The data in Figures 11.11 and 11.12 show the distribution of  $(1 - A)$  for  $\gamma = 10^8 \text{ m}^2/\text{S}$  as a function of the undistorted peak  $E_\infty$  of negative and positive return strokes. Observe that the initial peaks were normalised to 100 km by using the inverse distance dependence. Note that for a given undistorted initial peak the attenuation caused by the propagation effects may vary from one electric field signature to another. The reason for this is that different frequencies are attenuated by different amounts by propagation effects, and the frequency content of the electric field signatures vary from one waveform to another. In the data given in

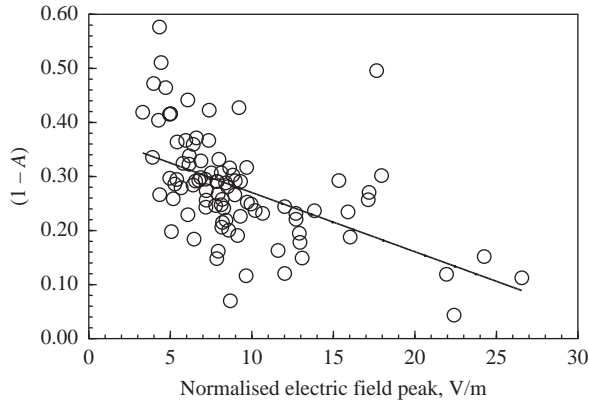


Figure 11.11 Distribution of  $1 - A$  for  $\gamma = 10^8 \text{ m}^2/\text{S}$  as a function of the undistorted peak  $E_\infty$  of negative return strokes. Note that the electric field peak was normalised to 100 km by using the inverse distance dependence. The best linear fit that represents the variation is also shown in the diagram.  $A = E_\sigma/E_\infty$ , where  $E_\sigma$  is the peak electric radiation field over finitely conducting ground and  $E_\infty$  is the peak electric radiation field that would be present if the ground was perfectly conducting.  $\gamma = D/\sigma$ , where  $D$  is the distance of propagation (in m) and  $\sigma$  is the conductivity in S/m. Adapted from [2]

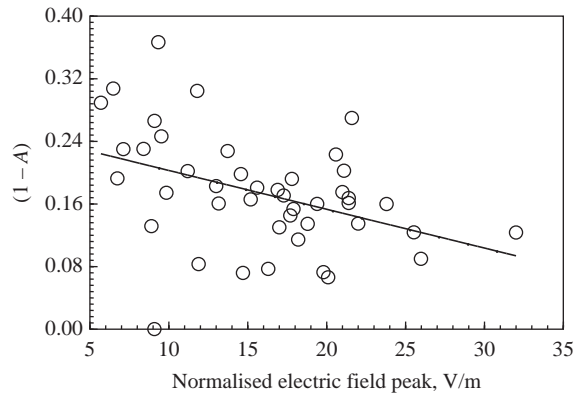


Figure 11.12 Distribution of  $1 - A$  for  $\gamma = 10^8 \text{ m}^2/\text{S}$  as a function of the undistorted peak  $E_\infty$  of positive return strokes. Note that the electric field peak was normalised to 100 km by using the inverse distance dependence. The best linear fit that represents the variation is also shown in the diagram.  $A = E_\sigma/E_\infty$ , where  $E_\sigma$  is the peak electric radiation field over finitely conducting ground and  $E_\infty$  is the peak electric radiation field that would be present if the ground was perfectly conducting.  $\gamma = D/\sigma$ , where  $D$  is the distance of propagation (in m) and  $\sigma$  is the conductivity in S/m. Adapted from [2]

these figures one can also observe a slight tendency for the attenuation of the initial peak to decrease with an increase in the initial peak of both the negative and positive return strokes, and the linear correlation coefficients between the two variables for different values of  $\gamma$  lie in the range of  $-0.58$  to  $-0.6$ . This decreasing attenuation indicates that the width of the initial peak of both the negative and positive first return stroke radiation fields increases as the peak increases.

According to the results of Cooray *et al.* [2], the mean value (based on a large number of return stroke waveforms) of the attenuation coefficient as a function of  $\gamma$  can be represented by the equations:

$$A_e = 0.24 \exp\left[\frac{-\gamma}{10^7}\right] + 0.24 \exp\left[\frac{-\gamma}{50 \times 10^7}\right] + 0.525$$

(for negative return strokes) (11.44)

$$A_e = 0.134 \exp\left[\frac{-\gamma}{1.5 \times 10^7}\right] + 0.312 \exp\left[\frac{-\gamma}{55 \times 10^7}\right] + 0.555$$

(for positive return strokes) (11.45)

It is important to note that these equations are valid for  $10^6 \text{ m}^2/\text{S} < \gamma < 2 \times 10^9 \text{ m}^2/\text{S}$ , and  $1 \text{ km} < D < 300 \text{ km}$ . The reason why  $D$  should not be allowed to exceed 300 km is that the equations used to estimate the propagation effects were derived by neglecting the curvature of the earth, which could lead to significant errors for distances larger than about 300 km. Comparison of the data obtained for positive return strokes with those obtained for negative ones shows that the propagation effects are more pronounced for negative return strokes and the differences are more important

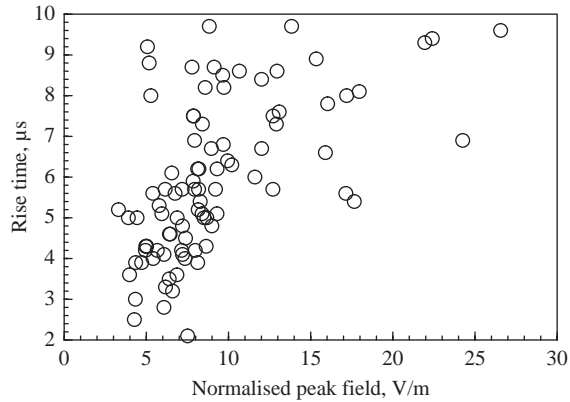


Figure 11.13 The variation of zero to peak rise time of the undistorted radiation fields of negative return strokes as a function of initial field peak. Adapted from [2]

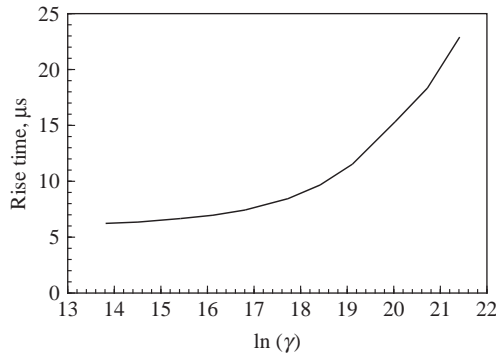


Figure 11.14 Variation of the mean value of the rise time of the negative return stroke radiation fields as a function of  $\gamma$ . Adapted from [2]

for small values of  $\gamma$ . The reason for the latter could be the much narrower initial peaks of negative return stroke fields than positive return stroke fields.

Another parameter of physical interest, especially in the case of lightning localisation by time of arrival, is the increase in the rise time of the waveforms when they propagate over finitely conducting ground. Figure 11.13 shows the variation of the zero to peak rise time of the undistorted negative return stroke waveforms as a function of the initial field peak. Figure 11.14 depicts the variation of the mean value of the rise time and Figure 11.15 the variation of the mean value of the increase in rise time as a function of  $\gamma$ . The data presented in Figure 11.15 show that the rise time of the radiation fields increases by about  $1 \mu\text{s}$  in propagating 100 km over finitely conducting ground of conductivity  $0.01 \text{ S/m}$ . Such information is of interest in evaluating the errors associated with lightning localisation by the time of arrival method.

#### 11.5.4 The reason why propagation effects vary with the shape of the radiation field

Cooray *et al.* [2] evaluated the average variation of the propagation effects as a function of  $\gamma$  for natural negative, positive and triggered return strokes. The results

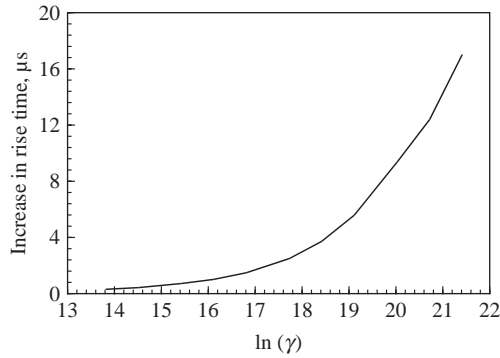


Figure 11.15 Variation of the mean value of the increase in rise time of the negative return stroke radiation fields as a function of  $\gamma$ . Adapted from [2]

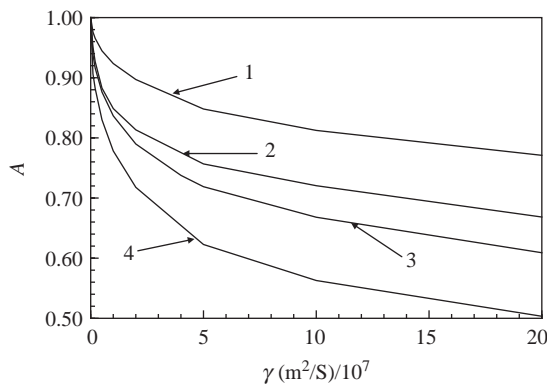


Figure 11.16 The mean value of the attenuation coefficient, as defined by (11.15), as a function of  $\gamma$ : (1) positive return strokes; (2) negative return strokes; (3) natural subsequent return strokes; (4) triggered subsequent return strokes. Adapted from [2]

are shown in Figure 11.16. The results show that the average attenuation of natural subsequent strokes lies somewhere between that for the natural first and the triggered subsequent strokes.

Let us now find out the reason why the attenuation is different for different types of return strokes. The attenuation of the initial peak mainly depends on the width of the initial peak of the radiation fields. In Figure 11.17, the average waveforms of first negative return strokes, first positive return strokes, triggered subsequent strokes and natural subsequent strokes are depicted. The average waveforms were generated by normalising each individual waveform to a common amplitude (i.e. setting the value of the peak to unity) and then aligning the peaks and averaging. Note that the average width of the positive return strokes is larger than that of the negative first return strokes and the average width of the natural subsequent return strokes lies between those of negative return strokes and the triggered subsequent return strokes. The attenuation of the waveforms owing to propagation depends mainly on the width of the initial peak, and the amount of

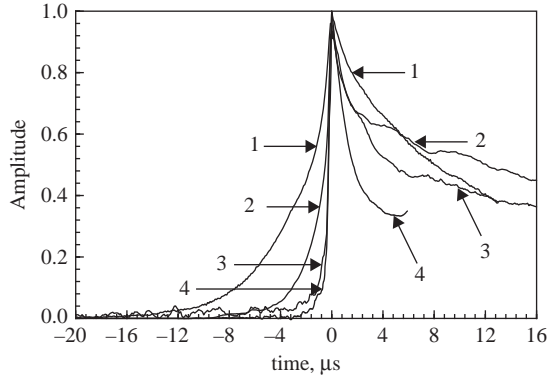


Figure 11.17 The average radiation fields of (1) positive first return strokes, (2) negative first return strokes, (3) natural negative subsequent return strokes and (4) triggered negative subsequent strokes. Adapted from [2]

attenuation decreases with increasing width. This fact explains the relative position of the curves given in Figure 11.16.

### 11.5.5 The effect of propagation on electromagnetic fields generated by cloud flashes

From the point of view of power engineers, the lightning events which are of most interest are the return strokes. Until recent times, the same was true for the lightning protection engineers. The rapid development of low voltage electronic devices and their incorporation in modern day decision-making apparatus, however, made it necessary for the engineers to consider the threats imposed by lightning events other than return strokes – cloud flashes, for example. This is because modern day electronics are sensitive to over-voltages of a few volts, and such voltage magnitudes can easily be generated by the interaction of electrical networks with electromagnetic fields generated by cloud flashes. A strong need exists today to categorise and quantify the electromagnetic fields generated by cloud flashes and to understand the way in which they can interact with the low voltage power installations. This, in turn, requires that one can explain the effects of propagation on radiation field pulses generated by cloud flashes as they propagate over finitely conducting ground. This problem was analysed by Cooray [36] and a brief description of the methodology is the following.

The geometry of the situation under consideration is shown in Figure 11.18. Let us assume that the cloud flash channel is vertical. Let  $Z_1$  be the height of origin of the discharge and  $Z_2$  is the height where it was terminated. The vertical electric field at the point of observation is given by

$$\begin{aligned}
 e_z(j\omega, \rho) = & \int_{Z_1}^{Z_2} \frac{I(j\omega) dz}{2\pi \epsilon_0} \left( \frac{2 - 3\sin^2\theta}{j\omega R^3} \right. \\
 & \left. + \frac{2 - 3\sin^2\theta}{cR^2} + j\omega \frac{\sin^2\theta}{c^2R} a(z, j\omega, \rho) \right) e^{-j\omega R/c} dz
 \end{aligned} \tag{11.46}$$



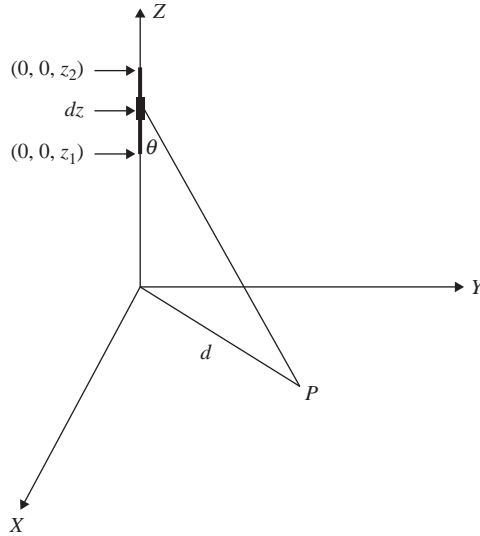


Figure 11.18 Geometry relevant to the calculation of propagation effects on electromagnetic fields generated by cloud flashes

where  $a(z, j\omega, \rho)$  is the attenuation function defined previously in (11.26). Now, as in the case return strokes, the attenuation function can be replaced by the function corresponding to height  $Z_1$ , i.e.  $a(Z_1, j\omega, \rho)$ . With this approximation the equation can be Fourier transformed into time domain as

$$E_{z,cl}(t, \rho) = E_{z,s,cl}(t, \rho) + E_{z,i,cl}(t, \rho) + \int_0^t E_{z,r,cl}(t - \tau, \rho) W(Z_1, t, \rho) d\tau \tag{11.47a}$$

where  $W(Z_1, t, \rho)$  is the inverse Fourier transformation of  $a(Z_1, j\omega, \rho)$ , and  $E_{z,s,cl}(t, \rho)$ ,  $E_{z,i,cl}(t, \rho)$  and  $E_{z,r,cl}(t, \rho)$  are the static, induction and radiation field components, respectively, of the electric fields generated by the cloud discharge over perfectly conducting ground. These field components are given by

$$E_{z,s,cl}(t, \rho) = \int_{Z_1}^{Z_2} \frac{dz}{2\pi\epsilon_0} \left\{ \frac{2 - 3 \sin^2\theta}{R^3} \int_0^t i(z, \tau - R/c) d\tau \right\} \tag{11.47b}$$

$$E_{z,i,cl}(t, \rho) = \int_{Z_1}^{Z_2} \frac{dz}{2\pi\epsilon_0} \frac{2 - 3 \sin^2\theta}{cR^2} i(z, t - R/c) \tag{11.47c}$$

$$E_{z,r,cl}(t, \rho) = \int_{Z_1}^{Z_2} \frac{dz}{2\pi\epsilon_0} \frac{\sin^2\theta}{c^2R} \frac{\partial i(z, t - R/c)}{\partial t} \tag{11.47d}$$

If the undistorted radiation fields generated by cloud flashes are available, they can be used in equation (11.47a) to evaluate the propagation effects.

### 11.5.5.1 Difference between propagation effects on electromagnetic fields from cloud flashes and ground flashes

In order to illustrate the difference between propagation effects on electromagnetic fields from cloud flashes and ground flashes, it is illuminating to calculate the effects of propagation when the undistorted radiation field is a step function. Such calculations are shown for  $D=1$  km,  $H=5$  km and  $\sigma=0.01$  and  $0.001$  S/m in Figure 11.19a. For comparison purposes, the step responses for the same parameters but with  $H=0$  (i.e. corresponding to a return stroke) are depicted in Figure 11.19b. Note that in the case of cloud flashes the field over finitely

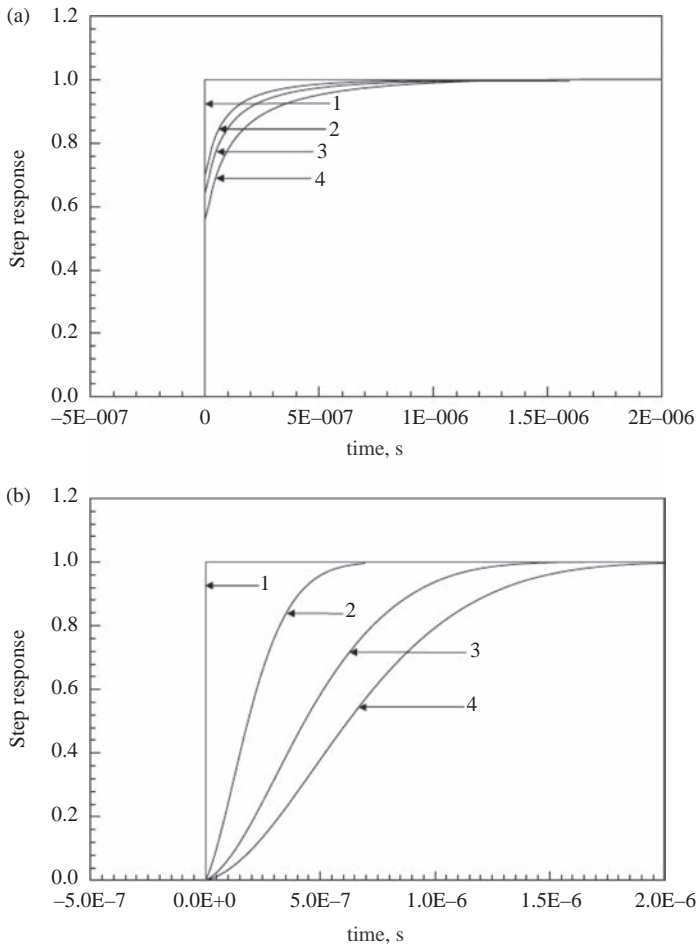


Figure 11.19 (a) The behaviour of  $E_{z,c}(t, \rho)$  in (11.47a) when  $E_{z,r,c}(t, \rho)$  is a unit step function and when the distance to the point of observation is such that the first two terms in (11.47a) can be neglected compared to the third term. The value of  $\rho$  is 1 km in (2), 5 km in (3) and 10 km in (4). In the calculation the lower end of the channel is assumed to be 5 km and the conductivity of ground is assumed to be 0.001 S/m. (b) As in (a), but in the calculations the lower end of the channel (i.e.  $Z_1$ ) was assumed to be at ground level. Adapted from [36]

conducting ground consists of two sections: Initially, the field rises like a step until it reaches an amplitude that is smaller than the amplitude of the undistorted waveform. Then, it rises slowly until it reaches the amplitude of the undistorted waveform. The reason for this behaviour is as follows: The radiation field from the discharge reaching the point of observation can be divided into a space wave (which arises from the first term in the square bracket of (11.26)) and a ground wave (which arises from the second term in the square bracket of (11.26)). The space wave is not attenuated by the finitely conducting ground, whereas the ground wave is strongly affected by it. The rapidly rising part of the waveform which occurs at  $t = 0$  in Figure 11.19a is generated by the space wave and the subsequent slow increase is caused by the ground wave. The amplitude of the space wave is zero for a channel section located at ground level. In the case of return strokes of ground flashes, the section of the channel which radiates during the first few microseconds of the radiation field is located close to ground. Thus the initial portion of the radiation field from a return stroke consists mainly of the surface wave. Since the high frequency components of the surface wave are strongly attenuated by the finitely conducting ground, the radiation fields from return strokes in ground flashes experience strong propagation effects. As the height of the radiating end of the channel increases, the contribution to the total field from the space wave increases. The sources of a cloud flash are located at altitudes of 3–8 km and a significant portion of the total radiation field is contributed by the space wave. Thus, for the reasons mentioned earlier, the attenuation of the radiation fields of cloud flashes is not as strong as that experienced by return strokes in ground flashes. These facts make the effect of propagation on the radiation fields from cloud flashes differ from that of the radiation fields from return strokes.

### 11.5.6 *Simplified expressions to calculate the horizontal electric field*

Horizontal electric field is of interest in many engineering studies. This field component plays a significant role in the source terms of the transmission line equations used to solve the problem of interaction of lightning-generated electromagnetic fields with power lines. Moreover, in lightning protection studies, this field component is of interest in evaluating the surface spark over probability at the point of strike and also in evaluating the step potential experienced by a person standing in the vicinity of a lightning strike point. Here several expressions that are being used to evaluate the horizontal electric field are presented together with their limits of accuracy.

#### 11.5.6.1 **Quasi-static expression to calculate horizontal electric field close to the lightning channel**

A popular approximation that is being used frequently to obtain the horizontal electric field at ground level in the vicinity of the return stroke channel is given by

$$E_{\rho}(t, \rho) = -\frac{I(t)}{2\pi\rho^2\sigma} \quad (11.48)$$

where  $E_{\rho}(t, \rho)$  is the horizontal electric field in time domain at ground level at a distance  $\rho$  from the strike point and  $I(t)$  is the current at the channel base. This quasi-static approximation is used frequently in lightning protection studies to estimate lightning hazards caused, for example, by step potentials.

### 11.5.6.2 Surface impedance expression

The surface impedance expression connects the horizontal electric field to the horizontal magnetic field present over finitely conducting ground. This is also a part of the Cooray–Rubinstein approximation used frequently in calculating induced over-voltages in power lines due to lightning [28, 37]. According to the surface impedance approximation, the horizontal electric field at ground level is given by

$$e_{\rho}(j\omega, \rho) = -c b_{\varphi, \sigma}(j\omega, \rho) \frac{k_0}{k_1} \quad (11.49)$$

where  $\rho$  is the horizontal distance to the point of observation from the strike point,  $e_{\rho}(j\omega, \rho)$  is the horizontal electric field at the surface of the ground and  $b_{\varphi, \sigma}(j\omega, \rho)$  is the azimuthal magnetic field at the surface of the ground. If one neglects the effects of finitely conducting ground on the magnetic field, one can write the above equation as

$$e_{\rho}(j\omega, \rho) = -c b_{\varphi}(j\omega, \rho) \frac{k_0}{k_1} \quad (11.50)$$

where  $b_{\varphi}(j\omega, \rho)$  is the magnetic field over perfectly conducting ground.

### 11.5.6.3 Comparison of the predictions of the quasi-static approximation and the surface impedance expression with exact calculations

Cooray [38] evaluated the horizontal electric field generated by first and subsequent return strokes using the exact theory and the results were compared with those predicted by (11.48–11.50). The results obtained by Cooray [38] are presented in Figures 11.20–11.27. The results of the comparison show the following on the quasi-static approximation: (a) The quasi-static approximation provides reasonable results at small distances and at long times. For a given distance and time, the agreement between the exact and the quasi-static approximation becomes better with decreasing conductivity. For a given conductivity and distance the agreement becomes better at longer times. For example, for a given conductivity and distance the error associated with the peak value of the subsequent stroke horizontal electric field is larger than that of the first strokes. The reason for this is that the peak value of the subsequent stroke occurs at times earlier than the first return stroke peak.

According to these calculations of Cooray [38], the surface impedance expressions as given in (11.50) provides accurate results at distances larger than about 50 m for 0.01 S/m, 200 m for 0.001 S/m (100 m if only the peak field is concerned), 400 m for 0.0003 S/m and about 600 m for 0.0001 S/m. The error associated with this expression at smaller distances is significant. Furthermore, for a given distance the agreement is better at short times than at long times. The results obtained for subsequent return strokes also show the same tendency as that of first return strokes. However, for a given distance the agreement between the peak field values generated by exact theory and the ones obtained from surface impedance expression is better in the case of subsequent return strokes than in the first. These results show clearly that the surface impedance expression can be used to evaluate the horizontal electric field at the surface of the ground, provided that the distance of interest is kept beyond a certain critical value which is a function of conductivity.

In the preceding paragraph comparison has been made between the predictions of (11.50) and the exact horizontal electric field. In this equation the magnetic field

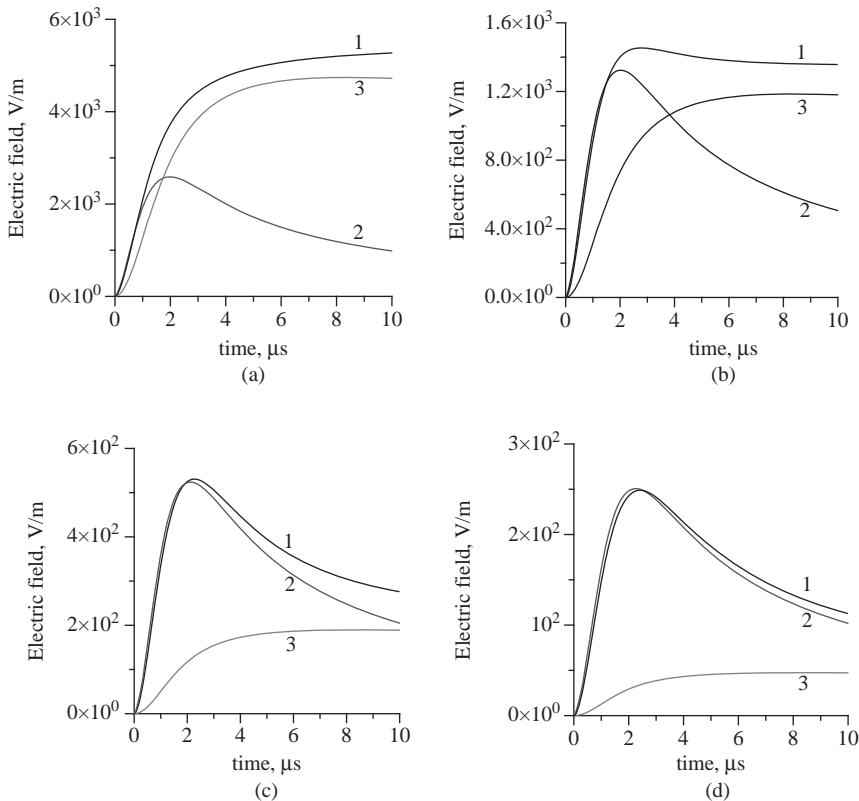


**Figure 11.20** First stroke horizontal electric field at ground level for (a)  $\rho = 10$  m,  $\sigma = 0.01$  S/m, (b)  $\rho = 20$  m,  $\sigma = 0.01$  S/m, (c)  $\rho = 50$  m,  $\sigma = 0.01$  S/m and (d)  $\rho = 100$  m,  $\sigma = 0.01$  S/m. Curve 1: Sommerfeld's integrals; Curve 2: Surface impedance expression (11.50); Curve 3: Quasi-static approximation. In the calculations, the return stroke is modelled by using the MTLE model with a current decay height constant  $\lambda_e$  equal to 2 km. The return stroke speed is kept at  $1.5 \times 10^8$  m/s. The current waveform at ground level is simulated by the analytical expression given by (11.21). Adapted from [38]

corresponds to the one that exists over perfectly conducting ground. However, the exact expressions as given by (11.49) involve the magnetic field over finitely conducting ground. The propagation effects on the magnetic field can be included using the simple procedure outlined in section 11.5.2. One can show that when this is done the agreement between the horizontal electric field calculated using the surface impedance expression and the exact one becomes better. When the distance to the lightning flash is large and the ground conductivity is poor, it is necessary to use (11.49) to obtain reasonable results. For example, Figure 11.28 shows the horizontal electric fields at a distance of 100 km obtained (1) using exact formulation, (2) using surface impedance expression with magnetic field over perfectly conducting ground as an input (i.e. (11.50)) and (3) using surface impedance expression with magnetic field over finitely conducting ground as an input (i.e. (11.49)). The conductivity of the ground in this example is 0.01 S/m. Note the

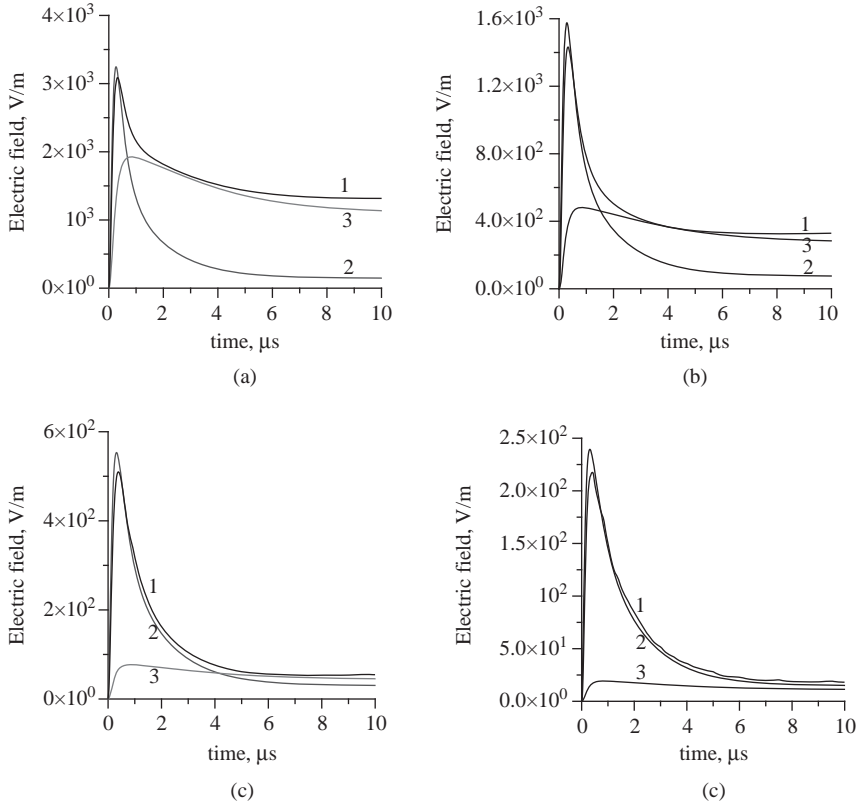


Figure 11.21 Subsequent stroke horizontal electric field at ground level for (a)  $\rho = 10$  m,  $\sigma = 0.01$  S/m, (b)  $\rho = 20$  m,  $\sigma = 0.01$  S/m, (c)  $\rho = 50$  m,  $\sigma = 0.01$  S/m and (d)  $\rho = 100$  m,  $\sigma = 0.01$  S/m. Curve 1: Sommerfeld's integrals; Curve 2: Surface impedance expression (11.50); Curve 3: Quasi-static approximation. In the calculations, the return stroke is modelled by using the MTL model with a current decay height constant  $\lambda_e$  equal to 2 km. The return stroke speed is kept at  $1.5 \times 10^8$  m/s. The current waveform at ground level is simulated by the analytical expression given by (11.21). Adapted from [38]

significant error in the horizontal electric field calculated without taking propagation effects on the magnetic field into account. Calculations by Cooray [38] show that propagation effects have to be included in the magnetic field already at distances larger than about 300 m for conductivities around  $10^{-3}$  S/m and at distances larger than about 200 m for  $10^{-4}$  S/m to obtain accurate results, especially in the case of subsequent strokes. This can also be seen in the data given in Figures 11.25–11.27 (dotted lines).

### 11.5.7 Barbosa and Paulino expression to calculate the horizontal electric field

Recently, Barbosa and Paulino [39] derived an expression to calculate the horizontal electric field in the vicinity of the lightning channel. Assume that the

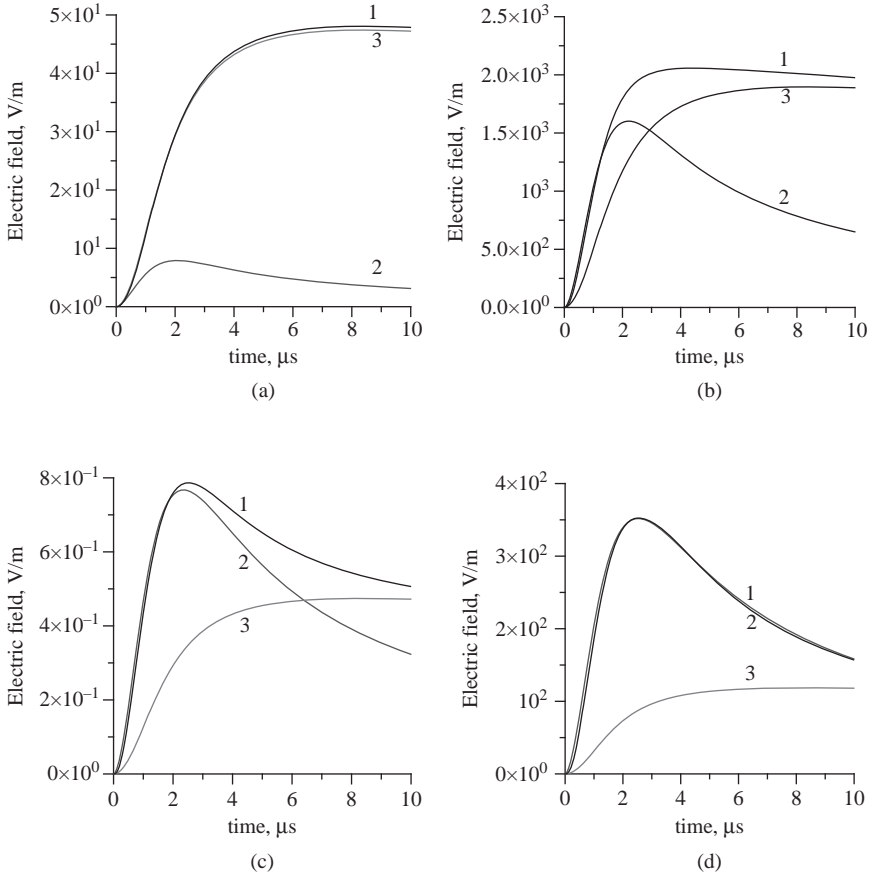


Figure 11.22 First stroke horizontal electric field at ground level for (a)  $\rho = 10 \text{ m}$ ,  $\sigma = 0.001 \text{ S/m}$ , (b)  $\rho = 50 \text{ m}$ ,  $\sigma = 0.001 \text{ S/m}$ , (c)  $\rho = 100 \text{ m}$ ,  $\sigma = 0.001 \text{ S/m}$  and (d)  $\rho = 200 \text{ m}$ ,  $\sigma = 0.001 \text{ S/m}$ . Curve 1: Sommerfeld's integrals; Curve 2: Surface impedance expression (11.50); Curve 3: Quasi-static approximation. In the calculations, the return stroke is modelled by using the MTLE model with a current decay height constant  $\lambda_e$  equal to 2 km. The return stroke speed is kept at  $1.5 \times 10^8 \text{ m/s}$ . The current waveform at ground level is simulated by the analytical expression given by (11.21). Adapted from [38]

magnetic field generated by a return stroke in the vicinity of its channel is a step of amplitude  $B_0$ . According to Barbosa and Paulino [39], the horizontal electric field induced in the vicinity of the lightning channel by such a return stroke is given by

$$E_\rho(\tau) = -\frac{Z_e B_0}{\mu_0} \left\{ \frac{2\epsilon_r + a\tau(1 + 3b\epsilon_r + 2ab\tau)}{2(1 + ab\tau)^{1/2}(\epsilon_r + a\tau)^{3/2}} \right\} \quad (11.51)$$

with  $a = \frac{\pi\sigma}{4\epsilon_0}$  and  $b = (\frac{1}{Z_e\sigma\rho})^2$  where  $Z_e$  is the impedance of free space,  $\sigma$  is the conductivity of soil,  $\epsilon_r$  is the relative dielectric constant of soil,  $\tau$  is the time from the arrival of the wave to the point of interest and  $\rho$  is the distance from the

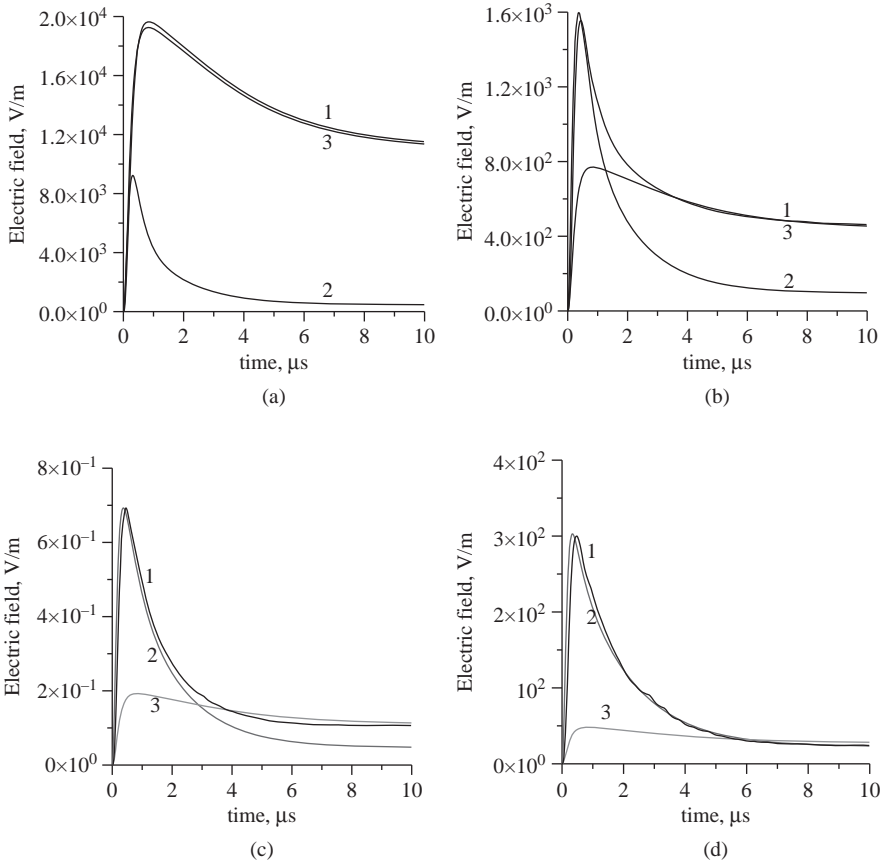


Figure 11.23 Subsequent stroke horizontal electric field at ground level for (a)  $\rho = 10 \text{ m}, \sigma = 0.001 \text{ S/m}$ , (b)  $\rho = 50 \text{ m}, \sigma = 0.001 \text{ S/m}$ , (c)  $\rho = 100 \text{ m}, \sigma = 0.001 \text{ S/m}$  and (d)  $\rho = 200 \text{ m}, \sigma = 0.001 \text{ S/m}$ . Curve 1: Sommerfeld's integrals; Curve 2: Surface impedance expression (11.50); Curve 3: Quasi-static approximation. In the calculations, the return stroke is modelled by using the MTLE model with a current decay height constant  $\lambda_e$  equal to 2 km. The return stroke speed is kept at  $1.5 \times 10^8 \text{ m/s}$ . The current waveform at ground level is simulated by the analytical expression given by (11.21). Adapted from [38]

lightning channel to the point of observation. The horizontal electric field caused by a return stroke of any arbitrary magnetic field can be obtained from (11.51) using Duhammel's integral.

Barbosa and Paulino [39] had compared the predictions of this equation with the exact horizontal electric field calculated in the vicinity of the lightning channel by Cooray [38]. They showed that the expression can predict the horizontal electric field to a reasonable accuracy. Figure 11.29 shows the predictions of this equation plotted together with the horizontal electric field calculated at 10 m from the lightning channel.



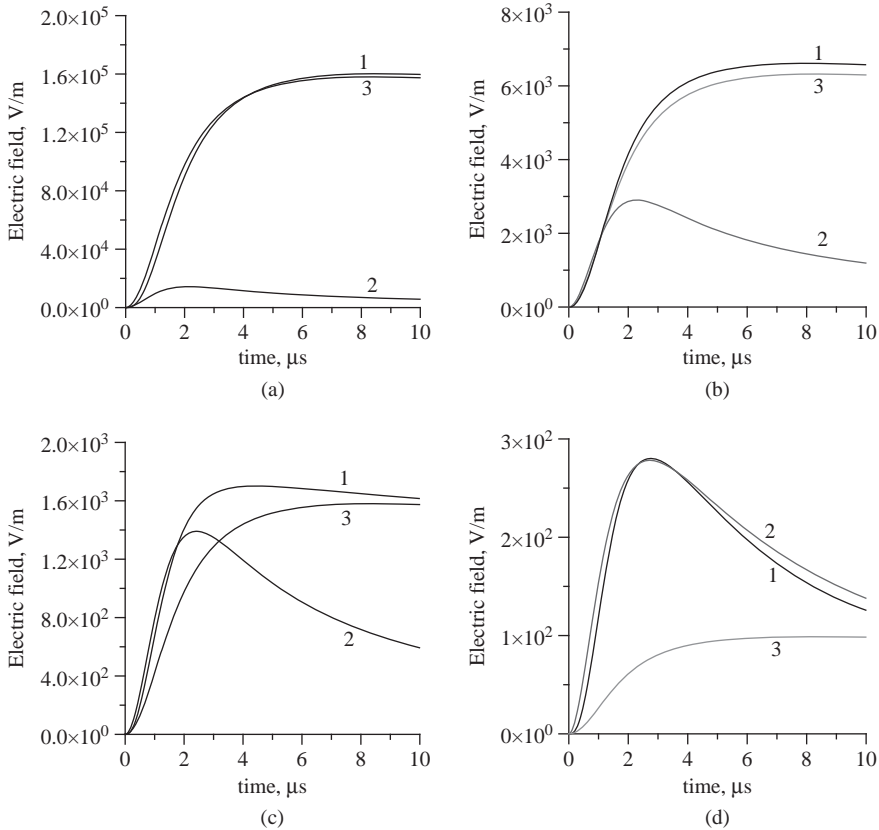


Figure 11.24 First stroke horizontal electric field at ground level for (a)  $\rho = 10 \text{ m}, \sigma = 0.0003 \text{ S/m}$ , (b)  $\rho = 50 \text{ m}, \sigma = 0.0003 \text{ S/m}$ , (c)  $\rho = 100 \text{ m}, \sigma = 0.0003 \text{ S/m}$  and (d)  $\rho = 400 \text{ m}, \sigma = 0.0003 \text{ S/m}$ . Curve 1: Sommerfeld's integrals; Curve 2: Surface impedance expression (11.50); Curve 3: Quasi-static approximation. In the calculations, the return stroke is modelled by using the MTL model with a current decay height constant  $\lambda_e$  equal to 2 km. The return stroke speed is kept at  $1.5 \times 10^8 \text{ m/s}$ . The current waveform at ground level is simulated by the analytical expression given by (11.21). Adapted from [38]

### 11.5.8 Approximate time domain expressions to calculate underground electric fields

Cooray [40] had utilised the dipole fields as derived by Bannister [19] to extract time domain expressions for the vertical electric field, azimuthal magnetic field and horizontal electric field at a given depth below a finitely conducting ground. The analysis conducted by Cooray [40] is presented in the following text.

#### 11.5.8.1 Vertical electric field at the surface and at different depths below the ground

According to Bannister [19], the vertical electric field at a depth  $\zeta$  below the surface of a finitely conducting ground produced by a dipole located at height  $z$  above ground level is given by

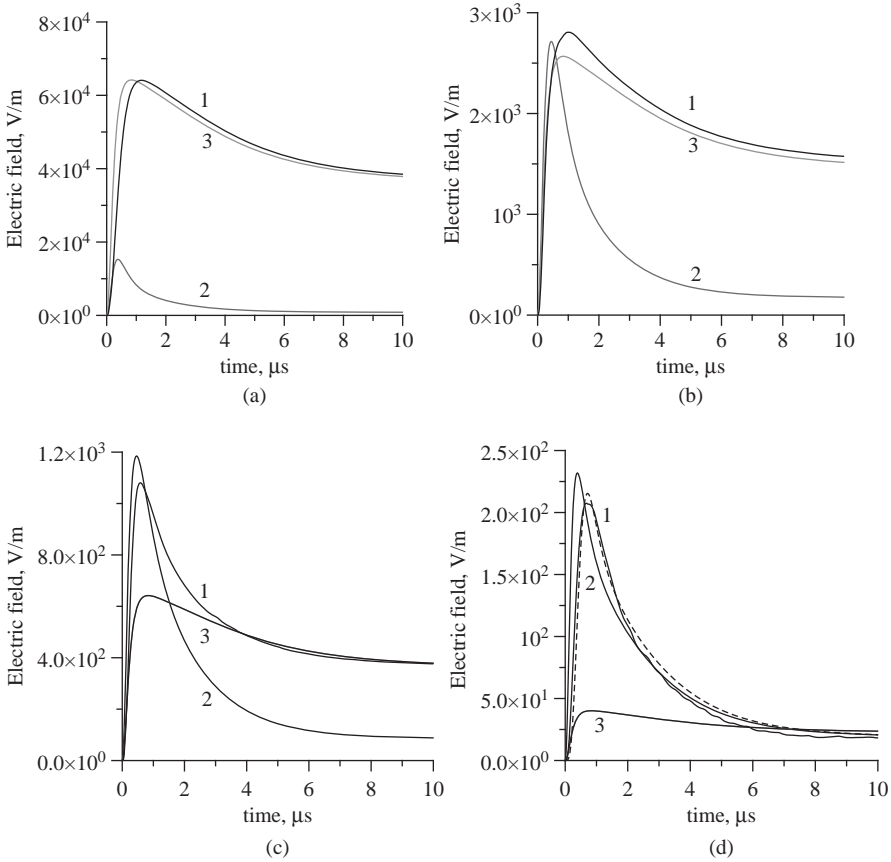


Figure 11.25 Subsequent stroke horizontal electric field at ground level for (a)  $\rho = 10\text{ m}$ ,  $\sigma = 0.0003\text{ S/m}$ , (b)  $\rho = 50\text{ m}$ ,  $\sigma = 0.0003\text{ S/m}$ , (c)  $\rho = 100\text{ m}$ ,  $\sigma = 0.0003\text{ S/m}$  and (d)  $\rho = 400\text{ m}$ ,  $\sigma = 0.0003\text{ S/m}$ . Curve 1: Sommerfeld's integrals; Curve 2: Surface impedance expression (11.50); Curve 3: Quasi-static approximation. The dotted line shows the prediction from (11.49). In the calculations, the return stroke is modelled by using the MTL model with a current decay height constant  $\lambda_e$  equal to 2 km. The return stroke speed is kept at  $1.5 \times 10^8\text{ m/s}$ . The current waveform at ground level is simulated by the analytical expression given by (11.21). Adapted from [38]

$$\begin{aligned}
 de_{z,b,under}(z, j\omega, \rho) = & \frac{I(j\omega) dz}{2\pi \epsilon_0} \left\{ \frac{j\omega e^{-jk_1 \zeta}}{(\sigma/\epsilon_0) + j\omega \epsilon_r} \right\} \left( \frac{2 - 3\sin^2\theta}{j\omega R^3} + \frac{2 - 3\sin^2\theta}{cR^2} \right. \\
 & \left. + j\omega \frac{\sin^2\theta}{c^2 R} a(z, j\omega, \rho) \right) e^{-j\omega R/c} \tag{11.52}
 \end{aligned}$$

All the parameters appearing in the above equation are defined in section 11.5.1.

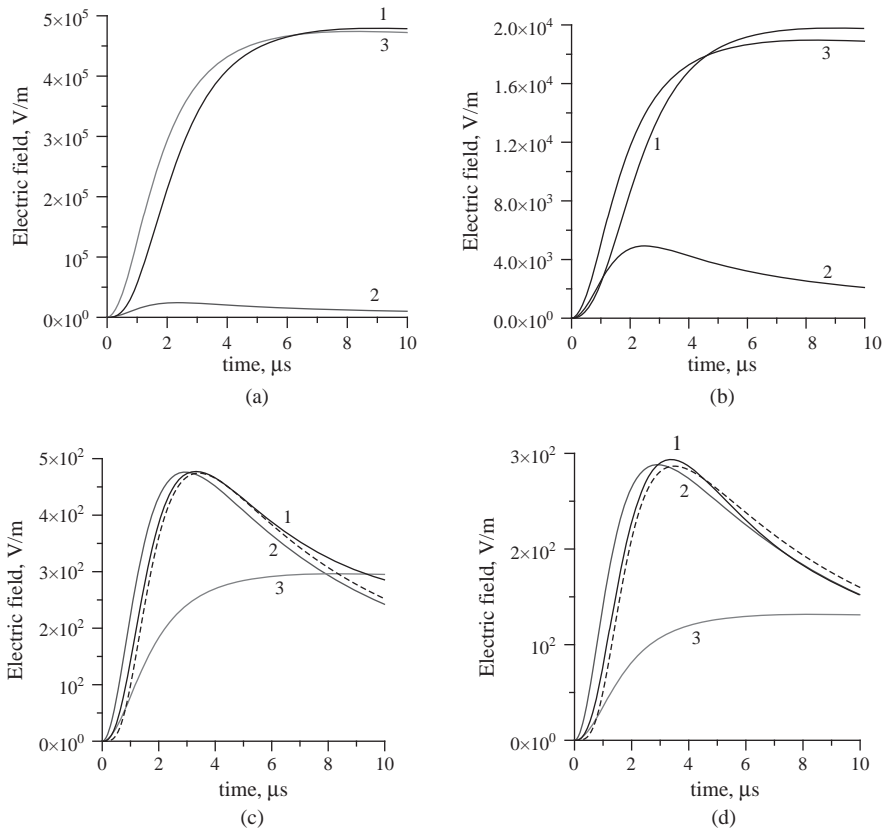


Figure 11.26 First stroke horizontal electric field at ground level for (a)  $\rho = 10$  m,  $\sigma = 0.0001$  S/m, (b)  $\rho = 50$  m,  $\sigma = 0.0001$  S/m, (c)  $\rho = 400$  m,  $\sigma = 0.0001$  S/m and (d)  $\rho = 600$  m,  $\sigma = 0.0001$  S/m. Curve 1: Sommerfeld's integrals; Curve 2: Surface impedance expression (11.50); Curve 3: Quasi-static approximation. The dotted lines show the prediction from (11.49). In the calculations, the return stroke is modelled by using the MTLE model with a current decay height constant  $\lambda_e$  equal to 2 km. The return stroke speed is kept at  $1.5 \times 10^8$  m/s. The current waveform at ground level is simulated by the analytical expression given by (11.21). Adapted from [38]

A comparison of (11.25) and (11.52) shows that the vertical electric field at a depth  $\zeta$  below the ground is related to the vertical electric field at the surface by

$$de_{z,under}(z, j\omega, \rho) = de_z(z, j\omega, \rho) \left\{ \frac{j\omega e^{-jk_1\zeta}}{(\sigma/\epsilon_0) + j\omega\epsilon_r} \right\} \quad (11.53)$$

Since the lightning return stroke channel can be represented by a series of dipoles distributed along the channel and the principle of superposition is valid, one can write

$$e_{z,under}(j\omega, \rho) = e_z(j\omega, \rho) \left\{ \frac{j\omega e^{-jk_1\zeta}}{(\sigma/\epsilon_0) + j\omega\epsilon_r} \right\} \quad (11.54)$$

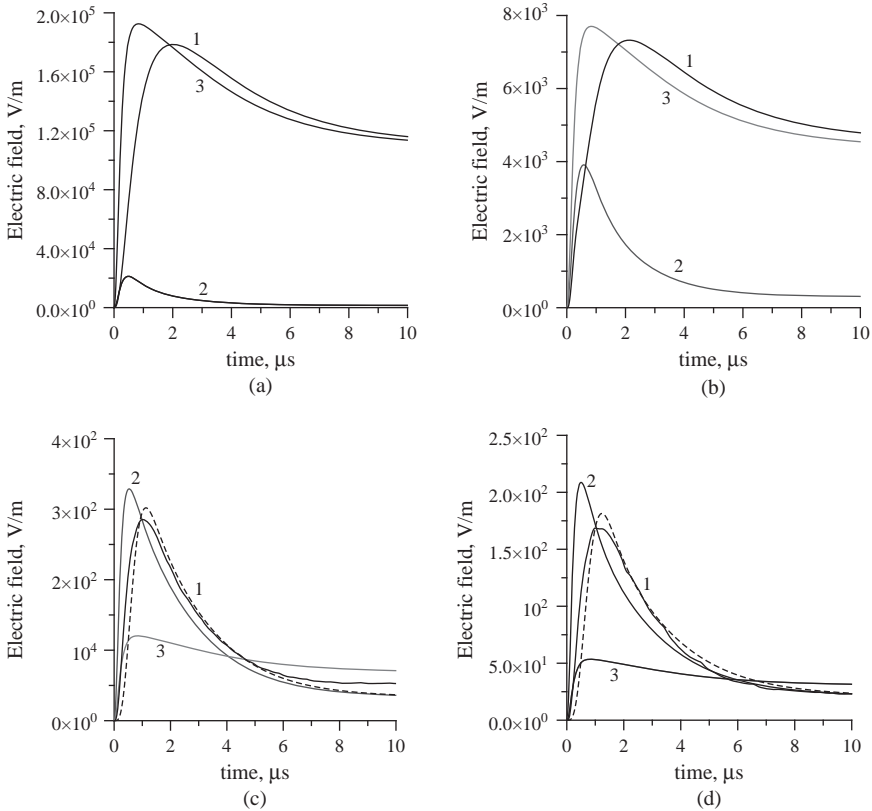


Figure 11.27 Subsequent stroke horizontal electric field at ground level for (a)  $\rho = 10$  m,  $\sigma = 0.0001$  S/m, (b)  $\rho = 50$  m,  $\sigma = 0.0001$  S/m, (c)  $\rho = 400$  m,  $\sigma = 0.0001$  S/m and (d)  $\rho = 600$  m,  $\sigma = 0.0001$  S/m. Curve 1: Sommerfeld's integrals; Curve 2: Surface impedance expression (11.50); Curve 3: Quasi-static approximation. The dotted lines show the prediction from (11.49). In the calculations, the return stroke is modelled by using the MTLE model with a current decay height constant  $\lambda_e$  equal to 2 km. The return stroke speed is kept at  $1.5 \times 10^8$  m/s. The current waveform at ground level is simulated by the analytical expression given by (11.21). Adapted from [38]

where  $e_{z,under}$  is the total vertical electric field at a depth  $\zeta$  below the ground surface and  $e_z$  is the total electric field at the ground surface. (Note that in equation 17 of Cooray [40] a term  $j\omega$  is missing in the numerator.) Transforming this into time domain one can obtain the vertical component of electric field at depth  $\zeta$  as a function of the vertical electric field at the surface. After some mathematical manipulation and by resorting to conventional Laplace transformations, one can write

$$E_{z,under}(t, \rho) = \int_0^t E_z(t - \tau, \rho) \Psi(\tau) d\tau \tag{11.55}$$

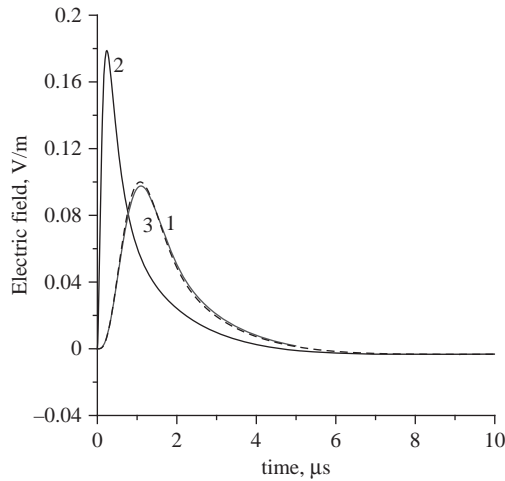


Figure 11.28 Horizontal electric field at ground level for  $\rho = 100$  km,  $\sigma = 0.01$  S/m. Curve (1) obtained from Sommerfeld's integrals. Curve (2) obtained from surface impedance expression with magnetic field over perfectly conducting ground as input (11.50). Curve (3) obtained from surface impedance expression with magnetic field over finitely conducting ground as input (11.49). In the calculations, the return stroke is modelled by using the MTLE model with a current decay height constant  $\lambda_e$  equal to 2 km. The return stroke speed is kept at  $1.5 \times 10^8$  m/s. The current waveform at ground level is simulated by the analytical expression given by (11.21). Adapted from [38]

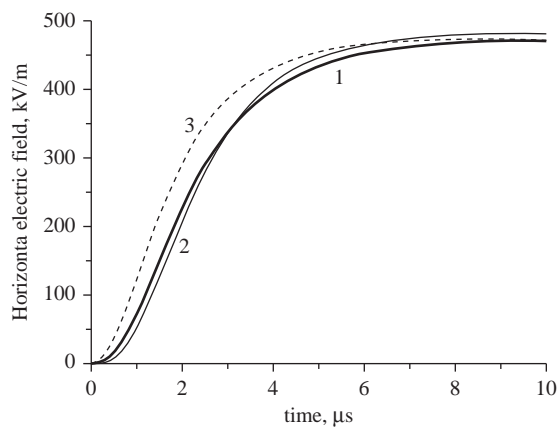


Figure 11.29 Horizontal electric field at the surface for the first stroke. Curve 1: Equation (11.51). Curve 2: Sommerfeld integrals from [38]. Curve 3: Quasi-static approximation (i.e. (11.48)). The distance to the point of observation is 10 m. Adapted from [39]

where

$$\Psi(t) = \int_0^t \Psi_1(t - \tau) \Psi_2(\tau) d\tau \tag{11.56}$$

$$\Psi_1(t) = \frac{1}{\epsilon} \left[ \delta(t) - \frac{\sigma}{\epsilon_0 \epsilon} u(t) \right] e^{-at} \tag{11.57}$$

$$\Psi_2(t) = \frac{e^{-\frac{a}{2} t} a k}{2\sqrt{t^2 - k^2}} I_1 \left( \frac{a\sqrt{t^2 - k^2}}{2} \right) u(t - k) + e^{-\frac{a}{2} t} \delta(t - k) \tag{11.58}$$

$$a = \frac{\sigma}{\epsilon_0 \epsilon} \quad k = \zeta \sqrt{\mu_0 \epsilon_0 \epsilon} \tag{11.59}$$

In these equations  $\delta(t)$  is the delta function,  $u(t)$  is the Heaviside's unit step function and  $I_1(t)$  is the modified Bessel function of order one. Note that there is a typographical error in the expressions for  $\Psi_1$  and  $\Psi_2$  given by Cooray [40] and they should be replaced by (11.57) and (11.58).

### 11.5.8.2 Azimuthal magnetic field at the surface and at different depths below ground

According to Bannister [19], the azimuthal magnetic field at the surface of a finitely conducting ground produced by a dipole located at height  $z$  above ground level is given by

$$db_\phi(z, j\omega, \rho) = \frac{I(j\omega) dz}{2\pi \epsilon_0 c} \left( \frac{\sin \theta}{cR^2} + \frac{j\omega \sin \theta}{c^2 R} a(z, j\omega, \rho) \right) e^{-j\omega R/c} \tag{11.60}$$

The azimuthal magnetic field at a depth  $\zeta$  at the same distance is given by

$$db_{\phi, \text{under}}(z, j\omega, \rho) = \frac{I(j\omega) dz}{2\pi \epsilon_0 c} e^{-jk_1 \zeta} \left( \frac{\sin \theta}{cR^2} + \frac{j\omega \sin \theta}{c^2 R} a(z, j\omega, \rho) \right) e^{-j\omega R/c} \tag{11.61}$$

Combination of (11.60) and (11.61) shows that the underground return stroke field can be connected to the surface field by

$$b_{\phi, \text{under}}(j\omega, \rho) = b_\phi(j\omega, \rho) e^{-jk_1 \zeta} \tag{11.62}$$

This can also be converted into the time domain after some mathematical manipulation with the result:

$$B_{\phi, \text{under}}(t, \rho) = \int_0^t B_\phi(t - \tau, \rho) Y(\tau) d\tau \tag{11.63}$$

with

$$Y(t) = \frac{e^{-\frac{a}{2} t} a k}{2\sqrt{t^2 - k^2}} I_1 \left( \frac{a\sqrt{t^2 - k^2}}{2} \right) u(t - k) + e^{-\frac{a}{2} t} \delta(t - k) \tag{11.64}$$

where  $B_\phi(t, \rho)$  is the azimuthal magnetic field in the time domain on the surface of the ground,  $B_{\phi, \text{under}}(t, \rho)$  is the azimuthal magnetic field at depth  $\zeta$  and  $I_1(t)$  is the

modified Bessel function of order one. (Note that in Cooray [40] it was written  $I_0(t)$  due to a typographical mistake.)

### 11.5.8.3 Horizontal electric field at the surface and at different depths below ground

According to the results of Bannister [19], the horizontal electric field penetrates into the ground exactly in the same way as the azimuthal magnetic field. Thus the horizontal electric field in the frequency domain at a depth  $\zeta$  below the surface of a finitely conducting ground,  $E_{\rho,under}(t, \rho)$ , is given by

$$E_{\rho,under}(t, \rho) = \int_0^t E_{\rho}(t - \tau, \rho) Y(\tau) d\tau \quad (11.65)$$

where  $E_{\rho}(t, \rho)$  is the horizontal electric field at the surface. The horizontal electric field at the surface can be calculated exactly using Sommerfeld's integrals or an approximate to this field can be obtained using the surface impedance expression. For example, (11.49) can be transferred into time domain giving the horizontal electric field as

$$E_{\rho}(t, \rho) = \int_0^t B_{\varphi,\sigma}(t - \tau, \rho) S(\tau) d\tau \quad (11.66)$$

with

$$S(t) = \frac{c}{\sqrt{\varepsilon}} \zeta e^{-\zeta t} [I_1(\zeta t) - I_0(\zeta t)] \quad (11.67)$$

where  $\zeta = \frac{\varepsilon \varepsilon_0}{\sigma}$ ,  $B_{\varphi,\sigma}(t, \rho)$  is the magnetic field at the surface of the ground and  $I_0(\zeta t)$  and  $I_1(\zeta t)$  are the modified Bessel functions of order zero and one, respectively. Cooray [38] had considered the prediction of (11.65) for both cases (i.e. calculating the horizontal electric field exactly at the surface or using (11.66) to obtain it) by comparing the results with the exact underground horizontal electric field calculated using the Sommerfeld's integrals. His results are presented in the next section.

#### 11.5.8.3.1 Comparison with exact calculations

Figures 11.30 and 11.31 show the examples of underground horizontal electric fields, which were calculated using three different procedures by Cooray [38]. Curve 1 gives the exact field calculated using Sommerfeld's integrals. Curve 2 shows the underground electric field calculated from (11.65) using the exact horizontal electric field at the surface of the ground. Curve 3 shows the underground electric field calculated using the same equation but with the horizontal electric field at ground level calculated using (11.66). The results presented in Figures 11.30 and 11.31 show that (11.65) can be used to obtain the underground electric fields, provided that the horizontal electric field at ground level is calculated (or measured) accurately. It is possible to show that the results obtained using the horizontal electric field calculated from (11.65), which connects the surface horizontal electric field to the underground horizontal electric field, is valid for ground conductivities encountered in practices and for depths much less than the lateral distance to the lightning strikes. One can also use these equations with high accuracy to calculate the underground electric field if the horizontal electric field at the surface of the ground is measured.

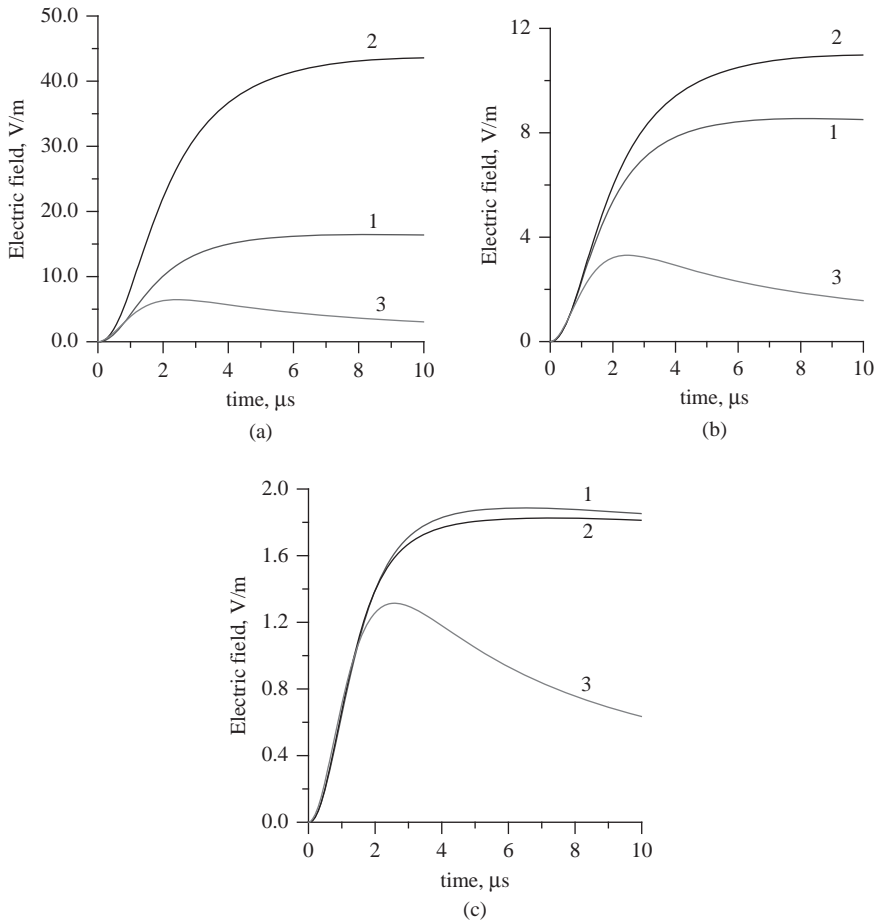
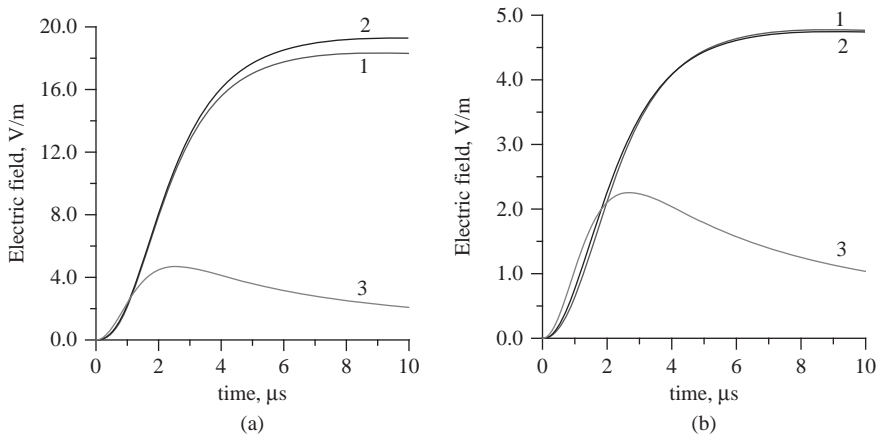


Figure 11.30 Underground first stroke horizontal electric fields at a depth of 10 m for (a)  $\rho = 10 \text{ m}, \sigma = 0.001 \text{ S/m}$ , (b)  $\rho = 20 \text{ m}, \sigma = 0.001 \text{ S/m}$ , (c)  $\rho = 50 \text{ m}, \sigma = 0.001 \text{ S/m}$ . Curve 1: Sommerfeld's integrals; Curve 2: Equation (11.65) with exact horizontal electric field at ground as input. Curve 3: Equation (11.65) with horizontal electric field calculated using surface impedance as input. In the calculations, the return stroke is modelled by using the MTLE model with a current decay height constant  $\lambda_e$  equal to 2 km. The return stroke speed is kept at  $1.5 \times 10^8 \text{ m/s}$ . The current waveform at ground level is simulated by the analytical expression given by (11.21). Adapted from [38]

If the depth is comparable to the distance to the lightning strike, as can be observed from Figures 11.30 and 11.31, equation 11.65 can generate large errors. Since the depths, which are of interest in practice, are on the order of metres, (11.65) – together with the exact horizontal electric field at ground level – can be used to evaluate underground fields at distances larger than about 50 m from the lightning strike. Note the significant error in the underground electric field when the surface horizontal electric field is calculated using the surface impedance expression. As shown in section 11.5.6.3 the surface impedance expression can introduce





*Figure 11.31 Underground first stroke horizontal electric fields at a depth of 10 m for (a)  $\rho = 50$  m,  $\sigma = 0.0001$  S/m, (b)  $\rho = 100$  m,  $\sigma = 0.0001$  S/m. Curve 1: Sommerfeld's integrals; Curve 2: Equation (11.65) with exact horizontal electric field at ground as input. Curve 3: Equation (11.65) with horizontal electric field calculated using surface impedance as input. In the calculations, the return stroke is modelled by using the MTLE model with a current decay height constant  $\lambda_e$  equal to 2 km. The return stroke speed is kept at  $1.5 \times 10^8$  m/s. The current waveform at ground level is simulated by the analytical expression given by (11.21). Adapted from [38]*

significant errors in the horizontal electric field when the point of observation is in the vicinity of the lightning channel and the same errors cause the underground electric field to deviate significantly from the exact one. However, when the distance to the point of observation is large or when the conductivity of the ground is high this procedure can give results to a reasonable accuracy. This was also illustrated in the work of Delfino *et al.* [41].

## 11.6 Propagation over vertically stratified ground or multi-section path

### 11.6.1 Expressions for the attenuation function for a dipole at ground level

The geometry relevant to the question under consideration is shown in Figure 11.32. Let us represent the path of propagation of the electromagnetic field as consisting of several laterally stratified sections or multi-section path. In each section the soil conductivity is assumed to be uniform. Each section is represented by a distance  $\rho_n$ , conductivity  $\sigma_n$  and relative dielectric constant  $\epsilon_r$ . The lightning channel is located at a distance  $\rho$  from the point of observation. In the calculation the lightning channel is assumed to be straight and vertical. In order to write down the equations corresponding to paths with many land sections in compact form, let us define the parameters  $\rho_{1,0} = 0$ ,  $\rho_{1,1} = \rho_1$ ,  $\rho_{1,2} = \rho_1 + \rho_2$ ,  $\rho_{1,3} = \rho_1 + \rho_2 + \rho_3$  etc. Then for a land path of  $M$  sections  $\rho_{1,M} = \rho$ , where  $\rho$  is the total path length.

Let us represent the attenuation function in the frequency domain for a dipole at ground level over finitely conducting uniform ground of surface impedance  $\Delta_1$  at

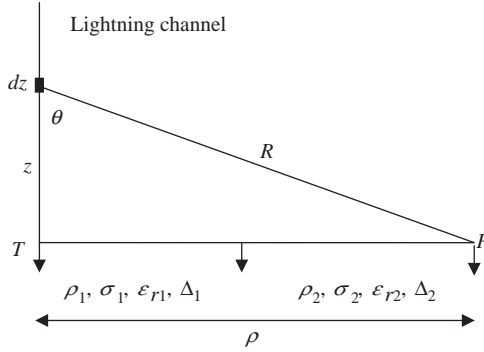


Figure 11.32 The geometry and the definition of various distances pertinent to the calculation of propagation effects caused by multi-section mixed path

a distance  $\rho$  from the dipole as  $w_{1-1}(\rho)$  (see (11.31)). With this notation the attenuation function corresponding to a dipole over homogeneous ground of surface impedance  $\Delta_s$  is represented by  $w_{s-s}(\rho)$ .

The attenuation function corresponding to a dipole at ground level over a two-section land path is given by [20, 42]

$$w_{1-2}(\rho) = w_{2-2}(\rho) - \left(\frac{j\rho}{2\lambda_0}\right)^{1/2} \int_0^{\rho_1} (\Delta_1 - \Delta_2)w_{1-1}(y_1)w_{2-2}(\rho - y_1) \frac{dy_1}{\sqrt{y_1(\rho - y_1)}} \tag{11.68}$$

where  $w_{1-2}(\rho)$  is the attenuation function for the two-section path,  $w_{2-2}(x)$  is the attenuation function associated with a path length of  $x$  over a ground of surface impedance  $\Delta_2$  and  $w_{1-1}(x)$  is the attenuation function corresponding to a similar path length over surface impedance  $\Delta_1$ .

$$w_{1-3}(\rho) = w_{3-3}(\rho) - \left(\frac{j\rho}{2\lambda_0}\right)^{1/2} \int_0^{\rho_{1,1}} (\Delta_1 - \Delta_3)w_{1-1}(y_1)w_{3-3}(\rho - y_1) \frac{dy_1}{\sqrt{y_1(\rho - y_1)}} - \left(\frac{j\rho}{2\lambda_0}\right)^{1/2} \int_{\rho_{1,1}}^{\rho_{1,2}} (\Delta_2 - \Delta_3)w_{1-2}(y_1)w_{3-3}(\rho - y_1) \frac{dy_1}{\sqrt{y_1(\rho - y_1)}} \tag{11.69}$$

where  $w_{1-2}(x)$  corresponds to the attenuation function of a two-section path with path length  $\rho_{1,1}$  over surface impedance of  $\Delta_1$  and a distance of  $x - \rho_{1,1}$  over surface impedance of  $\Delta_2$ . In the case of  $M$ -section land path:

$$w_{1-M}(\rho) = w_{M-M}(\rho) - \left(\frac{j\rho}{2\lambda_0}\right)^{1/2} \sum_{m=1}^M (\Delta_m - \Delta_M) \int_{\rho_{1,m-1}}^{\rho_{1,m}} w_{1-m}(y_1)w_{M-M}(\rho - y_1) \frac{dy_1}{\sqrt{y_1(\rho - y_1)}} \tag{11.70}$$

Note that in the above equation  $\rho_{1,0}=0$ . These equations define the attenuation function for multi-section path. For any given path this can be first calculated in frequency domain and the result can be Fourier transformed to get the time domain response that is necessary to get the time domain electromagnetic fields. In the next section we illustrate by example several interesting cases of propagation effects.

### 11.6.2 *Simplified expression for the electromagnetic fields from lightning over vertically stratified ground*

Recall that according to the approximations described in section 11.5.2.2, the radiation field at a distance  $\rho$  over homogeneous ground is given by

$$E_{z,\sigma}(t, \rho) = \int_0^t E_z(t - \tau, \rho) W_{s-s}(\rho) d\tau \quad (11.71)$$

where  $W_{s-s}(\rho)$  is the inverse Fourier transformation of the attenuation function corresponding to a dipole at ground level over the homogeneous ground surface of surface impedance  $\Delta_s$ , and  $E_z(t, \rho)$  is the radiation field over perfectly conducting ground. In the case of stratified ground of  $M$  sections the radiation field at a distance  $\rho$  is given by

$$E_{z,v\text{-stra}}(t, \rho) = \int_0^t E_z(t - \tau, \rho) W_{1-M}(\rho) d\tau \quad (11.72)$$

where  $W_{1-M}(\rho)$  is the inverse Fourier transformation of  $w_{1-M}(\rho)$  given by (11.70).

#### 11.6.2.1 **Validation of the simplified expression**

The accuracy of (11.72) was tested by Shoory *et al.* [13] taking as reference full-wave simulations obtained using the finite difference time domain technique. It was shown that this equation is capable of reproducing the distant peak field and the wave shape to a good accuracy. Several examples of the comparison as given by Shoory *et al.* are given in Figures 11.33 and 11.34.

### 11.6.3 *Some interesting effects of vertically stratified ground on radiation fields*

#### 11.6.3.1 **Sea gain effects**

Let us consider how the electromagnetic field varies in the case of two-section land, where one section is highly conducting and the other section relatively a poor conductor. This represents, for example, the case of an electromagnetic field generated by a lightning flash located over the sea and what happens to it as it propagates inland and vice versa. First, let us consider how an electromagnetic field generated by a return stroke located over the sea is modified as it penetrates into land. In the calculation, the conductivity of the ground is 0.001 S/m. Figure 11.35 shows what happens to the peak and the width of the pulse as it penetrates into the land path. The removal of high frequencies leads both to the attenuation and to the broadening of the initial peak and an increase in the rise time of the pulse. An interesting situation arises when the lightning flash is located over land but the electromagnetic field penetrates into the sea path. The length of the land path is

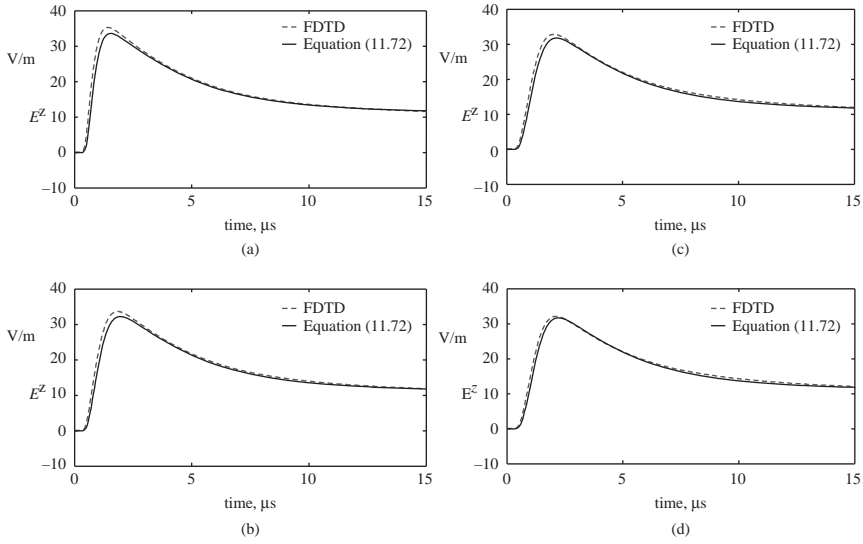


Figure 11.33 Vertical electric field at the surface of a mixed-path ground (two section) at a distance of  $\rho = 10$  km for  $\sigma_1 = 0.001$  S/m,  $\epsilon_{r1} = 10$ ,  $\sigma_2 = 4$  S/m,  $\epsilon_{r2} = 30$ . (a)  $\rho_2 = 7.5$  km, (b)  $\rho_2 = 2.5$  km, (c)  $\rho_2 = 0.5$  km and (d)  $\rho_2 = 0.1$  km. Adapted from [13]

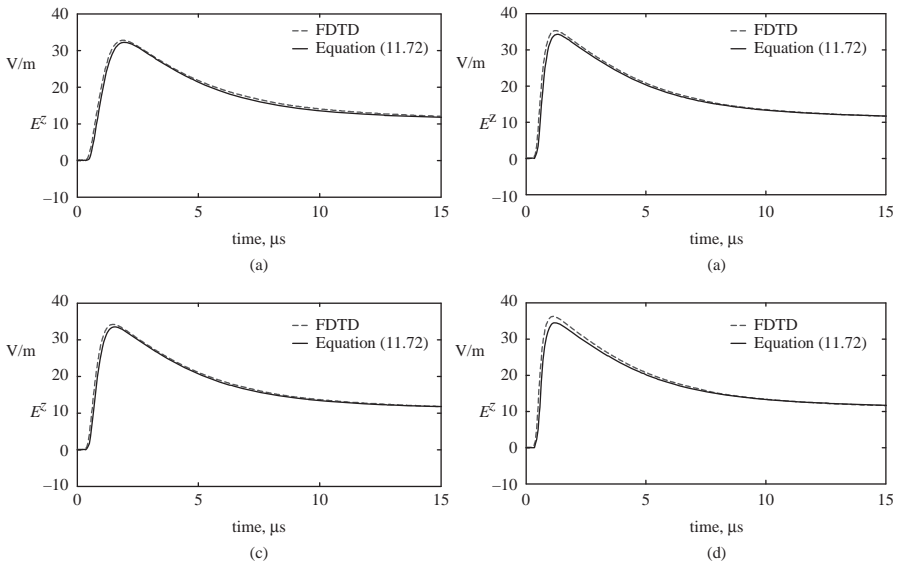
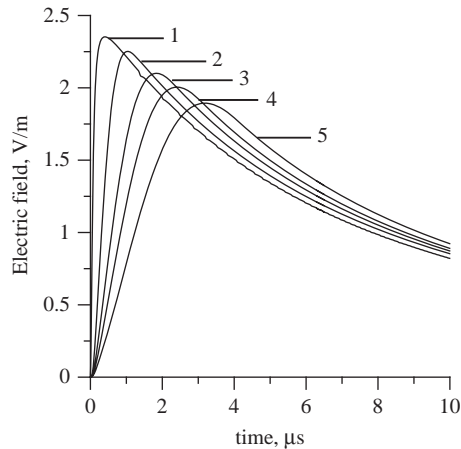


Figure 11.34 Vertical electric field at the surface of a mixed-path (two section) ground at a distance of  $\rho = 10$  km for  $\sigma_1 = 4$  S/m,  $\epsilon_{r1} = 30$ ,  $\sigma_2 = 0.001$  S/m,  $\epsilon_{r2} = 10$ . (a)  $\rho_2 = 7.5$  km, (b)  $\rho_2 = 2.5$  km, (c)  $\rho_2 = 0.5$  km and (d)  $\rho_2 = 0.1$  km. Adapted from [13]

now fixed at 100 km and the distance to the sea path is changed. The results are shown in Figure 11.36. Note that as the electromagnetic field propagates further into the sea it recovers some of the high frequencies. As a result the rise time starts decreasing and the peak amplitude starts increasing. The recovery can be seen



*Figure 11.35 Signature of the electric field of a lightning return stroke located over the sea at 100 km from the coast as it penetrates into land path. The conductivity of the land path is 0.002 S/m. The length of the land path is (2) 10 km, (3) 50 km, (4) 100 km and (5) 200 km. Curve 1 represents the electric field over perfectly conducting ground. Conductivity of sea water is 4 S/m and all waveforms are normalised to a common distance of 100 km. In the calculations, the return stroke is modelled by using the MTL model with a current decay height constant  $\lambda_e$  equal to 2 km. The return stroke speed is kept at  $1.5 \times 10^8$  m/s. The current waveform at ground level is simulated by the analytical expression given by (11.21). Adapted from [11]*

clearly in the case of electric field time derivatives shown in Figure 11.36b. This recovery is actually obtained by gaining some of the energy lost into the ground by the electromagnetic field propagating close to ground from the other parts of the field. It is actually not a reversal of the propagation effects.

### 11.6.3.2 Reciprocity

According to the principle of reciprocity, the same propagation effects should be observed when the receiver and the transmitter are interchanged. Though this is not apparent in the equations, calculations can be used to demonstrate its validity. An example of the calculation corresponding to the interchange of the path for a two-section layer is shown in Figure 11.37. As one can see the results are identical showing that the propagation effects are the same for the same path irrespective of the location of transmitter and receiver. This effect could actually be utilised to study whether there is any difference in the electromagnetic fields of return strokes of lightning flashes striking the ground and the sea. Measurements conducted at two stations one inland and the other located over the ocean can be used to check these effects. The measurements of electromagnetic fields of lightning striking at reciprocal locations in this case will provide information whether there is any difference in the electromagnetic fields. This is the case since the propagation effects have to be the same along the two paths. Such data can be obtained from the lightning location systems which provide the rise times and the amplitudes of lightning flashes striking at two locations. Of course, the experiment can be done completely over land sites if one can isolate lightning flashes in two regions – one

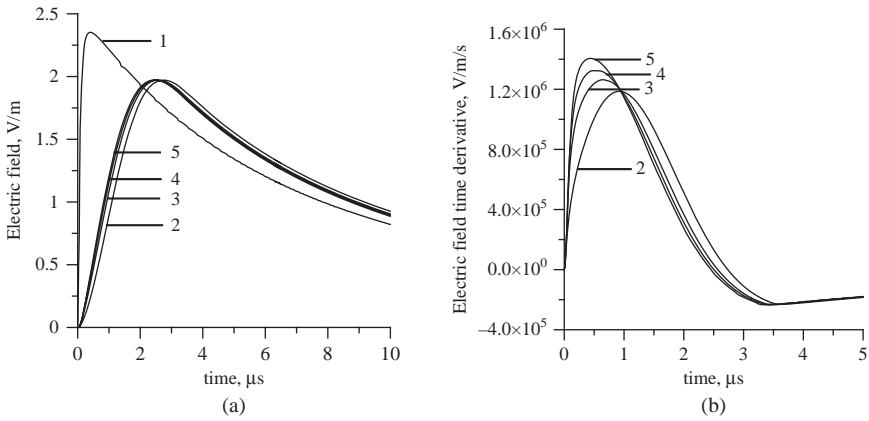


Figure 11.36 Signature of the (a) electric field and (b) electric field time derivative of a lightning return stroke located over land at 100 km from a coast line as it penetrates into the sea path. The length of the sea path is (2) 10 km, (3) 50 km, (4) 100 km and (5) 200 km. Curve 1 represents the electric field over perfectly conducting ground (this is not shown in (b)). Conductivity of sea water is 4 S/m and the conductivity of the land path is 0.002 S/m. All waveforms are normalised to a common distance of 100 km. In the calculations, the return stroke is modelled by using the MTLE model with a current decay height constant  $\lambda_e$  equal to 2 km. The return stroke speed is kept at  $1.5 \times 10^8$  m/s. The current waveform at ground level is simulated by the analytical expression given by (11.21). Adapted from [11]

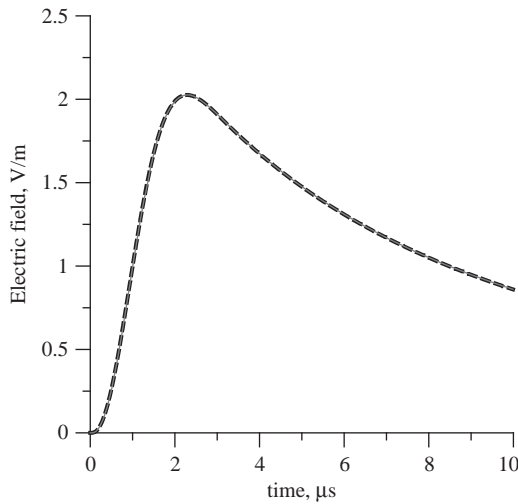
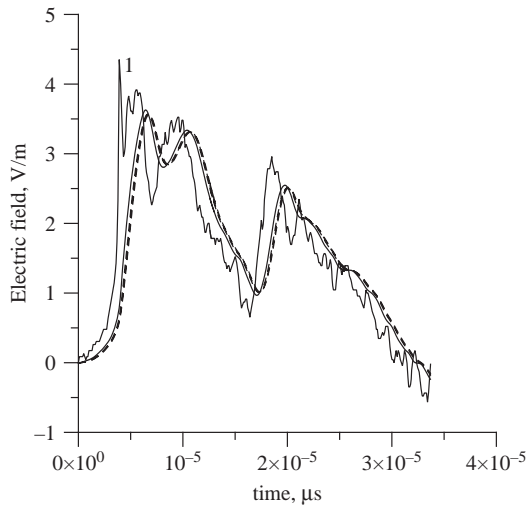


Figure 11.37 Effect of reversing the direction of the path of propagation. The solid line shows forward direction and the dashed line shows the reverse direction. Parameters of the calculation are  $\rho_1 = 200$  km,  $\sigma_1 = 0.01$  S/m,  $\rho_2 = 50$  km and  $\sigma_2 = 0.005$  S/m. In the calculations, the return stroke is modelled by using the MTLE model with a current decay height constant  $\lambda_e$  equal to 2 km. The return stroke speed is kept at  $1.5 \times 10^8$  m/s. The current waveform at ground level is simulated by the analytical expression given by (11.21). Adapted from [11]



*Figure 11.38 Signature of the waveform marked 1 after it has propagated along a three-section path. The path parameters are  $\rho_1 = 40$  km,  $\sigma_1 = 0.01$  S/m,  $\rho_2 = 40$  km,  $\sigma_2 = 0.001$  S/m,  $\rho_3 = 40$  km,  $\sigma_3 = 0.005$  S/m. The solid line shows the propagated waveform calculated using complete equations and the dashed line shows the one calculated using equivalent conductivity. The original waveform is obtained from a collection of range normalised first return stroke electric fields measured at a coastal station by Bailey and Willett [34] and Izumi and Willett [35]*

highly conducting and the other low conducting – and then study statistics of rise time of lightning flashes striking in one region as measured from the lightning location systems in the other region.

### 11.6.3.3 Equivalent conductivity

Cooray and Perez [43] and Cooray and Cummins [11] have investigated whether a multi-section ground can be replaced by a homogeneous ground with equivalent conductivity. They showed that the equivalent conductivity of  $M$ -section land can be written as

$$\sigma_e = \frac{\sum_{m=1}^M \rho_m}{\sum_{m=1}^M \frac{\rho_m}{\sigma_m}} \quad (11.73)$$

In the case of two-section land it reduces to

$$\sigma_e = \frac{\rho_1 + \rho_2}{\frac{\rho_1}{\sigma_1} + \frac{\rho_2}{\sigma_2}} \quad (11.74)$$

where  $\rho_1, \rho_2$  etc. are the lengths of different land paths and  $\sigma_1, \sigma_2$  etc. are the respective conductivities. Cooray and Cummins [11] have compared the exact results with the results obtained using equivalent conductivity and a good agreement is found between them. This confirmed the possibility of using this equivalent conductivity in calculating propagation effects caused by vertically stratified ground. An example based on three-section land is shown in Figure 11.38.

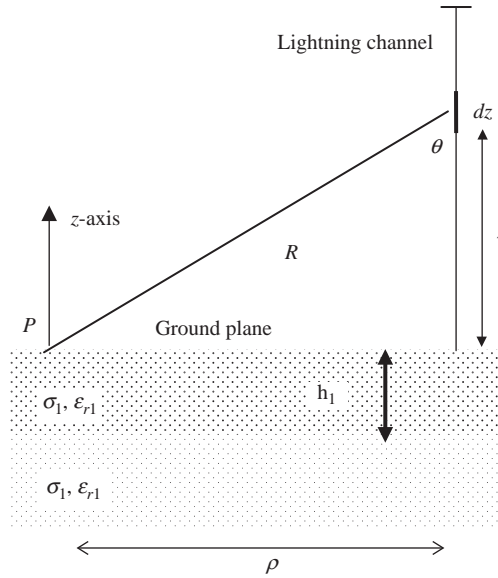


Figure 11.39 Geometry relevant to the analysis of propagation over horizontally stratified ground

## 11.7 Propagation effects over horizontally stratified ground

### 11.7.1 Wait's simplified expressions for the attenuation function for a dipole at ground level

The geometry relevant to the question under consideration is shown in Figure 11.39. Let us represent the ground as a stratum of thickness  $h_1$ , conductivity  $\sigma_1$  and relative dielectric constant  $\epsilon_{r1}$  below which the medium is semi-infinite with conductivity  $\sigma_2$  and dielectric constant  $\epsilon_{r2}$ . The surface impedance of the two layers are denoted by  $\Delta_1$  and  $\Delta_2$ . The dipole is located at a distance  $\rho$  from the point of observation.

According to Wait [44], the attenuation function corresponding to a dipole at ground level over horizontally stratified ground can be obtained by replacing the surface impedance in (11.26)–(11.31) by the effective surface impedance given by

$$\Delta_{eff} = \Delta_1 Q \quad (11.75)$$

where

$$Q = \frac{\Delta_2 + \Delta_1 \tanh(ju_1 h_1)}{\Delta_1 + \Delta_2 \tanh(ju_1 h_1)}; u_1 = k_1 \left[ 1 - \left( \frac{k_0}{k_1} \right)^2 \right] \quad (11.76a)$$

The ratios  $\left(\frac{k_0}{k_1}\right)^2$  and  $\left(\frac{k_0}{k_2}\right)^2$  are much less than unity in many cases. In those cases (11.76a) will be reduced to

$$Q = \frac{k_1 + k_2 \tanh(jk_1 h_1)}{k_2 + k_1 \tanh(jk_1 h_1)} \quad (11.76b)$$



In equations (11.76a) and (11.76b)

$$\Delta_1 = \frac{k_0}{k_1} \left( 1 - \frac{k_0^2}{k_1^2} \right)^{1/2} \quad (11.77a)$$

$$\Delta_2 = \frac{k_0}{k_2} \left( 1 - \frac{k_0^2}{k_2^2} \right)^{1/2} \quad (11.77b)$$

$$k_1 = k_0 [\varepsilon_{r1} - j60\sigma_1\lambda_0]^{1/2} \quad (11.78a)$$

$$k_2 = k_0 [\varepsilon_{r2} - j60\sigma_2\lambda_0]^{1/2} \quad (11.78b)$$

The attenuation function corresponding to a dipole at ground level over horizontally stratified ground is then given by

$$w_{h-str}(\rho) = 1 - j(\pi\eta)^{1/2} e^{-\eta} \operatorname{erfc}(j\eta^{1/2}) \quad (11.79)$$

with

$$\eta = -\frac{jk_0\rho}{2} [\Delta_{eff}]^2 \quad (11.80)$$

### 11.7.2 *Simplified expression for the electromagnetic fields from lightning over vertically stratified ground*

Again using the same approximation as in the case of vertically stratified ground, the radiation field at a distance  $\rho$  over horizontally stratified ground is given by

$$E_{z,h-stra}(t, \rho) = \int_0^t E_z(t - \tau, \rho) W_{h-str}(\rho) d\tau \quad (11.81)$$

where  $W_{h-str}(\rho)$  is the inverse Fourier transformation of the attenuation function  $w_{h-str}(\rho)$  corresponding to a dipole at ground level over horizontally stratified ground.

#### 11.7.2.1 **Validity of simplified expression**

The accuracy of (11.81) was tested by Shoory *et al.* [14], taking as reference the full-wave simulations obtained using the finite difference time domain technique. It was shown that (11.81) is capable of reproducing the distant peak field and the waveshape to a good accuracy. Several examples of the comparison as given by Shoory *et al.* are given in Figures 11.40 and 11.41.

### 11.7.3 *Some interesting effects of horizontally stratified ground on radiation fields*

#### 11.7.3.1 **Stratified ground with two layers – field enhancement cause by stratified ground**

The attenuation function in the frequency domain for several values of  $\sigma_2$  while keeping  $\sigma_1$  and  $h_1$  constant is shown in Figure 11.42. In the calculation the relative dielectric constants  $\varepsilon_{r1}$  and  $\varepsilon_{r2}$  were kept constant at 5. Note that for  $\sigma_1 < \sigma_2$  the attenuation function is larger than unity for certain frequencies. The reason for this is that when  $\sigma_1 < \sigma_2$ , the energy is being guided along the surface [44]. Of course,

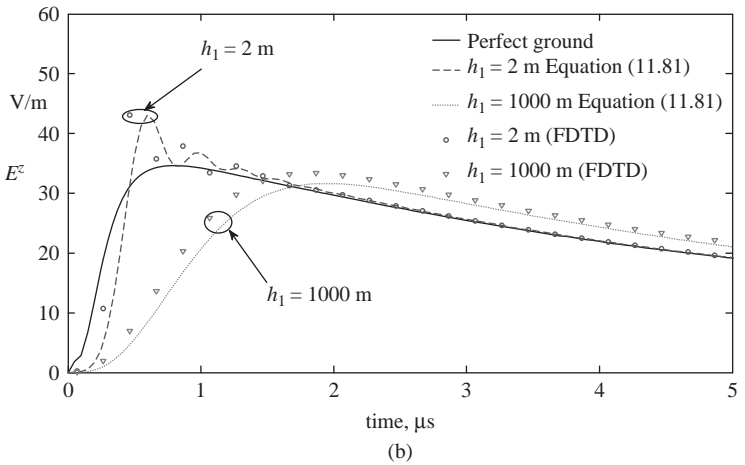
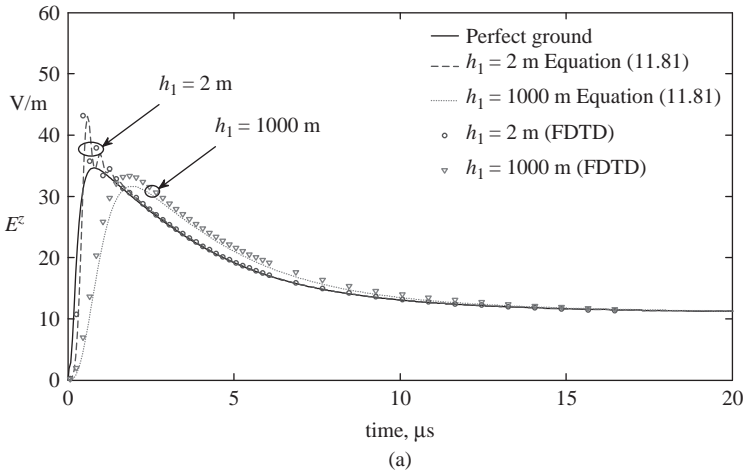


Figure 11.40 Vertical electric field at ground level at a distance of  $\rho = 10$  km with  $h_1 = 2$  m and  $h_1 = 1000$  m obtained using (11.81) and FDTD technique. (a) 20- $\mu$ s time window, (b) 5- $\mu$ s time window. The electrical parameters used in the calculation are  $\sigma_1 = 0.001$  S/m,  $\epsilon_{r1} = 10$ ,  $\sigma_2 = 4$  and  $\epsilon_{r2} = 30$ . Adapted from [14]

this enhancement of the field depends on the thickness of the upper layer. If the thickness of the upper layer is much larger than the skin depth corresponding to a certain frequency, then for that particular frequency the stratified ground behaves as homogeneous ground with conductivity  $\sigma_1$ . In the case of  $\sigma_1 > \sigma_2$  the amplitude of the attenuation function is always less than unity and it decreases monotonically with increasing frequency.

Figure 11.43 shows the electric field at 10 km generated by a lightning flash over stratified ground. For comparison purposes the electric fields that would be present over perfectly conducting ground and over homogeneous ground with conductivity equal to that of the upper or lower layer are also shown in the diagram. Figure 11.44 depicts the corresponding waveforms at 50 km distances. Note that when  $\sigma_1 > \sigma_2$ , the peak electric field is always lower than the one that is present over perfectly conducting ground. On the other hand, when  $\sigma_1 < \sigma_2$ ,

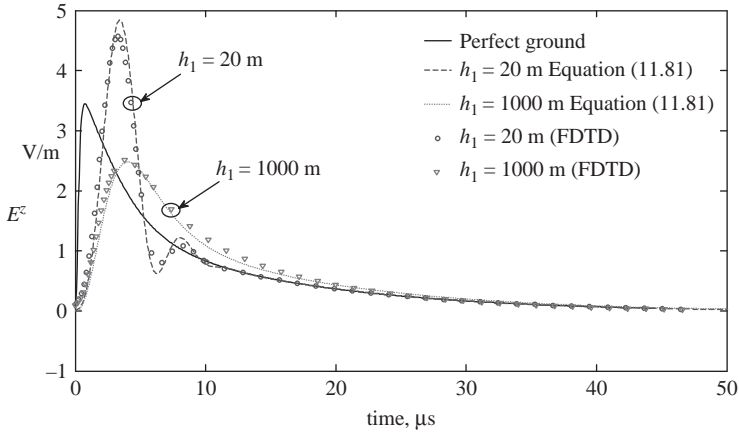


Figure 11.41 Vertical electric field at ground level at a distance of  $\rho = 100$  km with  $h_1 = 20$  m and  $h_1 = 1000$  m obtained using (11.81) and FDTD technique. The electrical parameters used in the calculation are  $\sigma_1 = 0.001$  S/m,  $\epsilon_{r1} = 10$ ,  $\sigma_2 = 4$  and  $\epsilon_{r2} = 30$ . Adapted from [14]

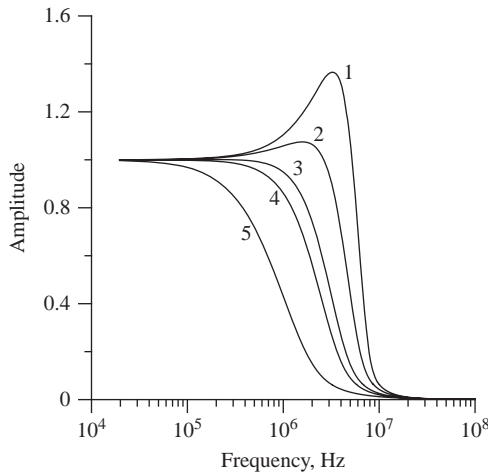
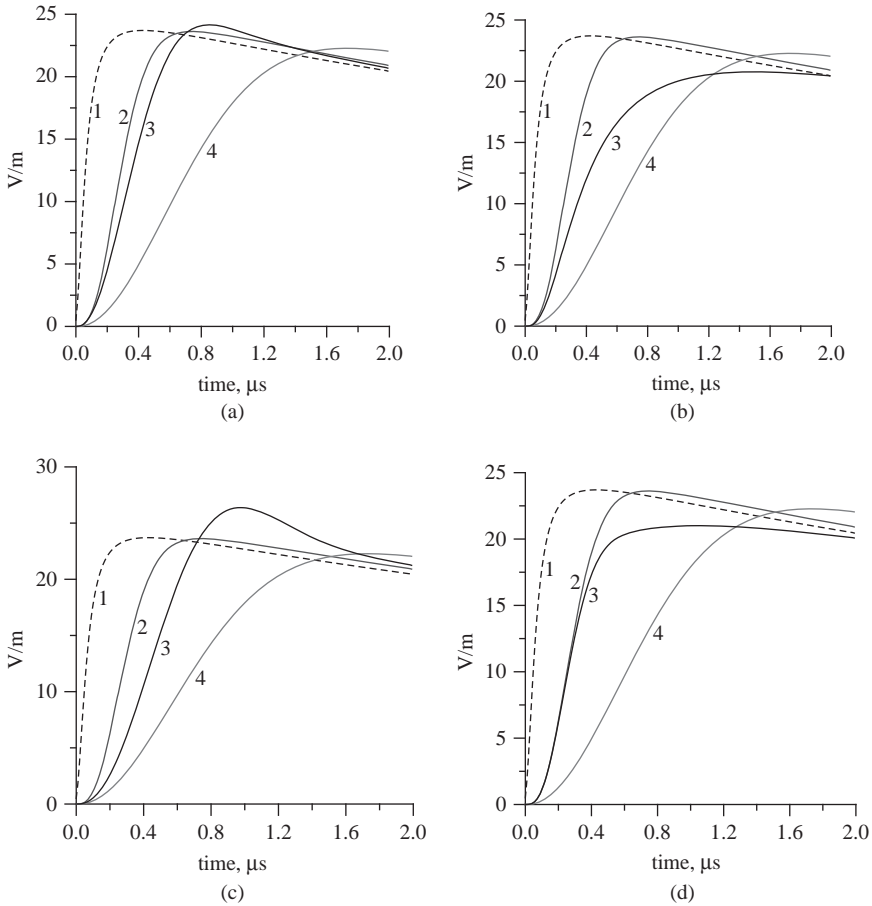


Figure 11.42 Attenuation function at 10 km as a function of frequency for stratified ground with two layers. The thickness of the upper layer,  $h_1$ , is 2 m. (1)  $\sigma_1 = 0.001$  S/m,  $\sigma_2 = 0.1$  S/m. (2)  $\sigma_1 = 0.001$  S/m,  $\sigma_2 = 0.01$  S/m. (3)  $\sigma_1 = 0.001$  S/m,  $\sigma_2 = 0.002$  S/m. (4)  $\sigma_1 = 0.001$  S/m,  $\sigma_2 = 0.001$  S/m. (5)  $\sigma_1 = 0.001$  S/m,  $\sigma_2 = 0.0001$  S/m. In the calculation  $\epsilon_{r1}$  and  $\epsilon_{r2}$  were kept constant at 5. Adapted from [12]

the electric field may contain a peak larger than its counterpart over perfectly conducting ground.

### 11.7.3.2 Continuously stratified ground

In reality, the conductivity of the soil depends on the moisture content. The moisture content in soil can change in a complicated manner depending on the weather conditions such as rain and dry seasons. This makes the conductivity profile of soil as a function of depth more complicated. During rain the



**Figure 11.43** Electric field at 10 km generated by a lightning flash over stratified ground. In each figure, curve 1 is the field over perfectly conducting ground, curve 2 is the field over finitely conducting homogeneous ground of conductivity 0.01 S/m and curve 4 is the field over finitely conducting homogeneous ground of conductivity 0.001 S/m. Curve 3 corresponds to the electric field over stratified ground. (a)  $\sigma_1 = 0.001$  S/m,  $\sigma_2 = 0.01$  S/m,  $h_1 = 2$  m; (b)  $\sigma_1 = 0.01$  S/m,  $\sigma_2 = 0.001$  S/m,  $h_1 = 2$  m; (c)  $\sigma_1 = 0.001$  S/m,  $\sigma_2 = 0.01$  S/m,  $h_1 = 5$  m; (d)  $\sigma_1 = 0.01$  S/m,  $\sigma_2 = 0.001$  S/m,  $h_1 = 5$  m. In the calculations, the return stroke is modelled by using the MTLE model with a current decay height constant  $\lambda_e$  equal to 2 km. The return stroke speed is kept at  $1.5 \times 10^8$  m/s. In the calculation  $\epsilon_{r1}$  and  $\epsilon_{r2}$  were kept constant at 5. The current waveform at ground level is simulated by the analytical expression given by (11.21). Adapted from [12]

conductivity of upper soil increases and as the moisture penetrates into the ground the soil layers located at different depths will gradually become conducting. So immediately after the rain the conductivity is high at the surface and it decreases with increasing depth. However, at the end of the rainy season the surface soil layers gradually dry up while the layer with high conductivity moves down. Thus

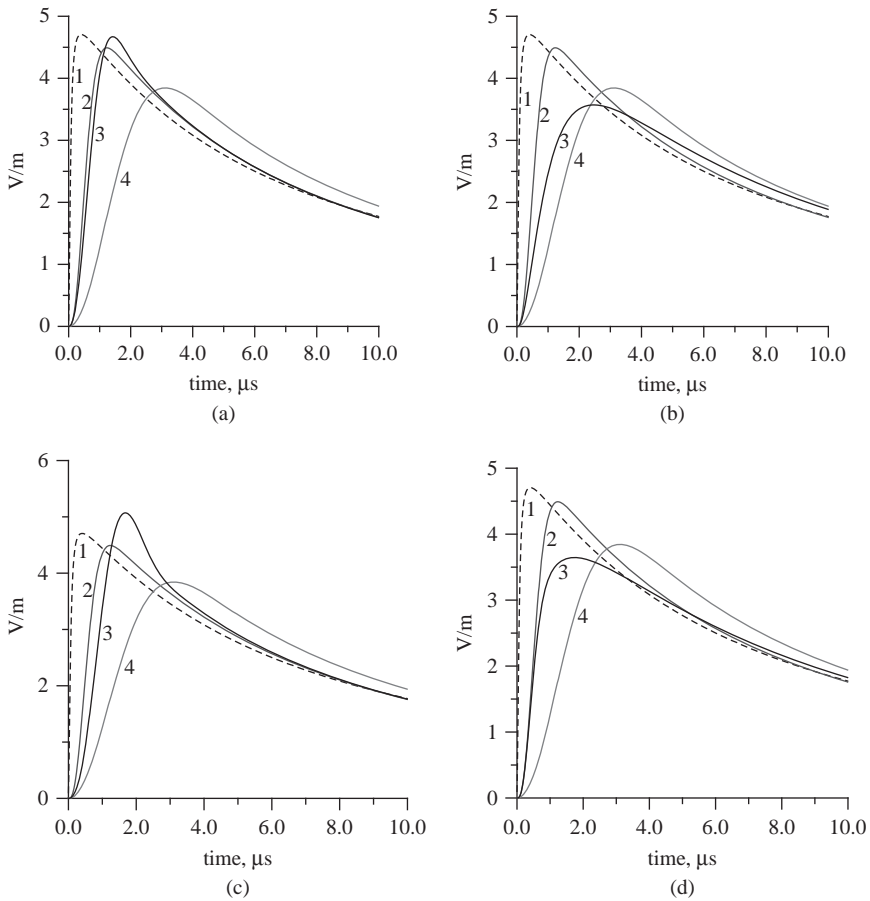


**Figure 11.44** *Electric field at 50 km generated by a lightning flash over stratified ground. In each figure, curve 1 is the field over perfectly conducting ground, curve 2 is the field over finitely conducting homogeneous ground of conductivity 0.01 S/m and curve 4 is the field over finitely conducting homogeneous ground of conductivity 0.001 S/m. Curve 3 corresponds to the electric field over stratified ground. (a)  $\sigma_1 = 0.001$  S/m,  $\sigma_2 = 0.01$  S/m,  $h_1 = 2$  m; (b)  $\sigma_1 = 0.01$  S/m,  $\sigma_2 = 0.001$  S/m,  $h_1 = 2$  m; (c)  $\sigma_1 = 0.001$  S/m,  $\sigma_2 = 0.01$  S/m,  $h_1 = 5$  m; (d)  $\sigma_1 = 0.01$  S/m,  $\sigma_2 = 0.001$  S/m,  $h_1 = 5$  m. In the calculations, the return stroke is modelled by using the MTL model with a current decay height constant  $\lambda_e$  equal to 2 km. The return stroke speed is kept at  $1.5 \times 10^8$  m/s. In the calculation  $\epsilon_{r1}$  and  $\epsilon_{r2}$  were kept constant at 5. The current waveform at ground level is simulated by the analytical expression given by (11.21). Adapted from [12]*

the conductivity profile varies with time and this provides a possibility to utilise the attenuation on high frequencies and electromagnetic fields to remote sense the soil parameters. Cooray and Cummins [12] studied the effects of such a conductivity profile on electromagnetic fields. Figure 11.45 shows two conductivity profiles analysed by Cooray and Cummins [12] that is in line with this description. In one

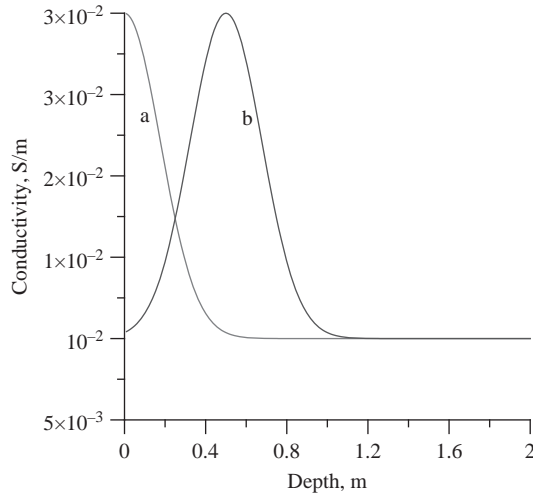


Figure 11.45 Two conductivity profiles selected in the calculations. In profile (a) the conductivity is maximum at the surface and in profile (b) it has moved to depth of about 0.6 m. The variation of conductivity with depth is assumed to be Gaussian. Adapted from [12]

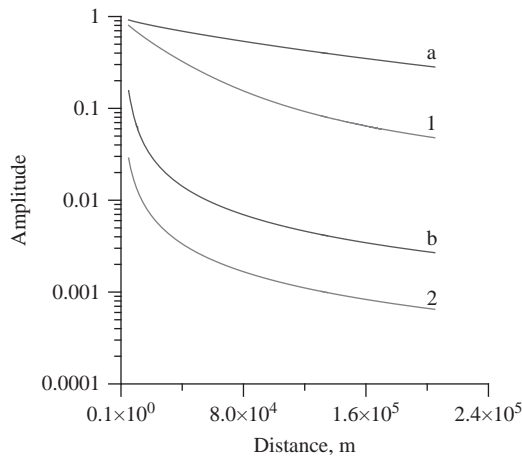
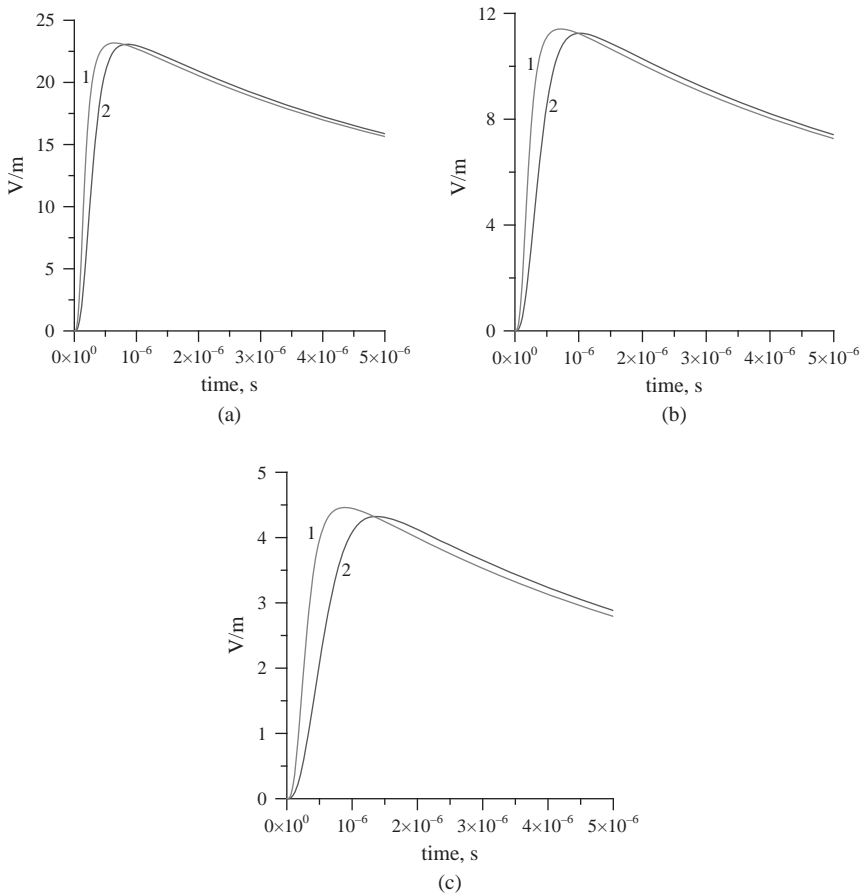


Figure 11.46 The amplitude of the electromagnetic field at different distances corresponding to conductivity profile (a) in Figure 11.45 (curves marked 1 and 2) and conductivity profile (b) in Figure 11.45 (curves marked a, b). The frequencies corresponding to the curves are  $10^6$  Hz (1 and a) and  $10^7$  Hz (2 and b). In the calculation the relative dielectric constant of all layers were fixed at 5. Adapted from [12]

profile the conductivity is high at the surface while in the other it increases with depth initially and then decreases again.

Figure 11.46 shows how the amplitude of the electromagnetic field at different frequencies varies as a function of distance when the ground is stratified according to Figure 11.45. Note that the shifting of the high conducting layer downwards



*Figure 11.47 Electric field corresponding to two conductivity profiles shown in Figure 11.45. (a) 10 km, (b) 20 km and (c) 50 km. The curves marked 1 correspond to profile b in Figure 11.45 and the curves marked 2 correspond to profile a in Figure 11.45. In the calculations, the return stroke is modelled by using the MTL model with a current decay height constant  $\lambda_e$  equal to 2 km. The return stroke speed is kept at  $1.5 \times 10^8$  m/s. The current waveform at ground level is simulated by the analytical expression given by (11.21). In the calculation the relative dielectric constant of all layers were fixed at 5. Adapted from [12]*

produces a significant change in the amplitude of the electromagnetic field at the two frequencies considered. They have also studied the effect of these conductivity profiles on the time domain electromagnetic fields radiated by lightning flashes. Figures 11.47 and 11.48 depict the electric field and the electric field derivative at 10, 20 and 50 km for the two conductivity profiles shown in Figure 11.45. Note that there is a significant difference in the field derivatives in the two cases. However, the difference is not that significant in the case of the rise time.

The results show that one can use single frequencies over the range of  $10^6$ – $10^7$ , the rise time of the radiation field or the time derivative of the radiation field to remote sense the seasonal variations of electrical parameters of the soil.

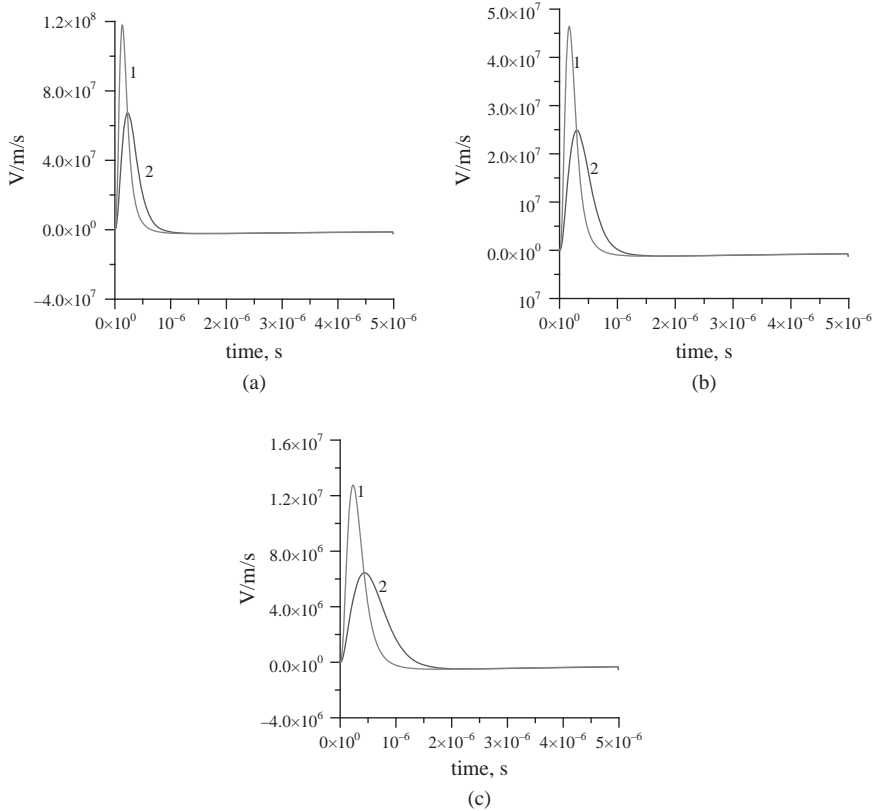


*Figure 11.48 Electric field time derivative corresponding to two conductivity profiles shown in Figure 11.45. (a) 10 km, (b) 20 km and (c) 50 km. The curves marked 1 correspond to profile b in Figure 11.45 and the curves marked 2 correspond to profile a in Figure 11.45. In the calculations, the return stroke is modelled by using the MTLE model with a current decay height constant  $\lambda_e$  equal to 2 km. The return stroke speed is kept at  $1.5 \times 10^8$  m/s. The current waveform at ground level is simulated by the analytical expression given by (11.21). In the calculation the relative dielectric constant of all layers were fixed at 5. Adapted from [12]*

## 11.8 Future studies

The large-scale deployment of lightning localisation systems based on the time of arrival and the demand on the accuracy of these systems, which to a large extent depends on the propagation effects, calls for more detailed experimental and theoretical studies of propagation effects. In this respect, not much research work has been conducted on the effects of propagation along irregular terrain especially propagation across mountains. In addition to advancing our knowledge of the effects of propagation, such studies would lead to more accurate lightning localisation systems.



## References

- [1] Uman, M. A., C. E. Swanberg, J. A. Tiller, Y. T. Lin, and E. P. Krider, Effects of 200 km propagation on lightning return stroke electric fields, *Radio Sci.*, 11, 985–990, 1976.
- [2] Cooray, V., M. Fernando, T. Sörensen, T. Götschl, and A. Pedersen, Propagation of lightning generated transient electromagnetic fields over finitely conducting ground, *J. Atmos. Terres. Phys.*, 62, 583–600, 2000.
- [3] Gardner, R. L., Effects of propagation on lightning induced transient fields, *Radio Sci.*, 16, 337–384, 1981.
- [4] Cooray, V., and S. Lundquist, Effects of propagation on the rise time and the initial peaks of radiation fields from return strokes, *Radio Sci.*, 18, 409–415, 1983.
- [5] Le Vine, D. M., L. Gesell, and M. Kao, Radiation from lightning return strokes over a finitely conducting earth, *J. Geophys. Res.*, 91, 11897–11908, 1986.
- [6] Cooray, V., Effects of propagation on the return stroke radiation fields, *Radio Sci.*, 22, 757–768, 1987.
- [7] Ming, Y., and V. Cooray, Propagation effects caused by a rough ocean surface on the electromagnetic fields generated by lightning return strokes, *Radio Sci.*, 29, 73–85, 1994.
- [8] Cooray, V., and Y. Ming, Propagation effects on the lightning generated electromagnetic fields for homogeneous and mixed sea land paths, *J. Geophys. Res.*, 99, 10641–10652, 1994.
- [9] Cooray, V., Propagation effects due to finitely conducting ground on lightning generated magnetic fields evaluated using Sommerfeld's equations, *IEEE Trans. EMC*, vol. 51, 526–531, 2009.
- [10] Cooray, V., On the accuracy of several approximate theories used in quantifying the propagation effects on lightning generated electromagnetic fields, *Trans. IEEE: Antenn Propag.*, 56(7), 1960–1967, 2008.
- [11] Cooray, V., and K. Cummins, Propagation effects caused by multi-section mixed paths on electric fields of lightning return strokes, *International Symposium on Lightning Protection*, Kirubita, Brazil, 2009.
- [12] Cooray, V., and K. L. Cummins, Propagation effects caused by stratified ground on electromagnetic fields of return strokes, in *20th International Lightning Detection Conference & 2nd International Lightning Meteorology Conference*, Tucson, Arizona, USA, 2008.
- [13] Shoory, A., A. Mimouni, F. Rachidi, V. Cooray, and M. Rubinstein, On the accuracy of approximate techniques for the evaluation of lightning electromagnetic fields along a mixed propagation path, *Radio Sci.*, 46, 2011.
- [14] Shoory, A. *et al.* Validity of simplified approaches for the evaluation of lightning electromagnetic fields above a horizontally stratified ground, *IEEE Trans. EMC*, 52(3), 657–663, 2010.
- [15] Delfino, F., R. Procopio, and M. Rossi, Lightning return stroke current radiation in presence of a conducting ground: 1. Theory and numerical evaluation of electromagnetic fields, *J. Geophys. Res.*, 115, doi:10.1029/2007JD008553, 2008.
- [16] Delfino, F., R. Procopio, M. Rossi, F. Rachidi, and C. A. Nucci, An algorithm for the exact evaluation of the underground lightning electromagnetic fields, *IEEE Trans. EMC*, 49, 401–411, 2007.

- [17] Sommerfeld, A., Über die Ausbreitung der Wellen in der drahtlosen Telegraphie, *Ann. Phys.*, 28, 665, 1909.
- [18] Norton, K. A., Propagation of radio waves over the surface of Earth and in the upper atmosphere, II, *Proc. IEEE*, 25, 1203–1236, 1937.
- [19] Bannister, P. R., Extension of finitely conducting Earth-image-theory results to any range, Technical Report, Naval Underwater systems center, January 1984.
- [20] Maclean, T. S. M., and Z. Wu, *Radio wave propagation over ground*, Chapman & Hall, London, 1993.
- [21] Gomes, C., and V. Cooray, Concepts of lightning return stroke models, *IEEE Trans. EMC*, 42(1), 82–96, 2000.
- [22] Nucci, C. A., C. Mazzetti, F. Rachidi, and M. Ianoz, On lightning return stroke models for LEMP calculations, Paper presented at the *19th International Conference on Lightning Protection*, Graz, Austria, 1988.
- [23] Nucci, C. A., G. Diendorfer, M. A. Uman, F. Rachidi, M. Ianoz, and C. Mazetti, Lightning return stroke models with specified channel base current: A review and comparison, *J. Geophys. Res.*, 95, 20395–20408, 1990.
- [24] Heidler, F., Analytische blitzstromfunktion zur LEMP-berechnung, *18th International Conference on Lightning Protection*, Munich, Germany, 1985.
- [25] Baba, Y., and V. A. Rakov, Evaluation of lightning return stroke electromagnetic models, *29th International Conference on Lightning Protection*, Uppsala, Sweden, 2008.
- [26] Mimouni, A., F. Rachidi, and A. Azzouz, Electromagnetic fields in the immediate vicinity of a tower struck by lightning, *29th International Conference on Lightning Protection*, Uppsala, Sweden, 2008.
- [27] Caligaris, C., F. Delfino, and R. Procopio, Cooray-Rubinstein formula for the evaluation of lightning radial electric fields: Derivation and implementation in the time domain, *IEEE Trans. EMC*, 50, 194–197, 2008.
- [28] Rubinstein, M., An approximate formula for the calculation of the horizontal electric field from lightning at close, intermediate and long range, *IEEE Trans. EMC*, 38, 531–535, 1996.
- [29] Wait, J. R., Transient fields of a vertical dipole over homogeneous curved ground, *Can. J. Phys.*, 36, 9–17, 1956.
- [30] Weidman, C. D., and E. P. Krider, Submicrosecond structure of the return stroke waveforms, *Geophys. Res. Lett.*, 7, 955–958, 1980.
- [31] Willett, J. C., and E. P. Krider, Rise times of impulsive high current processes in cloud to ground lightning, *IEEE (Antennas and Propagation)*, 48, 1442–1451, 2000.
- [32] Le Vine, D. M., J. C. Willett, and J. C. Bailey, Comparison of fast electric field changes from subsequent return strokes of natural and triggered lightning, *J. Geophys. Res.*, 94(D11), 13259–13265, 1989.
- [33] Krider, E. P., C. Leteinturier, and J. C. Willett, Submicrosecond fields radiated during the onset of first return strokes in cloud-to-ground lightning, *J. Geophys. Res.*, 101, 1589–1597, 1996.
- [34] Bailey, J. C., and J. C. Willett, Catalog of absolutely calibrated, range normalised, wideband, electric field waveforms from located lightning flashes in Florida, NRL memorandum Report 6497, Naval Research Laboratory, Washington, DC, USA, 1989.

- [35] Izumi, Y., and J. C. Willett, Catalog of absolutely calibrated, range normalised, wideband, electric field waveforms from located lightning flashes in Florida, Environmental Research Papers, No. 1082, Phillips Laboratory, Directorate of Geophysics, Hanscom Air Force Base, Massachusetts, USA, 1991.
- [36] Cooray, V., Propagation effects on radiation field pulses generated by cloud flashes, of lightning generated transient electromagnetic fields over finitely conducting ground, *J. Atmos. Solar-Terr. Phys.*, 69, 1397–1406, 2007.
- [37] Cooray, V., Horizontal fields generated by return strokes, *Radio Sci.*, 27, 529–537, 1992.
- [38] Cooray, V., Horizontal Electric Field Above- And Underground Produced By Lightning Flashes, *IEEE Trans. EMC*, 52, 936–943, 2010.
- [39] Barbosa, C. F., and J. O. Paulino, A time domain formula for the horizontal electric field at the Earth surface in the vicinity of lightning, *IEEE Trans. EMC*, 52(3), 640–645, 2010.
- [40] Cooray, V., Underground electromagnetic fields generated by the return strokes lightning flashes, *IEEE Trans. EMC*, 43, 75–84, 2001.
- [41] Delfino, F., R. Procopio, M. Rossi, F. Rachidi, and C. A. Nucci, Lightning return stroke current radiation in presence of a conducting ground: 2. Validity assessment of simplified approaches, *J. Geophys. Res.*, 113, D05111, doi:10.1029/2007JD008567, 2008.
- [42] Wait, J. R., On the theory mixed-path ground-wave propagation on a spherical Earth, *J. Res. Natl. Inst. Stand. Technol.*, 65D(4), 401–410, 1961.
- [43] Cooray, V., and H. Perez, Propagation effects on the first return stroke radiation fields: Homogeneous paths and mixed two section paths, Propagation effects on return stroke fields, 22nd ICLP, paper R1a-06, Budapest, 1994.
- [44] Wait, J. R., *Electromagnetic waves in stratified media*, Pergamon Press, Oxford, England, 1962.

---

## Chapter 12

# Interaction of electromagnetic fields generated by lightning with overhead electrical networks

*Carlo Alberto Nucci and Farhad Rachidi*

---

### 12.1 Introduction

Overvoltages induced by indirect lightning on overhead lines can cause damage to power systems, communication network or electronic control and management systems. Moreover, due to its more frequent occurrence, indirect lightning constitutes a more important cause of short interruptions and voltage sags than direct strikes, especially for distribution networks. Their estimation is therefore crucial for the correct protection and insulation co-ordination of overhead lines and, as a consequence, has been the subject of various studies during the past decades. The problem has been seriously reconsidered in the most recent years due to the increasing demand by customers for good quality in the power supply, and new models have been consequently developed to obtain a more accurate estimation of lightning-induced voltages.

The evaluation of lightning-induced voltages requires the knowledge of the electromagnetic field change along the line conductors of the considered electrical power network. This electromagnetic field is generally determined assuming that the lightning return stroke channel is a straight vertical antenna above a conducting plane (see Chapter 5). The spatial and temporal distribution of the current along the channel is specified using a return stroke model (see Chapter 6).

In this chapter, we present the theory describing the interaction of lightning electromagnetic fields with overhead lines, with particular reference to electrical power networks. In the first part of the chapter, we will present different approaches and formulations that can be used to describe the coupling between an external electromagnetic field and a transmission line. Then, we will extend the selected field-to-transmission line coupling model to include the effects of a lossy earth serving as a return conductor and to deal with the case of multiconductor lines. The time-domain representation of coupling equations, useful for analysing nonlinearities, will also be dealt with. The experimental test and validation of coupling models using data from natural and artificially triggered lightning, EMP simulators, or reduced scale models will also be presented in the first part of the chapter. In the second part of the chapter, we will apply the illustrated mathematical models to compute lightning-induced overvoltages on overhead power distribution lines.<sup>1</sup>

<sup>1</sup>In addition to what has been mentioned earlier, it is worth mentioning that lightning-induced voltages are of concern essentially for distribution overhead lines as transmission lines are characterised by insulation levels larger than typical magnitudes of lightning-induced voltages.

We will discuss, in particular, the influence on the amplitude and waveshape of lightning-induced voltages of

- the finite ground conductivity,
- the presence of shielding wires,
- the downward leader phase of the lightning discharge that precedes the return stroke phase and
- the corona effect.

## 12.2 Field-to-transmission line coupling models

### 12.2.1 Use of the transmission line theory

To solve the problem of lightning electromagnetic field coupling to an overhead line, the use could be made of the antenna theory, the general approach based on Maxwell's equations<sup>2</sup> [1]. However, due to the length of overhead lines, the use of such a theory for the calculation of lightning-induced voltages implies prohibitively long computation time, especially when statistical studies are desired (e.g. [2]). On the other hand, the use of quasi-static approximation [1], according to which propagation is neglected and coupling between incident electromagnetic fields and line conductors can be described by means of lumped elements, is not appropriate. In fact, such an approach requires that the overall dimensions of the circuit be smaller than about one tenth of the minimum significant wavelength of the electromagnetic field, an unacceptable assumption for the case of power lines illuminated by lightning electromagnetic pulse (LEMP).<sup>3</sup>

Assuming that the cross-sectional dimensions of the line are electrically small, we can consider that propagation occurs only along the line axis. This is one of the basic assumptions of the transmission line (TL) theory. In this way, the line can be represented by a distributed-parameter structure along its axis. Another fundamental assumption in the TL theory is that the response of the line is quasi-transverse electromagnetic (quasi-TEM). In other words, the electromagnetic field produced by the electric charges and currents along the line is confined in the transverse plane and perpendicular to the line axis. Finally, another assumption in the TL theory is that the sum of the line currents at any cross section of the line is zero. In other words, the ground – the reference conductor – is the return path for the currents in the  $n$  overhead conductors.

For uniform transmission lines with electrically small cross-sectional dimensions (not exceeding about one tenth of the minimum significant wavelength of the exciting electromagnetic field), several theoretical and experimental studies have shown a fairly good agreement between results obtained using the TL approximation and results obtained either by means of antenna theory or experiments (see section 12.2.12). A detailed discussion of the validity of the basic assumptions of the TL theory is beyond the scope of this chapter (see [1] and [3–6] for further discussion). However, it is worth making the following remarks:

- It is in practice impossible that the response of a line be purely TEM. In fact, a pure TEM mode could occur only for the case of a lossless line above a

<sup>2</sup>Different methods based on this approach generally assume that the wire's cross section is smaller than the minimum significant wavelength (thin-wire approximation).

<sup>3</sup>The LEMP frequency spectrum extends up to significant frequencies of a few MHz and beyond, which corresponds to minimum wavelengths of about 100 m or less.

perfectly conducting ground and when the exciting electromagnetic field has no electric field component tangential to the line conductors. Note, however, that for LEMP-illuminated power lines, the quasi-TEM line response can be considered as a reasonable approximation [1].

- By assuming that the sum of all the currents is equal to zero, we are considering only ‘transmission line mode’ currents and neglecting the so-called ‘antenna mode’ currents. If we desire to compute the load responses of the line, this assumption is adequate because the antenna mode current response is small near the ends of the line. Along the line, however, and even for electrically small line cross section, the presence of antenna mode currents makes that the sum of the currents at a cross section is not necessarily equal to zero [1, 3]. However, the quasi-symmetry due to the presence of the ground plane results in a very small contribution of antenna mode currents and consequently the predominant mode on the line will be transmission line [1].

### 12.2.2 Case of single-wire line above a perfectly conducting ground

We will consider first the simple case of a lossless single-wire line above a perfectly conducting ground. This simple case will be helpful to introduce various coupling models and to discuss some basic concepts. Later in this chapter (sections 12.2.8 and 12.2.10), we will cover the cases of lossy and of multiconductor lines. The transmission line is defined by its geometrical parameters (wire radius  $a$  and height above ground  $h$ ) and its termination impedances  $Z_A$  and  $Z_B$  (see Figure 12.1). The line is illuminated by an arbitrary external electromagnetic field. The problem of interest is the calculation of the induced voltages and currents along the line and at the terminations.

It is worth noting that the external exciting electric and magnetic fields  $\vec{E}^e, \vec{B}^e$  are defined as the sum of the lightning channel incident fields  $\vec{E}^i, \vec{B}^i$  and the ground-reflected fields  $\vec{E}^r, \vec{B}^r$  determined in absence of the line conductor.

### 12.2.3 Agrawal et al. model

By integrating Maxwell’s equations along the integration path defined in Figure 12.1 and using the transmission line approximation, Agrawal *et al.* [7] have derived a set

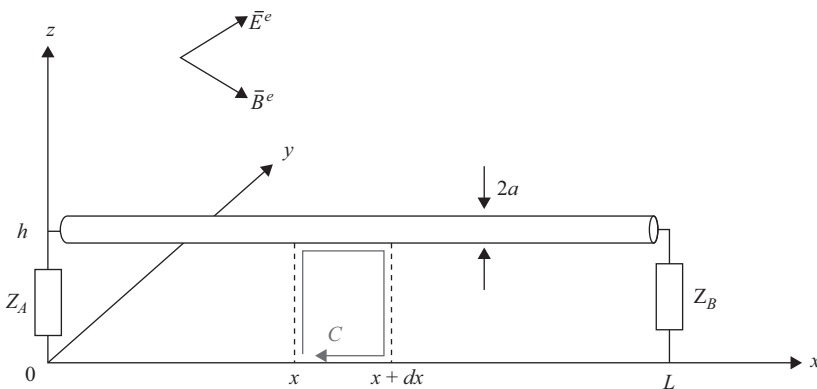


Figure 12.1 Geometry of the problem

of coupling equations, which, for the case of Figure 12.1, can be written in the frequency domain as [1]

$$\frac{dV^s(x)}{dx} + j\omega L'I(x) = E_x^e(x, 0, h) \tag{12.1}$$

$$\frac{dI(x)}{dx} + j\omega C'V^s(x) = 0 \tag{12.2}$$

in which

- $L'$  and  $C'$  are the per-unit-length inductance and capacitance of the line, respectively,<sup>4</sup>
- $I(x)$  is the induced current,
- $V^s(x)$  is the scattered voltage, related to the total voltage  $V(x)$  by the following expression:

$$V^s(x) = V(x) - V^e(x) \tag{12.3}$$

where  $V^e(x) = -\int_0^h E_z^e(x, z)dz$  is the exciting voltage,

- $E_x^e(x, h)$  and  $E_z^e(x, z)$  are the horizontal (along the conductor) and vertical components of the exciting electric field respectively.

The boundary conditions in terms of the scattered voltage and the total current as used in (12.1) and (12.2) are given by

$$V^s(0) = -Z_A I(0) + \int_0^h E_z^e(0, 0, z)dz \tag{12.4}$$

$$V^s(L) = Z_B I(L) + \int_0^h E_z^e(L, 0, z)dz \tag{12.5}$$

The equivalent circuit representation of (12.1), (12.2), (12.4) and (12.5) is shown in Figure 12.2. For this model, the forcing function is the exciting electric

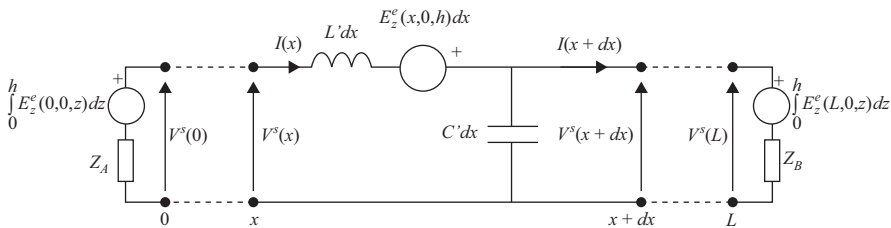


Figure 12.2 Equivalent circuit of a lossless, single-wire overhead line excited by an electromagnetic field (Agrawal et al. formulation)

<sup>4</sup>Expressions for the line inductance and capacitance will be given in section 12.2.8.

field tangential to the line conductor represented by distributed voltage sources along the line. Note that, in accordance with boundary conditions (12.4) and (12.5), two lumped voltage sources (equal to the line integral of the exciting vertical electric field) are inserted at the line terminations, which are generally denoted with the term ‘risers’.

### 12.2.4 Taylor, Satterwhite, and Harrison model

Although the Agrawal *et al.* model is the most adopted in the power/lightning literature, it is worth observing that an equivalent formulation of field-to-transmission line coupling equations was proposed earlier by Taylor, Satterwhite and Harrison in 1965 [8]. In the Taylor *et al.* formulation, the coupling equations are expressed in terms of the total induced current and the total induced voltage. They are given by

$$\frac{dV(x)}{dx} + j\omega L'I(x) = -j\omega \int_0^h B_y^e(x, 0, z) dz \tag{12.6}$$

$$\frac{dI(x)}{dx} + j\omega C'V(x) = -j\omega C' \int_0^h E_z^e(x, 0, z) dz \tag{12.7}$$

and the boundary conditions are expressed as

$$V(0) = -Z_A I(0) \tag{12.8}$$

$$V(L) = Z_B I(L) \tag{12.9}$$

These equations contain two forcing functions that are expressed in terms of the exciting transverse magnetic induction (distributed series voltage source), and of the exciting vertical electric field (distributed parallel current source) respectively, as shown in the equivalent circuit in Figure 12.3.

The Taylor formulation has been widely used in the electromagnetic compatibility literature, with particular reference to the interaction between nuclear electromagnetic pulse (NEMP) and transmission lines (e.g. [9]).

### 12.2.5 Rachidi model

Another form of coupling equations, equivalent to the Agrawal *et al.* and to the Taylor *et al.* models, has been derived by Rachidi [10]. In this formulation, only

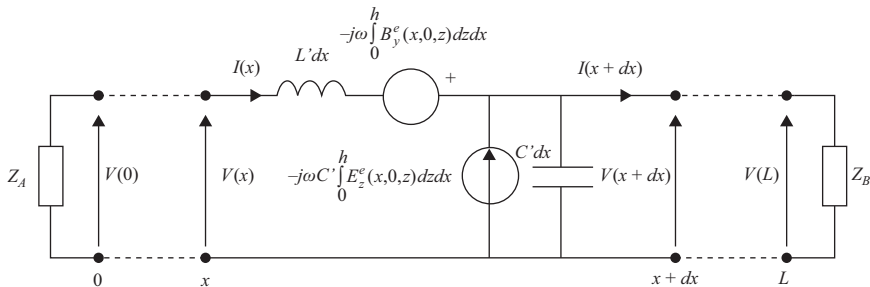


Figure 12.3 Equivalent circuit of a lossless single-wire overhead line excited by an electromagnetic field (Taylor *et al.* formulation)



the exciting magnetic field components appear explicitly as forcing functions in the equations

$$\frac{dV(x)}{dx} + j\omega L'I^s(x) = 0 \tag{12.10}$$

$$\frac{dI^s(x)}{dx} + j\omega C'V(x) = \frac{1}{L'} \int_0^h \frac{\partial B_x^e(x, 0, z)}{\partial y} dz \tag{12.11}$$

in which  $I^s(x)$  is the so-called scattered current related to the total current by

$$I(x) = I^s(x) + I^e(x) \tag{12.12}$$

where the excitation current  $I^e(x)$  is defined as

$$I^e(x) = -\frac{1}{L'} \int_0^h B_y^e(x, 0, z) dz \tag{12.13}$$

The boundary conditions corresponding to this formulation are

$$I^s(0) = -\frac{V(0)}{Z_A} + \frac{1}{L'} \int_0^h B_y^e(0, 0, z) dz \tag{12.14}$$

$$I^s(L) = \frac{V(L)}{Z_B} + \frac{1}{L'} \int_0^h B_y^e(L, 0, z) dz \tag{12.15}$$

The equivalent circuit corresponding to the above equivalent set of coupling equations is shown in Figure 12.4. Note that the equivalent circuit associated with the Rachidi model could be seen as the dual circuit – in the sense of electrical network theory – of the one corresponding to the Agrawal *et al.* model (Figure 12.2).

### 12.2.6 Contribution of the different components of the electromagnetic field in the coupling mechanism

In this section, we show that it is misleading to speak about the contribution of a given electromagnetic field component to the total induced voltage and current, without first specifying the coupling model one is using [11].

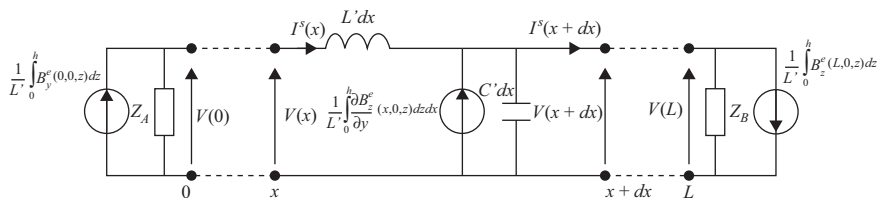


Figure 12.4 Equivalent circuit of a lossless single-wire overhead line excited by an electromagnetic field (Rachidi formulation)

Consider a 1 km long, 10 m high single-wire overhead line matched at both ends, above a perfectly conducting plane, illuminated by the electromagnetic field radiated by a nearby lightning return stroke. The components of the exciting electromagnetic field are calculated assuming a return stroke channel-base current typical of subsequent return strokes (peak value of 12 kA and maximum time derivative of 40 kA/ $\mu$ s) and using the MTLE return stroke current model [12, 13] (see Chapter 6). Nevertheless, the conclusions we will draw are independent of the nature of the transient electromagnetic source. The results predicted by the three coupling models are shown in Figure 12.5. These results have been obtained by solving numerically in the time-domain the coupling equations associated with the three considered formulations using the point-centred finite-difference time-domain (FDTD) technique. In addition to the total induced voltage at the line extremities, the contributions of the electromagnetic field components pertinent to each formulation are also shown.

Figure 12.5 shows that, as predicted theoretically, the total induced voltage waveforms obtained using the three coupling formulations are identical. However, the contribution of a given component of the exciting electromagnetic field to the total induced voltage varies depending on the adopted coupling model. For instance, for the considered case, the contribution of the vertical electric field  $E_z$ , significant in the model of Taylor *et al.* (Figure 12.5a), is practically negligible when using the model of Agrawal *et al.* (Figure 12.5b). This result can be explained considering that the source terms due to the vertical electric field are not the same in the two formulations: In the formulation of Taylor *et al.* the source term related to the vertical electric field acts along the whole line length, whereas in the formulation of Agrawal *et al.* the source related to the vertical electric field is localised only at the line terminations. The same reasoning can be applied to the contribution of other components, such as the transverse magnetic field  $B_y$  in the Taylor *et al.* and in the Rachidi formulations, or the horizontal electric field  $E_x$ , which contributes significantly to the total voltage in the Agrawal *et al.* model, but does not explicitly appear in the two other formulations.

The above illustrates that the three coupling models, which are equivalent and thus predicting the same total voltages, take into account the electromagnetic coupling in different ways, the various components of the electromagnetic field being related through Maxwell's equations. In other words, the three coupling models are different expressions of the same equations, cast in terms of different combinations of the various electromagnetic field components.

In conclusion, we have shown that the contribution of a given electromagnetic field in the coupling mechanism appears to strongly depend on the model used. Thus, when speaking about the contribution of a given electromagnetic field component to the induced voltages, one has first to specify the coupling model one is using.

### 12.2.7 Other models

Two other models have also been proposed and often used in the power literature to compute lightning-induced voltages on overhead lines, namely (1) the model by Rusck [14] and the model by Chowdhuri and Gross [15]. These two models are different from the Agrawal *et al.* model and its equivalent formulations, and the differences among these models have caused considerable discussion, disagreement and controversies among researchers and engineers dealing with lightning-induced

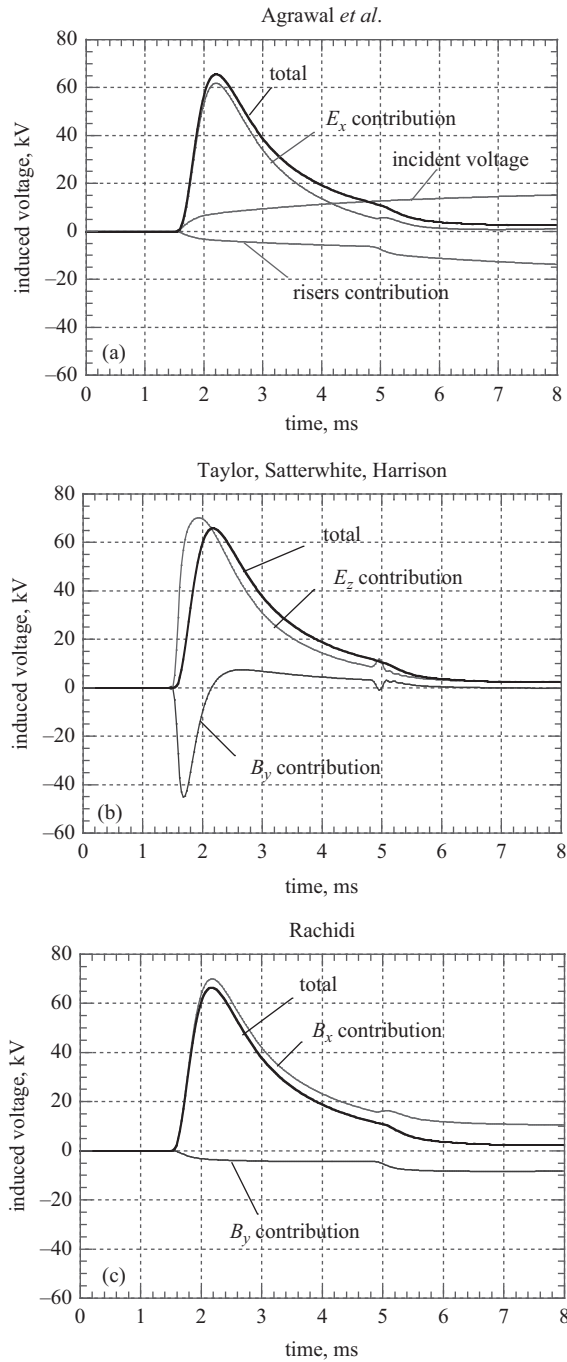


Figure 12.5 Illustration of the contribution of the various field components in the coupling mechanism: (a) Agrawal *et al.* model; (b) Taylor *et al.* model; (c) Rachidi model (adapted from Nucci and Rachidi [11])

voltage calculations (e.g. [16–23]). This is probably due to the fact that the models are expressed in terms of different quantities: the Rusck equations are written in terms of potentials, the Chowdhuri equations are expressed in terms of total voltage and the Agrawal *et al.* model is expressed in terms of scattered voltage. In two papers presented respectively by Nucci *et al.* [20] and Cooray [21], the different coupling equations have been rearranged in terms of similar quantities and it has been demonstrated that the Agrawal *et al.* model (or any of its equivalent formulations) is the only one that can be considered as rigorous within the limits of transmission line approximation, independently from the electromagnetic field source. In both Rusck and Chowdhuri–Gross models, some source terms are omitted. However, it is important to note that for the case of an electromagnetic field originated by a straight vertical channel,<sup>5</sup> the Rusck model becomes equivalent to the Agrawal *et al.* model and can therefore be adopted to predict the voltages induced by such a vertical lightning channel.

Since it is still adopted by some engineers and researchers, it is worth to remind here the analytical simplified Rusck formula [14], which applies to the case of an infinitely long single-conductor line above a perfectly conducting ground. This formula gives the maximum value  $V_{max}$  of the induced overvoltages at the point of the line nearest the stroke location:

$$V_{max} = Z_0 \frac{I \cdot h}{d} \left( 1 + \frac{1}{\sqrt{2}} \cdot \beta \cdot \frac{1}{\sqrt{(1 - 0.5 \cdot v^2)}} \right) \quad (12.16)$$

where

$$Z_0 = \frac{1}{4\pi} \sqrt{\frac{\mu_0}{\epsilon_0}} = 30 \, \Omega \quad (12.17)$$

in which  $I$  is the amplitude of the lightning current assumed to have a step function waveshape,  $h$  is the height of the line,  $d$  is the distance to the stroke location and  $\beta$  is the ratio of the return stroke speed to the speed of light.

Note that this formula does include not only the coupling model between the electromagnetic field and the line, but also the return stroke model for the calculation of the electromagnetic field radiated by the lightning current. The Rusck simplified formula will be compared with the Agrawal *et al.* model in section 12.3.3.

Finally, it is worth mentioning that the Agrawal *et al.* coupling model and its equivalent formulations (namely the models by Taylor *et al.*, by Rachidi, and – provided the lightning channel is straight and perpendicular to the ground plane – by Rusck) are the only ones that have been validated versus experimental results (see section 12.2.12).

### 12.2.8 Inclusion of losses

In the calculation of lightning-induced voltages, losses are, in principle, to be taken into account both in the wire and in the ground. Losses due to the finite ground conductivity are the most important ones, and affect both the electromagnetic field and the surge propagation along the line [24]. However, for relatively short lines

<sup>5</sup>Namely the geometry for which the Rusck model was originally developed.

(typically not exceeding 2 km), it is the influence of the ground losses on the electromagnetic field that is prominent [24].

Let us make reference to the same geometry of Figure 12.1, and take now into account losses both in the wire and in the ground plane. The wire conductivity and relative permittivity are denoted respectively as  $\sigma_w$  and  $\epsilon_{rw}$ , and the ground is characterised by its conductivity  $\sigma_g$  and its relative permittivity  $\epsilon_{rg}$ . The Agrawal *et al.* coupling equations extended to the present case of a wire above an imperfectly conducting ground can be written as (for a step by step derivation, see [1])

$$\frac{dV^s(x)}{dx} + Z'I(x) = E_x^e(x, h) \quad (12.18)$$

$$\frac{dI(x)}{dx} + Y'V^s(x) = 0 \quad (12.19)$$

where  $Z'$  and  $Y'$  are the longitudinal and transverse per-unit-length impedance and admittance respectively, given by [1] and [24]<sup>6</sup>

$$Z' = j\omega L' + Z'_w + Z'_g \quad (12.20)$$

$$Y' = \frac{(G' + j\omega C')Y'_g}{G' + j\omega C' + Y'_g} \quad (12.21)$$

in which

- $L'$ ,  $C'$  and  $G'$  are the per-unit-length longitudinal inductance, transverse capacitance and transverse conductance respectively, calculated for a lossless wire above a perfectly conducting ground:

$$\begin{aligned} L' &= \frac{\mu_0}{2\pi} \cosh^{-1} \left( \frac{h}{a} \right) \\ &\cong \frac{\mu_0}{2\pi} \ln \left( \frac{2h}{a} \right) \quad \text{for } h \gg a \end{aligned} \quad (12.22)$$

$$\begin{aligned} C' &= \frac{2\pi\epsilon_0}{\cosh^{-1}(h/a)} \\ &\cong \frac{2\pi\epsilon_0}{\ln(2h/a)} \quad \text{for } h \gg a \end{aligned} \quad (12.23)$$

$$G' = \frac{\sigma_{\text{air}}}{\epsilon_0} C' \quad (12.24)$$

- $Z'_w$  is the per-unit-length internal impedance of the wire; assuming a round wire and an axial symmetry for the current, the following expression for the wire internal impedance can be derived (e.g. [25]):

$$Z'_w = \frac{\gamma_w I_0(\gamma_w a)}{2\pi a \sigma_w I_1(\gamma_w a)} \quad (12.25)$$

where  $\gamma_w = \sqrt{j\omega\mu_0(\sigma_w + j\omega\epsilon_0\epsilon_{rw})}$  is the propagation constant in the wire and  $I_0$  and  $I_1$  are the modified Bessel functions of zero and first order respectively,

<sup>6</sup>In [1] the per-unit-length transverse conductance has been disregarded.

- $Z'_g$  is the per-unit-length ground impedance, which is defined as [24, 26]

$$Z'_g = \frac{j\omega \int_{-\infty}^h B_y^s(x, z) dx}{I} - j\omega L' \tag{12.26}$$

where  $B_y^s$  is the y-component of the scattered magnetic induction field.

Several expressions for the ground impedance have been proposed in the literature (e.g. [27–41]). Here, we will use the one proposed by Sunde [29] given by

$$Z'_g = \frac{j\omega\mu_0}{\pi} \int_0^\infty \frac{e^{-2hx}}{\sqrt{x^2 + \gamma_g^2 + x}} dx \tag{12.27}$$

where  $\gamma_g = \sqrt{j\omega\mu_0(\sigma_g + j\omega\epsilon_0\epsilon_{rg})}$  is the propagation constant in the ground.

The above expression is adopted essentially for two reasons:

1. Expression (12.27) is directly connected to the general expressions obtained from the scattering theory. As a matter of fact, it is shown in [1] that the general expression for the ground impedance derived using scattering theory reduces to the Sunde approximation when considering the transmission line approximation.
2. The results obtained using (12.27) are shown to be accurate within the limit of the transmission line approximation [1, p. 409].

The general expression (12.27) is not suitable for a numerical evaluation since it involves an integral over an infinitely long interval. Several approximations for the ground impedance of a single-wire line have been proposed in the literature (see [24] for a survey). One of the most simple and most accurate approximations was proposed by Sunde himself and is given by the following logarithmic function:

$$Z'_g \cong \frac{j\omega\mu_0}{2\pi} \ln\left(\frac{1 + \gamma_g h}{\gamma_g h}\right) \tag{12.28}$$

It has been shown [24] that the above logarithmic expression represents an excellent approximation to the general expression (12.27) over the whole frequency range of interest.

- Finally,  $Y'_g$  is the so-called ground admittance, given by [1, 26]

$$Y'_g \cong \frac{\gamma_g^2}{Z'_g} \tag{12.29}$$

### 12.2.9 Discussion on the relative importance of different transmission line parameters when calculating lightning-induced voltages

Figure 12.6 presents a comparison between ground and wire impedances for a 10 mm radius copper wire located 10 m above ground. The ground conductivity

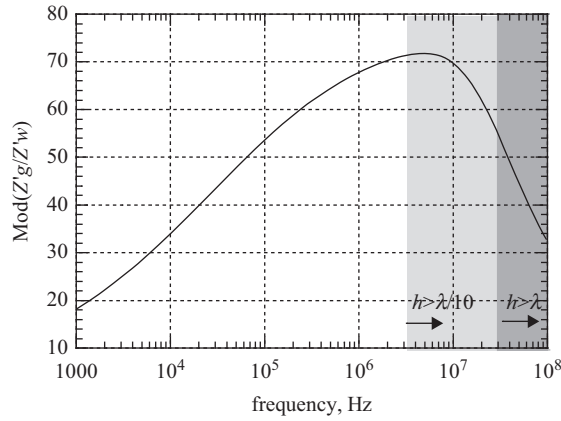


Figure 12.6 Ratio of the magnitude of the ground impedance to the wire impedance as a function of frequency. Copper wire of radius 10 mm is located at 10 m above the ground ( $\sigma_g = 0.01$  S/m,  $\epsilon_{rg} = 10$ ) (adapted from Rachidi et al. [24])

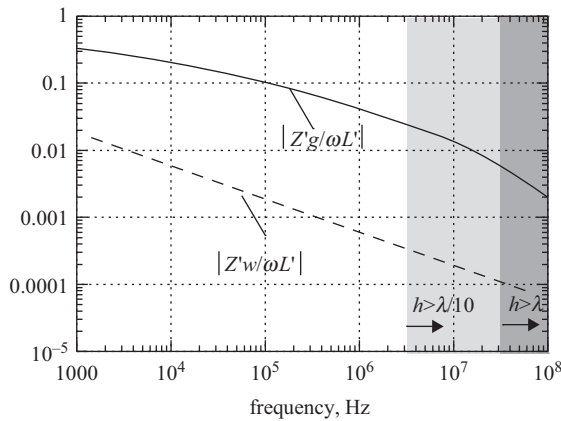


Figure 12.7 Comparison between longitudinal impedance terms: ground impedance, wire impedance, and  $j\omega L'$ . Copper wire of radius 10 mm is located at 10 m above the ground ( $\sigma_g = 0.01$  S/m,  $\epsilon_{rg} = 10$ ) (adapted from Rachidi et al. [24])

and relative permittivity are equal to 0.01 S/m and to 10, respectively. The results show that within the frequency range of interest, the wire impedance can be neglected as regard to the ground impedance. Note that for poorer conductivities, the ratio  $|Z'_g/Z'_w|$  will become even higher. We have also plotted in Figure 12.7 the ratios  $|Z'_g/j\omega L'|$  and  $|Z'_w/j\omega L'|$ . It can be seen that while  $|Z'_g|$  represents a non-negligible fraction of  $\omega L'$  over a wide frequency range, again  $|Z'_w|$  can be neglected.

In Figure 12.8, we have presented a comparison between  $1/|Y'_g|$  and  $1/\omega C'$  as a function of frequency. It can be seen that  $1/|Y'_g|$  is about five order of magnitude lower than  $1/\omega C'$ , and therefore it can be neglected in the computation of lightning-induced voltages on overhead power lines. Even though the computations in Figures 12.6–12.8 are performed up to 100 MHz, it is important to realise that for a

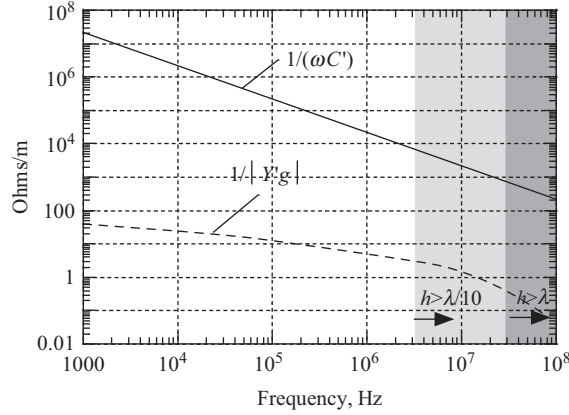


Figure 12.8 Comparison between the inverse of the ground admittance and  $1/j\omega C'$ . Copper wire of radius 10 mm is located at 10 m above the ground ( $\sigma_g = 0.01$  S/m,  $\epsilon_{rg} = 10$ ) (adapted from Rachidi et al. [44])

line height  $h = 10$  m, the transmission line (TL) approximation is valid up to a frequency of about 3 MHz corresponding to  $\lambda = 10 h$ ; for frequencies higher than about 30 MHz, corresponding in our case to  $\lambda = h$ , the validity of the TL approximation becomes seriously questionable. For this reason, computed results for these frequencies are presented in shaded areas.<sup>7</sup>

### 12.2.10 Case of multiconductor lines

Making reference to the geometry of Figure 12.9, the generalised<sup>8</sup> telegrapher’s equations for the case of a multi-wire system along the  $x$ -axis above an imperfectly conducting ground and in presence of an external electromagnetic excitation are given by [1, 41]

$$\frac{d}{dx} [V_i^s(x)] + j\omega [L'_{ij}] [I_i(x)] + [Z'_{gij}] [I_i(x)] = [E_x^e(x, 0, h_i)] \tag{12.30}$$

$$\frac{d}{dx} [I_i(x)] + [G'_{ij}] [V_i^s(x)] + j\omega [C'_{ij}] [V_i^s(x)] = [0] \tag{12.31}$$

in which

- $[V_i^s(x)]$  and  $[I_i(x)]$  are frequency-domain vectors of the scattered voltage and the current along the line;
- $[E_x^e(x, h_i)]$  is the vector of the exciting electric field tangential to the line conductors;

<sup>7</sup>It is worth mentioning that in Figures 12.6–12.8, we have neglected any variation of ground conductivity and relative permittivity as a function of frequency, even though there is experimental evidence that these two parameters are frequency-dependent (e.g., [42]). However, studies on the variation of ground parameters as a function of frequency [42, 43] show that (a) the ground conductivity variation becomes very appreciable only for frequencies higher than about 10 MHz, and (b) significant variation of the ground relative permittivity as a function of frequency occurs up to a few MHz, for which the ground impedance is not appreciably affected by the value of the ground relative permittivity.

<sup>8</sup>The word ‘generalised’ is here used to emphasise the presence of an external illumination of the line.



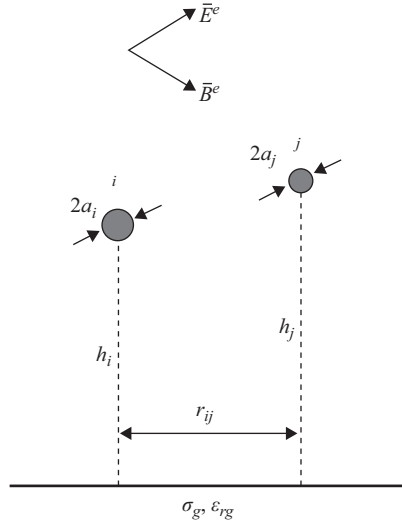


Figure 12.9 Cross-sectional geometry of a multiconductor line in presence of an external electromagnetic field

- $[0]$  is the zero-matrix (all elements are equal to zero);
- $[L'_{ij}]$  is the matrix of the per-unit-length line inductance. Assuming that the distances between conductors are much larger than their radii, the general expression for the mutual inductance between two conductors  $i$  and  $j$  is given by [1]

$$L'_{ij} = \frac{\mu_0}{2\pi} \ln\left(\frac{d^*}{d}\right) = \frac{\mu_0}{4\pi} \ln\left(\frac{r_{ij}^2 + (h_i + h_j)^2}{r_{ij}^2 + (h_i - h_j)^2}\right) \quad (12.32)$$

The self-inductance for the conductor  $i$  is given by

$$L'_{ii} = \frac{\mu_0}{2\pi} \ln\left(\frac{2h_i}{r_{ii}}\right) \quad (12.33)$$

- $[C'_{ij}]$  is the matrix of the per-unit-length line capacitance. It can be evaluated directly from the inductance matrix using the following expression [1]:

$$[C'_{ij}] = \epsilon_0 \mu_0 [L'_{ij}]^{-1} \quad (12.34)$$

- $[G'_{ij}]$  is the matrix of per-unit-length transverse conductance. The transverse conductance matrix elements can be evaluated starting either from the capacitance matrix or the inductance matrix using the following relations:

$$[G'_{ij}] = \frac{\sigma_{air}}{\epsilon_0} [C'_{ij}] = \sigma_{air} \mu_0 [L'_{ij}]^{-1} \quad (12.35)$$

However, for most practical cases, the transverse conductance matrix elements  $G'_{ij}$  are negligible in comparison with  $j\omega C'_{ij}$  [3] and can therefore be neglected in the computation.

- And, finally,  $[Z'_{gij}]$  is the matrix of the ground impedance. The general expression for mutual ground impedance between two conductors  $i$  and  $j$  derived by Sunde is given by [29]

$$Z'_{gij} = \frac{j\omega\mu_0}{\pi} \int_0^\infty \frac{e^{-(h_i+h_j)x}}{\sqrt{x^2 + \gamma_g^2 + x}} \cos(r_{ij}x) dx \tag{12.36}$$

In a similar way as for the case of a single-wire line, an accurate logarithmic approximation is proposed by Rachidi *et al.* [41] which is given by

$$Z'_{gij} \cong \frac{j\omega\mu_0}{4\pi} \ln \left[ \frac{\left(1 + \gamma_g \left(\frac{h_i+h_j}{2}\right)\right)^2 + \left(\gamma_g \frac{r_{ij}}{2}\right)^2}{\left(\gamma_g \frac{h_i+h_j}{2}\right)^2 + \left(\gamma_g \frac{r_{ij}}{2}\right)^2} \right] \tag{12.37}$$

Note that in (12.30) and (12.31), we have neglected the terms corresponding to wire impedance and the so-called ground admittance. Indeed, and as we have seen in the previous section, for typical overhead lines and for typical frequency range of interest (below 10 MHz), these parameters can be disregarded with reasonable approximation.

The boundary conditions for the two line terminations are given by

$$[V_i^s(0)] = -[Z_A][I_i(0)] + \left[ \int_0^{h_i} E_z^e(0, 0, z) dz \right] \tag{12.38}$$

$$[V_i^s(L)] = [Z_B][I_i(L)] + \left[ \int_0^{h_i} E_z^e(L, 0, z) dz \right] \tag{12.39}$$

in which  $[Z_A]$  and  $[Z_B]$  are the impedance matrices at the two line terminations.

### 12.2.11 Time-domain representation of coupling equations

A time-domain representation of field-to-transmission line coupling equations is sometimes preferable because it allows to handle in a straightforward manner non-linear phenomena such as corona, the presence of non-linear protective devices at the line terminals (see sections 12.3.4 and 12.3.5), and also variation in the line topology (opening and reclosure of switches). On the other hand, frequency-dependent parameters, such as the ground impedance, need to be represented using convolution integrals, which require important computation time and memory storage.

The field-to-transmission line coupling equations (12.30) and (12.31) can be converted into time domain to obtain the following expressions:

$$\frac{\partial}{\partial x} [v_i^s(x, t)] + [L'_{ij}] \frac{\partial}{\partial t} [i_i(x, t)] + [\xi'_{gij}] \otimes \frac{\partial}{\partial t} [i_i(x, t)] = [E_x^e(x, 0, h_i, t)] \tag{12.40}$$

$$\frac{\partial}{\partial x} [i_i(x, t)] + [G'_{ij}] [v_i^s(x, t)] + [C'_{ij}] \frac{\partial}{\partial t} [v_i^s(x, t)] = 0 \tag{12.41}$$

in which  $\otimes$  denotes convolution product and the matrix  $\left[ \xi'_{gij} \right]$  is called the transient ground resistance matrix; its elements are defined as

$$\left[ \xi'_{gij} \right] \cong F^{-1} \left\{ \frac{Z'_{gij}}{j\omega} \right\} \tag{12.42}$$

The inverse Fourier transforms of the boundary conditions written, for simplicity, for resistive terminal loads read

$$[v_i(0, t)] = -[R_A] [i_i(0, t)] + \left[ \int_0^{h_i} E_z^e(0, 0, z, t) dz \right] \tag{12.43}$$

$$[v_i(L)] = [R_B] [i_i(0)] + \left[ \int_0^{h_i} E_z^e(L, 0, z, t) dz \right] \tag{12.44}$$

where  $[R_A]$  and  $[R_B]$  are the matrices of the resistive loads at the two line terminals.

The general expression for the ground impedance matrix terms in the frequency domain (12.32) does not have an analytical inverse Fourier transform. Thus, the elements of the transient ground resistance matrix in time domain are to be, in general, determined using a numerical inverse Fourier transform algorithm.<sup>9</sup>

<sup>9</sup>However, the following analytical expressions are shown to be reasonable approximations to the numerical values obtained using an inverse FFT [44]

$$\xi'_{gii}(t) = \min \left\{ \frac{1}{2\pi h_i} \sqrt{\frac{\mu_0}{\epsilon_0 \epsilon_{rg}}}, \frac{\mu_0}{\pi \tau_{gii}} \left[ \frac{1}{2\sqrt{\pi}} \sqrt{\frac{\tau_{gii}}{t}} + \frac{1}{4} \exp(\tau_{gii}/t) \operatorname{erfc} \left( \sqrt{\frac{\tau_{gii}}{t}} \right) - \frac{1}{4} \right] \right\} \tag{12.45}$$

$$\xi'_{gij}(t) = \min \left\{ \frac{1}{2\pi h} \sqrt{\frac{\mu_0}{\epsilon_0 \epsilon_{rg}}}, \frac{\mu_0}{\pi T_{ij}} \left[ \frac{1}{2\sqrt{\pi}} \sqrt{\frac{T_{ij}}{t}} \cos(\theta_{ij}/2) + \frac{1}{4} e^{T_{ij} \cos(\theta_{ij})/t} \cos \left( \frac{T_{ij}}{t} \sin(\theta_{ij}) - \theta_{ij} \right) - \frac{1}{2\sqrt{\pi}} \sum_{n=0}^{\infty} a_n \left( \frac{T_{ij}}{t} \right)^{\frac{2n+1}{2}} \cos \left( \frac{2n-1}{2} \theta_{ij} \right) - \frac{\cos(\theta_{ij})}{4} \right] \right\} \tag{12.46}$$

in which

$$\tau_{gii} = h_i^2 \mu_0 \sigma_g \tag{12.47}$$

$T_{ij}$  and  $\theta_{ij}$  are defined as follows:

$$\hat{\tau}_{gij} = \hat{h}_{ij}^2 \mu_0 \sigma_g = \left( \frac{h_i + h_j}{2} + j \frac{T_{ij}}{2} \right)^2 \mu_0 \sigma_g = T_{ij} e^{j\theta_{ij}} \tag{12.48}$$

and  $\operatorname{erfc}$  is the complementary error function defined as

$$\operatorname{erfc}(x) = \frac{2}{\sqrt{\pi}} \int_x^{\infty} \exp(-t^2) dt = 1 - \frac{2 \exp(-x^2)}{\sqrt{\pi}} \sum_{n=0}^{\infty} a_n x^{2n+1} \tag{12.49}$$

where  $a_n = \frac{2^n}{1 \cdot 3 \cdot \dots \cdot (2n+1)}$

Equations (12.45) and (12.46) extend the well-known Timotin formula [45] to the early-time region, within the limits of the transmission line approximation [44].

### 12.2.12 Experimental validation of the field-to-transmission line coupling models

Rigorously, to test a coupling model it is necessary to know the incident electromagnetic field and the voltage (or current) induced by such a field on a given experimental line. This can be achieved by means of experimental installations and measurements; indeed, a number of experimental installations have been set up in different research centres in the world with such an aim. Then, using the exciting incident field as an input to the coupling model, one has to evaluate the voltage (or current) induced by such a field on the line as predicted by the model and to compare the calculated waveshape with the measured one.

The exciting field can be of different origin, such as the field radiated by natural or artificially triggered lightning (e.g. [46–57]), by EMP simulators (e.g. [58–61]), or by vertical antennas simulating a reduced-scale lightning channel (e.g. [62–64]). As a general comment, we can observe that the use of lightning is complicated by the intrinsic difficulty in performing a controlled experiment, although triggered lightning is clearly a better technique in this respect. More controlled conditions can be achieved using the above-mentioned EMP simulators or reduced-scale models. In what follows we give a brief description of the results that have been obtained using these techniques with the aim of testing the coupling models.

#### 12.2.12.1 Natural and triggered lightning experiments

Concerning the validation of coupling models, it is not crucial to distinguish between natural and triggered lightning, and for this reason we have grouped in the same paragraph the two types of experiments. We limit here to discuss only some of the experimental results published in the literature, as a complete survey of the existing publications is beyond the scope of this chapter.

A large number of experimental recordings has been published by Yokoyama *et al.* [46–48] using an experimental three-conductor, 820 m long, unenergised overhead line. The overvoltages measured by Yokoyama *et al.* were induced by lightning strokes having known impact point, a 200 m high tower, 200 m distant from the closest point of the line. Both current and overvoltages were recorded, but not the corresponding fields. Indeed Yokoyama *et al.* used their experimental data to test the model by Rusck, in the complete form, which uses as input the lightning current and gives as output the induced voltage. In this respect, the results by Yokoyama *et al.* cannot be used to test the coupling model as specified at the beginning of this section, but certainly provide an indication on the adequacy of the Rusck model.

The first simultaneous measurements of lightning electric and magnetic fields and the power line voltages induced by those fields were performed by Uman and co-workers in the Tampa Bay area of Florida during the summer of 1979 (Master *et al.* [16, 49]). Voltage measurements were made at one end of a 500 m unenergised overhead distribution line. Comparison of voltages calculated according to the Agrawal *et al.* coupling model and measured ones yielded reasonably good agreement in voltage waveshapes, but the magnitudes of the first were systematically about a factor of 4 smaller than the latter [16, 49]. Then, a series of experiments was carried out in the following years by the University of Florida research group (Rubinstein *et al.* [50], Georgiadis *et al.* [51]) in which some corrections were made on the first experiment procedure and in which, overall, a better agreement between theory and experimental results concerning voltage waveshapes

was reached, although the agreement between amplitudes was not always satisfactory. Possible causes for the disagreement can be calibration errors, imperfect determination of the angle of incidence of the electromagnetic wave, uncertainties about the ground conductivity value and the presence of trees and other objects in the vicinity of the line which may cause a field distortion.

De la Rosa and co-workers [52] presented measurements of voltage at one end of 13 kV three-phase overhead line of standard construction type. The line was 2.8 km long, nearly 10 m high. The three line conductors were bound together to a common point at both line ends, used to take a connection down to the voltage divider and matching resistor placed at ground level at both ends of the line. Amplitude, polarity and waveshape of the voltage at one end of the Mexican line were found to be a strong function of the position of lightning with respect to the line (in general quite distant from the line) and of ground conductivity. Their results were used by Cooray and De la Rosa [53], who found a good agreement between measured voltages and those calculated using the Agrawal *et al.* model.

Barker *et al.* [54] published the results of a study carried out at Camp Blanding in Florida to characterise lightning-induced voltages amplitude and waveshapes. They tested the Rusck simplified formula (12.16) (see section 12.2.7) and the Agrawal *et al.* model, finding a reasonable agreement between theory and measurements. The comparison presented in [54] is, however, affected by the assumption of a perfectly conducting ground, which was not the case in the field experiment.

More recently, Paolone *et al.* [65] presented results obtained during the summer of 2003 on a 0.75 km long line installed at the International Center for Lightning Research and Testing (ICLRT) [66] operated by the University of Florida. The line is composed of four conductors (three-phase conductors plus neutral, grounded at six locations) and equipped with surge arresters. The results were compared with simulations obtained using a second order FDTD implementation of the Agrawal *et al.* model and very good agreement was found.

### 12.2.12.2 EMP simulators

Coupling models can be tested also by means of EMP simulators. An EMP simulator is a facility able to radiate within the so-called working volume an electromagnetic wave with very short rise time (of the order of some ns) and with some tens of kV/m electric field intensity. EMP stands, as a matter of fact, for electromagnetic pulse [58]. The main components of an EMP simulator are a pulse generator and an antenna (of guided-wave type, conical, etc.) excited by the first one. With an EMP simulator it is possible, in principle, to avoid contaminations of the incident field due to the wire scattering, as might be the case when the field and the induced voltages are measured simultaneously (e.g. for lines illuminated by natural lightning fields). In this respect, the repeatability of the pulse generator is crucial, in that the electromagnetic field that is measured within the working volume in absence of the victim must be the same, which excites the victim when put within the working volume.

An example of comparison between measured and calculated results obtained by Guerrieri *et al.* [60, 61] using the SEMIRAMIS EMP simulator of the Swiss Federal Institute of Technology of Lausanne [59] is shown in Figure 12.10.

Tests using a more elaborate and complex network consisting of 27 branches illuminated by the electromagnetic field generated by the Swiss Defence Procurement Agency EMP simulator (called VERIFY) have also been performed and discussed by

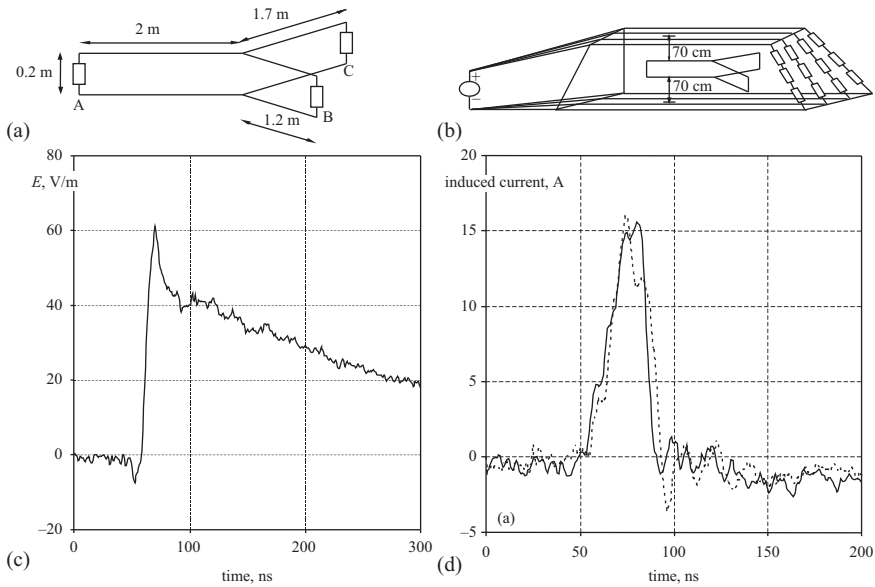


Figure 12.10 Example of comparison performed using the EMP simulator of the Federal Institute of Technology of Lausanne [59] between calculated (using the Agrawal *et al.* model) and induced currents on a Y-shaped test structure. (a) Test structure; (b) arrangement of the Y-shaped structure within the working volume of the simulator. (c) typical shape of the vertical electric field in the working volume of the simulator (measurement of the field is performed in absence of the Y-shaped structure). (d) measured (solid line) and calculated (dotted line) induced currents at point A of the structure (adapted from Guerrieri *et al.* [60, 61])

Paolone *et al.* [65]. The network actually represents a simple model for a car cable harness, flattened on the ground plane. Comparisons between experimental data and computer simulations for different load configurations of the reduced-scale model network were presented and it was found that the numerical simulations are in good agreement with the measurements.

### 12.2.12.3 Reduced-scale modelling

Another example of experiment that can be carried out under controlled conditions is the reduced-scale modelling. Ishii *et al.* [62] published voltage and current measurements obtained from a simple geometrical line model on a finitely conducting ground and found very good agreement between theory and calculations. The Japanese experiment was of interest since it allowed also for the assessment of the Agrawal *et al.* coupling model extended to the case of an overhead line above a lossy ground.

Piantini and Janiszewski [63] obtained a number of experimental data from a reduced-scale model of a distribution line at the University of Saõ Paulo in Brazil, which have been used by Nucci *et al.* [64] to test, successfully, the Agrawal *et al.* model. In Figure 12.11, we show an example of comparison between measurement and calculations taken from [60]. Another example will be given in section 12.3.5.

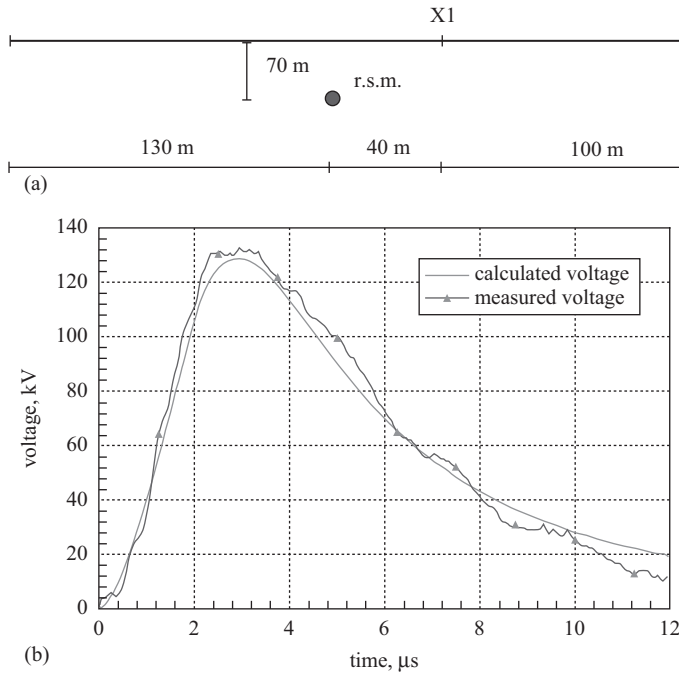


Figure 12.11 Test of the Agrawal *et al.* coupling model using a reduced-scale line model. (a) A simple single-conductor overhead line (top view). *r.s.m.* denotes the return stroke location. The real dimensions of the reduced-scale model are scaled by a factor 50. (b) Comparison between measurements and experimental results (adapted from Nucci *et al.* [64])

## 12.3 Lightning-induced voltages on overhead power lines

### 12.3.1 Return stroke current model, computation of the incident electromagnetic field, and coupling model

A computer program (LIOV, *l*ightning-*i*nduced *o*vervoltage) was developed by the authors of this chapter, which allows for the evaluation of lightning-induced voltages on a multiconductor overhead line above a lossy ground (see [24] and [67] for the theoretical background). LIOV has been developed in the framework of an international collaboration involving the University of Bologna (Department of Electrical Engineering), the Swiss Federal Institute of Technology (Power Systems Laboratory), and the University of Rome “La Sapienza” (Department of Electrical Engineering). The code is based on the field-to-transmission line coupling formulation of Agrawal *et al.*, suitably adapted for the calculation of induced overvoltages when lightning strikes near a horizontal overhead transmission line. In the LIOV code, the electromagnetic field radiated by the lightning channel is calculated using the field equations in the form given by Uman *et al.* [68] with the extension to the case of lossy ground introduced by Cooray and Rubinstein [69, 70] and assuming the modified transmission line (MTLE) return stroke current model for the description of the spatial-temporal distribution of the lightning current along the return stroke channel (Nucci *et al.* [12]; Rachidi and Nucci [13]). The

amplitude decay constant of the MTLE model,  $\lambda$ , is fixed at 2 km, as inferred by Nucci and Rachidi in [71] by means of simultaneously measured electromagnetic fields at two different distances.

The forcing functions in the Agrawal *et al.* coupling model are expressed, as seen in section 12.2.3, in terms of the vertical and horizontal electric field components. The vertical electric field radiated by the lightning channel is calculated assuming the ground as a perfectly conducting plane, since such a field component is not affected significantly by the soil resistivity in the frequency and distance range of interest, using the equations of Chapter 5. For the calculation of the horizontal electric field component, we adopt the earlier mentioned approximate formula proposed by Cooray and Rubinstein.<sup>10</sup>

The LIOV code allows for the calculation of lightning-induced voltages along an overhead line as a function of lightning current waveshape (amplitude, front steepness, duration), return stroke velocity, line geometry (height, length, number and position of conductors), stroke location with respect to the line, ground resistivity, ground relative permittivity, and termination impedances. Induction effects of downward leader electric fields [72] and corona effect on the induced voltages [70, 71] can also be dealt with. As a matter of fact, all calculation results presented in previous sections and those that will be presented in the next sections have been obtained using the LIOV code.<sup>11</sup>

### 12.3.2 Mechanism of voltage induction by a nearby lightning return stroke on an overhead line

Let us consider a 1 km long, 10 m high, single-wire overhead line, matched at both ends, to avoid reflections that would render less simple the following discussion. The stroke location is at a distance  $y = 50$  m from the line centre and equidistant to the line terminations. We now for simplicity assume the ground as a perfect conductor. The influence of ground losses will be dealt with in the following sections. The lightning return stroke field is calculated assuming the MTLE return stroke model, a channel-base current typical of subsequent return strokes (12 kA peak amplitude, 40 kA/s maximum-time derivative) and a return stroke velocity of  $1.3 \times 10^8$  m/s. The overvoltages at three different positions along the line calculated according to the Agrawal *et al.* model are shown in Figure 12.12 (Figure 12.12a:  $x = 0$ ; Figure 12.12b:  $x = 250$  m and Figure 12.12c:  $x = 500$  m). For illustrative purposes, the contributions to the total overvoltage of the incident voltage, of the voltage due to the horizontal electric field and of the voltage due to the vertical electric field at the line terminations ('risers' contribution), are shown in Figure 12.12; note that the first and the third terms represent the contribution of the vertical electric field to the total overvoltage according to this model. Although the total induced voltage has essentially the same waveshape independently of the observation point, the various contributions to the

<sup>10</sup> Cooray [75] has proposed an improved version of such a formula, taking into account remarks by Wait [76]. We assume in what follows that for the adopted values for ground conductivity, our results will not be significantly affected by the adoption of one expression instead of the other one. The improved Cooray–Rubinstein expression [75] has been recently implemented in an improved version of the LIOV code [77].

<sup>11</sup> It is worth adding that in the LIOV code, both the MTLE and the Agrawal *et al.* models equations are dealt with in the time domain; the field-to-transmission line coupling equations of the Agrawal *et al.* model are solved by means of the point-centred finite-difference time-domain method.



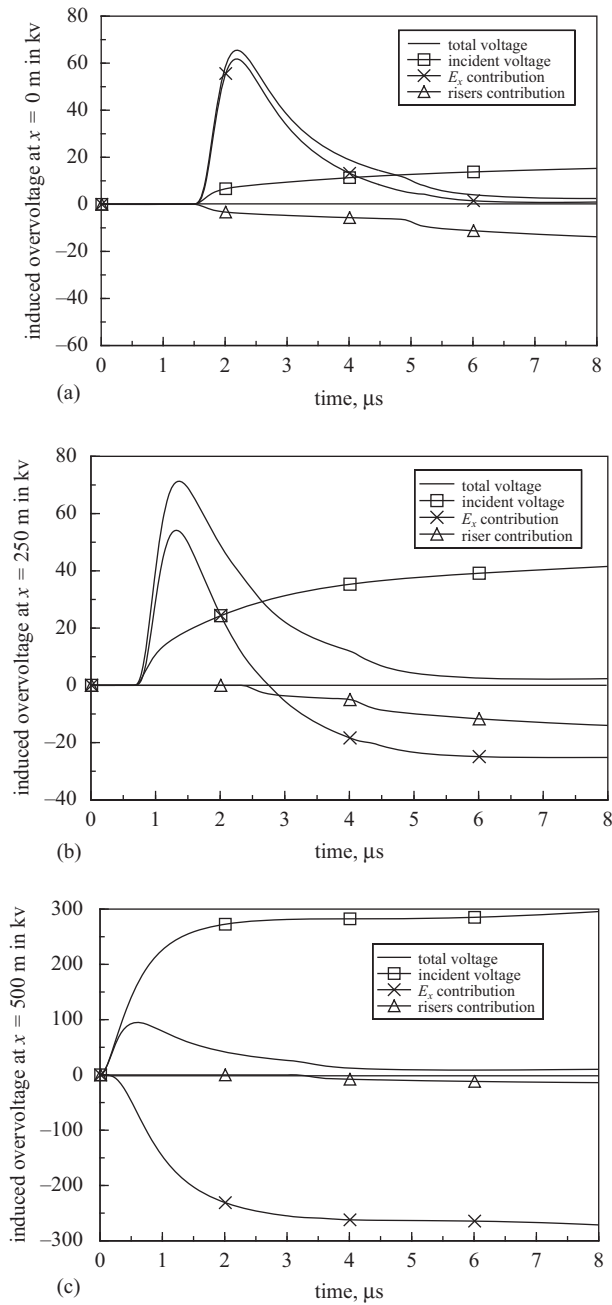


Figure 12.12 Overvoltages calculated at three different positions: (a)  $x = 0$ ; (b)  $x = 250$  m; (c)  $x = 500$  m along a 1 km long, matched overhead line, according to the Agrawal *et al.* coupling model. Stroke location: 50 m from the line centre and equidistant from line terminations. Channel-base current: typical of subsequent return stroke as shown in Figure 2 of [1]. Return stroke model: MTL model with  $\lambda = 2$  km and  $v = 1.9 \times 10^8$  m/s (adapted from Nucci *et al.* [67])

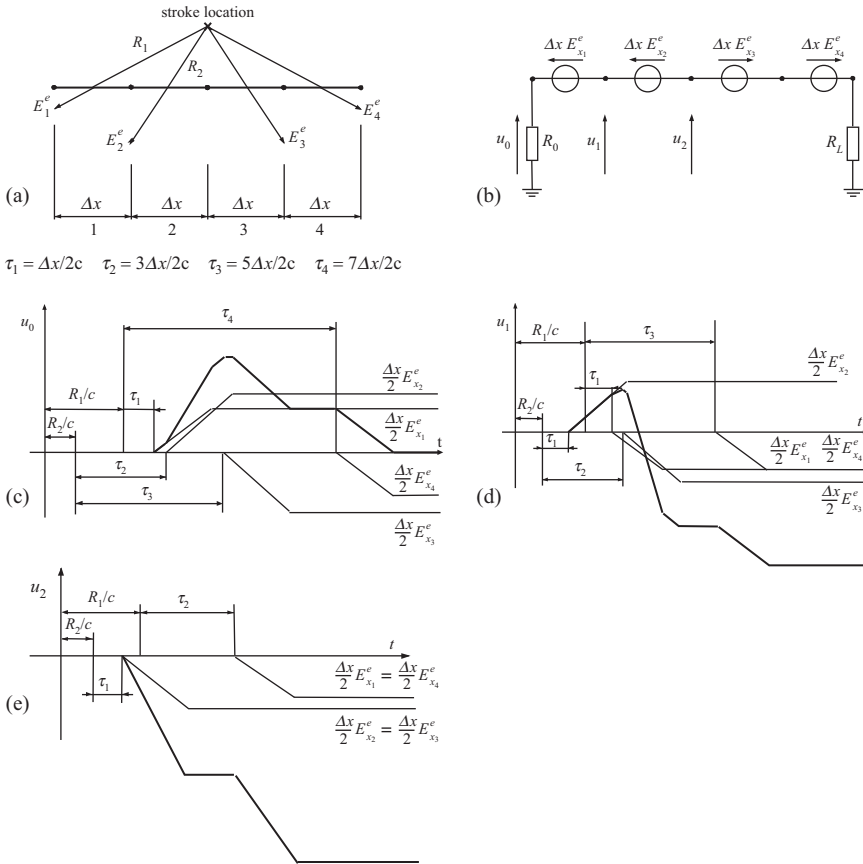


Figure 12.13 Schematic explanation of the different waveshapes of the induced voltage due to the horizontal field at three different positions according to the Agrawal et al. model: (a) line segmentation; (b) equivalent sources; (c)  $x = 0$  m; (d)  $x = 250$  m; (e)  $x = 500$  m (adapted from Diendorfer [18] and Nucci [77])

total overvoltage differ. See, for instance, the voltage produced by the horizontal electric field coupling. Figure 12.13 gives a schematic explanation of the different waveshapes at different observation points along the line of such a voltage contribution and explains the mechanism of formation of lightning-induced voltages. Note that due to the symmetry of the considered case, for low-frequency lightning electromagnetic fields or for short line lengths, no voltage would be induced along the line.

### 12.3.3 Preliminary remarks on the influence of the ground resistivity on the induced voltages

Ground resistivity is one of the most important parameters affecting the induced voltage amplitude and waveshape [24, 49, 78–82], and this is the case even for stroke locations close to the line. In the next paragraphs, we shall perform a systematic analysis, varying current waveshape, stroke location and observation point, aimed both at explaining the reasons for the different possible shapes and polarities of the induced voltages and at consolidating the knowledge on the subject. First, it

is useful, however, to make some preliminary remarks on the influence of the ground resistivity on the induced voltages.

Let us consider again a 1 km long, 10 m high, single-conductor overhead line. In order to clearly illustrate the influence of ground conductivity, a low value, namely 0.001 S/m, has been chosen. The ground relative permittivity is assumed to be equal to 10. The line is terminated at both ends on resistances of about 500  $\Omega$  (a value corresponding to the characteristic impedance of the line when considered as lossless). The same lightning strike location (equidistant from the line terminations and at 50 m from the line centre), return stroke current (12 kA peak amplitude, 40 kA/ $\mu$ s maximum time-derivative) and return stroke velocity ( $1.3 \times 10^8$  m/s) considered in section 12.3.2 are assumed.

The induced voltage calculated at the line terminations is presented in Figure 12.14a. In the same figure, we have also presented the results obtained for the same configuration but considering the ground as a perfectly conducting plane. It can be seen that the ground conductivity affects significantly the induced voltages in magnitude, shape and polarity. It is important to remind, as earlier mentioned in section 12.2.8, that the ground conductivity affects the induced voltages via two mechanisms: (i) in the calculation of the exciting electromagnetic fields and (ii) in the calculation of line parameters, which means in the propagation of the induced surges along the line. Now, the contribution of each of these two effects of the ground resistivity is shown, for the same line of Figure 12.14a, in Figure 12.14b, where the induced voltages for the three following cases are reproduced [24]:

- *case 1*: the ground conductivity is taken into account in both field calculation and surge propagation along the line (solid line in Figure 12.14b);
- *case 2*: the effect of the finite ground conductivity is taken into account only in the surge propagation along the line (curve ‘Ideal Field’ in Figure 12.14b). For this case, the exciting electric field has been calculated assuming a perfectly conducting ground;
- *case 3*: the effect of the finite ground conductivity is taken into account only in the calculation of the exciting electric field, neglecting the ground impedance (curve ‘Ideal Line’ in Figure 12.14b).

It can be clearly seen that for the considered case, namely for a relatively short line, the surge propagation along the line is not appreciably affected by the finite ground conductivity. This conclusion has important implications both for the computational aspects of the problem and for the interpretation of the results.

Note, however, that the influence of the ground on the surge propagation depends obviously on the line length. This issue is discussed in more detail in [24, 83]. We limit here to report that for line lengths in the range of 2 kilometres or so and for values of ground conductivity not lower than 0.001 S/m, for the evaluation of the early-time response of the line it is sufficient to take into account the presence of a lossy ground only in the calculation of the incident electromagnetic field.<sup>12</sup> In Figure 12.14c, we show results similar to those presented in Figure 12.14b, but considering a 5 km long line. It is clear that the surge attenuation and distortion along the line is no longer negligible and that the induced voltages are appreciably affected by the ground losses through both radiated field and surge propagation along the line.

<sup>12</sup> If the line is not matched, one has to be aware that the multiple reflections of surges propagating along it would be attenuated by the line losses.

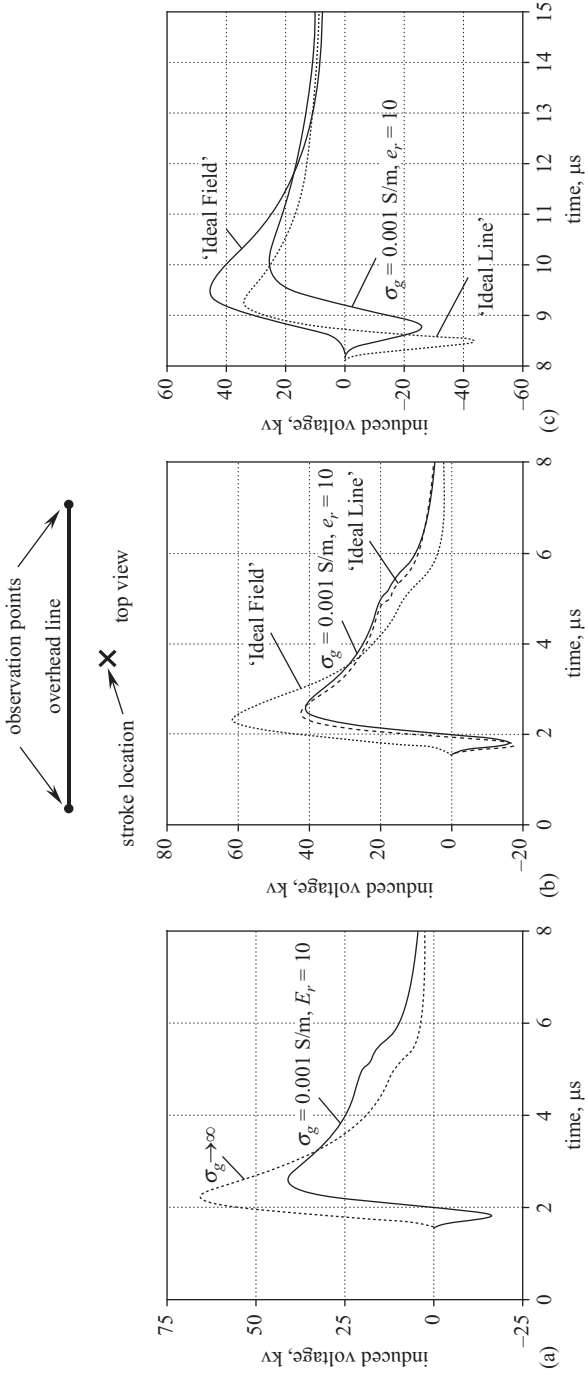


Figure 12.14 Influence of ground resistivity on lightning-induced voltages for the case of a stroke location equidistant to the line terminations. Lightning current: typical of subsequent return strokes (12 kA peak amplitude, 40 kA/ $\mu$ s maximum time-derivative). Observation points: line terminations. (a) Case of a 1 km overhead line.  $\sigma_g = 0.001$  S/m,  $\epsilon_r = 10$ . Dotted line: perfectly conducting ground. (b) As in (a). Dashed line ('Ideal Line'): induced voltage calculated taking into account the ground finite conductivity only when calculating the exciting electric field, and not in the surge propagation (ground impedance). Dotted line ('Ideal Field'): results obtained when the effect of ground finite conductivity is taken into account only in the surge propagation along the line. (c) As in (b), but for a 5 km long line (adapted from Rachidi et al. [24])

### 12.3.4 Sensitivity analysis and discussion

Although computer programs are nowadays popular and widely applied to solve a number of classical, yet complex problems in electrical engineering (load-flow, short circuits, stability), when dealing with the electromagnetic effects produced by lightning on distribution systems, often the need of a ‘simple’ equation, able to predict the amplitude of lightning-induced overvoltages without massive use of computer memory and/or numerical algorithms, is preferred. This somewhat obsolete concept to cope with the problem of interest can be due, on the one hand, to the random and unpredictable nature of the lightning discharge that apparently makes it worthless any effort towards the achievement of accurate calculations – as, according to the above-mentioned concern, what is really needed is just some order of magnitude of the amplitude that the induced voltages may reach – and, on the other hand, to the inherent complexity of the problem, which involves many aspects of several disciplines (physics, electromagnetics, power systems, numerical analysis, statistics). This partially explains the success of the simplified Rusck formula, which – as we shall see – in some simplified cases can still represent a valuable engineering tool. However, the results of the research activities on the subject carried out in the last decades in many countries have permitted the development of more realistic models and their implementation in relevant computer codes, which will be further discussed in the following section. These more recent models and computer programs can deal with more realistic cases than those considered by the previous models, where the overhead line was generally assumed to be of infinite length and above a perfectly conducting ground. They are applied in the following sections to perform a sensitivity analysis aimed at providing the magnitude and waveshape of lightning-induced surges as a function of the involved physical and geometrical parameters. Clearly, additional model improvements are still highly desirable, as even the most up-to-date ones do not still take into account some aspects of the problem (e.g. channel branches, lightning current attachment processes and relevant effects on the radiated electromagnetic field). In this respect it is worth mentioning that some recent research activity carried out by Borghetti *et al.* aimed at assessing the influence of the presence of buildings around the distribution line [84].

#### 12.3.4.1 Channel-base current and return stroke speed

The sensitivity analysis is carried out first assuming five different channel-base currents, whose main parameters (peak value and maximum front-steepness) are given in Table 12.1. Note that current A2 = D2, with a peak amplitude of 12 kA and a maximum time-derivative of 40 kA/μs, corresponds to a typical subsequent return stroke, according to Berger *et al.* [85]. Waveshapes A1, A2 and A3 correspond to channel-base currents with different maximum time-derivatives, the peak value being kept constant and equal to 12 kA. Waveshapes D1, D2 and D3 correspond to

Table 12.1 *Subsequent return stroke current peak values and maximum time derivatives of the adopted currents*

Parameter	Currents					
	A1	A2 = D2	A3	D1	D2 = A2	D3
$I_{peak}$ (kA)	12	12	12	4.6	12	50
$(di/dt)_{max}$ (kA/μs)	12	40	120	40	40	40

Table 12.2 Parameters of the two Heidler functions reproducing the adopted currents

	Currents					
	A1	A2 = D2	A3	D1	A2 = D2	D3
$I_{01}$ (kA)	10.7	10.7	7.4	4.3	10.7	47
$\tau_{11}$ ( $\mu$ s)	0.95	0.25	0.063	0.086	0.25	0.9
$\tau_{12}$ ( $\mu$ s)	4.7	2.5	0.5	3.3	2.5	66
$I_{02}$ (kA)	6.5	6.5	9	2.5	6.5	0
$\tau_{21}$ ( $\mu$ s)	4.6	2.1	0.27	2.8	2.1	0
$\tau_{22}$ ( $\mu$ s)	900	230	66	270	230	0
$n$	2	2	2	2	2	2

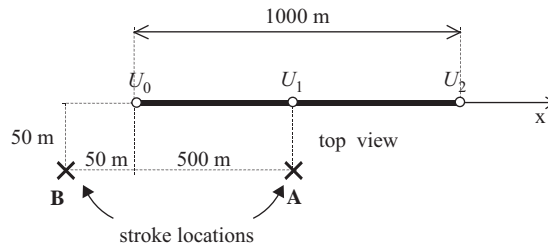


Figure 12.15 Geometry of the study. The line is matched at the two ends

currents having the same maximum time-derivative (40 kA/ $\mu$ s) but with different peak values. The selected minimum and maximum values for maximum time-derivative correspond to the 5 per cent and 95 per cent of cumulative probability according to [85].

All the channel-base currents A1, A2, A3, and D1, D2, D3 are reproduced by the sum of two Heidler functions [86], whose parameters are given in Table 12.2.

For all calculations, if not otherwise indicated, we will assume the return stroke velocity equal to  $1.9 \times 10^8$  m/s, a typical value along the first 500 m portion of the channel [87]. The effect of the variation of such a parameter will be discussed later in this section.

### 12.3.4.2 Ground electrical parameters

The calculations are performed considering (i) a perfectly conducting ground ( $\sigma_g$ ), and (ii) a ground characterised by a conductivity  $\sigma_g = 0.01$  S/m, and a relative permittivity  $\epsilon_{rg} = 10$ .

### 12.3.4.3 Line configuration and stroke location

As a base case we consider a 1 km long, 8 m high, single-conductor (diameter equal to 1 cm) overhead line. We can reasonably assume that the length of 1 km is significant enough to assess the influence of the various parameters involved in the sensitivity analysis, although distribution lines are, in general, longer than 1 km. Such an assumption will be discussed later (see later in section 12.3.4.8).

Two different stroke locations are selected: stroke location A, equidistant to the line terminations, and stroke location B, close to one of the line terminations (see Figure 12.15). The first is representative of all the stroke locations far from the distribution-line terminations; the second represents the stroke locations close to

one of the two line terminations. As the purpose of this section is a sensitivity analysis, for both cases, the line is assumed to be matched at both ends.

#### 12.3.4.4 Influence of channel-base current: stroke location A

In Figure 12.16, we show the induced voltages at the line terminations due to the channel-base currents, as shown in Table 12.1, for stroke location A. Curves with solid line refer to the case of a perfectly conducting ground (letter ‘P’ in figure’s legend), whereas the dotted curves refer to the ‘imperfect’ ground (letter ‘I’). It can be seen that, for the considered case (stroke location A and observation point at the line termination), the finite ground conductivity reduces both the peak value and the front-steepness of the induced voltages by about 20–30 per cent. Further, the ground resistivity plays a more important role for fast rising currents and is responsible for an

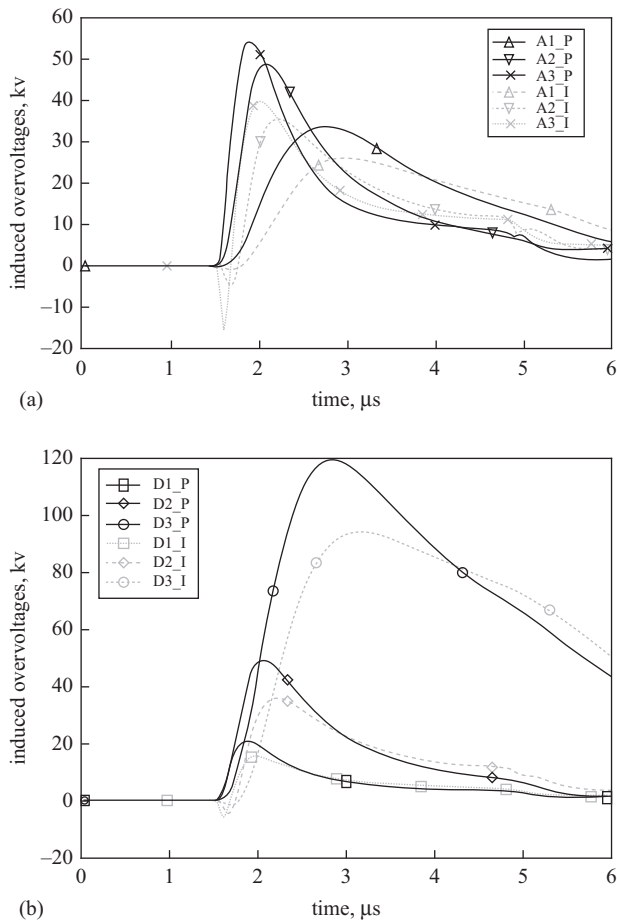


*Figure 12.16 Voltages induced at the line terminations for stroke location A. (a) Using channel-base currents with the same peak value but different time derivative (A1, A2 and A3 of Table 12.1). (b) vice-versa (currents D1, D2 and D3 of Table 12.1) (adapted from Guerrieri et al. [79])<sup>13</sup>*

<sup>13</sup> Letter ‘P’ in figure’s legend denotes a perfectly conducting ground and letter ‘I’ denotes an imperfectly conducting ground.

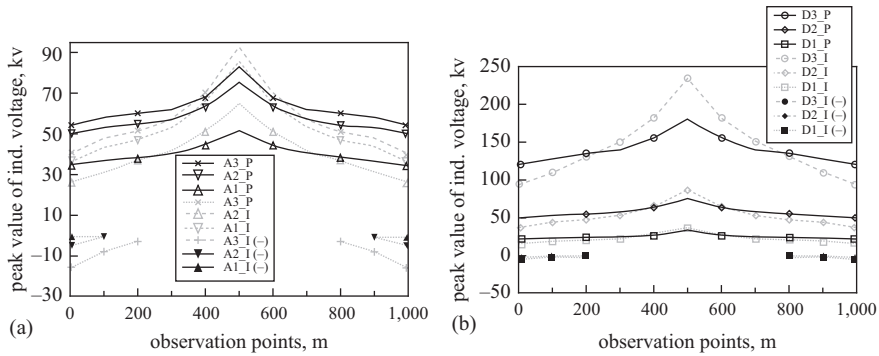


Figure 12.17 Maximum amplitude of the induced overvoltage along the line. Stroke location A. (a) Using channel-base currents with the same peak value but different time derivative ( $A_1$ ,  $A_2$  and  $A_3$  of Table 12.1); (b) vice versa (currents  $D_1$ ,  $D_2$ ,  $D_3$  of Table 12.1) (adapted from Guerrieri et al. [79])<sup>12</sup>

initial negative peak, which increases with the maximum time-derivative of the lightning current. These results can be explained by observing that, as shown in Figure 12.12a, for the considered stroke location and observation point, the induced voltage is practically given by the contribution of the horizontal electric field in the Agrawal *et al.* coupling model. As the ground conductivity decreases, the voltage due to the horizontal field contribution decreases as well, and results in an attenuation of the total induced voltage amplitude (see [88, 89] for additional details).

However, the situation changes if, for the same stroke location, we consider a different observation point. For instance, concerning the voltage at the middle point of the line, the soil resistivity produces an increase in the induced voltage, as it can be seen in Figure 12.17 where the peak value of the induced voltage is represented along the line, for the stroke location A. This can be explained considering that, for this observation point, as shown in Figure 12.12c, the contribution of the vertical electric field to the induced voltage (incident voltage plus risers) is, overall, positive (and, contrary to the previous case, can no longer be disregarded); on the other hand, for the considered observation point, the voltage due to the horizontal electric field is of negative polarity and, as its magnitude decreases with the ground resistivity, the total induced voltage increases (see Figures 12.12c and 12.13e).

Figure 12.17 shows also the negative initial peaks resulting from the finite ground conductivity (more pronounced for current A3 having the largest maximum steepness).

#### 12.3.4.5 Influence of channel-base current: stroke location B

For stroke location B, the results are presented in Figures 12.18 and 12.19. Figure 12.18a shows the induced voltages at the left line termination for currents A1, A2, and A3, whereas Figure 12.18b presents the induced voltages at the same termination for currents D1, D2, and D3. Again, solid line curves refer to the perfectly conducting ground assumption, and dotted line curves to a finitely conducting ground. Similarly, Figure 12.19 shows the induced voltages at the right line termination.

It can be seen that for an imperfectly conducting ground, the induced voltage at the near line termination (with respect to the stroke location) reaches larger magnitudes than for the case of a perfectly conducting ground. Note further that, at the



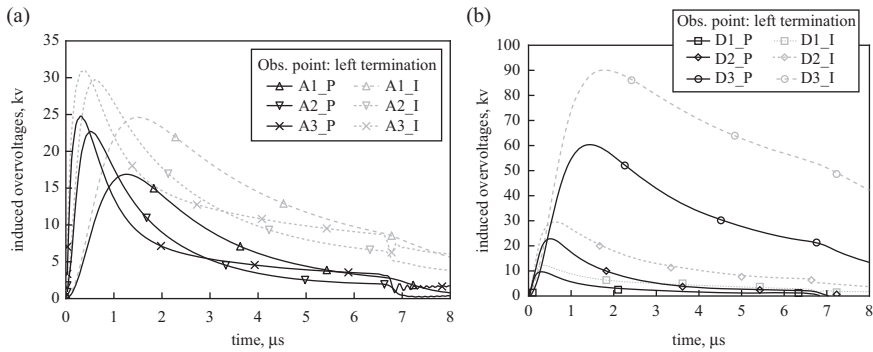


**Figure 12.18** Voltages induced at the left line termination for stroke location *B*. (a) Using channel-base currents with the same peak value but different time derivative ( $A_1$ ,  $A_2$  and  $A_3$  of Table 12.1); (b) vice versa (currents  $D_1$ ,  $D_2$ ,  $D_3$  of Table 12.1) (adapted from Guerrieri *et al.* [79])<sup>12</sup>

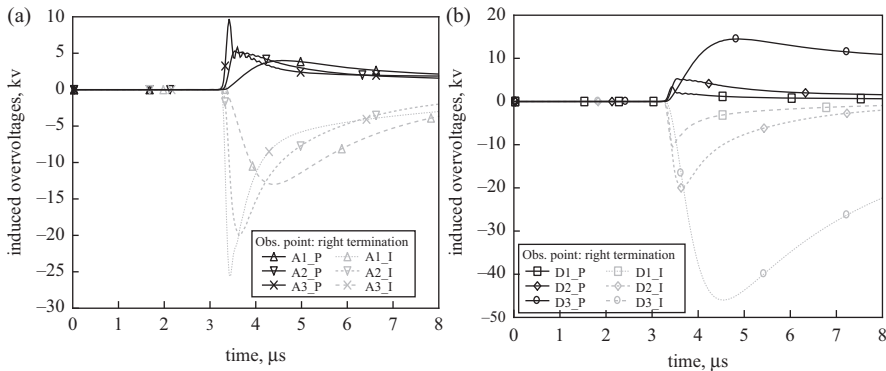


**Figure 12.19** Voltages induced at the right line termination for stroke location *B*. (a) Using channel-base currents with the same peak value but different time derivative ( $A_1$ ,  $A_2$  and  $A_3$  of Table 12.1); (b) vice versa (currents  $D_1$ ,  $D_2$ ,  $D_3$  of Table 12.1) (adapted from Guerrieri *et al.* [79])<sup>12</sup>

far line termination, the effect of the finite ground conductivity is even more evident, in that it produces an inversion of polarity in the induced voltages. For lossy soils, the induced voltage can indeed exhibit a bipolar waveshape. This can be explained, again, by considering the various contributions that form the total voltage (see [83] and [88] for additional details).

In Figure 12.20 we show the peak values of the induced voltages along the line for stroke location *B*. As for Figure 12.17, we have reported also the values of the negative peaks appearing when the ground is lossy.

It is interesting to note that while positive peaks decrease with distance from the near end, negative peaks increase, reaching their maximum value at the far end. For longer lines, the negative peak at the far termination of the line could even exceed the positive peak at the closest one. This is consistent with experimental results obtained by De la Rosa *et al.* [52], which revealed the occurrence of

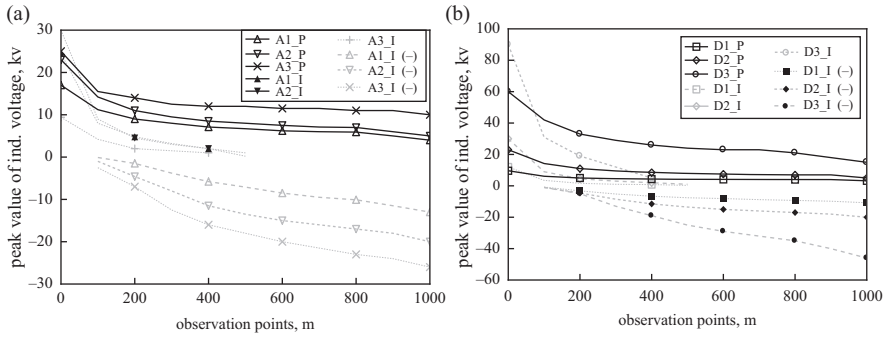


Figure 12.20 Induced overvoltage peaks along the line. Stroke location B. (a) Using channel-base currents with the same peak value but different time derivative ( $A_1$ ,  $A_2$  and  $A_3$  of Table 12.1); (b) vice versa (currents  $D_1$ ,  $D_2$ ,  $D_3$  of Table 12.1) (adapted from Guerrieri et al. [79])<sup>12</sup>

flashovers at the far end termination of an overhead line above a poor conducting soil in Mexico, and not at the close end one. It is important to realise however that beyond a certain length, depending on the ground characteristics and field wave-shape, such an enhancing effect will tend to be compensated by the attenuation of the surges due to line (ground) losses, as shown in Figure 12.21.

#### 12.3.4.6 Influence of line height

For a perfectly conducting ground, the induced voltage magnitude is nearly proportional to the line height [83, 91]. Considering the finite ground conductivity, the induced voltage peak still experiences an increase with the line height, but the increase is not rigorously linear and varies as a function of the ground conductivity, the position of the stroke location and the observation point along the line. The values of induced voltage peak as a function of line height and ground conductivity for the base case are presented in Table 12.3.

#### 12.3.4.7 Multiconductor lines

The induced voltage on one conductor of a multiconductor loaded line is, in general, affected by the presence of other conductors. The only two cases in which the shielding effect on one conductor due to the presence of the others is absent are those of an infinitely long lossless line and of a lossless matched/open line. For typical line constructions, the voltages induced on each of the line conductors are generally 15–25 per cent lower than those corresponding to a single conductor located at the same location [91]. The presence of ground wires helps in reducing the magnitude of induced voltages by a factor of about 20–40 per cent, depending on the line configuration [91]. For a comprehensive discussion on lightning-induced voltages on multiconductor lines, the interested reader is referred to [92].

#### 12.3.4.8 Influence of line length

It is useful to know up to which distance range the illumination of the line by the lightning electromagnetic field has to be considered in the evaluation of the induced overvoltages. As a matter of fact, when the LEMP response of a complex distribution network is to be evaluated, it might be useless to extend the coupling calculation beyond a certain distance.

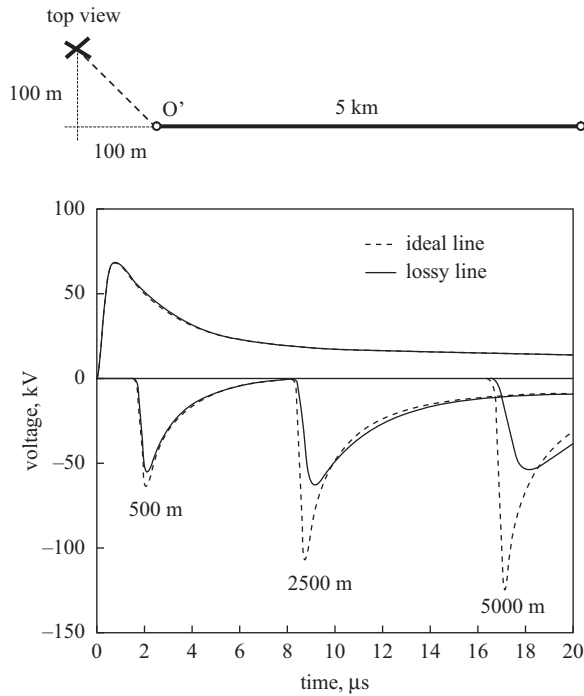


Figure 12.21 *Lightning-induced voltages at four observation points along a 5 km long line for a stroke location type B. Return stroke current A2. Ground conductivity is 0.001 S/m. In dashed lines we show the voltages calculated considering the ground resistivity only in the field calculation, but not in the surge propagation; in solid lines we show the voltages calculated considering the ground resistivity in both field calculation and surge propagation (adapted from Borghetti and Nucci [90])*

Table 12.3 *Effect of line height on the induced voltage peak for the base case, current waveshape A2 and stroke location at 50 m to the line centre and symmetrical to the line ends (adapted from [83])*

Observation point	Ground conductivity, S/m	Line height, m		
		7.5	9	10.5
$V_P$ at line end (kV)	$\infty$	49.5	59.5	69
	0.01	40.5	50	60
	0.001	26.5	35	44
$V_P$ at the line centre (kV)	$\infty$	67	81	95
	0.01	77.5	91.5	105.5
	0.001	101.5	115	128.5

Figure 12.22 shows the amplitude of the induced voltage calculated at two observation points along an overhead line, as a function of the line length, for the adopted current waveshapes and three values of ground conductivity. The stroke is located 50 m from the line centre and equidistant to the line terminations. Note that

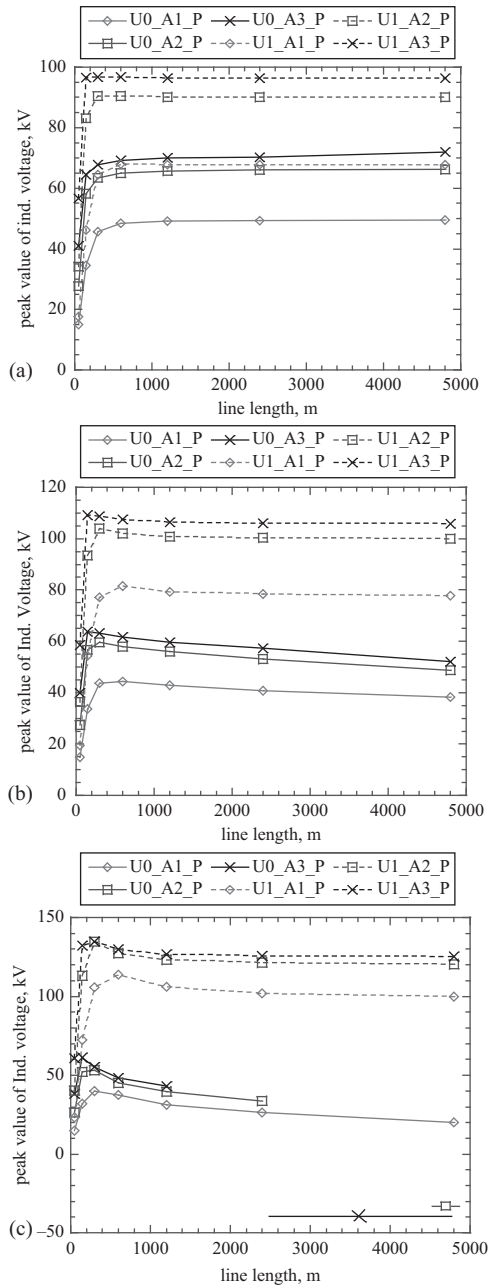


Figure 12.22 Influence of line length on the amplitude of the lightning-induced voltages along an overhead line. Stroke location equidistant from line terminations at 50 m from the line centre. Observation points:  $U_0$ , line terminations;  $U_1$ , line centre. Ground conductivity: (a) infinite, (b) 0.01 S/m, (c) 0.001 S/m. A1, A2 and A3 denote the different lightning current waveshapes adopted in the calculations (see Table 12.1).  $U_x_{Ay_Z}$ : Induced voltage  $U$  at observation point  $x$  (1 or 2) (see Figure 12.15), channel-base current  $A_y$  (A1, A2, or A3). Ground: perfectly ( $Z=P$ ) or imperfectly ( $Z=I$ ) conducting (adapted from Borghetti et al. [83])<sup>12</sup>

for line length exceeding about 2 km, for any of the examined current waveshapes the coupling between the LEMP and the line conductors becomes negligible. Note, further, that when the line is lossless, the voltage peak amplitude reaches a maximum value (that clearly depends on the current waveshape), and then remains constant with the line length. On the other hand, for poor conducting ground ( $\sigma_g = 0.001$  S/m), the voltage peak amplitude, after reaching a maximum value, exhibits first a pronounced decrease, followed by a slighter one. This is the result of the combined effect of the inversion of polarity of the excitation field that beyond a certain distance range acts in producing an inversion of polarity in the induced voltage [88], and of the surge propagation along the line. As the line length increases, the initial negative peak becomes predominant with respect to the positive one. For this reason, in Figure 12.20c, beyond a certain distance, we have plotted negative values.

If one repeats the computation for strokes located in the vicinity of one of the line terminations, it can be found that the induced voltage peak at termination close to the stroke location remains unvaried for line lengths beyond about 2 km. It is important to realise, however, that for such a case, the maximum induced voltage might occur along the line, faraway from the stroke location, as shown in Figure 12.21.

#### **12.3.4.9 Influence of the position of the stroke location with respect to the line and observation point**

For an overhead line above a perfectly conducting ground, in general, the maximum amplitude of the induced voltage is attained at the point of the line closest to the stroke location. However, as discussed earlier, when the resistivity of the ground cannot be neglected, the maximum amplitude may not be reached at the point of the line closest to the stroke location; additionally, the induced voltage can exhibit a bipolar wave-shape and a pronounced negative peak. Figure 12.23 shows the voltage induced at both ends of a 1-km-long line as a function of relative position of the stroke location, and provides an illustrative summary of the effect of stroke location and value of ground conductivity with respect to the line and to the observation point.

#### **12.3.4.10 Influence of return stroke velocity**

The induced voltage magnitude at distances not exceeding a few hundred metres is not appreciably affected by the return stroke speed [67, 83]. For more distant stroke locations (beyond a few kilometres), the induced voltage peak becomes nearly proportional to the return stroke speed, although at these distances, the magnitude of induced voltages, in general, does not represent a threat.

#### **12.3.4.11 Influence of distance of the stroke location to the line**

To analyse the effect of the distance of the stroke location to the line, we consider a stroke location symmetrical to the line terminations. The variation of the induced voltage at the line centre as a function of the distance to the stroke location is presented in Figure 12.24. For the analysis, we have considered the three current shapes of Table 12.1, two different values for the return stroke speed:  $1.3 \times 10^8$  m/s (left column) and  $1.9 \times 10^8$  m/s (right column), and the three adopted values for the ground conductivity. It can be seen that, for the considered stroke location, the voltage drops approximately inversely proportional to the distance. Also, for a given distance, the induced voltage is larger for poorer conductivities and/or higher current steepnesses.

In the same figures, we have plotted the results calculated using the simplified analytical Rusck formula [14] for the two different values of return stroke speed, namely  $1.3 \times 10^8$  and  $1.9 \times 10^8$  m/s, which we discuss next.

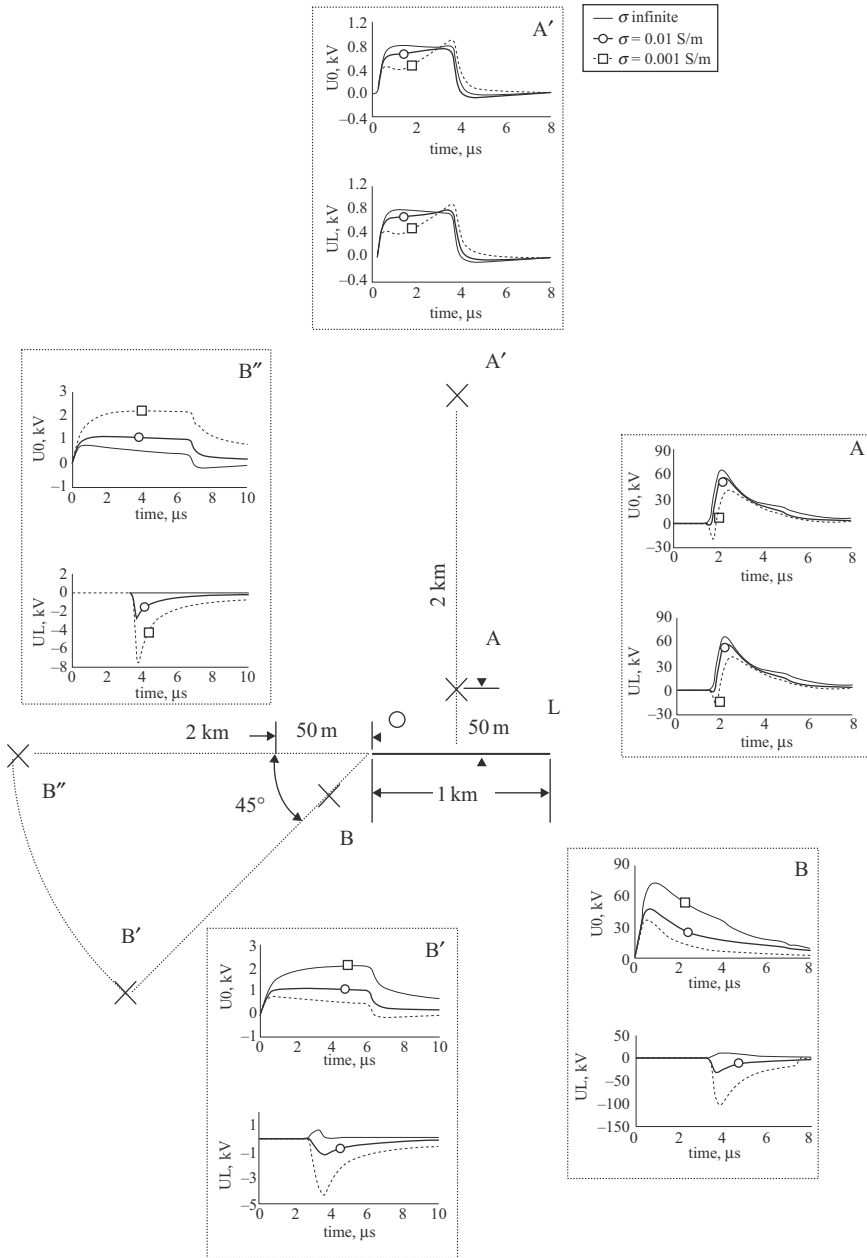
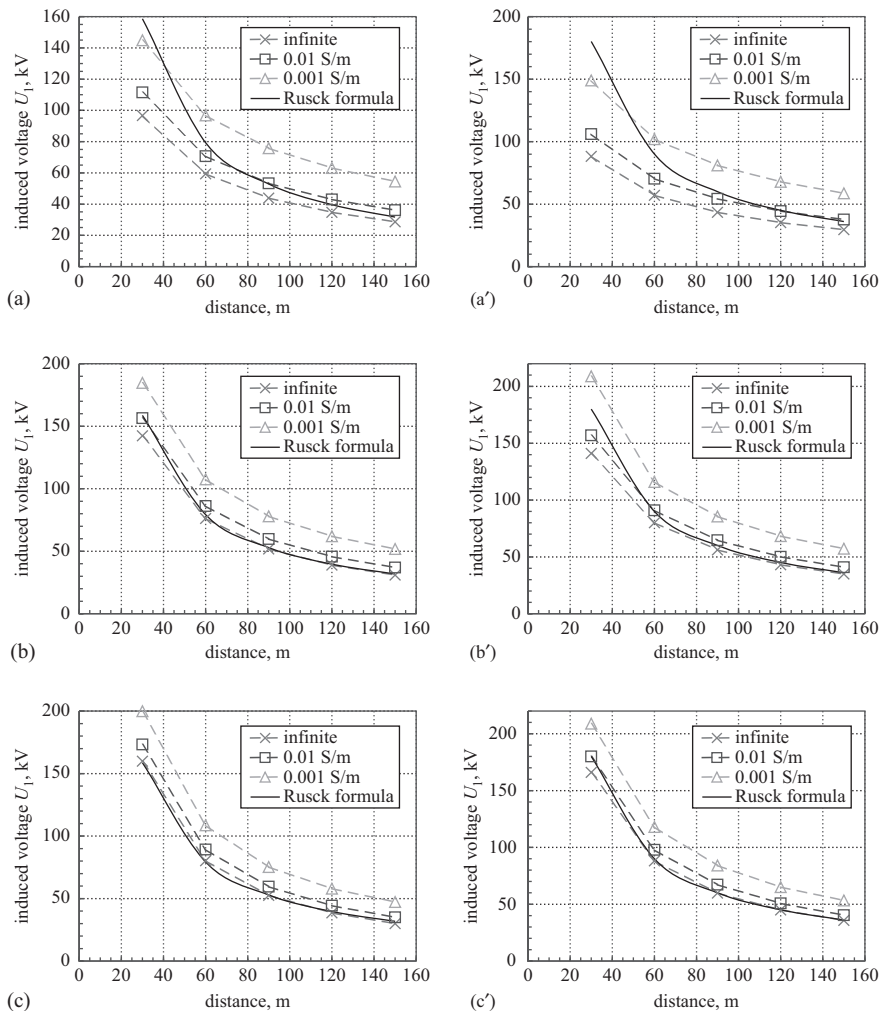


Figure 12.23 Effects of stroke location with respect to the line, with return stroke current A2, for two different observation points and for three different values of ground conductivity (adapted from Nucci et al. [89])

### 12.3.4.12 Comparison with the results obtained using the simplified Rusck formula

As mentioned earlier, the Rusck-simplified analytical formula (see (12.16) and (12.17)) gives the maximum value  $V_{max}$  of the induced overvoltages at the point of



**Figure 12.24** *Variation of the induced voltage magnitude at the line centre as a function of distance to the stroke location. Left column: return stroke velocity equal to  $1.3 \times 10^8$  m/s; right column: return stroke velocity equal to  $1.9 \times 10^8$  m/s. (a and d') Current A; (b and b') current A2; (c and c') current A3. In solid line we have reported the results obtained from the Rusck-simplified analytical expression (adapted from Borghetti et al. [83])*

an infinitely long line nearest to the stroke location (for convenience, we report the Rusck formula below):

$$V_{max} = Z_0 \frac{I \cdot h}{d} \left( 1 + \frac{1}{\sqrt{2}} \cdot \beta \cdot \frac{1}{\sqrt{(1 - 0.5 \cdot v^2)}} \right) \tag{12.16}$$

where

$$Z_0 = \frac{1}{4\pi} \sqrt{\frac{\mu_0}{\epsilon_0}} = 30 \Omega \tag{12.17}$$

where the various quantities have been already defined in section 12.2.7.

If we examine Figures 12.24a–c, we can conclude that, in general, when the channel-base currents exhibit a steep front (current A3), and when the ground is approximated as a perfectly conducting plane, the Rusck-simplified analytical expression provides an estimation for the induced voltages close to the one predicted by the more general Agrawal *et al.* model in which the forcing functions are calculated by means of the MTLE return stroke model. The disagreement between the voltage predicted by the two approaches (Rusck formula and Agrawal *et al.* MTLE models) increases with the return stroke velocity, the ground resistivity and the front duration of the lightning current. As a result, in general, the Rusck-simplified formula should not be applied to the case of overhead lines above a lossy ground.

### 12.3.5 Influence of additional factors (downward leader, corona, channel inclination and tortuosity)

#### 12.3.5.1 Downward leader electromagnetic field change

Most studies on lightning-induced voltages use as excitation source only the return stroke electric field change, neglecting any field changes prior to it. This assumption is based on theoretical considerations [93] and experimental observations made beyond a few hundred metres from the lightning channel, where the leader field change in a time scale of tens of microseconds is slow and small compared to the return stroke change [94]. More recent measurements, however, show that the leader electric field change due to triggered lightning at very close distance from the channel (e.g. 30 m) is comparable to that of the return stroke [95]. Although triggered lightning and natural lightning are dissimilar in that they are initiated by different physical processes, it is generally agreed that rocket-triggered lightning current and electromagnetic fields are very similar to those associated with natural subsequent return strokes. The implications of this observation to our understanding of lightning-induced voltages at close range have been studied in [72] and are summarised below.

In order to assess the inducing effect of the leader, the simple model originally proposed by Schonland [96] is adopted; it has been shown to produce satisfactory results at distances from the lightning channel not exceeding a few hundred metres [95]. According to this model [72, 95], a uniformly charged leader channel emerges from the centre of a volume of charge  $Q$  located in the cloud centre at height  $H_T$  and propagates vertically downward at a constant speed  $v_L$ . The return stroke is assumed to start when the leader channel reaches the ground, propagating upward at a constant speed  $v_{RS}$  and discharging the leader channel.

To calculate the return stroke fields, we assume that the return stroke discharges the previously established leader channel as it progresses towards the cloud at a constant speed. The model described above has the advantage that the electromagnetic field expressions can be evaluated analytically for both leader and return stroke phase (see [72]).<sup>14</sup>

<sup>14</sup> It is worth noting that several return stroke models specifying the spatial–temporal current distribution during the return stroke phase are proposed in the literature (see Chapter 6). If one assumes that, during the return stroke phase, all the charges deposited by the leader along the channel are removed, it follows that a specific leader charge distribution could be associated with a given return stroke model. It is therefore possible to consistently extend any return stroke model to take into account the leader phase and to calculate the electromagnetic field change.



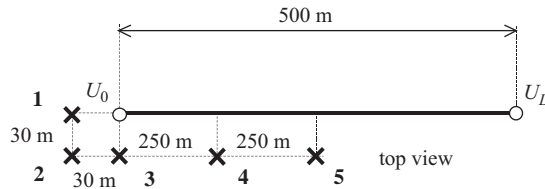


Figure 12.25 Map of considered stroke locations. The line is matched at both ends and its height above ground is 10 m (adapted from Rachidi *et al.* [72])

We here show the results of some simulations performed for a 500 m long, 10 m high, lossless single-wire overhead line matched at both ends. A relatively short line (500 m) is considered since, for such a case, the surge propagation over a finitely conducting ground could be neglected. Several stroke locations, shown in Figure 12.25, have been considered. For each case, the induced voltages  $U_0$  and  $U_L$  at both ends were computed in [72]. Some results of the simulations are shown in Figure 12.27. In it, the induced voltages calculated disregarding the leader electric field change are presented too (dashed lines). Note that in Figure 12.27, time  $t=0$  corresponds to the transition from the leader to the return stroke phase, as seen from the point of the line closest to the lightning channel. The values adopted for all the calculations are  $v_L = 107$  m/s [98],  $v_{RS} = 1.9 \times 10^8$  m/s [87],  $H_T = 5$  km. The linear charge density was assumed to be  $\rho_L = 10^{-4}$  C/m (consistent with the total charge lowered by subsequent strokes which ranges approximately from 0.2 to 1 C [94]).

The computed results show that, for stroke locations approximately along the line prolongation (Figure 12.26a,b), the dart leader electric field change contributes appreciably to the amplitude and waveshape of the induced voltages. For different stroke locations (e.g. stroke location 3), the effect of the leader is, for the considered observation points, less pronounced (Figure 12.26c,d). Note, additionally, that although the initial excursion exhibited by the dart leader-induced voltages had the same polarity for all the cases studied, its overall shape could be either unipolar, e.g. Figure 12.26a ( $U_0$ ), or bipolar, e.g. Figure 12.26b ( $U_L$ ).

One of the main conclusions of [72] is that voltage protection devices could be triggered by the leader-induced voltage, before the return stroke initiates.<sup>15</sup>

### 12.3.5.2 Effect of corona

The influence of corona on the voltages induced on overhead lines by nearby lightning has been investigated by Nucci *et al.* [73]. The first conclusion of that study is that only for particularly severe excitation conditions, e.g. lightning stroke locations very close to the line and/or large return stroke current amplitudes, corona needs to be taken into account. The corona process was described macroscopically by a charge-voltage diagram and included in Agrawal *et al.* field-to-transmission line coupling equations described by (12.18) and (12.19). Additionally, the results show that the influence of corona on the induced voltages is in general as important as the effect of the ground finite conductivity. This differs from the direct-strike behaviour, where corona, when present, affects the surge propagation more than the ground resistivity. Further, it has been shown that corona tends to increase the rise

<sup>15</sup> Continuing currents, which could also be responsible of protection operation [97], were disregarded in [72].

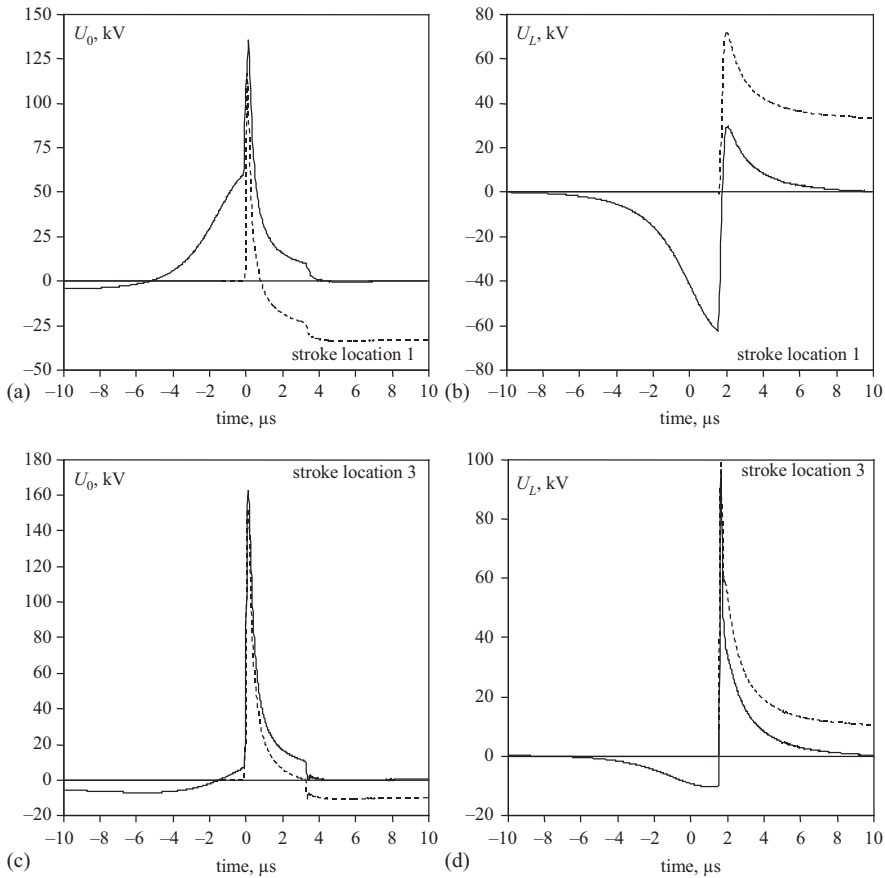


Figure 12.26 Lightning-induced voltages for stroke location 1 (a and b) and stroke location 3 (c and d) in Figure 12.25. Solid line: leader-return stroke induced voltage; Dotted line: return stroke induced voltage. Adapted from Rachidi et al. [72]

time and decrease the front steepness of the induced voltages, as for the case of direct strikes. The computation results also show a significant increase in the amplitude of the induced voltages in presence of corona, contrary to the case of direct strikes. Such a phenomenon can be explained, theoretically, by considering that the increase of the line capacitance produced by corona results in a decrease of the propagation velocity of the various surges induced by lightning.<sup>16</sup> This makes it possible for the total induced voltage – which results from the contributions of the various induced surges – to reach a larger value (see [73] for a more detailed explanation). An example showing the effect of corona on lightning-induced voltages, according to the model proposed in [99], is presented in Figure 12.27. The corona effect on multiconductor lines illuminated by LEMP has been studied in [99], where it has been found that taking into account the influence of corona on the mutual coupling between conductors can produce even higher increases of the

<sup>16</sup> If we think of the line as excited by a number of sources relevant to the impinging electromagnetic field – see, for instance, Figure 12.13 – we can associate each of these sources with the corresponding surge propagating on the line.

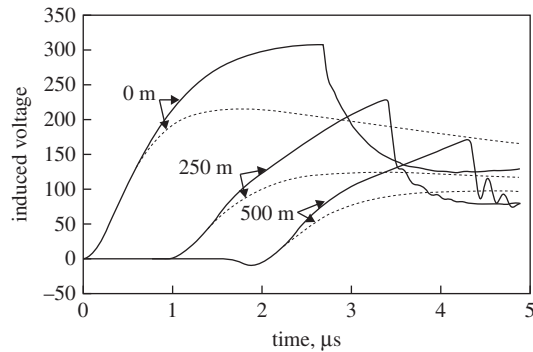


Figure 12.27 Voltages induced by a nearby lightning at three observation points along a 1 km long, 10 m high overhead line in presence of corona. Solid lines: taking into account corona; dotted lines: disregarding corona. Stroke location: 50 m from the line centre, equidistant from the line ends. Lightning current: peak value  $I_p = 35$  kA; maximum time derivative  $(di/dt)_{max} = 42$  kA/ $\mu$ s (adapted from Nucci *et al.* [73])

voltage amplitudes in the most exposed conductors, while in the less exposed ones a reduction of the voltage amplitudes is obtained.

The influence of corona on indirect lightning-induced transients on overhead transmission lines by taking into account different charge–voltage (Q–V) diagrams used to macroscopically model this phenomenon has been investigated by Dragan *et al.* [74]: for each of the examined cases of [74] corona results in an enhancement of lightning-induced overvoltages amplitude.

### 12.3.5.3 Channel inclination and tortuosity

The real geometry of a lightning channel differs from the one assumed in the analysis carried out so far, although, especially concerning subsequent return strokes, it may be a reasonable approximation.

Sakakibara [100] has first considered the effect of an inclined channel on the amplitude of the induced voltages, finding that such an effect, at least as far as the channel lies in a plane parallel to the line, is not extremely important. In [101] and [102], it is also shown that the channel inclination could affect very differently the field and induced voltage magnitudes. Indeed, depending on the channel orientation and its relative position to the observation point or to the line, the channel inclination could result either in an increase or in a decrease of the electromagnetic field and induced voltage magnitude.

### 12.3.6 Application to realistic cases: use of the LIOV–EMTP

In order to analyse the response of realistic configurations such as an electrical medium and low-voltage distribution network, to the excitation of a lightning electromagnetic field, the original LIOV code was interfaced with the electromagnetic transient program (EMTP) [103]. It is, in fact, unreasonable to expect from simplified formulas, such as the Rusck one, an accurate prediction of the amplitude and waveshape of the voltages induced by lightning on complex distribution systems (see Figure 12.28), as they were not developed to deal with those cases.

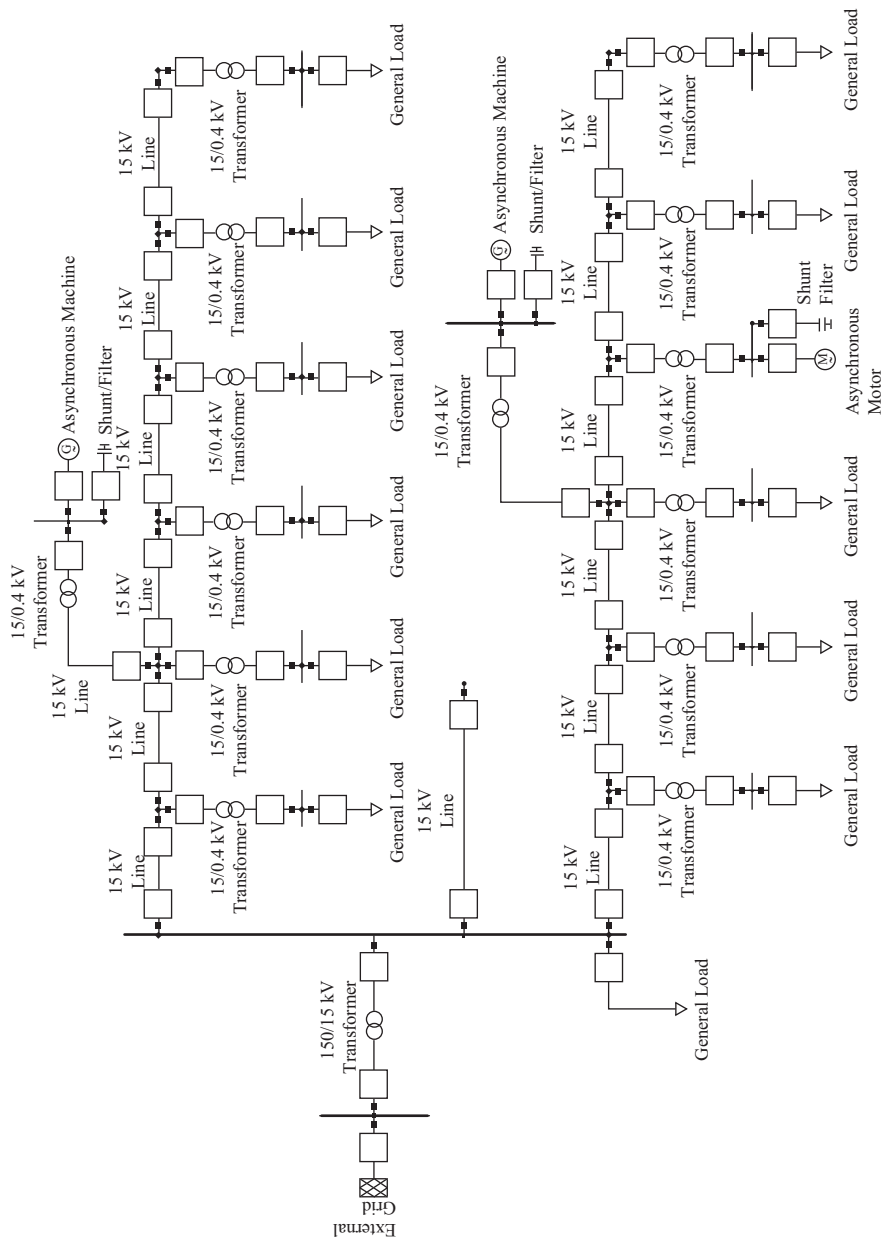


Figure 12.28 Power distribution network with complex topology (adapted from [104])

In principle, the LIOV code could serve for such a purpose, provided that the presence of the specific type of termination, as well as of the line discontinuities (e.g. surge arresters across the line insulators along the line) be properly taken into account. This procedure, however, requires that the boundary conditions for the transmission-line coupling equations be properly rewritten case by case, which can be a quite complex issue. Note, additionally, that when the termination is a power system component for which a complex circuit model is required (e.g. [105] and [106]) the boundary conditions assume a complex expression [61, 107, 108]. To deal with the problem of lightning-induced voltages on complex systems, two interfacing methods between LIOV and EMTP were then developed, the first one in collaboration with CESI [108] and the second one with EdF [109].

The concept at the basis of the first interface [108] is the following. A distribution line can be viewed as a group of lines as represented in Figure 12.1, and electrically connected by means of equivalent  $n$ -port circuits as shown in Figure 12.29. Each of these  $n$ -port circuits represents a power component located along the line (such as surge arresters, or distribution transformers), or the periodical grounding of neutral conductor for LV lines, of shielding wires for MV lines, etc. The LIOV code computes the voltages induced along the various lines that form the overall network (which we shall therefore call ‘LIOV-lines’), while the EMTP solves the boundary conditions equations relevant to the various  $n$ -port currents of the network.

The above concept has been applied to implement an improved LIOV–EMTP code [83, 104, 110, 111], based on EMTP96 [112].<sup>17</sup> With the developed LIOV–EMTP it is possible to compute the response of realistic distribution lines to nearby lightning, and therefore it can be used for insulation co-ordination of specific distribution lines, i.e. to determine the basic insulation level suitable for a given line, as well as to infer the optimal number and location of lightning surge arresters. An example of simulation using the LIOV–EMTP code is presented in Figure 12.30. The experimental results are obtained on the reduced scale model developed at the University of Saõ Paulo, earlier mentioned in section 12.2.12. More recently, LIOV has also been rewritten and interfaced with the revised version of EMTP (EMTP–RV), resulting in a new LIOV–EMTP–rv version of such an engineering tool that allows for more simulation capabilities (e.g. it is possible to take into account the interaction between grounding systems and nearby lightning [115] or the presence

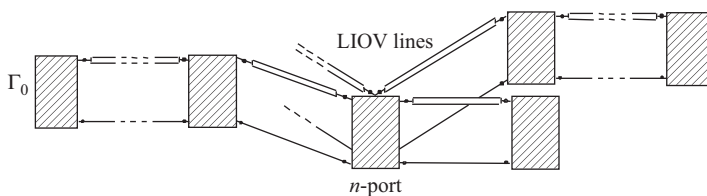


Figure 12.29 *Electrical distribution system illuminated by LEMP*

<sup>17</sup> The differences between this LIOV–EMTP programs compared to others previously developed [108, 109, 113] are discussed in [104, 114, 118]. We limit here to remind that besides all the features of the LIOV code, the LIOV–EMTP code allows for the evaluation of the LEMP response of any complicated overhead power network with any power system component connected to it, provided it is included in the EMTP library, the only limit being the computer memory.

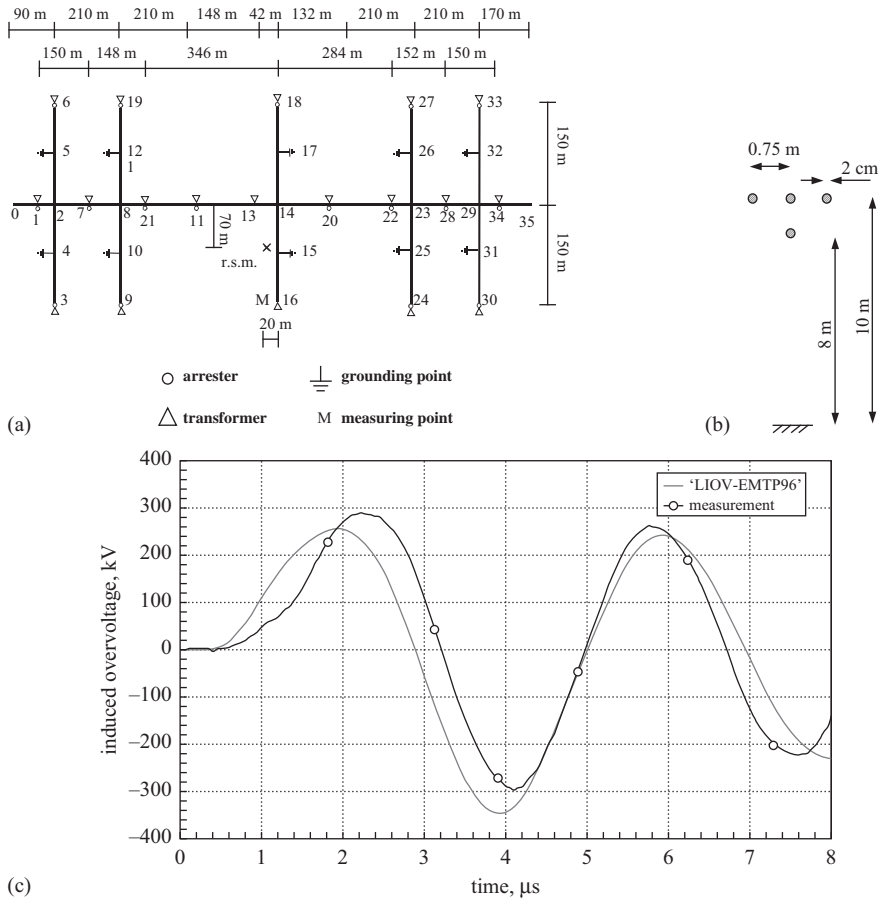


Figure 12.30 Computed and measured induced voltage on a reduced scale model of complex configuration. r.s.m. stands for stroke location (see [63] and [110] for details). (a) Topology of the analysed system; (b) line transverse geometry; (c) measured and calculated induced voltage

of resonant grounded distribution systems [116]), and that includes some powerful features that minimise the computational time, such as an analytical formulation for the electromagnetic field generated by lightning return strokes [117]. See [65] and [118] for more details.

## References

- [1] F.M. Tesche, M. Ianoz, and T. Karlsson, *EMC Analysis Methods and Computational Models*, John Wiley & Sons, New York, 1997.
- [2] A. Borghetti, C. A. Nucci, and M. Paolone, 'An improved procedure for the assessment of overhead line indirect lightning performance and its comparison with the IEEE std. 1410 method', *IEEE Transactions on Power Delivery*, vol. 22, no. 1, pp. 684–692, 2007.
- [3] C.R. Paul, *Analysis of Multiconductor Transmission Lines*, John Wiley & Sons, New York, 1994.

- [4] C.A. Nucci, F. Rachidi, and M. Rubinstein, 'Derivation of telegrapher's equations and field-to-transmission line interaction, in *Electromagnetic Field Interaction with Transmission Lines. From Classical Theory to HF Radiation Effects*, F. Rachidi and S. Tkachenko, ed., WIT Press, Southampton, UK, 2008.
- [5] F. Rachidi, 'A review of field-to-transmission line coupling models with special emphasis to lightning-induced voltages', *IEEE Transactions on Electromagnetic Compatibility*, vol. 54, no. 4, pp. 898–911, 2012.
- [6] F. Napolitano, A. Borghetti, C. A. Nucci, F. Rachidi, and M. Paolone, 'Use of the full-wave finite element method for the numerical electromagnetic analysis of LEMP and its coupling to overhead lines', *Electric Power Systems Research*, vol. 94, pp. 24–29, 2013.
- [7] A.K. Agrawal, H.J. Price, and S.H. Gurbaxani, 'Transient response of a multiconductor transmission line excited by a nonuniform electromagnetic field', *IEEE Transactions on Electromagnetic Compatibility*, vol. EMC-22, no. 2, pp. 119–129, May 1980.
- [8] C.D. Taylor, R.S. Satterwhite, and C.W. Harrison, 'The response of a terminated two-wire transmission line excited by a nonuniform electromagnetic field', *IEEE Transactions on Antennas and Propagation*, vol. AP-13, pp. 987–989, 1965.
- [9] M. Ianoz, C.A. Nucci, and F.M. Tesche, 'Transmission line theory for field-to-transmission line coupling calculations', *Electromagnetics*, vol. 8, no. 2–4, pp. 171–211, 1988.
- [10] F. Rachidi, 'Formulation of the field-to-transmission line coupling equations in terms of magnetic excitation fields', *IEEE Transactions on Electromagnetic Compatibility*, vol. 35, no. 3, August 1993.
- [11] C.A. Nucci and F. Rachidi, 'On the contribution of the electromagnetic field components in field-to-transmission lines interaction', *IEEE Transactions on Electromagnetic Compatibility*, vol. 37, no. 4, pp. 505–508, November 1995.
- [12] C.A. Nucci, C. Mazzetti, F. Rachidi, and M. Ianoz, 'On lightning return stroke models for LEMP calculations', *Proceedings of the 19th International Conference on Lightning Protection*, pp. 463–469, Graz, 25–29, April 1988.
- [13] F. Rachidi and C. A. Nucci, 'On the Master, Lin, Uman, Standler and the modified transmission line lightning return stroke current models', *Journal of Geophysical Research*, vol. 95, pp. 20389–20394, November 1990.
- [14] S. Rusck, 'Induced lightning overvoltages on power transmission lines with special reference to the overvoltage protection of low voltage networks', *Transactions of the Royal Institute of Technology, Stockholm*, no. 120, 1958.
- [15] P. Chowdhuri and E.T.B. Gross, 'Voltage surges induced on overhead lines by lightning strokes', *Proceedings of IEE*, vol. 114, no. 12, pp. 1899–1907, December 1967.
- [16] M.J. Master and M.A. Uman, 'Lightning induced voltages on power lines: Theory', *IEEE Transactions on Power Apparatus and Systems*, vol. PAS-103, no. 9, pp. 2502–2518, September 1984.
- [17] P. Chowdhuri, 'Analysis of lightning induced voltages on overhead lines', *IEEE Transactions on Power Delivery*, vol. 6, no. 1, pp. 479–492, January 1989.
- [18] G. Diendorfer, 'Induced voltage on an overhead line to nearby lightning', *IEEE Transactions on Electromagnetic Compatibility*, vol. EMC-32, no. 4, pp. 292–299, November 1990.

- [19] P. Chowdhuri, 'Response of overhead lines of finite length to nearby lightning strokes', *IEEE Transactions on Power Delivery*, vol. 6, no. 1, January 1991.
- [20] C.A. Nucci, F. Rachidi, M. Ianoz, and C. Mazzetti, 'Comparison of two coupling models for lightning-induced overvoltage calculations', *IEEE Transactions on Power Delivery*, vol. 10, no. 1, pp 330–338, January 1995.
- [21] V. Cooray, 'Calculating lightning-induced overvoltages in power lines: A comparison of two coupling models', *IEEE Transactions on Electromagnetic Compatibility*, vol. 36, no. 3, pp. 179–182, August 1994.
- [22] P. Chowdhuri, *Electromagnetic Transients in Power Systems* (Chapter 8), *Research Studies Press Ltd*, England, 1996.
- [23] P. Chowdhuri, S. Li, and P. Yan, 'Review of research on lightning-induced voltages on an overhead line', *IEE Proceedings on Generation, Transmission and Distribution*, vol. 148, no. 1, , pp. 91–95, January 2001.
- [24] F. Rachidi, C.A. Nucci, M. Ianoz, and C. Mazzetti, 'Influence of a lossy ground on lightning-induced voltages on overhead lines', *IEEE Transactions on Electromagnetic Compatibility*, vol. 38, no. 3, pp. 250–264, August 1996.
- [25] S. Ramo, J.R. Whinnery, and T. Van Duzer, *Fields and Waves in Communication Electronics*, John Wiley & Sons, New York, 1994.
- [26] F.M. Tesche, 'Comparison of the transmission line and scattering models for computing the HEMP response of overhead cables', *IEEE Transactions on Electromagnetic Compatibility*, vol. 34, pp. 93–99, May 1992.
- [27] J.R. Carson, Wave propagation in overhead wires with ground return, *Bell System Technical Journal*, vol. 5, pp. 539–554, 1926.
- [28] F. Pollaczek, 'On the field produced by an infinitely long wire carrying alternating current', *Elektrische Nachrichten Technik*, vol. III, no. 9, pp. 339–359, 1926, French translation by J.B. Pomey, *Revue Générale de l'Electricité*, vol. 29, no. 2, pp. 851–867, 1931.
- [29] E.D. Sunde, *Earth Conduction Effects in Transmission Systems*, Dover, New York, NY, 1968.
- [30] J.R. Wait, 'Theory of Wave Propagation along a Thin Wire Parallel to an Interface', *Radio Science*, vol. 7, pp. 675–679, June 1972.
- [31] R.W.P. King, T.T. Wu, and L.C. Shen, 'The horizontal wire antenna over a conducting or dielectric half space: current and admittance', *Radio Science*, vol. 9, pp. 701–709, July 1974.
- [32] M.C. Perz and M.R. Raghuvver, 'Generalized derivation of fields and impedance correction factors of lossy transmission lines. Part II: Lossy conductors above lossy ground', *IEEE Transactions on Power Apparatus and Systems*, vol. 93, pp. 1832–1841, 1974.
- [33] D.C. Chang and R.G. Olsen, 'Excitation of an infinite antenna above a dissipative earth', *Radio Science*, vol. 10, pp. 823–831, August–September 1975.
- [34] C. Gary, 'Approche complète de la propagation multifilaire en haute fréquence par l'utilisation des matrices complexe', *EDF Bulletin de la direction des études et recherches*, Série B, no. 3/4, pp. 5–20, 1976.
- [35] E.F. Vance, *Coupling to Shielded Cables*, R.E. Krieger, New York, FL, 1987.
- [36] A. Semlyen, 'Ground return parameters of transmission lines. An asymptotic analysis for very high frequencies', *IEEE Transactions on Power Apparatus and Systems*, vol. 100, no. 3, pp. 1031–1038, March 1981.



- [37] R.G. Olsen and T.A. Pankaskie, 'On the exact, Carson and image theories for wires at or above the earth's interface', *IEEE Transactions on Power Apparatus and Systems*, vol. 102, pp. 760–778, April 1983.
- [38] K.C. Chen, 'Time harmonic solutions for a long horizontal wire over the ground with grazing incidence', *IEEE Transactions on Antennas and Propagation*, vol. 33, pp. 233–243, March 1985.
- [39] M. D'Amore and M.S. Sarto, 'A new formulation of lossy ground return parameters for transient analysis of multiconductor dissipative lines', IEEE-PES Winter Meeting, Baltimore, MD, 1996.
- [40] G.J. Bridges and L. Shafai, 'Plane wave coupling to multiple conductor transmission lines above a lossy earth', *IEEE Transactions on Electromagnetic Compatibility*, vol. 31, no. 1, pp. 21–33, February 1989.
- [41] F. Rachidi, C.A. Nucci, and M. Ianoz, 'Transient analysis of multiconductor lines above a lossy ground', *IEEE Transactions on Power Delivery*, vol. 14, no. 1, pp. 294–302, January 1999.
- [42] J.H. Scott, 'Electrical and magnetic properties of rock and soil', Note 18 in AFWL EMP 2-1, Electromagnetic Pulse Theoretical Notes, April 1971.
- [43] C.L. Longmire and J.L. Gilbert, 'Theory of EMP coupling in the source region', DNA Report, Contract No. DNA 001-79-C-0186, 1980.
- [44] F. Rachidi, S.L. Loyka, C.A. Nucci, and M. Ianoz, 'A new expression for the ground transient resistance matrix elements of multiconductor overhead transmission lines', *Electric Power Systems Research*, vol. 65, pp. 41–46, 2003.
- [45] A. Timotin, 'Longitudinal transient parameters of a unifilar line with ground return', *Revue Roumaine des Sciences Techniques – Série Électrotechnique et Énergétique (RRST-EE)*, vol. 12, no. 4, pp. 523–535, Bucarest, 1967.
- [46] S. Yokoyama, K. Miyake, H. Mitani, and A. Takanishi, 'Simultaneous measurement of lightning induced voltages with associated stroke currents', *IEEE Transactions on Power Apparatus and Systems*, vol. PAS-102, no. 8, pp. 2420–2429, August 1983.
- [47] S. Yokoyama, K. Miyake, H. Mitani, and N. Yamazaki, 'Advanced observations of lightning induced voltage on power distribution lines', *IEEE Transactions on Power Systems*, vol. PWRD-1, no. 2, pp. 129–139, April 1986.
- [48] S. Yokoyama, K. Miyake, and S. Fukui, 'Advanced observations of lightning induced voltages on power distribution lines (II)', *IEEE Transactions on Power Delivery*, vol. 4, no. 4, pp. 2196–2203, October 1989.
- [49] M.J. Master, M.A. Uman, W.H. Beasley, and M. Darveniza, 'Lightning induced voltages on power lines: Experiment', *IEEE Transactions on Power Apparatus and Systems*, vol. PAS-103, no. 9, pp. 2519–2529, September 1984.
- [50] M. Rubinstein, A.Y. Tzeng, M.A. Uman, P.J. Medelius, and E.M. Thomson, 'An experimental test of a theory of lightning-induced voltages on an overhead wire', *IEEE Transactions on Electromagnetic Compatibility*, vol. 31, no. 4, pp. 376–383, November 1989.
- [51] N. Georgiadis, M. Rubinstein, M.A. Uman, P.J. Medelius, and E.M. Thomson, 'Lightning-induced voltages at both ends of a 488-m power distribution line', *IEEE Transactions on Electromagnetic Compatibility*, vol. 34, no. 4, November 1992.

- [52] F. de la Rosa, R. Valdiviva, H. Pérez, and J. Loza, 'Discussion about the inducing effects of lightning in an experimental power distribution line in Mexico', *IEEE Transactions on Power Delivery*, vol. 3, no. 3, July 1988.
- [53] V. Cooray and F. de la Rosa, 'Shapes and amplitudes of the initial peaks of lightning-induced voltage in power lines over finitely conducting earth: Theory and comparison with experiment', *IEEE Transactions on Antennas and Propagation*, vol. AP-34, no. 1, pp. 88–92, January 1986.
- [54] P.P. Barker, T.A. Short, A. Eybert-Berard, and J.B. Berlandis, 'Induced voltage measurements on an experimental distribution line during nearby rocket triggered lightning flashes', *IEEE Transactions on Power Delivery*, vol. 11, pp. 980–995, 1996.
- [55] M. Paolone *et al.* 'Lightning-induced disturbances in buried cables. Part II: Experiment and model validation', *IEEE Transactions on Electromagnetic Compatibility*, vol. 47, no. 3, pp. 509–520, August 2005.
- [56] E. Petrache *et al.* 'Lightning-induced currents in buried coaxial cables: A frequency-domain approach and its validation using rocket-triggered lightning', *Journal of Electrostatics*, doi:10.1016/j.elstat.2006.09.015, vol. 65, pp. 322–328, May 2007.
- [57] J. Schoene *et al.* 'Lightning currents flowing in the soil and entering a test power distribution line via its grounding', *IEEE Transactions on Power Delivery*, vol. 24, no. 3, pp. 1095–1103, July 2009.
- [58] C.E. Baum, 'EMP simulators, for various types of nuclear EMP environment: An interim categorization', *IEEE Transactions on Electromagnetic Compatibility*, vol. 20, no. 1, pp. 35–53, February 1978.
- [59] F. Arreghini, M. Ianoz, P. Zwiackner, and D.V. Giri, 'SEMIRAMIS: An asymmetrical bounded wave EMP simulator with a good confinement inside the transmission line', *Proceedings of the 10th International Zurich Symposium on Electromagnetic Compatibility*, March 1993.
- [60] S. Guerrieri *et al.* 'Effet d'une impulsion électro-magnétique sur des réseaux électriques à plusieurs branches. Modélisation et validation expérimentale', *Proceedings of the 7ème Colloque Int. sur la CEM*, pp. 475–480, Toulouse, March 1994.
- [61] S. Guerrieri, F. Rachidi, M. Ianoz, P. Zwiackner, and C.A. Nucci, 'A time-domain approach to evaluate induced voltages on tree-shaped electrical networks by external electromagnetic fields', *Proceedings of the 11th International Zurich Symposium on Electromagnetic Compatibility*, March 1995.
- [62] M. Ishii, K. Michishita, Y. Hongo, and S. Ogume, 'Lightning-induced voltage on an overhead wire dependent on ground conductivity', *IEEE Transactions on Power Delivery*, vol. 9, no. 1, January 1994.
- [63] A. Piantini and J.M. Janiszewski, 'An experimental study of lightning induced voltages by means of a scale model', *Proceedings of the 21st International Conference on Lightning Protection*, paper 4.08, pp. 195–199, Berlin, September 1992.
- [64] C.A. Nucci, A. Borghetti, A. Piantini, and J.M. Janiszewski, 'Lightning-induced voltages on distribution overhead lines: Comparison between experimental results from a reduced-scale model and most recent approaches', *Proceedings of the 24th International Conference on Lightning Protection*, pp. 314–320, Birmingham, 14–18 September 1998.

- [65] M. Paolone *et al.* 'Lightning electromagnetic field coupling to overhead lines: Theory, numerical simulations and experimental validation', *IEEE Transactions on Electromagnetic Compatibility*, vol. 51, no. 3, pp. 532–547, August 2009.
- [66] V.A. Rakov, 'Lightning discharges triggered using rocket-and-wire techniques', *Recent Research and Development in Geophysics*, vol. 2, pp. 141–171, 1999.
- [67] C.A. Nucci, F. Rachidi, M. Ianoz, and C. Mazzetti, 'Lightning-induced voltages on overhead lines', *IEEE Transactions on Electromagnetic Compatibility*, vol. 35, pp. 75–86, February 1993 (Corrections vol. 35, no. 4, p. 488, November 1993).
- [68] M.A. Uman, D.K. McLain, and E.P. Krider, 'The electromagnetic radiation from a finite antenna', *American Journal of Physics*, vol. 43, pp. 33–38, 1975.
- [69] V. Cooray, 'Lightning-induced overvoltages in power lines: Validity of various approximations made in overvoltage calculations', *Proceedings of the 22nd International Conference on Lightning Protection*, Budapest, 19–23 September 1994.
- [70] M. Rubinstein, 'An approximate formula for the calculation of the horizontal electric field from lightning at close, intermediate, and long range', *IEEE Transactions on Electromagnetic Compatibility*, vol. 38, no. 3, pp. 531–535, August 1996.
- [71] C.A. Nucci and F. Rachidi, 'Experimental validation of a modification to the transmission line model for LEMP calculations', 8th International Symposium on Electromagnetic Compatibility, pp. 389–394, Zurich, 7–9 March 1989.
- [72] F. Rachidi, M. Rubinstein, S. Guerrieri, and C.A. Nucci, 'Voltages induced on overhead lines by dart leaders and subsequent return-strokes in natural and rocket triggered lightning', *IEEE Transactions on Electromagnetic Compatibility*, vol. 39, no. 2, pp. 160–166, May 1997.
- [73] C.A. Nucci, S. Guerrieri, M.T. Correia de Barros, and F. Rachidi, 'Influence of corona on the voltages induced by nearby lightning on overhead distribution lines', *IEEE Transactions on Power Delivery*, vol. 15, no. 4, pp. 1265–1273, October 2000.
- [74] G. Dragan, G. Florea, C. A. Nucci, and M. Paolone, 'On the influence of corona on lightning-induced overvoltages', 30th International Conference on Lightning Protection, Cagliari, Italy, 13–17 September 2010.
- [75] V. Cooray, 'Some considerations on the 'Cooray-Rubinstein' approximation used in deriving the horizontal electric field over finitely conducting ground', *IEEE Transactions on Electromagnetic Compatibility*, vol. 44, no. 4, November 2002.
- [76] J.R. Wait, 'Concerning horizontal electric field of lightning', *IEEE Transactions on Electromagnetic Compatibility*, vol. 39, no. 2, pp. 186, May 1997.
- [77] C.A. Nucci, P. Chowdhuri, F. de la Rosa, G. Diendorfer, F. Heidler, W. Janischewskyj, *et al.*, 'Lightning-induced voltages on overhead power lines. Part II: Coupling models for the evaluation of the induced voltages', *Electra*, no. 162, pp. 121–145, October 1995.
- [78] V.F. Hermosillo and V. Cooray, 'Calculation of fault rates of overhead power distribution lines due to lightning induced voltages including the

- effect of ground conductivity', *IEEE Transactions on Electromagnetic Compatibility*, vol. 37, no. 3, pp. 392–399, 1995.
- [79] S. Guerrieri, M. Ianoz, C. Mazzetti, C.A. Nucci, and F. Rachidi, 'Lightning induced voltages on an overhead line above a lossy ground: A sensitivity analysis', *Proceedings of the 23rd ICLP*, Florence, 23–27 September 1996.
- [80] K. Michishita, M. Ishi, and Y. Imai, 'Lightning-induced voltages on multiconductor distribution line influenced by ground conductivity', 23rd International Conference on Lightning Protection, vol. I, pp. 30–35, Firenze, 23–27 September 1996.
- [81] H. K. Hoidalén, J. Sletbak, and T. Henriksen, 'Ground effects on induced voltages from nearby lightning', *IEEE Transactions on Electromagnetic Compatibility*, vol. 39, no. 4, pp. 269–278, 1997.
- [82] V. Cooray and V. Schuka, 'Lightning-induced overvoltages in power lines: Validity of various approximations made in overvoltage calculations', *IEEE Transactions on Electromagnetic Compatibility*, vol. 40, no. 4, pp. 355–363, 1998.
- [83] A. Borghetti, C.A. Nucci, M. Paolone, and F. Rachidi, 'Characterization of the response of an overhead line to lightning electromagnetic fields', 25th International Conference on Lightning Protection, ICLP'2000, Rhodes, Greece, September 2000.
- [84] A. Borghetti, F. Napolitano, C. A. Nucci, and M. Paolone, 'Effects of nearby buildings on lightning induced voltages on overhead power distribution lines', *Electric Power Systems Research*, vol. 94, pp. 38–45, 2013.
- [85] K. Berger, R.B. Anderson, and H. Kroninger, 'Parameters of lightning flashes', *Electra*, no. 1, pp. 23–27, 1975.
- [86] F. Heidler, 'Analytische Blitzstrom funktion zur LEMP-Berechnung', *Proceedings of the 18th International Conference on Lightning Protection*, paper 1.9, pp. 63–66, Munich, 16–20 September 1985.
- [87] D.M. Mach and W.D. Rust, 'Photoelectric return-stroke velocity and peak current estimates in natural and triggered lightning', *Journal of Geophysics Research*, vol. 94, no. D11, pp. 13237–13247, September 1989.
- [88] S. Guerrieri, C.A. Nucci, and F. Rachidi, 'Influence of the ground resistivity on the polarity and intensity of lightning induced voltages', *Proceedings of the 10th International Symposium on High Voltage Engineering*, Montreal, 24–30 August 1997.
- [89] C.A. Nucci, P. Chowdhuri, G.V. Cooray, M.T. Correia de Barros, M. Darveniza, F. De la Rosa, *et al.*, 'Lightning-induced voltages on overhead power lines. Part III: Sensitivity analysis', *Electra*, no. 222, pp. 27–30, October 2005.
- [90] A. Borghetti and C.A. Nucci, 'Frequency distribution of lightning-induced voltages on an overhead line above a lossy ground', *Proceedings of the 5th International Symposium on Lightning Protection*, São Paulo, 17–21 May 1999.
- [91] F. Rachidi, C.A. Nucci, M. Ianoz, and C. Mazzetti, 'Response of multiconductor power lines to nearby lightning return stroke electromagnetic fields', *IEEE Transactions on Power Delivery*, vol. 12, pp. 1404–1411, July 1997.
- [92] F. Napolitano, F. Tossani, C.A. Nucci, and F. Rachidi, 'LEMP response of multiconductor lines', *IEEE Transactions on Power Delivery*, doi:10.1109/TPWRD.2014.

- [93] C.F. Wagner and G.D. McCann, 'Induced voltages on transmission lines', *Electrical Engineering*, vol. 61, pp. 916–929, 1942.
- [94] M.A. Uman, *The Lightning Discharge*, Academic Press, San Diego, 1987.
- [95] M. Rubinstein *et al.* 'Characterization of vertical electric fields 500 m and 30 m from triggered lightning', *Journal of Geophysics Research*, vol. 100, no. D5, pp. 8863–8872, May 1995.
- [96] B.F. Schonland, 'The lightning discharge', *Handbook Physics*, vol. 22, pp. 576–628, 1956.
- [97] M.A. Uman, private communication.
- [98] D.M. Jordan *et al.* 'Observed dart leader speed in natural and triggered lightning', *Journal of Geophysics Research*, vol. 97, pp. 9951–9957, 1992.
- [99] M. T. Correia de Barros, J. Festas, C.A. Nucci, and F. Rachidi, 'Corona on multiconductor overhead lines illuminated by LEMP', *Proceedings of the 4th International Symposium on Power System Transients*, Budapest, June 1999.
- [100] A. Sakakibara, 'Calculation of lightning-induced voltages on overhead lines caused by inclined lightning strokes', *IEEE Transactions on Power Apparatus and Systems*, vol. 4, no. 1, pp. 683–693, Jan 1989.
- [101] B. Kordi, R. Moini, and F. Rachidi, 'Modeling an inclined lightning return stroke channel using the Antenna Theory model', *14th International Zurich Symposium on Electromagnetic Compatibility*, February 2001, Zurich.
- [102] R. Moini, S.H. Sadeghi, B. Kordi, and F. Rachidi, 'An antenna-theory approach for modeling inclined lightning return stroke channels', *Electric Power Systems Research Journal*, vol. 76, no. 11, pp. 945–952, July 2006.
- [103] *Electromagnetic Transient Program (EMTP) Rule Book*, Bonneville Power Administration, Portland, OR, 1984.
- [104] A. Borghetti, J.A. Gutierrez, C.A. Nucci, M. Paolone, E. Petrache, F. Rachidi, 'Lightning-induced voltages on complex distribution systems: models, advanced software tools and experimental validation', *Journal of Electrostatics*, 60, pp. 163–174, 2004.
- [105] P.T.M. Vaessen, 'Transformer model for high frequencies', *IEEE Transactions on Power Delivery*, vol. 7, no. 3, pp. 1761–1768, July 1992.
- [106] A. Morched, L. Martí, and J. Ottevangers, 'A high-frequency transformer model for the EMTP', *IEEE Transactions on Power Delivery*, vol. 8, no. 3, pp. 1615–1626, July 1993.
- [107] R. Iorio, C.A. Nucci, A. Porrino, and F. Rachidi, 'Lightning-induced overvoltages on distribution overhead lines in presence of distribution transformers or short cables', *Proceedings of the CIGRE Symposium on 'Power System Electromagnetic Compatibility'*, 6 pp., Losanna, 18–20 October 1993.
- [108] C.A. Nucci, V. Bardazzi, R. Iorio, A. Mansoldo, and A. Porrino, 'A code for the calculation of lightning-induced overvoltages and its interface with the electromagnetic transient program', *Proceedings of the 22nd International Conference on Lightning Protection*, Budapest, 19–23 September 1994.
- [109] D. Orzan, P. Baraton, M. Ianoz, and F. Rachidi, 'Comparaison entre deux approches pour traiter le couplage entre un champ EM et des réseaux de lignes' (in French), *Proceedings of the 8th Colloque International sur la CEM*, pp. 55–60, Lille, September 1996.
- [110] M. Paolone, C.A. Nucci, and F. Rachidi, 'A new finite difference time domain scheme for the evaluation of lightning induced overvoltages on

- multiconductor overhead lines', *Proceedings of the 5th International Conference on Power System Transients*, Rio de Janeiro, June 2001.
- [111] M. Paolone *et al.* 'A new interface for lightning induced overvoltages calculation between EMTP and LIOV code', IEEE Summer Meeting, 15–19 July 2001, Vancouver, British Columbia, Canada – EMTP user group meeting.
- [112] DCG, *EMTP96 Rule book*, DCG, 1996.
- [113] H.K. Høidalen, 'Calculation of lightning-induced overvoltages using MODELS', *Proceedings of the International Conference on Power Systems Transients*, Budapest, Hungary, pp. 359–364, 1999.
- [114] M. Paolone, *Modeling of Lightning-Induced Voltages on Distribution Networks for the Solution of Power Quality Problems, and Relevant Implementation in a Transient Program*, PhD thesis, University of Bologna, 2001.
- [115] F. Napolitano, *et al.*, 'Interaction between grounding systems and nearby lightning for the calculation of overvoltages in overhead distribution lines', *IEEE Trondheim PowerTech*, 19–23 June 2011.
- [116] A. Borghetti, *et al.*, 'Protection systems against lightning-originated overvoltages in resonant grounded power distribution systems', 2012 International Conference on Lightning Protection (ICLP), Vienna, Austria, pp. 1–7, 2012.
- [117] F. Napolitano, 'An analytical formulation of the electromagnetic field generated by lightning return strokes', *IEEE Transactions on Electromagnetic Compatibility*, vol. 53, no. 1, pp. 108–113, February 2011.
- [118] F. Napolitano, A. Borghetti, C. A. Nucci, M. Paolone, and F. Rachidi, 'A Link Between the LIOV code and the EMTP-RV for the calculation of lightning-induced voltages on distribution lines', 29th International Conference on Lightning Protection (ICLP), 2008.



---

## Chapter 13

# Principles of protection of structures against lightning

Carlo Mazzetti

---

Thunderstorms are natural weather phenomena and there are no devices and methods capable of preventing lightning discharges. Direct and nearby cloud-to-ground discharges can be hazardous to structures, persons, installations and other things in or on them, so that the application of lightning protection measures must be considered.

The decision for the need for protection and the selection of protection measures should be determined in terms of risk, which means that these measures should be adequate to reduce the risk to a tolerable level.

The modern approach is that of risk management, which integrates the need for protection and the selection of adequate protection measures taking into account both the efficiency of the measures and the cost of their provision. In the risk management approach, the lightning threats that create risk are identified, the frequencies of all risk events are estimated, the consequences of the risk events are determined and, if these are above a tolerable level of risk, protection measures are applied to reduce the risk ( $R$ ) to below the tolerable level ( $R_T$ ).

It should be stressed that the selection of adequate protection measures aims to reduce not only the risk by direct flashes to the structure but even the risk for low-voltage and electronic systems against indirect flashes, which means the risk due to flashes to ground near the structure, flashes direct to the lines or flashes to ground near the lines entering the structure.

According to the new publications' plan recently approved by IEC TC81 [1], the criteria for design, installation and maintenance of lightning protection measures may be distinguished in three separate groups:

- (i) protection measures to reduce physical damages (mechanical damages, fire and explosion danger) and life hazard due to direct lightning flashes to the structure
- (ii) protection measures against the electromagnetic effects of lightning on electrical and electronic systems in a structure
- (iii) protection measures to reduce the loss of services entering the structure, namely electrical and telecommunication lines.

### 13.1 Parameters of lightning current

Lightning parameters were investigated from the middle of the last century and a reliable synthesis of the collected data was published within CIGRE activities [2, 3].



Lightning current parameters are usually obtained from measurements taken on high objects. The statistical distributions, log-normal type, of lightning current parameters given in section 13.11 are used for the aim of lightning protection.

Also in section 13.11 are reported the values of the parameters and the wave-forms of lightning current used for protection purposes [4].

The most important parameters for the purpose of designing protection systems [5, 6] are:

- (a) *Peak value of the first stroke*: the lowest values of the statistical distribution of current amplitude of downward flashes are important for the choice of the number and position of the air termination system to prevent direct lightning flashes to the structure to be protected (see section 13.7); the highest values of the statistical distribution of current amplitude are important for sizing of protection measures (electrodynamic effects, etc.).
- (b) *Maximum rate of rise*: the highest values of the statistical distribution are important for dimensioning the protection measures in order to avoid inductive effects of lightning current (induced overvoltages) and dangerous sparking.
- (c) *Flash duration and total charge in the flash*: the highest values of the statistical distribution are important for sizing the air termination system aimed at limiting the thermal effects at the impact point of the lightning flash.
- (d) *Specific energy in a flash*: the highest values of the statistical distribution are important for the selection of a conductor for the protective system, aimed at preventing damage due to thermal effects and for setting up a suitable earthing system in order to prevent hazard to life.

For the protection of structures some additional information is necessary to assess more general models of lightning phenomenon, such a charge distribution in the channel and channel velocities [7].

Furthermore, in risk assessment it is crucial to know the average lightning flash density ( $N_g$ ) of the region where the structure and the incoming lines are placed.  $N_g$  values (expressing the number of flashes per km<sup>2</sup> per year) can be assessed by different methods – thunderstorm day maps, lightning flash counters – and, more recently, by lightning location systems.

## 13.2 Classification of structures

For the purposes of lightning protection, structures may be usefully classified according to consequential effects of lightning flash which can cause damage to the structure, their contents or their surroundings [8]:

- common structures
- structures with risk of explosion, containing solid explosive materials or hazardous zones type 0 as determined in IEC 60079-10; for the purposes of lightning protection, structures with hazardous zones type 1 or type 2 are not considered to be at risk of explosion due to very low probability of contemporary presence of lightning and explosive gas atmospheres
- structures with electronic systems, in which a large amount of electronic equipment is installed, such as systems including telecommunication equipment, control systems, measuring systems
- structures dangerous to the environment, which may cause biological, chemical and radioactive emission as a consequence of lightning, such as chemical, petrochemical, nuclear plants, etc.

Structures may be also classified according to the risk of fire:

- (i) Structures with a high risk of fire:
  - structures made by combustible materials
  - structures with a roof made of highly combustible materials
  - structures with a specific fire load larger than  $45 \text{ kg/m}^2$ .
- (ii) Structures with an ordinary risk of fire:
  - structures with a specific fire load between 20 and  $45 \text{ kg/m}^2$ .
- (iii) Structures with a low risk of fire:
  - structures with a specific fire load of less than  $20 \text{ kg/m}^2$
  - structures containing combustible materials only occasionally.

The specific fire load may be calculated as the ratio of the total amount of combustible material and the overall surface of the structure.

### **13.3 Damage due to lightning**

Lightning striking a structure can result in damage to the structure itself and to its occupants and contents, including failure of equipment and especially of electrical and electronic systems. The damages and failures may also extend to the surroundings of the structure and may even involve the local environment. The scale of this extension depends on the characteristics of the structure and characteristics of lightning flash.

#### *13.3.1 Effects of lightning*

The main characteristics of structures of relevance to lightning effects include [4]:

- construction (wood, brick, concrete, reinforced concrete, steel frame)
- function (dwelling house, office, farm, theatre, hotel, school, hospital, museum, church, prison, department store, bank, factory, industry plant, sports area)
- occupants and contents (persons and animals, nonflammable materials, inflammable materials, nonexplosive mixtures, explosive mixtures, equipment immune to electromagnetic fields or sensitive to electromagnetic fields)
- entering installations (electricity mains, telecommunication and data lines, other services)
- measures to limit consequential effects of damages (e.g. protection to reduce-mechanical damages, the consequences of fire, protection to limit the concentration of explosive mixtures, protection to limit the overvoltages, protection to limit step and touch voltages)
- scale of the extension of danger (structure with small local danger, structure with greater but confined danger, structure with danger to the surroundings, structure with danger to the environment).

#### *13.3.2 Causes and types of damage*

The lightning current is the source of damage. The following causes of damage are to be taken into account according to the position of the stricken point in relation to the structure [4]:

- flashes direct to a structure
- flashes direct to the incoming lines (mains, telecommunication and data lines) or other services

- flashes to ground near the structure
- flashes to ground near the incoming lines and services.

Direct flashes to the structure can cause:

- immediate mechanical damage, fire and/or explosion due to the lightning channel itself, or its current (overheated conductors) and its charge (molten metal)
- fire and/or explosion initiated by sparks caused by overvoltages resulting from resistive and inductive coupling
- injuries to people by step and touch voltages resulting from resistive and inductive coupling
- failure of electrical and electronic systems due to passage of part of the lightning currents and to overvoltages resulting from resistive and inductive coupling
- failure of apparatus internal to the structure due to direct coupling of lightning electromagnetic impulsive field (LEMP).

Direct flashes to the incoming lines can cause:

- fire and/or explosion triggered by sparks due to overvoltages appearing on external power lines entering the structure
- injuries to people due to overcurrents and to overvoltages appearing on external lines entering the structure
- failures of electrical and electronic systems due to overvoltages appearing on external lines entering the structure.

Flashes to the ground surface near the structure can cause:

- failures or malfunction of electrical and electronic systems due to overvoltages resulting from inductive coupling with lightning current
- failure of apparatus internal to the structure due to their direct coupling with LEMP.

Flashes to the ground surface near incoming lines can cause:

- failures or malfunction of electrical and electronic systems due to overvoltages induced in external lines entering the structure.

As result, the lightning can cause three basic types of damage:

- (i) shock to living beings due to touch and step voltages
- (ii) fire, explosion, mechanical destruction, chemical release (physical damages) due to mechanical and thermal effects by lightning current including sparking
- (iii) failure of electrical and electronic systems due to overvoltages.

### *13.3.3 Types of loss*

Each type of damage, alone or in combination with others, may produce different consequential loss in a structure. The type of loss that may appear depends on the characteristics of the structure.

According to [4] the following types of loss are to be considered:

- loss of human life
- loss of service to the public
- loss of cultural heritage
- loss of economic value (structure, content and loss of activity).

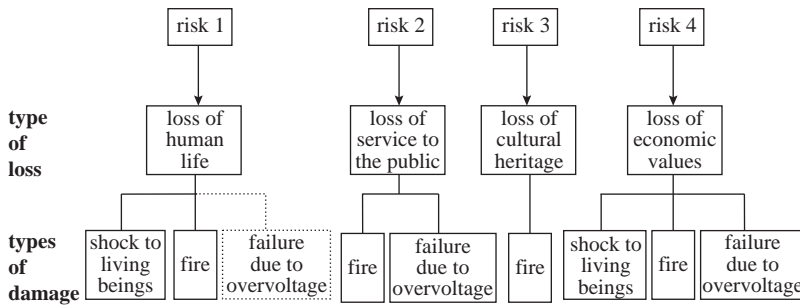


Figure 13.1 Types of loss resulting from different types of damage [9]

More than one loss may appear in a structure. Loss of economic value always appears. The first three losses belong to social value; the fourth loss belongs to private property.

The correspondence between causes of damage, types of damage and loss is shown in Figure 13.1.

### 13.4 Risk

The lightning hazard impending over a structure is a random process composed of a set of effects which are correlated with the parameters of lightning discharge, the characteristics of the structure, its content, the installation internal to the structure, the lines and other services entering the structure [10].

If the time of observation is fixed (usually  $t=1$  year), it is possible to demonstrate [10–12] that the risk, defined as the probability of having an annual loss in a structure due to lightning, may be calculated by the following expression:

$$R = 1 - \exp(-NPL) \tag{13.1}$$

where  $N$  is the average yearly number of flashes influencing the structure and its content,  $P$  is the damage probability of the structure due to a single flash and  $L$  is the average amount of loss, with consequential effects, due to a specified type of damage.

The quantity  $NPL$  is the level of risk or the number (or frequency) of annual loss in a structure due to lightning.

It is evident that if  $NPL \ll 1$  (in practice  $NPL < 0.1$ ), the risk (as probability) and the level of risk are coincident.

The International Standard [4] defines the risk as the probable annual loss in a structure due to lightning, and suggests [9] evaluating it by the following general formula:

$$R = NPL \tag{13.2}$$

where  $L$  is expressed as relative to the total amount of persons or goods.

#### 13.4.1 Number of flashes

It is generally accepted that the number of flashes  $N$  can be evaluated by the product of the lightning ground flash density  $N_g$  by an equivalent collection area  $A$  of the structure or the incoming line.

The lightning ground flash density, in number of lightning flashes per km<sup>2</sup> and per year, should be determined by measurements. Networks of flash counters or, more recently, of lightning location systems are installed in several countries to build maps of  $N_g$ .

If the map is not available, values of  $N_g$  may be estimated by different relationships [3, 13, 14] as a function of the number of thunderstorm days per year or keraunic level of the region  $T_d$ . The International Standard [9] suggests using the following approximate relation:

$$N_g \cong 0.1 T_d \quad (13.3)$$

where  $T_d$  may be obtained from the isokeraunic maps.

The equivalent collection area of the structure (or the incoming service), i.e. the surface crossed by all the lightning flashes (upwards and downwards) which hit the structure (or the service), depends on several parameters. The most significant are:

- structure (or service) characteristics: in particular the height, the position with respect to the other structures, the type of incoming line (MV or LV, overhead or underground, etc.)
- environment characteristics: orography, resistivity of soil
- lightning characteristics: electrical parameters and statistical distribution of the relevant values.

The methods for equivalent area calculation are based on different models (see section 13.12) used to evaluate the exposure of structures (or lines). A good summary of different models is reported in [7]; in [9] approximate formulas for equivalent collection area calculations are proposed for structures and incoming lines.

### 13.4.2 *Probability of damage*

Different difficulties are encountered when evaluating the probability of damage  $P$ . Reference [9] gives the guideline and table tools for evaluating the probabilities of different types of damage taking into account the effect of protection measures provided in reducing such probabilities.

It is important to note that in some cases the probability of a damage due to a single stroke is a result of the product of two probabilities of two events related in series sequence, but in some other cases the probability of damage has to be calculated as the parallel combination of two probabilities of two events in parallel sequence.

As an example, the first case is relevant to the probability of fire calculated as the product of the probability of spark ( $p_s$ ) and the probability that a spark could trigger a fire ( $p_f$ ):

$$P = p_s p_f \quad (13.4)$$

and the second case is related to the probability of a failure of a electronic system due to overvoltages by direct flash to a structure, calculated by the following relation:

$$P = [1 - (1 - pr)(1 - pi)] \quad (13.5)$$

where  $p_r$  is the probability of failure due to overvoltage by resistive coupling of the system with current flowing into the earth and  $p_i$  is the probability of failure due to overvoltage by inductive coupling of the internal loop installation with the lightning current flowing along the conductors.

### *13.4.3 Amount of loss*

The values of consequent loss  $L$  depend on the use to which the structure is assigned, the attendance time of persons in the structure, the type of service provided to public, the value of goods affected by damage, measures provided to limit the amount of damage.

For more detailed information on the methods of calculation of  $N, P$  and  $L$ , see Reference [9].

The following risks are to be taken into account, corresponding to the types of loss:

- $R_1$ : risk of loss of human life
- $R_2$ : risk of loss of services to the public
- $R_3$ : risk of loss of cultural heritage
- $R_4$ : risk of loss of economic value.

### *13.4.4 Risk components*

Each risk may be calculated as the sum of different risk components [9], each expressed by (13.2), depending on the cause of damage:

- (i) lightning flashes direct to the structure may generate:
  - $R_A$  component related to shock of living beings due to touch and step voltages
  - $R_B$  component related to fire, explosion, mechanical and chemical effects inside the structure due to mechanical and thermal effect including dangerous sparking
  - $R_C$  component related to the failure of electrical and electronic systems due to overvoltages on internal installations and incoming services.
- (ii) lightning flashes to ground near the structure may generate:
  - $R_M$  component related to the failure of electrical and electronic systems due to overvoltages on internal installations mainly caused by the magnetic field generated by the lightning current.
- (iii) lightning flashes direct to the incoming line may generate:
  - $R_U$  component related to shock of living beings due to touch and step voltages
  - $R_V$  component related to fire, explosion, mechanical and chemical effects inside the structure due to mechanical and thermal effect including dangerous sparking between incoming lines and metal installations (generally at the entrance point of the line into the structure)
  - $R_W$  component related to the failure of electrical and electronic systems due to overcurrents and overvoltages, transmitted by external lines to the structure.
- (iv) lightning flashes to ground near the incoming line may generate:
  - $R_Z$  component related to the failure of electrical and electronic systems due to induced overvoltages, transmitted through the incoming lines.

Table 13.1 Typical values of tolerable risk  $R_T$  [9]

Types of loss	$R_T$
Loss of human life	$10^{-5}$
Loss of service to the public	$10^{-3}$
Loss of cultural heritage	$10^{-3}$

For each type of loss, the value of risk  $R$  is then given by the sum of its components and may be calculated (see Figure 13.1) with reference to the point of strike with reference to the various types of damage.

With reference to the point of strike:

$$R = R_D + R_I \quad (13.6)$$

where  $R_D = R_A + R_B + R_C$  is the risk due to direct flashes to the structure and  $R_I = R_M + R_U + R_V + R_W + R_Z$  is the risk due to indirect flashes to the structure.

With reference to the various types of damage:

$$R = R_S + R_F + R_O \quad (13.7)$$

where  $R_S = R_A + R_U$ , the risk related to shock of living beings  $R_F = R_B + R_V$ , the risk related to physical damages and  $R_O = R_C + R_M + R_W + R_Z$ , the risk related to the failure of electrical and electronic systems due to overvoltages.

### 13.4.5 Tolerable value of risk

The aim of protection against lightning is to reduce the risk  $R$  to a maximum level  $R_T$  which can be tolerated for the structure to be protected:

$$R \leq R_T \quad (13.8)$$

If more than one type of damage could appear in the structure, the condition  $R \leq R_T$  shall be satisfied for each type of damage.

The values of tolerable risk  $R_T$  where lightning involves loss of social values should be under the responsibility of the national body concerned; representative values are given in Table 13.1.

The values of tolerable risk  $R_T$ , where lightning strikes involve only private economic loss, could be fixed by the owner of the structure or by the designer of protection measures according to a criterion of purely economic convenience.

For further information see [9].

#### 13.4.5.1 Procedure for selection of protection measures

For the structure to be protected, the lightning protection design engineer should decide if the protection is required and, if it is, suitable protection measures should be selected.

The main steps to be followed are:

- (a) identify the structure to be protected and its characteristics
- (b) identify the types of damage (and relevant risks) due to lightning in the structure
- (c) for each type of damage:
  - evaluate the risk  $R$
  - select the tolerable value of the risk  $R_T$

- compare  $R$  with  $R_T$
  - if  $R \leq R_T$  lightning protection is not necessary
  - if  $R > R_T$  protection measures shall be adopted in order to reduce  $R \leq R_T$
- (d) select all protection measures which reduce  $R \leq R_T$  for all damages relevant to the structure
- (e) select the most suitable protection according to the technical and economic aspects.

### **13.4.5.2 Protection measures**

The lightning protection measures include:

- (i) A lightning protection system (LPS) with adequate levels of protection in order to reduce the risk  $R_D$  by direct flashes to the structure. The LPS for the structure comprises an air termination system to intercept the lightning strike, a down conductor system to conduct the lightning current safely to earth and an earth termination system to dissipate the current into the earth. When an LPS is installed, equipotentialisation is a very important measure to reduce fire and explosion danger and life hazard. Equipotentialisation is achieved by means of bonding conductors or surge protective devices (SPD) where bonding conductors are not allowed.
- (ii) Protection against lightning electromagnetic impulse (LEMP) caused by direct and nearby flashes. LEMP protection includes a number of measures to protect electronic systems including the use of a mesh of down conductors to minimise the internal magnetic field, the selection of LEMP protection zones (LPZ), equipotential bonding and earthing, cable and equipment magnetic shielding (MS) and the installation of an SPD system.
- (iii) Protection against transient currents and voltages of electrical and communication services entering the structure. Includes the use of isolation devices, the shielding of cables and the installation and coordination of SPD adequately selected.

Additional measures, other than LPS/SPD/MS should be provided in order to limit:

- touch and step voltages (insulation of exposed conductors, etc.)
- the development and propagation of the fire (extinguishers, hydrants, fire alarm installations, fire compartment proof, protected escape routes, etc.)
- the overvoltages induced in internal installations (cable routing precautions, etc.).

The selection of the most suitable protection measures shall be made by the designer according to the share of each risk component in the total risk, and according to the technical and economic aspects of the different protection measures.

## **13.5 Basic criteria of protection**

### *13.5.1 Protection of structures against physical damages and life hazard*

The main and most effective protection measure, intended for protection of structures against mechanical damage, fire and explosion danger and life hazard due to direct flashes, is the lightning protection system (LPS). It consists of both external and internal lightning protection systems [8].



The functions of the external LPS are:

- (i) to intercept a direct lightning strike to the structure (with an air terminal system)
- (ii) to conduct the lightning current safely towards earth (using a down conductor system)
- (iii) to disperse it into the earth (using an earth termination system).

In addition, there is an internal LPS which prevents dangerous sparking within the structure using either equipotential bonding or a separation distance (and hence electrical insulation) between the LPS components and other electrically conducting elements internal to the structure.

Protection measures additional to external LPS may be required in order to avoid the hazard due to touch and step voltages for persons outside the structure in the vicinity of the down conductor system. Injuries to living beings due to touch and step voltages are mainly avoided by increasing the surface resistivity of the soil outside the structure, of the floor inside the structure and by insulation of the exposed conductive parts (see section 13.7.4).

Four types of LPS (I, II, III and IV) are defined as a set of construction rules, based on the corresponding lightning protection level. Each set includes level-dependent (e.g. rolling sphere radius, mesh width, etc.) and level-independent (e.g. cross sections, materials, etc.) construction rules.

For each lightning protection level, a set of maximum and minimum lightning current parameters values is fixed. The maximum values of lightning current parameters influence the sizing selection of protection measures.

Maximum values of lightning current parameters fixed by the International Standard [4] according to the lightning protection levels are shown in Table 13.3.

For protection level I, the fixed maximum values (see also black points in Figure 13.15) shall not be exceeded with a probability of 99 per cent. According to the polarity ratio (10 per cent positive and 90 per cent negative flashes), values taken from positive flashes must have probabilities below 10 per cent, those from negative flashes below 1 per cent. The maximum values of protection level I are reduced to 75 per cent for level II and to 50 per cent for levels III and IV (linear for  $I$ ,  $Q$  and  $di/dt$ , but quadratic for  $W/R$ ). The time parameters are unchanged.

The minimum values of lightning current amplitude have an influence on the positioning of the air termination system of an LPS in order to intercept the lightning flashes direct to the structure.

The minimum values of lightning current parameters fixed by International Standard [4] together with the related rolling sphere radius, according to the protection levels, are shown in Table 13.2. From the statistical distributions given in

*Table 13.2 Minimum values of lightning current and related rolling sphere radius corresponding to the lightning protection levels of LPS [8]*

Protection level	Rolling sphere radius $R$ , m	Minimum peak current $I$ , kA
I	20	3
II	30	5
III	45	10
IV	60	16

Note: Flashes with peak values lower than the minimum peak current of the relevant rolling sphere radius may still strike the structure.

Table 13.3 Maximum values of lightning current parameters corresponding to lightning protection levels [4, 15]

First short stroke			Protection level		
Current parameters	Symbol	Unit	I	II	III–IV
Peak current	$I$	kA	200	150	100
Short stroke charge	$Q_{short}$	C	100	75	50
Specific energy	$W/R$	MJ/ $\Omega$	10	5.6	2.5
Time parameters	$T_1/T_2$	$\mu\text{s}/\mu\text{s}$		10/350	
Subsequent short stroke			Protection level		
Current parameters	Symbol	Unit	I	II	III–IV
Peak current	$I$	kA	50	37.5	25
Average steepness	$di/dt$	kA/ $\mu\text{s}$	200	150	100
Time parameters	$T_1/T_2$	$\mu\text{s}/\mu\text{s}$		0.25/100	
Long stroke			Protection level		
Current parameters	Symbol	Unit	I	II	III–IV
Long stroke charge	$Q_{long}$	C	200	150	100
Time parameter	$T_{long}$	s		0.5	
Flash			Protection level		
Current parameters	Symbol	Unit	I	II	III–IV
Flash charge	$Q_{flash}$	C	300	225	150

Table 13.4 Probabilities for the limits of the lightning current parameters [8]

Probability	Lightning protection level			
Probability that value is	I	II	III	IV
Higher than minimum defined in Table 10.2	0.99	0.97	0.91	0.84
Lower than maximum defined in Table 10.3	0.99	0.98	0.97	0.97

Figure 13.15, a weighted probability can be determined, that the lightning current parameters are smaller than the maximum values and respectively greater than the minimum values defined for each protection level (see Table 13.4).

The protection measures are effective against lightning whose current parameters are in the range defined by the LPL assumed for design. Therefore, the efficiency of a protection measure is assumed equal to the probability with which lightning current parameters are inside such range.

### 13.5.2 Protection of electrical and electronic systems within the structure against lightning electromagnetic impulse (LEMP)

The protection of electrical and electronic systems within the structure against over-voltages due to LEMP is based on the principle of LEMP protection zones (LPZ). According to this principle [15] the structure to be protected shall be divided into lightning protection zones defined as zones of different LEMP severities and

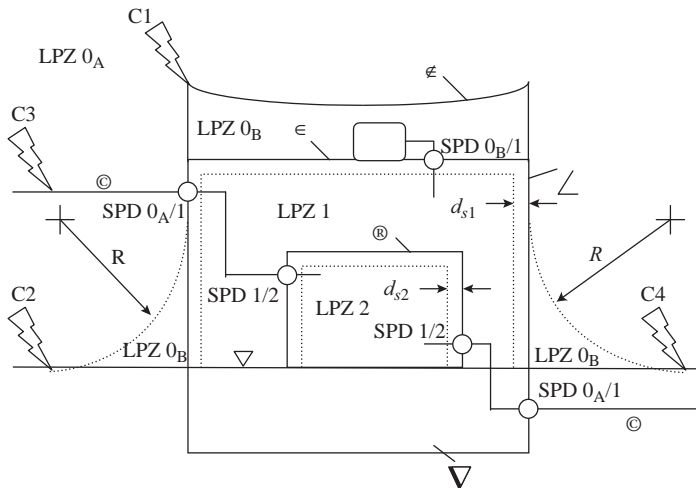
locations for bonding points designated on the zone boundaries. Each individual zone will be characterized by significant changes in the electromagnetic conditions at their boundaries. In general, the higher the number of the zones, the lower the electromagnetic environment parameters.

At the boundary of the individual zones, bonding of all metal penetrations shall be provided and screening measures might be installed.

The general principle for the division of a structure to be protected into different lightning protection zones is shown in Figure 13.2.

The protection should be completed by adequate measures of protection:

- earthing in order to achieve the maximum of equipotentiality between the equipment connected to the same earthing system; a meshed earthing system is suitable to fulfil this requirement;
- shielding, that is the basic measure to reduce the electromagnetic interference; shielding may include apparatus and lines or may be extended to whole zone; suitable routing of cables is an additional measure to reduce the electromagnetic interferences
- bonding in order to reduce the potential differences between metal parts and electronic systems inside the structure to be protected; bonding shall be provided at the boundaries of LPZs for metal parts and systems crossing the boundaries and may be performed by means of bonding conductors or, when necessary, by surge protection devices (SPDs).



ε	structure (shield of LPZ 1)	C1	strike to structure
E	air termination system	C2	strike near to structure
L	down conductor system	C3	strike to incoming service
V	earth termination system	C4	strike near to incoming service
R	room (shield of LPZ 2)	R	rolling sphere radius
C	incoming services	$d_s$	safety distance against too high magnetic field
O	lightning equipotential bonding (SPD 0A/X class I, other SPD class II tested)		
LPZ 0 <sub>A</sub>	direct strikes, full lightning current, full magnetic field		
LPZ 0 <sub>B</sub>	no direct strikes, partial lightning or induced current, full magnetic field		
LPZ 1	no direct strikes, partial lightning or induced current, damped magnetic field		
LPZ 2	no direct strikes, induced currents, further damped magnetic field		
	protected volumes inside LPZ 1 and LPZ 2 must respect safety distances $d_s$		

Figure 13.2 Protection by LEMP protection zones (LPZ) according to IEC [15]

### *13.5.3 Protection of services entering the structure*

Services entering the structures (e.g. telecommunication lines) and connected equipment must be protected against the direct and indirect influence of lightning by limiting the risk due to overvoltages and overcurrents, liable to occur in these services, to values which are lower than or equal to tolerable risk [16].

The main criteria of protection, which can also be combined, are:

- (a) to avoid as far as possible the lightning flashes striking the service directly by selecting underground instead of aerial routing or by using adequately positioned ground wires, where effective according to the line characteristics, or by increasing the pipe thickness to an adequate value and assuring the metallic continuity of pipes
- (b) to reduce the level of the overvoltages induced by lightning by means of adequate shielded cables
- (c) to divert overcurrent and to limit overvoltages by means of adequate SPD
- (d) to increase the rated impulse withstand voltage of lines and connected equipments, where convenient.

## **13.6 Protection by means of SPD**

SPDs are very effective protection measures for reducing the probability of occurrence of dangerous sparking or dangerous overvoltages due to direct and indirect flashes to the structure. They are the most convenient devices for achieving lightning equipotential bonding for live conductors in the form of incoming lines and internal live conductors with induced voltages.

The effectiveness of an SPD in reducing the overvoltage level is not easy to evaluate but recent International Standard [15, 17] help in the selection, coordination and installation of these protection measures.

SPDs should be located according to the LEMP protection zones (LPZs) concept (see Figure 13.2) at the boundary of each zone. In practice, SPDs are generally installed at the entrance point of incoming services and on the installation and equipment internal to the structure.

The protection of an SPD installed at the entry point of a line in a structure is effective, provided that SPDs:

- at the boundary LPZ 0/X, are dimensioned according to class I test requirements (impulse current 10/350  $\mu$ s)
- at the boundary LPZ X/Y ( $X > 0$ ,  $Y > 1$ ), are dimensioned according to class II test requirements (nominal current 8/20  $\mu$ s)
- comply with standard requirements [15]
- are coordinated with internal installations to be protected (and where together) in accordance with the requirements of [8] and [15].

The principles of coordination of SPDs are reported in [17], but effective operation of SPDs depends not only on their adequate selection and coordination but also on their proper installation.

One of the installation problems is the proper selection of the so-called protection distance, which means the maximum distance from the equipment, measured along the circuit, at which the SPD still protects the equipment.

The evaluation of the protection distance depends on the:

- level of protection of SPD
- type of SPD (spark gap, varistor, diode, etc.)
- impulse withstand voltage level (or the immunity level) of the equipment and its input surge impedance
- steepness of the lightning current
- characteristics of the conductors linking the SPD to the equipment (i.e. the mains supplying the equipment).

The evaluation of the protection distance of an SPD may be performed by means of the relations reported in [15] or, in a more accurate way, by computer simulation (e.g. PSICE or ATP programs) [18].

### **13.7 Main features of lightning protection system (LPS)**

#### *13.7.1 External lightning protection system*

The external LPS is intended to intercept direct lightning strokes, including flashes to the side of structure, to conduct lightning current from the point of strike to ground and to disperse it to earth without causing thermal, mechanical and electrical damages to the structure to be protected, including sparking and touch and step voltages dangerous for persons inside the structure. Protection measures additional to external LPS may be required in order to avoid the hazard due to touch and step voltages for persons outside the structure in the vicinity of the down conductor system. In most cases, the external LPS may be attached to the structure to be protected.

An isolated external LPS should be also considered when the thermal and explosive effects at the point of strike or on the conductors carrying the lightning current may cause damage to the structure or to the content. Typical cases are:

- structures with combustible covering
- structures with combustible walls
- areas with danger of explosion and fire.

Dangerous sparking between an LPS and structures shall be avoided:

- in an isolated external LPS by insulation or separation
- in a nonisolated external LPS by bonding or by insulation or separation.

Natural components made of conductive materials that will always remain in the structure and will not be modified (e.g. interconnected reinforced steel, metal framework of the structure, etc.) should preferably be used as part of the LPS. Other natural components should be used as additional to the LPS.

#### *13.7.2 Positioning of the air termination system*

The probability of the current of a lightning stroke penetrating the structure to be protected is considerably decreased by the presence of a properly designed air termination system.

##### **13.7.2.1 Principles of positioning**

The positioning of an air termination system would require knowledge of the physics of lightning discharge.

Basically, the lightning is characterised by downward leaders which progress to earth in successive steps following, approximately, a direction defined by the maximum field stress. The point of strike is found within those earthed points from which upward leaders may develop; these points, characterised by highest electrical fields, are usually localised on parts which are placed on the top of structures. It is therefore highly probable that an upward leader is initiated at the top of a high structure or a structure placed on a hill.

The complexity of the phenomenon has forced scientists to introduce assumptions and simplifications in order to assess models which allow them to obtain results more and more in accordance with experimental results.

One of the best known models, widely used for practical applications, is the model referring to the concept of striking distance, which is the particular distance between the downward leader and earth at which the stricken point is chosen. This parameter is usually related to the peak value of the lightning current (see Figure 13.4); reference is made to the electrogeometrical model (Golde, Whitehead and others) based on the striking distance concept [19].

As an improvement to this model, the configuration of the electric field at earth is also considered [13] in order to take into account the conditions of the inception of an upward leader at an earthed point. In particular, an improved electrogeometrical model for transmission line shielding analysis was proposed in 1987 by Eriksson [20] and a generalised leader inception model has been developed in 1990 by Rizk [21] and improved by Petrov and Waters in 1995 [22]. These models together with the leader progression model [23], based on the physics of the upward leader inception as derived from laboratory experiments, have proved to be of great value for evaluating the exposure of the structures and for providing a rough assessment of interception probability.

By application of these models the exposure of different simple structures (slim structures, horizontal conductors and square buildings and facades) located in various orographic conditions has been determined. In particular, the probability of lateral strikes is evaluated together with the height of structures at which the phenomenon becomes significant [7].

A more detailed overview of different models proposed in different times is outlined in section 13.12.

### **13.7.2.2 Types of air termination system**

The air termination systems can be composed of any combination of the following elements:

- rods
- catenary wires
- meshed conductors.

Radioactive air terminals are not allowed and the use of air terminations with intensified ionisation are to be positioned only as conventional ones.

In determining the position of the air termination system, particular care must be given to the interception protection of corners and edge surfaces under consideration, especially those at its top level(s) and on the upper 20 per cent of its facades.

Three methods are suggested by the International Standard [8] for the positioning of the air termination system, namely the protection angle method, the

rolling sphere method (which is an implementation of simple electrogeometrical model) and the mesh method, also known as the Faraday cage method.

The Standard was set up taking into account the technical data which was available on the basis of measurements of lightning parameters, practical experience and on theoretical approaches related to various models proposed to analyse the mechanism of the lightning impact.

The protection angle method is suitable for most simple shape buildings but it has the height limits indicated in Figure 13.3.

The rolling sphere method was first proposed by Lee [24] as an extension of the electrogeometric model to the design of air terminals for buildings and structures. It is suggested [8] in any cases with the radii given in Table 13.5.

Applying this method, the positioning of the air termination system is adequate if no point of the volume to be protected comes into contact with a sphere with radius  $R$  depending on the lightning protection level (Table 13.5), rolling around and on top of the structure in all possible directions. Therefore, the sphere will have to touch only the air termination system.

On tall structures higher than the rolling sphere radius  $R$ , side flashes may occur. Each lateral point of the structure touched by the rolling sphere is a possible point of strike. But the probability for side flashes is generally negligible for

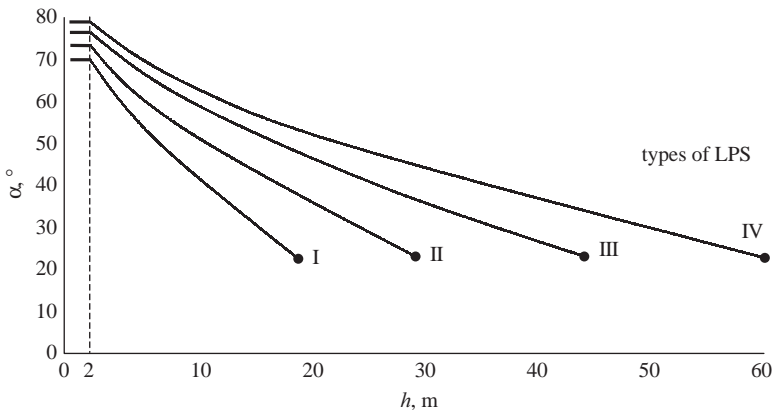


Figure 13.3 Height limits for protection angle method (not applicable beyond the values marked with •; only rolling sphere and mesh methods apply in these cases.  $h$  is the height of air termination above the area to be protected. The angle will not change for values of  $h$  below 2 m)

Table 13.5 Minimum values for rolling sphere radius, mesh size and protection angle corresponding to lightning protection levels [8]

Lightning protection level	Protection method		
	Rolling sphere radius $R$ , m	Mesh size $M$ , m	Protection angle $\alpha^\circ$
I	20	$5 \times 5$	
II	30	$10 \times 10$	See Figure
III	45	$15 \times 15$	13.3
IV	60	$20 \times 20$	

structures lower than 60 m. For taller structures the major part of all flashes will hit the top, horizontal leading edges and corners of the structure. Only a few per cent of all flashes will be side flashes to the structure.

Moreover, the probability for side flashes decreases rapidly as the height of the point of strike on tall structures decreases, when measured from the ground [7]. Therefore, it seems sufficient that consideration should be given to installing a lateral air termination system on the upper part of tall structures, typically the top 20 per cent of the height of the structure (see section 13.12 and Figure 13.19). The mesh method is a suitable form of protection where plane surfaces are to be protected.

The values for protection angle, rolling sphere radius and mesh size suggested by International Standards [8] are given in Table 13.5 according to the minimum value of the lightning current to be intercepted by the air termination system and to the types of LPS selected. These values are assessed in order to have equivalent protected volumes by using either protection angle or rolling sphere methods. The detailed information on the positioning of the air termination system is given in [25].

### *13.7.3 Down conductor systems*

In an LPS the down conductors have the task of carrying the current from the air termination to the earth termination system. In order to reduce the probability of damage due to lightning current flowing in the LPS, the following problems have to be considered:

- the conductor sizing depending on the lightning current flowing; in the case of tall structures, the upper parts of down conductors act also as air termination
- the conductor number and positioning in order to get a good sharing of the current in the various conductors and to minimise the electromagnetic field inside the structure
- the down conductor spacing from the conducting parts inside the structure, or equipotentialisation with them.

The down conductors are to be arranged in such way that from the point of strike to earth:

- (a) a several parallel current paths shall exist
- (b) the length of the current paths is kept to a minimum
- (c) equipotential bonding to conducting parts of the structure is performed everywhere it is necessary, connection of down conductors at the ground level and every 10/20 m of height is a good practice.

A great number of down conductors, as far as possible at equal spacing around the perimeter and interconnected by ring conductors, reduces the probability of dangerous sparking and facilitates the protection of the installations internal to the structure. This condition is fulfilled in metal framework structures and in reinforced concrete structures in which the interconnected steel is electrically continuous.

The down conductors shall be arranged so that they become, as far as possible, the direct continuation of the air termination conductors. They shall be installed straight and vertical such that they provide the shortest most direct path to earth. The formation of loops shall be avoided.



Down conductors of LPS not isolated from the structure to be protected may be installed as follows:

- if the wall is made of noncombustible material the down conductors may be positioned on the surface or in the wall
- if the wall is made of flammable material the down conductors can be positioned on the surface of the wall, provided that their temperature rise due to the passage of lightning current is not dangerous for the material of the wall
- if the wall is made of flammable material and the temperature rise of the down conductors is dangerous, the down conductors shall be placed in such a way that the distance between them and the wall is always greater than 0.1 m; mounting brackets may be in contact with the wall; with the dimensions given in the tables of the International Standard [8] the temperature rise is of the order of tens of degrees centigrade.

Metal installations of a structure, facade elements, profile rails and metallic sub-constructions of facades, provided that the electrical continuity between the various parts is made durable and their dimensions are at least equal to that specified for standard down conductors, as well as the metal or reinforced concrete framework of the structure and the interconnected reinforcing steel of the structure should be considered as natural down conductors.

#### *13.7.4 Protection measures against touch and step voltages*

Outside the structure, in the surrounding of the down conductors, in particular conditions the touch and step voltages may be hazardous to life even if the LPS has been designed and constructed according to the above-mentioned rules.

The risk for persons can be considered negligible [8] if one of the following conditions is fulfilled:

1. the probability of persons approaching or the time of their presence outside the structure and close to the down conductors is very low
2. insulation over the exposed conductor is provided giving a 100 kV, 1.2/50  $\mu$ s impulse withstand voltage, e.g. at least 3 mm cross linked polyethylene
3. the resistivity of the surface layer of the soil, in the range distance of 3 m from the conductor, is not less than 5000  $\Omega$ m; in general a layer of insulating material, e.g. asphalt of 5 cm thickness (or a layer of gravel of 10 cm thickness) satisfies this requirement
4. the natural down conductor system consists of several columns of the extensive metal framework of the structure or of several pillars of the interconnected steel of the structure, electrically continuous
5. for the case of step voltage, equipotentialisation by means of a meshed earthing system.

If none of these conditions is fulfilled, the down conductors should be placed in order to minimise the probability of being touched or persons should not be allowed to approach the down conductors to within 3 m or a panel indicating a warning hoarding should be placed.

#### *13.7.5 Earth termination system*

##### **13.7.5.1 Principles of design**

The earth termination of an LPS must be able to disperse lightning current into the ground without causing any danger to people or damage to installations inside the protected structure.

When dealing with the dispersion of the lightning current into the ground while minimising any potentially dangerous overvoltages, the transient behaviour of earthed electrodes under impulse current with high peak value should be considered.

The purpose of many of the studies published up to now was to acquire a deeper knowledge of the behaviour in transient conditions of earthed electrodes of various shapes (horizontal conductors, driven rods, grid systems) both from a theoretical [6, 26–29] and experimental [30–32] point of view, in frequency and in time domains. It is therefore possible to clarify some typical phenomena characterising the behaviour of earthed electrodes in transient conditions, namely:

- (i) The lightning current, independently from the polarity, propagates into the soil according to the typical laws of conducting, taking into account the range of frequencies involved in the lightning current (from some hundreds of kHz up to 1 MHz) and for soil resistivity up to 5000  $\Omega\text{m}$ . It is therefore of basic importance, even for dimensioning the earth termination system under lightning current, to have knowledge of the soil resistivity and to pay attention to the inhomogeneity of the soil involved in the current discharge.
- (ii) The transient behaviour of earthed electrodes is basically defined by inductive phenomena (see Figure 13.5). The rate of rise of the front of current impulses is therefore of major importance as it increases the importance of the inductive voltage drop in comparison with the resistive drop [6, 33, 34].
- (iii) The high values of lightning currents associated with very short front durations can result in high current density in the layers of soil nearest the surface of ground electrodes so that the critical gradients may be exceeded and discharges into the soil can occur [35].

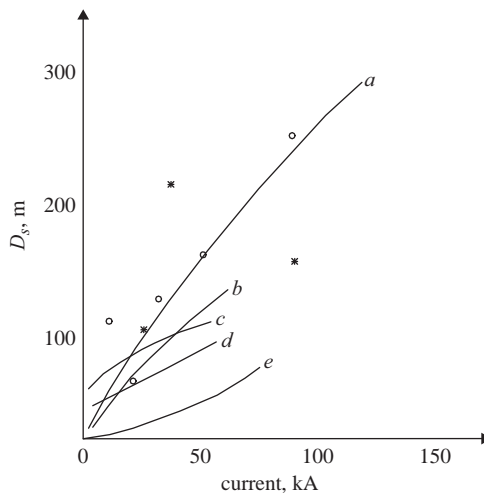


Figure 13.4 Striking distance as a function of peak value of the lightning current according to different authors; o estimates from two dimensional photos [36]; \* estimates from three dimensional photos [36]

- (a) ref. [37]
- (b) ref. [19]
- (c) ref. [38]
- (d) ref. [39]
- (e) ref. [40]

In order to analyse and compare the behaviour of different kinds of earth electrode it is convenient to define some typical parameters:

- transient, or surge, impedance, defined as the ratio between the instantaneous values of the earth termination voltage (potential difference between the earth termination system and the remote earth) and the earth termination current which, in general, do not occur simultaneously
- conventional earth resistance, defined as the ratio of the peak values of the earth termination voltage and the earth termination current, it is used conventionally to indicate the resistance of the earth termination system when subjected to lightning current
- the impulse factor, defined as the ratio between the conventional earth resistance and the low-frequency resistance of the earth electrode.

The main conclusions today widely accepted, based on comparison between theoretical studies and experimental works, may be summarised as follows:

- the earth electrode length which actually contributes to the impulsive current dispersion depends to a large extent on soil resistivity ( $\rho$ ), on time to crest ( $T_1$ ) and on peak value of the current ( $I$ )
- the analytical expression used to evaluate the effective length of earth electrodes is:

$$l_e = K_o(\rho T_1)^{1/2} \quad [m; \Omega m; \mu s] \quad (13.9)$$

where  $l_e$  is the effective length of the involved earth electrode from the current injection point to a distance at which the value of the conventional earth resistance does not undergo any significant reduction,  $K_o$  is a factor depending on the geometrical configuration of the earth electrode, ranging from 1.40 a single conductor energised at one end to 1.55 for a single conductor energised

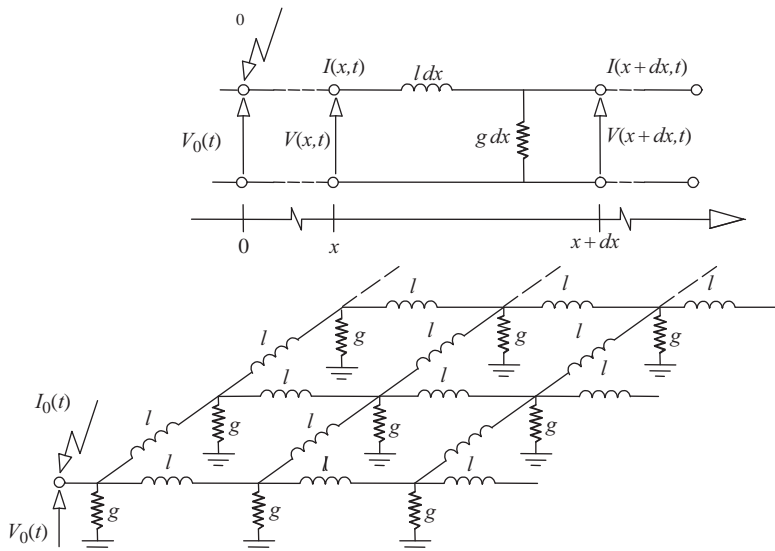


Figure 13.5 *Equivalent electric circuit for a single horizontal wire and for a meshed system.  $l$ : wire inductance for unit of length;  $g$ : earth conductance for unit of length*

- in the middle, to 1.65 for conductors arranged in star configuration energised in the centre
- (c) since amplitude and wave shape of the injected current, earth electrode dimensions and soil resistivity define the voltage distribution along the electrode (and consequently the contribution of different parts of the electrode to discharge current), these same parameters define the conventional earth resistance of the considered earth electrode; Figures 13.6–13.9 show the trends of the conventional earth resistance as a function of soil resistivity, current waveshape and earth conductor arrangement
  - (d) localised earth electrodes present conventional earth resistance lower than power frequency resistance if the value of the lightning impulse current is sufficiently high to cause soil ionisation.

In the designing of the earth termination system in order to disperse lightning current in the soil without danger to people, two items should be considered, namely, the maximum energy which can be tolerated by a human body in transient conditions typical of lightning, assumed equal to 20 W [6], and the risk, assumed as tolerable [9], that this maximum value of energy can be exceeded.

As a function of the tolerable risk, the values of the parameters of the lightning current have to be chosen from the relevant probabilistic distributions (see section 13.11); the earth termination system shall be designed so that the dispersion of the above fixed lightning current does not result in step voltages higher than necessary to dissipate the 20 W energy in the human body resistance of 500 Ω conventionally fixed.

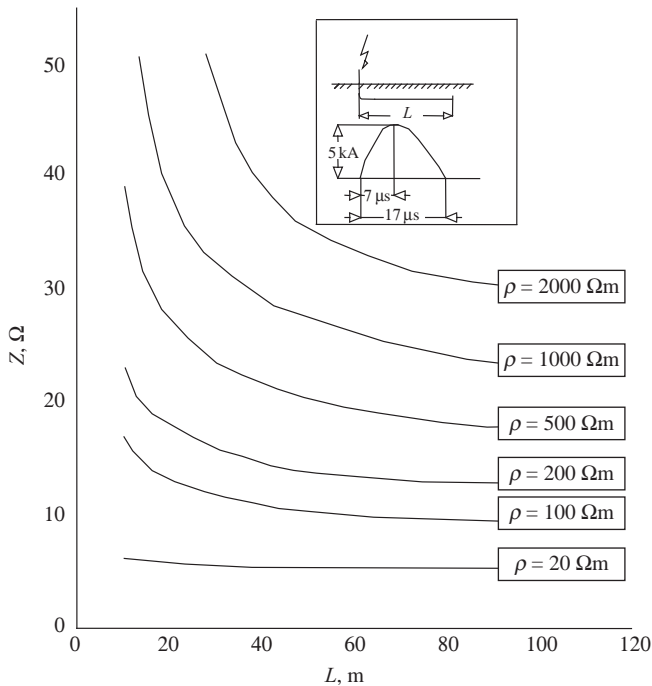


Figure 13.6 Conventional earth resistance of buried wires as a function of their length for different values of soil resistivity [6]

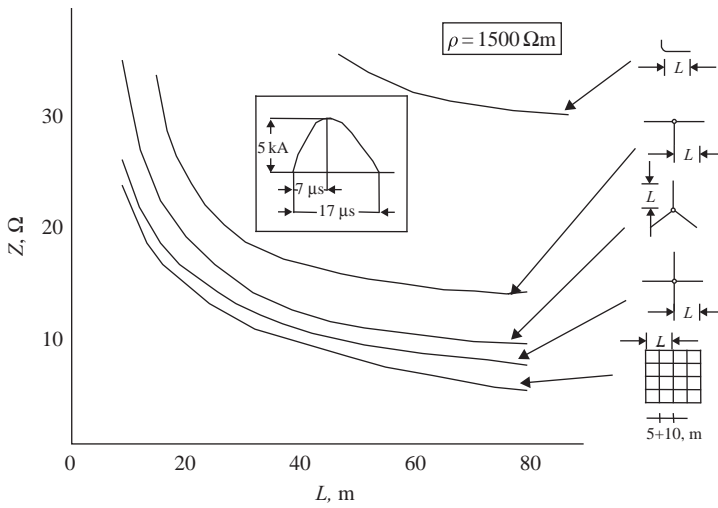


Figure 13.7 Conventional earth resistance of different arrangements of earth termination system [6]

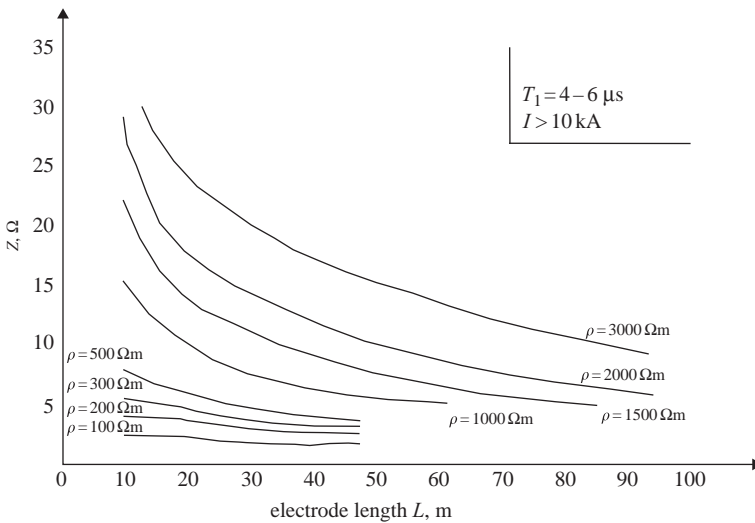


Figure 13.8 Conventional earth resistance of earth termination system (impulse current at the centre of a star arrangement) as a function of the length for different values of soil resistivity [6]

For different values of fixed risk the maximum admissible values of the conventional earth resistance may be evaluated in different earth termination system configurations in order to keep the step voltage within the safety limits. The results of application of this procedure allow us to establish the minimum required dimension of an earth termination system, as accepted by the International Standard [8] and discussed in section 13.7.5.2.

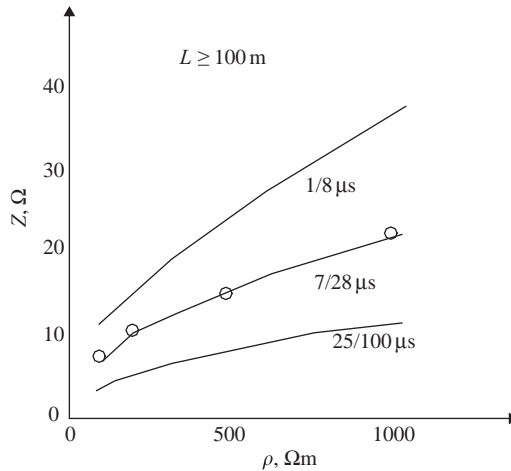


Figure 13.9 Conventional earth resistance as a function of soil resistivity; o experimental results [6]

### 13.7.5.2 Earthing arrangement in general conditions

From the viewpoint of lightning protection of buildings and structures, a single integrated structure earth termination system is preferable and is suitable for all purposes (i.e. lightning protection, power systems, telecommunication systems). Serious corrosion problems can occur when earthing systems made by different materials are connected to each other.

According to the International Standard [8] for earth termination systems, two basic types of earth electrode arrangement apply:

- (i) type A arrangement which comprises horizontal or vertical earth electrodes connected to each down conductor, in this case the minimum total number of earth electrodes shall be two
- (ii) type B arrangement which comprises either a ring conductor external to the structure in contact with the soil for at least 80 per cent of its total length or a foundation earth electrode; these earth electrodes may be also meshed.

For the ring earth electrode (or foundation earth electrode), the mean radius  $r$  of the area enclosed by the ring earth electrode (or foundation earth electrode) shall be not less than the value  $l_1$ :

$$r > l_1 \tag{13.10}$$

$l_1$  being represented in Figure 13.10 according to the types I, II and III and IV of LPS and then according to the values of lightning current parameters selected for dimensioning.

When the required value of  $l_1$  is larger than the convenient value of  $r$ , additional radial or vertical (or inclined) electrodes shall be added whose individual lengths  $l_r$  (horizontal) and  $l_v$  (vertical) are given by:

$$l_r = l_1 - r \tag{13.11}$$

and

$$l_v = (l_1 - r)/2 \tag{13.12}$$

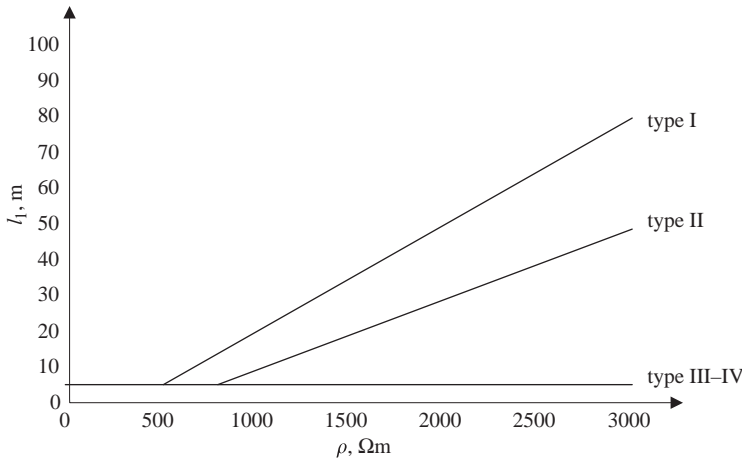


Figure 13.10 Minimum length  $l_1$  of earthing arrangement according to the type of LPS [8]. Types III and IV LPS are independent of soil resistivity

The number of additional electrodes shall not be less than the number of down conductors with a minimum of two. The additional electrodes should be connected to the ring earth electrode in correspondence to the down conductors and, as far as possible, with equal spacing.

The embedded depth and the type of the earth electrodes shall be such to minimise the effects of corrosion, soil drying and freezing and thereby stabilise the conventional earth resistance.

The interconnected reinforcing steel of concrete foundations or other suitable underground metal structures should preferably be used as an earth electrode. When the metallic reinforcement of concrete is used as an earth electrode, special care shall be exercised at the interconnections to prevent mechanical splitting of the concrete.

In the case of prestressed concrete, consideration should be given to the consequences of the passage of lightning discharge currents which may produce unacceptable mechanical stresses.

### 13.7.6 Materials and dimensions

The materials used for the LPS shall have the following main characteristics:

- good conductivity, to allow the flowing of the current
- suitable mechanical strength, to withstand the electrodynamic stresses caused by the high peak values of the current
- good resistance against the corrosion due to atmospheric environment.

The materials usually adopted are iron, copper and aluminium. Configuration and minimum cross sectional areas of air termination conductors, air termination rods, down conductors and earth electrodes are given in different Tables of [8].

## 13.8 Internal lightning protection system

### 13.8.1 General

The internal LPS should avoid the occurrence of dangerous sparking within the structure to be protected due to lightning current flowing in the external LPS or in

other conductive parts of the structure. Sparking occurring between the external LPS on the one hand and the metal installations, the electrical, signal and telecommunication installations, inside the structure to be protected, the external conductive parts and lines entering the structure on the other hand, should be considered dangerous. Dangerous sparking between different parts may be avoided with the aid of:

- lightning equipotential bonding
- adequate electrical insulation between the parts.

Damage to vulnerable instrumentation and control equipment due to their inductive coupling with partial lightning currents flowing through the external lightning protection system or through metal installations inside the building may be:

- avoided with the aid of low coupling impedance shielding of cables
- limited by means of surge protective devices (SPD).

Detailed information and requirements on the subject are reported in International Standard [15, 17].

### *13.8.2 Lightning equipotential bonding*

Equipotentialisation is achieved by interconnecting the LPS with metal elements of the structure construction, with the metal installations, with the external conductive parts and with electrical, signal and telecommunication installations within the structure to be protected.

Methods of interconnection are:

- bonding conductors, where the electrical continuity is not provided by natural bonding
- SPD where direct connections with bonding conductors are not allowed.

Lightning equipotential bonding connections shall be made as direct and straight as possible.

Lightning equipotential bonding to conducting parts of the structure at locations corresponding to ring conductors facilitates effective protection. When lightning equipotential bonding is established to conducting parts of the structure a part of the lightning current may flow into the structure and this effect should be taken into account. Therefore, lightning equipotential bonding at the level higher than the basement is only recommended if the required separation distance [8] can not be reached.

The SPD characteristics depend on the lightning current flowing along the relevant part of the external LPS. For external conductive parts, as well as for electrical, signal and telecommunication equipotential bonding, installations shall be performed at the entrance point into the structure.

Bonding conductors should withstand the part of the lightning current flowing through them. This current may be evaluated taking into account the conventional earth resistance of the earth termination system, the number of entering services (external conductive parts) bonded at the same point of entry and the number of conductors of each line entering into the structure, all connected in parallel. The details on the sharing of the current between different incoming services and formulae to evaluate the current flowing in each of them may be found in [15] and [17].



If the electrical, signal and telecommunication conductors are screened or located in metal conduit, it is normally sufficient to bond only these screens and conduits. If the electrical, signal and telecommunication conductors are neither screened nor located in metal conduit, they shall be bonded via SPDs.

All the conductors of each line should be bonded directly or with an SPD.

### 13.8.3 *Electrical insulation of the external LPS*

Analysis of the electromagnetic field caused by the flowing of lightning currents along the conductors of the protection system allows the assessment of rules for evaluating the spacing between air termination and protected structures in order to avoid side flash between them.

In order to avoid side flashes between the air termination or the down conductor on the one hand and the metal installations and electrical, signal and telecommunication installations internal to the structure to be protected on the other hand, a distance  $d$  between the parts shall be ensured not smaller than a separation distance  $s$ :

$$d > s \quad (13.13)$$

where the separation distance may be calculated with the following relation [8]:

$$s = k_i \frac{k_c}{k_m} l \quad [\text{m}] \quad (13.14)$$

where  $k_i$ ,  $k_c$ ,  $k_m$  depend, respectively, on the selected lightning protection level of LPS, the share of lightning current on the down conductors and the electrical insulation material (see [8] and [25] for more details) and  $l$  is the length, in metres, along the air termination or the down conductor from the point where the separation distance is to be considered to the nearest equipotential bonding point.

## 13.9 Shielding

Any lightning strike into the building causes partial currents flowing through metal installations inside the building and induces voltages between the individual conductors of a cable and between these conductors and earth. These voltages may be dangerous for the instrumentation and control equipment.

The dangerous voltages can be avoided by protective measures such as installation of SPD or shielding. Possible shielding measures are:

- a conductive cable screen, capable of carrying the individual partial lightning current
- laying the cables in well-closed conductive cable races
- laying the cables in a metal conduit.

## 13.10 Maintenance and inspection of LPS

The main objective of the inspections are to ascertain that all components of the LPS are in good condition and capable of performing their designed functions, and that there is no corrosion and any recently added services or constructions are incorporated into the LPS.

Inspections should be made as follows:

- during the construction of the structure, in order to check the embedded electrodes
- after the installation of the LPS
- periodically at such intervals as are determined with regard to the nature of the structure to be protected, the corrosion problems and the protection level
- after alterations or repairs, or when it is known that the structure has been struck by lightning.

During the periodic inspection, the deterioration and corrosion of air termination elements, conductors and connections and of earth electrodes must be particularly checked.

Regular inspections are among the fundamental conditions for a reliable maintenance of a LPS.

Further detailed information is given in [25].

## 13.11 Annex A: parameters of lightning current

### 13.11.1 Lightning flashes to earth

Two basic types of lightning flash exist, downward flashes initiated by a downward leader from cloud to earth and upward flashes initiated by an upward leader from an earthed structure to cloud. In flat territory and to lower structures mostly downward flashes occur, whereas for exposed and/or higher structures upward flashes become dominant. With the effective height the striking probability increases and the physical conditions change.

A lightning current consists of one or more different strokes, short strokes typically below 2 ms (Figure 13.11) and long strokes with more than 2 ms (Figure 13.12). Further differentiation of strokes comes from their polarity (positive or negative) and from their position during the flash (first, subsequent, superimposed). The possible components are shown in Figure 13.13 for downward flashes and in Figure 13.14 for upward flashes.

The additional component in upward flashes is the first long stroke without or with up to some ten superimposed short strokes. But all short stroke parameters of

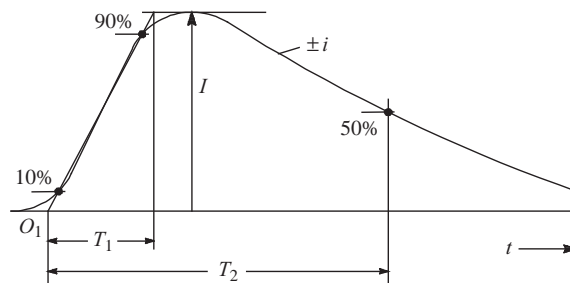


Figure 13.11 Definitions of short stroke parameters (typically  $T_2 < 2$  ms) [4, 15]

- $O_1$  = virtual origin
- $I$  = peak current
- $T_1$  = front time
- $T_2$  = time to half value

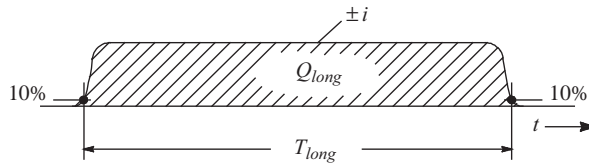


Figure 13.12 Definitions of long stroke parameters (typically  $2\text{ ms} < T_{long} < 1\text{ s}$ ) [4, 15]

$T_{long}$  = duration time  
 $Q_{long}$  = long stroke charge

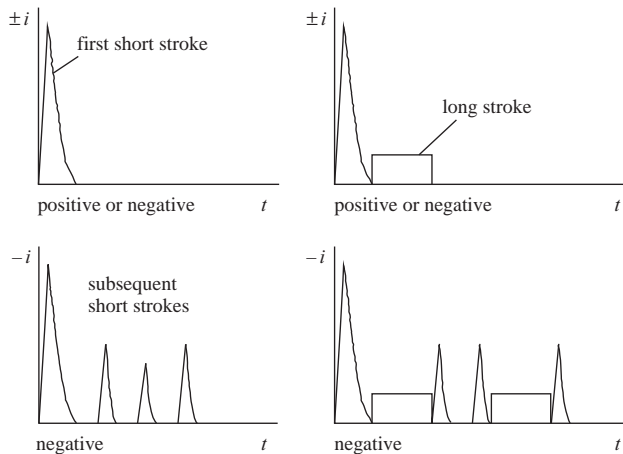


Figure 13.13 Possible components of downward flashes [4, 15] (typical in flat territory and to lower structures)

upward flashes are less than those of downward flashes. A higher long stroke charge of upward flashes is not yet confirmed. Therefore, for lightning protection, the lightning parameters of upward flashes are considered to be covered by the maximum values taken from downward flashes. A more precise evaluation of lightning parameters and their height dependency with regard to downward and upward flashes is still under consideration in the scientific community.

### 13.11.2 Lightning current parameters

The lightning current parameters in this standard are based on the results of CIGRE, which are given in Table 13.6. Their statistical distribution can be assumed to have a logarithmic normal distribution. The corresponding mean value  $\mu$  and the dispersion  $\sigma_{log}$  is given in Table 13.7 and the distribution function is shown in Figure 13.15. On this basis the probability of occurrence of any value of each parameter can be determined (see Figure 13.15).

A polarity ratio of 10 per cent positive and 90 per cent negative lightnings is assumed. The polarity ratio is a function of the territory. If no local information is available, the ratio given herein should be used.

For lightning protection level I the fixed maximum values in Table 13.3 shall not be exceeded with a probability of 99 per cent. According to the polarity ratio

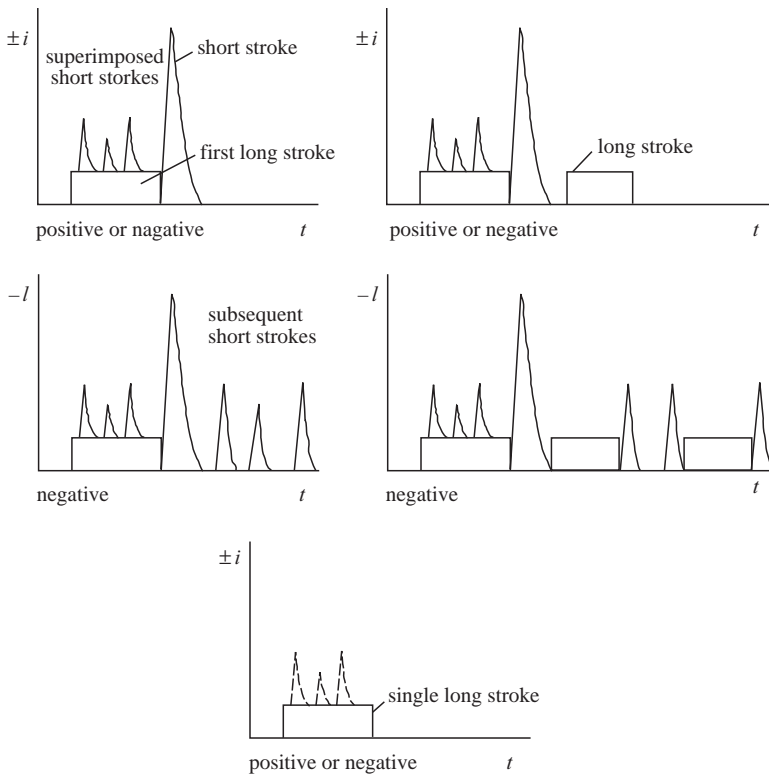


Figure 13.14 Possible components of upward flashes [4, 15] (typical to exposed and/or higher structures)

given above, values taken from positive flashes must have probabilities below 10 per cent, those from negative flashes below 1 per cent.

The maximum values of current parameters relevant to protection level I are reduced to 75 per cent for level II and to 50 per cent for level III and IV (linear for  $I$ ,  $Q$  and  $di/dt$ , but quadratic for  $W/R$ ). The time parameters are unchanged.

The minimum values in Table 13.2 are used to determine the interception probability of air terminals.

### 13.11.3 Maximum lightning current parameters used for dimensioning lightning protection systems

The mechanical effects of lightning are related to the peak value of the current ( $I$ ), and to the specific energy ( $W/R$ ). The thermal effects are related to the specific energy ( $W/R$ ) when resistive coupling is involved and to the charge ( $Q$ ) when arcs develop to the installation. The dangerous sparking caused by inductive coupling is related to the steepness ( $di/dt$ ) of the lightning current front.

Each of the single parameters ( $I$ ,  $Q$ ,  $W/R$ ,  $di/dt$ ) tends to dominate each failure mechanism. This is to be taken into account in establishing test procedures [4].

#### 13.11.3.1 First short stroke and long stroke

The values  $I$ ,  $Q$ ,  $W/R$  related to mechanical and thermal effects are determined from positive flashes (because their 10 per cent values are much higher than the

Table 13.6 Tabulated values of lightning current parameters taken from CIGRE and fixed values for lightning protection level I [4]

Parameter	Units	Values			Fixed value for level I	Stroke type	Line in Figure 10.14
		95%	50%	5%			
$I$	kA	4(98%) 4.9 4.6	20(80%) 11.8 35	90 28.6 250	— 50 200	*First negative short *Subsequent negative short First positive short (single)	1A + 1B 2 3
$Q_{flash}$	C	1.3 20	7.5 80	40 350	— 300	Negative flash Positive flash	4 5
$Q_{short}$	C	1.1 0.22	4.5 0.95	20 4	— 100	First negative short Subsequent negative short First positive short (single)	6 7 8
$W/R$	kJ/Q	2 6 0.55	16 55 6	150 550 52	— 10.000	First negative short Subsequent negative short First positive short	9 10 11
$di/dt_{max}$	kA/ $\mu$ s	9.1 9.9	24.3 39.9	65 161.5	—	*First negative short *Subsequent negative short	12 13
$di/dt_{30/90\%}$	kA/ $\mu$ s	0.2 4.1	2.4 20.1	32 98.5	20 200	First positive short *Subsequent negative short	14 15
$Q_{long}$	C				200	Long	
$T_{long}$	s				0.5	Long	
Front duration	$\mu$ s	1.8 0.22	5.5 1.1	18 4.5	— $T_1 = 0.25$	First negative short Subsequent negative short	
Stroke duration	$\mu$ s	3.5 30 6.5 25	22 75 32 230	200 200 140 2.000	$T_1 = 10$ $T_2 = 100$ $T_2 = 350$	First positive short (single) First negative short Subsequent negative short First positive short (single)	
Time interval	ms	7	33	150		Multiple negative strokes	
Total flash duration	ms	0.15 31 14	13 180 85	1.100 900 500		Negative flash (all) Negative flash (without single) Positive flash	

The values of  $I = 4$  kA and  $I = 20$  kA correspond to a probability of 98% and of 80%, respectively.

Table 13.7 Logarithmic normal distribution of lightning current parameters [4] mean  $\mu$  and dispersion  $\sigma_{\log}$  calculated from 95% and 5% values

Parameter	Units	Mean $\mu$	Dispersion $\sigma_{\log}$	Fixed value for level I	Stroke type	Line in Figure 13.14
$I$	kA	(61.1)	0.576	—	*First negative short (80%)	1A
		33.3	0.263	—	*First negative short (80%)	1B
$Q_{\text{flash}}$	C	11.8	0.233	50	*Subsequent negative short	2
		33.9	0.527	200	First positive short (single)	3
		7.21	0.452	—	Negative flash	4
		83.7	0.378	300	Positive flash	5
$Q_{\text{short}}$	C	4.69	0.383	—	First negative short	6
		0.938	0.383	—	Subsequent negative short	7
$W/R$	kJ/ $\Omega$	17.3	0.570	100	First positive short (single)	8
		57.4	0.596	—	First negative short	9
		5.35	0.600	—	Subsequent negative short	10
		612	0.844	10.000	First positive short	11
$di/dt_{\text{max}}$	kA/ $\mu\text{s}$	24.3	0.260	—	*First negative short	12
		40.0	0.369	—	*Subsequent negative short	13
$di/dt_{30/90\%}$	kA/ $\mu\text{s}$	2.53	0.670	20	First positive short	14
		20.1	0.420	200	*Subsequent negative short	15
$Q_{\text{long}}$	C	—	—	200	Long	—
$T_{\text{long}}$	s	—	—	0.5	Long	—
Front duration	$\mu\text{s}$	5.69	0.304	—	First negative short	—
		0.995	0.398	$T_1 = 0.25$	Subsequent negative short	—
Stroke duration	$\mu\text{s}$	26.5	0.534	$T_1 = 10$	First positive short (single)	—
		77.5	0.250	—	First negative short	—
		30.2	0.405	$T_2 = 100$	Subsequent negative short	—
		224	0.578	$T_2 = 350$	First positive short (single)	—
Time interval	ms	32.4	0.405	—	Multiple negative strokes	—
Total flash duration	ms	12.8	1.175	—	Negative flash (all)	—
		167	0.445	167	Negative flash (without single)	—
		83.7	0.472	—	Positive flash	—

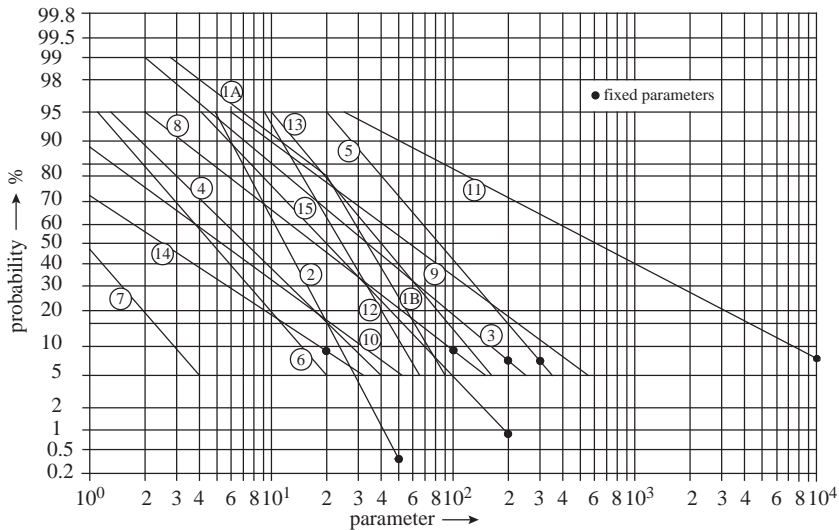


Figure 13.15 Cumulative frequency distribution of lightning current parameters (lines through 95% and 5% values) [4, 15]. (The meaning of the number and black points are in Tables 13.6 and 10.7)

corresponding 1 per cent values of the negative flashes). From Figure 13.15 (lines 3, 5, 8, 11 and 14) the following values with probabilities below 10 per cent can be taken:  $I = 200$  kA,  $Q_{flash} = 300$  C,  $Q_{short} = 100$  C,  $W/R = 10.000$  kJ/ $\Omega$  and  $di/dt = 20$  kA/ $\mu$ s. For a first short stroke according to Figure 13.11 these values give a first approximation for the front time:

$$T_1 = I / (di/dt) = 10 \mu\text{s} \tag{13.15}$$

$T_2$  is of minor interest. For an exponentially decaying stroke current the following approximately applies ( $T_1 \ll T_2$ ):

$$\begin{aligned} Q_{short} &= (1/0.7) \cdot I \cdot T_2 \\ W/R &= (1/2) \cdot (1/0.7) \cdot I^2 \cdot T_2 \end{aligned} \tag{13.16}$$

These formulas together with the values given above lead to a first approximation for the time to half value of  $T_2 = 350 \mu$ s.

For the long stroke its charge can be approximately calculated from:

$$Q_{long} = Q_{flash} - Q_{short} = 200 \text{ C} \tag{13.17}$$

Its duration time according to Figure 13.12 may be estimated from the flash duration time to  $T_{long} = 0.5$  s.

### 13.11.3.2 Subsequent short stroke

The value  $di/dt$  related to the dangerous sparking caused by inductive coupling is determined from subsequent short strokes of negative flashes (because their 1 per cent values are much higher than the 1 per cent values from first negative strokes or the corresponding 10 per cent values of the positive flashes). From Figure 13.15 (lines 2 and 15) the following values with probabilities below 1 per cent can be taken:  $I = 50$  kA and  $di/dt = 200$  kA/ $\mu$ s.

For a subsequent short stroke according to Figure 13.11 these values give as a first approximation for its front time:

$$T_1 = I/(di/dt) = 0.25 \mu\text{s}. \quad (13.18)$$

Its time to half value may be estimated from stroke duration of negative subsequent short strokes:  $T_2 = 100 \mu\text{s}$  ( $T_2$  is of minor interest).

#### 13.11.4 Minimum lightning current parameters used for interception efficiency of air terminals

Following the electrogeometric model the final jump distance (rolling sphere radius  $R$ ) is correlated with the peak value of the first short stroke. According to the IEEE working group report [41] the relation is given as:

$$R = 10 \cdot I^{0.65} \quad (13.19)$$

where  $R$  is the rolling sphere radius (m) and  $I$  is the peak current (kA).

For a given rolling sphere radius  $R$  it can be assumed that all flashes with peak values higher than the corresponding minimum peak value  $I$  will be intercepted by the air terminations. Therefore, the probability for the peak values of first strokes from Figure 13.15 is assumed as interception probability. Taking into account the polarity ratio of 10 per cent positive and 90 per cent negative flashes the total interception probability can be calculated.

### 13.12 Annex B: models for the evaluation of lightning exposure of structures and interception probability of air terminals

#### 13.12.1 Electrogeometric model

The electrogeometric model (EGM) was first proposed in Europe and was later further developed in America, notably by Whitehead and his team.

The position of a downward leader approaching the grounded structure defines a distance from the structure top called the striking distance. This parameter is usually related to the charge in the downward leader and then to the peak value of the lightning current, taking into account the correlation between the integrated leader charge and the current [13].

Different relations have been proposed to express the relationship between striking distance and peak value of the lightning current. Figure 13.4 shows some curves according to different authors together with some available data [36]. The curves exhibit a large spread due to different assumptions made by the authors to take care of the physics of the phenomenon. The comparison with recorded data [36] of striking distance to tall structures leads to the conclusion that the following relation fits well the recorded points:

$$D_s = 6.7 I^{0.8} \quad (13.20)$$

More recently, following the proposal of IEEE WG [41], the International Standard for lightning protection against direct strikes to the structure [10] accepted the following similar relation:

$$D_s = 10 I^{0.65} \quad (13.21)$$

The spaces protected by the application of the electrogeometric model for different conductor configurations are shown in Figures 13.16, 13.17 and 13.18. The design



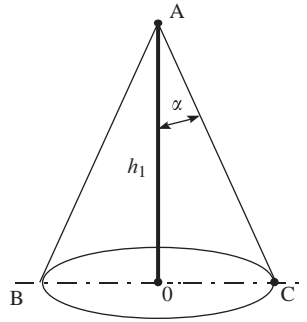


Figure 13.16 Volume protected by a vertical rod air termination [25]

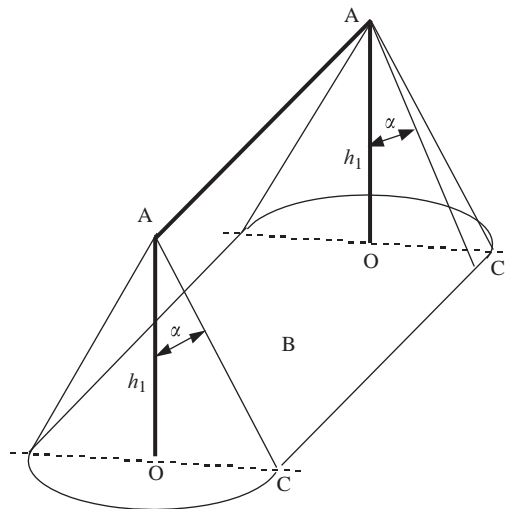


Figure 13.17 Volume protected by a catenary wire air termination [25] A: tip of an air termination; B: reference plane; OC: radius of protected area;  $h_1$ : height of an air termination rod above the reference plane;  $\alpha$ : protective angle according to Table 13.5

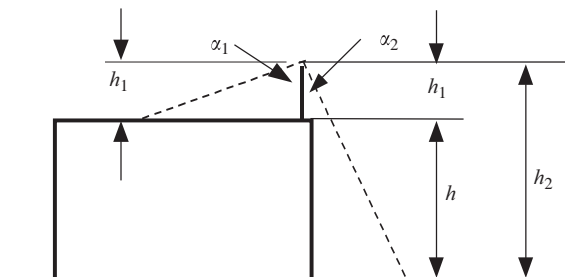


Figure 13.18 Volumes protected by a vertical air termination rod [25]  $h_1$  is the physical height of an air termination rod. The protective angle  $\alpha_1$  corresponds to the air termination height  $h_1$ , being the height above the roof surface to be protected (reference plane); the protective angle  $\alpha_2$  corresponds to the height  $h_2 = h_1 + h$ , being the soil reference plane;  $\alpha_1$  is related to  $h_1$  and  $\alpha_2$  is related to  $h_2$

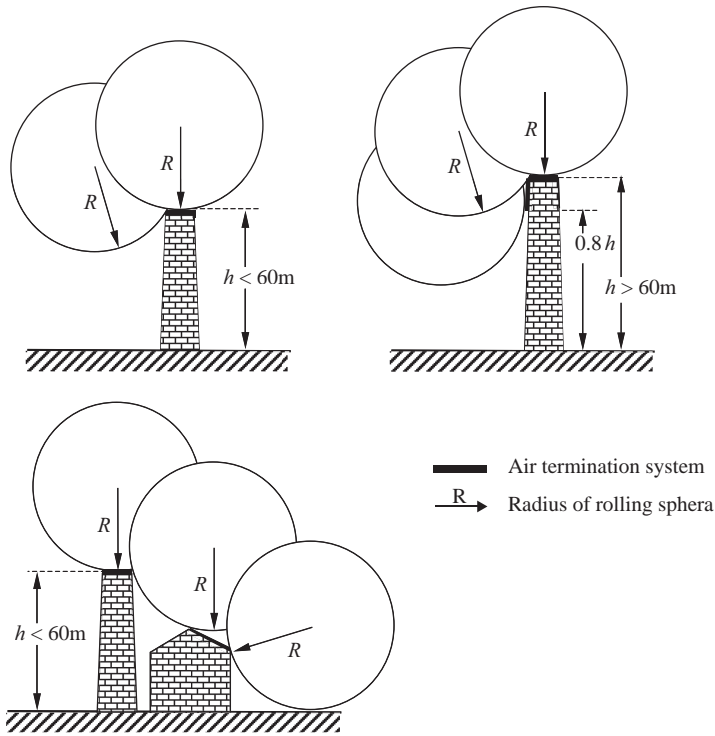


Figure 13.19 Design of an LPS air termination according to the rolling sphere method. The rolling sphere radius should comply with the selected lightning protection level (see Table 13.3)

of an LPS air termination system according to the rolling sphere method is shown in Figure 13.19.

### 13.12.2 Improved electrogeometric model

In contrast to earlier approaches, in which the striking distance is a function of current amplitude only, this model [20] provides a rational basis for taking account of the influence of structure height.

According to this model an attractive radius, defined as the maximum distance from the structure for which a downward leader having a defined charge is captured by the structure itself, may be evaluated as a function of downward leader charge. Consequently, a volume above the structure, within which leader interception is possible, can be evaluated on the basis of the attractive radius on the assumption that relative upward/downward leader approach velocity ratio be constant and equal to unity.

With the above assumption the impact of lightning to the structure is only possible when the tip of the downward leader reaches the volume above the structure defined by the attractive radius.

Application of the model over a broad range of structure heights and lightning current amplitudes allows us to derive the generalised curves. Regression through these curves allows us to estimate the structure attractive radius:

$$R = I^a 0.84 h^{0.6} \tag{13.22}$$

where  $a = 0.7 h^{0.02}$ .

From the model results relevant to structures with height ranging from 10 to 100 m, making reference to an average amplitude current of 35 kA, the following simplified formula is proposed:

$$R = 14 h^{0.6} \quad (13.23)$$

### 13.12.3 *Generalised leader inception model*

A further step in the simulation of the lightning impact mechanism is the representation of positive leader initiation from earthed objects under the influence of a negative descending leader and of the subsequent propagation of the two channels.

According to this model the conditions may be evaluated both for the corona inception at the earthed object and mainly for continuous positive leader inception and propagation from the corona critical dimension, which is generated by the negative leader charge approaching earth.

An iterative procedure is applied to determine the attractive radius as a function of the lightning current and of the height of the structure. For a free standing structure of up to 60 m height the following simplified formula has been proposed [21] for a lightning current of 31 kA:

$$R = 24.6 h^{0.4} \quad (13.24)$$

### 13.12.4 *Leader progression model*

A more detailed simulation of the lightning impact mechanism has been developed in 1990, and more recently (1996) refined, in which both the leader progression in time and space and the variation in time of the resulting electrical field can be considered. Detailed references of this dynamic model may be found in [23] and [7].

The model takes into account physical mechanisms investigated during the development of discharges in long air gaps and the investigations of the development of lightning channels. Of the involved phenomena, the model mainly takes into account the propagation of the downward negative channel and the inception and propagation of the upward positive leader from earthed structures.

A mathematical description of the phenomena requires a determination of the resulting electric field, repeated at different times, in order to simulate the charge in the cloud and the actual charge displaced by the leader channels during their progression.

This model allows us to simulate structures located in orographic conditions different from flat territory, such as valleys, hills and mountains with the presence of other structures in the vicinity.

Application of the model to different cases of structures and conductors together with considerations and comments on the model assumptions could be found in the report [7] prepared in the frame of CIGRE.

## References

- [1] IEC 81/170/Q: 'Questionnaire-approval of new publications' plan', April 2001
- [2] BERGER, K., ANDERSON, R.B., and KRONINGER, H.: 'Parameters of lightning flashes', *Electra*, 1975, (41), pp. 23–37
- [3] ANDERSON, R.B., and ERIKSSON, A.J.: 'Lightning parameters for engineering applications', *Electra*, 1980, (69), pp. 65–101

- [4] IEC 62305-1/CD 2002: 'Protection of structures against lightning – Part 1: general principles' (according to the new publications' plan)
- [5] WG of Italian Electrotechnical Committee (CEI), TC81-Lightning Protection: 'Lightning protection of structures', Part I to Part III, *Energ. Elettr.*, 1984, (5), pp. 185–214
- [6] WG of Italian Electrotechnical Committee (CEI), TC81-Lightning Protection: 'Lightning protection of structures', Part IV to Part VI, *Energ. Elettr.*, 1985, (11), pp. 447–475
- [7] GIGRE SC 33 WG 33.01 (TF03): 'Lightning exposures of structures and interception efficiency of air termination systems', 1989
- [8] IEC 61024-1: 'Protection of structures against lightning', Edn 1, 1990 (according to the new publications' plan: IEC 62305-3, Protection against lightning – Part 3: physical damages and life hazard). Draft IEC 81/215/CD, March 2003, produced by TC81/WG8
- [9] IEC 62305-2: Protection against lightning – Part 2: risk management. Draft IEC 81/214/CD, March 2003, produced by TC81/WG9 under revision of IEC 61662, TR 1995
- [10] FLISOWSKI, Z., and MAZZETTI, C.: 'A new approach to the complex assessment of the lightning hazard of buildings', *Bull. Pol. Acad. Tech. Sci.*, 1984, **32** (9–10), pp. 571–581
- [11] MAZZETTI, C., POMPILI, M., and FLISOWSKI, Z.: 'Review of application problems of probabilistic approach to the lightning hazard assessment', Proceedings of 23rd international conference on *Lightning protection* (ICLP), Florence, Italy, September 1996, paper 7.1, pp. 707–712
- [12] FLISOWSKI, Z., and MAZZETTI, C.: 'Risk assessment method for the protection of electronic systems against lightning overvoltages', IV SIPDA, Sao Paulo, Brazil, May 1999
- [13] UMAN, M.A.: 'Lightning discharge' (Academic Press, 1987)
- [14] POPLARSKY, F.: 'Relationship between the number of thunderstorm days and the lightning flash density registered by LFC in the world scale', *Proc. of 21st International Conference of Lightning Protection*, Berlin, Germany, paper 6.10
- [15] IEC 61312-1: 'Protection against LEMP – Part 1: general principles', 1995 (according to the new publications' plan: IEC 62305-4, Protection against lightning, Part 4: Failure of electrical and electronic systems within structures). Draft IEC 81/214/CD, March 2003, produced by TC81/WG3
- [16] IEC 61663-2: 'Lightning protection of telecommunication lines – Part 2: lines using metallic conductors', 2001
- [17] IEC 61312-3: 'Protection against LEMP – Part 3: requirements for surge protective device (SPD)', 1998
- [18] MAZZETTI, C., D'ELIA, B., TOMASSINI, R., DI GREGORIO, G., KUCA, B., and FLISOWSKI, Z.: 'LEMP disturbances in the mains incoming to the structures', Proceedings of international scientific conference on *Energy savings in electrical engineering*, Warsaw, May 2001, paper C-09, pp. 65–69
- [19] GOLDE, R.H.: 'Lightning vol. 1 and 2' (Academic Press, London 1977)
- [20] ERIKSSON, A.J.: 'The incidence of lightning strikes to power lines', *IEEE Trans. Power Deliv.*, 1987, **PWRD-2**, pp. 859–870
- [21] RIZK, F.A.M.: 'Modelling of transmission line exposure to direct lightning strokes', *IEEE Trans. Power Deliv.*, 1990, **5** (4), pp. 2009–2029

- [22] PETROV, N.I., and WATERS, R.T.: 'Determination of the striking distance of lightning to earthed structures', *Proc. Roy. Soc. A*, 1995, **450**, pp. 589–601
- [23] BERNARDI, M., DELLERA, L., GARBAGNATI, E., and SARTORIO, G.: 'Leader progression model of lightning: updating of the model on the basis of recent test results', Proceedings of 23rd ICLP, Florence, Italy, September 1996, paper 4.2, pp. 399–407
- [24] LEE, R.H.: 'Lightning protection of buildings', *IEEE Trans. on Industry Application*, 1979, **IA-15**, pp. 237–240
- [25] IEC 61024-1-2: 'Protection of structures against lightning – Part 2: application guide B', 1998
- [26] LIEW, A.C., and DARVENIZA, M.: 'Dynamic model of impulse characteristics of concentrated earths', *Proc. Inst. Electr. Eng.*, 1974, **121**, (2), pp. 2357–2362
- [27] VERMA, R., and MUKHEDKAR, D.: 'Impulse impedance of buried ground wire', *IEEE Trans. Power Appar. Syst.*, 1980, **PAS-99**, (5)
- [28] GUPTA, B.R., and THAPAR, B.: 'Impulse impedance of grounding grids', *IEEE Trans. Power Appar. Syst.*, 1980, **PAS-99**, (6)
- [29] MAZZETTI, C., and VECA, G.: 'Impulse behavior of ground electrodes', IEEE PES winter meeting, New York, 1983, paper 83 WM142-7
- [30] VAINER, A.L.: 'Impulse characteristics of complex earth grids', *Electrical Technology, USSR*, Vol. I, 1966
- [31] KOSTALUK, R., LOBODA, M., and MUKHEDKAR, D.: 'Experimental study of transient ground impedances', IEEE PES summer meeting, Portland, 1981, paper 81 SM 399-5
- [32] KOUTEYNIKONOFF, P.: 'Réponse impulsionnelle des prises de terre aux courantes de foudre', CIGRE symposium 22-81, Stockholm, 1981
- [33] OETTLÉ, E.E.: 'A new general estimation for predicting the impulse impedance of concentrated earth electrodes', *IEEE Trans. Power Deliv.*, 1988, **3**, (4), pp. 2020–2029
- [34] CRISHOLM, W.A., and JANISCHEWSKYJ, W.A.: 'Lightning surge response of ground electrodes', *IEEE Trans. Power Deliv.*, 1989, **4**, (2), pp. 1329–1337
- [35] POPOLANSKY, F.: 'Impulse characteristics of soil', 20th ICLP, Interlaken, September 1990, paper 3.2
- [36] ERIKSSON, A.J.: 'Lightning and tall structures', *Trans. SAIEE*, 1978, pp. 238–252
- [37] GILMAN, D.W., and WHITEHEAD, E.R.: 'The mechanism of lightning flashover on HV and EHV transmission lines', *Electra*, 1973, (27), pp. 65–96
- [38] YOUNG, F.S., CLAYTON, J.M., and HILEMAN, A.R.: 'Shielding of transmission lines', *IEEE Trans. Power Appar. Syst.*, 1963, special supplement, p. 132
- [39] WAGNER, C.F.: 'The lightning stroke as related to transmission line performance', *Electr. Eng.*, May–June, 1963
- [40] DAVIS, R.: 'Lightning flashovers on the British Grid', *Proc. Inst. Electr. Eng.*, 1963, pp. 969–974
- [41] IEEE WG report: 'Estimating lightning performance of transmission lines – updates to analytical models', SM 453-PWRD 1992

---

## Chapter 14

# Attachment of lightning flashes to grounded structures

Vernon Cooray

---

### 14.1 Introduction

A grounded structure can interact with a lightning flash in two different ways. It can interact either with a downward or upward lightning flash. The initiation of a downward lightning flash takes place in the cloud, whereas in the case of upward lightning flash, the point of initiation is usually at the tip of a tall structure. In other words, upward lightning flashes are created by the grounded structure itself. In this chapter, a brief description of various models used to study the lightning attachment is given together with some of their predictions. A portion of the material presented here is published previously in references [1, 2].

First, let us consider the events associated with the attachment of a downward negative lightning flash (i.e., a lightning flash that transport negative charges to ground) with a grounded structure (more details on this are presented in Chapter 4). Experimental investigations show that a downward lightning flash is initiated by a column of charge called the stepped leader that travels from cloud to ground in a stepped manner. As the stepped leader approaches the ground, the electric field at ground level increases steadily. The electric field at the pointed tips of a grounded structure which is immersed in this background electric field may reach values which are several times to several tens of times the magnitude of the background electric field produced by the stepped leader due to field enhancement. When the electric field at the tip of a structure reaches a critical value of about  $3.0 \times 10^6$  V/m electron avalanches will be generated from the tip. As the background electric field and hence the local electric field at the tip intensifies, the ionization taking place at the tip becomes more vigorous leading to an increase in the number of charge particles in the head of the electron avalanches. When this number reaches a value around  $10^8$ – $10^9$ , electron avalanches will be transformed to a streamer discharge [3, 4, see also Chapter 3]. This conversion of electron avalanches to a streamer, or the streamer inception, is called avalanche to streamer transition. Once the conditions necessary for streamer inception are satisfied, several streamer bursts will be issued from the point under consideration. These streamer bursts are generated from a common stem and if the charge in the streamer burst is larger than about  $1 \mu\text{C}$ , the streamer stem will be thermalized leading to the creation of a leader [3]. This transition is called streamer to leader transition. This leader, created by the action of the electric field generated by the stepped leader is called a connecting leader. Once incepted, a connecting leader starts to grow toward the down coming stepped leader. This growth of the connecting leader is mediated by streamer bursts generated at its tip.

The charge associated with each streamer burst depends on the background electric field and the potential gradient of the connecting leader channel. The potential gradient of the connecting leader channel (which is positively charged in this case) can be obtained by appealing to the thermodynamic model of the positive leaders as described by Gallimberti [3]. Each streamer burst extends the leader by a small amount. For example, if the charge in a streamer burst is  $Q$  then the amount of elongation of the positive leader is given by  $Q/q_1$ , where  $q_1$  is the amount of charge necessary to thermalize a unit length of the leader channel. For positive leaders this is equal to about  $65 \mu\text{C}/\text{m}$ . Recent studies conducted by Becerra and Cooray [5] show that  $q_1$  depends on the speed of the leader. Indeed, both the down coming stepped leader and the upward moving connecting leader moves with the aid of streamer bursts that generate enough charge to thermalize a section of the leader. As the positive leader approaches the negative one the average potential gradient between the two leader tips continues to increase and when it reaches a value equal to  $500 \text{ kV}/\text{m}$  all conditions necessary for the final attachment of the connecting leader to the stepped leader are satisfied. This situation is referred to as the final jump condition. Once the connection is made between the stepped leader and the connecting leader the resulting rapid neutralization of the stepped leader charge leads to the generation of a return stroke. The point of attachment of the downward flash on the structure is the point of initiation of the connecting leader that made the final connection with the stepped leader.

Now, let us consider the upward lightning flashes initiated by tall grounded structures. Upward lightning flashes are initiated by the tall structures themselves due to the field enhancement at the periphery of the structure when it is immersed in the background electric field generated by the thundercloud. As the electric field generated by the thundercloud increases and once all the stages that have been described above, namely, initiation of avalanches, initiation of streamers and initiation of a leader, had been completed an upward moving leader will be initiated from the structure. Once initiated the conditions necessary for its propagation are identical to that of the connecting leader described in the previous section except for the fact that here the background electric field remains more or less constant, whereas in the previous case it was increasing with time as the stepped leader approaches the structure. Once the leader initiated from the structure reaches the charge center in the cloud, dart leaders will follow this channel to ground initiating subsequent return strokes.

For a lightning attachment model to be self-consistent it should take into account all the processes mentioned above. However, due to the difficulties associated with including all these processes into a lightning striking model, engineers have constructed empirical models that can be applied easily in practice. In the following sections, some of the models utilized to analyze the problem of lightning attachment are described. However, before proceeding further let us describe the meaning of the striking distance as applied in lightning protection studies.

## 14.2 Striking distance

Let us first investigate the physical meaning of the striking distance. According to the definition of this parameter by Golde [6], the striking distance is the separation between the tip of the stepped leader and the tip of a grounded structure when a stable (i.e., continuously propagating) upward connecting leader is established from the

field enhanced tip of the structure. However, one can see immediately that this definition will lead to ambiguous situations in practice. For example, as a stepped leader approaches the ground several stable connecting leaders could be established either by several points on the same structure or by points in several structures. In this case, the above definition cannot be used to define the striking distance uniquely. Another situation where this definition may cause difficulties is when one tries to analyze lightning strikes to a flat ground. In this case, the final attachment may take place without the origin of a connecting leader in a conventional sense. However, one can get out of this ambiguous situation by redefining the striking distance as follows. It could be defined as *the separation between the tip of the structure, where a connecting leader is generated, and the tip of the stepped leader when the final jump condition is established between the connecting leader and the stepped leader*. This is illustrated in Figure 14.1. With this definition, a striking distance is associated only with a connecting leader that successfully intercepts the down coming stepped leader. It could also be applied without any ambiguity in situations where a connecting leader, in the conventional sense, is absent (or very short) during a lightning strike.

According to the Electro-Geometrical-Model (EGM) of lightning protection, the attachment between the stepped leader and the grounded structure takes place when the final jump condition is established between the tip of the stepped leader and the grounded structure. EGM does not envisage the presence of a connecting leader. In this chapter, the critical distance between the tip of the stepped leader and the grounded structure when the final jump condition is established between them is referred to as EGM-striking distance. This is the striking distance in the absence of a connecting leader. Thus, the striking distance defined in the previous section reduces to EGM-striking distance when the connecting leader is absent or negligibly short.

The final jump condition, borrowed from the jargon of high voltage research, is defined, in the case of long sparks, as the instant when the streamers generated from

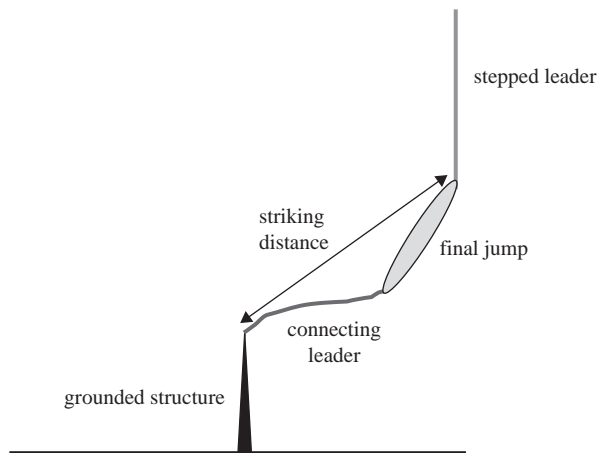


*Figure 14.1 The striking distance is defined in the figure as the separation between the tip of the structure, where a connecting leader is generated, and the tip of the stepped leader when the final jump condition is established between the connecting leader and the stepped leader*



the leader channel reaches the grounded electrode (see Chapter 3). Since the streamers maintain a constant potential gradient, one can assume that the final jump condition is reached when the average potential gradient between the leader tip and the grounded structure becomes equal to the potential gradient of streamer channels. Now consider a strike of a negative downward flash to flat ground. If the ground is completely flat, then the final jump condition is reached when the average electric field between the leader tip and the ground reaches a value 1–2 MV/m. This is the critical electric field necessary for negative streamer propagation. However, in practice, a completely flat ground does not exist and even on the surface of an ocean the turbulence created during thunderstorms may result in the formation of waves, which may act as temporary protrusions. In such cases, positive streamers could be generated from small protrusions on ground or on the ocean surface. If the breakdown is mediated purely by positive streamers, then it is reasonable to use  $E_s = 500$  kV/m. However, in the case of electrical breakdown between a negative stepped leader and a grounded structure both negative and positive streamers mediate the breakdown process and the electric field in the final jump region could be larger than 500 kV/m, the exact value depends on the relative extensions of negative and positive streamers in the final jump region. It is common practice in lightning protection studies to assume an electric field of 500 kV/m in the final jump region. In the case of encounter between the connecting leader and the stepped leader, the final jump condition is reached when the potential gradient between the two leader tips is equal to this critical potential gradient.

With the above definition, the striking distance in the absence of a connecting leader from a grounded structure becomes the separation between the tip of the structure and the tip of the stepped leader when the average electric field between them reaches a value of 500 kV/m. With increasing length of the connecting leader the striking distance increases.

In order to apply this concept of striking distance it is necessary to know when and where from the structure a connecting leader is incepted. There are several theories that can be utilized to find this information and some of the important ones are summarized below.

## 14.3 Leader inception models

### 14.3.1 *Critical radius and critical streamer length concepts*

Laboratory experiments conducted with rod-plane gaps in air show that for a given gap length the breakdown voltage remained the same with increasing electrode radius until a critical radius is reached [7, 8, see also Chapter 3]. Further increase of the radius led to an increase of the breakdown voltage. The radius at which the breakdown voltage starts to increase is named the critical radius. The critical radius is the minimum radius of a spherical electrode in a given gap length, which will produce leader inception immediately with the inception of streamers. The critical radius increases initially with gap length but reaches a more or less asymptotic value of about 38 cm for large gap lengths. Experiments conducted with inverted geometries gave values in the range 10–28 cm [9].

The critical radius concept is commonly applied in lightning research in the evaluation of the background electric field necessary for the generation of a continuous leader from a point on a grounded structure. This is done by replacing the extremity of the structure (or the tip of a lightning conductor) by a sphere of radius

equal to the critical radius and assuming that a leader will be incepted from the structure when the electric field at the surface of the sphere reaches breakdown value in air.

Laboratory experiments also show that the length of the streamers at the instant of leader inception from a sphere of critical radius is about 3 m [7, 8, see also Chapter 3]. In other words, the length of the streamers should exceed this critical value before the inception of a leader. Akyuz and Cooray [10] have used the critical streamer length as the criterion, instead of the critical radius, in evaluating the inception of connecting leaders. Based on the results of Chernov *et al.* [11], Petrov and Waters [12] assumed that the streamers initiated from a given point on a structure must extend to a critical length of 0.7 m, before an upward leader is initiated from that point. In a model developed by Bazelyan and Raizer [13] it is assumed that the unstable leader inception takes place when the potential drop between the electrode tip and a point about 1 m from it is equal to 400 kV. Since 400 kV/m is approximately equal to the potential gradient of positive streamers, this criterion implies that the inception of an unstable connecting leader takes place when the streamers extend to a length of about 1 m. According to them, for the unstable leader to transform into a stable leader and propagate continuously, the difference between the potential of the leader tip and the potential produced by the external field at the location of the leader tip should increase continuously. One advantage of the critical streamer length criterion over the critical radius criterion is that it can be easily implemented in any complicated structure that one may encounter in practice.

It is important to point out, however, that the critical radius and critical streamer length concepts are derived from breakdown characteristics of long rod-plane gaps under the application of switching impulses of critical time to crest. In the case of lightning attachment, the temporal variation of the electric field generated at the grounded structure by a down coming stepped leader is very different to that of an electric field generated by a switching impulse. For this reason, the validity of such concepts in the case of lightning flashes is still a topic of discussion.

### 14.3.2 Rizk's generalized leader inception equation

Based on the results from laboratory, Rizk [14] has constructed a theory to evaluate the inception of leaders from grounded structures. According to this theory, the ambient potential  $U$  (potential in the absence of the structure) at the height of a horizontal wire required to incept an upward connecting leader from the horizontal wire is given by

$$U = \frac{2247}{1 + \frac{5.15 - 5.49 \ln(a)}{h \ln(h/2a)}} \quad (14.1)$$

where  $h$  is the height of the horizontal conductor in meters and  $a$  is the radius of the wire in meters and  $U$  in kV. For a vertical tower the ambient potential at the top of the tower necessary for the inception of a connecting leader from it is given by

$$U = \frac{1556}{1 + 3.89/h} \quad (14.2)$$

where  $h$  is the height of the tower in meters.

Note that these results are based on laboratory data pertinent to switching impulses and the assessment of their validity in the case of electric fields generated by stepped leaders may require further research efforts. Recently, Rizk [15] has established theory that allows evaluation of leader inception from any structure.

### 14.3.3 *Lalande's stabilization field equation*

Lalande [16] used a physical model for the leader propagation in long gaps proposed by Goelian *et al.* [17] and combined it with the thermo-hydrodynamic model of the leader channel proposed by Gallimberti [3] in order to compute the leader inception condition. In constructing the model, it is also assumed that the ratio of the leader velocity to leader current remains constant during the development of the leader. Based on this analysis the background electric field (assumed to be uniform) necessary to initiate leaders from grounded structures was estimated as

$$E_0 \geq \frac{240}{1 + \frac{h}{10}} + 12 \text{ [kV m}^{-1}\text{]} \quad (14.3)$$

where  $h$  is the height of the structure in meters. In a later study, however, Lalande *et al.* [18] proposed the following equation, which is different from the above, for the stabilization electric field:

$$E_0 \geq \frac{306.7}{1 + \frac{h}{6.1}} + \frac{21.6}{1 + \frac{h}{132.7}} \text{ [kV m}^{-1}\text{]} \quad (14.4)$$

Unfortunately, the details as to the modifications necessary both in physics and in mathematics to change the results from (14.3) to (14.4) were not given in [18].

### 14.3.4 *Leader inception model of Becerra and Cooray (SLIM)*

Utilizing the same physics as developed by Gallimberti [3], Becerra and Cooray [5, 19] introduced a model to evaluate the inception of connecting leaders. The model can be applied to any grounded structure including conductors and towers of power transmission and distribution lines. The main steps that are included in the model are the following:

- (i) Formation of a streamer discharge (streamer inception) at the tip of a grounded object.
- (ii) Transformation of the stem of the streamer into thermalized leader channel (unstable leader inception).
- (iii) Extension of the positive leader and its self-sustained propagation (stable leader inception).

In the model, the streamer inception is evaluated using the well-known streamer inception criterion [3, 4] while the transition from streamer to leader is assumed to take place if the total charge in a streamer burst is equal to or larger than about  $1 \mu\text{C}$  [3]. Once incepted the propagation of the leader is evaluated in each time step by evaluating the charge in the streamer zones. This model not only predicts the conditions under which leaders are incepted but it provides the current and speed of the upward moving leaders. A detailed description of the procedure proposed by Becerra and Cooray to evaluate the leader inception can be found in Chapter 3.

## 14.4 Leader progression or lightning attachment models

In the previous section, we have described some of the important leader inception models. However, inception of a connecting leader itself does not guarantee lightning attachment. It is necessary for the connecting leader to propagate and make the final connection with the stepped leader. There are several models that attempt to do this and they are called leader progression models. Now, let us summarize several of these models.

One of the most simple and user friendly lightning strike models is the Electro Geometrical Model (EGM). As pointed out in section 14.2 this model assumes that when the stepped leader reaches a critical distance from a grounded structure where the average potential gradient in the gap between the leader tip and the grounded structure is equal to the streamer potential gradient, i.e., 500 kV/m, electrical breakdown takes place in the gap immediately and the lightning flash will be attracted to the grounded structure. This model neglects the presence and effects of connecting leaders.

For a complete description of the attachment of a leader to grounded structures, however, both the inception of a connecting leader and its subsequent propagation and final connection to the downward stepped leader have to be analyzed. The leader progression models attempt to simulate the dynamics associated with this process. In contrast to EGM, five models that take into account the formation of an upward leader exist today and they were introduced by Eriksson [20, this model is popularly known as Collection Volume Method (CVM)], Dellera and Garbagnati [21], Rizk [22], Becerra and Cooray [23], and Vargas and Torres [24–26]. Only in some of them, however, the dynamic progress of downward and upward leader is explicitly represented, as it will be illustrated in what follows. For ease of reference, refer to the models as A, B, C, D, and E, respectively. Basic features of these models are schematically depicted in Figure 14.2. Note that the description given here for the model C is based on reference [22]. In a recent paper, the model was updated and improved by Rizk [15].

- In models A, C, and D the downward stepped leader is assumed to take a straight path to ground without branches, while in B the path is determined step by step by the solution of subsequent electrostatic problems, in which the boundary conditions are represented essentially by the downward and upward leaders. In E, the downward leader channel may also be tortuous and branched and the channel geometry is based on the statistical characterizations of natural lightning channels as reported by Hill [27, 28] and Idone and Orville [29].
- The linear charge density on the downward stepped leader channel is assumed to decrease upward in A, C, D, and E. In B, the charge per unit length has two different values: one in the vicinity (last tens of meters) of the leader tip, which is uncorrelated to the amplitude of the lightning current and assumed equal to 100  $\mu\text{C}/\text{m}$  and the other one, the magnitude of which varies with the prospective return stroke current, along the rest of the leader channel. In D, the variation of the charge per unit length of the stepped leader is approximated by an analytical expression extracted by Cooray *et al.* [30] by analyzing the charge brought to ground by first return strokes within the first 100  $\mu\text{s}$ . More details on this charge distribution and the procedure utilized to derive it are given in Chapters 4 and 9 (see also section 14.5). In E, the charge distribution along the downward stepped leader, including the main channel and branches, is estimated by an electrostatic model of the lightning leader channel and the thundercloud [24, 25].

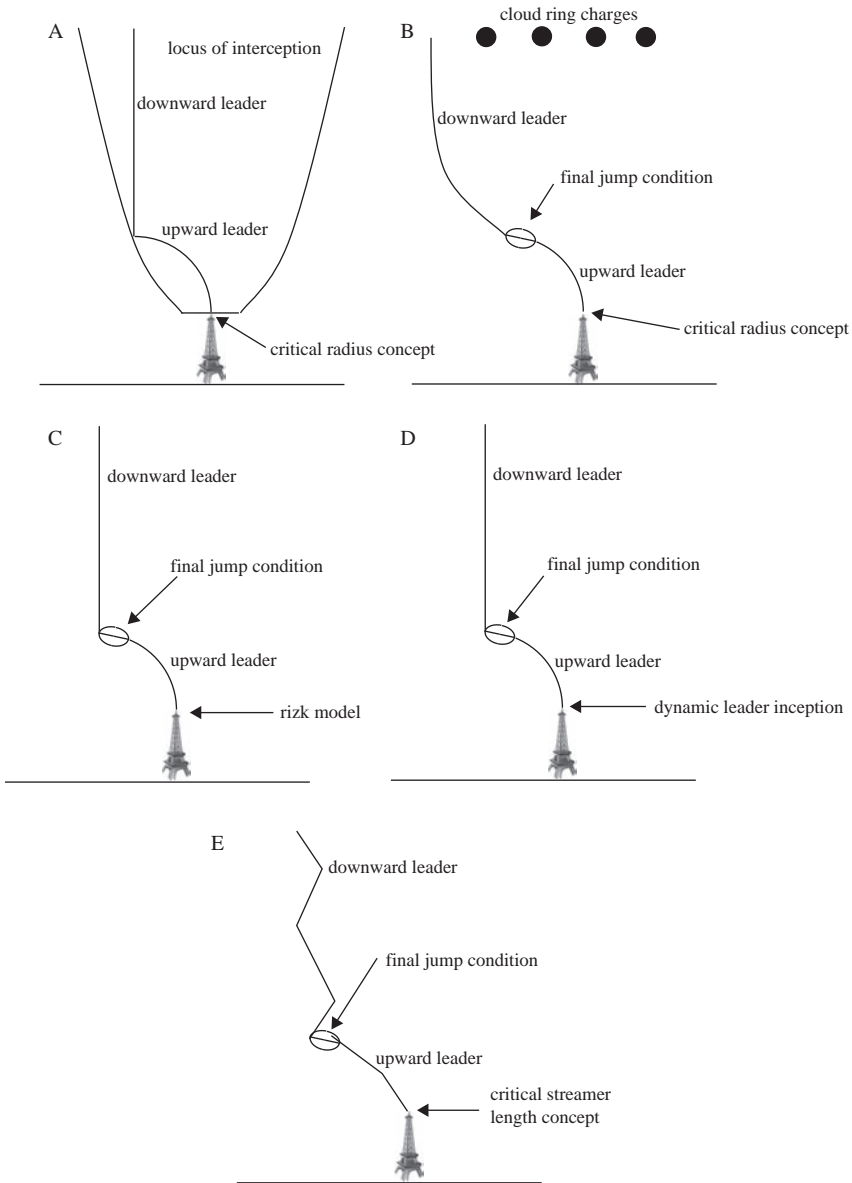


Figure 14.2 Schematics of the leader propagation models A, B, C, and E

- As the downward leader propagates toward the ground the conditions at the surface of the grounded structure is evaluated continuously to find the time of leader inception. The criterion for upward connecting leader inception used is either the critical radius concept (A and B), Rizk's generalized equation (C), Becerra and Cooray procedure (D) or the Vargas, and Torres criteria (E). The latter considers a streamer inception electric field assumption and the critical streamer length concept [25]. It is worth noticing that models A, B, and C are only applicable to horizontal wires and vertical earthed structures, whereas models D and E can be applied to any grounded structure, including complex

buildings. Recently, the procedure to apply model B and C to any grounded structure is illustrated in references [31] and [15], respectively.

- In models A, C, D, and E the downward stepped leader path is considered unaffected by the presence of upward connecting leaders. In models A, C, and D, the connecting leader travels in space in such a way that it will find the closest path for the connection with the stepped leader. However, recently Cooray [32] modified the model D in such a way that the connecting leader propagates in the direction of the maximum background electric field at the location of the tip of the connecting leader. In model B, both leaders propagate in the direction of the maximum electric field that exists along an equipotential line that is located at the outer boundary of the streamer region. The same criterion is applied in model E to simulate the propagation of the connecting leader.
- The ratio between the speed of propagation of the downward stepped leader and the upward moving stepped leader is assumed to be either 1 or 4. However, in model D the velocity of the upward leader is evaluated from first principles.
- In model A, the final attachment of the two leaders takes place when two tips of the leader channel meet each other. In model B, the final jump condition is reached when the streamer systems from the two leaders meet each other. In C, D, and E the final jump condition is reached when the average electric field between the two leader tips is 500 kV/m.

#### 14.4.1 Recent developments

Recently, Mazur *et al.* [33] introduced a model to describe the propagation of negative stepped leaders. They utilized the model to estimate the striking distance of lightning flashes. In the model, the direction of a new leader step is taken to be the direction in which the length of the negative streamers issued by the negative leader head is longest. The direction of the positive leader is given by the direction of the maximum electric field at the tip of the positive leader immediately outside the boundary region with an electric field of 3 MV/m. They also assumed that the striking distance is equal to the length of the final step of the stepped leader. The length of the final leader step was estimated by dividing the leader potential by the electric field of the negative streamer zone. Based on their simulations, it was claimed that the connecting leader does not play a significant role in determining the striking distance.

When considering the complexity of the lightning phenomena, it will always be necessary to make a large number of assumptions and simplifications in order to formulate a usable lightning strike model. However, the creation of leader progression models has been a major step forward and they are capable of predicting several phenomena observed in the field. Moreover, the models seem to be well suited for sensitivity analysis, where the effects of various parameters on the efficiency of lightning protection procedures are being studied by changing one parameter at a time. It is important to stress here that self-consistent leader progression models can also be utilized to compliment the simple engineering models that are being used in practice.

### 14.5 The potential of the stepped leader channel and the striking distance

As referred earlier, Cooray *et al.* [30] analyzed the negative first return stroke currents measured by Berger and Vogelsanger [34] and Berger [35] at Monte San Salvatore

to find out whether there is any relationship between the peak current and the charge brought to ground during the first 100  $\mu\text{s}$ . They reasoned that the time interval of 100  $\mu\text{s}$  is representative of the time for the return stroke front to reach the charge center in the cloud and therefore the charge brought to ground during this time is a result of the neutralization of the section of the leader channel located below the charge center. They found that there is a strong correlation between the two parameters. Cooray *et al.* [30] extended their analysis further to obtain the distribution of the linear charge density along the leader channel as a function of return stroke peak current (see Chapter 4 and the next section). This charge distribution could be used to calculate the electric field generated by the downward moving stepped leader channel as a function of current. In creating this charge distribution, Cooray *et al.* [30] used the charge simulation method. The derived charge distribution was then fitted with an analytical function so that it can be used conveniently in engineering studies. This analytical function is good enough to calculate the electric field generated by the leader when the tip of the leader is located at distances of 10 m or more from a grounded structure. However, in many applications the linear charge distribution alone is not enough to calculate the stepped leader potential. One also has to have information concerning the radius of the channel. For example, if it is assumed that the leader charge is located on an infinitesimally thin stepped leader channel, the potential of the stepped leader channel will go to infinity. However, such a simplification will still give the correct electric fields generated by a stepped leader as far as the point of observation is not located very close to the stepped leader channel. In the study conducted by Cooray *et al.* [30], the radius of the leader channel is assumed to vary depending on its charge density. Thus, to calculate the potential one has to plug in the radius used in the calculation. In many applications it is convenient to have the potential of the leader channel itself so that it can be used directly in evaluating the striking distance.

In calculating the striking distance it is necessary to know the potential of the stepped leader channel because the final jump condition is defined according to the average potential gradient across the gap between the connecting leader and the stepped leader channel or in the absence of a connecting leader, between the structure and the tip of the stepped leader. In a recent study, using the same data set that have been used by Cooray *et al.* [30] to extract the linear charge distribution of the stepped leader channel, Cooray [36] have evaluated the potential of the cloud as a function of the first return stroke peak current generated by a stepped leader originating from the cloud. The relationship between the two parameters was described by a polynomial regression curve. According to the results, the cloud potential  $V$  is connected to the peak first return stroke current,  $I_p$  by the equation

$$V = 5.86 \times 10^6 + 1.569 \times 10^6 I_p - 3.279 \times 10^3 I_p^2 \quad (14.5)$$

In this equation  $I_p$  is in kA and  $V$  is in volts. However, since it is convenient to use a power relationship in many engineering applications, Cooray and Becerra [2] used the following equation as an alternative to (14.5)

$$V = 3.0 \times 10^6 I_p^{0.813} \quad (14.6a)$$

The predictions of this equation agree with (14.5) reasonably well except for slight differences in the case of currents smaller than about 10 kA. The problem was reanalyzed again by Cooray [36] and it was found that the equation

$$V = 3.76 \times 10^6 I_p^{0.767} \quad (14.6b)$$

provides a better power fit to the relationship given by (14.5) than that provided by (14.6a). Of course the differences between (14.6a) and (14.6b) are so small either one of these could be used in engineering applications.

Note that (14.5), (14.6a), and (14.6b) describe the cloud potential as a function of the first return stroke peak current. Since the stepped leader channel can be treated as a good conductor the potential  $V$  is approximately equal to the tip potential of the stepped leader channel. Now, let us come back to the question of striking distance.

Now, if the connecting leader is short or absent then the striking distance,  $S$ , is given by  $S = V/E_s$ . In this expression,  $E_s$  is the average electric field between the stepped leader tip and the grounded structure when the final jump condition is reached. Thus the striking distance in the absence of a connecting leader, i.e., EGM-striking distance, is given by

$$R_{egm} = \frac{3.76 \times 10^6}{E_s} I_p^{0.767} \quad (14.7)$$

or

$$R_{egm} = \frac{5.86 \times 10^6 + 1.569 \times 10^6 I_p - 3.279 \times 10^3 I_p^2}{E_s} \quad (14.8)$$

As pointed out in section 14.2, the value of  $E_s$  that should be used in the above equation depends on the situation under consideration. If a strike to flat ground is considered then  $E_s \approx 10^6 - 2 \times 10^6$  V/m. In the case of a lightning strike to a structure the appropriate value of  $E_s$  is 500 kV/m. Let us consider the four levels of lightning protection classified as classes I, II, III, and IV. These classes provide protection from currents higher than 3, 5, 10, and 16 kA, respectively. According to IEC the striking distance (or the rolling sphere radii) corresponding to these classes are 20, 30, 45, and 60 m, respectively. Note, that if  $E_s = 500$  kV/m, according to (14.8) the striking distances corresponding to these currents are 21, 27, 42, and 60 m, respectively. These values are not far away from the values used in the IEC lightning protection standards. In the literature, one can find several expressions for the EGM striking distance [37–42]. They can be represented by the general equation

$$R_{egm} = a I_p^b \quad (14.9)$$

The parameters of this equation as presented in different publications are tabulated in Table 14.1. These relationships together with (14.7) are shown in Figure 14.3.

Table 14.1 Parameters  $a$  and  $b$  of (14.9) as given in different publications

Publication	$a$	$b$
Young <i>et al.</i> [37]	27	0.32
Brown and Whitehead [39]	6.4	0.75
Armstrong and Whitehead [Cigré WG 33-01, 1991] [38]	6	0.8
Love [40]	10	0.65
IEEE standard 1243 [41]	8	0.65
IEC standard 62305 [42]	10	0.65
Equation (14.7)	7.52	0.767



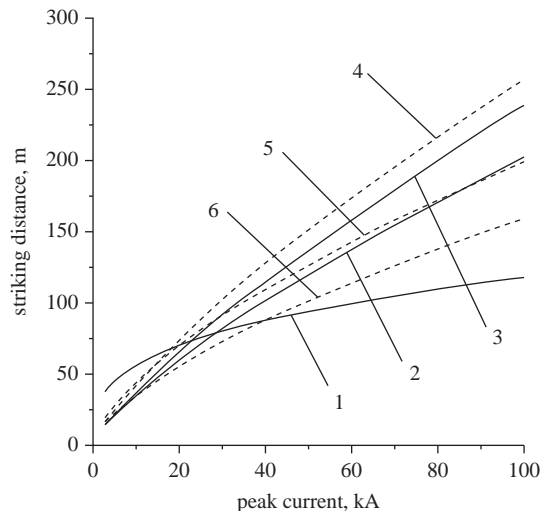


Figure 14.3 Striking distance as a function of first return stroke peak current according to different publications. (1) [37], (2) [39], (3) [38], (4) Equation (14.7), (5) [40, 42] and (6) [41]

### 14.6 Charge distribution on the stepped leader channel as a function of cloud potential

As described in Chapter 4 and the section 14.5, Cooray *et al.* [30] had derived the linear charge distribution along the leader channel as a function of return stroke peak current. An analytical expression for this charge distribution as a function of first return stroke peak current is given in Chapter 4. Sometimes in lightning protection studies it is convenient to express the charge distribution on the leader channel as function of cloud potential than that of the peak current. Now, the relationship given by (14.6b) can be written as

$$I_p = 2.67 \times 10^{-9} V^{1.304} \tag{14.10}$$

Using this relationship the charge distribution derived by Cooray *et al.* [30] can be written in terms of the cloud potential as follows. Let us assume that the height of the tip of the stepped leader at a given instant of time is located at a height  $z_o$ . Let  $\zeta$  represents the distance from the tip of the leader channel, measured along the stepped leader channel, to the point on the leader channel, say  $P$ , where the charge density is required. The linear charge density at this point on the stepped leader channel can be represented analytically by

$$\rho(l) = a_o \left( 1 - \frac{\zeta}{L - z_o} \right) G(z_o) V^{1.304} + \frac{V^{1.304} (a + b\zeta)}{1 + c\zeta + d\zeta^2} J(z_o) \tag{14.11}$$

$$\zeta = (z - z_o) \quad z > z_o \tag{14.12}$$

$$G(z_o) = 1 - \frac{z_o}{L} \tag{14.13}$$

$$J(z_o) = 0.3\alpha + 0.7\beta \quad (14.14)$$

$$\alpha = e^{-(z_o-10)}/75 \quad (14.15)$$

$$\beta = \left(1 - \frac{z_o}{L}\right) \quad (14.16)$$

where  $z_o$  is the height of the leader tip above ground in meters,  $z$  is the vertical height of the point P,  $L$  is the total vertical height (height of the point of origin) of the stepped leader channel in meters,  $\rho(z)$  is the charge per unit length (in C/m) of a leader section located at height  $z$ ,  $I_p$  is the return stroke peak current in kA,  $a_o = 3.94 \times 10^{-14}$ ,  $a = 1.3 \times 10^{-13}$ ,  $b = 1.044 \times 10^{-14}$ ,  $c = 0.522$ , and  $d = 3.73 \times 10^{-3}$ . Note that the above equation is valid for  $z_o \geq 10$  m. Since (14.11) describes the charge distribution as a potential of the cloud it can also be used with any other potential different from the one given by (14.6b).

## 14.7 Striking distance of subsequent return strokes

The triggered lightning experiments in combination with high speed photography have made it possible to study the attachment characteristics of subsequent strokes in details [43]. In the near future, these studies will gather information concerning the attachment of dart leaders to grounded structures. To the best of this author's knowledge, no theories on the striking distance of subsequent strokes are available in the literature. However, the potential of dart leader as a function of subsequent return stroke current is derived in Chapter 4. It is given by the equation

$$V = 5.86 \times 10^6 + 0.72 \times 10^6 I_p - 0.691 \times 10^3 I_p^2 \quad (14.17)$$

In the above equation,  $V$  is the potential (in volts) of the tip of the dart leader channel and  $I_p$  is the prospective subsequent return stroke peak current (in kA). Thus, the EGM striking distance of subsequent strokes is given by

$$R_{egm,sub} = \frac{5.86 \times 10^6 + 0.72 \times 10^6 I_p - 0.691 \times 10^3 I_p^2}{E_s} \quad (14.18)$$

In the above equation  $E_s = 5.0 \times 10^5$  V/m. Note, however, that the parameter that can be observed easily is the height of origin of the return stroke or the height at which the connecting leader met the down coming dart leader. The EGM does not specify what happens after the final jump condition is established between the down coming leader and the grounded structure. However, laboratory experiments with rod-plane gaps show that once the final jump condition is established a connecting leader starts from the grounded structure and move toward the tip of the leader. Thus, under the assumptions of EGM the connecting point takes place somewhere within the final jump distance (or the striking distance). The exact meeting point depends on the speed of connecting leader and the dart leader. To the best of our knowledge the only available experimental data in the literature shows that the speed ratio of connecting leader to the dart leader is equal to 1/2 [43]. Figure 14.4 shows the height of the meeting point as a function of subsequent return stroke peak current for the ratio of the speed of the connecting leader to the dart leader equal to 1/2. Note that the striking distance given by (14.18) is based on the

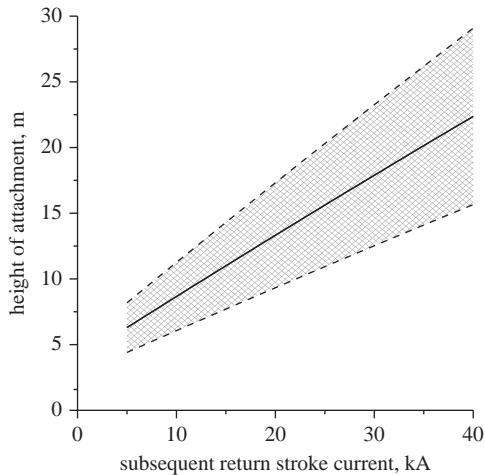


*Figure 14.4* The attachment height of subsequent return strokes, based on the ratio of the connecting leader speed to the dart leader speed equal to  $1/2$ , as a function of subsequent return stroke current. The possible spread of the estimated attachment height is also given in the diagram

relationship between the peak current of the subsequent return strokes as observed by Cooray *et al.* [30] (see Chapter 4). The spread in the data points used in the Cooray *et al.* [30] study is such that each individual data point may differ by about 30 per cent from the average curve that represents the relationship between the charge and the return stroke peak current. For this reason the calculated striking distance for a given peak return stroke current may also vary by about 30 per cent from (14.18). This spread is also shown in Figure 14.4. If this is correct, the height of the meeting point of a typical subsequent return stroke of 12 kA will be about 6–12 m and the one corresponding to a 20 kA will be about 9–17 m. Of course, the values given above are for the attachment of a dart leader to ground. In the case of lightning strikes to structures, the point of attachment will increase with increasing height of the structure because a connecting leader will be initiated in this case before the final jump condition is satisfied.

## 14.8 The effect of the height of the structure

The EGM was constructed by assuming that the effects of connecting leaders can be neglected in evaluating the attachment of lightning flashes to grounded conductors. This may very well be a reasonable assumption for lightning strikes to short structures where the probability of appearing of long connecting leaders is rather small. However, with increasing structure height the connecting leaders become longer and the predictions of EGM may be in error. This point was investigated by Cooray [32] and Cooray *et al.* [44]. The results presented below are based on the study are discussed in [44].

In order to evaluate the effect of structure height on lightning attachment one has to utilize an attachment model that is capable of taking into account the effect of connecting leaders. Any of the leader propagation models described earlier can

be used for this purpose. Cooray *et al.* [44] utilized the model SLIM for the task. Since the final jump, condition is defined according to the average electric field in the gap between the tips of the negative stepped leader and the connecting leader, in the analysis one has to have information concerning the potential of the stepped leader tip. For this purpose, one can use (14.5), (14.6a) or (14.6b) but Cooray [32] and Cooray *et al.* [44] used the potential function given by

$$V = 5 \times 10^6 I_p^{0.65} \quad (14.19)$$

instead of (14.5), (14.6a) or (14.6b). The reason for this choice is the following. At present, the decisions concerning the location of the lightning conductors on a structure to be protected are decided by the rolling sphere method of lightning protection. The rolling sphere method is based on the EGM which, as mentioned before, neglects the effects of connecting leaders and assume that the stepped leader is attracted to the structure when it comes within the final jump distance from the structure. In the current IEC standard the EGM striking distance is given as a function of the return stroke peak current by the following equation

$$S_{egm} = 10 I_p^{0.65} \quad (14.20)$$

Now, (14.20) gives the striking distance in the absence of a connecting leader (i.e., EGM striking distance). In other words, it gives the separation between the tip of the stepped leader and the grounded structure when the final jump condition is established between them. Thus, (14.20) can be utilized directly to estimate how the potential of the tip of the stepped leader vary as a function of the prospective return stroke peak current according to the IEC specifications. In order to obtain the potential of the leader channel that is in agreement with (14.20), one can appeal to the physics of the final jump condition and assume that the final jump condition occurs when the average potential gradient in the gap reaches 500 kV/m. The resulting potential (i.e.,  $E_s \times S_{egm}$ ) is given by (14.19). The use of potential given by (14.19) instead of (14.5), (14.6a) or (14.6b) will provide a possibility to directly evaluate how the striking distance and the attractive radii (the largest lateral distance that a stepped leader with a specified prospective return stroke current is attracted to the structure) as specified by IEC standard will vary as a function of structure height. For comparison purposes, the potential given by (14.6a) and (14.6b) are depicted together with (14.19) in Figure 14.5. Note that the two potential functions agree with each other at low currents but they deviate by about 25 per cent at high currents.

In the calculations the potential given by (14.19) is used together with (14.11) as input parameters of SLIM. The results obtained for the striking distance and attractive radii are presented below.

#### 14.8.1 Variation of striking distance with height

As mentioned previously, the striking distance is defined in the analysis presented here as the separation between the tip of the stepped leader and the tip of the grounded structure when a final jump condition is established between the connecting leader and the stepped leader. In the absence of a connecting leader, this definition reduces to the striking distance pertinent to EGM model. In the evaluation of striking distance, the stepped leader is assumed to come down directly above the structure. The structure that is being simulated is of cylindrical shape with a hemispherical tip. The radius of the cylinder in the calculation is assumed to

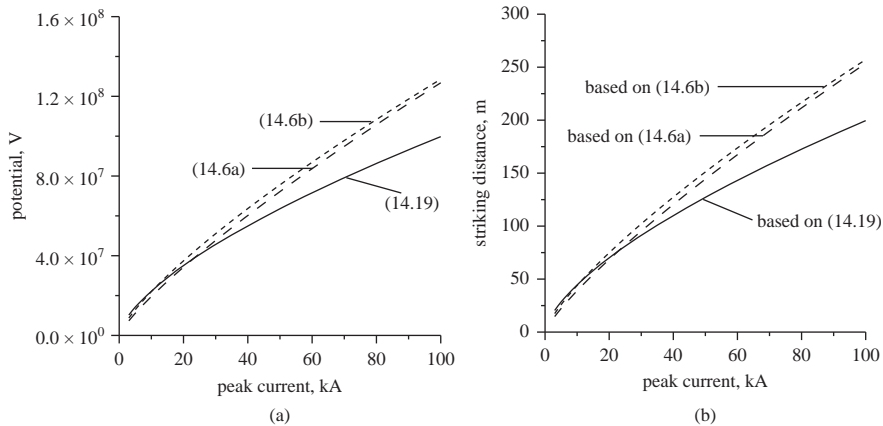


*Figure 14.5 (a) Leader tip potential as a function of return stroke peak current according to (14.6a), (14.6b), and (14.19). (b) EGM striking distance as a function of return stroke peak current based on (14.6a), (14.6b), and (14.19). In converting (14.6a), (14.6b), and (14.19) into striking distance the potentials given by these equations were divided by the streamer potential gradient of  $5 \times 10^5$  V/m*

be 0.1 m. Results are obtained for structure heights varying from 5 to 100 m and for return stroke current peaks varying from 5 to 100 kA. The striking distance as a function of return stroke current for several structure heights are depicted in Figure 14.6. In each diagram, the striking distance corresponding to (14.20) (i.e., the one used in the IEC standard) is also depicted. Moreover, an expression in the form  $S = aI_p^b$  that approximates the calculated striking distance is given in the figure caption.

Observe in these diagrams that the striking distance increases with increasing return stroke peak current and for a given return stroke peak current it increases with structure height. In contrast, the IEC striking distance (i.e., EGM striking distance) does not vary with structure height because it depends only on the potential of the stepped leader (or only on the return stroke peak current). Note also that, since we are using the charge distribution given by (14.11) with the stepped leader potential given by (14.19), the shorter the connecting leader the closer the value of striking distance obtained by SLIM to the striking distance used by the IEC lightning protection standard. Indeed, observe in the data presented in Figure 14.6 that for small structure heights the difference between the IEC striking distance and the one obtained from SLIM does not differ significantly. The reason for this being that the length of the connecting leader is smaller in the case of short structures for a given return stroke current.

### *14.8.2 Variation of attractive radii with distance*

In addition to the striking distance, the attractive radius of a grounded structure is a parameter that is often used in evaluating the number of lightning strikes that will be experienced by the structure over a given period of time. The attractive radius of a structure for a given stepped leader, with a specified prospective return stroke peak current, is defined as the maximum lateral distance from which the stepped leader could be attracted to the structure.

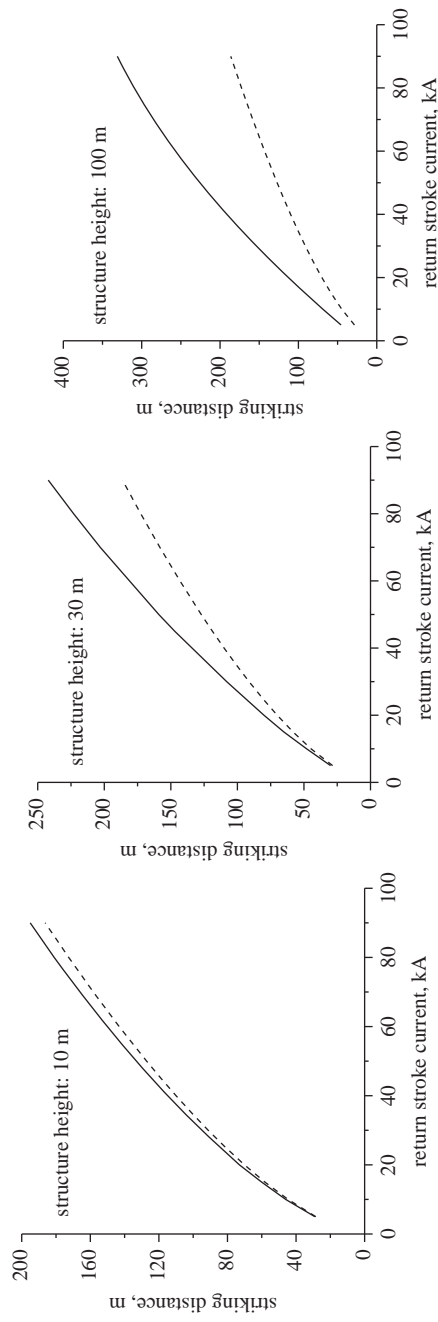


Figure 14.6 The striking distance of a stepped leader having different prospective return stroke currents for 10, 30, and 100 m high structures. The solid line is the results obtained using SLIM and the dashed line shows the results pertinent to EGM. The data pertinent to SLIM can be approximated by the equation  $S = 10I_p^{0.66}$  for 10-m high structure, by  $S = 9I_p^{0.73}$  for 30-m high structure and by  $S = 12I_p^{0.747}$  for the 100-m high structure

In the analysis presented here, the attractive radius of a grounded structure pertinent to a given stepped leader is evaluated as follows. First, the process of attachment between the structure and the stepped leader is analyzed by placing the path of the stepped leader directly above the structure. After that the stepped leader is gradually moved away from the structure evaluating in each case whether the stepped leader terminates on the structure or on the ground. The first distance at which the stepped leader terminates on the ground is the attractive radius of the structure pertinent to that particular stepped leader (or the prospective return stroke peak current).

Now, if one neglects the presence of a connecting leader, the attractive radius,  $R_{egm}$ , of a vertical or a horizontal conductor of height  $h$  is given according to EGM by

$$R_{egm} = \sqrt{S_{egm}^2 - (S_{egm} - h)^2} \quad \text{for } S_{egm} > h \quad (14.21a)$$

$$R_{egm} = S_{egm} \quad \text{for } S_{egm} \leq h \quad (14.21b)$$

In the presence of connecting leaders the value of the attractive radius for a given structure height increases from the EGM value due to the effect of the connecting leader. In the above equation,  $S_{egm}$  is the striking distance pertinent to EGM. In the analysis presented here, it was assumed to be given by (14.20). Thus, (14.21a) and (14.21b) are the attractive radii pertinent to the IEC lightning protection standard.

Figure 14.7 depicts the attractive radii calculated as a function of return stroke current peak for different heights of the structure. The attractive radii pertinent to IEC lightning protection standard is also depicted in each diagram. Note, again that, as in the case of striking distance, the difference between the attractive radii calculated using SLIM and the one pertinent to IEC lightning protection standard increases with increasing structure height. Moreover, for a given structure height the difference is smaller for smaller peak currents than for the larger peak currents. Again, one can see that for structure heights smaller than about 30 m the attractive radii is not that different to the ones pertinent to the IEC standard.

Note finally that, the values for the striking distance and attractive radii pertinent to IEC are always smaller than the ones predicted by the SLIM. As a result, adhering to the IEC standard would give rise to a conservative design of lightning protection system.

## 14.9 Comparison of different lightning attachment models

### 14.9.1 Comparison of attractive radii calculated using EGM and SLIM with CVM

The lightning attachment model introduced by Eriksson [20] is known as the Collection Volume Method (CVM). Recently, CVM has been utilized in making decisions concerning the placement of lightning conductors on buildings [45]. In order to evaluate the moment of inception of a connecting leader one has to calculate the electric field at the outer extremity of the structure during the progression of the stepped leader toward ground. This requires information concerning the charge distribution on the stepped leader channel and the field enhancement caused by the structure when placed in the electric field produced by the stepped leader. In his original model, Ericsson [20] assumed that the charge per unit length on the

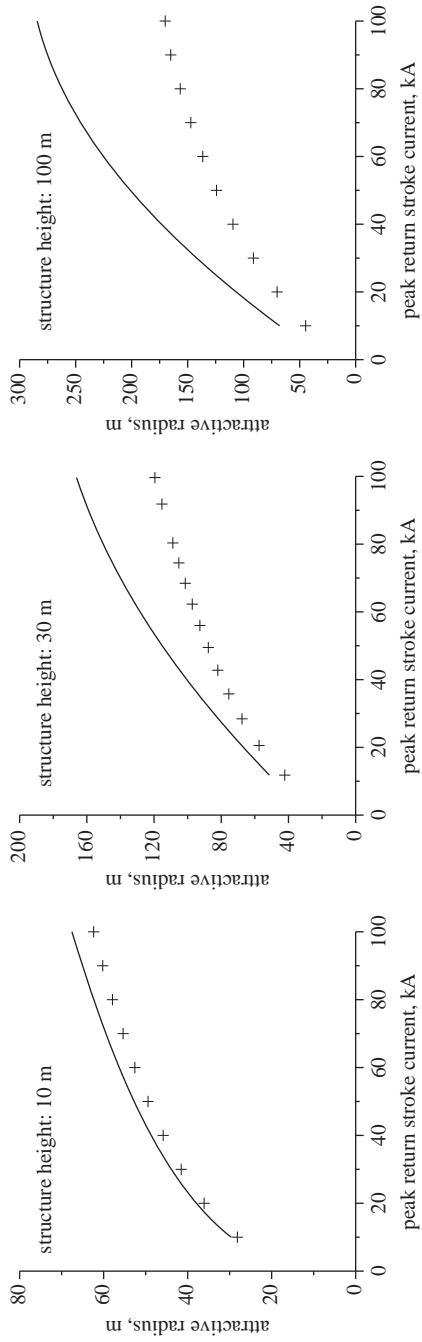


**Figure 14.7** The attractive radii of a stepped leader having different prospective return stroke currents for 10-, 30-, and 100-m high structures. The solid line is the result obtained using SLIM and the crosses shows the results pertinent to EGM



leader channel decreases linearly with height reducing to zero at the upper end of the channel. He assumed that the upper level of the leader channel is located at a height of 5 km from ground level. He also assumed that the relationship between the total charge on the stepped leader channel and the peak return stroke current is given by

$$I_p = 29.4 Q^{0.7} \quad (14.22)$$

In the above equation,  $I_p$  is the peak return stroke current in kA and  $Q$  is the total charge in coulombs. The above equation together with the assumed linear dependence specifies the charge distribution on the leader channel. It is important to mention here that in the recent applications of CVM in the location of lightning conductors the total charge on the leader channel is assumed to satisfy the relationship [45]

$$I_p = 10.7 Q^{0.7} \quad (14.23)$$

$Q$  in the above equation is really the one measured by Berger [46] for the charge brought to ground during the first 2 ms into the first return stroke. Eriksson assumed that (14.22) is more representative of the stepped leader channel because it agrees with Golde's suggestion that 1 C of charge should correspond to a return stroke current of about 25 kA. As we will show in the next section, the predictions of CVM differ considerably depending on whether (14.22) (as in [20]) or (14.23) (as in [45]) is used in estimating the charge distribution.

The results for the attractive radii obtained using CVM as a function of return stroke peak current for several structure heights are presented in Figure 14.8. In the calculation, the radius of the structure was fixed at 0.1 m. In these diagrams, the attractive radii as obtained (i) from SLIM, (ii) from IEC lightning protection standard, (iii) from CVM based on Eriksson's suggested charge distribution (let us refer to this as  $CVM_E$ ), and (iv) from CVM based on the charge distribution used by D'Alesandro and Gumley [45] (Let us refer to this as  $CVM_{A-G}$ ) are depicted. First, note that, similar to SLIM, CVM also predicts an increase in the attractive radii with increasing structure height. But, the attractive radii pertinent to  $CVM_{A-G}$  are considerably larger than the ones predicted by SLIM. On the other hand,  $CVM_E$  values are considerably lower than  $CVM_{A-G}$ . This shows that the attractive radii of lightning conductors as advocated by D'Alesandro and Gumley [45] (i.e.,  $CVM_{A-G}$ ) are much larger than the ones envisaged by Eriksson originally.

Concerning CVM, it is also important to make the following important remarks. First, in experiments conducted with inverted geometries, the critical radius was observed to lie in the range 10–28 cm [9]. The attractive radii obtained by CVM become larger than the ones depicted in Figure 14.8, if a value smaller than 38 cm is assumed for the critical radius. Second, note that in CVM, the attachment between the two leaders takes place when their tips meet each other. If it is assumed that the attachment takes place when the separation between the tips of the leaders reach the final jump distance, the predicted attractive radii of CVM would become even larger. Third, note that in CVM a connecting leader is essential for the attachment of a lightning flash to a grounded structure. If one neglects the presence or the effect of a connecting leader, CVM predicts that all lightning flashes strike the ground unless the stepped leader comes down directly over the structure.

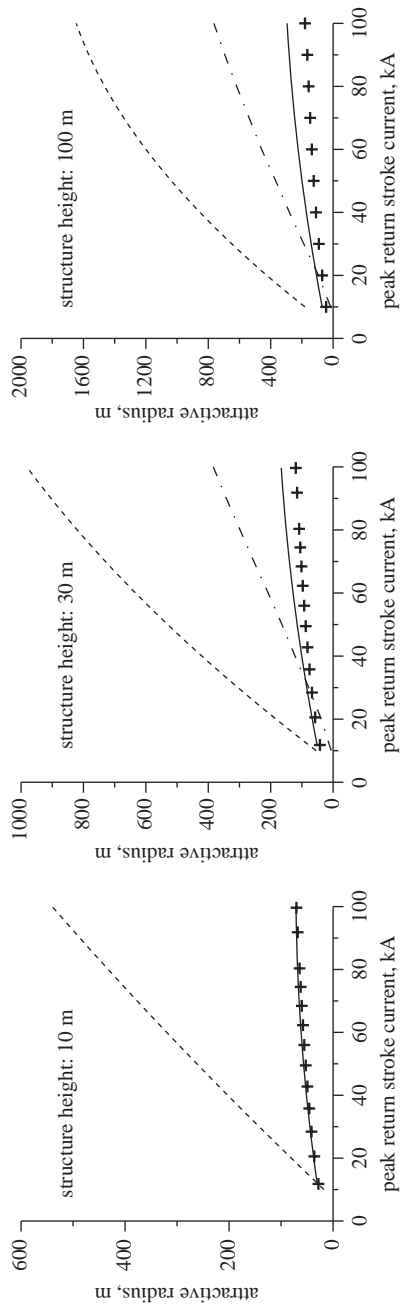


Figure 14.8 Attractive radii as predicted by CVM<sub>A-G</sub> (dashed line), SLIM (solid line) and EGM (crosses) corresponding to structure heights of 10, 30, and 100 m. The dashed-dot line in the diagrams corresponding to 30 and 100 m is the attractive radii as predicted by CVM when the charge distribution suggested by Eriksson [20] is used, i.e., CVM<sub>E</sub>

### 14.9.2 *Comparison of the predictions of SLIM with the predictions of other lightning attachment models*

Here we compare the results presented earlier with the leader progression models of Deller and Garbagnati [21] and Rizk [22]. The attractive radii of a structure of height  $h$  as a function of peak current  $I_p$  (in kA) as predicted by these two models can be represented by the equation

$$R = aI_p^b + c \quad (14.24)$$

In the model of Deller and Garbagnati,  $a = 0.028h$ ,  $b = 1.0$ , and  $c = 3h^{0.6}$ . The parameters corresponding to the Rizk model are:  $a = 4.27h^{0.41}$ ,  $b = 0.55$ , and  $c = 0$ . Note that similar to SLIM, both these models too predict the attractive radii to increase with increasing structure height. Let us now compare the predictions of these two models with the results presented in the previous sections.

Figure 14.9 shows the attractive radii as a function of peak current as predicted by these models for several values of structure heights. Recall that in calculating the attractive radii using SLIM, the potential function given by (14.19) was utilized. For comparison purposes the attractive radii as predicted by SLIM with the potential function given by (14.6b) is also given in the diagrams. Observe that all the models predict increasing attractive radii with increasing structure height. The values predicted by the model of Deller and Garbagnati [21] lies somewhat below the values predicted by SLIM and the values predicted by Rizk [22] lies somewhat above the values predicted by SLIM. With increasing structure height, the differences in the model predictions decrease. However, the predictions of these models are not that different to each other given the various uncertainties introduced into the results by assumptions made in these models. However, comparison of the data in these diagrams with the ones given in Figure 14.8 clearly shows that the CVM predicted attractive radii are significantly higher than the predictions of all the other models considered.

## 14.10 **Experimental test of lightning attachment models**

The only way to test the validity of the predictions of lightning strike models is to compare their predictions with time resolved photographs of attachment to structures of lightning flashes with measured return stroke currents. In this respect, time resolved photographs of lightning attachment to instrumented towers will provide examples that could be used to test the lightning strike models. For example, consider the two examples obtained by Berger [46, 47] which are depicted here in Figures 14.10 and 14.11. The return stroke current corresponding to the flash in Figure 14.10 is about 18 kA. The lateral displacement of the downward moving stepped leader channel from the tower was about 50 m. In this flash, the connecting leader issued from the tower met the stepped leader channel leader channel at a point A which is located at a height of about 30–40 m from the tip of the tower. The strike in Figure 14.11 had a peak return stroke current of 16 kA and the connecting leader met the down coming stepped leader channel at point marked C in Figure 14.11. The lateral displacement of the lightning channel from the tower was about 20 m. Figures 14.12 and 14.13 show the simulation of these events in SLIM using the potential function given by 14.5. The results would be the same irrespective of whether the potential given by (14.6a), (14.6b)

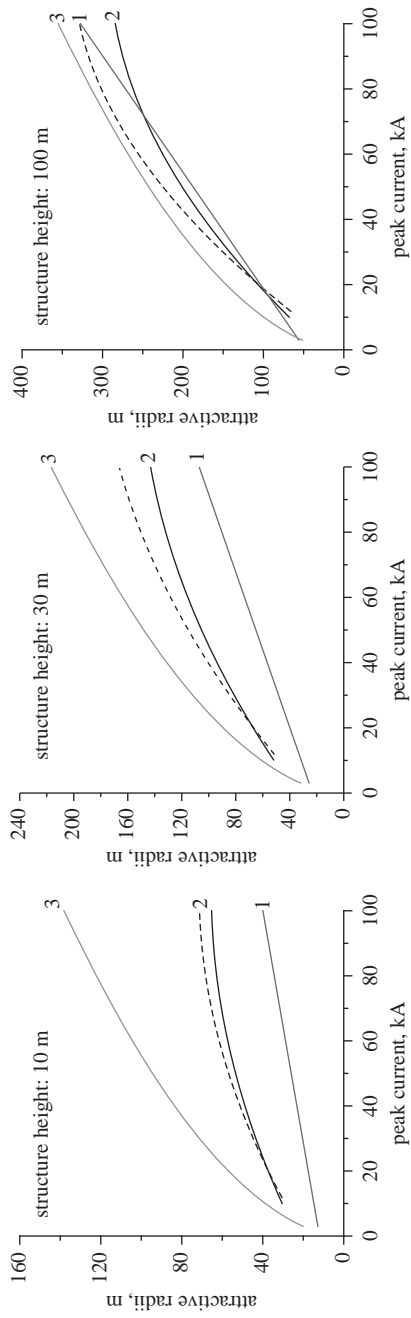


Figure 14.9 Attractive radii as predicted by (1) the model of Deller and Garbagnati [21], (2) SLIM and (3) the model of Rizk [22]. The dashed line corresponds to the prediction of SLIM with the potential function as given by (14.6a) is used as an input

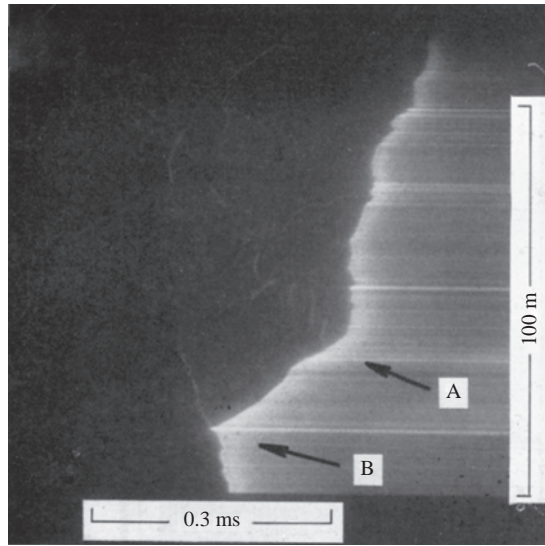


Figure 14.10 Time resolved photograph of a lightning strike to 70-m tall tower obtained by Berger [34] in Mount San Salvatore. In this flash, the connecting leader met with the down coming stepped leader at point A. The peak current in the first return stroke is 18 kA. Adapted from [47]

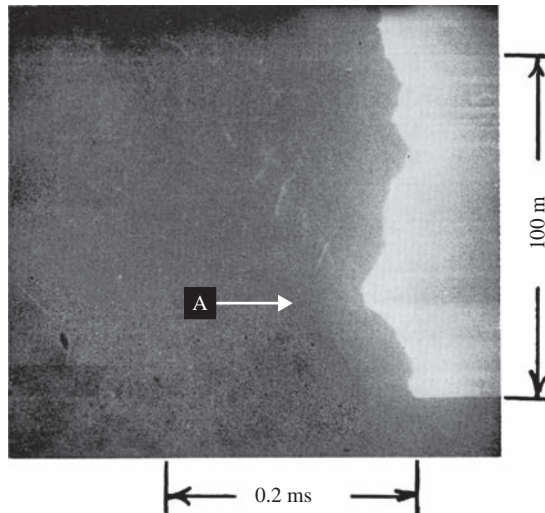


Figure 14.11 Time resolved photograph of a lightning strike to 70-m tall tower obtained by Berger [34] in Mount San Salvatore. In this flash, the connecting leader met with the down coming stepped leader at point A. The peak current in the first return stroke is 16 kA. Adapted from [46]

or the potential given by (14.19) is used in the calculations. The reason for this is that at the level of peak currents corresponding to these two return strokes both equations predict more or less the same leader tip potential. The simulations show that the connecting leader establishes the final jump condition when the tips of the

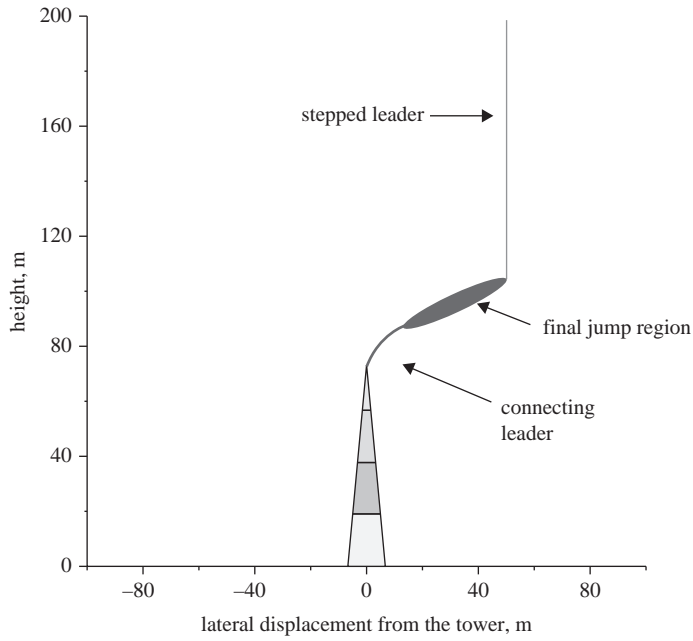


Figure 14.12 Results of simulation of the flash shown in Figure 14.10 using SLIM

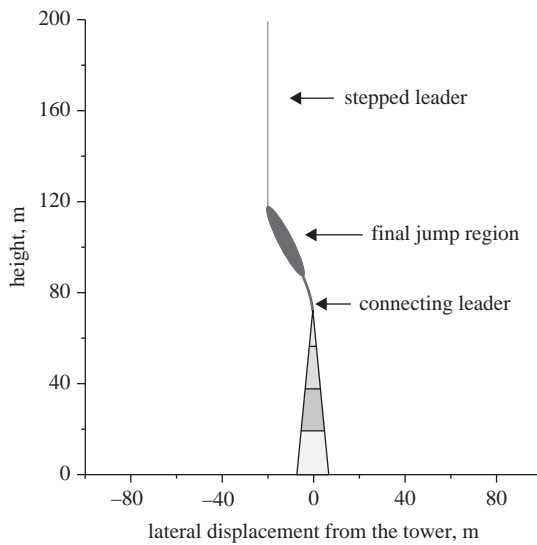
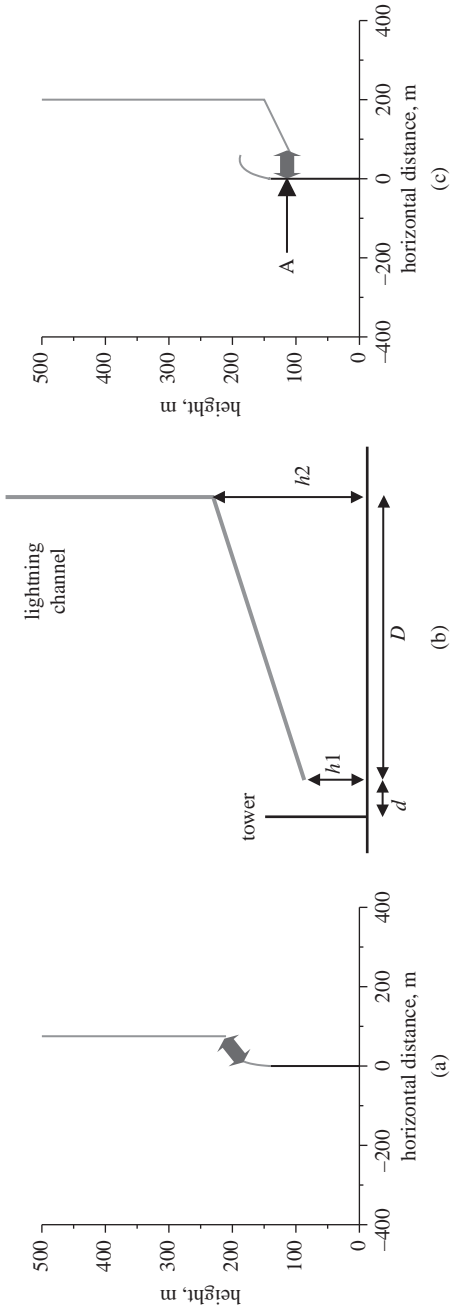


Figure 14.13 Results of simulation of the flash shown in Figure 14.11 using SLIM



**Figure 14.14** (a) The connecting leader and the vertical down coming stepped leader at the moment when the final jump condition is established between the connecting leader and the stepped leader. (b) Geometry of the slanted lightning channel used in the calculation. (c) The connecting leader and the inclined down coming stepped leader at the moment when the final jump condition is established between the grounded structure and the stepped leader. In (a) and (c) the final jump region is marked by two sided arrow. The thick arrow indicates the region where final jump condition is satisfied. Adapted from [32]

stepped leaders are roughly at the same heights as in the Figures 14.10 and 14.11. These results validate to some extent the predictions of SLIM.

### 14.11 Lightning strikes to the side of the structure

It is an established fact that lightning flashes can strike a tall structure at a point below the tip of the structure. Recently, for the first time in the literature, Cooray [36] utilized the lightning attachment model SLIM to simulate the attachment of lightning flashes to the side of the structure. The results obtained by Cooray [36] are the following. Consider a 150 m tall tower. For convenience, Cooray [36] assumed that the structure is cylindrical in shape with a radius 0.1 m and the tower top is a shaped like a hemisphere. Let us consider a stepped leader with a prospective return stroke current of 30 kA. First, consider the case where the stepped leader is vertical. In the simulation Cooray [36] has considered the lateral distance to the stepped leader from the tower to be 75 m. Simulations with SLIM shows that in this case the stepped leader is captured by a connecting leader issued from the top of the structure. Figure 14.14a shows the situation at the moment when the final jump condition is established between the connecting leader and the stepped leader. The final jump condition used in the simulation is that the average potential between the tip of the connecting leader and the tip of the stepped leader is 500 kV/m. Note that the length of the connecting leader is about 60 m. Now consider a stepped leader approaching the tower at an angle. The geometry assumed for the path of the stepped leader is shown in Figure 14.14b and the relevant distances are marked in the diagram. In the simulation it was assumed that  $D = 200$  m,  $h_1 = 100$  m,  $h_2 = 150$  m, and  $d = 15$  m. The simulation showed that the connecting leader issued from the tower was unable to make a connection with the stepped leader. The situation when the final jump condition is established is shown in Figure 14.14c. First, note that the stepped leader established final jump condition with a point on the side of the structure and this was the strike point of the lightning flash (marked A in Figure 14.14c). Note also that the connecting leader issued from the tower top, even though it was unsuccessful in establishing final jump condition, was about 80 m long. This example clearly demonstrates that side flashes to the tall structures takes place when the stepped leader approaches the structure at an angle.

### References

- [1] Cooray, V., A review of simulation procedures utilized to study the attachment of lightning flashes to grounded structures, Prepared on behalf of the CIGRE working group C4.405, ELECTRA, No. 257, 48–55, August 2011 (See also the comment and errata in ELECTRA, No. 260, pp. 18, 64, February, 2012)
- [2] Cooray, V. and M. Becerra, Attractive radii of vertical and horizontal conductors evaluated using a self consistent leader inception and propagation model – SLIM, Accepted for publication in *Atmos. Res.*, **117**, pp. 64–70, 2012
- [3] Gallimberti, I., The mechanism of long spark formation, *J. Physique Coll.*, **40**, C7, Suppl. 7, pp. 193–250, 1972
- [4] Bazelyan, E. M. and Y. P. Raizer, *Spark Discharge*, CRC Press, New York, 1977



- [5] Becerra, M. and V. Cooray, Time dependent evaluation of the lightning upward connecting leader inception, *J. Phys. D: Appl. Phys.*, **39**, pp. 4695–4702, 2006
- [6] R.H. Golde, *Lightning Protection*, Edward Arnold, London, 1973
- [7] Les Renardières Group, Research on long air gap discharges – 1973 results, *Electra*, **35**, pp. 47–155, 1974
- [8] Carrara, G. and L. Thione, Switching surge strength of large air gaps: a physical approach, *IEEE Trans.*, **PAS-95**(2), pp. 512–524, March/April 1976
- [9] Bernardi, M., L. Dellera, E. Garbagnati, G. Sartorio, Leader progression model of lightning: updating of the model on the basis of recent tests results, *Proc. of the 23rd International Conference on Lightning Protection (ICLP)*, September 1996
- [10] Akyuz, M. and V. Cooray, The Franklin lightning conductor: conditions necessary for the initiation of a connecting leader, *J. Electrostatics*, **51–52**, pp. 319–325, 2001
- [11] Chernov, E. N., A. V. Lupeiko, N. I. Petrov, Investigation of spark discharge in long air gaps using Pockel’s device, In *Proc. 7th Int. Symp. High Voltage Eng.*, Dresden, pp. 141–144, 1991
- [12] Petrov, N. I. and R. T. Waters, Determination of the striking distance of lightning to earthed structures, *Proc. R. Soc. A*, **450**, pp. 589–601, 1995
- [13] Bazelyan, E. M. and Y. P. Raizer, *Lightning physics and lightning protection*, Bristol, Institute of Physics, 2000
- [14] Rizk, F., A model for switching impulse leader inception and breakdown of long air-gaps, *IEEE Trans. on Power Delivery*, **4**(1), pp. 596–603, 1989
- [15] Rizk, F., Modeling of lightning exposure of buildings and massive structures, *IEEE Trans. on Power Delivery*, **24**(4), pp. 1987–1998, 2009
- [16] Lalande, P., Study of the lightning stroke conditions on a grounded structure, Doctoral thesis, Office National d’Etudes et de Recherches A’erospatiales ONERA, 1996
- [17] Goelian, N., P. Lalande, A. Bondiou-Clergerie, G. L. Bacchiega, A. Gazzani, I. Gallimberti, A simplified model for the simulation of positive-spark development in long air gaps, *J. Phys. D: Appl. Phys.*, **30**, pp. 2441–2452, 1997
- [18] Lalande, P., A. Bondiou-Clergerie, G. Bacchiega, I. Gallimberti, Observations and modeling of lightning leaders, *C.R. Physique*, **3**, pp. 1375–1392, 2002
- [19] Becerra, M. and V. Cooray, A simplified physical model to determine the lightning upward connecting leader inception, *IEEE Trans. Power Delivery*, **21**(2), pp. 897–908, 2006
- [20] Eriksson, A. J., An improved electrogeometric model for transmission line shielding analysis, *IEEE Trans.*, **PWDR-2**, pp. 871–877, 1987
- [21] Dellera, L. and E. Garbagnati, Lightning simulation by means of the leader progression model, I. Description of the model and evaluation of exposure of free standing structure, *IEEE Trans. Power Delivery*, **5**(4), pp.20009–20017, 1990
- [22] Rizk, F., Modeling of lightning incidence to tall structures Part I: Theory, *IEEE Trans. Power Delivery*, **PWRD-9**, pp. 162–171, 1994
- [23] Becerra, M. and V. Cooray, A self-consistent upward leader propagation model, *J. Phys. D: Appl. Phys.* **39**, pp. 3708–3715, 2006
- [24] Vargas, M., Novel integral model of the lightning discharge channel and its attachment to grounded structures, Doctoral thesis, Faculty of Engineering, National University of Colombia. Bogotá D.C., Colombia, 2006

- [25] Vargas, M. and H. Torres, On the development of a lightning leader model for tortuous or branched channels – Part I: Model description, *J. Electrostatics*, **66**(9+10), October, ISSN: 0304-3886, pp. 482–488, 2008
- [26] Vargas, M. and H. Torres, On the development of a lightning leader model for tortuous or branched channels – Part II: Model results, *J. Electrostatics*, **66**(9+10), October, ISSN: 0304-3886, pp. 489–495, 2008
- [27] Hill, R. D., Analysis of irregular paths of lightning channels, *JGR*, **73**(6), pp. 1897–1906, 1968
- [28] Hill, R. D., Tortuosity of lightning, *Atmos. Res.*, **22**(3), pp. 217–233, 1988
- [29] Idone, V. and R. Orville, Channel tortuosity variation in Florida triggered lightning, *Geophys. Res. Lett.*, **15**(7), pp. 645–648, 1988
- [30] Cooray, V., V. Rakov, N. Theethayi, The lightning striking distance – revisited, *J. Electrostatics*, **65**(5–6), pp. 296–306, 2007
- [31] Borghetti, A., F. Napolitano, C.A. Nucci, M. Paolone, M. Bernardi, Numerical solution of the leader progression model by means of the finite element method, *Proc. of the 30th Int. Conf. on Lightning Protection*, Cagliari, Italy, 2010
- [32] Cooray, V. On the attachment of lightning flashes to grounded structures with special attention to the comparison of SLIM with EGM and CVM, *J. Electrostatics*, **71**, pp. 577–581, 2013
- [33] Mazur, V., L. Ruhnke, A. Bondiou-Clergerie, P. Lalande, Computer simulation of a downward negative stepped leader and its interaction with a grounded structure, *J. Geophys. Res.*, **105**(D17), pp. 22361–22369, 2000
- [34] Berger, K. and E. Vogelsanger, Measurement and results of lightning records at Monte San Salvatore from 1955–1963 (in German), *Bull. Schweiz. Elektrotech.*, **56**, pp. 2–22, 1965
- [35] Berger, K., Methods and results of lightning records at Monte San Salvatore from 1963–1971 (in German), *Bull. Schweiz. Elektrotech. ver.*, **63**, pp. 21403–1422, 1972
- [36] Cooray, V., Attachment of lightning flashes to grounded structures, in *Lightning Electromagnetics* (ed. V. Cooray), IET publishers, London, UK, 2012
- [37] Young F.S., J. M. Clayton, A. R. Hileman, Shielding of transmission lines, *IEEE Trans. on PAS*, **82**, pp. 132–154, 1963
- [38] CIGRÉ WG 33-01 (convener A. Eriksson), Guide to Procedures for Estimating the Lightning Performance of Transmission Lines, Cigré Brochure 63, October 1991
- [39] Brown G.W. and E. R. Whitehead, Field and analytical studies of transmission line shielding, *IEEE Trans. on PAS*, **88**, pp. 617–626, 1969
- [40] Love E.R., Improvements on lightning stroke modelling and applications to the design of EHV and UHV transmission lines, M.Sc. Thesis, University of Colorado, 1973
- [41] IEEE Std. 1243, IEEE guide for improving the lightning performance of transmission lines, June 26, 1997
- [42] IEC 62305, International standard on protection against lightning, 2006
- [43] Wang, D., V. A. Rakov, M. A. Uman, N. Takagi, T. Watanabe, D. E. Crawford, *et al.*, Attachment process in rocket-triggered lightning strokes, *J. Geophys. Res.*, **104**, pp. 2143–2150, 1999
- [44] Cooray, V., U. Kumar, F. Rachidi, and C. A. Nucci, On the possible variation of the lightning striking distance as assumed in the IEC lightning

protection standard as a function of structure height, *Electric Power system Research*, **113**, 79–87, 2014

- [45] D'Alessandro, F. and J. R. Gumly, A 'Collection Volume Method' for placement of air terminals for the protection of structures against lightning, *J. Electrostatics*, **50**, pp. 279–302, 2001
- [46] Berger, K., Novel observations on lightning discharges: Results of research on Mount San Salvatore, *J. Franklin Institute*, **283**, pp. 478–525, 1967
- [47] Berger, K., The earth flash, In Golde, R. H. (Ed.), *Lightning*, vol. 1, Academic Press, London, UK, 1977

---

*Chapter 15*

## **Lightning and EMC**

*Michel Ianoz*

---

### **15.1 Introduction**

The very impressive natural phenomenon of lightning has been considered from the oldest times of humanity as a sign of power and as an instrument of punishment in the hands of the gods. The ancient Greeks imagined Zeus the ruler of the gods in Olympus as being the master of lightning, which he could use as a symbol of his supremacy. Similar stories can be found in the mythology of almost all cultures.

For many centuries, lightning has been a danger during thunderstorms for people, buildings and storage places where, for instance, wheat was stored. It can be assumed by extrapolating modern statistics that fires due to lightning took place often and that natural features, like a high tree in the proximity of a construction, were not always efficient protection.

When he began to use electricity, man had to build overhead lines to transport energy and information, lines which were exposed to lightning strokes causing disruption in the supply of energy or of the information. In the last case, direct danger for persons could occur due to the overvoltages, which, when the insulation level is inadequate, arrive on telephonic handsets and potentially kill people. The probability of direct impacts is however much higher for power lines due to their height over the ground. This explains the fact that practically from the beginning of the 20th century to the 1960s the attention of scientists was concentrated on protecting this kind of installation. The solution of installing a grounding wire at the top of towers used for the high-voltage lines proved to be quite efficient and after the 1960s, the interest in studying lightning was retained by only a small circle of scientists. It was no longer a necessity for engineers involved in practical applications such as power or even telecommunications.

In order to understand why lightning has again become a major item of concern for many applications of electricity a short look into the history of electromagnetic compatibility (EMC) is necessary.

### **15.2 Short overview of EMC history**

Contrary to what is usually thought, EMC is not such a young discipline. Its birth is in fact related to the beginning of radiocommunications, which were disturbed by natural noise or man-made interference. This problem was at the origin of the creation in 1935 of the Commission Internationale Spéciale pour les Perturbation Radio électriques (CISPR) in charge of specifying limits of electric and magnetic fields to avoid disturbing radiocommunications. The main sources of disturbance for

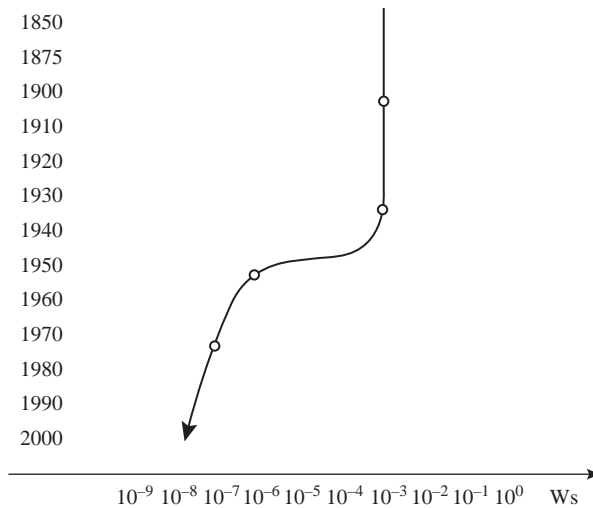


*Figure 15.1 Change of the level of energy needed for the destruction of electric and electronic components*

radio reception were thunderstorms which produced parasitic noise and corona in the proximity of high-voltage transmission lines. Direct lightning impacts could also represent a major threat for the antenna towers. Lightning rods with grounding wires connected to the earth were installed and in general this rather simple approach was sufficient to protect these towers. However, at that time the fight against electromagnetic noise did not yet use the term electromagnetic compatibility.

The increase of electromagnetic problems for various electric and electronic installation is related to the miniaturisation of the electronic components which began in the 1950s and 1960s. This miniaturisation, which was needed to reduce the weight of electronic devices, is of course connected to the development of various sciences and in particular to the use of satellites for military purposes. It increased the sensitivity of electronic components and therefore also the probability of interference. Figure 15.1 shows the decrease during the last 50 years of the energy needed to destroy different kinds of electric and electronic component. A constant decrease of the energy with a rather high slope can be noted around the 1960s and 1970s.

The fact that much less energy was needed made the indirect lightning effects, for example, the electromagnetic fields due to the lightning discharge, one of the major threats for electronics today.

### 15.3 Lightning as a disturbance source

In order to determine the potential danger that lightning can represent as a source of disturbance, it is necessary to use the knowledge we have about the characteristic lightning parameters. The important parameters to characterise the potentiality of lightning to become a source of interference are:

- the lightning current value
- the derivative of the lightning current
- the energy contained in a lightning discharge.

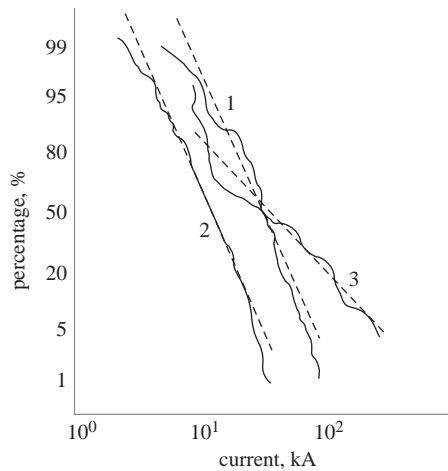


Figure 15.2 Probability curves of lightning amplitudes [2]

Characteristic values of the lightning discharge have been obtained by systematic measurement of natural lightning. The most complete data on natural lightning is probably that obtained by Berger [1] during more than 20 years of systematic recordings on Monte San Salvatore in Switzerland. Lightning parameters are discussed in Chapter 3 of this book.

The Berger data and data obtained by other scientists have permitted us to construct the probability curves of positive and negative lightning amplitudes shown in Figure 15.2 [2].

The main problem with this data is that it has mostly been recorded in the 1960s and 1970s, with techniques which probably did not obtain the fastest of rise times due to frequency limitation in the bandwidth. Another problem which modern techniques have revealed is that in order to increase the chances of capturing lightning, towers as high as possible have been used; new data has shown that the lightning current is reflected by the ground and it is probable that the recordings of the 1960s and 1970s have been polluted by these kinds of reflection, which could not have been observed with the technical capability of the time [3].

When considering lightning as a source of disturbance, two aspects should be regarded:

- (i) the direct lightning strike
- (ii) the indirect effects due to the electromagnetic field created by the discharge.

In both cases, the two parameters mentioned previously stay at the basis of the assessment. For the estimation of the indirect effects, more data is however necessary, as discussed in other chapters. This is essentially the following:

- the soil conductivity, which is the most important parameter as it determines the value of the horizontal electric field component radiated by the lightning channel
- the geometry of the victim which will determine, as discussed in Chapter 7, the value of the currents or voltages induced in the victim circuits.

These parameters are discussed in other chapters. As also discussed in Chapter 7, field-to-transmission line coupling models today permit numerical estimation of the indirect effects of lightning.

Using the existing measured data and other such approaches, and in spite of the probable errors in the data and the approximations in the models, the existing knowledge has permitted us to assess the electromagnetic effects of lightning on circuits and installations and develop protection concepts and mitigation methods.

## 15.4 Types of coupling between lightning and circuits or installations

### 15.4.1 Coupling modes

In order to permit modelling, the coupling modes between a disturbance source and a victim have been classified in different ways and under different criteria. One kind of classification is shown in Figure 15.3 [4] and it is this approach which will be used in what follows in order to discuss effects due to lightning. In this chapter, the following definition of direct and indirect lightning effects will be used. The term direct effect will be used only if a lightning strike hits an installation or a conductor galvanically connected to the installation. The term indirect effect will be used in two kinds of situation:

- (i) when a nearby lightning stroke induces a current in an installation or a conductor galvanically connected to the installation
- (ii) when a lightning current injected in a conductor or in a metallic structure induces a current in a nearby circuit or installation or gives a voltage drop at the input of an electronic circuit.

This means that only conductive coupling will generate direct lightning effects on installations, and all kinds of coupling mode can be at the origin of indirect lightning effects.

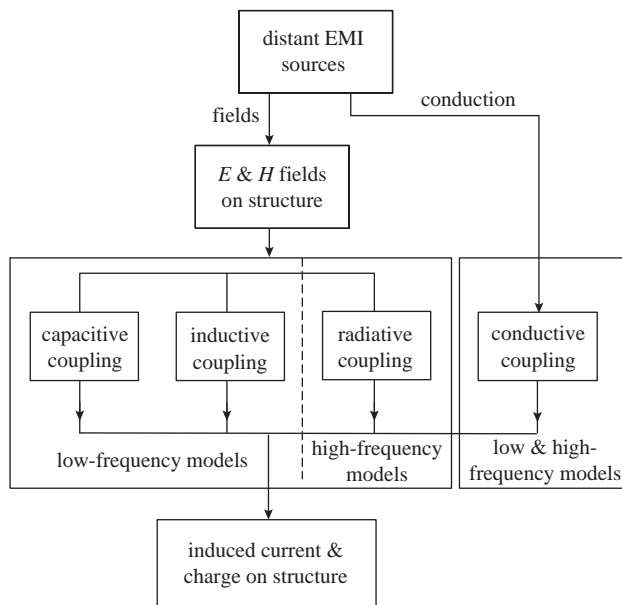


Figure 15.3 Classification of coupling modes [4]

### 15.4.2 Effects due to conductive coupling

As stated in the above paragraph, in the case of conductive coupling both direct or indirect lightning effects have to be considered. The conductive or galvanic coupling is defined as a direct penetration of a current into an installation. This current is initiated by a direct lightning strike. It will produce two types of effect:

- (i) a direct effect if the strike takes place on a conductor connected to the installation
- (ii) an indirect effect if the strike takes place on a metallic structure and, as stated previously, the potential difference created by this current will be transmitted at the input of an electronic circuit.

The probability of a direct strike on an overhead conductor connected to installation depends on the solution adopted in different countries for the construction of electric supply or telecommunication lines. This probability is very low in urban areas and in Europe where most of the distribution and telephone network is underground. In North and South America, for historical reasons, most of the low-power electric distribution is aerial even in towns. The same situation prevails in Japan where, due to frequent earthquakes, practically the whole energy and telephone network is constructed over the ground: the repair of an underground circuit is much more expensive than that of an aerial one. In general a rural network is also built using overhead lines. For aerial networks the probability of being hit by lightning is much higher. This probability can be calculated based on the keraunic level of the region.

### 15.4.3 Calculation of the average number of lightning strokes per year on an overhead line

The average density of lightning strokes per year on the ground (lightning strokes per km per year) can be calculated from the keraunic level of the region [5]:

$$N_s = N_k/7 \text{ 1/km}^2 \text{ per year} \quad (15.1)$$

where  $N_k$  is the keraunic level or coefficient, i.e., the number of thunderstorm days per year. A thunderstorm day is defined as a day during which at least one lightning stroke has been observed at a given location. The world keraunic level map is shown in Figure 15.4 [6].

As an example, for most regions of western Europe,  $N_k = 15 - 50$  (except the northern part which has a lower thunderstorm activity). This means that an average number of  $N_k = 30$  can be taken which gives an average density of  $N_s = 4.3$  lightning strokes/km<sup>2</sup> per year.

The average number of lightning strokes on an overhead line per year can be calculated with an empirical formula [6–8]:

$$N_l = N_s(b + 28H^{0.6})(1 - Sf) \cdot 10^{-1} \quad (15.2)$$

lightning strokes on 100 km of line, where  $N_s$  is the lightning stroke density on the ground previously defined,  $b$  (in metres) the horizontal distance between the lateral conductors of the three-phase line,  $H$  (in metres) is the line height and  $Sf$  the shielding factor due to the presence of other nearby objects. For heights of several



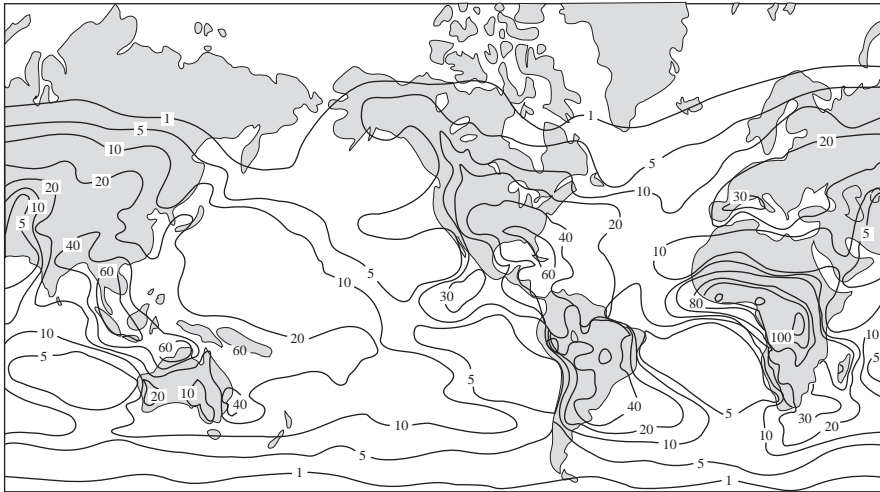


Figure 15.4 Map of the world keraunic levels

metres over the ground,  $b$  is much smaller than  $28H^{0.6}$  and can be neglected, (15.2) becomes

$$N_l = 2.8N_s \cdot H^{0.6} \cdot (1 - Sf) \quad (15.3)$$

lightning strokes on 100 km of line. And for a line of length  $L$

$$N_l = 2.8LN_s \cdot H^{0.6} \cdot (1 - Sf)/105$$

For western Europe with an  $N_s=4.3$  and an average shielding factor of 0.5 this gives 24 strokes per year on a distribution power line 10 m high and a length of 100 km.

Lightning current from a stroke on the ground can also arrive in an underground structure such as a water or a gas pipe. The probability for such a structure to collect lightning current flowing in the ground due to a nearby discharge can be even higher than for the line due to the larger surface around the structure on which the stroke can occur.

These structures usually penetrate into buildings and are therefore connected to the grounding network of the construction. For security reasons all the electronic installations inside the building are of course also connected to this grounding network. The lightning current can in this way penetrate inside the installation. It should also be noted that as grounding should usually have a low impedance, penetration of the lightning current is facilitated in this way.

#### 15.4.4 *Effects due to electromagnetic field coupling*

Two kinds of mechanism can be at the origin of electromagnetic field coupling:

- (i) a direct stroke on a building built in reinforced concrete and in which different devices and circuits are installed
- (ii) a lightning stroke near enough to the building in which sensitive devices are installed to create an electromagnetic field which can induce dangerous currents in the circuits of the installations.

### 15.4.4.1 Direct strokes on a building

If modern protection concepts are used, all the metallic parts of the building will be connected and the lightning current will be distributed in the rebars of the construction. This lightning current will create an electromagnetic field inside the building. Due to the high current value flowing in the rebars, the magnetic field will be predominant.

The technique of triggering lightning with small rockets carrying a wire that brings the lightning current to a chosen location has been used to strike the grounding rod of a real telecommunication tower. The measurements have shown that if the earthing of the tower is correctly achieved only 30 per cent of the lightning current flows into the metallic structure of the tower and the rest into the ground. However, if the lightning strike hits the top of a building and not its grounding rod the current will circulate in the whole metallic structure. Scale model measurements on a metallic cube of  $2 \times 2 \times 2$  m in high voltage laboratory [9] show that a lightning current of about 1 kA peak value creates a peak magnetic field of 20 A/m (Figure 15.5). In a loop of  $1 \text{ m}^2$ , a magnetic field variation of 20 A/m on  $10 \mu\text{s}$  can create an induced voltage of 2.5 V.

Other laboratory simulations [10] on a  $2 \times 2 \times 2$  m rebar cage (Figure 15.6a), show that the current induced in a loop inside a metallic structure in which a lightning current is flowing can in some cases (depending on the position in the cage and the rebar density) be higher than the current in the same loop but without

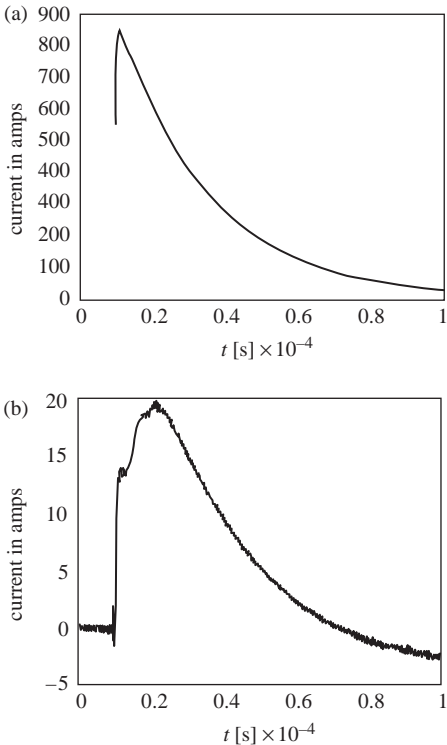


Figure 15.5 Laboratory simulation of magnetic field in a reinforced concrete building due to a lightning strike on it. (a) Simulated lightning current; (b) measured horizontal magnetic field component

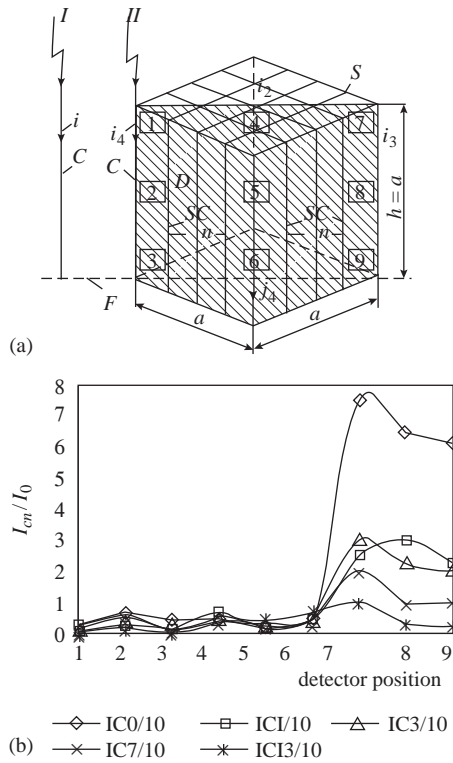


Figure 15.6 Laboratory simulation of the effect of rebars and position on current induced in a circuit due to a lightning strike on a building [10]. (a) Experimental cage; (b) ratio  $I_{cn}/I_0$  as a function of detector position in the cage, where  $I_{cn}$  is the current measured at different positions (from 1 to 9) when the cage has 1, 2, . . . , 13 rebars on each side and  $I_0$  is the current measured at different positions (from 1 to 9) without the cage

the presence of the cage (Figure 15.6b). This is due to the high lightning current flowing in a *rebar* near which the measurement loop was situated. This simulation shows that the solution of distributing the lightning current in the whole metallic structure of a reinforced concrete building can be, from the immunity point of view, worse for some installations than the solution of concentrating the discharge lightning current in a single descending conductor. These installations should be, in such a case, correctly protected.

#### 15.4.4.2 Lightning stroke near a building

The expressions ‘near’ or ‘near enough’ are relative and depend on the amplitude and derivative of the lightning current and of its energy content. Measurements using triggered lightning permit us to predict that lightning strokes at distances of about 50–500 m, with average amplitudes of 30 kA and average  $di/dt$  values of 30–100 kA/ $\mu$ s, can induce currents of tens of amperes in circuits forming a loop with a perimeter of a few metres [11]. Figure 15.7 shows the current measured in a line 8 m long and 1.8 m high and installed at 70 m from the impact point of triggered lightning on the Camp Blanding site in Florida. The measured value of

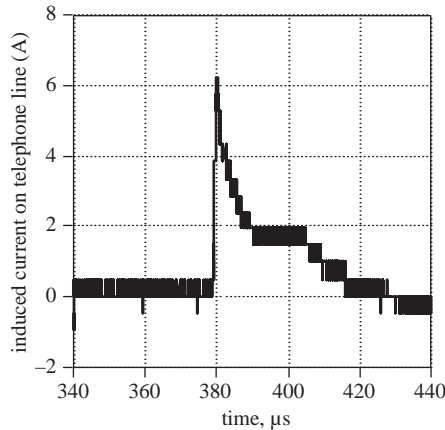


Figure 15.7 Lightning current measured on a 8 m long line situated at a distance of 70 m from a lightning stroke of about 6 kA

the lightning current was equal to about 6 kA. It can be seen that the induced current reached a peak value of 6 A. Assuming an attenuation of the electromagnetic field of about 6–10 dB inside a reinforced concrete building, the induced current amplitude in a circuit inside the building could be of about 2–3 A which would be a real threat for any electronics connected to this circuit.

## 15.5 Typical EMC problems due to lightning

In this section, we shall try to present a very summarised overview of different but typical EMC problems which can be experienced in different kinds of electricity application. These examples are far from being exhaustive but should give a good idea of kinds of specific problem that can arise in the particular applications which will be reviewed. Specific protection methods for each example will be briefly mentioned in this section and then discussed in general in section 15.6.

### 15.5.1 Lightning effects in power networks

The best known effect of lightning in power transmission or distribution networks is the direct lightning stroke either on a phase conductor or on a tower (or ground conductor). The protection of HV overhead lines against direct strikes is achieved by grounding wires mounted on towers where the wire is grounded. Today, the danger of a direct strike on a phase conductor is minimised by the presence of ground conductors for transmission lines of 125 kV and higher. However, there is a certain probability that distribution lines of 60 kV and lower voltage could be hit by a direct lightning strike.

Another possible outage danger comes from the backflash or return arc which occurs if a lightning stroke hits the grounding wire and the potential rise of the tower top exceeds the insulation strength of the insulator chain. In this case, an arc between the ground wire and a phase conductor takes place injecting at least a fraction of the total lightning current into the phase conductor (Figure 15.8).

Indirect lightning strokes, which can induce 50–60 kV or even higher over-voltages for the case of a nearby lightning stroke (50 m from the line) with a relatively low peak discharge current of 12 kA [12] should have little effect on

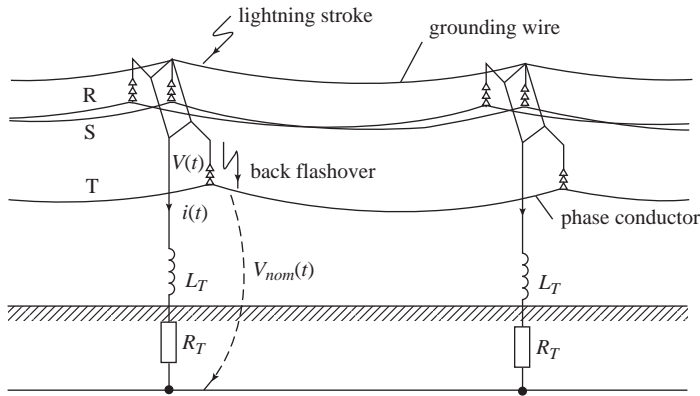


Figure 15.8 *The backflash from a ground to a phase conductor*

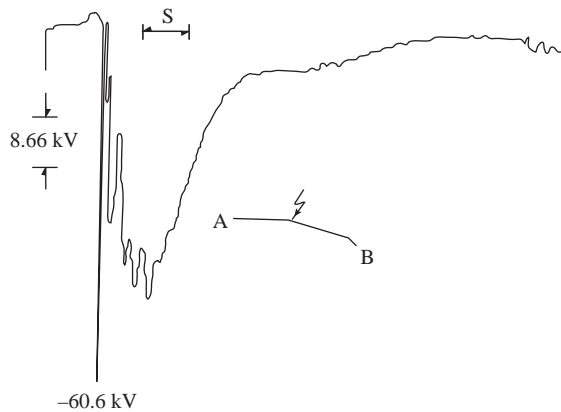


Figure 15.9 *Overvoltage recorded on a 13 kV distribution line induced by a natural lightning stroke of unknown amplitude and distance to the line. Here A–B figures the line position; the arrow indicates the direction from which the electromagnetic field produced by the lightning stroke came*

power HV transmission lines but could easily exceed the insulation strength of the distribution network causing short circuits and disruption of the energy supply.

A recorded overvoltage on a 13 kV distribution line in Mexico due to a natural lightning stroke of unknown amplitude and distance to the line is shown in Figure 15.9 [13].

Tests for protection efficiency on a real scale have been performed [14]. Lightning currents triggered using the rocket launching technique have been injected at the Camp Blanding site in Florida in a 730 m long overhead line. Several Metal-Oxide Varistor arresters were installed on the line. The injected current, the MOV discharge current and the arrester voltage are shown in Figure 15.10 [14].

In the cases discussed above, a direct strike of the line produces a galvanic coupling of the interference, but with the indirect effect all three components (electrostatic, inductive and radiation) enter the structure of the incident electromagnetic field, their respective contribution depending on the distance between the strike location and the line [15].

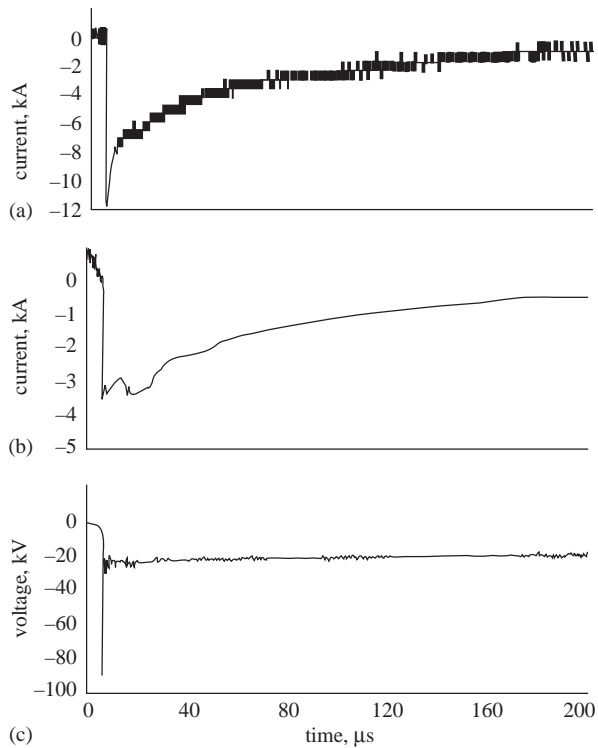


Figure 15.10 *Injected lightning current on the overhead line and responses of one MOV arrester. (a) Injected triggered lightning current; (b) arrester discharge current; (c) arrester voltage*

The increasing sensitivity of the different equipment used today in the power network has increased the threat represented by these induced voltages on medium or low-voltage distribution lines. Insulation coordination and definition of protection using lightning arresters, even at lower voltage levels, must take into account the danger due to indirect lightning.

### 15.5.2 *Lightning effects on power network substation equipment*

Here again direct and indirect lightning stroke effects can take place, related as above to galvanic or electromagnetic field coupling. However, the direct galvanic coupling acts on substation equipment through a chain of effects in a quite perverse way. Figure 15.11 shows a typical configuration for a circuit used for information transmission (data from equipment to the dispatching room, alarms, control). Two devices, T which is a translator used to convert information given for instance by a voltage or current transformer and A which is a receiver, are connected through a shielded coaxial cable. The shield is connected at the two extremities to the metallic box of the two devices which can be grounded or not. The substation ground is usually a metallic mesh buried at 30–50 cm under the Earth's surface. Any lightning current hitting an overhead line entering the substation will be conducted to the ground by the arrester usually installed at the entrance of the substation. The large lightning current flowing in the grounding mesh will create a voltage drop,  $U$ . If the equipment A is not grounded, this

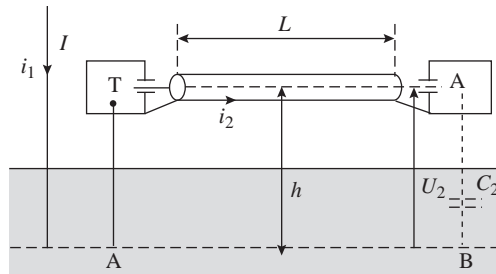


Figure 15.11 *Effect of a lightning current flowing in the ground plane of a power network substation*

voltage drop is found between A and the ground and this can be dangerous for the safety of the personnel. If A is grounded, the voltage drop appears between the internal conductor of the coaxial cable and the sheath, i.e., at the POE (point of entry) of the electronics of equipment A.

Currents induced in common or differential mode in the substation circuits due to indirect lightning effects also represent a large category of threats for sensitive electronic components. Usual EMC protection measures like proper grounding or bonding must be applied in order to avoid outages due to lightning in the power network.

### 15.5.3 *Lightning effects on telecommunication networks*

The effects of lightning on telecommunication networks are quite similar to those discussed for power networks, with the difference that telecommunication lines are lower than power lines and in many cases buried; this decreases the probability of direct strikes. However, the effects due to indirect lightning can be more dangerous as the telecommunication equipment is more sensitive than that connected in a power network. Figure 15.12 shows the results of a 2 year lightning-induced overvoltage measurement campaign in the French telecommunication network, which has been performed in five different sites in France: rural and urban, industrial and residential and in regions with different thunderstorm activity [16]. By counting the number of cases shown in Figure 15.12b, it can be seen that values 27 times higher than 2 kV have been measured in a network designed for a supply of 48 V or for transmitting signals at an even lower level.

Protection of the telecommunications equipment installed inside the switching entity is achieved by installing suppressors at the POE of the buildings or of the sensitive equipment (see primary and secondary protection discussed in section 15.6).

### 15.5.4 *Lightning effects on low-voltage power networks*

Less spectacularly, the effects of a lightning stroke in the proximity of low voltage power networks supplying residential areas can be quite damaging in many cases. Examples are not very often recorded, because they are mainly known to the insurance companies and not to scientists or engineers and are not published. However, a few cases can be referred to, like the destruction of all the TV sets in a residential building on the heights of the town of Montreux in 1996 and the destruction of TV sets through a current induced by a nearby lightning strike in the parabolic antenna of a big hotel in the town of Lausanne in 1997, both in Switzerland.

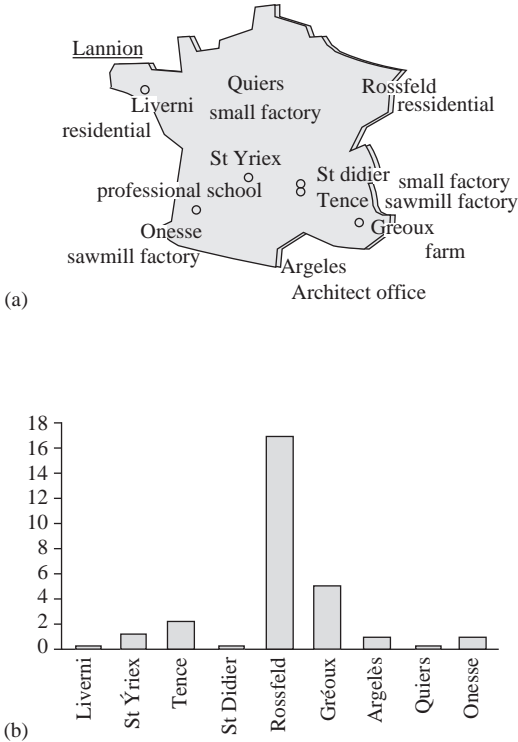


Figure 15.12 Results of a lightning-induced overvoltage measurement campaign in the French telecommunication network [15]. (a) Measurement sites; (b) histogram of overvoltages higher than 2 kV

Figure 15.13 shows the statistics of overvoltages due mainly to lightning strokes in different environments in Switzerland [17]. For comparison a composite curve for a 120 V distribution network in the United States is also shown.

Simulations of lightning-induced effects in the low-voltage network of a residential house have been performed by current injection in Sweden [18]. And for aircraft lightning immunity tests, the current injection was used as an approximation to assess the immunity of the residential distribution system instead of field radiation testing because of its low cost and high repeatability. The current injection was performed in:

- common mode between phase and ground
- differential mode between two phases of the three-phase domestic network.

Different transfer functions were tested and the example of Figure 15.14 shows the transfer voltage factor between the load response and the injected voltage at the house point of entry (POE).

### 15.5.5 Lightning effects on aircraft

Aeroplanes are often hit by lightning. Thunderstorm clouds cannot always be avoided by the aircraft and usually the plane forms a conducting bridge between two charged thunderclouds triggering a lightning discharge which flows on the metallic surface of the plane fuselage (Figure 15.15).



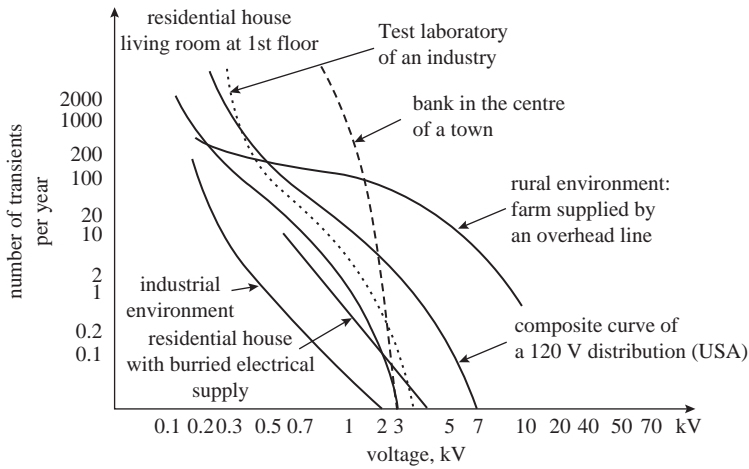


Figure 15.13 *Statistics of the number of transients per year in different types of low voltage networks in Switzerland [17]*

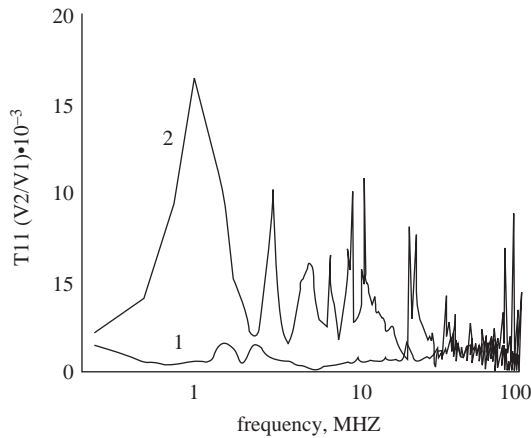


Figure 15.14 *Transfer voltage function between a load and the house POE for a current injected test in a residential house (1. CM injection; 2. DM injection) [18]*

Two trends in modern technology have increased the need to consider carefully the threat represented by lightning for an aircraft:

- (i) the increase of sensitive electronics used in aircraft
- (ii) the possible use of nonconductive or less conductive materials for the aeroplane body.

Both can be at the origin of EMC problems. In order to estimate the threat, experiments with an instrumented aircraft flying inside thunderstorms have been performed and currents induced by lightning discharges on the aeroplane have been recorded at real scale. Another way of estimating the threat and the protection level offered by the metallic envelope represented by the plane fuselage has been achieved by injecting pulses similar to lightning currents in an instrumented aircraft on ground [19]. These studies have permitted specific standards to be written which

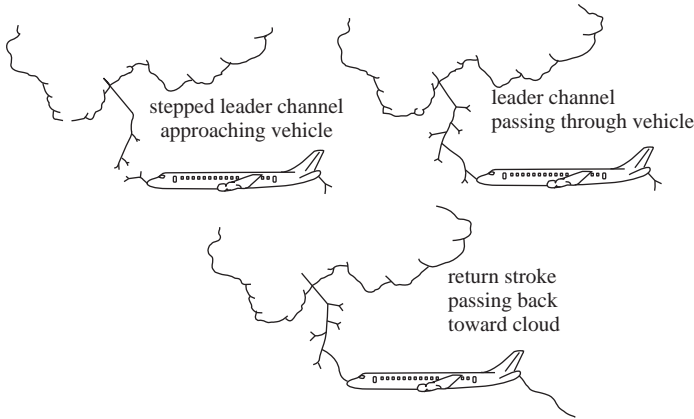


Figure 15.15 Lightning discharge through an aeroplane

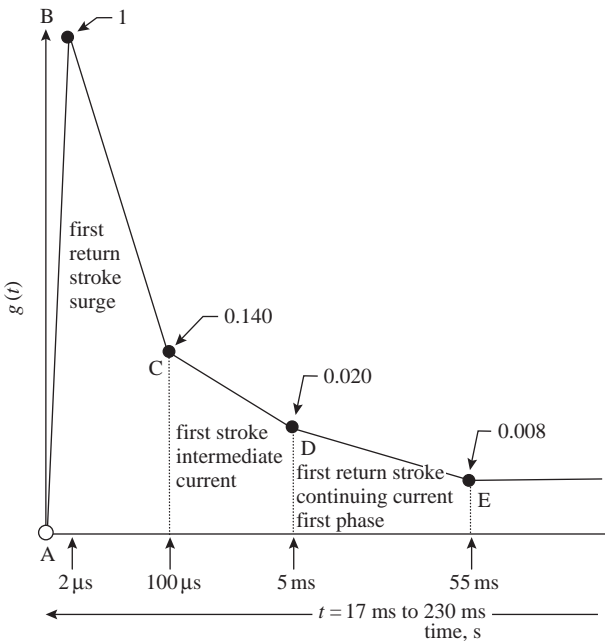


Figure 15.16 Shape of the impulse current injected in the aeroplane fuselage for the lightning test

define the test methods (Figure 15.15), the shape of the injected current and the test levels (Figure 15.16) [19].

### 15.6 Specific EMC lightning protection parameters

#### 15.6.1 General

Protection measures against the direct effects of lightning on buildings and relatively huge installations, which are discussed in Chapter 8, must be combined and coordinated with protection against direct or induced lightning effects on all kinds

Table 15.1 *Lightning current waveforms which can be used for tests [20]*

Event	Amplitude/waveform	Remarks
Lightning stroke:		
– direct stroke	30 kA/10 × 350 μs	Estimated average peak current values at the end of the line
– indirect stroke	5 kA/8 × 20 μs	Values may be 5–6 times higher

of sensitive equipment. This means that specific EMC lightning protection concepts have been developed and should be achieved. Lightning parameters which are important for EMC are the general parameters which characterise the physical process of a lightning discharge. In what follows they will be viewed from an EMC point of view with an emphasis on protection against effects which can create disturbances to sensitive circuits and equipment. The protection deals mainly with the primary lightning conducted environment due to direct strikes. However, more and more consideration is given to the secondary lightning conducted environment due to the indirect effect. As an example, Table 15.1 [20] shows test lightning parameters corresponding to average short circuit currents due to both the direct and indirect effects to be expected on an overhead telephone subscriberline of 1 km length. Note that the lightning currents that are given here as normed waveforms may be considerably different in practice.

As lines become shorter, the probability of lightning surge occurrence goes down, but direct strokes now have a higher probability of reaching the end of the line with all their energy.

It should be mentioned that currents and voltages due to very fast transients like those due to switches in GIS power networks, electrostatic discharges or other various sources of such kinds of interference always represent a certain probability for various installations together with the lightning threats. Combined protection measures against lightning and such very fast transients can be used. As EMC problems are usually viewed as being generated by HF phenomena (i.e., fast transients), in the following such combined protection measures are analysed by looking at basic surge parameters on long lines ( $L > 1$  km) and by considering the consequences of the two threats. As the very fast transient effects are very similar to high altitude EMP (HEMP) effects, the data which will be used for the following comparison has been taken from the HEMP literature, regarded here as representative for all kind of fast transient.

### 15.6.2 *Peak current*

The peak current is only responsible for voltage drops on ohmic resistances, for example, the grounding resistance. In a direct lightning stroke the local ground potential of a protected area may be raised by several hundred kV relative to a distant point. This may result in unpredictable dielectric breakdowns to ground in the protected area. The phenomena are clearly limited to lightning events and to installations with an imperfect shield or an unfavourable grounding system. In most cases the effect of  $di/dt$  on inductive voltage drops is much more important.

### 15.6.3 *Peak current derivative*

Inductive voltage drops and induced voltages are proportional to  $di/dt$ . In general, it is this parameter that gives rise to the most and severest problems in all protection

concepts. For direct lightning strokes the  $di/dt$  value chosen for the protection concept may be as high as 100–200 kA/ $\mu$ s. For fast transients this parameter may attain values as high as 150 kA/ $\mu$ s. Although sometimes higher than for lightning, it is still of the same order of magnitude and can be addressed with the same conceptual methods.

#### 15.6.4 Peak rate of change of voltage

Peak rate of change of voltage may only be applied to surge protectors with great precaution. Voltage rise times given in the literature are based on coupling calculations assuming certain field or current waveforms and linear line parameters. The theoretical peak voltage level may be as high as several 100 kV or even in the MV range for lightning. Typical values are in the range of 100 kV/ $\mu$ s–1 kV/ns for lightning and 1–10 kV/ns for fast transients. One does not usually consider non-linear effects like insulation breakdown and firing actions of gas filled surge arresters which may occur in the subnanosecond range even in the course of a lightning event. One also neglects ionisation effects and line losses in the 100 MHz frequency range. Assuming a low-pass characteristic for the line, the maximum  $du/dt$  will occur somewhere near half. There is no doubt that  $du/dt$  at lower levels (most primary protection elements switch from the insulating into the conducting state well below 10 kV) is smaller than  $(du/dt)_{max}$ . This uncertainty is mostly due to insufficient calculating models for frequencies above 100 MHz and a limited knowledge of nonlinear line parameters.

#### 15.6.5 Total charge

Total charge can be obtained by integrating the measured current. Values vary from  $50 \times 10^{-6}$  A for fast transients to 70 A in a very powerful direct lightning stroke. As most voltage breakdown and voltage limiting devices exhibit a distinct voltage stabilising action (a very low impedance above a typical threshold voltage), their current carrying capability may approximately be described in terms of the integral  $i \times dt$ . An  $8 \times 8$  mm gas filled arrester is about equally stressed by an indirect lightning stroke of 12 kA, 8/20  $\mu$ s and by another type of fast transient.

#### 15.6.6 The action integral: integral $i^2 \times dt$

The action integral is a parameter which is proportional to the energy. It has the units  $A^2s = J$ ; and it gives the energy that would be absorbed in a resistance of 1  $\Omega$  when the lightning current flows through it. As surge arresters have a low dynamic resistance in the m $\Omega$  range, they absorb only a comparatively small part of the potential energy. The capacity for energy absorbance of a surge arrester is therefore not relevant for its quality. The integral  $i^2 \times dt$  is several thousand times higher in a lightning stroke than in different fast transients. It is relevant for thermal effects in ohmic resistances, for example, current carrying capability of cable wires, and magneto-dynamic effects in current loops. Short powerful current surges (e.g., 40 kA, 8/20  $\mu$ s) may mechanically destroy an  $8 \times 8$  mm gas filled protector before it is thermally destroyed.

#### 15.6.7 Time to half value of the current

The time to half value of the current waveform is one of the most important determinants for protection circuits, i.e., combinations of primary and secondary protection elements. It varies from about 100 ns for fast transients to 350  $\mu$ s in a direct lightning stroke.

### 15.6.8 Conclusions on LEMP and fast transients protection comparison

Except for  $du/dt$  lightning represents a more severe threat than any other kind of fast transient as far as conducted disturbance is concerned. However, we must also consider the possible degradation of the shield attenuation by installing protection devices against conducted disturbance. For economic reasons and because a radiation shield is missing in most cases, lightning protection elements are usually not designed as feed through elements. They will therefore degrade the shield attenuation of a shielded protection concept unless special care is taken in their installation. The most important rule to observe is that the surge current should not radiate into the protected zone. This can be achieved by installing at least the primary protection element outside the shield or by adding a supplementary shield as shown in Figure 15.17.

Assuming that an installation is correctly done, then a well-designed only lightning protection concept may be completed into a lightning with fast transient concept at almost no additional cost. An only fast transient concept should not be chosen unless the lightning threat can be completely excluded.

## 15.7 Specific EMC lightning protection concepts

### 15.7.1 General EMC protection concepts

As lightning is one of the most powerful sources of electromagnetic disturbance, general EMC protection concepts can and are used for the protection against lightning.

The general EMC protection concepts are:

- (i) against conducted disturbances:
  - suppressing of overvoltages or overcurrents
- (ii) against radiated electromagnetic fields:
  - increase the distance between a potential disturbance source and the victim
  - shielding.

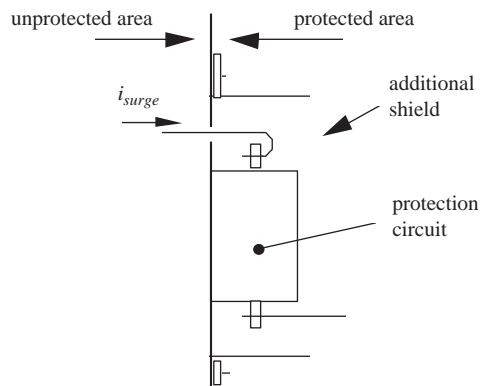


Figure 15.17 Solution to prevent the surge current for irradiating into the protected area

The concepts pertaining to conducted disturbances apply to direct lightning and those pertaining to radiated fields to indirect lightning effects. As the lightning discharge is an arbitrary phenomena regarding its parameters and also its striking point, an increase of distance between lightning and a potential victim is impossible to achieve. Therefore, only shielding will be considered as a possible protection against lightning electromagnetic fields.

### 15.7.2 Suppressors

Suppressors are protection elements which stop the penetration of conducted disturbances inside a protected volume. They can be:

- filters
- overvoltage suppressors
- separation transformers.

As lightning is a high energetic phenomena, filters and separation transformers are usually not used to stop the propagation and penetration of lightning currents inside protected areas. Therefore, only overvoltage suppressors will be discussed here.

The overvoltage suppressors are components with a nonlinear voltage–current characteristic. They pass rather abruptly from a nonconduction (or very low conduction) to a conduction mode if a certain voltage threshold is attained. Examples of such components and the way in which they pass through a shielded wall are:

- gas tubes (Figure 15.18a)
- varistors (Figure 15.18b)
- Zener diodes.

In both cases shown in Figures 15.18a and 15.18b, the protection elements are combined with an inductance which will increase the rise time of the surge wave.

Note that in the case of lightning only very sensitive and essential installations are installed in shielded cages. This in fact means that what has been called above a shielded wall is in many cases just the reinforced concrete structure of a building.

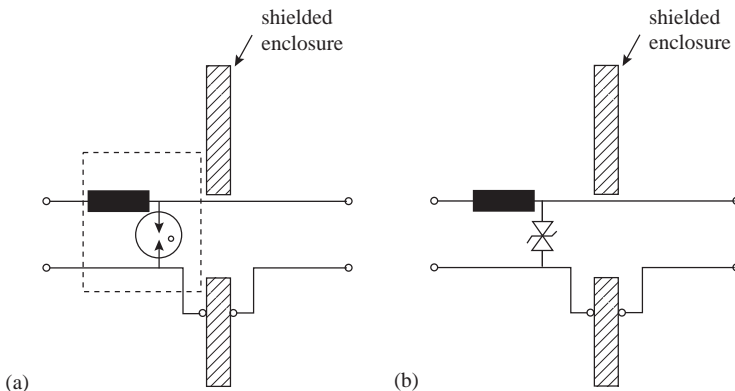


Figure 15.18 Protection elements at points of entry (POE) of buildings or shielded cages. (a) Protection using a gas tube and an inductance; (b) protection using a varistor and an inductance

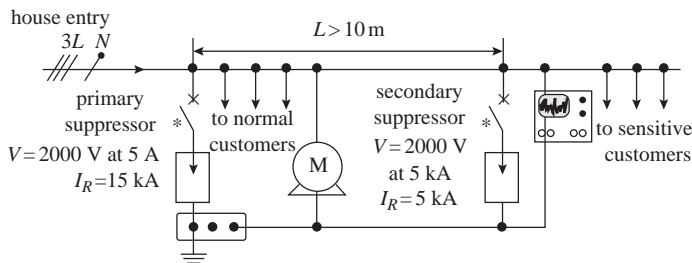


Figure 15.19 Protection cascade [17]

The protection of sensitive devices installed inside buildings is often achieved in several steps. A primary protection is installed at the point of entry (POE) where a conductor enters into a building. This primary protection is intended to absorb the high energy of a direct lightning stroke on the conductor and gas tubes can respond to such a stress. In case of sensitive and important equipment, a secondary protection can be installed inside the building (Figure 15.19) [17]. The lightning current remaining after the primary protection will have a much smaller energy content and a varistor can be used for this secondary step. This kind of protection design corresponds to the zoning concept.

### 15.7.3 Shielded cages

The shielded cage is a protection against electromagnetic fields. It can be used against lightning indirect effects if very sensitive equipment must be protected against possible lightning electromagnetic fields coming from nearby strikes.

In this case general EMC shielding concepts are applied, i.e., shielding continuity, penetration of conductors into the cage through filters, apertures closed by honeycombs.

However, protection by shielded cages against lightning is not really common. It can be combined for essential installations with protection against HEMP or high power microwaves (HPM).

## References

- [1] BERGER, K., ANDERSON, R.B., and KRONINGER, H.: 'Parameters of lightning flashes', *Electra*, 1975, (41), pp. 23–37
- [2] UMAN, M.A.: *The Lightning Discharge* (Academic Press, New York, 1987)
- [3] BERMUDEZ, J.L., RUBINSTEIN, M., RACHIDI, F., and PAOLONE, M.: 'A method to find the reflection coefficients at the top and bottom of elevated strike objects from measured lightning currents', *Proceedings of 14th International Symposium on EMC*, Zurich, February 20–22, 2001, paper 63J8
- [4] TESCHE, F.M., IANOZ, M., and KARLSSON, T.: *EMC Analysis Methods and Computational Models*, (J. Wiley & Sons, New York, 1996)
- [5] PRENTICE, S.A.: 'Lightning strike counter', *Electra*, CIGRE, 1972, (22), pp. 149–159
- [6] IEEE PES Power Transmission Distribution Committee Lightning Performance of Distribution Lines Working Group, 'Calculating lightning performance of distribution lines', *IEEE Trans. Power Deliv.*, 1990, (July), 5(3), pp. 1408–1417

- [7] PARISH, D.E. and KVALTINE, D.J.: 'Lightning faults on distribution lines', *IEEE Trans. Power Deliv.*, 1989, **4**(4), pp. 2179–2186
- [8] ERIKSSON, A.J.: 'The incidence of lightning strikes to power lines', *IEEE Trans. Power Deliv.*, 1987, **PWRD-2**, (3), pp. 859–870
- [9] NICOARA, B. and IANOZ, M.: 'Etude sur les effets électromagnétiques dues à un coup de foudre sur un bâtiment ou à proximité d'un bâtiment'. *Rapp. Int. LRE, EPFL*, October 1999
- [10] MAZZETTI, C. and FLISOWSKI, Z.: 'Spatial distribution of lightning interferences inside different LPS models', *Proceedings of 13th International Wroclaw symposium on EMC*, June 25–28, 1996, pp. 532–536
- [11] RACHIDI, F. *et al.* 'Indirect lightning effects on short overhead lines', *Proceedings of International Symposium EMC'98*, Roma, September 14–18, 1998, paper I – 1
- [12] RACHIDI, F., NUCCI, C.A., IANOZ, M., and MAZZETTI, C.: 'Response of multiconductor power lines to nearby lightning return stroke electromagnetic fields', *IEEE/PES Transmission and Distribution Conference*, Los Angeles, September 15–20, 1996
- [13] DE LA ROSA, F., VALDIVIVA, R., PEREZ, H., and LOSA, J.: 'Discussion about the induction effects of lightning in an experimental power distribution line in Mexico', *IEEE Trans. Power Deliv.*, 1988, **3**, (3), pp. 1080–1089
- [14] FERNANDEZ, M.I., RAMBO, K.J., RAKOV, V.A., and UMAN, M.A.: 'Performance of MOV arresters during very close, direct lightning strikes to a power distribution system', *IEEE Trans. Power Deliv.*, 1999, **14**, (2), pp. 411–418
- [15] MAZZETTI, C., NUCCI, C.A., IANOZ, M., and RACHIDI, F.: 'Frequency analysis of lightning stroke electromagnetic fields', *Proceedings of 7th Zürich International Symposium on EMC*, Zürich, March 3–5, 1987, paper 16D4
- [16] DJEBARI, B., GUÉRIN, L., and GLÉONEC, M.: 'Conducted EM disturbances on the telecommunication terminal equipment ports', *Proceedings of International Symposium on EMC'94*, Roma, September 13–16, 1994, paper B-5
- [17] SÉRAUDE, CH.: 'Surtensions et parafoudres en BT-Coordination de l'isolement en BT', *Cahier Technique Merlin Gérin* no. 179, September 1995
- [18] MING, Y., PEREZ, H., COORAY, G.V., and SCUKA, V.: 'Response characteristic of a low voltage power installation network to the EMP irradiation obtained by an impulse current injection method', *Proceedings of International Symposium on EMC'94*, Roma, September 13–16, 1994, pp. 543–548
- [19] FISHER, F.A. *et al.*: 'Lightning protection of aircraft', Lightning Technologies, Inc., Pittsfield, MA, 1990
- [20] BUECHLER, W., FLISOWSKI, Z., IANOZ, M., and MAZZETTI, C.: 'Comparisons between protection concepts against HEMP and LEMP', *Proceedings of International Symposium on EMC'95*, St. Petersburg, 26–30 June, 1995, pp. 369–374





---

## Chapter 16

# Electrical aspects of lightning strikes to humans

Chris Andrews

---

### 16.1 Introduction

In assessing any lightning injury, and indeed any electrical injury, the investigator is interested in the current pathway, and the magnitude of the current flowing. Without this, the assessment of any injury is conjectural, inaccurate, and poorly based. Current magnitude and pathway has not been well characterised in lightning injury.

Indeed some of the symptoms following a lightning strike have been enigmatic. Following a lightning strike or an electrical injury, physical symptoms can be experienced, such as pain and sensory abnormalities in the line of the strike peripherally. There is also, however, a substantial neuropsychiatric syndrome following the injury [1–3, 4]. It is presumed that these have some kind of origin in the disturbance of brain tissue and centres. How can this be, when an electric current has not passed through or near the brain? Recent research has indicated the importance of an area of the brain called the hippocampus [5], and its relation to depressive and post-traumatic syndromes. But more importantly, it has been demonstrated that electric current passing elsewhere in the body can induce these changes [6].

This then is the background against which this discussion is set. While knowledge is small, we set out attempts to calculate the currents involved in lightning strike impinging on the human body. This necessitates appreciating just what sort of strike there is to a person, and this is described below, as well as obtaining initial results in the magnitude of the current in each case.

These aspects are described and examined in turn.

### 16.2 Strike mechanisms – descriptive outline

To provide a feeling for the processes involved, a descriptive outline of each strike mechanism is given.

Lightning can impinge on an individual by five major mechanisms [7, 8]. The relative frequency of these has been estimated [9, 10]. Roeder provides a theoretical estimate for casualty risk adopting the mean of these (scaled to 100 per cent):

Direct strike	4%
Side flash	19%
Contact potential	23%
EPR shock <sup>a</sup>	42%
Upward streamer <sup>a</sup>	12%

<sup>a</sup>The likely division between these two mechanisms is not yet fully estimated.

These are purely estimates; however, provide a ‘feel’ for the risk of lightning strikes to individuals.

Roeder examines last resort emergency short-term protection for those left with no alternative but to be ‘in the open’ arising from prior planning (or lack of it). His figures derive from the relative frequency of each mechanism and correspond to the ‘native’ ‘in the open’ risks for victims.

Using behaviours for short-term lightning protection – for example the ‘lightning crouch’ – he gives a percentage Casualty Rate for each mechanism based on the perceived normal human behaviour in adopting this risk reduction method. He considers that the ‘lightning crouch’ reduces risk by reducing the individual’s area of vulnerability (using rolling spheres), and the risk can be tabulated as follows:

Direct strike	3%
Side flash	0% (assuming an individual in the open)
Contact potential	0% (assuming an individual in the open)
EPR shock	33%
Upward streamer	9%

The implication is that each of the mechanisms are not equally dangerous and the overall casualty figure arrived at is 41 per cent,  $\pm 9$  per cent. This is broadly in accord with previous estimated mortality of 30 per cent, though the recent success of awareness campaigns has reduced this to a much lower figure.

It is emphasised that these figures are for persons caught ‘in the open’ adopting inadvisable last minute precautions. They do not represent all lightning casualties in all circumstances. Similarly, they are not death rates. However, they do represent a plausible estimate of risk to individuals alone in the open.

### 16.2.1 *Direct strike*

An obviously dangerous situation is for an individual to be struck directly when in the open. The strike is geometrically based and is most likely when the individual presents a tall preferential point of attachment (see previous chapters regarding the attachment process).

Minimising this attractiveness is an important consideration. Crouching down has commonly regarded as a means of decreasing the geometric profile [11]. While this has both detractors and protagonists, this writer believes there is support for the individual at least being subjected to a lesser risk in adopting the crouch [12]. Roeder indeed considers the reduction to be of the order of 50 per cent [9].

Lightning injury, despite common conception, is not universally fatal [8]. Even direct strike, dangerous though it is, has only a percentage mortality.

### 16.2.2 *Contact potential and side flash*

There are similarities between these mechanisms in the sense that they require proximity with a stricken object.

When an individual is near a stricken object, and a streamer ‘jumps’ from that object to the individual, then a *side flash* is said to occur. If the individual is in direct contact with the stricken object, then voltage division occurs along the stricken object, and current flows from the point of contact through the individual. This is termed a shock via *contact potential*.

### 16.2.3 Earth potential rise

If an individual has points of contact with (non-ideal) ground within the field of current passage away from the base of a flash, then by virtue of the distributed ground resistance, a potential is set up between the points of contact. Current therefore flows through the individual. For a human this may be of little consequence if the points of contact are the feet, if close together, and of more consequence if spaced apart. Nonetheless the post-shock syndrome can still be profound.

If, however, a four footed animal like a cow stands in such a configuration, current may be conducted between fore- and hindlimbs, and the thorax may be involved – with much greater cardiac risk. Shock by this mechanism is variously termed *EPR shock*, *stride potential*, or similar. It is especially important in telephone related strike [13].

### 16.2.4 Aborted upward streamer

This mechanism, being recognized quite recently, is discussed in a little more detail.

The four mechanisms above do not account for all lightning injuries. For example, in a case known to the author, there were several individuals playing bowls on an outdoor grass rink. One man was directly struck by lightning; however, several others were knocked to the ground in varying degrees of consciousness. The stricken man did not survive, however all others did. In the past, the mechanism used to explain the fall of the other players might have been the mechanism of Earth Potential Rise (EPR) or the effect of blast. This is not entirely satisfying however. The players were probably too far from the stricken man for EPR effects to have been as dramatic as they seemed to have been. Cooper [14] reports similar relatively unsatisfying analyses, where existing mechanisms fail to explain the reported injuries.

It seems likely that a further mechanism, hitherto unrecognized, might have been active.

Anderson [15, 16] proposes such a mechanism, and that is the Unsatisfied Upward Streamer Mechanism.

Upward streamers have been known for some time. Krider [17], for example, refers to them in 1975, and quotes the first observations by McEachron *et al.* in 1936 [18]. He observes that as a stepped leader makes its way from a cloud to earth; when it gets within a certain distance of the ground, upward leaders emanate from possible strike points on the ground. He notes that several upward leaders can exist, and ultimately the return stroke results if one (for our purposes) of these connects with the stepped leader to form the lightning return stroke channel. In his paper, he shows several photographs demonstrating the existence of upward leaders though catching these on film is difficult.

Krider regards the length of these streamers as important. There is identified a *striking distance* for a point on the ground, this being the distance from that point within which the stepped leader must come to attach to that point and create the return stroke. He states that the upward leaders are, in length, approximately half the striking distance of their origin. After attachment with one upward streamer, unconnected leaders collapse, and Krider states ‘Unconnected upward streamers ranging in length from 26 to 92 m were sometimes photographed at the tip of a building when a cloud-to-ground discharge occurred in the vicinity’. Current to form the upward streamer from a living individual must flow upwards from the

ground, and then if unsatisfied, the fast collapse of the streamer returns current to ground. Thus the individual becomes a conduit for streamer current, both developing, and then collapsing. In the collapsing current  $di/dt$  will be large giving rise to potentially large voltages across the individual [19].

Anderson [15, 16] applied this to the mechanisms of lightning injury and suggested this mechanism can explain the hitherto unexplained injury mechanism. Carte *et al.* [20] discussed the event on which observations were made, and using this event the mechanism was postulated.

The event occurred at a camping scene where lightning struck the pole of a tent in which 26 schoolgirls, and 2 supervisors, along with 7 dogs were camped. The base was dry grass and sandy soil. The tent was supported by two 3.6 m poles at either end, with the bases embedded in concrete blocks on the ground. The poles were 5 m apart, and each was 2.5 m from the respective end of the tent. One pole was struck by a lightning impulse, and at the end of the tent where the pole was struck, four children were killed, along with three dogs. A further dog, slightly distant from the pole, was killed. Interestingly, in the detailed description of the various injuries, eye injuries were particularly highlighted – and this may bear on the discussion regarding entry portals below.

In appraising this situation, the authors suggest that one pole suffered a direct strike. It was possible that side flashes emanated to injure children close by, and ground current was thought to be a realistic possibility. Anderson examined technical aspects in detail, and considered that not all the cases could be explained simply by side flash or contact potential. For example clusters of individuals had such similar injuries that it was considered that they must have emanated from the same single process. Individual side flashes were considered unlikely in the situation of the unanimity of injuries. He postulated the streamer method of injury, and rather than suggesting streamers seeking to connect with a downward stepped leader, suggested streamers ultimately seeking to connect with a side flash. This is an interesting variation on the one theme.

These thoughtful and detailed appraisals provide very cogent support for defining the upward streamer mechanism. In passing also, this highlights the importance of detailed appraisal of a shock circumstance.

### 16.2.5 *Other classifications*

Zack *et al.* [21] consider that the mechanisms identified by Andrews *et al.* [13, 22, 23] for telephone mediated lightning shock should be considered as a separate mechanism of current impingement. This writer has not followed this suggestion because the telephone related events can be fitted into various combinations of existing mechanisms 1–4 above.

Blumenthal [24] considers a blast injury, which he documents, constitutes a sixth mechanism of injury. Blast injury is very important; however, the mechanisms 1–5 above are strictly electric current impingement methods, and blast takes existing current passage one further level as a consequential injury applicable to all the above electrical mechanisms. For electrical models, sufficient estimates of current can be made using the above. In addition, there are other ancillary injuries beside current injury which occur in lightning injury (e.g. burns, though minimal, Trauma, Perforation of Visci, eye injuries, and so on). It would seem excessive to number these 7, 8, 9, etc. At this point only purely electrical current passage is considered via mechanisms 1–5.

### 16.3 Current behaviour in biological material

The literature contains very little contemporary estimate of current pathways and magnitudes.

Blake-Pritchard [25] provided simplistic calculations. Other work (from Japanese researchers) [26–28] has been aimed more at determining lethal levels of flash current and the relationship between the development of flashover and the lethality of a given flash. They have also shown that respiratory support may save life after cardio-respiratory arrest [29] (see Andrews [30] also for support of this observation).

Ishikawa *et al.* [26] examined the lethal current level of a flash to live unanaesthetised rabbits using a multi-pulse technique. Their findings were that a threshold of approximately 62.6 J/kg existed beyond which death would occur. Further, their finding was that provided one stroke in a multi-stroke flash exceeded this level, then death would ensue. Specifically there was no ‘memory’ engendered for succeeding strokes, and no cumulative effect of multiple strokes was seen. The strokes were approximately 40 ms apart, three in number, and were applied directly to the animal’s head via a needle inserted in the scalp. Energy input was examined, and no account was taken of synchrony with the cardiac cycle – especially the probability of transgressing the ‘vulnerable window’ of late repolarisation. Nagai *et al.* [27] confirmed the order of the above energy level.

Ishikawa *et al.* [29] drew attention to the fact that if artificial ventilation was instituted after ‘death’ from a lightning strike, then survival was increased from 25 to 48 per cent.

Ohashi *et al.* [28] also drew attention to the protective effect of the development of external flashover in a human strike by survey of post mortem findings. Of 50 victims, 9 had evidence of flashover, and 41 showed no such evidence. Of the former, five survived, and of the latter only six survived. The division into groups was somewhat subjective, but nonetheless these results are impressive. If flashover occurs, it is protective. In an experimental determination they noted two separate groups of animals subjected to artificial shocks. In those developing ‘early’ flashover (sooner than 20  $\mu$ s from contact), the survival was markedly better than those developing later flashover. This bears obvious relation to energy dissipation internally and also duration of internal current passage.

In a different approach, Flisowski [31] used an analytical technique to predict the mortality level from strikes given the probability distributions of stroke current, local parameters, and known fatal current levels for the human body. Although the latter are an extrapolation of Dalziel’s well-known formula into regions of short impulses, the mortality level of 20–40 per cent found is of the same order as that given by Roeder, *supra*. The body model used, however, was simply resistive, and took no account of either reactive components, or the different nature of the skin from the internal milieu. The figure, however, is in accord with earlier estimated mortality.

There are extreme experimental difficulties in verifying any of the above data on humans. It is unacceptable to subject human beings to shocks under laboratory conditions. This may be one reason why considerations of current pathways and magnitudes in humans have received so little attention. Modelling is the major viable alternative. The author considers Finite Element Modelling to be of significant application for the future.

An interesting ‘side note’, however, exists in the work of Darveniza [32] who examined the electrical properties of wood used in power reticulation structures. This biological material is markedly more homogeneous than the animal body, but nonetheless contains possible channels for internal breakdown that parallel the tissue planes and channel structures of the mammalian body.

Darveniza found that the breakdown path seen when a wooden structure was submitted to an impulse was either entirely internal, or entirely external, never both. Which pathway was seen in an individual case was dependent on a number of factors, of which two were particularly important, viz., the moisture content of the wood (more moisture favouring the internal path), and the existence of an entry site (e.g. a bolt or the like) to the interior. In dry wood, moisture content less than 20 per cent, the pathway was invariably external. In ‘wet’ woods, moisture content greater than 50 per cent, the pathway was invariably internal. In the intermediate range other factors needed to be considered, such as length of wood sample, types of electrodes used, wet versus dry surface conditions, and associated hardware.

Using this information, the human body has some features favouring truly internal breakdown. These include high moisture content, relatively short ‘length’, and significant portals of entry. The latter include the special sense orifices of the cranium. It has been suggested that these orifices represent more important portals of entry than previously thought [30]. Hence, also, their vulnerability to injury in their own right. Nonetheless, the body possesses properties disposing to external flashover. These include the likelihood of being externally wet by rain, having less in the way of attached ‘hardware’, such as bolts and screws, and being less homogeneous.

Darveniza notes that evidence of internal flashover in wood is often easily seen, as the internal pathway almost always follows wood pores. The arc is of fine diameter, typically a few millimetres, and indeed tends to ‘fine down’ internally compared with external arcs. In the body, evidence of internal breakdown is rarely found. The most likely medium for transmission within the body is via the vascular tree or other fluid channels with their ionic liquid content. If current is transmitted internally via these self-sealing media, post-mortem evidence may not be present. Even so, such vascular conduction is likely to be quite dangerous, leading directly to the heart.

## **16.4 Models for lightning shock current estimates**

### *16.4.1 Body model*

The common theme for the model used is the simplified body model shown in International Standard IEC60479-1. The use of this model in direct strike illustrates the approach to modelling in the other cases. The body model is shown in Figure 16.1, and this is ‘driven’ in different ways to simulate different kinds of strike.

The discussion will initially centre on direct strike as this contains the fullest of the alternatives for the model of any of the subsequent circumstances.

It is hypothesised (and the models return results supporting these hypotheses) that the strike attaches to a superior part of the human anatomy, perhaps the head. Current is then transmitted internally and reaches a large magnitude. During this internal current passage period, there is no external current flashover, and therefore no consideration of any plasma properties over the body surface. Also during this internal conduction period, skin capacitance charges and ultimately a threshold is passed where skin breaks down locally, and internal current increases momentarily.

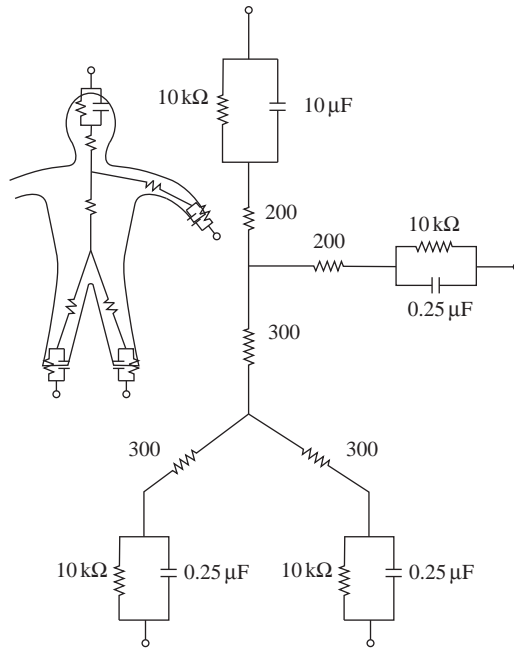


Figure 16.1 Body model

'Skin' in this case is taken to include shoe soles and the like, and breakdown of the skin includes breakdown of any skin covering like a shoe sole. Voltage builds up between the attachment point and (non-ideal) ground, until flashover occurs between the attachment point and ground. At this point, the internal current flow decreases dramatically.

'Skin breakdown' deserves comment. The essential point is that the field from the lightning attachment point reaches a magnitude where external transmission of the majority of the current occurs. Skin breakdown can be considered in two ways. In electrical terms it may be taken as the removal of the capacitive element of the skin, with no consideration of how. The major effect is simply a small increase in internal current before external current passage occurs. Should the capacitance not be removed from the circuit, flashover will still occur once a breakdown potential is reached. There is no consideration here of how such capacitance removal might occur, and this highlights the meaning of breakdown for the clinician. The clinician would consider breakdown of the skin to involve disruption of the skin elements, either from the trauma of the strike, or from burning. It will be seen that such physical breakdown is not a prerequisite for the production of flashover, and thus it might be postulated that severe cardiac injury might occur without physical skin disruption.

From the model, the internal current passage flow is short, and therefore major internal damage such as muscle burn needing fasciotomy is rarely seen in lightning injury. This is also the experience clinically in lightning injury.

Internally it is suggested that the majority of current flow is via ionic fluid – blood, CSF and similar. Muscle would seem to be next lowest in impedance, and this continues to higher and higher impedances up to bone. This writer feels that, contrary to popular belief, nerve tissue actually has relatively high impedance. While axonal tissue may be saltatory and ionic, significant nerve tissue is highly



inaccessible, being covered with multi-membranous layered fatty myelin. Further, the salutatory nature of conduction does not necessarily translate into electrical sensitivity of overwhelming degree –and possibly is capped.

External flashover may be modelled as an extremely low impedance pathway between attachment and Earth when the discharge electric field crosses a threshold, and the model proposed operates in this way. Thus the total current and majority path are accounted for. However, even though plasma exists over the skin surface after flashover, there will still be some current passage into the body from this plasma due to its potential, and the distributed skin impedance. This is, however, suggested to be low, as the potential of the plasma will be low, and the skin impedance (intact) will be high.

### *16.4.2 Factors for modelling*

A model of current flow within humans must take into account and be consistent with certain observed phenomena. It is against these factors that the effectiveness will be measured.

First, the body impedance is known to a greater or lesser degree. Until disruption of elements of this impedance occurs (due to mechanical forces, electrical breakdown, burns, electroporation, or similar) the impedance structure must be ‘respected’. The knowledge of physiological effects of impedance, as well as current behaviour, at the brevity of duration of lightning injury is very poor. Certain considerations by the IEC standards organisation are in progress, but are not yet adopted. These will be referred to in terms of dangerous thresholds below, but only as approximations.

Second, the model must allow for sufficient internal current to flow to be consistent with the functional consequences seen – particularly that of cardiac asystole.

Third, it must allow for the development of flashover.

Fourth, it must also allow for the fact that internal electrical injury or burn of a structural kind is extremely rarely seen. Thus any internal current must be short-lived.

In the light of these factors, three cases are considered in the estimates below and others follow simply by extension. We consider direct strike with no external flashover (this could also occur in side flash or contact potential), direct strike with external flashover (such as might occur in direct strike), and EPR shock. At least the first two cases are shown to engender shocks of lethal magnitude. A further examination of Upward Streamer Shock will be presented.

## **16.5 Current estimates**

### *16.5.1 Direct strike including side flash and contact potential*

In these mechanisms, there is direct impingement of lightning current on the individual. They are essentially the same mechanism, with only orders of magnitude being the differentiating factors. They are thus dealt with under the same mechanism.

The components in the model of Figure 16.1 follow commonly accepted lines, and include a 1 k $\Omega$  internal resistance split between arms, torso, and legs, as the internal component. This is purely resistive. The components for skin impedance

are significantly larger than for the internal resistance, and consist of a parallel resistance and capacitance of 10 kΩ and 0.25 μF. When this body model is placed in circuit with the lightning current source a means of modelling external and skin breakdown (should it occur, vide supra) is required. This is shown in Figure 16.2, where gaps G<sub>1</sub>–G<sub>4</sub> model the breakdown. G<sub>4</sub> represents external flashover, and G<sub>1</sub>, G<sub>2</sub> and G<sub>3</sub>, respectively model the cranial ‘skin’ breakdown and the two foot ‘skin’ breakdowns. The ‘skin’ is assumed to breakdown at a voltage of 5 kV across the parallel combination, and body surface breakdown to occur at a gradient of 2.7 kV/cm, and for a 1.8 m adult, approximately 500 kV. These are representative values and give useful current estimates.

**16.5.1.1 Earth resistance component**

Meliopoulos [33] has derived expressions for earth resistance applicable to these conditions. For an individual standing on a surface of Earth resistance ρ Ωm, the resistance measured from single foot to true earth is given by

$$R_e = \rho/8b$$

where ρ is the earth resistivity and b is the radius of the equivalent flat plate representing 1 ft.

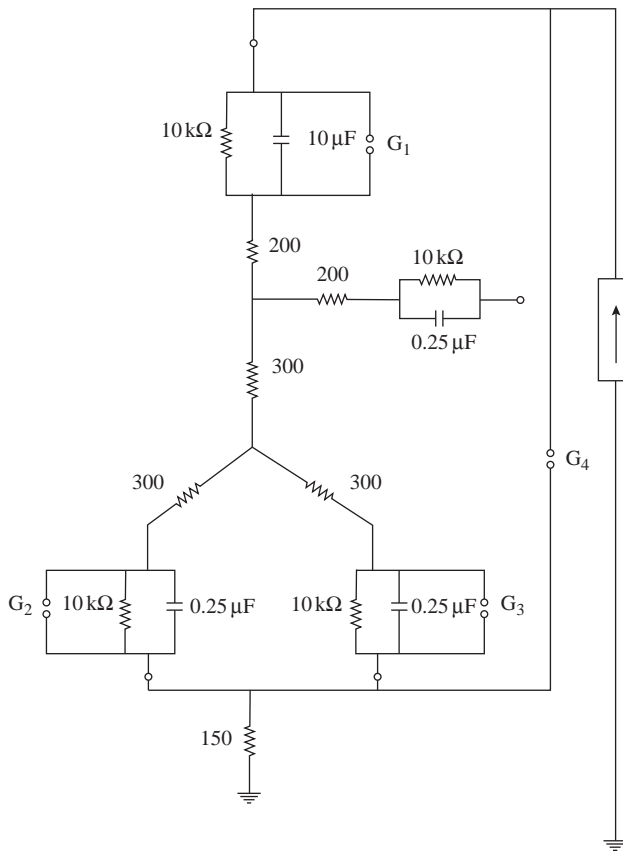


Figure 16.2 Equivalent circuit for direct strike ‘in the field’

Thus he shows that

$$R_e = 3\rho \text{ approximately, and 2ft in parallel is half that.}$$

In subsequent sections,  $\rho$  is taken to be  $100 \Omega\text{m}$ .

### 16.5.1.2 Direct strike – no flashover

The two cases of direct strike are now considered.

The first is assumed to be direct strike with no external breakdown. The equivalent circuit is shown in Figure 16.2. An impulse of 5 kA using an 8/20  $\mu\text{s}$  waveform is directly applied to the cranial skin and the sequence of events shown in Figure 16.3 are observed using this model.<sup>1</sup>

Even though no external flashover is modelled in this example, skin breakdown in the terms discussed above is highly likely (and the case of its occurrence is considered), and is programmed to occur at 5 kV. The sequence of events shows:

- (i) Voltage is generated across the body (here represented by the cranial-earth voltage) by the applied current, and leads the current which, in the internal milieu, rises exponentially. Voltage across the foot and cranial skin elements slightly lag the current;
- (ii) At 1.1  $\mu\text{s}$  and 1.7  $\mu\text{s}$ , respectively, breakdown of skin components occurs. This only has marginal impact on the internal current, and cannot be distinguished on the scale of the figure.
- (iii) Ultimately a maximum value of internal current is reached. This is 5 kA, and is an obviously harmful current.

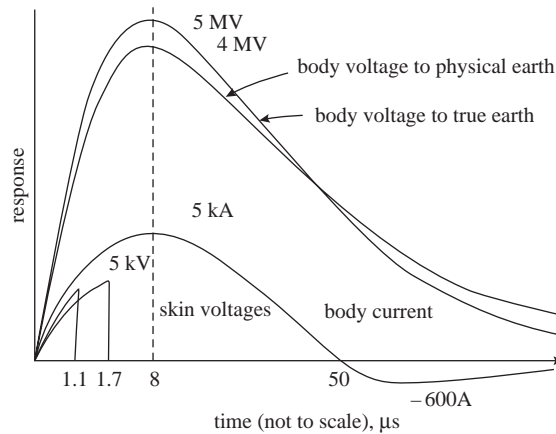


Figure 16.3 Sequence of events following direct strike 'in the field' without the occurrence of flashover

<sup>1</sup>The standard lightning parameters are accepted here. These are that the voltage potential of a lightning stroke attaching to an object at the point of contact can be modelled as a  $1/50 \mu\text{s}$  biexponential waveform. On application of this waveform the current that flows (the lightning stroke is actually a current source) is forced to be an  $8/20 \mu\text{s}$ , the lack of linear correspondence being brought about by the complex relation in the lightning channel of capacitance and inductance, i.e. energy storing and transforming model components. In the event, the applied lightning current here is modelled as an  $8/20$  current source.

- (iv) By 100  $\mu$ s the current wave has largely decayed and only a small component remains at 500  $\mu$ s. During the decay, the internal current becomes negative as capacitive elements discharge.

This situation is obviously harmful and the degree of harm depends on the localisation of the breakdown channel, and the current density in the channel. It seems a reasonable worst case assumption that this be conducted directly to the heart via the blood vessels, and probably is transmitted via the aorta with a cross-sectional area of around 7 cm<sup>2</sup>. The current density is thus extremely large. The likelihood of cardiac arrest is high, and the observed phenomenon of asystole is highly likely at this magnitude. Further discussion on this matter may be found in the section 'Heating'.

### 16.5.1.3 Direct strike – with flashover

The second case under consideration is that where the circumstances are as above, but external flashover occurs. The equivalent circuit is the same as the above and the sequence of events is shown in Figure 16.4.

The voltage between the cranium and local ground rises exponentially until 500 kV is reached when external flashover occurs at approximately 340 ns after attachment. This is remarkably small. At this stage the body current has risen to approximately 800 kA. At flashover the voltage and internal current drops dramatically to zero, and the vast majority of current is transmitted externally. The skin voltages now do not rise to 5 kV and so electrical breakdown does not occur. It is highly likely, however, that mechanical disruption of the skin surface occurs, and so skin resistance markedly decreases. Nonetheless the effect of this on body current is negligible.

Thus this circumstance also represents a dangerous situation.

### 16.5.1.4 Heating considerations

Other effects have been proposed for the effects of lightning damage to tissue, including heating effects. It is instructive to calculate possible temperature rises given the above possible scenarios.

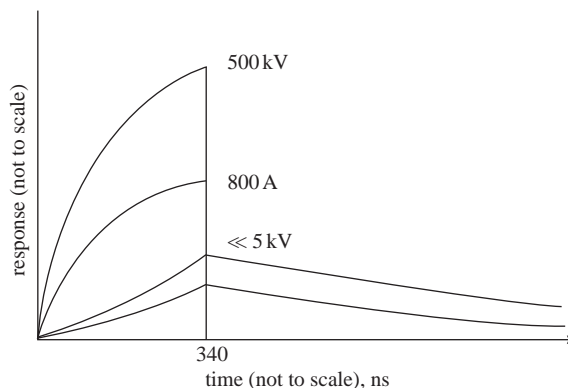


Figure 16.4 Sequence of events following direct strike 'in the field' with the occurrence of flashover

The internal current rises to approximately 800 A in 340 ns, and if as a first approximation this is considered linear, the energy input is approximately 33 J. If this is dissipated in the heart with a volume of about 200 mL, and the specific heat of water, then the temperature rise is around 0.04°C.

If on the other hand, no flashover occurs, the current is much larger and the energy absorption is around 188 kJ, and the cardiac temperature rise would be potentially 224°C, which is obviously capable of producing extreme thermal damage. Since damage of this magnitude is not seen, the worst case assumption that this dissipation occurs totally within the myocardium is not valid.

The situation for metal on the body surface is significant since imprints of individual metal objects (necklaces, belts, coins) can be seen on skin after a strike. Indeed the lesions below these items resemble burns and metal from the object can be embedded in the wound. The process can continue to the point where the whole object (most often a fine necklace) is incorporated into the wound.

Various metals with their relative resistivities are as follows (resistivity must be compared, to provide true comparison of metals irrespective of geometry:

<b>Metal</b>	<b>Resistivity <math>\times 10^{-8} \Omega\text{m}</math> (approx room temp)</b>
Aluminium	2.650
Copper	1.678
Gold	2.214
Iron	9.61
Lead	20.8
Nickel	6.93
Platinum	10.5
Silver	1.587
Zinc	42.1

Various alloys are similarly characterised.

<b>Alloy</b>	<b>Resistivity <math>\times 10^{-8} \Omega\text{m}</math> (approx room temp)</b>	
Aluminium-copper	6.55	50% each
Copper-gold	4.42	90% Cu
Copper-nickel	25.66	80% Cu
Copper-zinc	5.19	Brass – 80% copper (ranges 40–80% Cu)
Gold-silver	6.59	25% gold
Iron-nickel	31.6	80% iron

The resistance of a jewellery chain is difficult to quantify.<sup>2</sup> The reasons for this are that individual geometries are highly variable; that metal is often coated with a non-conductive lacquer for protection; many touch joints between links are involved and conduction at these is highly variable and proportional also to any lacquer coating.

<sup>2</sup>Andrews: informal measurements in a domestic environment. The simple resistance of a metal link in a chain seems to be a fraction of an ohm, however a fine linked chain can have a total resistance of hundreds of kilohms.

As an illustration, however, let us consider a small single piece of metal, say a 2 mm cube, this being the rough geometry of a single chain link. If we consider a copper-zinc alloy (brass), the resistance of this block is  $2.6 \times 10^{-5} \Omega$ . If this piece of metal is in the path of a 5 kA flashover, lasting 100  $\mu$ s, then the energy deposited will be approximately  $6.5 \times 10^{-2}$  J. The weight of the piece is 67.2 g (8 mL at a density of 8.4 g/mL 67.2 g). For brass the specific heat is 0.38 J/g/K and so the temperature rise will be  $2.5 \times 10^{-3}$ °C. This is unlikely to cause thermal burns from this element. But it is emphasised this is a single idealised element with current directly applied. The real situation is some hundreds of the links with high resistance joints between them. Just as an illustration, if we now consider a length of chain of the same material with a resistance of 10 k $\Omega$  (purely for argument sake) and weight 250 g, carrying, say, 10 per cent of the current of 5000 A, the temperature rise becomes  $2.63 \times 10^{-3}$ °C. This is above the melting point of brass.

Between these two extremes the real situation is likely to exist, and so burns from some necklace style metal geometries with metal melting is possible.

Imprints of metal on the body are seen in these cases. Other cases do exist, however. These are metal objects of much lower resistance and bigger mass (e.g. belt buckles), and somewhat protected from current passage (e.g. coins in pockets with intervening cloth between it and the skin). Thus the temperature rise may not be as extreme and melting is less likely. In this case an alternate explanation for the imprint may be that complex field interaction between metal and the skin beneath account for the imprints and metallisation. It may also account for imprints of metal which may still be seen when there is intervening clothing, despite there being no similar shaped imprint in the clothing.

There are six major types of burn seen in lightning injury. The linear burn has been postulated as a vaporisation of sweat in certain channels into steam [8, 14]. Current in the flashover pathways are conducted in plasma channels, and these reach substantial temperatures, though are brief. Certainly, linear burns may be due to this heat, possibly giving the linear burn pattern. Further, Cooper notes [8] that light clothing allows such steam to escape and the burn is relatively minor, whereas with heavy clothing such escape is less possible, and burns are correspondingly more severe.

It is important to note, however, that as opposed to technical electrical injury, burns from lightning are minor and rarely require major therapeutic intervention.

### 16.5.2 EPR mediated shock

The remaining case for consideration is EPR mediated shock. The equivalent circuit for this circumstance is shown in Figure 16.5a.

The equivalent circuit for the applied voltage is that given by Meliopoulos [33]. The magnitude of the voltage source is given by

$$V_{eq} = (\rho I / 2\pi)(1/r_1 - 1/r_2)$$

where  $r_1$  and  $r_2$  are the distances of the body parts in contact with physical ground from the base of the lightning stroke. The other quantities are defined as before.

$R_{eq}$  is given by 1.5  $\Omega$  being two 3  $\Omega$  resistances in parallel.

If we assume a 5 kA lightning stroke and a person 10 m distant with legs 1 m apart  $V_{eq}$  is 800 V, and is thus approximated as 1 kV in the model. If the person is 20 m from the base of the stroke, then the voltage falls to 200 V, and it may be seen that EPR (in-the-field) is a relatively small effect. These are illustrative figures only.

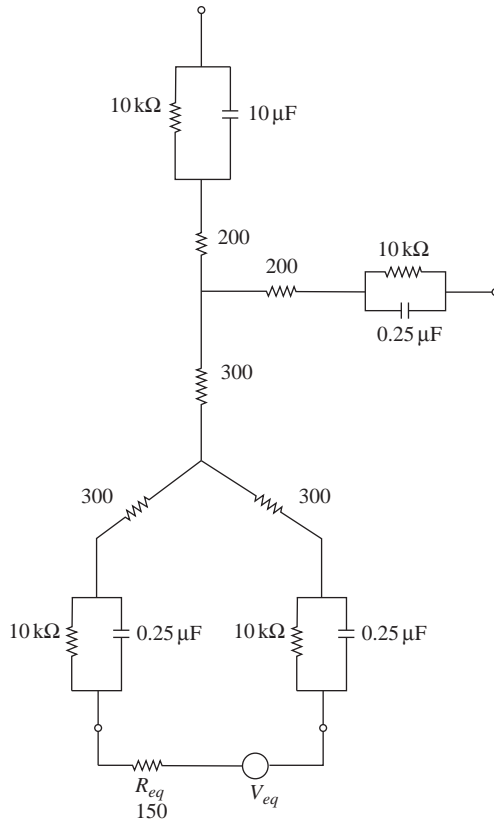


Figure 16.5a *Equivalent circuit for EPR mediated ‘in the field’ strike*

When these parameters are introduced to the model, a current of approximately 1.05 A peak, flows through the legs. Modelled in this way the myocardium seems at little risk, however it must be remembered that the internal resistance is distributed rather than discrete in reality. Thus, a small current will flow peripherally through the myocardium. The accepted factor applied due to a leg-to-leg current is less than 0.3, and so it is expected that less than 300 mA will flow. This is unlikely to be dangerous, on IEC criteria, given the small duration (45 μs) of the impulse. The effect for large animals, e.g. cattle, with legs up to 4 m apart, and direct trans-thoracic pathways, may well be dangerous.

More generally, the voltage distribution seen on a resistive ground as a function of a lightning stroke to ground can be illustrated.

The equation for  $V_{r1}$ , the ground potential at  $r_1$  is given by

$$V_{r1} = (\rho I / 2\pi) r_1$$

The parameter  $\rho$  is the earth resistivity, and  $I$  is the current in the stroke. This is a hyperbole and an example is given in Figure 16.5b.

### 16.5.3 *Aborted upward streamer*

The upward streamer case is complex and has been examined by Becerra and Cooray [12]. The calculations reported here are their calculations. They identify two processes of importance. First, a current will flow to extend the ionization of

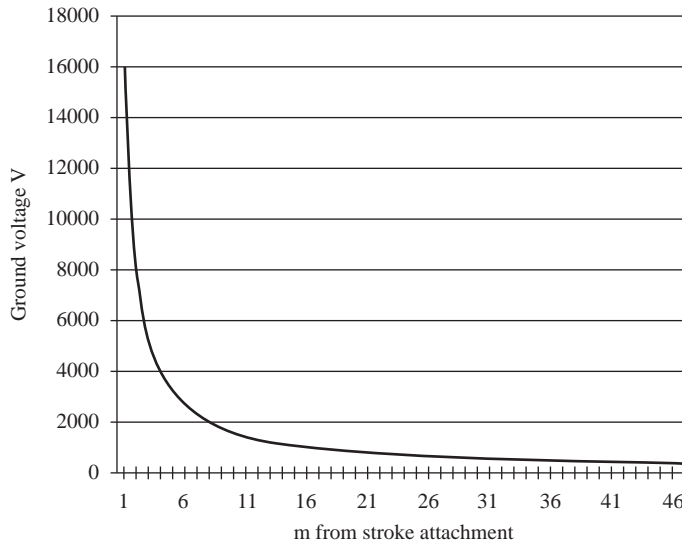


Figure 16.5b An example of ground potential versus distance from the base of a stroke, for  $\rho = 10 \Omega\text{m}$  and  $I = 10\,000 \text{ A}$ . Increases in  $\rho$  linearly shift the graph shape vertically, as do changes increases in  $I$ , increasing the ground potential. Decreases in either decrease the ground potential

the upward streamer as it reaches to ‘answer’ the downward stepped leader. Second, once attachment of the stepped leader has occurred elsewhere, reverse current flows back through the victim, and this will be a very short impulsive current as opposed to the former, which is a longer process.

Upward streamers from inanimate objects were thought to extend for a few tens to hundreds of microseconds, and have currents of 10–100 A. These however are from objects several tens of metres tall, and are not directly applicable to humans.

A numerical model was used, incorporating a dynamic upward leader model and then Finite Element analysis. The upward leader is modelled, and then backflow is calculated after the applied field collapses to zero, with each point in the leader modelled as a relaxing corona source with time constant  $\tau$ . In essence the capacitance of the streamer channel is discharged back through the victim, assumed resistive at this stage. The decay time constant  $\tau$  is estimated as being 0.4–1.2  $\mu\text{s}$ . Two cases were considered – where the return stroke is initiated by attachment to another object’s upward leader, or where there is no other upward leader and attachment occurs with ground. The attachment radius is relevant here; however, the attachment radius of a human being is somewhat conjectural.

For an average 30 kA lightning stroke, an upward leader was found to commence when the horizontal distance to the downward stepped leader was 42 m. The attractive radius was found to be 22 m. For an 80 kA stroke, the horizontal distance was found to be 93 m.

Given that the attractive radius defined a circle around the victim, the risk of direct strike was therefore

$$\text{Risk} = \frac{R_a^2}{R_1^2 - R_a^2}$$



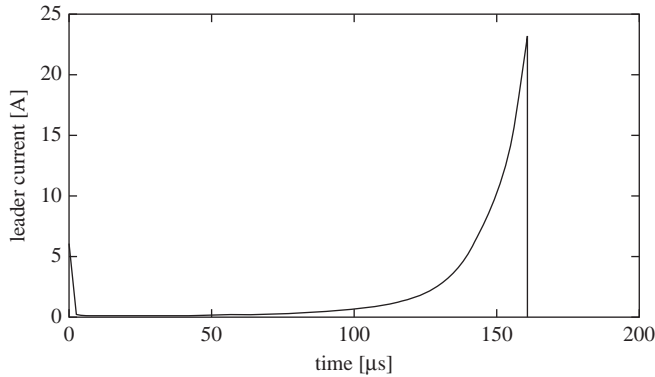


Figure 16.6 Streamer current versus time for a 30 kA lightning strike to earth (courtesy Dr Vernon Cooray with permission). Victim 1.75 m tall, strike 24 m distant horizontally

where  $R_a$  is the attractive radius, and  $R_1$  is the leader inception radius, that is, the radius at which the leader begins to emanate from the victim.

It was estimated that the attractive radius decreased by 30 per cent (to 15 m) in the squat position, and increased by 10 per cent when the hand was held above the head [12]. The squat was calculated to decrease risk by about 50 per cent, and extending the hand increased the risk by 20 per cent. The protection of the lightning squat has been debated and has achieved varying acceptance and discard. These figures, along with those quoted above [from 9] may point again to its credibility.

The currents are reported for the case of a return stroke to nearby ground. This is a worst case compared with discharge via another upward leader elsewhere.

For a stroke of 30 kA and  $R_1$  just greater than the attractive radius, the upward streamer charge is initiated with a charge injection of  $>5 \mu\text{C}$  – a large charge. This corresponds to an initial current of about 0.5 A. The current continues to rise to about 20 A before collapsing in about 160  $\mu\text{s}$ . (see Figure 16.6). For an 80 kA stroke, the current increases from 0.3 to 70 A in 350  $\mu\text{s}$ .

In the backflow segment, after the stepped leader attaches, much higher currents are reached due to the brevity of collapse and it assumed that they decay at the same rate as return stroke decays. Two decay time constants are nonetheless considered and the current decay is shown in Figure 16.7. The horizontal scale origin is the initial streamer inception. The relevant currents are approximately  $-5700 \text{ A}$  for a 30 kA stroke and  $-13200 \text{ A}$  for an 80 kA stroke for decay time constant of 0.1  $\mu\text{s}$ . For a 30 kA stroke and time constant of 1.0  $\mu\text{s}$ , the current reduces to approximately  $-600 \text{ A}$ .

These are again potentially injurious currents though they operate for a much shorter time period. Even so, the deposited energy in the most severe circumstance is 1.18 kJ, and this does not approach the direct stroke level, nor the energy reported by Ohashi [28].

#### 16.5.4 Telephone mediated strike

A research interest of the authors' is that of lightning shock delivered to individuals involving the public telephone system. Similar modelling has been undertaken for this circumstance.

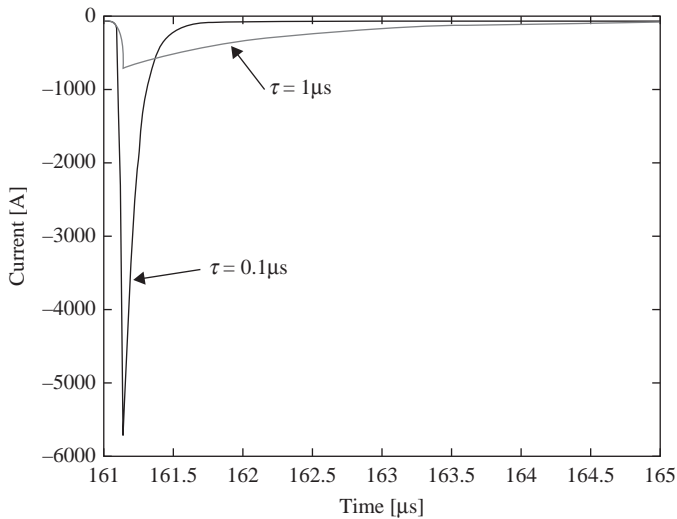


Figure 16.7 Backflow currents through a victim after collapse of the upward streamer (courtesy Dr Vernon Cooray with permission)

The ear in telephone-mediated lightning injury is at special risk, and is, in fact, subject to two distinct insults, one electrical and one acoustic [13, 34]. This section aims to quantify the order of electrical trauma to which the hearing organ is subjected, and consequently to indicate the order of electrical insult to which the whole body is subjected. The entry of current through the ear can be transmitted via one of several mechanisms to the remainder of the body.

The external connections to the body model above have been adjusted. In normal operation, the telephone handset is pressed to the ear using one hand. Coupling to the handset therefore is dual. The coupling is capacitive and the capacitance is taken as 88 pF, experimentally determined by the author.

Two circumstances of shock bear examination. The first is direct surge application through the telephone line through handset and cranium to a return path via the feet, or possibly another part of the body touching an earthed structure. In this case, the applied surge is a voltage surge, and compared with in-the-field strike, of somewhat less power. Breakdown of the handset/head interface may still occur, but surface flashover of the body is not considered at all likely. Occasional breakdown of skin entry/exit sites may occur. Using the previous model the earth resistance is set up in exactly the same way. The applied impulse is taken as a 10 kV 1/50  $\mu$ s voltage surge. Local measurement on lightning prone telephone lines indicate an upper limit of 5 kV unlikely to be exceeded, but 10 kV is taken as a worst case. The equivalent circuit and simulation result are shown in Figures 16.8 and 16.9.

The following may be seen. The 88 pF capacitor is modelled to breakdown at 5 kV, and prior to this body current is small, rising to a maximum of 700 mA. The handset coupling breaks down at approximately 1.5  $\mu$ s and when this occurs body current rises dramatically to a maximum of approximately 12 A at 10  $\mu$ s and then falls quickly to negligible values by 54  $\mu$ s. The possibility exists for skin breakdown to occur, but the model indicates that the skin voltage only rises to about 600 V. Given that a 10 kV surge is uncommon, and that the majority are less than 5 kV, the risk of death is low. Indeed below 5 kV handset flashover may not occur. When it

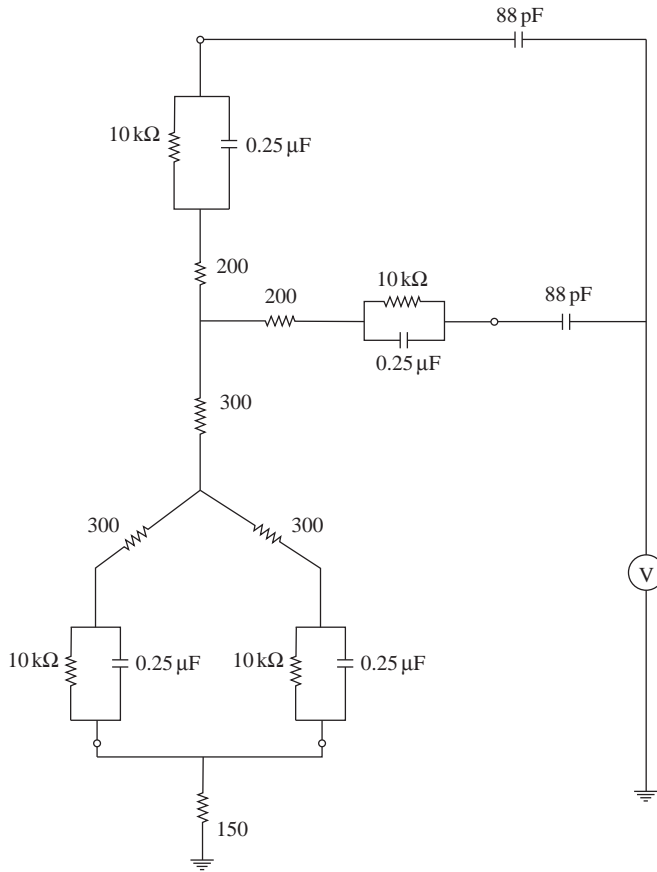


Figure 16.8 *Equivalent circuit for telephone mediated lightning strike with the impulses transmitted directly by the telephone cable*

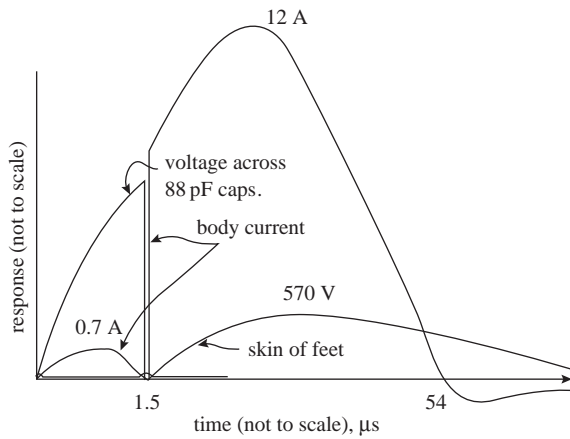


Figure 16.9 *Body response for telephone mediated lightning strike with the impulses transmitted directly by the telephone cable*

does, the spark will be local, and forms the ‘capacitive spark’ often seen. While unlikely to be fatal, such shocks are nonetheless highly perceivable, and unpleasant. Experience indicates that the neuropsychological syndrome after telephone related shock can be the same as other lightning shock.

Estimates are that the majority of telephone-mediated shocks in the author’s country (Australia) are mediated by local EPR causing current to be transmitted back to the remotely earthed telephone exchange. An equivalent circuit for such a circumstance is shown in Figure 16.10, using the same parameters as previously (a stroke 20 m away, and of  $100 \Omega\text{m}$ ). A voltage impulse of 1 kV is applied to both feet in parallel, and the results of simulation are shown in Figure 16.11. This is an appropriate level of impulse EPR given circumstances similar to that shown above. It may, however, underestimate the degree of the insult given modern construction of dwellings. It may be that power supply reticulation, or the structure itself may be struck, and the impulse transmitted to a highly conductive floor structure, e.g. concrete slab. This would increase the EPR voltage markedly. The 1 kV impulse used could, however, be scaled easily.

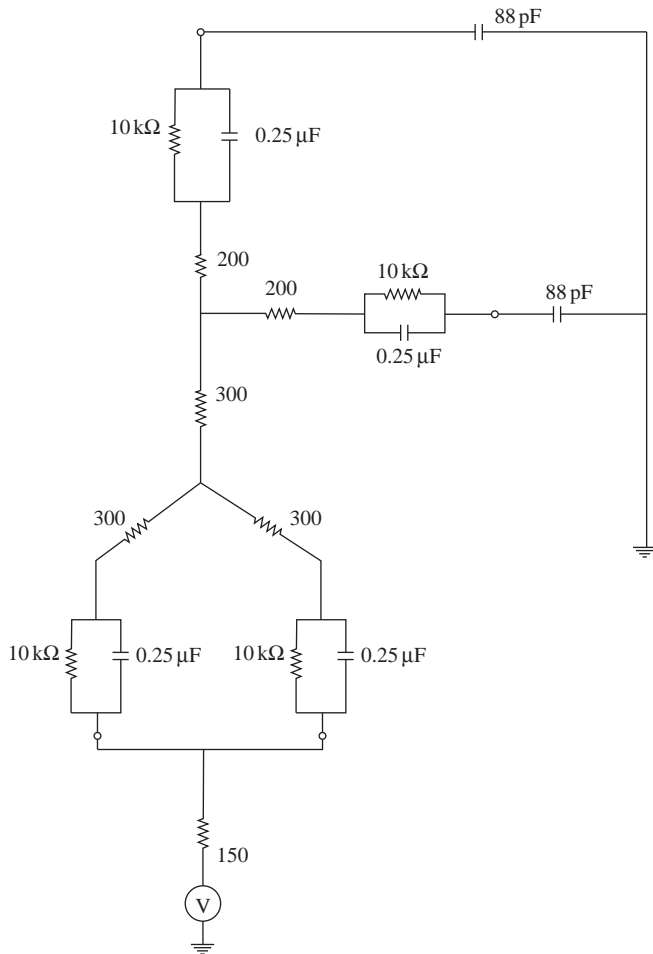


Figure 16.10 Equivalent circuit for telephone mediated lightning strike, with the impulse transmitted by EPR

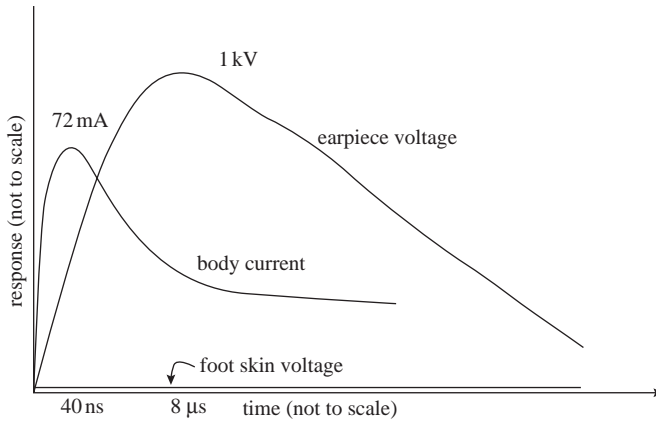


Figure 16.11 *Body response for telephone mediated lightning strike, with the impulse transmitted by EPR*

The simulation shows that the voltage across the 88 pF capacitors rises rapidly as expected, but does not necessarily break down. Body current rises to around 72 mA, and this is unlikely to be injurious. Even with an order of magnitude scaling, the results still represent the least dangerous of the strike circumstances. This is in terms of death, however sequelae certainly are seen clinically.

These results support the observation that no death has yet been seen in Australia from telephone-mediated lightning strike. If, however, high current strokes occur and circumstances conspire, such is not beyond possibility.

## 16.6 Experimental support

Experimental support for these models is hard to obtain, however one incidental observation may be important.

In other work [30], Australian sheep were subjected to cranial impulses, and flashover occurred. The impulses were multi-pulse, and indicated also the importance of cranial orifices as entry points. Tracings of the applied current pulse were obtained, and traces of the resulting cranium to hind-quarter voltage were also obtained. These are shown in Figure 16.12. In all cases where flashover occurred, the voltage dropped dramatically at approximately 500 nS, this being a rough limit

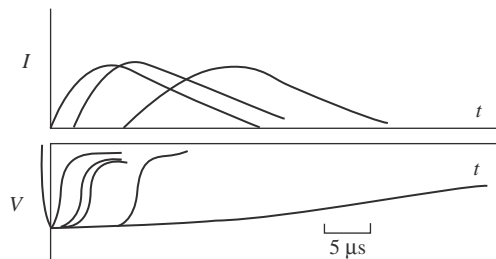


Figure 16.12 *Voltage tracing – cranium to earth (upper trace – multi-pulse traced from polaroid; lower trace – single pulse)*

of measurement. The trace of a single impulse in Figure 16.12 shows the drop in voltage, but a short tail which represents the limitation of the proposed model with respect to the plasma sheet after flashover.

## 16.7 Conclusion

In this segment models for in-the-field strike and telephone mediated strike have been developed, and proposals regarding pathways have been made. An estimation of the magnitude and the timecourse of the insult have been given.

## Acknowledgement

The author gratefully acknowledges the helpful comments made by Professor Mary Ann Cooper on earlier drafts of this chapter.

## References

- [1] COOPER, M.A., ANDREWS, C.J., and Ten DUIS, H.J., Psychological aspects of lightning injury, *9th Int. Conf. Atmosph. Elec., June 15–19, 1992*, Borisenkov, E., A.I. Voeikov Main Geophys Observ., St. Petersburg: St Petersburg, Russia
- [2] PLISKIN, N. *et al.*, Neuropsychological changes following electrical injury. *J. Int. Neuropsych. Soc.*, 2006. **12**: pp. 17–23
- [3] PRIMEAU, M., ENGELSTATTER, G.H., and BARES, K.K., Behavioral consequences of lightning and electrical injury. *Semin. Neurol.*, 1995. **15**(3): pp. 279–85
- [4] COORAY, V., COORAY, C., and ANDREWS, C., Lightning caused injuries in humans, in *Lightning Protection*, Edited by V. Cooray, Published by Institution of Engineering and Technology (IET, former IEE), London, UK, 2010
- [5] ANDREWS, C.J., The origin of remote symptoms in electrical and lightning injury: An attempt at explanation and a hypothesis for testing. *J. Lightn. Rsch.*, 2012. **4**(special issue 2): pp. 149–54
- [6] KURTULUS, A., ACAR, K., ADIGUZEL, E., and BOZ, B., Hippocampal neuron loss due to electric injury in rats: A stereological study. *Legal Medicine (Tokyo)*, 2008. **22**(12): pp. 2671–5
- [7] ANDREWS, C.J., COOPER, M.A., and Ten DUIS, H.J., Chapter 23a, Lightning and electrical injuries – medical and legal considerations, in *Forensic Science*, Wecht, C., Editor. 2000, Bender, USA
- [8] COOPER, M., HOLLE, R., ANDREWS, C., and BLUMENTHAL, R., Lightning injuries, in *Wilderness Medicine*, P. Auerbach, Editor. 2012, Elsevier: Philadelphia, USA
- [9] ROEDER, W.P., Short notice outdoor risk reduction – evaluating its performance and discussion on why it should not be taught, ICOLSE, EUROCAE, Paris France, 2007, Paper IC07-AB
- [10] COOPER, M.A., HOLLE, R. L., and ANDREWS, C., Distribution of lightning injury mechanisms, *20th International Lightning Detection Conference*, Vaisala, Tucson Arizona, 22–23 April, 2008. p. 4

- [11] ANDREWS, C.J., COOPER, M., DARVENIZA, M., and MACKERRAS, D., Lightning injury: Electrical medical and legal aspects. 1992, Florida: CRC Press
- [12] BECERRA, M., and COORAY, V., On the interaction of lightning upward connecting positive leaders with humans. *IEEE Trans EMC*, 2009. **51**(4): pp. 1001–1008
- [13] ANDREWS, C.J., and DARVENIZA, M., Telephone-mediated lightning injury: an Australian survey. *J. Trauma*, 1989. **29**(5): pp. 665–71
- [14] COOPER, M.A., A fifth mechanism of lightning injury. *Acad. Emerg. Med.*, 2002. **9**(2): pp. 172–4
- [15] ANDERSON, R.B., Does a fifth mechanism exist to explain lightning injuries? *IEEE Eng. Med. Biol. Mag.*, 2001. **20**(1): pp. 105–13.
- [16] ANDERSON, R.B., JANDRELL, I., and NEMATSWERANI, H., The Upward Streamer mechanism versus step potentials as a cause of injuries from close lightning discharges. *Trans. SA Inst. Elec. Eng.*, 2002: pp. 33–43
- [17] KRIDER, E., and LADD, C., Upward streamers in lightning discharges to mountainous terrain. *Weather*, 1975. **30**(3): pp. 77–81
- [18] McEACHRON, K., and McMORRIS, W., The lightning stroke: Mechanism of discharge. *Gen. Elec. Rev.*, 1936. **39**(10): pp. 487–96
- [19] BECERRA, M., and COORAY, V., On the interaction of lightning upward connecting positive leaders with humans, *Trans. IEEE (EMC)*, 2009. **51**: 1001–1008
- [20] CARTE, A.E., ANDERSON, R.B., and COOPER, M.A., A large group of children struck by lightning. *Ann. Emerg. Med.*, 2002. **39**(6): pp. 665–70
- [21] ZACK, F., ROTHSCOLD, M., and WEGENER, R., Lightning strike—mechanisms of energy transfer, cause of death, types of injury. *Dtsch. Arztebl.*, 2007. **104**(51–52): pp. A3545–9
- [22] ANDREWS, C.J., Telephone related lightning injury. *Med. J. Aust.*, 1992. **157**(11/12): pp. 823–5
- [23] ANDREWS, C.J., Further identification and treatment modalities in telephone mediated lightning strike, in *14th ICOLSE 1991*, NASA: Cocoa Beach, Fla.
- [24] BLUMENTHAL, R., JANDRELL, I., and WEST, N., Does a sixth mechanism exist to explain lightning injuries: Investigating a possible new injury mechanism to determine the cause of injuries related to close lightning flashes. *Am. J. Med. Pathol.*, 2012. **33**(3): pp. 222–6
- [25] BLAKE-PRITCHARD, E.A., Changes in the central nervous system due to electrocution. *Lancet*, 1934. **1**: p. 1163
- [26] ISHIKAWA, T., OHASHI, M., KITAGAWA, N., NAGAI, Y., and MIYAZAWA, M., Experimental study on the lethal threshold value of multiple successive voltage impulses to rabbits simulating multi-strike lightning flash. *Int. J. Biometeorol.*, 1985. **29**(2): pp. 157–68
- [27] NAGAI, Y., ISHIKAWA, T., OHASHI, M., and KITAGAWA, N., Study of lethal effects of multiple stroke flash lethal effects of rabbits subjected to 3 successive voltage impulses simulating multiple stroke flash. *Res. Lett. Atm. Phys.*, 1982. **2**: p. 87
- [28] OHASHI, M., KITAGAWA, N., and ISHIKAWA, T., Lightning injury caused by discharges accompanying flashovers – a clinical and experimental study of death and survival. *Burns Incl. Therm. Inj.*, 1986. **12**(7): pp. 496–501

- [29] ISHIKAWA, T. *et al.*, Experimental studies on the effect of artificial respiration after lightning accidents. *Res. Exp. Med. (Berl.)*, 1981. **179**(1): pp. 59–68
- [30] ANDREWS, C., Structural changes after lightning strike, with special emphasis on special sense orifices as portals of entry. *Semin. Neurol.*, 1995. **15**(3): pp. 296–303
- [31] FLISOWSKI, Z., and MAZZETTI, C., An approximate method of assessment of the electric shock hazard by lightning strike (Paper 6.9). *18th Int. conf. on Lightn. Protm.*, 1985. VDE Verlag GmbH: Munich
- [32] DARVENIZA, M., *Electrical Properties of Wood and Line Design*. 1978, Brisbane: University of Queensland Press, p. 197
- [33] MELIOPOULOS, A.P.S., *Power System Grounding and Transients*. 1990, NY USA: Marcel Dekker
- [34] ANDREWS, C.J., and DARVENIZA, M., Determination of the acoustic insult in telephone mediated lightning strike. *LM97 1997*, APERI: Chamonix Mont Blanc





---

## Chapter 17

# Upper atmospheric electrical discharges

*Ningyu Liu*

---

### 17.1 Introduction

The modern studies of electrical discharges in the middle and upper atmosphere related to thunderstorm/lightning activities began with several discovery works published in the late 1980s and early 1990s [Franz *et al.*, 1990; Sentman *et al.*, 1995; Wescott *et al.*, 1995; Pasko *et al.*, 2002; Neubert, 2003; Pasko, 2003], but observations of brief luminous discharges above thunderstorms were reported over a century ago [Lyons *et al.*, 2003a; Pasko, 2008]. Those luminous discharge phenomena are now collectively referred to as transient luminous events (TLEs). We know now they are driven by thunderstorm/lightning activities at tropospheric altitudes and are the manifestation of direct electrical coupling between tropospheric thunderstorms and the middle and upper atmosphere.

TLEs are categorized as jets, gigantic jets, sprites, halos, elves, etc., according to their different morphologies, altitude extents, and physical mechanisms. As shown in Figure 17.1, jets emanate from the top of thunderclouds up to an altitude of 40–50 km [Wescott *et al.*, 1995; Lyons *et al.*, 2003a]; gigantic jets are upward moving electrical discharges establishing a direct path of electrical contact between thundercloud tops and the lower ionosphere [Pasko *et al.*, 2002; Pasko, 2003; Su *et al.*, 2003; Cummer *et al.*, 2009]; sprites develop at the base of the ionosphere and move rapidly downwards at speeds up to a significant fraction of the speed of light [Franz *et al.*, 1990; Sentman *et al.*, 1995; Lyons, 1996; Stanley *et al.*, 1999]; halos (not shown in the figure) are brief diffuse glows centered around 78–80 km altitude with horizontal extent of 40–70 km and vertical thickness of a few kilometers [Barrington-Leigh *et al.*, 2001; Wescott *et al.*, 2001a]; and elves are lightning-induced optical flashes that can spread over 300 km laterally [Fukunishi *et al.*, 1996a; Inan *et al.*, 1997]. The overall atmospheric volumes occupied by TLEs appear to be as large as thousands of cubic kilometers. However, high spatial resolution images indicate that sprites, jets, and gigantic jets are highly structured. The lifetimes of the optical signatures of TLEs are generally very short: <1 ms for elves, ~2 ms for halos, one to tens of milliseconds and occasionally hundreds of milliseconds for sprites, and hundreds of milliseconds for jets and gigantic jets. According to the global survey obtained by the Imager of Sprites and Upper Atmospheric Lightning (ISUAL) experiment aboard the FORMOSAT-2 satellite, the global occurrence rates for elves, sprites, halos, and gigantic jets are 3.23, 0.5, 0.939, and 0.01 events per minute, respectively, indicating that elves are the most frequent type of TLEs.

The possibility of electrical discharges of air above thunderclouds was first recognized in 1925 by the Nobel Prize Laureate C.T.R. Wilson [Wilson, 1925].

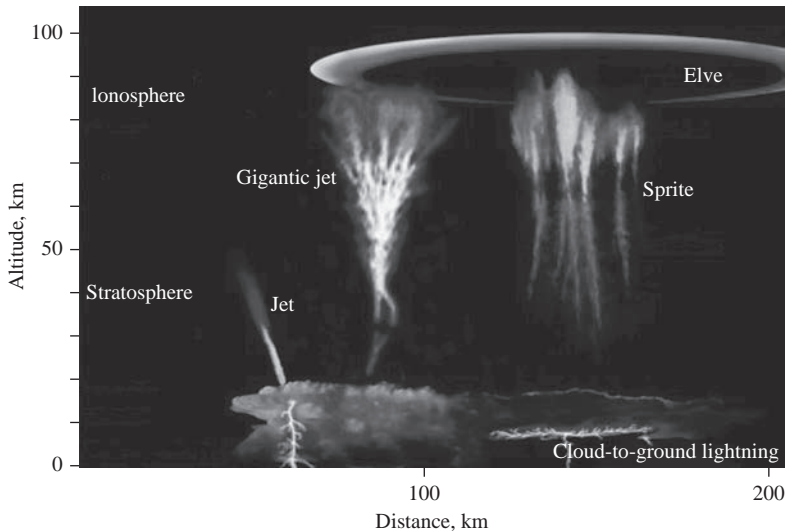


Figure 17.1 TLEs related to underlying thunderstorm/lightning activities [Pasko, 2003]. Reprinted with permission from *Nature*

He suggested that during thunderstorms, strong electric field may appear in the upper atmosphere due to charge rearrangement by lightning flashes or charge imbalances in thunderstorms. Under extreme circumstances, the electric field at high altitudes could be strong enough to accelerate electrons to energies sufficient to excite and ionize air molecules. This results in electrical discharges and optical flashes in the middle and upper atmosphere, which are now known as sprites. The physical mechanisms of TLEs are discussed in more detail later in this chapter.

Generally speaking, TLEs are driven by the electric field of thundercloud charge and lightning, and an important factor determining their temporal and spatial evolution is the field magnitude and duration at the corresponding atmospheric regions. Figure 17.2 shows the altitude profiles of air density and atmospheric conductivity from 0 to 100 km altitude. The air density decreases exponentially with the altitude. The atmospheric conductivity profile is broken down into two regions: the ion conductivity dominating region ( $< \sim 65$  km) and the electronic conductivity dominating region ( $> \sim 65$  km). In each region, the conductivity increases exponentially but the rate of increase is larger in the region dominated by the electronic component. The local Maxwellian relaxation time ( $\epsilon_0/\sigma$ , where  $\sigma$  is the local conductivity and  $\epsilon_0$  is the permittivity of free space) calculated by using the conductivity shown in Figure 17.2 is  $< 1$  ms above 80 km altitude, one to tens of milliseconds at 70 km, and  $\sim 1$  s at 30 km, which characterize the lifetimes of the electrical phenomena at those altitudes.

Our understanding of upper atmospheric discharges has advanced significantly since the early 1990s, and a large amount of dedicated observational, experimental, theoretical, and modeling efforts have been made to study various aspects of TLEs. Many papers, including a few recent extensive review papers, have been published in this field [Pasko, 2007, 2008; Neubert *et al.*, 2008; Roussel-Dupré *et al.*, 2008; Mishin and Milikh, 2008; Ebert and Sentman, 2008; Siingh *et al.*, 2008; Pasko, 2010; Ebert *et al.*, 2010; Pasko *et al.*, 2011; Stenbaek-Nielsen *et al.*, 2013; Pasko *et al.*, 2013]. A book dedicated to TLEs was also published in 2006

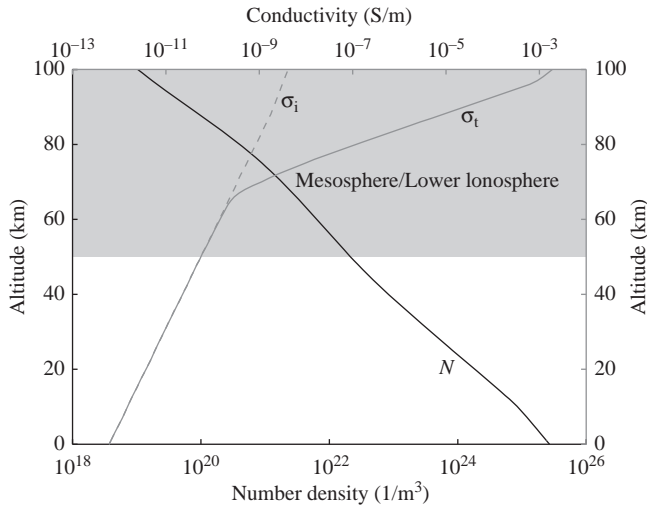


Figure 17.2 Altitude profiles of neutral density  $N$  and conductivity [Liu, 2012]. The neutral density is obtained from the MSIS profile ([http://omniweb.gsfc.nasa.gov/vitmo/msis\\_vitmo.html](http://omniweb.gsfc.nasa.gov/vitmo/msis_vitmo.html)). The ion conductivity is taken from Holzworth et al. [1985]. The electron density to calculate the electronic conductivity is taken from Wait and Spies [1964] and Pasko and Stenbaek-Nielsen [2002]. The total conductivity  $\sigma_t$  is dominated by the ion component below  $\sim 65$  km altitude and by the electronic component above that altitude

[Füllekrug et al., 2006], and discussions on different aspects of TLEs appear in several other books [Rakov and Uman, 2003; Leblanc et al., 2008; Cooray, 2012] and in journal special issues or sections [Ebert and Sentman, 2008; Sentman, 2010; Gordillo-Vázquez and Luque, 2013]. In this chapter, we attempt to give an overview of the TLE research and our knowledge of them. The general phenomenology of different types of TLEs is described in section 17.2. Section 17.3 discusses similarity laws for gas discharges at different pressures or gas densities, and presents an example illustrating possible distinctions between the discharges at different pressures. In section 17.4, we present example studies of modeling sprites (arguably the best documented TLEs) and their fine structures in order to show how TLE modeling is carried out and how it helps improve our understanding of TLEs.

## 17.2 General phenomenology

### 17.2.1 Jets and gigantic jets

#### 17.2.1.1 Jets

Jets are upward discharges developing from thundercloud tops and terminating at about 40–50 km altitude in the middle atmosphere. Observations of column optical flashes shooting upward from thundercloud tops to the middle atmosphere have been reported in the scientific literature since early last century. However, it is since the early 1990s that systematic studies of such unusual luminous phenomena have started to reveal their detailed characteristics. In June and July 1994, the Sprites94 aircraft campaign led by a team of researchers from the University of

Alaska conducted observations in the Midwest of the United States [Sentman *et al.*, 1995; Wescott *et al.*, 1995]. During the campaign, two jet aircraft were flown at  $\sim 12.5$  km altitude to make observations. Multiple cameras/photomultiplier tubes were mounted on each aircraft as well as GPS systems to track the positions of the aircraft and to obtain accurate timing information. This permitted accurate triangulation of the objects simultaneously recorded from the separate aircraft. A total of 51 incidents of narrow cones of blue light shooting upward from the tops of thunderstorms and terminating at  $\sim 40$  km altitude were recorded [Wescott *et al.*, 1995], which are now termed as “jets.” Most of the jets were observed from a distance of 100 km or so, and triangulating analysis indicated that they originated from an average altitude of 17.7 km and reached  $37.2 \pm 5.3$  km. The mean vertical speed of the jets was  $112 \pm 24$  km/s, and few of them developed in the vertical direction but with a mean angle off the axis of  $10.8^\circ \pm 7.0^\circ$ . It was also found that the average cone angle of the jets was  $14.7^\circ \pm 7.5^\circ$ . Note that the number following each mean value represents the range of the parameter not the error. The lifetimes of the jets varied from 200 to 300 ms. The instruments of the campaign included a color camera, and analysis of the color images of the jets showed that the spectrum of the jets is dominated by blue emissions below 480 nm. The optical emissions were believed to be from the second positive band system of  $N_2$  and might include contributions from the first negative band system of  $N_2^+$  as well [Wescott *et al.*, 1995].

During the same campaign, upward discharges from thundercloud tops but with a lower terminal altitude ranging from 18.1 to 25.7 km were also recorded, which were called “blue starters” but were likely related to the initial phase of jets [Wescott *et al.*, 1996]. They originated from a similar altitude as the jets observed in the same campaign [Wescott *et al.*, 1996] and their speeds varied in a wide range from 27 to 153 km/s. In a later aircraft campaign EXL98, which included a low-light-level camera with a narrow band 427.8 nm filter, the 427.8 nm band of the first negative band system of  $N_2^+$  was clearly recorded from a starter, providing conclusive evidence that starters are partially ionized [Wescott *et al.*, 2001b].

The jets and starters observed in the Sprites94 campaign occurred in two very active thunderstorm cells with an unusually large flash rate of 200–300 flashes/min [Wescott *et al.*, 1995, 1996, 1998]. In close vicinity (15–50 km) of the events, the negative CG flash rate increased 1–2 s before the events and then decreased significantly in a 1–3 s time window following the events. The flash rate within 30 km from the jets was about 25% higher than the rate for the starters within the same distance, suggesting that more charge transfer to ground preceded the jets than the starters. It was also found that neither jets nor starters were associated with a particular CG flash [Wescott *et al.*, 1995, 1996, 1998].

Figure 17.3 shows a high-resolution image of a jet that occurred above a thunderstorm over the Indian Ocean, as reported in Wescott *et al.* [2001b]. The main column of the jet has an apparent diameter of  $\sim 400$  m at its base from 18 to 22 km altitude, and its diffuse top has a diameter of  $\sim 2$  km at 30 km,  $\sim 3$  km at 35 km, and  $\sim 4.5$  km at 40 km altitude, respectively. A few very faint narrow channels branch off from the main column of the jet, and their apparent widths vary from 50 to 100 m. They were considered to be streamers [Wescott *et al.*, 2001b] (see section 3.7 in Chapter 3 for discussion on streamers), but the width of a typical streamer at 30 km altitude is two to three orders of magnitude smaller according to streamer modeling results reported later [Liu and Pasko, 2004, 2006]. Pasko [2010]

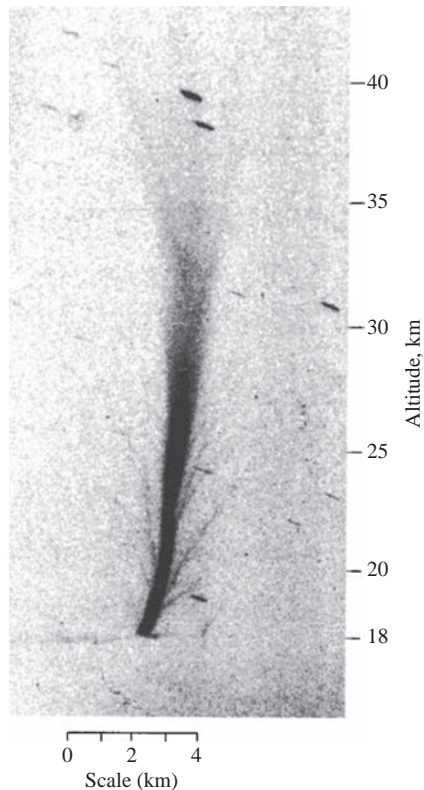


*Figure 17.3 Inverted black-and-white image of a blue jet above a large thunderstorm over the Indian Ocean, observed from St.-Denis, Réunion Island [Wescott et al., 2001b]. The exposure time of the image is 2 min, and the jet is about 145 km distant from the camera. The image is contrast adjusted to show the faint features. Reprinted with permission from the American Geophysical Union*

pointed out that those channels are likely to be produced by superposition and time-averaging of many streamers. The bright base of the jet in Figure 17.3 saturated the image, indicating that its brightness is at least 6.76 mega Rayleighs.

During the Severe Thunderstorm Electrification and Precipitation Study (STEPS) campaign conducted in summer 2000, 17 upward propagating optical flashes were observed over a small supercell-like storm above Kansas, the United States [Lyons et al., 2003a]. They were captured from a close distance of about 60 km by a low-light-level TV camera system with a GEN III intensifier. The durations of the events ranged from 33 to 136 ms, and their apparent vertical extent above the cloud tops was smaller than 1 km, with estimated speeds no more than 10 km/s. Compared to the starters reported in Wescott et al. [1996, 1998], they appeared to be brighter, more compact in shape, and more optically uniform [Lyons et al., 2003a]. The authors suggested that it is possible that they represent a different manifestation of the starters. During the same campaign, a jet was observed by a three-dimensional very high-frequency (VHF) lightning mapping array (LMA, see Rison et al. [1999]) that is efficient at detecting negative breakdown during

thunderstorms [Krehbiel *et al.*, 2008]. Although no optical images were recorded, this observation provided important data to understand the physical mechanism of jets. The jet occurred in a thunderstorm system with an inverted electrical structure, namely, the main negative cloud charge sitting above the main positive cloud charge. According to the LMA data, the jet was initiated midway between the upper negative charge and the positive screening charge at the upper cloud boundary, 10 s after an intracloud discharge selectively neutralized positive cloud charge in the volume right below the initiation location of the jet. The jet lasted for 120 ms and propagated 4 km upward to 13.5 km altitude, 2 km above the cloud top. Combined analysis of this observation and modeling results from a probabilistic lightning model led Krehbiel *et al.* [2008] to propose a unifying theory of how electrical discharges originating in thunderstorms escape from the cloud to form lightning, jets, etc., which is discussed in more detail in section 17.2.1.3.

Krehbiel *et al.* [2008]'s theory on how discharges originating inside thunderstorms escape from the cloud to form jets, starters, and lightning was supported by a recent observation of a starter by Edens [2011]. In contrast with the jet discussed in Krehbiel *et al.* [2008], the parent storm had a normal charge structure with upper positive cloud charge over midlevel cloud negative charge. The starter occurred during an NLDN (U.S. National Lightning Detection Network) negative CG flash of seven strokes. The LMA data showed that the starter originated as a bidirectional discharge at  $\sim 14$  km altitude between the upper positive charge region and negative screening charge at the cloud top. The positive discharge propagated upward, exited the top of the cloud at 15.2 km altitude, and terminated at 17 km. The part above the cloud was observed optically as the starter. The downward negative discharge extended into the positive charge region but the LMA sources associated with this discharge were only observed in a relatively localized volume, indicating only a small amount of positive cloud charge was tapped into by the negative discharge. The author suggested this was probably the reason why the starter did not evolve into a full-scale jet. The image of the starter showed that there appeared to be three diffuse streamer zones attached to lightning leader-like channels. It was concluded that both the upward leaders and streamers of the starter were of positive polarity based on the image and LMA data.

Chou *et al.* [2011] reported observations of 38 jets (37 jets/starters and 1 gigantic jet) over a small thunderstorm of  $\sim 100$  km diameter from a distance of  $\sim 400$  km. The instruments included a Watec low-light-level camera with a red band filter with a passband of 540–1000 nm. The recorded images show that significant red band emissions, presumably from the first positive band system of  $N_2$ , were produced by the jets.

The connection between jets/starters with lightning activities was further investigated by Suzuki *et al.* [2012]. Seventeen jets and 43 starters were observed in about 20 min by three low-light-level monochrome cameras and a high sensitivity color camera from a distance of 100 km. The parent storm was a small Japan summer storm with a size of  $185 \times 110$  km<sup>2</sup> at its fully developed stage. There were two convective cells, and the jets/starters occurred at the larger cell, when the cell top reached  $>16$  km altitude. This cell also generated most lightning activities. The lightning activities were monitored by a VHF/LF (low-frequency) lightning mapping system with a distance of 150–200 km between nearby sensors. At a separate site, extremely-low-frequency transients were recorded. Over a period of 4 hours, many CGs ( $>2800$  strikes) were detected, and 98.2% of them were negative CGs.

The durations of the jets varied between 30 and 450 ms, while the starters lasted shorter, with lifetimes varying from 30 to 150 ms. Analysis of the CG flashes within 5 s from the jets indicated that the lightning peak currents ranged from  $-80$  to  $10$ – $20$  kA with a  $-20$  kA peak for the peak current distribution. The charge moment changes within  $\pm 1$  s of jets/starters were on the order of  $-200$  to  $-100$  C km. Assuming that charge was removed from an altitude of 8 km, the corresponding charge transferred was about  $-12.5$  C to  $-25$  C. The authors also found that the CG and IC activities suddenly increased 1 s before the jets and then quickly decreased afterward, but although the CG activities exhibited the same pattern for the starter events, the IC flashes were very active within 1 s time window from the starters. In addition, the peak of the distribution of the time interval between two successive jets was 60–70 s, while the peak of the same distribution for the starters was smaller than 5 s. Given those differences in their connections with lightning discharges, *Suzuki et al.* [2012] speculated that jets and starters may not be the same phenomenon.

### 17.2.1.2 Gigantic jets

Like jets and starters, gigantic jets are also upward discharges originating in cloud tops but they reach a much higher altitude of 70–90 km [*Pasko et al.*, 2002; *Su et al.*, 2003; *Pasko*, 2003]. They electrically connect thundercloud tops with the lower ionosphere and are capable of rapidly transferring a large amount of charge between them [*Pasko et al.*, 2002; *Su et al.*, 2003; *Cummer et al.*, 2009]. The ISUAL global survey of TLEs indicates gigantic jets predominately occur above tropical storms over oceans and coasts [*Chen et al.*, 2008], but they are also observed above land [*van der Velde et al.*, 2007; *Chen et al.*, 2008] and winter storms [*van der Velde et al.*, 2010]. The altitude of the top of the parent cloud is typically about 15 km [*Pasko et al.*, 2002; *Su et al.*, 2003; *Cummer et al.*, 2009], but it can be as low as 6–7 km [*van der Velde et al.*, 2010]. Although gigantic jets predominately occur in tropical and subtropical regions, they have also been observed at latitudes as high as  $35.6$ – $42^\circ\text{N}$  [*van der Velde et al.*, 2010; *Yang and Feng*, 2012]. They are not associated with a particular CG flash but are connected to intracloud discharge activities [*Cummer et al.*, 2009; *Lu et al.*, 2011]. They may occur following sprites and are termed as secondary gigantic jets that extend from the cloud tops to the bases of sprites [*Lee et al.*, 2012], and the secondary gigantic jets may in turn trigger another sprite [*Lee et al.*, 2013]. Compared to other TLEs, they are extremely rare. However, a single storm can produce multiple gigantic jets [*Su et al.*, 2003; *Soula et al.*, 2011; *Huang et al.*, 2012].

Gigantic jets were first discovered in September 2001 over an oceanic thunderstorm, about 200 km northwest of the Arecibo Observatory, Puerto Rico [*Pasko et al.*, 2002]. The event lasted for  $\sim 800$  ms and was followed by an intense lightning flash in the underlying storm. Figure 17.4 shows selected image frames ( $\sim 33$  ms exposure time) of the gigantic jet that exhibited a tree-like structure. From frame 1 to frame 7, it developed relatively slowly, with speeds varying from  $0.5 \times 10^5$  to  $2.7 \times 10^5$  m/s, and reached an altitude of  $\sim 38$  km at frame 7. In the next video field (16.7 ms exposure time), the top of the gigantic jet reached 70 km altitude, indicating that the speed of the gigantic jet was at least  $\sim 2 \times 10^6$  m/s. The gigantic jet appeared to reach its full extent in frames 8 and 9, and then its luminosity gradually decayed. Rebrightening of the event occurred a few frames after frame 14. Sferics measurements indicated that negative charge was transferred



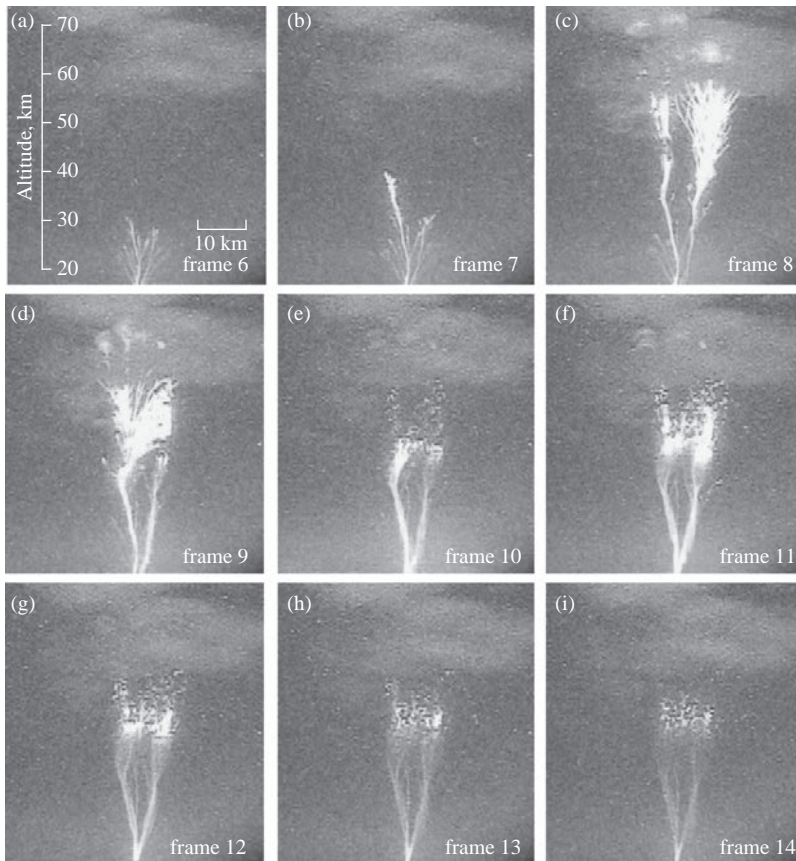


Figure 17.4 Selected frames of the first observation of gigantic jets [Pasko *et al.*, 2002]. Reprinted with permission from *Nature*

upward through the volume of the gigantic jet during the rebrightening, suggesting that the discharge responsible for the phenomenon was of negative polarity. The authors also concluded that the initial phase of the gigantic jet closely resembled the jets, as reported by *Wescott et al.* [1995, 1998, 2001b], in terms of the general geometrical shapes and propagation speeds, while the upper part of the gigantic jet exhibited the sprite-like features.

Observations of multiple gigantic jets above a single oceanic summer thunderstorm over the South China Sea near Luzon Island, the Philippines were reported by *Su et al.* [2003]. Five gigantic jets were recorded during a period of 12 min, and they appeared to be similar to the event reported by *Pasko et al.* [2002] in terms of the tree-like structure and propagation speeds. The jets emerged from the cloud at 16–18 km altitude and reached 86–91 km altitude. The authors found that the evolution of the gigantic jet might be divided into three distinct stages: leading jet, fully developed jet, and trailing jet. The leading jet describes the upward propagating stage of the event, the fully developed jet immediately follows the leading jet and connects the thundercloud top and the lower ionosphere, and the trailing jet is characterized by upward propagating luminous structures along the path established by the fully developed jet, which terminate at 60–68 km altitude, lower than the top of the fully developed jet. It was also found that the gigantic jets were not

associated with any particular CG flashes, and ELF (extremely low frequency) transients were found to be associated with four gigantic jet events, which showed that the jets were of negative polarity, i.e., transferring negative charge to the ionosphere. The inferred charge moment changes varied from 1000 to 2000 C km.

*van der Velde et al.* [2007] reported the first gigantic jet recorded over continental North America. The gigantic jet appeared to have a bright lower channel spanning from 14 to 50–59 km altitude, which developed into several dim branches that extended to 69–80 km altitude. The authors found the parent thunderstorm was a high-precipitation supercell cluster and the part of the supercell underlying the gigantic jet might have an inverted electrical structure. This thunderstorm region produced more +CG flashes than –CGs, and –CG activity practically ceased 4 min before the event, while +CG rate increased, reaching its maximum value in a 20 s time window from the gigantic jet. After the event, lightning activities of both polarities remained quiet for about 1.5 min.

Gigantic jets have also been caught from space by the ISUAL payload [*Chen et al.*, 2008]. Only 13 events were recorded from July 2004 to June 2007, which was about 60 times smaller than the number of sprites recorded during the same period of time. The majority (69%) of the events occurred over ocean and about 15% of the events occurred over either land or coast. Detailed analysis of a few selected ISUAL gigantic jets with photometric data of 0.05–0.5 ms resolution indicated that the speeds of the leading jets above  $\sim 40$  km altitude were as large as  $1.7\text{--}4.2 \times 10^7$  m/s and the speeds were increasing as the jets approached the lower ionosphere [*Kuo et al.*, 2009]. The upward propagating leading jets were seen by the ISUAL array photometer as a photometric peak propagating from the cloud top at  $\sim 20$  km altitude to the lower ionosphere at 90 km altitude. Within 1 ms from the moment that the jets made a contact with the bottom of the lower ionosphere, another photometric peak appeared and propagated downward from 50 km altitude to the cloud top. The authors suggested that the second peak was from a downward propagating current wave or potential wave. At the fully developed jet stage, the reduced electric field derived by considering the intensity ratios of different emission band systems varied from 3.3 to  $5.5E_k$ , which is similar to the magnitude of the electric field in the streamer head [*Kuo et al.*, 2005; *Liu et al.*, 2006], indicating that the fully developed gigantic jet consisted of streamers. Subsequent analysis of the ISUAL gigantic jets by *Chou et al.* [2010] showed that the ISUAL gigantic jets might be categorized into three types. Type I gigantic jets were negative discharges developing from cloud tops to the lower ionosphere, and their upward propagating stages were typically missed by the ISUAL instruments operated on a triggered mode. Type II gigantic jets began as jets and then developed into gigantic jets in about 110 ms. They generated very weak electromagnetic signals to be detected remotely, and the associated photometric features suggested that they were composed of positive streamers. The brightness of the fully developed type II gigantic jet was on average about 3.4 times smaller than that of the type I gigantic jet. Activities of jets and starters were often observed in the same general region before and after the type II gigantic jet. Type III gigantic jets were preceded by lightning and their brightness fell between types I and II. The associated electromagnetic signals were often contaminated by lightning, and it was therefore unable to determine the polarity of the gigantic jets.

That gigantic jets can result in a substantial charge transfer between the cloud tops and the ionosphere is clearly demonstrated by the work of *Cummer et al.* [2009],

who reported simultaneous low-light-level video images and low-frequency magnetic field measurements of a negative gigantic jet over a tropical storm. The gigantic jet developed from the cloud top at 14–14.5 km and reached 88 km altitude, and its optical signatures lasted for 400–500 ms. The total charge moment change of the gigantic jet was 10 800 C km, corresponding to a total charge transfer from the thunderstorm to the ionosphere of 144 C for an assumed channel length of 75 km. This is comparable in magnitude to the total charge transfer in large lightning flashes with significant continuing currents [Cummer *et al.*, 2009]. The authors suggested that in terms of charge transfer capability, gigantic jets can be viewed as upward lightning. In addition, a few fast pulses in the magnetic field waveform, which are consistent with typical in-cloud discharges, preceded the slow pulse associated with the current flowing through the gigantic jet. The authors suggested that the gigantic jet might be initiated as a negative leader developing in the parent thunderstorm. The connection between the in-cloud discharge activities with gigantic jets was investigated in more detail by using VHF lightning mapping networks [Lu *et al.*, 2011]. Two negative gigantic jets from two different storms were analyzed, and both of them occurred as part of flashes that began as normal intracloud lightning. The gigantic jets were developed from upward negative leaders that escaped from the cloud. Interestingly, one of the gigantic jets produced VHF sources at altitudes as high as 36 km, indicating that the gigantic jet might develop as a negative leader at that altitude.

First ground observation of gigantic jets in Europe was reported by *van der Velde et al.* [2010]. The gigantic jet occurred over a maritime winter thunderstorm only 6.5 km tall and its trailing jet was accompanied by a sprite that was triggered by a nearby CG lightning flash. The jet was of positive polarity and produced a charge moment change of 11 600 C km, and the ionization caused by the gigantic jet modified the conductivity of the D-region ionosphere, as suggested by the associated perturbations of VLF (very low frequency) signals propagating between a transmitter and a receiver.

Five negative gigantic jets were recorded, from a distance of ~50 km, with video and photograph cameras above an isolated tropical storm east of Reunion Island [Soula *et al.*, 2011]. The close range observations confirmed many features of gigantic jets from earlier studies including the tree-like structure and three development stages characterized as leading jet, fully developed jet, and trailing jet. It was also observed optically that all gigantic jets were accompanied by long, continuous cloud illumination, and they were preceded and followed by intermittent optical flashes from the thunderstorm. However, CG lightning was found to be inactive according to data from World Wide Lightning Location Network (WWLLN). The color images of the gigantic jets showed that the lower part (~20–40 km altitude) of the gigantic jets was bluish and there was a transition zone spanning between 40 and 65 km altitude that was dominated by red emission. The top sections of the events produced too little emission to be recorded by the photographic camera but were clearly visible in the video images.

### 17.2.1.3 Physical mechanisms of jets and gigantic jets

In this section, the origins and physical mechanisms of jets and gigantic jets are briefly discussed. Pasko [2008, 2010] conducted extensive reviews of the theories of jets and gigantic jets; readers are encouraged to refer to these two papers.

It has been established that conventional electrical breakdown processes of air, such as streamers and leaders, are the underlying processes driving jets and gigantic

jets. Immediately following the observations of jets during the Sprites94 campaign, streamer discharge theory was applied to explain the propagation and associated optical emissions of jets [Pasko *et al.*, 1996; Sukhorukov *et al.*, 1996]. However, the early theory considered jets as single streamer channels and was unable to explain the tree-like structure and blue-dominated spectrum of jets [Pasko, 2008, 2010]. The current theory of jets was based on the idea proposed by Petrov and Petrova [1999] that the development of jets is similar to the formation and propagation of ordinary lightning between thunderclouds and ground, and in particular, jets correspond qualitatively to the streamer zone of a leader (see section 3.15 in Chapter 3 for the concepts of streamer zone and leaders).

This idea was supported and further developed by the work of Pasko and George [2002], who reported a three-dimensional fractal modeling study of streamer coronas preceding a postulated leader channel. Their results indicated that if  $\sim 110\text{--}150$  C charge quickly accumulates ( $\sim 1$  s) in a volume with an effective radius of 3 km near the cloud top at  $\sim 15$  km altitude, the streamer coronas of a postulated leader above the charge can quickly fill a large volume of space above the thundercloud. In addition, although the initial volume filled by the streamers is determined by the thundercloud charge field, the streamer coronas self-consistently modify the electric field and develop into a unique conical shape. The streamer coronas obtained by their model are consistent with observed jets and starters in terms of their altitude extents, transverse sizes, and conical shapes, as reported in Wescott *et al.* [1995, 1996, 1998, 2001b]. It was also shown that starters are related to the initial phase of jets. Pasko and George [2002] also found that the intensity ratio of the combined red-and-green emission to the blue emission driven by a typical streamer head field agrees with the observed value reported by Wescott *et al.* [2001b], providing further support for the theory that jets are streamer coronas of a leader tip.

The necessity of the presence of leader channels in initiation and propagation of jets and gigantic jets was emphasized in theoretical work of Raizer *et al.* [2006, 2007]. They proposed that a jet is initiated as a bi-directional leader consisting of two leaders of opposite polarity. The upward positive leader escapes from the cloud and forms the trunk of the jet, and its streamer zone forms the branches appearing at the top of the jet. The downward negative leader propagates in thunderclouds to collect charge to support the propagation of the upward leader. The authors suggested that single streamer channels cannot support the propagation of jets because their conductivity lasts only for 1–10  $\mu\text{s}$  around 18 km altitude and is unable to supply the current flowing through the jets during their entire lifetime. The streamer zone instead consists of streamers produced at different times by the leader tip. The streamers have propagated through various distances, and each streamer head is followed by a short (about a few centimeters at ground), relatively conductive trail. In addition, the electric field in the streamer zone is maintained at the propagation threshold field of positive streamers (about 5 kV/cm at ground). Raizer *et al.* [2006, 2007] used a simplified streamer model to estimate the propagation threshold field of positive streamers at jet altitudes. They found that this field at altitudes  $>15$  km is about 35% smaller than the scaled ground value. Using the condition that the streamer zone field is equal to the streamer propagation threshold field, they found that in order for the streamers emitted at the leader tip to reach the lower ionosphere, the leader tip must reach altitudes of 23, 28, and 32 km for a leader potential of 100, 50, and 30 MV, respectively. According to the observation

reported by *Lu et al.* [2011], a VHF source, presumably associated with negative leader processes, was detected at 36 km altitude. It appears that the required leader tip altitude from the model of *Raizer et al.* [2006, 2007] is not unrealistic according to *Lu et al.* [2011]'s observation. However, it should be pointed out that the streamer zone structure and leader propagation are not well understood at present. Active research is currently carried out to understand the streamer-to-leader transition at the jet altitudes [*Riousset et al.*, 2010a; *da Silva and Pasko*, 2012].

Based on a combined analysis of LMA [*Rison et al.*, 1999] data of jets and fractal modeling [*Riousset et al.*, 2007] results, *Krehbiel et al.* [2008] proposed a unifying view of how electrical discharges originating inside thunderstorms escape to form cloud-to-ground (CG) lightning, bolt-from-the-blue discharges, jets, or gigantic jets. In order for the discharges to escape from a thundercloud, charge imbalance condition (either globally or locally) must be created in thunderstorms, for example, by intracloud or CG discharges. As to jets, they are believed to occur as a result of electrical discharges initiated between the upper storm charge and the screening charge at the cloud top. For normally electrified thunderstorms that are normally charged negatively (see the detailed discussion in *Riousset et al.* [2010b]), sudden negative CGs change their polarity and make it possible for the upward positive discharge originating between the upper positive charge layer and the screening charge to escape from the clouds. However, if the screening charge is mixed into the positive cloud charge, the chance for the positive discharge to start at the cloud top and escape from the cloud is largely reduced, and so the upward positive discharges occur much less frequently than negative CGs. For gigantic jets produced by normally electrified thunderstorms, the discharges are initiated as normal intracloud flashes between the main negative charge layer and positive charge layer. If the positive charge is depleted due to mixing with the screening charge, the upward negative discharge as part of the intracloud flash may continue to propagate upward upon reaching the cloud top and form gigantic jets. In this sense, gigantic jets share a similar scenario of development as more familiar "bolt-from-the-blue" lightning. The discharges leading to the bolt from the blue also originate inside the cloud but exit sideways and turn downward to ground, instead of exiting from the cloud top to form gigantic jets. According to this theory, the upward discharges producing the jets are of positive polarity while those forming gigantic jets are of negative polarity for normally electrified thunderstorms. For thunderstorms with inverted polarity, the polarities of the discharges leading to jets and gigantic jets are reversed. In addition, jets may be preceded by a CG or intracloud discharge by 5–10 s that creates favorable conditions to initiate discharges between the upper cloud charge and the screening charge and to help the discharges escape from the cloud.

The initiation theories of jets and gigantic jets proposed by *Krehbiel et al.* [2008] were later confirmed by a modeling study conducted by *Riousset et al.* [2010b], where the three-dimensional fractal model used by *Krehbiel et al.* [2008] was combined with a two-dimensional charge relaxation model to account for time-dependent conduction currents due to the conducting atmosphere and cloud screening charges. The results demonstrated the importance of the screening charges at cloud tops in jet and gigantic jet initiation. The accumulation of the screening charges facilitates initiation of jets, while effective mixing of these charges with the upper thundercloud charge may lead to the formation of gigantic jets. It was also found that prior occurrence of IC discharges can prevent the development of jets, and jets may be triggered when a CG lightning flash lowers

negative charge to ground, resulting in an enhanced field between the upper positive cloud charge and screening charge for normally electrified storms. It appears that the theories advanced by *Krehbiel et al.* [2008] and *Riousset et al.* [2010b] are generally consistent with the observational work on the discharge activities in the parent storms of jets and gigantic jets [*Wescott et al.*, 1996, 1998; *Cummer et al.*, 2009; *Edens*, 2011; *Lu et al.*, 2011; *Soula et al.*, 2011; *Suzuki et al.*, 2012].

In addition to thunderstorm charge reservoirs, electrical structures, and cloud top altitudes, the terminal altitudes of jets and gigantic jets are determined by other factors such as the middle and upper atmosphere conductivity profile. In the original discovery work of gigantic jets [*Pasko et al.*, 2002], the authors suggested that the relatively low night-time middle atmospheric conductivity typically observed in the tropical region may be favorable for upward discharges from thunderstorms to reach the lower ionosphere, because the corresponding longer Maxwellian relaxation times in that region of the atmosphere allow easier penetration of thundercloud electric fields. This is the result of the “moving capacitor plate” model of the electrodynamic of the middle atmosphere driven by fast charge redistribution at tropospheric altitudes [*Greifinger and Greifinger*, 1976; *Hale and Baginski*, 1987; *Pasko et al.*, 1997; *Pasko and George*, 2002]. According to this model, when considering the electrodynamic of the middle atmosphere in the context of jets and gigantic jets, an effective lower boundary of the ionosphere can be approximately set at the altitude where the Maxwellian relaxation time is equal to the characteristic timescale of the charge redistribution at tropospheric altitudes. Conduction current dominates above that altitude while displacement current dominates below. As a result, when the charge redistributing processes occur on a long timescale, the effective bottom boundary of the ionosphere is lowered. Therefore, upward discharges with a faster speed in a low conductivity atmosphere are more likely to reach higher altitudes.

### 17.2.2 Sprites

In contrast to jets and gigantic jets that appear to begin near cloud tops and propagate upward, sprites are initiated at the bottom boundary of the ionosphere and may span an altitude range of 40–90 km above thunderstorms [*Sentman et al.*, 1995; *Stenbaek-Nielsen et al.*, 2000; *Cummer et al.*, 2006a; *Pasko*, 2007, 2010; *Pasko et al.*, 2013]. They appear after intense CG lightning flashes that produce a temporary, strong quasi-electrostatic (QE) field above thunderclouds. They are predominately caused by +CGs [e.g., *Bocippio et al.*, 1995; *Williams*, 2006; *Williams et al.*, 2007, 2012], and only a very small fraction of observed sprites are caused by –CGs [*Barrington-Leigh et al.*, 2001; *Taylor et al.*, 2008; *Li et al.*, 2012]. The lateral extent of a sprite is typically 5–10 km, and, therefore, the total volume of the atmosphere affected by sprites can be as large as thousands of cubic kilometers. Their luminosity typically lasts for a few to tens of milliseconds, but the modifications of the atmospheric volume by sprites may last much longer [*Stenbaek-Nielsen et al.*, 2000]. In color images, sprites appear to be reddish above ~50 km altitude and transition to be bluish below [*Sentman et al.*, 1995]. Figure 17.5 shows a bright sprite captured with a digital, low-light-level, 1000 frame per second intensified CCD imager [*Stenbaek-Nielsen et al.*, 2000]. The event exhibited typical morphology of sprites including a few tens of kilometers vertical extent,

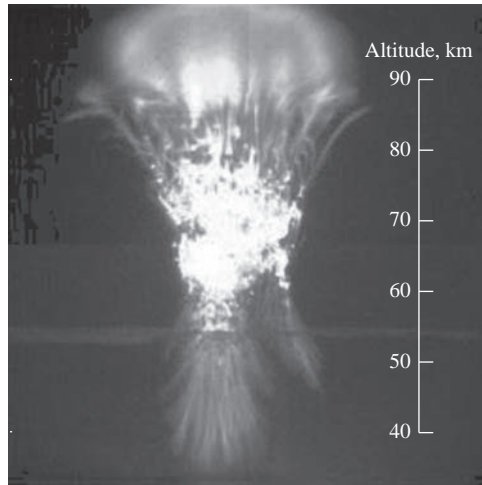


Figure 17.5 A large, bright sprite recorded on 18 August 1999 from the University of Wyoming Infrared Observatory [Stenbaek-Nielsen *et al.*, 2000; Pasko and Stenbaek-Nielsen, 2002]. Reprinted with permission from the American Geophysical Union

a diffuse glow at the top, tendril structures at the bottom, and a distinct transition region in the middle.

Halos or sprite halos are closely related to sprites, because they are also driven by the QE field of CG lightning [e.g., Barrington-Leigh *et al.*, 2001]. They normally appear within 1–2 ms after their parent CG and last for several milliseconds [e.g., Stenbaek-Nielsen *et al.*, 2000; Barrington-Leigh *et al.*, 2001; Cummer *et al.*, 2006a; Wescott *et al.*, 2001a; Newsome and Inan, 2010]. They may occur as an isolated event or may be preceded by elves (see section 17.2.3) and/or followed by sprites. In video images, they look like a relatively homogeneous glow that is centered around 78–80 km altitude with a horizontal extent of tens of kilometers and vertical thickness of several kilometers [Stenbaek-Nielsen *et al.*, 2000; Barrington-Leigh *et al.*, 2001; Wescott *et al.*, 2001a; Miyasato *et al.*, 2002; Moudry *et al.*, 2003; Gerken and Inan, 2003]. In comparison to sprites, which are predominantly caused by +CG, the occurrence of halos does not show a strong dependence on the polarity of CG. Negative CG that quickly transfers a large amount of charge from thunderclouds to the ground can produce halos as effectively as positive CG [Bering *et al.*, 2004; Williams, 2006; Frey *et al.*, 2007; Williams *et al.*, 2007; Taylor *et al.*, 2008; Newsome and Inan, 2010; Williams *et al.*, 2012; Li *et al.*, 2012].

### 17.2.2.1 Spatial structures and temporal dynamics of sprites

Complex fine structures in sprites, as shown in Figure 17.5, have been noted from early video observations [Sentman *et al.*, 1996; Taylor and Clark, 1996; Stanley *et al.*, 1996; Fukunishi *et al.*, 1996]. Pasko *et al.* [1998b] first proposed that the filamentary structures in sprites are the same electrical discharge process known as streamer discharges at atmospheric pressure. They also developed a theory to explain the vertical structuring of sprites, again as shown in Figure 17.5, by considering the interplay between electron attachment timescale, ambient dielectric

relaxation time, and streamer formation time at sprite altitudes [Pasko *et al.*, 1998b]. Since this work, a large body of experimental, observational, and modeling work has demonstrated that the streamer discharge theory is consistent with the temporal, spatial, and optical properties of the sprite filamentary structures [e.g., Raizer *et al.*, 1998; Stanley *et al.*, 1999; Gerken *et al.*, 2000; Gerken and Inan, 2002, 2003; Liu and Pasko, 2004, 2005; Marshall and Inan, 2005; Kuo *et al.*, 2005; Liu *et al.*, 2006; Liu and Pasko, 2006; Cummer *et al.*, 2006a; Ebert *et al.*, 2006; McHarg *et al.*, 2007; Stenbaek-Nielsen *et al.*, 2007; Chanrion and Neubert, 2008; Liu *et al.*, 2009a, 2009b; Li and Cummer, 2009; Luque and Ebert, 2009; Liu, 2010; Luque and Ebert, 2010; Ebert *et al.*, 2010; Liu *et al.*, 2011; Qin *et al.*, 2011, 2012a, 2012b; Li *et al.*, 2012; Kanmae *et al.*, 2012; Liu *et al.*, 2012; Kosar *et al.*, 2012; Qin *et al.*, 2013; Kosar *et al.*, 2013].

The streamer structures in sprites are clearly illustrated by Figure 17.6 that shows two images, with different spatial resolutions, of the same sprite event [Gerken *et al.*, 2000; Gerken and Inan, 2002, 2003]. The recording system consisted of an intensified narrow field of view (FOV) CCD camera and a bore-sighted wide FOV camera. In Figure 17.6, the left panel is the wide FOV image of the event, and the right panel is the narrow FOV image that corresponds to the small rectangle area in the center of the left panel. The right panel shows many streamer channels present in the sprite, the transverse spatial scales of which range from tens to a few hundreds of meters.

Due to the fast development of sprites, resolving their temporal dynamics requires an observation system with a high temporal resolution ( $<1$  ms). Stanley *et al.* [1999] obtained a temporal sequence ( $\sim 1$  ms) of images of a sprite event using a high-speed video system. The images show that the sprite was initiated at an altitude of  $\sim 75$  km and developed almost simultaneously upwards and downwards with an initial columniform shape. The speed of the vertical development of the column structure was measured to be  $>10^7$  m/s. The simultaneously downward and upward development of the column structure at the initial stage of sprite development was later confirmed by Stenbaek-Nielsen *et al.* [2000], McHarg *et al.* [2002], Moudry *et al.* [2002, 2003]. Observations of high-speed ( $>10^7$  m/s) development of sprites were also made by McHarg *et al.* [2002] using a multi-channel photometric system and by Moudry *et al.* [2002, 2003] using a high-speed

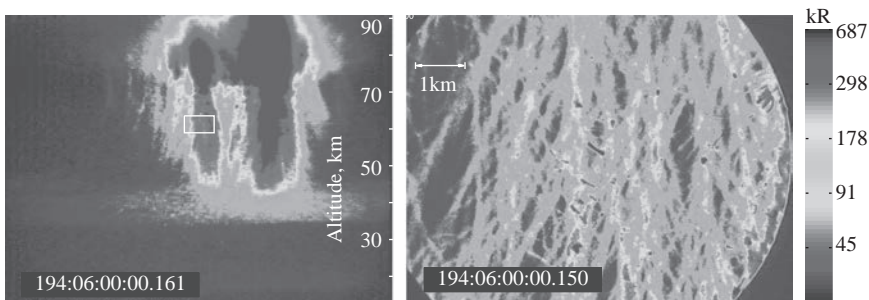


Figure 17.6 Telescopic imaging of sprites. Wide (left panel) and narrow (right panel) FOV images of a bright sprite event [Gerken *et al.*, 2000; Gerken and Inan, 2002, 2003]. Reprinted with permission from the American Geophysical Union



video system. High-speed telescopic imaging of sprites reported by *Marshall and Inan* [2005, 2006] confirmed the streamer structure of sprites and the high-speed downward and upward extension of streamers. Their results also demonstrated that the sprite streamer channel luminosity rarely persisted longer than 1–2 ms.

Recent high-speed video recordings made at  $\geq 5000$  fps have revealed detailed dynamics of sprite streamer initiation and propagation [*Cummer et al.*, 2006a; *McHarg et al.*, 2007; *Stenbaek-Nielsen et al.*, 2007; *Stenbaek-Nielsen and MchHarg*, 2008; *McHarg et al.*, 2010; *Stenbaek-Nielsen et al.*, 2010; *Stenbaek-Nielsen et al.*, 2013]. Those studies demonstrate that sprites caused by +CG are predominantly initiated with downward positive streamers that appear to originate either out of dark background or from the bottom of a halo. Upward negative streamers may appear later and seem to originate from structures forming near the initiation point of the positive streamers. Figure 17.7 shows an observation of a halo and a sprite made by *Cummer et al.* [2006a]. Sprite streamers were initiated at 73 km altitude from bright spots at the bottom of the halo that began 1.4 ms earlier. The downward streamers reached the terminal altitude of 40–45 km in about 2 ms, resulting in a propagation speed of as high as  $2 \times 10^7$  m/s. At the same time, the bright spots spawning the downward streamers expanded both downward and upward, forming bright columns, and upward streamers were later initiated from the bottom of the bright columns.

The temporal development of streamer tips was further resolved by the observations reported in *McHarg et al.* [2007], *Stenbaek-Nielsen et al.* [2007], *Stenbaek-Nielsen and MchHarg* [2008], *McHarg et al.* [2010], *Stenbaek-Nielsen et al.* [2010, 2013]. Those observations show that streamer heads accelerate, expand, and brighten, and streamer heads are the primary sources of the optical emission of sprites, confirming earlier streamer modeling results reported in *Liu and Pasko* [2004, 2005]. Figure 17.8 shows a downward propagating sprite streamer consisting of a bright streamer head and a relatively dark channel. The trajectory of the streamer head follows a parabolic curve indicating the accelerating

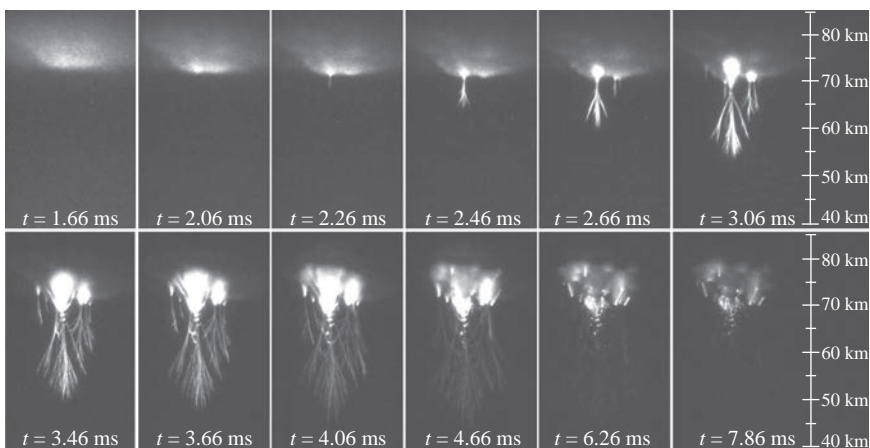


*Figure 17.7* High-speed images captured at 5000 fps of a halo and a sprite on 13 August 2005. Each image is labeled with its time from the lightning return stroke initiation [*Cummer et al.*, 2006a]. Reprinted with permission from the American Geophysical Union

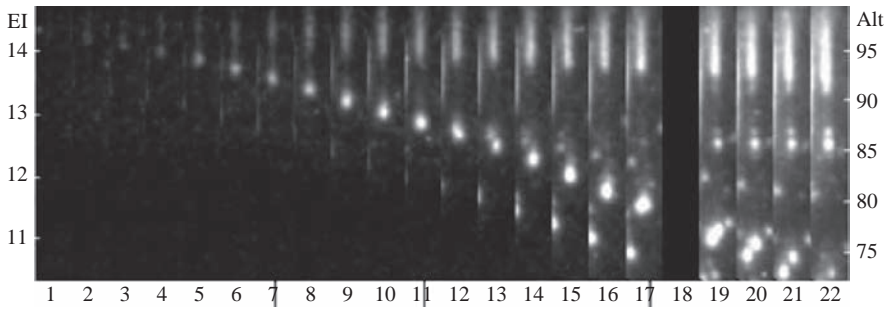


Figure 17.8 High-speed images ( $50 \mu\text{s}$  exposure time) of a downward sprite streamer [Stenbaek-Nielsen *et al.*, 2007]. Reprinted with permission from the American Geophysical Union

motion of the streamer. It can also be seen that the streamer head expands with increasing brightness.

Another interesting and not yet fully understood feature of sprites is the presence of apparently stationary glowing beads in the sprite body [Gerken and Inan, 2002, 2003; Moudry *et al.*, 2002, 2003; Marshall and Inan, 2005; Cummer *et al.*, 2006a], which last for  $\sim 100$  ms and generally exceed the optical lifetime of sprite streamers substantially [Marshall and Inan, 2005]. The observations presented by Cummer *et al.* [2006a] indicated that the tips of downward propagating sprite streamers were attracted to and, in some cases, collided with adjacent streamer channels. The points of streamer collision appeared to become long-persisting sprite beads [Cummer *et al.*, 2006a]. A theory to explain the formation of sprite beads was proposed by Luque and Gordillo-Vázquez [2011b] on the basis of their modeling results that sprite beads form as a result of sprite streamers passing through inhomogeneities of electron density in the upper atmosphere.

### 17.2.2.2 Sprite spectra

The spectrum of sprites has been a subject of study since the first color image was obtained in the Sprites94 campaign [Sentman *et al.*, 1995]. Mende *et al.* [1995] used an observation system consisting of a two-channel bore-sighted intensified CCD video camera system, with one channel as a spectrophotometer and the other channel as an imager to detect sprite events. The obtained results indicated that the sprite spectrum is dominated by the first positive band system of  $\text{N}_2$  ( $1\text{PN}_2$ ) emissions in the wavelength range of 430–850 nm [Mende *et al.*, 1995], which is consistent with the color image of sprites published in Sentman *et al.* [1995]. Around the same time, the sprite spectrum was also independently measured by Hampton *et al.* [1996]. Figure 17.9 shows a typical sprite spectrum obtained by Hampton *et al.* [1996], and all the features in the spectrum were identified to be from  $1\text{PN}_2$  [Hampton *et al.*, 1996].

Using a photometric system sensitive in the blue region of the visible light and with a high time resolution of 1.3 ms (the time resolutions of the systems used in the studies of Mende *et al.* [1995] and Hampton *et al.* [1996] were  $\sim 30$  ms), Armstrong *et al.* [1998] and Suszcynsky *et al.* [1998] demonstrated that the blue emissions of sprites are composed of the spectral lines from the second positive band system of  $\text{N}_2$  ( $2\text{PN}_2$ ) and the first negative band system of  $\text{N}_2^+$  ( $1\text{NN}_2^+$ ). The presence of the spectral signatures of  $2\text{PN}_2$  and  $1\text{NN}_2^+$  in the sprite spectrum was

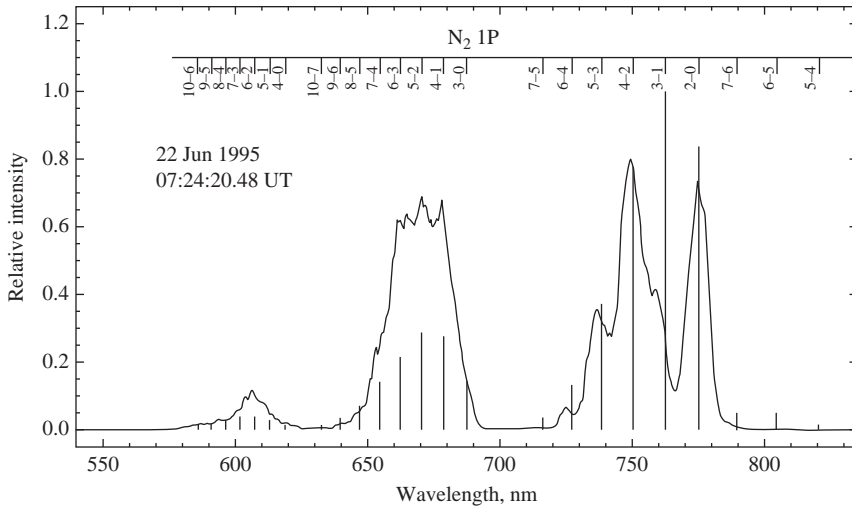


Figure 17.9 *Sprite spectrum reported by Hampton et al. [1996]. Reprinted with permission from the American Geophysical Union*

also documented by *Takahashi et al.* [2000] and *Morrill et al.* [2002]. Sprite spectra may also include features of Meinel bands of  $N_2^+$  in the red region of the visible light [*Morrill et al.*, 1998; *Bucselo et al.*, 2003]. The lack of OH spectral signatures in the sprite spectrum was noticed by *Sentman et al.* [2003], who reported simultaneous observations of mesospheric gravity waves and sprites.

Later, the ISUAL instrument on the FORMOSAT-2 satellite successfully detected the far ultraviolet (far-UV or FUV) emissions of the  $N_2$  Lyman–Birge–Hopfield (LBH) band system from sprites [*Mende et al.*, 2006]. The ISUAL instrument included a spectrophotometer with six individual photometers covering the spectral range from the far-UV to the near infrared, aiming to measure the spectral signatures of different emission band systems including the first positive and second positive band systems of  $N_2$ , the  $N_2$  LBH band system, and the first negative band system of  $N_2^+$  [*Chern et al.*, 2003; *Mende et al.*, 2005, 2006]. Figure 17.10 shows a temporal sequence of images (left column) of sprites and the corresponding spectrophotometer signatures (right column) recorded by the ISUAL spectrophotometer [*Mende et al.*, 2006]. Each panel in the right column corresponds to a photometer with the passband wavelength given next to the vertical axis of the panel. The vertical dashed lines in the top figure of the right column panel denote the time intervals corresponding to the images on the left. The second spectrophotometric peaks in the second and sixth time intervals are from sprites, following the peaks from lightning discharges.

Table 17.1 summarizes the four emission band systems that have been observed from sprites to date [*Liu and Pasko*, 2005; *Liu et al.*, 2006, 2009a]. The lifetimes and natural lifetimes of the excited states are calculated with and without the effects of quenching, respectively. For this calculation, the rate coefficients of the spontaneous transition and quenching are taken from *Vallance-Jones* [1974] except those for the  $N_2(a^1\Pi_g)$  states leading to the LBH emissions that were discussed in *Liu and Pasko* [2005], *Liu et al.* [2009a].

The possibility of detecting far-UV emissions of NO- $\gamma$  band system from space was discussed in *Liu and Pasko* [2007, 2010] on the basis of sprite streamer

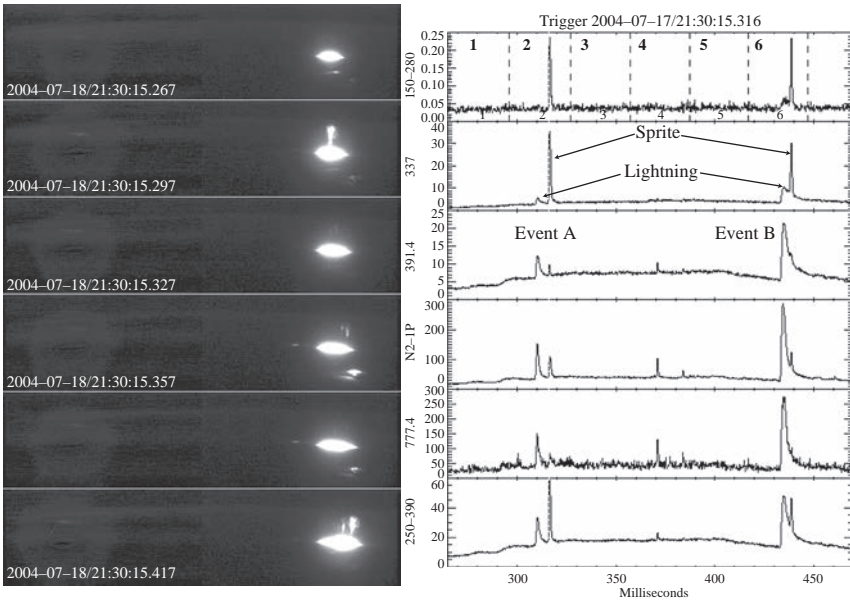


Figure 17.10 Images and spectrophotometer signatures of a sprite sequence recorded by the ISUAL instrument [Mende et al., 2006]

Table 17.1 Summary of emissions from sprites [Liu et al., 2006, 2009a]

Emission band system	Transition	Excitation threshold (eV)	Cross-section peak energy (eV)	Natural lifetime ( $\mu$ s)	Quenching altitude (km)	Lifetime at 70 km altitude ( $\mu$ s)
1PN <sub>2</sub>	$N_2(B^3\Pi_g) \rightarrow N_2(A^3\Sigma_u^+)$	$\sim 7.35$	12	5.9	$\sim 53$	5.4
2PN <sub>2</sub>	$N_2(C^3\Pi_u) \rightarrow N_2(B^3\Pi_g)$	$\sim 11$	14	0.05	$\sim 30$	0.05
LBH N <sub>2</sub>	$N_2(a^1\Pi_g) \rightarrow N_2(X^1\Sigma_g^+)$	$\sim 8.55$	17	55	$\sim 77$	14
1NN <sub>2</sub> <sup>+</sup>	$N_2^+(B^2\Sigma_u^+) \rightarrow N_2^+(X^3\Sigma_g^+)$	$\sim 18.8$	100	0.071	$\sim 48$	0.069

modeling results. The intensity of the far-UV emissions of the NO- $\gamma$  band system was found to be substantially weaker than that of the N<sub>2</sub> LBH system, but they may be detectable with a dedicated photometer with a passband of 240–260 nm [Liu and Pasko, 2007, 2010]. A recent comprehensive modeling work on sprite streamer chemistry and photochemistry conducted by Sentman et al. [2008] demonstrated that the sprite spectrum may also include long-lived signatures from weak atmospheric emissions OI 557.7 nm and O<sub>2</sub>( $b^1\Sigma_g^+ \rightarrow X^3\Sigma_g^-$ ) atmospheric airglow emissions, and very weak OH Meinel emissions and O<sub>2</sub>( $a^1\Delta_g \rightarrow X^3\Sigma_g^-$ ) infrared atmospheric emissions.

The results obtained from studying sprite spectra help understand the nature of sprites and the energetics of sprite electrons. For example, the presence of the 1NN<sub>2</sub><sup>+</sup> spectral components in the sprite spectrum indicates that ionization occurs in sprites. As another example, spectral analysis indicates that the streamer heads

are primary emission sources during the early stage of sprites [Liu and Pasko, 2004, 2005], which was later verified by high-speed video observations of sprite streamers [McHarg *et al.*, 2007; Stenbaek-Nielsen *et al.*, 2007], and the strength of the electric field and the mean energy of electrons in the streamer heads are about three times of the conventional breakdown field of air and 6.2–9.2 eV, respectively [Liu and Pasko, 2005; Kuo *et al.*, 2005; Liu *et al.*, 2006, 2009a; Celestin and Pasko, 2010].

### 17.2.2.3 Sprite charge, current and electromagnetic radiation

Measuring sprite charge, current, and electromagnetic radiation in the radio frequency range has also been undertaken since the early 1990s. A broad survey of ELF (0.3–3 kHz) and VLF (3–30 kHz) research on TLEs and causative lightning discharges was given by Inan *et al.* [2010], who discussed not only the electromagnetic radiation produced by TLEs but also the effects of the TLEs on the ELF/VLF signals propagating in the earth-ionosphere waveguide. Interested readers are referred to that paper for discussion on how ELF/VLF research has advanced our understanding of TLEs.

Cummer *et al.* [1998] first showed that the charge transfer and current flow in sprites resulted in detectable ELF signatures through simultaneous observations of ELF radio atmospheric waveforms and photometric measurements of sprite luminosity. They also found that no significant very low-frequency signature was associated with the ELF sferics, suggesting that the observed ELF transients were not likely to be produced by lightning discharges [Cummer *et al.*, 1998]. The ELF signatures of sprite currents were later confirmed by other measurements [Füllekrug and Reising, 1998; Reising *et al.*, 1999; Cummer and Stanley, 1999; Stanley *et al.*, 2000; Füllekrug *et al.*, 2001; Cummer *et al.*, 2006b]. The comparison between ELF data and high-speed sprite videos of submillisecond resolution showed that the ELF sprite current pulses appear to originate during the expansion of the upward streamers in sprites that typically forms the brightest stage of sprite development [Cummer and Stanley, 1999]. The unique sprite ELF signatures were used to detect daytime sprites by Stanley *et al.* [2000], who found that the parent lightning flashes of three daytime sprites transferred an exceptionally large amount of charge to ground compared to those causing night-time sprites. The sources of the ELF transients associated with sprites were triangulated to be electric currents in the mesosphere by using time arrival technique with a network of three magnetic field detectors [Füllekrug *et al.*, 2001].

Research work has also indicated that sprites are not always associated with ELF transients [Reising *et al.*, 1999; Füllekrug *et al.*, 2001; Price *et al.*, 2004] and that about 80% of ELF signatures produced by positive lightning are related to sprites [Füllekrug and Reising, 1998]. Cummer *et al.* [2006b] reported simultaneous observations of lightning and sprite optical emissions from the ISUAL instruments, which showed that the ELF pulses emitted by sprites were not associated with any visible low-altitude lightning process. ELF/VLF transients associated with sprites have also been detected by the instruments aboard the DEMETER satellite at 710 km altitude [Blecki *et al.*, 2009; Lefeuvre *et al.*, 2009].

Li and Cummer [2011] estimated electric charge in sprites and sprite streamers for the first time by conducting a coordinated analysis of the radio measurements of lightning and sprite currents, and high-speed videos of sprites. An example of the high-speed video dataset analyzed by Li and Cummer [2011] is

shown in Figure 17.7. For the events they analyzed, each sprite consisted of several sprite elements each of which contained a bright, generally vertical center core. Multiple positive streamers extended downward from this core, while a few upward negative streamers propagated with a significant horizontal component. Assuming that those upward negative streamers propagated in the direction of local electric field, *Li and Cummer* [2011] were able to derive the charge required in the sprite core to modify the background lightning electric field, which was found by full-wave FDTD (finite difference time domain method) simulation with the source lightning current derived from the radio measurements, so that the local electric field aligns with the propagation direction of the negative streamers. They found that individual sprite cores contain significant negative charge between  $-0.01$  and  $-0.03$  C that may be as much as 50% higher due to uncertainty in the assumed charge distribution along the core. An interesting result from such a large amount of charge distributed over the volume of the 100 m wide and 10 km long sprite core is that the maximum local electric field around it can reach a value close to the conventional breakdown threshold field. Assuming that the negative charge in the sprite core was deposited by the downward propagating positive streamers, they estimated that each downward positive streamer contains at least  $2-4 \times 10^{-3}$  C charge on average, which is consistent with the current measured for one bright sprite [*Li and Cummer*, 2011].

Charge rearrangement by sprites was recently investigated by *Hager et al.* [2012] using electric field data from Langmuir Electric Field Array, magnetic field data from the charge–moment network of Duke University, and high-speed video observations. For one bright sprite, a transient pulse, lasting for a few milliseconds, in the electric field and magnetic field waveforms matched the light intensity from the sprite in terms of shape and width, which was consistent with earlier studies by *Cummer et al.* [1998], *Stanley et al.* [2000]. According to *Hager et al.* [2012], the electric field pulse can be fitted by a sprite current that originates in the lower ionosphere and propagates downward. Assuming that the sprite current transported charge along a channel extending from 50 km to the ionosphere at an altitude of 100 km, the resulting charge transfer was 23.9 C for a transmission line model of the current with a speed of 0.25–0.55c. It was also found that the current was followed by impulsive electromagnetic radiation that may be similar to the “K-change” associated with lightning discharges.

*Pasko et al.* [1998a] first proposed a physical mechanism for the ELF radiation produced by sprite current. The model is based on the idea of the “moving capacitor plate” for estimating the altitude of the lower ionosphere boundary, which is briefly discussed in section 17.2.1.3. In the context of sprites, the cloud charge rearrangement due to the parent lightning generally takes place on a short timescale ( $\sim 1$  ms), so the altitude of the lower ionosphere boundary is set by the condition that the time elapsed from the lightning stroke is equal to the Maxwellian relaxation time at that altitude. The problem is then simplified as a cloud charge between two large plane conductors, and the induced charge on each conductor can be calculated, which turns out to be a function of the distance from the charge to the corresponding conductor. When the bottom boundary of the lower ionosphere is lowered, the resulting current can then be calculated by finding the changing rate of its induced charge. When modeling a sprite as a cylinder with elevated conductivity  $10^{-7}$  S/m, radius 50 km, and lower boundary that is defined by the “moving capacitor plate” model, *Pasko et al.* [1998a] found that the electric current flowing in the model sprite driven by the transient QE field of CG lightning can produce

significant electromagnetic radiation in the ELF frequency range, comparable in magnitude to that radiated by the causative lightning discharge. They also found that the ELF radiation depends weakly on the assumed values of the conductivity and radius of the model sprite.

The first theoretical study of electromagnetic radiation from sprite streamers was conducted by *Qin et al.* [2012c], who found that the spectrum of the radiation depends on the altitude of the sprite streamers. At 75 km altitude, sprites streamers produce electromagnetic radiation in the frequency range from 0 to  $\sim 3$  kHz, while at 40 km they can produce radiation with frequencies up to  $\sim 300$  kHz if they accelerate similarly as those observed at 75 km. They also speculated that the periodic branching of streamers might lead to a radiation spectrum enhancement in the VLF/LF range. They suggested that the radiation from sprite streamers could be partially responsible for the LF signals originating above thunderstorms, as reported in *Füllekrug et al.* [2010, 2011].

#### **17.2.2.4 Infrasound emissions from sprites**

Infrasonic (low-frequency acoustic waves) signals have also been identified to originate from sprites [*Liszka*, 2004; *Farges et al.*, 2005; *Liszka and Hobara*, 2006; *Farges and Blanc*, 2010]. *Liszka* [2004] first reported observations of possible infrasound signals from sprites that had a form of ascending chirps with frequencies varying between 1 and 6 Hz and lasted for 3–10 s. *Farges et al.* [2005] presented the first simultaneous observations of infrasound emissions and sprites. The infrasound spectrogram reported by them showed a chirp-like feature in the spectral band of 1–9 Hz, which is consistent with the observations of *Liszka* [2004], and the durations of the signals varied from several tenth to a few minutes. According to their ray-tracing modeling results, the sources of the infrasound signals were located between 60 and 80 km altitude, and had a transverse size similar to the optical width of the sprites. The sources of the observed infrasound signals were therefore unambiguously attributed to the sprites through close time correlation and matched source properties. They also found that the chirp-like dispersion is a result of propagation of the infrasound in the earth-thermosphere waveguide. More recent observations [*Liszka and Hobara*, 2006; *Farges and Blanc*, 2010] have confirmed the results of early studies. However, close range ( $< 100$  km) observations of infrasound signals that were possibly produced by sprites showed they exhibited the characteristics of inverted chirps, i.e., arrival of high frequencies before low frequencies [*Farges and Blanc*, 2010].

The observed infrasonic signatures are most likely produced by direct Ohmic heating of air caused by the electric current flowing in sprite structures [*de Larquier and Pasko*, 2010]. Temperature changes on the level of 0.2–2% were estimated to occur in sprite streamers [*Pasko et al.*, 1998b]. This is consistent with the analysis of energy budget of sprites by *Sentman et al.* [2003], which shows that the temperature change resulting from sprites is less than 0.5 K. Built on the electrostatic production model of infrasound from thunderclouds [*Pasko*, 2009], *de Larquier and Pasko* [2010] developed a two-dimensional FDTD model to study the propagation of the infrasound produced by a sprite in a realistic atmosphere. In their model, the sprite was represented by a series of isotropic sources arranged along vertical direction with transverse sizes that are consistent with the scaling laws (see section 17.3.1) of sprite streamers. Each source radiated a specific frequency content that varies from high to low frequencies as the altitude of the source

increases. Their results demonstrated that the inverted chirp infrasonic signals are consistent with general scaling of the diameters of sprites streamers, i.e., the sprite streamer diameters are inversely proportionally to the air density. According to their results, the smaller streamers at lower altitude radiate higher infrasonic frequencies that arrive first at the observational point on the ground, while the low-frequency components are delayed because they originate at lower air densities at higher altitudes. They also suggested that strong absorption of high-frequency infrasound components at high altitudes may also contribute to formation of inverted-chirp signals observed on the ground from a close range.

### 17.2.2.5 Sprite chemistry

The need to study the chemical effects of sprites and other TLEs was recognized right after the Sprites94 campaign, because a large atmospheric volume appears to be affected by TLEs and a unique pathway for the kinetics of atmospheric chemical species may be introduced by TLEs in the middle and upper atmosphere. This pathway differs from the normal chemical processes in the upper atmosphere initiated by photolysis of  $O_2$  and represents an example of the responses of the upper atmosphere upon impact by short, impulsive external forces [Sentman *et al.*, 2008]. An excellent example illustrating the chemical and electrical effects of sprites in the upper atmosphere is a high-speed video observation made by Stenbaek-Nielsen *et al.* [2000]. They reported that two sprites separated by  $\sim 50$  ms occurred in close proximity in space, and the second sprite appeared to reactivate the first one. An amazing aspect of this observation is that the 50 ms separation time is much longer than the optical lifetime of the first sprite ( $\sim 3\text{--}4$  ms). The reactivation of the first sprite implies that the modifications of the atmospheric volume by it lasted much longer than its optical lifetime [Stenbaek-Nielsen *et al.*, 2000].

Early kinetic modeling of sprite chemistry was attempted by Sentman *et al.* [2000] and Armstrong *et al.* [2001]. Later, Hiraki *et al.* [2004] evaluated the production of metastable oxygen  $O(^1D)$  in sprite halos due to electron impact dissociation of  $O_2$  and suggested that sprite halos could be a potential source of  $O(^1D)$  in the mesosphere at night. Enell *et al.* [2008] modeled the density changes of  $NO_x$  and  $O_3$  using a coupled ion-neutral model. Their results suggested although sprites are insignificant as a global source of  $NO_x$ , the local change of  $NO_x$  concentration may be significant. For extreme cases of very active sprite-producing thunderstorms, the  $NO_x$  concentration can be enhanced as much as five times the background concentration at 70 km altitude above the storms [Enell *et al.*, 2008]. The results of Enell *et al.* [2008] are generally consistent with the analysis conducted by Arnone *et al.* [2008, 2009], who analyzed MIPAS/GMTR satellite measurements of  $NO_2$  and concluded that there are no effects on a global scale but the  $NO_2$  enhancement at sprite altitudes can reach 10% of the ambient value. A contradictory result was reported by Rodger *et al.* [2008], who compared GOMOS satellite measurements of  $NO_2$  at TLE altitudes over lightning active regions and quiet regions but failed to find any significant difference on a regional scale.

The first comprehensive modeling study of plasma chemistry of sprites was recently reported by Sentman *et al.* [2008], where more than 80 chemical species and 800 chemical reactions were taken into consideration with a nonlinear plasma chemistry model. The study focused on the chemistry induced by the passage of a single sprite streamer through the mesosphere at 70 km altitude. The lifetimes of



various chemical species were obtained and the major loss and production mechanisms for each species were discussed. The representative important conclusions included that the lifetime of sprite electrons is about 1 s, the perturbation of NO density can be as large as 75% of the ambient background, and relatively large populations of long-lived ( $>1000$  s) metastable species are created by the streamer. By using the same model, *Sentman and Stenbaek-Nielsen* [2009] investigated the streamer channel plasma kinetics at a subbreakdown field of  $0.5E_k$  and found that the streamer channel field fixed at  $0.5E_k$  only has modest effects in the chemistry of the streamer channel plasma. Another recent modeling work solved balance equations for more than 75 chemical species together with Boltzmann's equation for electron energy distribution function (EEDF) in order to obtain accurate calculations of the rate coefficients of various electron-driven reactions [*Gordillo-Vázquez*, 2008]. It was found that the electron energy distribution rapidly reaches a steady state for the assumed streamer electric field, on a timescale much shorter than the lifetime of sprite streamers, suggesting that it is unnecessary to solve Boltzmann's equation when studying the chemical effects of sprite streamers. Model calculations for 63, 68, and 78 km altitudes indicated that the local enhancement of  $\text{NO}_x$  density varies with latitude and for 68 km altitude, the enhanced  $\text{NO}_x$  density is about ten times the ambient value [*Gordillo-Vázquez*, 2008]. This study also examined the vibrational kinetics of  $\text{N}_2$  and  $\text{CO}_2$  (see also *Gordillo-Vázquez* [2010]) in the plasma created by a sprite streamer and the effects of humidity (see also *Gordillo-Vázquez and Donko* [2009]).

In summary, a significant progress has been made in recent years in studying the chemistry induced by sprites in the upper atmosphere, and modeling studies have played a critical role in this achievement because it is generally difficult to measure the density perturbations of atmospheric species associated with sprites [*Arnone et al.*, 2008, 2009; *Rodger et al.*, 2008]. However, modeling studies of sprite streamer chemistry reported so far often simplify a streamer as one-dimensional electric field pulse, where important dynamical properties of the streamers are ignored, such as the acceleration and expansion of streamers and the time variation of the channel field. Self-consistent model to study sprite streamer chemistry has yet to be developed to confirm the results reported to date.

#### 17.2.2.6 Physical mechanism of sprites

A few recent review papers exist on this subject, including *Pasko* [2006, 2007, 2010], *Ebert et al.* [2010], and *Pasko et al.* [2013], and the readers are referred to those papers for detailed discussion. The following short discussion of the physical mechanism of sprites is partially adapted from *Pasko* [2006, 2007, 2010].

It was briefly mentioned at the beginning of this chapter that C.T.R. Wilson first predicted possible occurrences of large-scale electrical discharge phenomena above thunderclouds, which are currently called sprites. His idea can be illustrated by Figure 17.11. The thundercloud/lightning electric field in the upper atmosphere, which may be approximated as the field of a simple electric dipole consisting of a cloud charge and its image in the ground, decreases with altitude  $r$  as  $\sim r^{-3}$ , while the conventional breakdown threshold field  $E_k$  falls more rapidly with increasing altitude  $r$ , because it is proportional to air density that exponentially decreases with  $r$  (see Figure 17.2). As a result, "there will be a height above which the electric force due to the cloud exceeds the sparking limit" [*Wilson*, 1925], resulting in electrical discharges above thunderstorms.

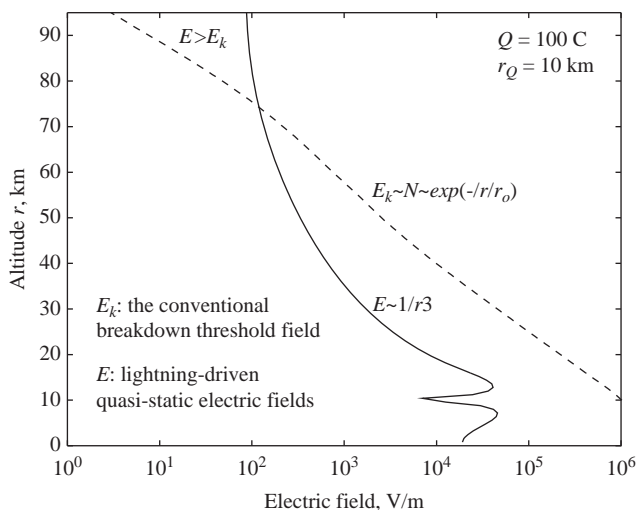


Figure 17.11 Physical mechanism of sprites [Wilson, 1925]: “While the electric force due to the thundercloud falls off rapidly as  $r$  increases, the electric force required to causing sparking (which for a given composition of the air is proportional to its density) falls off still more rapidly. Thus, if the electric moment of a cloud is not too small, there will be a height above which the electric force due to the cloud exceeds the sparking limit” [Pasko, 2007, 2010]. Reprinted with permission from the American Geophysical Union

It should be noted that due to the finite atmospheric conductivity above thunderclouds (see Figure 17.2), the dipole field configuration shown in Figure 17.11 is realized at mesospheric altitudes only during very transient time periods  $\sim 1\text{--}10$  ms after intense lightning discharges, in part defining similarly transient nature of the observed sprite phenomenon [Pasko *et al.*, 1997]. Figure 17.12 illustrates the mechanism for temporary penetration of the thundercloud/lightning electric fields to the higher-altitude regions. As the thundercloud charges slowly build up before a lightning discharge, high-altitude regions are shielded from the quasi-electrostatic fields of the thundercloud charges by the space charge induced in the conducting atmosphere at lower altitudes. The appearance of this shielding charge is a consequence of the vertical conductivity gradient of the atmosphere above thunderclouds. When one of the thundercloud charges (e.g., the positive charge shown in Figure 17.12) is quickly removed by a lightning discharge, the remaining charges of opposite sign above the thundercloud produce a large quasi-electrostatic field that appears at all altitudes above the thundercloud, and endures for a time equal to approximately (see related discussion in Pasko *et al.* [1997]) the local Maxwellian relaxation time at each altitude. This transient electric field leads to the heating of ambient electrons and the generation of ionization changes and optical emissions observed as sprites.

It should be emphasized that the simplified schematics, shown in Figure 17.12, are used to discuss the physical concept of penetration of the large electric field transient to mesospheric altitudes and by no means reflect the complexity of the charge distribution observed in thunderclouds. In cases of more realistic charge distributions in thunderclouds, which sometimes involve up to six charge layers in

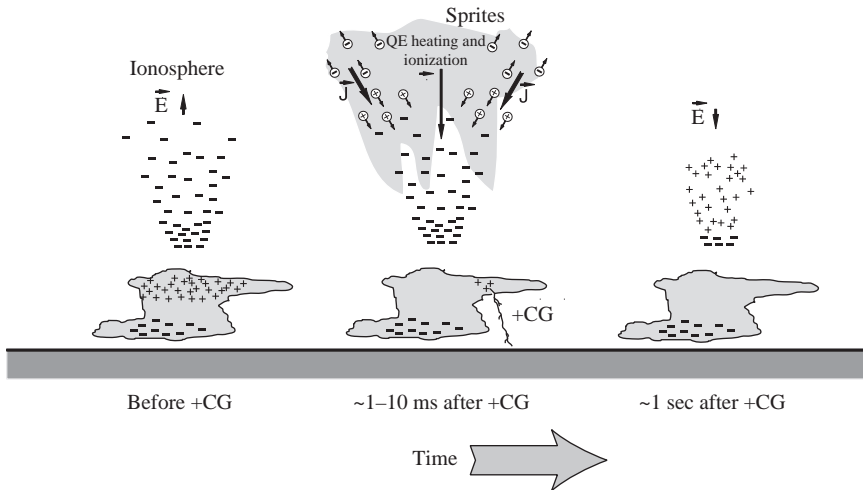


Figure 17.12 *Illustration of the mechanism of penetration of a large electric field to mesospheric altitudes following a positive cloud-to-ground (+CG) lightning discharge [Pasko et al., 1997]. Reprinted with permission from the American Geophysical Union*

the vertical direction [Marshall and Rust, 1993; Shepherd et al., 1996], each of the charge centers generates its own polarization charge in and above the thundercloud, and the resulting configuration of the electric field and charge density can be obtained by using the principle of superposition. This consideration is helpful in understanding the fact that the electric field appearing at mesospheric altitudes after the charge removal by a CG lightning discharge is defined mostly by the absolute value and altitude of the removed charge and is independent of the complexity of the charge configuration in the cloud. The charge removal can also be viewed as the “placement” of an identical amount of charge of opposite sign at the same location of the removed charge. Then the initial field above the cloud is simply the free space field due to the “newly placed” charge and its image in the ground that is assumed to be perfectly conducting, which makes it relatively straightforward to estimate the lightning electric field in the upper atmosphere. It should be noted that measurements indicated that most of the cloud charge removed by parent CG lightning of sprites may be located at relatively low altitudes between 2 and 5 km [Lyons et al., 2003b].

Detailed modeling results of the quasi-electrostatic field generated by CG lightning demonstrated that this field at mesospheric altitudes is almost directly proportional to the lightning charge moment change (i.e., charge removed by lightning times the altitude from which it is removed) [Pasko et al., 1997]. The charge moment change has since been established by experiments, observations, and simulations as the key parameter to measure the strength of lightning in terms of sprite production potential [Cummer and Inan, 1997; Hu et al., 2002; Cummer, 2003; Cummer and Lyons, 2005; Hu et al., 2007; Li et al., 2008, 2012; Cummer et al., 2013].

The physical mechanism of sprites discussed above has been tested by combined analysis of sprite video observations, remote measurements of lightning current moments, and FDTD simulations of lightning electromagnetic fields [Hu et al., 2007; Li et al., 2008; Gamerota et al., 2011; Li et al., 2012]. The results

indicated that for bright, short-delayed ( $<10\text{--}25$  ms from the parent lightning return stroke) sprites the simulated lightning electric field at the time of sprite initiation agrees within 20% with the threshold electric field for conventional breakdown. However, for long delayed sprite events and dimmer sprites, the measurement-inferred mesospheric electric field at sprite initiation can be as low as  $0.2\text{--}0.6E_k$  [Hu *et al.*, 2007; Li *et al.*, 2008; Gameraota *et al.*, 2011]. According to Li *et al.* [2008], about half of 83 sprites observed in a summer campaign in 2005 exhibited the characteristics of long-delayed sprites. The lightning discharges causing those delayed sprites all had continuing currents and slow (5–20 ms) intensifications (likely related to lightning M components) immediately preceded the sprite initiation. Sprite initiation in a lightning field below  $E_k$  is an outstanding problem in the research field of sprites. The recent studies to address this problem are reviewed in section 17.4.3.4.

### 17.2.3 *Elves*

Elves are fast expanding rings of optical emission in the lower ionosphere induced by lightning discharges. Similar to sprites, elves were theoretically predicted before their experimental documentation was published in scientific literature. Inan *et al.* [1991] theoretically studied the interaction between the electromagnetic radiation from lightning and the lower ionosphere at 90–95 km altitudes and found that ionospheric electrons can be heated by the lightning electromagnetic field pulse (EMP) to energies sufficient to excite and ionize neutral molecules. They suggested that the heating of ionospheric electrons by the lightning EMP pulse may result in a brief enhancement of airglow [Inan *et al.*, 1991], which is now called elves (an acronym for *Emissions of Light and VLF perturbations due to EMP Sources* [Fukunishi *et al.*, 1996]). Subsequent theoretical studies by Taranenko *et al.* [1992, 1993] investigated the optical emissions from elves in detail and concluded that the strongest emissions are from  $1\text{PN}_2$  and  $2\text{PN}_2$  band systems and weak emissions from  $\text{N}_2^+$  excited states are also produced. Self-consistent modeling of the EMP from a vertical lightning current and its interaction with the lower ionosphere conducted by Inan *et al.* [1996] indicated that the electromagnetic pulses generated by CG lightning return strokes with peak currents greater than 80 kA produce bright ( $>10^7$  R) elves and significant ionization changes at 80–95 km altitudes. The elve takes a form of a thin ( $\sim 30$  km) cylindrical shell that expands in time at speeds greater than the speed of light to radial distances up to  $\sim 250$  km. The time variations of the intensity pattern of the optical emissions that would be observed by an imager were studied for several representative-viewing geometries. When viewed from the limb, the time-integrated ( $>1$  ms) optical emissions from elves appear as a thin layer of lateral extent of 300–400 km; when viewed upward from aircraft altitudes at the horizontal location of the parent lightning, the time-integrated ( $>1$  ms) optical emissions appear as a ring with the maximum intensity located at radial distances between 40 and 110 km (see also Inan *et al.* [1997]; the minimum intensity at the center of the ring was attributed to the minimum in the radiated EMP intensity above the source lightning current); when viewed from a slanted direction on ground, the rapid expansion of the ring-shaped pattern of optical emissions results in apparent downward motion of elves. The lifetimes of the elves were estimated to be 300–500  $\mu\text{s}$ .

The first unambiguous observation (see Figure 17.13) of elves was made from space [Boeck *et al.*, 1992], which was described as a transient enhancement of the

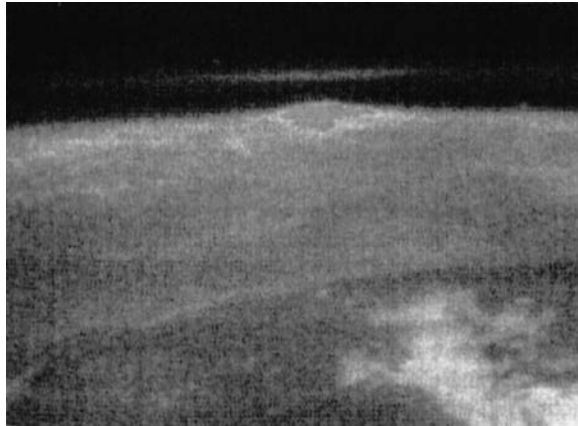


Figure 17.13 *Elve observed over the Caribbean from the Discovery Space Shuttle on 7 October 1990 [Boeck et al., 1992]. Reprinted with permission from the American Geophysical Union*

airglow layer ( $\sim 95$  km altitude) in coincidence with a lightning flash directly beneath it. The elve in Figure 17.13 appeared to be 10–20 km thick and 500 km wide, and its luminosity was about twice that of the background airglow [Boeck et al., 1992].

The first ground-based observations of elves were reported by *Fukunishi et al.* [1996]. The observations were made with a multichannel high-speed (15  $\mu$ s) photometer and image intensified CCD cameras from Yucca Ridge Field Station in Colorado. The elves were found to occur at 75–105 km altitudes, last for  $< 1$  ms, and span a horizontal region of 100–300 km. They appeared just after the onset of +CG lightning discharges and preceded the onset of sprites caused by the same lightning. *Inan et al.* [1997] reported high-speed photometric array (Fly’s Eye) data and low-light-level camera images of elves and compared them with modeling results obtained by a modified version of *Inan et al.* [1996]’s model. Their results demonstrated that the lightning EMP theory correctly explains the size, duration, rapid expansion, and optical intensity pattern of elves.

Observational data published later showed that elves can be produced by both +CG and –CG lightning strokes [Barrington-Leigh and Inan, 1999; Frey et al., 2005; Newsome and Inan, 2010]. Given that both elves and halos appear as brief diffuse glows in the lower ionosphere and can be triggered by both polarities of intense CG return strokes, it is generally difficult to capture them or differentiate one against the other with video recordings of standard TV frame rates [Barrington-Leigh and Inan, 1999; Barrington-Leigh et al., 2001; Newsome and Inan, 2010]. However, data from high-speed photometric arrays such as Fly’s Eye [Barrington-Leigh and Inan, 1999; Barrington-Leigh et al., 2001] and PIPER [Newsome and Inan, 2010] indicate that elves occur at a slightly higher altitude of  $\sim 90$  km, precede halos by 100–200  $\mu$ s, last for a shorter period of time ( $< 1$  ms for elves and  $< 2$  ms for halos), and have a much larger lateral extent. Newsome and Inan [2010] also reported observations of the so-called “elve doublets,” where pairs of elves seem to occur in rapid succession. The authors suggested that the elve doublets likely reflect that the EMP from the lightning return stroke has multiple peaks, perhaps resulting from the rise and fall of the return stroke current, as shown in *Inan et al.* [1996]’s modeling results.

According to space measurements by the ISUAL instruments, elves are the dominant type (about 81%) of the observed TLEs and 90% of them occur over ocean and coast regions [Mende *et al.*, 2005; Chen *et al.*, 2008]. The ISUAL measurements also indicated that the spectrum of elves consists of band systems of  $1\text{PN}_2$ ,  $2\text{PN}_2$ , and  $1\text{NN}_2^+$ , confirming the modeling results suggesting that ionization occurs in elves [Mende *et al.*, 2005; Kuo *et al.*, 2007]. In addition, far-UV emissions from  $\text{N}_2$  LBH band system has also been detected from elves [Mende *et al.*, 2005; Kuo *et al.*, 2007], which are normally difficult to be observed from ground because of severe attenuation by the dense atmosphere at lower altitudes [Mende *et al.*, 2005; Liu *et al.*, 2006; Kuo *et al.*, 2007]. The study performed by Kuo *et al.* [2007] also compared the elves observed by the ISUAL instruments with elve simulation results from an electromagnetic FDTD model. They found that the modeling results of elves produced by lightning return strokes agree well with the observed elves in terms of spatial-temporal evolution characteristics and brightness. In particular, the total photon counts of two ISUAL elves match with the model predictions when the peak currents of the parent CGs measured by NLDN are used as the inputs for the model. They also pointed out that the elves caught by the ISUAL instruments are mostly triggered by lightning currents greater than 80 kA because of high detection threshold setting and a long viewing distance ( $>2200$  km), and the elves produced by weaker lightning discharges may have therefore been missed by the ISUAL.

Recent three-dimensional FDTD modeling results presented by Marshall *et al.* [2010] and Marshall [2012] confirmed the doughnut-shaped optical emission pattern of elves and also showed that the pattern exhibits asymmetry if the Earth's magnetic field is taken into account. Marshall *et al.* [2010] also investigated the idea of lower ionospheric perturbations induced by successive horizontal in-cloud lightning discharges, as proposed by Marshall *et al.* [2008], and concluded that those discharges may produce observable optical emission with a different intensity pattern from normal elves, which is peaked at the center. Marshall [2012] also investigated how the rise and fall stages of the lightning return stroke current waveform produce elve doublets, as observed by PIPER [Newsome and Inan, 2010], and concluded that every elve is a doublet and the time separation and relative magnitudes between the two peaks of the lightning EMP determine whether it is observed as a doublet.

### 17.3 Elementary discharge processes

TLEs are high-altitude electrical discharges, and they are driven by the same elementary discharge processes as electrical discharges in air at high pressures. A detailed discussion of the elementary discharge processes such as electron drift, electron diffusion, electron impact ionization, two-body dissociative attachment, three-body attachment, electron detachment, photoionization, and recombination is presented in Chapter 3. However, as air density is significantly reduced at TLE altitudes, their relative roles in electrical discharges at TLE altitudes might be different. In general, three-body processes become less important because their reaction rates decrease faster than two-body processes as altitude increases. This may lead to striking differences in the dynamics of the electrical discharges at different altitudes. In this section, similarity laws of gas discharge physics are reviewed first, and then an example is presented to illustrate how the roles of elementary discharge processes may differ at different pressures.

### 17.3.1 Similarity laws

In gas discharge physics, the physical parameters of interest typically depend on a combination of two independent variables. For example, the coefficient for electron impact ionization discussed in section 3.3.1 of Chapter 3 is expressed as  $\frac{\alpha}{p} = f\left(\frac{E}{p}\right)$ , where  $\alpha$  is the ionization coefficient,  $p$  is the pressure, and  $E$  is the magnitude of electric field. Such expressions describing the relationship between combinations of the physical parameters of gas discharges are called similarity laws, because they relate the values of the parameters at different pressures or gas densities [Raizer, 1991, p. 11]. From  $\frac{\alpha}{p} = f\left(\frac{E}{p}\right)$ , it is clear that for a given  $E/p$ , the value of  $\alpha$  at a reduced pressure is reduced by the same factor from its ground value as the pressure. Therefore, similarity laws represent a useful tool in gas discharge physics, since they can be used with known properties of electrical discharges at one pressure to deduce the properties of discharges at other pressures of interest, at which experimental studies may not be feasible or even possible.

With the similarity laws of gas discharge parameters, similar discharges at different pressures may be obtained when certain conditions are satisfied [Achat *et al.*, 1992; Pasko *et al.*, 1998b; Liu and Pasko, 2004; Pasko, 2006; Liu and Pasko, 2006; Mesyats, 2006; Ebert *et al.*, 2006; Bolotov *et al.*, 2010]. Consider that an electron is placed in a homogeneous electric field  $E$  between two electrodes with a gap size  $d$ , the increase in energy of the electron is a function of the product  $E\lambda$ , where  $\lambda$  is the mean free path of electrons and is inversely proportional to the gas number density  $N$  or pressure  $p$ . In order to obtain similar discharges at different pressures, the product  $E\lambda$  and the mean free path number  $d/\lambda$  must be kept constant, or equivalently, the scaling factors  $E/p$  and  $pd$  must be kept constant [Achat *et al.*, 1992; Pasko, 2006; Liu and Pasko, 2006; Mesyats, 2006; Bolotov *et al.*, 2010]. In addition, only when a certain set of elementary processes, which are termed “allowed processes” in Mesyats [2006], occur in the discharges, similarity may be realized between the discharges at different pressures. The allowed processes are summarized in Mesyats [2006], which include electron impact ionization, electron attachment and detachment (from collisions between negative ions and neutral molecules), drift and diffusion, secondary processes at the electrodes such as electron emission due to ion bombardment and photoemission, the Penning effect, etc. When the discharges exhibit similarity at different pressures, it means that the physical quantities of the discharges  $G(\vec{r}, t)$  at similar spatiotemporal points related by linear transformations

$$\vec{r}' = s\vec{r}, t' = st$$

are also related by a linear transformation

$$G(\vec{r}', t') = s^{\gamma[G]} G(\vec{r}, t)$$

where  $s$  is a constant (e.g.,  $\frac{N_0}{N}$  in Table 17.2) and  $\gamma[G]$  is called the similarity factor [Bolotov *et al.*, 2010].

Pasko [2006] formulated many useful similarity relations for various physical quantities of gas discharges, which are summarized in Table 17.2. Note that neutral density  $N$  and pressure  $p$  are used interchangeably because a constant air temperature can be assumed for earth’s atmosphere. The physical quantities with the “0” subscript correspond to their reference values at ground pressure. Similar relations

Table 17.2 Similarity relations for various physical quantities of gas discharges [Pasko, 2006]

Length (i.e., mean free path, discharge tube length or diameter, streamer radius, etc.)	$L = L_0 \frac{N_0}{N}$
Time (i.e., between collisions, dielectric relaxation, two-body attachment, etc.)	$\tau = \tau_0 \frac{N_0}{N}$
Velocity does not scale (i.e., electron or ion drift velocity, streamer velocity, etc.)	$v = \frac{L}{\tau} = \text{const}$
Temperature and energy of electrons and ions do not scale, remaining the same in similar discharges	$T = \text{const}$ $\epsilon = \text{const}$
Electric field (i.e., in streamer head, in streamer body, etc.)	$E = E_0 \frac{N}{N_0}$
Mobility (electrons and ions)	$\mu = \frac{v}{E} = \mu_0 \frac{N_0}{N}$
The diffusion coefficient (electrons and ions)	$D = D_0 \frac{N_0}{N}$
Plasma and charge density (i.e., electron and ion densities in the streamer body, etc.)	$n = n_0 \frac{N^2}{N_0^2}$
Charge (i.e., in the streamer head)	$Q = Q_0 \frac{N_0}{N}$
The ionization and two-body attachment frequency	$\nu = \frac{1}{\tau} = \nu_0 \frac{N}{N_0}$
Conductivity	$\sigma = en\mu = \sigma_0 \frac{N}{N_0}$
Current density	$J = env = J_0 \frac{N^2}{N_0^2}$
Current	$I = JL^2 = \text{const}$

are also given in *Mesyats* [2006]. In the context of TLEs, *Pasko et al.* [1998b] first derived the similarity laws of streamer discharges at different pressures in the atmosphere. The similarity laws of streamer discharges are also implied by the dimensionless model of streamer discharges discussed in *Ebert et al.* [2006].

The processes that may result in violation of similarity laws are called “forbidden processes” [*Mesyats*, 2006]. Examples of those processes are electron three-body attachment, stepwise ionization, recombination, thermal ionization of gas, joule heating, etc. [*Pasko*, 2006; *Mesyats*, 2006]. The photoionization process involved in the propagation of streamers also does not obey similarity due to quenching of the excited states leading to the photoionizing radiation [*Liu and Pasko*, 2004; *Pasko*, 2006; *Liu and Pasko*, 2006; *Mesyats*, 2006; *Bolotov et al.*, 2010].

### 17.3.2 Electron density growth at subbreakdown condition at high altitudes

It is well known that the applied electric field must exceed a threshold value to initiate an electrical discharge at high pressure. This field is known as the conventional breakdown threshold field  $E_k$ , which is defined by the equality of the ionization and dissociative attachment coefficients [e.g., *Raizer*, 1991, p. 135]. When the applied field is greater than  $E_k$ , cumulative ionization of air becomes possible through a variety of discharge processes (see Chapter 3). The dissociative attachment process converts electrons to  $O^-$  ions (with an electron affinity of 1.46 eV) that are relatively unstable and may be converted back to electrons through the detachment process:  $O^- + N_2 \rightarrow e + N_2O$  [*Rayment and Moruzzi*, 1978; *Luque and Gordillo-Vázquez*, 2011a; *Liu*, 2012; *Neubert and Chanrion*, 2013].  $O^-$  ions may also be converted through a three-body process to more stable  $O_3^-$  ions:  $O^- + O_2 + M \rightarrow O_3^- + M$ . At high pressure, the three-body process is much faster than the detachment process, so it is the dominant sink for  $O^-$  ions; however, at



low pressure, the detachment process dominates, providing an additional source for free electrons [Luque and Gordillo-Vázquez, 2011a; Liu, 2012; Neubert and Chanrion, 2013]. In addition, at high pressure, the three-body attachment process:  $e + O_2 + M \rightarrow O_2^- + M$  is the dominant sink for electrons when electric field is about a factor of 2 smaller than  $E_k$ , which produces stable ions  $O_2^-$ , so even fewer  $O^-$  ions are produced. Because  $O^-$  ions are mainly converted back to electrons at low pressure, it becomes possible that electron density may increase even when the applied field is below  $E_k$ , as long as electron impact ionization is effective and other sink processes for electrons and  $O^-$  ions such as recombination are negligible.

A simple zero-dimensional ionization model can be formulated to illustrate how electron density may increase in a subbreakdown electric field at high altitudes. Considering the density changes of electrons and  $O^-$  ions under the influence of a constant electric field, the governing equations after ignoring slow processes such as recombination and three-body processes are

$$\frac{dn_e}{dt} = (v_i - v_a)n_e + v_d n_{O^-}$$

$$\frac{dn_{O^-}}{dt} = v_a n_e - v_d n_{O^-}$$

where  $n_e$  and  $n_{O^-}$  are the densities of electrons and  $O^-$  ions, respectively;  $v_i$ ,  $v_a$ , and  $v_d$  are the corresponding reaction frequencies of the ionization, attachment, and detachment. For constant electric field,  $v_i$ ,  $v_a$  and  $v_d$  are constant, and the two linear ordinary differential equations can be solved analytically. Assuming that the initial densities of electrons and  $O^-$  ions are  $n_e^0$  and  $0 \text{ m}^{-3}$ , respectively, the solution is

$$\begin{bmatrix} n_e \\ n_{O^-} \end{bmatrix} = \frac{n_e^0}{\bar{v}} \left\{ \begin{bmatrix} v_d + v_+ \\ v_a \end{bmatrix} \exp(v_+ t) - \begin{bmatrix} v_d + v_- \\ v_a \end{bmatrix} \exp(v_- t) \right\}$$

where  $\bar{v} = \sqrt{(v_i - v_d - v_a)^2 + 4v_i v_d}$  and  $v_{\pm} = 0.5[(v_i - v_d - v_a) \pm \bar{v}]$ . Figure 17.14 shows the time variation of the densities at various normalized electric fields  $E/E_k$  at 80 km altitude given an initial electron density of  $10^6 \text{ m}^{-3}$ . The electron density decreases initially and then either stays constant for lower field cases:  $0.17$  and  $0.33E_k$  or increases for other cases in the time window of 0–100 ms. The initial decrease is caused by the second term on the right hand of the solution while the increase by the first term. It should be emphasized that even when  $E = 0.67E_k$  a considerable increase in the electron density can be reached in a time period of 100 ms. In addition, changing  $n_e^0$  only results in vertical shifting of the curves in the figure while the shapes of the curves are preserved according to the solution.

It is also illustrative to consider the dependence of the growth rates  $v_{\pm}$  on the reduced electric field, which is shown in an air density independent form in Figure 17.15, where electron impact ionization and two-body attachment frequencies are also shown for comparison [Liu, 2012]. Note that  $|v_-|$  is plotted here and the corresponding exponential term in the solution only contributes initially for the ionization change. In the altitude range of 75–90 km,  $N_0/N$  varies from  $5 \times 10^4$  to  $5 \times 10^5$  and the reduced field must be greater than 70–80 Td, i.e.,  $E/E_k > 0.6$ – $0.7$ , to have a noticeable increase in electron density in several to tens milliseconds.

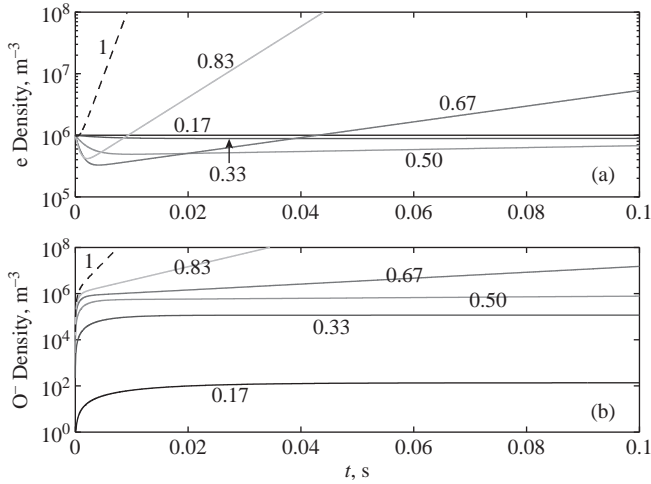


Figure 17.14 Density growth of (a) electrons and (b)  $\text{O}^-$  ions at constant electric field from a simple ionization model. The number labeling each curve is the value of  $E/E_k$  [Liu, 2012]. Reprinted with permission from the American Geophysical Union

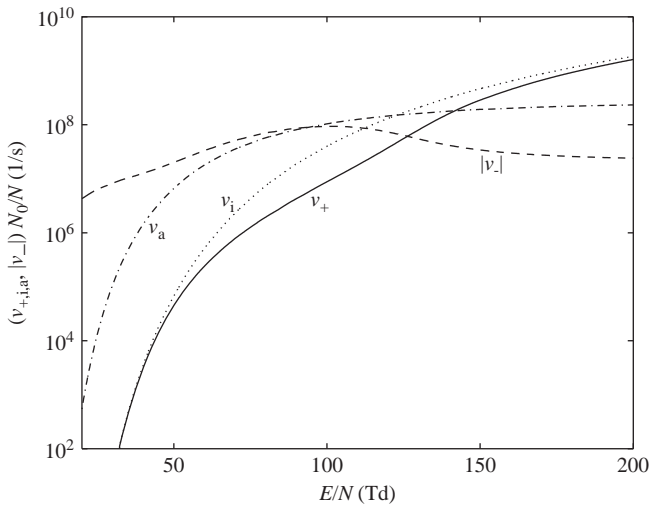


Figure 17.15 Comparison of  $v_{\pm}$  with electron impact ionization frequency  $v_i$  and two-body attachment frequency  $v_a$  in air [Liu, 2012]. Reprinted with permission from the American Geophysical Union

## 17.4 Modeling sprites and sprite streamers

### 17.4.1 Introduction

The dynamics of the electrical discharges responsible for TLEs may be described with plasma fluid equations that represent the first few moments of the Boltzmann equation [e.g., Guo and Wu, 1993]. The coefficients of the fluid equations are normally assumed to be a function of local reduced electric field  $E/N$ , where  $E$  is

the electric field magnitude and  $N$  is the air neutral density. This implies that the equilibrium electron distribution function is achieved instantaneously in time in response to the applied local electric field  $E$ . This assumption is justified as long as the relaxation times of the mean energy and momentum of the electron distribution are substantially smaller than the characteristic timescale of electric field variation. In particular, at ground pressure the energy relaxation timescales are on the order of 10 and 1 ps for typical electric field magnitudes in the streamer body and streamer head, respectively [Guo and Wu, 1993; Vitello *et al.*, 1993]. The local field approximation is therefore valid on typical timescales of streamer development at ground pressure, which are usually measured in nanoseconds. It should be noted that the variations of parameters of streamer plasmas due to the large space and time derivatives of the reduced electric field and electron density near the streamer head may introduce measurable corrections to the streamer dynamics [Naidis, 1997]. However, from the point of view of practical accuracy, the local field approach provides a satisfactory representation of the streamer characteristics [Naidis, 1997]. The 1–10 ps, scaled ( $\sim 1/N$ ) with atmospheric density, corresponds to 0.07–0.7 and 15–150 ns at altitudes 30 and 70 km, respectively. The validity of the local field approximation therefore remains in force for sprite streamers developing on timescales of hundreds of nanoseconds, and tens of microseconds at altitudes 30 and 70 km, respectively.

#### 17.4.1.1 Coefficients of plasma fluid equations

To model sprites and sprite streamers with plasma fluid equations, the field dependences of various coefficients need to be known. They have been either measured from experiments [e.g., Dutton, 1975; Gallagher *et al.*, 1983; Davies, 1983; Lowke, 1992; Morrow and Lowke, 1997; Petrovic *et al.*, 2007] or derived from the solution to the Boltzmann equation [e.g., Hagelaar and Pitchford, 2005; Moss *et al.*, 2006; Petrovic *et al.*, 2007]. Significant quantitative differences in the coefficients exist between different sources, and the modeling results of characteristics of the discharges using different coefficient sources show certain variability. However, the principle properties of sprites and sprite streamers found from modeling work are, in general, consistent when different sources of coefficients are used [Liu and Pasko, 2004].

In our modeling work, we typically use the coefficients from Hagelaar and Pitchford [2005] and Moss *et al.* [2006]. In Hagelaar and Pitchford [2005], the two-term approximation with Legendre polynomials to the Boltzmann equation was numerically solved, while in Moss *et al.* [2006], Monte Carlo model was used to follow electron dynamics in air under the influence of an applied electric field. The derived coefficients from those two studies agree in a wide range of electric field around  $E_k$ , but they may differ significantly from each other and also experimental measurements for very low fields that are typically unimportant for modeling sprites and sprite streamers. Hagelaar and Pitchford [2005] also provided a very useful software tool, BOLSIG+, to calculate the coefficients for fluid models, which can be freely downloaded at <http://www.bolsig.laplace.univ-tlse.fr>. A convenient MATLAB function resulting from the work of Moss *et al.* [2006] to find the coefficients of the most important processes for sprites and sprite streamers is available at <http://pasko.ee.psu.edu/air/>. The coefficients as functions of the reduced electric field can then be represented as a lookup table for fast model execution when solving the fluid equations to simulate the discharges.

### 17.4.2 Large-scale modeling of sprites/sprite halos

To reduce the complexity of the problem and improve simulation efficiency, an axisymmetric model is commonly used to simulate the dynamics of sprites/sprite halos. In such a model, the lower ionosphere is assumed to be axisymmetric, and simulation is initialized by introducing an axisymmetric, time-dependent charge distribution centered on the symmetry axis to model the charge deposited or removed by CG lightning flashes.

#### 17.4.2.1 Model equations

The dynamics of sprites/sprite halos can be described with drift–diffusion equations of charged particles and Poisson’s equation [Liu, 2012]:

$$\frac{\partial n_i}{\partial t} + \nabla \cdot \vec{J}_i = S_i - L_i$$

$$\nabla^2 \phi = -\frac{\rho}{\epsilon_0}$$

where  $n_i$  is the density of the  $i$ th charged species,  $\vec{J}_i$  the flux density,  $S_i$  and  $L_i$  the source and sink for the  $i$ th species;  $\phi$  is electric potential and electric field  $\vec{E} = -\nabla\phi$ ,  $\rho$  the charge density, and  $\epsilon_0$  the permittivity of free space. The flux density  $\vec{J}_i$  is defined as  $(n_i\vec{v}_i - D_i\nabla n_i)$ , where  $\vec{v}_i = \mu_i\vec{E}$  is the drift velocity,  $\mu_i$  the mobility, and  $D_i$  the diffusion coefficient. The terms  $S_i$  and  $L_i$  account for the change of the density due to ionization, attachment, recombination, and detachment, which are discussed next.

#### 17.4.2.2 Model species and reactions

Electrical discharges in air may produce many charged species in the middle and upper atmosphere, and tens of ion species and hundreds of reactions may be needed to fully understand the chemical kinetics involved in sprites/sprite halos [Sentman *et al.*, 2008; Gordillo-Vázquez, 2008; Sentman and Stenbaek-Nielsen, 2009; Liu, 2012]. However, it is computationally unrealistic to take into account such a large number of charged species and reactions for a two-dimensional model, and the ion chemistry is normally simplified in order to be able to simulate the principle physics and chemistry of sprites/sprite halos in a reasonable amount of computation time. In general, simple ions are produced by electron impact reactions during the active stage of the discharge process and then converted into complex ions such as hydrated positive ions and cluster negative ions following a chain of reactions. Because they have different recombination rates, it is necessary to differentiate between simple and complex ions.

To study the dissipation of ionization perturbations produced by gigantic jets, Lehtinen and Inan [2007] developed a five-constituent model of middle and upper atmospheric chemistry, based on the four-constituent model investigated earlier in Glukhov *et al.* [1992] and Pasko and Inan [1994]. According to their work, the charged species created by electric discharges in the middle and upper atmosphere can be grouped into electrons, light negative ions, cluster negative ions, light positive ions, and cluster positive ions. On the other hand, as discussed in section 17.3.2, electron detachment from  $O^-$  could be an important source for electrons when  $O^-$  ions are produced abundantly in the discharges, which requires a separate treatment of  $O^-$  ions from the rest of light negative ions. Therefore, a

chemistry model with six ion species is considered here, including electrons,  $O^-$  ions, light negative ions, cluster negative ions, light positive ions, and cluster positive ions. The list of reactions with their rate constants can be found in *Liu* [2012]. It should be noted that although such a simplified chemistry model works well within the first several hundred milliseconds after the beginning of the discharges, when the ion chemistry is dominated by a few number of ion species and electron impact reactions, it may be invalid on longer timescales as various forms of ions can be produced and characterizing the ion chemistry at this stage by using such a small set of ion species could introduce inaccuracy in the obtained results.

### 17.4.2.3 Lightning model

It has been established that the properties of CG discharges that define the development of sprites/sprite halos include the polarity of CGs, the charge moment change, and the duration of charge removal [e.g., *Pasko et al.*, 1997; *Cummer and Inan*, 1997; *Asano et al.*, 2008; *Qin et al.*, 2011]. *Pasko et al.* [1997] showed that the charge removal by CGs from thunderclouds to ground can be effectively modeled by depositing the opposite polarity of the removed charge at the same location in thunderclouds when the QE effects in the upper atmosphere are concerned (see section 17.2.2.6). However, it should be noted that such an equivalent model may give different results for the electric field in the lower mesosphere on a long timescale [*Pasko et al.*, 1997], but at that time the electric field is very small and its effects in the discharge itself could be negligible. For this model, the deposited charge  $Q(t)$  as a function of time  $t$  is described by *Pasko et al.* [1997]:

$$Q(t) = Q_0 \frac{\tanh\left(\frac{t}{\tau_f}\right)}{\tanh(1)}, \quad 0 \leq t < \tau_f$$

$$Q(t) = Q_0, \quad t \geq \tau_f$$

where  $\tau_f$  and  $Q_0$  are the duration of the lightning and the total amount of charge deposited, respectively. The spatial distribution of  $Q(t)$  is normally assumed to be a Gaussian distribution, which is centered at cloud altitudes, e.g., 10 km, and has a characteristic spatial scale of a few kilometers, e.g., 3 km.

### 17.4.2.4 Results

Figure 17.16 shows simulation results of a sprite halo caused by a +CG discharge removing 60 C charge from 10 km altitude in 1 ms. The deposited charge  $Q(t)$  is distributed in space following a Gaussian distribution centered on the symmetry axis, which has a height of 10 km and a characteristic spatial scale of 3 km. The corresponding charge moment change 600 C km is near the upper limit of the charge moment change threshold range for production of short delayed sprites [*Cummer and Lyons*, 2005; *Hu et al.*, 2007; *Li et al.*, 2008]. The figure shows the cross-sectional views of the distributions of normalized electric field, electron density, and  $O^-$  density at four different moments of time: 1, 1.9, 6.3, and 20 ms. It shows that a convex curvature of the lower ionosphere forms and develops above the parent lightning. The lightning field points predominantly downward so electrons drift upward (noting that ion motion is negligible for the timescale under consideration). The electrons therefore move in the same direction as the gradient of the electron density (see Figure 17.17), and the descending sprite halo on such a

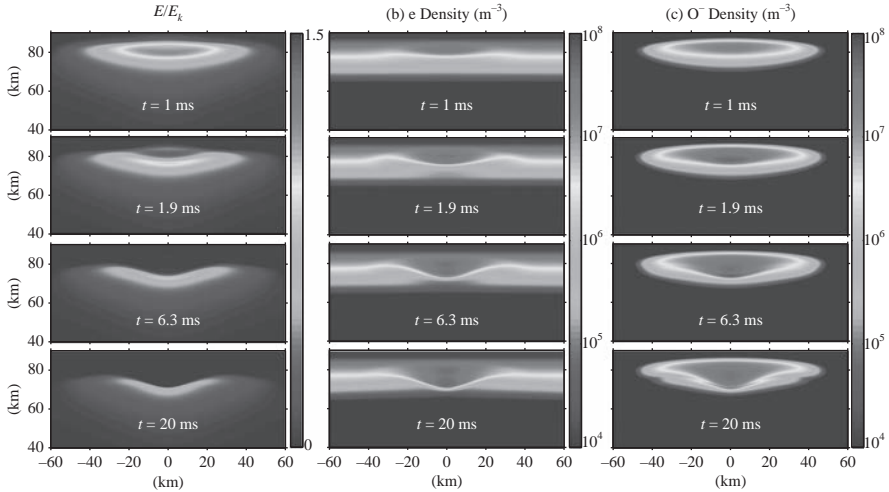


Figure 17.16 Simulation results of a halo caused by a +CG lightning flash transferring 60 C charge from 10 km altitude to ground in 1 ms. Cross-sectional views of the distributions of (a) normalized electric field, (b) electron density, and (c)  $O^-$  density at  $t = 1, 1.9, 6.3,$  and  $20$  ms [Liu, 2012]. Reprinted with permission from the American Geophysical Union

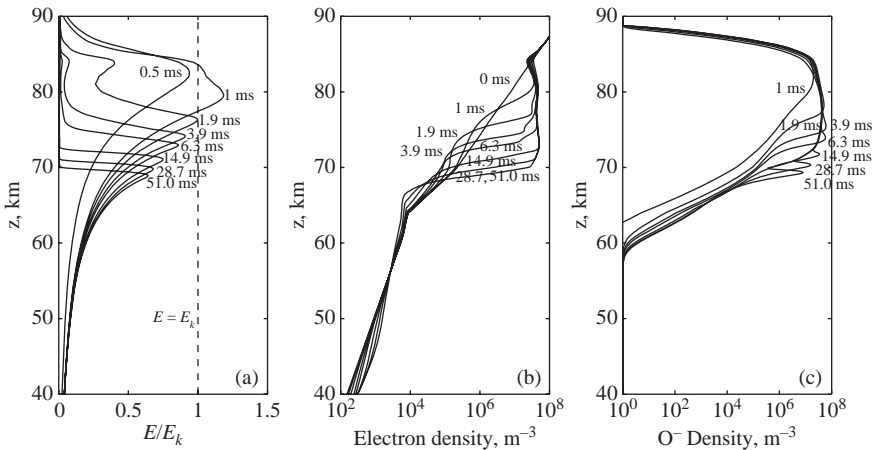


Figure 17.17 Simulation results of a halo caused by a +CG stroke transferring 60 C charge from 10 km altitude to ground in 1 ms. Altitude profiles of (a) normalized electric field, (b) electron density, and (c)  $O^-$  along symmetry axis for various moments of time [Liu, 2012]. Reprinted with permission from the American Geophysical Union

short timescale can only be explained by the development of an ionization wave. The  $O^-$  ions exist only in the region where the halo occupies or has passed through, as there is no initial background density for this species.

The altitude profiles of the same three quantities on the symmetry axis at more time instants are shown in Figure 17.17. The profiles of the normalized electric field

show that the region of strong electric field descends as time progresses and the peak normalized field decreases after 1 ms. It can also be seen that the strong electric field only lasts for  $\sim 1$  ms above 80 km altitude but an extended time period of tens of milliseconds around 69 km altitude. In addition, the electric field only exceeds  $E_k$  in a small altitude range around 80 km. The lowest altitude where  $E$  exceeds  $E_k$  is 76–77 km, which is reached at  $t = 1.9$  ms. Without the electron detachment from  $O^-$  ions, it would be expected that the strong field region would move down very slowly from 77 to 69 km altitude, because the ambient electron density decreases rapidly in this region and it could be further reduced by the two-body dissociative attachment due to  $E < E_k$  in this region so that the Maxwellian relaxation timescale would be very long. However, as shown by the field profiles, the peak field can still move relatively rapidly downward for a considerable distance even under the condition of  $E < E_k$ , although the speed decreases as it moves down. The front reaches about 69 km altitude at  $\sim 50$  ms and stays there until numerical instability occurs at  $\sim 70$  ms due to steepening electron density profile around that altitude.

The center panel of Figure 17.17 shows that the electron density in the altitude range of 70–85 km is highly elevated. It reaches a value close to the ambient electron density at about 85 km altitude. The sprite halo essentially brings down the lower ionosphere right above the parent lightning by about 15 km altitude. The increase in the electron density below 77 km altitude is quite interesting, where  $E$  never exceeds  $E_k$ . This increase in the electron density at the subbreakdown condition  $E > E_k$  is caused by the electron detachment from  $O^-$ , as discussed in section 17.3.2. Figures 17.16c and 17.17c show that  $O^-$  ions are produced abundantly on the timescale of the halo dynamics and their density in the altitude range of 70–85 km is comparable to electron density. The growth of electron density in  $E < E_k$  when there are abundant  $O^-$  ions in space can be understood as follows. Electrons are still produced below the breakdown threshold field due to electron impact ionization and they are constantly converted to  $O^-$  by the attachment process at the same time. Therefore, the total density of electrons and  $O^-$  ions increases as long as the ionization is effective (recombination takes place on a much longer timescale). When  $O^-$  ions accumulate to certain level, the detachment process becomes faster than the attachment process and then electron density increases together with the  $O^-$  density if significant ionization is continuously produced by the electron impact ionization.

After about  $t = 50$  ms, the halo stops descending but the electron density front becomes steeper and steeper, which eventually leads to numerical instability. In the end, a sharp electron density profile around 70 km is formed by the halo, but this is mostly caused by the increased electron density above and not by the loss of electrons below due to the attachment. Although the numerical grid size in this simulation is not fine enough to resolve sprite streamers, there is no indicative sign of formation of streamers. Particularly, the peak electric field of the halo continues to decrease, making initiation of streamers impossible. However, the parent lightning is quite impulsive, resulting in 600 C km charge moment change in 1 ms, and sprite streamer initiation would be expected according to studies on charge moment changes of sprite-inducing lightning [Cummer and Lyons, 2005; Hu *et al.*, 2007; Li *et al.*, 2008]. According to recent modeling results on sprite streamers, ionospheric inhomogeneities, which are not included in this simulation, are critical in initiation of sprite streamers [Qin *et al.*, 2011, 2012a, 2012b; Liu *et al.*, 2012; Kosar *et al.*, 2012; Qin *et al.*, 2013; Kosar *et al.*, 2013]. This might explain why there is no sign of streamer initiation shown by the simulation results presented in Figures 17.16 and 17.17.

### 17.4.3 Modeling of sprite streamers

Because of their small characteristic temporal and spatial scales, accurate simulation of sprite streamers requires a numerical grid with very fine temporal and spatial resolutions compared to modeling of sprites/sprite halos. As a result, typical streamer simulation employs a much smaller simulation region than that for modeling sprites/sprite halos. In addition, the propagation of sprite streamers is currently simulated only up to a couple of milliseconds because (1) streamer simulation is very time-consuming; (2) when streamers are forming, they quickly approach a stable/nearly stable state of propagation; and (3) the two-dimensional axisymmetric model is unable to simulate streamer branching that is often observed for expanding and accelerating sprite streamers [e.g., *McHarg et al.*, 2007; *Stenbaek-Nielsen et al.*, 2007; *McHarg et al.*, 2010]. Besides the elementary discharge processes included in the large-scale model of sprites/sprite halos, a critical process for streamer dynamics is photoionization, as discussed in Chapter 3. This process couples the production of electron–ion pairs with sources at different locations. Effects of photoionization on the streamer dynamics and development of efficient photoionization simulation models have been a subject of intensive research [*Zheleznyak et al.*, 1982; *Kulikovsky*, 2000; *Pancheshnyi et al.*, 2001; *Yi and Williams*, 2002; *Liu and Pasko*, 2004, 2006; *Ségur et al.*, 2006; *Luque et al.*, 2007; *Bourdon et al.*, 2007; *Liu et al.*, 2007]. Several photoionization models have been developed [*Zheleznyak et al.*, 1982; *Kulikovsky*, 2000; *Liu and Pasko*, 2004; *Ségur et al.*, 2006; *Luque et al.*, 2007; *Bourdon et al.*, 2007; *Liu et al.*, 2007], which give very similar streamer simulation results [*Bourdon et al.*, 2007; *Liu et al.*, 2007]. The SP<sub>3</sub> method developed in *Bourdon et al.* [2007] and *Liu et al.* [2007] is currently used in our streamer model, because it is accurate and easy to implement and the boundary conditions for this differential approach to photoionization calculation are also formulated.

It should be pointed out that photoionization may be ignored for large-scale modeling of sprites/sprite halos [*Liu*, 2012] because (1) the maximum field in the halo is much smaller than the streamer head field. The production of UV photons responsible for photoionization is less efficient at lower electric fields; (2) the spatial scales involved in the halo are much larger than the absorption length of the photons responsible for photoionization, which is about 100–200 m at halo altitudes [*Liu and Pasko*, 2004]; and (3) the electron detachment process of O<sup>−</sup> ions further makes the photoionization less important by providing additional source for free electrons ahead of the halo front.

#### 17.4.3.1 Model equations

Similar to the sprite halo model, the streamer model equations include the electron and ion drift–diffusion equations and Poisson’s equation [*Liu and Pasko*, 2004]:

$$\begin{aligned}\frac{\partial n_e}{\partial t} + \nabla \cdot \vec{J}_e &= (v_i - v_{a2} - v_{a3})n_e - \beta_{ep}b_en_p + S_{ph} \\ \frac{\partial n_p}{\partial t} &= v_in_e - \beta_{ep}n_en_p - \beta_{np}n_n n_p + S_{ph} \\ \frac{\partial n_n}{\partial t} &= (v_{a2} + v_{a3})n_e - \beta_{np}n_n n_p \\ \nabla^2 \phi &= -\frac{e}{\epsilon_0}(n_p - n_e - n_n)\end{aligned}$$



where  $n_e$ ,  $n_p$ , and  $n_n$  are the electron, positive ion, and negative ion number densities. The electron flux density  $\vec{J}_e = (n_e \vec{v}_e - D_e \nabla n_e)$ , where  $\vec{v}_e$  is the drift velocity of electrons and  $D_e$  is the electron diffusion coefficient;  $\nu_i$  is the ionization frequency;  $\nu_{a2}$  and  $\nu_{a3}$  are the two-body and three-body electron attachment frequencies, respectively;  $\beta_{ep}$  and  $\beta_{np}$  are the coefficients of electron–positive ion and negative–positive ion recombination, respectively; and  $S_{ph}$  is the rate of electron–ion pair production due to photoionization. Ions are assumed to be stationary, because mobilities of positive and negative ions are two to three orders of magnitude lower than the electron mobility.

### 17.4.3.2 Double-headed streamers developing in applied fields greater than $E_k$

Figure 17.18 shows development of double-headed streamers in applied electric fields  $E_0 = 1.5 E_k$  at three different altitudes: 0, 30, and 70 km. The simulations are initialized by placing spherically symmetric Gaussian plasma clouds with peak densities  $10^{14}$ ,  $2 \times 10^{10}$ , and  $5 \times 10^5 \text{ cm}^{-3}$ , and characteristic scales 0.2 mm, 1.4 cm, and 3 m, in the middle of the simulation domain at altitudes 0, 30, and 70 km, respectively. Test simulations show streamers can also be initiated by single electron avalanches and the streamers initiated by the clouds of relatively dense plasma attain similar characteristics as those initiated by single electron avalanches with a factor of  $\sim 10$  reduction in the model execution time. This approach to initiation of streamers is consistent with previous work of *Vitello et al.* [1993], indicating that the introduction of a relatively dense plasma cloud, with density and spatial scale of the same order of magnitude as streamers, allows to effectively bypass the initial avalanche phase of the streamer development.

As discussed in section 17.3.1, the streamer timescales, the streamer spatial scales, and the streamer electron densities scale with air density as  $\sim 1/N$ ,  $\sim 1/N$ , and  $\sim N^2$ , respectively, and the scaled streamer characteristics remain otherwise identical for the same values of the reduced electric field  $E/N$ . The results presented in Figures 17.18b and 17.18c correspond to the scaled ( $\sim 1/N$ ) moments of time at respective altitudes from the ground value of 2.7 ns shown in Figure 17.18a, thus illustrating the similarity properties of streamers at different altitudes/air densities. The horizontal and vertical dimensions of the simulation domain in Figures 17.18b and 17.18c also correspond to the scaled ( $\sim 1/N$ ) ground values shown in Figure 17.18a. The electron density scales in Figures 17.18b and 17.18c also correspond to scaled ( $\sim N^2$ ) values given in Figure 17.18a. Simple visual inspection of Figure 17.18 indicates that streamers at 30 and 70 km altitudes are very similar, but the positive and negative streamer heads at ground pressure exhibit radial scales, respectively,  $\sim 10\%$  and  $\sim 50\%$  smaller than the corresponding scaled values at higher altitudes. The three-body electron attachment and electron–positive ion recombination processes may lead to nonsimilar behavior of streamers at high gas pressures (see section 17.3.1). However, on the timescales of the simulations presented in Figure 17.18 these processes do not significantly affect the streamer properties. The photoionization model developed by *Zheleznyak et al.* [1982], which other photoionization models are based on, is fully similar at typical sprite altitudes  $\sim 40$ – $90$  km. However, the similarity is not preserved at lower altitudes due to the collisional quenching of the excited states responsible for the photoionizing radiation. The effective quenching altitude of those excited states is about 24 km, and therefore the quenching effects are negligible above this altitude, but at

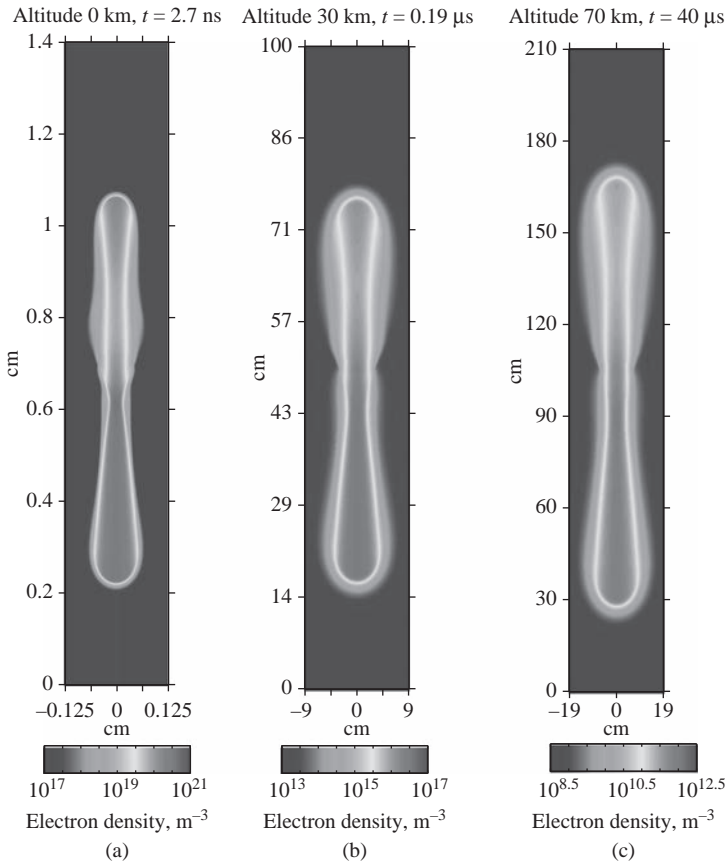


*Figure 17.18 A cross-sectional view of the distributions of the electron number density of double-headed streamers developing in applied electric fields  $E_0 = 1.5E_k$  at altitudes (a) 0 km, (b) 30 km, and (c) 70 km [Liu and Pasko, 2004]. The applied electric fields point vertically downward. The simulations are initialized by placing plasma clouds in the middle of the simulation domains. Each panel shows a downward propagating positive streamer and an upward propagating negative streamer that originate from the initial plasma cloud. The streamer heads propagate with expansion, and their speeds increase linearly with the lengths of the streamers [Liu and Pasko, 2004]. Reprinted with permission from the American Geophysical Union*

altitudes near or below it, an increasing fraction of the excited states are quenched, instead of radiating the UV photons, as the altitude decreases. Therefore, the differences observed between the streamer at ground and those at 30 and 70 km altitudes in Figure 17.18 are primarily due to the reduction in photoelectron production at high pressures [Liu and Pasko, 2004, 2006].

It seems that the formation of double-headed streamers is expected in the lower ionosphere when the lightning field exceeds  $E_k$ . However, high-speed videos of sprites show that sprite streamers are normally initiated with downward propagating positive streamers and negative streamers may be initiated later from the trail of

the positive streamer or may not form at all [Cummer *et al.*, 2006a; McHarg *et al.*, 2007; Stenbaek-Nielsen *et al.*, 2007; Stenbaek-Nielsen and McHarg, 2008; Stenbaek-Nielsen *et al.*, 2013]. Several factors may contribute to this difference between the modeling results and observations: (1) The zero background electron density and the dense plasma cloud to initialize the simulation may be unrealistic. Indeed, it has been recently found that double-headed streamers form at a lower ionospheric altitude only when the ambient lightning and halo field exceeds  $E_k$  at that altitude and it lasts longer than the streamer formation time at the same altitude, which depends on both the ambient field magnitude and the initial plasma cloud density [Qin *et al.*, 2011, 2012a, 2012b, 2013]. (2) The lightning electric field does not exceed  $E_k$ , and sprite streamers are initiated at subbreakdown condition. It has also been found recently that it is possible for streamers to be initiated in subbreakdown fields from ionospheric inhomogeneities with proper sizes and densities [Liu *et al.*, 2012; Kosar *et al.*, 2012, 2013]. In this scenario, a downward positive streamer naturally forms from the lower tip of an inhomogeneity in a downward pointing applied electric field, but no upward negative streamer forms from the upper tip (see section 17.4.3.4).

### 17.4.3.3 Streamers propagating in applied fields smaller than $E_k$

It is well known that a formed streamer can propagate in an electric field substantially lower than the conventional breakdown threshold field  $E_k$ . Experimental and numerical simulation results have established that the minimum field  $E_{cr}^+$  required for the propagation of positive streamers in air at ground pressure is about 5 kV/cm [e.g., Allen and Ghaffar, 1995; Morrow and Lowke, 1997; Babaeva and Naidis, 1997] and the minimum field  $E_{cr}^-$  for negative streamers is a factor of 2–3 higher than  $E_{cr}^+$  [Raizer, 1991, p. 361; Babaeva and Naidis, 1997]. For sprites, streamers developing in weak electric fields  $E < E_k$  likely occupy a substantial part of the overall sprite volume [Pasko *et al.*, 2000; Liu and Pasko, 2005; Liu *et al.*, 2009a, 2009b]. Therefore, the propagation of streamers in weak electric fields is an important subject for understanding spatial, temporal, and optical properties of sprites.

A positive streamer developing in an external electric field of 30  $N/N_0$  kV/cm at 75 km altitude is shown in Figure 17.19 [Liu *et al.*, 2009b]. Here,  $N$  and  $N_0$  are the air densities at 75 km altitude and ground level, respectively. The value of the external electric field is slightly smaller than the conventional breakdown threshold field of air that is about 32  $N/N_0$  kV/cm. To initiate streamers in an electric field smaller than  $E_k$ , a commonly used technique in streamer modeling studies is introducing a small conducting sphere with a fixed potential to enhance the electric field in its vicinity, where streamers can be initiated [Babaeva and Naidis, 1996, 1997; Liu and Pasko, 2005, 2006; Liu *et al.*, 2006, 2009a, 2009b]. For the simulation results shown in Figure 17.19, the conducting sphere is placed right above the top boundary of the simulation domain and the applied field points downward [Liu *et al.*, 2009b].

Similar to the streamers developing in strong fields  $>E_k$ , positive streamers propagating in weak electric fields  $>E_{cr}^+$  also expand and accelerate, and the brightness of their heads increases, as shown in Figures 17.19 and 17.20. According to Figures 17.19c and 17.19d, the maximum intensities of 1PN<sub>2</sub> and 2PN<sub>2</sub> are very similar, but the source size of 1PN<sub>2</sub> is larger than that of 2PN<sub>2</sub>. The emission intensities are highly enhanced in the streamer head in comparison with the streamer channel. Figure 17.20 shows a time sequence of intensity distributions

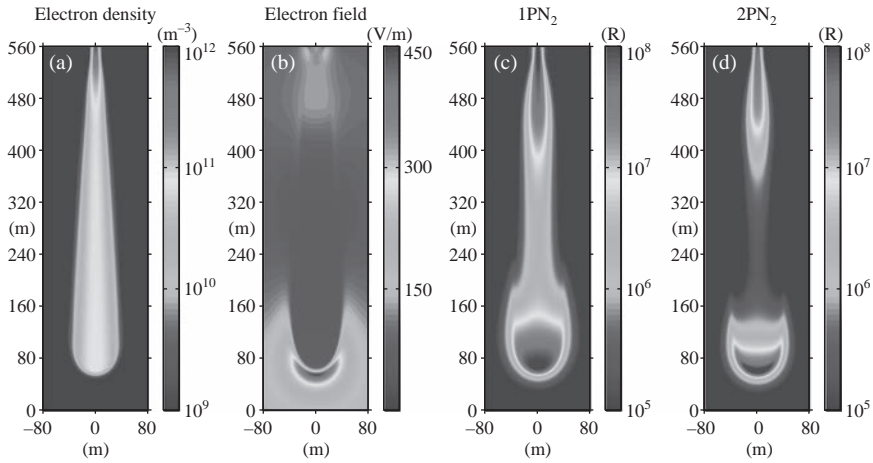


Figure 17.19 A cross-sectional view of (a) electron density, (b) electric field, (c)  $1PN_2$  intensity, and (d)  $2PN_2$  intensity at  $t = 300 \mu\text{s}$  for a downward propagating positive streamer in an electric field of  $30 N/N_0 \text{ kV/cm}$  at  $75 \text{ km}$  altitude [Liu et al., 2009b]. Reprinted with permission from the American Geophysical Union

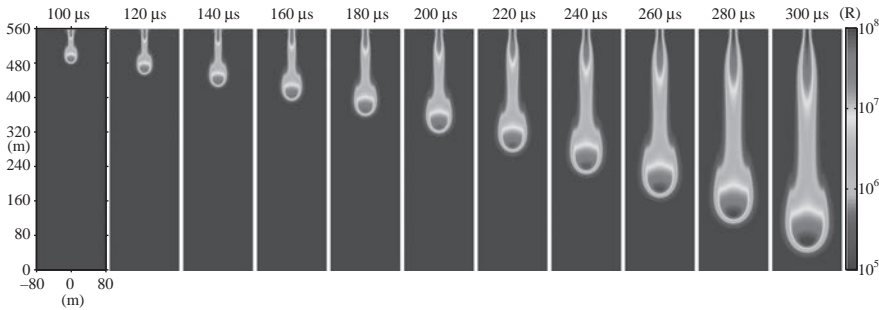


Figure 17.20 A time sequence of intensity distributions of  $1PN_2$  for a downward propagating model positive streamer at  $75 \text{ km}$  altitude. The sequence of images is shown with  $20 \mu\text{s}$  interval, starting at  $100 \mu\text{s}$  and ending at  $300 \mu\text{s}$  [Liu et al., 2009b]. The formatting is consistent with that of Figure 17.8. Reprinted with permission from the American Geophysical Union

of  $1PN_2$  for the streamer shown in Figure 17.19. The time interval between two successive images is  $20 \mu\text{s}$ . Each image shows the emission intensity in Rayleighs at the specific moment of time given at the top of the image.

The formatting of Figure 17.20 is consistent with streamer progression obtained experimentally in high-speed videos, as presented in Stenbaek-Nielsen et al. [2007] and shown in Figure 17.8. The trajectory of the streamer head follows a parabolic curve indicating the accelerating motion of the streamer, which is consistent with the accelerating streamer head in high-speed videos shown in Figure 17.8. The size of the streamer head keeps increasing and the radius of the visible head reaches about  $50 \text{ m}$  at  $t = 300 \mu\text{s}$ . In the model, the positive streamer with downward propagating direction is initiated due to the introduction of the

neutral plasma cloud in the high field region below the top boundary of the simulation domain. On the other hand, the observed streamer is initiated at the lower ionospheric boundary, so that no upward propagating negative streamers are formed because the lightning-induced electric field in this region relaxes on a timescale shorter than the streamer formation time [Pasko *et al.*, 1998b; Liu *et al.*, 2009b; Qin *et al.*, 2011, 2012a, 2012b, 2013].

#### 17.4.3.4 Modeling streamer initiation

Although many aspects of observed sprite streamers have been explained or even predicted by streamer modeling work, it is still not fully understood how sprite streamers are initiated in the lower ionosphere. According to triangulation analysis with multistation sprite videos including high-speed (>5000 fps) images, the initiation altitudes of sprite streamers vary between 65 and 90 km [Stenbaek-Nielsen *et al.*, 2010; Gamerota *et al.*, 2011], overlapping with the altitude range of sprite halos. In high-speed videos, sprite streamers appear to be initiated either at the bottom of a halo or out of the dark background [Stenbaek-Nielsen *et al.*, 2000; Cummer *et al.*, 2006a; McHarg *et al.*, 2007; Stenbaek-Nielsen *et al.*, 2007; Stenbaek-Nielsen and McHarg, 2008; Stenbaek-Nielsen *et al.*, 2013]. When they are initiated from the bottom of a halo, they appear to form from existing brightening luminous structures. High-speed videos also show that those structures descend downward with a decreasing speed and sprite streamers are initiated when their speeds are reduced so much that they appear to be stationary [Stenbaek-Nielsen *et al.*, 2011; Takahashi *et al.*, 2012]. The transverse sizes of those structures appear to be at least several times larger than the streamer head forming from them. On the other hand, coordinated analysis of sprite video images, remote measurements of lightning current moment, and finite difference time domain simulations of lightning electromagnetic fields has indicated that the simulated lightning electric field at the time of sprite initiation could be as low as 0.2–0.6  $E_k$  [Hu *et al.*, 2007; Li *et al.*, 2008; Gamerota *et al.*, 2011; Li *et al.*, 2012]. It has been a puzzle how sprite streamers can be initiated in such an electric field significantly smaller than  $E_k$ .

The sequence of sprite halo development and sprite streamer initiation has been the focus of several recent numerical studies [Luque and Ebert, 2009, 2010; Qin *et al.*, 2011, 2012a, 2012b, 2013; Kosar *et al.*, 2013]. It was concluded that sprite streamers are initiated as a result of the collapse of a sharpening halo front during its downward development and the pre-existing inhomogeneities can facilitate the streamer initiation but are not necessary [Luque and Ebert, 2009, 2010]. However, Qin *et al.* [2011] noted that the theory of streamer initiation from a collapsing halo has difficulty explaining some features shown by high-speed video observations, such as the spatial and temporal offsets between the halo and sprite streamers, and initiation of sprite streamers by small charge moment changes. They proposed that the pre-existing inhomogeneities are critical for streamer initiation in the lower ionosphere. They also found that it is easier for sprite streamers to be initiated from the pre-existing inhomogeneities located at the lower edge of the sprite halo where the conductivity is not significantly enhanced and strong electric field can last long enough for streamer formation [Qin *et al.*, 2012a, 2013]. The minimum density of the pre-existing inhomogeneities used in their studies is  $2 \times 10^9 \text{ m}^{-3}$ . In the above-mentioned modeling studies, the ambient electric field is generally greater than the conventional breakdown threshold field  $E_k$ , when

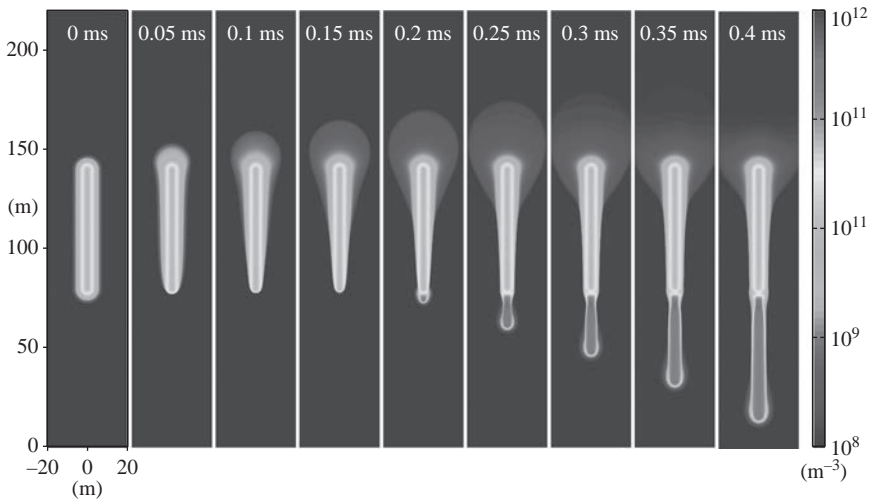
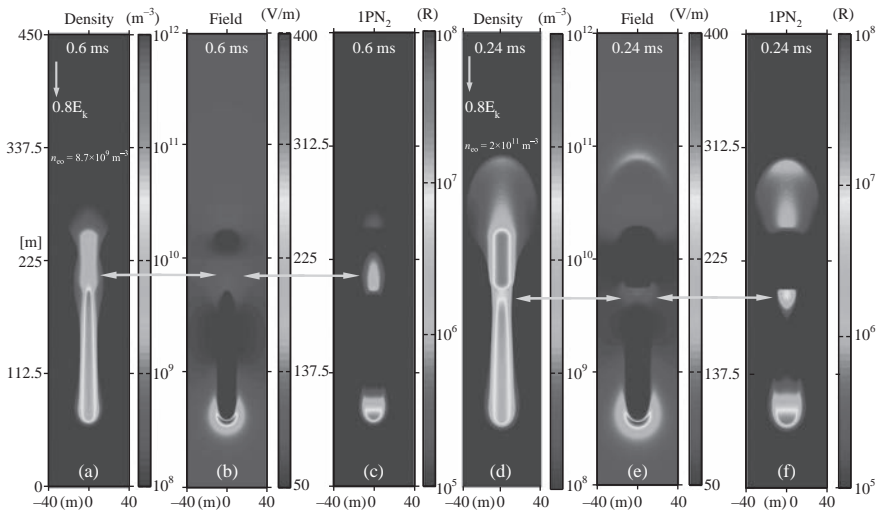


Figure 17.21 A cross-sectional view of the electron density distribution during the initiation of a positive sprite streamer from a columniform inhomogeneity [Liu *et al.*, 2012]. Reprinted with permission from the American Physical Society

streamers are forming. Streamer simulations reported in Liu *et al.* [2012] and Kosar *et al.* [2012] show that sprite streamers can be initiated in a subbreakdown field as low as  $0.3E_k$  from columniform inhomogeneities, which are typically 10 m wide, 100 m long and have a peak plasma density of  $\sim 10^{10} \text{ m}^{-3}$ .

Figure 17.21 shows that a sprite streamer is successfully formed at 70 km altitude in a downward-pointing lightning field with a magnitude of  $E_0 = 0.5E_k$  [Liu *et al.*, 2012]. The initial ionization column follows a Gaussian distribution with a characteristic spatial scale of 3 m, a length of 60 m, and a peak density of  $6 \times 10^{10} \text{ m}^{-3}$ . When  $E_0$  is suddenly applied at  $t = 0$  s, free electrons of the column start to drift upward. This exposes the positive ions in the lower tip (positive tip) of the column while resulting in an excess of electrons in the upper tip (negative tip). The continuous upward shifting of electrons accumulates positive and negative charge at the respective tip as well as in a thin shell around the column. As a result, the space charge screens an increasing fraction of the external field out of the ionization column and leads to an increasing enhancement of the electric field at the tip. However, asymmetric conditions are created at the two tips: a compact space charge region forms at the positive tip in contrast to a large, diffuse region at the negative tip. This is because the positive ions exposed are confined in the compact column but the excess electrons in the negative tip can continuously spread outward. Consequently, the electron density distribution becomes steeper at the positive tip, showing a slightly upward shifted tip and less steeper at the negative tip between 0 and 0.15 ms. During this period, the magnitude of electric field at the positive tip increases continuously but the location of the maximum field is fixed over time. At about 0.17 ms, the field reaches about  $2.5E_k$  ( $E_k = \sim 217 \text{ V/m}$  at 70 km altitude) and the location of the maximum field starts to move forward. The electron density in the tip also quickly increases when the field becomes greater than  $E_k$ , and the high density region finally extends forward as shown by electron density distributions at 0.2 ms and later. A positive streamer is



**Figure 17.22** Cross sections of electron density, electric field, and  $1PN_2$  intensity distributions for two streamers forming from ionization patches in  $E_0 = 0.8E_k$  at 75 km altitude. Panels (a)–(c) show the results of a streamer formed from an ionization patch with a peak plasma density of  $8.7 \times 10^9 \text{ m}^{-3}$ , while the streamer shown by panels (d)–(f) formed from a patch with a peak density of  $2 \times 10^{11} \text{ m}^{-3}$ . A luminous region around the initiation points of the streamers [Kosar et al., 2012]. Reprinted with permission from the American Geophysical Union

born from the positive tip of the initial ionization column. On the contrary, only a diffuse electron cloud appears around the negative tip.

It has also been shown that following the streamer initiation from isolated ionization patches, the region around the streamer initiation point brightens [Kosar et al., 2012], which seems to be consistent with the observed brightening of the origin of the sprite streamers, as reported in McHarg et al. [2007], Stenbaek-Nielsen et al. [2007], Stenbaek-Nielsen and McHarg [2008], and Stenbaek-Nielsen et al. [2013]. Figure 17.22 shows that the relative location of the brightening region to the tip of the column depends on the peak plasma density of the initial ionization column [Kosar et al., 2012]. In any case, a bright region near the streamer initiation point appears after the streamer initiation.

In addition, high-speed videos of sprites show that sprites initiated with downward propagating positive streamers and negative streamers may appear later and originate from existing structures in the positive streamer channels [Cummer et al., 2006a; Stenbaek-Nielsen and McHarg, 2008; Stenbaek-Nielsen et al., 2013]. The modeling results shown in Figures 17.21 and 17.22 also indicate that the initiation of positive streamers is much easier than negative streamers. However, it is possible that negative streamers will form eventually if the positive streamer propagates through a long enough distance. It is known that a positive streamer developing from a positive electrode in an electric field greater than its minimum field for stable propagation draws an exponentially increasing current [Liu, 2010]. This deposits a large amount of negative charge at the origin, leading to negative charging of the positive streamer trail and possible initiation of negative streamers

[Luque and Ebert, 2010]. The positive streamer developing from the ionization column also carries such a current, and the current will deposit negative charge to the column faster than the charge dissipation allowed by the conductive column, resulting in an electric field increase in the trail of the streamer [Liu, 2010; Liu et al., 2012; Kosar et al., 2012], which may eventually lead to initiation of a negative streamer from that tip.

However, it is unclear at present what are the sources of those inhomogeneities in the lower ionosphere. Some possible processes are briefly summarized in Kosar et al. [2012] and the candidates that are capable of generating high density inhomogeneities are rather limited, including meteor-related processes, intense filamentary electrical discharges like streamers, etc. However, Kosar et al. [2013] have demonstrated that large (hundreds of meter wide) ionospheric inhomogeneities with an electron density ( $\sim 9 \times 10^7 \text{ m}^{-3}$ ) close to the halo density obtained from halo modeling results [Liu, 2012] are capable of seeding sprite streamers even at subbreakdown condition. This result together with sprite halo modeling results presented in Liu [2012] suggests that if a sprite halo front is unstable, the instabilities developing from the pre-existing inhomogeneities in the lower ionosphere could be the sources of the ionospheric patches for streamer initiation [Kosar et al., 2013]. There is certainly more work that needs to be done to understand the initiation process of sprite streamers and the source of the inhomogeneity leading to their initiation.

## Acknowledgments

This research has been supported in part by an NSF grant ATM 0955379 and a DARPA grant HR0011-1-10-1-0061.

## References

- S. Achat, Y. Teisseyre, and E. Marode (1992), The scaling of the streamer-to-arc transition in a positive point-to-plane gap with pressure, *J. Phys. D: Appl. Phys.*, 25(4), 661–668.
- N. L. Allen and A. Ghaffar (1995), The conditions required for the propagation of a cathode-directed positive streamer in air, *J. Phys. D: Appl. Phys.*, 28, 331–337.
- R. A. Armstrong et al. (1998), Photometric measurements in the SPRITES' 95 and 96 campaigns of nitrogen second positive (399.8 nm) and first negative (427.8 nm) emission, *J. Atmos. Solar Terr. Phys.*, 60, 787–799.
- R. A. Armstrong, D. M. Suszcynsky, W. A. Lyons, and E. R. Williams (2001), Optical signatures, energy deposition, ionization and chemical dynamics in lightning-induced transient electrodynamic middle and upper atmospheric events (sprites), U.S. National Radio Science Meeting, Boulder, CO, 2001.
- E. Arnone et al. (2008), Seeking sprite-induced signatures in remotely sensed middle atmosphere NO<sub>2</sub>, *Geophys. Res. Lett.*, 35, L05807, doi:/10.1029/2007gl031791.
- E. Arnone et al. (2009), Seeking sprite-induced signatures in remotely sensed middle atmosphere NO<sub>2</sub>: Latitude and time variations, *Plasma Sources Sci. Technol.*, 18(3), 034014, doi:/10.1088/0963-0252/18/3/034014.



- T. Asano, M. Hayakawa, M. Cho, and T. Suzuki (2008), Computer simulations on the initiation and morphological difference of Japan winter and summer sprites, *J. Geophys. Res.*, 113(A2), A02308, doi:/10.1029/2007ja012528.
- N. Y. Babaeva and G. V. Naidis (1996), Two-dimensional modelling of positive streamer dynamics in non-uniform electric fields in air, *J. Phys. D: Appl. Phys.*, 29, 2423–2431, doi:/10.1088/0022-3727/29/9/029.
- N. Y. Babaeva and G. V. Naidis (1997), Dynamics of positive and negative streamers in air in weak uniform electric fields, *IEEE Trans. Plasma Sci.*, 25, 375–379.
- C. P. Barrington-Leigh and U. S. Inan (1999), Elves triggered by positive and negative lightning discharges, *Geophys. Res. Lett.*, 26, 683–686, doi:/10.1029/1999gl1900059.
- C. P. Barrington-Leigh, U. S. Inan, and M. Stanley (2001), Identification of sprites and elves with intensified video and broadband array photometry, *J. Geophys. Res.*, 106(A2), 1741–1750, doi:/10.1029/2000ja000073.
- E. A. Bering *et al.* (2004), Observations of transient luminous events (TLEs) associated with negative cloud to ground (–CG) lightning strokes, *Geophys. Res. Lett.*, 31(5), L05104, doi:/10.1029/2003gl018659.
- J. Błęcki, M. Parrot, and R. Wronowski (2009), ELF and VLF signatures of sprites registered onboard the low altitude satellite DEMETER, *Ann. Geophys.*, 27, 2599–2605, doi:/10.5194/angeo-27-2599-2009.
- D. J. Boccippio *et al.* (1995), Sprites, ELF transients, and positive ground strokes, *Science*, 269, 1088–1091.
- W. L. Boeck, O. H. Vaughan, R. J. Blakeslee, B. Vonnegut, and M. Brook (1992), Lightning induced brightening in the airglow layer, *Geophys. Res. Lett.*, 19, 99.
- O. V. Bolotov *et al.* (2010), Similarity laws for cathode-directed streamers in gaps with an inhomogeneous field at elevated air pressures, *Plasma Phys. Rep.*, 36(11), 1000–1011, doi:/10.1134/s1063780x10110097.
- A. Bourdon *et al.* (2007), Efficient models for photoionization produced by non-thermal gas discharges in air based on radiative transfer and the Helmholtz equations, *Plasma Sources Sci. Technol.*, 16, 656–678, doi:/10.1088/0963-0252/16/3/026.
- E. J. Bucsela *et al.* (2003),  $N_2(B^3\Pi_g)$  and  $N_2^+(A^2\Pi_u)$  vibrational distributions observed in sprites, *J. Atmos. Solar Terr. Phys.*, 65, 583–590.
- S. Célestin and V. P. Pasko (2010), Effects of spatial non-uniformity of streamer discharges on spectroscopic diagnostics of peak electric fields in transient luminous events, *Geophys. Res. Lett.*, 37, L07804, doi:/10.1029/2010gl042675.
- O. Chanrion and T. Neubert (2008), A PIC-MCC code for simulation of streamer propagation in air, *J. Comput. Phys.*, 227, 7222–7245, doi:/10.1016/j.jcp.2008.04.016.
- A. B. Chen *et al.* (2008), Global distributions and occurrence rates of transient luminous events, *J. Geophys. Res.*, 113, A08306, doi:/10.1029/2008ja013101.
- J. L. Chern *et al.* (2003), Global survey of upper atmospheric transient luminous events on the ROCSAT-2 satellite, *J. Atmos. Solar Terr. Phys.*, 65, 647–659, doi:/10.1016/s1364-6826(02)00317-6.

- J. K. Chou *et al.* (2010), Gigantic jets with negative and positive polarity streamers, *J. Geophys. Res.*, 115, A00E45, doi:/10.1029/2009ja014831.
- J. K. Chou *et al.* (2011), Optical emissions and behaviors of the blue starters, blue jets, and gigantic jets observed in the Taiwan transient luminous event ground campaign, *J. Geophys. Res.*, 116, A07301, doi:/10.1029/2010ja016162.
- V. Cooray (2012), *Lightning electromagnetics*, The Institution of Engineering and Technology, London.
- S. A. Cummer and U. S. Inan (1997), Measurement of charge transfer in sprite-producing lightning using ELF radio atmospherics, *Geophys. Res. Lett.*, 24(14), 1731–1734, doi:/10.1029/97gl51791.
- S. A. Cummer, U. S. Inan, T. F. Bell, and C. P. Barrington-Leigh (1998), ELF radiation produced by electrical currents in sprites, *Geophys. Res. Lett.*, 25, 1281.
- S. A. Cummer and M. Stanley (1999), Submillisecond resolution lightning currents and sprite development: Observations and implications, *Geophys. Res. Lett.*, 26, 3205–3208, doi:/10.1029/1999gl003635.
- S. A. Cummer (2003), Current moment in sprite-producing lightning, *J. Atmos. Sol.-Terr. Phys.*, 65, 499–508.
- S. A. Cummer and W. A. Lyons (2005), Implication of lightning charge moment changes for sprite initiation, *J. Geophys. Res.*, 110, A04304, doi:/10.1029/2004ja010812.
- S. A. Cummer *et al.* (2006a), Submillisecond imaging of sprite development and structure, *Geophys. Res. Lett.*, 33, L04104, doi:/10.1029/2005gl024969.
- S. A. Cummer *et al.* (2006b), Simultaneous radio and satellite optical measurements of high-altitude sprite current and lightning continuing current, *J. Geophys. Res.*, 111(A10), A10315, doi:/10.1029/2006ja011809.
- S. A. Cummer *et al.* (2009), Quantification of the troposphere-to-ionosphere charge transfer in a gigantic jet, *Nat. Geosci.*, 2, 617–620, doi:/10.1038/ngeo607.
- S. A. Cummer, W. A. Lyons, and M. A. Stanley (2013), Three years of lightning impulse charge moment change measurements in the United States, *J. Geophys. Res.*, 118, 5176–5189, doi:/10.1002/jgrd.50442.
- D. K. Davies (1983), Measurements of swarm parameters in dry air, in *Theoretical Notes, Note 346*, Westinghouse R&D Center, Pittsburgh, PA.
- C. L. da Silva and V. P. Pasko (2012), Simulation of leader speeds at gigantic jet altitudes, *Geophys. Res. Lett.*, 39, 13805, L13805, doi:/10.1029/2012gl052251.
- S. de Larquier and V. P. Pasko (2010), Mechanism of inverted-chirp infrasonic radiation from sprites, *Geophys. Res. Lett.*, 37, L24803, doi:/10.1029/2010gl045304.
- J. Dutton (1975), A survey of electron swarm data, *J. Phys. Chem. Ref. Data*, 4, 577–586.
- U. Ebert *et al.* (2006), The multiscale nature of streamers, *Plasma Sources Sci. Technol.*, 15, S118–S129.
- U. Ebert and D. D. Sentman (2008), Editorial review: Streamers, sprites, leaders, lightning: From micro- to macroscales, *J. Phys. D: Appl. Phys.*, 41(23), 230–301, doi:/10.1088/0022-3727/41/23/230301.
- U. Ebert *et al.* (2010), Review of recent results on streamer discharges and discussion of their relevance for sprites and lightning, *J. Geophys. Res.*, 115(A14), A00E43, doi:/10.1029/2009ja014867.

- H. E. Edens (2011), Photographic and lightning mapping observations of a blue starter over a New Mexico thunderstorm, *Geophys. Res. Lett.*, 38, L17804, doi:/10.1029/2011gl048543.
- C.-F. Enell *et al.* (2008), Parameterisation of the chemical effect of sprites in the middle atmosphere, *Ann. Geophys.*, 26, 13–27.
- T. Farges, E. Blanc, A. L. Pichon, T. Neubert, and T. H. Allin (2005), Identification of infrasound produced by sprites during the Sprite2003 campaign, *Geophys. Res. Lett.*, 32(1), L01813, doi:/10.1029/2004gl021212.
- T. Farges and E. Blanc (2010), Characteristics of infrasound from lightning and sprites near thunderstorm areas, *J. Geophys. Res.*, 115, A00E31, doi:/10.1029/2009ja014700.
- R. C. Franz, R. J. Nemzek, and J. R. Winckler (1990), Television image of a large upward electric discharge above a thunderstorm system, *Science*, 249, 48.
- H. U. Frey *et al.* (2005), Beta-type stepped leader of elve-producing lightning, *Geophys. Res. Lett.*, 32, L13824, doi:/10.1029/2005gl023080.
- H. U. Frey *et al.* (2007), Halos generated by negative cloud-to-ground lightning, *Geophys. Res. Lett.*, 34(18), L18801, doi:/10.1029/2007gl030908.
- H. Fukunishi *et al.* (1996a), Elves: Lightning-induced transient luminous events in the lower ionosphere, *Geophys. Res. Lett.*, 23(16), 2157–2160.
- H. Fukunishi, Y. Takahashi, M. Fujito, Y. Wanatabe, and S. Sakanoi (1996b), Fast imaging of elves and sprites using a framing/streak camera and a multi-anode array photometer, *Eos Trans. AGU*, 77(46).
- M. Füllekrug and S. C. Reising (1998), Excitation of Earth-ionosphere cavity resonances by sprite-associated lightning flashes, *Geophys. Res. Lett.*, 25, 4145–4148.
- M. Füllekrug, D. R. Moudry, G. Dawes, and D. D. Sentman (2001), Mesospheric sprite current triangulation, *J. Geophys. Res.*, 106, 20189–20194.
- M. Füllekrug, E. A. Mareev, and M. J. Rycroft (2006), *Sprites, elves and intense lightning discharges*, NATO Science Series II: Mathematics, Physics and Chemistry, vol. 225, Springer, Heidelberg, Germany.
- M. Füllekrug *et al.* (2010), Relativistic runaway breakdown in low-frequency radio, *J. Geophys. Res.*, 115, 0, A00E09, doi:/10.1029/2009ja014468.
- M. Füllekrug *et al.* (2011), Relativistic electron beams above thunderclouds, *Atmos. Chem. Phys.*, 11, 7747–7754, doi:/10.5194/acp-11-7747-2011.
- J. W. Gallagher, E. C. Beaty, J. Dutton, and L. C. Pitchford (1983), An annotated compilation and appraisal of electron swarm data in electronegative gases, *J. Phys. Chem. Ref. Data*, 12, 109–152.
- W. R. Gamerota *et al.* (2011), Comparison of sprite initiation altitudes between observations and models, *J. Geophys. Res.*, 116, A02317, doi:/10.1029/2010ja016095.
- E. A. Gerken, U. S. Inan, and C. P. Barrington-Leigh (2000), Telescopic imaging of sprites, *Geophys. Res. Lett.*, 27, 2637–2640.
- E. A. Gerken and U. S. Inan (2002), A survey of streamer and diffuse glow dynamics observed in sprites using telescopic imagery, *J. Geophys. Res.*, 107 (A11), 1344, doi:/10.1029/2002ja009248.
- E. A. Gerken and U. S. Inan (2003), Observations of decameter-scale morphologies in sprites, *J. Atmos. Solar Terr. Phys.*, 65, 567–572, doi:/10.1016/s1364-6826(02)00333-4.

- V. S. Glukhov, V. P. Pasko, and U. S. Inan (1992), Relaxation of transient lower ionospheric disturbances caused by lightning-whistler-induced electron-precipitation bursts, *J. Geophys. Res.*, 97(A11), 16971–16979, doi:/10.1029/92ja01596.
- F. J. Gordillo-Vázquez (2008), Air plasma kinetics under the influence of sprites, *J. Phys. D: Appl. Phys.*, 41(23), 234016, doi:/10.1088/0022-3727/41/23/234016.
- F. J. Gordillo-Vázquez and Z. Donko (2009), Electron energy distribution functions and transport coefficients relevant for air plasmas in the troposphere: Impact of humidity and gas temperature, *Plasma Sources Sci. Technol.*, 18, 034021, doi:/10.1088/0963-0252/18/3/034021.
- F. J. Gordillo-Vázquez (2010), Vibrational kinetics of air plasmas induced by sprites, *J. Geophys. Res.*, 115, A00E25, doi:/10.1029/2009ja014688.
- F. J. Gordillo-Vázquez and A. Luque (2013), Preface to the Special Issue on Thunderstorm Effects in the Atmosphere-Ionosphere System, *Surv. Geophys.*, 34(6), 697–700, doi:/10.1007/s10712-013-9256-9.
- C. Greifinger and P. Greifinger (1976), Transient ULF electric and magnetic fields following a lightning discharge, *J. Geophys. Res.*, 81(13), 2237–2247.
- J. M. Guo and C. H. Wu (1993), Comparisons of multidimensional fluid models for streamers, in *Non-Thermal Plasma Techniques for Pollution Control, NATO ASI Ser.*, vol. G34, part A, pp. 287–298, Springer-Verlag, New York.
- G. J. M. Hagelaar and L. C. Pitchford (2005), Solving the Boltzmann equation to obtain electron transport coefficients and rate coefficients for fluid models, *Plasma Sources Sci. Technol.*, 14, 722–733, doi:/10.1088/0963-0252/14/4/011.
- W. W. Hager *et al.* (2012), Charge rearrangement by sprites over a north Texas mesoscale convective system, *J. Geophys. Res.*, 117(D22), D22101, doi:/10.1029/2012jd018309.
- L. C. Hale and M. E. Baginski (1987), Current to the ionosphere following a lightning stroke, *Nature*, 329, 814–816.
- D. L. Hampton, M. J. Heavner, E. M. Wescott, and D. D. Sentman (1996), Optical spectral characteristics of sprites, *Geophys. Res. Lett.*, 23, 89–93.
- Y. Hiraki *et al.* (2004), Generation of metastable oxygen atom O(<sup>1</sup>D) in sprite halos, *Geophys. Res. Lett.*, 31, L14105, doi:/10.1029/2004gl020048.
- R. H. Holzworth, M. C. Kelley, C. L. Siefring, L. C. Hale, and J. T. Mitchell (1985), Electrical measurements in the atmosphere and the ionosphere over an active thunderstorm. 2. Direct current electric fields and conductivity, *J. Geophys. Res.*, 90, 9824.
- W. Y. Hu, S. A. Cummer, and W. A. Lyons (2002), Lightning charge moment changes for the initiation of sprites, *Geophys. Res. Lett.*, 29(8), 1279, doi:/10.1029/2001gl014593.
- W. Y. Hu, S. A. Cummer, and W. A. Lyons (2007), Testing sprite initiation theory using lightning measurements and modeled electromagnetic fields, *J. Geophys. Res.*, 112, D13115, doi:/10.1029/2006jd007939.
- S.-M. Huang *et al.* (2012), Optical and radio signatures of negative gigantic jets: Cases from Typhoon Lionrock (2010), *J. Geophys. Res.*, 117, A08307, doi:/10.1029/2012ja017600.

- U. S. Inan, T. F. Bell, and J. V. Rodriguez (1991), Heating and ionization of the lower ionosphere by lightning, *Geophys. Res. Lett.*, 18, 705–708, doi:10.1029/91gl00364.
- U. S. Inan, S. C. Reising, G. J. Fishman, and J. M. Horack (1996), On the association of terrestrial gamma-ray bursts with lightning and implications for sprites, *Geophys. Res. Lett.*, 23(9), 1017–1020.
- U. S. Inan *et al.* (1997), Rapid lateral expansion of optical luminosity in lightning-induced ionospheric flashes referred to as ‘elves’, *Geophys. Res. Lett.*, 24(5), 583–586.
- U. S. Inan, S. A. Cummer, and R. A. Marshall (2010), A survey of ELF and VLF research on lightning-ionosphere interactions and causative discharges, *J. Geophys. Res.*, 115, A00E36, doi:10.1029/2009ja014775.
- T. Kanmae, H. C. Stenbaek-Nielsen, M. G. McHarg, and R. K. Haaland (2012), Diameter-speed relation of sprite streamers, *J. Phys. D: Appl. Phys.*, 45(26), 275203, doi:10.1088/0022-3727/45/27/275203.
- B. C. Kosar, N. Y. Liu, and H. K. Rassoul (2012), Luminosity and propagation characteristics of sprite streamers initiated from small ionospheric disturbances at subbreakdown conditions, *J. Geophys. Res.*, 117(A16), 8328, A08328, doi:10.1029/2012ja017632.
- B. C. Kosar, N. Y. Liu, and H. K. Rassoul (2013), Formation of sprite streamers at subbreakdown conditions from ionospheric inhomogeneities resembling observed sprite halo structures, *Geophys. Res. Lett.*, 40, 6282–6287, doi:10.1002/2013GL058294.
- P. R. Krehbiel *et al.* (2008), Upward electrical discharges from thunderstorms, *Nat. Geosci.*, 1, 233–237, doi:10.1038/ngeo162.
- A. A. Kulikovskiy (2000), The role of photoionization in positive streamer dynamics, *J. Phys. D: Appl. Phys.*, 33, 1514–1524.
- C. L. Kuo *et al.* (2005), Electric fields and electron energies inferred from the ISUAL recorded sprites, *Geophys. Res. Lett.*, 32, L19103, doi:10.1029/2005gl023389.
- C. L. Kuo *et al.* (2007), Modeling elves observed by FORMOSAT-2 satellite, *J. Geophys. Res.*, 112(A11), A11312, doi:10.1029/2007ja012407.
- C. L. Kuo *et al.* (2009), Discharge processes, electric field, and electron energy in ISUAL-recorded gigantic jets, *J. Geophys. Res.*, 114(A13), A04314, doi:10.1029/2008ja013791.
- F. Leblanc *et al.* (2008), *Planetary Atmospheric Electricity*, 532 pp., Springer, New York, doi:10.1007/978-0-387-87664-1.
- L.-J. Lee *et al.* (2012), Characteristics and generation of secondary jets and secondary gigantic jets, *J. Geophys. Res.*, 117, A06317, doi:10.1029/2011ja017443.
- L.-J. Lee *et al.* (2013), Secondary gigantic jets as possible inducers of sprites, *Geophys. Res. Lett.*, 40, 1462–1467, doi:10.1002/grl.50300.
- F. Lefeuvre *et al.* (2009), On remote sensing of transient luminous events’ parent lightning discharges by ELF/VLF wave measurements on board a satellite, *J. Geophys. Res.*, 114, A09303, doi:10.1029/2009ja014154.
- N. G. Lehtinen and U. S. Inan (2007), Possible persistent ionization caused by giant blue jets, *Geophys. Res. Lett.*, 34, L08804, doi:10.1029/2006gl029051.

- J. Li, S. A. Cummer, W. A. Lyons, and T. E. Nelson (2008), Coordinated analysis of delayed sprites with high-speed images and remote electromagnetic fields, *J. Geophys. Res.*, 113(D12), D20206, doi:/10.1029/2008jd010008.
- J. Li and S. A. Cummer (2009), Measurement of sprite streamer acceleration and deceleration, *Geophys. Res. Lett.*, 36, L10812, doi:/10.1029/2009gl037581.
- J. Li and S. Cummer (2011), Estimation of electric charge in sprites from optical and radio observations, *J. Geophys. Res.*, 116, A01301, doi:/10.1029/2010ja015391.
- J. Li, S. A. Cummer, G. Lu, and L. Zigoneanu (2012), Charge moment change and lightning-driven electric fields associated with negative sprites and halos, *J. Geophys. Res.*, 117(A9), A09310, doi:/10.1029/2012JA017731.
- L. Liszka (2004), On the possible infrasound generation by sprites, *J. Low Freq. Noise, Vibration and Active Cont.*, 23(2), 85–93.
- L. Liszka and Y. Hobara (2006), Sprite-attributed infrasonic chirps – their detection, occurrence and properties between 1994 and 2004, *J. Atmos. Sol.-Terr. Phys.*, 68, 1179–1188.
- N. Y. Liu and V. P. Pasko (2004), Effects of photoionization on propagation and branching of positive and negative streamers in sprites, *J. Geophys. Res.*, 109, A04301, doi:/10.1029/2003ja010064.
- N. Y. Liu and V. P. Pasko (2005), Molecular nitrogen LBH band system far-UV emissions of sprite streamers, *Geophys. Res. Lett.*, 32, L05104, doi:/10.1029/2004gl022001.
- N. Y. Liu *et al.* (2006), Comparison of results from sprite streamer modeling with spectrophotometric measurements by ISUAL instrument on FORMOSAT-2 satellite, *Geophys. Res. Lett.*, 33, L01101, doi:/10.1029/2005gl024243.
- N. Y. Liu and V. P. Pasko (2006), Effects of photoionization on similarity properties of streamers at various pressures in air, *J. Phys. D: Appl. Phys.*, 39, 327–334, doi:/10.1088/0022-3727/39/2/013.
- N. Y. Liu and V. P. Pasko (2007), Modeling studies of NO- $\gamma$  emissions of sprites, *Geophys. Res. Lett.*, 34, L16103, doi:/10.1029/2007gl030352.
- N. Y. Liu *et al.* (2007), Application of photoionization models based on radiative transfer and the Helmholtz equations to studies of streamers in weak electric fields, *Appl. Phys. Lett.*, 91, 211501, doi:/10.1063/1.2816906.
- N. Y. Liu *et al.* (2009a), Assessment of sprite initiating electric fields and quenching altitude of a  $^1\Pi_g$  state of N<sub>2</sub> using sprite streamer modeling and ISUAL spectrophotometric measurements, *J. Geophys. Res.*, 114, A00E02, doi:/10.1029/2008ja013735.
- N. Y. Liu, V. P. Pasko, K. Adams, H. C. Stenbaek-Nielsen, and M. McHarg (2009b), Comparison of acceleration, expansion and brightness of sprite streamers obtained from modeling and high-speed video observations, *J. Geophys. Res.*, 114, A00E03, doi:/10.1029/2008ja013720.
- N. Y. Liu (2010), Model of sprite luminous trail caused by increasing streamer current, *Geophys. Res. Lett.*, 37, L04102, doi:/10.1029/2009gl042214.
- N. Y. Liu and V. P. Pasko (2010), NO- $\gamma$  emissions from streamer discharges: Direct electron impact excitation versus resonant energy transfer, *J. Phys. D: Appl. Phys.*, 43(8), 082001, doi:/10.1088/0022-3727/43/8/082001.
- N. Y. Liu, V. P. Pasko, H. C. Stenbaek-Nielsen, and M. G. McHarg (2011), Sprite streamers imaged at different exposure times, *IEEE Trans. Plasma Sci.*, 39, 2710–2711, doi:/10.1109/tps.2011.2159517.

- N. Y. Liu (2012), Multiple ion species fluid modeling of sprite halos and the role of electron detachment of  $O^-$  in their dynamics, *J. Geophys. Res.*, 117, A03308, doi:/10.1029/2011ja017062.
- N. Y. Liu, B. Kosar, S. Sadighi, J. R. Dwyer, and H. K. Rassoul (2012), Formation of streamer discharges from an isolated ionization column at subbreakdown conditions, *Phys. Rev. Lett.*, 109(2), 025002, doi:/10.1103/physrevlett.109.025002.
- J. J. Lowke (1992), Theory of electrical breakdown in air: The role of metastable oxygen molecules, *J. Phys. D: Appl. Phys.*, 25, 202–210.
- G. Lu *et al.* (2011), Lightning development associated with two negative gigantic jets, *Geophys. Res. Lett.*, 38, L12801, doi:/10.1029/2011gl047662.
- A. Luque, U. Ebert, C. Montijn, and W. Hundsdorfer (2007), Photoionization in negative streamers: Fast computations and two propagation modes, *Appl. Phys. Lett.*, 90, 081501, doi:/10.1063/1.2435934.
- A. Luque and U. Ebert (2009), Emergence of sprite streamers from screening-ionization waves in the lower ionosphere, *Nat. Geosci.*, 2(11), 757–760, doi:/10.1038/ngeo662.
- A. Luque and U. Ebert (2010), Sprites in varying air density: Charge conservation, glowing negative trails and changing velocity, *Geophys. Res. Lett.*, 37, L06806, doi:/10.1029/2009gl041982.
- A. Luque and F. J. Gordillo-Vázquez (2011a), Mesospheric electric breakdown and delayed sprite ignition caused by electron detachment, *Nat. Geosci.*, 5, 22–25, doi:/10.1038/ngeo1314.
- A. Luque and F. J. Gordillo-Vázquez (2011b), Sprite beads originating from inhomogeneities in the mesospheric electron density, *Geophys. Res. Lett.*, 38, L04808, doi:/10.1029/2010gl046403.
- W. A. Lyons (1996), Sprite observations above the U.S. high plains in relation to their parent thunderstorm systems, *J. Geophys. Res.*, 101, 29641.
- W. A. Lyons, T. E. Nelson, R. A. Armstrong, V. P. Pasko, and M. A. Stanley (2003a), Upward electrical discharges from thunderstorm tops, *Bull. Am. Meteorol. Soc.*, 84(4), 445–454, doi:/10.1175/bams-84-4-445.
- W. A. Lyons, T. E. Nelson, E. R. Williams, S. A. Cummer, and M. A. Stanley (2003b), Characteristics of sprite-producing positive cloud-to-ground lightning during the 19 July 2000 STEPS mesoscale convective systems, *Mon. Wea. Rev.*, 131(4), 2417–2427.
- T. C. Marshall and W. D. Rust (1993), Two types of vertical electrical structures in stratiform precipitation regions of mesoscale convective systems, *Bull. Am. Meteorol. Soc.*, 74(11), 2159–2170.
- R. A. Marshall and U. S. Inan (2005), High-speed telescopic imaging of sprites, *Geophys. Res. Lett.*, 32, L05804, doi:/10.1029/2004gl021988.
- R. A. Marshall and U. S. Inan (2006), High-speed measurements of small-scale features in sprites: Sizes and lifetimes, *Radio Sci.*, 41, RS6S43, doi:/10.1029/2005rs003353.
- R. A. Marshall, U. S. Inan, and T. W. Chevalier (2008), Early VLF perturbations caused by lightning EMP-driven dissociative attachment, *Geophys. Res. Lett.*, 35, L21807, doi:/10.1029/2008gl035358.
- R. A. Marshall, U. S. Inan, and V. S. Glukhov (2010), Elves and associated electron density changes due to cloud-to-ground and in-cloud lightning discharges, *J. Geophys. Res.*, 115, A00E17, doi:/10.1029/2009ja014469.

- R. A. Marshall (2012), An improved model of the lightning electromagnetic field interaction with the d-region ionosphere, *J. Geophys. Res.*, 117, A03316, doi:/10.1029/2011ja017408.
- M. G. McHarg, R. K. Haaland, D. R. Moudry, and H. C. Stenbaek-Nielsen (2002), Altitude-time development of sprites, *J. Geophys. Res.*, 107(A11), 1364, doi:/10.1029/2001ja000283.
- M. G. McHarg, H. C. Stenbaek-Nielsen, and T. Kammer (2007), Streamer development in sprites, *Geophys. Res. Lett.*, 34, L06804, doi:/10.1029/2006gl027854.
- M. G. McHarg, H. C. Stenbaek-Nielsen, T. Kanmae, and R. K. Haaland (2010), Streamer tip splitting in sprites, *J. Geophys. Res.*, 115, A00E53, doi:/10.1029/2009ja014850.
- S. B. Mende, R. L. Rairden, G. R. Swenson, and W. A. Lyons (1995), Sprite spectra; N<sub>2</sub> 1 PG band identification, *Geophys. Res. Lett.*, 22, 2633–2637.
- S. B. Mende *et al.* (2005), D region ionization by lightning-induced EMP, *J. Geophys. Res.*, 110, A11312, doi:/10.1029/2005ja011064.
- S. B. Mende *et al.* (2006), Spacecraft based studies of transient luminous events, in *Sprites, Elves and Intense Lightning Discharges, NATO Science Series II: Mathematics, Physics and Chemistry*, vol. 225, edited by M. Füllekrug, E. A. Mareev, and M. J. Rycroft, pp. 123–149, Springer, Heidelberg, Germany.
- G. A. Mesyats (2006), Reviews of topical problems: Similarity laws for pulsed gas discharges, *Phys.-Usp.*, 49, 1045–1065, doi:/10.1070/pu2006v049n10abeh006118.
- E. V. Mishin and G. M. Milikh (2008), Blue jets: Upward lightning, *Space Sci. Rev.*, 137, 473–488, doi:/10.1007/s11214-008-9346-z.
- R. Miyasato, M. J. Taylor, H. Fukunishi, and H. C. Stenbaek-Nielsen (2002), Statistical characteristics of sprite halo events using coincident photometric and imaging data, *Geophys. Res. Lett.*, 29(21), 2033, doi:/10.1029/2001gl014480.
- J. S. Morrill *et al.* (1998), Time resolved N<sub>2</sub> triplet state vibrational populations and emissions associated with red sprites, *J. Atmos. Solar Terr. Phys.*, 60, 811–829.
- J. S. Morrill *et al.* (2002), Electron energy and electric field estimates in sprites derived from ionized and neutral N<sub>2</sub> emissions, *Geophys. Res. Lett.*, 29(10), 1462, doi:/10.1029/2001gl014018.
- R. Morrow and J. J. Lowke (1997), Streamer propagation in air, *J. Phys. D: Appl. Phys.*, 30, 614–627.
- G. D. Moss, V. P. Pasko, N. Liu, and G. Veronis (2006), Monte Carlo model for analysis of thermal runaway electrons in streamer tips in transient luminous events and streamer zones of lightning leaders, *J. Geophys. Res.*, 111, A02307, doi:/10.1029/2005ja011350.
- D. R. Moudry, H. C. Stenbaek-Nielsen, D. D. Sentman, and E. M. Wescott (2002), Velocities of sprite tendrils, *Geophys. Res. Lett.*, 29(20), 1992, doi:/10.1029/2002gl015682.
- D. R. Moudry, H. C. Stenbaek-Nielsen, D. D. Sentman, and E. M. Wescott (2003), Imaging of elves, halos and sprite initiation at 1 ms time resolution, *J. Atmos. Solar Terr. Phys.*, 65, 509–518, doi:/10.1016/s1364-6826(02)00323-1.
- G. V. Naidis (1997), Effects of nonlocality on the dynamics of streamers in positive corona discharges, *Tech. Phys. Lett.*, 23, 493–494.



- T. Neubert (2003), On sprites and their exotic kin, *Science*, 300, 747–749.
- T. Neubert, M. Rycroft, T. Farges, E. Blanc, O. Chanrion, E. Arnone, A. Odzimek, N. Arnold, C.-F. Enell, E. Turunen, T. Bösinger, Á. Mika, C. Haldoupis, R. J. Steiner, O. van der Velde, S. Soula, P. Berg, F. Boberg, P. Thejll, B. Christiansen, M. Ignaccolo, M. Füllekrug, P. T. Verronen, J. Montanya, and N. Crosby (2008), Recent Results from Studies of Electric Discharges in the Mesosphere, *Surv. Geophys.*, 29, 71–137, doi:/10.1007/s10712-008-9043-1.
- T. Neubert and O. Chanrion (2013), On the electric breakdown field of the mesosphere and the influence of electron detachment, *Geophys. Res. Lett.*, 40, 2373–2377, doi:/10.1002/grl.50433.
- R. T. Newsome and U. S. Inan (2010), Free-running ground-based photometric array imaging of transient luminous events, *J. Geophys. Res.*, 115, A00E41, doi:/10.1029/2009ja014834.
- S. V. Pancheshnyi, S. M. Starikovskaia, and A. Y. Starikovskii (2001), Role of photoionization processes in propagation of cathode-directed streamer, *J. Phys. D: Appl. Phys.*, 34, 105–115.
- V. P. Pasko and U. S. Inan (1994), Recovery signatures of lightning-associated VLF perturbations as a measure of the lower ionosphere, *J. Geophys. Res.*, 99, 17523–17538, doi:/10.1029/94ja01378.
- V. P. Pasko, U. S. Inan, and T. F. Bell (1996), Blue jets produced by quasi-electrostatic pre-discharge thundercloud fields, *Geophys. Res. Lett.*, 23(3), 301–304.
- V. P. Pasko, U. S. Inan, T. F. Bell, and Y. N. Taranenko (1997), Sprites produced by quasi-electrostatic heating and ionization in the lower ionosphere, *J. Geophys. Res.*, 102(A3), 4529–4561, doi:/10.1029/96ja03528.
- V. P. Pasko, U. S. Inan, T. F. Bell, and S. C. Reising (1998a), Mechanism of ELF radiation from sprites, *Geophys. Res. Lett.*, 25(18), 3493.
- V. P. Pasko, U. S. Inan, and T. F. Bell (1998b), Spatial structure of sprites, *Geophys. Res. Lett.*, 25, 2123–2126.
- V. P. Pasko, U. S. Inan, and T. F. Bell (2000), Fractal structure of sprites, *Geophys. Res. Lett.*, 27(4), 497–500, doi:/10.1029/1999gl010749.
- V. P. Pasko and J. J. George (2002), Three-dimensional modeling of blue jets and blue starters, *J. Geophys. Res.*, 107(A12), 1458, doi:/10.1029/2002ja009473.
- V. P. Pasko and H. C. Stenbaek-Nielsen (2002), Diffuse and streamer regions of sprites, *Geophys. Res. Lett.*, 29(10), 1440, doi:/10.1029/2001gl014241.
- V. P. Pasko, M. A. Stanley, J. D. Matthews, U. S. Inan, and T. G. Wood (2002), Electrical discharge from a thundercloud top to the lower ionosphere, *Nature*, 416, 152–154, doi:/10.1038/416152a.
- V. P. Pasko (2003), Electric jets, *Nature*, 423, 927–929.
- V. P. Pasko (2006), Theoretical modeling of sprites and jets, in *Sprites, Elves and Intense Lightning Discharges, NATO Science Series II: Mathematics, Physics and Chemistry*, vol. 225, edited by M. Füllekrug, E. A. Mareev, and M. J. Rycroft, pp. 253–311, Springer, Heidelberg, Germany.
- V. P. Pasko (2007), Red sprite discharges in the atmosphere at high altitude: The molecular physics and the similarity with laboratory discharges, *Plasma Sources Sci. Technol.*, 16, S13–S29, doi:/10.1088/0963-0252/16/1/s02.
- V. P. Pasko (2008), Blue jets and gigantic jets: Transient luminous events between thunderstorm tops and the lower ionosphere, *Plasma Phys. Control. Fusion*, 50, 124050, doi:/10.1088/0741-3335/50/12/124050.

- V. P. Pasko (2009), Mechanism of lightning-associated infrasonic pulses from thunderclouds, *J. Geophys. Res.*, 114, D08205, doi:/10.1029/2008jd011145.
- V. P. Pasko (2010), Recent advances in theory of transient luminous events, *J. Geophys. Res.*, 115, A00E35, doi:/10.1029/2009ja014860.
- V. P. Pasko, Y. Yair, and C.-L. Kuo (2011), Lightning related transient luminous events at high Altitude in the Earth's atmosphere: Phenomenology, mechanisms and effects, *Space Sci. Rev.*, 168, 475–516, doi:/10.1007/s11214-011-9813-9.
- V. P. Pasko, J. Qin, and S. Celestin (2013), Toward better understanding of sprite streamers: Initiation, morphology, and polarity asymmetry, *Surv. Geophys.*, 34, 797–830, doi:/10.1007/s10712-013-9246-y.
- N. I. Petrov and G. N. Petrova (1999), Physical mechanisms for the development of lightning discharges between a thundercloud and the ionosphere, *Tech. Phys.*, 44, 472–475, doi:/10.1134/1.1259327.
- Z. L. Petrovic *et al.* (2007), Topical review: Kinetic phenomena in charged particle transport in gases, swarm parameters and cross section data, *Plasma Sources Sci. Technol.*, 16, doi:/10.1088/0963-0252/16/1/s01.
- C. Price *et al.* (2004), Ground-based detection of TLE-producing intense lightning during the MEIDEX mission on board the Space Shuttle Columbia, *Geophys. Res. Lett.*, 31, L20107, doi:/10.1029/2004gl020711.
- J. Qin, S. Célestin, and V. P. Pasko (2011), On the inception of streamers from sprite halo events produced by lightning discharges with positive and negative polarity, *J. Geophys. Res.*, 116, A06305, doi:/10.1029/2010ja016366.
- J. Qin, S. Célestin, and V. P. Pasko (2012a), Formation of single and double-headed streamers in sprite-halo events, *Geophys. Res. Lett.*, 39, 5810, L05810, doi:/10.1029/2012gl051088.
- J. Qin, S. Célestin, and V. P. Pasko (2012b), Minimum charge moment change in positive and negative cloud to ground lightning discharges producing sprites, *Geophys. Res. Lett.*, 39, 22801, L22801, doi:/10.1029/2012gl053951.
- J. Qin, S. Célestin, and V. P. Pasko (2012c), Low frequency electromagnetic radiation from sprite streamers, *Geophys. Res. Lett.*, 39, L22803, doi:/10.1029/2012gl053991.
- J. Qin, S. Célestin, and V. P. Pasko (2013), Dependence of positive and negative sprite morphology on lightning characteristics and upper atmospheric ambient conditions, *J. Geophys. Res.*, 118, 2623–2638, doi:/10.1029/2012ja017908.
- Y. P. Raizer (1991), *Gas Discharge Physics*, Springer, New York.
- Y. P. Raizer, G. M. Milikh, M. N. Shneider, and S. V. Novakovski (1998), Long streamers in the upper atmosphere above thundercloud, *J. Phys. D: Appl. Phys.*, 31, 3255–3264.
- Y. P. Raizer, G. M. Milikh, and M. N. Shneider (2006), On the mechanism of blue jet formation and propagation, *Geophys. Res. Lett.*, 33, L23801, doi:/10.1029/2006gl027697.
- Y. P. Raizer, G. M. Milikh, and M. N. Shneider (2007), Leader streamers nature of blue jets, *J. Atmos. Sol.-Terr. Phys.*, 69, 925–938, doi:/10.1016/j.jastp.2007.02.007.
- V. A. Rakov and M. A. Uman (2003), *Lightning: Physics and Effects*, Cambridge University Press, Cambridge, U.K.; New York.

- S. W. Rayment and J. L. Moruzzi (1978), Electron detachment studies between  $O^-$  ions and nitrogen, *J. Mass Spectrom. Ion Phys.*, 26, 321–326.
- S. C. Reising, U. S. Inan, and T. F. Bell (1999), ELF sferic energy as a proxy indicator for sprite occurrence, *Geophys. Res. Lett.*, 26, 987–990.
- J. A. Rioussset, V. P. Pasko, P. R. Krehbiel, R. J. Thomas, and W. Rison (2007), Three-dimensional fractal modeling of intracloud lightning discharge in a New Mexico thunderstorm and comparison with lightning mapping observations, *J. Geophys. Res.*, 112, D15203, doi:/10.1029/2006JD007621.
- J. A. Rioussset, V. P. Pasko, and A. Bourdon (2010a), Air-density-dependent model for analysis of air heating associated with streamers, leaders, and transient luminous events, *J. Geophys. Res.*, 115, A12321, doi:/10.1029/2010ja015918.
- J. A. Rioussset *et al.* (2010b), Modeling of thundercloud screening charges: Implications for blue and gigantic jets, *J. Geophys. Res.*, 115, A00E10, doi:/10.1029/2009ja014286.
- W. Rison, R. J. Thomas, P. R. Krehbiel, T. Hamlin, and J. Harlin (1999), A GPS-based three-dimensional lightning mapping system: Initial observations in central New Mexico, *Geophys. Res. Lett.*, 26(23), 3573–3576, doi:/10.1029/1999gl010856.
- C. J. Rodger, A. Seppälä, and M. A. Clilverd (2008), Significance of transient luminous events to neutral chemistry: Experimental measurements, *Geophys. Res. Lett.*, 35, L07803, doi:/10.1029/2008gl033221.
- R. Roussel-Dupré, J. J. Colman, E. Symbalisty, D. Sentman, and V. P. Pasko (2008), Physical Processes Related to Discharges in Planetary Atmospheres, *Space Sci. Rev.*, 137, 51–82, doi:/10.1007/s11214-008-9385-5.
- P. Ségur, A. Bourdon, E. Marode, D. Bessiéres, and J. H. Paillol (2006), The use of an improved Eddington approximation to facilitate the calculation of photoionization in streamer discharges, *Plasma Sources Sci. Technol.*, 15, 648–660, doi:/10.1088/0963-0252/15/4/009.
- D. D. Sentman, E. M. Wescott, D. L. Osborne, D. L. Hampton, and M. J. Heavner (1995), Preliminary results from the Sprites94 campaign: Red sprites, *Geophys. Res. Lett.*, 22, 1205–1208.
- D. D. Sentman, E. M. Wescott, M. J. Heavner, and D. R. Moudry (1996), Observations of sprite beads and balls, *Eos Trans. AGU*, 77(46).
- D. D. Sentman, D. R. Moudry, H. C. Stenbaek-Nielsen, E. M. Wescott, and F. T. São Sabbas (2000), Electric field effects on chemical reaction rates within sprites, *Eos Trans. AGU*, 81(45).
- D. D. Sentman *et al.* (2003), Simultaneous observations of mesospheric gravity waves and sprites generated by a midwestern thunderstorm, *J. Atmos. Solar Terr. Phys.*, 65, 537–550.
- D. D. Sentman, H. C. Stenbaek-Nielsen, M. G. McHarg, and J. S. Morrill (2008), Plasma chemistry of sprite streamers, *J. Geophys. Res.*, 113, D11112, doi:/10.1029/2007jd008941.
- D. D. Sentman and H. C. Stenbaek-Nielsen (2009), Chemical effects of weak electric fields in the trailing columns of sprite streamers, *Plasma Sources Sci. Technol.*, 18(3), doi:/10.1088/0963-0252/18/3/034012.
- D. D. Sentman (2010), Special Section: Effects of thunderstorms and lightning in the upper atmosphere, *J. Geophys. Res.*, [http://onlinelibrary.wiley.com/journal/10.1002/\(ISSN\)2169-9402/specialsection/THUNDER1](http://onlinelibrary.wiley.com/journal/10.1002/(ISSN)2169-9402/specialsection/THUNDER1).

- T. R. Shepherd, W. D. Rust, and T. C. Marshall (1996), Electric fields and charges near 0°C in stratiform clouds, *Mon. Wea. Rev.*, 124(5), 919–938.
- D. Singh *et al.* (2008), Thunderstorms, lightning, sprites and magnetospheric whistler-mode radio waves, *Surv. Geophys.*, 29, 499–551, doi:/10.1007/s10712-008-9053-z.
- S. Soula *et al.* (2011), Gigantic jets produced by an isolated tropical thunderstorm near Réunion Island, *J. Geophys. Res.*, 116(D15), D19103, doi:/10.1029/2010jd015581.
- M. Stanley *et al.* (1996), Observations of sprites and jets from Langmuir Laboratory, New Mexico, *Eos Trans. AGU*, 77(46).
- M. Stanley *et al.* (1999), High speed video of initial sprite development, *Geophys. Res. Lett.*, 26, 3201–3204.
- M. Stanley, M. Brook, P. Krehbiel, and S. A. Cummer (2000), Detection of daytime sprites via a unique sprite ELF signature, *Geophys. Res. Lett.*, 27, 871–874.
- H. C. Stenbaek-Nielsen, D. R. Moudry, E. M. Wescott, D. D. Sentman, and F. T. S. Ao Sabbas (2000), Sprites and possible mesospheric effects, *Geophys. Res. Lett.*, 27, 3829–3832.
- H. C. Stenbaek-Nielsen, M. G. McHarg, T. Kammae, and D. D. Sentman (2007), Observed emission rates in sprite streamer heads, *Geophys. Res. Lett.*, 34, L11105, doi:/10.1029/2007gl029881.
- H. C. Stenbaek-Nielsen and M. G. McHarg (2008), High time-resolution sprite imaging: Observations and implications, *J. Phys. D: Appl. Phys.*, 41(23), 234009, doi:/10.1088/0022-3727/41/23/234009.
- H. C. Stenbaek-Nielsen, R. Haaland, M. G. McHarg, B. A. Hensley, and T. Kanmae (2010), Sprite initiation altitude measured by triangulation, *J. Geophys. Res.*, 115, A00E12, doi:/10.1029/2009ja014543.
- H. C. Stenbaek-Nielsen, M. G. McHarg, R. Haaland, and T. Kanmae (2011), Sprite halo structures and streamer onset, *General Assembly and Scientific Symposium*, 2011 XXXth URSI.
- H. C. Stenbaek-Nielsen, T. Kanmae, M. G. McHarg, and R. Haaland (2013), High-Speed Observations of Sprite Streamers, *Surv. Geophys.*, 34, 769–795, doi:/10.1007/s10712-013-9224-4.
- H. T. Su *et al.* (2003), Gigantic jets between a thundercloud and the ionosphere, *Nature*, 423, 974–976, doi:/10.1038/nature01759.
- A. I. Sukhorukov, E. V. Mishin, P. Stubbe, and M. J. Rycroft (1996), On blue jet dynamics, *Geophys. Res. Lett.*, 23(13), 1625–1628.
- D. M. Suszcynsky, R. Roussel-Dupre, W. A. Lyons, and R. A. Armstrong (1998), Blue-light imagery and photometry of sprites, *J. Atmos. Solar Terr. Phys.*, 60, 801–809.
- T. Suzuki, M. Hayakawa, Y. Hobara, and K. Kusunoki (2012), First detection of summer blue jets and starters over Northern Kanto area of Japan: Lightning activity, *J. Geophys. Res.*, 117, A07307, doi:/10.1029/2011ja017366.
- Y. Takahashi, M. Fujito, Y. Watanabe, H. Fukunishi, and W. A. Lyons (2000), Temporal and spatial variations in the intensity ratio of N<sub>2</sub> 1st and 2nd positive bands in SPRITES, *Middle Atmosphere and Lower Thermosphere Electrodynamics Advances in Space Research*, 26(8), 1205–1208.
- Y. Takahashi, Y. Sanmiya, M. Sato, T. Kudo, and T. Inoue (2012), Lifetime and structures of TLEs captured by high-speed camera on board aircraft,

- Abstract AE41A-07 presented at 2012 Fall Meeting, AGU, San Francisco, Calif., 3–7 Dec.
- Y. N. Taranenکو, U. S. Inan, and T. F. Bell (1992), Optical signatures of lightning-induced heating of the D region, *Geophys. Res. Lett.*, 19, 1815–1818, doi:/10.1029/92gl02106.
- Y. N. Taranenکو, U. S. Inan, and T. F. Bell (1993), The interaction with the lower ionosphere of electromagnetic pulses from lightning: Excitation of optical emissions, *Geophys. Res. Lett.*, 20, 2675–2678, doi:/10.1029/93gl02838.
- M. J. Taylor and S. Clark (1996), High resolution CCD and video imaging of sprites and elves in the N<sub>2</sub> first positive band emission, *Eos Trans. AGU*, 77(46).
- M. J. Taylor *et al.* (2008), Rare measurements of a sprite with halo event driven by a negative lightning discharge over Argentina, *Geophys. Res. Lett.*, 35, L14812, L14812, doi:/10.1029/2008gl033984.
- A. V. Vallance-Jones (1974), *Aurora*, D. Reidel Publishing Co., Norwell, Mass.
- O. A. van der Velde *et al.* (2007), Analysis of the first gigantic jet recorded over continental North America, *J. Geophys. Res.*, 112, D20104, doi:/10.1029/2007jd008575.
- O. A. van der Velde *et al.* (2010), Multi-instrumental observations of a positive gigantic jet produced by a winter thunderstorm in Europe, *J. Geophys. Res.*, 115(D14), D24301, doi:/10.1029/2010jd014442.
- P. A. Vitello, B. M. Penetrante, and J. N. Bardsley (1993), Multidimensional modeling of the dynamic morphology of streamer coronas, in *Non-Thermal Plasma Techniques for Pollution Control, NATO ASI Ser.*, vol. G34, part A, edited by B. M. Penetrante and S. E. Schultheis, pp. 249–271, Springer-Verlag, New York.
- J. R. Wait and K. P. Spies (1964), Characteristics of the Earth-ionosphere waveguide for VLF radio waves, *Tech. Note 300*, Natl. Bur. of Stand., Boulder, Colo., 30 December.
- E. M. Wescott, D. Sentman, D. Osborne, D. Hampton, and M. Heavner (1995), Preliminary results from the Sprites94 aircraft campaign: 2. Blue jets, *Geophys. Res. Lett.*, 22(10), 1209–1212.
- E. M. Wescott *et al.* (1996), Blue starters: Brief upward discharges from an intense Arkansas thunderstorm, *Geophys. Res. Lett.*, 23(16), 2153–2156, doi:/10.1029/96gl01969.
- E. M. Wescott, D. D. Sentman, M. J. Heavner, D. L. Hampton, and O. H. Vaughan Jr. (1998), Blue jets: Their relationship to lightning and very large hailfall, and their physical mechanisms for their production, *J. Atmos. Solar Terr. Phys.*, 60, 713–724.
- E. M. Wescott *et al.* (2001a), Triangulation of sprites, associated halos and their possible relation to causative lightning and micrometeors, *J. Geophys. Res.*, 106(A6), 10467–10478, doi:/10.1029/2000ja000182.
- E. M. Wescott *et al.* (2001b), New evidence for the brightness and ionization of blue starters and blue jets, *J. Geophys. Res.*, 106, 21549–21554, doi:/10.1029/2000ja000429.
- E. R. Williams (2006), Problems in lightning physics—the role of polarity asymmetry, *Plasma Sources Sci. Technol.*, 15(2), S91–S108, doi:/10.1088/0963-0252/15/2/s12.

- E. Williams, E. Downes, R. Boldi, W. Lyons, and S. Heckman (2007), Polarity asymmetry of sprite-producing lightning: A paradox?, *Radio Sci.*, 42, RS2S17, doi:/10.1029/2006rs003488.
- E. Williams *et al.* (2012), Resolution of the sprite polarity paradox: The role of halos, *Radio Sci.*, 47, RS2002, doi:/10.1029/2011rs004794.
- C. T. R. Wilson (1925), The electric field of a thundercloud and some of its effects, *Proc. Phys. Soc. London*, 37(32D).
- J. Yang and G. L. Feng (2012), A gigantic jet event observed over a thunderstorm in mainland china, *Chinese Science Bulletin*, 57(36), 4791–4800, doi:/10.1007/s11434-012-5486-3.
- W. J. Yi and P. F. Williams (2002), Experimental study of streamer in pure N<sub>2</sub> and N<sub>2</sub>/O<sub>2</sub> mixtures and a  $\approx 13$  cm gap, *J. Phys. D: Appl. Phys.*, 35, 205–218.
- M. B. Zheleznyak, A. K. Mnatsakanyan, and S. V. Sizykh (1982), Photoionization of nitrogen and oxygen mixtures by radiation from a gas discharge, *High Temp.*, 20, 357–362.



---

## Chapter 18

# Energetic radiation from thunderstorms and lightning

*Joseph R. Dwyer and Hamid K. Rassoul*

---

### 18.1 Introduction

Electrical discharges in gases can be roughly divided into two categories: those whose behavior is governed by low-energy electrons, with energies less than a few tens of eV, and those whose behavior is governed by high-energy electrons, with energies often reaching several tens of MeV. The first category, which we shall refer to as low-energy discharges, is also called conventional discharges, which includes a wide range of phenomena such as corona discharges, including streamer and glow discharges, Trichel pulses, Townsend discharges, and spark breakdown [Loeb, 1965]. We note that low-energy here refers to the energy of the particles (electrons, photons, and ions) and does not necessarily describe the total energy of the discharge, which can be very large. In contrast to low-energy discharges, the discharges involving high-energy electrons, which we shall refer to as high-energy discharges, all involve energetic runaway electrons and include the mechanisms that produce terrestrial gamma-ray flashes (TGFs), x-rays from lightning and laboratory sparks, gamma-ray glows from thunderstorms, and probably neutron production associated with thunderstorms and lightning [Dwyer *et al.*, 2012; Dwyer and Uman, 2013].

Low-energy and high-energy discharges are often coupled, with low-energy discharges sometimes generating electric fields and providing seed particles for high-energy discharges, and the high-energy discharges sometimes enhancing electric fields and providing ionization, and hence free electrons, for low-energy discharges. Although, the two types of discharges may be coupled, in much of the literature they are treated separately. It is quite remarkable how similar low-energy and high-energy discharges are, despite having energies that differ by many orders of magnitude. Specifically, there are several examples of processes at low energies that have direct analogies at high energies. As a result, high-energy discharge processes often mirror those that occur at low energies, except that the former involve energetic particles and occur over much larger length scales.

In this chapter, we first review the observations of high-energy atmospheric physics processes within our atmosphere, including x-ray emissions from lightning and gamma-ray emissions, such as gamma-ray glows and TGFs, from thunderclouds. We then introduce and explain the mechanisms involved in high-energy discharges and compare these mechanisms to their low-energy counterparts. We also discuss recent models that have been developed to explain TGFs, including “dark lightning.”



## 18.2 Observations

### 18.2.1 X-rays from lightning

It is quite amazing that the fact that lightning emits hard x-rays ( $>100$  keV) was not established until ten years ago, especially considering that the x-ray emissions are very bright, often resulting in pulse pile-up and the saturation of readout electronics and that they occur for most lightning flashes [Dwyer *et al.*, 2012]. Two factors hampered earlier efforts to detect x-rays from lightning: x-rays with these energies usually propagate only a few hundred meters through air near sea level, and x-ray emissions recorded near the ground typically last less than about 1 msec for lightning stepped leaders, less than a few tens of microseconds for dart leaders, and somewhere in between for dart-stepped leaders. As a result, the lightning must strike relatively close to the detectors, and the detectors and their electronics must be fast enough to detect very short, high intensity bursts of x-rays. In recent years, such fast detector systems have become more readily available. Even some relatively cheap “off-the-shelf” systems are now adequate for the purpose. As for the issue of the lightning being close enough to the detectors to record x-rays, one possibility is to operate detectors for several years in a location with frequent lightning, such as central Florida. Sooner or later, a natural lightning strike will occur at a short enough distance to the detector for x-rays to be recorded.

There is a long history of searching for x-ray emissions from thunderstorms and lightning, starting shortly after C.T.R. Wilson first hypothesized that such radiation could be produced by strong electric fields in our atmosphere [Wilson, 1925]. Several of these measurements did report positive detections of energetic radiation associated with thunderstorms or lightning. However, roughly an equal number of observations reported that no significant x-ray emissions were detected [Suszcynsky *et al.*, 1996]. As a result, at the start of the 21st century, it was generally believed that lightning does not emit any significant number of x-rays. The situation changed in 2001 when Moore *et al.* reported bursts of energetic radiation, measured on a mountain top, associated with stepped leaders in natural cloud-to-ground lightning strikes. The energetic radiation began about 1 msec before the start of the return strokes and ended at the times of the return strokes [Moore *et al.*, 2001].

A productive way to investigate the x-ray emissions from lightning is to use rocket-triggered lightning, rather than waiting for natural lightning to strike nearby. For classical rocket-triggered lightning, a small rocket with a wire attached is launched when a thunderstorm is in the area and the electric fields at the ground are measured to be sufficiently elevated [Rakov and Uman, 2003; Uman, 2010]. The wire may either be on a spool that is lifted by the rocket, while one end of the wire is attached to the ground, or the spool may remain on the ground and the rocket lifts one end of the wire. In either case, a grounded wire rapidly extends upward. Often, when the wire reaches a length of a few hundred meters, the electric field at the tip of the grounded wire and the rocket becomes sufficiently enhanced to initiate an upward positive leader (hot discharge channel). During this process, the wire usually explodes due to the high currents flowing through it. The leader quickly propagates upward and eventually finds the cloud charge inside the thunderstorm. A downward lightning dart leader often follows the path of the leader and the remnants of the wire to the rocket launcher, resulting in a bright return stroke. Other leader/return stroke sequences may then follow the initial stroke. Figure 18.1 illustrates the sequence of events involved in classical rocket-triggered lightning.

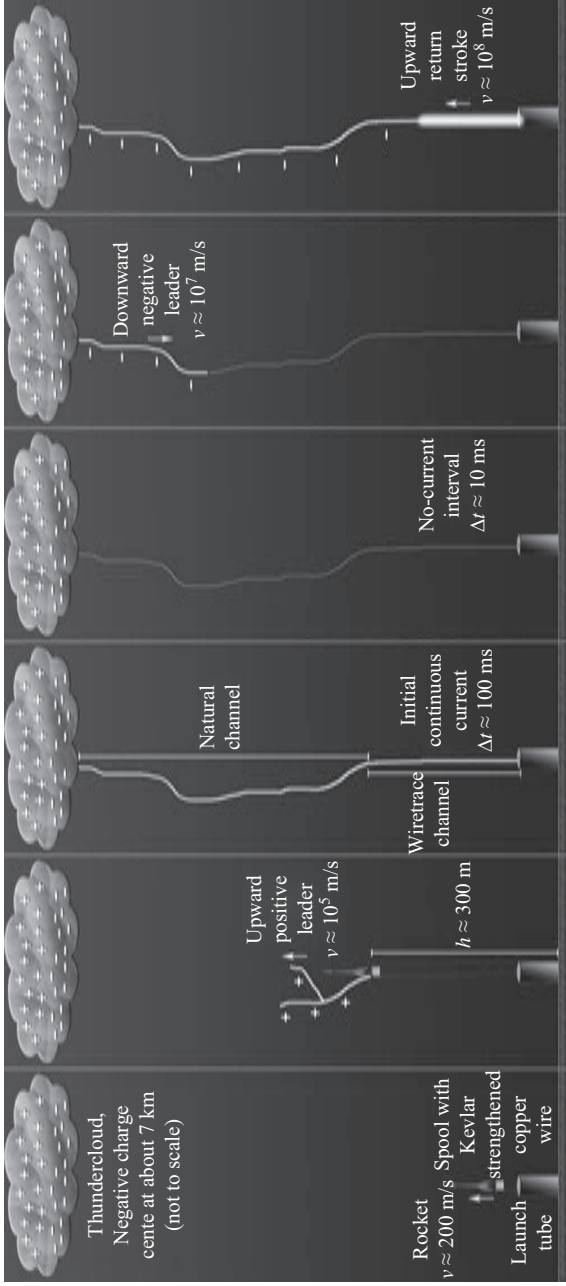


**Figure 18.1** Rocket-triggered lightning. Starting from the leftmost panel, a small rocket with a spool of Kevlar-coated copper wire is launched during thunderstorm conditions. As the rocket and spool rise, one end of the wire remains attached to the ground. Once the wire extends upward a few hundred meters, an upward positive leader initiates and propagates upward at a speed of about  $10^5$  m/s. After a short interval in which no current flows, a dart leader follows the warm channel back down to the launcher. This results in a return stroke, which propagates back up the channel at a speed of about  $10^8$  m/s and has a peak current of tens of kA. Figure from Uman [2010]

Rocket-triggered lightning is thought to be the same as the subsequent strokes of natural lightning. For natural lightning, rather than a rocket and wire, the gap between the cloud and the ground is breached by a stepped leader, which usually propagates downward from the cloud to the ground. When the stepped leader connects to the ground, a return stroke occurs. For natural lightning, this first return stroke usually has a peak current ( $\sim 30$  kA) that is larger than the peak current for subsequent strokes ( $\sim 15$  kA) [Rakov and Uman, 2003].

One advantage of rocket-triggered lightning is that the time and location of the lightning strike is known beforehand, allowing the detectors to be set up in close proximity to the lightning channel and the recording system to be armed and ready for the flash. A second advantage of rocket-triggered lightning is the experiment may be repeated many times. For example, at the International Center for Lightning Research and Testing (ICLRT) at Camp Blanding in north-central Florida, jointly run by the University of Florida and Florida Tech, about two dozen rocket-triggered lightning flashes are produced in a typical summer.

In 2003, Dwyer *et al.* reported the observation of energetic radiation during the dart and dart-stepped leader phase of rocket-triggered lightning [Dwyer *et al.*, 2003]. The energetic radiation was observed to occur before most return strokes, usually starting some tens of microseconds before the stroke and always terminating very close to the time of the return stroke. This work was followed by detailed studies of the properties of this energetic emission. It was shown that the energetic radiation is indeed x-ray emission, mostly in the few hundred keV range and occasionally reaching a few MeV [Dwyer *et al.*, 2004; Salah *et al.*, 2009; Schaal *et al.*, 2012]. As can be seen in Figure 18.2, the x-rays usually arrive in short ( $< 1$   $\mu$ sec) bursts, and the x-rays almost always stop near the beginning of the return stroke [Dwyer *et al.*, 2004; Salah *et al.*, 2009]. Measurements of the x-rays from natural lightning striking the ICLRT and other locations confirm that the x-ray emission from natural lightning stepped leaders is very similar to that from rocket-triggered lightning [Dwyer *et al.*, 2005a; Yoshida *et al.*, 2008; Mallick *et al.*, 2012]. It has also been shown that the x-ray bursts occur at the time of the step formation for dart-stepped leaders from triggered lightning and stepped leaders from natural lightning [Dwyer *et al.*, 2005a], possibly during the corona flash that occurs below the new leader segment [Howard *et al.*, 2008].

There appears to be a large amount of variation in the x-ray intensity from step to step and from stroke to stroke. It has been found that for triggered lightning, the return stroke current correlates with the fluence of the x-rays that preceded it, possibly because larger charges being transported by the leader causes both larger electric fields, which lead to the x-ray production, and larger return stroke currents [Schaal *et al.*, 2012]. However, this correlation only extends up to return stroke currents of about 10 kA. Above that, the x-ray fluence increases only gradually with increased return stroke current, with the maximum corresponding to a fluence of  $10^{17}$  electrons/sec at the lightning source.

Using the Thunderstorm Energetic Radiation Array (TERA) to measure x-rays from rocket-triggered lightning at the ICLRT, Saleh *et al.* [2009] found that the x-ray emission that preceded a return stroke during a bright dart-stepped leader appeared to be approximately isotropic into the lower hemisphere. Later, Schaal *et al.* [2012] showed that the x-ray emission may be more of a broad beam that rotates in the azimuthal direction, giving the appearance of being roughly isotropic on average. Howard *et al.* [2008, 2010] and Hill [2012] used a subset of TERA to

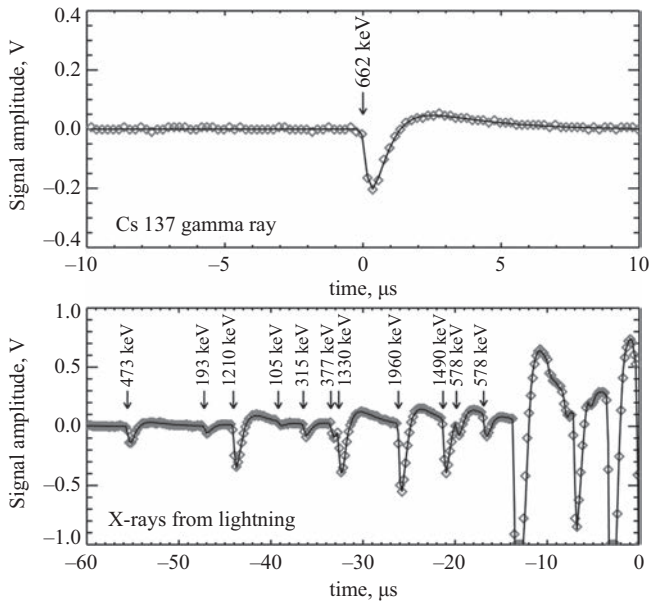
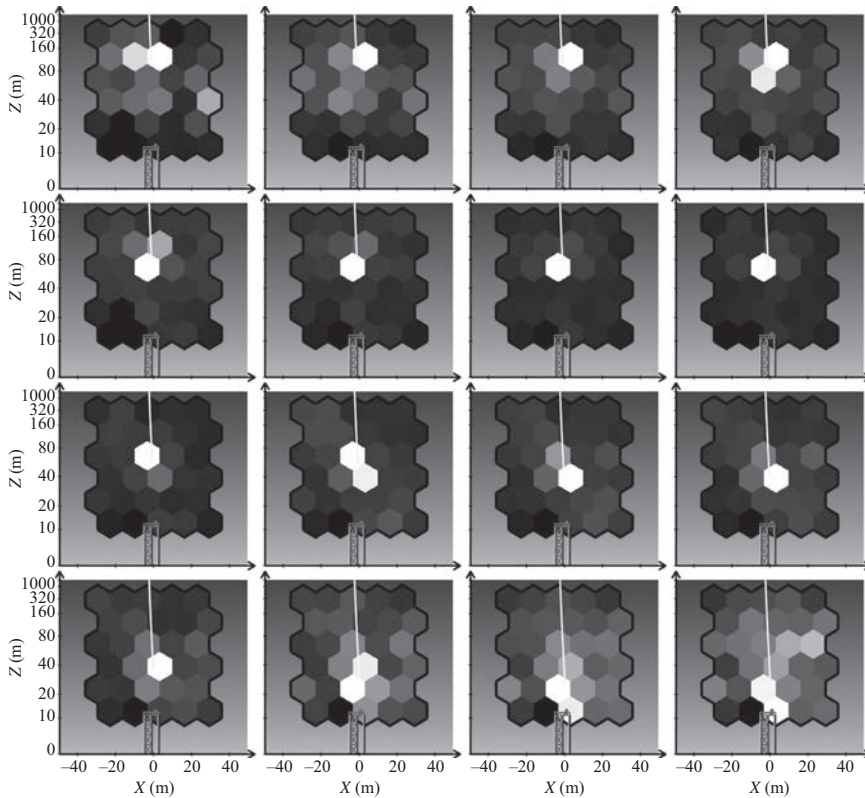


Figure 18.2 Top: Signals from one of the NaI(Tl)/PMT detectors for a single 662 keV gamma-ray from a Cs-137 radioactive source placed temporarily on top of the instrument. The diamonds show the data as recorded by the acquisition system, and the solid line is the detector response as calculated from the NaI light decay-time and the RC-times in the front-end electronics. Bottom: Signals for a time period just prior to a return stroke (at  $t = 0$ ) of triggered lightning. The detector response (solid line) is plotted over the measured data (diamonds). The arrows indicate the times and deposited energies of the x-ray pulses. Figure is from Dwyer *et al.* [2004]

do time-of-arrival (TOA) measurements of the x-ray pulses from natural and triggered lightning. They found that the x-ray pulses were produced in close association with the lightning leader step locations and times, as recorded by TOA measurements using an array of  $dE/dt$  sensors, confirming the earlier work [Dwyer *et al.*, 2005a] that showed a temporal relationship between the x-ray emission and the step formation and showing that there is also a close spatial relation. Indeed, with this technique, the x-ray source locations were seen to propagate downward with the leaders. Furthermore, for rocket-triggered lightning, the x-ray pulses could be seen both above and below the remnants of the triggering wire, demonstrating that the wire had no measurable effect on the production of the x-rays.

Finally, using a “pin-hole” type x-ray camera, x-ray emissions from triggered lightning leaders have been imaged, showing in some cases a rather compact source region that propagates downward near the tip of the leader [Dwyer *et al.*, 2011]. Figure 18.3 shows a sequence of sixteen 0.1  $\mu\text{s}$  images immediately before the return stroke for a chaotic leader [Hill *et al.*, 2012]. As can be seen, the source of the x-ray emission follows the tip of the lightning leader (as determined by  $dE/dt$  measurements) moving downward at about 1/7 the speed of light. These observations are consistent with the energetic electrons and the resulting x-ray emission



*Figure 18.3 Successive images of the x-ray emissions from rocket-triggered lightning, recorded at the ICLRT on 13 August 2010. The first image is in the upper left corner and time progresses from left to right. Each image is separated by 0.1  $\mu\text{sec}$ , and the exposures cover the emission times from  $-1.94$  to  $-0.087$   $\mu\text{sec}$  before the return stroke. The rocket launch tower is illustrated at the bottom along with the approximate location of the lightning channel. The intensity scale for each image has been adjusted so that the detector with the maximum deposited energy appears as white. From Dwyer et al. [2011]*

being generated by the high electric fields near the leader tip, possibly by the streamers in the streamer zone in front of the leader. In some of the images seen in Figure 18.3, a diffuse component of the x-ray emission is also visible. Because the background rate is so low compared with the high intensity of the x-ray emission from the lightning, nearly all of the emissions seen in the figure (non-black hexagons) are due to real x-rays from lightning. This diffuse component could possibly originate from an extended source region. However, Compton scattering and gamma-rays penetrating the sides of the camera may also contribute.

When the occurrence of x-ray emissions from lightning was first reported ten years ago, it was not clear what mechanisms were responsible for the emission. The emission could not be thermal x-ray emission due to the hot channel, since the emission always occurred before the return stroke, and the temperature of the return stroke channel (30 000 K) is many orders of magnitude too cold to account for such energetic x-rays [Rakov and Uman, 2003]. Relativistic Runaway Electron

Avalanche (RREAs), also called runaway breakdown [Gurevich *et al.*, 1992], was initially suggested, but it was quickly pointed out that the intensity and energy spectra of the x-rays were not consistent with this mechanism [Dwyer, 2004]. Instead, the production of energetic electrons in the very large electric fields near the leader or streamer tips was suggested [Dwyer, 2004; Moss *et al.*, 2006]. Measurements of the x-ray emissions from long laboratory sparks at atmospheric pressure, which appear to be very similar to the x-ray emission from lightning, support this basic picture [Dwyer *et al.*, 2005b; 2008; Rahman *et al.*, 2008; Nguyen *et al.*, 2008; 2010; March and Montanyà, 2011; Kochkin *et al.*, 2012]. The mechanisms involved in the production of energetic radiation are discussed in much detail, starting with section 18.3.

In order to understand how the energetic electrons are produced and what electric fields are present in the x-ray source region, it is important to know the energy spectrum of the x-rays from lightning. Such measurements are very challenging due to the high intensities of the x-rays. Some papers have reported pulses recorded in detectors that have more than an MeV of deposited energy, inferring that the individual x-ray photons reach that energy. Using bronze and lead attenuators of different thicknesses over scintillation detectors, it has been found that the large deposited energies for each pulse of x-rays are usually the result of pulse pile-up of x-rays in the 100 keV range and not individual photon with MeV energies, although occasionally MeV energies are recorded [Dwyer *et al.*, 2004; Saleh *et al.*, 2009; Mallick *et al.*, 2012].

Finally, we note that in addition to x-rays, neutrons have been reported in association with thunderstorms and lightning. These emissions appear to be the result of photo-nuclear reactions of the gamma-rays interacting with air nuclei [Babich and Roussel-Dupré, 2007]. As a result, the neutrons are probably an interesting side effect of the energetic radiation discussed here. We refer the interested reader to the following reviews for more information on neutrons: Milikh and Roussel-Dupré [2010] and Dwyer *et al.* [2012].

### 18.2.2 *Gamma-ray flashes from thunderstorms*

Since the 1980s, it has been known that thunderstorms emit x-rays and gamma-rays. These emissions can be divided into two types: gamma-ray glows and TGFs [Dwyer *et al.*, 2012]. Gamma-ray glows are second- to minute-long enhancements in the gamma-ray flux emitted by thunderstorms. These flux enhancements often terminate with the occurrence of lightning, suggesting that the glows are produced by large-scale electric fields within the clouds and not directly by lightning leaders. Glows have been measured by aircraft [Kelley *et al.*, 2010; Parks *et al.*, 1981; McCarthy and Parks, 1985], by balloons [Eack *et al.*, 1996a, b; 2000], and on the ground or on mountaintops [Alexeenko *et al.*, 2002; Brunetti *et al.*, 2000; Chilingarian *et al.*, 2010; 2012a,b; Chubenko *et al.*, 2000; 2003; Torii *et al.*, 2002; 2004; 2009; 2011; Tsuchiya *et al.*, 2007; 2009; 2011]. The name given to the phenomenon varies, depending upon the location where the gamma-rays were recorded. For example, energetic particle enhancements recorded on mountaintops by researchers in Armenia have been named Thunderstorm Ground Enhancements (TGEs) [Chilingarian *et al.*, 2012a]. A review of earlier measurements can be found in Suszcynsky *et al.* [1996].

The energy spectrum of gamma-ray glows often extends to several tens of MeV, suggesting that the mechanism that produces the energetic electrons

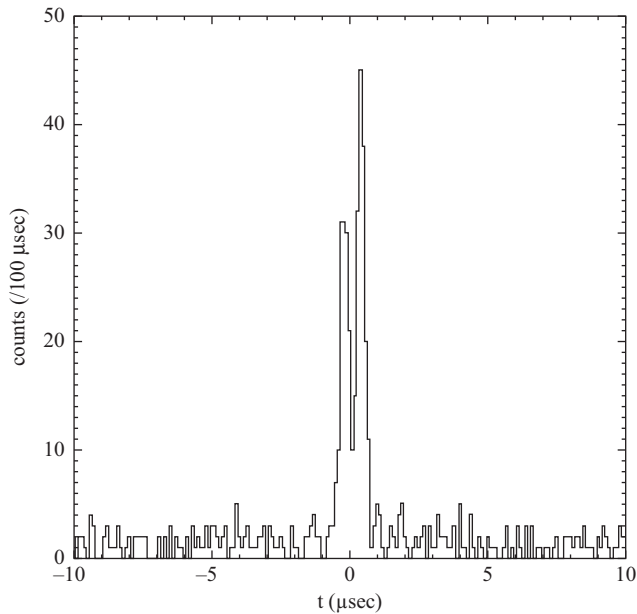


Figure 18.4 *Gamma-ray count rate for a TGF seen by CGRO/BATSE. Data courtesy Jerry Fishman*

responsible for the emission is fundamentally different from the mechanism that produces the energetic electrons responsible for the x-ray emissions associated with lightning leaders [Babich *et al.*, 2010], since the latter almost always has a much softer spectrum, usually in the few hundred keV range.

TGFs are a more powerful type of gamma-ray emission from thunderstorms. TGFs were discovered in 1994 by BATSE on the Compton Gamma-Ray Observatory (CGRO) [Fishman *et al.*, 1994]. TGFs were first identified as millisecond-long bursts of gamma-rays originating from the earth's atmosphere. The first TGF reported by BATSE is shown in Figure 18.4. Because of instrumental dead-time effects, we now know that the typical duration of a TGF is more like 100–200  $\mu\text{sec}$ , although there is a large variation in their duration ranging from a few tens of microseconds to a few millisecond. TGFs were initially inferred to originate from high-altitude discharges in association with sprites, which may reach altitudes of 80 km above the ground [Franz *et al.*, 1990; Inan *et al.*, 2006]. Indeed, when reviewing the seven years of research since the discovery of TGFs, Gurevich and Zybin [2001] concluded that TGFs could be regarded as a confirmation of the important role of runaway breakdown in high-altitude discharges such as sprites.

In an interesting turn of events, it was shown in 2005 that TGFs almost certainly do not originate from high-altitude discharges, sprites, or otherwise. Instead, they originate from ordinary thunderstorms deep within our atmosphere. This evidence was provided by new spacecraft, such as RHESSI [Smith *et al.*, 2005], AGILE [Marisaldi *et al.*, 2010a, b; Tavani *et al.*, 2011], and Fermi [Briggs *et al.*, 2010; 2011; Fishman *et al.*, 2011; Østgaard *et al.*, 2012], and from improved modeling, and ground-based radio observations of the TGFs. For example, the RHESSI spacecraft measured the energy spectrum of TGFs, which was modeled to include the effects of gamma-ray propagation up and out of the atmosphere

[Dwyer and Smith, 2005; Carlson *et al.*, 2007; Grefenstette *et al.*, 2008; Gjesteland *et al.*, 2010]. It was found that the gamma-rays pass through a considerable amount of atmosphere to get to the spacecraft from the source region. Specifically, the source regions of the TGFs were found to be less than about 20 km altitude, consistent with the heights of thunderstorms and far too low in the atmosphere to be associated with sprites.

It has been known for some time that TGFs are associated with radio sferics [Inan *et al.*, 1996; 2006; Cummer *et al.*, 2005; Cohen *et al.*, 2006; 2010; Connaughton *et al.*, 2010; Lu *et al.*, 2011]. VLF-LF radio measurements of the sferics associated with RHESSI and Fermi TGFs have shown that the charge moment changes of these are too small to produce sprites and are not consistent with earlier models of high-altitude production of the TGFs [Cummer *et al.*, 2005]. Furthermore, radio measurements show that the TGFs are closely associated with the early stage of normal positive intra-cloud (+IC) lightning within the thunderstorms, not the kind of lightning usually associated with sprites [Stanley *et al.*, 2006; Shao *et al.*, 2010; Lu *et al.*, 2010].

More recently, it has been found that sferics recorded in association with TGFs are probably produced directly by the high-energy electrons and the resulting ionization and not normal lightning [Cummer *et al.*, 2011; Dwyer, 2012; Connaughton *et al.*, 2013; Dwyer and Cummer, 2013]. As a result, radio observations of TGFs provide a new tool for directly studying how these events are generated inside the storms.

### **18.3 Discharges in air**

Because free electrons rapidly attach to air atoms, or recombine with ions when available, the conductivity of air is normally quite small. In fact, for clear air within our atmosphere, most of the electrical conductivity is provided by ions generated by radioactivity and cosmic rays. With the application of an electric field, a slow discharge of the field may follow. Inside clouds, where ions may attach to cloud particles, the conductivity is even lower than that for clear air.

In order for large currents to flow and for electric fields to be rapidly discharged, a large number of electrons must be liberated from air molecules. These electrons are then free to drift in the electric field, producing currents until they attach or recombine. The resulting ions also produce electric currents as they drift in the electric field, but these currents are usually small compared with the contribution from the electrons, at least for fast discharge processes. The issue is thus how to generate large numbers of free electrons on short timescales, for example, on sub-microsecond timescales.

One way to generate large numbers of free electrons is with an external source of ionizing radiation, that is, with energetic charged particles or UV photons, x-rays, or gamma-rays. Although this may produce a large electric current when an electric field is present, and indeed the electric field may rapidly decrease because of this current, this is usually not considered an electric breakdown, since it depends upon influences that are external to the system [Nasser, 1971]. For example, if the external source of ionization were suddenly stopped, then the discharge would, for the most part, also stop. Instead, an electrical breakdown is usually considered to be an internal state of the system, not dependent upon external influences. As a result, the production of free electrons should be



self-sustaining. For low-energy discharges, an example of the self-sustaining production of electrons is the Townsend breakdown [Cobine, 1958; Brown, 1966]. For high-energy discharges, the analogous process is called a relativistic feedback discharge, or in some cases “dark lightning” [Dwyer *et al.*, 2013].

## 18.4 Propagating electrons

For both low- and high-energy discharges, the key components are the propagating electrons. For low-energy discharges, these are the low-energy (few eV) drifting electrons [Raether, 1964]. For high-energy discharges, these are the runaway electrons [Wilson, 1925].

To understand the difference, consider Figure 18.5, which shows the rate at which electrons lose their kinetic energy in air per distance traveled [Dwyer, 2004]. The figure also shows that rate at which electrons gain energy from an electric field (50 kV/cm in this case) per distance traveled along the field line. For most of the graph, the electrons lose their energy predominantly through the ionization of air. However, at higher energies, above a few tens of MeV, energy losses from bremsstrahlung x-ray emissions (dashed line) become important. As can be seen in the figure, when we consider where the rate of energy gain exceeds the rate of energy loss from all sources, the figure is divided into two regions: the low-energy

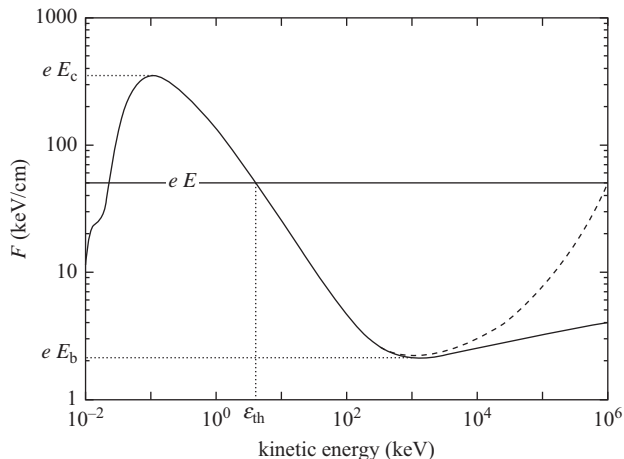


*Figure 18.5 Kinetic energy loss per unit length experienced by a free electron moving through air at STP as a function of the electrons' kinetic energy. The solid curve is mostly the result of ionization of air, and the dashed curve indicates the effects of bremsstrahlung emission. The horizontal line shows the electric force from a  $5.0 \times 10^6$  V/m electric field. Low-energy electrons in a conventional discharge are limited to a few tens of eV, shown on the left side of the plot. Runaway electrons occur when the kinetic energies are greater than the threshold energy,  $\epsilon > \epsilon_{th}$ . The critical electric field strength,  $E_c$ , is the field for which low-energy thermal electrons run away.  $E_b$  is the so-called breakeven field for runaway electrons. Figure from Dwyer [2004]*

regime on the left, which extends up to a few tens of eV, and the high-energy regime on the right, which begins at a few tens of keV (labeled  $\varepsilon_{th}$ ) and extends up to about 1 GeV. Outside of these two regimes, for example, around 100 eV, the electrons lose energy faster than they will gain energy from the field and thus slow down. In contrast, in the low- and high-energy regimes, the electrons may be accelerated by the electric field and gain energy.

At low energies, the situation is actually a bit more complicated, since the electrons also experience a large amount of elastic scattering, changing the direction of the electrons but not their energies. The electrons are also lost to two- and three-body attachment to oxygen in the air and to recombination, if ions are present [Liu and Pasko, 2004; Morrow and Lowke, 1997], all of which affects the energy distribution and motion of the electrons. The energy distribution is confined to the left side of the plot because of the rapid increase in the energy loss rate with the kinetic energy of the electrons. For simplicity, on average, we can visualize the low-energy electrons as drifting in the electric field,  $\vec{E}$ , with velocity  $\vec{v}_e = -\mu_e \vec{E}$  known as the drift velocity, where  $\mu_e$  is the mobility of the electrons. The motion of these electrons produces an electric current, which may help discharge the field.

At higher energies, above  $\varepsilon_{th}$ , the electrons gain energy from the field. Up to an MeV or so, the rate of energy loss actually decreases the faster the electrons go, which allows them to gain even more energy from the field. These are the runaway electrons. Depending upon the electric field strength and the total potential difference in the high-field region, the runaway electrons may gain very large energies, for example, up to a GeV for the example shown in Figure 18.5. However, electrons may only run away if their initial energy is above  $\varepsilon_{th}$ . Thus, there must be a source of energetic “seed” electrons with energies above  $\varepsilon_{th}$ . External sources of such seed electrons are atmospheric cosmic-ray secondary particles and radioactive decays. This runaway electron mechanism was first described by C.T.R Wilson in 1925 using cloud chamber measurements [Wilson, 1925]. As is discussed more below, positrons (the anti-particle of the electron) may run away just like electrons, but because their charges are positive rather than negative, they travel in the opposite direction of the electrons, similar to positive ions.

As can be seen in Figure 18.5, the low-energy electrons do not reach more than a few tens of eV in energy (for the electric field strength shown), since above that point, on average, they lose energy faster than they gain it from the field [Bazelyn and Raizer, 1998]. On the other hand, as the high-energy electrons move, they ionize the air, generating low-energy electron–ion pairs. Thus, there is a transport of energy and particles from high energy down to low energy, but no transport of energy and particles from the low-energy regime up to the high-energy regime, at least for the field strength shown.

The situation becomes quite different for stronger electric fields approaching and exceeding the critical field,  $E_c$ , shown in Figure 18.5. At this electric field, the free low-energy electrons on the left side of the plot may gain energy and enter the high-energy regime. In a sense, the low- and high-energy regimes join together at  $E_c$ , since nowhere is the rate of energy loss sufficient to prevent the electrons from gaining energy from the field. The situation for which strong electric fields allow the low-energy population to gain energy and run away is called “thermal runaway” or “cold runaway” [Gurevich, 1961; Moss *et al.*, 2006]. This mechanism is discussed in detail in the context of the x-ray emissions from lightning and laboratory sparks.

## 18.5 Avalanche multiplication

The higher the electric field strength, the higher the average energy of the low-energy electron distribution. Some of the electrons in this distribution have enough energy to ionize air molecules upon impact, which is a source of new free electrons [Bazelyn and Raizer, 1998]. Of course, some of the electrons are also lost to attachment processes; however, for strong enough electric fields, the overall effect is the exponential growth of free electrons with distance, that is, there is an “avalanche” of free electrons.

The rate of ionization,  $\alpha$  [ionizations per unit length], is called the first Townsend coefficient [Nasser, 1971; Cooray, 2012]. The rate at which electrons are lost due to two- and three-body attachment processes is  $\eta$ . For low electric field strengths,  $\alpha < \eta$ , so the rate at which free electrons are lost is faster than the rate at which new ones are created, and without a continuous source of new free electrons, the number of free electrons decreases. However, for air,  $\alpha$  increases with increased electric field strength quite rapidly, and for  $E > E_k \sim 3 \times 10^6$  V/m at STP we reach the condition  $\alpha > \eta$  [Raether, 1964]. That is, for electric field strengths above  $E_k$ , called the conventional breakdown field, new free electrons are generated within the gas at a rate faster than the rate at which free electrons are lost, resulting in a net gain in the number of free electrons with time and distance. In this way, even one free low-energy electron (produced, for example, from an external source of ionization radiation) may result in a very large number of free electrons via this avalanche multiplication process. It is convenient to define the avalanche length  $\eta = 1/(\alpha - \eta)$ . Then for a uniform electric field with  $E > E_k$ , the number of free electrons is given by

$$N_e = N_0 \exp(z/\lambda) \quad (18.1)$$

where  $N_0$  is the number of seed particles and  $z$  is the distance along the electric field line [Cooray, 2012].

In 1992, it was shown that avalanches of runaway electrons may also be produced in air [Gurevich *et al.*, 1992]. The process is quite similar to the production of low-energy avalanches described above in this section. As a relativistic runaway electron propagates through air, it will ionize the air, generating low-energy electrons, which quickly lose their energy and are eventually lost (no longer free). However, occasionally, the energetic runaway electron hard scatters with the electrons in an air atom (Møller scattering), generating an energetic secondary electron that has an energy above  $\varepsilon_{th}$ , the runaway electron threshold energy. This secondary electron may also run away along with the original electron. These two runaway electrons may experience additional hard scatters, generating more and more runaway electrons. Such RREAs may grow exponentially in time and space, quite similar to their low-energy cousins, except that the length and energy scales of the runaway electron avalanche are roughly a million times larger than those of the low-energy avalanche. For example, the average energy of the runaway electrons in an avalanche is about 7 MeV and the average energy of electrons in a low-energy electron avalanche is a few eV [Dwyer and Babich, 2011]. Likewise, the avalanche (e-folding) length of a runaway electron in an avalanche,  $\lambda$ , is often on the order of 100 m [Dwyer, 2003] and the avalanche (e-folding) length of a low-energy electron avalanche is often sub-millimeter in scale (see Figure 18.7).

Figure 18.6 shows the results of a Monte Carlo simulation of the propagation of electrons through air at standard conditions in a uniform electric field with 1000 kV/m.

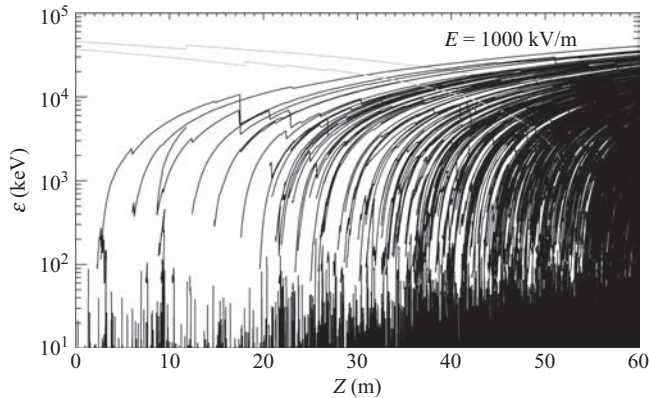


Figure 18.6 Monte Carlo simulation of electrons in air at standard conditions with an electric field of 1000 kV/m. Each line represents the trajectory of one electron or positron, showing the kinetic energy versus distance. In this simulation an avalanche of runaway electrons develops from left to right. The avalanche was initiated by injecting one 5 MeV energetic positron at the right side of the simulation region. A second positron can be seen to be produced by pair production (top light trace). Figure from Dwyer *et al.* [2013]

One 5 MeV positron (the seed particle in this case) is injected on the right side of the figure and gains energy as it propagates to the left (bottom trace rising from right to left). As can be seen, as the positron propagates, it gains energy from the field. It also generates secondary electrons when it scatters with atomic electrons (Bhabha scattering). Some of these secondary electrons have initial energies below the runaway electron threshold energy ( $\sim 30$  keV in this case) and rapidly lose their energy. A few secondary electrons in the figure are produced with sufficient energy so that they run away, gaining large energies from the electric field. This is the avalanche multiplication process [Gurevich *et al.*, 1992; Lehtinen *et al.*, 1999; Dwyer, 2003; Babich *et al.*, 2005; Celestin and Pasko, 2010; Roussel-Dupré *et al.*, 2008]. As the runaway electrons gain energy, more runaway electrons are created at lower energies, so the average energy of all runaway electrons in the avalanche remains approximately constant, equal to about 7 MeV. The occasional rapid dips in the electron energies seen in the figure are due to hard bremsstrahlung or Møller scattering events, which remove a significant fraction of the incident electron's energy. Note that the gamma-rays emitted by the electrons in the simulation produced another positron via pair production, which then also ran away to the left, generating more runaway electrons. This is the relativistic feedback mechanism, which is discussed in detail in section 18.6.

In Figure 18.6, both the high-energy and intermediate-energy electrons contribute to the ionization of the air. For fields much smaller than the conventional breakdown field, the total number of low-energy electrons created per energetic runaway electron is found to be about 7000 per meter traveled by each runaway electron along the electric field line [Dwyer and Babich, 2011]. These low-energy electrons drift in the electric field until they attach to air via either two- or three-body attachment. The contribution of the low-energy electrons and the

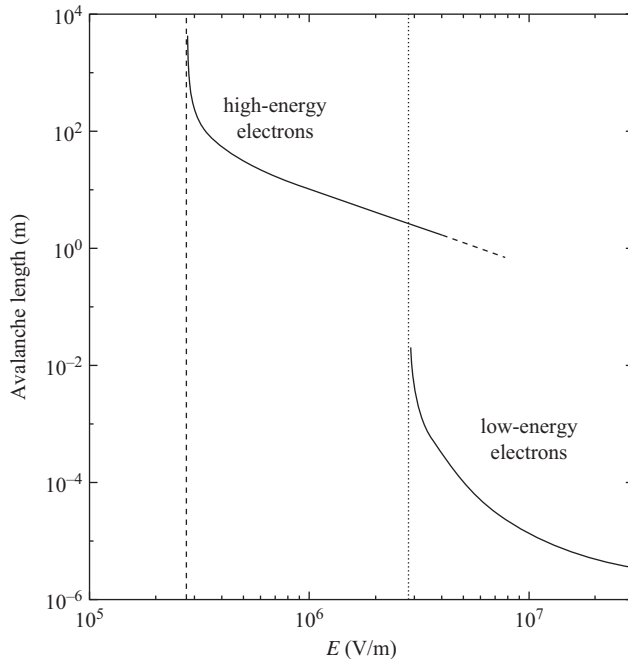


Figure 18.7 The avalanche (*e*-folding) length,  $\lambda$ , for high-energy runaway electrons and low-energy electrons as a function of electric field strength at standard conditions. The vertical dashed line is the threshold field for runaway electron avalanches to develop and the vertical dotted line is the conventional breakdown field, the field for low-energy electron avalanches to develop

accompanying positive and negative ions to the current is usually much larger than the contribution from the runaway electrons directly.

Figure 18.7 shows the avalanche length,  $\lambda$ , versus electric field strength at standard conditions for both low-energy and high-energy electron avalanches, that is, avalanches that are part of a conventional discharge and RREAs, respectively. The RREA curve is from Milikh and Roussel-Dupré [2010] and the low-energy curve is from a parameterization by Cooray [2012]. As can be seen, the high-energy avalanche begins at the lowest electric field strength,  $E_{th} = 2.84 \times 10^5$  V/m (vertical dashed line), and decreases rapidly with increased electric field strength [Dwyer, 2003; Babich *et al.*, 2004].  $E_{th}$  is comparable to or slightly less than the maximum electric fields directly measured inside thunderclouds, so it is very likely that RREAs are produced inside thunderstorms. Also, as can be seen in the figure, the avalanche length for the energetic electrons ranges from hundreds of meters down to a few meters over most of the electric field values. At higher electric fields, there is some disagreement about the runaway electron avalanche length (shown here as a dashed curve), since for such strong electric fields, part of the low-energy electron distribution may run away, affecting the production rate of the high-energy electrons [Colman *et al.*, 2010].

The low-energy avalanches occur for fields greater than the conventional breakdown field (vertical dotted line). Such avalanches occur when  $\alpha - \eta > 0$ , as discussed earlier in this section. Similar to the high-energy electrons, the

low-energy avalanche length drops rapidly with increased electric field strength. However, in this case, the avalanche length is about six orders of magnitude smaller than that of the high-energy electrons.

The energy spectrum of the runaway electrons is approximately exponential with an e-folding energy of about 7 MeV [Dwyer and Babich, 2011]:

$$N_{re} \propto \exp(\varepsilon/7 \text{ MeV}) \quad (18.2)$$

As long as there are at least a few avalanche lengths present in the high-field region, (18.2) is the steady state spectrum and is independent of the electric field strength and the air density. Individual runaway electrons may gain very large energies, reaching many tens of MeV, but because lower energy runaway electrons are continuously being created in the avalanche, the average energy of all electrons in the avalanche remains approximately equal to 7 MeV. Such high-energy electrons produce bremsstrahlung x-rays as they interact with air atoms. In fact, many of these x-rays are in the MeV range and so may be called gamma-rays. At sea level, the interaction length in air for runaway electrons to produce such energetic photons is on the order of about 100 m, which is similar to the avalanche length of the runaway electrons for typical electric field strengths considered. As a result, the number of gamma-rays produced is often close to the number of energetic runaway electrons in the avalanche. However, the gamma-rays travel much farther through the air than the electrons, so they are usually more easily observed away from the source region.

For both low-energy and high-energy electron avalanches, the production rate of electrons is tied to the injection rate of seed electrons that initiate the avalanches. In both cases, such seed particles may be provided by atmospheric cosmic-ray particles or by radioactive decays. Although an avalanche may greatly increase the number of free electrons in the gas, the avalanche mechanism alone is usually not sufficient to produce large electric currents and a rapid discharge of the field. The reason is that when the voltage is increased in a system, whether it is between electrodes in a laboratory or inside a thundercloud, before the avalanche multiplication can become very large, other discharge mechanisms usually come into play that result in electrical breakdown and the discharge of the field. These other discharge mechanisms are described in section 18.6.

## 18.6 Feedback mechanisms

In addition to creating more electrons, an avalanche also creates other particles that may play important roles in the discharge. For instance, for conventional discharges, electrons in an avalanche impact air molecules, resulting in atomic excitation, in addition to ionization events, resulting in ultraviolet (UV) photon emissions. Some of these UV photons may propagate to the start of the avalanche region and produce additional seed electrons, either via photoelectric emission from the cathode surface or via photoelectric interaction from the air. These seed electrons may then produce secondary avalanches, producing more UV photons and so forth. Similarly, positive ions, created by the electron avalanche may drift backwards (opposite the direction of the electrons) and interact with the cathode, liberating additional seed electrons, generating additional avalanches. As a result, a positive feedback loop is created, allowing an ever-increasing number of electron avalanches to be generated. Consequently, the production of free electrons

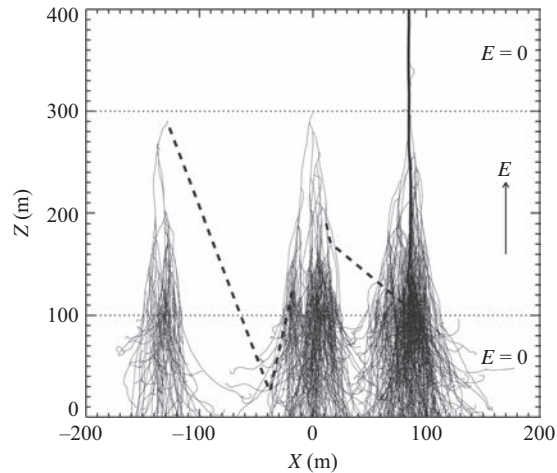


*Figure 18.8 The positron and x-ray feedback mechanisms. The figure shows the results of detailed Monte Carlo simulations. The light black lines show runaway electron trajectories. The dark solid line shows the trajectory of a runaway positron and the dashed lines illustrate the path taken by photons. Figure from Dwyer [2003]*

becomes self-sustaining, and the discharge would continue even if the external source of seed electrons were cut-off. For conventional discharges, this feedback mechanism is called a Townsend discharge and is involved in a wide range of phenomena including positive streamers, Trichel pulses, and glows [Brown, 1966; Nasser, 1971]. A self-sustaining Townsend discharge is sometimes called a Townsend breakdown, since it is a form of electrical breakdown. The Geiger mechanism, which takes place inside Geiger counter tubes, is a variation on the Townsend mechanism.

Interestingly, a very similar feedback phenomenon occurs with high-energy discharges, illustrated in Figure 18.8 [Dwyer, 2003]. As the runaway electrons in an avalanche propagate, they produce x-rays and gamma-rays ( $> \text{MeV}$  x-rays) via bremsstrahlung interactions with air. Some of these energetic photons pair-produce while still inside the avalanche region, resulting in an electron–positron pair, both of which may be energetic enough to run away. The electron may runaway in the forward direction adding to the avalanche of energetic electrons. On the other hand, the positron has the opposite charge sign as the electron and so turns around and runs away in the backwards direction (see Figure 18.6). Because the positrons are very energetic, reaching many tens of MeV, they may travel up to a few kilometers through a thundercloud before annihilating with electrons in the air. In fact, a significant fraction of the positrons created by pair-production propagate back to the start of the avalanche region. As the runaway positrons propagate through the air, they occasionally undergo a hard electric scatter with atomic electrons (Bhabha scattering) generating an energetic secondary electron, similar to how energetic runaway electrons generate an energetic secondary electrons via Møller scattering with atomic electrons. The secondary electrons generated by the positrons may then serve as seed particles for additional avalanches [Babich *et al.*, 2005].

Similarly, bremsstrahlung x-rays produced by the runaway electron avalanches, rather than undergoing pair production, may Compton backscatter, allowing

the x-ray to travel back to the start of the avalanche region. These x-rays may then produce new seed electrons and hence new avalanches, either by Compton scattering or from the photoelectric interaction with air.

The secondary avalanches of runaway electrons, produced either by the backward propagating positrons or the backscattered x-rays, produce more bremsstrahlung photons and the whole process repeats. In other words, a positive feedback cycle is created.

These feedback mechanisms, which together are called relativistic feedback, are almost exactly the same as the feedback mechanism that occurs during a Townsend discharge at low energies [Dwyer, 2007]. Instead of low-energy ions and UV photons, this mechanism involves positrons and x-rays. As with a Townsend breakdown, once relativistic feedback becomes self-sustaining, an ever increasing number of runaway electrons are created, resulting in very large electric currents that at least partially discharge the electric field.

As RREAs may be thought of as an exponential growth in the number of runaway electrons, the relativistic feedback mechanism may be thought of as the exponential growth in the number of RREAs. Since relativistic feedback discharges are composed of a very large number of RREAs, the energy spectrum produced by relativistic feedback discharges are about the same as for RREAs alone. However, relativistic feedback discharges may naturally produce fluxes of runaway electrons that are trillions of times larger than RREAs acting on cosmic-ray seed particles. As a result, relativistic feedback discharges may help explain TGFs [Dwyer, 2008; 2012; Liu and Dwyer, 2013].

## **18.7 Streamers**

When we consider a low-energy avalanche, as the electrons and ions propagate, they transport charge. With enough avalanche multiplication, a sufficient amount of charge may be transported to locally enhance the electric field. In some cases, the electric field produced by this charge transport may greatly exceed the ambient field and may exceed the conventional breakdown field, allowing the discharge to propagate into regions where the ambient electric field is below the conventional breakdown field [Nasser, 1971; Bazelyn and Raizer, 1998]. Such propagating discharge structures are called streamers. Raether estimated that a streamer would form when the number of electrons reached about  $10^8$  [Raether, 1940].

Streamers may be positive, negative, or bidirectional, and may be viewed as a discharge channel with an enhanced electric field at one or more of its tips. Negative streamers carry negative charge at their tip and propagate in the same direction as the electrons. Electron avalanches near the tip ionize the air and transport negative charge, allowing the avalanches to continue. In contrast, a positive streamer is composed of a partially discharged channel with a positive charge at its tip. Electron avalanches created in the air in front of the channel propagate toward the streamer tip, creating more ionization and causing the channel to extend in the direction opposite to the avalanche motion. UV photons emitted during the avalanche process help provide the seed electrons that make new avalanches, the same as for the Townsend discharge mechanism. An example of a positive streamer can be seen in Figure 18.9, which shows the results of numerical simulations.

Positive streamers involve converging electron avalanches that propagate into a region with a stronger electric field, whereas negative streamers involve diverging



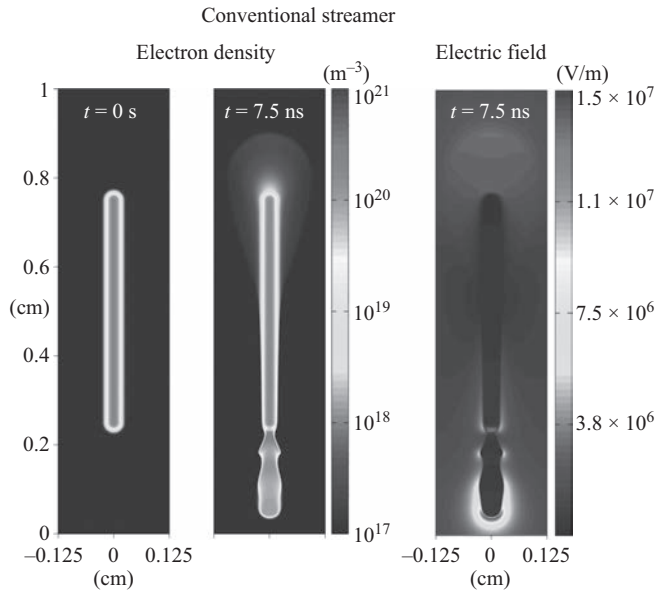


*Figure 18.9* Cross-sectional views of a positive streamer at sea level. The figure shows the results of numerical simulations of the electron density and electric field for a streamer initiated from a conductive region ( $t = 0 \text{ s}$ ). The positive streamer can be seen propagating downward at the bottom of the figure. In this simulation, no negative streamer initiated at the top of the column. Figure reprinted with permission from Liu et al. [2012]. Copyright 2012 by the American Physical Society

electron avalanches that propagate into regions with weaker electric fields. As a result, positive streamers are usually created before negative streamers and may propagate in lower ambient fields than negative streamers. For example, at standard conditions, positive streamers may propagate in fields as low as about 500 kV/m, but negative streamers require fields twice that large to propagate [Phelps and Griffiths, 1976]. Indeed, in the simulation shown in Figure 18.9, a positive streamer is initiated and propagates but a negative streamer never manages to form.

For both positive and negative streamers, at some point, the field must have exceeded the conventional breakdown field in order to create the streamer. For laboratory sparks, this usually happens near one of the electrodes. For thunderclouds, the fields may be enhanced near the surfaces of hydrometeors (water or ice particles). Streamers should be distinguished from leaders, which involve a hot, ionized channel. Streamers usually do not involve significant heating of the gas.

Modeling has shown that high-energy discharges produced by runaway electrons may generate propagating discharge structures very similar to positive streamers, except that they are hundreds of meters across rather than on a millimeter scale as with conventional streamers. This is seen in Figure 18.10. In fact, relativistic feedback can result in a propagating discharge that works in the exact same way as a positive streamer with positron feedback generating new runaway electron avalanches in front of the tip. These propagating discharge structures have been called relativistic feedback streamers [Dwyer, 2012; Liu and Dwyer, 2013].

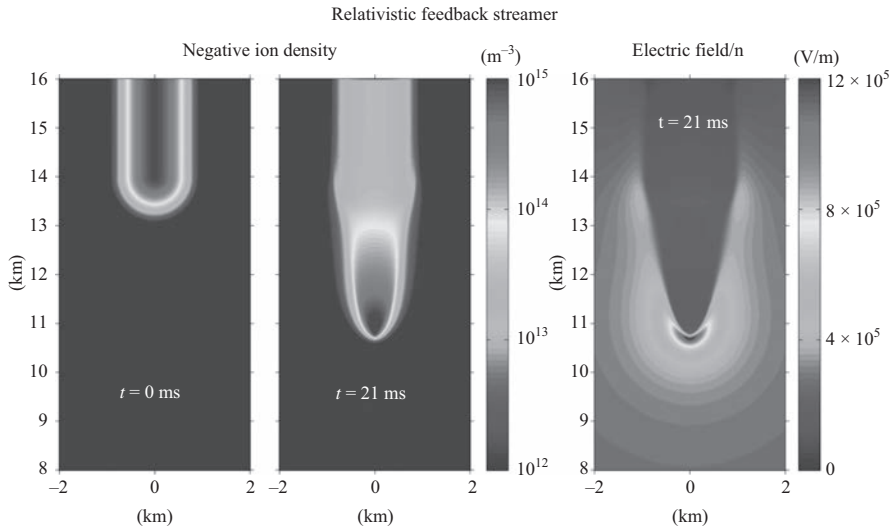


*Figure 18.10* Cross-sectional views of a relativistic feedback streamer at thunderstorm altitudes. The figure shows the results of numerical simulations of the low-energy ion density and electric field. The relativistic feedback streamer was initiated from a conductive region ( $t = 0$  s) and propagates downward toward the bottom of the figure. The structure of the relativistic feedback streamer is similar to that of the low-energy positive streamer seen in Figure 18.9, even though the length scales differ by a factor of 1 million. Figure from Liu and Dwyer [2013]

At this time, it is not clear if the high-energy analogy of negative streamers exists in our atmosphere.

## 18.8 Development of hot channels

As can be seen in Figures 18.6 and 18.7, the length scale of the runaway electron avalanche is many meters, if not hundreds of meters, long. Furthermore, elastic scattering of the runaway electrons causes the avalanche to spread out laterally [Dwyer, 2010]. This spreading can be seen in three avalanches shown in Figure 18.8. The effect of the long avalanche lengths and the spatial diffusion of the runaway electrons is that the density of the high-energy electrons and the accompanying ionization is many orders of magnitude lower than the density of low-energy electrons that may be achieved during conventional discharges.

In order to get a large-scale discharge across many kilometers, as happens with normal lightning, a hot conductive channel, called a leader, must form. Because the conductivity of air increases dramatically at high temperatures, current may be conducted over large distances through such channels, which have temperatures on the order of 10 000 K [Bazelyn and Raizer, 1998]. If the charges at the end of the channel produce a sufficiently large electric field, streamers may be emitted, causing the air to breakdown, allowing the leader to propagate forward, while feeding current into the existing channel to maintain its high temperature. In this

way, leaders may propagate over large distances. Indeed, lightning leaders have been recorded to travel over 100 km through thunderstorm systems.

Leaders may also form in long laboratory sparks in air. In laboratory sparks, a large number of streamers may be emitted from a small region on an electrode. The currents from these streamers are sufficient to heat the air to form a leader, which then may propagate into the gap. Leaders may also form in air away from electrodes. One example of this is the space leader that forms in front of negative leader channels, both for lightning and laboratory sparks. The space leader forms out of a space stem, presumably because of the heat provided to it by multiple streamers. In all cases, it is thought that the current from multiple streamers connected to a common location is sufficiently large and sufficiently concentrated to heat the air.

Because low-energy electrons attach quickly to air and become immobile, free electrons drift only a short distance (e.g., a few mm) before they are lost. Individual streamers do not produce much heating of the air, so once a streamer propagates more than a few mm, it becomes electrically isolated from its point of origin. Therefore, in order to heat the air to the point where a hot channel forms, multiple streamers must occur within a distance measured in mm. For conventional, low-energy discharges, this can happen because the avalanche length is very short for large electric fields, allowing streamers to form over very short distances. On the other hand, for high-energy discharges, the high-energy electrons are produced over distances typically measured in meters, if not hundreds of meters. Even taking into account the large number of low-energy electrons resulting from the ionization caused by the runaway electrons, nowhere does the density of electrons become large enough to produce significant heating of the air [Dwyer, 2010]. Dwyer and Babich [2012] estimated that a large runaway electron discharge, using the most optimistic conditions, would heat the air to about 0.1 K, far short of the thousands of Kelvin needed to form a hot leader channel. Therefore, some authors have questioned whether high-energy discharges could initiate lightning, as has been claimed in some work [Gurevich *et al.*, 1999; Solomon *et al.*, 2001].

Alternatively, if high-energy discharges are involved in the initiation of lightning, it is probably by locally enhancing the electric fields in some locations to the point where a conventional discharge may occur [Dwyer, 2005; Babich *et al.*, 2012]. For example, if the large-scale thunderstorm field is above  $E_{th}$  with a sufficiently large potential difference, a relativistic feedback streamer could form. As the relativistic feedback streamer propagates through the thundercloud, it discharges a large channel and enhances the field at its front (see Figure 18.10). Simulations show that in this way, the electric field may be sufficiently enhanced to allow lightning to initiate from hydrometeors (ice and water particles). It should be pointed out that whether or not high-energy particles are involved in lightning initiation, exactly how hot leader channels form in the thunderstorm environment is not well understood, and so much work remains to be done on this important topic.

## 18.9 High-energy versus low-energy discharges

As was discussed in the previous sections, many processes that occur during low-energy (conventional) discharges have direct analogies at much larger energies, that is, involving high-energy particles rather than low-energy particles. This is somewhat

Table 18.1. High-energy discharge mechanisms and their analogous low-energy discharge mechanisms.

High-energy discharge process	Low-energy discharge process
Wilson runaway electrons	Drifting low-energy electrons
RREAs	Low-energy electron avalanches
Relativistic feedback discharge	Townsend discharge
Relativistic feedback streamer	Positive streamer
Thermal runaway ( $E > E_c$ )	

Note: For very strong electric fields ( $E > E_c$ ) the two discharge mechanisms merge (adapted from Dwyer and Uman [2013]).

reminiscent of particle generations seen in particle physics, where particles have higher energy (mass) analogs that behave in similar ways. Table 18.1 compares the various low-energy and high-energy discharges discussed in this chapter.

Generally speaking, low-energy discharges dominate when electric fields are large and high-energy discharges dominate when the voltages are large. Of course, low-energy discharges may also occur when the voltages are large – normal lightning is a good example of this – but a large voltage is not required for such low-energy discharges to occur. What is required is that the electric field must exceed the conventional breakdown field,  $E_k$ , somewhere in the system. In contrast, high-energy discharges may occur if the electric field exceeds the runaway electron avalanche threshold,  $E_{th}$ , which is an order of magnitude smaller than  $E_k$ . However, it is important to emphasize that having the field exceed  $E_{th}$  is not sufficient for a substantial high-energy discharge to ensue. Such a field must also extend over a large distance with a potential difference of hundreds of MV sometimes needed. Because in our atmosphere, such large voltages occur only in association with thunderstorms and lightning, high-energy discharges are expected to be closely associated with thunderstorms and lightning activity.

At very large electric fields,  $E \sim E_c$ , the high-energy and low-energy discharges merge, resulting in thermal runaway electron production (also called cold runaway electron production), and high-energy discharge may develop with only moderate potential differences (e.g., kV and up). Because there are fluctuations in the energy loss rate experienced by electrons moving through air, even for a field below  $E_c$ , some electrons may gain enough energy from the field to run away. Colman *et al.* [2010] showed that this source of runaway electrons from the low-energy population may significantly affect the production rate of runaway electron above  $E_k$ , so the low- and high-energy populations must be considered together for strong fields, even for fields below  $E_c$ .

## 18.10 Modeling

As discussed in section 18.5, RREAs produce a characteristic exponential energy spectrum with an average energy of 7 MeV. Unlike RREAs, thermal runaway electrons have no characteristic energy spectrum. The energy obtained by the electrons depends upon the extent of the high-field region. For example, we might envision thermal runaway electrons being generated in the high-field region at the tip of a negative streamer. Once created, these energetic electrons may propagate

into a moderately strong field region ( $E_{th} < E < E_c$ ), which is too weak to make additional thermal runaway electrons, but is strong enough to allow the runaway electrons to continue to gain energy. This situation may be viewed as a combination of thermal runaway electron production coupled with Wilson's original runaway electron mechanism. The x-rays emitted by these electrons may explain the x-ray emissions seen from lightning and laboratory sparks, which often have energies reaching a few hundred keV.

On the other hand, if the thermal runaway electrons feed into an extended avalanche region with many RREA e-folding lengths, then the energy spectrum would become that of the RREAs, that is, with an average energy of 7 MeV. Such high x-ray energies are almost never seen from lightning leaders near the ground, suggesting that RREA multiplication (and relativistic feedback) is not important for describing the energetic electrons associated with lightning.

It has been suggested that lightning leaders inside thunderclouds may have sufficiently large potential differences in front of them to allow substantial RREA multiplication to occur. This combination of thermal runaway plus RREA multiplication has been suggested as a possible mechanism to explain TGFs [Dwyer, 2008; Carlson *et al.*, 2009; 2010; Celestin *et al.*, 2012; Xu *et al.*, 2012; Mallios *et al.*, 2013].

Relativistic feedback discharges may also explain TGFs. In particular, relativistic feedback streamers may explain multi-pulsed TGFs seen by CGRO/BATSE (e.g., see Figure 18.4). Simulations show that as relativistic feedback streamers propagate, they produce large fluxes of gamma-rays. Furthermore, these gamma-rays are often produced as a train of short pulses lasting several milliseconds, similar to some TGFs seen by BATSE. Dwyer [2012] and Liu and Dwyer [2013] developed detailed models of relativistic feedback discharges inside thunderclouds and found that these models could self-consistently generate gamma-ray flashes with properties (i.e., fluence, duration, pulse shapes, beaming directions) that are nearly identical to the observed properties of TGFs. Figure 18.11 shows an example of the gamma-ray emission from a relativistic feedback streamer. The wide range

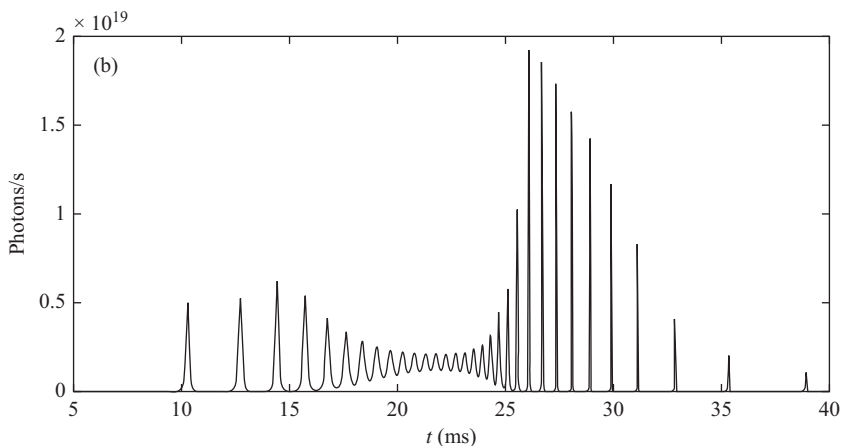


Figure 18.11 *Gamma-ray photons per second from a simulation of a relativistic feedback streamer. The simulation shows that such relativistic feedback streamers can produce gamma-ray pulsing similar to that sometimes seen in TGFs. Figure from Liu and Dwyer [2013]*

of pulse structures produced shows that interesting and unexpected behavior may occur, which has only begun to be investigated [Liu and Dwyer, 2013].

## 18.11 Dark lightning

As discussed in section 18.8, lightning involves the creation and propagation of a hot channel called the leader. When lightning leaders connect regions of opposite charge within the thunderstorm, or when they connect the cloud and the ground, very large currents (e.g., tens of kA) may flow through the channel. These large current pulses are called return strokes for cloud-to-ground (CG) lightning and are called recoil streamers or K-changes for intra-cloud (IC) lightning. For CG return strokes, the temperature of the channel has been measured to reach about 30 000 K. Such hot channels are incandescent and emit a large amount of light in the visible and UV range. For example, in the visible range the lightning channel has been found to emit about  $10^6$  W/m [Guo and Krider, 1983; Uman, 2001], that is, lightning is very bright. Although high-energy discharges may not directly result in a hot, incandescent channel as occurs with normal lightning, this does not mean that large electric currents are not produced. Indeed, simulations show that relativistic feedback discharges can generate many tens of kA of current, comparable to large lightning return strokes. Such large current pulses, which last tens of microseconds, should produce some of the largest LF/VLF radio pulses from the thunderstorm. Such radio pulses have indeed been seen in association with TGFs. For example, Cummer *et al.* [2011] compared two TGFs recorded by the GBM instrument onboard the Fermi spacecraft with LF/VLF radio measurements made at a distance of about 500 km. It was found that the shape and duration of the radio pulses closely matched the shape and direction that would be expected if the high-energy discharge that generated the TGF were also the source of the electric current that produced the radio pulse. Similarly, Connaughton *et al.* [2013] compared Fermi/GBM TGFs with “lightning” events recorded by the World-Wide-Lightning-Location-Network (WWLLN). They found that shorter TGFs, as measured by Fermi, had a much higher rate of detection by WWLLN than longer TGFs, and the peak TGF detection efficiency was higher than for normal IC lightning. Connaughton *et al.* suggested that these two facts could be naturally explained if WWLLN were not detecting IC lightning associated with the creation of the TGF but was instead detecting the radio pulse produced by the TGF itself. The high-energy discharge created both the gamma-rays and electric current that generated the radio pulse, supporting the work by Cummer *et al.* [2011]. Many previous papers had reported the detection of radio pulses in association with TGFs. However, this earlier work interpreted this association as evidence that lightning was very closely associated with specific lightning processes. It now appears that any association of TGFs with lightning is more indirect, and the radio pulses previously reported may have been misidentified.

Dwyer and Cummer [2013] modeled the radio emission from high-energy discharges involving RREAs and showed that the radio pulses expected from such discharges agreed well with those reported by Cummer *et al.* and detected by WWLLN as described in Connaughton *et al.* They also found that the LF/VLF radio pulses previously reported by Cummer *et al.* [2011] were consistent with the emission expected for relativistic feedback discharges. They found that such discharges could produce some of the largest current pulses associated with the

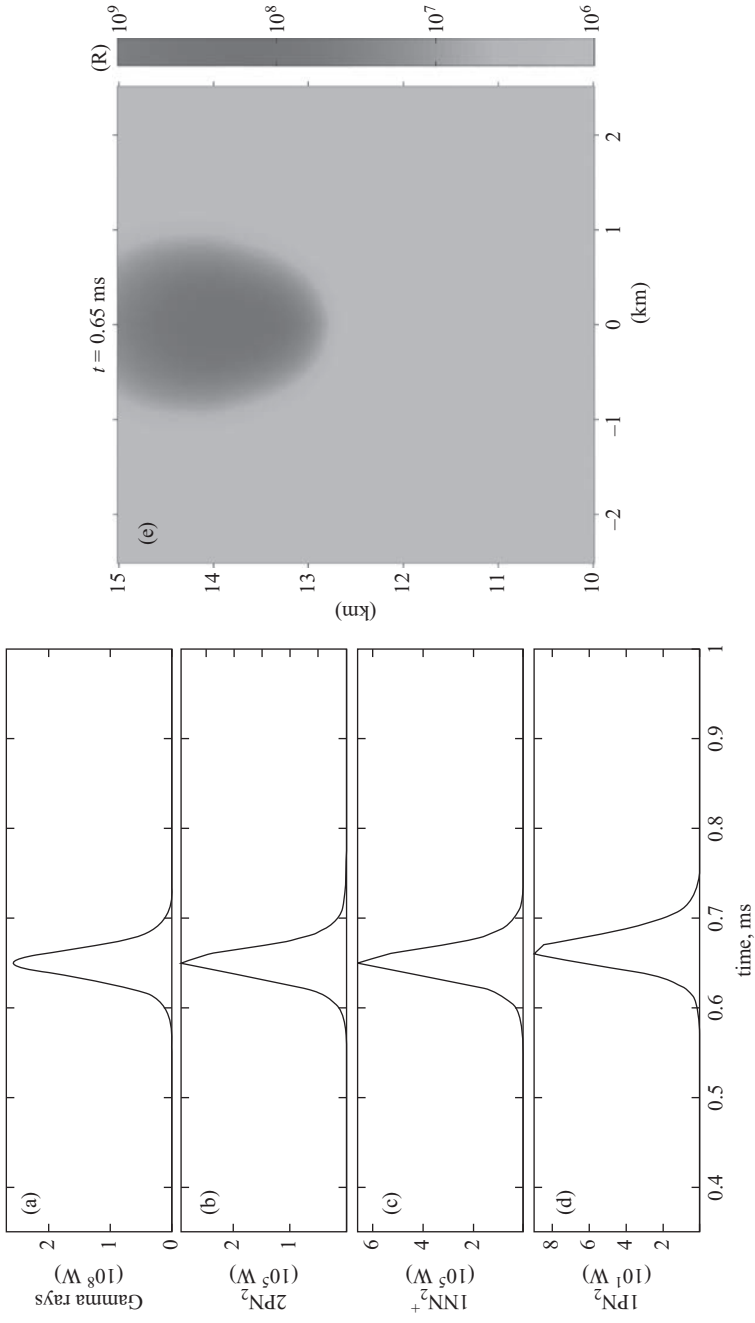


Figure 18.12 Simulation of a relativistic feedback discharge producing a single pulse TGF: (a) is the gamma-ray intensity; (b) to (d) are the volume integrated optical emission intensities of  $2PN_2$ ,  $1NN_2^+$ , and  $1PN_2$  as a function of time. The right panel shows the total emission intensity distribution in Rayleighs at the moment of the TGF peak produced by the relativistic feedback discharge (dark lightning). Figure from Dwyer et al. [2013]

thunderstorm. However, these lightning-like current pulses, which had also been recorded by lightning networks such as WWLLN as originating from lightning, are not produced by currents flowing through a hot, conductive channel. Instead, they are the result of a large but diffuse discharge generated by high-energy runaway electrons.

Dwyer *et al.* [2013] showed that although relativistic feedback discharges make large numbers of gamma-rays and lightning-like electric currents, they also produce very little visible light. Specifically, they found that a relativistic feedback discharge that produced the gamma-rays and radio pulses reported in Cummer *et al.* would emit only about 100 J of energy in the visible range, which is at least a few orders of magnitude less than the energy emitted by ordinary lightning. As a result, they referred to relativistic feedback discharges as “dark lightning.” Figure 18.12 shows the results of such simulations. According to this model, TGFs are a by-product of dark lightning, which is an alternative discharge path for thunderstorms that is different from ordinary lightning. Although dark lightning and ordinary lightning might both occur at the same time during a thunderstorm, unlike a lightning return stroke or a K-change, dark lightning would appear as a very large current pulse with almost no additional visible emission associated with it. Recent simultaneous observations of optical lightning and TGF from space also indicate that TGFs are not bright optically [Østgaard *et al.*, 2013], but more work is required to understand how these observations constrain the models.

## 18.12 Future work

The study of high-energy discharges and related phenomena has been named High-Energy Atmospheric Physics [Dwyer *et al.*, 2012]. Although the field originated with the work of C.T.R Wilson in the 1920s and has had many contributions over the years, a rapid development of theory, models, and observations has occurred in the last ten years. As of the writing of this chapter, this phase of rapid development appears to be continuing, so there may be more exciting discoveries to be made in the upcoming years. Promising research includes, but is not limited to improved modeling of high-energy processes, in situ measurements of energetic radiation inside thunderclouds using balloons and aircraft, radio observations of TGFs, improved ground-based measurements of energetic radiation from thunderstorms and lightning as well as laboratory sparks, and new spacecraft specifically designed to measure TGFs.

## Acknowledgments

This work has been primarily supported by DARPA grant HR0011-1-10-1-0061. Any opinions, findings, and conclusions or recommendations expressed in this material are those of the authors and do not necessarily reflect the views of DARPA.

## References

- V. V. Alexeenko, N. S. Khaerdinov, A. S. Lidvansky, V. B. Petkov, Transient variations of secondary cosmic rays due to atmospheric electric field and evidence for pre-lightning particle acceleration, *Phys. Lett. A* 301 (2002) 299.
- L. P. Babich, E. N. Donskoy, R. I. Il'kaev, I. M. Kutsyk, R. A. Roussel-Dupré, Fundamental parameters of a relativistic runaway electron avalanche in air, *Plasma Phys. Rep.* 30 (2004) 616–624.



- L. P. Babich, E. N. Donskoy, I. M. Kutsyk, R. A. Roussel-Dupré, The feedback mechanism of runaway air breakdown, *Geophys. Res. Lett.* 32 (2005) L09809, doi:10.1029/2004GL021744.
- L. P. Babich, R. A. Roussel-Dupré, Origin of neutron flux increases observed in correlation with lightning, *J. Geophys. Res.* 112 (2007) D13303, doi:10.1029/2006JD008340.
- L. P. Babich, E. I. Bochkov, E. N. Donskoi, I. M. Kutsyk, Source of prolonged bursts of high-energy gamma rays detected in thunderstorm atmosphere in Japan at the coastal area of the Sea of Japan and on high mountaintop, *J. Geophys. Res.* 115 (2010) A09317.
- L. P. Babich, E. I. Bochkov, J. R. Dwyer, I. M. Kutsyk, Numerical simulation of lightning initiation by cosmic rays, *J. Geophys. Res.* 117 (2012) A09316, doi:10.1029/2012JA017799.
- E. M. Bazelyn, Y. P. Raizer, *Spark Discharge*, 294 pp., CRC Press, Boca Raton, Florida, 1998.
- M. S. Briggs, G. J. Fishman, V. Connaughton, P. N. Bhat, W. S. Paciesas, R. D. Preece, C. Wilson-Hodge, V. L. Chaplin, R. M. Kippen, A. von Kienlin, C. A. Meegan, E. Bissaldi, J. R. Dwyer, D. M. Smith, R. H. Holzworth, J. E. Grove, A. Chekhtman, First results on terrestrial gamma ray flashes from the Fermi Gamma-ray Burst Monitor, *J. Geophys. Res.* 115 (2010) A07323, doi:10.1029/2009JA015242.
- M. S. Briggs *et al.*, Electron-positron beams from terrestrial lightning observed with Fermi GBM, *Geophys. Res. Lett.* 38 (2011) Issue 2, CiteID L02808.
- S. C. Brown, *Introduction to Electrical Discharges in Gases*, John Wiley & Sons, New York, 1966.
- M. Brunetti, S. Cecchini, M. Galli, G. Giovannini, A. Pagliarin, Gamma-ray bursts of atmospheric origin in the MeV energy range, *Geophys. Res. Lett.* 27 (2000) 1599–1602.
- B. Carlson, N. Lehtinen, and U. Inan, Constraints on terrestrial gamma-ray flash production derived from satellite observations, *Geophys. Res. Lett.* 34 (2007) Issue 8, CiteID L08809.
- B. Carlson, N. Lehtinen, and U. Inan, Terrestrial gamma ray flash production by lightning current pulses, *J. Geophys. Res.* 114 (2009) A00E08.
- B. Carlson, N. Lehtinen, and U. Inan, Terrestrial gamma ray flash production by active lightning leader channels, *J. Geophys. Res.* 115 (2010) Issue A10, A10324.
- S. Celestin, V. Pasko, Soft collisions in relativistic runaway electron avalanches, *J. Phys. D: Appl. Phys.* 43 (2010) 315206.
- S. Celestin, W. Xu, V. Pasko, Terrestrial gamma ray flashes with energies up to 100 MeV produced by nonequilibrium acceleration of electrons in lightning, *J. Geophys. Res.* 117 (2012) A05315, doi:10.1029/2012JA017535.
- A. Chilingarian *et al.*, Ground-based observations of thunderstorm-correlated fluxes of high-energy electrons, gamma rays, and neutrons, *Phys. Rev. D* 82 (2010) Issue 4, id. 043009.
- A. Chilingarian, H. Mkrtchyan, Role of the Lower Positive Charge Region (LPCR) in initiation of the Thunderstorm Ground Enhancements (TGEs), *Phys. Rev. D* 86 (2012a) 072003.
- A. Chilingarian, B. Mailyan, L. Vanyan, Recovering of the energy spectra of electrons and gamma rays coming from the thunderclouds, *Atmos. Res.* 114–115 (2012b) 1–16.

- A. P. Chubenko *et al.*, Intense x-ray emission bursts during thunderstorms, *Phys. Lett. A* 275 (2000) 90–100.
- A. P. Chubenko, I. V. Amurina, V. P. Antonova, M. M. Kokobaev, S. V. Kryukov, R. A. Nam, *et al.*, Effective growth of a number of cosmic ray electrons inside thundercloud, *Phys. Lett. A* 309 (2003) 90.
- J. D. Cobine, *Gaseous Conductors*, Dover Publishing, New York, 1958.
- M. B. Cohen, U. S. Inan, G. J. Fishman, Terrestrial gamma ray flashes observed aboard the Compton Gamma Ray Observatory/Burst and Transient Source Experiment and ELF/VLF radio atmospherics, *J. Geophys. Res.* 111 (2006) Issue D24, CiteID D24109.
- M. B. Cohen, U. S. Inan, R. K. Said, T. Gjestland, Geolocation of terrestrial gamma-ray flash source lightning, *Geophys. Res. Lett.* 37 (2010) Issue 2, CiteID L02801.
- J. J. Colman, R. A. Roussel-Dupré, L. Triplett, Temporally self-similar electron distribution functions in atmospheric breakdown: The thermal runaway regime, *J. Geophys. Res.* 115 (2010) A00E16.
- V. Connaughton, *et al.*, Associations between Fermi Gamma-ray Burst Monitor terrestrial gamma ray flashes and sferics from the World Wide Lightning Location Network, *J. Geophys. Res.* 115 (2010) Issue A12, CiteID A12307.
- V. Connaughton *et al.*, Radio signals from electron beams in Terrestrial Gamma-ray Flashes, *J. Geophys. Res.* 118 (2013) 118, 2313–2320.
- V. Cooray (Ed.), *The Lightning Electromagnetics*, Power & Energy Series 62, The Institute of Engineering and Technology, London, 2012.
- S. A. Cummer *et al.*, Measurements and implications of the relationship between lightning and terrestrial gamma ray flashes, *Geophys. Res. Lett.* 32 (2005) L08811, doi:10.1029/2005GL022778.
- S. A. Cummer *et al.*, The lightning-TGF relationship on microsecond timescales, *Geophys. Res. Lett.* 38 (2011) L14810, doi:10.1029/2011GL048099.
- J. R. Dwyer, A fundamental limit on electric fields in air, *Geophys. Res. Lett.* 30 (2003) 2055.
- J. R. Dwyer *et al.*, Energetic radiation produced during rocket-triggered lightning, *Science* 299 (2003) 694–697.
- J. R. Dwyer, Implications of x-ray emission from lightning, *Geophys. Res. Lett.* 31 (2004) L12102, doi:10.1029/2004GL019795.
- J. R. Dwyer, D. M. Smith, A Comparison between Monte Carlo simulations of runaway breakdown and terrestrial gamma-ray flash observations, *Geophys. Res. Lett.* 32 (2005) L22804, doi:10.1029/2005GL023848.
- J. R. Dwyer, The initiation of lightning by runaway air breakdown, *Geophys. Res. Lett.* 32 (2005) L20808, doi:10.1029/2005GL023975.
- J. R. Dwyer *et al.*, X-ray bursts associated with leader steps in cloud-to-ground lightning, *Geophys. Res. Lett.* 32 (2005a) L01803, doi:10.1029/2004GL021782.
- J. R. Dwyer *et al.*, X-ray bursts produced by laboratory sparks in air, *Geophys. Res. Lett.* 32 (2005b) L20809, doi:10.1029/2005GL024027.
- J. R. Dwyer, Relativistic breakdown in planetary atmospheres, *Phys. Plasmas* 14 (2007) Issue 4, pp. 042901–042901-17.
- J. R. Dwyer, The source mechanisms of Terrestrial Gamma-ray Flashes (TGFs), *J. Geophys. Res.* 113 (2008) Issue D10, CiteID D10103.
- J. R. Dwyer *et al.*, A study of X-ray emission from laboratory sparks in air at atmospheric pressure, *J. Geophys. Res.* 113 (2008) D23207, doi:10.1029/2008JD010315.

- J. R. Dwyer, Diffusion of relativistic runaway electrons and implications for lightning initiation, *J. Geophys. Res.* 115 (2010) CiteID A00E14.
- J. R. Dwyer, L. Babich, Low-energy electron production by relativistic runaway electron avalanches in air, *J. Geophys. Res.* 116 (2011) A09301, doi:10.1029/2011JA016494.
- J. R. Dwyer *et al.*, High-speed X-ray Images of Triggered Lightning Dart Leaders, *J. Geophys. Res.* 116 (2011) D20208.
- J. R. Dwyer, L. Babich, Reply to comment by A. V. Gurevich *et al.* on “Low-energy electron production by relativistic runaway electron avalanches in air,” *J. Geophys. Res.* 117 (2012) A04303 (6pp.), doi:10.1029/2011JA017487.
- J. R. Dwyer, D. Smith, S. A. Cummer, High energy atmospheric physics: Terrestrial gamma-ray flashes and related phenomena, *Space Sci. Rev.* (2012), doi:10.1007/s11214-012-9894-0.
- J. R. Dwyer, The relativistic feedback discharge model of terrestrial gamma ray flashes, *J. Geophys. Res.* 117 (2012) A02308, doi:10.1029/2011JA017160.
- J. R. Dwyer, S. A. Cummer, Radio emissions from terrestrial gamma-ray flashes, *J. Geophys. Res.* 118 (2013) 3769–3790.
- J. R. Dwyer, N.Y. Liu, H. K. Rassoul, Properties of the thundercloud discharges responsible for terrestrial gamma-ray flashes, *Geophys. Res. Lett.* 40 (2013) 4067–4073.
- J. R. Dwyer, M. A. Uman, *The Physics of Lightning*, Physics Reports, 534(4), 30 January 2014, 147–241.
- K. B. Eack, W.H. Beasley, W.D. Rust, T.C. Marshall, M. Stolzenburg, Initial results from simultaneous observation of X rays and electric fields in a thunderstorm, *J. Geophys. Res.* 101 (1996a) D23, 29637–29640.
- K. B. Eack, W.H. Beasley, W.D. Rust, T.C. Marshall, M. Stolzenburg, X-ray pulses observed above a mesoscale convective system, *Geophys. Res. Lett.* 23 (1996b) 21, 2915–2918.
- K. B. Eack, D.M. Suszcynsky, W.H. Beasley, R. Roussel-Dupré, E. Symbalisty, Gamma-ray emission observed in a thunderstorm anvil, *Geophys. Res. Lett.* 27 (2000) 185–188.
- G. J. Fishman, P. N. Bhat, R. Mallozzi, J. M. Horack, T. Koshut, C. Kouveliotou, *et al.*, Discovery of intense gamma-ray flashes of atmospheric origin, *Science* 264 (1994) 1313.
- G. J. Fishman, M. S. Briggs, V. Connaughton, P. N. Bhat, W. S. Pacias, A. von Kienlin, *et al.*, Temporal properties of the terrestrial gamma-ray flashes from the Gamma-Ray Burst Monitor on the Fermi Observatory, *J. Geophys. Res.* 116 (2011) A07304, doi:10.1029/2010JA016084.
- R. C. Franz, R. J. Nemzek, J. R. Winckler, Television image of a large upward electric discharge above a thunderstorm system, *Science* 249 (1990) 48–51.
- C. Guo, E. P. Krider, The optical power radiated by lightning return strokes, *J. Geophys. Res.* 88 (1983) Issue C13, 8621–8622.
- T. Gjesteland, N. Østgaard, P.H. Connell, J. Stadsnes, G.J. Fishman, Effects of dead time losses on terrestrial gamma ray flash measurements with the Burst and Transient Source Experiment, *J. Geophys. Res.* 115 (2010) Issue 3, A00E21.
- B. W. Grefenstette, D. M. Smith, J. R. Dwyer, G. J. Fishman, Time evolution of terrestrial gamma ray flashes, *Geophys. Res. Lett.* 35 (2008) Issue 6, CiteID L06802.
- A. V. Gurevich, On the theory of runaway electrons, *Soviet Phys. JETP*. 12(5) (1961) 904–912.

- A. V. Gurevich, G.M. Milikh, R.A. Roussel-Dupré, Runaway electron mechanism of air breakdown and preconditioning during a thunderstorm, *Phys. Lett. A* 165 (1992) 463–467.
- A. V. Gurevich, K. P. Zybin, R. A. Roussel-Dupré, Lightning initiation by simultaneous effect of runaway breakdown and cosmic ray showers, *Phys. Lett. A* 254 (1999) 79–87.
- A. V. Gurevich, K.P. Zybin, Runaway breakdown and electric discharges in thunderstorms, *Physics-Uspekhi* 44 (2001) 1119.
- J. D. Hill, M. A. Uman, D. M. Jordan, J. R. Dwyer, H. Rassoul, “Chaotic” dart leaders in triggered lightning: Electric fields, X-rays, and source locations, *J. Geophys. Res.* 117 (2012) D03118, doi:10.1029/2011JD016737.
- J. D. Hill, The Mechanisms of Lightning Leader Propagation and Ground Attachment, PhD Dissertation, University of Florida, 2012.
- J. Howard *et al.*, Co-location of lightning leader x-ray and electric field change sources, *Geophys. Res. Lett.* 35 (2008) L13817, doi:10.1029/2008GL034134.
- J. Howard *et al.*, RF and x-ray source locations during the lightning attachment process, *J. Geophys. Res.* 115 (2010), doi:10.1029/2009JD012055.
- U. S. Inan, S. C. Reising, G. J. Fishman, J. M. Horack, On the association of terrestrial gamma-ray bursts with lightning and implications for sprites, *Geophys. Res. Lett.* 23 (1996) 1017–1020.
- U. S. Inan, M. B. Cohen, R. K. Said, D. M. Smith, L. I. Lopez, Terrestrial gamma ray flashes and lightning discharges, *Geophys. Res. Lett.* 33 (2006) L18802, doi:10.1029/2006GL027085.
- N. A. Kelley, A. Lowell, D. M. Smith, J. R. Dwyer, S. A. Cummer, G. Lu, R. Blakeslee, Abstract AE11A-0332 presented at 2010 Fall Meeting, AGU, San Francisco, Calif., 13–17, 2010.
- P. O. Kochkin, C. V. Nguyen, A. P. J. van Deursen, U. Ebert, Experimental study of hard X-rays emitted from meter-scale positive discharged in air, *J. Phys. D: Appl. Phys.* 45 (2012) 425202 (10pp.).
- N. G. Lehtinen, T. F. Bell, U. S. Inan, Monte Carlo simulation of runaway MeV electron breakdown with application to red sprites and terrestrial gamma ray flashes, *J. Geophys. Res.* 104 (1999) 24699–24712, doi:10.1029/1999JA0900335.
- N. Liu, V. P. Pasko, Effects of photoionization on propagation and branching of positive and negative streamers in sprites, *J. Geophys. Res.* 109 (2004) A04301, doi:10.1029/2003JA010064.
- N. Liu, J. R. Dwyer, Modeling terrestrial gamma-ray flashes produced by relativistic feedback discharges, *J. Geophys. Res.* 118 (2013) 2359–2376.
- N. Liu, B. Kosar, S. Sadighi, J. R. Dwyer, H. K. Rassoul, Formation of streamer discharges from an isolated ionization column at subbreakdown conditions, *Phys. Rev. Lett.* 109 (2012) 025002.
- L. B. Loeb, *Electrical Coronas*, University of California Press, Berkeley and Los Angeles, 1965.
- G. Lu *et al.*, Lightning mapping observation of a terrestrial gamma-ray flash, *Geophys. Res. Lett.* 37 (2010) Issue 11, CiteID L11806.
- G. Lu *et al.*, Characteristics of broadband lightning emissions associated with terrestrial gamma ray flashes, *J. Geophys. Res.* 116 (2011) Issue A3, CiteID A03316.
- S. Mallick, V. A. Rakov, J. R. Dwyer, A study of x-ray emissions from thunderstorms with emphasis on subsequent strokes in natural lightning, *J. Geophys. Res.* 117 (2012) doi:10.1029/2012JD017555.

- S. A. Mallios, S. Celestin, V. P. Pasko, Production of very high potential differences by intra-cloud lightning discharges in connection with terrestrial gamma ray flashes, *J. Geophys. Res.* 118 (2013), doi:10.1002/jgra.50109, 912–918.
- V. March, J. Montanyà, X-rays from laboratory sparks in air: The role of the cathode in the production of runaway electrons, *Geophys. Res. Lett.* 38 (2011) L04803, doi:10.1029/2010GL046540.
- M. Marisaldi, F. Fuschino, C. Labanti, M. Galli, F. Longo, E. Del Monte, Detection of terrestrial gamma-ray flashes up to 40-MeV by the AGILE Satellite, *J. Geophys. Res.* 115 (2010a) A00E13.
- M. Marisaldi, A. Argan, A. Trois, A. Giuliani, M. Tavani, C. Labanti, Gamma-Ray Localization of Terrestrial Gamma-Ray Flashes, *Phys. Rev. Lett.* 105 (2010b) 128501.
- M. McCarthy, G. K. Parks, Further observations of x-rays inside thunderstorms, *Geophys. Res. Lett.* 12 (1985) 393–396.
- G. Milikh, R. Roussel-Dupré, Runaway breakdown and electrical discharges in thunderstorms, *J. Geophys. Res.* 115 (2010) A00E60, doi:10.1029/2009JA014818.
- C. B. Moore, K. B. Eack, G. D. Aulich, W. Rison, Energetic radiation associated with lightning stepped-leaders, *Geophys. Res. Lett.* 28 (2001) 2141–2144.
- R. Morrow, J. J. Lowke, Streamer propagation in air, *J. Phys. D: Appl. Phys.* 30 (1997) 614–627.
- G. D. Moss, V. P. Pasko, N. Liu, G. Veronis, Monte Carlo model for analysis of thermal runaway electrons in streamer tips in transient luminous events and streamer zones of lightning leaders, *J. Geophys. Res.* 111 (2006) A02307, doi:10.1029/2005JA011350.
- E. Nasser, *Fundamentals of Gaseous Ionization and Plasma Electronics*, Wiley-Interscience, New York, 1971.
- C. V. Nguyen, A. P. J. van Deursen, U. Ebert, Multiple x-ray bursts from long discharges in air, *J. Phys. D: Appl. Phys.* 41 (2008) 234012.
- C. V. Nguyen, A.P.J. van Deursen, E.J.M. van Heesch, C.J.J. Winands, A.J.M. Pemen, X-ray emission in streamer-corona plasma, *J. Phys. D.: Appl. Phys.* 43 (2010) 025202 (5pp.), doi:10.1088/0022-3727/43/2/025202.
- N. Østgaard, T. Gjesteland, R. S. Hansen, A. B. Collier, B. Carlson, The true fluence distribution of terrestrial gamma flashes at satellite altitude, *J. Geophys. Res.* 117 (2012) A03327 (8pp.), doi:10.1029/2011JA017365.
- Østgaard *et al.*, Simultaneous observations of optical lightning and terrestrial gamma ray flash from space, *Geophys. Res. Lett.* <http://onlinelibrary.wiley.com/doi/10.1002/grl.v40.10/issuetoc> 40 (2013) 2423–2426.
- G. K. Parks, B. H. Mauk, R. Spiger, J. Chin, X-ray enhancements detected during thunderstorm and lightning activities, *Geophys. Res. Lett.* 8 (1981) 1176–1179.
- C. T. Phelps, R. F. Griffiths, Dependence of positive corona streamer propagation on air pressure and water vapor content, *J. Appl. Phys.* 47 (1976) 7.
- H. Raether, Zur Entwicklung von Kanalentladungen, *Arch. Elektrotech* 34 (1940) 49–56.
- H. Raether, *Electron Avalanches and Breakdown in Gases*, Butterworth & Co. Ltd., 1964.
- M. Rahman *et al.*, X-rays from 80 cm long sparks in air, *Geophys. Res. Lett.* 35 (2008) L06805, doi:10.1029/2007GL032678.

- V. A. Rakov, M. A. Uman, *Lightning: Physics and Effects*, Cambridge University Press, Cambridge, UK, 2003, 687 pages; paperback edition, Cambridge University Press, 2006.
- R. Roussel-Dupré, J. J. Colman, E. Symbalisty, D. Sentman, V. P. Pasko, Physical processes related to discharges in planetary atmospheres, *Space Sci. Rev.* 137 (2008) 51–82.
- Z. Saleh *et al.*, Properties of the x-ray emission from rocket-triggered lightning as measured by the Thunderstorm Energetic Radiation Array (TERA), *J. Geophys. Res.* 114 (2009) D17, doi:10.1029/2008JD011618.
- M. M. Schaal *et al.*, Spatial energy spatial and energy distributions of X-ray emissions from leaders in natural and rocket triggered lightning, *J. Geophys. Res.* 117 (2012) D15201, doi:10.1029/2012JD017897.
- X.-M. Shao, T. Hamlin, D. M. Smith, A closer examination of terrestrial gamma-ray flash-related lightning processes, *J. Geophys. Res.* 115 (2010) Issue 9, CiteID A00E30.
- D. M. Smith, L. I. Lopez, R. P. Lin, C. P. Barrington-Leigh, Terrestrial gamma-ray flashes observed up to 20 MeV, *Science* 307 (2005) 1085–1088.
- R. Solomon, V. Schroeder, M. B. Baker, Lightning initiation – conventional and runaway-breakdown hypotheses, *Q.J.R. Meteorol. Soc.* 127 (2001) 2263–2704.
- Mark A. Stanley, Xuan-Min Shao, David M. Smith, Liliana I. Lopez, Morris B. Pongratz, Link between terrestrial gamma-ray flashes and intra-cloud lightning discharges, *Geophys. Res. Lett.* 33 (2006) Issue 6, CiteID L06803.
- D. M. Suszcynsky, R. Roussel-Dupré, G. Shaw, Ground-based search for X rays generated by thunderstorms and lightning, *J. Geophys. Res.* 101 (1996) 23505.
- M. Tavani, M. Marisaldi, C. Labanti, F. Fuschino, A. Argan, A. Trois, Terrestrial gamma-ray flashes as powerful particle accelerators, *Phys. Rev. Lett.* 106 (2011) Issue 1, id. 018501.
- T. Torii, M. Takeishi, T. Hosono, Observation of gamma-ray dose increase associated with winter thunderstorm and lightning activity, *J. Geophys. Res.* 107 (2002) 4324.
- T. Torii, T. Nishijima, Z.-I. Kawasaki, T. Sugita, Downward emission of runaway electrons and bremsstrahlung photons in thunderstorm electric fields, *Geophys. Res. Lett.* 31 (2004) L05113.
- T. Torii *et al.*, Gradual increase of energetic radiation associated with thunderstorm activity at the top of Mt. Fuji, *Geophys. Res. Lett.* 36 (2009) L13804.
- T. Torii, T. Sugita, M. Kamogawa, Y. Watanabe, K. Kusunoki, Migrating source of energetic radiation generated by thunderstorm activity, *Geophys. Res. Lett.* 38 (2011) L24801, doi:10.1029/2011GL049731.
- H. Tsuchiya, T. Enoto, S. Yamada, T. Yuasa, M. Kawaharada, T. Kitaguchi, Detection of high-energy gamma rays from winter thunderclouds, *Phys. Rev. Lett.* 99 (2007) 165002.
- H. Tsuchiya, T. Enoto, T. Torii, K. Nakazawa, T. Yuasa, S. Torii, Observation of an energetic radiation burst from mountain-top thunderclouds, *Phys. Rev. Lett.* 102 (2009) 255003.
- H. Tsuchiya, T. Enoto, S. Yamada, T. Yuasa, K. Nakazawa, T. Kitaguchi, Long-duration  $\gamma$  ray emissions from 2007 and 2008 winter thunderstorms, *J. Geophys. Res.* 116 (2011) D09113.
- M. A. Uman, *The Lightning Discharge*, Academic Press, London, 1987, 376 pages; revised paperback edition, Dover, New York, 2001.

- M. A. Uman, *The Art and Science of Lightning Protection*, 2008, Cambridge University Press, Cambridge, 2010.
- S. Yoshida *et al.*, High energy photon and electron bursts associated with upward lightning strokes, *Geophys. Res. Lett.* 37 (2008) L10804, doi:10.1029/2007GL032430.
- C. T. R. Wilson, The acceleration of beta-particles in strong electric fields such as those of thunder-clouds, *Proc. Cambridge Phil. Soc.* 22 (1925) 534–538.
- W. Xu, S. Celestin, and V. Pasko, Source altitudes of terrestrial gamma-ray flashes produced by lightning leaders, *Geophys. Res. Lett.* 39 (2012) L08801, doi:10.1029/2012GL051351.

---

## Chapter 19

# Global lightning nitrogen oxides production

*William Koshak*

---

### 19.1 The importance of lightning nitrogen oxides

The intense heating of air molecules by a lightning discharge and subsequent rapid cooling of the hot lightning channel results in the production of nitrogen oxides (Chameides, 1986). The lightning nitrogen oxides, or “LNO<sub>x</sub>” for brevity (where  $\text{NO}_x = \text{NO} + \text{NO}_2$ ), indirectly influences our climate since these molecules are important in controlling the concentration of ozone (O<sub>3</sub>) and hydroxyl radicals (OH) in the atmosphere (Huntrieser *et al.*, 1998; see also Crutzen 1970, 1973, 1979; Chameides and Walker, 1973; Hidalgo and Crutzen, 1977). Analyses of Tropospheric Emission Spectrometer (TES) data show that tropical upper tropospheric ozone has the largest radiative impact (Aghedo *et al.*, 2011). In addition, the distribution of ozone forcing can have a substantial influence on regional rainfall patterns, even more so than its global mean annual average forcing would suggest (Shindell *et al.*, 2012). Since LNO<sub>x</sub> controls ozone and is the most important source of NO<sub>x</sub> in the upper troposphere (particularly in the tropics), lightning is important to climate (see the review by Schumann and Huntrieser, 2007). Furthermore, a substantial amount of LNO<sub>x</sub> is transported to higher latitudes via the stratosphere, extending its influence even farther (Grewe *et al.*, 2002, 2004).

Observations of lightning provide one of the most vital, simple, and direct means for examining the spatial and temporal evolution of atmospheric convection across large geographic regions. The cloud buoyancy that drives vertical motions in thunderstorms results from a temperature differential on the order of only 1°C; this means that temperature perturbations of this order are clearly important in the context of both cloud electrification and global warming (Williams, 2005).

In order to optimally track the co-varying nature of lightning and climate, and provide useful indicators that help decision makers mitigate and adapt to adverse lightning-caused impacts, it is important to employ satellite lightning data that provides not just ground flash information but also cloud flash information. Cloud flashes outnumber ground flashes over the United States by a factor of 2.94 to 1 on average (Boccippio *et al.*, 2001), and this factor can exceed 70 for individual severe storms (Carey and Rutledge, 1998; Figure 11a). Indeed, cloud flash information is required to fully assess lightning/climate covariance. Lightning is also uniquely coupled to thunderstorm updraft intensity (as associated with extreme weather events), and to ice precipitation based processes. Therefore, observations of lightning provide a simple and direct means of probing and tracking changes in both convection and convective cold cloud precipitation.





“ice factory” at tropopause levels and contribute to upper tropopause water vapor via sublimation (Baker *et al.*, 1995, 1999). Price (2000) found excellent agreement between lightning activity and upper tropospheric water vapor, which is a more important greenhouse substance than boundary layer water vapor (Williams, 2005).

Other interconnections potentially exist. First, according to the Intergovernmental Panel on Climate Change (IPCC) Report (1995) and Kunkel (2003), a warmer climate implies a larger number of extreme events (e.g., flash floods and severe storms that are associated with much lightning). However, Williams (2005) indicates that mean thunderstorm flash rate (a reasonable indicator of storm severity) is not larger in a warmer climate. Second, a three-fold enhancement of ground flash lightning frequency over Houston, Texas, has raised the issue of heat island and pollution effects (Huff and Changnon, 1972; Orville *et al.*, 2001; Steiger *et al.*, 2002). Albrecht *et al.* (2011) provide additional connections between ground flash lightning and pollution/deforestation. Finally, increases in positive polarity ground flashes (i.e., those that deposit positive charge to the Earth’s surface) have been attributed to elevated equivalent potential temperatures (Williams *et al.*, 2004, 2005), and to the thunderstorm’s ingestion of smoke from fires (Lyons *et al.*, 1998; Murray *et al.*, 2000).

Emissions of LNO<sub>x</sub> are not only important in global chemistry/climate modeling but are also important in regional air quality modeling; see for example the importance of LNO<sub>x</sub> on air pollution control problems involving tropospheric ozone (Biazar and McNider, 1995). The U.S. Environmental Protection Agency (EPA) Community Multiscale Air Quality (CMAQ) modeling system is applied by federal, state, local agencies, and other stakeholders to evaluate the impact of air quality management practices for multiple pollutants at a variety of spatio-temporal scales. The CMAQ improves the scientific understanding and modeling capability of chemical and physical atmospheric interactions, and guides the development of air quality regulations and standards. Specifically, many state and local air quality agencies use the CMAQ modeling system to determine compliance with the National Ambient Air Quality Standards (NAAQS). At the national level, billions of dollars in emission reduction scenarios are tested using CMAQ, with an aim of determining the most efficient and cost-effective strategies for attaining the NAAQS. Therefore, improvements in the LNO<sub>x</sub> emission inventory directly translate into appreciable cost savings.

## 19.2 Estimating global annual LNO<sub>x</sub> production

### 19.2.1 Flash extrapolation method

The most common method for estimating the global annual LNO<sub>x</sub> production, the so-called *flash extrapolation method* (Lawrence *et al.*, 1995), is to employ the following formula (Liaw *et al.*, 1990):

$$G = \gamma PF \quad (19.1)$$

where  $G$  is the global LNO<sub>x</sub> production per year (measured in teragrams of N per year, i.e., Tg(N)/yr),  $P$  is the average NO<sub>x</sub> production per flash (in units of number of molecules per lightning flash), and  $F$  is the global lightning flash rate (number of flashes per second). The conversion factor  $\gamma$  is the ratio of the atomic mass ( $M = 14.0067$  g/mol) of nitrogen to Avogadro’s constant ( $N_A = 6.02214129 \times 10^{23}$  molecules per mole) times (1 Tg/10<sup>12</sup> g) times the number of seconds in a year (365.25 days/yr)(24 h/day)(3600 s/h). This gives a value for  $\gamma$  of approximately

$7.34 \times 10^{-28} \text{ Tg(N) yr}^{-1}/(\text{molecule s}^{-1})$ , where each molecule of NO or NO<sub>2</sub> has one atom of nitrogen).

Often in the literature, the variables  $G$  and  $P$  are defined in terms of the production of lightning NO instead of lightning NO<sub>x</sub>. But, the difference is fairly minor. According to the chemiluminescent detector measurements of laboratory sparks made by Wang *et al.* (1998), it was found that in all cases the measured NO<sub>x</sub> fraction in the sampling was only about 5–10 percent greater than the NO fraction. So “lightning NO<sub>x</sub>” and “lightning NO” are sometimes loosely used interchangeably in the literature.

Variability in  $G$  is attributable in part to the variability in  $P$ . Several estimates of  $P$  by various investigators have been summarized (Schumann and Huntrieser, 2007; Labrador *et al.*, 2004; Lawrence *et al.*, 1995). These estimates were inferred in a variety of ways: theoretical, laboratory observations, field observations, and by synthesizing all or combinations of these estimates. Table 19.1 provides a summary and an update of the various values of  $P$  obtained.

The variability in  $P$  has two basic sources. First, variability occurs due to the estimation method employed. For example, laboratory sparks do not exactly simulate lightning discharges and field observations of lightning are not as nicely controlled as in a laboratory setting. Rocket triggered lightning experiments, such as in Uman *et al.* (1997), represent an interesting compromise between the two extremes of a laboratory setting and field observations of nature. Second, some of the variability in the estimate of  $P$  is likely due to the natural variability of lightning and the thunderstorm environment in which it occurs. Clearly, lightning channel current, channel length, channel altitude, and the number of strokes in a flash, all affect the amount of LNO<sub>x</sub> produced by a flash. The chemical reaction rates and scavenging processes associated with LNO<sub>x</sub> are directly tied to the chemical, microphysical, and dynamical processes associated with a thundercloud, and these properties vary from storm to storm in general. From Table 19.1, the range of estimates for  $P$  is large; i.e., from  $4.0 \times 10^{24}$  all the way up to  $3.0 \times 10^{27}$  molecules per flash.

Another source of variability in the estimate of  $G$  is the uncertainty in the estimate of the global flash rate,  $F$ . Before the launch of the first space-based lightning mappers (see section 19.5.2) for examining the global distribution of total (i.e., ground and cloud) flashes, the estimation of  $F$  was difficult.

An early estimate of  $F$  is attributed to Brooks (1925). Based on available observations, he estimated the number of lightning flashes per thunderstorm and combined this estimate with a survey of global annual thunderstorm occurrence. Specifically, he estimated that there were approximately 1800 thunderstorms occurring worldwide at any given moment, each lasting about one hour and producing about 200 flashes per hour. This gives 360,000 flashes per hour, or  $F = 100$  flashes per second, implying over 3.15 billion flashes annually.

The range of values in the global flash rate provided in Table 8.1.1 of the summary review of Lawrence *et al.* (1995) is 50–500 flashes per second. Rakov and Uman (2003) remark that some of the variability in  $F$  is due to confusion about whether cloud or ground flashes or both are described by published flash rates, or confusion between the terms “lightning stroke” and “lightning flash.”

An interesting and novel approach for inferring the global flash rate was provided by Heckman *et al.* (1998). Radiation with frequencies of 5–30 Hz is ducted between the ionosphere and the surface of the Earth with little attenuation. Assuming all of this radiation is from lightning, they attempted to invert the electric and magnetic fields obtained from 10 days of observation. Their inferred average

Table 19.1 Comparison of LNO<sub>x</sub> estimates on a per flash basis from several studies (adapted from Peterson and Beasley (2011) and Koshak et al. (2014), but expanded with additional entries from Schumann and Huntrieser (2007) and with updates for the LNO<sub>M</sub> results; see section 19.4 for a discussion of LNO<sub>M</sub> data analyses)

Study	Methodology	$P$ ( $\times 10^{25}$ molecules per flash)	$P/N_A$ (moles/flash)
Noxon (1976)	Field observations	10	166.05
Tuck (1976)	Theoretical	1.1	18.27
Chameides et al. (1977)	Theoretical	6–14	99.63–232.48
Chameides (1979)	Theoretical	16–34	265.69–564.58
Hill et al. (1980)	Theoretical	1.2, 6*	19.93, 99.63*
Dawson (1980)	Theoretical	0.8, 4*	13.28, 66.42*
Levine (1981)	Laboratory	0.5	8.30
Hameed et al. (1981)	Review and NO <sub>y</sub> model	0.74	12.29
Kowalczyk & Bauer (1982)	Theoretical	10	166.05
Peyroux & Lapeyre (1982)	Laboratory	3.2, 2.8*	53.14, 46.50*
Drapcho et al. (1983)	Field observations	40, (10–80)*	664.22 (166.05–1328.43)*
Borucki & Chameides (1984)	Theoretical and Laboratory	3.6	59.78
Bhetanabhotla et al. (1985)	Theoretical	1.6	26.57
Franzblau & Popp (1989)	Field observations	300	4981.62
Sisterson and Liaw (1990)	Theoretical	8.2	136.16
Goldenbaum & Dickerson (1993)	Model	3.8	63.10
Lawrence et al. (1995)	Review	2.3	38.19
Kumar et al. (1995)	Field observations	0.5, 6*	8.30, 99.63*
Ridley et al. (1996)	Field observations	2.8–3.6	46.50–59.78
Jadhav et al. (1996)	Field observations	6.4	106.27
Price et al. (1997)	Theoretical	6.7–67	111.26–1112.56
Huntrieser et al. (1998)	Field observations	4–30	66.42–498.16
Wang et al. (1998)	Laboratory	3.1	51.48
Höller et al. (1999)	Field observations	7	116.24
Stith et al. (1999)	Field observations	1.25–12.5	20.76–207.57
DeCaria et al. (2000)	Theoretical	15.6, (14–28)*	259.05, (232.48–464.95)*
Bradshaw et al. (2000)	Review	10–20	166.05–332.11
Cook et al. (2000)	Laboratory	0.4–7.4	6.64–122.88
Nesbitt et al. (2000)	Field observations	2.67	44.34
Huntrieser et al. (2002)	Field observations	2.7, 8.1*	44.84, 134.50*
Skamarock et al. (2003)	Model and field observations	2.6	43.17
Fehr et al. (2004)	Field observations	21	348.71
Langford et al. (2004)	Field observations	58	963.11
Ridley et al. (2004)	Field observations	3.2, (3.3–23)*	53.14, (54.80–381.92)*
Beirle et al. (2004)	Satellite	6	99.63
DeCaria et al. (2005)	Theoretical	27.7, (21–28)*	459.97, (348.71–464.95)*
Beirle et al. (2006)	Satellite	5.4	89.67
Rahman et al. (2007)	Field observations	24 (10 km channel)	398.53

(Continued)

Table 19.1 (Continued)

Study	Methodology	$P$ ( $\times 10^{25}$ molecules per flash)	$P/N_A$ (moles/flash)
Ott <i>et al.</i> (2007)	Model and field observations	21.7	360.34
Fraser <i>et al.</i> (2007)	Field observations	10–33	166.05–547.98
Koike <i>et al.</i> (2007)	Field observations	2–49	33.21–813.66
Schumann & Huntrieser (2007)	Review	15	249.08
Cooray <i>et al.</i> (2009)	Theoretical	2	33.21
Beirle <i>et al.</i> (2010)	Satellite	1	16.61
Ott <i>et al.</i> (2010)	Theoretical	30.1	499.82
Jourdain <i>et al.</i> (2010)	Theoretical	31.3	519.75
Bucsela <i>et al.</i> (2010)	Satellite	10.5	174.36
Martini <i>et al.</i> (2011)	Theoretical	28.9	479.90
Huntrieser <i>et al.</i> (2011)	Field observations	15.1	250.74
Koshak (this chapter)	LNOM data analyses	13.7	226.89

Values with asterisks are from Schumann and Huntrieser (2007) that differed from summary values given in Lawrence *et al.* (1995), Labrador *et al.* (2004), or Peterson and Beasley (2011).

rate of vertical charge transfer squared was  $1.7 \times 10^5$  (C km)<sup>2</sup> per second, and by making additional assumptions about the nature of lightning, including the typical charge moments deposited in a flash, they arrived at an estimate of 22 flashes per second. This (low-end) estimate could easily be adjusted upward by “tuning” some of the assumptions made in the inversion technique.

Satellite observations of lightning provided a unique vantage point to better understand global lightning counts. A value of 123 flashes per second was estimated by Orville and Spencer (1979) using data from two Defense Meteorological Satellite Program (DMSP) satellites; this value had a factor of 2 uncertainty. A value of 80 flashes per second was obtained using a silicon photodiode detector on a DMSP satellite (Turman and Edgar, 1982); this value ranged from 40 to 120 flashes per second. Using a set of high-frequency radio receivers on the Ionospheric Sounding Satellite-b (ISS-b), a value of 63 flashes per second was obtained by Kotaki *et al.* (1981). Data from the DMSP and ISS-b were used in conjunction with the Cloud-Ground Ratio #3 (CGR3) observations to obtain the latitudinal variation of total flash density over each major land mass and each major ocean; the information was combined in a computational model of global lightning occurrence and resulted in a value of 65 flashes per second (Mackerras *et al.*, 1998). Finally, low Earth orbiting satellite lightning mappers (section 19.5.2) have provided what are considered the best estimates of  $F$  to date: 44 flashes per second (Christian *et al.*, 2003) and a value of 46 flashes per second (Cecil *et al.*, 2012).

Given the variability in the estimates of  $F$  and  $P$ , the range of values 0.9–220 Tg(N)/yr for  $G$  reported in Labrador *et al.* (2004) is quite large. But, because of the advent of lightning mappers, the uncertainties in estimating  $F$  have decreased substantially. According to Fehr *et al.* (2004), a more likely range of  $G$  is 2–20 Tg(N)/yr. The in-depth review by Schumann and Huntrieser (2007) suggests a range of 0.6–13 Tg(N)/yr, which is based on their (2–40)  $\times 10^{25}$  molecules per flash value of  $P$ , and the 44 flashes per second global rate of Christian *et al.* (2003). In any case, it appears that the primary difficulty in estimating the global production  $G$  using the flash extrapolation method is in estimating the per flash LNO<sub>x</sub> production  $P$ .

### 19.2.2 Thunderstorm extrapolation method

An alternative approach to estimating the global production of LNO<sub>x</sub> was introduced in Chameides *et al.* (1987). It is based on making in-situ measurements (or inferences) of the concentration of NO<sub>x</sub> in thundercloud anvils. The form of the estimate is

$$G = \kappa[\text{NO}_x]F_cS \quad (19.2)$$

where [NO<sub>x</sub>] is the average volume mixing ratio (in units of ppbv) in the anvil produced by lightning,  $F_c$  is the average air mass flux out of the anvil (in units of g(air)/s), and  $S$  is the number of active thunderstorm cells across the globe at a given time. Here, the conversion factor  $\kappa = abc$ , where  $a$  is equal to the number of seconds per year times 14 g(N)/mole times 1 mole/(29 g (air)); that is,  $a \approx 1.5 \times 10^7 \text{ g(N) g(air)}^{-1} \text{ s yr}^{-1}$ ,  $b = (10^{-9}/\text{ppbv})$ , and  $c = 10^{-12} \text{ Tg(N)/g(N)}$  so that the units of  $G$  are in Tg(N)/yr. In addition, the estimate,  $F_c = (v_a - v_s)\rho_a\Delta y\Delta z$  was employed by Chameides, where  $v_a$  is the horizontal wind speed *inside* the anvil,  $v_s$  is the storm system (steering level) speed taken as about half the ambient wind speed at the anvil altitude,  $\rho_a \sim 500 \text{ g(air)/m}^3$  is the air density in the anvil,  $\Delta y$  is the width of the anvil, and  $\Delta z$  is the depth of the anvil.

The Chameides *et al.* (1987) study employed (19.2) using data obtained from a NASA Convair 990 aircraft equipped to measure NO levels. The aircraft penetrated the anvils of two cumulonimbus clouds over the North Pacific Ocean. The value of [NO<sub>x</sub>] was estimated from the NO measurements by making assumptions about the chemical conversion rates of NO to NO<sub>2</sub> and the associated photostationary state.

According to the review in Schumann and Huntrieser (2007), the thunderstorm extrapolation method provides a range on  $G$  between about 1 and 25 Tg(N)/yr. Though the method does not require knowledge of flash properties, it is difficult to estimate the true number of thunderstorms active at any one moment across the globe.

### 19.2.3 Global model fit method

The value of  $G$  can also be inferred by adjusting the production of LNO<sub>x</sub> in a Chemical Transport Model (CTM) such that the model results best fit the aircraft measurements of trace gases that are affected by LNO<sub>x</sub> sources (Levy *et al.*, 1996). For example, the concentrations of upper tropospheric NO<sub>x</sub> and NO<sub>y</sub> (i.e., all reactive odd nitrogen or fixed nitrogen, which are any N–O combinations except the very stable N<sub>2</sub>O) are directly affected by LNO<sub>x</sub>. In addition, LNO<sub>x</sub> indirectly affects O<sub>3</sub>, CO, HNO<sub>3</sub>, and others, via photochemistry. According to the review by Schumann and Huntrieser (2007), systematic comparisons between LNO<sub>x</sub>-sensitive measurements and CTM results suggest a range of  $G$  between 2 and 8 Tg(N)/yr. However, several authors expressed doubts about the feasibility of this approach citing, for example, either missing or highly variable data (see Schumann and Huntrieser (2007; section 3.3) for additional details). Nonetheless, applications of this method using satellite observations offer important “top-down” constraints to the value of  $G$  (see section 19.5.3 of this chapter).

## 19.3 Observations and inferences of LNO<sub>x</sub>

In this section, and sections 19.4 and 19.5 to follow, a closer look at the variety of ways investigators have observed or inferred LNO<sub>x</sub> is discussed. This provides additional context to the difficulties associated with estimating  $G$ . Although there

have been improvements in the measurements and methods for estimating  $P$ , there is still considerable debate in the lightning/chemistry community regarding what the best estimate of  $P$  should be; clearly, more work is needed to improve confidence.

To begin, some early ground-based measurements of historical importance are discussed (sections 19.3.1 and 19.3.2). Next, a few examples of field campaigns notable for their highly coordinated measurements are provided, including in situ aircraft measurements (section 19.3.3). Finally, section 19.3.4 provides some unique insight about LNO<sub>x</sub> from artificially triggered lightning.

### 19.3.1 *Early examinations of thunderstorm rainwater*

The work of von Liebig (1827) suggested that lightning contributes to the global source of NO<sub>x</sub>. In addition, von Liebig hypothesized that the concentration of dissolved nitrate, NO<sub>3</sub><sup>-</sup>, in rainwater can be explained in part by the following reactions:



where the third body M is any inert molecule (e.g., N<sub>2</sub> or O<sub>2</sub>), HNO<sub>3</sub> is the highly water-soluble nitric acid gas, and the last reaction takes place in the rainwater.

This hypothesis motivated several follow-on studies that looked for a correlation between the concentration of NO<sub>3</sub><sup>-</sup> in rainwater and lightning frequency (Hutchinson, 1954; Viemeister, 1960; Visser, 1961). However, these studies found that typically only a relatively small percent of the NO<sub>3</sub><sup>-</sup> was attributable to lightning. In other words, even if there were copious amounts of lightning in a region and associated lightning NO, not much of this lightning NO would show up as NO<sub>3</sub><sup>-</sup> in the thunderstorm rainwater. Eventually, an explanation of this result was that the conversion time (12–20 h) of the first two reactions in (19.3) is substantially larger than the typical (~ 1 h) lifetime of a thunderstorm (Tuck, 1976; Chameides, 1977).

### 19.3.2 *Clarifying observations*

The difficulties associated with examining thunderstorm rainwater clearly implied a need to find improved methods for measuring lightning nitrogen oxides. Some milestone observations in the 1970s provided substantial confirmation and clarification.

Early preliminary observations of trace nitrogen dioxide (NO<sub>2</sub>) from lightning are provided in Reiter (1970). The NO<sub>2</sub> measurements were taken at a mountain recording station 1780 m above sea level. A special instrument was used to measure the NO<sub>2</sub>. It functioned on the basis of a chemical reaction that involved the oxidation of potassium iodide ions by NO<sub>2</sub>; a current is eventually generated that is proportional to the concentration of the NO<sub>2</sub>. The instrument had a low-end sensitivity of 0.002 mg NO<sub>2</sub> per cubic meter (see Reiter (1970) for additional details). No NO<sub>2</sub> was detectable during times of clear air or showers, but measurable NO<sub>2</sub> traces were obtained during 17 thunderstorms located at or very near the recording station. Peak readings were typically 0.005 mg, but there were four cases in which peak concentrations ranged from 0.01 to 0.08 mg.

Subsequently, a spectrometer was used to infer the amount of NO<sub>2</sub> produced by a lightning storm that occurred on July 20, 1975 (Noxon, 1976). The

spectrometer was used to scan the spectrum of the cloud deck above the Fritz Peak Observatory in the range 4300–4500 Å. This spectrum was then divided by a solar spectrum taken at small solar zenith angle. The ratio yielded a spectrum that contained atmospheric absorption features generated by the thunderstorm. It was concluded by Noxon (1976) that the local troposphere NO<sub>2</sub> abundance was enhanced by a factor of 500 over the normal level due to the lightning storm, and it was estimated that there were approximately  $2 \times 10^{26}$  molecules per stroke generated. The enhancement, along with additional evidence from Noxon (1978), confirmed the tentative results in Reiter (1970).

### 19.3.3 Some field campaigns

The list of field campaigns discussed below is by no means comprehensive; see the many additional airborne-measurement-related field campaigns discussed in Table 3 of Schumann and Huntrieser (2007). Nonetheless, the field experiments discussed here are noteworthy examples of experiments that were dedicated toward making measurements of chemical species in the inflow and outflow regions of thunderstorms in conjunction with measurements of the cloud structure, kinematics, and lightning activity. Therefore, these field campaigns are good examples of how investigators can connect chemistry measurements in the convective outflow to specific cloud and lightning characteristics.

#### 19.3.3.1 STERAO-A

The Stratospheric-Tropospheric Experiment: Radiation, Aerosols, and Ozone (STERAO) series of field experiments was initiated to better address the complex and interdependent chemical, dynamical, electrical, and radiative processes associated with thunderstorms that directly and/or indirectly influence weather and climate (Dye *et al.*, 2000). The first in the series, STERAO-A, addressed deep convection and the composition of the upper troposphere and lower stratosphere. The primary objective of STERAO-A was to determine the effects of thunderstorms on the chemical structure of the middle and upper troposphere, particularly the production of LNO<sub>x</sub>, and the transport of NO<sub>x</sub> from the boundary layer. The field experiment was conducted during the summer of 1996 in northeastern Colorado; the primary observations included (see Dye *et al.* (2000) for additional details):

- Colorado State University (CSU) CHILL multi-parameter Doppler radar to observe storm structure evolution
- National Oceanic and Atmospheric Administration (NOAA) WP3D Orion aircraft for characterizing the chemical environment, including determining the entrance/exit of chemical species in the boundary layer and mid-cloud levels and storm airflow
- North Dakota Citation jet for observing chemistry, microphysics, and airflow in or near thundercloud anvils
- French Office Nationale d'Etudes et de Recherches Aerospatiales (ONERA) 3-D lightning interferometer for determining the location and time-of-occurrence of ground flashes
- The National Lightning Detection Network<sup>TM</sup> (NLDN) for determining the location and time-of-occurrence of ground flashes
- The National Center for Atmospheric Research (NCAR) Atmospheric Technology Division mobile Cross-Chain Loran Atmospheric Sounding System (CLASS) for acquiring atmospheric soundings



The STERAO-A study in Dye *et al.* (2000) focused on a severe storm that occurred on July 10, 1996 and that had mostly (i.e., > 95 percent) cloud flashes throughout most of the storm's life cycle. They deduced that lightning contributed a minimum of 45 percent (and more likely 60–90 percent) of the total NO<sub>x</sub> observed in the anvil.

Although it was difficult to correlate individual flashes with aircraft-measured spikes in NO mean mixing ratio, a simple model of the NO plume from lightning was introduced to estimate lightning NO production (Stith *et al.*, 1999). The plume model has the form

$$\lambda = b \frac{[\text{NO}]p\pi D^2}{4kT} \quad (19.4)$$

where [NO] is the concentration of NO above the background (in units of ppbv),  $p$  is pressure (in Pa),  $T$  is temperature (in absolute K),  $D$  is the NO plume diameter (in meters), and  $\lambda$  is the resulting NO production efficiency (in molecules NO per meter of channel). The Boltzmann constant is  $k = 1.381 \times 10^{-23} \text{ m}^2 \text{ kg s}^{-2} \text{ K}^{-1}$ , and as before the conversion factor is  $b = (10^{-9}/\text{ppbv})$ . They obtained a range from  $2 \times 10^{20}$  to  $1 \times 10^{22}$  molecules of NO per meter of lightning channel.

The study by DeCaria *et al.* (2000) performed a 2-D cloud-scale model simulation of the STERAO-A storm that occurred on July 12, 1996. One of their objectives was to infer from the simulations and available measurements the relative production of NO<sub>x</sub> by ground and cloud flashes. Defining  $P_g$  to be the NO<sub>x</sub> production per ground flash, and  $P_c$  the NO<sub>x</sub> production per cloud flash, they estimated that  $P_g$  should be in the range 200–500 moles and that the model results agree best with the observations when the ratio  $P_c/P_g$  is in the range 0.5–1. See subsection 19.5.4.1 for additional estimates of this ratio.

Three-dimensional cloud-scale chemical transport models have also been developed and applied to STERAO-A storms (e.g., Skamarock *et al.*, 2000; Stenchikov *et al.* 2005). DeCaria (2005) applied the Stenchikov *et al.* (2005) model to again examine lightning NO<sub>x</sub> production in the July 12, 1996 storm (as well as trace gas transport and photochemical ozone production). In their analysis, they concluded that the values  $P_g = P_c = 460$  moles give the best reproduction of the observed mixing ratios and shape of the anvil NO<sub>x</sub> plume.

### 19.3.3.2 EULINOX

The European Lightning Nitrogen Oxides (EULINOX) field experiment was coordinated by the Deutsches Zentrum für Luft- und Raumfahrt (DLR) located near Munich, Germany and conducted in July 1998 (Höller and Schumann, 2000). An important objective of the experiment was to estimate the importance of LNO<sub>x</sub> in comparison to other sources of NO<sub>x</sub>; there was a desire to reduce the uncertainties involved in both the production and effect of LNO<sub>x</sub> from the flash scale to the synoptic scale. The idea was that an improved understanding of the relevant processes on the small scale is necessary for a better representation of the effects on the larger scale. An important specific question asked by the EULINOX project was, “Can one deduce the LNO<sub>x</sub> source per flash, or per thunderstorm, from the planned observations?”

Two DLR aircraft were used to make in-situ chemical, particle, and meteorological measurements: a Dornier-228 turboprop completed measurements in the boundary layer, and a Falcon jet made measurements primarily in the upper troposphere. Both aircraft were equipped with instruments for measuring NO, ozone, and carbon dioxide, and the Falcon jet additionally measured NO<sub>2</sub>, other

chemical and particle measurements, and some standard data (position, altitude, temperature, humidity, pressure, and the three components of the wind field) (Huntrieser *et al.*, 2002). The Falcon completed several flights over much of central Europe, whereas the Dornier-228 completed fewer flights and covered a region more local to the DLR operation center in Oberpfaffenhofen, Germany.

For lightning observations, the ONERA VHF interferometric lightning mapper was used to locate the fast streamer processes in ground and cloud flashes; 3-D reconstruction of flash channels was possible within about 50 km of the DLR operation center and 2-D channel location was possible for flashes within about 100 km (Fehr *et al.*, 2004). Two lightning position and tracking system (LPATS) (Casper and Bent, 1992) sensors were employed to obtain 2-D locations of ground flashes. NASA satellite lightning observations from the Optical Transient Detector (OTD; 1999–2000, see section 19.5.2) were also available for EULINOX.

In addition, several other measurements were available for EULINOX. Radar data included: DLR Polarization Diversity Radar (POLDIRAD) polarimetric doppler radar, and data from the German Weather service doppler/reflectivity radars. Sounding data (profiles of pressure, temperature, humidity) and mesonet data (surface pressure, temperature, humidity, wind) were available. Finally, EULINOX benefitted from a variety of additional satellite observations (infrared, visible, WV images, ozone, NO<sub>2</sub>). See Höller and Schumann (2000) for additional details.

For an average EULINOX thunderstorm, ~70 percent of the anvil NO<sub>x</sub> was produced by lightning and ~30 percent was transported from the boundary layer; the amount of LNO<sub>x</sub> was found to exceed 80 percent in larger EULINOX thunderstorms (Huntrieser *et al.*, 2002). The Huntrieser *et al.* (2002) study found that the maximum NO mixing ratio measured inside a thundercloud near lightning was 25 ppbv. In addition, they employed the thunderstorm extrapolation method (section 19.2.2) to estimate the annual global LNO<sub>x</sub> production  $G$ . They assumed the values:  $S \sim 2000$ , and  $F_c \sim 1.05 \times 10^{11}$  g(air)/s, where  $(v_a - v_s) \sim 7$  m s<sup>-1</sup>,  $\rho_a \sim 500$  g/m<sup>3</sup>,  $\Delta y \sim 30\,000$  m, and  $\Delta z \sim 1000$  m. They used the estimate anvil [NO<sub>x</sub>]  $\sim 0.9$  ppbv, where the value 0.9 ppbv represented the average of all EULINOX cases. From (19.2) they obtained  $G \sim 3$  Tg(N)/yr. (They also applied the simple plume model given in (19.4) and obtained  $2.7 \times 10^{21}$  molecules NO per meter of channel. This gave  $G \sim 4$  Tg(N)/yr when an ONERA interferometer-derived channel length of 30 km was used in conjunction with an assumed global flash rate of 65 s<sup>-1</sup>.)

A 3-D cloud model, with LNO<sub>x</sub> emissions represented by a Lagrangian particle approach, was applied to study the EULINOX supercell storm that occurred on July 21, 1998 (Fehr *et al.*, 2004). The simulation used both parameterized and observed ground and cloud flash frequencies. Experimentally deduced values for the ground flash NO<sub>x</sub> production of 4.9 kg(N), or equivalently  $2.1 \times 10^{26}$  molecules NO (348.7 moles) and a ratio between cloud and ground NO<sub>x</sub> production of 1.4 were confirmed by the model. This ratio of 1.4 is substantially larger than the ratio of 0.1 initially assumed by Price *et al.* (1997).

### 19.3.3.3 TROCCINOX

During February–March 2004 and February 2005, airborne in-situ measurements of NO, NO<sub>y</sub>, CO, and O<sub>3</sub> mixing ratios, J(NO<sub>2</sub>) photolysis rate, and meteorological variables were obtained in the anvil outflow of thunderstorms over southern Brazil as part of the Tropical Convection, Cirrus and Nitrogen Oxides Experiment (TROCCINOX) field experiment (Schumann *et al.* 2004; Huntrieser *et al.* 2007; Schumann and Huntrieser 2007). The NO<sub>2</sub> (and NO<sub>x</sub>) mixing ratios were inferred

from the measurements of NO, O<sub>3</sub>, J(NO<sub>2</sub>), pressure, and temperature by assuming a photostationary steady state. The airborne measurements were carried out using the DLR Falcon aircraft (maximum flight altitude of 12.5 km), and also in part with a high altitude (~20 km) Russian M55 Geophysica aircraft. During this wet season, both subtropical and tropical thunderstorms were investigated. In addition to ancillary satellite and radar information, lightning observations in southern Brazil were obtained using a six-station VLF/LF lightning detection network (LINET) developed by the University of Munich (Betz *et al.*, 2004; Betz *et al.*, 2007), the operational Brazilian network RINDAT (Rede Integrada Nacional de Detecção de Descargas Atmosféricas), and satellite Lightning Imaging Sensor (LIS; 1997–present, see section 19.5.2).

The composition of the anvil outflow from a large, long-lived Mesoscale Convective System (MCS) was, for the first time, investigated (Huntrieser *et al.*, 2007). The MCS, which had advected from northern Argentina and Uruguay, was found to have significantly enhanced NO<sub>x</sub>, CO, and O<sub>3</sub> mixing ratios. From the penetrations of TROCCINOX thunderstorms, Huntrieser *et al.* (2007) found that NO<sub>x</sub> mixing ratios in the anvil outflow region between 8 and 12.5 km were enhanced with average mixing ratios varying between 0.2 and 1.6 nmol mol<sup>-1</sup>, or ppbv. They estimated that the NO<sub>x</sub> from the anvil outflow of a subtropical thunderstorm was about 80% due to lightning, and only a minor contribution from the boundary layer.

Correlating the spatial distribution of measured anvil NO<sub>x</sub> enhancement with individual lightning flashes is difficult. To help, the distribution of LNO<sub>x</sub> in and near thundercloud cells was simulated with the Lagrangian particle dispersion model FLEXPART. Huntrieser *et al.* (2008) found that the amount of nitrogen produced by lightning in a thunderstorm is not well correlated with the number of (LINET) strokes; they stated that stroke length, peak current, and release height also need to be considered. Nonetheless, they estimated that the average LNO<sub>x</sub> per LIS flash was ~1 and ~2–3 kg(N) for three tropical and one subtropical Brazilian thunderstorms, respectively. Consequently, they suggested that tropical flashes may be less productive than subtropical flashes. With these values and an assumed global flash rate of 44 flashes per second, they estimated mean values of  $G$  of 1.6 and 3.1 Tg(N)/yr, for the respective storms mentioned.

Finally, the study by Höller *et al.* (2009) asserted that the effective lightning stroke length is the dominant factor for LNO<sub>x</sub> production, and that stroke peak current and emission height were less significant.

### 19.3.4 Rocket triggered lightning

By launching a small (~1 m) plastic or steel rocket with a trailing wire, either grounded or ungrounded, into a thundercloud, it is possible to artificially trigger a lightning discharge. This so-called *rocket-and-wire* technique is described in Rakov and Uman (2003). The trailing wire is composed of copper or steel and has a diameter of ~0.2 mm; it is spooled out either from the ground or from the rocket.

The first rocket-triggered lightning occurred in 1960 from a research vessel situated off the west coast of Florida (Newman, 1965); the study employed grounded trailing wires. The first triggering over land occurred in 1973 in Saint Privat d'Allier, France (Fieux *et al.*, 1975). In addition to the triggered-lightning program developed in France, other triggered-lightning programs were developed in Japan (Kahokugata, Hokuriku coast, Okushishiku), the United States (New Mexico, Florida, Alabama), China (multiple sites over the northern and southeastern regions), and Brazil (Cachoeira Paulista).

One of the triggered-lightning programs in Florida was developed in 1993 in Camp Blanding (Uman *et al.*, 1997) and is presently still operational. It has been found that the characteristics of the leader-return-stroke sequences in triggered-lightning are similar in most, if not all, respects to the *subsequent* leader-return stroke sequences in natural ground flashes (Rakov and Uman, 2003; Depasse, 1994). Evidently, the first leader-return stroke sequence in a natural ground flash is not as well represented by triggered-lightning.

Acknowledging the fact that triggered-lightning is not exactly the same as natural lightning, one can still attempt to make measurements of triggered-lightning  $\text{NO}_x$  (TLNO $_x$ ) as a proxy to LNO $_x$ . An obvious benefit of such an approach is that one controls where and when the discharge occurs, so that the placement and operation of chemistry measurements are optimized. In addition, one can also isolate a section of the triggered-lightning channel in a given volume so that no assumptions have to be made about the wind velocity or the dispersion of  $\text{NO}_x$  from the channel.

In July 2005 at the Camp Blanding, Florida triggering site, i.e., the International Center for Lightning Research and Testing (ICLRT), Rahman *et al.* (2007) obtained the first direct measurements of TLNO $_x$ . Three negative polarity lightning flashes were triggered using the rocket-and-wire technique. Two electrodes were used; one was connected to the rocket launcher where the lightning channel terminates, and the other electrode was grounded. The separation distance between the electrodes was 3 cm, and they were placed within a cylindrical chamber. The apparatus effectively isolated a 3-cm section of channel. Atmospheric air entered the chamber continuously, and evacuated air from the chamber passed through a calibrated  $\text{NO}_x$  Analyzer (model 9841B, Monitor Labs).

From their study of the three triggered lightning events, they concluded that relatively slow discharge processes, those occurring on timescales of milliseconds to hundreds of milliseconds (such as continuing currents in ground flashes), can contribute significantly to  $\text{NO}_x$  production. Moreover, they asserted that the return strokes within a ground flash are not the primary producers of  $\text{NO}_x$ ; i.e., their data showed that the  $\text{NO}_x$  production is primarily from long-duration, steady currents, as opposed to microsecond-scale impulsive return stroke currents. Since cloud flashes transfer large amounts of charge via steady currents on the order of 100 A, the implication was that cloud flashes could be as (or more) efficient at producing  $\text{NO}_x$  than ground flashes (Rahman *et al.*, 2007).

Overall, the Rahman study found a production of  $2.0 \times 10^{22}$   $\text{NO}_x$  molecules per meter of channel for one triggered flash, and  $2.4 \times 10^{22}$  molecules per meter for each of the other two triggered flashes. The value of  $P = 24 \times 10^{25}$  molecules per flash expressed in Table 19.1 was based on the latter value, and it was arbitrarily multiplied here by a 10-km channel length for order-of-magnitude purposes only. The value of 10 km is an underestimate (see following section regarding channel length estimation based on VHF lightning mapping data).

## 19.4 The Lightning Nitrogen Oxides Model (LNOM)

The previous section discussed various conventional methods for estimating the amount of nitrogen oxides produced by a flash. In this section, a more recent method for estimating LNO $_x$  is discussed. The approach is based on a research-grade software package, named the Lightning Nitrogen Oxides Model (LNOM),

which was developed at the NASA Marshall Space Flight Center (MSFC). The LNOm analyzes multiple lightning datasets in order to make detailed estimates of LNOx on a flash-by-flash basis. As such, LNOm data analyses represent the most detailed “bottom-up” constraints on the value of  $P$  in (19.1).

### 19.4.1 Motivations

Given the importance of LNOx in global climate studies as discussed in section 19.1, the ability to accurately model LNOx production within global climate models is paramount. For example, in the NASA Goddard Institute for Space Studies (GISS) ModelE2 global climate model (Schmidt *et al.*, 2006), the parameterization employed is based on the study by Price *et al.* (1997) who described LNOx production from a single flash as follows:

$$P = EY \quad (19.5)$$

Here,  $E$  is the estimated mean *energy* of the flash (Joules per flash),  $Y$  is the *yield* (# molecules of NO<sub>x</sub> per Joule), and so  $P$  is the estimated average amount of NO<sub>x</sub> *production* per flash (# molecules of NO<sub>x</sub> per flash). As mentioned above, most of the NO<sub>x</sub> yield (~ 90 percent or more) is in the form of NO (Wang *et al.*, 1998). Price *et al.* (1997) arrived at the estimates:  $E \sim 6.7 \times 10^9$  J (for ground flashes),  $E \sim 6.7 \times 10^8$  J (for cloud flashes), and  $Y \sim 10^{17}$  molecules per joule.

Note that (19.5) pertains only to the *LNOx production per flash* portion of the actual parameterization provided in Price *et al.* (1997; equation (15)) which includes various temporal and molecular weight conversion factors and flash count information that are not pertinent to the present discussion. In addition, GISS multiplies the Price *et al.* (1997) production parameterization by their own tuning factor, called `tune_NOx` in the ModelE2 code, in an attempt to improve results.

The estimates of  $E$  and  $Y$  are simply coarse-educated guesses, or the so-called “back of the envelope” calculations based on reasonable syntheses of the appropriate lightning literature. Moreover, one should recognize that the production parameterization in (19.5) provides only two numbers: the production  $P_g$  from ground flashes and the production  $P_c$  from cloud flashes. In reality, the production is not fixed for all ground flashes or for all cloud flashes. Presently, these fixed values are being applied within ModelE2 in conjunction with the flash count parameterization (discussed later) to arrive at the total LNOx source.

By today’s standards, the Price *et al.* (1997) estimates are overly simplistic since we now have advanced ground-based lightning detection systems capable of deeply probing the nature of lightning flashes, and accumulating realistic distributions of their properties that are critical for making accurate estimates of LNOx production. In particular, the bulk and estimative parameterization in equation (19.5) glosses over many important variables that can now be accounted for in part, or fully:

- Variable lightning channel lengths (longer channels → more LNOx).
- Variable lightning currents (larger and/or longer lasting currents → more LNOx).
- Variable lightning channel altitude (lower altitude → higher air density → more LNOx). That is, the yield  $Y$  in equation (19.5) is actually altitude dependent not a fixed constant (see Chameides (1986; equation (6.2)), and Wang *et al.* (1998; equation (9))).
- Variable # of return strokes in ground flashes (more strokes → more LNOx).
- Variable production physics (i.e., certain physical processes, if they occur in a flash, would produce additional LNOx (see Cooray *et al.*, 2009)).

In addition, there are deficiencies in the flash count parameterizations. For example, to calculate the number of ground and cloud flashes in each ModelE2 grid box, NASA GISS applied a parameterization described in Price and Rind (1992, 1993, 1994) and Price *et al.* (1997) that has the following form:

$$\begin{aligned} f_g &= \alpha[qH^p] && (\text{\#ground flashes per minute}) \\ f_c &= (1 - \alpha)[qH^p] && (\text{\#cloud flashes per minute}) \end{aligned} \quad (19.6)$$

The quantity in square brackets  $[qH^p]$  is the *total lightning flash rate*  $f$  (# flashes per minute), where  $H$  is the cloud top height in kilometers. The empirical constants  $q$  and  $p$  depend on whether it is a continental thunderstorm ( $q = 3.44 \times 10^{-5}$ ,  $p = 4.90$ ) or a maritime thunderstorm ( $q = 6.40 \times 10^{-4}$ ,  $p = 1.73$ ). The variable  $\alpha = (aD^4 + bD^3 + cD^2 + dD + e)^{-1}$  is the *ground flash fraction* (i.e., the proportion of ground flashes in an individual thunderstorm), where  $D$  is the *cold cloud thickness* in kilometers (i.e., the vertical thickness between the altitude of the 0°C isotherm and cloud-top height). The empirical constants are:  $a = 0.021$ ,  $b = -0.648$ ,  $c = 7.49$ ,  $d = -36.54$ , and  $e = 64.09$ .

GISS applies their own tuning factors (one for continental storms, and one for maritime storms) in an attempt to improve the parameterizations. Moreover, the values of the constants  $q$  and  $p$  have been adjusted over the years to drive the geographical distribution of ModelE2 lightning frequencies as close as possible to NASA Optical Transient Detector (OTD) lightning observations (see model/observation comparisons provided in Plate 2 of Shindell *et al.* (2001), Figure 8 of Shindell *et al.* (2003), and Figure 11 of Shindell *et al.* (2006)). Despite these improvements, there are still several shortcomings which need to be addressed:

- (a) *Documented Deficiencies*: ModelE2 tends to overestimate lightning over SE Asia and Indonesia, and this leads to overestimates of the total flashes of 5 percent during boreal summer and 17 percent during boreal winter; overestimates are pronounced over South America during the boreal winter (Shindell *et al.*, 2006).
- (b) *Separate Verification Needed*: Comparisons of ModelE2 flash frequency with OTD data are fundamentally incomplete because OTD only provides the total flash number (i.e., the sum of both ground and cloud flashes). Since the parameterizations in (19.6) provide both ground flash and cloud flash counts, it is important to separately verify the accuracy of each of these parameterizations, particularly since the typical amount of LNO<sub>x</sub> produced per ground and per cloud flash could differ.
- (c) *Low Detection Efficiency*: OTD was a prototype sensor that had daytime and nighttime flash detection efficiencies of only 44 and 56 percent, respectively (Boccippio *et al.*, 2002). In addition, the limited view-time associated with its low Earth orbit required that one perform 55 day sampling strategies in an attempt to alleviate biases associated with the diurnal cycle of lightning. Even though the Lightning Imaging Sensor (LIS) offers higher detection efficiency and better location accuracy, it only covers the tropics/subtropics, and like OTD, does not discriminate between ground and cloud flashes. Therefore, a high detection efficiency, *continuous* monitoring system that detects (and discriminates between) ground and cloud flashes is needed to fully investigate the accuracy of the parameterizations in (19.6).
- (d) *Limitations Associated with Ground Flash Fraction*: The polynomial expression given above for the ground flash fraction  $\alpha$  is only based on 139 thunderstorms which occurred only in the summer and only over the United States (Price and

Rind, 1993), yet is being applied globally and seasonally within the ModelE2. In addition, the value of  $D$  in the parameterization is restricted to the range  $5.5 \text{ km} < D < 14 \text{ km}$ .

- (e) *Theoretical Inconsistencies*: The parameterization for total flash rate in maritime thunderstorms contains a formal derivational inconsistency and predicts nonphysical cloud-top heights when the parameterization is inverted (Boccippio, 2002).

### 19.4.2 *Functionality*

Since lightning has highly variable channel lengths, currents, altitudes, and stroke number, and since there are a variety of discharge types within a flash that produce different amounts of LNO<sub>x</sub>, it is crucial that the variability of lightning be addressed to obtain accurate estimates of LNO<sub>x</sub> production, including its vertical profile. This implies that a very large number of flashes should be analyzed on a flash-by-flash basis (using the appropriate lightning detection technologies and data analysis techniques) so that quantitative and realistic statistical distributions of LNO<sub>x</sub> production can be obtained.

In order to accomplish these objectives, the LNO<sub>x</sub> Model (LNOM) was developed (Koshak *et al.*, 2009, 2010, 2011; Koshak and Peterson, 2011; Koshak *et al.*, 2014). The LNOM implements a realistic description of lightning while at the same time combines useful laboratory findings with state-of-the-art lightning observations to obtain specific LNO<sub>x</sub> estimates of individual flashes.

Figure 19.2 provides an overview of the basic function of the LNOM. It ingests VHF lightning channel mapping data such as obtained from the North Alabama Lightning Mapping Array (NALMA; Koshak *et al.*, 2004). The VHF data provide

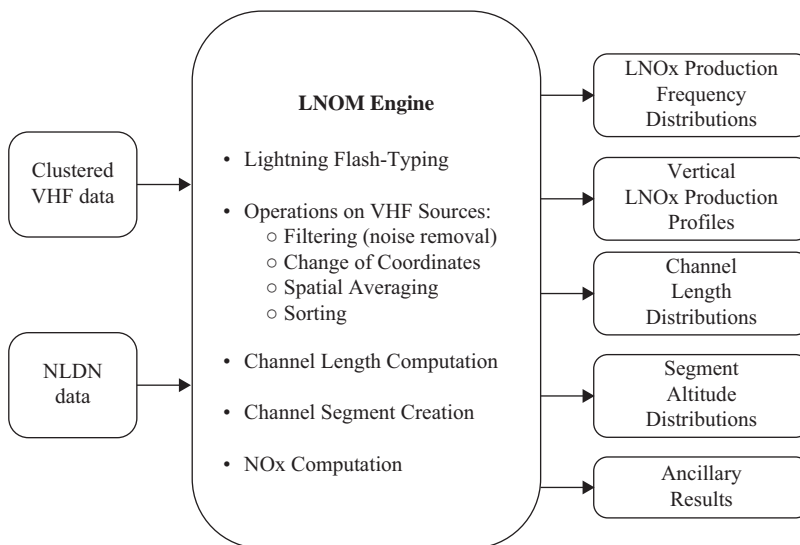


Figure 19.2 *The LNOM ingests 4-D VHF lightning channel mapping data and NLDN data to obtain the products shown on the right side of the flow diagram. These products are produced for ground flashes, for cloud flashes, and for all flashes.*

remarkable information about the spatial and temporal evolution of the lightning channel; over the LNOm analysis region the VHF data provides 4-D channel mapping with a location accuracy measured in tens of meters and with a time resolution of 80–100  $\mu\text{sec}$  (Thomas *et al.*, 2004). The LNOm also ingests ground flash data from the National Lightning Detection Network<sup>TM</sup> (NLDN, Cummins *et al.*, 2006; Cummins and Murphy, 2009). Note that the focus of LNOm is on the production of  $\text{NO}_x$ , not its subsequent chemical conversion, transport (convective, advective), or removal (e.g., wet scavenging).

In summary, the LNOm analyzes each flash individually by examining the VHF and NLDN data associated with the flash. It performs the following basic processing steps:

1. *Flash Typing*: Based on the VHF and NLDN data, LNOm categorizes the flash as either a ground flash or a cloud flash; this is an important initial step because many physical processes associated with LNO<sub>x</sub> production depend on flash type.
2. *Channel Length Computation*: LNOm spatially averages the VHF data, and computes the total channel length.
3. *Channel Chopping*: LNOm dices up the lightning channel into 10-m segments, and stores both the orientation and 3-D location of each of these segments.
4. *NO<sub>x</sub> Computation*: LNOm applies algorithms to compute the LNO<sub>x</sub> from each 10-m segment based on empirical and theoretical formulas provided in Wang *et al.* (1998) and Cooray *et al.* (2009). Note that there are several typos in the equations of Cooray *et al.* (2009) and these were corrected in Cooray *et al.* (2012). These algorithms account for many physical mechanisms that produce  $\text{NO}_x$ , and the algorithms are only applied if the mechanism is present. For example, ~75 percent of positive polarity ground flashes are associated with *continuing currents*, but only about 30 percent of negative polarity ground flashes contain such currents. Similarly, 10-m segments that are a part of a ground flash channel, but that are not located within the channel(s) to ground (i.e., are not associated with the return stroke) would not be associated with return stroke  $\text{NO}_x$  production. LNOm accounts for these and other nuances. Because of the arbitrary geometrical orientation and altitude of the individual 10-m lightning channel segments, several of the formulas for computing LNO<sub>x</sub> provided in Wang *et al.* (1998) and Cooray *et al.* (2009, 2012) are appropriately generalized within the LNOm computational algorithms. The production mechanisms accounted for by LNOm include the following:
  - (a)  $\text{NO}_x$  production from return strokes (based on Wang *et al.* (1998)):
    - accounts for peak current magnitude using NLDN data
    - accounts for the number of strokes in the flash using NLDN data
    - accounts for air density (channel segment altitude) using VHF data
  - (b)  $\text{NO}_x$  production from processes other than return strokes (Cooray *et al.*, 2009, 2012):
    - production from the hot core of stepped leaders
    - production from stepped leader corona sheath
    - production from the hot core of dart leaders
    - production from K-changes
    - production from continuing currents and associated M-components



5. *LNOM Data Product Creation*: Based on all these computations, the LNOM creates the final LNOM data products, typically for monthly, annual, or multi-annual analysis periods within the LNOM analysis domain (see right-hand boxes in Figure 19.2 and further description to follow).

The standard LNOM analysis domain is a fixed (i.e., Eulerian) cylinder, having a height range extending from the surface to 20 km, and having a horizontal radial range of 20.31 km. This radius was chosen since it produces the areal equivalent of a 36 km × 36 km Community Multiscale Air Quality (CMAQ) grid cell, i.e., an initial application of the LNOM was for improving CMAQ air quality forecasts. The LNOM cylinder dimensions can be adjusted as needed for other applications.

In fact, the most recent applications of the LNOM, still being conducted at the time of this writing, involve a Lagrangian LNOM analysis domain cylinder that moves with individual storms or storm complexes to track LNO<sub>x</sub> production. In these applications, the period over which the LNOM products are produced is much shorter, i.e., on the order of the duration of a thunderstorm cell, rather than the much longer monthly or annual periods mentioned above. This effort is being led by researchers at the University of Alabama – Huntsville (UAH), the Universities Space Research Association (USRA), and NASA MSFC as part of the Deep Convective Clouds and Chemistry Experiment (DC3; <http://www.eol.ucar.edu/projects/dc3/>).

### 19.4.3 *Data products*

There are several LNOM output data products, including channel length distribution (CLD), segment altitude distribution (SAD), vertical LNO<sub>x</sub> production profile (LNPP), and LNO<sub>x</sub> distribution (LND). These are provided for ground flashes alone, for cloud flashes alone, and for all flashes. The ancillary products shown in Figure 19.2 are primarily for research purposes; for example, the channel connection summary (CCS) is an ancillary product used to visually evaluate the accuracy of the LNOM channel computation module. It provides various cross-sectional plots of the VHF sources for an individual lightning flash, the linear connections made between the spatially averaged sources, and the resulting channel length computation.

The SAD provides the number of 10-m channel segments in each 100-m altitude interval of the LNOM analysis cylinder during a prescribed LNOM analysis time period. This product gives the user an idea of how much LNO<sub>x</sub> might be expected in a certain vertical layer of the atmosphere during a given period just due to the amount of lightning activity in that layer and/or due to the occurrence of some relatively long channel discharges in the layer. The left panel in Figure 19.3 provides an example of a (one month) SAD product; for an additional example of a SAD see the air quality study in Koshak et al. (2014).

Figure 19.3 (right panel) shows an example of the LNPP data product. It is important to note that the LNPPs are not dynamically mixed profiles, but are strictly production profiles. Therefore, the LNPPs should not be confused with the baseline “C shape” LNO<sub>x</sub> profile due to Pickering et al. (1998), or the “backward C shape” profiles found in the 3 D cloud scale chemical transport model simulations of Ott et al. (2010, Table 2).

The LND is a frequency distribution of the LNO<sub>x</sub>. So given  $N = N_g + N_c$  flashes analyzed by the LNOM, where  $N_g$  is the number of ground flashes and  $N_c$  is

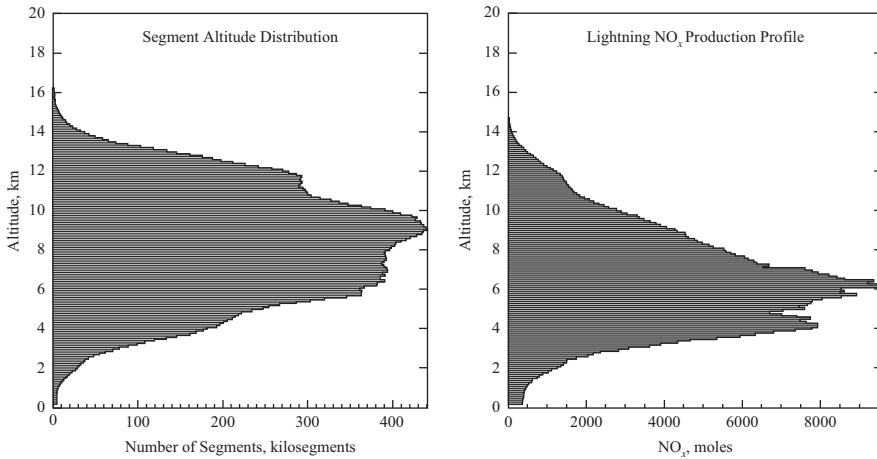


Figure 19.3 Examples of altitude dependent LNOx products: SAD (left), and LNPP (right) for June 2011 North Alabama thunderstorms.

the number of cloud flashes, the ground and cloud flash LNOx frequency distributions can be denoted as  $\Phi(p_g)$  and  $\Phi(p_c)$ , respectively. Here,  $p_g$  is the independent variable for ground flash LNOx, and  $p_c$  is the independent variable for cloud flash LNOx. Since the LNOx analysis domain has a finite radial range, it is always possible to truncate flashes that cross the vertical cylindrical wall of the LNOx domain. However, the LNOx keeps track of those flashes that are truncated, and additionally computes the LNOx produced by the portion of the channel outside the cylinder wall. Hence, the total LNOx from each flash is calculated, and this stored information allows LNOx to generate the LND product.

#### 19.4.4 Data archive

At the time of this writing, the LNOx data archive contains LNOx analyses for 468 928 flashes. Most of these flashes are derived from 9 years (2004–2012) of North Alabama thunderstorms. The remaining flashes are from 4 years of data derived from the DC metropolitan LMA network.

Figure 19.4 provides the channel length distributions (CLD product) for the entire 9 years of North Alabama thunderstorms; this corresponds to a total of 404 197 flashes. The distribution of channel length is given for all flashes, for just cloud flashes, and for just ground flashes. Again, the CLDs can be generated for any analysis time period desired (such as the 1-month time period employed in Figure 19.3). Note from Figure 19.4 that the mean channel length for ground flashes is about 66.9 km, whereas the mean channel length for cloud flashes is about 47.6 km. Longer channel length implies more NO<sub>x</sub> production, all else being equal. In addition, more of the ground flash channel is at lower altitude (higher air density) than the cloud flash channel, so in the case of ground flash channel there are more air molecules available to produce more LNOx. Indeed, the laboratory measurements of Wang *et al.* (1998) show an increase of NO<sub>x</sub> production with increasing pressure, all else being equal. Finally, LNOx production also depends on the current waveform associated with the lightning discharge. This is a more complicated comparison to make, as there are several discharge types even with a

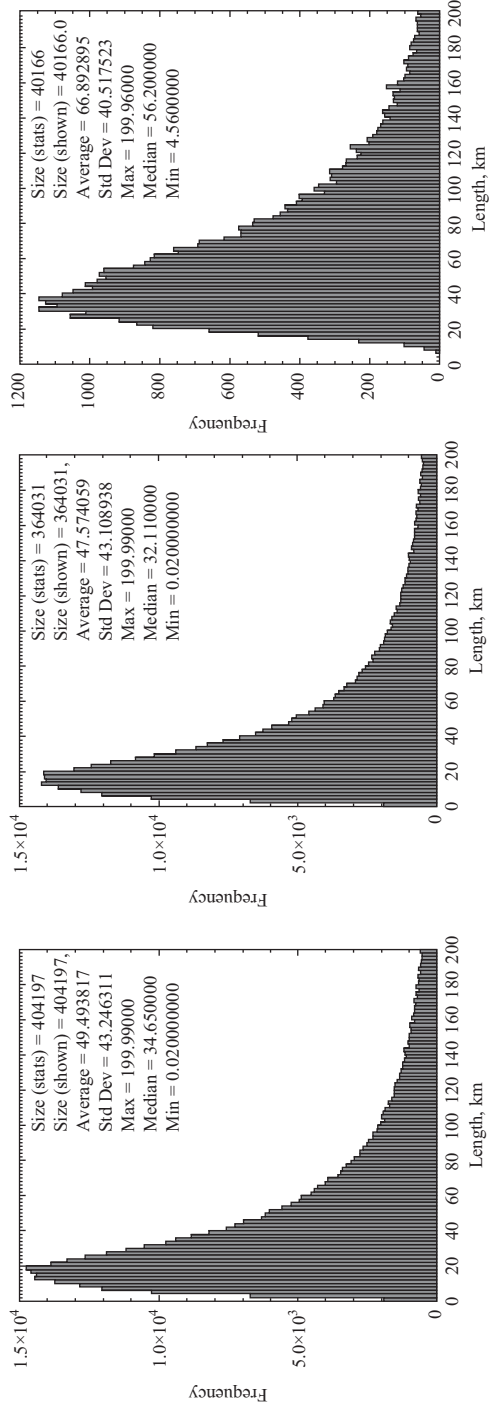


Figure 19.4 The LNOM-derived frequency distributions of lightning channel lengths for all flashes (left), cloud flashes (middle), and ground flashes (right). These results are for 9 years (2004–2012) of North Alabama thunderstorms.

given flash type (ground or cloud). The peak current and current duration clearly are important parameters to consider.

Given the longer channel lengths and lower channel altitudes of ground flashes, and all the available  $\text{NO}_x$  production mechanisms available in Wang *et al.* (1998) and Cooray *et al.* (2009, 2012), including those production mechanisms related to the current waveform, the LNDOM obtains the LNO<sub>x</sub> distributions (LND product) shown in Figure 19.5 (for the same 9-year period mentioned above). It is interesting to see that the average LNO<sub>x</sub> per ground flash is 604.3 moles, whereas it is only 36.4 moles for cloud flashes. Averaging the entire sample of flashes gives a value of 94.4 moles per flash. In the total sample of 404 197 flashes there are far more cloud flashes (364 031 or 90.1 percent) than there are ground flashes (40 166 or 9.9 percent).

It should be noted that LNDOM flash counts are not suitable for estimating the ratio of the number of cloud flashes to ground flashes, or the so-called “Z ratio.” For example, flashes are removed from all LNDOM data products if the flash type cannot be confidently determined by the non-exhaustive but efficient analysis of the NLDN and LMA data.

One should also note that Table 19.1 shows updated values of  $P$  and  $P/N_A$  for the LNDOM data analysis based on the 9 years of North Alabama data in the LNDOM archive. Previously, the best values shown for LNDOM data analyses given in Koshak *et al.*, (2014) were based on just five summer months of analyses (i.e., August 2005, August 2006, August 2007, August 2008, and August 2009), or a total of 32 705 flashes. Of the 32 705 flashes, 4832 were ground flashes and 27 873 were cloud flashes. The average LNO<sub>x</sub> per ground flash was 484.15 moles, and the average for cloud flashes was 34.78 moles. So the average LNO<sub>x</sub> per flash was computed as  $[4832(484.15) + (27\ 873)(34.78)]/(32\ 705) = 101.17$  moles per flash. However, this (correct) result is susceptible to misinterpretation. Obviously, it is biased downward because the number of cloud flashes employed in the computation far outnumbers the number of ground flashes used. Hence, it is more meaningful to properly weight the relative frequencies of ground and cloud flashes. To do this, one can use the value of the mean Z ratio equal to 3 for the months of August that Koshak *et al.* (2014) found from the 4-year climatological Z-ratio dataset obtained by Boccippio *et al.* (2001). The computation then becomes:  $[1(484.15) + 3(34.78)]/4 = 147.12$  moles per flash (for the month of August in North Alabama). As seen in Figure 19.5, the 9-year North Alabama data from the LNDOM archive consists of a total of 404 197 flashes (40 166 ground flashes + 364 031 cloud flashes). Using the mean LNO<sub>x</sub> per ground and per cloud flash from Figure 19.5, the mean is  $[(40\ 166)(604.28) + (364\ 031)(38.19)]/(404\ 197) = 94.4$  moles per flash as stated above. But again, it is more meaningful to use an estimate of the relative frequencies of ground and cloud flashes. Across all months and for the North Alabama region, the mean value of the Z-ratio is about 2 (Boccippio *et al.*, 2001). Therefore, a more meaningful value for the mean LNO<sub>x</sub> per flash is  $[1(604.28) + 2(38.19)]/3 = 226.89$  moles per flash, which is the value used in Table 19.1.

The LNDOM archive continues to grow, and this trend is expected to continue especially with the proliferation of VHF networks. The LNDOM database will likely expand by analyzing flashes detected by other VHF networks in the following areas: Oklahoma, West Texas, Houston, White Sands in New Mexico, Fort Collins (as part of the National Science Foundation (NSF) DC3 Experiment), Sao Paulo,

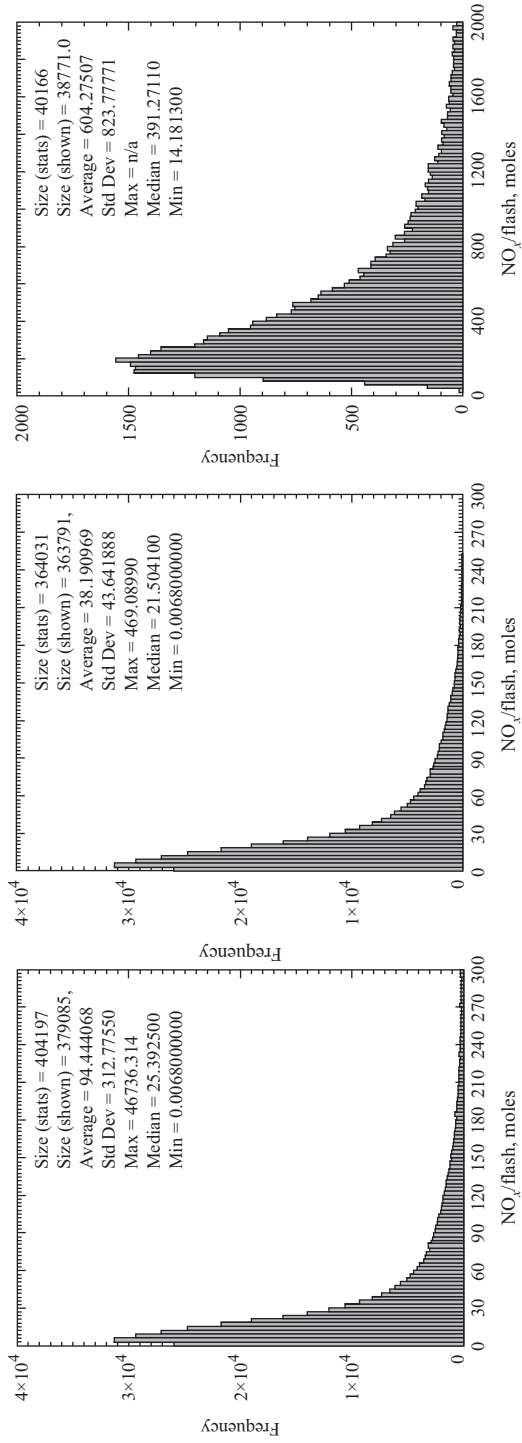


Figure 19.5 The LNOM-derived frequency distributions of flash LNO<sub>x</sub> for all flashes (left), cloud flashes (middle), and ground flashes (right). These results are for 9 years (2004–2012) of North Alabama thunderstorms.

Brazil (as part of the CHUVA Experiment), Dugway Proving Ground in Utah, Camp Blanding Florida, Kennedy Space Center Florida, and potentially other regions.

Overall, the frequency distributions of LNO<sub>x</sub> production,  $\Phi(p_g)$  and  $\Phi(p_c)$ , derived from LNO<sub>x</sub> and provided in Figure 19.5 could be considered for replacing the two fixed educated guesses ( $P_g$ ,  $P_c$ ) for production currently employed within ModelE2 as discussed in section 19.4.1. That is, there is no longer a need to restrict the LNO<sub>x</sub> production parameterization to a single fixed “back-of-the-envelope” estimate (i.e., one estimate for ground flashes and one estimate for cloud flashes). With the processing of detailed lightning observations by LNO<sub>x</sub>, the statistical frequency distributions,  $\Phi(p_g)$  and  $\Phi(p_c)$ , of LNO<sub>x</sub> production from *actual* ground and cloud flashes is available. Specifically, instead of assigning to each ground flash the same fixed LNO<sub>x</sub> production value, one can randomly pick the LNO<sub>x</sub> production value from the LNO<sub>x</sub>-derived distribution  $\Phi(p_g)$ . A similar comment holds for the cloud flashes. Because of the random sampling, this general approach also makes it possible to create more realistic simulations of the temporal evolution of the LNO<sub>x</sub> source within models, particularly in those models that are geared toward shorter-term forecasts (such as with CMAQ ozone predictions).

#### 19.4.5 Future evolution

Although the LNO<sub>x</sub> has made significant advances in combining theory, lab results, and flash-specific measurements to acquire optimal estimates of LNO<sub>x</sub>, it is recognized that it is still an imperfect tool.

First, a comprehensive list of LNO<sub>x</sub> production mechanisms is not available for LNO<sub>x</sub> to apply, and of those mechanisms identified in the scientific literature, there is still debate as to their relative importance. In particular, less is known about the discharge physics processes within cloud flashes, so it is possible that LNO<sub>x</sub> presently does not correctly parameterize LNO<sub>x</sub> from cloud flashes. For example, and as discussed above, there is evidence that cloud flashes might produce as much NO<sub>x</sub> as ground flashes; i.e., the rocket-triggered lightning study of Rahman *et al.* (2007) indicated that the discharge processes associated with small, slower, steady currents produced substantial NO<sub>x</sub>. Yet, the present cloud flash LNO<sub>x</sub> parameterizations employed by LNO<sub>x</sub> lead to relatively small values of cloud flash NO<sub>x</sub>. It is too early to tell how such an issue will eventually be resolved, and debate on whether a typical cloud flash produces less, about the same, or even more NO<sub>x</sub> than a typical ground flash continues. As such, the LNO<sub>x</sub> architecture is highly modular so that LNO<sub>x</sub> parameterizations for different discharge processes can be easily refined, or new parameterizations added via a “plug-and-play” methodology. As the LNO<sub>x</sub> matures along these lines, reprocessing of the LNO<sub>x</sub> input (NLDN and VHF) data archive will provide updated LNO<sub>x</sub> results for the lightning/chemistry community.

Second, estimating lightning channel length from LMA VHF sources is fundamentally difficult. Environmental radio frequency noise, source-strength degradation as a function of source range from the LMA network, and the lack of a consistent 1:1 relationship between the optical channel geometry and that defined by the channel VHF emission, all give rise to channel length estimation errors. Therefore, the LNO<sub>x</sub> software package is built in such a way that testing of alternative channel length modules is fairly easy.

The longer-term plans of the NASA Marshall Space Flight Center are to internally upgrade the main modules of LNO<sub>x</sub> and reprocess the data archive with

the latest LNOm version. Following the completion of this internal developmental phase (IDP), a broader community of expertise will be sought to further improve and test the LNOm. This community developmental phase (CDP) is anticipated to improve the accuracy and expand the applicability of the LNOm exponentially. This phase need not be limited to just software module improvements, but can also include ingestion of additional lightning/chemistry related measurements that “open the doors” for further improvements in estimating LNOx.

## 19.5 Benefits of satellite observations

In this section, some satellite-based observations of lightning, as well as satellite observations of the trace gas species affected by lightning, are discussed. In just the past  $\sim 50$  years, advancements in space-borne measurements of lightning and its chemistry have provided a much better understanding of the global-scale spatio-temporal distribution of lightning and associated LNOx production. These global-scale features are difficult to obtain by conventional ground-based and aircraft observations alone.

### 19.5.1 *Two early studies employing photometers*

Space-based optical observations of lightning were conducted in the studies by Vorpahl *et al.* (1970) and Sparrow and Ney (1971) as part of the Orbiting Solar Observatory (OSO) series of satellites. The OSO Program was the name of a series of science satellites primarily for studying the sun (i.e., to observe an 11-year sun spot cycle in UV and X-ray spectra), which also included important non-solar experiments. Eight satellites in the series were successfully launched by NASA between 1962 and 1975 using Delta rockets.

The study by Vorpahl *et al.* (1970) reported on night-time lightning activity from the OSO-2 satellite during the new moon periods from February to October 1965. Three of four photometers sensitive to broad spectral bands and suitable for the detection of lightning within a  $10^\circ$  field-of-view were employed. The minimum threshold of  $\sim 3 \times 10^5$  photons  $\text{cm}^{-2}$  at the satellite was used, below which lightning could not be readily detected. The accuracy in determining the lightning source location was claimed to be better than  $\sim 3^\circ$  in latitude and longitude. Within the satellite observation limits of  $35^\circ$  N to  $35^\circ$  S, they determined that ten times as many lightning storms occur over land than over the ocean.

The investigation by Sparrow and Ney (1971) consisted of six photometers aboard the OSO-5 satellite. Four of the six photometers could be used to detect lightning, and the study reported on results from two of the four. The study confirmed Vorpahl’s OSO-2 results that the distribution of night-time thunderstorms is heavily biased toward land areas rather than over the ocean.

### 19.5.2 *Space-based lightning mappers*

Since the early satellite photometer measurements mentioned above, additional optical observations of lightning have been made from the VELA and DMSP series of satellites and from the space shuttle (Suszcynsky *et al.*, 2001; Mackerras *et al.*, 1998, and references therein).

However, an important advancement in better fixing the global annual lightning frequency, i.e., the variable  $F$  in (19.1), as well as vastly improving the

understanding of the diurnal, seasonal and geographical variations in lightning and storm activity, was made possible by the advent of two satellite lightning mappers: the Optical Transient Detector (OTD; 1995–2000) and the Lightning Imaging Sensor (LIS; 1997–present). These instruments detect total (i.e., ground flash and cloud flash) lightning from low Earth orbit during both daytime and night (Christian *et al.*, 1992, 1996, 1999, 2003). Calibration and performance characteristics of the sensors are additionally given in Koshak *et al.*, (2000) and Boccippio *et al.*, (2000, 2002), respectively.

The OTD/LIS lightning mappers are based on Charge Coupled Device (CCD) technology that provides accurate geolocation with millisecond-scale time resolution. OTD, a payload on the MicroLab-1 satellite (later renamed OV-1), had an average orbital altitude of about 740 km and a nadir pixel footprint of  $\sim 8 \times 8 \text{ km}^2$ . The LIS is aboard the Tropical Rainfall Measuring Mission (TRMM) satellite which had an average orbital altitude of about 350 km, but was later boosted to about 402.5 km in August 2001. The LIS nadir pixel footprint is  $\sim 4 \times 4 \text{ km}^2$ . Both the OTD and LIS employ a  $128 \times 128$  pixel CCD array for geolocating lightning.

Since a flash typically lasts a few tenths of a second, and the OTD and LIS CCD frame times are  $\sim 2$  ms, these instruments are ideal for examining the optical components of a flash. The nomenclature used to describe these components includes *event*, *group*, and *flash* (Mach *et al.*, 2007). Basically, an optical event is one (instrument threshold-breaking) pixel illumination in one CCD frame time; hence, an event is the basic unit of OTD/LIS data. An optical group is any collection of adjacent events in one frame time; “adjacent” here means that the pixels touch either on a side or a corner. Finally, the clustering of groups into a flash is performed in Earth-based coordinates. A global lightning flash density distribution based on OTD/LIS data is provided in Figure 3 of Mach *et al.* (2007).

Although the optical event, group, and flash data provide useful insight into lightning physics, the 2-ms frame time resolution is not sufficient for time-resolving individual lightning optical pulse waveforms, which typically have a pulse width at half maximum of  $\sim 400 \mu\text{s}$ , but with variability depending on the lightning discharge type (Goodman *et al.*, 1988). By comparison, photodiode/photometer sensors typically have excellent temporal resolution (e.g., 10–100  $\mu\text{s}$ ), but poor spatial resolution.

In addition to OTD and LIS, a Fast on-Orbit Recording of Transient Events (FORTE) satellite carrying VHF broadband receivers and an Optical Lightning System (OLS) was launched in 1997 (Suszcynsky *et al.*, 2000). The OLS consists of two optical systems. The first was the Lightning Location System (LLS), a  $128 \times 128$  pixel CCD array for geolocating lightning flashes within 10 km. The front-end optical and CCD assemblies are identical to LIS. The second component of the OLS is a fast (15  $\mu\text{s}$  resolution) broadband (0.4–1.1  $\mu\text{m}$ ) photometer with an  $80^\circ$  field of view. This (augmented) lightning mapper was a joint Los Alamos National Laboratory and Sandia National Laboratories satellite experiment designed primarily to address technology issues associated with treaty verification and the monitoring of nuclear tests from space (Suszcynsky *et al.*, 2000). Inter-comparisons between the VHF and OLS datasets have been used in an attempt to discriminate flash type (ground flash or cloud flash) from space, and in identifying specific discharge processes (e.g., return stroke signatures).



Recently, plans have been made to place a spare LIS on the International Space Station (ISS) in early 2016. The high (>50 degree) orbital inclination of the ISS will allow the ISS/LIS to capture more lightning (such as thunderstorms over the upper midwest of the United States) that is presently missed by the 35° orbital inclination of TRMM/LIS.

In addition, the future Geostationary Lightning Mapper (GLM), described in Goodman *et al.* (2013), is expected to have a profound impact on our understanding of LNO<sub>x</sub> production. It will map the locations and time-of-occurrence of total lightning activity *continuously* day and night with near-uniform storm-scale spatial resolution and with a product refresh rate of under 20s over the Americas and adjacent oceanic regions. The GLM is based on the two heritage low Earth orbiting lightning mappers OTD and LIS, and it is planned as a payload on the Geostationary Operational Environmental Satellite R-series (GOES-R), which is presently scheduled to launch in early 2016. Although the primary objective of GLM is for severe weather warning (e.g., abrupt increases or “jumps” in lightning activity provide warning lead time to tornadic storms), the enormous lightning dataset that will be obtained through continuous monitoring will offer unprecedented detail and lightning statistics from which optimal estimates of LNO<sub>x</sub> production can be made. Likewise, other countries are planning similar missions (the Geostationary Lightning Imager (GLI) on China’s Fengyun-4 (FY4) satellite series and Europe’s Lightning Imager (LI) as part of the Meteosat Third Generation (MTG) satellite series).

### 19.5.3 *Top-down constraints on LNO<sub>x</sub>*

The global model fit method (section 19.2.3) for estimating the global annual LNO<sub>x</sub> production  $G$  originally employed airborne observations of NO<sub>x</sub> (Levy *et al.*, 1996). But, the method can also be applied using satellite observations of trace gases. For example, Boersma *et al.* (2005) extended the work of Levy *et al.* (1996) by employing satellite measurements of tropospheric NO<sub>2</sub> columns from the Global Ozone Monitoring Instrument (GOME). Satellite observations of this type offer a powerful “top-down” constraint on LNO<sub>x</sub> production when used in conjunction with a mature chemical transport model (CTM).

Another example of employing satellite observations is described in Martin *et al.* (2007). Measurements of trace-gases from three satellite platforms were employed to provide independent top-down constraints on the LNO<sub>x</sub> source. The space-based measurements included: tropospheric NO<sub>2</sub> columns from the Scanning Imaging Absorption Spectrometer for Atmospheric Chartography (SCIAMACHY) (Bovensmann *et al.*, 1999), tropospheric O<sub>3</sub> columns from the Ozone Monitoring Instrument (OMI) (Levelt *et al.*, 2006) and Microwave Limb Sounder (MLS) (Waters *et al.*, 2006), and upper tropospheric HNO<sub>3</sub> from the Atmospheric Chemistry Experiment Fourier Transform Spectrometer (ACE-FTS) (Bernath *et al.*, 2005). The global CTM employed was the GEOS-Chem model (Bey *et al.*, 2001); it was used to identify the locations and time periods in which lightning would be expected to dominate the trace gas observations. The space-based measurements were then sampled at those locations and time periods. All three measurements exhibited a maximum in the tropical Atlantic and a minimum in the tropical Pacific; the overall pattern was driven by injection of lightning NO into the upper troposphere over the tropical continents, followed by photochemical

production of  $\text{NO}_2$ ,  $\text{HNO}_3$ , and  $\text{O}_3$  during transport. Using the distribution of lightning  $\text{NO}_x$  emissions in GEOS-Chem, the study found that a global emission rate of  $6 \pm 2 \text{ Tg(N) yr}^{-1}$  from lightning in the model best represents the satellite observations of tropospheric  $\text{NO}_2$ ,  $\text{O}_3$ , and  $\text{HNO}_3$ . If one applies (19.1) with the Cecil *et al.* (2012) global flash rate of 46 flashes per second, one obtains an estimate  $P = G/(\gamma F) = 17.8 \times 10^{25}$  molecules per flash = 295.08 moles per flash. The LNOm estimate of 226.89 moles per flash given in Table 19.1 is within 23 percent [= (226.89 – 295.08)/295.08] of this value.

There is more than one way to view the inter-play or optimization process between bottom-up and top-down constraints for purposes of constraining the estimate of LNO<sub>x</sub> production. Figure 19.6 provides one way of conceptualizing the process. The various model parameterizations in the CTM involving lightning typically include the thundercloud lightning flash rate parameterization (RP), the flash energy parameterization (EP), the LNO<sub>x</sub> yield parameterization (YP), and possibly even a vertical LNO<sub>x</sub> profile parameterization (PP). Additionally, OTD/LIS data, ground-based lightning data, lab data, algorithms, and advanced models are used to improve these parameterizations. In principle, the EP, YP, and PP can all be adjusted in an attempt to maintain consistency with archived LNOm results.

Unfortunately, standard convective parameterizations in global CTMs fail to reproduce observations from OTD/LIS. But, the study by Murray *et al.* (2012) introduced an optimal regional scaling algorithm for CTMs to fit the LNO<sub>x</sub> source to the satellite lightning data in a way that preserves the coupling to deep convective transport; the coarse regional scaling preserves sufficient statistics in the satellite data to constrain the inter-annual variability of lightning. Using GEOS Chem as a test bed, they obtained a value of  $G = 6.0 \pm 0.5 \text{ Tg(N) yr}^{-1}$ .

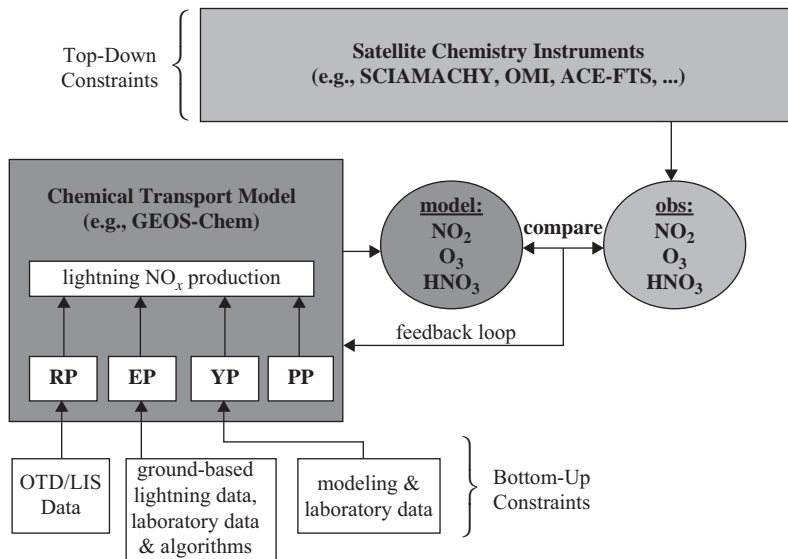


Figure 19.6 An example of optimizing various lightning parameterizations within a model to best fit satellite chemistry measurements (see main text for description of variables shown).

Recently, the uncertainties associated with applying top-down constraints have been examined (Stavrakou *et al.*, 2013). The top-down constraint approach implicitly assumes that the relationship between the emission fluxes and the atmospheric abundances is reasonably well simulated by the CTM, so that the CTM and measurement data mismatch can be mostly attributed to the errors in the emission inventories. However, studies mentioned in Stavrakou *et al.* (2013) point to flaws in the current mechanisms implemented in CTMs that imply potentially large impacts on simulated  $\text{NO}_x$  concentrations, and hence on the top-down  $\text{NO}_x$  emission estimates.

#### 19.5.4 *Discriminating flash type from space*

Although the lightning mappers discussed in section 19.5.2 are designed to provide total lightning activity, these optical instruments do not directly provide flash type (ground flash or cloud flash) classification, i.e., they do not identify which flashes strike the ground. This is understandable since the optically thick thundercloud obscures the view making it difficult to determine flash type. Early examinations of data from the OTD and LIS confirm this difficulty. At optical frequencies, the thundercloud multiply scatters the lightning source, resulting in a diffuse cloud top emission that prevents one from deciding whether or not the lightning channel below cloud top connects to ground. The following subsection highlights the importance of determining flash type information when estimating LNO<sub>x</sub> production, and the last three subsections provide some recent advances in the development of retrieval algorithms that can be used to help segregate ground flashes from cloud flashes.

##### 19.5.4.1 **Why discriminate?**

In order to accurately estimate LNO<sub>x</sub> production for purposes of regional air quality and global chemistry/climate models, one needs to know how many flashes occur, and what amount of  $\text{NO}_x$  each flash produces. In addition, modelers need to know when and where the flashes occur and at what altitude; this information allows them to simulate the time-dependent horizontal and vertical distributions of the LNO<sub>x</sub> source within their model grid system.

Rather than attempting to specify the LNO<sub>x</sub> produced from each flash, modelers usually assign a single, typical value of  $\text{NO}_x$  production  $P_g$  to all ground flashes, and a single, typical value  $P_c$  to all cloud flashes. This is done because ground and cloud flashes involve fundamentally different discharge processes and occur at different mean altitudes, and hence there is a reasonable expectation that the two flash types produce different amounts of  $\text{NO}_x$ .

Thus, modelers typically employ LNO<sub>x</sub> production parameterizations that specifically require estimates of the values of  $P_g$  and  $P_c$ . This implicitly implies that some knowledge of the relative number of ground and cloud flashes is needed. Even if a modeler assumes that  $P_g = P_c$ , there would still be a desire to discriminate the flash type of flashes observed from space because cloud flashes deposit  $\text{NO}_x$  at higher altitudes than ground flashes. Differences in the vertical distribution of the LNO<sub>x</sub> source directly affect predictions of ozone in both regional air quality and global climate/chemistry models.

Cloud flashes usually outnumber ground flashes by a typical ratio of 3:1, and this ratio can be substantially larger, particularly in severe storms. So even if  $P_c$  is chosen smaller than  $P_g$ , it is still possible that cloud flashes could be the dominant  $\text{NO}_x$  source.

Previous studies have used vertical profiles from Pickering *et al.* (1998) that were determined for a  $P_c/P_g$  ratio of 0.1, based on the work of Price *et al.* (1997). However, some studies suggest that the  $P_c/P_g$  ratio might be closer to, or even above, unity (Gallardo and Cooray, 1996; DeCaria *et al.*, 2000; Zhang *et al.*, 2003; Fehr *et al.*, 2004); see Ott *et al.* (2010) for additional summary comments on the size of this ratio.

Presently however, the detailed analyses of the LNOM show that  $P_g$  is substantially larger than  $P_c$  (Koshak *et al.*, 2014; Koshak and Peterson, 2011). The difference is primarily attributable to differences in channel length, channel altitude, current magnitude, the number of strokes in a flash, and types of discharge-dependent  $\text{NO}_x$  production mechanisms present. In fact, because of the variable nature of lightning and thunderstorms,  $\text{LNO}_x$  production can substantially vary from one set of ground flashes to another, or from one set of cloud flashes to another. But, since less empirical data exists on cloud flashes overall, it is acknowledged that the parameterization of  $\text{NO}_x$ -production mechanisms within cloud flashes could be lacking and that future improvements to all  $\text{LNO}_x$  parameterizations within the LNOM could tighten, or even close, the gap between the two flash types.

In any case, since the probability that  $P_g$  is *identically* equal to  $P_c$  is small, and since cloud flashes deposit more  $\text{NO}_x$  at higher altitudes than ground flashes, the best estimate of the overall  $\text{LNO}_x$  source is obtained when one can segregate in some way the ground flashes from the cloud flashes. The next three subsections briefly summarize some methods for performing this segregation when satellite-based lightning mapper observations are employed.

#### 19.5.4.2 The mean method

As mentioned previously, space-based optical observations of lightning normally cannot directly detect the discharge channel since it is typically obscured by the cloud. However, the spatio-temporal pattern of the diffuse lightning cloud top optical emission itself provides key information about whether or not the channel connects to ground. For example, by comparing OTD and NLDN data, Koshak (2010) showed that the mean Maximum Group Area (MGA) for ground flashes was appreciably larger than the mean MGA for cloud flashes, so that, for satellite lightning mappers, MGA is a fundamental variable for discriminating ground flashes from cloud flashes. Here, a flash is composed of one or more optical groups, and the group of largest area is the MGA. It was hypothesized by Koshak (2010) that the return stroke, along with any accompanying simultaneous discharges, produces a relatively large optical group within the flash, so that a statistically large MGA is useful as a type of “return stroke detector.”

The follow-on study by Koshak and Solakiewicz (2011) introduced a first attempt to retrieve the *ground flash fraction* based on the MGA variable suggested by Koshak (2010). That is, given a set of  $N$  flashes observed by a satellite lightning mapper, the algorithm would estimate the fraction  $\alpha = N_g/N$  of the flashes that strike the ground, where  $N_g$  is the number of ground flashes. The value of  $N$  must be large, typically 5000. Denoting  $x$  for the value of MGA and applying some straightforward algebra, Koshak and Solakiewicz (2011) established a mathematical relationship between the mean MGA values and the ground flash fraction given by

$$\bar{x} = \alpha \bar{x}_g + (1 - \alpha) \bar{x}_c \quad (19.7)$$

where  $\bar{x}$ ,  $\bar{x}_g$ , and  $\bar{x}_c$  are the mean MGA for all  $N$  flashes, for all  $N_g$  ground flashes, and for all  $N_c = N - N_g$  cloud flashes, respectively. This equation is easily solved for  $\alpha$  in terms of  $\bar{x}$ ,  $\bar{x}_g$ , and  $\bar{x}_c$ . The value of  $\bar{x}$  is computed directly from the  $N$  lightning mapper-observed values of MGA, and the values of  $\bar{x}_g$ , and  $\bar{x}_c$  were estimated from the conterminus United States (CONUS) by comparing NLDN and OTD observations. Thus, retrieval errors obtained from this simple method are expected to increase when other geographical regions and seasons are considered.

### 19.5.4.3 The mixed exponential distribution method

A more sophisticated retrieval algorithm was introduced in Koshak (2011). Rather than estimating the values of  $\bar{x}_g$ , and  $\bar{x}_c$  with fixed CONUS means as was done in the mean method described above, this algorithm modeled the ground and cloud flash MGA density functions with distinct models. Each model had an exponential form after the low-ends of the ground, and cloud flash MGA distributions were appropriately modified (i.e., shifted by the instrument nadir pixel footprint). By superpositioning these two exponential density function models, a single mixed exponential distribution model was obtained that could be used to describe the distribution of measured MGAs. The mixed exponential distribution model had three parameters ( $\alpha$ ,  $\mu_g$ ,  $\mu_c$ ), where the last two parameters are the population means of the ground and cloud flash MGA distributions, respectively. The specific form of the mixed exponential distribution model is

$$p(y) = \frac{\alpha}{\mu_g} e^{-y/\mu_g} + \frac{(1-\alpha)}{\mu_c} e^{-y/\mu_c} \quad (19.8)$$

where  $y$  is the shifted MGA, and  $p(y)$  is its associated density function. The values of these three parameters were retrieved from the MGA observations using a formal Bayesian inversion process and the maximum a posteriori (MAP) solution (see Koshak (2011) for additional details).

### 19.5.4.4 The analytic perturbation method

Note that the mixed exponential distribution model discussed above is a *fixed* model and one attempts to find the optimum parameters of that fixed model. However, one can still argue that a different geographical region and/or season might have ground and cloud flash MGA population distributions that deviate too much from the fixed mathematical model employed. In addition, both the mean method and mixed exponential distribution method provide no way for flash typing specific flashes.

These limitations have motivated a very recent study by Koshak and Solakiewicz (2014). They introduce a *model-independent* method for retrieving the ground flash fraction; the method also subsequently determines the flash type of each of the  $N$  flashes. Once again, the value of  $N$  must be large, typically 5000 (although reasonably small solution retrieval errors are obtained for values of  $N$  as low as 2000). The model-independent approach is called the Analytic Perturbation Method (APM).

The idea behind the APM is to avoid making any assumptions about how the MGAs are distributed in a particular geographical region for a particular period of time (e.g., season); the region and period are collectively referred to as the “target.” To accomplish this, one carries out an instrument “burn-in” phase wherein the lightning mapper samples (typically thousands) of lightning in the

target of interest. Using independent ground flash observations (e.g., NLDN, or GLD360 data) one can flash-type the sampled flashes observed by the lightning mapper, and therefore estimate the true ground and cloud flash MGA density functions. These “climate” density function estimates are then used as baselines or starting points in any actual subsequent retrieval.

In the subsequent operational retrieval, the lightning mapper makes an observation of  $N \sim 5000$  flashes in the target of interest. Next, the mathematical theory of the APM provides a way to perturb away from the climate baselines in order to retrieve, for the set of  $N$  observed flashes, the ground and cloud flash MGA density functions, the ground flash fraction, and the flash type of each flash. The APM solution for the retrieved ground flash fraction  $\alpha_r$  and the retrieved ground and cloud flash MGA density functions, described by the vectors ( $\mathbf{g}_r$ ,  $\mathbf{c}_r$ ), is given by (see derivation given in Koshak and Solakiewicz (2014)):

$$\begin{aligned} \alpha_r &= \frac{(\mathbf{m} - \mathbf{b})^T (\mathbf{a} - \mathbf{b})}{(\mathbf{a} - \mathbf{b})^2} \\ \mathbf{g}_r &= \mathbf{m} + (1 - \alpha_r)(\mathbf{a} - \mathbf{b}) \\ \mathbf{c}_r &= \mathbf{m} - \alpha_r(\mathbf{a} - \mathbf{b}) \end{aligned} \quad (19.9)$$

Here, the climate ground and cloud flash MGA density functions are described, respectively, by the “climate vectors” ( $\mathbf{a}$ ,  $\mathbf{b}$ ). The frequency distribution of the observed MGA values can be described by a vector  $\mathbf{M}$ ; dividing this vector by the sample size  $N$  gives the vector  $\mathbf{m}$ . So  $\mathbf{m}$  is a measured quantity provided by the lightning mapper. Mathematically,  $\mathbf{m}$  is a vector that describes the MGA mixture density; i.e.,  $\mathbf{m} = \alpha \mathbf{g} + (1 - \alpha)\mathbf{c}$ , where ( $\mathbf{g}$ ,  $\mathbf{c}$ ) are vectors that describe the true ground and cloud flash MGA density functions. The APM solutions in (19.9) provide the retrieval estimates to each term on the right-hand side of this expression of  $\mathbf{m}$ .

Using the results in (19.9), Koshak and Solakiewicz (2014) obtained the probability,  $P_{gr}(x)$ , that a flash, having an MGA value equal to  $x$ , is a ground flash. The expression they derived is given by

$$P_{gr}(x) = \frac{\alpha_r g_r(x)}{\alpha_r g_r(x) + (1 - \alpha_r) c_r(x)} \quad (19.10)$$

The values on the right-hand side of (19.10) are given in (19.9) where the density functions  $g_r(x)$  and  $c_r(x)$  are described by the vectors  $\mathbf{g}_r$  and  $\mathbf{c}_r$ , respectively. The flash typing approach is straightforward; i.e.,  $P_{gr}(x) > 0.5 \Rightarrow$  ground flash, and  $P_{gr}(x) \leq 0.5 \Rightarrow$  cloud flash. Koshak and Solakiewicz (2014) performed detailed simulations and found that the APM performed quite well; the mean ground flash fraction retrieval errors were below 0.04 across the full range 0 – 1, and the fraction of flashes accurately flash typed averaged better than 78 percent.

If it is not feasible or possible to conduct a burn-in process for a particular target, call it target A, it is possible to apply to target A the burn-in results (i.e., climate vectors) from a different target (target B). However, retrieval errors will be large if the thunderstorm and lightning characteristics of target A differ from those of target B.

Overall, the basic idea is to provide the lightning mapper sufficient “training” via the burn-in approach so that the lightning mapper can then run

autonomously for a wide range of targets, including possibly those targets that may have no, or inadequate, independent lightning flash type validation measurements available.

The ideal future application of the APM is to apply it to the global OTD/LIS climatology in order to partition the lightning climatology into separate ground and cloud flash climatologies. Optimal estimates of the NO<sub>x</sub> produced per ground and per cloud flash, possibly by future improved versions of the LNO<sub>x</sub> containing updated parameterizations for cloud flashes, could then be applied to these climatologies to recalculate the global LNO<sub>x</sub> production, *G*. Of course, this estimate could be updated once again in the same manner as future ISS/LIS, GLM, GLI, and LI data become available.

## References

- Aghedo, A. M. *et al.*, The vertical distribution of ozone instantaneous radiative forcing from satellite and chemistry climate models, *J. Geophys. Res.*, **116**, D01305, doi:10.1029/2010JD014243, 2011.
- Albrecht, R. I., C. A. Morales, and M. A. F. Silva Dias, Electrification of precipitating systems over the Amazon: Physical processes of thunderstorm development. *J. Geophys. Res.*, **116**, D08209, doi:10.1029/2010JD014756, 2011.
- Baker, M. B., H. J. Christian, and J. Latham, A computational study of the relationships linking lightning frequency and other thundercloud parameters, *Quart. J. Roy. Met. Soc.*, **121**, 1525–1548, 1995.
- Baker, M. B. *et al.*, Relationships between lightning activity and various thundercloud parameters: satellite and modeling studies, *Atmos. Res.*, **51**, 221–236, 1999.
- Beirle, S., U. Platt, M. Wenig, and T. Wagner, NO<sub>x</sub> production by lightning estimated with GOME, *Adv. Space Res.*, **34**, 793–797, 2004.
- Beirle, S., N. Spichtinger, A. Stohl, *et al.*, Estimating the NO<sub>x</sub> produced by lightning from GOME and NLDN data: a case study in the Gulf of Mexico, *Atmos. Chem. Phys.*, **6**, 1075–1089, <http://www.atmos-chem-phys.net/6/1075/2006/>, 2006.
- Beirle, S., H. Huntrieser, and T. Wagner, Direct satellite observation of lightning-produced NO<sub>x</sub>, *Atmos. Chem. Phys.*, **10**, 10965–10986, 2010.
- Bernath, P. F., C. T. McElroy, M. C. Abrams, *et al.*, Atmospheric Chemistry Experiment (ACE): mission overview, *Geophys. Res. Lett.*, **32**, L15S01, doi:10.1029/2005GL022386, 2005.
- Betz, H.-D., K. Schmidt, W. P. Oettinger, and M. Wirz, Lightning detection with 3D-discrimination of intracloud and cloud-to-ground discharges, *Geophys. Res. Lett.*, **31**, L11108, doi:10.1029/2004GL019821, 2004.
- Betz, H.-D., K. Schmidt, B. Fuchs, W. P. Oettinger, and H. Höller, Cloud lightning: detection and utilization for total lightning measured in the VLF/LF regime, *J. Lightning Res.*, **2**, 1–17, 2007.
- Bey, I. *et al.*, Global modeling of tropospheric chemistry with assimilated meteorology: model description and evaluation, *J. Geophys. Res.*, **106**, 23073–23096, 2001.
- Bhetanabhotla, M. N., B. A. Crowell, A. Coucouvinos, R. D. Hill, and R. G. Rinker, Simulation of trace species production by lightning and corona discharge in moist air, *Atmos. Environ.*, **19**, 1391–1397, 1985.

- Biazar, A. P., and R. T. McNider, Regional estimates of lightning production of nitrogen oxides, *J. Geophys. Res.*, **100**, D11, 22861–22874, 1995.
- Boccippio D. J. *et al.*, The Optical Transient Detector (OTD): instrument characteristics and cross-sensor validation, *J. Atmos. Oceanic Technol.*, **17**, 441–458, 2000.
- Boccippio, D. J., K. L. Cummins, H. J. Christian, and S. J. Goodman, Combined satellite and surface-based estimation of the intracloud: cloud-to-ground lightning ratio over the continental United States, *Mon. Weather Rev.*, **129**, 108–122, 2001.
- Boccippio, D. J., W. J. Koshak, and R. J. Blakeslee, Performance assessment of the Optical Transient Detector and Lightning Imaging Sensor. Part I: predicted diurnal variability, *J. Atmos. Oceanic Technol.*, **19**, 1318–1332, 2002.
- Boccippio, D. J., Lightning scaling relations revisited, *J. Atmos. Sci.*, **59**, 1086–1104, 2002.
- Boersma, K. F., H. J. Eskes, E. W. Meijer, and H. Kelder, Estimates of lightning NO<sub>x</sub> production from GOME satellite observations, *Am. Chem. Phys.*, **5**, 2311–2331, 2005.
- Borucki, W. J., and W. L. Chameides, Lightning: estimates of the rates of energy dissipation and nitrogen fixation, *Rev. Geophys. Space Phys.*, **22**, 363–372, 1984.
- Bovensmann, H. *et al.* SCIAMACHY: mission objectives and measurement modes, *J. Atmos. Sci.*, **56**(2), 127–150, 1999.
- Bradshaw, J. *et al.*, Observed distributions of nitrogen oxides in the remote free troposphere from the NASA Global Tropospheric Experiment programs, *Rev. Geophys.*, **38**, 61–116, doi:10.1029/1999RG900015, 2000.
- Brooks, C. E. P., The distribution of thunderstorms over the globe, *Geophys Mem.*, **3** (4), 147–164, 1925.
- Bucsel, E. J. *et al.*, Lightning-generated NO<sub>x</sub> seen by the Ozone Monitoring Instrument during NASA's Tropical Composition, Cloud and Climate Coupling Experiment (TC4), *J. Geophys. Res.*, **115**, D00J10, doi:10.1029/2009JD013118, 2010.
- Carey, L. D., and S. A. Rutledge, Electrical and multiparameter radar observations of a severe hailstorm, *J. Geophys. Res.*, **103**, 13979–14000, 1998.
- Casper, P. W., and R. B. Bent, Results from the LPATS USA national lightning detection and tracking system for the 1991 lightning season, *Proc. 21st Int. Conf. Lightning Protection*, Berlin, Germany, pp. 339–342, Sept., 1992.
- Cecil, D. J., D. E. Buechler, and R. J. Blakeslee, Gridded lightning climatology from TRMM-LIS and OTD: dataset description, *Atmo. Res.*, doi:10.1016/j.atmosres.2012.06.028, 2012.
- Chameides, W. L., and J. C. G. Walker, A photochemical theory of tropospheric ozone, *J. Geophys. Res.*, **78**, 8751–8760, 1973.
- Chameides, W. L., D. H. Stedman, R. R. Dickerson, D. W. Rusch, and R. J. Cicerone, NO<sub>x</sub> production in lightning, *J. Atmo. Sci.*, **34**, 143–149, 1977.
- Chameides, W. L., Effect of variable energy input on nitrogen fixation in instantaneous linear discharges, *Nature*, **277**, 123–125, 1979.
- Chameides, W. L., The role of lightning in the chemistry of the atmosphere. In *The Earth's Electrical Environment*, Chapter 6, National Academy Press, Washington, D. C., ISBN 0-309-03680-1, 1986.
- Chameides, W. L. *et al.*, An estimate of the NO<sub>x</sub> production rate in electrified clouds based on NO observations from the GTE/CITE 1 fall 1983 field operation, *J. Geophys. Res.*, **92**, 2153–2156, 1987.



- Christian, J. J., R. J. Blakeslee, and S. J. Goodman, Lightning Imaging Sensor for the Earth Observing System, in *Tech. Rep. NASA TM-4350*, NASA, Washington, D. C., 1992.
- Christian, J. J. *et al.*, The Optical Transient Detector (OTD), in *Proc. 10th Int. Conf. on Atmospheric Electricity*, 368–371, ICAE, Osaka, Japan, 1996.
- Christian, H. J. *et al.*, The Lightning Imaging Sensor, in *Proc. 11th Int. Conf. on Atmospheric Electricity*, 746–749, ICAE, Guntersville, AL, 1999.
- Christian, H. J. *et al.*, Global frequency and distribution of lightning as observed from space by the Optical Transient Detector, *J. Geophys. Res.*, **108**, No. D1, doi:10.1029/2002JD002347, 2003.
- Cook, D. R., Y. P. Liaw, D. L. Sisterson, and N. L. Miller, Production of nitrogen oxides by a large spark generator, *J. Geophys. Res.*, **105**, 7103–7110, doi:10.1029/1999JD901138, 2000.
- Cooray, V., M. Rahman, and V. Rakov, On the NO<sub>x</sub> production by laboratory electrical discharges and lightning, *J. of Atmos. & Solar-Terres. Phys.*, **71**, 1877–1889, 2009.
- Cooray, V., M. Rahman, and V. Rakov, On the NO<sub>x</sub> production by laboratory electrical discharges and lightning, in *Lightning Electromagnetics*, edited by V. Cooray, Published by The Institution of Engineering and Technology (IET – former IEE), London, UK, 2012.
- Crutzen, P. J., The influence of nitrogen oxides on the atmospheric ozone content, *Quart. J. Roy. Meteor. Soc.*, **96**, 320–327, 1970.
- Crutzen, P. J., A discussion of the chemistry of some minor constituents in the stratosphere and troposphere, *Pure Appl. Geophys.*, **106**, 1385–1399, 1973.
- Crutzen, P. J., The role of NO and NO<sub>2</sub> in the chemistry of the troposphere and stratosphere, *Ann. Rev. Earth Planet. Sci.*, **7**, 443–472, 1979.
- Cummins, K. L. *et al.*, The US National Lightning Detection Network: post-upgrade status, *Second Conference on Meteorological Applications of Lightning Data*, Am. Meteorol. Soc., Atlanta, Ga., 29 January to 2 February, 2006.
- Cummins, K. L., and M. J. Murphy, An overview of lightning locating systems: history, techniques, and data uses, with an in-depth look at the U. S. NLDN, *IEEE Trans. on Electromag. Comp.*, **51**, No. 3, 499–518, 2009.
- Dawson, G. A., Nitrogen fixation by lightning, *J. Atmos. Sci.*, **37**, 174–178, 1980.
- DeCaria, A. J. *et al.*, A cloud-scale model study of lightning-generated NO<sub>x</sub> in an individual thunderstorm during STERAO-A, *J. Geophys. Res.*, **105**, 11601–11616, 2000.
- DeCaria, A. J., K. E. Pickering, G. L. Stenchikov, and L. E. Ott, Lightning-generated NO<sub>x</sub> and its impact on tropospheric ozone production: a three-dimensional modeling study of a Stratosphere-Troposphere Experiment: Radiation, Aerosols, and Ozone (STERAO-A) thunderstorm, *J. Geophys. Res.*, **110**, D14303, doi:10.1029/2004JD005556, 2005.
- Depasse, P., Statistics on artificially triggered lightning, *J. Geophys. Res.*, **99**, D9, 18515–18522, 1994.
- Drapcho, D. L., D. Sisterson, and R. Kumar, Nitrogen fixation by lightning activity in a thunderstorm, *Atmos. Environ.*, **17**, 729–734, 1983.
- Dye, J. E., B. A. Ridley, W. Skamarock, *et al.*, An overview of the stratospheric-tropospheric experiment: radiation, aerosols, and ozone (STERAO)-deep convection experiment with results for the July 10, 1996 storm, *J. Geophys. Res.*, **105**, 10023–10045, 2000.

- Edwards, D. P., J. F. Lamarque, J. L. Attie, L. K. Emmons, A. Richter, J. P. Cammas, *et al.*, Tropospheric ozone over the tropical Atlantic: a satellite perspective, *J. Geophys. Res.*, **108**, No. D8, 4237–4257, 2003.
- Fehr, T., H. Holler, and H. Huntrieser, Model study on production and transport of lightning-produced NO<sub>x</sub> in an EULINOX supercell storm, *J. Geophys. Res.*, **109**, D09102, doi:10.1029/2003JD003935, 2004.
- Fieux, R., C. Gary, and P. Hubert, Artificially triggered lightning above land, *Nature*, **257**, 212–214, 1975.
- Franzblau, E., and C. J. Popp, Nitrogen oxides produced from lightning, *J. Geophys. Res.*, **94**, 11089–11104, doi:10.1029/89JD00694, 1989.
- Fraser, A., F. Goutail, C. A. McLinden, S. M. L. Melo, and K. Strong, Lightning-produced NO<sub>2</sub> observed by two ground-based UV-visible spectrometers at Vanscoy, Saskatchewan in August 2004, *Atmos. Chem. Phys.*, **7**, 1683–1692, <http://www.atmos-chem-phys.net/7/1683/2007/>, 2007.
- Gallardo, L., and V. Cooray, Could cloud-to-cloud discharges be as effective as cloud-to-ground discharges in producing NO<sub>x</sub>?, *Tellus*, **48B**, 641–651, 1996.
- Goldenbaum, G. C., and R. R. Dickerson, Nitric oxide production by lightning discharges, *J. Geophys. Res.*, **98**, 18333–18338, 1993.
- Goodman, S. J., H. J. Christian, and W. D. Rust, A comparison of the optical pulse characteristics of intracloud and cloud-to-ground lightning as observed above clouds, *J. Appl. Meteorol.*, **27**, 1369–1381, 1988.
- Goodman, S. J. *et al.*, The GOES-R Geostationary Lightning Mapper (GLM), *Atmos. Res.*, **125–126**, 34–49, 2013.
- Grewe, V., C. Reithmeier, and D. Shindell, Dynamic-chemical coupling of the upper troposphere and lower stratosphere region, *Chemosphere*, **47/8**, 55–65, 2002.
- Grewe, V., D. T. Shindell, and V. Eyring, The impact of horizontal transport on the chemical composition in the tropopause region: lightning NO<sub>x</sub> and streamers, *Adv. Space Res.*, **33**, 1058–1061, doi:10.1016/S0273-1177(03)00589-1, 2004.
- Hameed, S., O. G. Paidoussis, and R. W. Stewart, Implication of natural sources for the latitudinal gradients of NO<sub>y</sub> in the unpolluted troposphere, *Geophys. Res. Lett.*, **8**, 591–594, 1981.
- Heckman, S. J., Williams, E. R., and Boldi, R., Total global lightning inferred from Schumann resonance measurements, *J. Geophys. Res.*, **103**, D24, 31775–31779, 1998.
- Hidalgo, H., and P. J. Crutzen, The tropospheric and stratospheric composition perturbed by NO<sub>x</sub> emissions of high-altitude aircraft, *J. Geophys. Res.*, **82**, 5833–5866, 1977.
- Hill, R. D., R. G. Rinker, and H. D. Wilson, Atmospheric nitrogen fixation by lightning, *J. Atmos. Sci.*, **37**, 179–192, 1980.
- Höller, H., U. Finke, H. Huntrieser, M. Hagen, and C. Feigl, Lightning-produced NO<sub>x</sub> (LINOX): experimental design and case study results, *J. Geophys. Res.*, **104**, 13911–13922, doi:10.1029/1999JD900019, 1999.
- Höller, H., and U. Schumann (Eds.), EULINOX-The European Lightning Nitrogen Oxides Project, *Rep. DLR-FB 2000-28*, 240 pp., Deutsche Luftund Raumfahrt Oberpfaffenhofen, Wessling, Germany, 2000.
- Höller, H. *et al.*, Lightning characteristics observed by a VLF/LF lightning detection network (LINET) in Brazil, Australia, Africa and Germany, *Atmos. Chem. Phys.*, **9**, 7795–7824, 2009.

- Huff, F. A., and S. A. Changnon Jr., Inadvertent precipitation modification by urban areas, *Preprints in 3rd Conf. on Weather Modification*, AMS, Boston, MA, pp. 73–78, 1972.
- Huntrieser, H., H. Schlager, C. Feigl, and H. Höller, Transport and production of  $\text{NO}_x$  in electrified thunderstorms: survey of previous studies and new observations at midlatitudes, *J. Geophys. Res.*, **103**, 28247–28264, 1998.
- Huntrieser, H. H., C. Feigl, H. Schlager, *et al.*, Airborne measurements of  $\text{NO}_x$ , tracer species, and small particles during the European Lightning Nitrogen Oxides Experiment, *J. Geophys. Res.*, **107**, 4113, doi:10.1029/2000JD000209, 2002.
- Huntrieser, H. *et al.*, Lightning-produced  $\text{NO}_x$  over Brazil during TROCCINOX: airborne measurements in tropical and subtropical thunderstorms and the importance of mesoscale convective systems, *Atmos. Chem. Phys.*, **7**, 2987–3013, <http://www.atmos-chem-phys.net/7/2987/2007/>, 2007.
- Huntrieser, H. *et al.*, Lightning activity in Brazilian thunderstorms during TROCCINOX: implications for  $\text{NO}_x$  production, *Atmos. Chem. Phys.*, **8**, 921–953, 2008.
- Huntrieser, H. *et al.*, Mesoscale convective systems observed during AMMA and their impact on the  $\text{NO}_x$  and  $\text{O}_3$  budget over West Africa, *Atmos. Chem. Phys.*, **11**, 2503–2536, doi:10.5194/acp-11-2503-2011, 2011.
- Hutchinson, G. E., The biogeochemistry of the terrestrial atmosphere. In *The Earth as a Planet*, edited by G. P. Kuiper, University of Chicago Press, Chicago, 1954.
- IPCC Second Assessment Report: Climate Change 1995, A report of the Intergovernmental Panel on Climate Change (IPCC).
- Jadhav, D. B., A. L. Londhe, and S. Bose, Observations of  $\text{NO}_2$  and  $\text{O}_3$  during thunderstorm activity using visible spectroscopy, *Adv. Atmos. Sci.*, **13**, 359–374, 1996.
- Jourdain, L., S. S. Kulawik, H. M. Worden, K. E. Pickering, J. Worden, and A. M. Thompson, Lightning  $\text{NO}_x$  emissions over the USA constrained by TES ozone observations and the GEOS-Chem model, *Atmos. Chem. Phys.*, **10**, 107–119, 2010.
- Koike, M., Y. Kondo, K. Kita, *et al.*, Measurements of reactive nitrogen produced by tropical thunderstorms during BIBLE-C, *J. Geophys. Res.*, **112**, D18304, doi:10.1029/2006JD008193, 2007.
- Koshak, W. J. *et al.*, Laboratory Calibration of the Optical Transient Detector and the Lightning Imaging Sensor, *J. Atmos. Oceanic Technol.*, **17**, 905–915, 2000.
- Koshak, W. J. *et al.*, North Alabama Lightning Mapping Array (LMA): VHF source retrieval algorithm and error analyses, *J. Atmos. Oceanic Technol.*, **21**, 543–558, 2004.
- Koshak, W. J., M. N. Khan, A. P. Biazar, M. Newchurch, and R. T. McNider, A NASA model for improving the lightning  $\text{NO}_x$  emission inventory for CMAQ, *Joint Session: 4th Conference on the Meteorological Applications of Lightning Data and the 11th Conference on Atmospheric Chemistry; 89th Annual AMS Conference*, Phoenix, AZ, January 11–15, 2009.
- Koshak, W. J., H. S. Peterson, E. W. McCaul, and A. Biazar, Estimates of the lightning  $\text{NO}_x$  profile in the vicinity of the North Alabama Lightning Mapping Array, *International Conference on Lightning Detection*, Orlando, FL, April 19–21, 2010.
- Koshak, W. J., Optical characteristics of OTD flashes and the implications for flash-type discrimination, *J. Atmos. Oceanic Technol.*, **27**, 1822–1838, 2010.

- Koshak, W. J., and R. J. Solakiewicz, Retrieving the fraction of ground flashes from satellite lightning imager data using CONUS-based optical statistics, *J. Atmos. Oceanic Technol.*, **28**, 459–473, 2011.
- Koshak, W. J., A mixed exponential distribution model for retrieving ground flash fraction from satellite lightning imager data, *J. Atmos. Oceanic Technol.*, **28**, 475–492, 2011.
- Koshak, W., H. Peterson, M. Khan, A. Biazar, and L. Wang, The NASA Lightning Nitrogen Oxides Model (LNOM): application to air quality modeling, *XIV International Conference on Atmospheric Electricity*, Rio de Janeiro, Brazil, August 8–12, 2011.
- Koshak, W., and H. Peterson, A summary of the NASA Lightning Nitrogen Oxides Model (LNOM) and recent results, *10th Annual Community Modeling and Analysis System (CMAS) Conference*, Chapel Hill, NC, October 24–26, 2011.
- Koshak, W. J., H. S. Peterson, A. P. Biazar, M. Khan, and L. Wang, The NASA Lightning Oxides Model (LNOM): application to air quality modeling, *Atmos. Res.*, 135–136, 363–369, 2014.
- Koshak, W. J., and R. J. Solakiewicz, A method for retrieving the ground flash fraction and flash type from satellite lightning mapper observations, in review, *J. Atmos. Oceanic Technol.*, 2014.
- Kotaki, M., I. Kuriki, C. Katoh, and H. Sugiuchi, Global distribution of thunderstorm activity observed with ISS-b, *J. Radio Res. Lab. Jpn.*, **28**, 49–71, 1981.
- Kowalczyk, M., and E. Bauer, Lightning as a source of  $\text{NO}_x$  in the troposphere, Tech. Rep. FAA-EE-82-4, 76 pp., *Inst. For Def. Anal.*, Alexandria, Virginia, 1982.
- Kumar, P. P., G. K. Manohar, and S. S. Kandalgaonkar, Global distribution of nitric oxide produced by lightning and its seasonal variation, *J. Geophys. Res.*, **100**, 11203–11208, 1995.
- Kunkel, K. E., Sea surface temperature forcing of the upward trend in US extreme precipitation, *J. Geophys. Res.*, **108**, D1, 4020, doi:10.1029/2002JD002404, 2003.
- Labrador, L. J., R. von Kuhlmann, and M. G. Lawrence, The effects of lightning-produced  $\text{NO}_x$  and its vertical distribution on atmospheric chemistry: sensitivity simulations with MATCH-MPIC, *Atmos. Chem. Phys. Discuss.*, **4**, 6239–6281, 2004.
- Langford, A. O., R. W. Portmann, J. S. Daniel, H. L. Miller, and S. Solomon, Spectroscopic measurements of  $\text{NO}_2$  in a Colorado thunderstorm: determination of the mean production by cloud-to-ground lightning flashes, *J. Geophys. Res.*, **109**, D11304, doi:10.1029/2003JD004158, 2004.
- Lawrence, M. G., W. L. Chameides, P. S. Kasibhatla, H. Levy, II, and W. Moxim, Lightning and atmospheric chemistry: the rate of atmospheric NO production, in *Handbook of Atmospheric Electrodynamics*, vol. **1**, edited by H. Volland, pp. 189–202, CRC Press, Boca Raton, Florida, 1995.
- Levelt, P. F. *et al.*, The ozone monitoring instrument, *IEEE Trans. Geosci. Remote Sens.*, **44**, 1093–1101, doi:10.1109/TGRS.2006.872333, 2006.
- Levine, J. S., Simultaneous measurements of  $\text{NO}_x$ , NO, and  $\text{O}_3$  production in a laboratory discharge: atmospheric implications, *Geophys. Res. Lett.*, **8**, 357–360, 1981.

- Levy, H., W. J. Moxim, and P. S. Kasibhatla, A global three-dimensional time-dependent lightning source of tropospheric NO<sub>x</sub>, *J. Geophys. Res.*, **101**, 22911–22922, 1996.
- Liaw, Y. P., D. L. Sisterson, and N. L. Miller, Comparison of field, laboratory, and theoretical estimates of global nitrogen fixation by lightning, *J. Geophys. Res.*, **95**, D13, 22489–22494, 1990.
- Lyons, W. A., T. E. Nelson, E. R. Williams, J. Cramer, and T. Turner, Enhanced positive cloud-to-ground lightning in thunderstorms ingesting smoke, *Science*, **282**, 77–81, 1998.
- Mach, D. M., H. J. Christian, R. J. Blakeslee, D. J. Boccippio, S. J. Goodman, and W. L. Boeck, Performance assessment of the optical transient detector and lightning imaging sensor, *J. Geophys. Res.*, **112**, D09210, doi:10.1029/2006JD007787, 2007.
- Mackerras, D., M. Darveniza, R. E. Orville, E. R. Williams, and S. J. Goodman, Global lightning: total, cloud and ground flash estimates, *J. Geophys. Res.*, **103**, 19791–19809, 1998.
- Martin, R. V., D. J. Jacob, and J. A. Logan, Detection of lightning influence on tropical tropospheric ozone, *Geophys. Res. Lett.*, **27**(11), 1639–1642, 2000.
- Martin, R. V. *et al.*, Space-based constraints on the production of nitric oxide by lightning, *J. Geophys. Res.*, **112**, D09309, doi:10.1029/2006JD007831, 2007.
- Martini, M. *et al.*, The impact of North American anthropogenic emissions and lightning on long-range transport of trace gases and their export from the continent during summers 2002 and 2004, *J. Geophys. Res.*, **116**, D07305, doi:10.1029/2010JD014305, 2011.
- Murray, N. D., R. E. Orville, and G. R. Huffines, Effect of pollution from Central American fires on cloud-to-ground lightning in May 1998, *Geophys. Res. Lett.*, **27**, 2249–2252, 2000.
- Murray, L. T., D. J. Jacob, J. A. Logan, R. C. Hudman, and W. J. Koshak, Optimized regional and interannual variability of lightning in a global chemical transport model constrained by LIS/OTD satellite data, *J. Geophys. Res.*, **117**, D20307, doi:10.1029/2012JD017934, 2012.
- Nesbitt, S. W., R. Zhang, and R. E. Orville, Seasonal and global NO<sub>x</sub> production by lightning estimated from the optical Transient Detector (OTD), *Tellus*, **52B**, 1206–1215, 2000.
- Newman, M. M., Use of triggered lightning to study the discharge channel. In *Problems of Atmospheric and Space Electricity*, pp. 482–490, New York, Elsevier, 1965.
- Noxon, J. F., Atmospheric nitrogen fixation by lightning, *Geophys. Res. Lett.*, **3**, 463–465, 1976.
- Noxon, J. F., Tropospheric NO<sub>2</sub>, *J. Geophys. Res.*, **83**, 3051–3057, 1978.
- Orville, R. E., and W. Spencer, Global lightning flash frequency, *Mon. Wea. Rev.*, **107**, 934–943, 1979.
- Orville, R. E. *et al.*, Enhancement of cloud-to-ground lightning activity over Houston, Texas, *Geophys. Res. Lett.*, **28**, 2597–2600, 2001.
- Ott, L. E., K. E. Pickering, G. L. Stenchikov, H. Huntrieser, and U. Schumann, Effects of lightning NO<sub>x</sub> production during the 21 July European Lightning Nitrogen Oxides Project storm studied with a three-dimensional cloud-scale

- chemical transport model, *J. Geophys. Res.*, **112**, D05307, doi:10.1029/2006JD007365, 2007.
- Ott, L. E. *et al.*, Production of lightning NO<sub>x</sub> and its vertical distribution calculated from three-dimensional cloud-scale chemical transport model simulations, *J. Geophys. Res.*, **115**, D04301, doi:10.1029/2009JD011880, 2010.
- Petersen, D., M. Bailey, W. H. Beasley, and J. Hallett, A brief review of the problem of lightning initiation and a hypothesis of initial lightning leader formation, *J. Geophys. Res.*, **113**, D17205, doi:10.1029/2007JD009036, 2008.
- Peterson, H. S., and W. H. Beasley, Possible catalytic effects of ice particles on the production of NO<sub>x</sub> by lightning discharges, *Atmos. Chem. Phys.*, **11**, 10259–10268, doi:10.5194/acp-11-10259-2011, 2011.
- Peterson, H. S., and J. Hallett, Ice particle growth in the presence of nitric oxide, *J. Geophys. Res.*, **117**, D06302, doi:10.1029/2011JD016986, 2012.
- Pickering, K.E., Y.S. Wang, W.K. Tao, C. Price, and J.F. Muller, Vertical distributions of lightning NO<sub>x</sub> for use in regional and global chemical transport models, *J. Geophys. Res.*, **103** (D23), 31203–31216, 1998.
- Peyrous, R., and R. M. Lapeyre, Gaseous products created by electrical discharges in the atmosphere and condensation nuclei resulting from gaseous phase reactions, *Atmos. Environ.*, **16**, 959–968, 1982.
- Price, C., and D. Rind, A simple lightning parameterization for calculating global lightning distributions, *J. Geophys. Res.*, **97**, 9919–9933, 1992.
- Price, C., and D. Rind, What determines the cloud-to-ground lightning fraction in thunderstorms?, *Geophys. Res. Lett.*, **20**, No. 6, 463–466, 1993.
- Price, C., and D. Rind, Possible implications of global climate change on global lightning distributions and frequencies, *J. Geophys. Res.*, **90**, D5, 10823–10831, 1994.
- Price, C., J. Penner, and M. Prather, NO<sub>x</sub> from lightning: 1. Global distribution based on lightning physics, *J. Geophys. Res.*, **102**, D5, 5929–5941, 1997.
- Price, C., Evidence for a link between global lightning activity and upper tropospheric water vapor, *Nature*, **406**, 290–293, 2000.
- Rahman, M. *et al.*, Measurements of NO<sub>x</sub> produced by rocket-triggered lightning, *Geophys. Res. Lett.*, **34**, L03816, doi:10.1029/2006GL027956, 2007.
- Rakov, V. A., and M. A. Uman, *Lightning: Physics and Effects*, Cambridge University Press, Cambridge, United Kingdom, ISBN 0 521 583276 6, 687 pp., 2003.
- Reeve, N., and R. Toumi, Lightning activity as an indicator of climate change, *Quart. J. Roy. Met. Soc.*, **125**, 893–903, 1999.
- Reiter, R., On the causal relation between nitrogen-oxygen compounds in the troposphere and atmospheric electricity, *Tellus*, **22**, 122–135, 1970.
- Ridley, B. A., J. E. Dye, J. G. Walega, J. Zheng, F. E. Grahek, and W. Rison, On the production of active nitrogen by thunderstorms over New Mexico, *J. Geophys. Res.*, **101**, 20985–21005, doi:10.1029/96JD01706, 1996.
- Ridley, B., L. Ott, K. Pickering, *et al.*, Florida thunderstorms: a faucet of reactive nitrogen to the upper troposphere, *J. Geophys. Res.*, **109**, 1–19, doi:10.1029/2004JD004769, 2004.
- Schmidt, G.A., R. Ruedy, J. E. Hansen, *et al.*, Present day atmospheric simulations using GISS ModelE: Comparison to in-situ, satellite and reanalysis data. *J. Climate*, **19**, 153–192, doi:10.1175/JCLI3612.1, 2006.

- Schumann, U., H. Huntrieser, H. Schlager, L. Bugliaro, C. Gatzen, and H. Hoeller, Nitrogen oxides from thunderstorms – results from experiments over Europe and the continental tropics, *Deutsch-Österreichisch-Schweizerische Meteorologen-Tagung (DACH)*, Deutsche Meteorologische Gesellschaft, Karlsruhe, Germany, 7–10 September, 2004.
- Schumann, U., and H. Huntrieser, The global lightning-induced nitrogen oxides source, *Atmos. Chem. Phys.*, **7**, 3823–3907, 2007.
- Shindell, D.T., J. L. Grenfell, D. Rind, V. Grewe, and C. Price, Chemistry-climate interactions in the Goddard Institute for Space Studies general circulation model: 1. Tropospheric chemistry model description and evaluation. *J. Geophys. Res.*, **106**, 8047–8076, doi:10.1029/2000JD900704, 2001.
- Shindell, D.T., G. Faluvegi, and N. Bell, Preindustrial-to-present-day radiative forcing by tropospheric ozone from improved simulations with the GISS chemistry-climate GCM. *Atmos. Chem. Phys.*, **3**, 1675–1702, doi:10.5194/acp-3-1675-2003, 2003.
- Shindell, D.T. *et al.*, Simulations of preindustrial, present-day, and 2100 conditions in the NASA GISS composition and climate model G-PUCCINI, *Atmos. Chem. Phys.*, **6**, 4427–4459, doi:10.5194/acp-6-4427-2006, 2006.
- Shindell, D. T., A. Voulgarakis, G. Faluvegi, and G. Milly, Precipitation response to regional radiative forcing, *Atmos. Chem. Phys. Disc.*, **12**, 5015–5037, 2012.
- Sisterson, D. L., and Y. P. Liaw, An evaluation of lightning and corona discharges on thunderstorm air and precipitation chemistry, *J. Atmos. Chem.*, **10**, 83–96, 1990.
- Skamarock, W. C. *et al.*, Numerical simulations of the July 10 Stratospheric-Tropospheric Experiment: Radiation, Aerosols, and Ozone – Deep Convection Experiment convective system: kinematics and transport, *J. Geophys. Res.*, **105**, 19973–19990, 2000.
- Skamarock, W. C. *et al.*, Observational- and modeling-based budget of lightning-produced NO<sub>x</sub> in a continental thunderstorm, *J. Geophys. Res.*, **108**, 4305, doi:10.1029/2002JD002163, 2003.
- Sparrow, J. G., and E. P. Ney, Lightning observations by satellite, *Nature*, **232**, 540–541, 1971.
- Stavrakou, T. *et al.*, Key chemical NO<sub>x</sub> sink uncertainties and how they influence top-down emissions of nitrogen oxides, *Atmos. Chem. Phys. Discuss.*, **13**, 7871–7929, 2013.
- Steiger, S. M., R. E. Orville, and G. Huffines, Cloud-to-ground lightning characteristics over Houston, Texas: 1989–2000, *J. Geophys. Res.*, **107**, doi:10.1029/2001JD001142, 2002.
- Stenchikov, G. *et al.*, Simulation of the fine structure of the 12 July 1996 Stratosphere-Troposphere Experiment: Radiation, Aerosols, and Ozone (STERAO-A) storm accounting for the effects of terrain and interaction with mesoscale flow, *J. Geophys. Res.*, **110**, D14304, doi:10.1029/2004JD005582, 2005.
- Stith, J. *et al.*, NO signatures from lightning flashes, *J. Geophys. Res.*, **104**, 16081–16089, 1999.
- Suszcynsky, D. M., M. W. Kirkland, A. R. Jacobson, R. C. Franz, and S. O. Knox, FORTE observations of simultaneous VHF and optical emissions from lightning: basic phenomenology, *J. Geophys. Res.*, **105**, D2, 2191–2201, 2000.

- Suszczynsky, D. M. *et al.*, Coordinated observations of optical lightning from space using the FORTE photodiode detector and CCD imager, *J. Geophys. Res.*, **106**, D16, 17897–17906, 2001.
- Thomas, R. J. *et al.*, Accuracy of the lightning mapping array, *J. Geophys. Res.*, **109**, D14207, doi:10.1029/2004JD004549, 2004.
- Tuck, A. F., Production of nitrogen oxides by lightning discharges, *Q. J. R. Meteor. Soc.*, **102**, 749–755, 1976.
- Turman, B. N., and B. C. Edgar, Global lightning distributions at dawn and dusk, *J. Geophys. Res.*, **87**, 1191–1206, 1982.
- Uman, M. A. *et al.*, Triggered-lightning experiments at Camp Blanding, Florida (1993-1995), *Trans. IEE Japan*, **117-B**, 446–452, 1997.
- Viemeister, P. E., Lightning and the origin of nitrates found in precipitation, *J. Meteor.*, **17**, 6811–683, 1960.
- Visser, S., Chemical composition of rain water in Kampala, Uganda, and its relation to meteorological and topographical conditions, *J. Geophys. Res.*, **66**, 3759–3765, 1961.
- von Liebig, J., Une note sur la nitrification, *Ann. Chem. Phys.*, **35**, 329–333, 1827.
- Vorpahl, J. A., J. G. Sparrow, and E. P. Ney, Satellite observations of lightning, *Science*, **169**, 860–862, 1970.
- Wang, Y., A. W. DeSilva, and G. C. Goldenbaum, Nitric oxide production by simulated lightning: dependence on current, energy, and pressure, *J. Geophys. Res.*, **103**, 19149–19159, 1998.
- Waters, J. W., *et al.*, The Earth Observing System Microwave Limb Sounder (EOS MLS) on the Aura satellite, *IEEE Trans. Geosci. Remote Sens.*, **44**, 1075–1092, doi:10.1109/TGRS.2006.8, 2006.
- Williams, E. R., T. Chan, and D. Boccippio, Islands as miniature continents: another look at the land-ocean lightning contrast, *J. Geophys. Res.*, **109**, D16206, 2004.
- Williams, E. R., Lightning and climate: a review, *Atmo. Res.*, **76**, 272–287, 2005.
- Zhang, X., J. H. Helsdon Jr., and R. D. Farley, Numerical modeling of lightning-produced NO<sub>x</sub> using an explicit lightning scheme: 1. Two-dimensional simulation as a ‘proof of concept’, *J. Geophys. Res.*, **108**, D18, 4579, doi:10.1029/2002JD003224, 2003.





---

## Chapter 20

# Lightning and global temperature change

Colin Price

---

### 20.1 Introduction

Lightning is one of nature's most beautiful and awesome sights. Yet it can also be extremely dangerous, presenting a major natural hazard in many different environments, from power utility companies to civil aviation, to golfers, and more. Thousands of people are killed every year by lightning bolts, while tens of thousands are injured (Cooray *et al.*, 2007). Lightning impacts both our daily commercial and recreational activities. In the United States alone, damages due to lightning strikes amount to tens of millions of dollars annually (Curran *et al.*, 2000). In recent years, with great interest in renewable energy, wind turbines have become extremely vulnerable to lightning damage (Glushakow, 2007). Furthermore, most commercial airliners are struck about once a year by lightning; however, due to the protective metal skin, generally little damage is incurred. Tens of thousands of fires are also ignited by lightning every year, generally in temperate or high latitudes (e.g., Canada, Siberia, etc.) (Stocks *et al.*, 2002). In such cases, tens of fires can be ignited locally on the same day as a storm passes through, causing major problems for fire crews and fire management. Hence, knowledge of how lightning activity may change as the Earth's temperature changes is of critical importance and interest.

In section 20.2 of this paper, we will discuss global lightning activity and the distribution of thunderstorms around the Earth. The connection between lightning and cloud microphysics and dynamics will be discussed in section 20.3. In section 20.4, the links with global temperatures will be presented on different timescales, from diurnal to inter-annual, including predictions for the future. The discussion and conclusions will be presented in section 20.5.

### 20.2 Global distribution of thunderstorms

While it was thought for many decades that the global lightning frequency was  $\sim 100$  flashes/sec, recent satellite observations give the best estimate of 45 flashes/sec (Christian *et al.*, 2003). The distribution of these lightning discharges around the globe is not random, following the general circulation patterns of the atmosphere, driven by solar heating (Price, 2006). Solar heating in the tropics results in the creation of warm moist air that initiates vertical convection and mixing of the atmosphere. Lightning activity in thunderstorms is an indication of the intensity of atmospheric convection. Atmospheric convection occurs under unstable

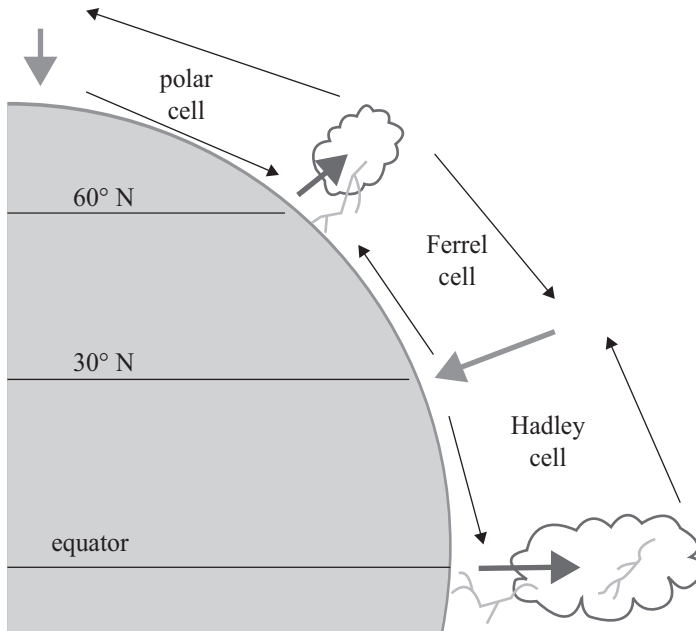


*Figure 20.1 Schematic representation of the general circulation cells in the atmosphere, between the equator and the pole, showing the thunderstorms in the equatorial regions and in mid-latitudes (60°N), while in areas of subsidence few thunderstorms are found (30°N and polar regions)*

atmospheric conditions due to the heating of the boundary layer either by solar radiation during the day or by the mixing of air masses of different densities. Depending on the level of atmospheric instability, the convection will lead to the development of thunderstorms of different intensities. However, this region of tropical convection decreases with increasing latitude due to the circulation patterns in the atmosphere that result in sinking air (subsidence) in the subtropical regions around 30°N and 30°S. The rising air in the tropics, and the sinking air in the subtropics, produces the meridional Hadley cell (Figure 20.1), where the latitude of subsidence over the global deserts is primarily determined by the amplitude of the Coriolis force, which is directly linked to the Earth's rate of rotation. Hence, if the planet was to rotate slower/faster, the tropical band of thunderstorms would expand/contract due to changes in the Coriolis force. The descending air at 30 degrees will diverge at the surface and spread either toward the equator (resulting in the easterly trade winds) or towards the pole (resulting in the westerly mid-latitude winds). These poleward winds eventually meet the cold dry polar air around 50–60 degrees along the polar front. This area of convergence between the cold polar air and the warmer subtropical air results in an additional region of thunderstorms in mid-latitudes. This north–south meridional circulation results in three circulation cells: the Hadley cell between the equator and 30 degrees latitude, the Ferrel cell between 30 and 60 degrees latitude, and the polar cell between 60 degrees and the pole (Figure 20.1). These cells occur in both the northern and southern hemispheres, and shift with the seasons.

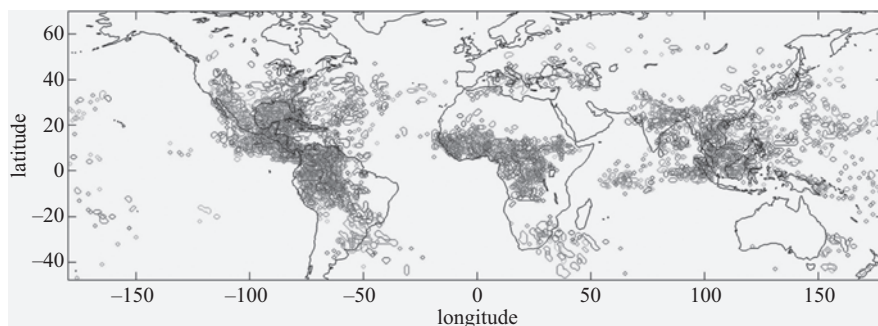


Figure 20.2 Global distribution of thunderstorms (based on WLLN data) for the month of September 2012

In addition to solar heating, water vapor, and particularly the release of latent heat during condensation and freezing, plays a vital role in thunderstorm development. Since the saturation water vapor concentrations increase  $\sim 7$  per cent for every  $1^\circ\text{C}$  increase in temperature (Clausius–Clapeyron relationship), the tropical atmosphere has an order of magnitude more water vapor to condense into rain and ice than the polar atmospheres. Hence, there is much more energy available for the formation of thunderstorms in the tropical atmosphere compared with the higher latitudes.

In the longitudinal direction, the Earth is separated into tropical continental regions (Americas, Africa, and Asia) separated by the various oceans (Atlantic, Indian, and Pacific). While solar radiation during the day is absorbed in only a few centimeters of soil, the same radiation is absorbed in a few tens of meters of water in the ocean. This, together with the different heat capacity of water and soil, results in the surface air temperature over the continents heating much more rapidly in the daytime compared with the oceans. Hence, atmospheric convection and thunderstorms are much more common over the tropical continents compared with the tropical oceans. For the above reasons, the vast majority of lightning (75 per cent) occurs in the tropics between  $30^\circ\text{N}$  and  $30^\circ\text{S}$ , while 90 per cent of all lightning occurs over summertime continental regions (Christian *et al.*, 2003) (Figure 20.2). The remaining 10 per cent in the winter hemisphere is primarily over the warm ocean currents such as the Gulf stream and the Mediterranean Sea.

It should be noted that not all tropical continental thunderstorms are intense lightning generators. The tropical monsoon periods are characterized by the seasonal onshore flow of moist oceanic air, resulting in heavy rainfall in continental thunderstorms, however with low lightning rates (Petersen *et al.*, 2002; Williams *et al.*, 2002). This generally occurs in the Indian monsoon, the African monsoon, the Brazilian monsoon, and the Australian monsoon. Intense lightning activity prefers a somewhat drier environment, which may also explain the difference between the African and the South American lightning activity (Williams and Satori, 2004; Price, 2009).

Global thunderstorms can therefore occur in two very different environments. First, the tropical air mass type thunderstorms resulting from the diurnal solar heating of the surface of the Earth. These late afternoon continental thunderstorms occur mainly in the tropics but can also occur during summer months in mid-latitudes where “static” instabilities can develop in the afternoons on hot summer

days. Second, the frontal thunderstorms occur primarily in mid- to high latitudes where different types of air masses interact and result in baroclinic instabilities along cold, warm, and stationary fronts. Frontal thunderstorms can occur at any hour of the day, over continent and ocean, and during summer and winter. What is needed for these thunderstorms to develop is a strong density gradient between adjacent air masses. These density gradients can be caused either by temperature differences, humidity differences, or a combination of both.

It should be noted that in addition to the above ways of producing thunderstorms we also observe thunderstorms due to orographic forcing (uplift over topography). Mountain ranges and islands force air to flow upwards and can initiate instabilities that trigger the formation of precipitation and thunderstorms. For example, locations to the south of the Himalayas have very intense lightning activity due to the forced uplift of moist air penetrating inland from the Indian Ocean.

### 20.3 Microphysics and dynamics of thunderstorms

Lightning activity in thunderstorms depends on both the microphysics and the dynamics of the clouds, both of which are related to atmospheric temperatures and more specifically temperature *gradients*. It is now well known that the electrification process in thunderstorms is related to the existence of hydrometeors in different phases and sizes interacting with each other through collisions, freezing, melting, coalescence, and breakup (Williams *et al.*, 1991). In thunderstorms, there is a layer where we can find liquid water (supercooled), ice crystals, snow, hail, and graupel (soft hail) all existing together. This is at altitudes between the 0°C and the -40°C isotherm. At temperatures higher than 0°C, all ice will start melting and turn to water drops. At temperatures below -40°C, all hydrometeors will be frozen solid. However, water can exist in the liquid form at temperatures below 0°C and above -40°C, called *supercooled* water. It has been shown in laboratory studies that collision between all these particles (especially ice and graupel), in this mixed-phase region of clouds, is the key for the charge transfer between cloud particles (Takahashi, 1978; Saunders *et al.*, 1991). Cloud particle collisions are thought to be the main mechanism for cloud electrification. Rebounding particles carry away equal and opposite charges. Observations show that clouds having predominantly ice crystals in the mixed phase region, and small amounts of supercooled water and graupel, show little electrification (Takahashi, 2006) and little lightning. However, it should be noted that in thunderstorm anvils with no liquid water or graupel, in situ charging has been documented (Kuhlman *et al.*, 2009).

What determines which clouds have hail, graupel, and supercooled water in the mixed phase region of convective clouds? This region in summer thunderstorms can extend from around 2 to 10 km altitude, and therefore we need significant updrafts (unstable atmosphere) in these clouds to carry the heavier particles up above the freezing level. Observations show that updraft velocities in oceanic thunderstorms may reach a maximum of 10 m/s, while over continental regions the updrafts can reach 50 m/s or greater (Price and Rind, 1992; Williams and Stanfill, 2002; Williams *et al.*, 2004; Deierling and Petersen, 2008). Since updraft intensity plays a major role in thunderstorm electrification and lightning frequencies (Baker *et al.*, 1995, 1999), this dramatic difference in thunderstorm dynamics results in the lightning activity over the oceans being an order of magnitude less than over the

continents. In addition to the transport of larger hydrometeors into the mixed phase region of clouds, the stronger updrafts also enhance the collision efficiency between different sized particles. Increased collisions result in increased charge transfer between particles, leading to rapid charge buildup in clouds.

While lightning activity in thunderstorms is directly related to the microphysics and dynamics of thunderstorms, the dynamics impacts the microphysics (charge transfer, phase changes, rate of collisions, etc.), while the microphysics also feedbacks on the dynamics during the storm development (latent heat release during condensation and freezing, downdrafts due to rainfall and hail formation, etc.).

## 20.4 Temperature and lightning

It has been shown by many studies that lightning activity, thunderstorm days, or indices linked to global lightning activity (ionospheric potential, Schumann resonances, etc.) are sensitive indicators of surface temperature changes (Williams, 1992; Price, 1993; Williams, 2005; Reeve and Toumi, 1999; Markson and Price, 1999; Price and Asfur, 2006; Markson, 2007; Williams, 2009). These studies show that on different temporal and spatial scales, small increases in surface temperature result in large nonlinear increases in thunderstorm and lightning activity (Williams, 2005, 2009).

### 20.4.1 Diurnal variations

Global thunderstorm activity has a clear diurnal cycle that has been studied since the 1920s (Whipple, 1929). This diurnal cycle peaks around 1900 universal time (UT) and has a minimum around 0300 UT (Figure 20.3). The data in Figure 20.3 represent the number of global thunderstorm clusters, based on the WWLLN

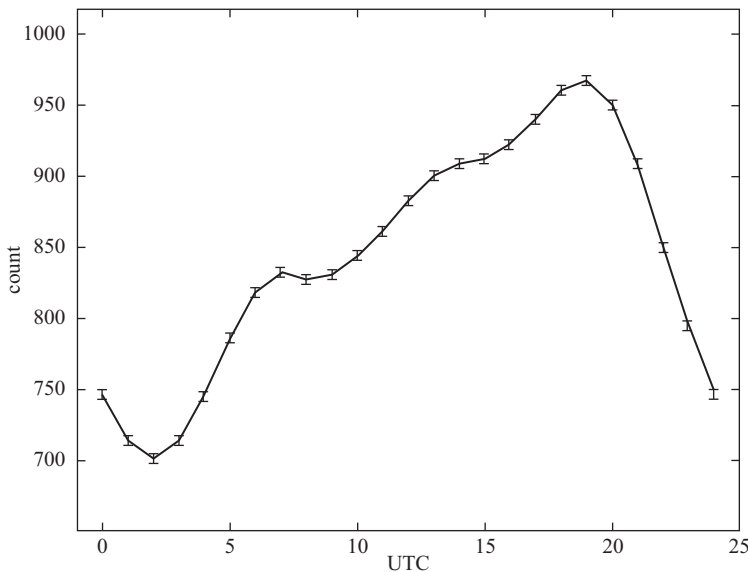


Figure 20.3 Diurnal variations in global thunderstorms (y-axis) based on WWLLN lightning data clusters for six years (2006–2012) (Mezuman, 2013)

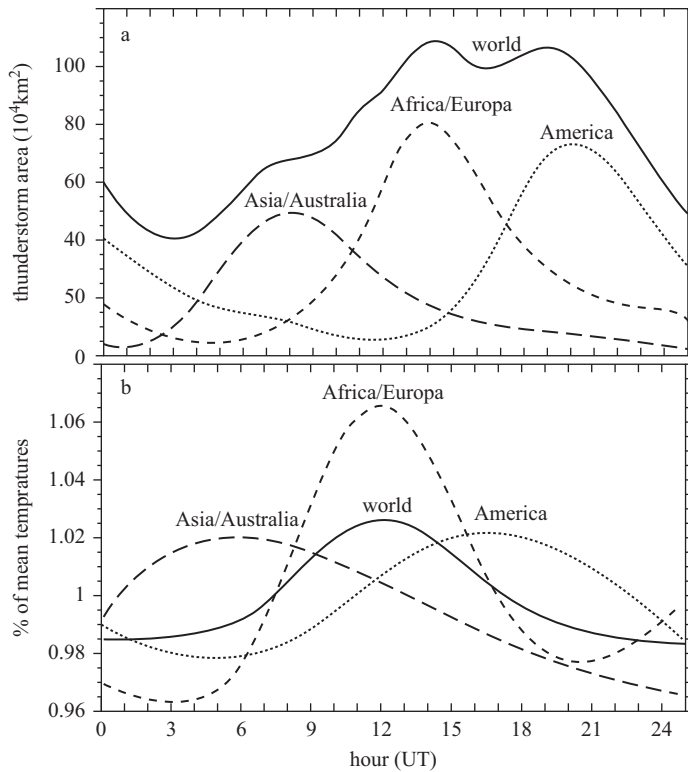


Figure 20.4 (a) Global thunderstorm area as a function of UT time adapted from Whipple (1929); (b) regional and global temperature changes on the diurnal cycle adapted from Price (1993)

ground-based lightning detection network (wwln.net) (Mezuman, 2013). This diurnal cycle is very similar to that found by Whipple (1929) using independent data of “thunderdays” observed at many meteorological stations around the globe (Figure 20.4a).

Whipple (1929) showed that the global diurnal thunderstorm pattern can be broken down into three parts, representing the three major tropical thunderstorm regions of the globe (Asia/Australia, Africa/Europe, and the Americas). Since the tropical thunderstorm activity is driven on a daily basis by solar heating of the surface, inducing atmospheric instability, and hence the development of thunderstorms, the maximum in each of these three regions occurs locally in the late afternoon hours, close to 4–5 pm. However, this time is very different on the global UT clock. Late afternoon in Asia is around 0800–0900 UT, in Africa and Europe late afternoon occurs around 1400 UT, and in the Americas late afternoon occurs around 2000 UT, and hence the shift between the regional curves in Figure 20.4a.

In Figure 20.4b is shown the surface temperature data for the same regions (tropical land regions and global), showing the variability of the temperature throughout the diurnal cycle for the different regions and the globe as a whole. It can be seen that the maximum of each curve occurs a few hours before the maximum in thunderstorm activity in that region. This can be explained by the lag between the maximum heating by the sun and the time it takes to develop an unstable atmosphere, convection, and lightning in thunderstorms. It does appear

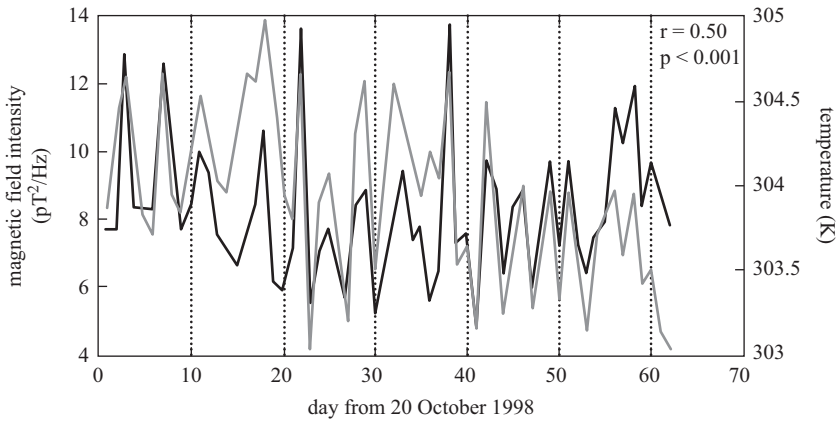


Figure 20.5 Daily variations of surface temperature over tropical Africa and lightning activity over Africa measured using the Schumann resonance method (Price and Asfur, 2006)

therefore that the diurnal cycle in thunderstorm activity is related to the heating and cooling of the continents every day, and hence the temperature of the surface is a driving force in the diurnal cycle of lightning and thunderstorms. It should be noted that other studies also show positive correlations between diurnal surface temperatures and parameters related to global lightning activity, such as the ionospheric potential (Markson and Price, 1999).

If we look at the day-to-day variability of lightning activity, here too we see a positive correlation between lightning activity and surface temperatures. In Figure 20.5 presents two months of daily lightning activity over Africa (black curve) and the mean daily tropical African surface temperatures (gray curve). While the correlation coefficient is only  $r = 0.5$ , the correlation is statistically significant, implying that in this case the day-to-day variations of temperature can explain 25 per cent of the variability of the regional lightning activity over tropical Africa.

While daily temperatures in the tropics are extremely important for the development of convection and thunderstorms, day-to-day temperature changes may be less important in higher mid-latitudes, where storms are less dependent on the daily surface temperatures for initiating convection. Nevertheless, 75 per cent or more of the global lightning and thunderstorms occur in the tropical regions, and hence temperature variations on a daily scale should have a strong influence on global lightning activity.

#### 20.4.2 Semi-annual variations

The next temporal scale worth investigating is the semi-annual variation, or in other words, the two maxima in solar heating that impact the tropical regions due to the sun's crossing of the equator twice every year at the equinox (due to the tilt of the Earth's axis of rotation). Many studies have been performed related to the semi-annual cycle of thunderstorm activity (Williams, 1994; Satori and Zieger, 1999; Fullekrug and Fraser-Smith, 1998; Nickolaenko *et al.*, 1999; Manohar *et al.*, 1999; Christian *et al.*, 2003; and Satori *et al.*, 2009). Figure 20.6a shows the monthly variations of the tropical (25°N–25°S) wet bulb temperature (Williams, 1994),



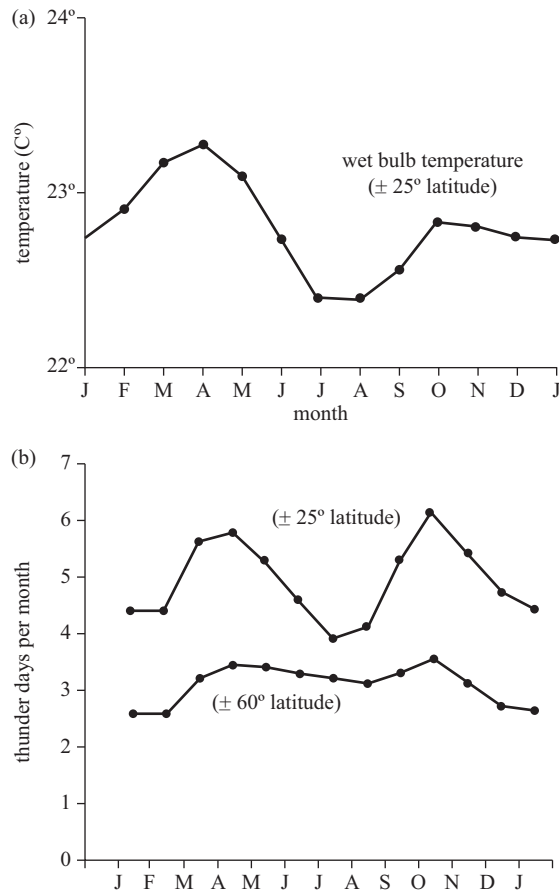


Figure 20.6 (a) Monthly variations of the tropical wet bulb temperature showing two peaks around the equinoxes; (b) Tropical and global monthly thunder days per month (adapted from Williams, 1994)

which represents a combination of the actual temperature and the amount of moisture in the air, both of which are important for the production of thunderstorms. The wet bulb temperature is actually the temperature to which we need to cool the air until it becomes saturated (condensation occurs). Hence, the dry bulb temperature (actual air temperature) is always greater than the wet bulb temperature if the air is unsaturated. The figure shows that the temperatures in the tropics have two maxima every year, the first around April and the second around October. These months are shortly after the spring and autumn equinoxes when the sun is 90 degrees above the equator at 12 noon (21 March and 22 September). As in the diurnal plots, the Earth system takes time to heat up (especially the oceans), and hence the maximum temperatures lag about 1 month after the maximum solar radiation that occurs in the tropics at the equinoxes. This is the same reason that summer temperatures in the northern hemisphere peak in July/August and not on the 21 June (the longest day of the year, and hence the maximum solar radiation in the northern hemisphere).

The same monthly patterns can be seen in the thunderstorm activity (measured as thunderdays) (Figure 20.6b), where both tropical and global ( $60^\circ\text{N}$ – $60^\circ\text{S}$ )

thunderday statistics are presented. Since the semi-annual cycle is non-existent outside the tropics (the sun “travels” north–south of the equator to the maximum latitude of 23.5 degrees north and south), the semi-annual cycle in global thunderstorms is much weaker than the signal in the tropical thunderstorm activity. Similar semi-annual variability is also seen in the more recent LIS/OTD lightning data from satellite (Christian *et al.*, 2003), where the lightning exhibits a clear semi-annual cycle in the tropics, but when all the global lightning is binned together, the semi-annual cycle disappears, with the global lightning showing a single maximum during northern hemisphere summer. This global northern hemisphere maximum is primarily due to the asymmetric distribution of the mid-high latitude lightning in the summer hemispheres, with the northern hemisphere having much more lightning during its summer, compared with the southern hemisphere summer. The reason for this lightning asymmetry is due to the asymmetry in the land distribution in the two hemispheres, since thunderstorms develop more readily over land surfaces than over the oceans (Christian *et al.*, 2003).

Hence, on the semi-annual cycle, there also appears to be a link between temperatures and lightning activity, implying the solar forcing, and hence surface temperatures are an important factor in determining the monthly variability in tropical and global thunderstorm activity.

### 20.4.3 Annual variations

When moving to the annual timescale there are many parameters that vary on this scale, forced by the sun, and the seasons. Even sunbathers in Miami have a clear annual cycle that would correlate very nicely with global lightning activity, and hence particularly on this timescales we need to be careful with correlations, and understanding cause-and-effect.

In Figure 20.7a, the land-area global lightning flash count from the OTD satellite is presented, together with the land-area global wet bulb temperatures (Reeve and Toumi, 1999). It is clear that the global temperatures and lightning both peak in the north hemisphere summer (June–August) while the minimum temperatures and lightning are during the southern hemisphere summer (December–February). In Figure 20.7b, the mean annual cycle is removed from the data, to show only the anomalies of temperature and lightning. Although the scatter is quite large, it is still clear that the two parameters are positively correlated, with a slope of the line implying that for every 1°C increase of wet bulb temperature on the annual scale, the lightning activity should increase by around 40 per cent.

Other studies have also shown the clear annual cycle of global lightning and temperatures (Williams *et al.*, 1994; Price, 2000; Christian *et al.*, 2003), further supporting the connection between seasonal temperature changes and seasonal lightning activity.

### 20.4.4 ENSO variations

After the annual cycle of temperatures (summer/winter) the largest influence on the Earth’s climate is the El Nino–Southern Oscillation (ENSO) phenomenon. This swing in the Earth’s climate occurs with a periodicity of between 3 and 7 years, and is caused by shifts in ocean temperatures in the tropical Pacific Ocean. These shifts influence weather patterns around the globe and also have a small impact on global temperatures. The last major El Nino of 1997–98 caused ocean and global air temperatures to warm slightly, making 1998 the warmest year in recent records.

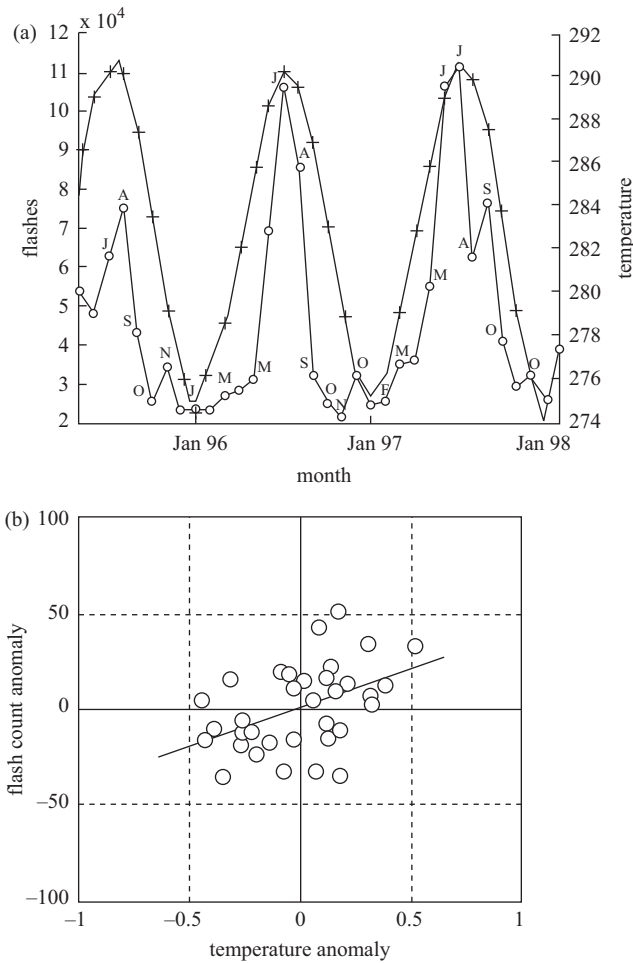


Figure 20.7 (a) Annual variations in wet bulb temperature (+) and lightning activity for land areas of the globe; (b) scatter plot of same data after removing the mean seasonal cycle (Reeve and Toumi, 1999)

The slight decrease in global temperatures due to the La Ninas of the last decade has also been “blamed” for the stagnation of the rising global temperatures due to increasing greenhouse gases in the atmosphere (Kosaka and Xie, 2013).

On a regional scale many authors have shown that during the warmer El Nino phase of the ENSO, regional lightning activity increases (Hamid *et al.*, 2001; Yoshida *et al.*, 2007; Chronis *et al.*, 2008; Pinto, 2009; Satori *et al.*, 2009; Kumar and Kamra, 2012). On a global scale Williams (1992) presented a clear correlation between monthly global lightning activity (measured via the Schumann resonances) and monthly mean tropical temperature anomalies (Figure 20.8). These data show the ENSO cycle in the temperature data, peaking in the winter (northern hemisphere) of 1969–70 and again in the winter of 1972–73, both warm El Nino years. The monthly lightning data tracks the temperature anomalies ( $\pm 0.5^\circ\text{C}$ ) surprisingly well during this period. It should be noted that such a good correlation

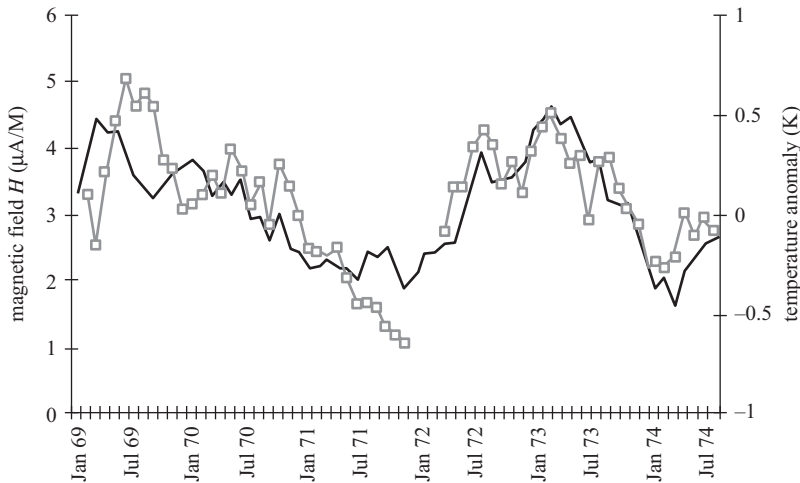


Figure 20.8 Monthly tropical temperature anomalies from 1969 to 1974 (bold curve) and monthly global lightning estimates (boxes) using the Schumann resonance method (Williams, 1992)

between ENSO temperature anomalies and global lightning has not been found by other researchers, and therefore this relationship needs additional research. Nevertheless, both regional and global studies point to more lightning occurring during the warmer phase of the ENSO cycle, implying a positive link between global surface temperatures on the El Niño timescale and global and regional lightning activity.

#### 20.4.5 Inter-annual variations

Due to the increased interest in global warming, as well as the increased evidence that global temperatures are increasing (IPCC, 2013), we also would like to know if global lightning is sensitive to these long-term changes. If we look back in time, we do not have more than 10–20 years of global lightning data. For this reason, many studies have been performed using “thunderday” data, representing the number of days per month (or year) that thunder is heard at a specific station. One example is given in Figure 20.9 for Sao Paulo, Brazil (Pinto *et al.*, 2013). Figure 20.9a shows the annual mean number of thunderdays, while Figure 20.9b shows the annual mean temperatures from 1950 until the present. There has been a clear increase in the annual number of thunderdays from around 60 in the 1950s up to 90 in the 1990s. This was associated with an increase in temperatures of 2–3°C over the same period in Sao Paulo, implying a 10 per cent increase in thunderdays for every 1°C warming.

Whether these temperature changes are due to local urban heat island effects (UHI) in Sao Paulo, or due to global warming, is irrelevant for the comparison of the graphs. These results, together with other thunderday studies from Alaska (Williams, 2009), ionospheric potential measurements (Markson, 2007), and air-Earth current measurements in the United Kingdom (Harrison and Ingram, 2005) imply a slight increase in the thunderstorm activity over the 20th century as temperatures warmed.

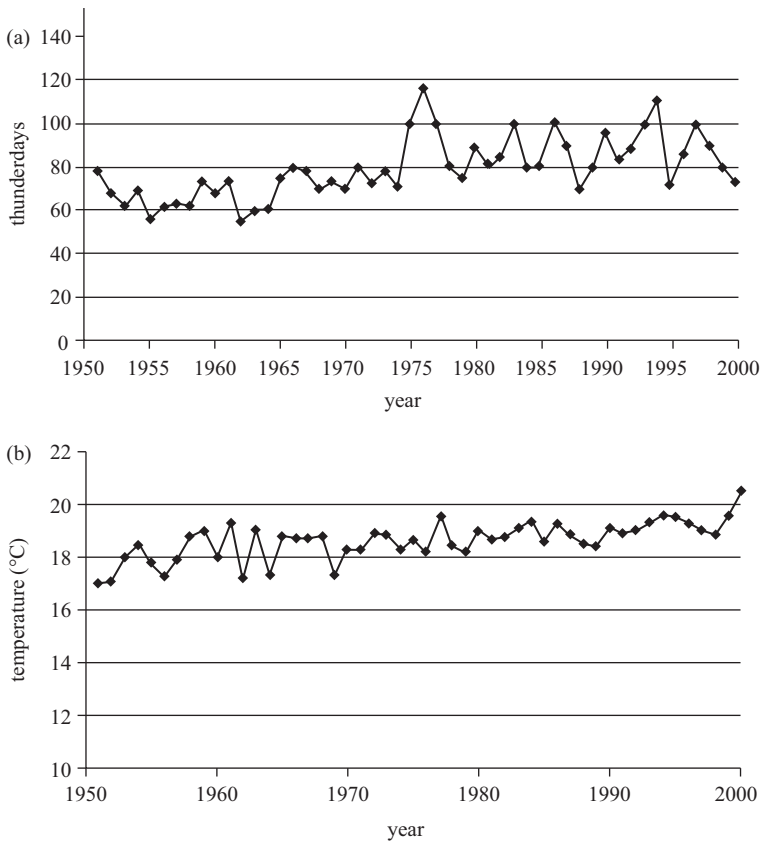


Figure 20.9 Long-term trend in thunder days (a) and temperature (b) in Sao Paulo, Brazil (Pinto *et al.*, 2013)

#### 20.4.6 Future predictions

The recent Intergovernmental Panel on Climate Change (IPCC) report (IPCC, 2013) predicts a global warming of 1–4°C by the end of this century, depending on the scenario we assume for future uses of energy and land use. However, one of the weaknesses of all the models used for these predictions is the simulation of convective clouds, which is a sub-grid scale process that needs to be parameterized in climate models (Del Genio *et al.*, 2007; Fuytan and Del Genio, 2007). While climate models have problems accurately modeling convective clouds, they are even more problematic modeling lightning activity, although this has been attempted (Price and Rind, 1994a; 1994b; Shindell *et al.*, 2006; Grenfell *et al.*, 2003).

For understanding lightning changes in a warmer world, we need to look at not only surface temperatures but also the temperature profile (lapse rate) in the atmosphere as greenhouse gases increase. There are three possibilities regarding the mean vertical temperature profile in the lower troposphere, as greenhouse gases increase and surface temperatures warm (Figure 20.10). If the surface warms more than the upper troposphere, the atmosphere will become more unstable (on average), and we would expect more convection and thunderstorms. If the surface and the upper troposphere warm at the same rate, then no change will be seen in the

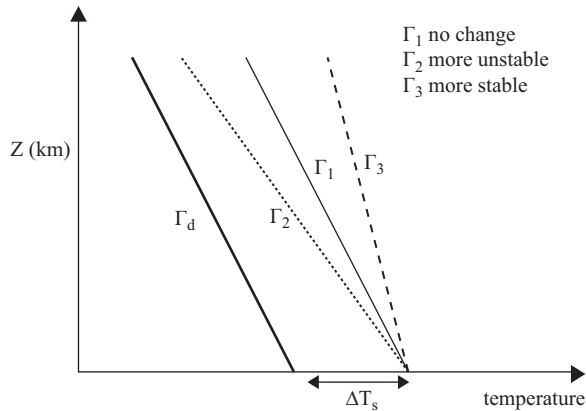


Figure 20.10 The atmospheric dry adiabatic lapse rate of  $9.8^{\circ}\text{C}/\text{km}$  ( $\Gamma_d$ ) is the equilibrium profile of the dry atmosphere.  $\Gamma_1$ ,  $\Gamma_2$ , and  $\Gamma_3$  give three scenarios of average future profiles due to global warming

lapse rate, and hence there will be no change in the mean stability (or instability) of the troposphere. Finally, if the upper troposphere warms more than the surface temperatures, this will stabilize the atmosphere, with fewer thunderstorms developing in a warmer world. Climate models of all complexity and sizes show that as the climate warms at the surface, the tropical upper troposphere (exactly the location of most of the global thunderstorms) warms even more (IPCC, 2013). The reason for this is that increased convection transports additional water vapor into the upper atmosphere where it acts as a strong greenhouse gas, absorbing infrared radiation emitted from the surface of the Earth. The increase in water vapor results in a larger warming in the upper troposphere than at the surface, resulting in the average stabilization of the tropical atmosphere ( $\Gamma_3$  in Figure 20.10).

However, within the thunderstorms themselves the instability measured by the convective available potential energy (CAPE) tends to increase in a warmer climate (Del Genio *et al.*, 2007), especially for the most intense thunderstorms. And increases in CAPE in the present climate show clear increases in lightning activity (Williams *et al.*, 1992; Pawar *et al.*, 2012; Singh *et al.*, 2012). Therefore, when these same climate models are run under a scenario with a doubled- $\text{CO}_2$  atmosphere (a situation we will reach by the middle of this century), the models show increases in lightning activity, of approximately 10 per cent for every  $1^{\circ}\text{C}$  global warming (Price and Rind, 1994b; Grenfell *et al.*, 2003; Shindell *et al.*, 2006). Locally that increase can be much larger (Figure 20.11). In the tropics the model shows an approximate 40 per cent increase for a doubled- $\text{CO}_2$  atmosphere.

This apparent paradox was dealt with in more depth by Del Genio *et al.* (2007) where they showed that in a doubled- $\text{CO}_2$  climate the updrafts strengthen by  $\sim 1\text{m/s}$ , due to a rise in the height of the freezing level in the model. They showed that in certain regions, such as the western United States, the drying in a warmer climate reduces the frequency of thunderstorms, but the strongest storms (highest CAPE values) occur 26 per cent more often (Figure 20.12). In other words, the drier climate produces less thunderstorms overall, but those storms that do develop are more intense in a warmer climate. This agrees with recent observations (Williams *et al.*, 2005) showing increased electrification in the drier regions of the Great

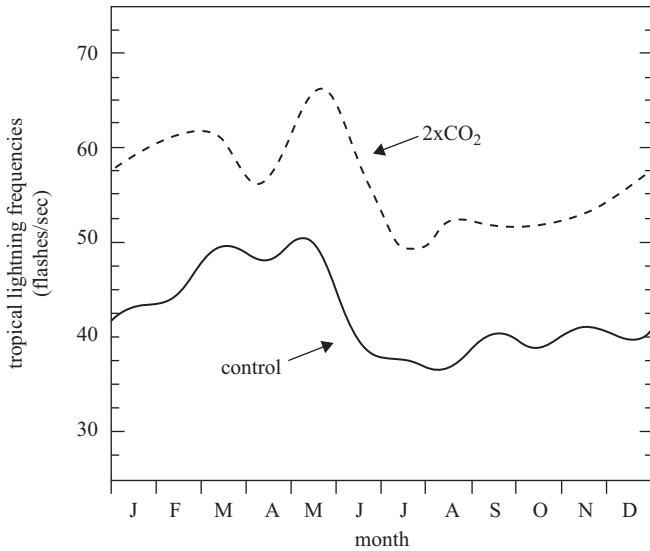


Figure 20.11 Results from the NASA GISS climate model run  $1xCO_2$  (control) and  $2xCO_2$  atmospheric concentrations of  $CO_2$ . An increase in tropical lightning is observed during all months (Price and Rind, 1994b; Goldammer and Price, 1998)

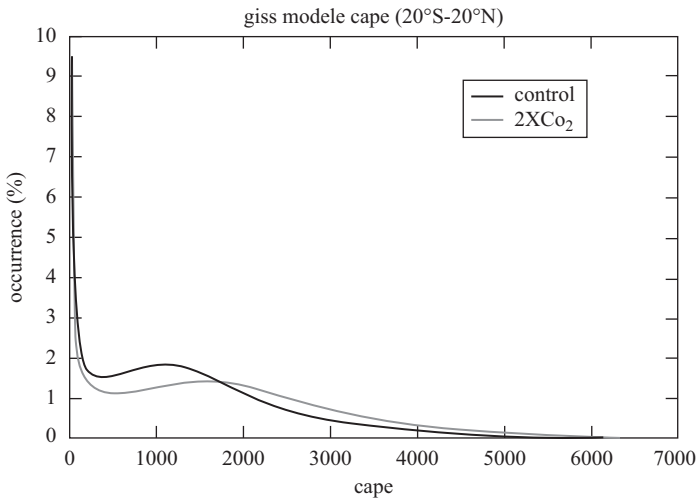


Figure 20.12 The convective available potential energy (CAPE) that represents the potential explosiveness of storms, in the NASA GISS climate model, for the present climate, and a  $2xCO_2$  climate (Del Genio *et al.*, 2007)

Plains of the United States, and increased lightning activity in Southeast Asia during the dry warm El Nino periods (Hamid *et al.*, 2001).

Hence, here too, using climate models to predict the future, there appears to be a positive correlation between a warmer world and more lightning and thunder-storm activity.

## 20.5 Conclusions and discussion

Lightning is a major natural hazard that impacts many commercial and recreational sectors, while also often causing death or severe injury due to the high temperatures and high peak currents in the lightning channel. Global lightning and thunderstorm activity is driven first and foremost by the Earth's climate, which is driven by solar insolation that varies with latitude, longitude (land/ocean), season, and hour. The climate drives circulation patterns that promote thunderstorms in the tropics and mid-latitudes, and inhibit thunderstorms in the subtropics and polar regions. Locally, thunderstorm activity depends on surface temperature, water vapor, the tropospheric lapse rate, as well as aerosol loading (not discussed here). These parameters can impact the intensity of lightning activity in thunderstorms.

On short timescales (hourly, daily, semi-annual, and annual) there is a robust positive correlation between tropical lightning activity and surface temperature. There is also evidence for increasing thunderstorm activity over the 20th century, although we have limited data to study long-term trends over the last century. Finally, climate models further support the positive correlation between lightning and global temperatures, with increases of 10 per cent per 1°C as the climate warms due to increasing greenhouse gas concentrations in the atmosphere.

One factor that has not been addressed here is the role of aerosols in thunderstorms electrification and how changes in aerosol loading in the atmosphere may impact thunderstorm and lightning activity. It is possible that warmer, drier climates will result in more suspended aerosols and cloud condensation nuclei, hence influencing cloud microphysics and cloud electrification (Williams *et al.*, 2002; Rosenfeld *et al.*, 2008), and it should be pointed out that all model simulations of future lightning activity do not include any aerosol effects on lightning and address only thermodynamic changes in their simulations. Whether aerosol effects would amplify or reduce these changes is a topic for future studies.

## References

- Baker, M.B., H.J. Christian, and J. Latham, 1995: A computational study of the relationships linking lightning frequency and other thundercloud parameters, *Quart. J. Roy. Met. Soc.*, 121, 1525–1548.
- Baker, M.B. *et al.*, 1999: Relationship between lightning activity and various thundercloud parameters: Satellite and modeling studies, *Atmos. Res.*, 51, 221–236.
- Christian, H.J., R.J. Blakeslee, D.J. Boccippio, W.L. Boeck *et al.*, 2003: Global frequency and distribution of lightning as observed from space by the Optical Transient Detector, *J. Geophys. Res.*, 108, 4005, doi:10.1029/2002JD0023.
- Chronis, T.G. *et al.*, 2008: Global lightning activity from the ENSO perspective, *Geophys. Res. Lett.*, 35, L19804, doi:10.1029/2008GL034321.
- Cooray, V., C. Cooray, and C.J. Andrews, 2007: Lightning casued injuries in humans, *J. Electrostat.*, 65, 386–394.
- Curran, E.B., R.L. Holle, and R.E. Lopez, 2000: Lightning casualties and damages in the United States from 1959–1994, *J. Climate*, 13, 3448–3464.
- Del Genio, A.D., Y. Mao-Sung, and J. Jonas, 2007: Will moist convection be stronger in a warmer climate? *Geophys. Res. Lett.*, 34, L16703, doi:10.1029/2007GL030525.



- Deierling, W., and W.A. Petersen, 2008: Total lightning activity as an indicator of updraft characteristics, *J. Geophys. Res.*, 113, D16210, doi:10.1029/2007JD009598.
- Fullekrug, M., and A. Fraser-Smith, 1998: Global lightning and climate variability inferred from ELF field variations, *Geophys. Res. Lett.*, 24, 2411–2414.
- Futyan, J.M., and A.D. Del Genio, 2007: Relationships between lightning and properties of convective cloud clusters, *Geophys. Res. Lett.*, 34, L15705, doi:10.1029/2007GL030227.
- Glushakow, B., 2007: Effective lightning protection for wind turbine generators, *IEEE Trans. on Energy Conversion*, 22, 214–222.
- Goldammer, J.G., and C. Price, 1998: Potential impacts of climate change on fire regimes in the tropics based on MAGICC and a GISS GCM-derived lightning model, *Climate Change*, 39, 273–296.
- Grenfell, J.L., D.T. Shindell, and V. Grewe, 2003: Sensitivity studies of oxidative changes in the troposphere in 2100 using the GISS GCM, *Atmos. Chem. Phys. Discuss.*, 3, 1805–1842.
- Hamid, E.Y., Z. Kawasaki, and R. Mardiana, 2001: Impact of the 1997–98 El Niño on lightning activity over Indonesia, *Geophys. Res. Lett.*, 28, 147–150.
- Harrison, R.G., and W.J. Ingram, 2005: Air-Earth current measurements at Kew, London, 1909–1979, *Atmos. Res.*, 76, 49–64.
- Intergovernmental Panel on Climate Change (IPCC), 2013: Climate Change 2013: The Physical Science Basis. World Meteorological Organization (WMO) and UN Environment Programme (UNEP).
- Kosaka, Y., and S.P. Xie, 2013: Recent global-warming hiatus tied to equatorial Pacific surface cooling, *Nature*, doi:10.1038/nature12534.
- Kuhlman, K.M., D.R. MacGorman, M.I. Biggerstaff, and P.R. Krehbiel, 2009: Lightning initiation in the anvils of two supercell storms. *Geophys. Res. Lett.*, 36, L07802, doi:10.1029/2008GL036650.
- Kumar, P.R., and A.K. Kamra, 2012: Land-sea contrast in lightning activity over the sea and peninsular regions of South/Southeast Asia, *Atmos. Res.*, 118, 52–67.
- Manohar, G.K., S.S. Kandalgaonkar, and M.I.R. Tinmaker, 1999: Thunderstorm activity over India and the Indian southwest, *J. Geophys. Res.*, 104, 4169–4188.
- Markson, R., 2007: The global circuit intensity: Its measurement and variation over the last 50 years, *Bull. Amer. Meteor. Soc.*, 88, 1–19.
- Markson, R., and C. Price, 1999: Ionospheric potential as a proxy index for global temperatures, *Atmos. Res.*, 51, 309–314.
- Mezuman, K., 2013: Detecting global thunderstorm distribution from lightning clusters, MSc thesis, Tel Aviv University, Israel.
- Nickolaenko, A.P., M. Hayakawa, and Y. Hobara, 1999: Long-term periodical variations in global lightning activity deduced from Schumann resonance monitoring, *J. Geophys. Res.*, 104, 27585–27591.
- Pawar, S.D., D.M. Lal, and P. Murugavel, 2012: Lightning characteristics over central India during Indian summer monsoon, *Atmos. Res.*, 106, 44–49.
- Petersen, W.A. *et al.*, 2002: TRMM observations of intraseasonal variability in convective regimes over the Amazon, *J. Clim.*, 15, 1278–1294.
- Pinto, O., Jr., 2009: Lightning in the tropics: from a source of fire to a monitoring system of climate change, *Nova Science Publishers*, 109p.
- Pinto, O., Jr., I.R.C.A. Pinto, and M.A.S. Ferro, 2013: A study of the long-term variability of thunderstorm days in southeast Brazil, *J. Geophys. Res. Atmos.*, 118, 5231–5246, doi:10.1002/jgrd.50282.

- Price, C., 1993: Global surface temperatures and the atmospheric electrical circuit, *Geophys. Res. Lett.*, 20, 1363–1366.
- Price, C., 2000: Evidence for a link between global lightning activity and upper tropo-spheric water vapor, *Nature*, 406, 290–293.
- Price, C., 2006: Global thunderstorm activity, in *Sprites, Elves and Intense Lightning Discharges*, edited by M. Fullekrug *et al.*, Springer, Amsterdam, The Netherlands, 85–99.
- Price, C., 2009: Will a drier climate result in more lightning? *Atmos. Res.*, 91, 479–484.
- Price, C., and D. Rind, 1992: A simple lightning parameterization for calculating global lightning distributions, *J. Geophys. Res.*, 97, 9919–9933.
- Price, C., and D. Rind, 1994a: Modeling global lightning distributions in a General Circulation Model, *Mon. Wea. Rev.*, 122, 1930–1939.
- Price, C., and D. Rind, 1994b: Possible implications of global climate change on global lightning distributions and frequencies, *J. Geophys. Res.*, 99, 10823–10831.
- Price, C., and M. Asfur, 2006: Can lightning observations be used as an indicator of upper-tropospheric water vapor variability? *Bull. Amer. Meteor. Soc.*, 87, 291–298.
- Reeve, N., and R. Toumi, 1999: Lightning activity as an indicator of climate change, *Quart. J. Roy. Met. Soc.*, 125, 893–903.
- Rosenfeld, D. *et al.*, 2008: Flood or drought: How do aerosols affect precipitation? *Science*, 1309–1313.
- Satori, G., and B. Zieger, 1999: El Nino related meridional oscillations of global lightning activity, *Geophys. Res. Lett.*, 26, 1365–1368.
- Satori, G., E. Williams, and V. Mushtak, 2009: ELF electromagnetic signatures of global lightning activity, in *Lightning: Principles, Instruments and Applications*, edited by H.D. Betz, U. Schumann, and P. Laroche, Springer, New York.
- Saunders, C.P.R., W.D. Keith, and R.P. Mitzewa, 1991: The effect of liquid water on thunderstorm charging, *J. Geophys. Res.*, 96, 11007–11017.
- Shindell, D.T. *et al.*, 2006: Simulations of preindustrial, present-day, and 2100 conditions in the NASA GISS composition and climate model G-PUCCINI, *Atmos. Chem. Phys.*, 6, 4427–4459.
- Siingh, D., P. Ramesh Kumar, M.N. Kulkarni, *et al.*, 2012: Lightning, convective rain and solar activity – Over the South/Southeast Asia, *Atmos. Res.*, 120–121, 99–111.
- Stocks, B.J., J.A. Mason, J.B. Todd, *et al.*, 2002: Large forest fires in Canada, 1959–1997, *J. Geophys. Res.*, 107, 8149, doi:10.1029/2001JD000484.
- Takahashi, T., 1978: Riming electrification as a charge generation mechanism in thunderstorms, *J. Atmos. Sci.*, 55, 1536–1548.
- Takahashi, T., 2006: Precipitation mechanisms in East Asian monsoon: Video-sonde study, *J. Geophys. Res.*, 111, D09202, doi:10.1029/2005JD006268.
- Whipple, F.J.W., 1929. On the association of the diurnal variation of electric potential gradient in fine weather with the distribution of thunderstorms over the globe, *Quart. J. Roy. Met. Soc.*, 55, 1– 17.
- Williams, E.R., R. Zhang, and J. Rydock, 1991: Mixed-phase microphysics and cloud electrification, *J. Atmos. Sci.*, 48, 2195–2203.
- Williams, E.R., 1992: The Schumann resonance: a global tropical thermometer, *Science*, 256, 1184–1187.

- Williams, E.R., 1994: Global circuit response to seasonal variations in global surface air temperature, *Mon. Wea. Rev.*, 122, 1917–1929.
- Williams, E.R., 2005: Lightning and climate: A review, *Atmos. Res.*, 76, 272–287.
- Williams, E.R., 2009 The global electric circuit: A review, *Atmos. Rev.*, 91, 140–152.
- Williams, E.R., *et al.*, 2002: Contrasting convective regimes over the Amazon: Implications for cloud electrification, *J. Geophys. Res., LBA Special Issue*, 107, D20, 8082, doi:10.1029/2001JD000380, 2002.
- Williams, E.R., V. Mushtak, D. Rosenfeld, S. Goodman, and D. Boccippio, 2005: Thermodynamic conditions favorable to superlative thunderstorm updraft, mixed phase microphysics and lightning flash rate, *Atmos. Res.*, 76, 288–306.
- Williams, E.R., S.A. Rutledge, S.C. Geotis, *et al.*, 1992: A radar and electrical study of tropical hot tower, *J. Atmos. Sci.*, 49, 1386–1395.
- Williams, E.R., and G. Satori, 2004: Lightning, thermodynamic and hydrological comparisons of the two tropical continental chimneys, *J. Atmos. Solar-Terr. Phys.*, 66, 1213–1231.
- Williams, E., and S. Stanfill, 2002: The physical origin of the land-ocean contrast in lightning activity, *C. R. Physique*, 3, 1277–1292.
- Williams, E., T. Chan, and D. Boccippio, 2004: Islands as miniature continents: Another look at the land-ocean lightning contrast, *J. Geophys. Res.*, 109, D16206, doi:10.1029/2003JD003833.
- Yoshida, S., T. Morimoto, T. Ushio, and Z. Kawasaki, 2007: ENSO and convective activities in Southeast Asia and western Pacific, *Geophys. Res. Lett.*, 34, doi:10.1029/2007GL030758.

---

# Index

---

- aborted upward streamer 703,  
714–16
- accretion 1, 21, 32, 33
- action integral 279, 695
- aerial networks 683
- aerosol concentrations 7–8
- Agrawal *et al.* model 562–3
- air
  - DC corona modes in 95
  - diffusion of electrons in 56
  - discharges in 795–6
  - electrical breakdown of 45
    - and underground
      - azimuthal magnetic field in 502
      - horizontal electric field in 502–3
      - vertical electric field in 501–2
- aircraft 691–3, 825
  - lightning immunity tests 691
- aircraft campaign EXL98 728
- airport runway lighting system
  - cable currents 313
  - current decay along counterpoise 311–12
  - currents in vertical ground rods 312–13
  - lightning damage to system 313
- air terminals 612, 624–7, 636
  - deterioration and corrosion of 637
  - interception probability 643–6
- altitude triggering technique 272–4,  
278–9
- ambipolar diffusion 55
- analytic perturbation method (APM) 848–50
- anodes, fall 89
- antennas
  - crossed loop 209–10
  - horizontal/vertical 211
  - parabolic 690
  - plate (whip) 204–8
- arresters 301, 303, 306, 308
- atmosphere 28–86
  - baroclinity of 8, 11
  - barotropic 8
  - vertical temperature structure 7
- Atmospheric Chemistry Experiment
  - Fourier Transform Spectrometer (ACE-FTS) 844
- atmospheric conditions
  - dependence of electrical breakdown on 99–101
  - instability 7
- atmospheric convection 863–4
- atoms
  - electron affinity of 52
  - electronegative 71, 95, 99, 108
  - excitations of 41, 45–6, 49
  - ionisation of 45, 48, 79
  - meta-stable 50–1, 57, 82
- ATP program 624
- attenuation function 512, 541
- Australia, telephone-mediated shocks in 719
- Austrian Lightning Detection & Information System (ALDIS) 343
- avalanches 649, 805
  - anode reaching 97
  - electron 61–3
  - head of 60
  - multiplication 798–801
  - secondary 64
- azimuthal magnetic field 527
  - in air and underground 502
  - at surface and at different depths below ground 537–8
- backflash 687, 688
- background electric fields 42, 61, 126,  
130, 132, 141, 202, 204–5, 427,  
649
- critical 72, 76
- streamers in 64, 127–9

- Barbosa and Paulino expression to calculate horizontal electric field 529–31
- baroclinity 8, 10
- Bergeron process 2
- bidirectional discharge 64
- bidirectional leader 148–50, 278
- biological material, current behaviour in 705–6
- bipolar cloud-to-ground flashes 251–3
- bipolar lightning 341
  - upward 341–2
- bipolar upward-initiated flashes 342
- blue starters 728
- BOLSIG+ 758
- “bolt-from-the-blue” lightning 736
- Boltzmann’s constant 49, 56, 58, 828
- Boltzmann’s equation 42, 748, 758
- bonding, equipotential 619, 627, 635–6, 623
- Boys camera 152, 231
- broadband 174
  - measurements 141
  - optical pulse 154–5
- Bruce-Golde model 385
- buildings
  - direct strokes on 685–6
  - strokes near 686–7
- cable currents 313
- cables, underground 308–9
- camera photography 234
- Camp Blanding, triggering facility at 274, 298
- capacitance
  - per-unit-length line 572
  - transverse 568
- CAPE (Convective Available Potential Energy) 7, 8
- cathode 78, 81, 95
  - collision of positive ions with 79
  - dark space 90
  - drop 89
  - fall 92
  - processes 56–9
- channel length distribution (CLD) 836, 837
- characteristic pulses 133, 134
  - physical nature of 135–7
- charge distribution 351, 374, 468, 658
  - along streamer channels 74
- charge per unit length 187, 412, 480, 655, 666
- Chemical Transport Model (CTM) 825, 844–6
- CHILL multi-parameter Doppler radar 827
- Chowdhuri–Gross model 565, 567
- classical dipole method of electric field calculation 483–5
- classical mechanism 125, 132
- classical triggering technique 269–72, 276–8
- Clausius–Clapeyron relation 7, 10, 11
- climate models 832, 874, 875, 832
- close lightning electromagnetic environment
  - characterization of 295–6
- cloud base 11, 139, 186, 190
- cloud buoyancy 819
  - integrated 7
  - modest 10
  - vertical extent of 7
- cloud chamber photographs 64, 67
- cloud condensation nuclei 7–8, 35
- cloud flash 121–3
  - electromagnetic fields generated by 193–9
- cloud particle collisions 866
- cloud potential 202
  - and energy dissipation in first return strokes 202–3
  - and energy dissipation in subsequent return strokes 203–4
- clouds
  - flashes 846
  - formation of 1
  - M components inside 180
  - origin of dart leader in 187
  - stratiform 5
  - water content 22, 26–8, 29–31
  - see also* thunderclouds
- cloud screening charges 736
- cloud-to-ground (CG) discharges 343
- cloud-to-ground (CG) flashes
  - leaders 233
  - leader speed 235
  - negative 233

- positive 233
- recoil leaders 235–7
- upward connecting leader 237
- cloud-to-ground (CG) lightning 352–3, 736, 737, 809
- cloud to ground flash ratio 124
- cold cloud thickness 833
- cold runaway electron production 807
- Collection Volume Method (CVM) 655, 666, 668
- collisional detachment 54
- collisions
  - elastic 41, 75, 93
  - electrons-gas particles 44–5
  - excitation 41
  - ice crystal, graupel with 31, 136
  - ice–ice 28, 34
  - inelastic 41, 45
  - ionisation 41, 45–6, 49, 61, 79, 87, 97
  - ions–molecules 51
- Community Multiscale Air Quality (CMAQ) system 821, 836
- compact cloud discharges (CID) 198
- Compton Gamma-Ray Observatory (CGRO) 794
- concrete foundations 634
- condensation 7
- conducting plane 354, 368, 382
- conductive coupling 682–3
- conductors
  - air termination 634
  - bonding 619, 635
  - down 619, 620, 627–8, 634, 636
  - horizontal 625, 629
  - meshed 625
  - mutual coupling between 597
  - mutual inductance between 572
  - neutral, periodical grounding of 600
  - overhead 560, 683
  - ring 627, 633, 635
- conduits 636
- connecting leader 649
- conservation equations 408
- contact potential 702, 708–9
- continuing current (CC) 177, 244–5
  - detection of strokes 249
  - duration 246–8
  - electric field change caused by 178
  - presence of 245–6
  - return stroke peak current and waveshapes and M-components 248–9
  - 249–51
- continuity equation 358, 365–8, 371–3
  - ground level, fields at 368
  - image channel 368
- convective available potential energy (CAPE) 875
- convective mechanism 19–20
  - mesoscale 2, 4–6
- conventional breakdown threshold field 755
- Cooray, on return stroke speed 482–3
  - classical dipole method of electric field calculation 483–5
  - electric field calculation using electromagnetic fields of accelerating charges 485–90
- Cooray model 433–5, 439
  - Version I 439–40
- corona 127, 646, 680
  - brush and leader branching 258–9
  - burst 97–9, 132
  - decay time constant 426
  - discharge 94–9, 106
    - lateral 137
    - time constant 478
  - effect 596–8
  - influence on development at initiation of long sparks 114–15
  - negative modes 95–7
  - sheath 104, 137, 157, 174
- corrosion 634, 637
- coupling 597, 682–7
  - inductive 635, 614, 617
  - models 560–78
  - resistive 617, 639
- CPTs (chaotic pulse trains) 192
- critical radius 110–11, 652–3
- critical risetime 104
- critical streamer length concepts 652–3
- critical volume 102, 109, 114, 126
- Cross-Chain Loran Atmospheric Sounding System (CLASS) 827
- crossed magnetic loops 212
- cumulative ionisation 61, 69
- cumulonimbus cloud 1

- current at ground level 478
- current decay, along counterpoise 311–12
- current dissipation models (CD models) 461–2, 477
  - advantages of 462–3
  - description 452–4
  - generalisation of 460–1
  - mathematical background 455–6
  - predictions of 457–9
  - return stroke models 456–7
- current estimates 708–9
- current generation models (CG models) 477
  - channel base current 444
  - concept 425–9
  - generalisation of 459–60
  - ground conductivity in 463–4
  - mathematical background 429–31
  - in practice 431–2
  - predictions of 445
    - connecting leader 450
    - electromagnetic fields 446–7
    - field and current parameters 447–50
    - return stroke current 445–6
    - slow front 450
  - to represent first return strokes 441–4
  - value of model parameters 444–5
- current pathway 701
- current propagation models (CP models) 461–2, 477
  - concept 420
  - description 420–5
  - features of 423
- currents
  - antenna mode 561
  - associated with steps 147–8
  - average 146–7
  - cable 313
  - channel-base 584–5
  - leader 146–8, 187–8
  - point discharge 20
  - retarded 361, 372–3
  - rise time of dart leaders 189
  - streamer 73
  - thermionic 58
  - time to half value of 695
  - transient 619
  - triggered 688
  - in vertical ground rods 312–13
- current waveforms 276–8
  - parameters for negative strokes in rocket-triggered lightning 281
  - return-stroke 279–89
- damage
  - causes and types of 613–14
  - lightning 313
    - effects of 613–15
    - limiting risk of 623
    - mechanical 624
    - probability of 616–17
    - thermal 624
- dark lightning 809–11
- dark period 106, 107, 114–15
- dark spaces 90
- dart leaders 155, 184–93, 260–1
  - charge per unit length on 187
  - current and charge 187–8
  - electric field change 596
  - length 185–6, 190
  - optical signature 186–7
  - origin in cloud 187
  - propagation 121
  - return strokes and 190
  - RF radiation from 189
  - spectrum and temperature 186
  - speed 185–90
  - static fields generated by 188–9
  - strong source of RF radiation 172
- dart stepped leaders 191–2, 197
- day-to-day temperature changes 869
- Defense Meteorological Satellite Program (DMSP) satellites 824
- de-ionisation processes 51–2
- DEMETER satellite 744
- detection of upward lightning 343
- Diendorfer model 435–6
  - modification by Thottappillil *et al.* 436–8
- Diendorfer-Uman model 386
- diffusion 55–6, 72
- dipole
  - electrostatic field from 351–2
  - vertical electric field 135
- direct strikes
  - heating considerations 711–13

- no flashover 710–11
  - probability 683
  - protection against 643
  - with flashover 711
- direct triggered-lightning strikes 301
  - horizontal configuration distribution
    - line 301, 303–6
  - vertical configuration distribution
    - line 306–8
- discharge time constant 479
- distance–voltage diagram 112
- distribution line
  - horizontal configuration 301, 303–6
  - vertical configuration 306–8
- disturbance
  - conducted 696, 697
  - electromagnetic 696
- DLR Polarization Diversity Radar (POLDIRAD) polarimetric Doppler radar 829
- DMSP satellite observations 10
- Dornier-228 turboprop aircraft 828–9
- doubled-CO<sub>2</sub> atmosphere 875
- down-coming corona current 488
- downraughts 19–20
- downward negative leader 274
- drift–diffusion equations 759
- drift velocity 42–3, 56, 60, 97
- drop breakup theory 20–1
- droplet size effect 31–4
- DU model 371
  
- earth(ing)
  - equipotential 619
  - termination system 620, 635
- earth potential rise (EPR) 703
  - mediated shock 713–14
- earth resistance component 709–10
- earth's magnetic field 753
- effective height 327
  - of tall objects 326–30
- EGM (electrogeometric model) 626, 643–5
- electrical aspects
  - of lightning strikes to humans 701
  - strike mechanisms 701
    - aborted upward streamer 703
    - contact potential and side flash 702
    - current estimates 708–9
    - direct strike 702
    - earth potential rise 703
- electrical breakdown 41–115, 86, 119, 120, 126, 136
  - and corona 99
  - critical value necessary for 97
  - dependence on atmospheric conditions 99–101
  - small gaps 78–85
  - statistical nature of 101–3
- electrical discharges, upper
  - atmospheric: *see* upper atmospheric electrical discharges
- electric and magnetic fields calculation over finitely conducting ground 508
- electric fields 387, 390
  - breakdown 126–7, 132
  - broadband 172
  - calculation 483–90
  - change generated by M component 179
  - created by stepped leaders 143
  - critical 74, 95, 100, 109, 114, 130, 189
  - generated by M components 121
  - generated by stepped leader 139–42
  - measuring 204–10
  - measuring polarity of 212
  - minimum necessary for inception of corona 108
  - pulses generated by preliminary breakdown process 136
  - return stroke 133, 377–9
  - stable streamer propagation 114
- Electro Geometrical Model (EGM) 655, 663
  - of lightning protection 651
  - striking distance 651
- electromagnetic field pulse (EMP) 751
  - self-consistent modeling 751
- electromagnetic fields 500
  - azimuthal magnetic field in air and underground 502
  - cloud flashes 193–9
  - computation of, from lightning discharge 351–401



- of dipole over finitely conducting ground 501
- downward leader 595–6
- electromagnetic fields of return strokes 503
- ground flashes 132–93
- horizontal electric field in air and underground 502–3
- lightning-generated 212, 559–609
- measurements 119
- overhead electrical networks 559–609
- return strokes 503
- simplified expression for 548
- vertical electric field in air and underground 501–2
- electromagnetic models 419
- electron avalanches 61–3, 101, 803
  - formation of 95
- electron energy distribution function (EEDF) 748
- electrons
  - attachment and detachment 52–4
  - emission of 82
  - mean energy 56
  - primary 79, 83, 97
  - recombination of positive ions and 64, 89–90
  - runaway mechanism 131–2
  - secondary 79, 83
  - temperature 50, 75–6
  - thermalised 53
  - wave nature of 58
- electrostatic approximation 384
- electrostatic discharges 694
- electrostatic fields 122, 143, 161, 211, 356–7, 368
  - change caused by stepping process 148
  - nonuniqueness of 369–71
- electro-thermodynamic models 407–10
- El Niño–Southern Oscillation (ENSO) phenomenon 871–3
- elve doublets 752–3
- elves 725, 751–3
- EMC (electromagnetic coupling) 679–98
- EMP (electromagnetic pulse)
  - simulators 560, 575
  - see also* HEMP; LEMP
- EMTP (electromagnetic transient program) 598–601
- energetic radiation from thunderstorms and lightning 787–811
- energy
  - collision 51
  - dissipation, return strokes and lightning flashes 200–4
  - ionisation 45–6, 48, 89
  - optical 155
  - recombination 51–2
  - thermal 56, 114
  - translational 48, 55, 76, 103, 114
  - vibrational 75–6, 114
- engineering models 420
  - current generation models (CG models)
    - concept 425–9
    - in practice 431–2
    - mathematical background 429–31
  - current propagation models (CP models)
    - concept 420
    - description 420–5
- equilibrium
  - thermodynamic 44, 49, 76, 155
  - vapour pressure 2
- equipotential bonding 619–20, 623, 635–6, 636
- equipotentialisation 619, 627, 635–6
- European Lightning Nitrogen Oxides (EULINOX) field experiment 828–9
- excitations 90, 97, 114
  - atomic 41, 45, 49
  - electronic 42
  - free paths for 41
  - of molecular vibrations 54–5
  - rotational 42
  - vibrational 42, 114
- exclusion zone 248
- Falcon jet 828–9
- Faraday
  - cage method 626
  - dark space 90
- Fast on-Orbit Recording of Transient Events (FORTE) satellite 843
- FDTD (finite difference time domain method) 745, 746, 753
- feedback mechanisms 801–3

- Fermi energy levels 56
- fibre glass plates 157
- field emission 59, 87
  - arcs 91
- field of view (FOV) CCD camera 739
- field-to-transmission line coupling
  - models 560–78, 681
- final jump 110
  - condition 650, 651
  - initiation of 109
- finitely conducting ground, vector
  - potential of dipole over 500–1
- first corona 103, 107, 114–15
  - inception and characteristics of 108–9
- first return strokes 120–1, 155, 166, 192
  - current derivatives of 160
  - initiation of 172
  - model 163
  - peak current 184
  - radiation field 133
  - RF radiation generated by 171–4
- flash duration 239–40
- flash extrapolation method 821–4
- flash type, discriminating
  - analytic perturbation method 848–50
  - mean method 847–8
  - mixed exponential distribution
    - method 848
  - reasons for 846–7
  - from space 846–50
- formative time lag 102
- FORMOSAT-2 satellite 742
- Franklin conductors 152
- Franklin rod 111
- freezing 7, 21
- French Office Nationale d'Etudes et de Recherches Aérospatiales (ONERA) 3-D lightning interferometer 827
- frequencies
  - spectra 175
  - see also* HF; LF; RF; UHF; LHF; VLF
- frictional force 131
- Fritz Peak Observatory 827
- frontal thunderstorms 866
- galvanic coupling: *see* conductive coupling
- gamma-ray flashes from thunderstorms 793–5
- gases
  - critical volume of 102
  - electronegative 52, 85, 97
  - explosive 612
  - ionisation of 48, 81–2
- gas tubes 697–8
- generalised leader inception model 646, 653–4
- generating voltmeter 204–5
- Geostationary Lightning Mapper (GLM) 844
- Geostationary Operational Environmental Satellite R-series (GOES-R) 844
- geostationary satellites 200
- gigantic jets 725, 731–4
  - negative 734
  - physical mechanisms of 734–7
- GIS power networks 694
- global annual LNO<sub>x</sub> production, estimation of
  - flash extrapolation method 821–4
  - global model fit method 825
  - thunderstorm extrapolation method 825
- global lightning nitrogen oxides production 819–77
- global model fit method 825
- global temperature change 863
- glow
  - abnormal 88, 90–1
  - negative 90, 95
  - positive 99
  - pulseless 95
- glow discharge 88–99
  - normal 88
- glow to arc transition 91–3
- Goddard Institute for Space Studies (GISS) ModelE2 global climate model 832–3
- graupels 1–2, 30–1, 33, 125, 136
  - charged 31
  - negative 31, 33, 35
  - positive 33
  - riming 31
  - simulated 29

- surface 26, 33, 35
- temperature 22
- gravitational separation 2, 22
- greenhouse gases 874
- ground admittance 569, 573
- grounded structures 649
  - attachment of lightning flashes to 649–75
  - charge distribution on stepped leader channel 660–1
  - effect of height of structure 662–6
  - leader inception models 652–4
  - leader progression/lightning attachment models 655–7
  - lightning attachment models
    - comparison of 666–70
    - experimental test of 670–5
  - lightning strikes to side of structure 675
  - striking distance 650–2
    - potential of stepped leader channel and 657–9
    - of subsequent return strokes 661–2
- ground flashes 4, 11, 119–21, 135, 199–200, 211, 212, 846, 849
  - cloud flashes and 199–200
  - density 124
  - fraction 833, 847
  - negative 119, 212
  - physical processes and
    - electromagnetic fields 132–93
  - positive 4, 5, 11, 119, 212
- grounding rods 685
- grounding wires 679–80, 687
  - mounted on towers 687
- ground levels, fields at 364–5
- ground rod current 312–13
  
- hailstones 2, 10, 17, 22
  - positively charged 22
- half-peak width 279, 287, 288
- halos 725, 738
- Heidler function 504
- Heidler model 432–3
  - channel base current 432
- HEMP (high altitude EMP) effects 694, 698
- Hermitian glow 99
  
- HF (high frequency) 213, 694
  - radiation 134, 172–4
  - see also* UHF; LHF
- high-energy discharges 787
  - versus low-energy discharges 806–7
- high-energy particles 806
- high-speed video observations 768, 770
- high-speed video recordings
  - features of lightning flashes obtained from 231–61
- horizontal configuration distribution line 301, 303–6
- horizontal electric field
  - in air and underground 502–3
  - Barbosa and Paulino expression to calculate 529–31
  - quasi-static expression to calculate 526
  - simplified expressions to calculate 526
    - at surface and at different depths below ground 538
    - surface impedance expression 527
- horizontally stratified ground,
  - propagation effects over 547
  - simplified expression for electromagnetic fields 548
  - validity of simplified expression 548
    - continuously stratified ground 550–5
    - stratified ground with two layers 548–50
    - Wait's simplified expressions 547–8
- horizontal magnetic field, calculating 512
- hot channels, development of 805–6
- HPM (high power microwaves) 698
- Hubert model 432–3
- human, electrical aspects of lightning strikes to 701
- hyperbolic direction finding 213
  
- ICC pulses, parameters of 336–7
- ice
  - breaking of hydrogen bonds in 28
  - charging due to fragmentation of 28
  - melting of 21

- ice crystals 2, 17–18, 23, 26, 28–31, 125
  - crystals vapour-grown 22, 29, 31
  - impacting on still-freezing droplet
    - on graupel surface 35
  - vapour-grown 22
- ice–ice 18
  - collisions 28, 34
  - noninductive charging mechanism 35
- ice–liquid interface 21
- image channel 364, 382
- Imager of Sprites and Upper Atmospheric Lightning (ISUAL) experiment 725
- impedance
  - ground 569, 573–4
  - per-unit-length 568
  - surge 624, 630
- impulsive current components in
  - upward negative lightning 336
- impulsive voltage waveforms 298
- induced-voltage waveforms 298–9
- induction fields 161, 368
- inductive mechanism/phenomena 16–19, 629
- initial continuous current (ICC) 245, 270, 278
- interception probability 625, 639, 643–6
- Intergovernmental Panel on Climate Change (IPCC) 874
- International Center for Lightning Research and Testing (ICLRT) 576
  - at Camp Blanding 274, 298, 302
- interstroke intervals 279, 280, 284
- interstroke time intervals 244
- intra-cloud (IC) 232, 795
  - flash 4
  - lightning 809
- ionisation
  - cumulative 69, 100, 102
  - electron collision 60
  - free paths for 41
  - primary 80
  - probability of 87
  - soil 631
  - thermal 48–50, 76, 87, 93
  - virgin air 174
- ionosphere 123, 212
- ionospheric sounding satellite-b (ISS-b) 824
- ions 56
  - collision of 89
  - collision of meta-stable 82
  - common, mobility in air 42
  - different mobilities in ice and water 35
  - hydrated 54
  - ionisation due to positive 51
  - molecular 54
- ISUAL gigantic jets 733
- ISUAL instruments with elve simulation 753
- ITCZ (intertropical convergence zone) 10
- jets 725, 727–31
  - physical mechanisms of 734–7
- junction processes 121
- K changes 122, 182–3, 187, 197
- keraunic level 616, 683–4
- Lalande’s stabilization field equation 654
- latent heat 7, 21, 33
- latitude 124–5, 183
- LCL (lifted condensation level) 1, 11
- LCR models 410–19
- leader channels
  - charge density 143–5
  - potential gradient 110
  - total charge 143–5
  - uniformly charged 189
- leader electric fields 383–4
- leader inception model of
  - Becerra and Cooray (SLIM) 654, 664
- leader inception models 652–4
- leader progression model 625, 646, 655–7
- leader/return-stroke electric field waveforms 295
- leaders
  - attempted 121
  - chaotic 192–3
  - connecting 120

- mathematical modelling of positive discharges 111–14
  - negative 110
  - positive 135, 149, 650, 657
  - propagation of 115, 130
  - upward 645
- LEMP (lightning electromagnetic pulse) 560, 589, 597, 619, 621–2, 696
- LF (low-frequency) 581
- lightning 863, 877
  - airport runway lighting system 311–13
  - grounding impedance 289
  - interaction with objects and systems 296–7
  - miscellaneous experiments 313
  - power distribution lines 297–308
  - power transmission lines 309
  - residential building 309
  - temperature and 867–76
  - in thunderstorms 866
    - energetic radiation from 787–811
    - underground cables 308–9
    - see also* triggered lightning
- lightning attachment models 655–7
  - comparison of 666–70
  - experimental test of 670–5
- lightning channels
  - temperature estimation 155–6
  - thickness 157
- lightning detection network (LINET) 830
- lightning discharge
  - computation of electromagnetic fields from 351–401
  - frequency 123–5
  - inception 125–32
- lightning flashes 405, 649
  - cloud-to-ground 3
  - duration 612
  - number of 615–16
  - positive 638, 639
  - strike point of 675
  - triggered 154, 160, 178, 186, 190, 575–6, 595, 685, 686
  - upward 650
  - see also* cloud flashes; ground flashes
- lightning-generated electromagnetic fields 518
- Lightning Imaging Sensor (LIS) 830, 833
  - lightning mappers 843
- lightning initiation
  - conditions necessary for 130
- lightning locating system (LLS) 232, 330, 343, 843
- lightning mapping arrays (LMA) 232, 729–30
- lightning model 760
- lightning nitrogen oxides
  - importance of 819–21
- Lightning Nitrogen Oxides Model (LNOM) 831
  - data archive 837–41
  - data products 836–7
  - functionality 834–6
  - future evolution 841
  - motivations 832–4
- lightning position and tracking system (LPATS) sensors 829
- lightning protective system (LPS) 310
- lightning return stroke 387
  - generated electromagnetic fields 499
- lightning shock current estimates
  - body model 706–8
  - factors for modelling 708
- lightning strikes electrical aspects, to humans 701
- lightning-triggering facility 274–6
- linear charge density 144
- LIOV (lightning-induced overvoltage) 578–9, 598–601
- LNB (level of neutral buoyancy) 7
- LNOx
  - clarifying observations 826
  - field campaigns 827–30
  - global annual production 821–5
  - importance of 819–21
  - observations and inferences 825–31
  - rocket triggered lightning 830–1
  - thunderstorm rainwater, early examinations of 826
  - top-down constraints on 844
- LNOx distribution (LND) 836, 839

- local thermodynamic equilibrium (LTE) 409
- long sparks 103–14, 150, 155, 186
  - laboratory 174
- Lorentz condition approach 361–5
- low-energy discharges 787
- low-energy particles 806
- LPS (lightning protection systems) 619
  - external 619–20
- LPZs (LEMP protection zones) 619, 622–3
- luminosity 332
- lumped circuit model 410
- Lundholm, on return stroke speed 480–1
- Lundholm's derivation 481
  
- magnetic direction finding 123, 212
- magnetic field 364, 381–2, 392
  - measuring 204–10
  - return stroke 364, 377–9
- magnetic induction field 569
- magnetostatic field 357
- MATLAB function 758
- Maximum Group Area (MGA) 847
- Maxwell–Boltzmann distribution 49
- Maxwellian distribution 44
- Maxwellian relaxation time 737, 762
- M-components 178–82, 187, 193, 260–1
  - electric fields generated by 121
- mean free path and cross section 41–2
- mean Maximum Group Area (MGA), for ground flashes 847–8
- mesoscale convective systems 2, 4–6, 830
- mixed exponential distribution
  - method 848
- mixed-mode concept 337
- mixed-phase region 2, 4, 5, 10–11
  - central 4
  - elevation of 7
- ModelE2 832–4
- model-independent method: *see* Analytic Perturbation Method
- modeling 807–9
- molecules 52
  - electronegative 52, 73
  - vibrational excitation of 54–5, 114
- moment approximation 383
- monopole technique 358
- Monte Carlo model 758
- MOV (Metal-Oxide Varistorov) arresters 688
- moving capacitor plate model 737, 745
- MTLE (modified transmission line model, exponential) 371, 387, 420, 504, 578–9
  - return stroke 565, 578–9, 595
- MTLL (modified transmission line model, linear) 386–7, 420
- multiconductor lines 5714–573, 589
- multigrounded lightning flashes 240–4
- Møller scattering 798
  
- N<sub>2</sub> Lyman–Birge–Hopfield (LBH) band system 742
- National Lightning Detection Network<sup>TM</sup> (NLDN) 827
- National Oceanic and Atmospheric Administration (NOAA) WP3D Orion aircraft 827
- natural lightning 790
- nearby triggered-lightning strikes 297–301
- negative ions 19, 20, 25, 52, 53–4, 84, 97, 108
  - hydrated 114
- negative lightning flash 649
- negative streamers 803, 804
- negative upward lightning 332
- NEMP (nuclear electromagnetic pulse) 563
- net electric field
  - changing due to dart leaders in triggered lightning 295
- nitrogen dioxide (NO<sub>2</sub>), from lightning 826
- nitrogen oxides 200
- North Dakota Citation jet 827
- Norton equivalent 289
- Norton's and Bannister's approximations 508
  - for vertical electric field with exact calculations 509–12
- Norton's equation 510

- optical fibre ground wires (OPGW) 245
- optical Lightning System (OLS) 843
- optically determined properties 152–4, 185–7
- optical signals 123
  - energy released in 155
- Optical Transient Detector (OTD) 829
  - lightning mappers 843
  - lightning observations 833
- Orbiting Solar Observatory (OSO) Program 842
- oscillatory voltage waveforms 298
- “other-triggered” upward lightning 330
- overvoltage suppressors 697
- ozone 200
  
- particle interaction 125
- Paschen curve 101
- Paschen’s law 85–7, 90
- PCP (positive charge pocket) 135–7
- peak current 282, 285, 288, 625, 643
  - derivative 190
  - determination of 161
  - first return stroke 184
- Peek’s formula 101
- Penning ionisation 50
- photoelectric emission 58
- photoionization 48, 82, 114
  - model 763, 764
- photometers 842
- photons
  - ionisation of gas by 82–3
- plasma fluid equations 758
- positive cloud-to-ground (+CG) flashes 234–5
- positive return strokes
  - electromagnetic fields of 451
  - extension of model 450–1
- positive streamer 803, 804
- potential barrier 57–9
- power distribution lines 297–308
- power installations
  - low-voltage 142
- power lines 560, 679
- power networks
  - lightning effects in 687–9
  - low-voltage 690–1
  - substation equipment 689–90
- power transmission lines 309
- precipitation 18
  - ice-based 16
  - vertical development of 7
- precursors 270
- preliminary breakdown process 119, 133–4
  - duration 134–5
  - location 135
  - physical nature 135–7
- propagating electrons 796–7
- propagation
  - dart leader 121
  - leader 107, 115, 130
  - stepped leader 138
  - streamer 64, 69–71, 76, 114, 130
- propagation effects 499
  - on electromagnetic fields and cloud and ground flashes 525–6
  - on electromagnetic fields generated by cloud flashes 523
  - on radiation fields 517–21
  - varying with shape of radiation field 521–3
- protection
  - EMC measures 690, 693–396
  - primary 690, 695, 698
  - secondary 690, 695
  - tests for efficiency 688
- protective devices 159
- PSICE program 624
- pulse propagation
  - vertical lightning channel 401
  - on vertical wire antenna 399–400
- pulses
  - bipolar 195, 199
  - broadband optical 154–5
  - characteristic 133–4, 139
  - K 182
  - leader 142
  - microsecond scale 183, 194, 199
  - narrow isolated 198–9
  - optical 154–5, 186, 191
  - preliminary breakdown 132
  
- quasi-liquid layer theory 25–8, 35
- quasi-static approximation

- Rachidi model 563–4
- radiation  
 HF 134, 172–4  
 UHF 173–4  
 VHF 149, 185, 187  
 visible 89  
*see also* RF
- radiation fields 369, 372  
 amplitude of stepped leader 147  
 calculation of 486, 487  
 characteristics 164–71  
 measurement of 208  
 peak 183–4, 212  
 propagation effects on 517–21  
 return stroke 199  
 signature of, generated by stepped leader 141–2
- radio  
 interferometric systems 211  
 interferometry 214–15
- Rai, on return stroke speed 481–2
- Rakov model  
 Version I 439–40
- rate of rise (steepness) 279, 286–7, 288
- recoil leader negative end (RLNE) 260
- recoil leader positive end (RLPE) 260
- recombination 51–2, 64, 90  
 dissociative 52  
 radiative 51–2  
 three-body 52
- Relativistic Runaway Electron  
 Avalanche (RREAs) 792–3
- residential building 309
- restrikes 107
- retardation effects, treatment of 359–61
- return current radius 414, 418
- return stroke (RS) models 237–9  
 future of 470  
 ground conductivity in 463–4  
 with special attention to engineering applications 405–70
- return stroke channel 182, 187, 377, 565, 578  
 defunct 189
- return-stroke current peak  
 versus grounding conditions 289–95
- return-stroke current waveforms  
 parameters of 279–89
- return stroke fields 500
- return stroke models 153, 371, 567, 578–9
- return stroke peak current and CC 248–9
- return strokes 107, 120–1, 133–5, 141–3, 147, 260–1, 365  
 calculation of fields from 385–7  
 detector 847  
 distribution of peak radiation fields 170  
 electric and magnetic fields 377–9  
 electromagnetic fields of 503  
 electromagnetic fields generated by 161–76  
 energy dissipation in 200–4  
 modelling of 405–7  
 negative 167–9  
 optical radiation generated by 154–7  
 origin 152  
 parameters of 337–9  
 positive 167–9, 172  
 properties of currents measured at base of channel 157–61  
 speed 120–1, 152–4, 361, 369, 567, 584–5  
 utilised in testing approximate expressions 504–5  
 velocity 184, 579, 582, 592, 595
- return stroke speed 152, 477–90  
 Cooray on 482–3  
 Lundholm on 480–1  
 Rai on 481–2  
 Wagner on 480–1
- return stroke velocity 489
- RF (radiofrequency) radiation 171–4, 189, 198
- rime 7, 11, 26, 35  
 accretion rate 33  
 experiments 29–31  
 graupel 31  
 substrate 33
- RINDAT (Rede Integrada Nacional de Detecção de Descargas Atmosféricas) 830
- risetime 279, 285–6, 288
- Rizk-model method 327, 330
- Rizk's generalized leader inception equation 653–4



- rocket-and-wire triggered lightning
  - experiments 267–314
- rocket-triggered lightning 336, 789, 790, 830
- rod-plane gaps 78, 652
  - impulse breakdown in 104–11
- rods 625, 680
  - air termination 634
  - driven 629
- runaway breakdown 792–3
- runaway electron hypothesis 131–2
- runway lighting system 311–13
- Rusck model 565, 567
  
- satellite observations, of lightning
  - benefits of 842–50
  - discriminating flash type from space 846–50
  - space-based lightning mappers 842–4
  - top-down constraints on LNO<sub>x</sub> 844
  - two early studies employing photometers 842
- Scanning Imaging Absorption Spectrometer for Atmospheric Chartography (SCIAMACHY) 844
- Schottky effect 58–9
- screening charges at cloud tops 736
- seasonal occurrence of upward lightning 331–2
- segment altitude distribution (SAD) 836
- selective ion capture theory 20
- semi-infinite vertical thin-wire antenna
  - electrostatic fields from 354
  - magnetostatic fields from 354
- Severe Thunderstorm Electrification and Precipitation Study (STEPS) campaign 729
- shielding 622, 636
  - cables 619, 623, 635
  - cages 698
  - imperfect 694
  - radiation 696
  - wires 600
- short-circuit lightning current 289
- Shumann resonances 123
- side flashes 626, 702
  
- similarity 87
- similarity laws 754–5
- simplified expression
  - validation of 542
- validity of 548
  - continuously stratified ground 550–5
  - stratified ground with two layers 548–50
- simulated house experiment 309
- single return stroke 407
- single wire lines 561
  - impedance 569
  - overhead 564, 579
- SLIM model 654, 663, 664, 670
- slow electric fields 133
- soil 629
  - conductivity 681
  - ionisation 631
  - lossy 588
  - resistivity 579, 620
- solar heating 863
- solid–liquid interface 25
- Sommerfeld's equations 513
- space-based lightning mappers 842–4
- space charge 114–15
  - electric field due to avalanche 63–4
- space stem 107
- sparks/sparking 76, 624
  - channels 93–4
  - formation of 61, 75
  - probability 616
  - see also* long sparks
- SPDs (surge protective devices) 619, 622–3, 635–6
- specific energy 279
- spectrometer 826–7
- spectroscopic measurements 104
- spider lightning 5
- sprites 725, 737–8
  - charge, current and electromagnetic radiation 744–6
  - chemistry 747–8
  - emissions from 743
  - infrasound emissions from 746–7
  - modeling 757–71
  - physical mechanism of 748–51

- spatial structures and temporal dynamics of 738–41
  - spectra 741–4
- Sprites94 campaign 735, 741, 747
- sprite streamers, modeling of 763–71
- stabilization field equation 654
- static field, calculation of 486
- statistical time lag 102, 109
- stepped leader channel 174, 649
  - charge distribution on 660–1
  - and striking distance 657–9
- stepped leaders 72, 120, 132, 160, 175
  - dart 191–2
  - electric field generated by 139–42
  - initiation of 133
  - interception of 150–2
  - optimally determined properties 137–9
  - pulses 197–8
  - source of disturbance 150
  - speed 139
  - structure 137
  - temperature 139
- stratosphere 7
- Stratospheric-Tropospheric Experiment: Radiation, Aerosols, and Ozone (STERA0) series
  - of field experiments 827–8
- streak cameras 119, 152
- streamer channels 75
  - charge distribution along 74
  - physical properties 71–2
  - potential gradient of 73–4
- streamer discharges 61, 64, 68, 174
  - chain of water drops 127–9
  - electrical breakdown criterion in presence of 76–8
  - single water drop 125–7
- streamer propagation 69–71, 76
  - conditions necessary for 130
  - critical electrical field necessary for 114
- streamers 127, 137, 154, 166, 803–5
  - anode directed 64
  - breakdown 86, 99
  - bursts 111–12
  - cathode directed 64
  - criterion 86, 95
  - current in 73
  - discharges 738
  - double-headed 764–6
  - formation 64–8
  - initiation 768–71
  - mid gap 67
  - negative 64, 71, 72, 78, 95, 110, 120, 148
  - onset 99
  - physical processes taking place at head 69
  - positive 64, 67, 71–2, 74, 149, 157, 766, 770–1
  - radial 99
  - speed 73
  - Trichel 97
  - zone 112
- streamer-to-leader transition 130, 649
  - and initiation of leader 103–4
- streamer to spark transition 93–4
  - and thermalisation 74–6
- striking distance 643, 650–2, 703
  - of subsequent return strokes 661–2
  - stepped leader channel and 657–9
  - variation with height 663–4
- supercooled water 866
- suppressors 697–8
- surface arcing 290, 292
- surface impedance expression 527–9
- surface potential theories 22–5
- surface temperatures 874–5
- surge arresters 600, 695
  - gas filled 695
- Swiss Defence Procurement Agency
  - EMP simulator 576–7
- tall objects
  - effective height of 326–30
  - lightning studies conducted at 328–9
- Taylor *et al.* formulation 563
- Taylor-Satterwhite-Harrison model 563
- TCS (travelling current source) model 371, 385–6
- telecommunications 679
  - equipment 612
  - lines 611, 623, 683
  - networks 690
  - systems 142, 633
  - tower 685

- telegrapher's equations 571
- telephone mediated strike 716–20
- TEM (transverse electromagnetic)  
560–1  
spherical 400
- temperature  
dart leader 186  
defunct return stroke channel 189  
electron 44, 50, 93, 155  
gradients 866  
high-pressure arc 92  
and lightning 867  
annual variations 871  
diurnal variations 867–9  
ENSO variations 871–3  
future predictions 874–6  
inter-annual variations 873  
semi-annual variations 869–71  
stepped leader 139
- terrestrial gamma-ray flashes (TGFs)  
787
- thermal effects 612, 624, 639, 695
- thermalisation 74–6, 93
- thermal runaway 797
- thermionic emission 58, 87
- thermodynamic equilibrium 44, 155
- thermoelectric effect/theory 22, 28
- 3-D cloud-scale chemical transport  
models, of STERAO-A storm  
828
- thundercloud charges 749
- thundercloud/lightning electric field  
748
- thunderclouds 132, 691  
charge structure 2–4, 351  
electrical charges involved in 132  
geographical variability 6–11  
local conditions necessary for 1–2  
mature 158  
sprite-producing: mesoscale  
convective systems 4–6
- thunderday studies 873
- thunderstorm days 616, 683
- Thunderstorm Energetic Radiation  
Array (TERA) 790
- thunderstorms 123, 199, 611  
electrification mechanisms 15–35  
extrapolation method 825  
frontal 866  
global distribution of 863–6  
and lightning, energetic radiation  
from 787–811  
microphysics and dynamics of 866–7  
midlatitude 10–11  
rainwater, early examinations of  
826  
summer 2  
tropical 8, 10  
winter 11
- time domain technique 298
- time lags 102, 103, 109  
formative 102
- time of arrival technique  
VHF 133
- time of arrival technique 124, 213
- TL (transmission line) models 369,  
379, 386, 398–9  
*see also* MTL; MTLE; MTL
- Toepler's law 480, 481
- top-down constraints, on LNO<sub>x</sub> 844
- total lightning flash rate 833
- total stroke action integral 279, 284
- total stroke charge 279, 283
- tower initiated lightning discharges  
325–43  
effective height of tall objects  
326–30  
ICC pulses, parameters of 336–7  
negative upward lightning,  
impulsive current components  
in 336  
return strokes, parameters of  
337–9  
upward bipolar lightning,  
characteristics of 341–2  
upward lightning, detection of 343  
upward lightning, initiation of 330–1  
upward lightning, seasonal  
occurrence of 331–2  
upward negative lightning, general  
characterization of 332–5  
upward positive lightning,  
characteristics of 339–41
- towers 158, 160, 679, 681  
grounding wires mounted on 687  
potential rise of top 687  
telecommunication 685
- Townsend coefficient 798

- Townsend's breakdown mechanism  
78–85, 86, 91, 95
- Townsend's ionisation coefficient 61
- trailing wire 830
- transient ground resistance matrix 574
- transient luminous events (TLEs)  
725–7, 744, 753
- transmission line 410–19
- trichel streamers 97
- triggered lightning  
altitude triggering 272–4  
classical triggering 269–72  
current 160, 301  
distribution of 309  
injection point 310, 311  
parameters 158–9  
discharges 267  
lightning-triggering facility 274–6  
programs 268, 831  
techniques for 269–74
- triggered-lightning NO<sub>x</sub> (TLNO<sub>x</sub>)  
measurements 831
- triggered-lightning technique 151
- tripole structure 3–4
- tropical continental regions 865
- Tropical Convection, Cirrus and  
Nitrogen Oxides Experiment  
(TROCCINOX) field  
experiment 829–30
- tropical storms 134
- tropopause 7, 11
- troposphere 819
- Tropospheric Emission Spectrometer  
(TES) 819
- tune\_NO<sub>x</sub> code 832
- 2-D cloud-scale model simulation, of  
STERAO-A storm 828
- UHF (ultra high frequency) 173
- Uman model 435–6  
modification by Thottappillil *et al.*  
436–8
- underground  
cables 308–9  
electric fields  
time domain expressions to  
calculate 532  
structures 634, 684  
telephone network 683
- ungrounded-wire technique 272–3
- unidirectional leader concept 149–50
- uniform transmission line 411
- updrafts 137
- updraughts 19–20, 30
- upper atmospheric electrical  
discharges 725–71  
elementary discharge processes  
753–7  
elves 751–3  
gigantic jets 731–7  
jets 727–31, 734–7  
sprites 737–51  
modeling 757–71
- upward bipolar lightning,  
characteristics of 341–2
- upward connecting leader 151, 237
- continuing current (CC) 244–5  
flash duration 239–40  
interstroke time intervals 244
- multigrounded lightning flashes  
240–4
- return stroke (RS) 237–9
- upward lightning 325, 326  
detection of 343  
flashes 253–7, 327, 637–8, 639  
initiation of 330–1  
negative 326  
positive 326  
seasonal occurrence of 331–2
- upward negative lightning 332–5  
characteristics of impulsive current  
components in 336  
general characterization of  
parameters of ICC pulses 336–7  
parameters of return strokes  
following ICC 337–9
- upward positive leaders (UPLs) 254,  
270
- upward positive lightning,  
characteristics of 339–41
- vapour deposition 7
- varistors 159
- varistors 697, 698
- vector potential of dipole over finitely  
conducting ground 500–1
- vertical configuration distribution line  
306–8

- vertical electric field 508–9
  - in air and underground 501–2
  - calculating 512
  - at point of observation 523
  - at surface and at different depths
    - below ground 532–7
- vertical LNO<sub>x</sub> production profile (LNPP) 836
- vertically stratified ground/multi-section path 540
  - equivalent conductivity 546
  - expressions for attenuation function
    - for dipole at ground level 540–2
  - reciprocity 544–6
  - sea gain effects 542–4
  - simplified expression for
    - electromagnetic fields 542
- VHF (very high frequency) 182
  - imaging techniques 133
  - lightning mapping array (LMA) 729
  - lightning mapping techniques 123
  - observations 149
  - radiation 149, 173–4, 185, 187
  - radio imaging techniques 121, 135
- vicinity of channel
  - exact propagation effects in 505–8
- VLF (very low frequency) 175, 199, 212–13
  - mapping technique 149
- voltages 711
  - breakdown 52, 85, 100, 104
  - developed across resistive devices
    - during lightning strikes 158
  - peak rate of change of 695
  - sags 559
  - scattered 562
  - touch and step 617, 620, 624
- VT (vibrational–translational)
  - relaxation 55, 75, 103, 114
- Wagner
  - channel base current 432
  - corona current per unit length 432
  - return stroke speed 432
  - model 432
  - on return stroke speed 480–1
  - speed of corona current 432
- Wait's simplified expressions 547–8
- waveshapes and M-components 249–51
- wet bulb temperature 870
- Wilson, C.T.R. 725–6, 788
- work function 56, 58, 82
- Workman–Reynolds effect 21–2, 34
- World Meteorological Organisation 123
- World-Wide-Lightning-Location-Network (WWLLN) 809
- X-rays from lightning 788–93
- zener diodes 697
- zero crossing time 167, 197
- zero-dimensional ionization model 756
- Z ratio 839



# The Lightning Flash

## 2nd Edition

This updated and expanded new edition of Cooray's classic text provides the reader with a thorough background in almost every aspect of lightning and its impact on electrical and electronic equipment. The contents range from basic discharge processes in air through transient electromagnetic field generation and interaction with overhead lines and underground cables, to lightning protection and testing techniques. New to this edition are discussions of high-speed video recordings of lightning; rocket-and-wire triggered lightning experiments; tower initiated lightning discharges; upper atmospheric electrical discharges; attachment of lightning flashes to grounded structures; energetic radiation from thunderstorms and lightning; global lightning nitrogen oxides production; and lightning and global temperature change.

*The Lightning Flash, 2nd Edition* is a sound introduction to researchers and advanced students working in the field and of value for anyone designing, installing or commissioning equipment which needs to be secured against lightning strikes.

**Vernon Cooray** is a leading Professor of lightning research at Uppsala University, where his research interests include experimental and theoretical aspects of electromagnetic compatibility, electromagnetic wave propagation, lightning physics, lightning protection and the physics of electrical discharges. He has published more than 270 scientific articles on lightning and electrical discharges, is the vice president of the scientific committee of the International Conference on Lightning Protection and the editor-in-chief of the Journal of Lightning Research. Professor Cooray has edited three books on lightning with the IET: *The Lightning Flash*, *Lightning Protection* and *Lightning Electromagnetics*.

ISBN 978-1-84919-691-8



9 781849 196918 >

The Institution of Engineering and Technology  
[www.theiet.org](http://www.theiet.org)  
978-1-84919-691-8